DEVELOPMENTS IN GEOTECHNICAL ENGINEERING VOL. 53

NONLINEAR ANALYSIS IN SOIL MECHANICS

Theory and Implementation

W.F. CHEN
and
E. MIZUNO

ELSEVIER

DEVELOPMENTS IN GEOTECHNICAL ENGINEERING 53

NONLINEAR ANALYSIS IN SOIL MECHANICS

Theory and Implementation

Further titles in this series
Volumes 2, 3, 5, 6, 7, 9, 10, 13, 16 and 26 are out of print

1 G. SANGLERAT — THE PENETROMETER AND SOIL EXPLORATION
4 R. SILVESTER — COASTAL ENGINEERING, 1 and 2
8 L.N. PERSEN — ROCK DYNAMICS AND GEOPHYSICAL EXPLORATION
Introduction to Stress Waves in Rocks
11 H.K. GUPTA AND B.K. RASTOGI — DAMS AND EARTHQUAKES
12 F.H. CHEN — FOUNDATIONS ON EXPANSIVE SOILS
14 B. VOIGHT (Editor) — ROCKSLIDES AND AVALANCHES, 1 and 2
15 C. LOMNITZ AND E. ROSENBLUETH (Editors) — SEISMIC RISK AND ENGINEERING DECISIONS
17 A.P.S. SELVADURAI — ELASTIC ANALYSIS OF SOIL-FOUNDATION INTERACTION
18 J. FEDA — STRESS IN SUBSOIL AND METHODS OF FINAL SETTLEMENT CALCULATION
19 Á. KÉZDI — STABILIZED EARTH ROADS
20 E.W. BRAND AND R.P. BRENNER (Editors) — SOFT-CLAY ENGINEERING
21 A. MYSLIVE AND Z. KYSELA — THE BEARING CAPACITY OF BUILDING FOUNDATIONS
22 R.N. CHOWDHURY — SLOPE ANALYSIS
23 P. BRUUN — STABILITY OF TIDAL INLETS
Theory and Engineering
24 Z. BAŽANT — METHODS OF FOUNDATION ENGINEERING
25 Á. KÉZDI — SOIL PHYSICS
Selected Topics
27 D. STEPHENSON — ROCKFILL IN HYDRAULIC ENGINEERING
28 P.E. FRIVIK, N. JANBU, R. SAETERSDAL AND L.I. FINBORUD (Editors) — GROUND FREEZING 1980
29 P. PETER — CANAL AND RIVER LEVÉES
30 J. FEDA — MECHANICS OF PARTICULATE MATERIALS
The Principles
31 Q. ZÁRUBA AND V. MENCL — LANDSLIDES AND THEIR CONTROL
Second completely revised edition
32 I.W. FARMER (Editor) — STRATA MECHANICS
33. L. HOBST AND J. ZAJÍC — ANCHORING IN ROCK AND SOIL
Second completely revised edition
34 G. SANGLERAT, G. OLIVARI AND B. CAMBOU — PRACTICAL PROBLEMS IN SOIL MECHANICS AND FOUNDATION ENGINEERING, 1 and 2
35. L. RÉTHÁTI — GROUNDWATER IN CIVIL ENGINEERING
36. S.S. VYALOV — RHEOLOGICAL FUNDAMENTALS OF SOIL MECHANICS
37 P. BRUUN (Editor) — DESIGN AND CONSTRUCTION OF MOUNDS FOR BREAKWATERS AND COASTAL PROTECTION
38 W.F. CHEN AND G.Y. BALADI — SOIL PLASTICITY
Theory and Implementation
39 E.T. HANRAHAN — THE GEOTECTONICS OF REAL MATERIALS: THE ϵ_{ij}, ϵ_k METHOD
40 J. ALDORF AND K. EXNER — MINE OPENINGS
Stability and Support
41 J.E. GILLOTT — CLAY IN ENGINEERING GEOLOGY
42. A.S. CAKMAK (Editor) — SOIL DYNAMICS AND LIQUEFACTION
42. A.S. CAKMAK (Editor) — SOIL-STRUCTURE INTERACTION
44. A.S. CAKMAK (Editor) — GROUND MOTION AND ENGINEERING SEISMOLOGY
45. A.S. CAKMAK (Editor) — STRUCTURES, UNDERGROUND STRUCTURES, DAMS, AND STOCHASTIC METHODS
46. L. RÉTHÁTI — PROBABILISTIC SOLUTIONS IN GEOTECTONICS
47 B.M. DAS — THEORETICAL FOUNDATION ENGINEERING
48. W. DERSKI, R. IZBICKI, I. KISIEL AND Z. MROZ — ROCK AND SOIL MECHANICS
49. T. ARIMAN, M. HAMADA, A.C. SINGHAL, M.A. HAROUN AND A.S. CAKMAK (Editors) — RECENT ADVANCES IN LIFELINE EARTHQUAKE ENGINEERING
50 B.M. DAS — EARTH ANCHORS
51 K. THIEL — ROCK MECHANICS IN HYDROENGINEERING
52 W.F. CHEN AND X.L. LIU — LIMIT ANALYSIS IN SOIL MECHANICS
53 W.F. CHEN AND E. MIZUNO — NONLINEAR ANALYSIS IN SOIL MECHANICS
54 F.H. CHEN — FOUNDATIONS ON EXPANSIVE SOILS
55. J. VERFEL — ROCK GROUTING AND DIAPHRAGM WALL CONSTRUCTION
56. B.N. WHITTAKER AND D.J. REDDISH — SUBSIDENCE
Occurrence, Prediction and Control
57 E. NONVEILLER — GROUTING, THEORY AND PRACTICE
58. V. KOLÁŘ AND I. NĚMEC — MODELLING OF SOIL-STRUCTURE INTERACTION
59A. R.S. SINHA — UNDERGROUND STRUCTURES
Design and Instrumentation

DEVELOPMENTS IN GEOTECHNICAL ENGINEERING 53

NONLINEAR ANALYSIS IN SOIL MECHANICS

Theory and Implementation

W.F. CHEN

School of Civil Engineering, Purdue University, West Lafayette, IN 47907, U.S.A.

and

E. MIZUNO

Department of Civil Engineering, Nagoya University, Nagoya 464, Japan

ELSEVIER
Amsterdam — Oxford — New York — Tokyo 1990

ELSEVIER SCIENCE PUBLISHERS B.V.
Sara Burgerhartstraat 25
P.O. Box 211, 1000 AE Amsterdam, The Netherlands

Distributors for the United States and Canada:

ELSEVIER SCIENCE PUBLISHING COMPANY INC.
655, Avenue of the Americas
New York, NY 10010, U.S.A.

ISBN 0-444-43043-1

This book is printed on acid-free paper

Printed in The Netherlands

PREFACE

A complete analysis of stress and strain in a structure, as the load is increased to failure, is known to be very complicated. This is particularly true in soil mechanics and soil structure interaction problems where, unlike traditional structural engineering, the analysis almost always involves two- and three-dimensional continua. With the present state of development of finite-element computer softwares and high-speed digital computer hardwares, we can confidently say that an almost unlimited range of solutions can now be obtained. These are not limited to linear elastic small-deformation solid mechanics but can be extended to include problems of various kinds involving material and geometric nonlinearities. This book is concerned with the development of numerical tools for solutions of nonlinear analysis problems in soil mechanics.

The mathematical theories of elasticity and plasticity are employed for the constitutive modeling of the soil behavior. The theoretical foundation and basic concepts of material modeling are described in details in PART II including critical discussions of the Theory of Elasticity and Modeling in Chapter 3, the Theory of Perfect Plasticity and Modeling in Chapter 4, and the Theory of Hardening Plasticity and Modeling in Chapter 5.

The material nonlinearity is represented in PART III by an elastic-plastic cap-type model which can treat either strain-hardening or strain-softening materials. The plasticity formulation and calibration (Chapter 6) together with the numerical algorithm developed for its implementation and predictions (Chapter 7) provide a general format for incorporating various plasticity models described previously in PART II into the cap-type of plasticity relationship of PART III suitable for direct finite-element applications. In particular, the Drucker-Prager model with an elliptic hardening cap illustrated in details in Chapter 6 and coded in Chapter 7 as a SUBROUTINE CAPMDL represents an adequate constitutive model for the short-time behavior of many geological materials over a wide range of loadings.

The geometric nonlinearity for large-deformation analyses is described in details in PART IV. The theoretical foundation of large-deformation formulation and its simplification are described in details in Chapter 8. The nonlinear finite-element equations for large deformation and material inelasticity are solved by a combined incremental and iterative solution technique (Chapter 9). Two types of iterations are carried out, the first being iteration on the material parameters and the second equilibrium iterations. The method of analysis is based on a displacement formulation of the finite-element method. Large displacements are accounted for using a total Lagrangian formulation and an updated Lagrangian formulation.

Applications of the nonlinear theory are presented for a wide range of numerical examples throughout the book. In particular, several case studies using the computer program developed are presented in PART V (Chapter 10). First the material nonlinearities involving associated as well as non-associated flow rules with different procedures for the determination of the material parameters from the experimental data are examined for strip footings on stratum of clay. The algorithms for the behavior of the clay are then tested and checked for the simplification of small-strain small-rotation formulation. Finally, small-strain large-rotation analyses of elasto-plastic behavior are carried out for vertical slopes under seismic loading. This analytical simplification is reasonable for most large-displacement problems in geotechnical engineering applications and results in symmetric governing equations in the large-displacement finite-element analysis. The complete progressive failure behavior of slopes at all stress levels leading up to collapse is obtained. The collapse loads of the slopes and their associated failure mechanisms by the finite-element method are compared with those of the limit analysis method.

The book can be used for nonlinear analysis courses in geotechnical engineering of various lengths, involving mathematical modeling of materials (PART II and PART III), large-deformation finite-element description of structures (PART IV), and computer implementation and numerical predictions (PART V). In writing this book, we have endeavored to make the prerequisites as few as possible. Some background on the theory of linear elasticity and the finite-element method is assumed. The book is aimed to the graduate student in civil engineering who has sufficient background in soil mechanics and is learning about inelastic behavior of materials and large-displacement description of structures for the first time. The inclusion of computer subroutines for soil cap models is intended to encourage the reader to try out these models in a direct manner.

May, 1988

W.F. Chen
E. Mizuno

CONTENTS

Part I

FUNDAMENTALS

Chapter 1

INTRODUCTION

1.1 INTRODUCTION

For a long time, soil mechanics has been based on Hooke's law of linear elasticity for stress and deformation analysis for a soil mass under a footing, or behind a retaining wall, when no failure of the soil is involved. This is known as the *elasticity problem* in soil mechanics. On the other hand, the theory of *perfect plasticity* is used to deal with the conditions of ultimate failure of a soil mass. Problems of earth pressure, retaining walls, bearing capacity of foundations, and stability of slopes are all considered in the realm of perfect plasticity. These are called *stability problems*. Long-term settlement problems and consolidation problems, however, are treated in soil mechanics as essentially *viscoelastic problems*.

Partly for simplicity in practice and partly because of the historical development of mechanics of solids, the elasticity problems and the stability problems in soil mechanics are treated separately and in unrelated ways. The essential connection between the elasticity problems and the stability problems is known as the *progressive failure problems*. The progressive failure problems deal with the elastic-plastic transition from the initial linear elastic state to the ultimate state of the soil by plastic flow. The essential set of equations for the solutions of progressive failure problems is the *constitutive equations* of soils, which give a unique relationship of stress and strain for different geotechnical materials. These relationships and applications to soils and rocks are discussed in the following Chapters.

1.2 CHARACTERISTICS OF SOIL BEHAVIOR

Some typical stress-strain curves for soils in the triaxial tests are shown in Fig. 1.1. As can be seen from Fig. 1.1a, the relation of the deviatoric stress σ_3-σ_1 v.s. axial strain ϵ_1 for a *normally consolidated* clay in a *drained test* is characterized by a nonlinear response curve which rises at a slower rate after reaching a certain stress level. Here, the further straining is always associated with an increase in stress. This phenomenon is known as *strain-hardening*. The stress-strain curve for *overconsolidated* clay in an *undrained test* exhibits the same behavior as that of normally consolidated clay in a drained test. The overconsolidated clay in a drained test and normally consolidated clay in an undrained test behave differently from those mentioned above. The stress-strain curves both have a clearly defined peak occurring at a low strain level. An element of these clays, strained beyond the strain

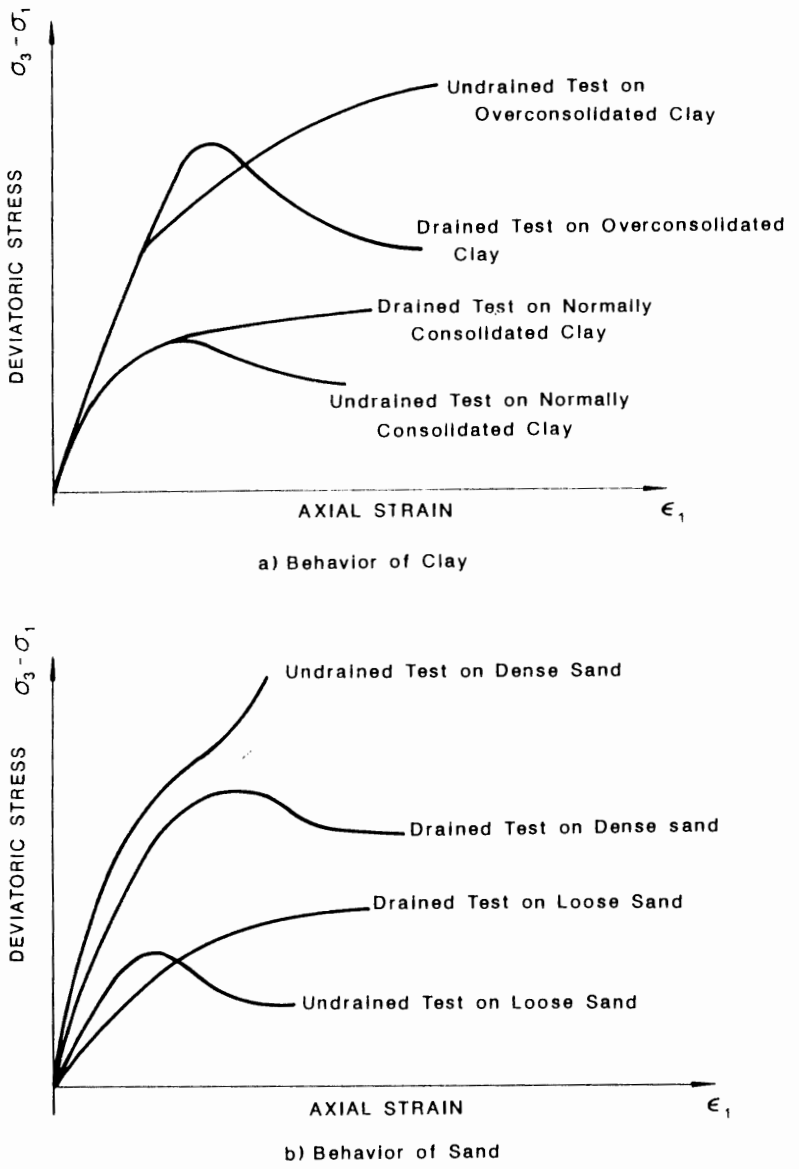

Fig. 1.1. Typical soil stress-strain curves.

corresponding to the peak stress point, becomes weaker than it was at this peak point. This phenomenon is known as *strain-softening*.

Similar conclusions can be made from Fig. 1.1b for the behavior of sand. Dense sand in an undrained test and loose sand in a drained test show the strain-hardening. Dense sand in a drained test and loose sand in an undrained test show a peak

stress followed by strain-softening to a residual stress. The behavior of dense sand in a drained test is similar to that of overconsolidated clay in a drained test. The similar behavior also occurs in the other corresponding cases for clay and sand.

1.3 IDEALIZATIONS AND MATERIAL MODELING

The typical stress-strain behavior of soils presented in the previous Section is not linearly elastic for the entire range of loading of practical interest. In fact, actual behavior of soils is much complicated and they show a great variety of behavior when subjected to different conditions. Drastic idealizations are therefore essential in order to develop simple mathematical models for practical applications. No mathemetical model can completely describe the complex behavior of real soils under all conditions. Each soil model aims at a certain class of phenomena, captures their essential features, and disregards what is considered to be of minor importance in that class of applications. Thus, this constitutive model meets its limits of applicability where a disregarded influence becomes important. As mentioned previously, Hooke's law has been used successfully in soil mechanics to describe the general behavior of soil media under short-term working load condition, but it fails to predict the behavior and strength of a soil–structure interaction problem near ultimate strength condition, because plastic deformation at this load level attains a dominating influence, while elastic deformation becomes of minor importance.

Under a short-term loading, soil behavior may be idealized as time-independent where the effects of time can be neglected. This time-independent idealization of soils can be further idealized as *elastic* behavior and *plastic* behavior. As the first step in constitutive modeling of soils, it is therefore logical to utilize and refine the classical theories of elasticity and plasticity as developed for such an idealized material. However, there are in many cases considerable differences between the properties of soils and those of the idealized bodies. These differences may have a significant influence on the solution of some boundary value problems in soil mechanics. In such cases, the classical theories must be modifed and extended so that the special properties of soils in certain practical applications are taken into consideration.

A material for which there exists a one-to-one coordination between stress and strain is known as *elastic material*. Thus, a body that consists of this idealized material returns to its original shape whenever all stresses are reduced to zero. The linear theory of elasticity used most commonly is the *Hooke* type or *Cauchy* type of constitutive models for soils, in spite of its obvious shortcomings. These linear elastic models can be significantly improved by assuming bilinear or higher polynomial type of nonlinear fit for the stress-strain relationship of soil in the form of *secant formulations*. This is known as the *Hooke type* or *Cauchy type of elastic formulation*. These types of elastic models must be combined with criteria defining "failure" of the soil.

In a more restricted sense, an elastic material must satisfy the energy equation of thermodynamics. The elastic material characterized by this additional requirement is known as *hyperelastic material*. On the other hand, the minimal requirement for a material to qualify as elastic in any sense is that there exists a one-to-one coordination between stress increment and strain increment. Thus, a body that consists of this material returns to its original state of deformation whenever all stress increments are reduced to zero. This reversibility in the infinitesimal sense justifies the use of the term *hypoelastic* for elastic materials satisfying only this minimal requirement. The *incremental* constitutive formulations based on hypoelastic models have been increasingly used in recent years by geotechnical engineers for soils in which the state of stress is generally a function of the current state of stresses and strains as well as of the stress path followed to reach that state (Chen and Saleeb, 1982).

The elastic modeling in the form of secant or incremental formulations can be quite accurate for soils sustaining proportional loading. However, this *reversibility* associated with these formulations is not the case for a *plastic material*. Thus, these formulations fail to identify plastic deformations when unloading occurs. This can, to some extent, be rectified by introducing loading criteria as in the *deformation theory of plasticity*. Although the deformation theory and the existence of loading function are incompatible even in the most limited sense, it is still a very attractive alternative for solution of large classes of soil and soil structure interaction problems, because of its simplicity.

The *flow theory of plasticity* represents a necessary and correct extension of elastic stress-strain relations into the plastic range at which permanent plastic strain is possible in addition to elastic strain. This plastic strain remains when the stresses are removed. Thus, the strain in a plastic material may be considered as the sum of the reversible elastic strain and the permanent irreversible plastic strain. Since an elastic stress-strain law as mentioned above is usually assumed to provide the relation between the incremental changes of stress and elastic strain, the stress-strain law for a plastic material reduces, essentially, to a relation involving the current state of stresses and strains and the incremental changes of stress and plastic strain. This relation is generally assumed to be homogeneous and linear in the incremental changes of the components of stress and plastic strain. This assumption precludes viscosity effects and thus constitutes the time-independent idealization.

The first step towards such a mathematical model is to establish the yield limit of an elastic material. This is known as the *yield function* which is a certain function of the stress components. A plastic material is called *perfectly plastic* or *work-hardening* or *softening* according to whether the yield function as represented by a certain hypersurface in six-dimensional stress space is fixed or it admits changes (expansion or contraction) as plastic strain develops. For moderate strains, mild steel behaves approximately like a perfectly plastic material. It is therefore not surprising that in early years (1950–1965) this perfect plasticity model was used almost exclusively and extensively in the analysis and design of steel structures because of its simplicity. The general theorems of limit analysis, developed on the basis of perfect

plasticity, furnish simple, direct and realistic estimates of the load-carrying capacity of these structures. However, perfect plasticity is not nearly as appropriate for soils as for metals.

The use of strain- or work-hardening plasticity theories to describe the stress-strain behavior of soils under cyclic loading condition has been highly developed in recent years in soil mechanics. As a result of these advances, the theory of soil plasticity is now in a position to lead that of metal plasticity. In the next Section, soil plasticity is reviewed historically. Some of these theoretical developments will be described in details in Chapters 4 through 6 for soils idealized as elastic-perfectly plastic or elastic-plastic materials with work-hardening.

1.4 HISTORICAL REVIEW OF PLASTICITY IN SOIL MECHANICS

In the 1950's major advances were made in the *theory of metal plasticity* by the development of (1) the fundamental theorems of limit analysis, Drucker et al. (1952), (2) Drucker's postulate or definition of stability of material, and (3) the concept of normality condition or associated flow rule. The theory of *limit analysis of perfectly plasticity* leads to practical methods that are needed to estimate the load-carrying capacity of structures in a more direct manner. The concept of a *stable material* provides a unified treatment and broad point of view of the stress-strain relations of plastic solids. The idea of *normality condition* provides the necessary connection between the yield criterion or loading function to the plastic stress-strain relations. All these have led to a rigorous basis for the theory of classical plasticity, and laid down the fundations for subsequent notable developments.

The initial applications of the classical theory of plasticity were almost exclusively concerned with perfectly plastic metallic solids such as mild steel for which it behaves approximately like a perfectly plastic material (Prager and Hodge, 1950). For these materials, the angle of internal friction ϕ is zero, no plastic volume change occurs and the only material property is the shear strength k or cohesion c in the terminology of soil mechanics. Numerical calculations were restricted to the *method of characteristics* based on the theory of the plane *slip-line field* analysis to derive the stress and velocity distribution in the plastic region (Hill, 1950). Since the plane slip-line field analysis is rarely applicable to structures, exact and approximate calculations of the plastic collapse load were made exclusively by the methods of limit analysis (Drucker, 1960).

The development of the modern *theory of soil plasticity*, as a new field, was strongly influenced by the well-established theory of metal plasticity. Soil mechanics specialists have been preoccupied with extending these concepts to answer the complex problems of soil behavior. Tresca's yield condition, used widely in metal plasticity, can be regarded as a special case of the condition of Coulomb's criterion on which the important concept of the *limiting equilibrium* of a soil media had been firmly established in soil mechanics (Terzaghi, 1943).

It is a relatively straightforward matter to extend the method of characteristics to cover Coulomb material where c and ϕ can either remain constant (Sokolovskii, 1965) or vary throughout the stress field in some specified manner (Booker and Davis, 1972). In the theory of limit equilibrium, the introduction of stress-strain relations was obviated by the restriction to the consideration of equations of equilibrium and a yield condition. This produces what appears to be and sometimes is static determinancy for the solutions of slip-line field equations. However, in many soil–structure interaction problems, the boundary conditions involve rates of displacement and the slip-line equations are generally statically indeterminate. The key to obtain a valid solution for such cases requires the basic knowledge of the stress-strain relations. Otherwise, a so-called solution is merely a guess.

The *general theory of limit analysis*, developed in early 1950's, considers the stress-strain relation of a soil in an idealized manner. This idealization, termed normality or the associated flow rule, establishes the limit theorems on which limit analysis is based. Although the applications of limit analysis to soil mechanics are relatively recent, there have been an enormous number of practical solutions available (Chen, 1975). Many of the solutions obtained by the method are remarkably good when comparing with the existing results for which satisfactory solutions already exist. As a result of this development, the meaning of the limit equilibrium solutions becomes clear in the light of the *upper-* and *lower-bound theorems* of limit analysis.

The first major advance in the extension of metal plasticity to soil plasticity was made in the paper "Soil Mechanics and Plastic Analysis or Limit Design" by Drucker and Prager (1952). In this paper, the authors extended the Coulomb criterion to three-dimensional soil mechanics problems. The Coulomb criterion was interpreted by Drucker (1953) as a modified Tresca as well as an extended von Mises yield criterion. The yield criterion obtained by Drucker and Prager for the latter case is now known as the *Drucker-Prager model* or the *extended von Mises model*.

One of the main stumbling blocks in the further development of the stress-strain relations of soil based on the Drucker-Prager type or Coulomb type of yield surfaces to define the limit of elasticity and beginning of a continuing irreversible plastic deformation was the excessive prediction of dilation, which was the result of the use of the *associated flow rule*. It became necessary, therefore to extend classical plasticity ideas to a "*non-associated*" form in which the plastic potential functions and yield surfaces are defined separately (Davis, 1968). However, this modification eliminated the validity of the use of limit theorems for bounding collapse loads and created doubts about the uniqueness of solutions. Attempts have been made to revise the bounding theorems and to resolve the uniqueness problem, but to date not much success has been achieved through this route (Palmer, 1973).

In 1957, an important advance was made in the paper "Soil Mechanics and Work-Hardening Theories of Plasticity" by Drucker et al. In this paper the authors introduced the concept of work-hardening plasticity into soil mechanics. There are two important innovations in the paper. The first is the introduction of the idea of a

work-hardening cap to perfectly plastic yield surface such as the Coulomb type or Drucker-Prager type of yield criterion. The second innovation is the use of current *soil density* (or *voids ratio*, or *plastic compaction*) as the *state variable* or the strain-hardening parameter to determine the successive loading cap surfaces.

These ideas have led in turn to the generation of many soil models, most notably the development of the *critical state soil mechanics* at Cambridge University, U.K. These new soil models have grown increasingly complex as additional experimental data have been gathered, interpreted, and matched. This extension marks the beginning of the modern development of a consistent theory of soil plasticity (Chen, 1975, 1982; Chen and Baladi, 1985).

1.5 NONLINEAR STRESS ANALYSES IN GEOTECHNICAL ENGINEERING

Various methods exist for incorporating the material constitutive models developed for soils and rocks into finite-element computer programs for solving practical geotechnical problems that require nonlinear stress analyses involving both material and geometric nonlinearities. Iterative calculations based on linear incremental formulation can now be treated with comparative ease within the framework of finite-element software. Consequently, practical problems which previously could not have been solved analytically, can now be analyzed, and reasonable data for use in practical design can be generated using finite-element calculations.

Since geotechnical engineering problems are so complex, however, moderate idealizations must be performed with great care to obtain reliable solutions by the finite-element analysis. In recent years, the development of more sophisticated material models based on the concept of continuum mechanics has rapidly advanced with the aid of finite-element computational work. Consequently, the range of application for the finite-element method has been extended not only to nonlinear stress analyses of foundation, slope, embankment and excavation problems, but also those of discontinuity problems and interaction problems between structure and soil under dynamic as well as static loading conditions. Although the finite-element method has had a profound effect on the rapid development of the analysis based on the nonlinear stress-strain behavior of geotechnical materials, there are still some analytical and theoretical difficulties associated with the present nonlinear stress analysis in geotechnical engineering problems. These are:

1. Selection or evaluation of material models
2. Selection or evaluation of material constants
3. Idealization of ground conditions
4. Assessment of analytical results, and
5. Evaluation of analytical procedures in the finite-element method.

In item (1), although several models such as the nonlinear elastic model, the classical elastic-plastic model and the advanced strain-hardening models have been widely used in the nonlinear stress analysis of geotechnical materials, the selection of an appropriate model depends on the material characteristics assumed in the

analysis, the accuracy required for the analysis, and the type of loading condition, e.g. undrained or drained condition. However, there has been little critical evaluation of material models as they are generally applied to geotechnical problems. Items (2) and (3) should be considered with particular care in the case of dynamic loadings. As for item (4), results of a finite-element method may be checked against those obtained by conventional methods, such as limit equilibrium and limit analysis methods. In item (5), selection of the analytical procedures must be based on the loading condition, required accuracy of analysis, material model, capacity of the computer to be used, and computational time.

When an elaborate idealization of the problem is made, the finite-element nonlinear stress analysis becomes meaningful and powerful. Considering all the elaborate calculations involved, however, it is easy to forget that the numerical results are only response to idealized conditions and may not be taken as the real behavior. Such obtained results must be assessed by experimental data from laboratory and test data *in situ*. Then, the applicability of the material models used and their numerical implementation procedures adopted in a nonlinear stress analysis can be re-evaluated.

1.6 NEED, OBJECTIVES AND SCOPE

To aid the rapid development in recent years in the application of advanced computational procedures to nonlinear stress analyses, more research study related to material modeling and material strength characterization is still needed in order to provide a better prediction of material behavior such as strain-hardening, strain-softening, yielding or failure and creep, etc. However, since the mechanical behavior of soils is influenced by many factors such as density, residual stresses, stress history, existence of discontinuity, void ratio, temperature, time, and pore water pressure, etc., the difficult problem is to represent these factors adequately in a simple mathematical model and to implement it realistically into a computer-based numerical analysis, within the framework of *continuum theory*. Consequently, the modeling of mechanical behaviors of geomaterials for use in analytical studies still remains one of the most difficult challenges in geotechnical engineering.

Although the limit equilibrium method has been widely used in geotechnical practice, it neglects the important fact that the stress-strain relations are an essential consideration for a complete theory in any branch of continuum mechanics for deformable soils. On the other hand, the modern limit analysis methods take into consideration the stress-strain relations of soils in an idealized manner. Although its application to geotechnical problems has been in the area of soil statics and more recently in the area of soil dynamics, the progressive failure behavior prior to collapse state has not yet been fully analyzed. For a valid assessment of geotechnical engineering problems, a complete progressive failure analysis under dynamic as well as static loading conditions is required. This in turn requires the consideration of a suitable material model, that adequately describes the basic characteristics of soil behavior under various stress conditions.

Recent research in soil mechanics is directed toward a better understanding of the mechanical behavior of soil and the development of more advanced material models, within the framework of the principles of continuum mechanics. Although various types of material models for soils have been developed in recent years for use in geotechnical and earthquake engineering problems, the relative advantages and disadvantages, the limitations and ranges of applications of these models have not been assessed critically, particularly as applied to soil progressive failure problems. Therefore, a critical assessment of existing material models is needed from the viewpoint of experimental and theoretical considerations as well as from the viewpoint of application of these models to solve specific benchmark problems under seismic and static loading conditions.

Thus, the primary objective of this book is to review and assess the plasticity-based material models such as the perfectly plastic, strain/work-hardening material models with respect to their advantages and limitations as they applied to numerical analyses of geotechnical engineering problems. More specifically, the objectives of the book are: (1) to describe the theoretical development of various existing plasticity models in general and the cap models in particular; (2) to present the numerical techniques for their finite-element implementations; and (3) to show the applicability of these models by conducting a comparative progressive failure analysis of selected soil problems. In this book, the cap model is selected as the basis for evaluating other existing constitutive models because this model appears to be the most satisfactory from the experimental, theoretical, and numerical standpoint (Chen and Baladi, 1985).

The book is divided into five parts. The contents of each part are briefly summarized as follows:

In PART I entitled FUNDAMENTALS, the general background necessary for a nonlinear stress analysis of geotechnical engineering problems, such as concepts of stresses and strains in three dimensions, is described in Chapter 2.

In PART II entitled MATERIAL MODELING—BASIC CONCEPTS, elasticity-based material models such as Cauchy elastic, hyperelastic, hypoelastic models are reviewed and their stress-strain relations are derived from the secant and incremental formulations in Chapter 3. The advanced strain-hardening plasticity models as well as the classical perfect plasticity models are reviewed and discussed with respect to their advantages and limitations for applications to geotechnical engineering problems. Incremental constitutive matrices of several types of plasticity models, including *isotropic hardening*, *kinematic hardening*, and *mixed* type, are then presented in a form that is suitable for direct use in a numerical analysis, under both *associated* and *non-associated flow rule* assumptions (Chapters 4 and 5).

In PART III entitled MATERIAL NONLINEARITY—CAP MODELS, the cap types of plasticity models are reviewed and the models are calibrated under several simple stress or strain tests such as uniaxial strain, triaxial shear tests in drained and undrained conditions. The cap models are first applied to three embankments on Boston blue clay and the applicability is then assessed critically by comparing the model predictions with measured values in situ (Chapter 6). For elastic-plastic

finite-element analyses, integration techniques such as the mid-point integration rule and iterative method are employed to demonstrate the finite-element implementation of existing plasticity models. Here, the models adopted for an illustrative computer implementation are: (1) the Coulomb model (elastic-perfectly plastic model); (2) the Drucker-Prager model (elastic-perfectly plastic model); and (3) the strain-hardening cap models (plane and elliptic cap models). The computer codes corresponding to the Coulomb model, the Drucker-Prager model and cap model are developed in detail in Chapter 7.

In PART IV entitled GEOMETRIC NONLINEARITY—LARGE-DEFORMATION ANALYSES, incremental equilibrium equations considering the effects of large deformation and geometric change of soil are developed by utilizing the total and updated Lagrangian formulations. Implementations of this development in a finite-element analysis are explained in some details in Chapters 8 and 9.

In PART V entitled CASE STUDY, as illustrative example problems, a footing problem and a slope stability problem under static or seismic loading conditions are solved, compared and evaluated. Finally, the applicability and limitations of the plasticity-based models (cap models in particular) as applied to geotechnical engineering problems are discussed in Chapter 10, based on the finite-element results.

REFERENCES

Booker, J.R. and Davis, E.H., 1972. A note on a plasticity solution to the stability of slopes in inhomogeneous clay. Geotechnique, 22: 509–513.

Chen, W.F., 1975. Limit Analysis and Soil Plasticity. Elsevier, Amsterdam, 638 pp.

Chen, W.F., 1982. Plasticity in Reinforced Concrete. McGraw-Hill, New York, NY, 474 pp.

Chen, W.F. and Baladi, G.Y., 1985. Soil Plasticity: Theory and Implementation. Elsevier, Amsterdam, 231 pp.

Chen, W.F. and Saleeb, A.F., 1982. Constitutive Equations for Engineering Materials, Vol. 1-Elasticity and Modeling. Wiley-Interscience, New York, NY, 580 pp.

Davis, E.H., 1968. Theories of plasticity and the failure of soil masses. In: I.K. Lee (Editor), Soil Mechanics: Selected Topics. Butterworths, London, pp. 341–380.

Drucker, D.C., 1953. Limit analysis of two- and three-dimensional soil mechanics problems. J. Mech. Phys. Solids, 1: 217–226.

Drucker, D.C., 1960. Plasticity. In: Structural Mechanics. Pergamon Press, London, pp. 407–455.

Drucker, D.C. and Prager, W., 1952. Soil mechanics and plastic analysis or limit design. Q. Appl. Math., 10 (2): 157–165.

Drucker, D.C., Greenberg, H.J. and Prager, W., 1952. Extended limit design theorems for continuous media. Q. Appl. Math., 9: 381–389.

Drucker, D.C., Gibson, R.E. and Henkel, D.J., 1957. Soil mechanics and work hardening theories of plasticity. Trans., ASCE, 122: 338–346.

Hill, R., 1950. The Mathematical Theory of Plasticity. Clarendon Press, Oxford, 355 pp.

Palmer, A.C. (Editor), 1973. Proceedings of the Symposium on the Role of Plasticity in Soil Mechanics. Cambridge University, Cambridge, England, 314 pp.

Prager, W. and Hodge, P.G., 1950. Theory of Perfectly Plastic Solids. John Wiley, New York, NY, 264 pp.

Sokolovskii, V.V., 1965. Statics of Granular Media. Pergamon Press, New York, NY, 232 pp.

Terzaghi, K., 1943. Theoretical Soil Mechanics. John Wiley, New York, NY, 510 pp.

Chapter 2

BASIC CONCEPT OF CONTINUUM MECHANICS

2.1 INTRODUCTION

Since soils are multi-phase materials comprised of mineral grains, air voids and water, the mathematical characterization of their behavior should ideally be based on a consideration of the behavior of individual constituent elements and their interaction. However, such an approach can be rather complex and would not be particularly fruitful in *geotechnical engineering* applications. For the problems treated in geotechnical engineering, the scale of practical interest is in the range of tens to hundreds of feet. Thus, these "microscopic" effects may be averaged and the soil can be idealized as a *continuum*. *Soil mechanics*, which is treated within the framework of such idealization, is therefore a branch of *mechanics of solids*. In the following Sections, the general background necessary for this book will be described in some details.

2.2 NOTATIONS

For purposes of generalization, symbolic forms of the equations, using index notation and summation convention, will be introduced. The notations used in the text are those conventionally found in continuum mechanics.

For computer programming purposes, *matrix notations* are most convenient. Thus, for specific material models, the numerical procedures for a solution have been illustrated in matrix notations in a Cartesian coordinate system.

In this book, we shall restrict ourselves to a *right-handed Cartesian coordinate system* with a set of three mutually orthogonal x-, y-, and z-axes. For future convenience, the axes are more conveniently named as x_1, x_2, and x_3 for a general discussion, rather than the more familiar axes x, y, and z for a specific engineering application.

In the continuum mechanics, it is convenient to use tensile stress as a positive quantity and compressive stress as a negative quantity. Problems of engineering analysis and design in soil structures, however, are generally concerned with compressive stresses in most cases. For convenience, therefore, the continuum mechanics sign convention will be followed in this book for general discussion but the soil mechanics sign convention will be utilized in later Chapters when specific numerical solutions of typical soil–structure problems are presented. Detailed

discussion of *index notation* and *summation convention* can be found in the book by Chen and Saleeb (1982).

2.3 STRESSES IN THREE DIMENSIONS

In the theory of soil mechanics, the soils are regarded as continua as a rule. This permits the use of the notations of stress and strain. The relationship between stress and strain in an idealized material forms the basis of the mathematical theories of *elasticity*, *plasticity* and *viscosity* which can in turn be applied to actual soil materials to estimate stress or strain in a specified force field.

An understanding of stress and strain and principles of stress and strain analysis is therefore essential to the engineer who models the behavior of soil, and designs structures in soil. These principles are summarized briefly in what follows.

2.3.1 Definitions and notations

The analysis of stress is essentially a branch of statics which is concerned with the detailed description of the way in which the stress at a point of a body varies. In two dimensions, this involves only elementary trigonometry, and the use of *Mohr's circle* is found to be most convenient. In three dimensions, however, *index notation* is preferred for the calculation of stresses across any plane at the point. Herein, only the three-dimensional case will be worked out.

The stress at a point P in solid body may be obtained by considering a small plane area dA at a random orientation with a unit normal vector n_i originating at P (Fig. 2.1). Then, if dF_i is the resultant of all the forces exerted on dA, the limit of

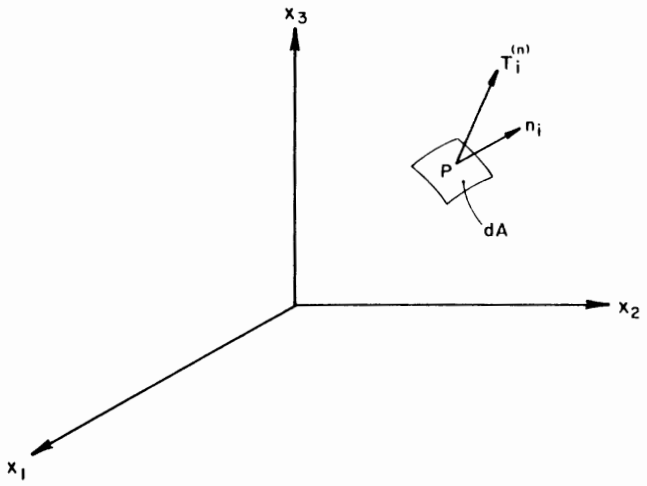

Fig. 2.1. Stress vector T_i at point P on an area element with a unit normal vector n_i.

the ratio dF_i/dA as dA tends to zero is called the *stress vector* $T_i^{(n)}$ at the point across the plane whose normal vector is n_i, that is:

$$T_i^{(n)} = \lim_{dA \to 0} \frac{dF_i}{dA} \tag{2.1}$$

The dimensions of $T_i^{(n)}$ are force per unit area.

The *state of stress* at the point P is completely specified or defined if we know all the values of $T_i^{(n)}$ corresponding to various n_i. Since there are an infinite number of n_i through the point P, we shall have an infinite number of values of $T_i^{(n)}$ which, in general, differ from each other. Thus, the infinite number of values of $T_i^{(n)}$ are needed in order to characterize the state of stress at the point. It turns out, however, that these stress vectors are related to each other through Newton's law of motion or equilibrium. In fact, the value of $T_i^{(n)}$ for any n_i can be calculated once the stress vectors $T_i^{(1)}$, $T_i^{(2)}$, and $T_i^{(3)}$ are known for the three mutually perpendicular area elements whose normals are in the direction of the coordinate axes x, y, z or equivalently x_1, x_2, and x_3, respectively.

Let us consider the equilibrium condition of an element OABC with the stress vectors $T_i^{(-1)}$, $T_i^{(-2)}$, $T_i^{(-3)}$, and $T_i^{(n)}$ acting on its faces OBC, OAC, OAB, and ABC, respectively, as shown in Fig. 2.2. F_i acts as the body forces of the element OABC per unit volume, and h is the length of the perpendicular distance from O to plane ABC. Let A be the area of plane ABC. Then the area of each face perpendicular to the x_i-axis, denoted by A_i, is given by:

$$A_i = An_i \tag{2.2}$$

The volume of the element OABC is given by:

$$V = \tfrac{1}{3}Ah \tag{2.3}$$

From equilibrium condition of the element OABC and using Eqs. (2.2) and (2.3), we have:

$$T_i^{(n)}(A) + T_i^{(-1)}(An_1) + T_i^{(-2)}(An_2) + T_i^{(-3)}(An_3) + F_i(\tfrac{1}{3}Ah) = 0 \tag{2.4}$$

Dividing Eq. (2.4) by A and letting $h \to 0$, we get:

$$T_i^{(n)} = -T_i^{(-1)}n_1 - T_i^{(-2)}n_2 - T_i^{(-3)}n_3 \tag{2.5}$$

Since $T_i^{(-1)} = -T_i^{(1)}$, $T_i^{(-2)} = -T_i^{(2)}$, and $T_i^{(-3)} = -T_i^{(3)}$, Eq. (2.5) has therefore the simple form:

$$T_i^{(n)} = T_i^{(1)}n_1 + T_i^{(2)}n_2 + T_i^{(3)}n_3 \tag{2.6}$$

This is known as *Cauchy's formula*. The stress vector $T_i^{(n)}$ at the point P with a unit

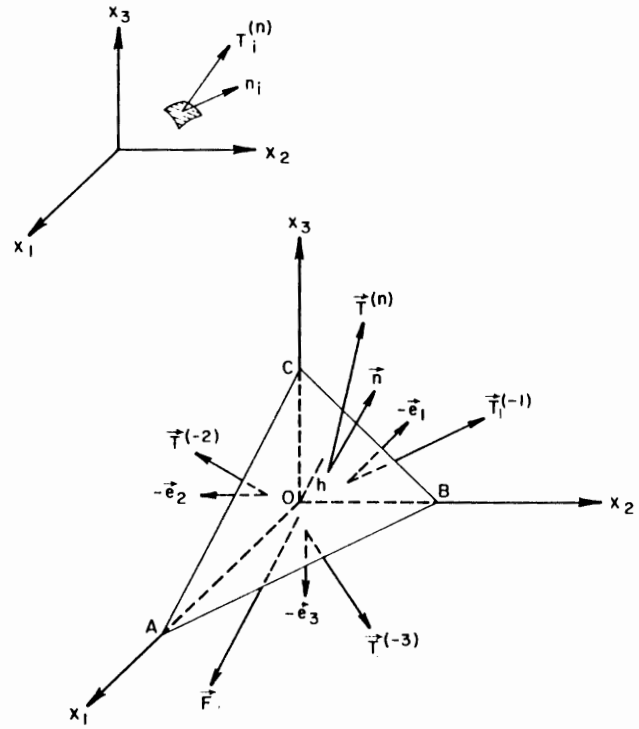

Fig. 2.2. Relation between stress vector acting on an arbitrary plane n_i and the three stress vectors acting on the coordinate planes.

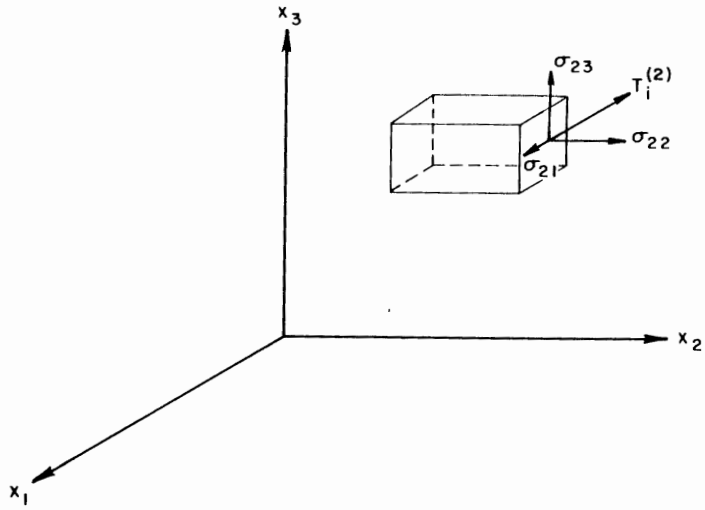

Fig. 2.3. Typical components of stress tensor σ_{ij} acting on the x_2-coordinate plane.

normal $n_i = (n_1, n_2, n_3) = (l, m, n)$ is expressed as a linear combination of the three stress vectors on the plane-area elements perpendicular to the three coordinates at the point. Therefore, it is clear that the three stress vectors $T_i^{(1)}$, $T_i^{(2)}$, $T_i^{(3)}$ define the state of stress at the point completely.

Since T_i is a vector quantity, it can be more conveniently represented by three components: A normal stress component and two tangential stress components. For example, the stress vector $T_i^{(2)}$ associated with the coordinate plane y or x_2 has the three components: Normal stress σ_y or σ_{22} and shear stresses τ_{yx} and τ_{yz} or σ_{21} and σ_{23} in the direction of the three coordinate axes y, x, and z or x_2, x_1, and x_3, respectively as shown in Fig. 2.3, or:

$$T_i^{(2)} = [\sigma_{21}, \sigma_{22}, \sigma_{23}] = [\tau_{yx}, \sigma_y, \tau_{yz}] \tag{2.7}$$

in which the index notation of σ_{22} for *normal stress* and σ_{21}, σ_{23} for *shearing stresses*, and the engineering notation of σ_y for normal stress and τ_{yx}, τ_{yz} for shearing stresses will always be used interchangeably. In the former case, the first suffix denotes the normal direction on the small area $\mathrm{d}A$ and the second suffix the direction in which the component acts. In the latter case, only one suffix is used for the normal stress since the direction of the component is the same as that of the normal to the surface. If the normal component of the stress across a surface is positive, it is called a *tensile stress* and if it is negative it is called a *compressive stress*.

In the same way the stress at P across a plane whose normal is in the direction of x_1 or x will have components:

$$T_i^{(1)} = [\sigma_{11}, \sigma_{12}, \sigma_{13}] = [\sigma_x, \tau_{xy}, \tau_{xz}] \tag{2.8}$$

and that across a plane whose normal is in the direction x_3 or z will have components:

$$T_i^{(3)} = [\sigma_{31}, \sigma_{32}, \sigma_{33}] = [\tau_{zx}, \tau_{zy}, \sigma_z] \tag{2.9}$$

The nine quantities in Eqs. (2.7) to (2.9), which define the three stress vectors $T_i^{(1)}$, $T_i^{(2)}$, and $T_i^{(3)}$, are called the components of the *stress tensor* σ_{ij} at the point P, which are collected in Eq. (2.10):

$$\sigma_{ij} = \begin{bmatrix} T_i^{(1)} \\ T_i^{(2)} \\ T_i^{(3)} \end{bmatrix} = \begin{bmatrix} \sigma_{11} & \sigma_{12} & \sigma_{13} \\ \sigma_{21} & \sigma_{22} & \sigma_{23} \\ \sigma_{31} & \sigma_{32} & \sigma_{33} \end{bmatrix} = \begin{bmatrix} \sigma_x & \tau_{xy} & \tau_{xz} \\ \tau_{yx} & \sigma_y & \tau_{yz} \\ \tau_{zx} & \tau_{zy} & \sigma_z \end{bmatrix} \tag{2.10}$$

The components of σ_{ij} are shown in the positive directions in Fig. 2.4 referred to

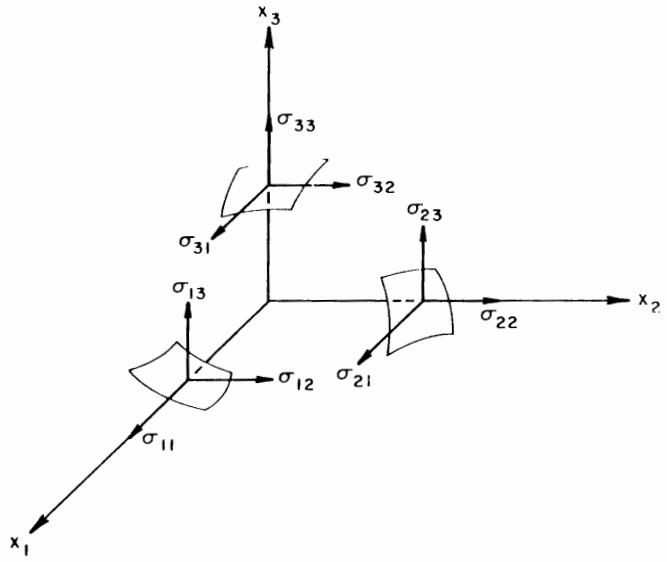

Fig. 2.4. Typical components of stress tensor σ_{ij} acting on the three coordinate planes.

the x_i coordinate system. The dual notation in Eq. (2.10), where σ represents a normal component of stress and τ a shearing component of stress, is known as *von Karman's notation* used widely in practice as well as in the well-known book by Timoshenko and Goodier (1951).

The nine components in Eq. (2.10) are the components of a mathematical entity called a *second-order tensor*. A second-order tensor is defined completely by three vectors just as a vector is defined completely by three scalars. A *vector* is therefore called a *first-order tensor*. Tensor analysis is much used in developing the higher parts of the continuum theory. The main change, from the present point of view is that the notation x, y, z for the coordinate is replaced by x_1, x_2, x_3, so that they are specified by the numbers 1, 2, 3. The nine components of the stress tensor are denoted by σ_{ij}, where values of i and j are running from 1 to 3.

Example 2.1: The state of stress at a point is represented by the given stress tensor σ_{ij}:

$$\sigma_{ij} = \begin{bmatrix} -80 & 16 & 26 \\ 16 & 26 & -28 \\ 26 & -28 & -36 \end{bmatrix} \text{(units of stress)}$$

For a plane with unit normal $n_i = (1/\sqrt{2}, 1/\sqrt{3}, 1/\sqrt{6})$, calculate the magnitude of the stress vector, $T_i^{(n)}$.

Solution: The components $T_i^{(n)}$ of stress vector are calculated using Eq. (2.6), which gives respectively:

$$T_1^{(n)} = T_1^{(1)}n_1 + T_1^{(2)}n_2 + T_1^{(3)}n_3 = -80 \times \frac{1}{\sqrt{2}} + 16 \times \frac{1}{\sqrt{3}} + 26 \times \frac{1}{\sqrt{6}} = -36.72$$

$$T_2^{(n)} = T_2^{(1)}n_1 + T_2^{(2)}n_2 + T_2^{(3)}n_3 = 14.89$$

$$T_3^{(n)} = T_3^{(1)}n_1 + T_3^{(2)}n_2 + T_3^{(3)}n_3 = -12.48$$

Thus, the magnitude of the stress vector is calculated by:

$$|T^{(n)}| = \sqrt{\left[T_1^{(n)}\right]^2 + \left[T_2^{(n)}\right]^2 + \left[T_3^{(n)}\right]^2} = 41.54$$

2.3.2 Cauchy's formulas, index notation, and summation convention

Unlike the two-dimensional stress analysis which can be conveniently described by the simple geometric construction of Mohr's circle, many of difficulties of the three-dimensional stress analysis are caused by the complication of three-dimensional geometry. This can be handled by the use of *index notation* and *summation convention*. These relations are summarized briefly in the following.

From the consideration of equilibrium of forces acting on an arbitrary small volume of material, it can be shown that the components of the stress vector $T_i^{(n)}$, or simply T_i, in the x_i-coordinate direction can be written as:

$$T_i = \sum_{j=1}^{3} \sigma_{ji} n_j \tag{2.11}$$

where we take it for granted that, since the subscript i is unspecified, the equation must hold for each of the three possible values of this subscripts. The index i is therefore called *free index*. The index j in Eq. (2.11) is, however, a *dummy* subscript because of the fact that the particular letter used in this subscript is not important; thus:

$$T_i = \sum_{j=1}^{3} \sigma_{ji} n_j = \sum_{k=1}^{3} \sigma_{ki} n_k \tag{2.12}$$

To allow for further brevity, we adopt the following summation convention: when a subscript occurs twice in the same term, it will be understood that the subscript is to be summed from 1 to 3. Thus, Eq. (2.12) can be abbreviated as:

$$T_i = \sigma_{ji} n_j = \sigma_{ki} n_k \tag{2.13}$$

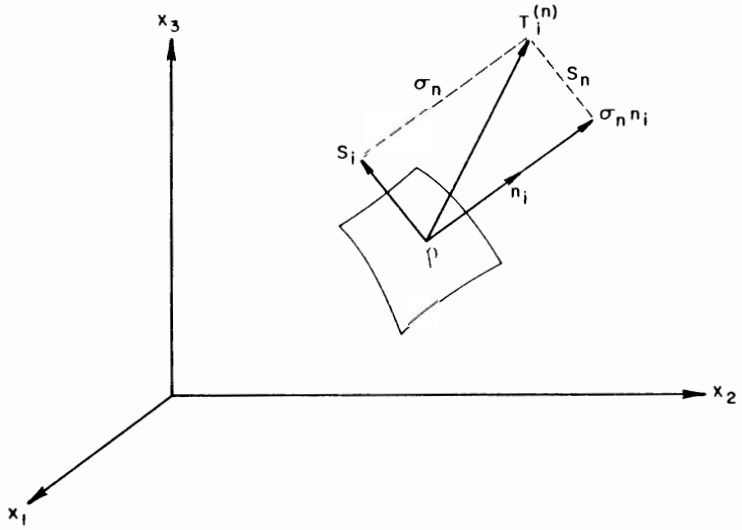

Fig. 2.5. Normal and shearing stress components of stress vector T_i acting on an arbitrary area element n_i.

where the free index must occur precisely once in each term of the expression or equation. It represents a vector with three components, $i = 1, 2, 3$ respectively. The dummy index j or k is to be summed from 1 to 3. The dummy index may or may not occur precisely twice in any other terms. Note that if a subscript occurs more than twice in one term of an expression or equation, it is a mistake in the use of the index notation and summation convention.

From the consideration of equilibrium of moments of a material element, it can be shown that the stress tensor σ_{ij} is symmetric, i.e.:

$$\sigma_{ij} = \sigma_{ji} \tag{2.14}$$

Thus, Eq. (2.13) can be rewritten somewhat more conveniently and conventionally as:

$$T_i = \sigma_{ij} n_j \tag{2.15}$$

and it therefore follows that T_i for the unit normal n_i can be calculated from knowledge of the nine basic quantities as given in Eq. (2.10).

The stress vector T_i acting on the area element n_i at P can be resolved into normal stress components $\sigma_n n_i$ and shear stress component S_i, as shown in Fig. 2.5.

The magnitude of the normal stress σ_n is clearly $T_i n_i$, so that the normal stress component can be expressed in terms of the stress tensor through Eq. (2.15) as:

$$\sigma_n = T_i n_i = \sigma_{ij} n_i n_j \tag{2.16}$$

The magnitude of the shearing stress component S_n is given by:

$$S_n = (S_i S_i)^{\frac{1}{2}} = \left(T_i T_i - \sigma_n^2\right)^{\frac{1}{2}} \tag{2.17}$$

Using Eqs. (2.15) and (2.16), the above equation becomes:

$$S_n = \left[\sigma_{ij}\sigma_{ik} n_j n_k - (\sigma_{ij} n_i n_j)^2\right]^{\frac{1}{2}} \tag{2.18}$$

Equations (2.16) and (2.18) allow the determination of the normal and shearing components of the stress vector T_i acting on the plane n_i (Fig. 2.5). Equations (2.6), (2.16) and (2.18) all are called *Cauchy's formulas*. The vector $\sigma_n n_i$ is in the direction of the normal vector n_i, and the vector S_i, lies in the plane formed by two vectors T_i and n_i, or:

$$S_i = T_i - \sigma_n n_i \tag{2.19}$$

Example 2.2: The state of stress at a point represented by the given stress tensor σ_{ij}:

$$\sigma_{ij} = \begin{bmatrix} 3 & 4 & 0 \\ 4 & 9 & 0 \\ 0 & 0 & 3 \end{bmatrix} \text{(units of stress)}$$

For a plane with unit normal $n_i = (1/2,\ 1/2,\ 1/\sqrt{2}\,)$, calculate the normal and shear stress components, σ_n and S_n, for plane with normal vector n_i.

Solution: Let us first calculate the components $T_i^{(n)}$ of the stress vector employing Eq. (2.15):

$$T_1^{(n)} = \sigma_{1j} n_j = 3.5$$

$$T_2^{(n)} = \sigma_{2j} n_j = 6.5$$

$$T_3^{(n)} = \sigma_{3j} n_j = 2.12$$

Thus, the magnitude of the stress vector has the value:

$$|T^{(n)}| = \sqrt{\left[T_1^{(n)}\right]^2 + \left[T_2^{(n)}\right]^2 + \left[T_3^{(n)}\right]^2} = 7.68$$

Substituting into Eq. (2.16), we get the normal stress component σ_n, that is:

$$\sigma_n = \sigma_{ij} n_i n_j = \sigma_{11} n_1 n_1 + \sigma_{12} n_1 n_2 + \sigma_{13} n_1 n_3 + \sigma_{21} n_2 n_1 + \sigma_{22} n_2 n_2 + \sigma_{23} n_2 n_3 + \sigma_{31} n_3 n_1 + \sigma_{32} n_3 n_2 + \sigma_{33} n_3 n_3 = 6.5$$

or

$$\sigma_n = T_1^{(n)} n_1 + T_2^{(n)} n_2 + T_3^{(n)} n_3 = 6.5$$

The shear stress component, S_i, is given by Eq. (2.19):

$$S_1 = T_1^{(n)} - \sigma_n n_1 = 0.25$$

$$S_2 = T_2^{(n)} - \sigma_n n_2 = 3.25$$

$$S_3 = T_3^{(n)} - \sigma_n n_3 = -2.48$$

Thus, the magnitude of the shear stress component, S_n, is calculated by Eq. (2.17):

$$|S_n| = \left[|T|^2 - \sigma_n^2 \right]^{\frac{1}{2}} = \left[7.68^2 - 6.5^2 \right]^{\frac{1}{2}} = 4.09$$

or

$$|S_n| = \left[S_1^2 + S_2^2 + S_3^2 \right]^{\frac{1}{2}} = 4.09$$

Example 2.3: Let us consider two area elements passing through any point P and having unit normals m_i and n_i. The associated stress vectors are denoted by $T_i^{(m)}$ and $T_i^{(n)}$, respectively. Prove that the projection of $T_i^{(m)}$ on the direction n_i is equal to the projection of $T_i^{(n)}$ on the direction of m_i (the *projection theorem*).

Proof: We can find the projection of $T_i^{(m)}$ on the direction of n_i by the dot product of the two vectors. Using $T_i^{(m)}$ expressed in terms of the stress tensor at point P, we have:

$$T_i^{(m)} n_i = \sigma_{ji} m_j n_i \tag{2.20}$$

On the other hand, the projection of $T_i^{(n)}$ on the direction of m_i is in a similar way given by:

$$T_i^{(n)} m_i = \sigma_{ji} n_j m_i \tag{2.21}$$

Noting that i and j are dummy indexes and σ_{ij} is a symmetrical tensor ($\sigma_{ij} = \sigma_{ji}$), Eq. (2.21) can be written as:

$$T_i^{(n)} m_i = \sigma_{ji} n_i m_j \tag{2.22}$$

From Eqs. (2.20) and (2.22), therefore, we obtain:

$$T_i^{(m)} n_i = T_i^{(n)} m_i \tag{2.23}$$

Equation (2.23) is called the *projection theorem*.

2.3.3 Principal axes of stresses

The Cauchy's formulas of Eqs. (2.16) and (2.18) give a complete picture of the variation of stress at P with direction, showing that both σ_n and S_n are related to the direction cosines $n_i = (n_1, n_2, n_3)$. If a particular unit normal n_i is chosen in such a way that only the normal stress component exists while the shear stress component vanishes, this is known as the *principal direction*. This condition for principal direction implies that the stress vector T_i at P is perpendicular to the area element with n_i, that is, $T_i = \sigma\, n_i$, or using Eq. (2.15), we have:

$$\sigma_{ij} n_j = \sigma n_i \tag{2.24}$$

which can be written as:

$$(\sigma_{ij} - \sigma\delta_{ij}) n_j = 0 \tag{2.25}$$

where δ_{ij} is the *Kronecker delta*, it has the value 1 if $i = j$ and 0 if $i \neq j$. Equation (2.25) can be expressed in the expanded form:

$$\begin{aligned} (\sigma_{11} - \sigma) n_1 + \sigma_{12} n_2 + \sigma_{13} n_3 &= 0 \\ \sigma_{21} n_1 + (\sigma_{22} - \sigma) n_2 + \sigma_{23} n_3 &= 0 \\ \sigma_{31} n_1 + \sigma_{32} n_2 + (\sigma_{33} - \sigma) n_3 &= 0 \end{aligned} \tag{2.26}$$

The above is a set of three simultaneous linear homogeneous equations for n_i (n_1, n_2, n_3). This set possesses solutions if and only if the determinant of the coefficient vanishes:

$$\det |\sigma_{ij} - \sigma\delta_{ij}| = 0 \tag{2.27}$$

or

$$\begin{vmatrix} \sigma_{11} - \sigma & \sigma_{12} & \sigma_{13} \\ \sigma_{21} & \sigma_{22} - \sigma & \sigma_{23} \\ \sigma_{31} & \sigma_{32} & \sigma_{33} - \sigma \end{vmatrix} = 0 \tag{2.28}$$

Expanding Eq. (2.28) leads to the *characteristic equation* expressed by:

$$\sigma^3 - I_1\sigma^2 + I_2\sigma - I_3 = 0 \tag{2.29}$$

where I_1, the sum of the diagonal terms of σ_{ij}, is:

$$I_1 = \sigma_{ii} = \sigma_{11} + \sigma_{22} + \sigma_{33} \tag{2.30}$$

I_2, the sum of the principal two-rowed minors of the determinant of σ_{ij}, is:

$$I_2 = \begin{vmatrix} \sigma_{22} & \sigma_{23} \\ \sigma_{32} & \sigma_{33} \end{vmatrix} + \begin{vmatrix} \sigma_{11} & \sigma_{13} \\ \sigma_{31} & \sigma_{33} \end{vmatrix} + \begin{vmatrix} \sigma_{11} & \sigma_{12} \\ \sigma_{21} & \sigma_{22} \end{vmatrix} = \tfrac{1}{2}\left(I_1^2 - \sigma_{ij}\sigma_{ji}\right) \tag{2.31}$$

and I_3, the determinant of σ_{ij}, is:

$$I_3 = \det|\sigma_{ij}| = \tfrac{1}{6}\left(2\sigma_{ij}\sigma_{jk}\sigma_{ki} - 3I_1\sigma_{ij}\sigma_{ji} + I_1^3\right) \tag{2.32}$$

The quantities I_1, I_2, and I_3 are called the *invariants of the stress tensor* σ_{ij}. As their names imply, these invariants are unaffected by rotation of the coordinate axes. Note here that the above invariants I_1, I_2, and I_3 are not the only invariants of the stress tensor σ_{ij}. In general, there are a number of combinations of the stress tensor σ_{ij} that are not altered by a rotation of the coordinate axes. The easy way of constructing such invariants is to use the fact that σ_{ij} is a tensor, so that any scalar quantity generated out of stress tensor must be an invariant (Chen and Saleeb, 1982).

Equation (2.29) has three roots, σ_1, σ_2, σ_3. Using these roots, Eq. (2.26) can be solved to give three directions of n_i at right angles to each other on which maximum, intermediate, and minimum normal stresses corresponding to zero shear stress exist. These three directions are called *principal directions* at P, and the corresponding normal stresses are called *principal stresses*. A right-handed coordinate system can be oriented to line up with the principal directions at P, such a coordinate system is called *principal axes* for the stress state at P.

Once this principal direction is known, it is convenient to use the principal axes as the axes of reference. Thus, if the principal stresses σ_1, σ_2, σ_3 are substituted for the stress tensor σ_{ij}, in the Cauchy formulas (2.16) and (2.18), the normal and shear stresses in the direction n_i have the simple forms:

$$\sigma_n = \sigma_{ij}n_in_j = \sigma_1n_1^2 + \sigma_2n_2^2 + \sigma_3n_3^2 \tag{2.33a}$$

$$S_n = \left[(\sigma_1n_1)^2 + (\sigma_2n_2)^2 + (\sigma_3n_3)^2 - \left(\sigma_1n_1^2 + \sigma_2n_2^2 + \sigma_3n_3^2\right)^2\right]^{\frac{1}{2}} \tag{2.33b}$$

An *octahedral plane* is a plane whose normal makes equal angles with each of the principal axes of the stress, and thus it follows that the normal stress σ_{oct} and shear stress τ_{oct} on the octahedral plane whose normal n_i is defined by:

$$n_i = (n_1, n_2, n_3) = \frac{1}{\sqrt{3}}(1, 1, 1) \tag{2.34}$$

are given by Cauchy's formulas of Eqs. (2.33a) and (2.33b) in the form:

$$\sigma_{oct} = \tfrac{1}{3}(\sigma_1 + \sigma_2 + \sigma_3) = \tfrac{1}{3}I_1$$

$$\tau_{oct} = \tfrac{1}{3}\left[(\sigma_1 - \sigma_2)^2 + (\sigma_2 - \sigma_3)^2 + (\sigma_3 - \sigma_1)^2\right]^{\frac{1}{2}} \tag{2.35}$$

Once the values of principal stresses are known, the Mohr circle construction can be proceeded in the usual manner. That is, on the normal stress axis, lengths are marked off to represent σ_1, σ_2 and σ_3, respectively. From this construction of Mohr's circles, it follows that there are three principal shear stresses τ_1, τ_2, and τ_3, corresponding to the radii of the three Mohr's circles with:

$$\tau_1 = \tfrac{1}{2}|\sigma_2 \quad \sigma_3|, \ \tau_2 = \tfrac{1}{2}|\sigma_1 - \sigma_3|, \quad \text{and } \tau_3 = \tfrac{1}{2}|\sigma_1 - \sigma_2| \tag{2.36}$$

each of which occurs on an area element whose unit normal makes an angle of 45 degrees with each of the corresponding principal axes. The largest numerical value of the *principal shears* is called the *maximum shear stress*:

$$\tau_{\max} = \tfrac{1}{2}|\sigma_1 - \sigma_3| \quad \text{or } \tau_{\max} = \max(\tau_1, \tau_2, \tau_3) \tag{2.37}$$

for $\sigma_1 > \sigma_2 > \sigma_3$. The maximum shear stress is half the difference of the major (greatest) and minor (least) principal stresses and occurs on a plane whose normal bisects the major and minor principal axes. Thus, if materials such as soil and rock are known to fail in shear, it will obviously tend to fail in the plane of maximum shear. It is a relatively easy matter to define the likely direction and magnitude of failure stress from a given state of stress at a point.

Example 2.4: Find the principal stresses, their principal directions, and the principal shear stresses for the given stress tensor σ_{ij}:

$$\sigma_{ij} = \begin{bmatrix} 5 & 0 & 3 \\ 0 & 0 & 2 \\ 3 & 2 & 0 \end{bmatrix} \text{(units of stress)}$$

Show that the three principal directions are orthogonal to each other. Calculate the octahedral normal and shearing stresses.

Solutions: Three invariants I_1, I_2, and I_3 are calculated from Eqs. (2.30), (2.31), and (2.32), respectively:

$I_1 \quad \sigma_{ii} \quad 5 + 0 + 0 = 5$

$I_2 \quad 13$

$I_3 = \quad -20$

The characteristic equation (2.29) becomes:

$\sigma^3 \quad 5\sigma^2 \quad 13\sigma + 20 = 0$

which has three roots:

$\sigma_1 = 6.52, \quad \sigma_2 = 1.15, \quad \text{and } \sigma_3 = -2.67$

As a check, the sum of these principal values must equal to:

$$\sigma_1 + \sigma_2 + \sigma_3 = I_1 = 5$$

The principal directions are obtained as follows: for $\sigma_1 = 6.52$, Eqs. (2.26) becomes:

$$\begin{aligned}
&(5 - 6.52)n_1^{(1)} + (0)n_2^{(1)} + (3)n_3^{(1)} = 0\\
&(0)n_1^{(1)} + (0 - 6.52)n_2^{(1)} + (2)n_3^{(1)} = 0\\
&(3)n_1^{(1)} + (2)n_2^{(1)} + (0 - 6.52)n_3^{(1)} = 0
\end{aligned}$$

Noting that one of the three equations is not independent, we must use the remaining two equations with the condition $n_i^{(1)}\, n_i^{(1)} = 1$, leading to the solution:

$$n_i^{(1)} = (\pm 0.883,\ \pm 0.137,\ \pm 0.448)$$

The other two principal directions $n_i^{(2)}$ and $n_i^{(3)}$ can be solved in a similar manner:

$$n_i^{(2)} = (\pm 0.362,\ \mp 0.808,\ \mp 0.465)$$

$$n_i^{(3)} = (\pm 0.299,\ \pm 0.572,\ \mp 0.764)$$

The dot products of these three principal directions are:

$$n_i^{(1)} n_i^{(2)} = (0.319) + (-0.111) + (-0.208) = 0$$

$$n_i^{(2)} n_i^{(3)} = (0.108) + (-0.463) + (0.355) = 0$$

$$n_i^{(3)} n_i^{(1)} = (0.264) + (0.079) + (-0.343) = 0$$

which indicate that the three principal directions are *orthogonal* to each other. Octahedral stresses, σ_{oct} and τ_{oct}, are determined by Eqs. (2.35):

$$\sigma_{oct} = \tfrac{1}{3} I_1 = \tfrac{5}{3}$$

$$\tau_{oct} = \tfrac{1}{3}\left[(\sigma_1 - \sigma_2)^2 + (\sigma_2 - \sigma_3)^2 + (\sigma_3 - \sigma_1)^2\right]^{\frac{1}{2}} = 3.77$$

The octahedral shearing stress τ_{oct} can also be expressed in terms of the components of a general state of stress σ_{ij} (see Example 2.7):

$$\tau_{oct} = \tfrac{1}{3}\left[(\sigma_{11} - \sigma_{22})^2 + (\sigma_{22} - \sigma_{33})^2 + (\sigma_{33} - \sigma_{11})^2 + 6(\sigma_{12}^2 + \sigma_{23}^2 + \sigma_{31}^2)\right]^{\frac{1}{2}} \qquad (2.38)$$

Substituting the numerical values of stress components σ_{ij} into Eq. (2.38), we have:

$$\tau_{oct} = 3.77$$

Example 2.5: Show that the principal normal stresses assume the stationary values.

Proof: From Eq. (2.16), the normal stress σ_n has the value:

$$\sigma_n = \sigma_{ij} n_i n_j$$

where the values of n_i must satisfy the condition for directional cosines:

$$n_1^2 + n_2^2 + n_3^2 = 1$$

To find the stationary values for σ_n, define the function Y with the Lagrange multipher, σ:

$$Y = \sigma_n - \sigma\left(n_1^2 + n_2^2 + n_3^2 - 1\right)$$

and use the following three conditions:

$$\frac{\partial Y}{\partial n_1} = 0 \tag{2.39a}$$

$$\frac{\partial Y}{\partial n_2} = 0 \tag{2.39b}$$

$$\frac{\partial Y}{\partial n_3} = 0 \tag{2.39c}$$

Equation (2.39a) yields:

$$2\sigma_{11} n_1 + 2\sigma_{12} n_2 + 2\sigma_{13} n_3 - 2\sigma n_1 = 0$$

or

$$(\sigma_{11} - \sigma) n_1 + \sigma_{12} n_2 + \sigma_{13} n_3 = 0 \tag{2.39d}$$

In a similar manner, Eqs. (2.39b) and (2.39c) lead to:

$$\sigma_{21} n_1 + (\sigma_{22} - \sigma) n_2 + \sigma_{23} n_3 = 0 \tag{2.39e}$$

$$\sigma_{31} n_1 + \sigma_{32} n_2 + (\sigma_{33} - \sigma) n_3 = 0 \tag{2.39f}$$

Equations (2.39d–f) are identical to those in Eq. (2.26). Thus, the principal normal stresses assume the stationary values.

2.3.4 *Deviatoric stress*

The stress state σ_{ij} can be decomposed into two stress states, one representing *pure shear state* s_{ij} and the other *hydrostatic state* $p\delta_{ij}$ where p is the *mean stress* value given by:

$$p = \tfrac{1}{3}(\sigma_{11} + \sigma_{22} + \sigma_{33}) = \tfrac{1}{3}I_1 \tag{2.40}$$

The *deviatoric stress* tensor s_{ij} is defined by:

$$s_{ij} = \sigma_{ij} - p\delta_{ij} \tag{2.41}$$

which can be shown to be a state of pure shear (Chen and Saleeb, 1982).

Since subtracting a constant normal stress in all directions will not change the principal directions, s_{ij} and σ_{ij} have the same principal axes. The *principal values of the deviatoric stress tensor* s_1, s_2, s_3 can be found in the same manner just as the principal values of the stress tensor, σ_1, σ_2, σ_3, i.e.:

$$\det|s_{ij} - s\delta_{ij}| = 0 \tag{2.42}$$

or

$$s^3 - J_1 s^2 - J_2 s - J_3 = 0 \tag{2.43}$$

where:

$$J_1 = s_{ii} = s_{11} + s_{22} + s_{33} = s_1 + s_2 + s_3 = 0 \tag{2.44}$$

$$J_2 = \tfrac{1}{2}s_{ij}s_{ij} = \tfrac{1}{2}\left(s_1^2 + s_2^2 + s_3^2\right) = -\left(s_1 s_2 + s_2 s_3 + s_3 s_1\right)$$

$$= \tfrac{1}{6}\left[(\sigma_{11} - \sigma_{22})^2 + (\sigma_{22} - \sigma_{33})^2 + (\sigma_{33} - \sigma_{11})^2\right]$$

$$+ \sigma_{12}^2 + \sigma_{23}^2 + \sigma_{31}^2 \text{ (see Example 2.7)} \tag{2.45}$$

$$J_3 = \tfrac{1}{3}s_{ij}s_{jk}s_{ki} = \det|s_{ij}| = s_1 s_2 s_3 \tag{2.46}$$

The quantities, J_1, J_2, J_3, defined analogously to the invariants of the stress tensor I_1, I_2, I_3, are called the *invariants of the deviatoric stress tensor*. A single subscript indicates a principal value. The deviatoric stress tensor and their invariants play a very important role in the stress-strain modeling of both elastic and plastic materials. The hydrostatic pressure and the deviatoric stress, respectively, cause *volumetric change* and *shape change* in the material element within the framework of the theory of elasticity (see Chapter 3).

Example 2.6: The stress tensor σ_{ij} is given by:

$$\sigma_{ij} = \begin{bmatrix} 1 & 2 & 1 \\ 2 & 2 & 1 \\ 1 & 1 & 3 \end{bmatrix} \text{ (units of stress)}$$

Calculate:
(a) The hydrostatic stress and the stress deviatoric tensor, s_{ij}.
(b) The principal values of deviatoric stress tensor.

Solutions: (a) Hydrostatic stress p is given by:

$$p = \tfrac{1}{3}\sigma_{ii} = \tfrac{1}{3}(1 + 2 + 3) = 2$$

The stress deviatoric tensor, s_{ij}, is:

$$s_{ij} = \sigma_{ij} \quad p\delta_{ij} = \begin{bmatrix} 1 & 2 & 1 \\ 2 & 2 & 1 \\ 1 & 1 & 3 \end{bmatrix} - \begin{bmatrix} 2 & 0 & 0 \\ 0 & 2 & 0 \\ 0 & 0 & 2 \end{bmatrix} = \begin{bmatrix} -1 & 2 & 1 \\ 2 & 0 & 1 \\ 1 & 1 & 1 \end{bmatrix}$$

(b) Using Eq. (2.42) or (2.43), the characteristic equation is:

$$\det |s_{ij} - s\delta_{ij}| = \begin{vmatrix} -1 - s & 2 & 1 \\ 2 & 0 - s & 1 \\ 1 & 1 & 1 - s \end{vmatrix} = 0$$

or

$$s^3 \quad 7s \quad 1 = 0$$

Solving the cubic equation, we obtain the three principal values of deviatoric stress tensor:

$$s_1 = 2.714, \quad s_2 = -0.143, \quad s_3 = -2.571$$

Example 2.7: Prove that:

(a) $J_2 = \frac{1}{6}\left[(\sigma_{11} \quad \sigma_{22})^2 + (\sigma_{22} \quad \sigma_{33})^2 + (\sigma_{33} \quad \sigma_{11})^2\right] + \sigma_{12}^2 + \sigma_{23}^2 + \sigma_{31}^2$

(b) $\tau_{oct} \quad \sqrt{\frac{2}{3}}J_2$

Proof: (a) Similar to the definition for I_2, J_2 can be written as:

$$J_2 = -\begin{vmatrix} s_{22} & s_{23} \\ s_{32} & s_{33} \end{vmatrix} - \begin{vmatrix} s_{11} & s_{13} \\ s_{31} & s_{33} \end{vmatrix} - \begin{vmatrix} s_{11} & s_{12} \\ s_{21} & s_{22} \end{vmatrix}$$

$$= -(s_{11}s_{22} + s_{22}s_{33} + s_{33}s_{11}) + s_{12}^2 + s_{23}^2 + s_{31}^2$$

Substituting $s_{11} = \frac{1}{3}(2\sigma_{11} - \sigma_{22} - \sigma_{33})$, $s_{22} = \frac{1}{3}(2\sigma_{22} - \sigma_{11} - \sigma_{33})$, $s_{33} = \frac{1}{3}(2\sigma_{33} - \sigma_{11} - \sigma_{22})$, $s_{12} = \sigma_{12}$, $s_{23} = \sigma_{23}$, $s_{31} = \sigma_{31}$, we obtain:

$$J_2 = -\frac{1}{9}\left[(2\sigma_{11} - \sigma_{22} - \sigma_{33})(2\sigma_{22} - \sigma_{11} - \sigma_{33}) + (2\sigma_{22} - \sigma_{11} - \sigma_{33})(2\sigma_{33} - \sigma_{11} - \sigma_{22}) + (2\sigma_{11} - \sigma_{22} - \sigma_{33})(2\sigma_{33} - \sigma_{11} - \sigma_{22})\right] + \sigma_{12}^2 + \sigma_{23}^2 + \sigma_{31}^2$$

$$= \frac{1}{6}\left[(\sigma_{11} - \sigma_{22})^2 + (\sigma_{22} - \sigma_{33})^2 + (\sigma_{33} - \sigma_{11})^2\right] + \sigma_{12}^2 + \sigma_{23}^2 + \sigma_{31}^2$$

(b) The second invariant J_2 derived just above, being expressed in terms of the components of a general state of stress σ_{ij}, can now be expressed in terms of principal stresses, σ_1, σ_2, σ_3:

$$J_2 = \frac{1}{6}\left[(\sigma_1 - \sigma_2)^2 + (\sigma_2 - \sigma_3)^2 + (\sigma_3 - \sigma_1)^2\right] \tag{2.47}$$

Comparing the expression for octahedral shear stress τ_{oct} derived previously in Eq. (2.35) with the expression for J_2 derived above in Eq. (2.47), we find:

$$\tau_{oct} = \frac{1}{3}\sqrt{6J_2} = \sqrt{\frac{2}{3}J_2} \tag{2.48a}$$

or

$$\tau_{oct} = \frac{1}{3}\left[(\sigma_{11} - \sigma_{22})^2 + (\sigma_{22} - \sigma_{33})^2 + (\sigma_{33} - \sigma_{11})^2 + 6(\sigma_{12}^2 + \sigma_{23}^2 + \sigma_{31}^2)\right]^{\frac{1}{2}} \tag{2.48b}$$

2.3.5 Geometrical representation of stresses

A simple geometric interpretation of the *stress invariants* is given below. Point A in Fig. 2.6 represents the state of stress $(\sigma_1, \sigma_2, \sigma_3)$ at a material point in the principal stress coordinate system. Stress vector $\overrightarrow{OA}$ is decomposed into vector $\overrightarrow{OB}$ along the ξ-axis which is called the *hydrostatic axis* $(\sigma_1 = \sigma_2 = \sigma_3)$ and vector $\overrightarrow{BA}$ in the *deviatoric plane* which is perpendicular to the ξ-axis. Since the unit vector n_i in ξ-axis is given by:

$$n_i = (1/\sqrt{3}\,,\ 1/\sqrt{3}\,,\ 1/\sqrt{3}\,) \tag{2.49}$$

and the magnitude of vector $\overrightarrow{OB}$ is obtained by the dot product of vector $\overrightarrow{OA}$ and the unit vector n_i, we have:

$$|\overrightarrow{OB}| = \sigma_i n_i = \frac{1}{\sqrt{3}}(\sigma_1 + \sigma_2 + \sigma_3) = \frac{1}{\sqrt{3}} I_1 \tag{2.50}$$

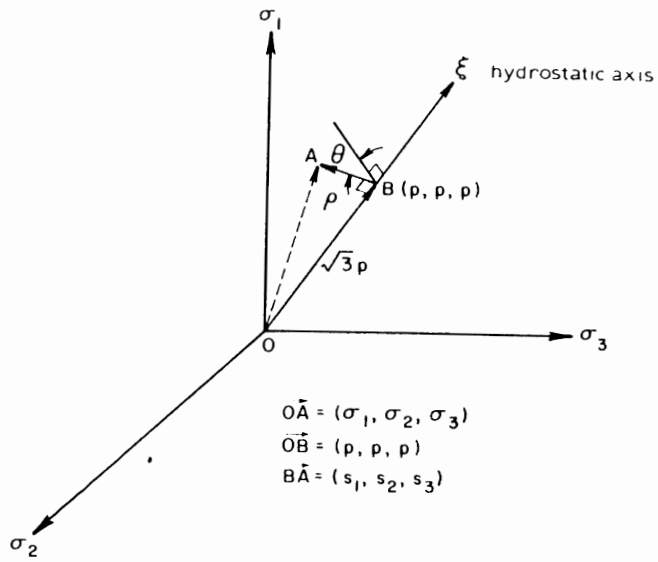

Fig. 2.6. Stress state in principal stress space.

The components of vector $\vec{BA}$ are given by:

$$\dot{BA} = \dot{OA} - \dot{OB} \tag{2.51}$$

where:

$$\dot{OB} = |\vec{OB}|\, n_i = \left[\tfrac{1}{3}(\sigma_1 + \sigma_2 + \sigma_3),\ \tfrac{1}{3}(\sigma_1 + \sigma_2 + \sigma_3),\ \tfrac{1}{3}(\sigma_1 + \sigma_2 + \sigma_3)\right] \tag{2.52}$$

or

$$\vec{OB} = (p,\ p,\ p) \tag{2.53}$$

Substituting Eq. (2.53) into Eq. (2.51) leads to:

$$\vec{BA} = (\sigma_1,\ \sigma_2,\ \sigma_3) - (p,\ p,\ p)$$

$$= \left[(\sigma_1 - p),\ (\sigma_2 - p),\ (\sigma_3 - p)\right] \tag{2.54}$$

or, from the definition of deviatoric stress, $\vec{BA}$ can be written as:

$$\vec{BA} = (s_1,\ s_2,\ s_3) \tag{2.55}$$

The length ρ of vector $\vec{BA}$ is given by:

$$\rho = \sqrt{s_1^2 + s_2^2 + s_3^2} = \sqrt{2J_2} \tag{2.56}$$

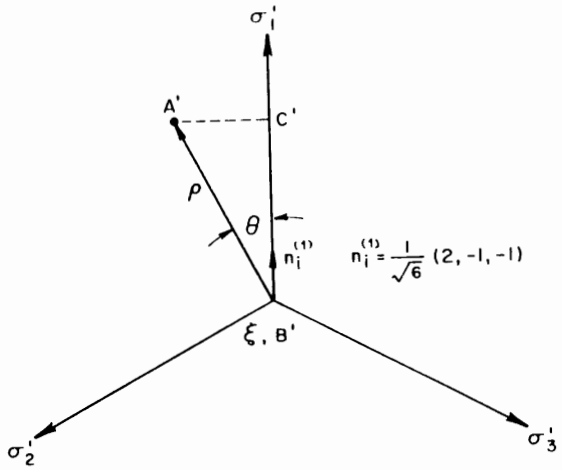

Fig. 2.7. Stress state on π-plane with $\sigma_1 > \sigma_2 > \sigma_3$.

Further, since octahedral shearing stress τ_{oct} and the second invariant of deviatoric stress tensor J_2 are related by Eq. (2.48a), ρ is represented by:

$$\rho = \sqrt{3}\,\tau_{oct} \tag{2.57}$$

If the stress vector $\overrightarrow{OA}$ is viewed from the hydrostatic ξ-axis, the actual length and direction of $\overrightarrow{BA}$ can be projected onto the *π-plane* (Fig. 2.7) which is defined by:

$$\sigma_1 + \sigma_2 + \sigma_3 = 0 \tag{2.58}$$

In this figure, the axes σ_1', σ_2', and σ_3' are the projections of the axes σ_1, σ_2, and σ_3 on the π-plane, and $B'A'$ is the projection of vector $\overrightarrow{BA}$ on the same plane. Since, in the principal stress space, the unit vector $n_i^{(1)}$ along the σ_1'-axis has the components:

$$n_i^{(1)} = \frac{1}{\sqrt{6}}(2,\ -1,\ -1) \tag{2.59}$$

the projection of vector $\overrightarrow{B'A'}$ along the unit vector, denoted by $B'C'$, is given by:

$$B'C' = \rho\cos\theta = \overrightarrow{B'A'}\cdot n^{(1)} = (s_1,\ s_2,\ s_3)\frac{1}{\sqrt{6}}(2,\ -1,\ -1) \tag{2.60}$$

or

$$\rho\cos\theta = \frac{1}{\sqrt{6}}(2s_1 - s_2 - s_3) \tag{2.61}$$

Utilizing the relation of $s_1 + s_2 + s_3 = 0$, Eq. (2.61) becomes:

$$\rho\cos\theta = \sqrt{\tfrac{3}{2}}\,s_1 \tag{2.62}$$

Replacing ρ in terms of J_2, we have:

$$\cos\theta = \frac{\sqrt{3}}{2}\frac{s_1}{\sqrt{J_2}} \tag{2.63}$$

Utilizing the trigonometric identity $\cos 3\theta = 4\cos^3\theta - 3\cos\theta$ and substituting for $\cos\theta$ from Eq. (2.63) lead to:

$$\cos 3\theta = 4\left(\frac{\sqrt{3}}{2}\frac{s_1}{\sqrt{J_2}}\right)^3 - 3\left(\frac{\sqrt{3}}{2}\frac{s_1}{\sqrt{J_2}}\right)$$

or

$$\cos 3\theta = \frac{3\sqrt{3}}{2J_2^{3/2}}\left(s_1^3 - s_1 J_2\right) \tag{2.64}$$

Using $J_2 = -(s_1s_2 + s_2s_3 + s_3s_1)$ as given in Eq. (2.45), Eq. (2.64) becomes:

$$\cos 3\theta = \frac{3\sqrt{3}}{2J_2^{3/2}}\left[s_1^3 + s_1^2(s_2 + s_3) + s_1s_2s_3\right] \tag{2.65}$$

Finally, substituting for $s_2 + s_3 = -s_1$ and $J_3 = s_1s_2s_3$ leads to:

$$\cos 3\theta = \frac{3\sqrt{3}}{2}\frac{J_3}{J_2^{3/2}} \tag{2.66}$$

The angle θ is called *Lode* angle and given by:

$$\theta = \frac{1}{3}\cos^{-1}\left[\frac{3\sqrt{3}}{2}\frac{J_3}{J_2^{3/2}}\right] \tag{2.67}$$

The range in which the angle θ varies is given by (for $\sigma_1 \geq \sigma_2 \geq \sigma_3$):

$$0 \leq \theta \leq \frac{\pi}{3} \tag{2.68}$$

since in this range, σ_1 is the maximum, σ_2 is the intermediate, and σ_3 is the minimum principal stresses as shown clearly in Fig. 2.7. For other stress condition such as $\sigma_1 \geq \sigma_2 \geq \sigma_3$, the angle θ must now be measured from σ_3'-axis and the same equation as Eq. (2.67) can be still applied.

Any state of stress can be expressed in terms of I_1, J_2, and J_3 in the *principal stress space*. Details of physical interpretations of these stress invariants can be found elsewhere (see, for example, Chen, 1982).

Example 2.8: The principal stress states at three different points in a material are respectively given by $(\sigma_1, \sigma_2, \sigma_3) = (11, 1, 3)$, $(1, 3, 11)$, and $(3, 11, 1)$. Plot their stress states in the principal stress space and on the π-plane.

Solution: The principal stress states are respectively plotted by points, A, B, and C in Fig. 2.8. The stress vectors $\overrightarrow{OA}$, $\overrightarrow{OB}$, and $\overrightarrow{OC}$ can be decomposed into the hydrostatic part and the deviatoric part. The hydrostatic parts are represented by the vector $\overrightarrow{OD}$ whose component and magnitude are respectively given by:

$$\overrightarrow{OD} \quad (I_1/3,\ I_1/3,\ I_1/3) \quad (5, 5, 5)$$

$$|\overrightarrow{OD}| = 5\sqrt{3}$$

On the other hand, the deviatoric parts, denoted by $\overrightarrow{DA}$, $\overrightarrow{DB}$, and $\overrightarrow{DC}$, have the components such as:

$$\overrightarrow{DA} = \overrightarrow{OA} - \overrightarrow{OD} = (11, 1, 3) - (5, 5, 5) = (6, -4, -2)$$

$$\overrightarrow{DB} = \overrightarrow{OB} - \overrightarrow{OD} = (1, 3, 11) - (5, 5, 5) = (-4, -2, 6)$$

$$\overrightarrow{DC} = \overrightarrow{OC} - \overrightarrow{OD} = (3, 11, 1) - (5, 5, 5) = (-2, 6, -4)$$

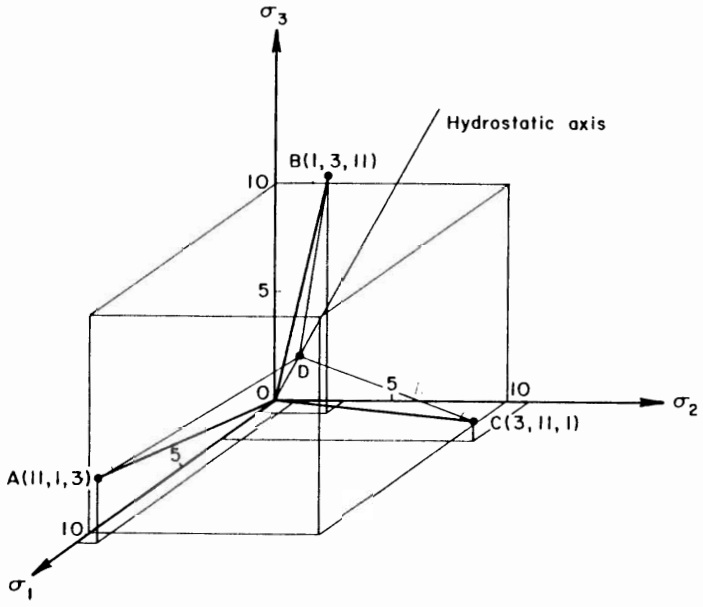

Fig. 2.8. Stress states in principal stress space.

all of which result in the same value of:

$$J_3 = s_1 s_2 s_3 = 48$$

and the same value of:

$$J_2 \quad \rho^2/2 \quad 28$$

where:

$$\rho = |\overrightarrow{DA}| = |\overrightarrow{DB}| = |\overrightarrow{DC}| = \sqrt{6^2 + (-4)^2 + (-2)^2} = 2\sqrt{14}$$

To plot the stress point for each state on the π-plane, we use the two invariants of deviatoric stress tensor J_2, and J_3. For the first set of stress state $(\sigma_1, \sigma_2, \sigma_3) = (11, 1, 3)$, the ordering of relative magnitude of the three principal values is:

$$\sigma_1 > \sigma_3 > \sigma_2 \tag{2.69}$$

Thus, the Lode angle θ must be measured clockwise from the largest principal value, i.e., the σ_1'-axis. Substituting the deviatoric stress invariants $J_2 = 28$ and $J_3 = 48$ into Eq. (2.67), the angle θ can be determined:

$$\theta = \frac{1}{3} \cos^{-1}\left[\frac{3\sqrt{3}}{2} \frac{J_3}{J_2^{3/2}}\right] = 10.89°$$

The second and third stress states $(\sigma_1, \sigma_2, \sigma_3) = (1, 3, 11)$ and $(3, 11, 1)$ can be

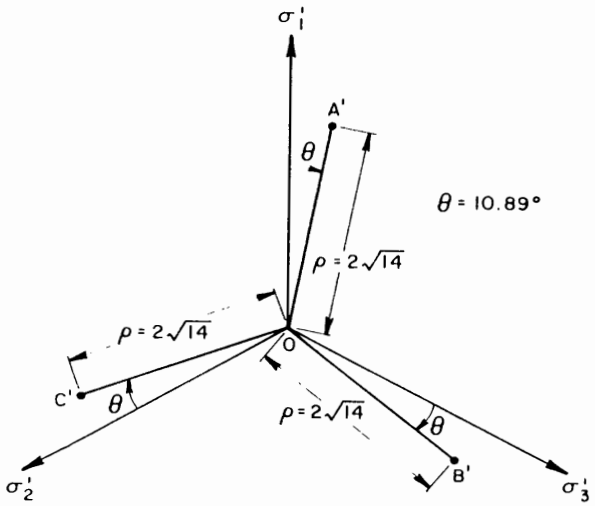

Fig. 2.9 Stress states on π-plane.

plotted on the π-plane in a similar manner. Since the stress conditions are $\sigma_3 > \sigma_2 > \sigma_1$ for the second stress state and $\sigma_2 > \sigma_1 > \sigma_3$ for the third stress state, the angle θ ($\theta = 10.89°$) must be measured clockwise from the σ_3'-axis for state B and the σ_2'-axis for state C, respectively. These stress states represented by points A′, B′, C′ on the π-plane are shown in Fig. 2.9.

Example 2.9: The well-known Coulomb criterion for the failure of geological materials (to be discussed in Chapter 4) is given by:

$$|\tau| = c - \sigma \tan \phi \tag{2.70}$$

where τ, σ, c and ϕ are respectively the shearing stress, normal stress, strength of cohesion, and angle of internal friction. Construct the cross-sectional shape of the Coulomb failure surface on the π-plane.

Solution: The Coulomb criterion implies that failure occurs when the largest Mohr's circle passing through two principal stresses (the maximum and minimum stresses) touches the failure line, as shown in Fig. 2.10. Using these two stresses, Eq. (2.70) can be rewritten as:

$$\tfrac{1}{2}(\sigma_{max} - \sigma_{min}) = -\tfrac{1}{2}(\sigma_{max} + \sigma_{min}) \sin \phi + c \cos \phi \tag{2.71}$$

In order to project the failure surface of Eq. (2.71) onto the π-plane, we define the new Cartesian coordinate system (X, Y, Z) where the X-axis on the π-plane is perpendicular to the σ_1'-axis, the Y-axis is taken to be the same as the σ_1'-axis, and the Z-axis is coincident with the hydrostatic pressure axis as shown in Fig. 2.11. The

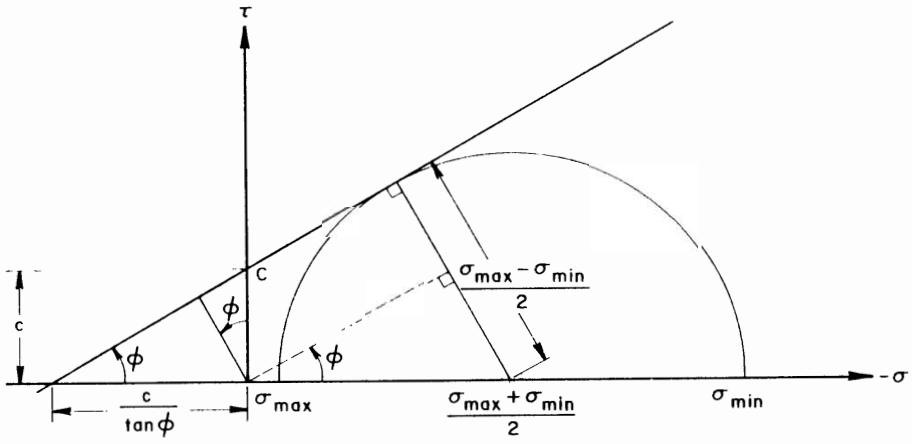

Fig. 2.10. Coulomb criterion in σ-τ space.

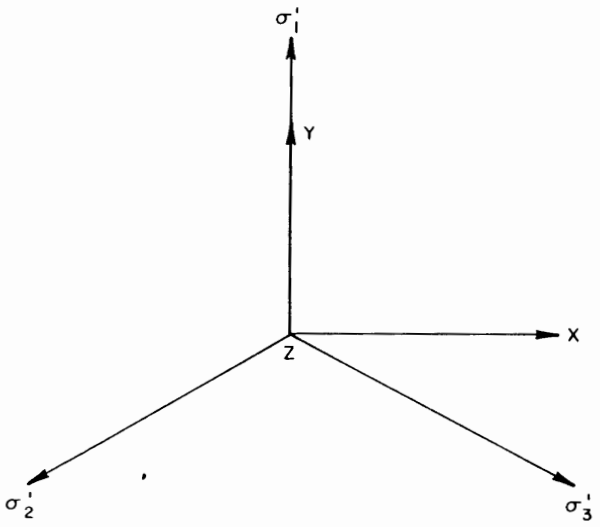

Fig. 2.11 Cartesian coordinate system on π-plane.

relationship between the principal coordinate system and the new coordinate system on the π-plane is given by:

$$\begin{Bmatrix} \sigma_1 \\ \sigma_2 \\ \sigma_3 \end{Bmatrix} = \begin{bmatrix} 0 & \frac{2}{\sqrt{6}} & \frac{1}{\sqrt{3}} \\ \frac{1}{\sqrt{2}} & -\frac{1}{\sqrt{6}} & \frac{1}{\sqrt{3}} \\ \frac{1}{\sqrt{2}} & -\frac{1}{\sqrt{6}} & \frac{1}{\sqrt{3}} \end{bmatrix} \begin{Bmatrix} X \\ Y \\ Z \end{Bmatrix} \tag{2.72}$$

Here, the maximum and minimum stresses used in Eq. (2.71) are considered to have six sets of stress conditions on the π-plane (see Fig. 2.12). As an example, for the condition $\sigma_1 > \sigma_2 > \sigma_3$, the maximum and minimum stresses are respectively σ_1 and σ_3. Therefore, Eq. (2.71) can be written as:

$$\tfrac{1}{2}(\sigma_1 - \sigma_3) \qquad \tfrac{1}{2}(\sigma_1 + \sigma_3)\sin\phi + c\cos\phi \tag{2.73}$$

Substituting Eq. (2.72) and setting $Z = 0$, Eq. (2.73) is transferred into the X,Y,Z-coordinate system and represents the partial shape of the cross-section of the Coulomb criterion on the π-plane under the condition $\sigma_1 > \sigma_2 > \sigma_3$. Namely:

$$Y = -\frac{\sqrt{3}(1 - \sin\phi)}{3 + \sin\phi} X + \frac{2\sqrt{6}\, c\cos\phi}{3 + \sin\phi} \tag{2.74}$$

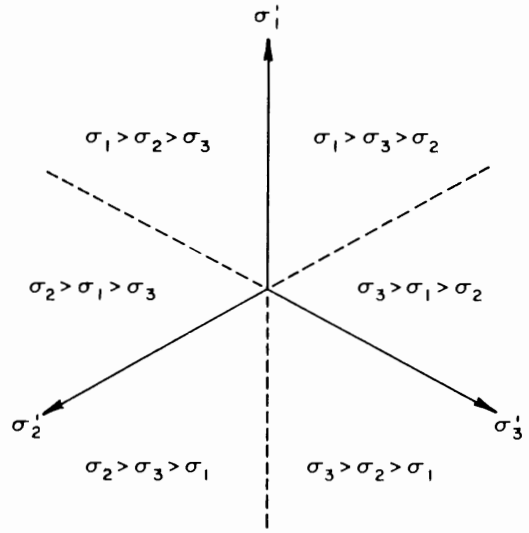

Fig. 2.12. Stress conditions on π-plane.

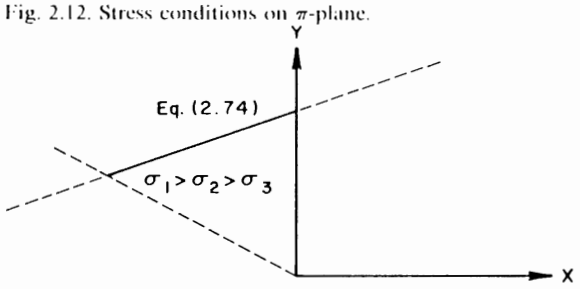

Fig. 2.13 Coulomb shape on π-plane under $\sigma_1 > \sigma_2 > \sigma_3$.

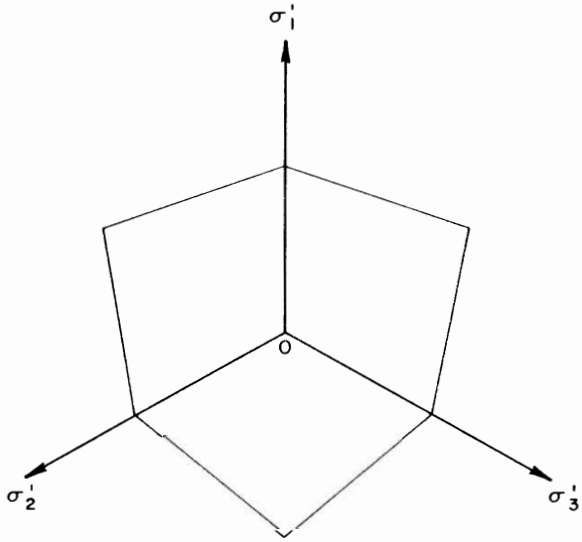

Fig. 2.14. Coulomb shape on π-plane.

This projection is shown in Fig. 2.13. A similar examination for the other five cases results in an *irregular hexagonal shape*, as shown in Fig. 2.14, describing the failure cross-section on the π-plane based on the Coulomb criterion.

2.4 STRAINS IN THREE DIMENSIONS

The analysis of strain is essentially a branch of geometry which deals with the deformation of an assemblage of particles. For the present Section, only the case of infinitesimal strain will be considered. This development is formally very similar to that of stress. Thus, there is no need to write all the details explicitly here because almost every step would be identical after the substitution of components of *strain vector* δ_i for components of stress vector T_i, of components of strain ϵ_{ij} for components of stress σ_{ij}, of components of *strain deviation* e_{ij} for stress deviation s_{ij}, and the associated word changes. Here, as before, only three-dimensional cases will be discussed. For a more detailed discussion on finite strain, the reader is referred to Chapter 8.

2.4.1 Definitions and notations

In the analysis of stress, the stress at a point is defined by the process of cutting a small element at the point and taking limits of force divided by area (Fig. 2.1). The strain at a point, however, is defined by the process of drawing line elements through the point and taking the limits of the change in length of the line element divided by its original length and also comparing the change in angle between any two line elements radiating from this point. Thus, *rigid-body rotation* or *translation* produces no changes in length or angle and therefore causes no strain.

Denote the changes in length per unit of length in the directions of the coordinate axes by ϵ_{11}, ϵ_{22}, ϵ_{33}, and the decreases in angle between the positive directions of the two coordinate line elements by $\gamma_{12} = \gamma_{21}$, $\gamma_{23} = \gamma_{32}$, and $\gamma_{13} = \gamma_{31}$. Then, for any line element at the point P in any direction n_i having the normal strain ϵ_n in the direction of n_i and shear strain ϵ_{nt} between the direction n_i and a perpendicular direction t_i (see Fig. 2.15), the corresponding Cauchy's formulas for strain have the form:

$$\epsilon_n = \delta_i n_i = (\epsilon_{ij} n_j) n_i = \epsilon_{ij} n_i n_j \tag{2.75}$$

$$\epsilon_{nt} = \delta_i t_i = (\epsilon_{ij} n_j) t_i = \epsilon_{ij} n_j t_i \tag{2.76}$$

where the strain tensor ϵ_{ij} is defined as:

$$\epsilon_{ij} = \begin{bmatrix} \epsilon_{11} & \epsilon_{12} & \epsilon_{13} \\ \epsilon_{21} & \epsilon_{22} & \epsilon_{23} \\ \epsilon_{31} & \epsilon_{32} & \epsilon_{33} \end{bmatrix} = \begin{bmatrix} \epsilon_{11} & \frac{1}{2}\gamma_{12} & \frac{1}{2}\gamma_{13} \\ \frac{1}{2}\gamma_{21} & \epsilon_{22} & \frac{1}{2}\gamma_{23} \\ \frac{1}{2}\gamma_{31} & \frac{1}{2}\gamma_{32} & \epsilon_{33} \end{bmatrix} \tag{2.77}$$

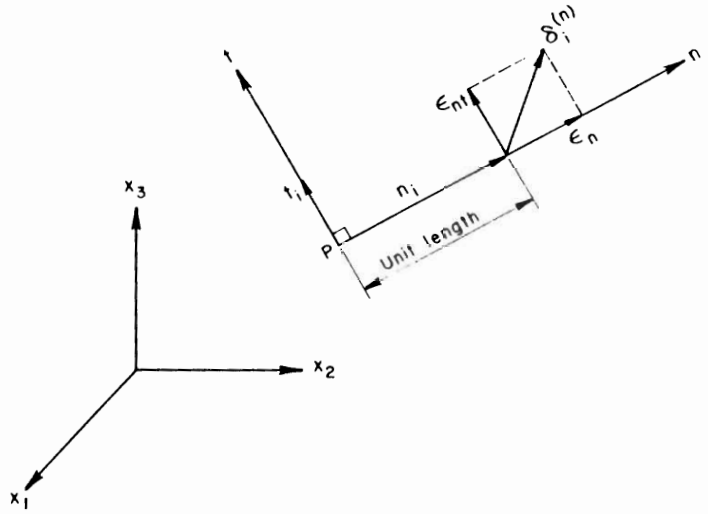

Fig. 2.15. Normal and shear strain components of strain vector at a point for arbitrary fiber n_i

Here, as in stress, the corresponding Cauchy's formula for strain vector $\delta_i = \epsilon_{ij} n_j$ has been used.

Note an important difference between the results for stress and strain; for example, $\epsilon_{12} = \frac{1}{2}\gamma_{12}$ or $\epsilon_{xx} = \frac{1}{2}\gamma_{xx}$ appears in Eq. (2.77) in place of γ_{12} or γ_{xx}, which would correspond to τ_{xy} in the engineering sense. The shear-strain components ϵ_{12}, ϵ_{23}, ϵ_{13} are called the *tensorial shear strains*, while the shear strains γ_{12}, γ_{23}, γ_{31} are called *engineering shear strains*. When the components of the strain array are chosen appropriately (ϵ_{11}, $\epsilon_{12} = \frac{1}{2}\gamma_{12}$, etc.) as in Eq. (2.77), the array has a second order tensorial character and indicates the existence of Mohr's circle construction for coordinate transformation.

The *state of strain* at a point is defined as the *totality* of all the changes in length of line elements divided by their original lengths which pass through the point and also the totality of all the changes in the angle between any pair of line elements radiating from this point. Here, as in stress, these changes can be determined by the corresponding Cauchy's formulas of Eqs. (2.75) and (2.76). Thus, the strain tensor ϵ_{ij} defines the state of strain at the point completely.

2.4.2 *Deviatoric strain*

Like the stress tensor, the strain tensor can be decomposed into two parts: a *spherical* part associated with a change in *volume* and a *deviatoric* part associated with a change in *shape (distortion)*:

$$\epsilon_{ij} = e_{ij} + \tfrac{1}{3}\epsilon_v \delta_{ij} \tag{2.78}$$

where e_{ij} is defined here as the deviatoric strain tensor which is a pure shear state, and:

$$\epsilon_v = \epsilon_{kk} = \epsilon_{11} + \epsilon_{22} + \epsilon_{33} = \epsilon_x + \epsilon_y + \epsilon_z \tag{2.79}$$

is the volume change per unit volume, or dilatation. Note that e_{ij} and ϵ_{ij} have the same principal axes.

2.4.3 Octahedral strains and principal shear strains

An *octahedral fiber* is a fiber of material which before deformation is equally inclined to the three principal strain axes 1, 2, and 3. The corresponding octahedral normal strain is given by:

$$\epsilon_{oct} = \tfrac{1}{3}(\epsilon_1 + \epsilon_2 + \epsilon_3) = \tfrac{1}{3}\epsilon_v \tag{2.80}$$

which represents the mean of the three *principal strains*, and the *engineering octahedral shear strain* is:

$$\gamma_{oct} = \tfrac{2}{3}\left[(\epsilon_{11} - \epsilon_{22})^2 + (\epsilon_{22} - \epsilon_{33})^2 + (\epsilon_{33} - \epsilon_{11})^2 + 6\epsilon_{12}^2 + 6\epsilon_{23}^2 + 6\epsilon_{31}^2\right]^{\frac{1}{2}} \tag{2.81}$$

Similar to principal shear stresses, τ_1, τ_2 and τ_3, the *engineering principal shear strains* are:

$$\gamma_1 = |\epsilon_2 - \epsilon_3|, \quad \gamma_2 = |\epsilon_1 - \epsilon_3|, \quad \text{and } \gamma_3 = |\epsilon_1 - \epsilon_2| \tag{2.82}$$

and the *maximum shear strain* is the largest value of the principal shear strains:

$$\gamma_{max} = \max(\gamma_1, \gamma_2, \gamma_3) \quad \text{or } \gamma_{max} = |\epsilon_1 - \epsilon_3|, \quad \text{for } \epsilon_1 > \epsilon_2 > \epsilon_3. \tag{2.83}$$

Example 2.10: Define the invariants of strain tensor, I_1', I_2', and I_3' and the invariants of deviatoric strain tensor, J_1', J_2', and J_3' in the manner similar to that of the stress invariants, I_1, I_2, I_3 and stress deviatoric invariants, J_1, J_2, J_3:

$$I_1' = \epsilon_{ii} = \epsilon_{11} + \epsilon_{22} + \epsilon_{33} = \epsilon_x + \epsilon_y + \epsilon_z = \epsilon_v \tag{2.84a}$$

$$I_2' = \begin{vmatrix} \epsilon_{22} & \epsilon_{23} \\ \epsilon_{32} & \epsilon_{33} \end{vmatrix} + \begin{vmatrix} \epsilon_{11} & \epsilon_{13} \\ \epsilon_{31} & \epsilon_{33} \end{vmatrix} + \begin{vmatrix} \epsilon_{11} & \epsilon_{12} \\ \epsilon_{21} & \epsilon_{22} \end{vmatrix} = \tfrac{1}{2}\left(I_1'^2 - \epsilon_{ij}\epsilon_{ji}\right) \tag{2.84b}$$

$$I_3' = \det|\epsilon_{ij}| = \tfrac{1}{6}\left(I_1'^3 - 3I_1'\epsilon_{ij}\epsilon_{ji} + 2\epsilon_{ij}\epsilon_{jk}\epsilon_{ki}\right) \tag{2.84c}$$

$$J_1' = e_{ii} = e_{11} + e_{22} + e_{33} = e_x + e_y + e_z = 0 \tag{2.84d}$$

$$J_2' = \tfrac{1}{2}e_{ij}e_{ji} = \tfrac{1}{6}\left[(\epsilon_{11} - \epsilon_{22})^2 + (\epsilon_{22} - \epsilon_{33})^2 + (\epsilon_{33} - \epsilon_{11})^2\right] + \epsilon_{12}^2 + \epsilon_{23}^2 + \epsilon_{31}^2 \tag{2.84e}$$

$$J_3' = \tfrac{1}{3}e_{ij}e_{jk}e_{ki} = \det|e_{ij}| \tag{2.84f}$$

Show that:

(a) $J_2' = \frac{1}{3}\left(I_1'^2 - 3I_2'\right)$ (2.85)

(b) $J_3' = \frac{1}{27}\left(2I_1'^3 - 9I_1'I_2' + 27I_3'\right)$ (2.86)

Solution: (a) From the definition in Eq. (2.84e):

$$J_2' = \tfrac{1}{2}e_{ij}e_{ji} = \tfrac{1}{2}\left(\epsilon_{ij} - \tfrac{1}{3}\epsilon_{kk}\delta_{ij}\right)\left(\epsilon_{ji} - \tfrac{1}{3}\epsilon_{ll}\delta_{ji}\right)$$

$$= \tfrac{1}{2}\left(\epsilon_{ij}\epsilon_{ji} - \tfrac{2}{3}\epsilon_{kk}\epsilon_{ij}\delta_{ji} + \tfrac{1}{9}\epsilon_{kk}\epsilon_{ll}\delta_{ij}\delta_{ji}\right)$$

Substituting $\delta_{ij}\delta_{ji} = 3$ and $\epsilon_{ij}\delta_{ij} = \epsilon_{ii}$:

$$J_2' = \tfrac{1}{2}\left(\epsilon_{ij}\epsilon_{ji} - \tfrac{1}{3}\epsilon_{kk}\epsilon_{ii}\right) = \tfrac{1}{3}\left[\epsilon_{kk}\epsilon_{ii} - \tfrac{3}{2}\left(\epsilon_{kk}\epsilon_{ii} - \epsilon_{ij}\epsilon_{ji}\right)\right]$$

From Eqs. (2.84a) and (2.84b), we have:

$$J_2' = \tfrac{1}{3}\left(I_1'^2 - 3I_2'\right)$$

(b) From Eq. (2.84f):

$$J_3' = \tfrac{1}{3}e_{ij}e_{jk}e_{ki} = \tfrac{1}{3}\left(\epsilon_{ij} - \tfrac{1}{3}\epsilon_{ll}\delta_{ij}\right)\left(\epsilon_{jk} - \tfrac{1}{3}\epsilon_{mm}\delta_{jk}\right)\left(\epsilon_{ki} - \tfrac{1}{3}\epsilon_{nn}\delta_{ki}\right)$$

$$= \tfrac{1}{3}\left[\epsilon_{ij}\epsilon_{jk}\epsilon_{ki} - \tfrac{1}{3}\epsilon_{ll}\left(\epsilon_{ij}\epsilon_{jk}\delta_{ki} + \epsilon_{ij}\epsilon_{ki}\delta_{jk} + \epsilon_{jk}\epsilon_{ki}\delta_{ij}\right)\right.$$

$$\left. + \tfrac{1}{9}\epsilon_{ll}\epsilon_{mm}\left(\epsilon_{ij}\delta_{jk}\delta_{ki} + \epsilon_{jk}\delta_{ij}\delta_{ki} + \epsilon_{ki}\delta_{ij}\delta_{jk}\right) - \tfrac{1}{27}\epsilon_{ll}\epsilon_{mm}\epsilon_{nn}\delta_{ij}\delta_{jk}\delta_{ki}\right]$$

$$= \tfrac{1}{3}\left[\epsilon_{ij}\epsilon_{jk}\epsilon_{ki} - \tfrac{1}{3}\epsilon_{kk}\left(\epsilon_{ij}\epsilon_{ji} + \epsilon_{ij}\epsilon_{ji} + \epsilon_{ij}\epsilon_{ij}\right) + \tfrac{1}{9}\epsilon_{ll}\epsilon_{kk}\left(\epsilon_{ii} + \epsilon_{ii} + \epsilon_{ii}\right) - \tfrac{1}{9}\epsilon_{ii}\epsilon_{ll}\epsilon_{kk}\right]$$

$$= \tfrac{1}{27}\left[2\epsilon_{ii}\epsilon_{ll}\epsilon_{kk} + 9\epsilon_{ij}\epsilon_{jk}\epsilon_{ki} - 9\epsilon_{kk}\epsilon_{ij}\epsilon_{ji}\right]$$

$$= \tfrac{1}{27}\left[2\epsilon_{ii}\epsilon_{ll}\epsilon_{kk} - \tfrac{9}{2}\epsilon_{kk}\left(\epsilon_{ii}\epsilon_{ll} - \epsilon_{ij}\epsilon_{ji}\right) + \tfrac{27}{6}\left(\epsilon_{ii}\epsilon_{ll}\epsilon_{kk} - 3\epsilon_{kk}\epsilon_{ij}\epsilon_{ji} + 2\epsilon_{ij}\epsilon_{jk}\epsilon_{ki}\right)\right]$$

Using Eqs. (2.84a), (2.84b), and (2.84c), it reduces to:

$$J_3' = \tfrac{1}{27}\left(2I_1'^3 - 9I_1'I_2' + 27I_3'\right)$$

Example 2.11: Given the strain tensor ϵ_{ij} as:

$$\epsilon_{ij} = \begin{bmatrix} 23 & -15 & 1 \\ -15 & 9 & 8 \\ 1 & 8 & 13 \end{bmatrix} \times 10^{-3}$$

find:

(a) The principal strains and the principal directions;
(b) The maximum shear strains;
(c) The octahedral strains;
(d) The normal strain component ϵ_n and the resultant shear strain component ϵ_s for a fiber element with the direction $n_i = (0.25, 0.58, 0.775)$;
(e) The deviatoric strain tensor e_{ij} and its invariants J_2' and J_3';
(f) The volumetric change per unit volume (dilation);
(g) The strain invariants I_2' and I_3'.

Solutions: (a) The *characteristic equation* $|\epsilon_{ij} - \epsilon\delta_{ij}| = 0$ for the strain tensor ϵ_{ij} is:

$$\begin{vmatrix} 23 - 10^3\epsilon & -15 & 1 \\ -15 & 9 - 10^3\epsilon & 8 \\ 1 & 8 & 13 - 10^3\epsilon \end{vmatrix} = 0$$

or

$$10^9\epsilon^3 - 45 \times 10^6\epsilon^2 + 333 \times 10^3\epsilon + 1955 = 0$$

Solving the cubic equation for the principal strains, we obtain:

$$\epsilon_1 = 0.0332, \quad \epsilon_2 = 0.01558, \quad \epsilon_3 = -0.00378$$

The principal directions are then obtained as follows: for $\epsilon_1 = 0.0332$:

$$\begin{aligned} (0.023 - 0.0332)n_1^{(1)} - 0.015n_2^{(1)} + 0.001n_3^{(1)} &= 0 \\ -0.015n_1^{(1)} + (0.009 - 0.0332)n_2^{(1)} + 0.008n_3^{(1)} &= 0 \\ 0.001n_1^{(1)} + 0.008n_2^{(1)} + (0.013 - 0.0332)n_3^{(1)} &= 0 \end{aligned}$$

Since one of the three simultaneous equations is not independent, we use the directional cosine condition $n_1^2 + n_2^2 + n_3^2 = 1$, to find the components of the unit vector $n_i^{(1)}$ for the principal direction associated with the principal value $\epsilon_1 = 0.0332$:

$$n_i^{(1)} \quad (+0.8071, +0.5611, +0.1840)$$

Similarly, we can find the other principal directions associated with the principal values ϵ_2 and ϵ_3:

$$n_i^{(2)} \quad (+0.3712, \pm 0.2433, \pm 0.8961)$$

$$n_i^{(3)} \quad (+0.4583, \pm 0.7913, +0.4047)$$

(b) The maximum shear strain is:

$$\gamma_{max} = \epsilon_{max} - \epsilon_{min} = 0.0332 - (-0.00378) = 0.03698$$

(c) The octahedral normal and shear strains, ϵ_{oct} and γ_{oct} are calculated from Eqs. (2.80) and (2.81):

$$\epsilon_{oct} = \tfrac{1}{3}I_1' = \tfrac{1}{3}(0.023 + 0.009 + 0.013) = 0.015$$

$$\gamma_{oct} = \tfrac{2}{3}\left[(\epsilon_{11} - \epsilon_{22})^2 + (\epsilon_{22} - \epsilon_{33})^2 + (\epsilon_{33} - \epsilon_{11})^2 + 6(\epsilon_{12}^2 + \epsilon_{23}^2 + \epsilon_{31}^2)\right]^{\frac{1}{2}} = 0.0302$$

(d) The components of strain vector δ_i associated with the fiber element whose direction is $n_i = (0.25, 0.58, 0.775)$ are:

$$\delta_i = \epsilon_{ij} n_j = (-0.002175, 0.00767, 0.014965)$$

Therefore, the normal strain component ϵ_n of the strain vector δ_i is:

$$\epsilon_n = \delta_i n_i = -0.002175 \times 0.25 + 0.00767 \times 0.58 + 0.014965 \times 0.775 = 0.0155$$

The components of shear vector ϵ_s associated with the strain vector δ_i are:

$$\epsilon_s = \delta_i - \epsilon_n n_i = (-0.00605, -0.00132, 0.00295)$$

from which the magnitude of the resultant shear strain can be determined:

$$|\epsilon_s| = \sqrt{(-0.00605)^2 + (-0.00132)^2 + (0.00295)^2} = 0.00686$$

(e) The deviatoric strain tensor e_{ij} is:

$$e_{ij} = \epsilon_{ij} - \tfrac{1}{3}\epsilon_{kk}\delta_{ij} = \begin{bmatrix} 23-15 & -15 & 1 \\ -15 & 9-15 & 8 \\ 1 & 8 & 13-15 \end{bmatrix} \times 10^{-3}$$

$$= \begin{bmatrix} 8 & -15 & 1 \\ -15 & -6 & 8 \\ 1 & 8 & -2 \end{bmatrix} \times 10^{-3}$$

Using e_{ij} above, the second and third deviatoric strain invariants J_2' and J_3' are:

$$J_2' = -\begin{vmatrix} -0.006 & 0.008 \\ 0.008 & -0.002 \end{vmatrix} - \begin{vmatrix} 0.008 & 0.001 \\ 0.001 & -0.002 \end{vmatrix} - \begin{vmatrix} 0.008 & -0.015 \\ -0.015 & -0.006 \end{vmatrix}$$

$$= 342 \times 10^{-6}$$

$$J_3' = \det|e_{ij}| = 0.008\begin{vmatrix} -0.006 & 0.008 \\ 0.008 & -0.002 \end{vmatrix} + 0.015\begin{vmatrix} -0.015 & 0.008 \\ 0.001 & -0.002 \end{vmatrix}$$

$$+ 0.001\begin{vmatrix} -0.015 & -0.006 \\ 0.001 & 0.008 \end{vmatrix} = -2 \times 10^{-7}$$

(f) The volumetric change per unit volume ϵ_v is:

$$\epsilon_v = \epsilon_{ii} = I_1' = 45 \times 10^{-3}$$

(g) The second and third strain invariants, I_2' and I_3' are written in terms of principal strains as:

$$I_2' = \begin{vmatrix} \epsilon_2 & 0 \\ 0 & \epsilon_3 \end{vmatrix} + \begin{vmatrix} \epsilon_1 & 0 \\ 0 & \epsilon_3 \end{vmatrix} + \begin{vmatrix} \epsilon_1 & 0 \\ 0 & \epsilon_2 \end{vmatrix} = \epsilon_2\epsilon_3 + \epsilon_1\epsilon_3 + \epsilon_1\epsilon_2$$

$$= (0.01558)(-0.00378) + (0.0332)(-0.00378) + (0.0332)(0.01558)$$

$$= 3.33 \times 10^{-4}$$

$$I_3' = \epsilon_1\epsilon_2\epsilon_3 = (0.0332)(0.01558)(-0.00378) = -1.955 \times 10^{-6}$$

2.5 EQUATIONS OF SOLID MECHANICS

The word "*mechanics*" implies a mathematical formulation of the problem and of the basic equations to be used in its solution. In the continuum theory of soil mechanics that includes the mathematical theory of elasticity, plasticity, and viscosity, the following three basic sets of equations must be applied:

1. Equations of *equilibrium* of motion for a static or dynamic analysis, respectively.
2. Conditions of *geometry* or the *compatibility* of strains and displacements.
3. Material *constitutive* laws or *stress-strain* relations.

The initial and boundary conditions on forces and displacements which also must be satisfied in a particular problem are included for brevity under items (1) and (2). A brief discussion of each of the items listed above is given as follows.

2.5.1 Equations of equilibrium (or motion)

From consideration of statics (or dynamics), one can relate the components of the stress fields, σ_{ij}, in a body to the components of body forces, F_i (forces per unit volume), and external surface forces, T_i (forces per unit area), acting on the boundaries of the body. Stress fields which satisfy these statical (or dynamical) conditions are said to be *statically* (or *dynamically*) *admissible*. For example, in the static analysis of the body shown in Fig. 2.16a, a statically admissible set of stresses σ_{ij}, and external surface and body forces, T_i and F_i, respectively, must satisfy the following equilibrium equations:

At surface points: $$T_i = \sigma_{ji} n_j \tag{2.87}$$

At interior points: $$\sigma_{ji,j} + F_i = 0 \tag{2.88}$$

$$\sigma_{ji} = \sigma_{ij} \tag{2.89}$$

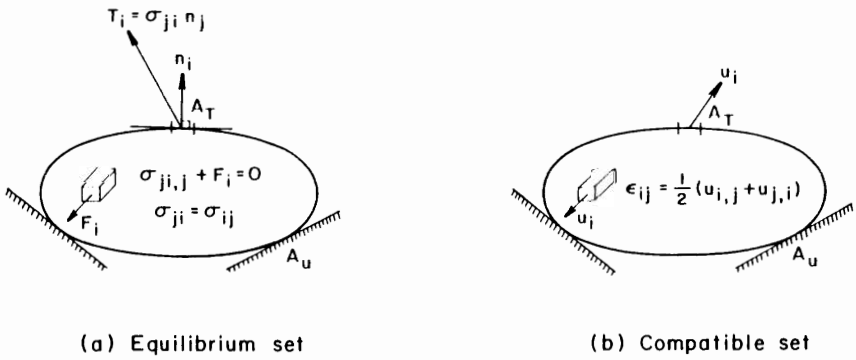

(a) Equilibrium set (b) Compatible set

Fig. 2.16. Conditions of equilibrium and compatibility (geometry) in the static analysis of a solid mechanics problem.

where n_i is the outward unit normal vector to a surface element on which T_i is acting, as shown in Fig. 2.16a. In the above equations, summation convention for repeated indices is employed, and a comma in the term denotes partial differentiation with respect to the coordinate axes (space variables), x_i, with $i = 1, 2, 3$.

As can easily be seen from Eqs. (2.88), only three equations of equilibrium (or motion) are obtained at any point in the body for prescribed body forces F_i. Thus, we have three equilibrium equations with six unknowns, namely the stress components σ_{ij} at a given point in the body. Here, an equilibrium set is merely a set and by no means a unique one. In general, an infinite number of stress states can be found which will satisfy the stress boundary conditions of Eq. (2.87) and the equilibrium equations (2.88) and (2.89).

2.5.2 Geometric (compatibility) conditions

Compatibility or geometry conditions are derived from kinematic considerations which relate the components of a strain field, ϵ_{ij}, to the components of a displacement field, u_i. It may also be necessary to impose the *condition of compatibility (integrability)* of strains and displacements in order to ensure that these strain-displacement relations are integrable for a prescribed strain field. A set of displacements, u_i, and strains, ϵ_{ij}, which satisfies these geometry conditions in addition to the imposed displacement boundary conditions is called a *kinematically admissible* set or simply a *compatible* set. Referring to Fig. 2.16b, kinematic considerations lead to the following conditions for small deformations:

Strain-displacement relations:

$$\epsilon_{ij} = \tfrac{1}{2}(u_{i,j} + u_{j,i}) \tag{2.90}$$

Compatibility (integrability) conditions:

$$\epsilon_{ij,kl} + \epsilon_{kl,ij} - \epsilon_{ik,jl} - \epsilon_{jl,ik} = 0 \tag{2.91}$$

Compatibility conditions are the geometrical relationship that strain tensor ϵ_{ij} at each material point must satisfy in order to ensure a continuous deformation for the continuum as a whole. These conditions consist of 81 equations, however, only the following six equations are independent to each other, if the symmetry of strain tensor, $\epsilon_{ij} = \epsilon_{ji}$, is taken into consideration:

$$
\begin{aligned}
&\frac{\partial^2 \epsilon_x}{\partial y^2} + \frac{\partial^2 \epsilon_y}{\partial x^2} = 2\frac{\partial^2 \epsilon_{xy}}{\partial x \partial y} \\
&\frac{\partial^2 \epsilon_y}{\partial z^2} + \frac{\partial^2 \epsilon_z}{\partial y^2} = 2\frac{\partial^2 \epsilon_{yz}}{\partial y \partial z} \\
&\frac{\partial^2 \epsilon_z}{\partial x^2} + \frac{\partial^2 \epsilon_x}{\partial z^2} = 2\frac{\partial^2 \epsilon_{zx}}{\partial x \partial z} \\
&\frac{\partial}{\partial x}\left(-\frac{\partial \epsilon_{yz}}{\partial x} + \frac{\partial \epsilon_{zx}}{\partial y} + \frac{\partial \epsilon_{xy}}{\partial z}\right) = \frac{\partial^2 \epsilon_x}{\partial y \partial z} \\
&\frac{\partial}{\partial y}\left(-\frac{\partial \epsilon_{zx}}{\partial y} + \frac{\partial \epsilon_{xy}}{\partial z} + \frac{\partial \epsilon_{yz}}{\partial x}\right) = \frac{\partial^2 \epsilon_y}{\partial z \partial x} \\
&\frac{\partial}{\partial z}\left(-\frac{\partial \epsilon_{xy}}{\partial z} + \frac{\partial \epsilon_{yz}}{\partial x} + \frac{\partial \epsilon_{zx}}{\partial y}\right) = \frac{\partial^2 \epsilon_z}{\partial x \partial y}
\end{aligned}
\tag{2.92}
$$

Therefore, a compatible set of displacements, u_i, and strains, ϵ_{ij}, must satisfy Eqs. (2.90) and (2.91) together with the prescribed displacement boundary conditions. In many practical applications such as the popular finite-element method, a displacement field u_i is usually assumed. In such cases, the corresponding compatible strain components, ϵ_{ij}, can always be derived directly from the assumed displacement field using Eq. (2.90). This compatible set of strains and displacements is, of course, only a set among many other possible sets of strain and displacement fields.

It is important to note that the strain integrability conditions given in Eq. (2.91), are needed only when the displacements u_i, are not explicity retained as unknowns in the formulation of a problem. For instance, for solutions in the classical theory of elasticity, stress functions are frequently introduced as the only unknown functions (e.g., Airy's stress function in the two-dimensional elasticity). In such cases, Eq. (2.91) must be imposed on the strain field to ensure the existence of a continuous single-valued displacement field. In most practical problems, the displacements are generally taken explicitly as unknowns in the formulation (e.g., in the finite-element technique for numerical solutions). Then, the integrability conditions of Eq. (2.91) are not needed, and only Eq. (2.90) is used to derive the strains from the displacements. In such cases, there are nine independent unknowns (namely, six stress components, σ_{ij}, plus three displacement components, u_i, while strains are expressed in terms of the displacements). On the other hand, only three equations of equilibrium (or motion) are available (for example, Eq. (2.88) in the static analysis).

Thus, six additional equations are needed to complete the formulation of the problem. These additional equations are furnished by the constitutive or stress-strain relations of the material.

Example 2.12: Determine the relations among the constants a_0, a_1, b_0, b_1, c_0, c_1, and c_2 so that the following equations become a possible state of strain:

$$\epsilon_x = a_0 + a_1(x^2 + y^2) + (x^4 + y^4)$$

$$\epsilon_y = b_0 + b_1(x^2 + y^2) + (x^4 + y^4)$$

$$\gamma_{xy} = c_0 + c_1 xy(x^2 + y^2 + c_2)$$

$$\epsilon_z = \gamma_{yz} = \gamma_{xz} = 0$$

Solution: Strain functions are substituted into the compatibility equations (2.92). The strain functions satisfy automatically all the compatibility conditions except the first one, irrespective of the value of the coefficients. Therefore, if the functions satisfy the first condition the strain functions become admissible. The first condition of compatibility is:

$$\frac{\partial^2 \epsilon_x}{\partial y^2} + \frac{\partial^2 \epsilon_y}{\partial x^2} = 2\frac{\partial^2 \epsilon_{xy}}{\partial x \partial y}$$

Substituting the functions ϵ_x, ϵ_y, and γ_{xy}, we have:

$$2a_1 + 2b_1 + 12x^2 + 12y^2 = 3c_1x^2 + 3c_1y^2 + c_1c_2$$

or

$$(3c_1 - 12)x^2 + (3c_1 - 12)y^2 = 2a_1 + 2b_1 - c_1c_2$$

Since this equation must be satisfied for any values of x and y, it follows that:

$$3c_1 - 12 = 0$$

$$2a_1 + 2b_1 - c_1c_2 = 0$$

or

$$c_1 = 4$$

$$c_2 = \tfrac{1}{2}(a_1 + b_1)$$

It should be noted that the values of a_0, b_0, and c_0 can be arbitrarily taken.

2.5.3 *Constitutive relations*

Since both static (dynamic) and kinematic (or geometric) conditions are treated independently and no relating conditions are introduced, they are valid for elastic as well as inelastic or plastic materials. The differentiating feature of various material behaviors is accounted for in the *material constitutive laws*. These laws give the relations between stress components σ_{ij} and strain components ϵ_{ij} at any point in the body. They may be simple or extremely complex depending upon the material of the body and the conditions to which it has been subjected.

Once the material constitutive law is established, the general formulation for the solution of a solid mechanics problem can be completed. The six stress components, σ_{ij}, six strain components, ϵ_{ij}, and three displacement components, u_i, are connected by the three equilibrium equations, six kinematic equations, and six constitutive equations. These 15 unknown quantities of stresses, strains, and displacements inside a body are determined from the system of 15 equations expressing laws of nature. The interrelationships of variables (F_i, T_i, σ_{ij}, ϵ_{ij} and u_i) encountered in a general formulation are shown schematically in Fig. 2.17 in the case of static analysis.

The constitutive relations for a particular material are determined experimentally and they may involve measurable physical quantities other than stresses and strains, such as temperature and time, or internal parameters which cannot be measured directly. The effects of such internal parameters on the stress-strain behavior of the material can often be more conveniently expressed in terms of history of stress and strain, or memory of past mechanical events inherent in the material.

The constitutive relationship for a material depends on many factors, including the homogeneity, isotropy and continuity of the body material, its reaction to

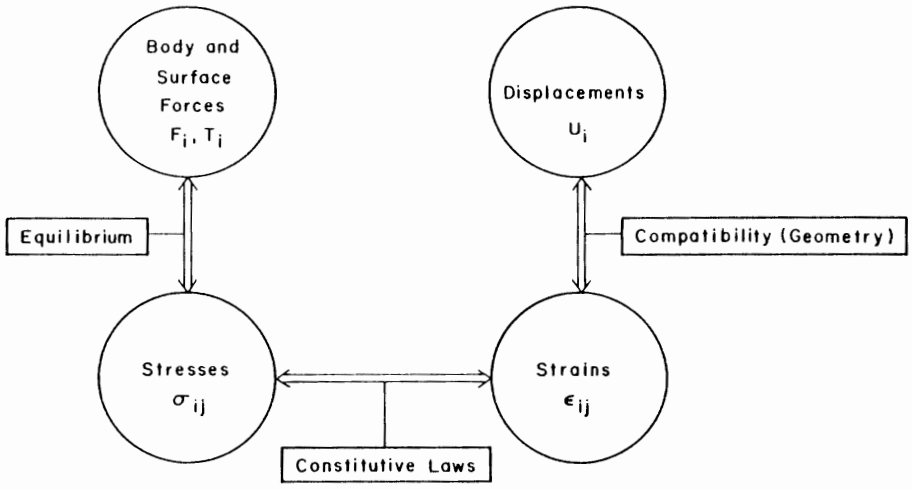

Fig. 2.17. Interrelationships of variables in the solution of a static solid mechanics problem

loading over a period and the rate and magnitude of loading. The behavior of an actual material varies enormously with temperature, confining pressure, rate of strain, and other factors. However, under certain limited conditions, it is possible to idealize the soils as elastic, plastic, or viscous materials for the purpose of stress and strain analysis. With the present state of development of *finite-element* computer programs, we can confidently say that an almost unlimited range of solutions in soil mechanics can now be obtained. They are not limited to linear elastic problems, but can be extended to include various kinds of problems with material and geometric nonlinearities (Chen, 1982).

2.6 SUMMARY

In soil mechanics, as in continuum mechanics, the basic quantities are stress and strain. The *stress* has the dimension of force per unit area, a quantity expressing the intensity of force induced in the soil body. The *strain* is a dimensionless quantity expressing deformation of soil in terms of the original dimension. The relationship between stress and strain in an idealized material forms the basis of the mathematical theories of *elasticity*, *plasticity* and *viscosity*. These theories can in turn be applied to real soils to estimate stress, strain, or displacement of a soil body subjected to a specified force field. The *nonlinear analysis* of soils based on the theories of elasticity and plasticity is the subject of the present book.

An understanding of stress and strain and the principles of stress and strain analysis in three dimensions is therefore essential to the engineer analyzing structures in soil. These principles are developed and summarized briefly in the first two parts of this Chapter (Sections 2.3 and 2.4). In three dimensions, we show that: (1) Cauchy's formulas in index notation are simple to derive and easy to use; (2) the decomposition of a state of stress or a state of strain at a material point into the hydrostatic (or volumetric) part and the deviatoric (or shear) parts provides a clear physical picture of these basic quantities; and (3) the interrelationships between the hydrostatic (or volumetric) part with the first invariant of stress (or strain) tensor, and the deviatoric (or shear) part with the second invariant of stress (or strain) deviatoric tensor give the necessary link between the physical and geometrical interpretations of these basic quantities of stress and strain at a material point. The Lode angle, that is somewhat directly related to the third invariant of deviatoric stress tensor, is also an important invariant enabling one to locate the stress point on the deviatoric plane.

The analysis of stress and strain at a point holds for all materials, since each of these quantities is treated independently, the former based on equilibrium consideration while the latter is based on geometrical consideration. These two quantities are not related in any way. The mechanical properties of a soil are governed by the stress-strain relationship. For the mathematical theories of elasticity, plasticity, and viscosity, the real materials are idealized as elastic, plastic, or viscous materials for

the purposes of stress/strain analysis, thus providing a direct stress-strain relationship, a strain-time, stress-time relationship or a combination of the two or three.

This stress-strain relationship for a material under general loading and environmental conditions is generally called the *constitutive relation* or *equation*. The six stress components σ_{ij}, six strain components ϵ_{ij}, and three displacement components u_i are connected by the three equilibrium equations (2.88), six compatibility equations (2.91), and six constitutive equations. These 15 unknown quantities of stresses, strains, and displacements inside a body are determined from the system of 15 equations of solid mechanics expressing laws of nature. These equations are discussed briefly in the last part of this Chapter (Section 2.5). Further developments of elasticity- and plasticity-based constitutive relations for soils will be presented in details in the following four Chapters.

REFERENCES

Chen, W.F., 1982. Plasticity in Reinforced Concrete. McGraw-Hill, New York, NY, 474 pp.

Chen, W.F. and Saleeb, A.F., 1982. Constitutive Equations for Engineering Materials, Vol. 1 Elasticity and Modeling. Wiley-Interscience, New York, NY, 580 pp.

Timoshenko, S.P. and Goodier, J.N., 1951. Theory of Elasticity. McGraw-Hill, New York, NY, 567 pp.

Part II

MATERIAL MODELING—BASIC CONCEPTS

Chapter 3

ELASTICITY AND MODELING

3.1 INTRODUCTION

As mentioned in the previous Chapter, soil mechanics along with all other branches of mechanics of solids requires the consideration of geometry or compatibility and of equilibrium or dynamics. The essential set of equations that differentiate the soil from other solids is the relation between stress and strain. The behavior of soils is very complicated. Therefore, any attempt to incorporate various features of soil properties in a single mathematical model is not likely to be successful. Even if such a model could be constructed, it would be far too complex to serve as the basis for the solution of practical geotechnical engineering problems. Simplifications and idealizations are essential in order to produce simpler models that can represent those properties that are essential to the considered problem. Thus, any such simpler models should not be expected to be valid over a wide range of conditions.

With the present state of development of computer programs, such simple but inadequate material models are often one of the major factors in limiting the capability of stress analysis. This is especially true in soil mechanics where generally accepted constitutive relations for soils under triaxial states of stress do not exist. Nevertheless, there exists a large variety of models which have been proposed in recent years to characterize the stress-strain and failure behavior of soil medium. All these models have certain inherent advantages and limitations which depend to a large degree on their particular application.

This book attempts to evaluate critically these existing soil constitutive relations in general and plasticity models in particular, within the context of their use in the numerical analysis of geotechnical engineering problems, to determine the range of applicability, relative merits, and limitations and to identify the specific need for further modifications and developments.

The evaluation of these models is in general based on the following three considerations:

1. Theoretical evaluation of the models with respect to the basic principles of continuum mechanics to ascertain their consistency with the theoretical requirements of continuity, stability and uniqueness.
2. Experimental evaluation of the models with respect to their suitability to fit experimental data from a variety of available test, and the ease of the determination of the material parameters from standard test data.
3. Numerical and computational evaluation of the models with respect to the facility with which they can be implemented in computer calculations. Particular

emphasis will be placed on the implementation of these models in nonlinear incremental finite-element computer codes for obtaining solutions of geotechnical problems under general stress conditions including monotonic as well as cyclic loadings.

The basis of model evaluation described above will provide the balance between the requirements of rigor from the continuum mechanics viewpoint, the requirements of realistic representation of soil behavior from the experimental-testing viewpoint, as well as the requirements for simplicity in application from the computation viewpoint.

The scope covered in this book is limited to time-independent soil models based on the *continuum mechanics approach*. Specifically, various types of geotechnical material models based on the theories of elasticity and plasticity are considered.

In this Chapter, various elasticity-based material models are reviewed briefly with respect to their advantages and limitations when they are applied to numerical stress analyses in geotechnical problems. Subsequently, their stress-strain relations are presented in some details for a direct use in finite-element applications.

3.2 ELASTIC MODELS IN GEOTECHNICAL ENGINEERING

Elastic material models based on the theory of *continuum mechanics* can be generally classified as linear elastic (generalized Hooke's law), Cauchy elastic, hyperelastic, and hypoelastic models. These models are described briefly in what follows.

3.2.1 Linear elastic model (generalized Hooke's law)

The *linear elastic model* is the oldest and simplest model which gives a unique and linear relation between the state of stress and strain, and it can be classified further as isotropic, transversely isotropic, orthotropic or anisotropic depending on the materials assumed in the analysis (see Section 3.4). The most general form of linear stress-strain relations for an elastic material can be represented by the *generalized Hooke's law* as:

$$\sigma_{ij} = B_{ij} + C_{ijkl}\epsilon_{kl} \tag{3.1}$$

where B_{ij} are components of initial stress tensor corresponding to the initial strain free state and C_{ijkl} is a fourth-order tensor of elastic material constants. As implied by the elastic description in Chapter 1, materials described by this relation return to their original undeformed configuration upon unloading. Thus, this type of linear relationship has a very limited range of applicability to geological materials.

For the stress level not very different from the in situ condition, and significantly below failure, stress distributions and immediate settlements may be predicted by this elastic procedure. However, the limitation of this model is that a proper

selection of the elastic moduli is not an obvious one. A reasonable solution in an analysis with this model depends to a large extent on the experience of the user. To overcome the material nonlinearity, a simple modification of the linear elastic model to a *piecewise linear elastic model* may be considered. This modification assumes that the stress-strain curve can be represented by a piecewise linear relationship. As a result, the conventional linear elastic model is modified with different material constants for each linear interval. Because of its simplicity, the linear elastic model has formed the basis of various nonlinear elastic stress-strain relations used in engineering practice.

3.2.2 *Cauchy elastic model*

For a *Cauchy elastic material*, the current state of stress, σ_{ij}, depends *only* on the current state of deformation, ϵ_{ij}; that is, stress is a function of strain (or vice versa). The constitutive relation of this material has the general form:

$$\sigma_{ij} = F_{ij}(\epsilon_{kl}) \tag{3.2}$$

where F_{ij} is the elastic response function of the material. The elastic response function F_{ij} for an *isotropic* material, for example, can be expressed in a polynomial form of the strain tensor ϵ_{ij}, that is:

$$F_{ij} = a_0\delta_{ij} + a_1\epsilon_{ij} + a_2\epsilon_{ik}\epsilon_{kj} + a_3\epsilon_{ik}\epsilon_{kl}\epsilon_{lj} + \ldots \tag{3.3}$$

where a_0, a_1, a_2, a_3, ... are coefficients. Employing the *Cayley-Hamilton Theorem* which implies that any second-order tensor satisfies its own characteristic equation [see Eq. (2.29)], Eq. (3.2) can therefore be reduced to:

$$\sigma_{ij} = A_0\delta_{ij} + A_1\epsilon_{ij} + A_2\epsilon_{ik}\epsilon_{kj} \tag{3.4}$$

where A_0, A_1, and A_2 are elastic response coefficients which are polynomial functions of strain invariants, I_1', I_2', and I_3'. Alternatively, the strain tensor ϵ_{ij} can be expressed in terms of the stress tensor σ_{ij}, that is:

$$\epsilon_{ij} = B_0\delta_{ij} + B_1\sigma_{ij} + B_2\sigma_{ik}\sigma_{kj} \tag{3.5}$$

where B_0, B_1, and B_2 are elastic response coefficients which are polynomial functions of stress invariants, I_1, I_2, and I_3. Using the transformation law of a second-order tensor, it can be shown that Eq. (3.4) or Eq. (3.5) is of form invariant with respect to rigid motion of a spatial coordinate system, i.e.:

$$\begin{aligned}\sigma'_{mn} &= l_{mi}l_{nj}\sigma_{ij} = A_0 l_{mi}l_{nj}\delta_{ij} + A_1 l_{mi}l_{nj}\epsilon_{ij} + A_2 l_{mi}l_{nj}\epsilon_{ik}\epsilon_{kj} \\ &= A_0\delta'_{mn} + A_1\epsilon'_{mn} + A_2\epsilon'_{mk}\epsilon'_{kn}\end{aligned} \tag{3.6}$$

or

$$\epsilon'_{mn} - l_{mi}l_{nj}\epsilon_{ij} = B_0 l_{mi}l_{nj}\delta_{ij} + B_1 l_{mi}l_{nj}\sigma_{ij} + B_2 l_{mi}l_{nj}\sigma_{ik}\sigma_{kj}$$

$$= B_0\delta'_{mn} + B_1\sigma'_{mn} + B_2\sigma'_{mk}\sigma'_{kn} \tag{3.7}$$

where σ'_{mn} or ϵ'_{mn} is referred to the primed (rotated) coordinate system.

The behavior of such models described above is both *reversible* and *path-independent* in the sense that stresses are uniquely determined by the current state of strain (or vice versa). In general, although stresses are uniquely determined from strains (or vice versa), the converse is not necessarily true. Furthermore, reversibility and path-independency of the *strain energy* and *complementary energy density functions*, $W(\epsilon_{ij})$ and $\Omega(\sigma_{ij})$ respectively, are not generally guaranteed. In fact, the Cauchy type of elastic models may generate energy for certain loading-unloading cycles (see, for example, Chen and Saleeb, 1982). That is, the model may violate the law of thermodynamics, which is not acceptable on physical grounds. This has led to the consideration of the secant type of formulation (for example, *hyperelastic model*) discussed in the next Section.

In spite of these theoretical reservations, some simplified versions of nonlinear Cauchy elastic constitutive models have been proposed for practical use in soil mechanics. For example, the simplest approach to formulate such nonlinear models is to simply replace the elastic constant in the linear stress-strain relations with secant moduli dependent on the stress and/or strain invariant. Nonlinear models of this type have been discussed in the papers by Boyce, 1980; Girijavallabhan and Reese, 1968; Hardin and Drnevich, 1972; and Katona et al., 1976; among others. These models are mathematically and conceptually very simple. The models account for two of the main characteristics of soil behavior; *nonlinearity* and the *dependence* on the hydrostatic stress.

The main disadvantage of the models is that they describe a path-independent behavior. Therefore, their applications are primarily directed toward monotonic or proportional loading regimes. For arbitrarily assumed functions for the secant

TABLE 3.1

Modifications of Cauchy elastic models

Advantages	Limitations
conceptually and mathematically simple	path-independent, reversible
	– no coupling between volumetric and deviatoric responses
easy to determine the constants and wide data base is established for many parameters	
	for arbitrary functions of the moduli, energy generation may occur in certain stress cycles

moduli, there is no guarantee that the energy functions W and Ω will be path-independent and energy generation may occur in certain stress cycles, which is physically not acceptable.

The advantages and limitations of Cauchy elastic models based on modifications of the linear elasticity are summarized in Table 3.1.

3.2.3 *Hyperelastic model*

To the contrary of the engineering or empirical approach described in previous Section, the *classical hyperelastic model*, which will not generate energy over any load-unload stress cycles, provides a more rational approach in formulating secant stress-strain relations for soils.

The development of constitutive equation for this type of material is based on *Green's method* which employs the two fundamental laws of mechanics: the first law of thermodynamics and the law of kinetic energy. Therefore, the hyperelastic model is sometimes called *Green elastic model* which assumes, to begin with, the existence of a *strain energy density function* W, or a *complementary energy density function* Ω.

The first law of thermodynamics can be expressed in mathematical form:

$$\delta W_e + \delta \tilde{Q} = \delta \tilde{T} + \delta U \tag{3.8}$$

where δW_e is a change in work done onto the system by external agency, $\delta \tilde{Q}$ a change in heat flow into the system, $\delta \tilde{T}$ a change in kinetic energy, δU a change in internal energy.

On the other hand, the law of kinetic energy can be written as:

$$\delta W_e + \delta W_i = \delta \tilde{T} \tag{3.9}$$

where δW_i is a change in work done inside the system by internal agency. Substitution of δW_e $\delta \tilde{T}$ δW_i from Eq. (3.9) into Eq. (3.8) leads to:

$$\delta W_i \quad \delta \tilde{Q} \quad \delta U \tag{3.10}$$

If we assume that the heat flow $\delta \tilde{Q}$ is zero, we have:

$$\delta W_i = -\delta U \tag{3.11}$$

Considering the case that a material with volume V and surface area S undergoes an infinitesimal displacement δu_i, the variation in the work by the external traction force T_i $\sigma_{ji} n_j$ and body force F_i can be expressed as:

$$\delta W_e \quad \int_S \sigma_{ji} n_j \delta u_i \, dS + \int_V F_i \delta u_i \, dV \tag{3.12}$$

where n_j are directional cosines of the outward vector normal to the surface S. Employing the *Divergence Theorem*, the first term in Eq. (3.12) can be transformed into a form for volume integral, that is:

$$\int_S \sigma_{ji} n_j \delta u_i \, dS = \int_V (\sigma_{ji} \delta u_i)_{,j} \, dV = \int_V \sigma_{ji} (\delta u_i)_{,j} \, dV + \int_V \sigma_{ji,j} \delta u_i \, dV \tag{3.13}$$

where a subscript j after a comma represents a derivative with respect to the coordinate axis x_j. Substituting Eq. (3.13) into Eq. (3.12), we have:

$$\delta W_e = \int_V \left[\sigma_{ji} (\delta u_i)_{,j} + (\sigma_{ji,j} + F_i) \delta u_i \right] dV \tag{3.14}$$

Since $\sigma_{ji,j} + F_i = 0$ from the equilibrium condition, Eq. (3.14) becomes:

$$\delta W_e = \int_V \sigma_{ji} (\delta u_i)_{,j} \, dV \tag{3.15}$$

The infinitesimal displacement gradient $(\delta u_i)_{,j}$ can be written as:

$$(\delta u_i)_{,j} = \tfrac{1}{2} \left[(\delta u_i)_{,j} + (\delta u_j)_{,i} \right] + \tfrac{1}{2} \left[(\delta u_i)_{,j} - (\delta u_j)_{,i} \right] \tag{3.16}$$

where the first and second terms in Eq. (3.16) are respectively symmetric and skew-symmetric tensors. Therefore, substitution of Eq. (3.16) into Eq. (3.15) yields:

$$\delta W_e = \int_V \tfrac{1}{2} \sigma_{ji} \left[(\delta u_i)_{,j} + (\delta u_j)_{,i} \right] dV \tag{3.17}$$

Using the strain-displacement relations in Eq. (2.90), Eq. (3.17) can be represented as:

$$\delta W_e = \int_V \sigma_{ji} \delta \epsilon_{ij} \, dV \tag{3.18}$$

where $\delta \epsilon_{ij}$ is a change in strain tensor ϵ_{ij}. From $\delta \tilde{Q} = 0$ and the assumption that $\delta \tilde{T} = 0$ during an infinitesimal displacement, Eq. (3.8) can be written as:

$$\delta W_e = \delta U \tag{3.19}$$

Denoting the internal energy per unit volume (internal energy density function or strain energy density function) by W, δU associated with the material volume V can be expressed as:

$$\delta U = \int_V \delta W \, dV \tag{3.20}$$

From Eqs. (3.18), (3.19), and (3.20), we have:

$$\int_V \sigma_{ij}\delta\epsilon_{ij}\,dV = \int_V \delta W\,dV \tag{3.21}$$

which leads to:

$$\delta W = \sigma_{ij}\delta\epsilon_{ij} \tag{3.22}$$

Since the internal (or strain) energy density function W depends on the strain components ϵ_{ij}, the variation δW can be expressed in terms of $\delta\epsilon_{ij}$, i.e.:

$$\delta W = \frac{\partial W}{\partial \epsilon_{ij}}\delta\epsilon_{ij} \tag{3.23}$$

Comparing Eqs. (3.22) and (3.23), the stress tensor σ_{ij} ($= \sigma_{ji}$) is given by:

$$\sigma_{ij} = \frac{\partial W}{\partial \epsilon_{ij}} \tag{3.24}$$

Equation (3.24) is a basis for the Green elastic model. For an *isotropic* material, the strain energy density function W is a function of any three independent invariants of strain tensor ϵ_{ij}. If we choose the invariants given by:

$$I_1' = \epsilon_{ii} \tag{3.25a}$$

$$I_2' = \tfrac{1}{2}\epsilon_{ij}\epsilon_{ji} \tag{3.25b}$$

$$I_3' = \tfrac{1}{3}\epsilon_{ij}\epsilon_{jk}\epsilon_{ki} \tag{3.25c}$$

Equation (3.24) can be rewritten as:

$$\sigma_{ij} = \frac{\partial W}{\partial I_1'}\frac{\partial I_1'}{\partial \epsilon_{ij}} + \frac{\partial W}{\partial I_2'}\frac{\partial I_2'}{\partial \epsilon_{ij}} + \frac{\partial W}{\partial I_3'}\frac{\partial I_3'}{\partial \epsilon_{ij}} \tag{3.26}$$

Since:

$$\frac{\partial I_1'}{\partial \epsilon_{ij}} = \delta_{ij} \tag{3.27a}$$

$$\frac{\partial I_2'}{\partial \epsilon_{ij}} = \epsilon_{ij} \tag{3.27b}$$

$$\frac{\partial I_3'}{\partial \epsilon_{ij}} = \epsilon_{ik}\epsilon_{kj} \tag{3.27c}$$

Equation (3.26) can thus be expressed as:

$$\sigma_{ij} = \frac{\partial W}{\partial I_1'}\delta_{ij} + \frac{\partial W}{\partial \bar{I}_2'}\epsilon_{ij} + \frac{\partial W}{\partial \bar{I}_3'}\epsilon_{ik}\epsilon_{kj} \tag{3.28}$$

Equation (3.4) in the Cauchy formulation and Eq. (3.28) in the Green formulation have the same form except the difference that the response coefficients A_0, A_1, and A_2 in Eq. (3.4) are independent while the response coefficients $\partial W/\partial I_1'$, $\partial W/\partial \bar{I}_2'$, and $\partial W/\partial \bar{I}_3'$ in Eq. (3.28) are dependent on each other under the following *integrability conditions*:

$$\frac{\partial}{\partial \bar{I}_2'}\left(\frac{\partial W}{\partial I_1'}\right) = \frac{\partial}{\partial I_1'}\left(\frac{\partial W}{\partial \bar{I}_2'}\right) \tag{3.29a}$$

$$\frac{\partial}{\partial \bar{I}_3'}\left(\frac{\partial W}{\partial I_1'}\right) = \frac{\partial}{\partial I_1'}\left(\frac{\partial W}{\partial \bar{I}_3'}\right) \tag{3.29b}$$

$$\frac{\partial}{\partial \bar{I}_3'}\left(\frac{\partial W}{\partial \bar{I}_2'}\right) = \frac{\partial}{\partial \bar{I}_2'}\left(\frac{\partial W}{\partial \bar{I}_3'}\right) \tag{3.29c}$$

The Green type of constitutive equation can therefore be regarded as a special case of the Cauchy type of equation. Similarly, the counterpart of Eq. (3.28) can be derived by assuming the existence of complementary energy density function Ω which is a function of stress tensor σ_{ij}. Using the relationship:

$$W + \Omega = \sigma_{ij}\epsilon_{ij} \tag{3.30}$$

and differentiating Eq. (3.30) with respect to σ_{kl}, we have:

$$\frac{\partial \Omega}{\partial \sigma_{kl}} = -\frac{\partial W}{\partial \sigma_{kl}} + \sigma_{ij}\frac{\partial \epsilon_{ij}}{\partial \sigma_{kl}} + \frac{\partial \sigma_{ij}}{\partial \sigma_{kl}}\epsilon_{ij} = \left(\sigma_{ij} - \frac{\partial W}{\partial \epsilon_{ij}}\right)\frac{\partial \epsilon_{ij}}{\partial \sigma_{kl}} + \frac{\partial \sigma_{ij}}{\partial \sigma_{kl}}\epsilon_{ij} \tag{3.31}$$

Using Eq. (3.24), Eq. (3.31) reduces to:

$$\frac{\partial \Omega}{\partial \sigma_{kl}} = \frac{\partial \sigma_{ij}}{\partial \sigma_{kl}}\epsilon_{ij} \tag{3.32}$$

Since $\partial \sigma_{ij}/\partial \sigma_{kl} = \delta_{ik}\delta_{jl}$, we finally have:

$$\epsilon_{kl} = \frac{\partial \Omega}{\partial \sigma_{kl}} \quad \text{or} \quad \epsilon_{ij} = \frac{\partial \Omega}{\partial \sigma_{ij}} \tag{3.33}$$

For an isotropic material, the complementary energy density function Ω is a function of any three independent invariants of stress tensor. By taking the following invariants such as:

$$I_1 = \sigma_{ii} \tag{3.34a}$$

$$I_2 = \tfrac{1}{2}\sigma_{ij}\sigma_{ji} \tag{3.34b}$$

$$I_3 = \tfrac{1}{3}\sigma_{ij}\sigma_{jk}\sigma_{ki} \tag{3.34c}$$

Eq. (3.33) can be expressed as:

$$\epsilon_{ij} = \frac{\partial \Omega}{\partial I_1}\frac{\partial I_1}{\partial \sigma_{ij}} + \frac{\partial \Omega}{\partial I_2}\frac{\partial I_2}{\partial \sigma_{ij}} + \frac{\partial \Omega}{\partial I_3}\frac{\partial I_3}{\partial \sigma_{ij}} \tag{3.35}$$

Since:

$$\frac{\partial I_1}{\partial \sigma_{ij}} = \delta_{ij} \tag{3.36a}$$

$$\frac{\partial I_2}{\partial \sigma_{ij}} = \sigma_{ij} \tag{3.36b}$$

$$\frac{\partial I_3}{\partial \sigma_{ij}} = \sigma_{ik}\sigma_{kj} \tag{3.36c}$$

Equation (3.35) can then be written as:

$$\epsilon_{ij} = \frac{\partial \Omega}{\partial I_1}\delta_{ij} + \frac{\partial \Omega}{\partial I_2}\sigma_{ij} + \frac{\partial \Omega}{\partial I_3}\sigma_{ik}\sigma_{kj} \tag{3.37}$$

Equation (3.37) has the same form as that of Eq. (3.5), except that the difference between the characteristics of the response coefficients in Eq. (3.5) and Eq. (3.37). It can be readily understood that similar integrability relations to Eq. (3.29) exist among the response coefficients, $\partial\Omega/\partial I_1$, $\partial\Omega/\partial I_2$, and $\partial\Omega/\partial I_3$.

Based on any assumed functional relationship of W in terms of strain invariants, or Ω in terms of stress invariants, various nonlinear elastic stress-strain relations in the form of secant formulation can be obtained from Eq. (3.28) or (3.37). Such hyperelastic formulation yields a one-to-one relationship between the states of stress and strain, i.e., reversibility and path-independency of stresses and strains. Note that the stress tensor σ_{ij} in Eq. (3.24) and strain tensor ϵ_{ij} in Eq. (3.33) are respectively normal to the surfaces of strain energy density function W and complementary energy density function Ω (see normality condition in Section 3.3.4).

On the other hand, differentiation of Eqs. (3.24) and (3.33) results in the incremental stress-strain relations given by:

$$d\sigma_{ij} = \frac{\partial^2 W'}{\partial \epsilon_{ij} \partial \epsilon_{kl}} d\epsilon_{kl} = H_{ijkl}\, d\epsilon_{kl} \tag{3.38a}$$

$$d\epsilon_{ij} = \frac{\partial^2 \Omega}{\partial \sigma_{ij} \partial \sigma_{kl}} d\sigma_{kl} = H'_{ijkl}\, d\sigma_{kl} \tag{3.38b}$$

where the symmetrical matrices of the components of the fourth-order tensors H_{ijkl} and H'_{ijkl} are known mathematically as the *Hessian matrices* and are functions of W' and Ω, respectively (see Section 3.3.4).

From Eqs. (3.38a) and (3.38b), it is observed that tangent moduli are identical for loading and unloading. Thus, the hyperelastic model yields a constitutive relation which is incapable of describing material behavior with load history-dependence and rate-dependence. Incremental formulation of hyperelasticity can exhibit *strain-* or *stress-induced anisotropy* in the material. Material instability of this model occurs when:

$$\det | H_{ijkl} | = 0 \quad \text{or} \quad \det | H'_{ijkl} | = 0 \tag{3.39}$$

Despite its shortcomings, hyperelastic model has been utilized as nonlinear constitutive relations for soils.

In the early applications of the finite-element method to soil mechanics problems, simplified forms of hyperelasticity were generated and used through a simple extension of the linear theory of elasticity. Later, it is to assume strain- or stress-dependent and coupled or uncoupled bulk and shear moduli and to construct a secant constitutive relation for coupled or uncoupled volumetric and deviatoric stresses and strains. A third-order model, based on the classical theory of hyperelasticity, has been formulated by Evans and Pister (1966) and subsequently used by Ko and Masson (1976), and Saleeb and Chen (1981) among others in soil mechanics.

The hyperelastic formulation can be quite accurate for soils strained in proportional loading and may represent several characteristics associated with soil behavior; *nonlinearity*, *dilation*, *stress-induced anisotropy*, and *strain-softening*. Moreover, use of these models in such cases satisfies the rigorous theoretical requirements of continuity, stability, uniqueness, and energy consideration of continuum mechanics, as will be described in Section 3.3. However, as noted previously, models of the hyperelastic type fail to identify the inelastic character of soil deformation because of its path-independency that is the result of a one-to-one coordination between stress and strain.

The main objection to the hyperelastic formulation is the complications involved with the material constants. Even when initial isotropy is assumed, a nonlinear

TABLE 3.2

Hyperelastic models

Advantages	Limitations
satisfy stability and uniqueness	path-independent, reversible
shear-dilatancy, and effect of all stress invariants may be included	difficult to fit and requires large number of tests
	most models confined to small regions
attractive from programming and computer economy points of view	of applications

hyperelastic model often contains too many material parameters. For instance, a third-order hyperelastic model, in which the stress (or strain) components can be represented by the third-order polynomial functions of strain (or stress) components, requires 9 constants; while 14 constants are needed for the fifth-order hyperelastic model. A large number of tests are generally required to determine these constants, which limit the practical usefulness of the models.

The advantages and limitations of hyperelastic models are summarized in Table 3.2.

3.2.4 Hypoelastic model

An obvious shortcoming in both of the previous types of nonlinear elasticity models is the path-independent behavior implied in the secant stress-strain formulation, which is certainly not true for soils in general. A further improved description of soil behavior is provided by the *hypoelastic formulation* in which the stress rate can in general be represented by the material response function that is a function of the current stress or strain state and strain rate. The general form of the constitutive equation for this type of material is mathematically expressed as:

$$\dot{\sigma}_{ij} = F_{ij}(\sigma_{mn}, \dot{\epsilon}_{kl}) \tag{3.40a}$$

or

$$\dot{\sigma}_{ij} = F_{ij}(\epsilon_{mn}, \dot{\epsilon}_{kl}) \tag{3.40b}$$

where the dot indicates the rate of stress or strain.

As a special case of hypoelastic model, consider the stress-strain relation described by Eq. (3.40a) in the following. It can be shown that the most general form of the constitutive relations of Eq. (3.40a) which satisfies the *isotropic* conditions

may be expressed by employing the *Cayley-Hamilton Theorem* as (e.g., Rivlin and Ericksen, 1955):

$$\dot{\sigma}_{ij} = \alpha_0\delta_{ij} + \alpha_1\dot{\epsilon}_{ij} + \alpha_2\dot{\epsilon}_{ik}\dot{\epsilon}_{kj} + \alpha_3\sigma_{ij} + \alpha_4\sigma_{ik}\sigma_{kj} + \alpha_5(\dot{\epsilon}_{ik}\sigma_{kj} + \sigma_{ik}\dot{\epsilon}_{kj})$$
$$+ \alpha_6(\dot{\epsilon}_{ik}\dot{\epsilon}_{kl}\sigma_{lj} + \sigma_{ik}\dot{\epsilon}_{kl}\dot{\epsilon}_{lj}) + \alpha_7(\dot{\epsilon}_{ik}\sigma_{kl}\sigma_{lj} + \sigma_{ik}\sigma_{kl}\dot{\epsilon}_{lj})$$
$$+ \alpha_8(\dot{\epsilon}_{ik}\dot{\epsilon}_{kl}\sigma_{lm}\sigma_{mj} + \sigma_{ik}\sigma_{kl}\dot{\epsilon}_{lm}\dot{\epsilon}_{mj}) \tag{3.41}$$

where the response coefficients α_0, α_1, ..., and α_8 are polynomial functions of the invariants of $\dot{\epsilon}_{ij}$ and σ_{kl} and the following four joint invariants:

$$Q_1 = \dot{\epsilon}_{pq}\sigma_{qp} \qquad Q_2 = \dot{\epsilon}_{pq}\sigma_{qr}\sigma_{rp} \tag{3.42a}$$
$$Q_3 = \dot{\epsilon}_{pq}\dot{\epsilon}_{qr}\sigma_{rp} \qquad Q_4 = \dot{\epsilon}_{pq}\dot{\epsilon}_{qr}\sigma_{rs}\sigma_{sp} \tag{3.42b}$$

Assuming that the material is time-independent, we eliminate all terms in Eq. (3.41) containing second and higher powers of $\dot{\epsilon}_{ij}$ so that Eq. (3.41) becomes homogeneous in time. Therefore, the response coefficients α_2, α_6, and α_8 must vanish. On the other hand, the coefficients α_1, α_5, and α_7 must be independent of $\dot{\epsilon}_{ij}$ and be functions of stress invariants alone while α_0, α_3, and α_4 must be of degree one in $\dot{\epsilon}_{ij}$. Imposing these restrictions on the response coefficients in Eq. (3.41), we obtain:

$$\dot{\sigma}_{ij} = \alpha_0\delta_{ij} + \alpha_1\dot{\epsilon}_{ij} + \alpha_3\sigma_{ij} + \alpha_4\sigma_{ik}\sigma_{kj} + \alpha_5(\dot{\epsilon}_{ik}\sigma_{kj} + \sigma_{ik}\dot{\epsilon}_{kj}) + \alpha_7(\dot{\epsilon}_{ik}\sigma_{kl}\sigma_{lj} + \sigma_{ik}\sigma_{kl}\dot{\epsilon}_{lj}) \tag{3.43}$$

where the response coefficients α_0, α_3, and α_4 may be written as:

$$\alpha_0 = \beta_0\dot{\epsilon}_{nn} + \beta_1 Q_1 + \beta_2 Q_2 \tag{3.44a}$$

$$\alpha_3 = \beta_3\dot{\epsilon}_{nn} + \beta_4 Q_1 + \beta_5 Q_2 \tag{3.44b}$$

$$\alpha_4 = \beta_6\dot{\epsilon}_{nn} + \beta_7 Q_1 + \beta_8 Q_2 \tag{3.44c}$$

where, similar to the coefficients, α_1, α_5, and α_7, the response coefficients β_0, β_1, ..., and β_8 are independent of $\dot{\epsilon}_{ij}$ and are functions of stress invariant alone. Substitution of Eq. (3.44) into Eq. (3.43) leads to the incremental constitutive equations given by the following form:

$$\dot{\sigma}_{ij} = (\beta_0\dot{\epsilon}_{nn} + \beta_1 Q_1 + \beta_2 Q_2)\delta_{ij} + \alpha_1\dot{\epsilon}_{ij} + (\beta_3\dot{\epsilon}_{nn} + \beta_4 Q_1 + \beta_5 Q_2)\sigma_{ij}$$
$$+ (\beta_6\dot{\epsilon}_{nn} + \beta_7 Q_1 + \beta_8 Q_2)\sigma_{ik}\sigma_{kj} + \alpha_5(\dot{\epsilon}_{ik}\sigma_{kj} + \sigma_{ik}\dot{\epsilon}_{kj})$$
$$+ \alpha_7(\dot{\epsilon}_{ik}\sigma_{kl}\sigma_{lj} + \sigma_{ik}\sigma_{kl}\dot{\epsilon}_{lj}) \tag{3.45}$$

Since each term in Eq. (3.45) contains a time derivative d/dt, both sides of the equation can be multiplied by dt, resulting in the following form:

$$\begin{aligned} d\sigma_{ij} = {} & (\beta_0\, d\epsilon_{nn} + \beta_1\, d\epsilon_{pq}\sigma_{qp} + \beta_2\, d\epsilon_{pq}\sigma_{qr}\sigma_{rp})\delta_{ij} \\ & + (\beta_3\, d\epsilon_{nn} + \beta_4\, d\epsilon_{pq}\sigma_{pq} + \beta_5\, d\epsilon_{pq}\sigma_{qr}\sigma_{rp})\sigma_{ij} \\ & + (\beta_6\, d\epsilon_{nn} + \beta_7\, d\epsilon_{pq}\sigma_{pq} + \beta_8\, d\epsilon_{pq}\sigma_{qr}\sigma_{rp})\sigma_{ik}\sigma_{kj} + \alpha_1\, d\epsilon_{ij} \\ & + \alpha_5(d\epsilon_{ik}\sigma_{kj} + \sigma_{ik}\, d\epsilon_{kj}) + \alpha_7(d\epsilon_{ik}\sigma_{kl}\sigma_{lj} + \sigma_{ik}\sigma_{kl}\, d\epsilon_{lj}) \end{aligned} \tag{3.46}$$

where $d\sigma_{ij}$ and $d\epsilon_{ij}$ are the stress and strain increment tensors, respectively. Equation (3.46) is the most general form of incremental constitutive equation for isotropic time-independent materials. The 12 response coefficients which are polynomial functions of stress invariants can be determined by experiments and curve and model fitting to the available test data. Equation (3.46) may be conveniently written in the incrementally linear form given by:

$$d\sigma_{ij} = C_{ijkl}(\sigma_{mn})\, d\epsilon_{kl} \tag{3.47}$$

where C_{ijkl} is often called the *tangential stiffness tensor* of the material. The most general form of C_{ijkl} which satisfies the condition of material isotropy may be written as:

$$\begin{aligned} C_{ijkl} = {} & A_1\delta_{ij}\delta_{kl} + A_2(\delta_{ik}\delta_{jl} + \delta_{jk}\delta_{il}) + A_3\sigma_{ij}\delta_{kl} + A_4\delta_{ij}\sigma_{kl} \\ & + A_5(\delta_{ik}\sigma_{jl} + \delta_{il}\sigma_{jk} + \delta_{jk}\sigma_{il} + \delta_{jl}\sigma_{ik}) + A_6\delta_{ij}\sigma_{km}\sigma_{ml} + A_7\delta_{kl}\sigma_{im}\sigma_{mj} \\ & + A_8(\delta_{ik}\sigma_{jm}\sigma_{ml} + \delta_{il}\sigma_{jm}\sigma_{mk} + \delta_{jk}\sigma_{im}\sigma_{ml} + \delta_{jl}\sigma_{im}\sigma_{mk}) + A_9\sigma_{ij}\sigma_{kl} + A_{10}\sigma_{ij}\sigma_{km}\sigma_{ml} \\ & + A_{11}\sigma_{im}\sigma_{mj}\sigma_{kl} + A_{12}\sigma_{im}\sigma_{mj}\sigma_{km}\sigma_{ml} \end{aligned} \tag{3.48}$$

in which the 12 material coefficients A_1, A_2, ..., and A_{12} depend only on the invariants of the stress tensor σ_{ij}.

The inverse constitutive form of Eq. (3.47) is usually written as:

$$d\epsilon_{ij} = D_{ijkl}(\sigma_{mn})\, d\sigma_{kl} \tag{3.49}$$

where D_{ijkl} is the *tangential compliance tensor* which is a function of the stress tensor σ_{ij} in the same manner as that of C_{ijkl} in Eq. (3.47).

These incremental stress-strain relations provide a natural mathematical model for materials with limited memory. This can be seen by an integration of Eq. (3.47):

$$\sigma_{ij} = \int_0^{\epsilon_{ij}} C_{ijkl}(\sigma_{mn})\, d\epsilon_{kl} + \sigma_{ij}^0 \tag{3.50}$$

where σ_{ij}^{0} indicates the initial stress state. The integral expression clearly indicates the *path-dependency* and *irreversibility* of the process. The hypoelastic response is therefore stress history(path)-dependent. In the linear case for which $C_{ijkl}(\sigma_{mn})$ is constant, the hypoelasticity degenerates to the Cauchy type of elasticity, which corresponds to the history-independent secant modulus formulation. The integration in Eq. (3.50) can be carried out explicitly and leads to the Cauchy elastic formulation.

As observed from Eq. (3.47), the tangential stiffness is identical in loading and unloading. This reversibility requirement only in the infinitesimal (or incremental) sense justifies the use of the term hypoelastic or *minimum elastic*. Material instability or failure occurs when:

$$\det | C_{ijkl}(\sigma_{mn}) | = 0 \tag{3.51}$$

Equation (3.51) leads to an eigenvalue problem of which the eigenvectors span a surface, the failure surface, in the stress space.

There are two problems associated with the hypoelasticity modeling. The first problem is that, in the nonlinear range, the hypoelasticity-based models exhibit *stress-induced anisotropy*. This anisotropy implies that the principal axes of stress and strain are different, introducing coupling effect between normal stresses and shear strains. As a result, a total of 21 material moduli for general triaxial conditions have to be defined for every point of the material loading path. This is a difficult task for paractical application.

The second problem is that, under the uniaxial stress condition, the definition of loading and unloading is clear. However, under multiaxial stress conditions, the hypoelastic formulation provides no clear criterion for loading or unloading. Thus, a loading in shear may be accompanied by an unloading in some of the normal stress components. Therefore, additional assumptions are needed for defining loading-unloading criterion.

In the simplest class of hypoelastic models, the incremental stress-strain relations are formulated directly as a simple extension of the isotropic linear elastic model with the elastic constants replaced by variable tangential moduli which are taken to be functions of the stress and/or strain invariants. A particularly popular hypoelastic model is the *Duncan-Chang model* (Duncan and Chang, 1970; Duncan, 1981), among others (Kondner, 1963; Kulhawy et al., 1969). The *Duncan-Chang model* represents a simplification of Eq. (3.40) in that the material stiffness is incrementally isotropic with stress-dependent moduli. The moduli are described as parabolic functions of stress level. Failure is implied when these moduli approach zero. Models of this type are attractive from both computational and practical viewpoints. They are well suited for implementation of finite-element computer codes. The material parameters involved in the models can be easily determined from standard laboratory tests using well defined procedures; and many of these parameters have a broad data base.

The early incremental finite-element analyses were conducted with these sim-

plified forms of hypoelasticity. In the simplest approach, the incremental constitutive model is based on an isotropic formulation using test data from a single parameter load set-up, resulting in, for example, a stress- or strain-dependent modulus of elasticity. To this end, three classes of formulations have emerged: *hyperbolic*, *parabolic*, and *exponential relations*. In spite of the theoretical reservations against isotropic modeling with identical moduli in the principal directions and no coupling with the shear response, the hyperbolic type of models and their generalizations have been applied extensively in the past and used successfully in the finite-element solution of nonlinear soil mechanics problems (see Chen and Saleeb, 1982).

A more sophisticated model is based on the decoupling of volumetric and deviatoric stress and strain with two parameters. In this case, the nonlinear deformation model is developed on the basis of an isotropic formulation with variable bulk moduli and shear moduli.

The application of this type of hypoelasticity models should be confined to monotonic loading situations which do not basically differ from the experimental tests from which the material constants were determined or curve fitted. Thus, the isotropic models should not be used in cases such as nonhomogeneous stress states, nonproportional loading paths or cyclic loadings.

TABLE 3.3

Hypoelastic models

Advantages	Limitations
Modification of the linear elastic models	
conceptually and mathematically simple	incrementally reversible
suitable for finite element implementation	no coupling between volumetric and deviatoric responses
easy to fit	when G_t and K_t are used, the behavior near failure can not be described adequately
many of the parameters have wide data base	
have been used successfully in many practical applications	- possible energy generation for certain stress cycles if arbitrary functions for the moduli are used
First-order hypoelastic models	
stress path dependency	incrementally reversible
stress-induced anisotropy	tangent stiffness matrix is generally unsymmetric; thus requires increased storage and computation
	difficult to fit and requires large number of tests
	– possible energy generation for certain stress cycles
	no uniqueness proof in general

Examples of the classical formulations and applications of the first-order hypoelastic models can be found in the papers by Coon and Evans (1972), Desai (1980), Davis and Mullenger (1979), and Tokuoka (1971). Again, as for the hyperelastic models, the practical usefulness of the hypoelastic models is limited by the nature and number of tests required to determine the material constants. There is no unique way to determine these constants. Also, as has been shown in the thesis (Saleeb, 1981), the material tangential stiffness matrix for a hypoelastic model is generally unsymmetric which results in a considerable increase in both storage and computational time. Further, in such cases, uniqueness of the solution of boundary value problems can not generally be assured.

The advantages and limitations for two of hypoelastic models are summarized in Table 3.3.

3.3 UNIQUENESS, STABILITY, NORMALITY, AND CONVEXITY FOR ELASTIC MATERIALS

It is a desirable feature for a boundary-value problem that any mathematical theory describing the mechanical behavior of materials provides strongly a *unique* solution which exhibits *stable* equilibrium configurations. These characteristics are generally to be expected for most actual physical problems. However, it must be recognized that if the real body deforms in a nonunique manner, or assumes unstable equilibrium configurations, no amount of mathematical modeling on materials can compel it to do otherwise.

In this Section, the uniqueness and stability requirements for solutions together with their implications for elastic materials are discussed.

3.3.1 Uniqueness

Let us consider an elastic material body with volume V and surface area A. The part of the surface area where surface tractions are prescribed is denoted by A_T, and that where surface displacements are prescribed is denoted by A_u (see Fig. 2.16). When the body forces, F_i, and the surface forces, T_i, act upon the body, the resulting stresses, strains, and displacements are given by σ_{ij}, ϵ_{ij}, and u_i, respectively. Now assume that we further impose small changes of the applied forces and displacements denoted by the increments $\mathrm{d}T_i$ on A_T, $\mathrm{d}F_i$ in V, and $\mathrm{d}u_i$ on A_u. For this case, it is important to investigate whether the resulting stress and strain increments $\mathrm{d}\sigma_{ij}$ and $\mathrm{d}\epsilon_{ij}$, respectively, are determined uniquely by the increments of the applied forces and displacements $\mathrm{d}T_i$, $\mathrm{d}F_i$, and $\mathrm{d}u_i$. If it is not, there must then exist at least two different solutions corresponding to the applied changes $\mathrm{d}T_i$, $\mathrm{d}F_i$, and $\mathrm{d}u_i$. Let two solutions be respectively solution (a) with increments $\mathrm{d}\sigma_{ij}^{\mathrm{a}}$, $\mathrm{d}\epsilon_{ij}^{\mathrm{a}}$ and solution (b) with increments $\mathrm{d}\sigma_{ij}^{\mathrm{b}}$, $\mathrm{d}\epsilon_{ij}^{\mathrm{b}}$.

Each of these solutions must satisfy the equilibrium and compatibility (or geometry) requirements. For solution (a), $\mathrm{d}T_i$, $\mathrm{d}F_i$, and $\mathrm{d}\sigma_{ij}^{\mathrm{a}}$ constitute an equilibrium set, whereas $\mathrm{d}u_i$ and $\mathrm{d}\epsilon_{ij}^{\mathrm{a}}$ represent a compatible set. Similarly, the set $\mathrm{d}T_i$,

dF_i, and $d\sigma_{ij}^{b}$ is statically admissible and the set du_i and $d\epsilon_{ij}^{b}$ is kinematically admissible, for solution (b). Because of the linearity of the equilibrium equations (2.88), the difference between the two statically admissible sets of solutions (a) and (b) is also statically admissible; that is, the stresses $(d\sigma_{ij}^{a} - d\sigma_{ij}^{b})$, corresponding to zero surface forces on A_1 and zero body forces in V, constitute an equilibrium set. Similarly, because of the linearity of the strain-displacement relations, Eq. (2.90), the strains $(d\epsilon_{ij}^{a} - d\epsilon_{ij}^{b})$, and the displacements $(du_i^{a} - du_i^{b})$, which are zero on A_u, are kinematically admissible, and therefore constitute a compatible set. Applying the *principle of virtual work* to these two "difference" sets, we obtain:

$$0 = \int_V \left(d\sigma_{ij}^{a} - d\sigma_{ij}^{b}\right)\left(d\epsilon_{ij}^{a} - d\epsilon_{ij}^{b}\right) dV \tag{3.52}$$

since $(dT_i^{a} - dT_i^{b}) = 0$ on A_1, $(du_i^{a} - du_i^{b}) = 0$ on A_u, and $(dF_i^{a} - dF_i^{b}) = 0$ in V.

If it can be shown that the integrand in Eq. (3.52) is *positive definite*, uniqueness is proved. As an example, let us consider the case of a *linear hyperelastic (first-order hyperelastic)* material body. If the "difference" states of stress and strain are denoted respectively by:

$$d\sigma_{ij}' = d\sigma_{ij}^{a} - d\sigma_{ij}^{b} \tag{3.53a}$$

$$d\epsilon_{ij}' = d\epsilon_{ij}^{a} - d\epsilon_{ij}^{b} \tag{3.53b}$$

then the incremental constitutive relation gives:

$$d\sigma_{ij}' = C_{ijkl}\, d\epsilon_{kl}' \tag{3.54}$$

where the components of *symmetrical* elastic response tensor C_{ijkl} are constants. Substitution of above relation into Eq. (3.52) leads to:

$$\int_V C_{ijkl}\, d\epsilon_{kl}'\, d\epsilon_{ij}'\, dV = 0 \tag{3.55}$$

The integrand in Eq. (3.55) is a positive definite quadratic form since the determinant of the elastic response coefficients in the tensor C_{ijkl} is always positive, as will be seen in Section 3.3.4. Hence, the integral in Eq. (3.55) is zero only if $d\epsilon_{ij}' = 0$; that is, $d\epsilon_{ij}^{a} = d\epsilon_{ij}^{b}$. Furthermore, it follows from the constitutive relation of Eq. (3.54) that $d\sigma_{ij}' = 0$; that is $d\sigma_{ij}^{a} = d\sigma_{ij}^{b}$. Thus, uniqueness is proved for this kind of material, and either $d\sigma_{ij}$ or $d\epsilon_{ij}$ can have a unique value at each point of the body.

For different classes of nonlinear elastic materials described in the preceding Section, additional restrictions must be considered in order to establish the proof of positive definiteness of the integrand in Eq. (3.52). This leads to a consideration of Drucker's *material stability postulate* (Drucker, 1951), to be discussed in the next Section. As will be seen, this postulate provides sufficient conditions for uniqueness proof (see Example 3.1).

3.3.2 *Drucker's stability postulate*

Let us consider a material body with volume V and surface area A, as shown in Fig. 3.1a. The applied surface and body forces are denoted by T_i and F_i, respectively. The corresponding induced displacements, stresses, and strains are denoted by u_i, σ_{ij}, and ϵ_{ij}, respectively. This existing set of forces, stresses, displacements, and strains satisfies both equilibrium and compatibility (or geometry) conditions.

We shall consider next an external agency which is entirely distinct from the agency that causes the existing states of stress σ_{ij} and strain ϵ_{ij}. This external agency applies additional surface and body forces, $\mathrm{d}T_i$ and $\mathrm{d}F_i$, which cause the additional set of stress increments $\mathrm{d}\sigma_{ij}$, strain increments $\mathrm{d}\epsilon_{ij}$, and displacement increments $\mathrm{d}u_i$, to the body as illustrated in Fig. 3.1b.

Definition of a *stable material* is followed by conditions which are known as *Drucker's stability postulates* (Drucker, 1951):

1. The work done by *the external agency* during the application of the added set of forces on the changes in displacements it produces is positive.
2. The net work performed by *the external agency* over the cycle of application and removal of the added set of forces and the changes in displacements it produces is nonnegative.

It should be noted here that the work referred to is only the work done by the added set of forces $\mathrm{d}T_i$ and $\mathrm{d}F_i$ on the "change" in displacements $\mathrm{d}u_i$ it produces, not the total forces on $\mathrm{d}u_i$. Mathematically, the following two stability requirements can be specified:

$$\int_A \mathrm{d}T_i \, \mathrm{d}u_i \, \mathrm{d}A + \int_V \mathrm{d}F_i \, \mathrm{d}u_i \, \mathrm{d}V > 0 \tag{3.56}$$

$$\oint_A \mathrm{d}T_i \, \mathrm{d}u_i \, \mathrm{d}A + \oint_V \mathrm{d}F_i \, \mathrm{d}u_i \, \mathrm{d}V > 0 \tag{3.57}$$

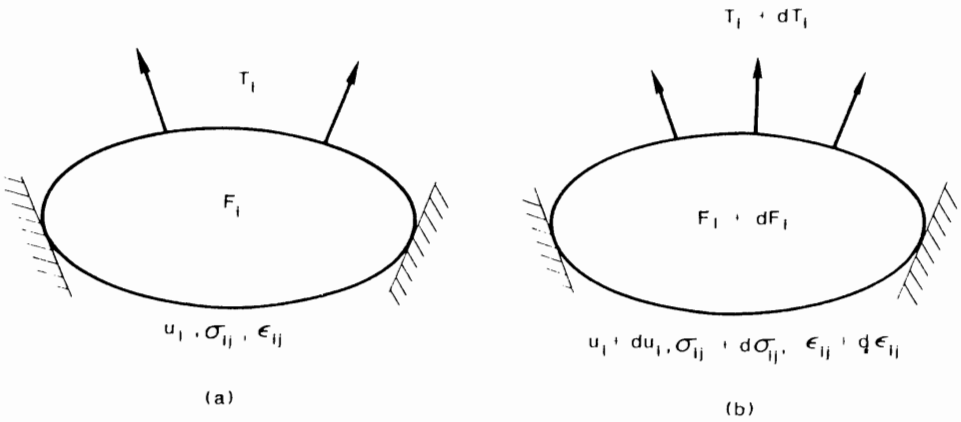

Fig. 3.1 External agency and Drucker's stability postulate. (a) Existing system. (b) Existing system and external agency

in which $\oint$ indicates integration over a cycle of addition and removal of the additional set of forces and stresses.

The first postulate, Eq. (3.56), is called *stability in small*, while the second one, Eq. (3.57), is termed *stability in cycle*. Note that these stability requirements are more restrictive than the laws of thermodynamics, which require only that the work done by the total (existing) forces F_i and T_i on $\mathrm{d}u_i$ be nonnegative.

Employing the principle of virtual work to the "added" equilibrium set, $\mathrm{d}F_i$, $\mathrm{d}T_i$, and $\mathrm{d}\sigma_{ij}$, and the corresponding compatible set, $\mathrm{d}u_i$ and $\mathrm{d}\epsilon_{ij}$, the stability conditions in Eqs. (3.56) and (3.57) can be reduced to the following inequalities (V is an arbitrary volume of body considered):

Stability in small

$$\mathrm{d}\sigma_{ij}\,\mathrm{d}\epsilon_{ij} > 0 \tag{3.58}$$

Stability in cycle

$$\oint \mathrm{d}\sigma_{ij}\,\mathrm{d}\epsilon_{ij} \geq 0 \tag{3.59}$$

3.3.3 Existence of W and Ω

According to Drucker's postulate, useful net energy can not be extracted from the material and the system of forces acting upon it in a cycle of application and removal of the added set of forces and displacements. Furthermore, energy must be put in if only irrecoverable (permanent or plastic) deformation is to take place. For elastic materials, all deformations are recoverable and stability condition requires that the work done by the external agency in such a cycle be zero; that is, the integral of inequality in Eq. (3.59) is always zero for elastic materials. It can be shown that this provides a necessary and sufficient condition for the *existence* of strain energy and complementary energy density functions, W and Ω, respectively.

For example, let the existing states of stress and strain in an elastic material body be σ_{ij}^* and ϵ_{ij}^*, respectively. We consider a case that an external agency which applies and then releases an additional set of stresses to the existing state of stress. For an elastic material, when the stress state returns back to the original state σ_{ij}^*, the strain state also returns to ϵ_{ij}^*. Over such a cycle the second postulate in Eq. (3.59) requires:

$$\oint (\sigma_{ij} - \sigma_{ij}^*)\,\mathrm{d}\epsilon_{ij} = 0 \tag{3.60}$$

since no permanent (or plastic) strains have occurred. Choosing the initial existing state to be both stress and strain free, we find:

$$\oint \sigma_{ij}\,\mathrm{d}\epsilon_{ij} = 0 \tag{3.61}$$

which must be true irrespective of the path followed during the cycle. This implies that integrand in Eq. (3.61) must be an exact (or perfect) differential. This naturally suggests the consideration of the elastic strain energy density function, W, written as a function of strains alone, such that:

$$W(\epsilon_{ij}) = \int_0^{\epsilon_{ij}} \sigma_{ij}\, d\epsilon_{ij} \quad \text{and} \quad \sigma_{ij} = \frac{\partial W}{\partial \epsilon_{ij}}$$

These are the same relations derived previously for hyperelastic materials in Section 3.2.3.

Similarly, without providing a detailed argument, it can be shown that the second stability postulate (3.59) leads to the existence of the elastic complementary energy density, Ω, as a function of stresses alone; as also given previously.

Not only does the second stability postulate assure the existence of W and Ω, but, as will be seen in Example 3.1, the first postulate also guarantees that for any elastic constitutive model based on an assumed function for W (or Ω), a *unique inverse* constitutive relation can always be obtained.

The close relation between the stability postulate and the existence of a unique inverse of the stress-strain relation can best be illustrated by considering the symbolic uniaxial σ-ϵ curves in Fig. 3.2. For cases (a) to (c) in this figure, the stress σ is uniquely determined from the strain ϵ, and the converse is also true. An additional stress $d\sigma > 0$ gives rise to an additional strain $d\epsilon > 0$, with the product $d\sigma d\epsilon > 0$. That is, the additional stress $d\sigma$ does positive work which is represented by the shaded triangles in the diagrams. Behaviors of this kind are stable in Drucker's sense.

In case (d), the deformation curve has a descending branch, where the strain increases as stress decreases. Although the stress σ is uniquely determined from the value of strain ϵ, the converse is not true. On the descending branch, additional stress does negative work, i.e. $d\sigma d\epsilon < 0$. Such a *strain-softening* behavior is unstable.

In case (e), on the other hand, the strain decreases as stress increases. Therefore, the stress, σ, can not be uniquely determined from the value of the strain. Since $d\sigma d\epsilon < 0$, the material is again unstable. In the mechanical scheme, this case contradicts the laws of thermodynamics because it allows "free" extraction of useful work.

Example 3.1: Prove the uniqueness of solution from the first stability postulate described above.

Proof: We shall again consider the two solutions (a) and (b) discussed at the beginning of Section 3.3.1. The "difference" state of stress $(d\sigma_{ij}^a - d\sigma_{ij}^b)$ may be considered as applied by an external agency which produces the corresponding strain $(d\epsilon_{ij}^a - d\epsilon_{ij}^b)$. The fundamental stability postulate, inequality (3.58), then becomes:

$$\left(d\sigma_{ij}^a - d\sigma_{ij}^b\right)\left(d\epsilon_{ij}^a - d\epsilon_{ij}^b\right) > 0 \tag{3.62}$$

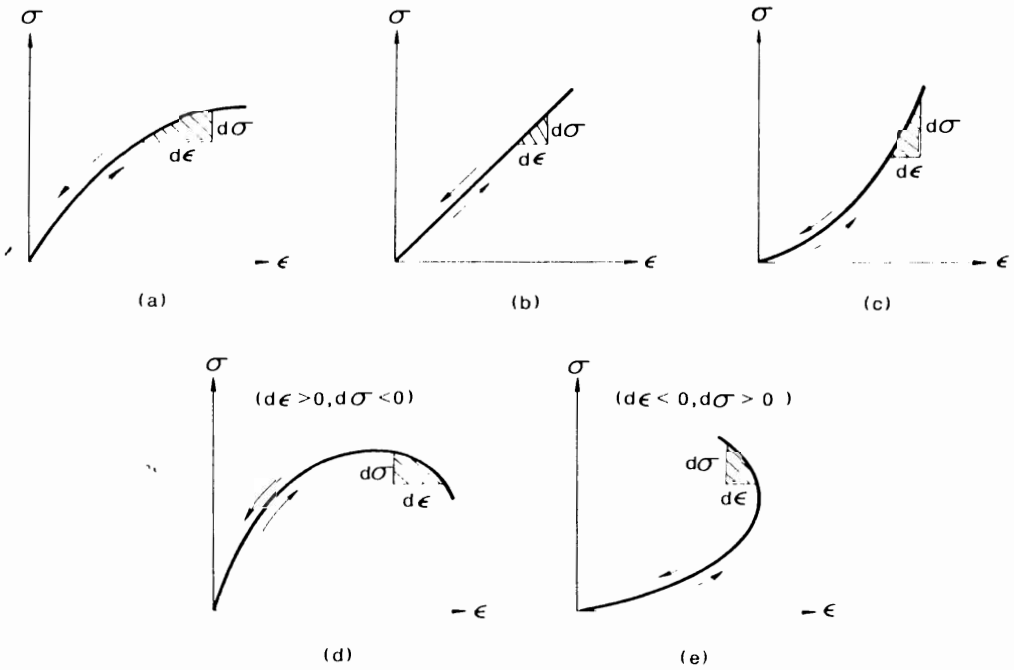

Fig. 3.2. Stable and unstable stress-strain curves for elastic materials. (a), (b), (c) Stable materials, $d\sigma\, d\epsilon > 0$. (d), (e) Unstable materials, $d\sigma\, d\epsilon < 0$.

that is, the integrand in Eq. (3.52) is always positive. Therefore, the integral of Eq. (3.52) can be zero if and only if the integrand is identically zero at each point in the body. Thus:

$$\left(d\sigma_{ij}^{a} - d\sigma_{ij}^{b}\right)\left(d\epsilon_{ij}^{a} - d\epsilon_{ij}^{b}\right) = 0 \tag{3.63}$$

which is satisfied when either $d\sigma_{ij}^{a} = d\sigma_{ij}^{b}$ or $d\epsilon_{ij}^{a} = d\epsilon_{ij}^{b}$. However, for stable elastic materials, the state of stress (or strain) is *uniquely* determined by the state of strain (or stress). Hence $d\sigma_{ij}^{a} = d\sigma_{ij}^{b}$ implies that $d\epsilon_{ij}^{a} = d\epsilon_{ij}^{b}$, and uniqueness of solution is guaranteed.

The uniqueness proved above is in an *incremental* sense (uniqueness in small) for elastic materials which satisfy Drucker's stability postulate. It has been shown that the changes in the stress and strain fields, corresponding to incremental changes in the applied loads and imposed displacements, are uniquely determined, provided that the current existing values such as loads, displacements, stresses, and strains are known. After the application of the increment, the existing values are updated, and another incremental problem is then solved. By solving a succession of incremental loading problems, therefore, one can determine the response of the material body to finite load changes. Thus, uniqueness in small entails uniqueness in large, since each

incremental step produces a unique solution. Separate proof of uniqueness in large may be established for path-independent elastic stable materials. However, the proof outlined here for stability in small is more general and can be easily extended for path-dependent constitutive models such as plasticity models and incremental stress-strain relations in Chapters 4 through 6.

Comments: It should be noted here that the uniqueness proof established before arises partly because of the *linearity* of the equilibrium and strain-displacement relations, Eqs. (2.88) and (2.90), and partly because of the material stability postulates. It is convenient, then, to distinguish between *geometric stability* and *material stability*. Uniqueness may be lost in a real structure because the equilibrium and kinematic equations are not in general linear. The most common example is the *buckling phenomenon* of structural elements as a result of geometry changes leading to nonlinear equilibrium equations. On the other hand, linear equilibrium and kinematic equations may be applicable in the considered structure, but the material may not be intrinsically stable, and as a result the solution becomes nonunique. Materials such as concrete and some soils under certain conditions (e.g., in the strain-softening range) are examples for such behavior. One consequence of the assumptions such as material stability postulate and linearity of the equilibrium and kinematic equations is that the solutions obtained from these assumptions are always stable and unique. This avoids many difficulties that might otherwise be encountered in the numerical computations.

3.3.4 Restrictions—normality and convexity

As discussed in the previous Section, the second stability postulate requires that the constitutive relations for elastic materials be always of hyperelastic (or Green) type written as Eqs. (3.24) and (3.33). Moreover, these relations must satisfy the first stability postulate in Eq. (3.58) which imposes additional conditions on the general form of the constitutive equations.

By differentiating constitutive relations of Eq. (3.24), the incremental stress components $d\sigma_{ij}$ can be expressed in terms of the incremental strains $d\epsilon_{ij}$, that is:

$$d\sigma_{ij} = \frac{\partial \sigma_{ij}}{\partial \epsilon_{kl}} d\epsilon_{kl} = \frac{\partial^2 W}{\partial \epsilon_{ij} \partial \epsilon_{kl}} d\epsilon_{kl} \tag{3.64}$$

Substituting for $d\sigma_{ij}$ from this equation into the first stability condition of Eq. (3.58), we obtain:

$$\frac{\partial^2 W}{\partial \epsilon_{ij} \partial \epsilon_{kl}} d\epsilon_{ij}\, d\epsilon_{kl} > 0 \tag{3.65a}$$

That is, the quadratic form $(\partial^2 W / \partial \epsilon_{ij} \partial \epsilon_{kl})\, d\epsilon_{kl} d\epsilon_{ij}$ must be *positive definite* for

arbitrary values of the components $d\epsilon_{ij}$. The inequality (3.65a) may be rewritten in another convenient form as:

$$H_{ijkl}\, d\epsilon_{ij}\, d\epsilon_{kl} > 0 \tag{3.65b}$$

where H_{ijkl} is a fourth-order tensor given by:

$$H_{ijkl} = \frac{\partial^2 W}{\partial \epsilon_{ij} \partial \epsilon_{kl}} \tag{3.66}$$

As can be easily seen in Eq. (3.66), tensor H_{ijkl} satisfies the symmetry conditions (ϵ_{ij} is symmetrical) such as $H_{ijkl} = H_{jikl} = H_{ijlk} = H_{jilk} = H_{klij}$. Hence, there will be only 21 independent elements in H_{ijkl}.

Mathematically, the matrix of the components of $H_{ijkl} = \partial^2 W / \partial \epsilon_{ij} \partial \epsilon_{kl}$ is known as the *Hessian matrix* of the function W. When ϵ_{ij} is expressed in a vector form with six components such as $[\epsilon_{11}, \epsilon_{22}, \epsilon_{33}, \gamma_{12}, \gamma_{23}, \gamma_{31}]$, then the elements of the Hessian matrix for W are written as

$$[H] = \begin{vmatrix} \dfrac{\partial^2 W}{\partial \epsilon_{11}^2} & \dfrac{\partial^2 W}{\partial \epsilon_{11} \partial \epsilon_{22}} & \dfrac{\partial^2 W}{\partial \epsilon_{11} \partial \epsilon_{33}} & \dfrac{\partial^2 W}{\partial \epsilon_{11} \partial \gamma_{12}} & \dfrac{\partial^2 W}{\partial \epsilon_{11} \partial \gamma_{23}} & \dfrac{\partial^2 W}{\partial \epsilon_{11} \partial \gamma_{31}} \\ & \dfrac{\partial^2 W}{\partial \epsilon_{22}^2} & \dfrac{\partial^2 W}{\partial \epsilon_{22} \partial \epsilon_{33}} & \dfrac{\partial^2 W}{\partial \epsilon_{22} \partial \gamma_{12}} & \dfrac{\partial^2 W}{\partial \epsilon_{22} \partial \gamma_{23}} & \dfrac{\partial^2 W}{\partial \epsilon_{22} \partial \gamma_{31}} \\ & & \dfrac{\partial^2 W}{\partial \epsilon_{33}^2} & \dfrac{\partial^2 W}{\partial \epsilon_{33} \partial \gamma_{12}} & \dfrac{\partial^2 W}{\partial \epsilon_{33} \partial \gamma_{23}} & \dfrac{\partial^2 W}{\partial \epsilon_{33} \partial \gamma_{31}} \\ & & & \dfrac{\partial^2 W}{\partial \gamma_{12}^2} & \dfrac{\partial^2 W}{\partial \gamma_{12} \partial \gamma_{23}} & \dfrac{\partial^2 W}{\partial \gamma_{12} \partial \gamma_{31}} \\ \text{Symmetric} & & & & \dfrac{\partial^2 W}{\partial \gamma_{23}^2} & \dfrac{\partial^2 W}{\partial \gamma_{23} \partial \gamma_{31}} \\ & & & & & \dfrac{\partial^2 W}{\partial \gamma_{31}^2} \end{vmatrix} \tag{3.67}$$

and condition (3.65b) requires that $[H]$ must be positive definite.

Alternatively, inequality (3.58) can be written in terms of Ω and σ_{ij}. Thus, we finally get:

$$H'_{ijkl}\, d\sigma_{ij}\, d\sigma_{kl} > 0 \tag{3.68}$$

where

$$H'_{ijkl} = \frac{\partial^2 \Omega}{\partial \sigma_{ij} \partial \sigma_{kl}} \tag{3.69}$$

and the elements of the Hessian matrix $[H']$ for Ω are exactly of the same form as that for W in Eq. (3.67) with W, ϵ and γ being replaced by Ω, σ, and τ, respectively.

The restrictions imposed by Drucker's material stability postulate and their implications are summarized as follows:

1. The strain energy and complementary energy density functions W and Ω exist and are always *positive definite*. This follows directly from the positive definiteness character of their Hessian matrices, $[H]$ and $[H']$, respectively, and agrees with the requirement of the laws of thermodynamics.
2. Furthermore, the positive definiteness of $[H]$ and $[H']$ assures that a unique inverse of the constitutive relations always exists. That is, for any constitutive law $\sigma_{ij} = F(\epsilon_{ij})$ based on an assumed function for W, a unique inverse relation $\epsilon_{ij} = F'(\sigma_{ij})$ can always be obtained.
3. The stress tensor or strain tensor is respectively *normal* to the *convex* surface corresponding to constant W or Ω in strain or stress space.

The *normality* and *convexity* conditions are discussed in the following.

Normality

Equation (3.33) implies the *normality condition* that the total strain tensor ϵ_{ij} is outward normal to the surface of constant Ω at a given point σ_{ij}. In Fig. 3.3, for example, the surface Ω = constant is illustrated symbolically in the nine-dimensional stress space. The state of stress σ_{ij} is represented by a point in this space. The components ϵ_{ij}, corresponding to stresses σ_{ij}, are plotted as a free vector in the

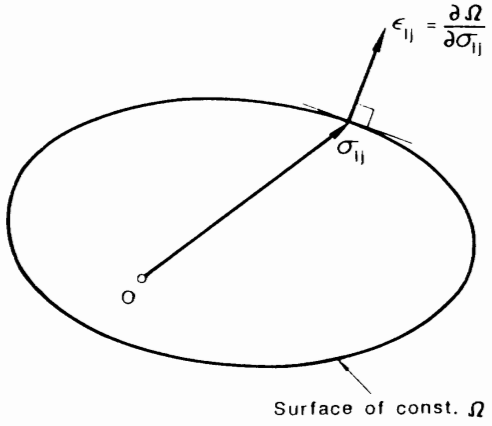

Fig. 3.3. Normality of ϵ_{ij} to the surface Ω = const. in the general nine-dimensional stress space

stress space (with ϵ_{11} as the component in the σ_{11} direction, etc.) with its origin at the stress point σ_{ij}.

Normality provides a very strong and significant restriction on the possible form of the stress-strain relations. Suppose, as an example, that the complementary energy density function Ω is a function of J_2 alone: $\Omega = \Omega(J_2)$. Then, based on the normality relation (3.33), we have:

$$\epsilon_{ij} = \frac{\partial \Omega}{\partial \sigma_{ij}} = \frac{\partial \Omega}{\partial J_2}\frac{\partial J_2}{\partial \sigma_{ij}} = f(J_2)s_{ij} \tag{3.70}$$

which indicates that the volumetric strain $\epsilon_{ii} = \epsilon_v$ is always zero in such case.

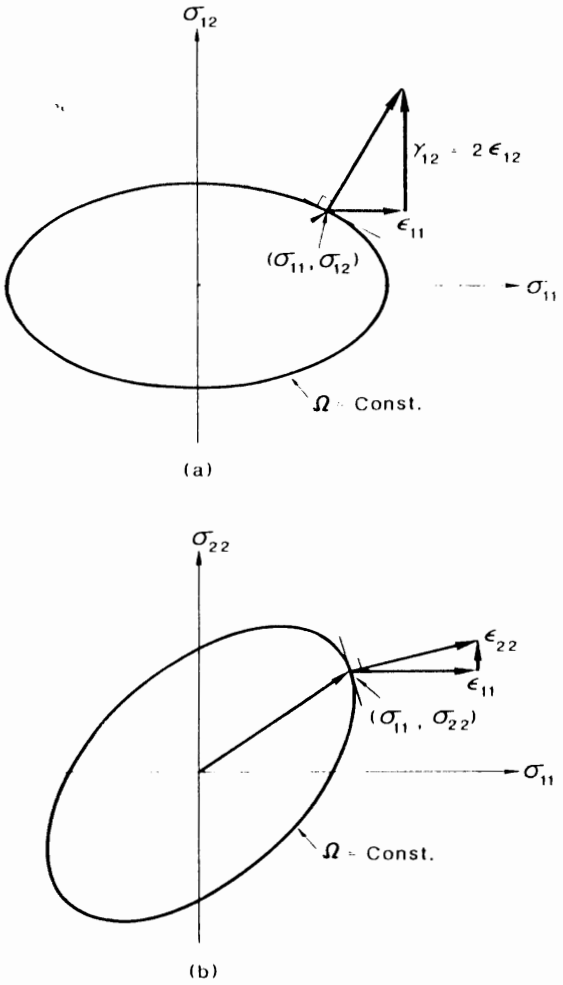

Fig. 3-4 Normality in two-dimensional stress subspaces for an isotropic linear elastic material. (a) Combined tension σ_{11} and shear σ_{12}. (b) Biaxial tension σ_{11} and σ_{22}.

Because of the symmetry of σ_{ij} and ϵ_{ij}, it is just permissible (and more convenient) to work in a six-dimensional stress space σ_{11}, σ_{22}, σ_{33}, σ_{12}, σ_{23}, and σ_{31}, with the normal strain vector representing ϵ_{11}, ϵ_{22}, ϵ_{33}, γ_{12}, γ_{23}, and γ_{31} as in the full nine-dimensional space. In such a case, the normality conditions give:

$$\epsilon_{11} = \frac{\partial \Omega}{\partial \sigma_{11}}, \quad \gamma_{12} = \frac{\partial \Omega}{\partial \sigma_{12}} \tag{3.71}$$

in which Ω is expressed in terms of the six independent stress components. Of course, much of the time we deal with fewer nonzero components of stress and a subspace of the six-dimensional space is used. For instance, combined tension σ_{11} and shear σ_{12} $(= \sigma_{21})$, and biaxial tension σ_{11} and σ_{22}, are represented in the two-dimensional subspaces $(\sigma_{11}, \sigma_{12})$ and $(\sigma_{11}, \sigma_{22})$, respectively, as shown in Fig. 3.4 for an isotropic linear elastic material. Similarly, normality condition can be said for Eq. (3.24).

Convexity

Here, a pictorial proof of convexity based on the stability and normality definitions is described below.

Consider any existing states of stress and strain σ_{ij}^{a} and ϵ_{ij}^{a} with the corresponding surface $\Omega(\sigma_{ij}^{a}) = \text{constant}$. Assume that this surface is nonconvex, as shown in Fig. 3.5. Then, it is always possible to reach a state of stress σ_{ij}^{b} on the same surface $\Omega(\sigma_{ij}^{a}) = \text{constant}$ by adding the stress set $\Delta\sigma_{ij}$ to σ_{ij}^{a} along a straight-line path which lies outside the surface. Stability postulate requires that the net work done by the added stress set on the resulting strain changes be positive; that is:

$$\int_{\sigma_{ij}^{a}}^{\sigma_{ij}^{b}} (\epsilon_{ij} - \epsilon_{ij}^{a})\, d\sigma_{ij} > 0 \tag{3.72}$$

which can be rewritten as:

$$\int_{0}^{\sigma_{ij}^{b}} \epsilon_{ij}\, d\sigma_{ij} \quad \int_{0}^{\sigma_{ij}^{a}} \epsilon_{ij}\, d\sigma_{ij} \quad \epsilon_{ij}^{a} \Delta\sigma_{ij} > 0 \tag{3.73}$$

The first two terms give $\Omega(\sigma_{ij}^{b}) - \Omega(\sigma_{ij}^{a}) = 0$, since the two states σ_{ij}^{a} and σ_{ij}^{b} lie on the same surface of constant Ω. Therefore, inequality (3.73) reduces to:

$$\epsilon_{ij}^{a} \Delta\sigma_{ij} < 0 \tag{3.74}$$

that is, the angle between the two vectors ϵ_{ij}^{a} (normal to the surface $\Omega = \text{constant}$ at σ_{ij}^{a}) and $\Delta\sigma_{ij}$ must be obtuse for all σ_{ij}^{b} and $\Delta\sigma_{ij}$. However, if the surface is nonconvex, as assumed, one can always find a vector $\Delta\sigma_{ij}$ at an acute angle to the vector ϵ_{ij}^{a} (such as $\Delta\sigma_{ij}$ in Fig. 3.5 with θ less than 90°), in which case $\epsilon_{ij}^{a} \Delta\sigma_{ij} > 0$ and inequality (3.74) is violated. Therefore, the surface $\Omega = \text{constant}$ must be

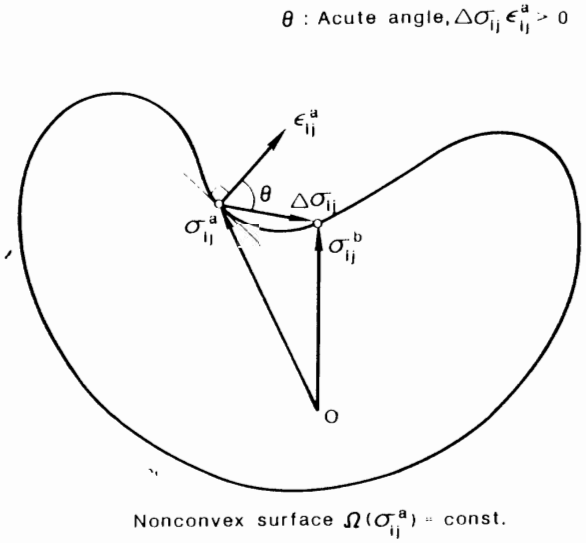

Fig. 3.5. Normality of the surface $\Omega = \text{const}$ without convexity.

convex; and in this case all the possible vectors $\Delta\sigma_{ij}$ lie inside the surface satisfying inequality (3.74).

3.4 LINEAR ELASTIC STRESS-STRAIN RELATIONS

3.4.1 Generalized Hooke's law

Assuming the initial strain-free state corresponds to an initial stress-free state, that is, $B_{ij} = 0$, then Eq. (3.1) reduces to:

$$\sigma_{ij} = C_{ijkl}\epsilon_{kl} \tag{3.75}$$

Equation (3.75) is the simplest generalization of the linear dependence of stress on strain observed in the familiar Hooke's experiment in a simple tension test and is often referred to as the *generalized Hooke's law*.

Since both stress σ_{ij} and strain ϵ_{ij} are second-order tensors, it follows that C_{ijkl} is a fourth-order tensor which consists of $(3)^4 = 81$ material constants. From $\sigma_{ij} = \sigma_{ji}$ and $\epsilon_{ij} = \epsilon_{ji}$, the number of 81 material constants is reduced to 36 under the symmetric conditions of $C_{ijkl} = C_{jikl} = C_{ijlk} = C_{jilk}$. Further, for a *Green elastic material* that requires an energy conservation, additional restrictions on C_{ijkl} are required. This is shown in the following. Expanding the strain energy density function $W(\epsilon_{ij})$ in a polynomial form and keeping only second-order terms, we have:

$$W = c_0 + \alpha_{ij}\epsilon_{ij} + \beta_{ijkl}\epsilon_{ij}\epsilon_{kl} \tag{3.76}$$

where c_0, α_{ij}, and β_{ijkl} are constants. Employing Eq. (3.24), the stress tensor σ_{ij} can be written as:

$$\sigma_{ij} = \alpha_{ij} + (\beta_{ijkl} + \beta_{klij})\epsilon_{kl} \tag{3.77}$$

Assuming the initial strain-free state corresponding to an initial stress-free state, i.e., $\alpha_{ij} = 0$, we have:

$$\sigma_{ij} = (\beta_{ijkl} + \beta_{klij})\epsilon_{kl} \tag{3.78}$$

Comparing Eq. (3.78) with Eq. (3.75), the response constants C_{ijkl} can be written as:

$$C_{ijkl} = \beta_{ijkl} + \beta_{klij} \tag{3.79}$$

This relation requires that for a Green elastic material, the order of the pairs of subscripts (ij) and (kl) can be interchanged, i.e.:

$$C_{(ij)(kl)} = C_{(kl)(ij)} \tag{3.80}$$

As a result, the number of material constant needed for a linearly elastic material becomes 21. The material consisting of such 21 material constants is called *linearly anisotropic material*. Using the six stress components (σ_{11}, σ_{22}, σ_{33}, σ_{12}, σ_{23}, σ_{31}) and six strain components (ϵ_{11}, ϵ_{22}, ϵ_{33}, γ_{12}, γ_{23}, γ_{31}), the general matrix form of the stress-strain relation for a linearly anisotropic elastic material is written as:

$$\begin{Bmatrix} \sigma_{11} \\ \sigma_{22} \\ \sigma_{33} \\ \sigma_{12} \\ \sigma_{23} \\ \sigma_{31} \end{Bmatrix} = \begin{bmatrix} C_{11} & C_{12} & C_{13} & C_{14} & C_{15} & C_{16} \\ & C_{22} & C_{23} & C_{24} & C_{25} & C_{26} \\ & & C_{33} & C_{34} & C_{35} & C_{36} \\ & & & C_{44} & C_{45} & C_{46} \\ & \text{Symmetric} & & & C_{55} & C_{56} \\ & & & & & C_{66} \end{bmatrix} \begin{Bmatrix} \epsilon_{11} \\ \epsilon_{22} \\ \epsilon_{33} \\ \gamma_{12} \\ \gamma_{23} \\ \gamma_{31} \end{Bmatrix} \tag{3.81}$$

If there are additional symmetries existed in the material, these 21 independent constants can be further reduced. This is illustrated in the forthcoming.

3.4.2 A plane of symmetry

A material with a plane of symmetry requires that the elastic property is unchanged under 180-degree rotation about one of the coordinate axes x_1, x_2, and x_3 which are taken inside a material. Figure 3.6 shows the coordinate axes x_1, x_2, and x_3 where the relation between stress components and strain components is defined by utilizing Eq. (3.81). We now define a new coordinate axes x_1', x_2', and x_3' in order to take into account a plane of symmetry with respect to the x_2-x_3-plane, as shown in Fig. 3.6. Stress tensor σ_{ij}^* and strain tensor ϵ_{ij}^* transformed into the new

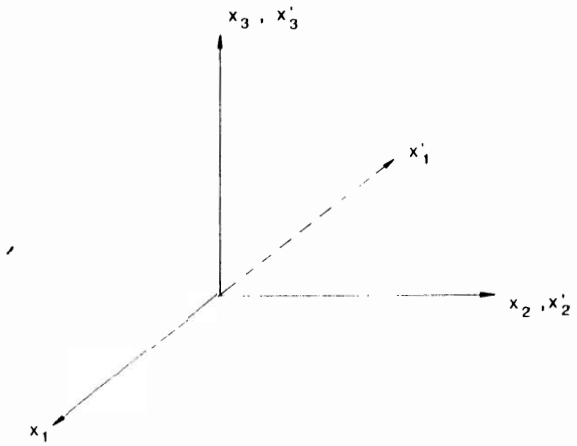

Fig. 3.6. A plane of symmetry about x_1-x_3-plane.

coordinate system are expressed in terms of the stresses σ_{ij} and strains ϵ_{ij} in (x_1, x_2, x_3) coordinate axes, that is:

$$\sigma_{ij}^* = l_{ik} l_{jl} \sigma_{kl} \tag{3.82a}$$

$$\epsilon_{ij}^* = l_{ik} l_{jl} \epsilon_{kl} \tag{3.82b}$$

where l_{ij} represents the cosines of the angles between the x_i' and x_j axes for i and j ranging in values from 1 to 3. The tensor l_{ij} is now written in the matrix form as:

$$l_{ij} = \begin{vmatrix} 1 & 0 & 0 \\ 0 & 1 & 0 \\ 0 & 0 & 1 \end{vmatrix} \tag{3.83}$$

Substituting Eq. (3.83) into Eq. (3.82), stress tensor σ_{ij}^* and strain tensor ϵ_{ij}^* transformed into the new coordinate become in a matrix form:

$$\sigma_{ij}^* = \begin{vmatrix} \sigma_{11} & -\sigma_{12} & -\sigma_{13} \\ \sigma_{21} & \sigma_{22} & \sigma_{23} \\ -\sigma_{31} & \sigma_{32} & \sigma_{33} \end{vmatrix} \tag{3.84a}$$

$$\epsilon_{ij}^* \quad \begin{vmatrix} \epsilon_{11} & \epsilon_{12} & \epsilon_{13} \\ \epsilon_{21} & \epsilon_{22} & \epsilon_{23} \\ \epsilon_{31} & \epsilon_{32} & \epsilon_{33} \end{vmatrix} \tag{3.84b}$$

Stress tensor σ_{ij}^* and strain tensor ϵ_{ij}^* should be in a relation of Eq. (3.75), that is:

$$\sigma_{ij}^* \quad C_{ijkl}' \epsilon_{kl}^* \tag{3.85}$$

Thus, the following coefficients in Eq. (3.81) should be zero:

$$C_{14}' \quad C_{16}' = C_{24}' = C_{26}' = C_{34}' = C_{36}' = C_{45}' = C_{56}' = 0 \tag{3.86}$$

The 21 material constants are now reduced to 13. The general matrix form of a linearly elastic material with *a plane of symmetry* is thus written as:

$$\begin{Bmatrix} \sigma_{11} \\ \sigma_{22} \\ \sigma_{33} \\ \sigma_{12} \\ \sigma_{23} \\ \sigma_{31} \end{Bmatrix} = \begin{bmatrix} C_{11} & C_{12} & C_{13} & 0 & C_{15} & 0 \\ & C_{22} & C_{23} & 0 & C_{25} & 0 \\ & & C_{33} & 0 & C_{35} & 0 \\ & & & C_{44} & 0 & C_{46} \\ & \text{Symmetric} & & & C_{55} & 0 \\ & & & & & C_{66} \end{bmatrix} \begin{Bmatrix} \epsilon_{11} \\ \epsilon_{22} \\ \epsilon_{33} \\ \gamma_{12} \\ \gamma_{23} \\ \gamma_{31} \end{Bmatrix} \tag{3.87}$$

3.4.3 Two planes of symmetry (orthotropic symmetry)

In addition to a plane of symmetry about x_2-x_3-plane, consider the case of a plane of symmetry about x_1-x_3-plane as shown in Fig. 3.7. A similar procedure to that of one plane of symmetry is taken by utilizing the following transformation tensor l_{ij}:

$$l_{ij} = \begin{bmatrix} 1 & 0 & 0 \\ 0 & -1 & 0 \\ 0 & 0 & 1 \end{bmatrix} \tag{3.88}$$

The stress tensor σ_{ij}^* and the strain tensor ϵ_{ij}^* transformed into the new coordinate system (x_1', x_2', x_3') are respectively written as:

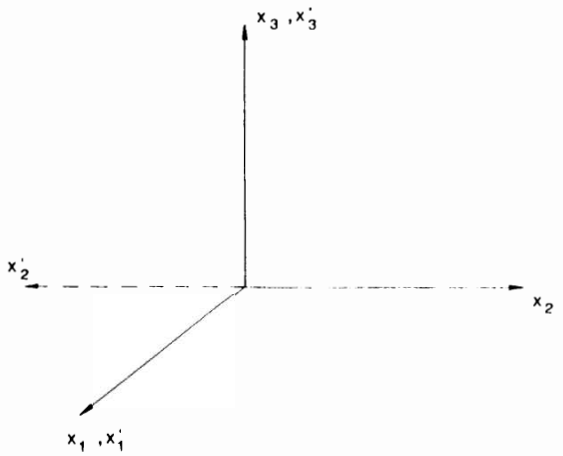

Fig. 3.7. A plane of symmetry about x_1-x_3-plane.

$$\sigma_{ij}^{*} = \begin{bmatrix} \sigma_{11} & \sigma_{12} & \sigma_{13} \\ \sigma_{21} & \sigma_{22} & -\sigma_{23} \\ \sigma_{31} & -\sigma_{32} & \sigma_{33} \end{bmatrix} \tag{3.89a}$$

$$\epsilon_{ij}^{*} = \begin{bmatrix} \epsilon_{11} & \epsilon_{12} & \epsilon_{13} \\ \epsilon_{21} & \epsilon_{22} & -\epsilon_{23} \\ \epsilon_{31} & -\epsilon_{32} & \epsilon_{33} \end{bmatrix} \tag{3.89b}$$

Using Eqs. (3.89) and (3.87), it is found that $C_{15} = C_{25} = C_{35} = C_{46} = 0$. Thus, the material constants are reduced to 9. The *two planes of symmetry* implies also the symmetry about the third orthogonal plane (called *orthotropic symmetry*), and the number of material constants for a linear elastic orthotropic material is nine.

The general matrix form of such a material is expressed as:

$$\begin{Bmatrix} \sigma_{11} \\ \sigma_{22} \\ \sigma_{33} \\ \sigma_{12} \\ \sigma_{23} \\ \sigma_{31} \end{Bmatrix} = \begin{bmatrix} C_{11} & C_{12} & C_{13} & 0 & 0 & 0 \\ & C_{22} & C_{23} & 0 & 0 & 0 \\ & & C_{33} & 0 & 0 & 0 \\ & & & C_{44} & 0 & 0 \\ & \text{Symmetric} & & & C_{55} & 0 \\ & & & & & C_{66} \end{bmatrix} \begin{Bmatrix} \epsilon_{11} \\ \epsilon_{22} \\ \epsilon_{33} \\ \gamma_{12} \\ \gamma_{23} \\ \gamma_{31} \end{Bmatrix} \tag{3.90}$$

3.4.4 Transverse and cubic isotropies

In the case of a *transversely isotropic material*, the material exhibits a rotationally elastic symmetry about one of the coordinate axes, x_1, x_2, and x_3. Figure 3.8 shows

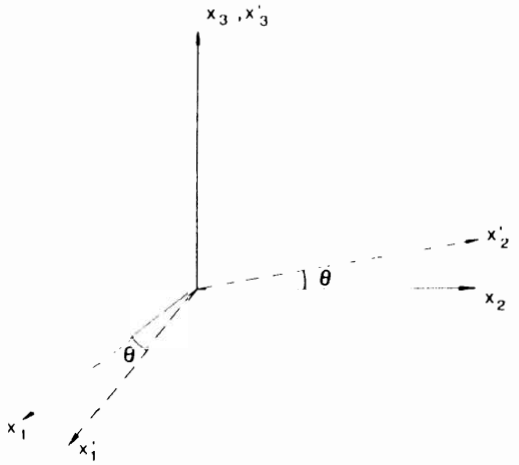

Fig. 3.8. Transverse isotropy.

the coordinate system corresponding to the transverse isotropy of material about the coordinate axis x_3. Transformation tensor l_{ij} is given by:

$$l_{ij} = \begin{bmatrix} \cos\theta & \sin\theta & 0 \\ -\sin\theta & \cos\theta & 0 \\ 0 & 0 & 1 \end{bmatrix} \tag{3.91}$$

In a similar manner to the previous cases, σ_{ij}^* and ϵ_{ij}^* are obtained, and material constants have the following relationship such as:

$$C_{11} = C_{22}, \quad C_{13} = C_{23}, \quad C_{44} = \tfrac{1}{2}(C_{11} - C_{12}), \quad \text{and } C_{55} = C_{66} \tag{3.92}$$

Thus, the matrix form of a transversely isotropic material with five constants can be written as:

$$\begin{Bmatrix} \sigma_{11} \\ \sigma_{22} \\ \sigma_{33} \\ \sigma_{12} \\ \sigma_{23} \\ \sigma_{31} \end{Bmatrix} = \begin{bmatrix} C_{11} & C_{12} & C_{13} & 0 & 0 & 0 \\ & C_{11} & C_{13} & 0 & 0 & 0 \\ & & C_{33} & 0 & 0 & 0 \\ & & & \tfrac{1}{2}(C_{11} - C_{12}) & 0 & 0 \\ & \text{Symmetric} & & & C_{55} & 0 \\ & & & & & C_{55} \end{bmatrix} \begin{Bmatrix} \epsilon_{11} \\ \epsilon_{22} \\ \epsilon_{33} \\ \gamma_{12} \\ \gamma_{23} \\ \gamma_{31} \end{Bmatrix} \tag{3.93}$$

For a linearly elastic material with *cubic symmetry* for which the properties along the x_1, x_2, and x_3 directions are identical, we can not distinguish between directions x_1, x_2, and x_3 as shown in Fig. 3.9. It follows that the cubic symmetric material has only three independent material constants. The matrix form of the stress-strain relation can be expressed as:

$$\begin{Bmatrix} \sigma_{11} \\ \sigma_{22} \\ \sigma_{33} \\ \sigma_{12} \\ \sigma_{23} \\ \sigma_{31} \end{Bmatrix} = \begin{bmatrix} C_{11} & C_{12} & C_{12} & 0 & 0 & 0 \\ & C_{11} & C_{12} & 0 & 0 & 0 \\ & & C_{11} & 0 & 0 & 0 \\ & & & C_{44} & 0 & 0 \\ & \text{Symmetric} & & & C_{44} & 0 \\ & & & & & C_{44} \end{bmatrix} \begin{Bmatrix} \epsilon_{11} \\ \epsilon_{22} \\ \epsilon_{33} \\ \gamma_{12} \\ \gamma_{23} \\ \gamma_{31} \end{Bmatrix} \tag{3.94}$$

3.4.5 Full isotropy

For a material whose elastic properties are not a function of direction at all, only two independent elastic material constants are sufficient to describe its behavior completely. This material is called *isotropic linear elastic*. The stress-strain relationship for this material is thus written as an extension of that of a transversely isotropic material, i.e.:

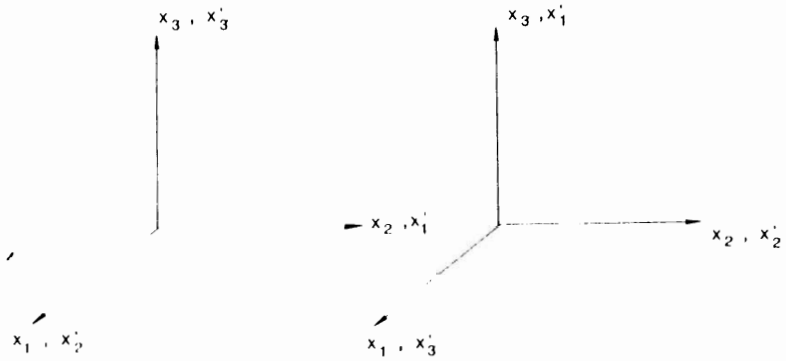

Fig. 3.9. Cubic isotropy.

$$\begin{Bmatrix}\sigma_{11}\\ \sigma_{22}\\ \sigma_{33}\\ \sigma_{12}\\ \sigma_{23}\\ \sigma_{31}\end{Bmatrix} = \begin{bmatrix} C'_{11} & C'_{12} & C'_{12} & 0 & 0 & 0 \\ & C'_{11} & C'_{12} & 0 & 0 & 0 \\ & & C'_{11} & 0 & 0 & 0 \\ & & & \tfrac{1}{2}(C'_{11}-C'_{12}) & 0 & 0 \\ & \text{Symmetric} & & & \tfrac{1}{2}(C'_{11}-C'_{12}) & 0 \\ & & & & & \tfrac{1}{2}(C'_{11}-C'_{12}) \end{bmatrix} \begin{Bmatrix}\epsilon_{11}\\ \epsilon_{22}\\ \epsilon_{33}\\ \gamma_{12}\\ \gamma_{23}\\ \gamma_{31}\end{Bmatrix} \tag{3.95}$$

Replacing C'_{12} and $\frac{1}{2}(C'_{11} - C'_{12})$ respectively by λ and μ which are called *Lamé's constants*, Eq. (3.95) is rewritten as:

$$\begin{Bmatrix}\sigma_{11}\\ \sigma_{22}\\ \sigma_{33}\\ \sigma_{12}\\ \sigma_{23}\\ \sigma_{31}\end{Bmatrix} = \begin{bmatrix} \lambda+2\mu & \lambda & \lambda & 0 & 0 & 0 \\ & \lambda+2\mu & \lambda & 0 & 0 & 0 \\ & & \lambda+2\mu & 0 & 0 & 0 \\ & & & \mu & 0 & 0 \\ & \text{Symmetric} & & & \mu & 0 \\ & & & & & \mu \end{bmatrix} \begin{Bmatrix}\epsilon_{11}\\ \epsilon_{22}\\ \epsilon_{33}\\ \gamma_{12}\\ \gamma_{23}\\ \gamma_{31}\end{Bmatrix} \tag{3.96}$$

3.5 ISOTROPIC LINEAR ELASTIC STRESS-STRAIN RELATIONS

In this Section, the tensor forms of isotropic linear stress-strain relations are shown, and the physical meaning of Lamé's constants λ and μ is explained from simple tests under simple states of stresses. Subsequently, the matrix forms of isotropic linear elastic stress-strain relations which are suitable for a direct use in stress analysis are given for various cases such as the three-dimensional, plane stress, plane strain, and axisymmetric conditions.

3.5.1 Tensor forms

The general form of the isotropic elastic tensor C_{ijkl} in Eq. (3.96) can be expressed in terms of the isotropic tensors:

$$C_{ijkl} = \lambda\delta_{ij}\delta_{kl} + \mu(\delta_{ik}\delta_{jl} + \delta_{il}\delta_{jk}) \tag{3.97}$$

and substitution of Eq. (3.97) into Eq. (3.75) yields the following tensorial form:

$$\sigma_{ij} = 2\mu\epsilon_{ij} + \lambda\epsilon_{kk}\delta_{ij} \tag{3.98}$$

where ϵ_{kk} is an elastic volumetric strain, i.e., $\epsilon_{kk} = \epsilon_{11} + \epsilon_{22} + \epsilon_{33}$. The volumetric strain ϵ_{kk} is given by setting a tensorial index, $i = j$, then:

$$\epsilon_{kk} = \frac{\sigma_{kk}}{3\lambda + 2\mu} \tag{3.99}$$

where σ_{kk} is the sum of three normal stress components, i.e., $\sigma_{kk} = \sigma_{11} + \sigma_{22} + \sigma_{33}$.

Substituting Eq. (3.99) into Eq. (3.98) and solving for ϵ_{ij}, we find:

$$\epsilon_{ij} = -\frac{\lambda}{2\mu(3\lambda + 2\mu)}\sigma_{kk}\delta_{ij} + \frac{1}{2\mu}\sigma_{ij} \tag{3.100}$$

It can be understood from both Eqs. (3.98) and (3.100) that the principal directions of stress and strain coincide. The Lamé's constants λ and μ are determined from simple tests corresponding to simple states of stresses. Some of these tests suitable for soil materials are as follows:

Hydrostatic pressure test (Fig. 3.10a): If $\sigma_{ij} = \sigma_m\delta_{ij}$ where σ_m is the hydrostatic pressure, the ratio of the pressure σ_m to the change in volumetric strain, ϵ_{kk} is defined as the *bulk modulus K*. From Eq. (3.99), it can easily be expressed as:

$$K = \frac{\sigma_m}{\epsilon_{kk}} = \lambda + \tfrac{2}{3}\mu \tag{3.101}$$

Simple compression test (Fig. 3.10b): In this case, only a compressive stress σ_{11} exists and the others are zero. Equation (3.98) can be expressed as:

$$\sigma_{11} = 2\mu\epsilon_{11} + \lambda\epsilon_{kk} \tag{3.102a}$$

$$0 = 2\mu\epsilon_{22} + \lambda\epsilon_{kk} \tag{3.102b}$$

$$0 = 2\mu\epsilon_{33} + \lambda\epsilon_{kk} \tag{3.102c}$$

Using the above equations, the ratio of $\sigma_{11}/\epsilon_{11}$, defined as the *Young's modulus* E, is given by:

$$E = \frac{\sigma_{11}}{\epsilon_{11}} = \frac{\mu(3\lambda + 2\mu)}{\lambda + \mu} \tag{3.103}$$

On the other hand, the ratio of the fractional expansion ϵ_{22} to the linear strain ϵ_{11}, defined as the *Poisson's ratio* ν, is given by:

$$\nu = -\frac{\epsilon_{22}}{\epsilon_{11}} = -\frac{\epsilon_{33}}{\epsilon_{11}} = \frac{\lambda}{2(\lambda + \mu)} \tag{3.104}$$

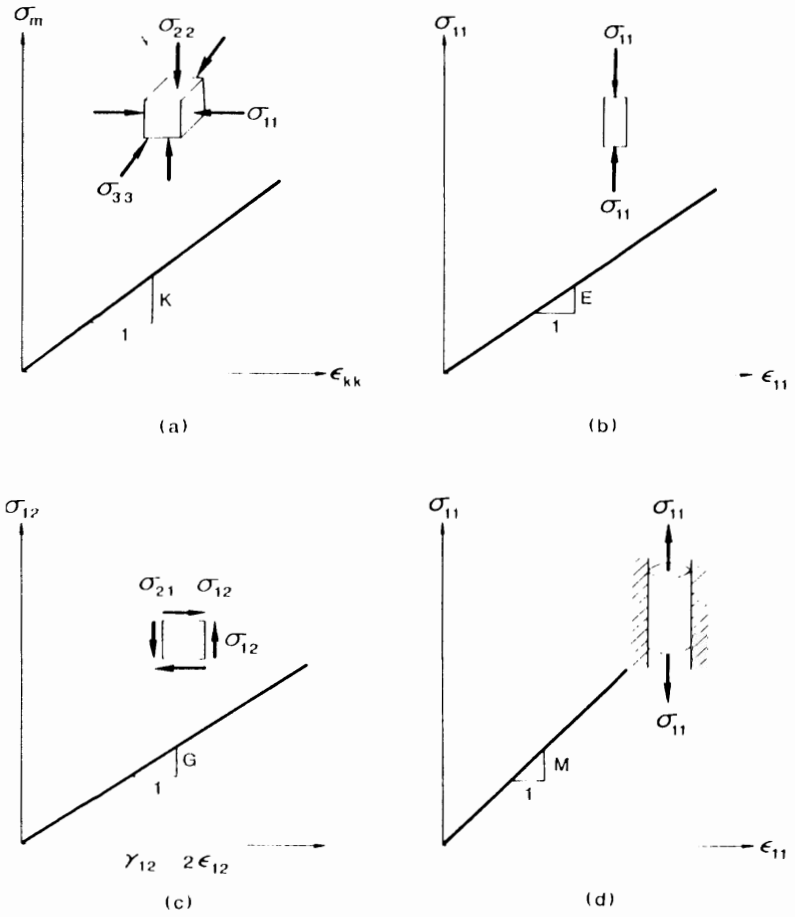

Fig. 3.10. Behavior of isotropic linear elastic material in simple tests. (a) Hydrostatic compression test ($\sigma_{11} = \sigma_{22} = \sigma_{33} = p$). (b) Simple compression test. (c) Pure shear test. (d) Uniaxial strain test.

Pure shear test (Fig. 3.10c): Only a shear stress $\sigma_{12} = \sigma_{21}$ is not zero. The ratio $\sigma_{12}/2\epsilon_{12}$ or σ_{12}/γ_{12}, defined as the *shear modulus* G, is written from Eq. (3.98) as:

$$G = \mu \tag{3.105}$$

Uniaxial strain test (Fig. 3.10d): This test is performed by applying a uniaxial stress component σ_{11} in the axial direction of a cylindrical test sample so that the lateral surface is restrained against lateral movement. Consequently, in this case an axial strain ϵ_{11} is the only nonvanishing component. The ratio between σ_{11} and ϵ_{11}, defined as the *constrained modulus*, M, is given from Eq. (3.98) by:

$$\sigma_{11} = \lambda\epsilon_{11} + 2\mu\epsilon_{11} \tag{3.106a}$$

or

$$M = \frac{\sigma_{11}}{\epsilon_{11}} = \lambda + 2\mu \tag{3.106b}$$

By knowing these relationships, any one of the elastic constants E, ν, K, λ, μ or M can be expressed in terms of any other two of the constants. In particular, the following relationships for soil parameters are frequently used in the mathematical modeling of a linear isotropic elastic material:

$$K = \frac{E}{3(1-2\nu)}, \qquad G = \frac{E}{2(1+\nu)} \tag{3.107a}$$

or

$$E = \frac{9KG}{3K+G}, \qquad \nu = \frac{3K-2G}{2(3K+G)} \tag{3.107b}$$

For real elastic materials, experiments have shown that the material constants E, G, and K are always positive, that is:

$$E > 0, \quad G > 0, \quad \text{and} \quad K > 0 \tag{3.108}$$

These conditions imply that, for example, a uniaxial tensile stress causes an extension of the material in the same direction. Similarly, a shear strain caused by a simple shear stress has the same direction of the shear stress. From the inequalities in Eq. (3.108) and the relationship (3.107a), we note the following restriction imposed on the Poisson's ratio ν:

$$-1 < \nu < \tfrac{1}{2} \tag{3.109}$$

At present, we have no practical experience for any existing material that will exhibit a negative value of ν.

Example 3.2: Using the strain-displacement relation in Eq. (2.90) and the stress-strain relations of an isotropic linear elastic material, show that the equations of equilibrium, Eq. (2.88), can be written in the following form (these equations are known as *Navier's displacement equations*):

$$u_{i,jj} + \frac{1}{1-2\nu} u_{j,ji} + \frac{F_i}{G} = 0 \tag{3.110}$$

in which u_i, ν, and G are displacement components, Poisson's ratio, and shear modulus, respectively.

Solutions: Substituting the strain-displacement relations in Eq. (2.90), $\epsilon_{ij} = \frac{1}{2}(u_{i,j} + u_{j,i})$, into stress-strain relations in Eq. (3.98), we have:

$$\sigma_{ij} = \sigma_{ji} = \mu(u_{i,j} + u_{j,i}) + \lambda u_{k,k}\delta_{ij} \tag{3.111}$$

Differentiation of the above equation with respect to the x_j-coordinate axis leads to:

$$\sigma_{ji,j} = \mu(u_{i,jj} + u_{j,ij}) + \lambda u_{k,kj}\delta_{ij} = \mu(u_{i,jj} + u_{j,ij}) + \lambda u_{k,ki} \tag{3.112}$$

since $u_{k,kj}\delta_{ij} = u_{k,ki}$. Substitution of Eq. (3.112) into equations of equilibrium yields:

$$\mu(u_{i,jj} + u_{j,ij}) + \lambda u_{k,ki} + F_i = 0 \tag{3.113a}$$

or

$$\mu(u_{i,jj} + u_{j,ji}) + \lambda u_{j,ji} + F_i = 0 \tag{3.113b}$$

since $u_{j,ij} = u_{j,ji}$ and $u_{k,ki} = u_{j,ji}$.

Further substitution of $\lambda = 2\nu\mu/(1-2\nu)$ from Eq. (3.104) and $\mu = G$ gives Navier's displacement equations, that is:

$$u_{i,jj} + \frac{1}{1-2\nu} u_{j,ji} + \frac{F_i}{G} = 0$$

Example 3.3: Show that the first-order isotropic formulation of the Cauchy elastic model and hyperelastic model gives the identical stress-strain relations to those in Eq. (3.98).

Solutions:

First-order Cauchy elastic model. In order for Eq. (3.4) to be first-order (linear) elastic stress-strain relation, A_0 is a linear function of the first strain invariant I_1', A_1 is constant, and A_2 is zero. Thus, Eq. (3.4) can be written as:

$$\sigma_{ij} = \alpha_0\delta_{ij} + \alpha_1 I_1'\delta_{ij} + \alpha_2\epsilon_{ij} \tag{3.114}$$

where α_0, α_1, and α_2 are material constants. If the initial strain-free state corresponds to an initial stress-free state, Eq. (3.114) becomes:

$$\sigma_{ij} = \alpha_1 I_1' \delta_{ij} + \alpha_2 \epsilon_{ij} \tag{3.115}$$

Replacing respectively α_1 and α_2 by λ and 2μ leads to the identical forms to Eq. (3.98) for an isotropic linear elastic material.

First-order hyperelastic (Green) model. In order for Eq. (3.28) to present the first-order stress-strain relation, the strain energy density function W needs to keep all quadratic terms in strains. Assuming again that the initial strain-free state corresponds to an initial stress-free state, the function W can be written as:

$$W = \beta_1 I_1'^2 + \beta_2 \bar{I}_2' \tag{3.116}$$

where β_1 and β_2 are material constants. Substituting Eq. (3.116) into Eq. (3.28), we find:

$$\sigma_{ij} = \frac{\partial\left(\beta_1 I_1'^2 + \beta_2 \bar{I}_2'\right)}{\partial I_1'} \delta_{ij} + \frac{\partial\left(\beta_1 I_1'^2 + \beta_2 \bar{I}_2'\right)}{\partial \bar{I}_2'} \epsilon_{ij} + \frac{\partial\left(\beta_1 I_1'^2 + \beta_2 I_3'\right)}{\partial I_3'} \epsilon_{ik}\epsilon_{kj}$$

$$= 2\beta_1 I_1' \delta_{ij} + \beta_2 \epsilon_{ij} \tag{3.117}$$

Replacing respectively β_1 and β_2 by $\lambda/2$ and 2μ, then, we have again the identical expressions to Eq. (3.98).

Example 3.4: Show that for an isotropic linear elastic material the hydrostatic stress and deviatoric stress respectively cause the volumetric strain and devatoric strain.

Solutions: Using Eqs. (3.103) through (3.105), the strain-stress relation in Eq. (3.100) can be written as:

$$\epsilon_{ij} = \frac{1}{2G}\sigma_{ij} - \frac{\nu}{E}\sigma_{kk}\delta_{ij} \tag{3.118}$$

A neat and logical separation exists between the hydrostatic response and the deviatoric response. Substitution of $(s_{ij} + \frac{1}{3}\sigma_{kk}\delta_{ij})$ for σ_{ij} and $(e_{ij} + \frac{1}{3}\epsilon_{kk}\delta_{ij})$ for ϵ_{ij} into Eq. (3.118) leads to:

$$e_{ij} + \tfrac{1}{3}\epsilon_{kk}\delta_{ij} = \frac{1}{2G}s_{ij} + \frac{1-2\nu}{3E}\sigma_{kk}\delta_{ij} \tag{3.119}$$

Thus, we find the following relationships:

$$e_{ij} = \frac{1}{2G}s_{ij} \tag{3.120}$$

$$\epsilon_{kk} = \frac{3(1-2\nu)}{E}\sigma_{\mathrm{m}} = \frac{1}{K}\sigma_{\mathrm{m}} \tag{3.121}$$

where σ_{m} is $\frac{1}{3}\sigma_{kk}$.

Equations (3.120) and (3.121) indicate that the distortion e_{ij} is produced by the stress deviations s_{ij}, and that the volumetric change ϵ_{kk} or ϵ_v is produced by the mean normal stress σ_m. Each is independent of the other. Consequently, the stress-strain relationships can be expressed in a simple form of K and G:

$$\epsilon_{ij} = \frac{1}{2G} s_{ij} + \frac{1}{9K} \sigma_{kk} \delta_{ij} \tag{3.122}$$

$$\sigma_{ij} = 2Ge_{ij} + K\epsilon_{kk}\delta_{ij} \tag{3.123}$$

3.5.2 Three-dimensional matrix forms

Replacing Lamé's material constants λ and μ in Eq. (3.96) by Young's modulus E and Poisson's ratio ν, the stress-strain relations for the three-dimensional case can be written in the following matrix form:

$$\begin{Bmatrix} \sigma_{11} \\ \sigma_{22} \\ \sigma_{33} \\ \sigma_{12} \\ \sigma_{23} \\ \sigma_{31} \end{Bmatrix} = \frac{E}{(1+\nu)(1-2\nu)} \times \begin{bmatrix} 1 & \nu & \nu & \nu & 0 & 0 & 0 \\ & 1 & \nu & \nu & 0 & 0 & 0 \\ & & 1 & \nu & 0 & 0 & 0 \\ & & & & \frac{(1-2\nu)}{2} & 0 & 0 \\ & & & & & \frac{(1-2\nu)}{2} & 0 \\ & \text{Symmetric} & & & & & \frac{(1-2\nu)}{2} \end{bmatrix} \begin{Bmatrix} \epsilon_{11} \\ \epsilon_{22} \\ \epsilon_{33} \\ \gamma_{12} \\ \gamma_{23} \\ \gamma_{31} \end{Bmatrix} \tag{3.124}$$

where it should be noted that the strain components consist of the engineering shear strains. Substituting Eq. (3.107b) into Eq. (3.124), we have an alternative form:

$$\begin{Bmatrix} \sigma_{11} \\ \sigma_{22} \\ \sigma_{33} \\ \sigma_{12} \\ \sigma_{23} \\ \sigma_{31} \end{Bmatrix} = \begin{bmatrix} (K + \frac{4}{3}G) & (K - \frac{2}{3}G) & (K - \frac{2}{3}G) & 0 & 0 & 0 \\ & (K + \frac{4}{3}G) & (K - \frac{2}{3}G) & 0 & 0 & 0 \\ & & (K + \frac{4}{3}G) & 0 & 0 & 0 \\ & & & G & 0 & 0 \\ & \text{Symmetric} & & & G & 0 \\ & & & & & G \end{bmatrix} \begin{Bmatrix} \epsilon_{11} \\ \epsilon_{22} \\ \epsilon_{33} \\ \gamma_{12} \\ \gamma_{23} \\ \gamma_{31} \end{Bmatrix} \tag{3.125}$$

3.5.3 *Plane stress case*

The three-dimensional stress-strain relations can be reduced to the two-dimensional plane stress case as shown in Fig. 3.11a. The stress conditions are:

$$\sigma_{31} = \sigma_{32} = \sigma_{33} = 0 \tag{3.126}$$

Using Eq. (3.126), the expression in Eq. (3.124) can be reduced to the matrix form:

$$\begin{Bmatrix} \sigma_{11} \\ \sigma_{22} \\ \sigma_{12} \end{Bmatrix} = \frac{E}{1-\nu^2} \begin{bmatrix} 1 & \nu & 0 \\ \nu & 1 & 0 \\ 0 & 0 & \dfrac{1-\nu}{2} \end{bmatrix} \begin{Bmatrix} \epsilon_{11} \\ \epsilon_{22} \\ \gamma_{12} \end{Bmatrix} \tag{3.127}$$

or

$$\begin{Bmatrix} \epsilon_{11} \\ \epsilon_{22} \\ \gamma_{12} \end{Bmatrix} = \frac{1}{E} \begin{bmatrix} 1 & -\nu & 0 \\ -\nu & 1 & 0 \\ 0 & 0 & 2(1+\nu) \end{bmatrix} \begin{Bmatrix} \sigma_{11} \\ \sigma_{22} \\ \sigma_{12} \end{Bmatrix} \tag{3.128}$$

Although in the plane stress case, we have:

$$\epsilon_{23} = \epsilon_{31} = 0 \quad \text{or} \quad \gamma_{23} = \gamma_{31} = 0 \tag{3.129}$$

the component ϵ_{33} is non-zero and has the form given by:

$$\epsilon_{33} = \frac{\nu}{E}(\sigma_{11} + \sigma_{22}) = \frac{\nu}{1-\nu}(\epsilon_{11} + \epsilon_{22}) \tag{3.130}$$

It is clear from Eq. (3.130) that the normal strain ϵ_{33} is a linear function of ϵ_{11} and ϵ_{22} and for this reason it has not been included in Eq. (3.128).

3.5.4 *Plane strain case*

The plane strain condition is commonly found in an elongated body of constant cross-section subjected to a uniform loading along its longitudinal axis (x_3-axis in Fig. 3.11b). The following conditions generally hold:

$$\epsilon_{31} = \epsilon_{32} = \epsilon_{33} = 0 \quad \text{or} \quad \gamma_{31} = \gamma_{32} = \epsilon_{33} = 0 \tag{3.131}$$

In a similar manner to the case of the plane stress condition, the matrix form of Eq. (3.124) can be reduced to:

$$\begin{Bmatrix} \sigma_{11} \\ \sigma_{22} \\ \sigma_{12} \end{Bmatrix} = \frac{E}{(1+\nu)(1-2\nu)} \begin{bmatrix} 1-\nu & \nu & 0 \\ \nu & 1-\nu & 0 \\ 0 & 0 & \dfrac{1-2\nu}{2} \end{bmatrix} \begin{Bmatrix} \epsilon_{11} \\ \epsilon_{22} \\ \gamma_{12} \end{Bmatrix} \tag{3.132}$$

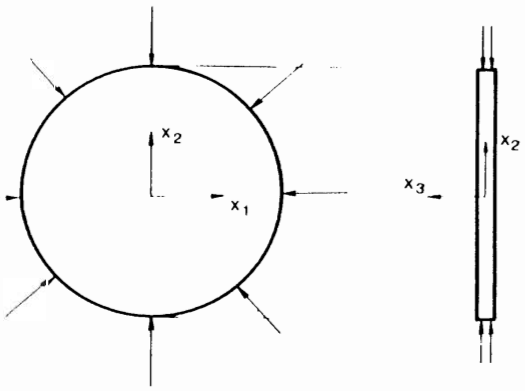

(a) Plane Stress case

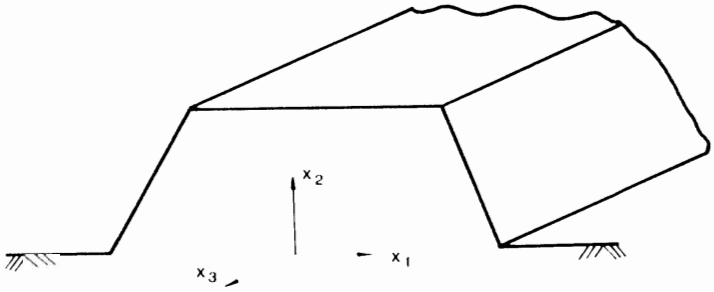

(b) Plane Strain case

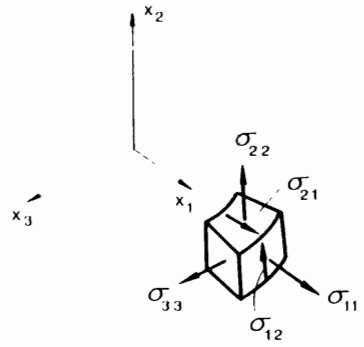

(c) Axisymmetric case

Fig. 3.11 Two-dimensional conditions. (a) Plane stress case (b) Plane strain case (c) Axisymmetric case

while the stress components σ_{23} and σ_{31} are zero, and the stress component σ_{33} has the value:

$$\sigma_{33} = \nu(\sigma_{11} + \sigma_{22}) \tag{3.133}$$

Solving Eq. (3.132) for the strains, we have the inverse form:

$$\begin{Bmatrix} \epsilon_{11} \\ \epsilon_{22} \\ \gamma_{12} \end{Bmatrix} = \frac{1+\nu}{E} \begin{bmatrix} 1-\nu & -\nu & 0 \\ -\nu & 1-\nu & 0 \\ 0 & 0 & 2 \end{bmatrix} \begin{Bmatrix} \sigma_{11} \\ \sigma_{22} \\ \sigma_{12} \end{Bmatrix} \tag{3.134}$$

3.5.5 *Axisymmetric case*

Analysis of the body of revolution under the axisymmetric loading is similar to those of plane stress and plane strain cases since it is also a two-dimensional case. The states of stress and strain can be completely defined by the two components of displacements in any plane section of the body along its axis of symmetry. Referring to Fig. 3.11c, there are in this case three strain components ϵ_{11}, ϵ_{22}, and γ_{12}, in the x_1-x_2-plane, and one strain component ϵ_{33} in the direction normal to the x_1-x_2-plane. The matrix form can be written as:

$$\begin{Bmatrix} \sigma_{11} \\ \sigma_{22} \\ \sigma_{33} \\ \sigma_{12} \end{Bmatrix} = \frac{E}{(1+\nu)(1-2\nu)} \begin{bmatrix} 1-\nu & \nu & \nu & 0 \\ \nu & 1-\nu & \nu & 0 \\ \nu & \nu & 1-\nu & 0 \\ 0 & 0 & 0 & \dfrac{(1-2\nu)}{2} \end{bmatrix} \begin{Bmatrix} \epsilon_{11} \\ \epsilon_{22} \\ \epsilon_{33} \\ \gamma_{12} \end{Bmatrix} \tag{3.135}$$

or

$$\begin{Bmatrix} \epsilon_{11} \\ \epsilon_{22} \\ \epsilon_{33} \\ \gamma_{12} \end{Bmatrix} = \frac{1}{E} \begin{bmatrix} 1 & -\nu & -\nu & 0 \\ -\nu & 1 & -\nu & 0 \\ -\nu & -\nu & 1 & 0 \\ 0 & 0 & 0 & 2(1+\nu) \end{bmatrix} \begin{Bmatrix} \sigma_{11} \\ \sigma_{22} \\ \sigma_{33} \\ \sigma_{12} \end{Bmatrix} \tag{3.136}$$

3.6 ISOTROPIC NONLINEAR ELASTIC STRESS-STRAIN RELATIONS BASED ON TOTAL FORMULATION

In this Section, various nonlinear elastic stress-strain relations based on *total* (or *secant) stress-strain formulations* are presented in some details for nonlinear elastic model with secant moduli, Cauchy elastic, and hyperelastic (or Green) models.

3.6.1 *Nonlinear elastic model with secant moduli*

A simple extension of the linear elastic stress-strain relation with the elastic material constants being replaced by scalar functions associated with either the stress and/or the strain invariants will have the property of isotropy and reversibility. As an example, consider the linear form of Eq. (3.122) modified by replacing the material constants K and G with $K_s(I_1, J_2, J_3)$ and $G_s(I_1, J_2, J_3)$ which are respectively secant bulk and secant shear modulus functions of the first stress invariant I_1, the second and third deviatoric stress invariants, J_2, and J_3. Thus, we have:

$$\epsilon_{ij} = \frac{1}{2G_s(I_1, J_2, J_3)} s_{ij} + \frac{1}{9K_s(I_1, J_2, J_3)} \sigma_{kk}\delta_{ij} \tag{3.137}$$

There is, of course, a neat and logical separation between the mean response and the deviatoric or shear response of the material, exactly as for the linear elastic material. Specifically, we can write respectively as:

$$\epsilon_{kk} = \frac{1}{3K_s(I_1, J_2, J_3)} \sigma_{kk} \tag{3.138a}$$

$$e_{ij} = \frac{1}{2G_s(I_1, J_2, J_3)} s_{ij} \tag{3.138b}$$

However, unlike the linear elastic relations, Eqs. (3.138a) and (3.138b) show that there is an interaction between the two responses through the change in magnitude of the invariants I_1, J_2, and J_3. This implies that volume change ϵ_{kk} does not depend solely on σ_{kk}. Similarly, distortion or shear deformation, e_{ij}, does not depend only on the stress deviation or shear stresses, s_{ij}. They depend on each other, and interact through the variation of the scalar functions G_s and K_s. Recently, stress-strain models based on this formulation have been extensively used in nonlinear finite-element analysis for concrete and granular materials.

In principle, any scalar function of the stress and/or the strain invariants may be used for the isotropic nonlinear elastic moduli. Obviously, the constitutive models formulated on this basis are of the *Cauchy elastic type*. This formulation does not imply that the strain energy density function W and the complementary energy density function Ω, calculated from such stress-strain relations, are *path-independent*. Therefore, certain restrictions must be imposed on the chosen scalar functions G_s and K_s in order to ensure the path-independence character of W and Ω.

Utilizing the stress-strain relations of Eq. (3.137), the expression of the complementary energy density function Ω can be written as:

$$\Omega = \int_0^{\sigma_{ij}} \epsilon_{ij}\, \mathrm{d}\sigma_{ij}$$

$$= \int_0^{\sigma_{ij}} \left[\frac{1}{2G_s(I_1, J_2, J_3)} s_{ij} + \frac{1}{9K_s(I_1, J_2, J_3)} \sigma_{kk}\delta_{ij} \right] \left[\mathrm{d}s_{ij} + \tfrac{1}{3}\, \mathrm{d}\sigma_{mm}\delta_{ij} \right]$$

$$= \int_0^{J_2} \frac{1}{2G_s(I_1, J_2, J_3)}\, \mathrm{d}J_2 + \int_0^{I_1} \frac{1}{18K_s(I_1, J_2, J_3)}\, \mathrm{d}(I_1)^2 \tag{3.139}$$

where $\mathrm{d}J_2 = s_{ij}\, \mathrm{d}s_{ij}$ and $\mathrm{d}(I_1)^2 = 2I_1\, \mathrm{d}I_1$.

In order for the above function Ω to be independent of stress path, the integrals in Eq. (3.139) have to depend only on the current values of I_1 and J_2, respectively. Therefore, the bulk and shear moduli have to be expressed as:

$$K_s = K_s(I_1) \quad \text{or} \quad K_s = K_s(\sigma_{\mathrm{oct}}) \tag{3.140}$$

$$G_s = G_s(J_2) \quad \text{or} \quad G_s = G_s(\tau_{\mathrm{oct}}) \tag{3.141}$$

On the other hand, using Eq. (3.123) and the scalar functions K_s and G_s which are taken as functions of the three strain invariants I_1', J_2', and J_3', it can be shown that the strain energy density function W is given by:

$$W = \int_0^{\epsilon_{ij}} \sigma_{ij}\, \mathrm{d}\epsilon_{ij}$$

$$= \int_0^{\epsilon_{ij}} \left[2G_s(I_1', J_2', J_3')e_{ij} + K_s(I_1', J_2', J_3')\epsilon_{kk}\delta_{ij} \right] \left[\mathrm{d}e_{ij} + \tfrac{1}{3}\, \mathrm{d}\epsilon_{kk}\delta_{ij} \right]$$

$$= \int_0^{J_2'} 2G_s(I_1', J_2', J_3')\, \mathrm{d}J_2' + \int_0^{I_1'} \tfrac{1}{2}K_s(I_1', J_2', J_3')\, \mathrm{d}(I_1')^2 \tag{3.142}$$

in which $\mathrm{d}J_2' = e_{ij}\, \mathrm{d}e_{ij}$ and $\mathrm{d}(I_1')^2 = 2I_1'\mathrm{d}I_1'$.

In a similar manner to the previous case, the strain path-independency of W can always be satisfied if moduli K_s and G_s are expressed as:

$$K_s = K_s(I_1') \tag{3.143a}$$

$$G_s = G_s(J_2') \tag{3.143b}$$

or

$$K_s = K_s(\epsilon_{\mathrm{oct}}) \tag{3.144a}$$

$$G_s = G_s(\gamma_{\mathrm{oct}}) \tag{3.144b}$$

It should be noted that K_s and G_s must, of course, be positive. Consequently, the integrals in Eq. (3.139) and (3.142) are always positive. This result confirms that W and Ω are *always positive definite*.

Example 3.5: Show the conditions under which W and Ω are path-independent, when K_s and G_s are taken as functions of both I_1' and J_2' (or I_1 and J_2).

Solutions: The strain energy density function W which consists of I_1' and J_2' can be expressed from Eq. (3.142) as:

$$W = \int_0^{J_2'} 2G_s(I_1', J_2')\, \mathrm{d}J_2' + \int_0^{I_1'} \tfrac{1}{2}K_s(I_1', J_2')\, \mathrm{d}(I_1')^2 \tag{3.145}$$

In order for the above expression to be strain-path-independent, each integrand in Eq. (3.145) must have the following *integrability condition*, that is:

$$\frac{\partial\left[2G_s(I_1', J_2')\right]}{\partial(I_1')^2} = \frac{\partial\left[\tfrac{1}{2}K_s(I_1', J_2')\right]}{\partial J_2'} \tag{3.146a}$$

The relation in Eq. (3.146a) leads finally to:

$$\frac{2}{I_1'}\frac{\partial G_s}{\partial I_1'} \qquad \frac{\partial K_s}{\partial J_2'} \tag{3.146b}$$

On the other hand, the complementary energy density function Ω can be written from Eq. (3.139) as:

$$\Omega = \int_0^{J_2} \frac{1}{2G_s(I_1, J_2)}\, \mathrm{d}J_2 + \int_0^{I_1} \frac{1}{18K_s(I_1, J_2)}\, \mathrm{d}(I_1)^2 \tag{3.147}$$

In a similar manner to the previous case, the integrability condition under which Eq. (3.147) is stress-path independent is given by:

$$\frac{\partial\left(\dfrac{1}{2G_s(I_1, J_2)}\right)}{\partial(I_1)^2} \qquad \frac{\partial\left(\dfrac{1}{18K_s(I_1, J_2)}\right)}{\partial J_2} \tag{3.148a}$$

Equation (3.148a) can be rewritten in the form:

$$\frac{9}{2G_s^2}\frac{\partial G_s}{\partial I_1} \qquad \frac{I_1}{K_s^2}\frac{\partial K_s}{\partial J_2} \tag{3.148b}$$

Example 3.6: Express the complementary energy density function Ω in terms of the stress invariants I_1 and J_2, and the strain energy density function W in terms of the strain invariants I_1' and J_2', for an isotropic linear elastic material.

Solutions: Replacing $G_s(I_1, J_2, J_3)$ and $K_s(I_1, J_2, J_3)$ in Eq. (3.139) by G and K which are constant values, the complementary energy density function Ω can be written as:

$$\Omega = \int_0^{J_2} \frac{1}{2G}\, \mathrm{d}J_2 + \int_0^{I_1} \frac{1}{18K}\, \mathrm{d}(I_1)^2 = \int_0^{J_2} \frac{1}{2G}\, \mathrm{d}J_2 + \int_0^{I_1} \frac{2I_1}{18K}\, \mathrm{d}I_1$$

$$= \frac{J_2}{2G} + \frac{I_1^2}{18K} \tag{3.149}$$

Similarly, the strain energy density function W in Eq. (3.142) can be written as:

$$W = \int_0^{J_2'} 2G\, \mathrm{d}J_2' + \int_0^{I_1'} \tfrac{1}{2}K\, \mathrm{d}(I_1')^2 = \int_0^{J_2'} 2G\, \mathrm{d}J_2' + \int_0^{I_1'} KI_1'\, \mathrm{d}I_1'$$

$$= 2GJ_2' + \tfrac{1}{2}K(I_1')^2 \tag{3.150}$$

Noted that the first and second terms in Eqs. (3.149) and (3.150) are respectively the *distortinal energy* associated with the shear stresses or distortion and the *dilation energy* associated with the hydrostatic pressure or volumetric change.

3.6.2 Cauchy elastic model

In the stress-strain relation (3.4), for example, we choose the response functions A_0, A_1, and A_2 to be functions of strain invariants, so that the stress tensor σ_{ij} can be written as a second-order polynomial expression of strain invariants. Assuming that the initial strain-free state corresponds to the initial stress-free state, these functions are expressed as:

$$A_0 = a_1 I_1' + a_2 I_1'^2 + a_3 I_2' \tag{3.151a}$$

$$A_1 = a_4 + a_5 I_1' \tag{3.151b}$$

$$A_2 = a_6 \tag{3.151c}$$

where a_1, ..., and a_6 are material constants.
Substituting Eqs. (3.151) into Eq. (3.4), we have the following *second-order stress-strain relationship* given by:

$$\sigma_{ij} = \left(a_1 I_1' + a_2 I_1'^2 + a_3 I_2'\right)\delta_{ij} + (a_4 + a_5 I_1')\epsilon_{ij} + a_6 \epsilon_{ik}\epsilon_{kj} \tag{3.152}$$

As a special case, the second-order polynomial expression can be reduced to the first-order expression (linear elastic stress-strain relation), that is:

$$\sigma_{ij} = a_1 I_1' \delta_{ij} + a_4 \epsilon_{ij} \tag{3.153}$$

Therefore, the material constants a_1 and a_4 may take identical constants to respectively λ and 2μ where λ and μ are Lamé's constants [see Eq. (3.98)]. Thus, Eq. (3.152) becomes:

$$\sigma_{ij} = \left(\lambda I_1' + a_2 I_1'^2 + a_3 I_2'\right)\delta_{ij} + (2\mu + a_5 I_1')\epsilon_{ij} + a_6 \epsilon_{ik}\epsilon_{kj} \tag{3.154a}$$

or using K and G

$$\sigma_{ij} = \left[\left(K - \tfrac{2}{3}G\right) I_1' + a_2 I_1'^2 + a_3 I_2'\right]\delta_{ij} + (2G + a_5 I_1')\epsilon_{ij} + a_6 \epsilon_{ik}\epsilon_{kj} \tag{3.154b}$$

Similarly, the inverse of the second-order form in Eq. (3.5) can be written as:

$$\epsilon_{ij} = \left[-\frac{\lambda}{2\mu(3\lambda + 2\mu)} I_1 + b_2 I_1^2 + b_3 I_2\right]\delta_{ij} + \left(\frac{1}{2\mu} + b_5 I_1\right)\sigma_{ij} + b_6 \sigma_{ik}\sigma_{kj} \tag{3.155a}$$

or

$$\epsilon_{ij} = \left[\frac{2G - 3K}{18GK} I_1 + b_2 I_1^2 + b_3 I_2\right]\delta_{ij} + \left(\frac{1}{2G} + b_5 I_1\right)\sigma_{ij} + b_6 \sigma_{ik}\sigma_{kj} \tag{3.155b}$$

The six material constants in Eq. (3.154) or (3.155) are determined from simple tests corresponding to simple states of stresses. Some of model behaviors in tests for soil materials are expressed as follows:

Hydrostatic pressure test: The components of stresses are $\sigma_{11} = \sigma_{22} = \sigma_{33} = \sigma$ and $\sigma_{12} = \sigma_{23} = \sigma_{31} = 0$. For this case, the stress invariants I_1 and I_2 are respectively 3σ and $3\sigma^2$. Substitution of this condition into Eq. (3.155a) yields:

$$\begin{aligned}\epsilon_{11} = \epsilon_{22} = \epsilon_{33} &= \left[-\frac{\lambda}{2\mu(3\lambda + 2\mu)} 3\sigma + 9b_2\sigma^2 + 3b_3\sigma^2\right] + \left(\frac{1}{2\mu} + 3b_5\sigma\right)\sigma + b_6\sigma^2 \\ &= \frac{1}{3\lambda + 2\mu}\sigma + (9b_2 + 3b_3 + 3b_5 + b_6)\sigma^2\end{aligned} \tag{3.156a}$$

or

$$\epsilon_{11} = \epsilon_{22} = \epsilon_{33} = \frac{1}{3K}\sigma + (9b_2 + 3b_3 + 3b_5 + b_6)\sigma^2 \tag{3.156b}$$

$$\epsilon_{12} = \epsilon_{23} = \epsilon_{31} = 0 \tag{3.156c}$$

The first term in Eqs. (3.156a) and (3.156b) gives the linear relationship which is the same as that of the first-order model and the second term shows the nonlinear relationship which is usually observed in a test on soil materials.

Simple compression test: Only a compressive stress σ_{11} acts and the other stress components are zero. The stress invariants I_1 and I_2 for this case are respectively σ_{11} and 0. Therefore, Eq. (3.155b) can be written as:

$$\epsilon_{11} = -\frac{2G - 3K}{18GK}\sigma_{11} + b_2\sigma_{11}^2 + \left(\frac{1}{2G} + b_5\sigma_{11}\right)\sigma_{11} + b_6\sigma_{11}^2$$

$$= \frac{G + 3K}{9GK}\sigma_{11} + (b_2 + b_5 + b_6)\sigma_{11}^2 \tag{3.157a}$$

$$\epsilon_{22} = \epsilon_{33} = \frac{2G - 3K}{18GK}\sigma_{11} + b_2\sigma_{11}^2 \tag{3.157b}$$

$$\epsilon_{12} = \epsilon_{23} = \epsilon_{31} = 0 \tag{3.157c}$$

As can be seen from Eqs. (3.157a) and (3.157b), the relationship between the stress and the strain is nonlinear due to the second term. The coefficient $(G + 3K)/9GK$ in the first term of Eq. (3.157a) is identical to $1/E$ in the linear elastic model.

Simple shear test: Only the shear stress $\sigma_{12} = \sigma_{21}$ acts. In this case, the stress invariants I_1 and I_2 are respectively zero and $-\sigma_{12}^2$. Therefore, we have the following relations from Eq. (3.155b):

$$\epsilon_{11} = b_3 I_2 + b_6\sigma_{1k}\sigma_{k1} = (b_6 - b_3)\sigma_{12}^2 \tag{3.158a}$$

$$\epsilon_{22} = (b_6 - b_3)\sigma_{12}^2 \tag{3.158b}$$

$$\epsilon_{33} = -b_3\sigma_{12}^2 \tag{3.158c}$$

$$\epsilon_{12} = \frac{1}{2G}\sigma_{12} \tag{3.158d}$$

$$\epsilon_{23} = \epsilon_{31} = 0 \tag{3.158e}$$

From Eqs. (3.158a) through (3.158c), a volumetric change $\epsilon_v = (2b_6 - 3b_3)\sigma_{12}^2$, is caused by the shear stress. This implies that there exists a nonlinear relationship between shear stress and volumetric strain. On the other hand, the linear relation between the shear stress and the shear strain as in the linear elastic model remains.

Uniaxial strain test: An axial strain ϵ_{11} is the only nonvanishing component and the other strain components are zero. Therefore, the strain invariants I_1' and I_2' are respectively ϵ_{11} and 0. Substituting the above condition into Eq. (3.154b), we find:

$$\sigma_{11} = \left(K - \tfrac{2}{3}G\right)\epsilon_{11} + a_2\epsilon_{11}^2 + (2G + a_5\epsilon_{11})\epsilon_{11} + a_6\epsilon_{11}^2$$

$$= \left(K + \tfrac{4}{3}G\right)\epsilon_{11} + (a_2 + a_5 + a_6)\epsilon_{11}^2 \tag{3.159a}$$

$$\sigma_{22} = \sigma_{33} = \left(K - \tfrac{2}{3}G\right)\epsilon_{11} + a_2\epsilon_{11}^2 \tag{3.159b}$$

$$\sigma_{12} = \sigma_{23} = \sigma_{31} = 0 \tag{3.159c}$$

The coefficient $\left(K + \frac{4}{3}G\right)$ in the first linear term of Eq. (3.159a) is the *constrained modulus* M obtained in the linear elastic model. The relationship between each normal stress and axial strain in the second-order elastic model is nonlinear.

3.6.3 Hyperelastic (Green) model

For the hyperelastic model in Eq. (3.28) to include the second-order expression of strain, the strain energy density function W must include the third-order polynomial as:

$$W = c_0 + c_1 I_1' + c_2 I_1'^2 + c_3 \bar{I}_2' + c_4 I_1'^3 + c_5 I_1' \bar{I}_2' + c_6 \bar{I}_3' \tag{3.160}$$

where $c_0, \ldots,$ and c_6 are material constants.
Assuming the initial strain-free state corresponds to the initial stress-free state, that is, $c_0 = c_1 = 0$, then Eq. (3.160) reduces to:

$$W = c_2 I_1'^2 + c_3 \bar{I}_2' + c_4 I_1'^3 + c_5 I_1' \bar{I}_2' + c_6 \bar{I}_3' \tag{3.161}$$

Substitution of Eq. (3.161) into Eq. (3.28) leads to:

$$\sigma_{ij} = \left(2c_2 I_1' + 3c_4 I_1'^2 + c_5 \bar{I}_2'\right)\delta_{ij} + (c_3 + c_5 I_1')\epsilon_{ij} + c_6 \epsilon_{ik}\epsilon_{kj} \tag{3.162}$$

As a special case, when the second-order terms are neglected, Eq. (3.162) reduces to the linear relation:

$$\sigma_{ij} = 2c_2 I_1' \delta_{ij} + c_3 \epsilon_{ij} \tag{3.163}$$

As a result, the material constants c_2 and c_3 may be matched with the material constants λ and μ or K and G in the linear elastic model, i.e.,

$$c_2 = \frac{\lambda}{2} \quad \text{or} \quad c_2 = \frac{3K - 2G}{6} \tag{3.164a}$$

$$c_3 = 2\mu \quad \text{or} \quad c_3 = 2G \tag{3.164b}$$

Finally, we have the second-order stress-strain relation written in the general form as:

$$\sigma_{ij} = \left[\left(K - \tfrac{2}{3}G\right)I_1' + 3c_4 I_1'^2 + c_5 I_2'\right]\delta_{ij} + (2G + c_5 I_1')\epsilon_{ij} + c_6\epsilon_{ik}\epsilon_{kj} \tag{3.165}$$

In a similar manner, the inverse of the second-order stress-strain relation based on the complementary energy density function Ω can be written from Eq. (3.37) as:

$$\epsilon_{ij} = \left[\frac{2G - 3K}{18GK} I_1 + 3d_4 I_1^2 + d_5 \bar{I}_2\right]\delta_{ij} + \left(\frac{1}{2G} + d_5 I_1\right)\sigma_{ij} + d_6\sigma_{ik}\sigma_{kj} \tag{3.166}$$

Note that the stress-strain relationships obtained from either the Cauchy formulation or the hyperelastic formulation have a similar form to each other, except that they are different in the number of material constants. The five material constants in Eq. (3.165) or (3.166) are determined from simple tests corresponding to simple states of stresses. Some of the model behavior in simple tests for soil materials can be obtained in a similar manner to those of Cauchy elastic model described previously.

3.7 ISOTROPIC NONLINEAR ELASTIC STRESS-STRAIN RELATIONS BASED ON INCREMENTAL FORMULATION

In this Section, the *incremental* (or *tangential) forms* of stress-strain relations for the nonlinear elastic model with secant moduli, Cauchy elastic, hyperelastic (Green), and hypoelastic models are described.

3.7.1 Nonlinear elastic model with secant moduli

Consider the incremental nonlinear stress-strain relations based on the secant moduli K_s and G_s that are respectively functions of ϵ_{oct} and γ_{oct}, that is:

$$K_s = K_s(\epsilon_{oct}) \tag{3.167}$$

$$G_s = G_s(\gamma_{oct}) \tag{3.168}$$

Using these secant moduli, the mean response and the deviatoric response of soils are treated separately as:

$$p = K_s\epsilon_{kk} \tag{3.169a}$$

$$s_{ij} = 2G_s e_{ij} \tag{3.169b}$$

Since $\epsilon_{kk} = 3\epsilon_{oct}$ and $p = \sigma_{oct}$, Eq. (3.169a) can be rewritten as:

$$\sigma_{oct} = 3K_s\epsilon_{oct} \tag{3.170}$$

On the other hand, taking the sum of the square for both sides of Eq. (3.169b), we have:

$$s_{ij}s_{ij} = 4G_s^2 e_{ij}e_{ij} \tag{3.171}$$

Substituting the relations $s_{ij}s_{ij} = 3\tau_{oct}^2$ and $e_{ij}e_{ij} = \frac{1}{4}\gamma_{oct}^2$, and taking a square root, we find:

$$\tau_{oct} = G_s\gamma_{oct} \tag{3.172}$$

The incremental forms of Eqs. (3.170) and (3.172) are expressed as:

$$d\sigma_{oct} = 3\left(K_s + \epsilon_{oct}\frac{dK_s}{d\epsilon_{oct}} \right) d\epsilon_{oct} \tag{3.173a}$$

$$d\tau_{oct} = \left(G_s + \gamma_{oct}\frac{dG_s}{d\gamma_{oct}} \right) d\gamma_{oct} \tag{3.173b}$$

Equation (3.173) may be rewritten as:

$$d\sigma_{oct} = 3K_t\, d\epsilon_{oct} \tag{3.174a}$$

$$d\tau_{oct} = G_t\, d\gamma_{oct} \tag{3.174b}$$

where K_t and G_t are defined as the *tangent bulk* and *tangent shear moduli* respectively, i.e.:

$$K_t = K_s + \epsilon_{oct}\frac{dK_s}{d\epsilon_{oct}} \tag{3.175a}$$

$$G_t = G_s + \gamma_{oct}\frac{dG_s}{d\gamma_{oct}} \tag{3.175b}$$

The schematic relationships between K_t and K_s, and G_t and G_s are shown in Fig. 3.12.

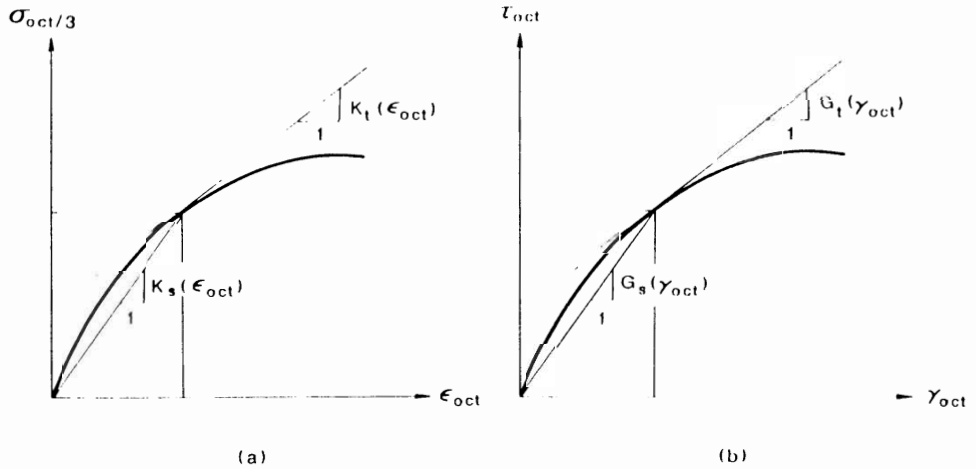

Fig. 3.12. Octahedral normal and shear stress-strain relations. (a) Octahedral normal stress-strain relation. (b) Octahedral shear stress-strain relation.

The stress increment tensor $d\sigma_{ij}$ can be decomposed into the deviatoric and hydrostatic parts, ds_{ij} and $d\sigma_{oct}\delta_{ij}$, respectively:

$$d\sigma_{ij} = ds_{ij} + d\sigma_{oct}\delta_{ij} \tag{3.176}$$

From Eq. (3.174a), $d\sigma_{oct}$ can be written as:

$$d\sigma_{oct} = 3K_t\, d\epsilon_{oct} = K_t\, d\epsilon_{kk} = K_t\delta_{kl}\, d\epsilon_{kl} \tag{3.177}$$

On the other hand, the deviatoric stress increment ds_{ij} can be obtained from Eq. (3.169b) as:

$$ds_{ij} = 2\left(e_{ij}\frac{dG_s}{d\gamma_{oct}}\, d\gamma_{oct} + G_s\, de_{ij}\right) \tag{3.178}$$

Solving for $dG_s/d\gamma_{oct}$ from Eq. (3.175b), we have:

$$\frac{dG_s}{d\gamma_{oct}} = \frac{G_t - G_s}{\gamma_{oct}} \tag{3.179}$$

Differentiating the relation $\gamma_{oct}^2 = \frac{4}{3}e_{rs}e_{rs}$ (see Chapter 2), we obtain:

$$d\gamma_{oct} = \frac{4}{3}\frac{e_{rs}}{\gamma_{oct}}\, de_{rs} \tag{3.180}$$

Substitution of Eqs. (3.179) and (3.180) into Eq. (3.178) and factoring de_{rs} result in:

$$ds_{ij} = 2\left[G_s\delta_{ri}\delta_{js} + \frac{4}{3}\frac{(G_t - G_s)}{\gamma_{oct}^2}e_{ij}e_{rs}\right]de_{rs} \tag{3.181}$$

Using the relationship between the total strain increment tensor $d\epsilon_{rs}$ and the deviatoric strain increment tensor de_{rs}:

$$de_{rs} = d\epsilon_{rs} - \tfrac{1}{3}\,d\epsilon_{mm}\delta_{rs} = \left(\delta_{rk}\delta_{sl} - \tfrac{1}{3}\delta_{rs}\delta_{kl}\right)d\epsilon_{kl} \tag{3.182}$$

Equation (3.181) can be written as:

$$ds_{ij} = 2\left(G_s\delta_{ik}\delta_{jl} - \tfrac{1}{3}G_s\delta_{ij}\delta_{kl} + \eta e_{ij}e_{kl}\right)d\epsilon_{kl} \tag{3.183}$$

where

$$\eta = \frac{4}{3}\frac{G_t - G_s}{\gamma_{oct}^2} \tag{3.184}$$

Now, substituting Eqs. (3.177) and (3.183) into Eq. (3.176), we obtain the required incremental stress-strain relations (Murray, 1979):

$$d\sigma_{ij} = 2\left[\left(\frac{K_t}{2} - \frac{G_s}{3}\right)\delta_{ij}\delta_{kl} + G_s\delta_{ik}\delta_{jl} + \eta e_{ij}e_{kl}\right]d\epsilon_{kl} \tag{3.185}$$

which can be written in the matrix form as:

$$\{d\sigma\} = [C_t]\{d\epsilon\} \tag{3.186a}$$

where

$$\{d\sigma\} = [d\sigma_{11}, d\sigma_{22}, d\sigma_{33}, d\sigma_{12}, d\sigma_{23}, d\sigma_{31}]^t \tag{3.186b}$$

$$\{d\epsilon\} = [d\epsilon_{11}, d\epsilon_{22}, d\epsilon_{33}, d\gamma_{12}, d\gamma_{23}, d\gamma_{31}]^t \tag{3.186c}$$

and the material tangential stiffness matrix $[C_t]$ may be expressed as:

$$[C_t] = [A] + [B] \tag{3.187a}$$

in which:

$$[A] = \begin{bmatrix} \alpha & \beta & \beta & 0 & 0 & 0 \\ \beta & \alpha & \beta & 0 & 0 & 0 \\ \beta & \beta & \alpha & 0 & 0 & 0 \\ 0 & 0 & 0 & G_s & 0 & 0 \\ 0 & 0 & 0 & 0 & G_s & 0 \\ 0 & 0 & 0 & 0 & 0 & G_s \end{bmatrix} \tag{3.187b}$$

$$[B] = 2\eta\{e\}\{e\}^{\mathrm{t}} \tag{3.187c}$$

where

$$\alpha = K_t + \tfrac{4}{3}G_s \tag{3.188a}$$

$$\beta = K_t - \tfrac{2}{3}G_s \tag{3.188b}$$

and $\{e\}^{\mathrm{t}}$ is the transpose matrix of the deviatoric strain vector $\{e\}$:

$$\{e\}^{\mathrm{t}} = [e_{11}, e_{22}, e_{33}, e_{12}, e_{23}, e_{31}] \tag{3.189}$$

Note that the symmetric matrix $[A]$ in Eq. (3.187b) has the same isotropic form as that of Eq. (3.125) for an isotropic linear elastic material with K and G being replaced by K_t and G_s, respectively. On the contrary, the matrix $[B]$ is symmetric but does not have such an isotropic form. The second-order values of the deviatoric strains $\{e\}\{e\}^{\mathrm{t}}$ in Eq. (3.187c) are offset by the value η which contains the second-order strain γ_{oct}^2 in Eq. (3.184), and thus the quotients are not necessarily small with respect to unity. The numerical comparison of the relative magnitudes of both matrices $[A]$ and $[B]$ has been shown in some details in the book by Chen and Saleeb (1982).

Owing to the path-independent behavior implied in the total stress-strain formulation, the incremental form derived above represents the most restricted class of hypoelastic stress-strain relations that are integrable.

3.7.2 Cauchy elastic model

Herein, an incremental form of the second-order stress-strain relations in Eq. (3.4) is formulated. If Eq. (3.4) is differentiated, the stress increment tensor $d\sigma_{ij}$ can be written as:

$$d\sigma_{ij} = \left[\frac{\partial A_0}{\partial \epsilon_{kl}}\delta_{ij} + A_1 \frac{\partial \epsilon_{ij}}{\partial \epsilon_{kl}} + \epsilon_{ij}\frac{\partial A_1}{\partial \epsilon_{kl}} + A_2 \frac{\partial(\epsilon_{im}\epsilon_{mj})}{\partial \epsilon_{kl}} + \epsilon_{im}\epsilon_{mj}\frac{\partial A_2}{\partial \epsilon_{kl}} \right] d\epsilon_{kl} \tag{3.190}$$

where $d\epsilon_{kl}$ is the strain increment tensor, and A_0, A_1, and A_2 are elastic response coefficients and they are polynomial functions of strain invariants, I_1', I_2', and I_3'. For the second-order model, these are again expressed from Eq. (3.151) as:

$$A_0 = \left(K - \tfrac{2}{3}G\right)I_1' + a_2 I_1'^2 + a_3 I_2' \tag{3.191a}$$

$$A_1 = 2G + a_5 I_1' \tag{3.191b}$$

$$A_2 = a_6 \tag{3.191c}$$

The partial derivatives in Eq. (3.190) are calculated using the above expressions for A_0, A_1, and A_2, and the results are given by:

$$\frac{\partial A_0}{\partial \epsilon_{kl}} = \left(K - \tfrac{2}{3}G\right)\delta_{kl} + 2a_2 I_1'\delta_{kl} + a_3(I_1'\delta_{kl} - \epsilon_{kl}) \tag{3.192a}$$

$$\frac{\partial A_1}{\partial \epsilon_{kl}} = a_5\delta_{kl} \tag{3.192b}$$

$$\frac{\partial A_2}{\partial \epsilon_{kl}} = 0 \tag{3.192c}$$

$$\frac{\partial \epsilon_{ij}}{\partial \epsilon_{kl}} = \delta_{ik}\delta_{jl} \tag{3.192d}$$

$$\frac{\partial(\epsilon_{im}\epsilon_{mj})}{\partial \epsilon_{kl}} = \epsilon_{lj}\delta_{ik} + \epsilon_{ik}\delta_{jl} \tag{3.192e}$$

since $I_2' = \frac{1}{2}(I_1'^2 - \epsilon_{ij}\epsilon_{ji})$.
Substituting Eqs. (3.192a–e) into Eq. (3.190), we finally obtain:

$$d\sigma_{ij} = \Big[\left(K - \tfrac{2}{3}G\right)\delta_{kl}\delta_{ij} + 2a_2 I_1'\delta_{kl}\delta_{ij} + a_3(I_1'\delta_{kl} - \epsilon_{kl})\delta_{ij} + (2G + a_5 I_1')\delta_{ik}\delta_{jl} + a_5\epsilon_{ij}\delta_{kl} + a_6(\epsilon_{lj}\delta_{ik} + \epsilon_{ik}\delta_{jl})\Big]d\epsilon_{kl} \tag{3.193}$$

The above equation represents the incremental form of the second-order Cauchy elastic constitutive model. In a similar manner to the previous model in Section 3.7.1, Eq. (3.193) can always be written in a matrix form as:

$$\{d\sigma\} = [C_t]\{d\epsilon\} \tag{3.194}$$

in which $[C_t]$ is an *unsymmetrical tangential stiffness matrix* and its value depends on the current state of strain ϵ_{ij} and the material constants such as K, G, a_2, a_3, a_5 and a_6.

As an example of Eq. (3.194), the matrix form representing the incremental relations for a general three-dimensional case is given below:

$$\begin{Bmatrix} d\sigma_{11} \\ d\sigma_{22} \\ d\sigma_{33} \\ d\sigma_{12} \\ d\sigma_{23} \\ d\sigma_{31} \end{Bmatrix} = \begin{bmatrix} C_{11} & C_{12} & C_{13} & C_{14} & C_{15} & C_{16} \\ C_{21} & C_{22} & C_{23} & C_{24} & C_{25} & C_{26} \\ C_{31} & C_{32} & C_{33} & C_{34} & C_{35} & C_{36} \\ C_{41} & C_{42} & C_{43} & C_{44} & C_{45} & C_{46} \\ C_{51} & C_{52} & C_{53} & C_{54} & C_{55} & C_{56} \\ C_{61} & C_{62} & C_{63} & C_{64} & C_{65} & C_{66} \end{bmatrix} \begin{Bmatrix} d\epsilon_{11} \\ d\epsilon_{22} \\ d\epsilon_{33} \\ d\gamma_{12} \\ d\gamma_{23} \\ d\gamma_{31} \end{Bmatrix} \tag{3.195}$$

where

$$C_{11} = \left(K + \tfrac{4}{3}G\right) + (2a_2 + a_3 + a_5)I_1' + (-a_3 + a_5 + 2a_6)\epsilon_{11}$$

$$C_{12} = \left(K - \tfrac{2}{3}G\right) + (2a_2 + a_3)I_1' + a_5\epsilon_{11} - a_3\epsilon_{22}$$

$$C_{13} = \left(K - \tfrac{2}{3}G\right) + (2a_2 + a_3)I_1' + a_5\epsilon_{11} - a_3\epsilon_{33}$$

$$C_{14} = \tfrac{1}{2}(-a_3 + a_6)\gamma_{12}$$

$$C_{15} = -\tfrac{1}{2}a_3\gamma_{23}$$

$$C_{16} = \tfrac{1}{2}(-a_3 + a_6)\gamma_{31}$$

$$C_{21} = \left(K - \tfrac{2}{3}G\right) + (2a_2 + a_3)I_1' - a_3\epsilon_{11} + a_5\epsilon_{22}$$

$$C_{22} = \left(K + \tfrac{4}{3}G\right) + (2a_2 + a_3 + a_5)I_1' + (-a_3 + a_5 + 2a_6)\epsilon_{22}$$

$$C_{23} = \left(K - \tfrac{2}{3}G\right) + (2a_2 + a_3)I_1' + a_5\epsilon_{22} - a_3\epsilon_{33}$$

$$C_{24} = C_{14}$$

$$C_{25} = \tfrac{1}{2}(-a_3 + a_6)\gamma_{23}$$

$$C_{26} = -\tfrac{1}{2}a_3\gamma_{31}$$

$$C_{31} = \left(K - \tfrac{2}{3}G\right) + (2a_2 + a_3)I_1' - a_3\epsilon_{11} + a_5\epsilon_{33}$$

$$C_{32} = \left(K - \tfrac{2}{3}G\right) + (2a_2 + a_3)I_1' - a_3\epsilon_{22} + a_5\epsilon_{33}$$

$$
\begin{aligned}
C_{33} &= (K + \tfrac{4}{3}G) + (2a_2 + a_3 + a_5)I_1' + (-a_3 + a_5 + 2a_6)\epsilon_{33} \\
C_{34} &= -\tfrac{1}{2}a_3\gamma_{12} \\
C_{35} &= C_{25} \\
C_{36} &= C_{16} \\
C_{41} &= \tfrac{1}{2}(a_5 + a_6)\gamma_{12} \\
C_{42} &= C_{41} \\
C_{43} &= \tfrac{1}{2}a_5\gamma_{12} \\
C_{44} &= G + \tfrac{1}{2}a_5 I_1' + \tfrac{1}{2}a_6\epsilon_{11} + \tfrac{1}{2}a_6\epsilon_{22} \\
C_{45} &= \tfrac{1}{4}a_6\gamma_{31} \\
C_{46} &= \tfrac{1}{4}a_6\gamma_{23} \\
C_{51} &= \tfrac{1}{2}a_5\gamma_{23} \\
C_{52} &= \tfrac{1}{2}(a_5 + a_6)\gamma_{23} \\
C_{53} &= C_{52} \\
C_{54} &= C_{45} \\
C_{55} &= G + \tfrac{1}{2}a_5 I_1' + \tfrac{1}{2}a_6\epsilon_{22} + \tfrac{1}{2}a_6\epsilon_{33} \\
C_{56} &= \tfrac{1}{4}a_6\gamma_{12} \\
C_{61} &= \tfrac{1}{2}(a_5 + a_6)\gamma_{31} \\
C_{62} &= \tfrac{1}{2}a_5\gamma_{31} \\
C_{63} &= C_{61} \\
C_{64} &= C_{46} \\
C_{65} &= C_{56} \\
C_{66} &= G + \tfrac{1}{2}a_5 I_1' + \tfrac{1}{2}a_6\epsilon_{11} + \tfrac{1}{2}a_6\epsilon_{33}
\end{aligned}
\tag{3.196}
$$

3.7.3 *Hyperelastic model*

In a similar manner to the previous case, the incremental form of the second-order hyperelastic model can be derived by differentiating Eq. (3.165). Thus, we have:

$$\mathrm{d}\sigma_{ij} = \Big[\big\{\big(K - \tfrac{2}{3}G\big)\delta_{kl} + 6c_4 I_1'\delta_{kl} + c_5\epsilon_{kl}\big\}\delta_{ij} + c_5\delta_{kl}\epsilon_{ij} + (2G + c_5 I_1')\delta_{ik}\delta_{jl} + c_6\big(\delta_{ik}\epsilon_{lj} + \epsilon_{ik}\delta_{lj}\big)\Big]\mathrm{d}\epsilon_{kl} \tag{3.197}$$

Comparing Eq. (3.193) of the Cauchy elastic model with Eq. (3.197) of the hyperelastic model, the matrix form of Eq. (3.194) for a three-dimensional case can be readily obtained. Namely, replacing the material constants a_2, a_3, a_5, and a_6 in Cauchy elastic model by:

$$2a_2 + a_3 = 6c_4 \tag{3.198a}$$

$$a_3 = c_5 \tag{3.198b}$$

$$a_5 = c_5 \tag{3.198c}$$

$$a_6 = c_6 \tag{3.198d}$$

We have the following matrix form where the tangential stiffness matrix is symmetric:

$$\begin{Bmatrix} \mathrm{d}\sigma_{11} \\ \mathrm{d}\sigma_{22} \\ \mathrm{d}\sigma_{33} \\ \mathrm{d}\sigma_{12} \\ \mathrm{d}\sigma_{23} \\ \mathrm{d}\sigma_{31} \end{Bmatrix} = \begin{bmatrix} C_{11} & C_{12} & C_{13} & C_{14} & C_{15} & C_{16} \\ & C_{22} & C_{23} & C_{24} & C_{25} & C_{26} \\ & & C_{33} & C_{34} & C_{35} & C_{36} \\ & & & C_{44} & C_{45} & C_{46} \\ & \text{Symmetric} & & & C_{55} & C_{56} \\ & & & & & C_{66} \end{bmatrix} \begin{Bmatrix} \mathrm{d}\epsilon_{11} \\ \mathrm{d}\epsilon_{22} \\ \mathrm{d}\epsilon_{33} \\ \mathrm{d}\gamma_{12} \\ \mathrm{d}\gamma_{23} \\ \mathrm{d}\gamma_{31} \end{Bmatrix} \tag{3.199}$$

where

$$C_{11} = \big(K + \tfrac{4}{3}G\big) + (6c_4 + c_5)I_1' + 2(c_5 + c_6)\epsilon_{11}$$

$$C_{12} = \big(K - \tfrac{2}{3}G\big) + 6c_4 I_1' + c_5\epsilon_{11} + c_5\epsilon_{22}$$

$$C_{13} = \big(K - \tfrac{2}{3}G\big) + 6c_4 I_1' + c_5\epsilon_{11} + c_5\epsilon_{33}$$

$$C_{14} = \tfrac{1}{2}(c_5 + c_6)\gamma_{12}$$

$$C_{15} = \tfrac{1}{2}c_5\gamma_{23}$$

$$C_{16} = \tfrac{1}{2}(c_5 + c_6)\gamma_{31}$$

$$C_{22} = \left(K + \tfrac{4}{3}G\right) + (6c_4 + c_5)I_1' + 2(c_5 + c_6)\epsilon_{22}$$

$$C_{23} = \left(K - \tfrac{2}{3}G\right) + 6c_4 I_1' + c_5\epsilon_{22} + c_5\epsilon_{33}$$

$$C_{24} = C_{14}$$

$$C_{25} = \tfrac{1}{2}(c_5 + c_6)\gamma_{23}$$

$$C_{26} = \tfrac{1}{2}c_5\gamma_{31} \tag{3.200}$$

$$C_{33} = \left(K + \tfrac{4}{3}G\right) + (6c_4 + c_5)I_1' + 2(c_5 + c_6)\epsilon_{33}$$

$$C_{34} = \tfrac{1}{2}c_5\gamma_{12}$$

$$C_{35} = C_{15}$$

$$C_{36} = C_{16}$$

$$C_{44} = G + \tfrac{1}{2}c_5 I_1' + \tfrac{1}{2}c_6\epsilon_{11} + \tfrac{1}{2}c_6\epsilon_{22}$$

$$C_{45} = \tfrac{1}{4}c_6\gamma_{13}$$

$$C_{46} = \tfrac{1}{4}c_6\gamma_{23}$$

$$C_{55} = G + \tfrac{1}{2}c_5 I_1' + \tfrac{1}{2}c_6\epsilon_{22} + \tfrac{1}{2}c_6\epsilon_{33}$$

$$C_{56} = \tfrac{1}{4}c_6\gamma_{12}$$

$$C_{66} = G + \tfrac{1}{2}c_5 I_1' + \tfrac{1}{2}c_6\epsilon_{11} + \tfrac{1}{2}c_6\epsilon_{33}$$

3.7.4 Hypoelastic model

Here, the incremental stress-strain relation of the first-order hypoelastic model is formulated. Defining the material coefficients A_1, A_2, ..., and A_{12} in Eq. (3.48) by:

$$A_1 = a_1 + a_3 I_1 \tag{3.201a}$$

$$A_2 = \tfrac{1}{2}(a_2 + a_4 I_1) \tag{3.201b}$$

$$A_3 = a_5 \tag{3.201c}$$

$$A_4 = a_7 \tag{3.201d}$$

$$A_5 = \tfrac{1}{2}a_6 \tag{3.201e}$$

$$A_6 = A_7 = \ldots = A_{12} = 0 \tag{3.201f}$$

the general form of the tangential stiffness tensor C_{ijkl} for the first-order hypoelastic model can thus be written as:

$$C_{ijkl} = (a_1 + a_3 I_1)\delta_{ij}\delta_{kl} + \tfrac{1}{2}(a_3 + a_4 I_1)(\delta_{ik}\delta_{jl} + \delta_{jk}\delta_{il}) + a_5\sigma_{ij}\delta_{kl}$$
$$+ \tfrac{1}{2}a_6(\delta_{ik}\sigma_{jl} + \delta_{il}\sigma_{jk} + \delta_{jk}\sigma_{il} + \delta_{jl}\sigma_{ik}) + a_7\sigma_{kl}\delta_{ij} \tag{3.202}$$

where a_1 to a_7 are material constants.
Substitution of Eq. (3.202) into Eq. (3.47) yields the following constitutive relations:

$$d\sigma_{ij} = a_1\, d\epsilon_{kk}\delta_{ij} + a_2\, d\epsilon_{ij} + a_3 I_1\, d\epsilon_{kk}\delta_{ij} + a_4 I_1\, d\epsilon_{ij} + a_5\sigma_{ij}\, d\epsilon_{kk}$$
$$+ a_6(\sigma_{jk}\, d\epsilon_{ik} + \sigma_{ik}\, d\epsilon_{jk}) + a_7\sigma_{kl}\, d\epsilon_{kl}\delta_{ij} \tag{3.203}$$

The above relations in Eq. (3.203) represent the most general form of the first-order hypoelastic constitutive law for an initially isotropic material. The material behavior described by Eq. (3.203) revolves around the seven material constants a_1 to a_7. Note that if all material constants other than a_1 and a_2 are eliminated (zero-order hypoelasticity), then the stress-strain relations in Eq. (3.203) reduce to those of the generalized Hooke's law for an isotropic linear elastic material, with the additional freedom that an initial stress can now be prescribed for the zero initial strain state. Therefore, the material constants a_1 and a_2 might be written as:

$$a_1 = K - \tfrac{2}{3}G \tag{3.204a}$$

$$a_2 = 2G \tag{3.204b}$$

The matrix form of the incremental constitutive relation for the three-dimensional case can be written as:

$$\begin{Bmatrix} d\sigma_{11} \\ d\sigma_{22} \\ d\sigma_{33} \\ d\sigma_{12} \\ d\sigma_{23} \\ d\sigma_{31} \end{Bmatrix} = \begin{bmatrix} C_{11} & C_{12} & C_{13} & C_{14} & C_{15} & C_{16} \\ C_{21} & C_{22} & C_{23} & C_{24} & C_{25} & C_{26} \\ C_{31} & C_{32} & C_{33} & C_{34} & C_{35} & C_{36} \\ C_{41} & C_{42} & C_{43} & C_{44} & C_{45} & C_{46} \\ C_{51} & C_{52} & C_{53} & C_{54} & C_{55} & C_{56} \\ C_{61} & C_{62} & C_{63} & C_{64} & C_{65} & C_{66} \end{bmatrix} \begin{Bmatrix} d\epsilon_{11} \\ d\epsilon_{22} \\ d\epsilon_{33} \\ d\gamma_{12} \\ d\gamma_{23} \\ d\gamma_{31} \end{Bmatrix} \tag{3.205}$$

where the tangential stiffness matrix becomes unsymmetric and their components are respectively given by:

$$C_{11} = \left(K + \tfrac{4}{3}G\right) + (a_3 + a_4)I_1 + (a_5 + 2a_6 + a_7)\sigma_{11}$$

$$C_{12} = \left(K - \tfrac{2}{3}G\right) + a_3 I_1 + a_5\sigma_{11} + a_7\sigma_{22}$$

$$
\begin{aligned}
C_{13} &= \left(K - \tfrac{2}{3}G\right) + a_3 I_1 + a_5\sigma_{11} + a_7\sigma_{33} \\
C_{14} &= (a_6 + a_7)\sigma_{12} \\
C_{15} &= a_7\sigma_{23} \\
C_{16} &= (a_6 + a_7)\sigma_{31} \\
C_{21} &= \left(K - \tfrac{2}{3}G\right) + a_3 I_1 + a_7\sigma_{11} + a_5\sigma_{22} \\
C_{22} &= \left(K + \tfrac{4}{3}G\right) + (a_3 + a_4) I_1 + (a_5 + 2a_6 + a_7)\sigma_{22} \\
C_{23} &= \left(K - \tfrac{2}{3}G\right) + a_3 I_1 + a_5\sigma_{22} + a_7\sigma_{33} \\
C_{24} &= C_{14} \\
C_{25} &= (a_6 + a_7)\sigma_{23} \\
C_{26} &= a_7\sigma_{31} \\
C_{31} &= \left(K - \tfrac{2}{3}G\right) + a_3 I_1 + a_7\sigma_{11} + a_5\sigma_{33} \\
C_{32} &= \left(K - \tfrac{2}{3}G\right) + a_3 I_1 + a_7\sigma_{22} + a_5\sigma_{33} \\
C_{33} &= \left(K + \tfrac{4}{3}G\right) + (a_3 + a_4) I_1 + (a_5 + 2a_6 + a_7)\sigma_{33} \\
C_{34} &= a_7\sigma_{12} \\
C_{35} &= C_{25} \\
C_{36} &= C_{16} \\
C_{41} &= (a_5 + a_6)\sigma_{12} \\
C_{42} &= C_{41} \\
C_{43} &= a_5\sigma_{12} \\
C_{44} &= G + \tfrac{1}{2}a_4 I_1 + \tfrac{1}{2}a_6\sigma_{11} + \tfrac{1}{2}a_6\sigma_{22} \\
C_{45} &= \tfrac{1}{2}a_6\sigma_{31} \\
C_{46} &= \tfrac{1}{2}a_6\sigma_{23} \\
C_{51} &= a_5\sigma_{23}
\end{aligned}
\tag{3.206}
$$

$$C_{53} = (a_5 + a_6)\sigma_{23}$$

$$C_{53} = C_{52}$$

$$C_{54} = C_{45}$$

$$C_{55} = G + \tfrac{1}{2}a_4 I_1 + \tfrac{1}{2}a_6\sigma_{22} + \tfrac{1}{2}a_6\sigma_{33}$$

$$C_{56} = \tfrac{1}{2}a_6\sigma_{12}$$

$$C_{61} = (a_5 + a_6)\sigma_{31}$$

$$C_{62} = a_5\sigma_{31}$$

$$C_{63} = C_{61}$$

$$C_{64} = C_{46}$$

$$C_{65} = C_{56}$$

$$C_{66} = G + \tfrac{1}{2}a_4 I_1 + \tfrac{1}{2}a_6\sigma_{11} + \tfrac{1}{2}a_6\sigma_{33}$$

Example 3.7: Consider the first-order isotropic hypoelastic model described by the incremental stress-strain relation:

$$\mathrm{d}\sigma_{ij} = C_{ijkl}(\epsilon_{rs})\,\mathrm{d}\epsilon_{kl} \tag{3.207}$$

where the tangential stiffness tensor is given by:

$$C_{ijkl} = (b_1 + b_2 I_1')\delta_{ij}\delta_{kl} + \tfrac{1}{2}(b_3 + b_4 I_1')(\delta_{ik}\delta_{jl} + \delta_{jk}\delta_{il}) + b_5\epsilon_{ij}\delta_{kl}$$
$$+ \tfrac{1}{2}b_6(\epsilon_{jk}\delta_{il} + \epsilon_{jl}\delta_{ki} + \epsilon_{ik}\delta_{lj} + \epsilon_{il}\delta_{kj}) + b_7\epsilon_{kl}\delta_{ij} \tag{3.208}$$

where b_1, b_2, ..., and b_7 are material constants and I_1' is the first invariant of strain tensor ϵ_{ij}.

(a) Show that this incremental law provides a total stress-strain relationship when it satisfies the integrability conditions:

$$\frac{\partial C_{ijkl}}{\partial \epsilon_{mn}} = \frac{\partial C_{ijmn}}{\partial \epsilon_{kl}} \tag{3.209}$$

(b) Show that in order for the hypoelastic material described above to be Cauchy

elastic, the integrability conditions in (a) give the following condition:

$$b_3 = b_5 \tag{3.210}$$

(c) Show that if the material behavior is required to be Green elastic (or hyperelastic), the condition:

$$b_5 = b_1 \tag{3.211}$$

must be satisfied in addition to the condition given in (b).
(d) Using the two conditions given in (b) and (c), show that the incremental law may be integrated to give the hyperelastic constitutive relations (assume initial stress- and strain-free states):

$$\sigma_{ij} = b_1 I_1' \delta_{ij} + b_3 \epsilon_{ij} + \tfrac{1}{2} b_2 I_1'^2 \delta_{ij} + b_4 I_1' \epsilon_{ij} + b_6 \epsilon_{ik} \epsilon_{jk} + \tfrac{1}{2} b_4 \epsilon_{kl} \epsilon_{kl} \delta_{ij} \tag{3.212}$$

(e) Using the result obtained in (d), show that the strain energy density function, W', is given by:

$$W' = \tfrac{1}{2} b_1 I_1'^2 + \tfrac{1}{2} b_3 \epsilon_{ij} \epsilon_{ij} + \tfrac{1}{6} b_2 I_1'^3 + \tfrac{1}{2} b_4 I_1' \epsilon_{ij} \epsilon_{ij} + \tfrac{1}{3} b_6 \epsilon_{ik} \epsilon_{ij} \epsilon_{jk} \tag{3.213}$$

(f) Derive the simple stress-strain relation in uniaxial strain test ($\epsilon_{11} = \epsilon$, all other $\epsilon_{ij} = 0$) for the material described by the constitutive relations in (d).

Solutions:
(a) *Integrability condition*: Since stresses are single-valued continuous functions of strains for the total stress-strain relations, we have the following incremental stress-strain relations:

$$d\sigma_{ij} = \frac{\partial \sigma_{ij}}{\partial \epsilon_{kl}} \, d\epsilon_{kl} \tag{3.214}$$

As the integrability conditions for Eq. (3.214), we must have:

$$\frac{\partial \left(\dfrac{\partial \sigma_{ij}}{\partial \epsilon_{kl}} \right)}{\partial \epsilon_{mn}} = \frac{\partial \left(\dfrac{\partial \sigma_{ij}}{\partial \epsilon_{mn}} \right)}{\partial \epsilon_{kl}} \tag{3.215}$$

If the incremental stress-strain relation of the first-order hypoelastic model is taken into consideration for this case, the above integrability conditions become:

$$\frac{\partial C_{ijkl}}{\partial \epsilon_{mn}} = \frac{\partial C_{ijmn}}{\partial \epsilon_{kl}}$$

(b) *Integrability condition for the Cauchy elastic model*: The left-hand side of Eq. (3.209) can be expressed as:

$$\frac{\partial C_{ijkl}}{\partial \epsilon_{mn}} = b_2\delta_{mn}\delta_{ij}\delta_{kl} + \tfrac{1}{2}b_4\delta_{mn}(\delta_{ik}\delta_{jl} + \delta_{jk}\delta_{il}) + \tfrac{1}{2}b_5(\delta_{im}\delta_{jn} + \delta_{in}\delta_{jm})\delta_{kl}$$
$$+ \tfrac{1}{4}b_6(\delta_{jm}\delta_{kn}\delta_{il} + \delta_{in}\delta_{km}\delta_{jl} + \delta_{im}\delta_{jn}\delta_{kl} + \delta_{jn}\delta_{im}\delta_{kl} + \delta_{jm}\delta_{kn}\delta_{il} + \delta_{in}\delta_{km}\delta_{jl}$$
$$+ \delta_{jm}\delta_{in}\delta_{kl} + \delta_{in}\delta_{jm}\delta_{kl}) + \tfrac{1}{2}b_7(\delta_{km}\delta_{jn} + \delta_{kn}\delta_{jm})\delta_{il} \quad (3.216a)$$

On the other hand, the right-hand side of Eq. (3.209) can be written as:

$$\frac{\partial C_{ijmn}}{\partial \epsilon_{kl}} = b_2\delta_{kl}\delta_{ij}\delta_{mn} + \tfrac{1}{2}b_4\delta_{kl}(\delta_{im}\delta_{jn} + \delta_{jm}\delta_{in}) + \tfrac{1}{2}b_5(\delta_{ik}\delta_{jl} + \delta_{il}\delta_{jk})\delta_{mn}$$
$$+ \tfrac{1}{4}b_6(\delta_{ik}\delta_{ml}\delta_{nj} + \delta_{jl}\delta_{mk}\delta_{ni} + \delta_{jk}\delta_{nl}\delta_{mi} + \delta_{jl}\delta_{nk}\delta_{mi} + \delta_{ik}\delta_{ml}\delta_{nj} + \delta_{il}\delta_{mk}\delta_{nj}$$
$$+ \delta_{ik}\delta_{nl}\delta_{mj} + \delta_{il}\delta_{nk}\delta_{mj}) + \tfrac{1}{2}b_7(\delta_{mk}\delta_{nl} + \delta_{ml}\delta_{nk})\delta_{ij} \quad (3.216b)$$

It can be concluded from Eqs. (3.216a) and (3.216b) that if $b_4 = b_5$, the integrability condition of Eq. (3.209) is satisfied.

(c) *Hyperelastic condition*: For the stress-strain relations to satisfy the hyperelastic condition, $C_{ijkl} = C_{klij}$ must hold. Comparison of C_{ijkl} with C_{klij} leads to the condition:

$$b_5 = b_7$$

(d) *Hyperelastic constitutive relations*: Substituting $b_5 = b_7 = b_4$ into Eq. (3.208), and integrating with respect to strains $d\epsilon_{kl}$ lead to:

$$\sigma_{ij} = \int_0^{\epsilon_{ij}}\Big[(b_1 + b_2 I_1')(\delta_{ij}\delta_{kl} + \tfrac{1}{2}(b_3 + b_4 I_1')(\delta_{ik}\delta_{jl} + \delta_{jk}\delta_{il}) + b_4\epsilon_{ij}\delta_{kl}$$
$$+ \tfrac{1}{2}b_6(\epsilon_{jk}\delta_{il} + \epsilon_{jl}\delta_{ki} + \epsilon_{ik}\delta_{lj} + \epsilon_{il}\delta_{kj}) + b_4\epsilon_{kl}\delta_{ij}\Big]d\epsilon_{kl}$$
$$= \int_0^{I_1'}(b_1 + b_2 I_1')\delta_{ij}\,dI_1' + \int_0^{\epsilon_{ij}}(b_3 + b_4 I_1')\,d\epsilon_{ij} + \int_0^{I_1'} b_4\epsilon_{ij}\,dI_1'$$
$$+ \int_0^{\epsilon_{ij}} b_6(d\epsilon_{ik}\epsilon_{kj} + \epsilon_{ik}\,d\epsilon_{kj}) + \int_0^{\epsilon_{kl}} b_4\epsilon_{kl}\delta_{ij}\,d\epsilon_{kl}$$

Utilizing $I_1'd\epsilon_{ij} + dI_1'\epsilon_{ij} = d(I_1'\epsilon_{ij})$ and $d\epsilon_{ik}\epsilon_{kj} + \epsilon_{ik}d\epsilon_{kj} = d(\epsilon_{ik}\epsilon_{kj})$, we have:

$$\sigma_{ij} = b_1 I_1'\delta_{ij} + b_3\epsilon_{ij} + \tfrac{1}{2}b_2 I_1'^2\delta_{ij} + b_4 I_1'\epsilon_{ij} + b_6\epsilon_{ik}\epsilon_{kj} + \tfrac{1}{2}b_4\epsilon_{kl}\epsilon_{kl}\delta_{ij}$$

(e) *Strain energy density function*: From the definition of strain energy density, W:

$$W = \int_0^{\epsilon_{ij}} \sigma_{ij}\, d\epsilon_{ij}$$

$$\int_0^{\epsilon_{ij}} \left(b_1 I_1' \delta_{ij} + b_3 \epsilon_{ij} + \tfrac{1}{2} b_2 I_1'^2 \delta_{ij} + b_4 I_1' \epsilon_{ij} + b_6 \epsilon_{ik}\epsilon_{kj} + \tfrac{1}{2} b_4 \epsilon_{kl}\epsilon_{kl}\delta_{ij} \right) d\epsilon_{ij}$$

$$= \int_0^{I_1'} b_1 I_1'\, dI_1' + \int_0^{\epsilon_{ij}} b_3 \epsilon_{ij}\, d\epsilon_{ij} + \int_0^{I_1'} \tfrac{1}{2} b_2 I_1'^2\, dI_1' + \int_0^{\epsilon_{ij}} b_4 I_1' \epsilon_{ij}\, d\epsilon_{ij}$$

$$+ \int_0^{\epsilon_{ij}} b_6 \epsilon_{ik}\epsilon_{kj}\, d\epsilon_{ij} + \int_0^{I_1'} \tfrac{1}{2} b_4 \epsilon_{kl}\epsilon_{kl}\, dI_1'$$

Since $\epsilon_{ij} d\epsilon_{ij} = d(\frac{1}{2}\epsilon_{ij}\epsilon_{ij})$, $I_1' \epsilon_{ij} d\epsilon_{ij} + \frac{1}{2}\epsilon_{ij}\epsilon_{ij} dI_1' = d(\frac{1}{2}\epsilon_{ij}\epsilon_{ij} I_1')$, and $\epsilon_{ik}\epsilon_{kj} d\epsilon_{ij} = d(\frac{1}{3}\epsilon_{ij}\epsilon_{jk}\epsilon_{ki})$, we have:

$$W = \tfrac{1}{2} b_1 I_1'^2 + \tfrac{1}{2} b_3 \epsilon_{ij}\epsilon_{ij} + \tfrac{1}{6} b_2 I_1'^3 + \tfrac{1}{2} b_4 I_1' \epsilon_{ij}\epsilon_{ij} + \tfrac{1}{3} b_6 \epsilon_{ik}\epsilon_{ij}\epsilon_{jk}$$

(f) *Stress-strain relations in the uniaxial strain test*: Substituting $\epsilon_{11} = \epsilon$, and all other $\epsilon_{ij} = 0$ into the stress-strain relations obtained in (d), we have:

$$\sigma_{11} = (b_1 + b_3)\epsilon + \left(\tfrac{1}{2} b_2 + \tfrac{1}{2} b_4 + b_6\right)\epsilon^2 \tag{3.217a}$$

$$\sigma_{22} = \sigma_{33} = b_1 \epsilon + \left(\tfrac{1}{2} b_2 + \tfrac{1}{2} b_4\right)\epsilon^2 \tag{3.217b}$$

$$\sigma_{12} = \sigma_{23} = \sigma_{31} = 0 \tag{3.217c}$$

3.8 SUMMARY

In this Chapter, the elasticity-based material models have been reviewed theoretically with respect to their applicability to geotechnical engineering problems, and their stress-strain relations have been derived and put in suitable forms for direct use in a numerical stress analysis. The elasticity-based models may be categorized as *total* or *incremental stress-strain formulations*. A more detailed treatment of these theories has been presented by Chen and Saleeb (1982), and Desai and Siriwardane (1984). Based on the discussions presented in this Chapter, the essential points concerning the characteristics, advantages, and limitations of elasticity-based constitutive models can be summarized as follows:

TOTAL ELASTIC STRESS-STRAIN RELATIONS

Cauchy elastic type

General form:

$$\sigma_{ij} = F_{ij}(\epsilon_{mn}) \quad \text{or} \quad \epsilon_{ij} = F'_{ij}(\sigma_{mn})$$

Characteristics

1. Stresses, σ_{ij}, and strains, ϵ_{ij}, are *reversible* and *path-independent*.
2. Reversibility and path independency of strain energy and complementary energy density functions, W and Ω, are *not* in general guaranteed. That is, thermodynamic laws may be violated since the models may generate energy for some load-unload stress paths (not acceptable on physical grounds).
3. The material *secant stiffness* and *compliance* matrices are generally *asymmetrical*.
4. In general, when stresses are determined *uniquely* from strains or vice versa, the converse is *not* necessarily true. In order to satisfy thermodynamic laws and uniqueness of stresses and strains, additional conditions must be imposed.
5. The most commonly used models for this type are formulated by simple modifications of the isotropic linear elastic stress-strain relations based on *variable secant moduli* (e.g., K_s and G_s). Often, the material parameters in such models have *well-defined physical relations* to the observed stress-strain behavior of the material, and they can be *easily determined* from experimental data.

Hyperelastic (Green) type

General form:

$$\sigma_{ij} = \frac{\partial W}{\partial \epsilon_{ij}} \quad \text{or} \quad \epsilon_{ij} = \frac{\partial \Omega}{\partial \sigma_{ij}}$$

Characteristics

1. Stresses, σ_{ij}, and strains, ϵ_{ij}, are both *reversible* and *path-independent*.
2. These types of models *satisfy the laws of thermodynamics* since W and Ω are reversible and path independent.
3. Although the constitutive laws based on assumed functions W or Ω have great *mathematical capabilities* and different *general* relations can be derived, the material constants involved have no direct physical interpretation in most cases. Also, the procedure of determining these constants often requires *complicated testing programs*.
4. Functional forms for W or Ω can be easily assumed to reproduce the desired physical phenomena of the behavior of materials, such as *nonlinearity*, *dilatation* and *cross effects*, and *stress-* or *strain-induced anisotropy*.

5. By imposing the restriction of *convexity* on the energy density functions W and Ω, the *uniqueness* of stresses and strains in a general Green type of material is always satisfied (Drucker's *stability postulate*).
6. Material *secant stiffness* and *compliance* matrices are always *symmetrical*.

INCREMENTAL STRESS-STRAIN RELATIONS

Hypoelastic type

General forms:

$$d\sigma_{ij} = C_{ijkl}(\sigma_{pq})\, d\epsilon_{kl}$$

$$d\sigma_{ij} = C_{ijkl}(\epsilon_{pq})\, d\epsilon_{kl}$$

$$d\epsilon_{ij} = D_{ijkl}(\epsilon_{pq})\, d\sigma_{kl}$$

$$d\epsilon_{ij} = D_{ijkl}(\sigma_{pq})\, d\sigma_{kl}$$

where C_{ijkl} and D_{ijkl} are general functions of their indicated arguments.

Characteristics

1. The state of stress depends in general on the current state of strain as well as on the stress path followed to reach this state (i.e., the behavior is *path-dependent*).
2. The behavior is *incrementally reversible* (i.e., infinitesimal deformations in a hypoelastic material under initial stresses are reversible).
3. *Initial conditions* must be prescribed to obtain unique solutions. Different stress paths and initial conditions lead to different stress-strain relations.
4. In general, a hypoelastic model *may* violate laws of thermodynamics in some load-unload cycles since it may generate energy.
5. The determination of the material constants in the classical hypoelastic models requires *complicated testing programs*. Moreover, there is no obvious physical relation between these constants and the established material properties. No clearly defined relationship exists between the effect of varying any constant and the resulting change in the stress-strain behavior of the material. The models are *difficult* to *fit* to available test data.

REFERENCES

Boyce, H.R., 1980. A non-linear model for the elastic behavior of granular materials under repeated loading. Int. Symp. Soils under Cyclic and Transient Loading, Swansea, U.K., Vol. 1, 1980, pp. 285–294.

Chen, W.F. and Saleeb, A.F., 1982. Constitutive Equations for Engineering Materials, Vol. 1 - Elasticity and Modeling. John-Wiley, New York, NY, 580 pp.

Coon, M.D. and Evans, R.J., 1972. Incremental constitutive laws and their associated failure criteria with applications to plain concrete. Int. J. Solids Struct., 8: 1169-1183.

Davis, R.O. and Mullenger, G., 1979. A simple rate-type constitutive representation for granular media. Proc. 3rd Int. Conf. Numerical Methods in Geomechanics, Aachen Germany, Vol. 1, pp. 415-421.

Desai, C.S., 1980. A general basis for yield, failure and potential functions in plasticity. Int. J. Numer. Anal. Methods Geomech., 4: 361-375.

Desai, C.S. and Siriwardane, H.J., 1984. Constitutive Laws for Engineering Materials. Prentice-Hall, Englewood Cliffs, NJ, 468 pp.

Drucker, D.C., 1951. A more fundamental approach to plastic stress-strain relations. Proc., 1st U.S. National Congress on Applied Mechanics, ASME, pp. 487-491.

Duncan, J.M., 1981. Hyperbolic stress-strain relationships. In: R.N. Yong and H.-Y. Ko (Editors), Limit Equilibrium Plasticity and Generalized Stress-Strain in Geotechnical Engineering, ASCE, New York, NY, 443-460.

Duncan, J.M. and Chang, C.Y., 1970. Nonlinear analysis of stress and strain in soils. J. Soil Mech. Found. Div. ASCE, 96 (SM5): 1629-1653.

Evans, R.J. and Pister, K.S., 1966. Constitutive equations for a class of nonlinear elastic solids. Int. J. Solids Struct., 2(3): 427-445.

Girijavallabhan, C.V. and Reese, L.C., 1968. Finite element method for problems in soil mechanics. J. Soil Mech. Found. Div., ASCE, 94(SM2): 473-496.

Hardin, B.O. and Drnevich, V.P., 1972. Shear modulus and damping in soils: measurement and parameter effects. J. Soil Mech. Found. Div., ASCE, 98(SM6): 603-624.

Katona, M.G., Smith, J.M., Odello, R.S. and Allgood, J.R., 1976. CANDE - A modern approach for structural design and analysis of buried culverts. Rep. No. FHWA-RD-77-5, Naval Civil Engineering Laboratory.

Ko, H.Y. and Masson, R.M., 1976. Nonlinear characterization and analysis of sand. In: Numerical Methods in Geomechanics, ASCE, New York, NY, pp. 294-304.

Kondner, R.L., 1963. Hyperbolic stress-strain response: cohesive soils. J. Soil Mech. Found. Div., ASCE, 89(SM1): 115-143.

Kulhawy, F.H., Duncan, J.M. and Seed, H.B., 1969. Finite element analyses of stresses and movements in embankments during construction. Geotech. Eng. Rep. No. TE 69-4, Dep. Civ. Eng., University of California, Berkeley, CA.

Murray, D.W., 1979. Octahedral based incremental stress-strain matrices. J. Eng. Mech. Div., ASCE, 105(EM4): 501-513.

Rivlin, R.S. and Ericksen, J.L., 1955. Stress-deflection relation for isotropic materials. J. Ration. Mech. Anal., 4(1): 323-425.

Saleeb, A.F., 1981. Constitutive models for soils in landslides. PhD Thesis, School of Civil Engineering, Purdue Univ., West Lafayette IN, 489 pp.

Saleeb, A.F. and Chen, W.F., 1981. Nonlinear hyperelastic (Green) constitutive models for soils, part I - Theory and Calibration, pp. 265-285, Part II - Predictions and Comparisons, pp. 492-538. Proc. North American Workshop on Limit Equilibrium, Plasticity, and Generalized Stress-Strain in Geotechnical Engineering, ASCE Publication, New York, 1981.

Tokuoka, T., 1971. Yield conditions and flow rules derived from hypoelasticity. Arch. Ration. Mech. Anal., 42: 239-252.

Chapter 4

PERFECT PLASTICITY AND MODELING

4.1 INTRODUCTION

In the preceding Chapter, several elasticity-based soil material models have been reviewed for engineering practice. The fundamental difference between *elasticity-based* and *plasticity-based models* lies in the treatment of loading and unloading. In the plastic theories, the concept of *loading criterion* is introduced to treat separately the different behaviors of materials in loading and in unloading.

In the most fundamental sense, the soil behaves as an *elastic-plastic material* (see Fig. 1.1), i.e., soil deformations are basically inelastic since upon load removal, unloading follows an entirely different path from that followed by loading. If an elasticity-based model is used to describe the soil behavior under a general loading condition, a special loading criterion must be defined for loading and for unloading. Such a formulation is known as the *deformation theory of plasticity* (Chen, 1982). A generalization of the deformation theory of plasticity in the form of incremental stress-strain relationships is called the *variable moduli models*.

There are limitations for the deformation theory of plasticity and the variable moduli models. These limitations can be overcome by the introduction of the *flow* (or *incremental*) *theory of plasticity*. The flow theory is based on three fundamental assumptions: (1) the existence of an *initial yield surface*; (2) the evolution of *subsequent loading surfaces (hardening rule)*; and (3) the formulation of an appropriate *flow rule*. For soils, as for metals, *perfect plasticity* is an excellent design simplification, while more complex stress-strain behaviors of soil may be approximated by the more sophisticated hardening plasticity theory. This will be described in the following Chapter.

The formulation based on the flow theory of plasticity generally gives a good fit of data from laboratory tests. Existing plasticity models are generally defined by a few material parameters that can usually be determined from standard tests. In general, these models can represent such important soil characteristics as *dilatancy*, *dependency* of strength on *stress* or *strain history*, *nonlinear hysteretic behavior* under cyclic loading, and coincidence of the principal axes of strain increment and stress increment axes at low stress levels, with smooth transition to the coincidence of the principal axes of strain increment with the principal stress axes at high stress levels. These models rigorously satisfy the basic requirements of continuum mechanics such as *uniqueness*, *stability*, and *continuity*.

In this Chapter, the deformation theory of plasticity and the flow theory of perfect plasticity are reviewed in some details. Complete stress increment-strain

increment relationships are derived for a general perfectly plastic material. The perfect plasticity of the Prandtl-Reuss, Tresca, von Mises, Coulomb, and Drucker-Prager materials is then developed and assessed with respect to their applicability for practical geotechnical engineering problems.

4.2 DEFORMATION THEORY

The stress-strain relations for soil deformed beyond the elastic range into the inelastic state represent an area of great importance to soil mechanics. This is because deformation of soil in the elastic range is usually small and does not represent a realistic stress range in geotechnical engineering problems. Within the framework of deformation theory of plasticity, the total deformations ϵ_{ij} are decomposed into the elastic and the plastic components ϵ^{e}_{ij} and ϵ^{p}_{ij} by a simple superposition:

$$\epsilon_{ij} = \epsilon^{e}_{ij} + \epsilon^{p}_{ij} \tag{4.1}$$

The plastic strain is obtained from the flow rule:

$$\epsilon^{p}_{ij} = \phi \frac{\partial F}{\partial \sigma_{ij}} \tag{4.2}$$

where ϕ is a scalar function relating to a one-dimensional test curve, positive during loading and zero during unloading, and F is a scalar function of the stress state and possibly also of some hardening parameters.

In the deformation theories of plasticity for work-hardening materials, it postulates that the state of stress determines the state of strain uniquely as long as plastic deformation continues. Thus, they are identical with nonlinear elastic stress-strain relations of secant type as long as unloading does not occur.

Thus, for such elasticity-based models to describe adequately the soil behavior under general loading and unloading conditions, we need to establish a special criterion defining loading-unloading. Such a treatment is closely in the realm of the deformation theory of plasticity.

4.2.1 An illustrative example

An example of the deformational plasticity formulation has been given in the book by Chen and Saleeb (1982) where the third-order hyperelastic model was augmented by a loading-unloading criterion. This criterion is expressed in terms of the complementary energy density function Ω. Unloading is indicated by the condition $d\Omega < 0$, where $d\Omega = \epsilon_{ij} d\sigma_{ij}$ is the incremental change in Ω. The condition $d\Omega > 0$ indicates loading. Reloading is defined by the condition $d\Omega > 0$ and $\Omega < \Omega_{max}$, where Ω_{max} is the maximum previous value of Ω at the material point.

Mathematically, these general conditions may be written as:

$$\text{Loading:} \quad \text{when } \Omega = \Omega_{\max} \quad \text{and } d\Omega > 0 \tag{4.3a}$$

$$\text{Unloading:} \quad \text{when } \Omega \leq \Omega_{\max} \quad \text{and } d\Omega < 0 \tag{4.3b}$$

$$\text{Reloading:} \quad \text{when } \Omega < \Omega_{\max} \quad \text{and } d\Omega > 0 \tag{4.3c}$$

For the cases of unloading or reloading, the initial tangential moduli may be applied, whereas for loading, the following general form of the deformation theory for an isotropic material may be used:

$$\epsilon_{ij}^{p} = P\delta_{ij} + Qs_{ij} + Rt_{ij} \tag{4.4}$$

where $t_{ij} = s_{ik}s_{kj} - \frac{2}{3}J_2\delta_{ij}$, s_{ij} is the stress deviation tensor, $J_2 = \frac{1}{2}s_{ij}s_{ij}$ and ϵ_{ij}^{p} is the plastic strain components. In general, the scalar functions P, Q, and R depend on the three invariants of the stress tensor σ_{ij}. For the special case of $P = R = 0$, Eq. (4.4) reduces to the *Hencky relations* commonly used for metals.

The only objection to the present definition of loading and unloading in Eq. (4.3) is the ambiguity encountered at the *neutral loading* condition $d\Omega = 0$ where one may arbitrarily assign either value of the loading or unloading moduli. The result is that an infinitesimal stress changes near the neutral loading may produce finite strain changes, and the *continuity condition* may be violated. This is not physically acceptable.

Considering the loading criterion of Eq. (4.3), it appears that apart from severe multi-dimensional loading conditions, neutral loading paths are not likely to occur in many practical situations where moderate loading conditions are generally encountered. However, the validity of such a statement, and the consequences can not be ascertained unless extensive numerical studies of practical problems are performed. Such numerical studies are not presently available for the third-order hyperelastic models combined with a loading criterion such as the complementary energy density function, Ω.

In general, it has been clearly demonstrated that, except for certain special cases of loading, e.g., increasing proportional loading, the deformation type of theories can not lead to meaningful results, and sometimes they lead to contradictions. As mentioned previously, these types of models do not satisfy the *continuity* requirement for loading conditions near or at the neutral loading. Basically, the difficulty lies in the fact that the deformation theory and the existence of the loading function, f, even in the most limited sense, are incompatible. This has led naturally to the consideration of the second type of formulation based on the incremental theory of plasticity. This will be described in Section 4.3.

4.2.2 *Variable moduli models*

The generalization of the deformation theory of plasticity in the form of incremental stress-strain relationships is called the variable moduli models (Nelson and Baron, 1971; Nelson et al., 1971; Nelson and Baladi, 1977). Different forms of material response functions are applied in initial loading, and in subsequent unloading and reloading, i.e., the models are generally irreversible, even for an incremental loading.

The mathematical description of the variable moduli model is given in the incremental forms as:

$$\mathrm{d}p = K\,\mathrm{d}\epsilon_{kk} \quad \text{and} \quad \mathrm{d}s_{ij} = 2G\,e_{ij} \tag{4.5}$$

where $\mathrm{d}p$ and $\mathrm{d}\epsilon_{kk}$ are the mean hydrostatic stress and the volumetric strain increments and $\mathrm{d}s_{ij}$ and $\mathrm{d}e_{ij}$ are the deviatoric stress and the deviatoric strain increments, respectively. Different functions for shear modulus G and bulk modulus K generally are applied in initial loading, and in subsequent unloading, and reloading.

Variable moduli models have many advantages. They generally give a good over-all fit to the full set of tests available, and they are capable of fitting repeated hysteretic data in cyclic loading. In addition, they are computationally simple and relatively easy to fit the data for the determination of material constants. However, phenomena such as dilatation, cross effects, and noncoincidence of the principal axes of stress and strain increments can not be described by such relations as Eq. (4.5). The other problem associated with this type of formulation is that the model may not satisfy all rigorous theoretical requirements for all stress histories. For

TABLE 4.1
Advantages and limitations of deformational plastic models

Advantages	Limitations
Deformation theory of plasticity	
simple formulation	continuity problem near or at neutral loading
allow hysteretic behavior	with the exception of unloading, behavior is still path-independent
Variable moduli models	
simple	continuity problem near or at neutral loading
good fit of data	
allow hysteretic behavior	
easy to fit	
suitable for finite element implementation	

instance, at or near the neutral loading conditions in shear, the model fails to satisfy the continuity condition (Chen and Saleeb, 1982). Thus, the model is restricted to practical applications in which no substantial neutral loading, or near neutral loading occurs. For the proportional loading case, the model is theoretically correct.

The advantages and limitations of constitutive models based on the deformational type of plasticity theory are summarized in Table 4.1.

4.3 FLOW THEORY

In the development of stress increment-strain increment relationship, the total strain increment $d\epsilon_{ij}$ is assumed to be the sum of the elastic strain increment $d\epsilon^e_{ij}$ and the plastic strain increment $d\epsilon^p_{ij}$, i.e.:

$$d\epsilon_{ij} = d\epsilon^e_{ij} + d\epsilon^p_{ij} \tag{4.6}$$

The elastic strain increment is assumed to be completely described within the framework of incremental Hooke's law where two material parameters such as the bulk modulus, K, and the shear modulus, G, are either constants or function of stress invariants and/or strain invariants. On the other hand, to estimate the plastic strain increment, the following concepts of flow, or incremental theory of plasticity for perfectly plastic materials are needed:

1. The existence of a yield surface.
2. The determination of flow rule that specifies the general form of the stress to the incremental plastic strain relationship.

These subjects are discussed in the forthcoming.

4.3.1 Yield criteria

It is necessary to define the onset of plasticity or the point at which elastic relations cease to be valid. For simple tests such as tension, compression and shear, the onset of plasticity can be taken as the yield point which may be obtained from the stress-strain curve by either the direct, tangent or off-set method. For combined tests under bi-axial stress conditions, the yield curves rather than yield points must be established. Further, from the most general combination of three-dimensional tests, yield surfaces can be constructed. These surfaces or curves are represented mathematically as the *yield criteria*. These yield criteria serve to define the stress conditions under which plastic deformation will occur for a material element and also to separate zones of elastic behavior from those of elastic-plastic behavior. Stress paths within the yield surface result in purely recoverable deformations, while paths which intersect the yield surface produce both recoverable and permanent deformations (plastic strains).

In general, the initial yield function f (or criterion) can be described as:

$$f(\sigma_{ij}) = f_c \tag{4.7}$$

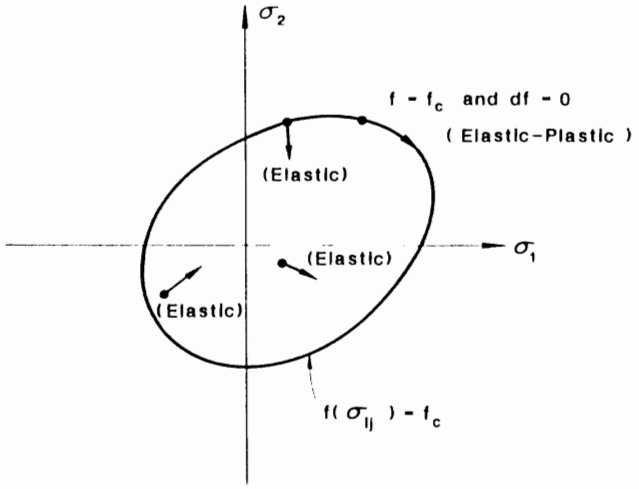

Fig. 4.1. Yield surface for a perfectly plastic material.

where f_c is a constant value for a perfectly plastic material but a variable for strain- or work-hardening materials (see Chapter 5).

Consider first the yield surface in biaxial stress space. For a perfectly plastic material, the yield surface is fixed in stress space, and therefore plastic deformation occurs only when the stress path moves on the yield surface (Fig. 4.1). Thus, the loading condition for plastic flow is given by:

$$f = f_c \quad \text{and} \quad \mathrm{d}f = \frac{\partial f}{\partial \sigma_{ij}} \mathrm{d}\sigma_{ij} = 0 \tag{4.8}$$

On the other hand, elastic behavior occurs if, after an increment of stress, the new state of stress is within the elastic domain, that is:

$$f < f_c \tag{4.9}$$

For the special case of a stress path originating on the yield surface, the loading condition for the elastic behavior is expressed as:

$$f = f_c \quad \text{and} \quad \mathrm{d}f = \frac{\partial f}{\partial \sigma_{ij}} \mathrm{d}\sigma_{ij} < 0 \tag{4.10}$$

4.3.2 Flow rule

The flow rule defines the relationship between the next increment of the plastic strain increment $\mathrm{d}\epsilon_{ij}^{p}$, and the present state of stress σ_{ij} for a yielded element

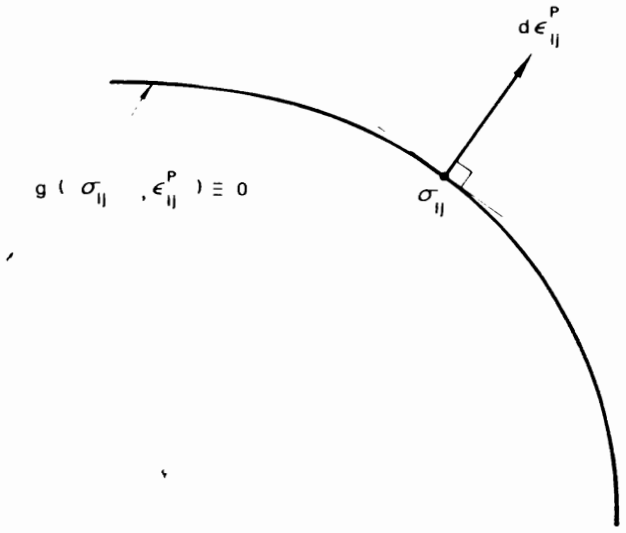

Fig. 4.2. Representation of flow rule.

subjected to further loading. This relationship is established using the concept of *plastic potential function* g. In the theory of plasticity, the direction of the plastic strain increment is defined by the plastic potential function g in the form:

$$d\epsilon^p_{ij} = d\lambda \frac{\partial g}{\partial \sigma_{ij}} \tag{4.11}$$

where $d\lambda$ is a positive scalar of proportionality dependent on the state of stress and load history. If the potential and yield surfaces coincide with each other ($f = g$), the flow rule is called the *associated* type, otherwise it is the *non-associated* type. As can be understood from Eq. (4.11), the direction of the plastic strain increment vector, $d\epsilon^p_{ij}$, is normal to the surface of plastic potential g at the current stress point, σ_{ij}. This normality condition is shown schematically in Fig. 4.2. As a result, the directions of principal axes of plastic strain increment are in general not coincident with those for stress increment.

4.3.3 Basic requirements

As will be shown later, the associated flow rule assumption will lead to the uniqueness of the solution of a boundary value problem for perfectly plastic and work-hardening materials.

The irreversible character of plastic deformations predicted by the theory leads to the *irreversibility condition* that may be simply stated as follows: the work done by stresses on the change of plastic strain is positive whenever a change of plastic strain occurs. Consider a unit volume of perfectly plastic material subjected to a homoge-

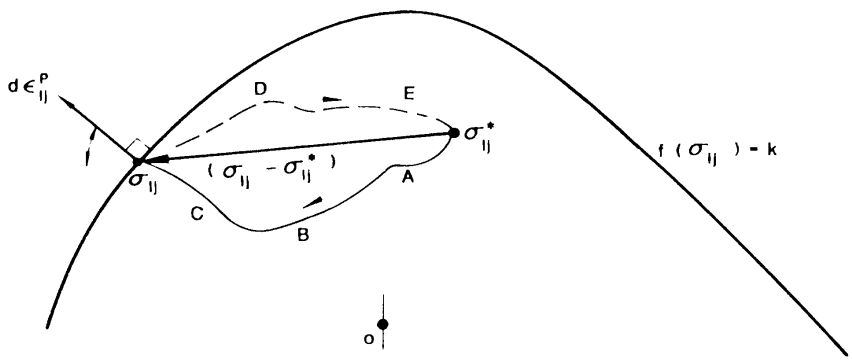

Fig. 4.3. Stress path produced by an external agency (plastic-strain coordinates are superimposed).

neous state of stress σ^*_{ij} on or inside the yield surface (see Fig. 4.3). Suppose that an external agency adds stresses along a path ABC lying inside the surface until the state of stresses reaches the yield surface. Only elastic work has taken place along the stress path ABC. Now, suppose the external agency keeps the stress state σ_{ij} on the yield surface for a short time. Plastic flow must therefore occur, and only the plastic work takes place during the flow. The external agency then releases stresses and returns the state of stress to the original stress σ^*_{ij} along the elastic path DE. As all purely elastic changes are completely reversible and independent of the path from σ^*_{ij} to σ_{ij} and return to σ^*_{ij}, all the elastic energy is recovered. The plastic work done by the external agency on this loading and unloading cycle is represented by the scalar product of the stress vector $(\sigma_{ij} - \sigma^*_{ij})$ and the plastic strain increment vector $d\epsilon^p_{ij}$. The requirement that this work be positive for the changes in the plastic deformations leads to:

$$(\sigma_{ij} - \sigma^*_{ij})\, d\epsilon^p_{ij} \geq 0 \tag{4.12}$$

If the plastic-strain coordinates are superimposed upon the stress coordinates, the geometrical interpretation of Eq. (4.12) is shown in Fig. 4.3. The positive scalar product requires an acute angle between the stress vector $(\sigma_{ij} - \sigma^*_{ij})$ and the plastic-strain-increment vector $d\epsilon^p_{ij}$. If the normality condition for plastic flow is taken, the plastic-strain-increment vector $d\epsilon^p_{ij}$ is normal to the yield surface. Since Eq. (4.12) must be satisfied for all stress vectors, $(\sigma_{ij} - \sigma^*_{ij})$, this condition requires that the yield surface be *convex*. The restrictions imposed on the plastic stress-strain relations by the *normality condition* for the plastic-strain-increment vector $d\epsilon^p_{ij}$ and the *convexity property* of the yield surface are of general nature.

4.4 PERFECT PLASTICITY MODELS

The origin of metal plasticity dates back to a series of papers by Tresca, beginning in 1864. The first proposed yield criterion for metals is now known as the

Tresca criterion (or the *maximum shear stress criterion*). In 1870, Saint Venant used the Tresca criterion to determine the state of stress in a plastically deforming cylinder subjected to two dimensional states of stress. In this process, he developed a constitutive relation for a *rigid*, perfectly plastic material. Recognizing that no unique relationship existed between the state of stress and the total plastic strain, Saint Venant proposed that the plastic strain-rate coincides with the direction of maximum shear stress. Here, the concept of flow rule, or the plastic potential surface was introduced. Later, Levy extended Saint Venant's equation to the three-dimensional case. Prandtl, in 1924, made the important step of considering the elastic components of strain-rates when formulating the constitutive equations. Thus, the tools for representing the constitutive behavior of an elastic-perfectly plastic material were in place.

Von Mises, in 1913, introduced a new yield criterion for metals which proved to be more convenient for numerical solutions than the Tresca criterion. This yield condition is known as the *von Mises criterion* (or the *octahedral shear* or *distortion energy criterion*). In 1928, von Mises used this criterion and developed a constitutive relation based on the normality concept that relates the plastic strain rate to the yield surface. On the other hand, the concept of perfect plasticity based on the Coulomb criterion, the Tresca criterion, and the von Mises criterion has been used extensively in the past in the conventional soil mechanics to assess the collapse load in stability problems. However, perfect plasticity is not nearly appropriate for soils, as for metals. Some of the troubles and their justifications for practical use were discussed in the paper "Concepts of Path Independence and Material Stability for Soils" by Drucker (1966).

In general, the yield function f depends on various parameters such as stresses, strains and history of loading. We may exclude the strains from the parameters in the yield function since, for the classical perfectly plastic models, they are uniquely related to the stress level. Therefore, the general form of f may be given by Eq. (4.7). Furthermore, we shall restrict ourselves to isotropic materials which would require the function f to be unchanged with respect to any transformation of coordinates. This isotropic condition calls for the use of invariants of stresses. Thus, the form of f can be represented by:

$$f(\text{invariants of } \sigma_{ij}) \quad f_c \tag{4.13a}$$

or

$$f(I_1, J_2, J_3) \quad f_c \tag{4.13b}$$

In the followings, classical perfectly plastic models such as Tresca, von Mises, Coulomb and Drucker-Prager models will be reviewed in some details and assessed with respect to their advantages and limitations for solving practical problems in geotechnical engineering.

Since the hydrostatic pressure has little or no effect on the plastic deformation and yielding of metals, the invariants of deviatoric stresses s_{ij}, not the total stresses σ_{ij} are critical and play the key roles. Equation (4.13) takes the form:

$$f(\text{invariants of } s_{ij}) = f_c \tag{4.14}$$

Among various invariants of deviatoric stress tensor s_{ij}, only two are independent and other invariants can be expressed in terms of these two. For reasons that will become clear later, we shall choose the two invariants J_2 and J_3 as the two independent invariants and express the yield criterion in the form:

$$f(J_2, J_3) = f_c \tag{4.15}$$

The Tresca criterion (or the maximum shear stress criterion) implies that metal yielding occurs when the maximum shear stress reaches a critical level. For the special case $\sigma_1 \geq \sigma_2 \geq \sigma_3$, the Tresca yield condition can be written as:

$$\tfrac{1}{2}(\sigma_1 - \sigma_3) = k \tag{4.16}$$

where σ_1, σ_3 are the maximum and minimum principal stresses, respectively and k is the yield stress of material determined from the pure shear test. More generally, Eq. (4.16) can be written in the form:

$$\left[(\sigma_1 - \sigma_2)^2 - 4k^2\right]\left[(\sigma_2 - \sigma_3)^2 - 4k^2\right]\left[(\sigma_3 - \sigma_1)^2 - 4k^2\right] = 0 \tag{4.17}$$

or in terms of stress invariants J_2 and J_3, Eq. (4.17) can be expressed by:

$$f - f_c = 4J_2^3 - 27J_3^2 - 36k^2J_2^2 + 96k^4J_2 - 64k^6 = 0 \tag{4.18}$$

The three-dimensional view of the Tresca yield criterion in principal stress space is shown in Fig. 4.4a where Eq. (4.17) or (4.18) represents a cylindrical surface whose generator is parallel to the hydrostatic axis ($\sigma_1 = \sigma_2 = \sigma_3$), and whose cross sectional shape is a regular hexagon.

The von Mises yield criterion (or the maximum shear energy criterion) implies that the plastic behavior begins when the distortional energy reaches a critical value. The *distortional energy* per unit volume of the material, W'_d, stored in the material due to the elastic shear deformation prior to yielding can be represented by (see Example 3.6, Chapter 3):

$$W'_d = \frac{1+\nu}{E} J_2 \tag{4.19}$$

where ν and E are respectively the Poisson's ratio and the modulus of elasticity.

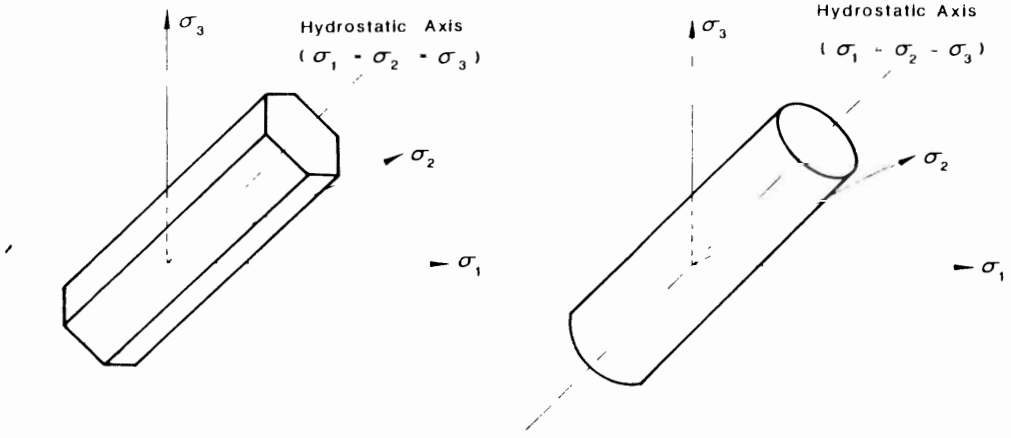

a) Tresca Criterion

b) Von Mises Criterion

Fig. 4.4. Classical yield critera for metals.

Since the distortional energy W'_d is related to the second invariant of the deviatoric stress tensor, J_2, the von Mises criterion is also called the *J_2-theory* or the *octahedral shear stress criterion*. It has the simple form:

$$J_2 = k^2 = 0 \tag{4.20a}$$

or using the components of a general state of stress, we have:

$$\frac{1}{6}\left[(\sigma_{11} - \sigma_{22})^2 + (\sigma_{22} - \sigma_{33})^2 + (\sigma_{33} - \sigma_{11})^2 + 6\sigma_{12}^2 + 6\sigma_{23}^2 + 6\sigma_{31}^2\right] - k^2 = 0 \tag{4.20b}$$

where k is again the yield stress of material in pure shear state. This criterion has the simplest mathematical form that is compatible with the general postulate for an isotropic material. The three-dimensional view of the von Mises yield criterion in the principal stress space is shown in Fig. 4.4b where Eq. (4.20) represents a circular cylinder whose generator is parallel to the hydrostatic axis, and whose cross sectional shape on the π-plane is a circle.

Consider the yield stress in simple tension test with $\sigma_1 = \sigma_y$, $\sigma_2 = \sigma_3 = 0$. Substitution of these values into the Tresca criterion leads to:

$$\sigma_y = 2k \tag{4.21}$$

while a similar consideration for the von Mises criterion gives:

$$\sigma_y = \sqrt{3}\,k \tag{4.22}$$

If the two criteria are matched at the simple tension yield stress σ_y, the ratio of the

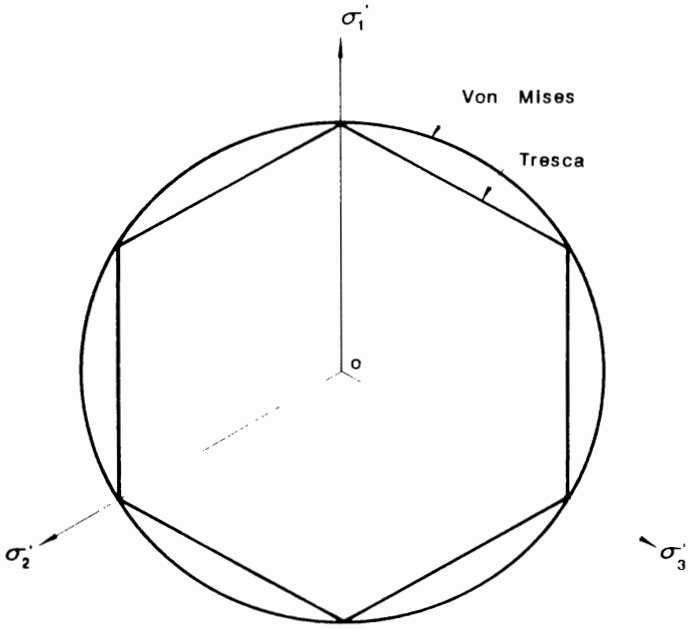

Fig. 4.5. Tresca and von Mises criteria on the π-plane.

yield stress in pure shear k predicted by the von Mises criterion to that of the Tresca criterion is $2/\sqrt{3} = 1.15$. In this case, the circular cylinder circumscribes the Tresca hexagon (see Fig. 4.5) and it follows that the maximum difference between the Tresca and the von Mises criteria can not exceed 15 percent. If the two criteria are matched at the pure shear test, the von Mises circle will inscribe the Tresca hexagon.

The von Mises criterion considers the effect of intermediate principal stress on the yield strength, while the Tresca criterion neglects this principal stress and considers only the maximum shear stress. Because of the possible numerical complications required for the corner treatment along the edges of the Tresca hexagon, the von Mises criterion is mathematically more convenient for practical

TABLE 4.2
Advantages and limitations of the Tresca and von Mises models

Advantages	Limitations
Tresca	
simple	only for undrained saturated soils of clay type (total stress)
	corner
von Mises	
- simple	only for undrained saturated soils of clay type (total stress)
- smooth	

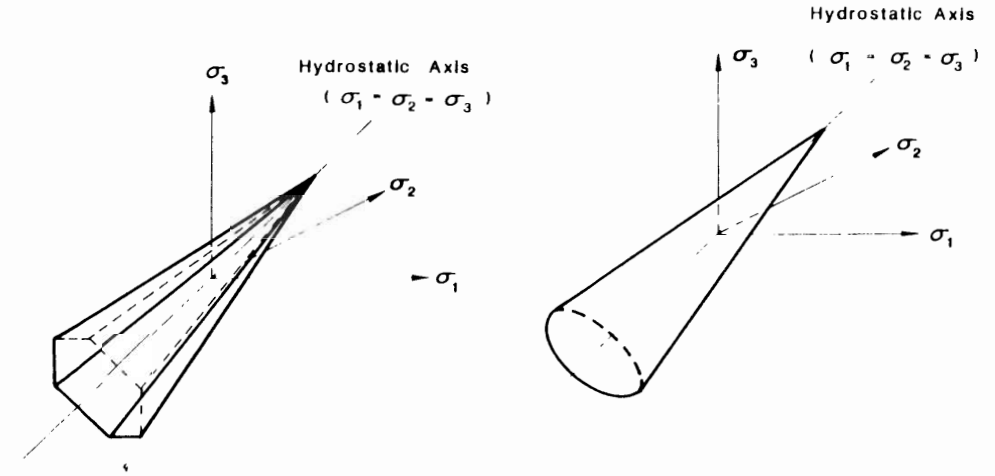

a) Extended Tresca Criterion b) Extended von Mises Criterion

Fig. 4.6. Classical yield criteria for soils.

use. Since both criteria are developed primarily for metals whose yield strength is insensitive to the hydrostatic pressure, they are not generally suitable for application to stability problems in soil mechanics. The advantages and limitations of Tresca and von Mises models are summarized in Table 4.2.

To include the effect of the hydrostatic pressure on soil strength, the Tresca and the von Mises criteria can be extended to the so-called extended Tresca and extended von Mises criteria as follows:
for the *extended Tresca criterion*,

$$\frac{|\sigma_1 - \sigma_3|}{I_1 + c_1} = c_2 \tag{4.23}$$

and for the *extended von Mises criterion*,

$$\frac{\sqrt{J_2}}{I_1 + c_3} = c_4 \tag{4.24}$$

where c_1, c_2, c_3 and c_4 are constants.
These extended criteria in the principal stress space are sketched in Fig. 4.6.

Example 4.1: The initial yield curve is formed by joining all possible initial yield points observed from a series of combined stress tests. Here, we shall demonstrate the construction of a rather complete yield curve for metals in the biaxial stress space only from one simple test, based on the following three assumptions:
(1) Isotropy
(2) Equality of properties in tension and in compression

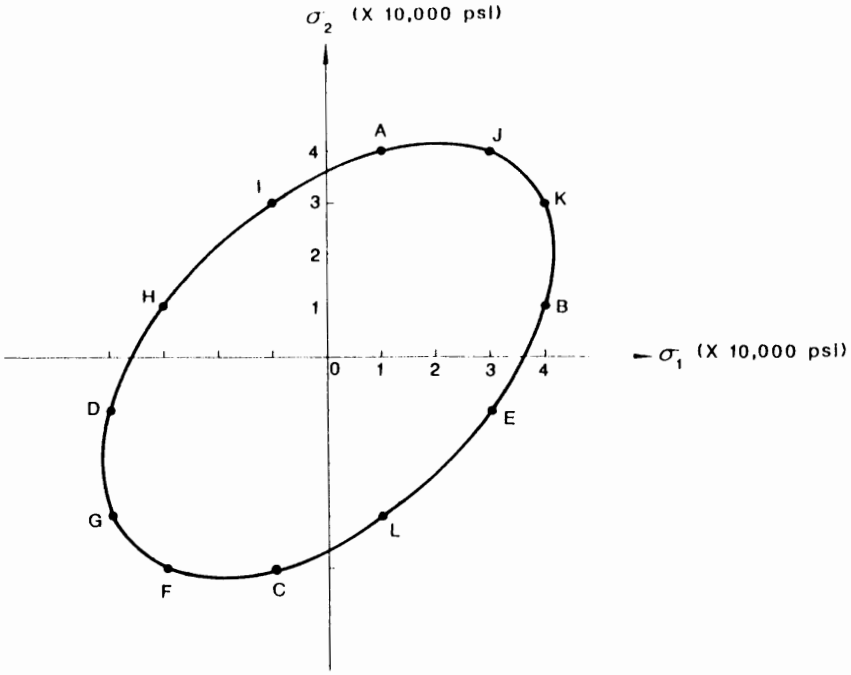

Fig. 4.7. Yield curve in the biaxial stress space.

(3) Insensitivity to hydrostatic pressure

If a metal yields at a stress state $(\sigma_1, \sigma_2) = (10{,}000 \text{ psi}, 40{,}000 \text{ psi})$.

(a) Find all other biaxial states of stress in $\sigma_1 - \sigma_2$-space at which the metal must yield.

(b) Estimate the yield stress in axial tension and in simple shear.

Solutions:

(a) *Yielding in biaxial states:* The given initial yield state is plotted as Point A in $\sigma_1 - \sigma_2$-space shown in Fig. 4.7. From the first assumption of isotropy, this metal must yield also at the stress state denoted by Point B:

$$(\sigma_1, \sigma_2) = (40{,}000 \text{ psi}, 10{,}000 \text{ psi})$$

From the second assumption of equality of properties in tension and in compression, we have other two stress states C and D corresponding to Points A and B such as:

$$(\sigma_1, \sigma_2) = (-10{,}000 \text{ psi}, -40{,}000 \text{ psi})$$

$$(\sigma_1, \sigma_2) = (-40{,}000 \text{ psi}, -10{,}000 \text{ psi})$$

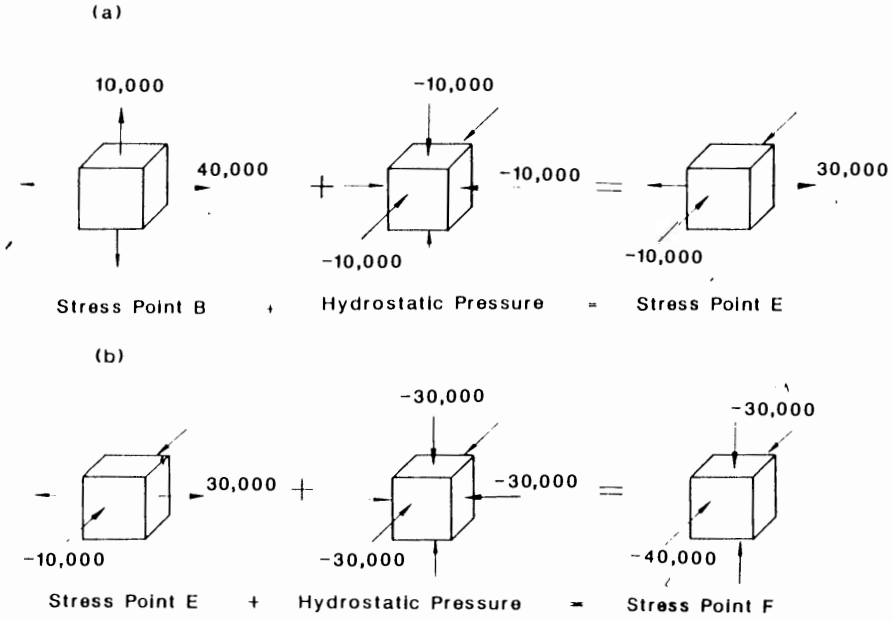

Fig. 4.8 Insensitivity to hydrostatic pressure.

Employing the third assumption, we may add a hydrostatic pressure of $p = -10{,}000$ psi to the stress state at Point B (see Fig. 4.8a) and this results in a biaxial tension-compression state as represented by Point E as the new yield state. In a similar manner, addition of a further hydrostatic pressure of $p = -30{,}000$ psi to the stress state at Point E leads to the new stress state F in the biaxial compression region (see Fig. 4.8b).

Using the first two assumptions again, we obtain the other six stress states such as *G*, *H*, *I*, *J*, *K*, and *L* as shown in Fig. 4.7.

(b) *Estimate of yield stress:* Connecting all twelve points obtained in (a) with a smooth curve which is convex, we obtain a yield curve in the biaxial stress space. From this curve, we can estimate the yield stresses for any combined stress conditions. For example, for the yield stress in simple tension, we have:

$\sigma_1 = 35{,}050$ psi

and in simple shear ($\sigma_1 = -\sigma_2$), we find:

$\sigma_1 = 20{,}800$ psi

Example 4.2. Show that the Tresca and von Mises criteria in the (a) $\sigma_1 - \sigma_2$-space are respectively a hexagon and an ellipse, and in the (b) $\sigma_{11} - \sigma_{12}$-space are both ellipses.

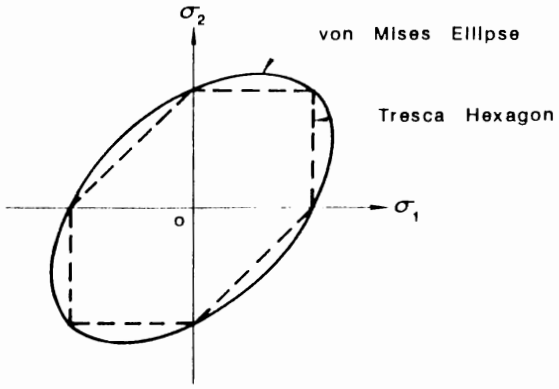

Fig. 4.9. Yield curves in the $\sigma_1 - \sigma_2$ stress space.

Solutions: (a) The general form of the Tresca criterion in the principal stress space is:

$$\left[(\sigma_1 - \sigma_2)^2 - 4k^2\right]\left[(\sigma_2 - \sigma_3)^2 - 4k^2\right]\left[(\sigma_3 - \sigma_1)^2 - 4k^2\right] = 0 \tag{4.25}$$

Substitution of $\sigma_3 = 0$ leads to:

$$\left[(\sigma_1 - \sigma_2)^2 - 4k^2\right]\left[\sigma_2^2 - 4k^2\right]\left[\sigma_1^2 - 4k^2\right] = 0 \tag{4.26}$$

Equation (4.26) is satisfied under the following conditions:

$$\sigma_1 - \sigma_2 = \pm 2k \tag{4.27a}$$

$$\sigma_1 = +2k \tag{4.27b}$$

$$\sigma_2 = \pm 2k \tag{4.27c}$$

These conditions describe the yielding of the material in the biaxial stress space and are shown as a hexagon in Fig. 4.9.
The von Mises criterion (or J_2-theory) as given by Eq. (4.20) is reduced to the biaxial stress state ($\sigma_3 = 0$):

$$\sigma_1^2 - \sigma_1\sigma_2 + \sigma_2^2 = 3k^2 \tag{4.28}$$

Equation (4.28) can be shown as an ellipse in Fig. 4.9.
(b) Using Mohr's circle for stress state (σ_{11}, σ_{12}), the maximum shear stress τ_{max} can be found as:

$$\tau_{max} = \left(\tfrac{1}{4}\sigma_{11}^2 + \sigma_{12}^2\right)^{1/2} \tag{4.29}$$

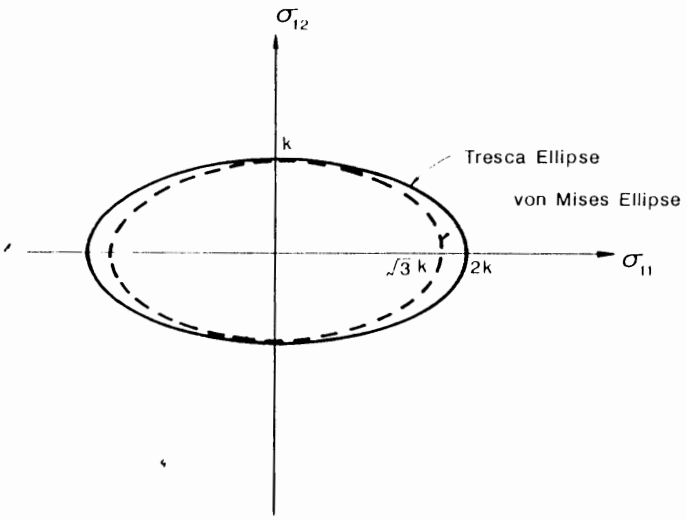

Fig. 4.10. Yield curves in the $\sigma_{11} - \sigma_{12}$ stress space.

From the Tresca's condition $\tau_{max} = k$, we have:

$$\sigma_{11}^2 + 4\sigma_{12}^2 = 4k^2 \tag{4.30}$$

which is an ellipse in the $\sigma_{11} - \sigma_{12}$ space (Fig. 4.10).

On the other hand, substitution of σ_{11}, σ_{12}, and $\sigma_{22} = \sigma_{33} = \sigma_{23} = \sigma_{31} = 0$ into the von Mises criterion in Eq. (4.20) leads to:

$$\sigma_{11}^2 + 3\sigma_{12}^2 = 3k^2 \tag{4.31}$$

which also is an ellipse in the $\sigma_{11} - \sigma_{12}$ space (see Fig. 4.10).

4.6 COULOMB MODEL

Realizing that soil strength depends on the hydrostatic pressure, a general yield function of Eq. (4.13) may be written as:

$$f(I_1, J_2, J_3) = f_c \tag{4.32}$$

A typical example representing the characteristic of Eq. (4.32) is the *Coulomb criterion*, dating back to 1773.

The Coulomb criterion is certainly the best known failure criterion in soil mechanics. This criterion, which was proposed for geotechnical materials much earlier than the Tresca and von Mises yield criteria for metals, is the first type of failure criterion that takes into consideration the effect of the hydrostatic pressure

on the strength of granular materials. This criterion states that failure occurs when the shear stress τ and the normal stress σ acting on any element in the material satisfy the linear equation (refer to Fig. 2.10):

$$|\tau| + \sigma \tan\phi - c = 0 \tag{4.33}$$

where c and ϕ denote the cohesion and the angle of internal friction,respectively. For the special case of frictionless materials for which $\phi = 0$, Eq. (4.33) reduces to the *maximum shear stress criterion* of Tresca, $\tau = c$, and the cohesion becomes equal to the yield stress in pure shear $c = k$.

We consider a state of principal stress $(\sigma_1, \sigma_2, \sigma_3)$ which satisfies the Coulomb criterion of Eq. (4.33). If the condition of stress state is $\sigma_1 > \sigma_2 > \sigma_3$, the Coulomb criterion can be written as:

$$\tfrac{1}{2}(\sigma_1 - \sigma_3) = \tfrac{1}{2}(\sigma_1 + \sigma_3)\sin\phi + c\cos\phi \tag{4.34}$$

Each principal stress can be represented in terms of I_1, $\sqrt{J_2}$, θ (Lode angle), using Eqs. (2.41) and (2.63) and referring to Fig. 2.7. These are:

$$\sigma_1 = \frac{2}{\sqrt{3}}\sqrt{J_2}\cos\theta + \tfrac{1}{3}I_1 \tag{4.35a}$$

$$\sigma_2 = \frac{2}{\sqrt{3}}\sqrt{J_2}\cos\left(\theta - \tfrac{2}{3}\pi\right) + \tfrac{1}{3}I_1 \tag{4.35b}$$

$$\sigma_3 = \frac{2}{\sqrt{3}}\sqrt{J_2}\cos\left(\theta + \tfrac{2}{3}\pi\right) + \tfrac{1}{3}I_1 \tag{4.35c}$$

Therefore, substitution of Eqs. (4.35a) and (4.35c) into Eq. (4.34) leads to the stress invariant form of the Coulomb criterion, that is:

$$\tfrac{1}{3}I_1\sin\phi + \sqrt{J_2}/3\left[(1+\sin\phi)\cos\theta - (1-\sin\phi)\cos\left(\theta + \tfrac{2}{3}\pi\right)\right] - c\cos\phi = 0 \tag{4.36a}$$

or

$$I_1\sin\phi + \tfrac{1}{2}\left[3(1-\sin\phi)\sin\theta + \sqrt{3}(3+\sin\phi)\cos\theta\right]\sqrt{J_2} - 3c\cos\phi = 0 \tag{4.36b}$$

As shown by Shield (1955), the Coulomb's failure criterion is an irregular hexagonal pyramid in the principal stress space (Fig. 4.11). The cross-sectional shape of this pyramid on the π-plane is shown in Fig. 2.14.

To obtain a better approximation when tensile stress occurs, it is sometimes

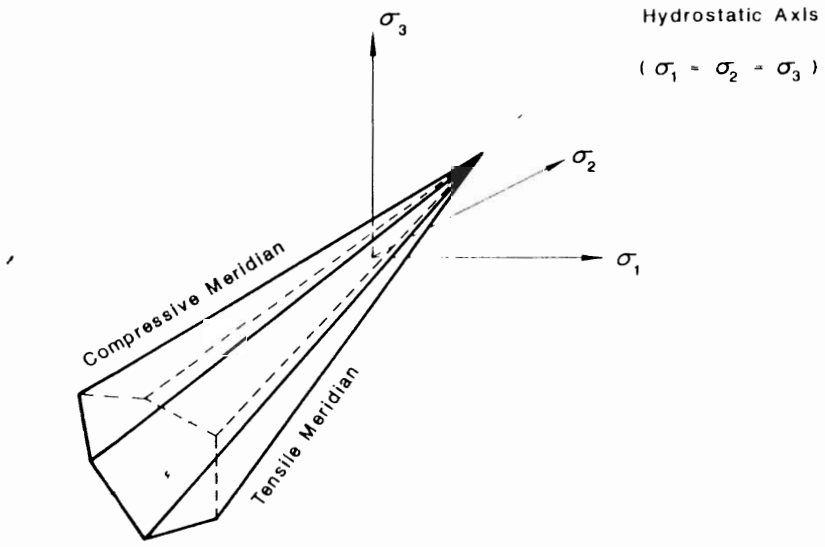

Fig. 4.11 Coulomb criterion.

necessary to combine the Coulomb criterion with a maximum-tensile-strength cut-off (Chen, 1982):

$$\sigma \quad f_t \cdot 0 \tag{4.37}$$

where f_t is a tensile strength obtained from an experiment. This *modified Coulomb criterion* with a tension cut-off is defined by three material constants such as c, ϕ, and f_t. Note that the uniaxial tensile strength as predicted by the Coulomb criterion [Eq. (4.33)] should be thought of as a fictitious tensile strength which is not the same as the true uniaxial tensile strength of a material from experiment. The main advantages and limitations of the Coulomb criterion with a tension cut-off are summarized in detail in the book by Chen (1982).

Even though the Coulomb criterion as mentioned above is generally simple in graphical form, the Coulomb surface exhibits corners or singularities in a three-dimensional generalization. The resulting general yield or failure function with singularities gives rise to some difficulties in numerical analysis. In addition to this

TABLE 4.3
Advantages and limitations of the Coulomb model

Advantages	Limitations
simple	corners
its validity is well established for many soils	neglects the effects of intermediate principal stress

limitations, the Coulomb criterion neglects the influence of intermediate principal stress on shear strength. Nevertheless, for the most part, this criterion has in the past been used for necessity and simplicity to obtain reasonable solutions to important and practical problems in geotechnical engineering.

The advantages and limitations of the Coulomb criterion are summarized in Table 4.3.

Example 4.3: Construct the cross-sectional shape of the Coulomb criterion in the biaxial stress space, and find its uniaxial compressive and tensile strength predicted by the Coulomb criterion.

Solution: In the biaxial stress state with σ_1, σ_2, $\sigma_3 = 0$, the following six sets of stress conditions are considered:

(i) $\sigma_1 > \sigma_2 > 0$ (4.38a)

(ii) $\sigma_1 > 0 > \sigma_2$ (4.38b)

(iii) $\sigma_2 > \sigma_1 > 0$ (4.38c)

(iv) $\sigma_2 > 0 > \sigma_1$ (4.38d)

(v) $0 > \sigma_1 > \sigma_2$ (4.38e)

(vi) $0 > \sigma_2 > \sigma_1$ (4.38f)

From condition (i), the Coulomb equation (4.34) with $\sigma_3 = 0$ leads to:

$$\tfrac{1}{2}\sigma_1 = -\tfrac{1}{2}\sigma_1 \sin\phi + c\cos\phi \tag{4.39a}$$

or

$$\sigma_1 = \frac{2c\cos\phi}{1+\sin\phi} \tag{4.39b}$$

From condition (ii), changing σ_3 to σ_2 in Eq. (4.34) leads to:

$$\tfrac{1}{2}(\sigma_1 - \sigma_2) = -\tfrac{1}{2}(\sigma_1 + \sigma_2)\sin\phi + c\cos\phi \tag{4.40a}$$

or

$$\sigma_2 = \frac{1+\sin\phi}{1-\sin\phi}\,\sigma_1 - \frac{2c\cos\phi}{1-\sin\phi} \tag{4.40b}$$

The other conditions can be examined in a similar manner. Using these six

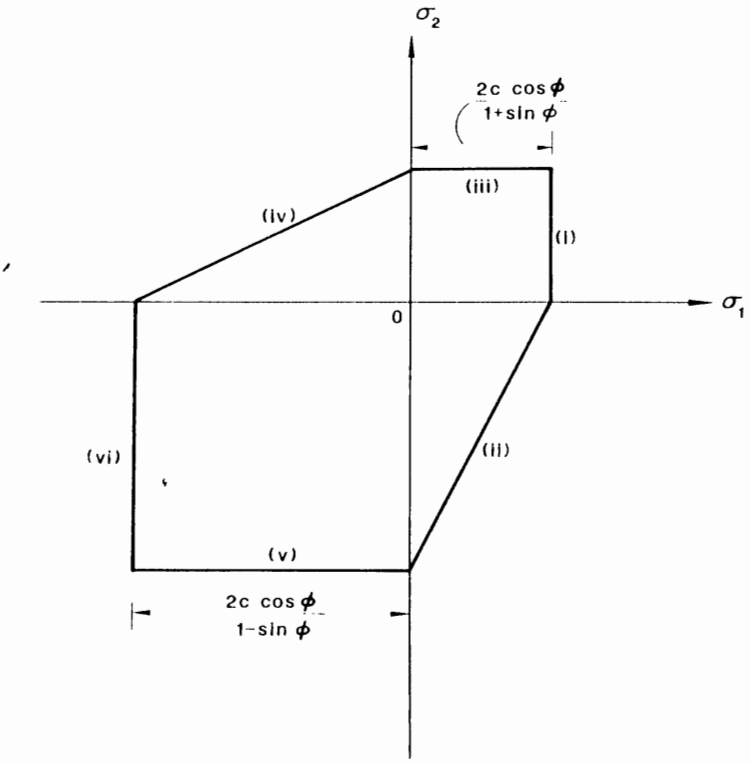

Fig. 4.12. Coulomb criterion in the biaxial stress space.

conditions based on the six stress conditions [Eqs. (4.38a–f)], a hexagonal-shaped failure surface of the Coulomb criterion in the biaxial stress space is constructed in Fig. 4.12. The uniaxial compressive strength f_c^* and tensile strength f_t^* predicted by the Coulomb criterion in terms of c and ϕ are, respectively:

$$f_c^* = \frac{2c\cos\phi}{1-\sin\phi} \tag{4.41}$$

$$f_t^* = \frac{2c\cos\phi}{1+\sin\phi} \tag{4.42}$$

4.7 DRUCKER-PRAGER MODEL

The stress invariant form of the Coulomb criterion consisting of I_1, J_2, and J_3 (or θ) is rather complicated and causes some difficulties in treatment regarding the plastic flow at corners. For practical purposes, therefore, a smooth surface is often

used to approximate the yield surface with singularities in elastic-plastic finite-element analyses under a more general stress condition. The *Drucker-Prager perfectly plastic model* (Drucker and Prager, 1952), which neglects the influence of J_3 on the cross-sectional shape of failure surface, can be considered as the first attempt to approximate the well-known Coulomb criterion by a simple smooth function. This criterion is expressed as a simple stress invariant function of the first invariant of stress tensor, I_1, and the second invariant of deviatoric stress tensor, J_2, together with two material constants α and k. It has the simple form:

$$f = \alpha I_1 + \sqrt{J_2} = k \tag{4.43}$$

where the constants α and k may be related to the Coulomb's material constants c and ϕ in several ways, as described later.

The yield or failure surface of Eq. (4.43) in the principal stress space depicts clearly a right-circular cone with the symmetry about the hydrostatic axis (Fig. 4.13). The Drucker-Prager surface can be looked upon as an extension of the von Mises surface for pressure-dependent materials such as soil and concrete. Thus, this criterion is also called the *extended von Mises criterion*.

If α is zero, Eq. (4.43) reduces to the well-known von Mises yield condition for metal. When ϕ is zero, the Coulomb criterion reduces to the Tresca criterion for metal. In a sense, the von Mises criterion may be considered as an approximate version of the Tresca yield criterion.

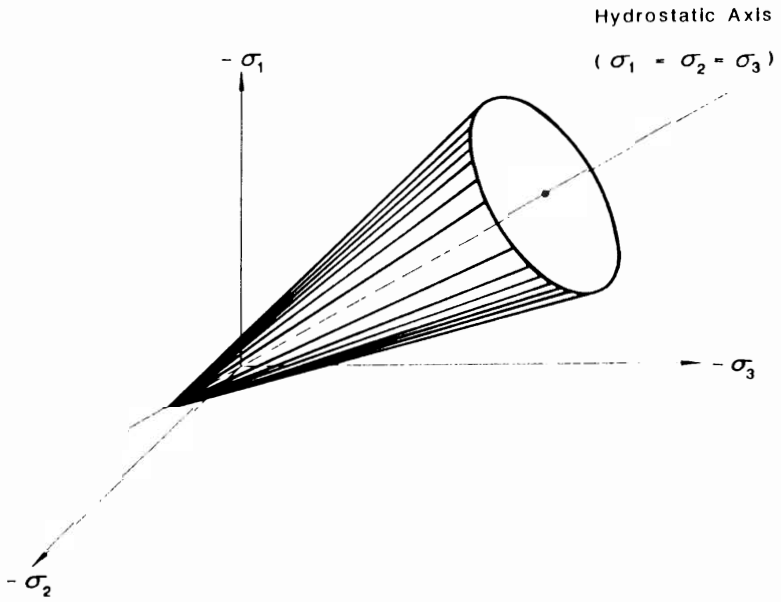

Fig. 4.13. Drucker-Prager criterion

TABLE 4.4
Advantages and limitations of the Drucker-Prager model

Advantages	Limitations
simple to use	excessive plastic dilatancy at yielding
can be matched with the Coulomb model by a proper selection of constants	can not reproduce the hysteretic behavior within the failure surface
computer codes available	can not predict the pore pressure build-up during an undrained sub-failure cyclic shear loading
limit analysis techniques can be used	
satisfy the uniqueness requirement (associated flow rule)	

The Drucker-Prager model cannot predict plastic volumetric strain or compaction of soil materials during hydrostatic loading. To improve this limitation, an extended von Mises model with a convex end cap was proposed by Drucker et al. (1957). However, the failure surface of this model results in a much higher prediction of dilatancy than that observed in experiments. As a result, a modified failure or yield surface, which is asymptotically parallel to the I_1-axis for high values of I_1, as subsequently proposed by DiMaggio and Sandler (1971). Details of this will be given in Chapter 6. The advantages and limitations of the Drucker-Prager model are summarized in Table 4.4.

Drucker-Prager material constants

Since the Drucker-Prager criterion has been established as an approximation of the Coulomb criterion, it is natural to determine the material constants α and k in the Drucker-Prager criterion by matching two particular points with those of the Coulomb criterion, and thus expressing the two Drucker-Prager parameters α and k in terms of the given Coulomb constants c and ϕ.

Three-dimensional matching: In the three dimensional principal stress space, the Drucker-Prager criterion can be matched with the apex of the Coulomb criterion for either Point A or B on its π-plane as shown in Fig. 4.14. In the former case, the cone circumscribes the hexagonal pyramid. Since a line element (*compressive meridian*) connecting the apex O with the Point A contains the same line for both criteria, we can find the relations between α, k, and c, ϕ. Namely, substituting $\theta = \pi/3$ into Eq. (4.36), we have the line element OA given by:

$$\frac{2 \sin \phi}{\sqrt{3}\,(3 - \sin \phi)} I_1 + \sqrt{J_2} = \frac{6c \cos \phi}{\sqrt{3}\,(3 - \sin \phi)} \tag{4.44}$$

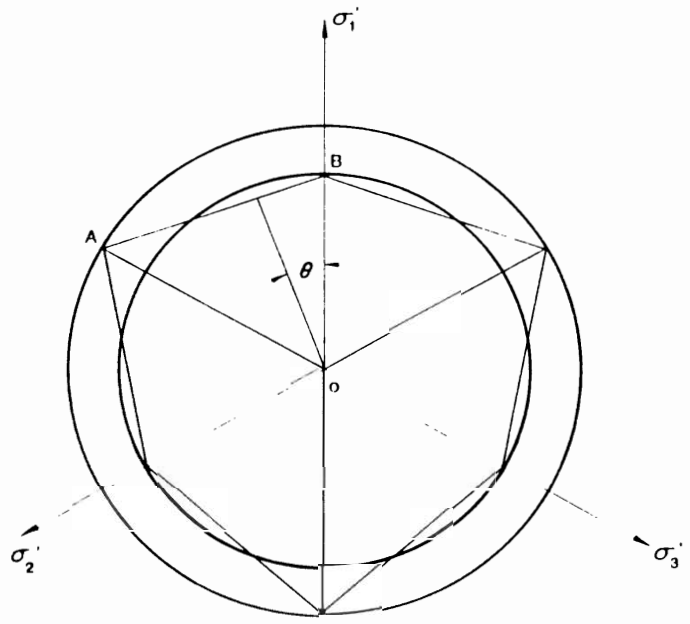

Fig. 4.14. Shape of yield criteria on the π-plane.

Comparing Eq. (4.44) with Eq. (4.43) of the Drucker-Prager criterion, the parameters α and k are, respectively:

$$\alpha = \frac{2 \sin \phi}{\sqrt{3}\,(3 - \sin \phi)} \tag{4.45a}$$

$$k = \frac{6c \cos \phi}{\sqrt{3}\,(3 - \sin \phi)} \tag{4.45b}$$

These material constants are the same as those given by Zienkiewicz et al. (1975) and Zienkiewicz (1978). The latter case results in an inner cone and the corresponding constants for a *tensile meridian* ($\theta = 0$ degree) are:

$$\alpha = \frac{2 \sin \phi}{\sqrt{3}\,(3 + \sin \phi)} \tag{4.46a}$$

$$k = \frac{6c \cos \phi}{\sqrt{3}\,(3 + \sin \phi)} \tag{4.46b}$$

Plane stress matching: In the biaxial stress space with $\sigma_3 = 0$, the shape of the Coulomb yield surface is an unsymmetrical hexagon (solid line) as shown in Fig.

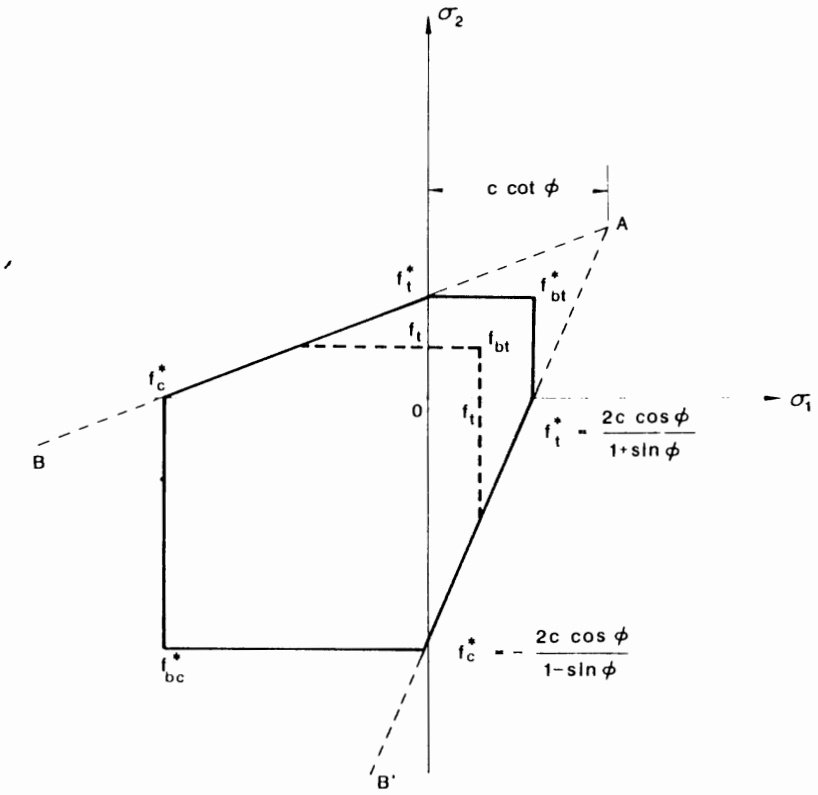

Fig. 4.15. Shapes of the Coulomb and the modified Coulomb criteria in the biaxial stress space

4.15. The Drucker-Prager or extended von Mises criterion is an off-center ellipse when parameter α is less than $1/2\sqrt{3}$, but becomes a parabola or a hyperbola when it is equal to or exceeds $1/2\sqrt{3}$, respectively.

To relate the Drucker-Prager constants α and k with those of the Coulomb criterion c and ϕ in this space, two conditions are needed. In the present case of plane stress condition, we can match, for example, the simple tensile strength f_t^* and simple compressive strength f_c^* of the two criteria. The two material constants α and k in the Drucker-Prager criterion are determined as:

$$\alpha = \frac{1}{\sqrt{3}} \sin\phi \tag{4.47a}$$

$$k = \frac{2}{\sqrt{3}} c\cos\phi \tag{4.47b}$$

There are several ways to match the two criteria and the corresponding material constants. As shown in Table 4.5, the material constants matched with the biaxial

TABLE 4.5
Material constants matched with the Coulomb criterion (plane stress)

Matching points	α	k
f_t^*, f_c^*	$\frac{1}{\sqrt{3}}\sin\phi$	$\frac{2}{\sqrt{3}}c\cos\phi$
f_{bt}^*, f_c^*	$\frac{2\sin\phi}{\sqrt{3}(3-\sin\phi)}$	$\frac{6c\cos\phi}{\sqrt{3}(3-\sin\phi)}$
f_t^*, f_{bc}^*	$\frac{2\sin\phi}{\sqrt{3}(3+\sin\phi)}$	$\frac{6c\cos\phi}{\sqrt{3}(3+\sin\phi)}$
f_{bt}^*, f_{bc}^*	$\frac{1}{2\sqrt{3}}\sin\phi$	$\frac{2}{\sqrt{3}}c\cos\phi$

tensile strength f_{bt}^* and the simple compressive strength f_c^*, and those matched with the biaxial compressive strength f_{bc}^* and the simple tensile strength f_t^* are respectively identical to those obtained previously in the three-dimensional matching.

The simple tensile strength f_t^* of the Coulomb criterion, however, is generally found to be greater than the actual strength f_t obtained from a simple tension test. Hence, the *modified Coulomb criterion with a tension cut-off* is employed when a tensile strength affects significantly the behavior of soil or concrete structures. This modified Coulomb criterion is drawn in Fig. 4.15 where the tension region (solid line $f_{bt}^* - f_t^*$) is cut off by the broken line ($f_{bt} - f_t$).

The material constants α and k matched with the modified Coulomb criterion are listed in Table 4.6 where the parameter β is the ratio of the simple compressive strength to the actual tensile strength, f_c^*/f_t.

Plane strain matching: On the other hand, if the Drucker-Prager and Coulomb criteria are expected to give identical limit loads (plastic collapse loads) for the plane strain case, then the following two conditions must be used: (1) same limit

TABLE 4.6
Material constants matched with the modified Coulomb criterion (plane stress)

Matching points	α	k
f_{bt}, f_c^*	$\frac{\beta-1}{\sqrt{3}(\beta+2)}$	$\frac{\sqrt{3}\beta}{\beta+2}f_t$
f_{bt}, f_{bc}^*	$\frac{\beta-1}{2\sqrt{3}(\beta+1)}$	$\frac{2\beta}{\sqrt{3}(\beta+1)}f_t$
f_t, f_c^*	$\frac{\beta-1}{\sqrt{3}(\beta+1)}$	$\frac{2\beta}{\sqrt{3}(\beta+1)}f_t$
f_t, f_{bc}^*	$\frac{\beta-1}{\sqrt{3}(2\beta+1)}$	$\frac{\sqrt{3}\beta}{2\beta+1}f_t$

load; and (2) plane strain. In order to derive the form of the Drucker-Prager criterion in a plane strain condition, we state the basic theorem of limit analysis method: "when the limit load is reached for any body or assemblage of bodies of perfectly plastic material, collapse takes place at constant stress and only plastic (not elastic) increments of strain occur" (Chen, 1975). This means that at the instant of collapse, the strain rates of increments are purely plastic and the total strain increment $d\epsilon_{ij}$ at this limiting state is equal to the plastic strain increment $d\epsilon^p_{ij}$. Using the concept of flow rule or normality condition, the plastic stress-strain relation for the Drucker-Prager criterion, Eq. (4.43), is:

$$d\epsilon^p_{ij} = d\lambda \frac{\partial f}{\partial \sigma_{ij}} = d\lambda \left(\alpha \delta_{ij} + \frac{1}{2\sqrt{J_2}} s_{ij} \right) \tag{4.48}$$

For the plane strain case, the following conditions must be met:

$$d\epsilon^p_{33} \quad d\epsilon^p_{31} \quad d\epsilon^p_{32} = 0 \tag{4.49}$$

Equations (4.48) and (4.49) lead to:

$$s_{33} = -2\alpha\sqrt{J_2} \tag{4.50a}$$

$$s_{31} - s_{32} = 0 \tag{4.50b}$$

Thus, the stress invariant I_1 can be expressed as:

$$\begin{aligned} I_1 &= \sigma_{11} + \sigma_{22} + \sigma_{33} = \sigma_{11} + \sigma_{22} + s_{33} + \tfrac{1}{3} I_1 \\ &= \sigma_{11} + \sigma_{22} - 2\alpha\sqrt{J_2} + \tfrac{1}{3} I_1 \end{aligned} \tag{4.51}$$

Solving for I_1, we find:

$$I_1 = \tfrac{3}{2}(\sigma_{11} + \sigma_{22}) - 3\alpha\sqrt{J_2} \tag{4.52}$$

Using Eqs. (4.50), (4.52) and $J_2 = \frac{1}{2}(s_{11}^2 + s_{22}^2 + s_{33}^2 + 2\sigma_{12}^2 + 2\sigma_{23}^2 + 2\sigma_{31}^2)$, J_2 can be expressed as:

$$J_2 = \left| \left(\frac{\sigma_{11} \quad \sigma_{22}}{2} \right)^2 + \sigma_{12}^2 \right| / (1 \quad 3\alpha^2) \tag{4.53}$$

Substituting Eq. (4.52) into Eq. (4.43), we find:

$$f = 3\alpha \frac{\sigma_{11} + \sigma_{22}}{2} + (1 \quad 3\alpha^2)\sqrt{J_2} \quad k \tag{4.54}$$

Further substitution of Eq. (4.53) into Eq. (4.54) gives:

$$\frac{k}{\sqrt{(1-3\alpha^2)}} = \frac{3\alpha}{\sqrt{(1-3\alpha^2)}}\frac{\sigma_{11}+\sigma_{22}}{2} + \left[\left(\frac{\sigma_{11}-\sigma_{22}}{2}\right)^2 + \sigma_{12}^2\right]^{1/2} \tag{4.55}$$

If we denote:

$$k/\sqrt{(1-3\alpha^2)} = c\cos\phi \tag{4.56a}$$

and

$$3\alpha/\sqrt{(1-3\alpha^2)} = \sin\phi \tag{4.56b}$$

Equation (4.55) becomes identical to that of the Coulomb criterion under the plane strain condition (for more details, see the paper by Drucker and Prager, 1952). The material constants α and k can therefore be written explicitly in term of c and ϕ in the form by Drucker and Prager (1952):

$$\alpha = \tan\phi/\sqrt{9+12\tan^2\phi} \tag{4.57a}$$

and

$$k = 3c/\sqrt{9+12\tan^2\phi} \tag{4.57b}$$

The broken lines AB and AB′ in Fig. 4.15 are the projection of the Coulomb criterion onto the biaxial stress space for the plane strain case. It should be noted that stress σ_3 is now not zero.

In the case of metal, the simple tension yield value is usually used to determine the material constant k for both the Tresca and von Mises criteria. It follows from the previous Section 4.5 that the maximum deviation between the Tresca and von Mises prediction occurs in pure shear, and this can not exceed 15 percent. In the case of soil, rock, or concrete, replacement of the Coulomb criterion, or other well-known criteria with singularities, by the smooth Drucker-Prager function is more complicated. For example, if the simple tension and simple compression states are used to relate the Drucker-Prager constants α and k with the Coulomb's constants c and ϕ, the matching may be reasonable for stress analysis in the tension-compression domains under plane stress condition, but their use in the plane strain problems may result in a significantly different prediction of the plastic collapse load. Critical evaluation of these constants is obviously necessary before a proper choice can be made for use in a particular application. An assessment of various possible matching schemes has been given by Chen and Mizuno (1979).

4.8 PRANDTL-REUSS STRESS-STRAIN RELATIONS

Before going to derive the generalized elastic-perfectly plastic constitutive equations for geotechnical engineering materials, we shall here present the Prandtl-Reuss constitutive relations for an elastic-perfectly plastic metal which does not exhibit work-hardening but flows plastically under a constant stress.

Plastic strain rates

In dealing with plastic rates, we need to know the directions of the axes of the principal strain rates. For isotropic materials, we expect these to coincide with the axes of the principal stresses. In other words, a rectangular element of an isotropic material under a simple compression will flow plastically in such a way that its faces remain mutually perpendicular. The assumption of coincidence of the principal axes of plastic strain rate and stress determines only the *directions* of the strain rate components and not their magnitudes. To obtain the actual *magnitudes*, we need to make use of a yield function.

The physical explanation of such an assumption can be put in mathematical form as follows:

Let us decompose the increment of plastic strain into the deviatoric and hydrostatic components:

$$d\epsilon_{ij}^{p} = de_{ij}^{p} + \tfrac{1}{3}\, d\epsilon_{kk}^{p}\delta_{ij} \tag{4.58}$$

The incompressibility of plastic volume for metals requires that:

$$\tfrac{1}{3}\, d\epsilon_{kk}^{p}\delta_{ij} = 0 \tag{4.59}$$

so that:

$$d\epsilon_{ij}^{p} = de_{ij}^{p} \tag{4.60}$$

Equation (4.60) means that the total and the deviatoric strain increments are equal and therefore interchangeable. We will, however, use $d\epsilon_{ij}^{p}$ in our derivation.

In the same manner, a state of stress can be written separately as:

$$\sigma_{ij} = s_{ij} + \tfrac{1}{3}\sigma_{kk}\delta_{ij} \tag{4.61}$$

Hydrostatic pressure has been found to produce only the elastic component of the strain increment. As a result, the deviatoric stress tensor s_{ij} is solely responsible for plastic deformation.

Prandtl-Reuss equations

The coincidence of the plastic strain increment and the principal stress axes implies that the two terms are proportionally related:

$$d\epsilon_{ij}^{p} = d\lambda s_{ij} \tag{4.62}$$

where $d\lambda$ is a positive factor of proportionality or a scalar multiplier which is not determined by the stress but is a measure of the amount of plastic strain. In the work-hardening case to be discussed in Chapter 5, this proportionality factor becomes a function of $d\sigma_{ij}$, σ_{ij} and the prior history of loading.

Equation (4.62) may be written in terms of the general stresses:

$$\begin{aligned}
d\epsilon_{11}^p &= \tfrac{2}{3}d\lambda\left[\sigma_{11} - \tfrac{1}{2}(\sigma_{22} + \sigma_{33})\right] \\
d\epsilon_{22}^p &= \tfrac{2}{3}d\lambda\left[\sigma_{22} - \tfrac{1}{2}(\sigma_{33} + \sigma_{11})\right] \\
d\epsilon_{33}^p &= \tfrac{2}{3}d\lambda\left[\sigma_{33} - \tfrac{1}{2}(\sigma_{11} + \sigma_{22})\right] \\
d\epsilon_{12}^p &= d\lambda\sigma_{12} \\
d\epsilon_{23}^p &= d\lambda\sigma_{23} \\
d\epsilon_{31}^p &= d\lambda\sigma_{31}
\end{aligned} \tag{4.63}$$

Equations (4.63) represent the general form of plastic stress-strain relations (or flow rule) and are often known as the *Prandtl-Reuss equations*. Obviously, the equations themselves merely give a relationship between the ratios of plastic strain increments in different directions. That is, we can generate the following proportionality under the principal strain increments and principal deviatoric stresses:

$$\frac{d\epsilon_1^p}{s_1} = \frac{d\epsilon_2^p}{s_2} = \frac{d\epsilon_3^p}{s_3} = d\lambda \tag{4.64}$$

or

$$\frac{d\epsilon_1^p - d\epsilon_2^p}{s_1 - s_2} = \frac{d\epsilon_2^p - d\epsilon_3^p}{s_2 - s_3} = \frac{d\epsilon_3^p - d\epsilon_1^p}{s_3 - s_1} = d\lambda \tag{4.65}$$

where subscripts 1, 2, and 3 denote the principal directions of plastic strain increments and deviatoric stresses.

Scalar function $d\lambda$

To obtain the actual magnitudes of the plastic strain increments, we need to solve for $d\lambda$. Since we deal the condition at the onset of plasticity, it would be appropriate to make use of a yield function to arrive at $d\lambda$ as follows. By means of Eq. (4.63), we can have the following relation:

$$\begin{aligned}
&(d\epsilon_{11}^p - d\epsilon_{22}^p)^2 + (d\epsilon_{22}^p - d\epsilon_{33}^p)^2 + (d\epsilon_{33}^p - d\epsilon_{11}^p)^2 + 6(d\epsilon_{12}^p)^2 + 6(d\epsilon_{31}^p)^2 + 6(d\epsilon_{23}^p)^2 \\
&= (d\lambda)^2\left[(\sigma_{11} - \sigma_{22})^2 + (\sigma_{22} - \sigma_{33})^2 + (\sigma_{33} - \sigma_{11})^2 + 6\sigma_{12}^2 + 6\sigma_{23}^2 + 6\sigma_{31}^2\right]
\end{aligned} \tag{4.66}$$

Now, defining the effective plastic strain increment $d\bar{e}_p$ as:

$$d\bar{e}_p = \sqrt{\tfrac{1}{2}\, de^p_{ij}\, de^p_{ij}}$$

$$\left[\tfrac{1}{6}(d\epsilon^p_{11} - d\epsilon^p_{22})^2 + \tfrac{1}{6}(d\epsilon^p_{22} - d\epsilon^p_{33})^2 + \tfrac{1}{6}(d\epsilon^p_{33} - d\epsilon^p_{11})^2 + (d\epsilon^p_{12})^2 + (d\epsilon^p_{23})^2 + (d\epsilon^p_{31})^2\right]^{1/2} \qquad (4.67a)$$

and recalling that the right-hand side is proportional to the square of the octahedral shear stress τ_{oct}, see Eq. (2.48b), we may rewrite Eq. (4.66) as:

$$d\lambda = \sqrt{\frac{2}{3}}\,\frac{d\bar{e}_p}{\tau_{oct}} \qquad (4.67b)$$

Realizing also that, from Eq. (2.48b), we have:

$$\tau_{oct} = \sqrt{\tfrac{2}{3}}\,J_2$$

Eq. (4.67b) now becomes:

$$d\lambda = \frac{d\bar{e}_p}{\sqrt{J_2}} \qquad (4.68)$$

If the von Mises yield function [Eq. (4.20a)] is employed, we have:

$$\sqrt{J_2} = \frac{1}{\sqrt{3}}\,\sigma_y \qquad (4.69)$$

where σ_y is the yield strength of a material in simple tension. Substititing Eq. (4.69) into Eq. (4.68), we have:

$$d\lambda = \sqrt{3}\,\frac{d\bar{e}_p}{\sigma_y} \qquad (4.70)$$

The Prandtl-Reuss equations utilizing the von Mises yield criterion finally lead to:

$$d\epsilon^p_{ij} = \left[\sqrt{3}\,\frac{d\bar{e}_p}{\sigma_y}\right] s_{ij} \qquad (4.71)$$

It is appropriate now to point out that, if we accept a unifying concept of *normality* (see Sect. 4.3.3.), the Prandtl-Reuss equations will have identical form as the normality condition of the von Mises or J_2 yield function only. In other words, we can derive the flow rules based on the normality condition for yield functions

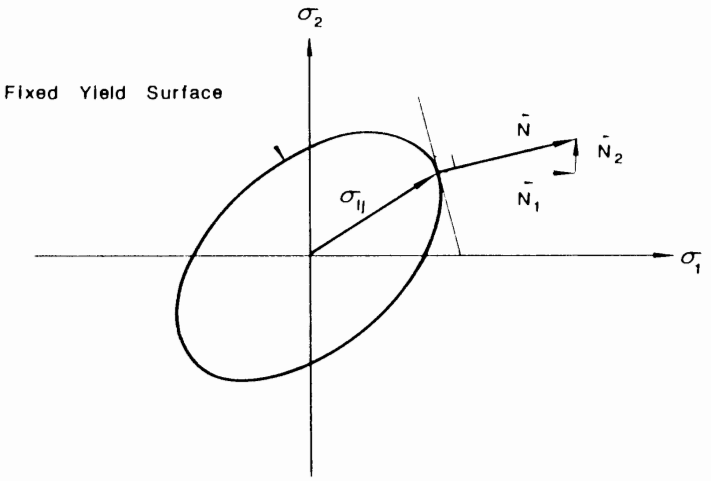

Fig. 4.16. Normality condition of fixed yield surface for perfect plasticity.

other than J_2, but these flow rules will be different from the Prandtl-Reuss equations. A proof can be made as follows:

Loading criterion

First let us define the three types of loading for the J_2 theory as:

(a) Loading $\quad dJ_2 = s_{ij}\, ds_{ij} > 0$ (4.72a)

(b) Neutral Loading $\quad dJ_2 = s_{ij}\, ds_{ij} = 0$ (4.72b)

(c) Unloading $\quad dJ_2 = s_{ij}\, ds_{ij} < 0$ (4.72c)

For a perfectly plastic behavior, the yield surface is fixed and the loading type (a) does not exist. Unloading is possible but should not be concerned since it only involves the elastic strain. Neutral loading is therefore responsible for plastic flow. Referring to Fig. 4.16, the von Mises yield surface for a perfectly-plastic material is drawn in the two-dimensional principal stress space. From Eq. (2.45), we have:

$$J_2 = \tfrac{1}{3}\left(\sigma_1^2 - \sigma_1\sigma_2 + \sigma_2^2\right) \tag{4.73}$$

so that:

$$dJ_2 = \tfrac{2}{3}\left[\left(\sigma_1 - \tfrac{1}{2}\sigma_2\right) d\sigma_1 + \left(\sigma_2 - \tfrac{1}{2}\sigma_1\right) d\sigma_2\right] \tag{4.74}$$

The condition of neutral loading where $dJ_2 = 0$ results in:

$$\frac{d\sigma_2}{d\sigma_1} = -\frac{\sigma_1 - \tfrac{1}{2}\sigma_2}{\sigma_2 - \tfrac{1}{2}\sigma_1} \tag{4.75}$$

Normality condition

From Fig. 4.16, if the horizontal and vertical components of the vector $\dot{N}$ (the outward normal to the ellipse) are designated by N_1 and N_2, the slope of the normal is simply N_2/N_1. The normal and the tangent are two mutually perpendicular lines, therefore, the product of their slopes must be -1, that is:

$$\frac{N_2}{N_1}\frac{\mathrm{d}\sigma_2}{\mathrm{d}\sigma_1} = -1 \tag{4.76}$$

or

$$\frac{N_2}{N_1} = -\frac{\mathrm{d}\sigma_1}{\mathrm{d}\sigma_2} = \frac{\sigma_2 - \frac{1}{2}\sigma_1}{\sigma_1 - \frac{1}{2}\sigma_2} = \frac{s_2}{s_1} = \frac{\mathrm{d}\epsilon_2^{\mathrm{p}}}{\mathrm{d}\epsilon_1^{\mathrm{p}}} \tag{4.77}$$

Equation (4.77) states that the increment of plastic strain is represented to an arbitrary scale by a vector that is normal to the curve of constant J_2. Equation (4.77) is in fact identical to the Prandtl-Reuss equations.

In conclusion, we derive a flow rule from the normality concept for any yield function. However, if we select J_2 or the von Mises yield function, the normality condition and the Prandtl-Reuss equations will have an identical form.

The Prandtl-Reuss equations give us the plastic strain increment which once integrated along the entire loading path will result in the total plastic strain. In the meantime, the elastic strain can be computed using the elastic stress-strain relations in Chapter 3, in particular, Eq. (3.98) or Eq. (3.123). In some plasticity problems, the plastic strain is large and the elastic strain becomes negligible so that the assumption of a rigid-plastic behavior is adequate. As such, the plastic strain increment $\mathrm{d}\epsilon_{ij}^{\mathrm{p}}$ is equal to the total strain $\mathrm{d}\epsilon_{ij}$ since $\mathrm{d}\epsilon_{ij}^{\mathrm{e}} = 0$. The Prandtl-Reuss equations of Eq. (4.62) now become:

$$\mathrm{d}\epsilon_{ij} = \mathrm{d}\lambda s_{ij} \tag{4.78}$$

Equation (4.78) is often known as the *Levy-Mises equation*.

Stress-strain relations

The incremental stress-strain relation of Hooke's law can be written as:

$$\mathrm{d}\sigma_{ij} = C_{ijkl}\,\mathrm{d}\epsilon_{kl}^{\mathrm{e}} \tag{4.79}$$

where C_{ijkl} is the isotropic elastic response function and $\mathrm{d}\epsilon_{kl}^{\mathrm{e}}$ is an increment of elastic strain.

Using Eq. (4.6), Eq. (4.79) can be represented by:

$$\mathrm{d}\sigma_{ij} = C_{ijkl}(\mathrm{d}\epsilon_{kl} - \mathrm{d}\epsilon_{kl}^{\mathrm{p}}) \tag{4.80}$$

Substituting $C_{ijkl} = \lambda\delta_{ij}\delta_{kl} + \mu(\delta_{ik}\delta_{jl} + \delta_{il}\delta_{jk})$ where λ and μ are the Lamé's material constants and the Prandtl-Reuss equation (4.62) into Eq. (4.80), we find:

$$d\sigma_{ij} = \lambda\, d\epsilon_{kk}\delta_{ij} + 2\mu\, d\epsilon_{ij} - 2\, d\lambda\, \mu s_{ij} \tag{4.81}$$

where proportionality factor $d\lambda$ given in Eq. (4.67b) is changed to the form consisting of the deviatoric strain increments de_{ij}. Taking the square of the proportionality factor $d\lambda$ in Eq. (4.67b), and substituting $(\tau_{oct})^2 = \frac{2}{3}J_2$, and $(de_p)^2 = \frac{1}{2}de_{ij}^p de_{ij}^p$, we find:

$$(d\lambda)^2 = de_{ij}^p\, de_{ij}^p/2J_2 \tag{4.82}$$

Using the relation $de_{ij}^p = d\lambda s_{ij}$, $d\lambda$ can be rewritten as:

$$d\lambda = s_{ij}\, de_{ij}^p/2J_2 \tag{4.83a}$$

or

$$d\lambda = s_{ij}\, de_{ij}/2J_2 \tag{4.83b}$$

since

$$s_{ij}\, de_{ij} = s_{ij}(de_{ij}^e + de_{ij}^p) = s_{ij}\frac{1}{2G}ds_{ij} + s_{ij}\, de_{ij}^p = s_{ij}\, de_{ij}^p \tag{4.84}$$

where the quantity $s_{ij}ds_{ij}$ is the increment of the second invariant of the deviatoric stress tensor and is zero for the perfectly plastic Prandtl-Reuss material associated with the J_2-theory. Substituting Eq. (4.83b) into Eq. (4.81), the Prandtl-Reuss stress-strain relations can be written as:

$$d\sigma_{ij} = \lambda\, d\epsilon_{kk}\delta_{ij} + 2\mu\, d\epsilon_{ij} - (\mu s_{mn}\, de_{mn}/J_2)s_{ij} \tag{4.85a}$$

or by replacing Lamé's constants λ and μ with G and K:

$$d\sigma_{ij} = 2G\, de_{ij} + K\, d\epsilon_{kk}\delta_{ij} - (Gs_{mn}\, de_{mn}/J_2)s_{ij} \tag{4.85b}$$

Example 4.4: Examine the behavior of the Prandtl-Reuss material under condition of uniaxial strain.

Solution: Under the uniaxial strain condition, the principal strain, principal deviatoric strain increments, and principal stresses are given as:

$$d\epsilon_i = [d\epsilon_1 \quad 0 \quad 0] \tag{4.86a}$$

$$de_i = \tfrac{1}{3}d\epsilon_1[2 \quad -1 \quad -1] \tag{4.86b}$$

$$\sigma_i = [\sigma_1 \quad \sigma_2 \quad \sigma_3] \tag{4.86c}$$

In the elastic range the behavior of the material is governed by the incremental Hooke's law, that is:

$$d\sigma_1 = \left(K + \tfrac{4}{3}G\right) d\epsilon_1 = M\, d\epsilon_1 = \left[(3K + 4G)/9K\right] dI_1 \tag{4.87a}$$

$$d\sigma_1 - d\sigma_2 = d\sigma_1 - d\sigma_3 = 2G\, d\epsilon_1 = (2G/3K)\, dI_1 \tag{4.87b}$$

where $M = K + \frac{4}{3}G$ is known as the *constrained modulus*.
For a virgin loading in the elastic range, Eq. (4.87) governs the behavior of the material. It should be noted that if the initial states of stress and strain are free, for a virgin loading, Eq. (4.87) can be used in terms of the total rather than the incremental quantities. In the uniaxial-tension strain test, the von Mises yield criterion has the simple form:

$$\sqrt{J_2} = \frac{1}{\sqrt{3}}(\sigma_1 - \sigma_2) \tag{4.88}$$

Thus, the material will yield when:

$$\frac{1}{\sqrt{3}}(\sigma_1 - \sigma_2) = k \tag{4.89}$$

where k is the yield stress in pure shear.
From Eqs. (4.87) and (4.89), the value of vertical stress σ_1 at yield becomes:

$$\sigma_1 = \frac{\sqrt{3}\,(3K + 4G)}{6G} k = \frac{\sqrt{3}\,M}{2G} k \tag{4.90}$$

Thus, when σ_1 reaches the value given by Eq. (4.90), the material yields and further application of vertical stress causes the material to move along the fixed yield surface, undergoing plastic as well as elastic strains. In the plastic range, the deviatoric stress increment ds_1 is given from Eq. (4.85b):

$$ds_1 = 2G\, de_1 - (Gs_{mn}\, de_{mn}/J_2)s_1 \tag{4.91}$$

The rate of work $s_{mn}de_{mn}$ in Eq. (4.91) reduces to:

$$s_{mn}\, de_{mn} = s_1\, de_1 + 2s_2\, de_2 \tag{4.92}$$

Utilizing the fact that $s_{ii} = de_{ii} = 0$, Eq. (4.92) reduces to:

$$s_{mn}\, de_{mn} = \tfrac{3}{2}s_1\, de_1 \tag{4.93}$$

From Eq. (4.93) and $de_1 = \frac{2}{3}d\epsilon_1$, Eq. (4.91) becomes:

$$ds_1 = \tfrac{1}{3}G\, d\epsilon_1 - \left(Gs_1^2/J_2\right) de_1 \tag{4.94}$$

In the plastic range, $J_2 = \frac{1}{4}s_1^2$ and Eq. (4.94) reduces to:

$$ds_1 = 0 \tag{4.95}$$

Since $ds_{11} = 0$, Eq. (4.95) indicates that $ds_2 = ds_3 = 0$, and the stress changes beyond the initial yield are of purely hydrostatic pressure type:

$$d\sigma_1 = ds_1 + \tfrac{1}{3}dI_1 = \tfrac{1}{3}dI_1 \tag{4.96a}$$

$$d\sigma_2 = ds_2 + \tfrac{1}{3}dI_1 = \tfrac{1}{3}dI_1 \tag{4.96b}$$

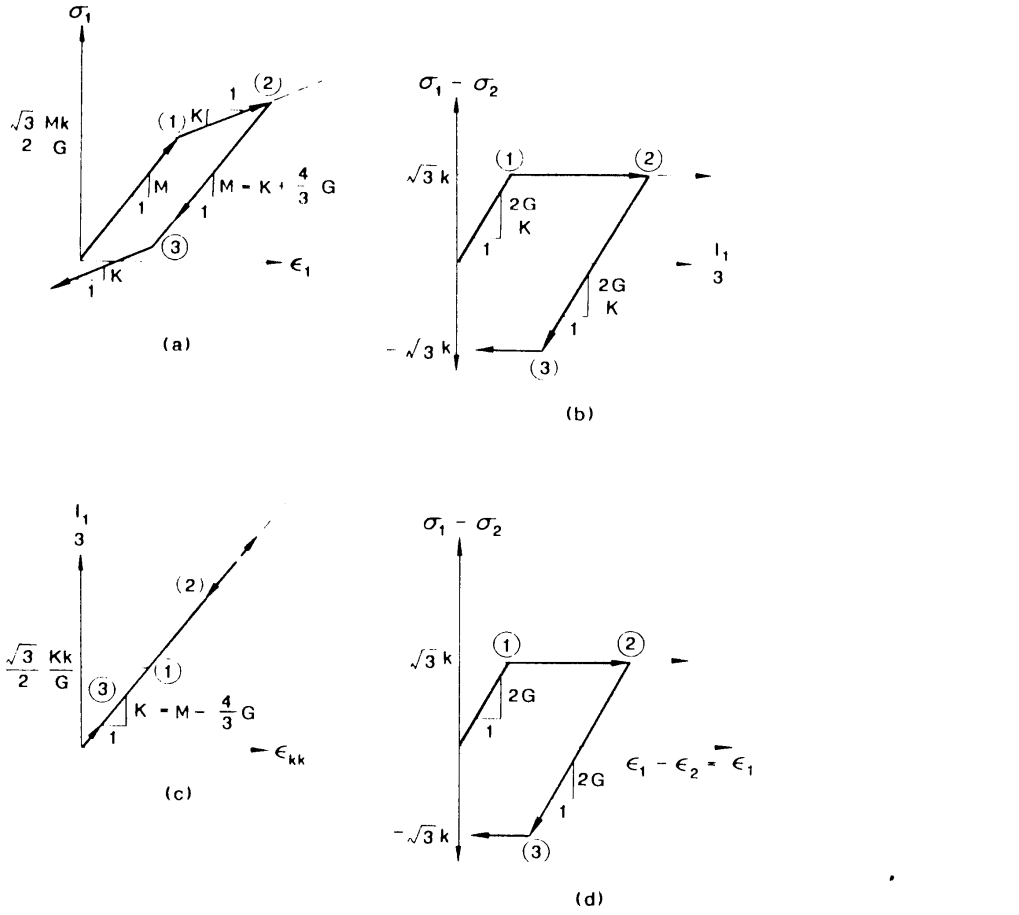

Fig. 4.17 Behavior of Prandtl-Reuss material under the condition of uniaxial strain: (a) vertical stress–strain relation, (b) principal stress difference–hydrostatic pressure relation; (c) hydrostatic pressure–volumetric strain relation; and (d) principal stress difference–strain difference relation

Equation (4.96) indicates that the Prandtl-Reuss material behaves as though it were a fluid once it has reached its limiting shear resistance. From Eqs. (4.85b) and (4.86a), it follows that:

$$\tfrac{1}{3}\mathrm{d}I_1 = K\,\mathrm{d}\epsilon_1 \tag{4.97}$$

Substituting Eq. (4.97) into Eq. (4.96a), the vertical stress-strain increment relation in the plastic range becomes:

$$\mathrm{d}\sigma_1 = K\,\mathrm{d}\epsilon_1 \tag{4.98}$$

Figure 4.17 depicts schematically the behavior of a uniaxial strain test for the Prandtl-Reuss material. The loading slope of the σ_1 versus ϵ_1 curve (Fig. 4.17a) breakes, or softens, when yielding occurs and becomes equal to the bulk modulus. Accordingly, the loading slopes of the principal stress difference-hydrostatic pressure curve (Fig. 4.17b) and the principal stress difference-strain difference curve (Fig. 4.17d) become zero. Since $\mathrm{d}\epsilon^{\mathrm{p}}_{kk} = 0$, the slope of the hydrostatic pressure-volumetric strain curve remains constant (Fig. 4.17c). Once the material unloads, it follows the linear elastic relations until it reaches the yield surface again on the opposite side of the yield surface, corresponding to:

$$\frac{1}{\sqrt{3}}(\sigma_1 - \sigma_2) = k \tag{4.99}$$

and then the material flows plastically again, according to Eq. (4.85b). This unloading behavior is also shown in Fig. 4.17.

Example 4.5: Examine the behavior of the Prandtl-Reuss material under the plane stress condition defined by $\sigma_i = [\sigma_1\ 0\ \sigma_3]$.

Solution: From this stress state, the Prandtl-Reuss material will yield when:

$$J_2 = \tfrac{1}{3}\left(\sigma_1^2 + \sigma_3^2 - \sigma_1\sigma_3\right) = k^2 \tag{4.100}$$

Equation (4.100) exhibits an ellipse in the $\sigma_1 - \sigma_3$ stress space (Fig. 4.18). We now consider a biaxial compresson-compression test where for example, the lateral stress σ_3 is held constant at the $-k$ value (k is a positive value) while the vertical stress σ_1 is increased to the compressive direction from Point A to B. Before reaching the yield Point B, the behavior of the material is linearly elastic. Substituting $\mathrm{d}\sigma_2 = \mathrm{d}\sigma_3 = 0$ into the incremental Hooke's law, we find the following relations:

$$\mathrm{d}\sigma_1 = \left[9KG/(3K + G)\right]\mathrm{d}\epsilon_1 = E\,\mathrm{d}\epsilon_1 \tag{4.101a}$$

$$\mathrm{d}\epsilon_3 = -\left[(3K - 2G)/(6K + 2G)\right]\mathrm{d}\epsilon_1 = -\nu\,\mathrm{d}\epsilon_1 \tag{4.101b}$$

$$\mathrm{d}\epsilon_2 = \mathrm{d}\epsilon_3 \tag{4.101c}$$

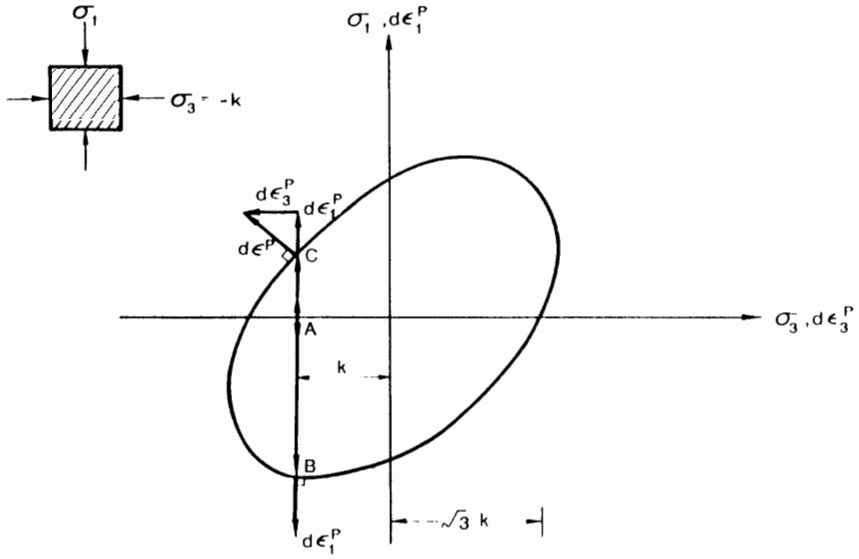

Fig. 4.18 Von Mises yield curve for a special plane stress condition.

At Point B, the material yields, and unlimited plastic deformation takes place at $\sigma_1 = -2k$; the corresponding components of plastic strain increments are respectively:

$$d\epsilon_1^p = d\lambda s_1 = d\lambda\left[\sigma_1 - \tfrac{1}{3}(\sigma_1 + \sigma_3)\right] = d\lambda\left[-2k - \tfrac{1}{3}(-2k - k)\right] = -d\lambda k \qquad (4.102a)$$

$$d\epsilon_2^p = d\lambda s_2 = d\lambda\left[\sigma_2 - \tfrac{1}{3}(\sigma_1 + \sigma_3)\right] = d\lambda\left[0 - \tfrac{1}{3}(-2k - k)\right] = d\lambda k \qquad (4.102b)$$

$$d\epsilon_3^p = d\lambda s_3 = d\lambda\left[\sigma_3 - \tfrac{1}{3}(\sigma_1 + \sigma_3)\right] = d\lambda\left[-k - \tfrac{1}{3}(-2k - k)\right] = 0 \qquad (4.102c)$$

If we repeat the same test and change the direction of σ_1 to the tension side (a biaxial tension-compression test), we find that the material yields when $\sigma_1 = k$, Point C in Fig. 4.18. At Point C the unlimited plastic flow has the value:

$$d\epsilon_1^p = d\lambda s_1 = d\lambda\sigma_1 = d\lambda k \qquad (4.103a)$$

$$d\epsilon_2^p = d\lambda s_2 = d\lambda\sigma_2 = 0 \qquad (4.103b)$$

$$d\epsilon_3^p = d\lambda s_3 = d\lambda\sigma_3 = -d\lambda k \qquad (4.103c)$$

If the plastic strain increment coordinates are superimposed on the stress coordinates, as shown in Fig. 4.18, the concept of normality or associated flow rule can be demonstrated clearly from this simple example. In the biaxial compression test $d\epsilon_3^p = 0$, and the plastic strain increment vector $d\epsilon_1^p$ is perpendicular to the yield

surface at Point B. In the biaxial tension-compression test, on the other hand, $d\epsilon_1^p = -d\epsilon_3^p$, indicating that the plastic strain increment vector is perpendicular to the yield surface at Point C.

4.9 GENERALIZED STRESS-STRAIN RELATIONS

In the previous Section, the Prandtl-Reuss stress-strain relations have been derived from the condition that the principal axes of plastic strain increments are identical with those of the current deviatoric stresses. In this Section, from the *associated flow rule assumption (normality condition)*, $d\epsilon_{ij}^p = d\lambda(\partial f/\partial\sigma_{ij})$, we will derive the general stress-strain relations for an ideal plastic material whose yield function f (or yield surface) is fixed in the principal stress space, i.e., it does not move or expand during plastic deformation. The yield surface treated in the development of the incremental stress-strain relations is only a function of stress tensor, or function of invariants of stress tensor for an isotropic material.

Substituting the incremental Hooke's law and the flow rule equations into Eq. (4.6), the complete strain-stress relations for an elastic-perfectly plastic material can be represented as:

$$d\epsilon_{ij} = d\epsilon_{ij}^e + d\epsilon_{ij}^p = \frac{dI_1}{9K}\delta_{ij} + \frac{ds_{ij}}{2G} + d\lambda\frac{\partial f}{\partial\sigma_{ij}} \tag{4.104}$$

where $d\lambda$ is an as yet undetermined proportionality factor with the value:

$$d\lambda = 0 \text{ wherever } f < f_c \quad \text{or } f = f_c \quad \text{but } df < 0 \tag{4.105a}$$

$$d\lambda > 0 \text{ wherever } f = f_c \quad \text{and } df = 0 \tag{4.105b}$$

We shall determine the form of the factor $d\lambda$ below. This can be accomplished by combining the strain-stress relations (4.104) with the *consistency condition*:

$$df = \frac{\partial f}{\partial\sigma_{ij}}d\sigma_{ij} = 0 \tag{4.106}$$

which assures that the new stress state $(\sigma_{ij} + d\sigma_{ij})$ after the incremental change $d\sigma_{ij}$ still satisfies the yield criterion:

$$f(\sigma_{ij} + d\sigma_{ij}) = f(\sigma_{ij}) + df = f(\sigma_{ij}) \tag{4.107}$$

Solving Eq. (4.104) for ds_{ij}, we can determine the stress increment tensor

$$d\sigma_{ij} = ds_{ij} + \tfrac{1}{3}dI_1\delta_{ij} = 2G\,d\epsilon_{ij} - 2G\,d\lambda\frac{\partial f}{\partial\sigma_{ij}} + \left(\frac{1}{3} - \frac{2G}{9K}\right)dI_1\,\delta_{ij} \tag{4.108}$$

Substituting Eq. (4.108) into the consistency condition (4.106), we have:

$$2G\frac{\partial f}{\partial \sigma_{ij}}\,d\epsilon_{ij} - 2G\,d\lambda\frac{\partial f}{\partial \sigma_{ij}}\frac{\partial f}{\partial \sigma_{ij}} + \left(\frac{1}{3} - \frac{2G}{9K}\right)dI_1\frac{\partial f}{\partial \sigma_{ij}}\delta_{ij} = 0 \tag{4.109}$$

To eliminate dI_1 from Eq. (4.109), we use Eq. (4.104) with $i = j$:

$$dI_1 = 3K\left(d\epsilon_{kk} - d\lambda\frac{\partial f}{\partial \sigma_{ij}}\delta_{ij}\right) \tag{4.110}$$

Substituting Eq. (4.110) into Eq. (4.109), the proportionality factor $d\lambda$ can now be obtained as:

$$d\lambda = \frac{\dfrac{\partial f}{\partial \sigma_{ij}}\,d\epsilon_{ij} + \dfrac{3K - 2G}{6G}\,d\epsilon_{kk}\dfrac{\partial f}{\partial \sigma_{ij}}\delta_{ij}}{\dfrac{\partial f}{\partial \sigma_{mn}}\dfrac{\partial f}{\partial \sigma_{mn}} + \dfrac{3K - 2G}{6G}\left(\dfrac{\partial f}{\partial \sigma_{mn}}\delta_{mn}\right)^2} \tag{4.111}$$

Once the yield function f is substituted for a particular material of interest and total strain increments $d\epsilon_{ij}$ are prescribed, the factor $d\lambda$ can be determined uniquely. When dI_1 in Eq. (4.110) is used, the stress increment $d\sigma_{ij}$ in Eq. (4.108) becomes:

$$d\sigma_{ij} = 2G\,de_{ij} + K\,d\epsilon_{kk}\,\delta_{ij} - d\lambda\left[\left(K - \tfrac{2}{3}G\right)\frac{\partial f}{\partial \sigma_{mm}}\delta_{mm}\delta_{ij} + 2G\frac{\partial f}{\partial \sigma_{ij}}\right] \tag{4.112}$$

Thus, the corresponding stress increments are also determined uniquely by the yield function $f(\sigma_{ij})$ and the strain increments $d\epsilon_{ij}$. In other words, if the current stress state σ_{ij} is known and the increments of strain $d\epsilon_{ij}$ are prescribed, Eq. (4.112) can be used to find the corresponding stress increments $d\sigma_{ij}$. In general, however, if the current stress state is known and the stress increments are prescribed, the corresponding strain increments can not be uniquely determined because the plastic strain increments can be defined only within the indeterminate factor $d\lambda$ [Eq. (4.111)].

For a number of geotechnical materials, particularly soils, the yield functions in perfectly plastic models in Sections 4.5 through 4.7 are generally expressed in terms of the stress invariants I_1, J_2, and J_3 in the form:

$$f(\sigma_{ij}) = f(I_1, J_2, J_3) = f_c \tag{4.113}$$

It follows that:

$$\frac{\partial f}{\partial \sigma_{ij}} = \frac{\partial f}{\partial I_1}\frac{\partial I_1}{\partial \sigma_{ij}} + \frac{\partial f}{\partial J_2}\frac{\partial J_2}{\partial \sigma_{ij}} + \frac{\partial f}{\partial J_3}\frac{\partial J_3}{\partial \sigma_{ij}} \tag{4.114}$$

Since:

$$\frac{\partial I_1}{\partial \sigma_{ij}} = \delta_{ij} \tag{4.115a}$$

$$\frac{\partial J_2}{\partial \sigma_{ij}} = s_{ij} \tag{4.115b}$$

$$\frac{\partial J_3}{\partial \sigma_{ij}} = t_{ij} = s_{ik}s_{kj} - \tfrac{2}{3}J_2\delta_{ij} \tag{4.115c}$$

Equation (4.114) can thus be represented by:

$$\frac{\partial f}{\partial \sigma_{ij}} = \frac{\partial f}{\partial I_1}\delta_{ij} + \frac{\partial f}{\partial J_2}s_{ij} + \frac{\partial f}{\partial J_3}t_{ij} \tag{4.116}$$

Substitution of Eq. (4.116) into Eq. (4.112) results in:

$$d\sigma_{ij} = 2G\,de_{ij} + K\,d\epsilon_{kk}\delta_{ij} - d\lambda\left[3K\frac{\partial f}{\partial I_1}\delta_{ij} + 2G\left(\frac{\partial f}{\partial J_2}s_{ij} + \frac{\partial f}{\partial J_3}t_{ij}\right)\right] \tag{4.117}$$

where $d\lambda$ has the form:

$$d\lambda = \frac{1}{H}\left[3K\frac{\partial f}{\partial I_1}d\epsilon_{kk} + 2G\left(\frac{\partial f}{\partial J_2}s_{kl} + \frac{\partial f}{\partial J_3}t_{kl}\right)d\epsilon_{kl}\right] \tag{4.118a}$$

in which:

$$H = 9K\left(\frac{\partial f}{\partial I_1}\right)^2 + 4GJ_2\left(\frac{\partial f}{\partial J_2}\right)^2 + 12GJ_3\frac{\partial f}{\partial J_2}\frac{\partial f}{\partial J_3} + 2G\left(s_{ik}s_{kj}s_{ij}s_{ji} - \tfrac{4}{3}J_2^2\right)\left(\frac{\partial f}{\partial J_3}\right)^2 \tag{4.118b}$$

In the next Section, we shall derive the stiffness matrices for perfect plasticity models which can be applied directly in a stress-strain subroutine of the existing finite-element programs.

4.10 STIFFNESS FORMULATION

4.10.1 General description

For the direct use in a finite-element displacement formulation, Eq. (4.117) can be written in the preferable tensorial form as:

$$d\sigma_{ij} = C^{ep}_{ijkl}\,d\epsilon_{kl} \tag{4.119a}$$

where C^{ep}_{ijkl} is referred to here as the *elastoplastic stiffness tensor*, that is:

$$C^{ep}_{ijkl} = 2G\delta_{ik}\delta_{jl} + \left(K - \tfrac{2}{3}G\right)\delta_{ij}\delta_{kl} - \frac{1}{H}H_{ij}H_{kl} \tag{4.119b}$$

in which:

$$H = 9KA^2 + 4GJ_2B^2 + 12GJ_3BC + 2G\left(s_{ik}s_{kj}s_{il}s_{lj} - \tfrac{4}{3}J_2^2\right)C^2 \tag{4.119c}$$

$$H_{ij} = 3KA\delta_{ij} + 2G\left(Bs_{ij} + Ct_{ij}\right) \tag{4.119d}$$

$$A = \frac{\partial f}{\partial I_1}, \quad B = \frac{\partial f}{\partial J_2}, \quad \text{and } C = \frac{\partial f}{\partial J_3} \tag{4.119e}$$

Equation (4.119a) can be written in a general three-dimensional matrix form:

$$\begin{Bmatrix} d\sigma_{11} \\ d\sigma_{22} \\ d\sigma_{33} \\ d\sigma_{12} \\ d\sigma_{23} \\ d\sigma_{31} \end{Bmatrix} = \begin{bmatrix} K+\frac{4}{3}G & K-\frac{2}{3}G & K-\frac{2}{3}G & 0 & 0 & 0 \\ K-\frac{2}{3}G & K+\frac{4}{3}G & K-\frac{2}{3}G & 0 & 0 & 0 \\ K-\frac{2}{3}G & K-\frac{2}{3}G & K+\frac{4}{3}G & 0 & 0 & 0 \\ 0 & 0 & 0 & G & 0 & 0 \\ 0 & 0 & 0 & 0 & G & 0 \\ 0 & 0 & 0 & 0 & 0 & G \end{bmatrix} \begin{Bmatrix} d\epsilon_{11} \\ d\epsilon_{22} \\ d\epsilon_{33} \\ d\gamma_{12} \\ d\gamma_{23} \\ d\gamma_{31} \end{Bmatrix}$$

$$- \frac{1}{H} \begin{bmatrix} H_{11}^2 & H_{11}H_{22} & H_{11}H_{33} & H_{11}H_{12} & H_{11}H_{23} & H_{11}H_{31} \\ H_{22}H_{11} & H_{22}^2 & H_{22}H_{33} & H_{22}H_{12} & H_{22}H_{23} & H_{22}H_{31} \\ H_{33}H_{11} & H_{33}H_{22} & H_{33}^2 & H_{33}H_{12} & H_{33}H_{23} & H_{33}H_{31} \\ H_{12}H_{11} & H_{12}H_{22} & H_{12}H_{33} & H_{12}^2 & H_{12}H_{23} & H_{12}H_{31} \\ H_{23}H_{11} & H_{23}H_{22} & H_{23}H_{33} & H_{23}H_{12} & H_{23}^2 & H_{23}H_{31} \\ H_{31}H_{11} & H_{31}H_{22} & H_{31}H_{33} & H_{31}H_{12} & H_{31}H_{23} & H_{31}^2 \end{bmatrix} \begin{Bmatrix} d\epsilon_{11} \\ d\epsilon_{22} \\ d\epsilon_{33} \\ d\gamma_{12} \\ d\gamma_{23} \\ d\gamma_{31} \end{Bmatrix} \tag{4.120}$$

4.10.2 Stiffness coefficients

The forms for A, B, and C in the stiffness matrix are derived in the forthcoming for the material models of Tresca, von Mises, Coulomb, and Drucker-Prager, under the associated flow rule assumption.

(A) Tresca model

The stress invariant form of the Tresca model can be rewritten as:

$$f = f_s = 4J_1^3 - 27J_3^2 - 36k^2J_2^2 + 96k^4J_2 - 64k^6 = 0 \tag{4.121}$$

By taking derivatives of Eq. (4.121) with respect to I_1, J_2, and J_3, we obtain:

$$A = \frac{\partial f}{\partial I_1} = 0 \tag{4.122a}$$

$$B = \frac{\partial f}{\partial J_2} = 12J_2^2 - 72k^2J_2 + 96k^4 \tag{4.122b}$$

$$C = \frac{\partial f}{\partial J_3} = -54J_3 \tag{4.122c}$$

(B) von Mises model

The von Mises model is given by:

$$f = f_s = \sqrt{J_2} - k = 0 \tag{4.123}$$

In a similar way, we can obtain the stiffness coefficients such as:

$$A = \frac{\partial f}{\partial I_1} = 0, \quad B = \frac{\partial f}{\partial J_2} = \frac{1}{2\sqrt{J_2}}, \quad \text{and} \quad C = \frac{\partial f}{\partial J_3} = 0 \tag{4.124}$$

The stress-strain relations are identical with those derived from the Prandtl-Reuss equation.

(C) Coulomb model

The Coulomb model in terms of stress invariants is given by:

$$f = f_s = I_1 \sin\phi + \frac{1}{2}\left[3(1 - \sin\phi)\sin\theta + \sqrt{3}\,(3 + \sin\phi)\cos\theta\right]\sqrt{J_2} - 3c\cos\phi = 0 \tag{4.125}$$

where

$$\theta = \frac{1}{3}\cos^{-1}\left(\frac{3\sqrt{3}}{2}\frac{J_3}{J_2^{3/2}}\right)$$

Differentiating Eq. (4.125) with respect to I_1, J_2, and J_3, we find:

$$A = \frac{\partial f}{\partial I_1} = \sin\phi \tag{4.126a}$$

$$B = \frac{\partial f}{\partial J_2} = \frac{1}{4}\left[3(1 - \sin\phi)\sin\theta + \sqrt{3}(3 + \sin\phi)\cos\theta\right]\frac{1}{\sqrt{J_2}}$$

$$+ 3\sqrt{3}J_3\left[3(1 - \sin\phi)\cos\theta - \sqrt{3}(3 + \sin\phi)\sin\theta\right]/(8J_2^2\sin 3\theta) \tag{4.126b}$$

$$C = \frac{\partial f}{\partial J_3} = -\sqrt{3}\left[3(1 - \sin\phi)\cos\theta - \sqrt{3}(3 + \sin\phi)\sin\theta\right]/(4J_2\sin 3\theta) \tag{4.126c}$$

If ϕ is set equal to zero, then, stiffness coefficients become those for the Tresca model.

(D) Drucker-Prager model

The equation is written again as:

$$f - f_c = \alpha I_1 + \sqrt{J_2} - k = 0 \tag{4.127}$$

Therefore, in a similar manner to the previous cases, the stiffness coefficients are:

$$A = \alpha, \quad B = \frac{1}{2\sqrt{J_2}} \quad \text{and} \quad C = 0 \tag{4.128}$$

If α is set equal to zero, the coefficients become the same as those for the von Mises model.

Example 4.6: Write explicitly the plane strain constitutive matrix for the Drucker-Prager material.

Solution: For the plane strain case ($\gamma_{23} = \gamma_{31} = \epsilon_{33} = 0$), the matrix form of Eq. (4.120) can be reduced to:

$$\begin{Bmatrix} d\sigma_{11} \\ d\sigma_{22} \\ d\sigma_{12} \\ d\sigma_{33} \end{Bmatrix} = [C^{ep}] \begin{Bmatrix} d\epsilon_{11} \\ d\epsilon_{22} \\ d\gamma_{12} \end{Bmatrix} \tag{4.129}$$

where the x_3-axis is normal to the plane. Using $A = \alpha$, $B = 1/(2\sqrt{J_2})$, and $C = 0$, the components of matrix $[C^{ep}]$ can be expressed as:

$$[C^{ep}] = \begin{bmatrix} K + \frac{4}{3}G & K - \frac{2}{3}G & 0 \\ K - \frac{2}{3}G & K + \frac{4}{3}G & 0 \\ 0 & 0 & G \\ K - \frac{2}{3}G & K - \frac{2}{3}G & 0 \end{bmatrix} - \frac{1}{H} \begin{bmatrix} H_{11}^2 & H_{11}H_{22} & H_{11}H_{12} \\ H_{22}H_{11} & H_{22}^2 & H_{22}H_{12} \\ H_{12}H_{11} & H_{12}H_{22} & H_{12}^2 \\ H_{33}H_{11} & H_{33}H_{22} & H_{33}H_{12} \end{bmatrix} \tag{4.130}$$

and

$$H = 9K\alpha^2 + G \tag{4.131a}$$

$$H_{11} = 3K\alpha + \frac{G}{\sqrt{J_2}} s_{11} \tag{4.131b}$$

$$H_{22} = 3K\alpha + \frac{G}{\sqrt{J_2}} s_{22} \tag{4.131c}$$

$$H_{12} = \frac{G}{\sqrt{J_2}} s_{12} = \frac{G}{\sqrt{J_2}} \sigma_{12} \tag{4.131d}$$

$$H_{33} = 3K\alpha + \frac{G}{\sqrt{J_2}} s_{33} \tag{4.131e}$$

Example 4.7: Examine the behavior of the Drucker-Prager material under an uniaxial state of strain test such as:

$$d\epsilon_1 = [d\epsilon_1 \quad 0 \quad 0] \tag{4.132a}$$

$$d\epsilon_1 = \frac{1}{3} d\epsilon_1 [2 \quad 1 \quad 1] \tag{4.132b}$$

$$d\sigma_1 = [d\sigma_1 \quad d\sigma_2 \quad d\sigma_2] \tag{4.132c}$$

Solution: The elastic behavior of the material is governed by:

$$d\sigma_1 = \left(K + \frac{4}{3}G\right) d\epsilon_1 - M\, d\epsilon_1 = \frac{3K + 4G}{9K} dI_1 \tag{4.133a}$$

and

$$d\sigma_1 = d\sigma_2 = 2G\, d\epsilon_1 = \frac{2G}{3K} dI_1 \tag{4.133b}$$

The Drucker-Prager material yields when:

$$\frac{1}{\sqrt{3}} |\sigma_1 - \sigma_2| + \alpha(\sigma_1 + 2\sigma_2) = k \tag{4.134}$$

since $\sigma_2 = \sigma_3$.

From Eqs. (4.133) and (4.134), we find the values of vertical principal stress σ_1 at yield:

$$\sigma_1 = \frac{\sqrt{3}\,(3K + 4G)k}{\pm 6G + 9\sqrt{3}\,K\alpha} = \frac{\sqrt{3}\,Mk}{\pm 2G + 3\sqrt{3}\,K\alpha} \tag{4.135}$$

When α is equal to zero, Eq. (4.135) reduces to Eq. (4.90), corresponding to the Prandtl-Reuss material. The effect of α in this case is to decrease the value of the vertical stress σ_1 at yield for uniaxial tension test (upper sign) and to increase the value σ_1 at yield for uniaxial compression test (lower sign). Further increase of the vertical stress σ_1 results in the stress state in the material moving along the yield surface undergoing both elastic and plastic deformation. The incremental elastic-plastic stress-strain relation is obtained from previous discussion of generalized constitutive relations (4.117), that is:

$$d\sigma_{ij} = 2G\,de_{ij} + K\,d\epsilon_{kk}\delta_{ij} - d\lambda\left(\frac{G}{\sqrt{J_2}}s_{ij} + 3K\alpha\delta_{ij}\right) \tag{4.136}$$

where

$$d\lambda = \frac{\left(G/\sqrt{J_2}\right)s_{mn}\,de_{mn} + 3K\alpha\,d\epsilon_{kk}}{G + 9K\alpha^2} \tag{4.137}$$

Thus, the relation between the vertical stress increment and vertical strain increment is written as:

$$d\sigma_1 = \left(K + \tfrac{4}{3}G\right)d\epsilon_1 - \frac{\left\{\left[2\sqrt{3}/3\right]G \pm 3K\alpha\right\}^2}{9K\alpha^2 + G}\,d\epsilon_1 \tag{4.138}$$

Again, it is noted that when α is set equal to zero, Eq. (4.138) reduces to the corresponding equation (4.98) for the Prandtl-Reuss material.

The stress-strain relation in uniaxial strain-compression test is shown in Fig. 4.19 for both the Prandtl-Reuss and Drucker-Prager Materials. For the Prandtl-Reuss material (Fig. 4.19a), the curve is elastic until the yield condition is reached at a stress proportional to k. In the plastic region, the slope is simply the bulk modulus K. Unloading is elastic until the opposite side of the yield surface is reached and

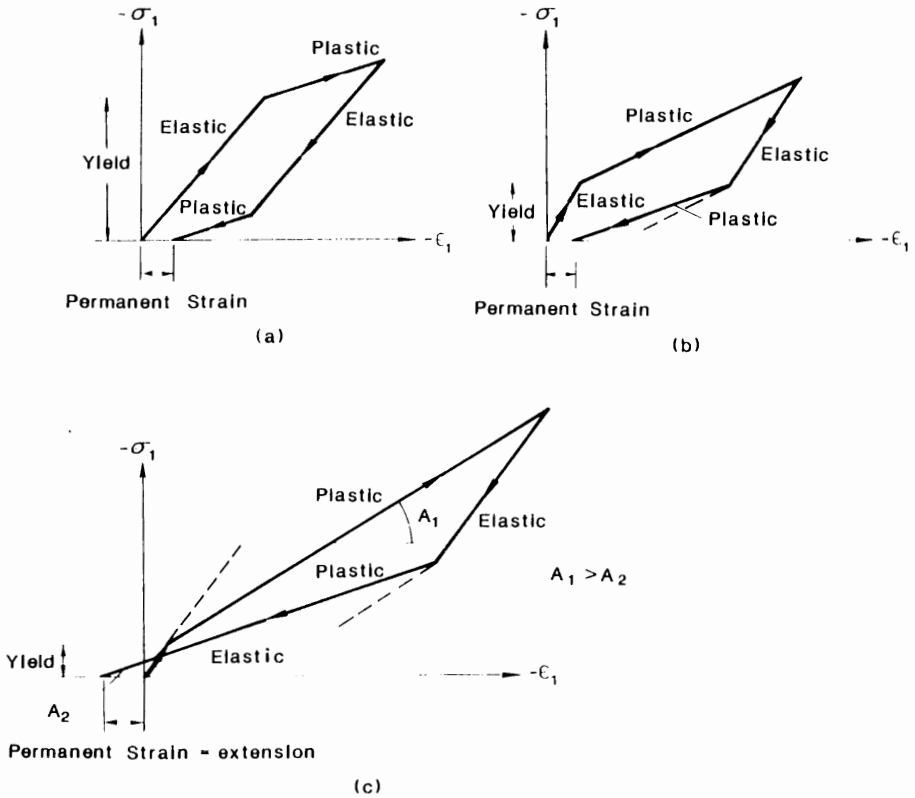

Fig. 4.19. Behavior of the Prandtl-Reuss and Drucker-Prager materials under the condition of uniaxial strain: (a) Prandtl-Reuss relations; (b) Drucker-Prager in stress small; (c) Drucker-Prager in stress large.

then plastic again with the slope K. At the completion of the stress cycle, a permanent strain remains.

For the case of the Drucker-Prager material when loaded not too far beyond the elastic range, it is similar (Fig. 4.19b). Here, the plastic slope as given by the form:

$$\frac{d\sigma_1}{d\epsilon_1} = K\frac{(1 + 2\sqrt{3}\,\alpha)^2}{1 + 9\alpha^2 K/G} \tag{4.139}$$

is larger than K in compression loading (upper sign) and smaller in unloading (lower sign). The permanent strain at the end of a load-unload cycle is still in compression. However, when this material is loaded far away beyond the elastic range (Fig. 4.19c), the permanent strain becomes an extension.

From Eqs. (4.110), (4.137) and (4.138), the incremental relation between the hydrostatic pressure and the compressive volumetric strain for uniaxial strain test is

obtained:

$$dI_1 = \frac{9K\alpha\left\{\left[(2\sqrt{3})/3\right]G - 3K\alpha\right\}}{G + 9K\alpha^2} d\epsilon_{kk} + 3K\, d\epsilon_{kk} \tag{4.140}$$

When α is set equal to zero, Eq. (4.140) reduces to the corresponding expression for the Prandtl-Reuss material. The increment of the plastic volumetric strain becomes:

$$d\epsilon^p_{kk} = \frac{\alpha(-2\sqrt{3}G + 9K\alpha)}{3KG(1 + 2\sqrt{3}\alpha)} dI_1 \tag{4.141}$$

For the uniaxial stran-stress path to reach the yield surface in the compression test, the following condition must hold from Eq. (4.135):

$$\frac{2G}{\sqrt{3}K} > 3\alpha \tag{4.142}$$

Therefore, as expected, the incremental plastic volumetric stran is positive (expansion).

4.11 SUMMARY

In developing suitable stress-strain relations for plastic materials, two basic approaches have been discussed in the first part of this Chapter. The first is the so-called *deformation* or *total-stran* type. Deformation theory of plasticity postulates that for *work-hardening material* (to be discussed in Chapter 5) the state of stress determines the state of stran uniquely as long as plastic deformation continues. This theory is identical with nonlinear elastic stress-strain relations in Chapter 3, as unloading does not occur. For example, if material isotropy is assumed, the most general form of the deformation theory can be written as:

$$\epsilon^p_{ij} = P(I_1, J_2, J_3)\delta_{ij} + Q(I_1, J_2, J_3)s_{ij} + R(I_1, J_2, J_3)t_{ij}$$

where ϵ^p_{ij} is the plastic strain component given by $(\epsilon_{ij} - \epsilon^e_{ij})$; the elastic component is assumed to be given by Hooke's law. Such a formulation can be used for general stress histories only when the criterion of loading or further plastic deformation, $f(I_1, J_2, J_3)$, is explicitly stated. When its magnitude increases, the plastic strain ϵ^p_{ij} changes in accordance with the plastic stress-strain relation; when it decreases, unloading takes place in accordance with some other relations such as linear or nonlinear elastic stress-strain relations.

In general, it has clearly been demonstrated that, except for certain special cases of loading, for example, when all stress components increase proportionally, deformation theory can not lead to meaningful results and sometimes leads to contradic-

tions. The main limitation is that loading and unloading expressions do not coincide for neutral changes in stress, i.e., for stress changes in which $f(I_1, J_2, J_3)$ remains constant so that there is neither loading nor unloading. This is known as the *condition of continuity*. Basically, the difficulty lies in the fact that the deformation theory and existence of $f(I_1, J_2, J_3)$, even in the most limited sense, are incompatible.

Next type of theory known as the *flow* or the *incremental theory of plasticity* is consistent with the assumption of criterion of loading $f(I_1, J_2, J_3)$ and therefore avoids the difficulty encountered in a deformation theory. This theory relates the *increment* of plastic strain $d\epsilon_{ij}^p$ to the state of stress σ_{ij} and stress increment $d\sigma_{ij}$. The simplest type of flow theory is the *theory of perfect plasticity*.

The basic concept used in the development of stress-strain relations for elastic-perfectly plastic materials postulates that a *yield surface* $f(\sigma_{ij})$ exists which depends only upon the state of stress. Each stress point inside the fixed surface represents an *elastic state* of stress and each point on the yield surface a *plastic state*. The strain in an elastic state is assumed to be given by a generalized Hooke's law. The strain in the plastic state is assumed as the sum of the reversible *elastic strain* and the permanent *plastic strain*. Plastic flow occurs when $f = 0$ and $df = 0$. This is used as the criterion for *loading* for a perfectly plastic material. Thus, $f = 0$ and $df < 0$ indicate *unloading*, and $f < 0$ indicates the elastic state. During loading, both elastic and plastic strain occur. Plastic flow is developed along the exterior normal of the fixed yield surface. This is known as the *normality principle* for the associated flow rule material.

The condition of *uniqueness* for the solution of a boundary value problem and the condition of *irreversibility* of plastic deformation lead to the following two important restrictions on the yield surface and the stress-strain relations:

1. The yield surface in stress space must be *convex*.
2. The plastic strain increment vector $d\epsilon_{ij}^p$ must be *normal* to the yield surface in stress space, that is, $d\epsilon_{ij}^p = d\lambda\, \partial f/\partial \sigma_{ij}$.

Perfect plasticity models such as the Tresca and von Mises criteria for metals are used for determining the collapse or limiting state of a structure. Since the shear strength of soils increases with the effective mean normal stress, it can not be described by these models which depict respectively the hexagonal and circular cylinders in the principal stress space. The only case in which these models may be used is for the total stress analysis of saturated undrained soil of clay type. The Coulomb criterion is certainly the best known failure model for hydrostatic pressure sensitive soils. This criterion is, however, not mathematically convenient in three-dimensional situations due to the existence of corners (singularities). Representative perfect plasticity model of the Drucker-Prager type is the simplest model which approximates the well-known yield or failure criterion such as the Coulomb or the modified Coulomb. For the progressive failure analysis of soil, rock, or concrete, this model may give reasonable results, as long as the particular material constants, α and k, are adequately or reasonably assumed for the particular problems considered.

The Prandtl-Reuss relation for metals assumes that the principal axes of plastic strain increments $d\epsilon^p_{ij}$ are identical with those of the current stresses, that is, $d\epsilon^p_{ij} = d\lambda s_{ij}$. This condition incorporated with the J_2-criterion leads to the *normality condition* that the plastic strain increment is normal to the J_2 yield surface.

Generalized stress-strain relations for perfect plasticity models such as Tresca, von Mises, Coulomb, and Drucker-Prager models are formulated under the assumption of the associated flow rule (normality condition). The incremental stress-strain relations are written as:

$$d\sigma_{ij} = C^{ep}_{ijkl}\, d\epsilon_{ij}$$

where C^{ep}_{ijkl} is a fourth-order constituent tensor which consists of the different stiffness coefficents for different yield functions.

REFERENCES

Chen, W.F., 1975. Limit Analysis and Soil Plasticity. Elsevier, Amsterdam, 638 pp.

Chen, W.F., 1982. Plasticity in Reinforced Concrete. McGraw-Hill, New York, NY, 474 pp.

Chen, W.F. and Mizuno, E., 1979. On material constants for soil and concrete models. Proc. Third ASCE/EMD Specialty Conference Austin, Texas, September 17–19, ASCE Publication, New York, pp. 539–542.

Chen, W.F. and Saleeb, A.F., 1982. Constitutive Equations for Engineering Materials, Vol. 1 – Elasticity and Modeling. John Wiley Interscience, New York, NY, 580 pp.

DiMaggio, F.L. and Sandler, I.S., 1971. Material models for granular soils. J. Eng. Mech. Div. ASCE, 97 (EM3): 935–950.

Drucker, D.C., 1966. Concept of path independence and material stability for soils. In: J. Kravtchenko and P.M. Sirieys (Editors), Rheol. Mecan. Soils Proc. IUTAM Sym., Grenoble, Springer, Berlin, pp. 23–43.

Drucker, D.C. and Prager, W., 1952. Soil mechanics and plastic analysis or limit design. Q. Appl. Math. 10 (2): 157–175.

Drucker, D.C., Gibson, R.E. and Henkel, D.J., 1957. Soil mechanics and work-hardening theories of plasticity. Trans., ASCE, 122: 338–346.

Nelson, I. and Baladi, G.Y., 1977. Outrunning ground shock computed with different models. J. Eng. Mech. Div. ASCE, 103 (EM3): 377–393.

Nelson, I. and Baron, M.L., 1971. Application of variable moduli models to soil behavior. Int. J. Solids Struct. 7: 399–417.

Nelson, I., Baron, M.L. and Sandler, I.S., 1971. Mathematical models for geological materials for wave propagation studies. Shock Waves and the Mechanical Properties of Solids. Syracuse University Press, Syracuse, NY.

Shield, R.T., 1955. On Coulomb's law of failure in soils. J. Mech. Phys. Solids, 4 (1): 10–16.

Zienkiewicz, O.C., 1978. The Finite Element Method. McGraw-Hill, New York, NY, 787 pp.

Zienkiewicz, O.C., Humpheson, C. and Lewis, R.W., 1975. Associated and non-associated visco-plasticity and plasticity in soil mechanics. Géotechnique, 25(4): 671–689.

Chapter 5

HARDENING PLASTICITY AND MODELING

5.1 INTRODUCTION

The general techniques mentioned in the preceding Chapter in the discussion of stress-strain relations for an elastic-perfectly plastic material can readily be extended to the material with hardening. The incremental theory of plasticity for hardening materials is based on three fundamental assumptions: (1) the shape of an *initial yield surface*; (2) the evolution of subsequent *loading surfaces (hardening rule)*; and (3) the formulation of an appropriate *flow rule*. The fundamental difference between the theory of perfect plasticity and the theory of hardening plasticity is that the yield surface is now *not* fixed in stress space and a stress state σ_{ij} is permitted to move outside the yield surface. The concept of a yield surface fixed in the stress space for a perfectly plastic material is now generalized to the idea of a *loading surface* for a hardening material. The *hardening rule* is used to define the motion of the yield surface during plastic loading.

There are a number of hardening rules, such as isotropic hardening, kinematic hardening, and mixed hardening (Chen, 1982). Isotropic hardening rule allows for a uniform expansion of the loading surface, while the kinematic hardening rule permits the loading surface to move as a rigid body in stress space. Mixed hardening, on the other hand, which combines both of these types of hardening, permits the loading surface to expand or to contract uniformly and to translate in stress space. It is well known that the models associated with isotropic hardening rule apply mainly to monotonic loading while for cyclic loadings and pronounced Bauschinger effects, the models associated with kinematic hardening rule or mixed hardening rule would be more appropriate.

Nonmetallic materials such as soils exhibit hardening as well as softening effects in the post-failure regime. As the first step to construct a stress-strain model for such a complicated material as soil, it is logical to utilize the classical theories of hardening plasticity as well developed for materials such as metals. It must be noted, however, that any explicit descriptions in phenomenological or mathematical terms are bound to be a drastic idealization of actual behavior of soils and can not be expected to be valid over a wide range of conditions. Thus, when comparing the hardening models with experiments, we should accordingly be satisfied with agreement in trends and not expect agreement in details in general.

The assumptions made concerning the hardening rule introduce the major distinction among various *advanced hardening plasticity models* developed for soils in recent years. These hardening models are directed towards a more realistic

representation of soil behavior. A more comprehensive discussion of the historical development of the modern theory of soil plasticity is given elsewhere (Chen, 1984).

In the present Chapter, the basic concepts of plasticity for hardening materials are reviewed and several plasticity models with more complex hardening rules combining the concepts of kinematic and isotropic hardenings are presented for the description of soils under monotonic and cyclic loading conditions. In the later part of this Chapter, the incremental stress-strain relations concerning isotropic, kinematic, or mixed type of both are derived in some details for their direct applications into numerical stress analysis in geotechnical engineering problems.

5.2 FLOW THEORY

In this Section, the basic assumptions of flow theory for work-hardening materials such as loading function, hardening rule, flow rule, and Drucker's postulate for stable (or hardening) material are discussed in some details.

5.2.1 Loading function

The loading function is the yield function for the deformed material. At any stage of plastic deformation, the loading function can be represented, geometrically, like the yield function in the theory of perfect plasticity, by a surface in a stress space. This surface is called the *subsequent yield surface* or the *loading surface*. Its geometry changes with the plastic flow. In general, the loading function is expressed in terms of the stress state σ_{ij}, the plastic strain ϵ_{ij}^{p}, and the hardening parameter k, that is:

$$f = f(\sigma_{ij}, \epsilon_{ij}^{p}, k) \tag{5.1}$$

As shown in Fig. 5.1, the elastic-plastic behavior occurs if the state of stress intersects the yield surface and attempts to move beyond the present boundary. In this case, the loading condition for the plastic deformation is defined by:

$$f = 0 \quad \text{and} \quad \mathrm{d}f = \frac{\partial f}{\partial \sigma_{ij}} \mathrm{d}\sigma_{ij} > 0 \tag{5.2}$$

In a similar manner to that for the perfectly plastic material, the elastic behavior occurs under the conditions such that:

$$f < 0 \quad \text{or} \quad f = 0 \quad \text{and} \quad \mathrm{d}f = \frac{\partial f}{\partial \sigma_{ij}} \mathrm{d}\sigma_{ij} < 0 \tag{5.3}$$

However, note that the neutral loading occurs when the initial and subsequent stresses fall on the same yield surface, with no attempt to move beyond the current

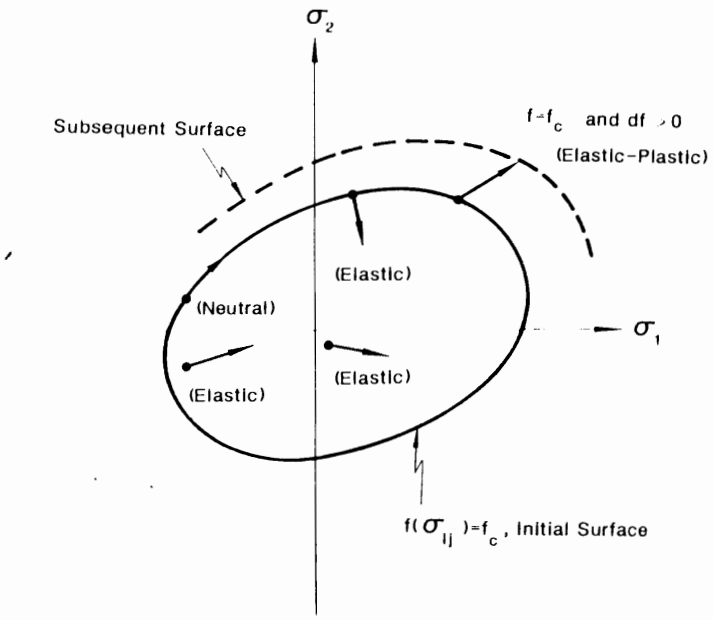

Fig. 5.1 Yield surface for a hardening material.

surface ($f = 0$ and $df = 0$). In this case of neutral loading, deformations are assumed to be purely elastic.

5.2.2 *Hardening rule*

Perfectly plastic material descriptions represent a fair first approximation to soil behavior. According to experimental evidence, however, it is generally known that during the process of incremental plastic deformation, the yield surface changes size, shape, and location. A law governing this aspect of the problem, i.e., one which defines the manner of constructing the subsequent yield surfaces, is called the *hardening rule*. The manner in which hardening occurs for geological materials is expected to be complex. Limited experimental data, therefore, require that some simplified assumptions be made. Mathematically, hardening is characterized by parameters (memory) which vary with the plastic load history. The hardening parameter may vary in form from material to material. For metals, the hardening parameter is often a function of the plastic trajectory or the total plastic work, while for soils it may be dependent on the amount of plastic compaction (see cap models in Chapter 6).

There are several hardening rules that have been proposed to describe the growth of subsequent yield surfaces for strain-hardening (or softening) materials. The choice of a specific hardening rule depends primarily on the ease with which it can be applied and its ability to represent the hardening behavior of a particular

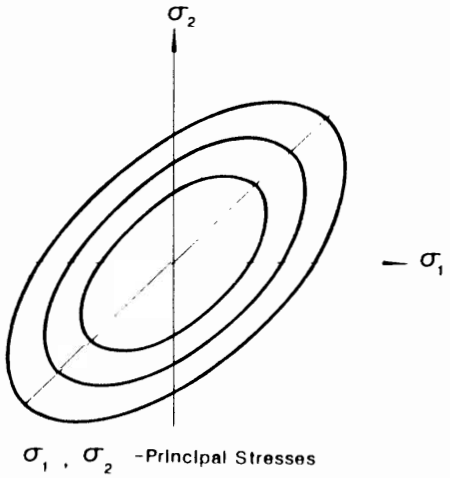

Fig. 5.2. Isotropic hardening.

material. In general, three types of hardening rules have been commonly utilized (Chen, 1982). These are:

1. Isotropic hardening
2. Kinematic hardening
3. Mixed hardening

In the isotropic hardening rule, as shown in Fig. 5.2, the initial yield surface is assumed to expand (or contract) uniformly without distortion as plastic flow continues. On the other hand, the kinematic hardening rule assumes that, during plastic deformations, the loading surface translates without rotation as a rigid body in the stress space, maintaining the size and shape of the initial yield surface (Fig. 5.3). This rule provides a means of accounting for the Bauschinger effect, which refers to one particular type of directional anisotropy induced by the plastic deformations; namely that the initial plastic deformation of one sign reduces the resistance of the material with respect to the subsequent plastic deformation of the opposite sign. Therefore, plasticity models incorporated with the kinematic hardening rule are particularly suitable for materials with pronounced Bauschinger effect such as soils under cyclic and reversed types of loadings.

A combination of isotropic and kinematic hardening rules leads to the more general hardening rule, and therefore provides for a more flexibility in describing the hardening behavior of the material. For the mixed (combined) hardening rule, the loading surface in its plasticity model experiences translation as well as expansion (contraction) in all directions, and different degrees of the Bauschinger effect may be simulated. The plasticity models incorporated into kinematic and mixed types of hardening rules are generally known as the *anisotropic hardening models*.

In the last few years, several plasticity models with more complex hardening rules combining the concepts of kinematic and isotropic hardenings have been developed

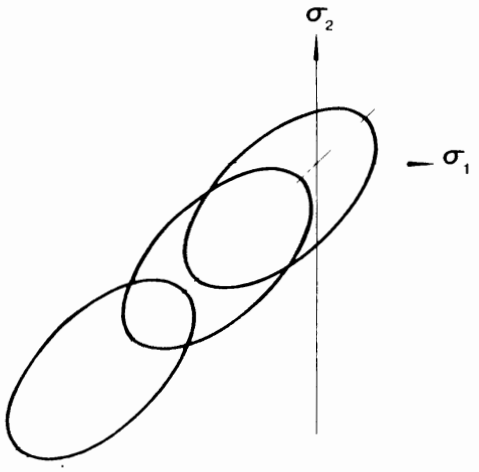

Fig. 5.3. Kinematic hardening.

and applied to describe the behavior of soils under cyclic and dynamic loadings. Some of these models will be discussed later.

5.2.3 Flow rule

We may start by separating any stress increment $d\sigma_{ij}$ into two components: the tangent and normal stress components to the loading or the yield surface. Only the normal stress component produces the plastic strain increment which is also proportional to this stress increment. Mathematically speaking, here, as for the perfectly plastic materials, we may write:

$$d\epsilon_{ij}^{p} = d\lambda \frac{\partial f}{\partial \sigma_{ij}} \tag{5.4}$$

where $d\lambda$ is a proportionality factor representing the magnitude while $\partial f/\partial \sigma_{ij}$ is the direction. This is shown schematically in Fig. 5.4. The magnitude of $d\epsilon_{ij}^{p}$ can be further specified by determining the geometry of Fig. 5.5 where we can write $d\lambda$:

$$d\lambda = \frac{1}{H'} \frac{\partial f}{\partial \sigma_{mn}} d\sigma_{mn} \tag{5.5}$$

where H' is termed the *hardening modulus* which depends generally on stress, strain and history of loading. Substitution of Eq. (5.5) into Eq. (5.4) leads to:

$$d\epsilon_{ij}^{p} = \frac{1}{H'} \left(\frac{\partial f}{\partial \sigma_{mn}} d\sigma_{mn} \right) \frac{\partial f}{\partial \sigma_{ij}} \tag{5.6}$$

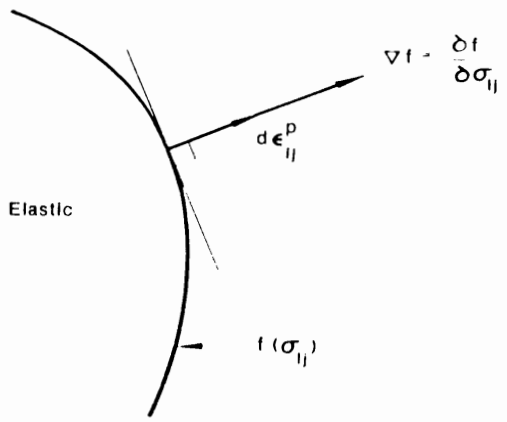

Fig. 5.4. Direction of $d\epsilon_{ij}^{p}$.

The form described above is based on the *associated flow rule* assumption (normality condition). However, this is not satisfied well in a general behavior of engineering materials such as soil, rock, and concrete. Therefore, the *non-associated flow rule* assumption that the plastic strain increment is normal to the *plastic potential function* g is most often applied. Thus, Eq. (5.6) can be rewritten as:

$$d\epsilon_{ij}^{p} = \frac{1}{H'}\left(\frac{\partial f}{\partial \sigma_{mn}} d\sigma_{mn}\right)\frac{\partial g}{\partial \sigma_{ij}} \tag{5.7}$$

The non-associated form of Eq. (5.7) is used to derive the generalized elastic-plastic constitutive equations in Section 5.10. The constitutive equations based on the associated flow rule can be easily obtained by replacing the function g with f.

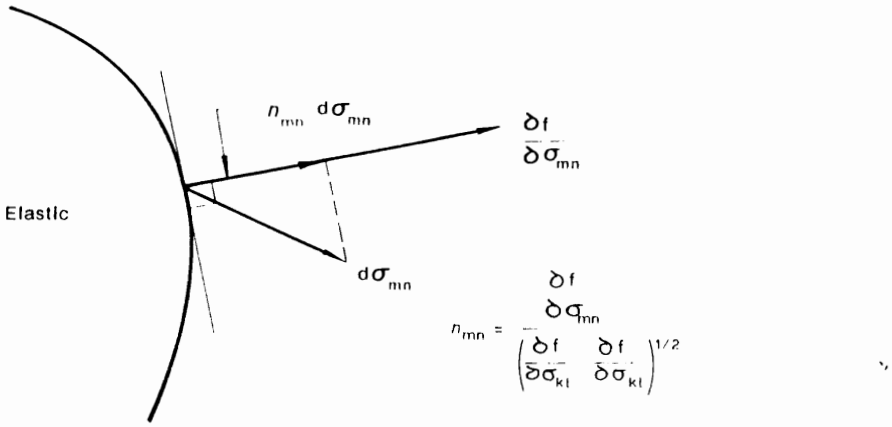

Fig. 5.5. Magnitude of $d\epsilon_{ij}^{p}$ is proportional to the projection of the stress increment, $d\sigma_{ij}$, onto the direction of the normal n_{ij}, that is $n_{ij}d\sigma_{ij} = n_{mn}d\sigma_{mn}$.

5.2.4 *Drucker's postulate*

For work-hardening materials, *Drucker's stability postulate* for *stable materials* (Drucker, 1951) can be introduced as the third basic requirement in addition to the two basic requirements explained for the perfectly plastic materials. Drucker's postulate discussed previously in Chapter 3 gives a more precise definition of the hardening material. The explanation of this postulate is briefly repeated in what follows.

As the stress-strain curve given in Fig. 5.6a, an increment of stress $d\sigma_{ij}$ gives rise to an increment of strain $d\epsilon_{ij}$ with the scalar product of $d\sigma_{ij}\, d\epsilon_{ij} > 0$. The shaded triangle in the figure therefore represents a positive work done by the external agency, and the material of this kind is defined as the *stable* (or *work-hardening*) *material*. On the other hand, the stress-strain curve in Fig. 5.6b has a descending branch, where the strain increases with descending stress. On this branch, the external agency does negative work since $d\sigma_{ij}\, d\epsilon_{ij} < 0$. This material is thus regarded as the *unstable* (or *work-softening*) *material*. Let us suppose that the work hardening material is in an equilibrium under a state of stress σ_{ij}, and then apply additional stresses $d\sigma_{ij}$ and slowly remove them. For this case, Drucker (1951) postulated that:

1. During the application of these additional stresses, a positive work is taken place.
2. For a complete cycle of additional loading and unloading, additional stresses are said to produce positive work if the plastic deformation takes place. The work will be equal to zero only when the deformation is totally elastic.

It should be emphasized that the work referred to here is not the work of the total stresses, but rather the work of the additional stresses on the additional strains.

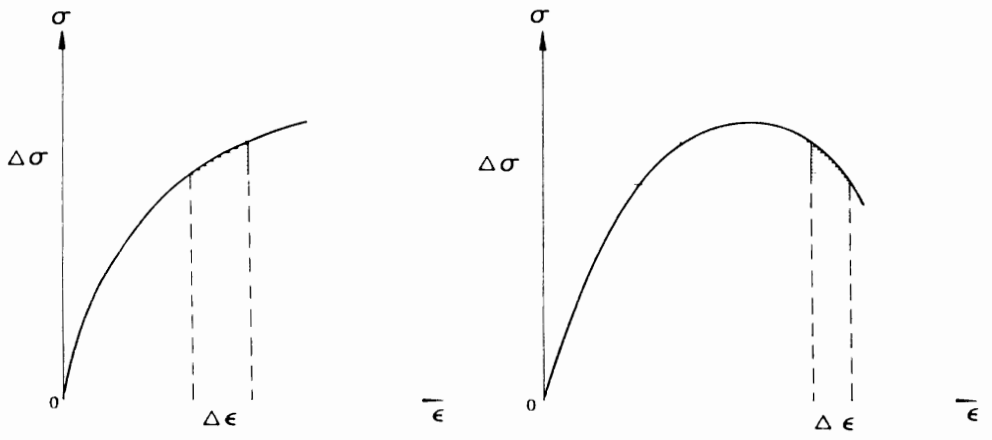

Fig. 5.6. Drucker's stability postulate for hardening materials: (a) stable material, (b) unstable material.

Drucker's postulate leads to an important inequality which can be put into the mathematical form as follows:
For the loading process:

$$d\sigma_{ij}\, d\epsilon_{ij} > 0 \tag{5.8}$$

or using the decomposition of the strain increment, i.e., $d\epsilon_{ij} = d\epsilon^{e}_{ij} + d\epsilon^{p}_{ij}$:

$$d\sigma_{ij}(d\epsilon^{e}_{ij} + d\epsilon^{p}_{ij}) > 0 \tag{5.9}$$

For the cycle of loading and unloading:

$$d\sigma_{ij}\, d\epsilon^{p}_{ij} \geq 0 \tag{5.10}$$

since the work on elastic strains is zero.

As for the case of a perfectly plastic material, consider a unit volume of a hardening material in which there is a homogeneous state of stress σ^{*}_{ij} on or inside the loading surface (see Fig. 4.3). Suppose that an external agency adds stresses along path ABC lying inside the current loading surface until the state of stresses reaches σ_{ij} on the loading surface. Only elastic work has taken place along stress path ABC. Now suppose the external agency again increases the stress state σ_{ij} by $d\sigma_{ij}$. Consequently, plastic deformation must occur, and both elastic and plastic works take place during this increment of stresses. The external agency then releases stresses and returns the state of stress to the original stress σ^{*}_{ij} along the elastic path DE. Since all purely elastic changes are completely reversible and independent of the path from σ^{*}_{ij} to σ_{ij} and return to σ^{*}_{ij}, all the elastic energy is recovered. The plastic work done by the external agency on this loading and unloading cycle is represented by the scalar product of the stress vectors $(\sigma_{ij} - \sigma^{*}_{ij})$, $d\sigma_{ij}$ and the plastic strain increment vector $d\epsilon^{p}_{ij}$. The irreversibility requirement that this work be positive for plastic deformations leads to:

$$(\sigma_{ij} - \sigma^{*}_{ij})\, d\epsilon^{p}_{ij} + d\sigma_{ij}\, d\epsilon^{p}_{ij} \geq 0 \tag{5.11}$$

Since σ^{*}_{ij} is an arbitrarily chosen state of stress, it follows that Eqs. (5.10) and (5.11) lead to the same inequality as that given previously for a perfectly plastic material, that is:

$$(\sigma_{ij} - \sigma^{*}_{ij})\, d\epsilon^{p}_{ij} \geq 0 \tag{5.12}$$

where σ^{*}_{ij} is any state of stress lying on or inside the loading surface and σ_{ij} is on the loading surface (see Fig. 4.3). If the plastic strain coordinates are superimposed upon stress coordinates, as for the perfectly plastic material in Fig. 4.3, the expression (5.12) can be interpreted as scalar products of stress increment and strain increment vectors. A positive scalar product requires an acute angle between two

vectors. Thus, the same conclusions as those mentioned for the perfectly plastic material in Chapter 4 can be made:

1. The initial yield surface and all subsequent yield or loading surfaces must be convex.
2. The plastic strain increment vector $d\epsilon_{ij}^{p}$ must be normal to the yield or loading surface.

Note that the equality condition of Drucker's postulate, $d\sigma_{ij}\, d\epsilon_{ij}^{p} = 0$, leads to the case of the perfectly plastic material. The important requirements such as the *convexity* of the yield or loading surface and the *normality* of the plastic flow, together with the assumption that the plastic strain increment must be *linear* in the stress increment, enable one to develop the plastic stress-strain relations of various geotechnical materials which will be discussed in detail later.

5.3 HARDENING PLASTICITY MODELS

The general form of hardening plasticity models, as described in the previous Section, may be written as:

$$f(\sigma_{ij}, \epsilon_{ij}^{p}, k) = F(\sigma_{ij}, \epsilon_{ij}^{p}) - k^{2}(\epsilon_{p}) = 0 \tag{5.13}$$

where ϵ_{p} is the *effective plastic strain* to be explained in Section 5.9.1. In other words, at each stage of plastic deformation or unloading, there exists a loading surface $F(\sigma_{ij}, \epsilon_{ij}^{p})$ such that no additional plastic deformation takes place when F is smaller than k^{2}, which depends on the history of loading or the effective plastic strain path ϵ_{p}.

Since the work-hardening model tends to introduce anisotropies in initially isotropic materials, it does not suffice to represent the yield surface in the space of principal stresses.

In the following, three types of hardening plasticity models with isotropic hardening, kinematic hardening, and mixed hardening rules are summarized conceptually and mathematically.

5.3.1 Isotropic hardening model

For a perfectly plastic material, the equation for the fixed yield surface has the form $F(\sigma_{ij}) = k^{2}$, where k is a constant. The simplest work-hardening model is to assume that the yield surface expands uniformly without distortion as plastic flow occurs. The size of the yield surface is now governed by the value k^{2}, which depends upon plastic strain history. The equation for the subsequent yield surface or loading surface can be written as the following form:

$$F(\sigma_{ij}) = k^{2}(\epsilon_{p}) \tag{5.14}$$

where the scalar $k^2 > 0$ is some measure of isotropic hardening and the effective plastic strain ϵ_p is an integrated increasing function of the plastic strain increments but not the plastic strain itself.

If the von Mises equation is taken as F, then Eq. (5.14) becomes:

$$J_2 = \tfrac{1}{2} s_{ij} s_{ij} = k^2(\epsilon_p) \tag{5.15}$$

Since the loading surface expands uniformly (or isotropically), it can not account for the Bauschinger effect exhibited by most structural materials. In fact, contrary to the experimental observations, this hardening model implies that because of isotropic hardening the material will exhibit an increase in the compressive yield stress equal to the increase in the tensile yield stress. Since the plastic deformation is an anisotropic process, it can not be expected that this model predicting isotropy in the plastic range will lead to realistic results when complex loading paths, involving significant changes in the direction of the stress vector in the stress space (not necessarily completely reversed) are considered.

The Lade-Duncan model (Lade and Duncan, 1973, 1975), the Lade model (Lade, 1977) to be discussed in Sections 5.4 and 5.5 and the Cap type of strain-hardening models in Chapter 6 are examples for isotropic hardening plasticity models.

5.3.2 Kinematic hardening model

As mentioned previously, the kinematic hardening model assumes that during the plastic deformation, the loading surface translates as a rigid body in the stress space, keeping the size, shape, and orientation of the initial yield surface. The kinematic hardening model has the following form for loading surface:

$$f(\sigma_{ij}, \epsilon^p_{ij}) = F(\sigma_{ij} - \alpha_{ij}) - k^2 = 0 \tag{5.16}$$

where k is a constant and α_{ij} are the coordinates of the center of the loading surface which change as the plastic deformation continues. The simplest version for determining parameter α_{ij} is to assume a linear dependence of $d\alpha_{ij}$ on $d\epsilon^p_{ij}$. This is known as the *Prager's hardening rule* (Prager, 1955, 1956), which has the simple form given by:

$$d\alpha_{ij} = c\, d\epsilon^p_{ij} \quad \text{or} \quad \alpha_{ij} = c\epsilon^p_{ij} \tag{5.17}$$

where c is the work-hardening constant, characteristic for a given material. Equation (5.17) may be taken as the definition of the *linear work hardening*.

Some inconsistency may arise when the Prager's hardening equation is employed in a *subspace* of stress. Namely, if some of the stress components are set equal to zero in Eq. (5.16), for example, $\sigma''_{ij} = 0$ and $\sigma'_{ij} \neq 0$, Eq. (5.16) can be written as:

$$F(\sigma'_{ij} - \alpha'_{ij} - \alpha''_{ij}) - k^2 = 0 \tag{5.18}$$

As $d\alpha''_{ij} = c\, d\epsilon^{p}_{ij}$ is not necessarily zero from Eq. (5.17), Eq. (5.18) no longer necessarily represents a loading surface which is merely translating in stress space; it may be deforming as well, due to the changing values of α''_{ij}.

In order to develop the kinematic hardening model that is also valid in subspace of stress, Ziegler (1959) modified Prager's hardening rule and assumed the rate of translation to take place in the direction of the *reduced-stress vector* $\bar{\sigma}_{ij} = \sigma_{ij} - \alpha_{ij}$ in the form:

$$d\alpha_{ij} = d\mu \bar{\sigma}_{ij} = d\mu(\sigma_{ij} - \alpha_{ij}) \tag{5.19}$$

where $d\mu$ is a positive proportionality factor which depends on the history of the deformation. For simplicity, the factor can be assumed in the form:

$$d\mu = a\, d\epsilon_{p} \tag{5.20}$$

where a is a positive constant, characteristic for a given material.

Example of the kinematic hardening model is the original multi-surface model proposed by Mróz (1967) to be described in Section 5.6.

5.3.3 *Mixed hardening model*

A combination of the two previous models leads to the more realistic *mixed hardening model* (Hodge, 1957) whose loading function can be expressed as:

$$f(\sigma_{ij}, \epsilon^{p}_{ij}, k) = F(\sigma_{ij} - \alpha_{ij}) - k^{2}(\epsilon_{p}) = 0 \tag{5.21}$$

In this case, the loading surface experiences translation and uniform expansion in all directions; i.e., it retains its original shape. With the mixed hardening rule, different degrees of the Bauschinger effect can now be simulated.

Anisotropic hardening plasticity models such as the nested yield surface models, the generalized multi-surface models, the bounding surface models explained in Section 5.6 are based on the general formulations mentioned above.

In the following Section, we shall summarize briefly the advanced hardening plasticity models: the Lade-Duncan model and the Lade model for isotropic work-hardening materials, and the nested yield surface models, the generalized multi-surface models, and the bounding surface models for anisotropic strain- or work-hardening materials.

5.4 LADE-DUNCAN MODEL

Failure and loading criteria

Lade and Duncan (1973) investigated the characteristics of cohesionless soil, performing cubical triaxial tests on Monterey No. 0 Sand. Among various test

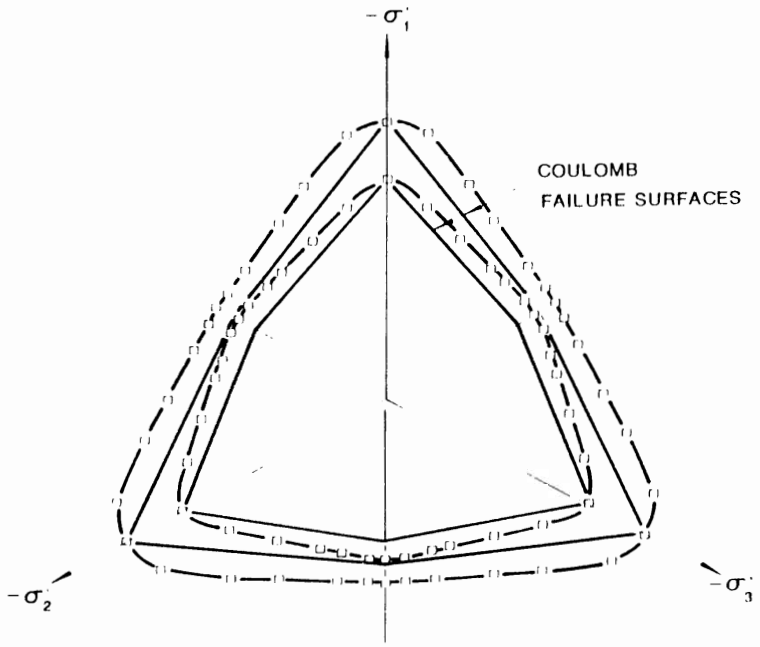

Fig. 5.7 Failure surfaces on deviatoric plane for dense and loose Monterey No. 0 sand (Lade and Duncan, 1973).

results, failure states had been examined for different relative magnitudes of the intermediate principal stress, b, which is defined as:

$$b = (\sigma_2 - \sigma_3)/(\sigma_1 - \sigma_3) \tag{5.22}$$

under stress conditions for which $\sigma_1 \leq \sigma_2 \leq \sigma_3 \leq 0$. The value of b is zero for the triaxial compression test in which $\sigma_2 = \sigma_3$, and it is unity for the triaxial extension test in which $\sigma_1 = \sigma_2$. The value b changes between zero and unity due to the intermediate value of σ_2. Such experimentally obtained failure points are plotted on the deviatoric plane for dense and loose Monterey No. 0 Sands, as shown in Fig. 5.7. In this figure, the cross-sections of the Coulomb failure surfaces which correspond to the failure strengths from triaxial compression tests are also shown for a relative comparison. The shapes of the experimentally obtained failure surfaces seem to be smooth throughout their lengths, while those of the Coulomb failure surfaces show an irregular hexagon with singularities. In this model development, it has been assumed that the confining pressure (I_1) has no influence on the shape of the cross-section of the failure surface on the deviatoric plane. Consequently, the failure surface in the principal stress space is a cone whose cross-sections have similar shapes but different sizes under different hydrostatic pressures.

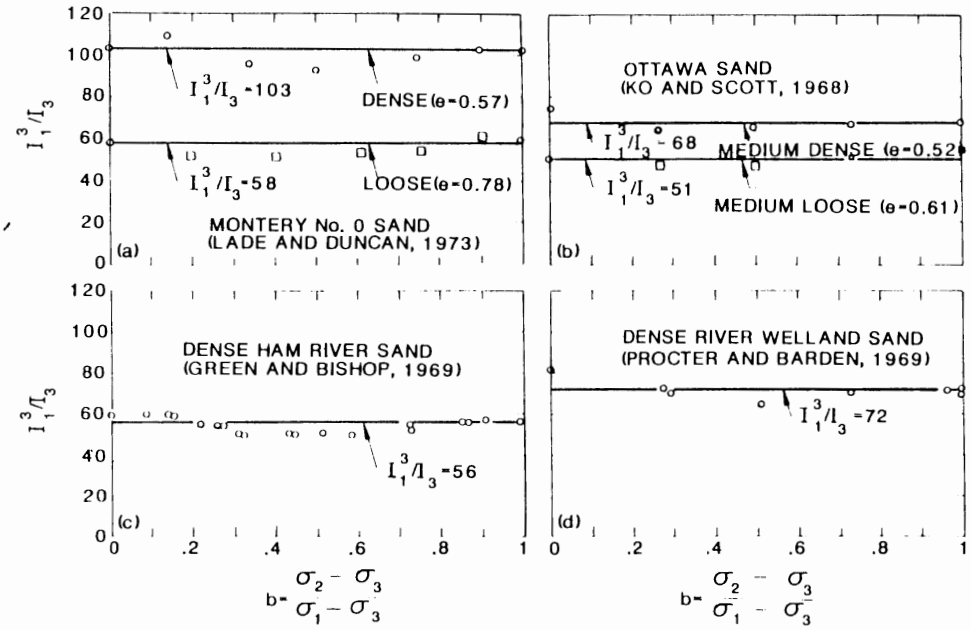

Fig. 5.8. Comparisons of failure criterion with data from cubical triaxial tests on four different sands (Lade and Duncan, 1975).

Thus, Lade and Duncan (1975) proposed the failure criterion that can be expressed in a simple combination of stress invariants, that is:

$$\kappa_1 = I_1^3/I_3 \tag{5.23}$$

where I_1 and I_3 are respectively the first and third invariants of the stress tensor, and κ_1 is a value of stress level at failure which depends on the density of sands.

The suitability of the failure criterion was examined by using the failure data from the cubical triaxial tests on four different sands. The relationships between the b-value and the stress level κ_1 from four tests are plotted in Fig. 5.8 together with the prediction by the failure criterion of Eq. (5.23). As can be seen from Fig. 5.8a, reasonably good agreement is obtained for both dense and loose sands, although there is some scatter within which the failure criterion (Eq. 5.23) seems to overestimate slightly the failure strength of the loose and dense sands at the intermediate value of b.

In addition, Fig. 5.8b to 5.8d show comparisons between the results predicted by Eq. (5.23) and the published results of the cubical triaxial tests performed on different cohesionless soils by Green and Bishop (1969), Ko and Scott (1968), and Procter and Barden (1969). Although there is also some scatter for three cases, it can be seen that the failure criterion describes the strength characteristics of these soils quite well.

Lade and Duncan (1975) have consequently developed the isotropic elastic-plastic work-hardening model, based on the failure criterion mentioned above as well as the results from the cubical triaxial tests. Their model contains subsequent yield (or loading) surfaces and a failure surface. The form of the failure surface f_f is again expressed in terms of the stress invariants, I_1 and I_3, as:

$$f_f = I_1^3 - \kappa_1 I_3 = 0 \tag{5.24}$$

or using other stress invariants I_1, J_2, and J_3, Eq. (5.24) can be represented by:

$$f_f = J_3 - \frac{1}{3} I_1 J_2 + \left(\frac{1}{27} - \frac{1}{\kappa_1} \right) I_1^3 = 0 \tag{5.25}$$

On the other hand, the form of loading surfaces f_1 is given by:

$$f_1 = I_1^3 - \kappa I_3 = 0 \tag{5.26}$$

or

$$f_1 = J_3 - \frac{1}{3} I_1 J_2 + \left(\frac{1}{27} - \frac{1}{\kappa} \right) I_1^3 = 0 \tag{5.27}$$

where κ is a value which is determined from the current stress level and varies from 27 for hydrostatic stress condition ($\sigma_1 = \sigma_2 = \sigma_3$) up to the value of κ_1 at failure.

In the principal stress space, the three-dimensional view of the failure surfaces with different values of κ_1 is shown in Fig. 5.9a as conical with its apex at the origin of the stress axes. Also, the shapes of the failure surfaces on the π-plane are respectively shown in Fig. 5.9b, for three values of $\kappa_1 = 41.7$, 62.5, and 115.3.

On the other hand, the inner loading (or yield) surface enclosed by the failure surface has the same general surface as the failure surface, except the difference in the value of κ, and it expands isotropically around the hydrostatic axis as the current stress level approaches the failure condition, that is, the value of κ increases from the original value of 27 to the specified value κ_1. Therefore, the yield surface approaches asymptotically the failure surface with an increase in the stress level, κ.

Flow rule

Lade and Duncan (1973) examined the directions of the plastic strain increment vectors whether the normality condition of classical theory of plasticity is satisfied on the failure surface with respect to their test results. The directions on the experimental failure surfaces projected in triaxial plane are shown in Fig. 5.10, respectively, for dense and loose sands. As can be seen, the directions of plastic increments are caused with acute angles to the failure surface for dense and loose sands in both compression and extension sides. Therefore, the normality condition is not satisfied for the failure surfaces in the triaxial plane. Further, the projections

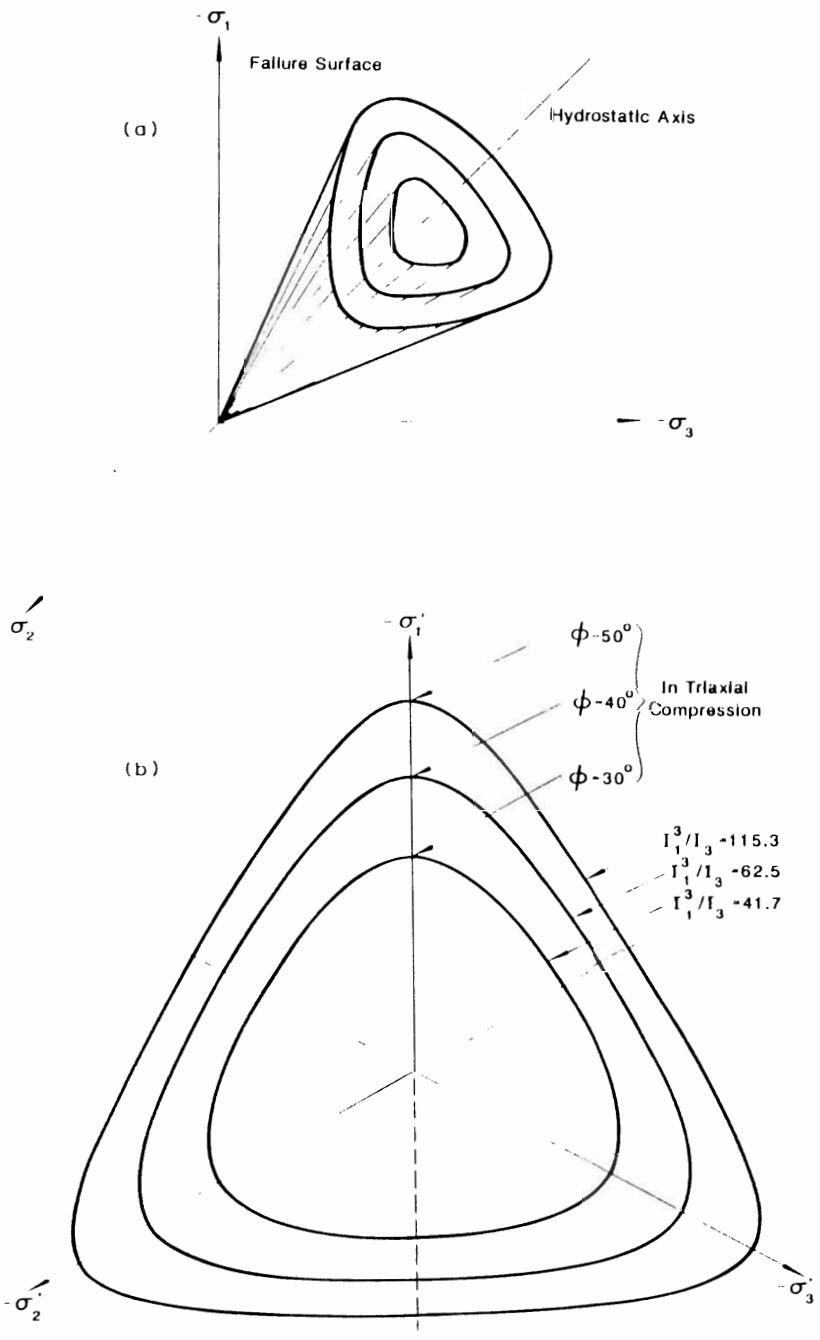

Fig. 5.9. Lade-Duncan model. (a) general shape in principal stress space, (b) cross section on π-plane (Lade and Duncan, 1975).

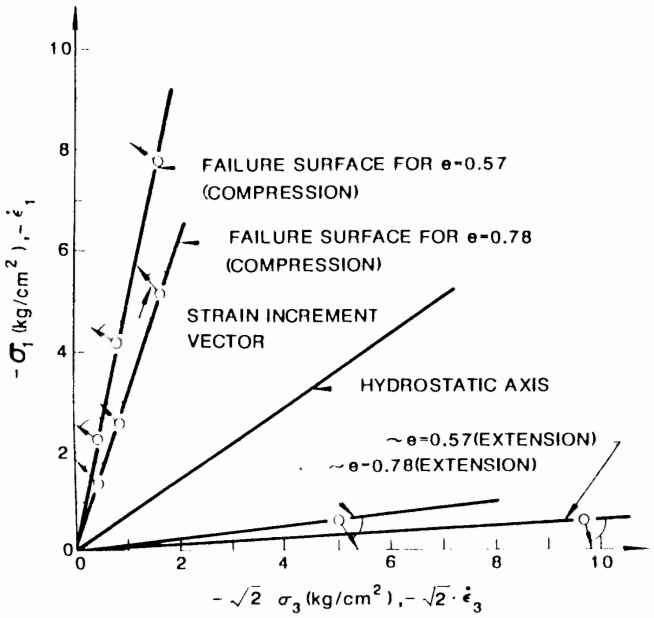

Fig. 5.10. Directions of strain increment vectors in triaxial plane for dense and loose Monterey No. 0 sand (Lade and Duncan, 1973).

of the plastic strain increment vectors on the deviatoric plane are shown in Fig. 5.11, for dense and loose sands. It can be understood that their projections keep a close perpendicularity to the failure surfaces except a few of vectors at intermediate values. From both Figs. 5.10 and 5.11, we may therefore state that the normality condition is almost satisfied on the deviatoric plane, but not on the triaxial plane.

From these observations, Lade and Duncan (1975) introduced the *plastic potential function* g that is expressed in a similar form to that of the yield function:

$$g = I_1^3 - \kappa_2 I_3 = 0 \tag{5.28}$$

or using other stress invariants:

$$g = J_3 - \tfrac{1}{3} I_1 J_2 + \left(\frac{1}{27} - \frac{1}{\kappa_2} \right) I_1^3 = 0 \tag{5.29}$$

where κ_2 has a constant value which depends on a given stress level. The value of κ_2 is related to the directions of the plastic strain increment in the triaxial plane for both the triaxial compression and extension conditions. From an examination of the experimental results shown in Fig. 5.12 for dense Monterey No. 0 sand, the variation of κ_2 is represented as a function of the current stress level, κ, that is:

$$\kappa_2 = A\kappa + 27(1 - A) \tag{5.30}$$

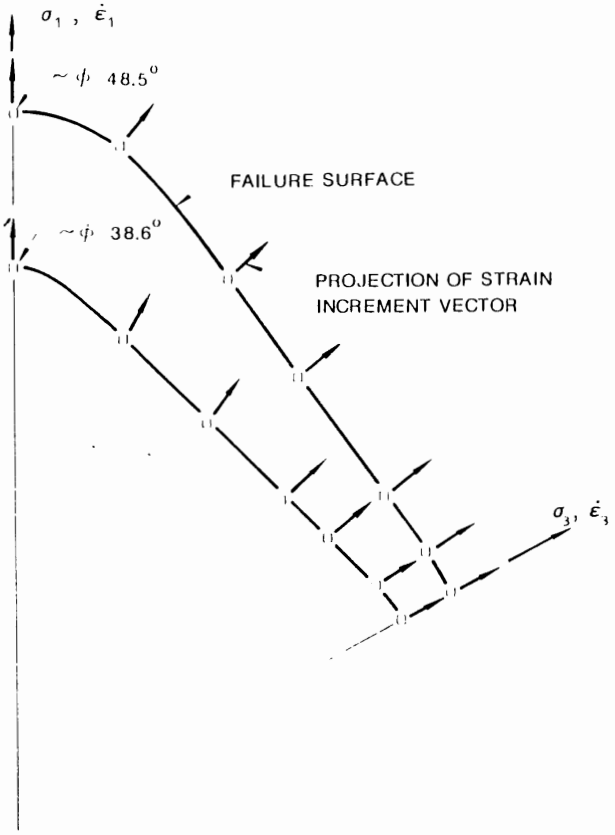

Fig. 5.11. Directions of strain increment vectors on deviatoric plane for dense and loose Monterey No. 0 sand (Lade and Duncan, 1973).

where A is the inclination of straight line which can be determined from experimental data. The value of κ_2 varies from 27 for $\kappa = 27$ under the hydrostatic stress conditions to A (κ_1 27) + 27 for $\kappa = \kappa_1$ at failure.

The plastic potential function given by Eq. (5.29) depicts the same view in three-dimensional principal stress space (Fig. 5.9a) and the same shape on the deviatoric plane (Fig. 5.9b) as that of the yield surface, except the difference in the values of κ and κ_2.

Isotropic work-hardening rule

The magnitudes of the plastic strain increments corresponding to the stress increments can be calculated by employing the work-hardening rule discussed in the following as well as a non-associated flow rule. A relation between the plastic work given by:

$$W_p = \int \sigma_{ij} \, d\epsilon_{ij}^p \tag{5.31}$$

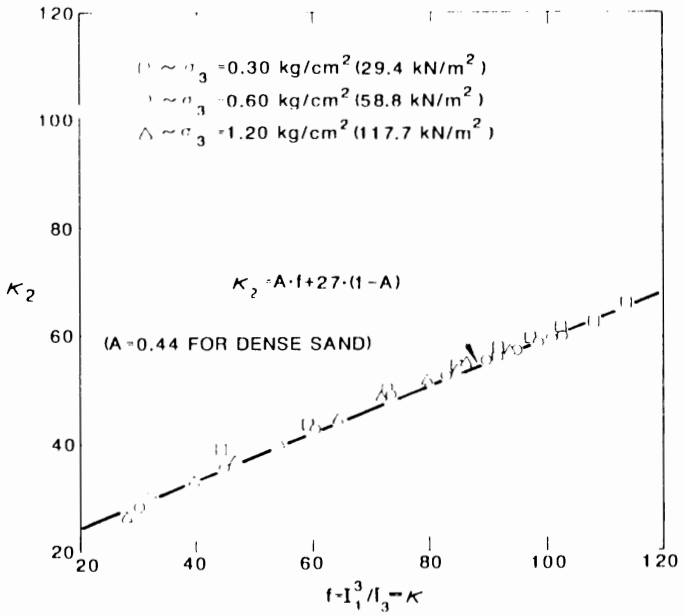

Fig. 5.12. Variation of κ_2 with $f = I_1^3/I_3$ for dense Monterey No. 0 sand (Lade and Duncan, 1975).

and the current stress level, $\kappa = I_1^3/I_3$, was examined from experimental results, and its experimental relation is shown in Fig. 5.13 for dense Monterey No. 0 sand, as an example. Mathematically, the relation can be approximated by the following hyperbolae:

$$\kappa \quad \kappa_t = W_p/(a + dW_p) \tag{5.32}$$

where κ_t is a threshold stress level. It is assumed in their model that for the value from 27 up to κ_t, no plastic strain occurs and no plastic work is done. Only elastic behavior dominates until the current stress level reaches $\kappa = \kappa_t$. The parameter, a, which is the initial slope of the W_p-$(\kappa - \kappa_t)$ relationship, may be expressed as:

$$a = Mp_a(\sigma_3/p_a)^l \tag{5.33}$$

in which p_a is the atmospheric pressure and σ_3 is the initial confining pressure. Both M and l are dimensionless numbers which may be determined by plotting the a-values versus σ_3-values on log-log scales and fitting a straight line to the data. The reciprocal of parameter d is the ultimate value of $(\kappa - \kappa_t)$ which Eq. (5.32) approaches asymptotically at large values of the plastic work, W_p. Thus, the plastic work increment, dW_p, can be written as:

$$dW_p = \frac{a\, d\kappa}{[1 - d(\kappa - \kappa_t)]^2} \tag{5.34}$$

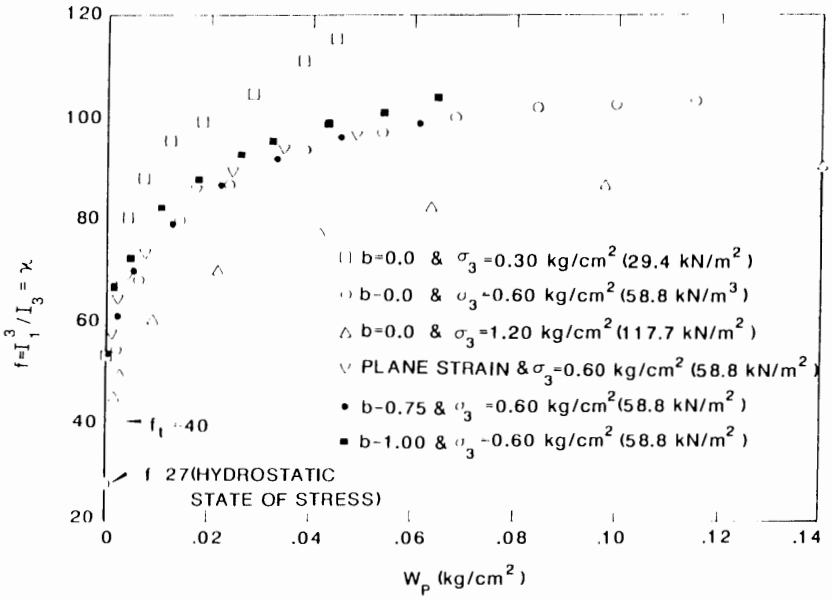

Fig. 5.13. Relation between plastic work and stress level for dense Monterey No. 0 sand (Lade and Duncan, 1975).

Once knowing the current value of the stress level and the difference, $d\kappa$, in κ between two successive stress states, dW_p can be calculated from Eq. (5.34) and then from the non-associated flow rule assumption the plastic strain increments, $d\epsilon_{ij}^p$, are calculated as follows:

$$d\epsilon_{ij}^p = d\lambda \frac{\partial g}{\partial \sigma_{ij}} \tag{5.35}$$

where the positive scalar function $d\lambda$ is now expressed by:

$$d\lambda = \frac{dW_p}{3g} \tag{5.36}$$

On the other hand, the elastic strain increments are calculated from Hooke's law, using the unloading-reloading moduli which were developed by Duncan and Chang (1970).

The model has an improved capacity for representing several characteristics of the stress-strain for cohesionless soils, such as the effects of the intermediate principal stress, shear dilatancy effects, and stress-path effects. Further, this model has been examined for the three-dimensional behavior of remolded Grundite clay (Lade and Musante, 1978).

TABLE 5.1

Advantages and limitations of the Lade-Duncan model

Advantages	Limitations
simple	suitable for cohesionless soils
effect of intermediate principal stress	straight line meridian causes some contradictions at high compressive pressure
smooth	

The advantages and limitations of this model are summarized in Table 5.1.

5.5 LADE MODEL

Failure and loading criteria

The Lade and Duncan model (1975) for a cohesionless soil described in the previous Section has been modified by Lade (1977) with curved yield (or loading) surfaces, instead of yield surfaces with straight meridian line, and with the cap type of yield surfaces similar to those of the generalized cap models (see *generalized cap models* in Chapter 6). The scheme of a curved conical yield surface with a spherical cap superimposed in triaxial plane is shown in Fig. 5.14. Cap type of spherical yield surface is controlled by the plastic collapse strains occurring during isotropic compression. Failure of soils is controlled entirely by the curved-conical yield surface which yields the plastic expansive strains, but not by the yield cap. Therefore, in this model development, the total strain increments, $d\epsilon_{ij}$, are divided into an elastic component, $d\epsilon_{ij}^{e}$, a plastic collapse component, $d\epsilon_{ij}^{c}$, and a plastic expansive component, $d\epsilon_{ij}^{p}$, such that:

$$d\epsilon_{ij} = d\epsilon_{ij}^{e} + d\epsilon_{ij}^{c} + d\epsilon_{ij}^{p} \tag{5.37}$$

The cap type of yield surface is expressed in terms of the first and second invariants of the stress tensor, I_1, and I_2 as follows:

$$f_c = I_1^2 - 2I_2 \tag{5.38}$$

The cap surface expands isotropically as the value of f_c increases. The plastic potential surface corresponding to the yield surface is taken the same as f_c in this portion (an associated flow rule).

On the other hand, in order to make the failure surface curved as observed for most cohesionless soils, the frictional angle is assumed to decrease with increasing magnitude of the hydrostatic pressure. In this way, the modified yield surface of Lade and Duncan model (1975) has been developed in terms of the first and the

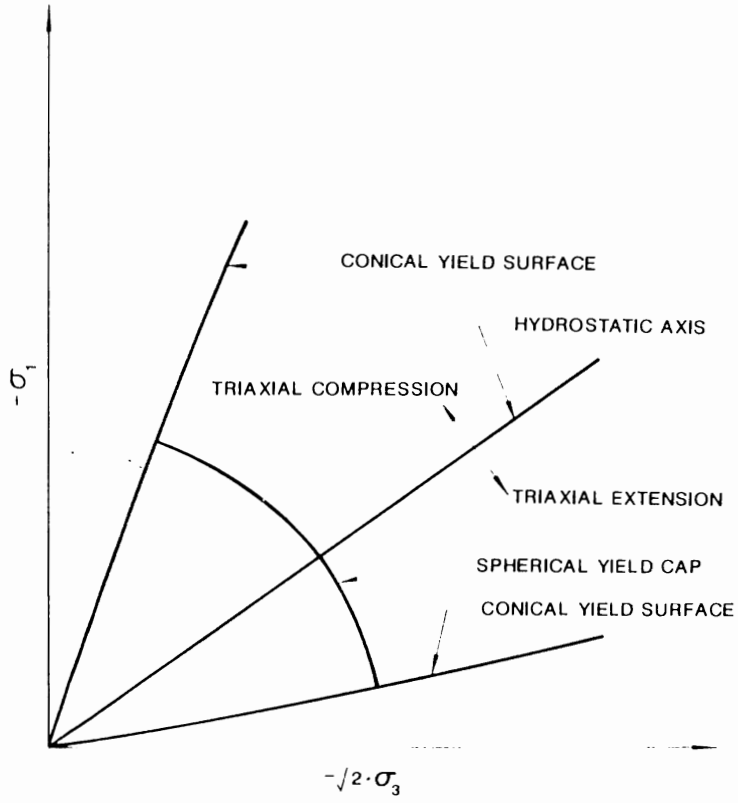

Fig. 5.14. Conical yield surface and spherical yield surface in triaxial plane (Lade, 1977).

third invariants of the stress tensor, I_1 and I_3:

$$f_p = (I_1^3/I_3 - 27)(I_1/p_a)^m \tag{5.39}$$

where f_p has a value of η_1 at failure. The value of η_1 and m in Eq. (5.39) can be determined by plotting $(I_1^3/I_3 - 27)$ vs. p_a/I_1 at failure in a log-log diagram. The apex angle increases as the value of η_1 increases, and the curvature of the failure surface increases as the value of m increases. For the special case of $m = 0$, the failure surface becomes straight, and it is identical to that of the Lade-Duncan model in Section 5.4. Although the plastic potential function is assumed to be identical to the yield surface for the behavior of plastic collapse strains, this assumption is not accurate for that of the plastic expansive strains.

Flow rule

The plastic potential surface for conical yield surfaces is expressed in a form similar to the failure or yield function described above, that is:

$$\eta_1 = (I_1^3/I_3 - 27)(I_1/p_a)^m \tag{5.40}$$

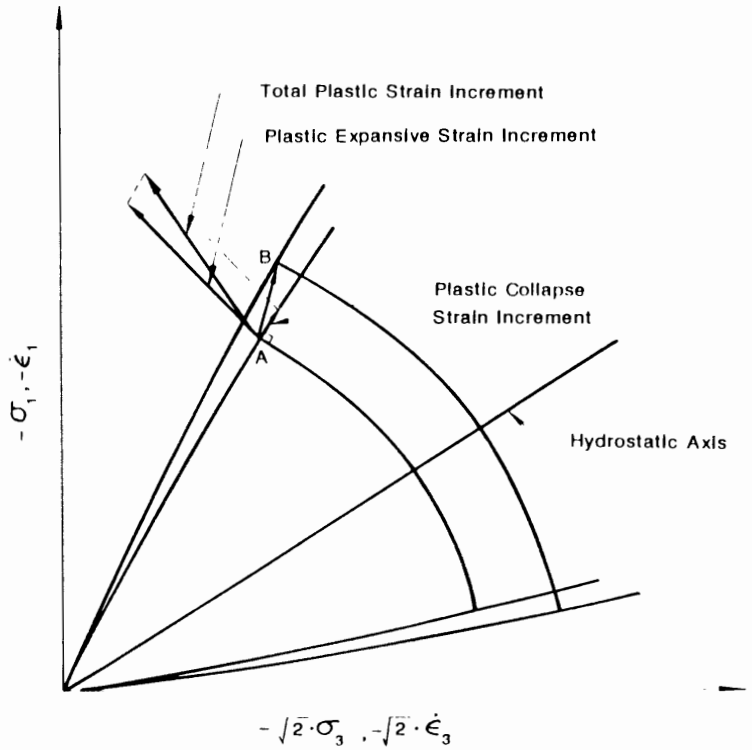

Fig. 5.15. Schematic diagram of yielding process with plastic strain components superimposed in triaxial plane (Lade, 1977).

where η_2 is a constant for given values of f_p and σ_3, and m is the same constant in the yield function (5.39). In a similar manner to the treatment of material constant in the Lade-Duncan model discussed in the previous Section, the value of η_2 may be determined from the directions of plastic strain increments in the triaxial plane. Details of the form on η_2 are given in the paper by Lade (1977).

The shapes of plastic potential surfaces are like asymmetric bullets with their apices at the origin of the principal stress space (see Fig. 5.14). Also, their shapes on π-plane are the same as those of the yield surfaces shown in Fig. 5.9b.

The plastic expansive strains, $d\epsilon_{ij}^p$, occurred on the curved-conical yield surface are thus calculated from a non-associated flow rule assumption, whereas the plastic collapse strains, $d\epsilon_{ij}^c$, occurred on the cap-type yield surface are calculated from the associated flow rule assumption. For the particular case when the state of stress moves from Point A to B as shown in Fig. 5.15, both plastic expansive and collapse strains occur, because both yield surfaces are pushed outward. Thus, the resultant plastic strains are calculated as the vector sum of the two plastic strain incremental vectors. The mathematical treatment at corners will be shown later in some details.

As for the calculation of the elastic strains, the hypoelasticity model proposed by Duncan and Chang (1970) is used.

Work-hardening rule

In order to calculate the plastic collapse strains with the associated flow rule, work-hardening relationship is determined from an isotropic compression test. The total plastic work, W_c, accumulated due to the collapse strain is expressed in terms of f_c in Eq. (5.38), that is:

$$W_c = F_c(f_c) \tag{5.41}$$

where F_c is a monotonically increasing, positive function, implying that the work-hardening relationship is independent of the stress-path. It is noted that for an isotropic compression test, the plastic work, $W_c = \int \sigma_{ij}\, d\epsilon^c_{ij}$, reduces to $\int \sigma_m\, d\epsilon^c_{kk}$ where σ_m is the hydrostatic pressure and $d\epsilon^c_{kk}$, the increment of volumetric plastic collapse strain, and also f_c in Eq. (5.38) reduces to $3\sigma_m^2$. From such simplified test results, the relationship between W_c and f_c plotted on log-log scales as a straight line can be expressed by:

$$W_c = C p_a \left(f_c / p_a^2\right)^q \tag{5.42}$$

where the value of collapse modulus C is determined at $f_c/p_a^2 = 1$, the collapse exponent q is the slope of the straight line, and p_a is atmospheric pressure.

On the other hand, to calculate the plastic expansive strains using a non-associated flow rule, both isotropic work-hardening and -softening relationships are determined from the triaxial compression tests. The plastic work due to the plastic expansive strains at each stage of triaxial compression tests can be calculated as $W_p = \int \sigma_{ij}\, d\epsilon^p_{ij}$ where $d\epsilon^p_{ij}$ is an increment of plastic expansive strains. In a similar manner to that of the hardening relation between f_c and W_c, the following expression corresponding to the function f_p in Eq. (5.39) and the plastic work W_p can be experimentally obtained:

$$f_p = a \exp(-bW_p)\left(W_p/p_a\right)^{1/r}, \quad r > 0 \tag{5.43}$$

where the parameters, a, b, and r, are constants for a given value of confining pressure, σ_3. Since the value of f_p increases until W_p reaches the peak value of W_p^{peak} and then f_p decreases with further increase in W_p, the expression in Eq. (5.43) can represent not only the work-hardening behavior but also the work-softening behavior of cohesionless soils.

From both above-mentioned work-hardening relationships of the cap yield surface and the conical yield surface, the corresponding plastic strains are obtained utilizing the flow rules.

Almost all aspects of soil behavior described in the previous simpler theory by the Lade-Duncan model have been modified in the development of the more refined

TABLE 5.2

Advantages and limitations of the Lade model

Advantages	Limitations
simple	suitable only for cohesionless soils
smooth	
curved meridian	
wider range of pressure than with other criteria	

Lade model. This model has been examined to some extent for the prediction of soil and pore pressure behavior in the undrained triaxial compression tests on saturated sand by Lade (1978).

The advantages and limitations of this model are summarized in Table 5.2.

5.6 NESTED YIELD SURFACE MODELS

Although isotropic strain- or work-hardening models described above have been widely used in soil mechanics because of their simplicity in direct computational applications, these models are not adequate for the prediction of soil behavior undergone loading-unloading reversals. The isotropic model predicts elastic behavior solely until the stress is fully reversed to the original state. However, it is observed in soil experiments that upon unloading, both elastic and plastic deformations occur well before the stress is fully reversed. Hence, an alternative approach to the isotropic hardening type of model is provided by the kinematic type of strain-hardening rules or a combination of isotropic and kinematic types of strain-hardening rules. Recently, this approach has been employed by several researchers to provide for a more realistic representation of soil behavior under reversed, and particularly cyclic, loading conditions.

One-dimensional illustration

Before going to discuss the recently advanced *nested yield surface models*, let us consider two bars in parallel which carry the load P through a rigid plate, as shown in Fig. 5.16a. Two bars have respectively different cross sectional areas A_1, A_2 and different stress-strain relations shown in Fig. 5.16b. As the load P increases gradually, the relation between the equivalent (or averaged) stress given by $P/(A_1 + A_2)$ and strain follows the path (O → A → B → C) in Fig. 5.17. Both bars behave elastically until Bar 1 yields first at point A (path O → A). However, Bar 2 remains elastic for further loading until it yields later at point B (path A → B). After point B, both bars can no longer sustain additional loadings (path B → C). Upon unloading from point C, both bars show again an elastic behavior until Bar 1 yields in compression at point D (path C → D). For further compressive loading, Bar 2 yields

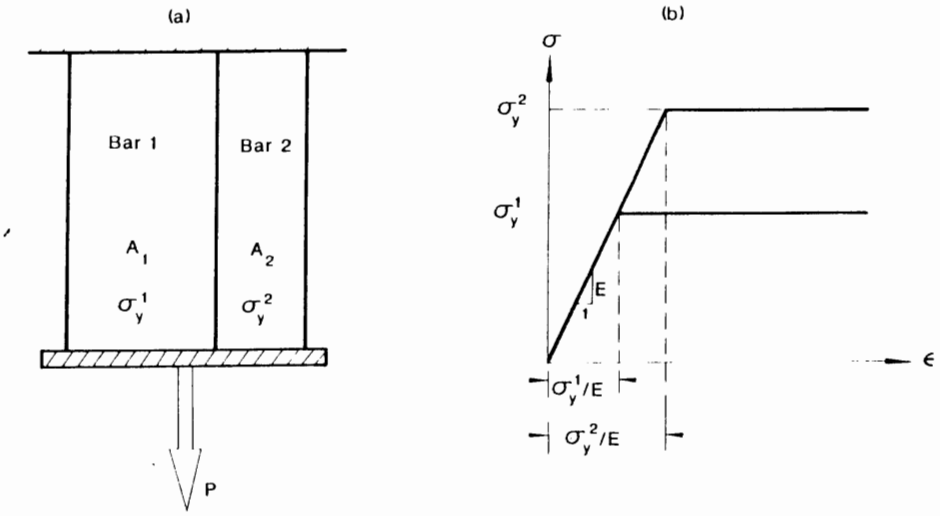

Fig. 5.16. Simple sublayer model: (a) parallel two-bar system; (b) stress-strain relations.

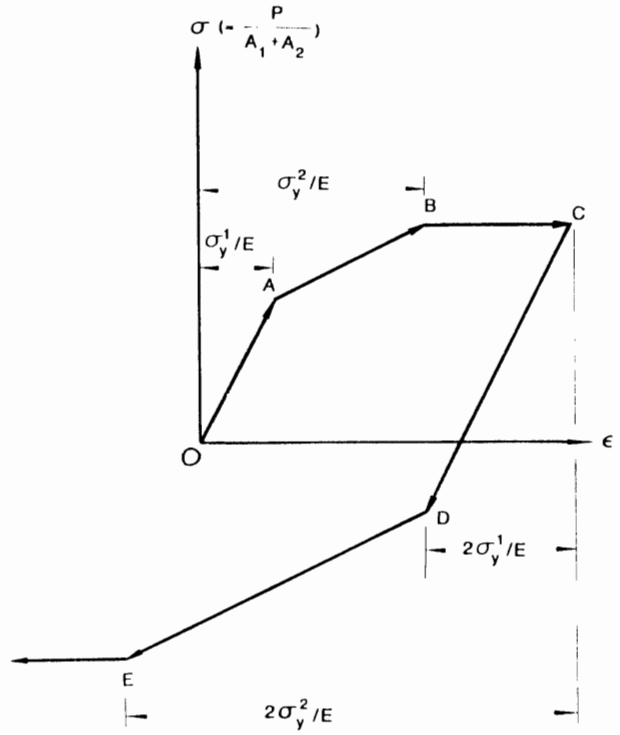

Fig. 5.17. Stress-strain relation by a sublayer model.

at point E, and then the system loses its resistance. The behavior of the two-bar system for reloading case can be examined in a similar manner to those for loading and unloading. It should be noted here that segments such as CD and DE in unloading branch are respectively twice as long as segments, OA and AB in loading branch. This is the well-known *Masing criterion* (Masing, 1926) for establishing the unloading and reloading curves from an initial loading curves. Iwan (1967), following the related work of Masing, first proposed such a one-dimensional plasticity model (for example, see Fig. 5.16a). In the more general case, it consists of a collection of perfectly elastic and rigid-plastic or slip elements arranged in either a series-parallel or a parallel-series combination. The model can contain a very large number of elements, and the properties of these elements can be distributed such that they can match the particular form of hysteretic behavior of a certain type of soil. Such models are known as the *overlay* or *mechanical sublayer models* (e.g. Zienkiewicz et al., 1977). The concept of sublayer model was originally introduced by Duwez (1935) and further developed later by Besseling (1958).

Iwan / Mróz models

In order to extend the one-dimensional model to three-dimensional situations, an extended formulation of the classical incremental theory of plasticity has been proposed by Iwan (1967). Instead of using a single yield surface in stress space, he postulated a family (nest) of yield surfaces (Fig. 5.18) with each surface translating independently in a pure kinematic manner, or individually obeying a linear work-hardening model. Their combined action, in general, gives rise to a nonlinear work-hardening behavior for the material as a whole. The approach leads to a realistic Bauschinger effect of the type that could not be obtained by using a single yield surface and the nonlinear work-hardening rule even with kinematic hardening.

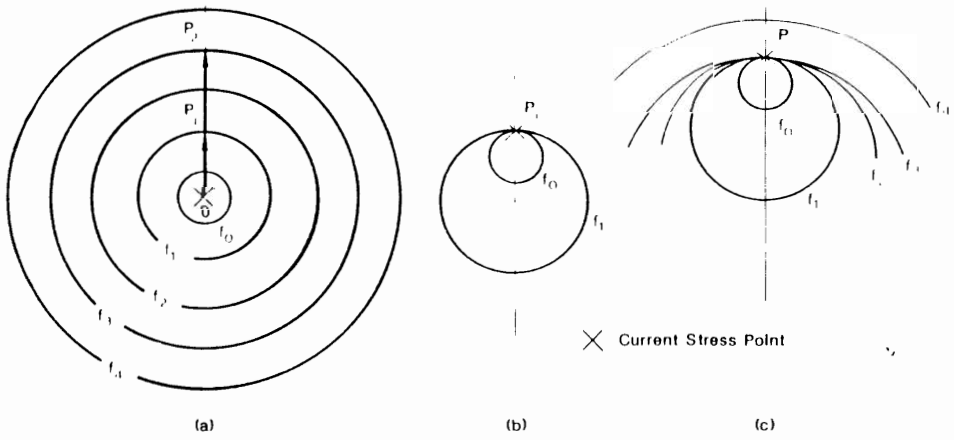

Fig. 5.18. Series of nested yield surfaces in Mróz/Iwan type of strain-hardening models.

The same concept of using a field of nested yield surface was also proposed independently by Mróz (1967). The Iwan/Mróz models are usually known as the *multi-surface plasticity models (nested yield surface models)*. These models have been used by Joyner and Chen (1976) to study the seismic response of two-dimensional configurations of soils. The model has been found to be particularly promising for use in calculating the response of earth dams subjected to earthquake ground shaking. In all the proposed models of this type, associated flow rule has been utilized to estimate plastic strain increment. The plastic strain increment can be represented using the hardening modulus H' which determines the stiffness of surface f, namely:

$$d\epsilon_{ij}^{p} = \frac{1}{H'}\left(\frac{\partial f}{\partial \sigma_{mn}} d\sigma_{mn}\right)\frac{\partial f}{\partial \sigma_{ij}} \tag{5.44}$$

Figure 5.18 demonstrates the qualitative behavior of a multi-surface model with pure kinematic hardening rule during the process of proportional loading. The initial positions of the yield surface f_0, f_1, f_2, f_3, and f_4 are shown in Fig. 5.18a. When the stress point moves from O to P_1, elastic strains first occur until the surface f_0 is reached, where the plastic flow begins and the surface f_0 starts to move towards the surface f_1. Before their contact, the hardening modulus H_0' associated with f_0 governs the plastic flow according to the associated flow rule. However, when f_0 engages f_1 at P_1 (Fig. 5.18b), the first nesting yield surface f_1 becomes the active surface and, upon further loading, the hardening modulus H_1' applies to the flow rule. Both f_0 and f_1 are then translated by the stress point, and they remain tangent to each other on the stress path until they touch the yield surface f_2 which then becomes the active surface. For subsequent contacts of consecutive surfaces, the process is repeated with applying corresponding new values of hardening moduli. The situation when the stress state reaches f_3 is illustrated in Fig. 5.18c. The process of unloading and subsequent loading in reverse direction can be similarly treated.

This discussion is helpful to understand the characteristic of *multi-surface plasticity model*. In order to discuss further the behavior of these surfaces for general stress paths deviating from proportional loading, the mathematical forms of the multi-surfaces $f_0, f_1, \ldots, f_m, \ldots, f_p$ with respective sizes $k^{(0)} < k^{(1)} < \ldots < k^{(m)} < \ldots < k^{(p)}$ are defined by:

$$f_m \quad f_m\left[\sigma_{ij} \quad \alpha_{ij}^{(m)}, k^{(m)}\right] - 0 \quad (m = 0, \ldots, p) \tag{5.45}$$

where $\alpha_{ij}^{(m)}$ are the coordinates of center of yield surface in stress space and $k^{(m)}$ is its current size. $\alpha_{ij}^{(m)}$ and $k^{(m)}$ are, under a certain conditions, assumed to be functions of plastic strain, ϵ_{ij}^{p}. The function f_m is conveniently chosen to be a homogeneous function with respect to the terms of $[\sigma_{ij} - \alpha_{ij}^{(m)}]$ and $k^{(m)}$. After an arbitrary stress path when the stress point reaches the yield surface, f_m, the yield

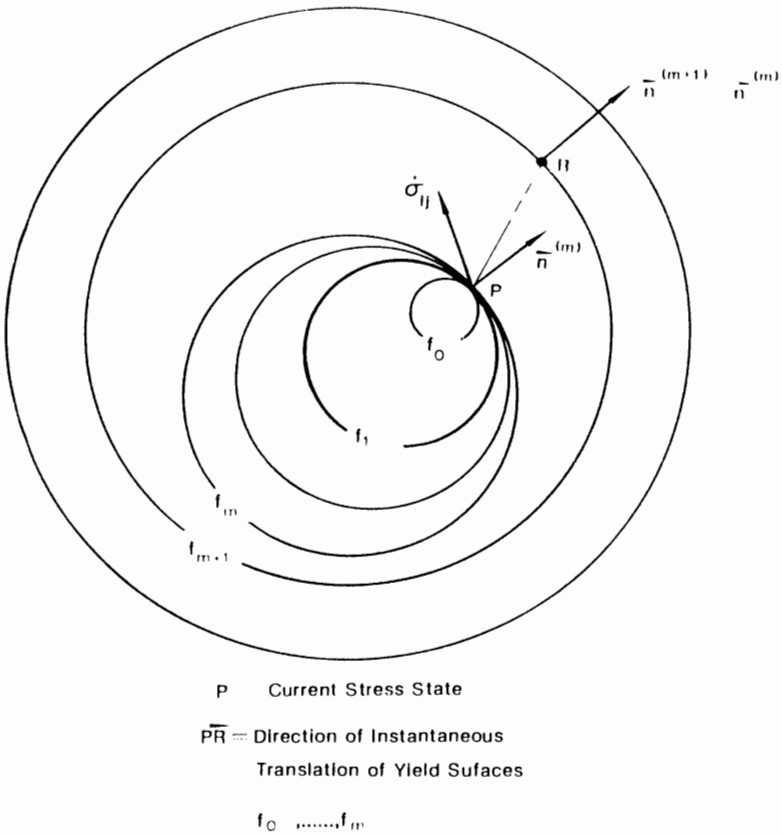

Fig. 5.19. Translation rule of multi-surfaces in stress space.

surfaces, $f_0, f_1, \ldots, f_m$, are tangent to each other at the contact point P as shown in Fig. 5.19. We have the following mathematical relationship from Eq. (5.45):

$$\frac{\sigma_{ij} - \alpha_{ij}^{(0)}}{k^{(0)}} = \frac{\sigma_{ij} - \alpha_{ij}^{(1)}}{k^{(1)}} = \cdots = \frac{\sigma_{ij} - \alpha_{ij}^{(m)}}{k^{(m)}} \tag{5.46}$$

If the stress increment $d\sigma_{ij}$ is further applied at the point P on the yield surface, f_m, such that $d\sigma_{ij}$ points out of the yield surface, the plastic strain increments, $d\epsilon_{ij}^p$, are given by Eq. (5.44) which uses the hardening modulus $H' = H'_m$ associated with the outermost yield surface, f_m. The hardening modulus H'_m may take the constant value for each surface, f_m, or the form which is a function of the plastic strain, ϵ_{ij}^p. The original nested yield surface model proposed by Mróz (1967) has constant hardening modulus, H'_m, determined from a simple test.

To describe mathematically the motion of the m-th yield surface, let us consider again a typical situation as shown in Fig. 5.19. Two similar surfaces f_m and f_{m+1}

have their centers denoted by the vectors $\alpha_{ij}^{(m)}$ and $\alpha_{ij}^{(m+1)}$ from the origin in the stress space. These yield functions are expressed by:

$$f_m\left[\sigma_{ij} \quad \alpha_{ij}^{(m)},\ k^{(m)}\right] = 0 \tag{5.47}$$

$$f_{m+1}\left[\sigma_{ij} \quad \alpha_{ij}^{(m+1)},\ k^{(m+1)}\right] = 0 \tag{5.48}$$

If the stress point P lies on the surface f_m as shown in Fig. 5.19, the instantaneous translation of f_m associated with the stress increment, $d\sigma_{ij}$, will occur along PR where R is a point on the yield surface f_{m+1} corresponding to the same direction of outward normal as that at the point P on the surface f_m. Denoting the states of stress at P and R by $\sigma_{ij}^{(m)}$ and $\sigma_{ij}^{(m+1)}$ respectively, we have the following relationship from Eq. (5.46):

$$\sigma_{ij}^{(m+1)} \quad \alpha_{ij}^{(m+1)} \quad \frac{k^{(m+1)}}{k^{(m)}}\left[\sigma_{ij}^{(m)} \quad \alpha_{ij}^{(m)}\right] \tag{5.49}$$

Assuming now the translation of yield surface, f_m, denoted by $d\alpha_{ij}^{(m)} = d\mu\ \mu_{ij}$ where μ_{ij} is expressed by the tensor, $[\sigma_{ij}^{(m+1)} - \sigma_{ij}^{(m)}]$, we find from Eq. (5.49):

$$d\alpha_{ij}^{(m)} = \frac{d\mu}{k^{(m)}}\left[\left\{k^{(m+1)} - k^{(m)}\right\}\sigma_{ij}^{(m)} - \left\{\alpha_{ij}^{(m)}k^{(m+1)} - \alpha_{ij}^{(m+1)}k^{(m)}\right\}\right] \tag{5.50}$$

For the special case when the centers of the two surfaces are identical, that is, $\alpha_{ij}^{(m)} \quad \alpha_{ij}^{(m+1)}$, Eq. (5.50) reduces to:

$$d\alpha_{ij}^{(m)} = d\mu \frac{k^{(m+1)} \quad k^{(m)}}{k^{(m)}}\left[\sigma_{ij}^{(m)} - \alpha_{ij}^{(m)}\right] \tag{5.51}$$

It follows that the instantaneous translation is identical to the rule proposed by Ziegler (1959), i.e., along the vector connecting the center of the yield surface with the current stress point. The magnitude of $d\mu$ is determined from the *consistency condition* that the current stress point remains on the subsequent yield surface, i.e., $df_m \quad 0$. Thus:

$$df_m \quad \frac{\partial f_m}{\partial \sigma_{ij}}\left[d\sigma_{ij} \quad d\alpha_{ij}^{(m)}\right] \quad 0 \tag{5.52}$$

Substituting $d\alpha_{ij}^{(m)} = d\mu[\sigma_{ij}^{(m+1)} \quad \sigma_{ij}^{(m)}]$ into Eq. (5.52), we find:

$$d\mu = \frac{(\partial f_m/\partial \sigma_{ij})\, d\sigma_{ij}}{(\partial f_m/\partial \sigma_{kl})\left[\sigma_{kl}^{(m+1)} - \sigma_{kl}^{(m)}\right]} \tag{5.53}$$

5.7 GENERALIZED MULTI-SURFACE MODELS

The original Mróz model can further be extended and generalized by assuming that each surface with constant hardening modulus is allowed to expand or contract. This means that $k^{(m)}$ is not constant but a function of a scalar parameter which is the length of a plastic strain trajectory monotonically increasing in the course of plastic deformation. A scalar parameter ξ is written as:

$$\xi = \int \left(d\epsilon_{ij}^{p} \, d\epsilon_{ij}^{p} \right)^{1/2} \tag{5.54}$$

It follows from the experimental fact that the initial yield surface f_0 enclosing the elastic region contracts during the plastic deformation process, while the yield surface with small hardening modulus expands. The *generalized multi-surface plasticity models* proposed by Prévost (1977, 1978) will be explained in some details in the following.

Prévost models

Prévost (1977, 1978) developed two anisotropic strain-hardening or softening models: (1) the *undrained* or *hydrostatic pressure-nonsensitive model*, and (2) the *drained* or *hydrostatic pressure-sensitive model*, extending the original Mróz model. The undrained model, which is based on the von Mises type of nested yield surfaces with the associated flow rule, is defined completely in the deviatoric stress space, and it is independent of the hydrostatic pressure (or mean effective normal stress). On the other hand, the drained or hydrostatic pressure-sensitive model, which has many characteristics common to the extended von Mises (or Drucker-Prager) and the modified Cam-clay models (see Section 6.3 in Chapter 6), takes into consideration the effect of hydrostatic pressure and its flow rule is a non-associated type on all the surfaces except on the outermost surface where the associated type is employed.

In the following, two types of plasticity models will be explained.

Undrained model

This model has been developed for the undrained behavior of clays under monotonic and cyclic loading conditions. Prévost (1977) utilized the von Mises types of multi-surfaces whose functions are expressed as follows:

$$f_m = \tfrac{1}{2} \left[s_{ij} - \beta_{ij}^{(m)} \right] \left[s_{ij} - \beta_{ij}^{(m)} \right] - \left[k^{(m)} \right]^2 = 0 \tag{5.55}$$

where s_{ij} is the deviatoric stress tensor, $k^{(m)}$ is the size of the yield surface and $\beta_{ij}^{(m)}$ is the deviatoric stress coordinate of its center which is usually given by $\beta_{ij}^{(m)} = \alpha_{ij}^{(m)} - \frac{1}{3}\alpha_{kk}^{(m)}\delta_{ij}$ where $\alpha_{ij}^{(m)}$ is the center coordinate corresponding to the general stress tensor σ_{ij}. Equation (5.55) presents a circle on the deviatoric plane with its center defined by the deviatoric stress coordinates $\beta_{ij}^{(m)}$.

In general, the circle has been displaced from the origin of the stress space, as

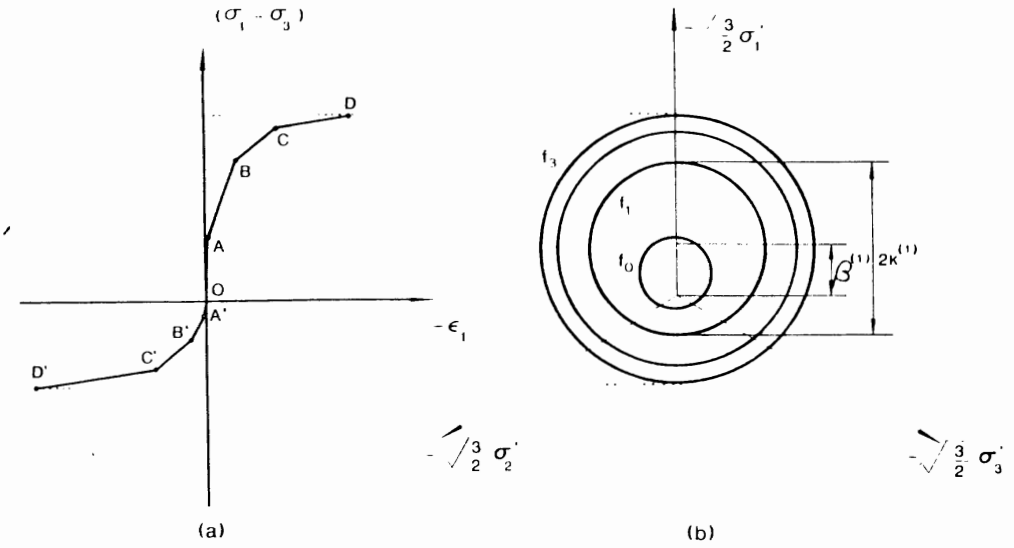

Fig. 5.20. Relationship between uniaxial stress-strain curve and initially located multi-surfaces on deviatoric plane: (a) discretized uniaxial stress-strain relation; (b) multi-surfaces on deviatoric plane.

shown in Fig. 5.19. If the center of all the yield surfaces is located at the origin, the soil is said *initially isotropic*. However, in most practical cases, soils are under K_0-conditions where only three principal stresses σ_1 and $\sigma_2 = \sigma_3$ are acting. Therefore, the initial location of each yield surface of undrained model for such K_0-consolidated soil is determined from the undrained stress-strain curves obtained in both triaxial compression and extension tests (Fig. 5.20a). These experimental stress-strain curves are replaced by linear segments along which the tangent modulus is constant. Although segments with the same slope exist in both the compression and extension regions, the behavior in both is different due to K_0-consolidation. The von Mises type of yield surfaces which delimit regions with similar mechanical properties are shown on the deviatoric plane in Fig. 5.20b. Note that the scale has been increased by the factor $\sqrt{3/2}$ for a simple comparison. The parameters $\beta_{ij}^{(m)}$ and $k^{(m)}$ corresponding to each yield surface are easily determined in the following manner:

In a triaxial test, the deviatoric stresses are s_{11}, $s_{22} = s_{33}$, and $s_{ij} = 0$ for $i \neq j$. Therefore, defining $q = \sigma_{11} - \sigma_{33}$, these are respectively represented by:

$$s_{11} - \sigma_{33} = \tfrac{2}{3}q \tag{5.56a}$$

$$s_{22} = s_{33} = -\tfrac{1}{3}q \tag{5.56b}$$

Noting that $\beta_{11}^{(m)}$, $\beta_{22}^{(m)} = \beta_{33}^{(m)} = -\frac{1}{2}\beta_{11}^{(m)}$ and substituting Eqs. (5.56a) and (5.56b) into Eq. (5.55), the yield function f_m is written as:

$$q - \tfrac{3}{2}\beta_{11}^{(m)} = \pm k^{(m)} \tag{5.57}$$

Consider, for example, the yield surface f_2 corresponding to the points C and C′ in Fig. 5.20a, stress difference q in Eq. (5.57) is respectively given by:

$$q_c = \tfrac{3}{2}\beta_{11}^{(2)} - k^{(2)} \quad \text{(compression negative)} \tag{5.58a}$$

and

$$q_{c'} = \tfrac{3}{2}\beta_{11}^{(2)} + k^{(2)} \quad \text{(tension positive)} \tag{5.58b}$$

Solving Eqs. (5.58a) and (5.58b) with respect to $\beta_{11}^{(2)}$ and $k^{(2)}$:

$$\beta_{11}^{(2)} = \tfrac{1}{3}(q_c + q_{c'}) \tag{5.59a}$$

and

$$k^{(2)} = \tfrac{1}{2}(q_{c'} - q_c) \tag{5.59b}$$

From Eq. (5.59a), the coordinate of $\beta_{22}^{(2)} = \beta_{33}^{(2)}$ is also found:

$$\beta_{22}^{(2)} = \beta_{33}^{(2)} = -\tfrac{1}{6}(q_c + q_{c'}) \tag{5.60}$$

Repeating this in a similar manner, the locations and sizes for all yield surfaces can be initialized, and then the model can be applied for the predictions of soils under various cyclic triaxial tests.

The generalized model assumes that the radius size $k^{(m)}$ and the hardening modulus H'_m are functions of the scalar parameter ξ, which monotonically increases in the course of plastic deformation, being defined in a similar manner to Eq. (5.54) as:

$$\xi = \int \left(\tfrac{2}{3} \mathrm{d}e_{ij}^{\mathrm{p}}\, \mathrm{d}e_{ij}^{\mathrm{p}}\right)^{1/2} \tag{5.61}$$

where $\mathrm{d}e_{ij}^{\mathrm{p}}$ are the plastic deviatoric strain increments. According to Prévost (1978), variations in H'_m usually occur only once large values of ξ have been reached, whereas the $k^{(m)}$ functions usually start to vary upon the first loading reversal.

In this model development, the rule used to govern the translation of the multi-surfaces during plastic loading is still that suggested by Mróz (1967), but a simultaneous isotropic hardening (or softening) is allowed. The kinematic rule leads to a different expression of parameter $\mathrm{d}\mu$ from Eq. (5.53). From the consistency condition of Eq. (5.55), $\mathrm{d}f_m = 0$, we obtain:

$$\mathrm{d}f_m = \frac{\partial f_m}{\partial s_{ij}} \mathrm{d}s_{ij} + \frac{\partial f_m}{\partial \beta_{ij}^{(m)}} \mathrm{d}\beta_{ij}^{(m)} + \frac{\partial f_m}{\partial k^{(m)}} \mathrm{d}k^{(m)} = 0 \tag{5.62}$$

Substituting now $d\beta_{ij}^{(m)} = d\mu\, \mu_{ij}$ where μ_{ij} is expressed as $[s_{ij}^{(m+1)} - s_{ij}^{(m)}]$, and $\partial f_m/\partial \beta_{ij} = -\partial f_m/\partial s_{ij}$, we find $d\mu$ written as:

$$d\mu = \frac{(\partial f_m/\partial s_{ij})\, ds_{ij} + (\partial f_m/\partial k^{(m)})\, dk^{(m)}}{(\partial f_m/\partial s_{pq})\mu_{pq}} \tag{5.63}$$

After substitution of Eq. (5.55) and a rigorous arrangement, we can simplify Eq. (5.63) to:

$$d\mu = \frac{\frac{3}{2}\left[s_{ij} - \beta_{ij}^{(m)}\right] ds_{ij} - k^{(m)}\, dk^{(m)}}{k^{(m+1)}k^{(m)} - \frac{3}{2}\left[s_{pq} - \beta_{pq}^{(m+1)}\right]\left[s_{pq} - \beta_{pq}^{(m)}\right]} \tag{5.64}$$

where $dk^{(m)}$ is estimated by utilizing the plastic strain increments $d\epsilon_{ij}^{p}$ which are calculated by the flow rule associated with the hardening modulus H_m', for the stress increments, $d\sigma_{ij}$.

This model has been adopted by Prévost et al. (1981) in the finite-element analyses of soil structure interaction of centrifugal models under both monotonic and cyclic loadings simulating the situation encountered in the analysis of offshore gravity structure foundations under wave forces. The results obtained from the analysis agree quite well with those measured experimentally in the centrifuge. This study has demonstrated the ability of the multi-surface model to provide realistic representation of soil behavior under complex loadings.

Drained model

Prévost (1978) has also extended the idea of multi-surface plasticity model for undrained conditions to that for drained conditions, by taking into consideration the effect of hydrostatic pressure, $\frac{1}{3} I_1$, as well as the deviatoric stress s_{ij} on the yielding of soils. The yield function for the m-th yield surface has the following form:

$$f_m = \frac{3}{2}\left[s_{ij} - \beta_{ij}^{(m)}\right]\left[s_{ij} - \beta_{ij}^{(m)}\right] + C^2\left[\frac{1}{3} I_1 - \gamma^{(m)}\right]^2 - \left[k^{(m)}\right]^2 = 0 \tag{5.65}$$

where $\gamma^{(m)} = \frac{1}{3}\alpha_{kk}^{(m)}$ is the center of the yield surface along the hydrostatic axis, and C is a material parameter which is usually taken to be $3/\sqrt{2}$. As a special case, the yield function f_m can be reduced to that under the stress condition in triaxial test:

$$f_m = \left[q - \frac{3}{2}\beta_{11}^{(m)}\right]^2 + C^2\left[p - \gamma^{(m)}\right]^2 - \left[k^{(m)}\right]^2 = 0 \tag{5.66}$$

where $p = \frac{1}{3} I_1$ and $q = \sigma_1 - \sigma_3$. The quantities $\frac{3}{2}\beta_{11}^{(m)}$ and $\gamma^{(m)}$ are the center coordinates of the elliptic surfaces in the $p - q$ plane. A schematic view is shown in Fig. 5.21.

It is assumed in this model that the hardening modulus H_m' and the current size of yield surface, $k^{(m)}$, are functions of the plastic volumetric strains ϵ_v^p ($= \epsilon_{11}^p + \epsilon_{22}^p$

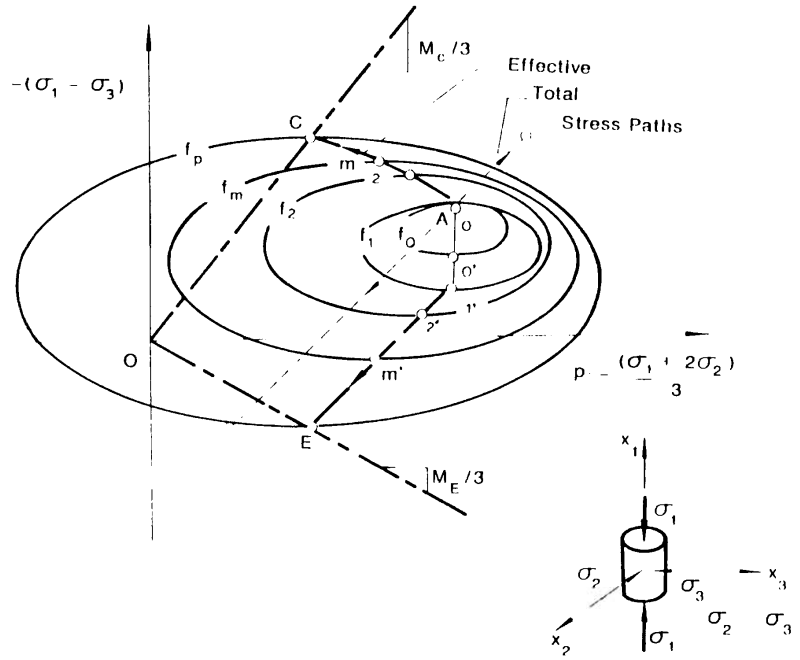

Fig. 5.21. Multi-surfaces in triaxial plane (Prévost, 1978).

$+\epsilon_{ij}^p$) or the plastic shear distortions ξ in Eq. (5.61), or both, in order to use a combination of the isotropic and new kinematic strain-hardening rules where each yield surface is allowed to translate in stress space by the stress point and to change in size simultaneously. Non-associated flow rule is employed for the inner yield surfaces, whereas the associated flow rule is taken for the outermost yield surface.

Plastic potential function

The plastic potential function, g_m, associated with f_m is made from the experimental facts such that the vector of plastic deviatoric strain increments becomes normal to the projection of the yield surface onto the deviatoric stress space. According to the expression by Prévost (1978), the vectors $\partial f_m/\partial \sigma_{ij}$ and $\partial g_m/\partial \sigma_{ij}$ are respectively decomposed into the hydrostatic stress axis and the deviatoric stress space, that is:

$$\frac{\partial f_m}{\partial \sigma_{ij}} = Q'^{(m)}_{ij} + Q''^{(m)}\delta_{ij} \tag{5.67}$$

$$\frac{\partial g_m}{\partial \sigma_{ij}} = P'^{(m)}_{ij} + P''^{(m)}\delta_{ij} \tag{5.68}$$

where $P'^{(m)}_{ij}$, $Q'^{(m)}_{ij}$ are their projections onto the deviatoric stress space, and $P''^{(m)}$, $Q''^{(m)}$ are those along the hydrostatic axis. The following relationship can be made:

$$P'^{(m)}_{ij} = Q'^{(m)}_{ij} \tag{5.69}$$

As for $P''^{(m)}$, it is conveniently taken as a function of both $\left|Q'^{(m)}_{ij}\right| = (Q'^{(m)}_{ij}Q'^{(m)}_{ij})^{1/2}$ and $Q''^{(m)}$, that is:

$$P''^{(m)} = Q''^{(m)} + A_m\left|Q'^{(m)}_{ij}\right| \tag{5.70}$$

where $A_m = [\gamma^{(m)} - \gamma^{(p)}]a_m$, and $\gamma^{(p)}$ is the center of the outermost yield surface f_p along the hydrostatic axis, and a_m is a material parameter determined from the experiments. Since A_m becomes zero, the associated flow rule is thus employed on the outermost surface, f_p.

Hardening modulus

We shall now explain the characteristics of the hardening modulus H'_m. Substitution of Eqs. (5.67) and (5.68) into the non-associated flow rule equation leads to the following expression for the plastic strain increment written as:

$$\mathrm{d}\epsilon^{\mathrm{p}}_{ij} = \frac{1}{H'_m}\left[Q'^{(m)}_{kl}\,\mathrm{d}s_{kl} + Q''^{(m)}\,\mathrm{d}I_1\right]\left[P'^{(m)}_{ij} + P''^{(m)}\delta_{ij}\right] \tag{5.71}$$

Further, the plastic strain increments in Eq. (5.71) can be decomposed into two parts: the plastic volumetric strain $\mathrm{d}\epsilon^{\mathrm{p}}_v$ and the plastic deviatoric strain $\mathrm{d}e^{\mathrm{p}}_{ij}$ such as:

$$\mathrm{d}\epsilon^{\mathrm{p}}_v = \frac{3}{H'_m}\left[Q'^{(m)}_{kl}\,\mathrm{d}s_{kl} + Q''^{(m)}\,\mathrm{d}I_1\right]P''^{(m)} \tag{5.72}$$

$$\mathrm{d}e^{\mathrm{p}}_{ij} = \frac{1}{H'_m}\left[Q'^{(m)}_{kl}\,\mathrm{d}s_{kl} + Q''^{(m)}\,\mathrm{d}I_1\right]P'^{(m)}_{ij} \tag{5.73}$$

The hardening modulus H'_m can be reduced to the important indices when $Q'^{(m)}_{ij}$ or $Q''^{(m)}$ is respectively identical to zero. When $Q'^{(m)}_{ij} = 0$, the hardening modulus, H'_m, then plays the role of the *plastic bulk modulus*, and from Eq. (5.72) we obtain:

$$H'_m = 3Q''^{(m)}P''^{(m)}\frac{\mathrm{d}I_1}{\mathrm{d}\epsilon^{\mathrm{p}}_v} \tag{5.74}$$

when $Q''^{(m)} = 0$, H'_m then plays the role of the *plastic shear modulus*, and from Eq. (5.73) we find:

$$H'_m = \frac{\left|P'^{(m)}_{ij}\right|}{(\mathrm{d}e^{\mathrm{p}}_{ij}\,\mathrm{d}e^{\mathrm{p}}_{ij})^{1/2}}Q'^{(m)}_{kl}\,\mathrm{d}s_{kl} \tag{5.75}$$

Prévost (1978) assumed that in general case, H'_m has the combined form of the plastic bulk modulus and plastic shear modulus, and its value varies along the yield surface, f_m.

As for the outermost surface, f_p, whose size, position, and movement are functions of the current plastic volumetric strain, that is:

$$k^{(p)} = k^{(p)}(\epsilon_v^p) \tag{5.76a}$$

$$d\beta_{ij}^{(p)} = dk^{(p)} a_{ij} \tag{5.76b}$$

$$d\gamma^{(p)} = dk^{(p)} b \tag{5.76c}$$

where a_{ij}, b are determined from experimental test results, the hardening modulus H'_p for the outermost surface f_p can be calculated from the consistency condition and it follows that H'_p varies along the yield surface, f_p, with the value of $\partial f_p / \partial p$.

Since the hardening modulus H'_m varies in general along the yield surface, from the requirement of consistency condition, experimental observation such as "*consolidation*", "*dilatant*", and "*critical state*" can be explained particularly on the outermost surface which plays the role of a failure surface, according to the conditions of hardening modulus such as $H'_p > 0$, $H'_p < 0$ and $H'_p = 0$.

Theoretical interpretation of this model is given in detail by Prévost (1978) for the case of undrained axial soil tests and consolidation tests.

Hardening rule

We shall explain now the hardening rule proposed by Prévost (1978) in some details. As mentioned above, the nested yield surfaces should move in the stress space in order not to overlap the outer yield surface. Referring to Fig. 5.22, let R denote the point on the yield surface, f_{m+1} at which the direction of normal vector is the same as that at the point P where the current state of stress lies. The vector μ_{ij}

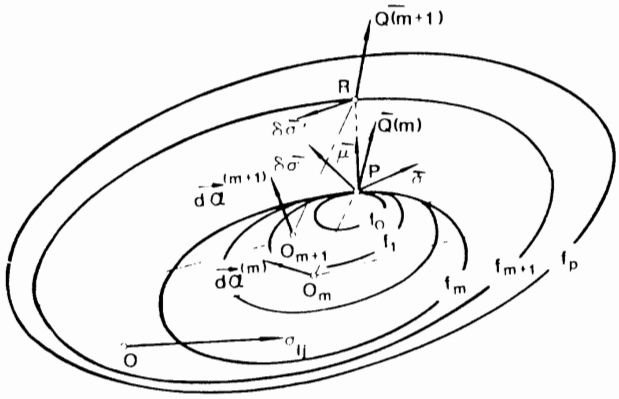

Fig. 5.22. Field of yield surfaces in stress space — hardening rule (Prévost, 1978).

connecting the points between P and R is written from the homogeneity of the function as:

$$\mu_{ij} = \frac{k^{(m+1)}}{k^{(m)}}\left[s_{ij} - \beta_{ij}^{(m)}\right] - \left[s_{ij} - \beta_{ij}^{(m+1)}\right]$$

$$+ \left[\frac{k^{(m+1)}}{k^{(m)}}\left\{\tfrac{1}{3}I_1 \quad \gamma^{(m)}\right\} \quad \left\{\tfrac{1}{3}I_1 \quad \gamma^{(m+1)}\right\}\right]\delta_{ij} \tag{5.77}$$

Let $\delta\sigma_{ij}$ and $\delta\sigma'_{ij}$ denote the increments of motions in stress space of points, P and R. The increments, $\delta\sigma_{ij}$ and $\delta\sigma'_{ij}$, which are decomposed into the deviatoric stresses δs_{ij}, $\delta s'_{ij}$ and hydrostatic pressures $\frac{1}{3}\delta I_1$, $\frac{1}{3}\delta I'_1$, can be obtained from the consistency condition $\mathrm{d}f_m = 0$, that is:

$$\delta\sigma_{ij} \quad \delta s_{ij} + \tfrac{1}{3}\delta I_1\delta_{ij}$$

$$= \mathrm{d}\beta_{ij}^{(m)} + \mathrm{d}\gamma^{(m)}\delta_{ij} + 2k^{(m)}\,\mathrm{d}k^{(m)}Q_{ij}^{(m)}/\left|Q_{kl}^{(m)}\right|^2 \tag{5.78}$$

$$\delta\sigma'_{ij} \quad \delta s'_{ij} + \tfrac{1}{3}\delta I'_1\delta_{ij}$$

$$\mathrm{d}\beta_{ij}^{(m+1)} + \mathrm{d}\gamma^{(m+1)}\delta_{ij} + 2k^{(m+1)}\,\mathrm{d}k^{(m+1)}Q_{ij}^{(m)}/\left|Q_{kl}^{(m)}\right|\left|Q_{pq}^{(m+1)}\right| \tag{5.79}$$

where $Q_{ij}^{(m)}$ is expressed by:

$$Q_{ij}^{(m)} = \frac{\partial f_m}{\partial\sigma_{ij}} = 3\left[s_{ij} - \beta_{ij}^{(m)}\right] + 3\left[\tfrac{1}{3}I_1 - \gamma^{(m)}\right]\delta_{ij} \tag{5.80}$$

since C' is now $3/\sqrt{2}$.
In order to avoid the overlapping of the surfaces, instantaneous translation, $\mathrm{d}\alpha_{ij}^{(m)}$, $\mathrm{d}\alpha_{ij}^{(m+1)}$ denoted by $\mathrm{d}\beta_{ij}^{(m)} + \mathrm{d}\gamma^{(m)}\delta_{ij}$, $\mathrm{d}\beta_{ij}^{(m+1)} + \mathrm{d}\gamma^{(m+1)}\delta_{ij}$, must satisfy the condition such as:

$$\delta\sigma_{ij} \quad \delta\sigma'_{ij} + \delta\mu\,\mu_{ij} \tag{5.81}$$

In this case, the surfaces, f_m and f_{m+1}, can move each other along $\overline{\mathrm{PR}}$. Substituting Eqs. (5.78) and (5.79) into Eq. (5.81), we finally get:

$$\mathrm{d}\alpha_{ij}^{(m)} - \mathrm{d}\alpha_{ij}^{(m+1)} = 2\left|\frac{k^{(m+1)}}{\left|Q_{ij}^{(m+1)}\right|}\mathrm{d}k^{(m+1)} - \frac{k^{(m)}}{\left|Q_{ij}^{(m)}\right|}\mathrm{d}k^{(m)}\right|\frac{Q_{ij}^{(m)}}{\left|Q_{ij}^{(m)}\right|} + \delta\mu\,\mu_{ij} \tag{5.82}$$

where the parameter, $\delta\mu$, is obtained from Eq. (5.81) as:

$$\delta\mu = \frac{Q_{kl}^{(m)}(\delta\sigma_{kl} - \delta\sigma'_{kl})}{Q_{rs}^{(m)}\mu_{rs}} \tag{5.83}$$

However, the quantity of $\delta\mu$ is not known unless the magnitudes of $d\alpha_{ij}^{(m)}$ and $d\alpha_{ij}^{(m+1)}$ are evaluated. In what follows, we shall refer to the kinematic rule proposed by Prévost (1978). He adopted the following kinematic rule to describe the drained soil behavior:

$$d\alpha_{ij}^{(m)} = d\beta_{ij}^{(m)} + d\gamma^{(m)}\delta_{ij} = d\eta\,\mu'_{ij} + d\gamma^{(m)}\delta_{ij} \tag{5.84}$$

where $d\eta$ is a scalar, μ'_{ij} is the projection of the vector μ_{ij} onto the deviatoric plane, and $d\gamma^{(m)}$ is selected so that the projections onto the hydrostatic axis of the translation-increment $\delta\sigma_{ij}$ and of the stress-increment $d\sigma_{ij}$ at the point P are the same. Thus, from the consistency condition, we have:

$$d\gamma^{(m)} = \tfrac{1}{3}dI_1 - 2k^{(m)}\,dk^{(m)}Q'^{(m)}/\left|Q_{ij}^{(m)}\right|^2 \tag{5.85}$$

and further substitution of Eq. (5.85) and $d\beta_{ij}^{(m)} = d\eta\,\mu'_{ij}$ into the consistency condition leads to:

$$d\beta_{ij}^{(m)} = \frac{Q_{kl}^{\prime(m)}\,ds_{kl} - 2k^{(m)}\,dk^{(m)}\left|Q_{ij}^{\prime(m)}\right|^2/\left|Q_{ij}^{(m)}\right|^2}{Q_{rs}^{\prime(m)}\mu'_{rs}}\,\mu'_{ij} \tag{5.86}$$

where μ'_{ij} is expressed from Eq. (5.77) by:

$$\mu'_{ij} = \frac{k^{(m+1)}}{k^{(m)}}\left[s_{ij} - \beta_{ij}^{(m)}\right] - \left[s_{ij} - \beta_{ij}^{(m+1)}\right] \tag{5.87}$$

For the special case when $P'^{(m)} = Q'^{(m)} = \gamma^{(m)} = 0$, the kinematic rule is reduced to that of the undrained model discussed previously. Also, when $dk^{(m)} = dk^{(m+1)} = 0$, it is reduced to the case of the purely kinematic hardening.

5.8 BOUNDING SURFACE MODELS

Nested yield surface models discussed in the previous Section may be capable of representing anisotropic behavior of soils which can not be described by the classical plasticity models. However, the necessity to define, renew and keep in memory each yield surface in the model may make the computer implementation of the model more complicated and also expensive. In what follows, the alternative anisotropic plasticity models such as *two-surface models* are briefly reviewed.

Two-surface models

Extending a number of observations on the macroscopic behavior of metals subjected to uniaxial random cyclic loading, Dafalias and Popov (1975) have constructed a *bounding surface model* to describe the material behavior for complex multi-axial loadings, especially for cyclic loadings. This model consists of a *bounding surface* and *loading surface*, as shown schematically in Fig. 5.23a. The bounding surface always encloses the loading surface inside which only the elastic behavior is observed, and it is ordinarily taken congruent to the loading surface. The loading surface is defined as:

$$f(\sigma_{ij} - \alpha_{ij}, q_n) = 0 \tag{5.88}$$

where α_{ij} are the center coordinates of the loading surface represented as Point k in Fig. 5.23a and q_n are the plastic internal variables (PIV) such as the plastic strain. The loading surface is allowed to translate as well as to deform under any hardening rule assumed appropriately, and it may contact the bounding surface, but not intersect it. Within the framework of the associated flow rule assumption, the generalized hardening modulus H' related to the loading surface is given by:

$$H' = H'(\delta, W_p) \tag{5.89}$$

where the δ is the distance (usually measured in Euclidean metric) between the current stress state σ_{ij} represented as point a on the loading surface and the stress state $\bar{\sigma}_{ij}$ at the point b which is obtained by the intersection of the line $\overline{ka}$ with the bounding surface as shown in Fig. 5.23a, and W_p is the plastic work which is integrated in the plastic strain space along the loading path during the plastic deformation prior to the elastic deformation preceding the current plastic state.

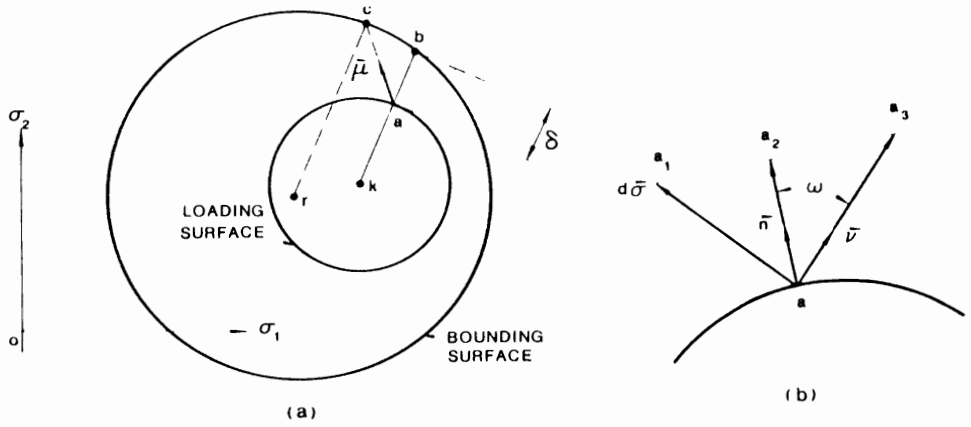

Fig. 5.23. Schematic representation of a loading and a bounding surface and illustration of their motions (Dafalias and Popov, 1975).

Plastic hardening modulus on the loading surface is assumed to vary depending on the relative configuration of the loading and bounding surfaces. This is an important assumption that distinguishes the present formulation from the previous multi-surface models.

On the other hand, the bounding surface is defined as the homogeneous function of the form:

$$F(\sigma_{ij} - \alpha^*_{ij},\ q_n) = 0 \tag{5.90}$$

where α^*_{ij} are the center coordinates of point r for the bounding surface. The bounding surface translates in the stress space, following the rule given by:

$$\mathrm{d}\alpha^*_{ij} = \frac{\mathrm{d}\sigma}{\cos\omega} n_{ij} - (1 - H'_0/H')\,\mathrm{d}\sigma\,\mu_{ij} \tag{5.91}$$

where $\mathrm{d}\alpha^*_{ij}$ is the increment of the center translation of the bounding surface, $(\mathrm{d}\sigma/\cos\omega)n_{ij}$ represents the increment of point a in the direction of the unit vector n_{ij} due to the translation of the loading surface, H'_0 hardening modulus for contact with $\delta = 0$, $\mathrm{d}\sigma$ the projection of $\mathrm{d}\sigma_{ij}$ onto the normal vector n_{ij} at point a, and μ_{ij} the unit vector along points a and c at which the normal vectors are identical (see Fig. 5.23a). Note that if the loading surface moves as a rigid body, the first term $(\mathrm{d}\sigma/\cos\omega)n_{ij}$ in Eq. (5.91) becomes identical to the incremental translation $\mathrm{d}\alpha_{ij}$ of the center of the loading surface. Further, if the two surfaces come in contact, $H' = H'_0$, they move together at the same rate, that is:

$$\mathrm{d}\alpha^*_{ij} = \mathrm{d}\alpha_{ij} \tag{5.92}$$

Hardening rules

As a special case, if the Prager's kinematic rule is incorporated into this model, $\mathrm{d}\alpha_{ij}$ can be represented as:

$$\mathrm{d}\alpha_{ij} = c\,\mathrm{d}\epsilon^p_{ij} \tag{5.93}$$

where c is the material parameter. Using $\partial f/\partial\alpha_{ij} = -(\partial f/\partial\sigma_{ij})$, Eqs. (5.44) and (5.93), the consistency condition $\mathrm{d}f = 0$ becomes:

$$\begin{aligned}\mathrm{d}f &= \frac{\partial f}{\partial\sigma_{ij}}\mathrm{d}\sigma_{ij} + \frac{\partial f}{\partial\alpha_{ij}}\mathrm{d}\alpha_{ij} \\ &= \frac{\partial f}{\partial\sigma_{ij}}\mathrm{d}\sigma_{ij} - \frac{\partial f}{\partial\sigma_{ij}} c \frac{1}{H'}\left(\frac{\partial f}{\partial\sigma_{mn}}\mathrm{d}\sigma_{mn}\right)\frac{\partial f}{\partial\sigma_{ij}} = 0\end{aligned} \tag{5.94}$$

Equation (5.94) leads to:

$$c = \frac{H'}{(\partial f/\partial \sigma_{ij})(\partial f/\partial \sigma_{ij})} \tag{5.95}$$

Using Eq. (5.44) and substituting Eq. (5.95) into Eq. (5.93), we obtain:

$$d\alpha_{ij} = c\, d\epsilon^{p}_{ij} = c\, \frac{1}{H'} \left(\frac{\partial f}{\partial \sigma_{mn}} d\sigma_{mn} \right) \frac{\partial f}{\partial \sigma_{ij}}$$

$$- \frac{(\partial f/\partial \sigma_{mn})\, d\sigma_{mn}}{\left[(\partial f/\partial \sigma_{kl})(\partial f/\partial \sigma_{kl})\right]^{1/2}} \frac{(\partial f/\partial \sigma_{ij})}{\left[(\partial f/\partial \sigma_{rs})(\partial f/\partial \sigma_{rs})\right]^{1/2}} \tag{5.96}$$

Noting that $(\partial f/\partial \sigma_{mn})/[(\partial f/\partial \sigma_{kl})(\partial f/\partial \sigma_{kl})]^{1/2}$ is the unit normal n_{mn}, Eq. (5.96) can be written as:

$$d\alpha_{ij} = n_{mn}\, d\sigma_{mn} n_{ij} = d\sigma\, n_{ij} \tag{5.97}$$

Since $\nu_{ij} = n_{ij}$, $\omega = 0$ for the Prager's kinematic hardening rule, $d\alpha^{*}_{ij}$ in Eq. (5.91) becomes:

$$d\alpha^{*}_{ij} = d\sigma\, n_{ij} - d\sigma \left(1 - \frac{H'_0}{H'}\right) \mu_{ij} = d\alpha_{ij} - d\sigma \left(1 - \frac{H'_0}{H'}\right) \mu_{ij} \tag{5.98}$$

In this case, the translation increment $d\alpha^{*}_{ij}$ of the bounding surface is described by incorporating into the Prager's hardening rule.

If the Ziegler's kinematic hardening rule is used in this model, $d\alpha_{ij}$ can be written as:

$$d\alpha_{ij} = d\mu(\sigma_{ij} - \alpha_{ij}) \tag{5.99}$$

where $d\mu$ is the proportionality factor. Referring to Fig. 5.24, we have:

$$\sigma_{ij} - \alpha_{ij} = \rho u_{ij} \tag{5.100}$$

where u_{ij} is the unit vector along the $\overline{ka}$ and ρ is the distance between the points k and a. Therefore, Eq. (5.99) is represented by:

$$d\alpha_{ij} = d\mu\, \rho\, u_{ij} \tag{5.101}$$

In a similar manner to that of the Prager's case, the consistency condition $df = 0$ becomes:

$$df = \frac{\partial f}{\partial \sigma_{ij}} d\sigma_{ij} - \frac{\partial f}{\partial \alpha_{ij}} d\mu\, \rho\, u_{ij} = 0 \tag{5.102}$$

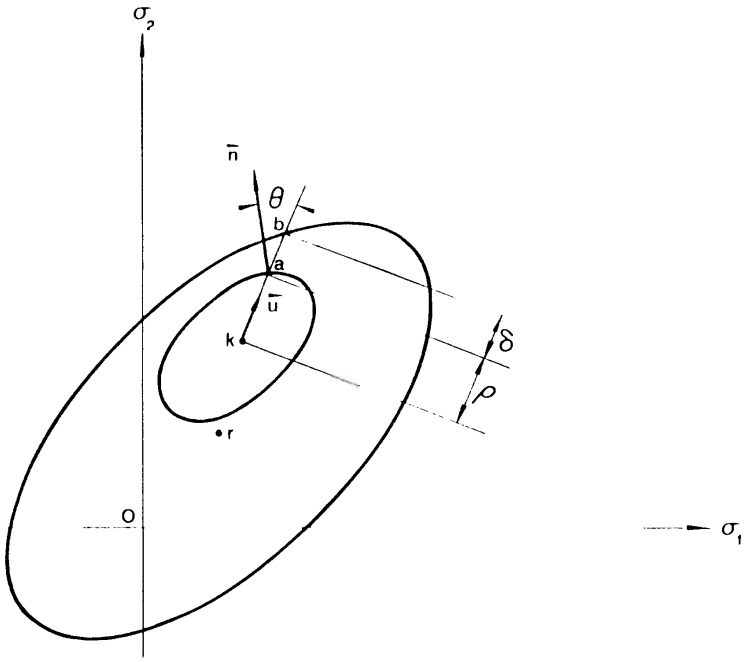

Fig. 5.24. Schematic representation of the loading and bounding surfaces for Ziegler's model (Dafalias and Popov, 1975).

Equation (5.102) yields:

$$d\mu = \frac{(\partial f/\partial \sigma_{ij})\, d\sigma_{ij}}{\rho(\partial f/\partial \sigma_{kl}) u_{kl}} \tag{5.103}$$

or using the unit normal n_{ij}:

$$d\mu = \frac{n_{ij}\, d\sigma_{ij}}{\rho n_{kl} u_{kl}} \tag{5.104}$$

Noting $n_{ij}\, d\sigma_{ij} = d\sigma$, $n_{kl}u_{kl} = \cos\theta$ (see Fig. 5.24), $d\alpha_{ij}$ in Eq. (5.101) becomes:

$$d\alpha_{ij} = \frac{d\sigma}{\cos\theta} u_{ij} \tag{5.105}$$

Substitution of $r_{ij} = u_{ij}$ and $\omega = \theta$ into $d\alpha^*_{ij}$ in Eq. (5.91) leads to:

$$d\alpha^*_{ij} = \frac{d\sigma}{\cos\theta} u_{ij} - d\sigma\left(1 - \frac{H'_0}{H'}\right)\mu_{ij} = d\alpha_{ij} - d\sigma\left(1 - \frac{H'_0}{H'}\right)\mu_{ij} \tag{5.106}$$

As can be understood from the above discussion, any kinematic and deformation law for the loading surface may be assumed in the general development of the bounding surface model proposed by Dafalias and Popov (1975).

Two-surface models for soils

Much simpler models of anisotropic strain-hardening plasticity have been recently developed for soils based on the bounding surface concept introduced earlier for metals (e.g., Dafalias and Popov, 1975, 1976; Krieg, 1975).

A two-surface model of this type was proposed by Mróz et al. (1978, 1979) for clays. A bounding surface, $F = 0$, representing the consolidation history of the soil, and a yield surface or loading surface, $f = 0$, defining the elastic domain within the bounding surface (Fig. 5.25) are employed in the model.

The bounding surface is assumed to expand or contract isotropically, but the yield surface is allowed to translate, expand or contract within the domain enclosed by the bounding surface. The translation of the yield surface is governed by the same rule as the multi-surface models described earlier (i.e., the yield surface f will translate towards the bounding surface along $\overline{PR}$ in Fig. 5.25). An interpolation rule to define the variation of the hardening moduli between the loading and the bounding surfaces follows the work by Dafalias and Popov (1976), where the hardening modulus of yield surface, H', is taken as a function of the distance (Fig. 5.25) between the current stress point, P, on the yield surface and its conjugate point R, on the bounding surface. Very detailed discussions of the present model and its application to represent the behavior of clays under monotonic and cyclic triaxial tests conditions have been given by Mróz et al. (1979).

Mróz et al. (1981) further introduced the concept of the accumulated strain fatigue parameter which determines the degree of soil stiffness degradation, in order to account for the rearrangement of soil structure in the course of cyclically plastic deformation and inelastic behavior such as the progressive densification/dilatation

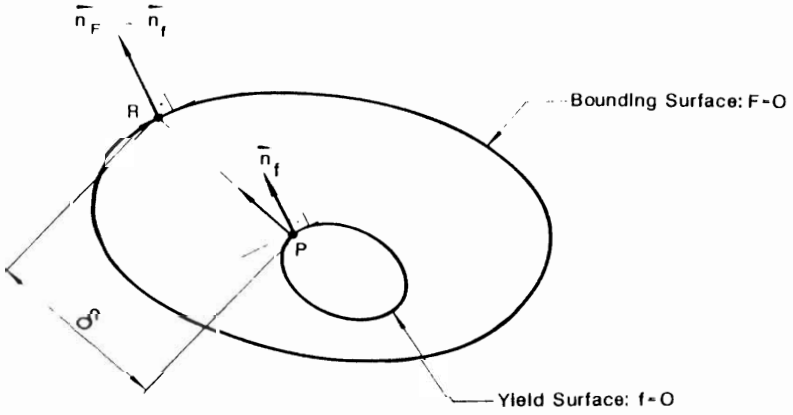

Fig. 5.25. Yield and bounding surfaces in stress space.

and/or the corresponding pore-water pressure changes. The two-surface anisotropic hardening model has been extended to the *three-surface model* consisting of a yield surface, a bounding surface (consolidation surface) and an intermediate surface which divides the domain within the consolidation surface into two sub-domains. This is known as the *extended two-surface model*. In the extended two-surface model, the progressive material degradation is simulated by the intermediate surface. Further, an alternative description has been provided by the new version of the hardening model (Mróz et al., 1978) with infinite number of intermediate surfaces, accounting for the cyclic degradation effect into the hardening modulus. Development of the models of similar type can be found in the papers by Pietruszczak and Mróz (1983) and Mróz and Pietruszczak (1983).

Dafalias and Herrmann (1980) have also used the bounding surface formulation to describe the behavior of clay under cyclic loadings. However, no explicit yield surface was postulated within the bounding surface. The associated flow rule was utilized for the bounding surface. In this model, the variation of the hardening modulus within the boundary surface is defined on the basis of a very simple radial mapping rule. For each actual stress point within (or on) the bounding surface, a corresponding "*image*" point on the surface is specified as the intersection of the surface with the straight (radial) line connecting the origin with the current stress point (the origin was assumed to be always within the bounding surface). The actual hardening modulus is then assumed to be a function of the hardening modulus on the bounding surface, at the "*image*" point, and the distance between the actual stress point and its "*image*". In order to take into account the difference in the soil behavior between compression and tension stress conditions, an improved bounding surface theory has been presented by introducing all three stress invariants for initially isotropic materials and then the qualitative behavior of the model is assessed in detail under various conditions of monotonic, cyclic, drained, and undrained loadings (Dafalias and Herrmann, 1982).

The advantages and limitations of anisotropic plasticity models described in this Section are summarized in Table 5.3.

TABLE 5.3

Advantages and limitations of the anisotropic plasticity models

Advantages	Limitations
Multi-surface model	
powerful for cyclic loading	difficult to memorize the size and location of each surface in a computer numerical analysis
relatively simple determination of the initial parameters	
Two-surface model	
powerful for cyclic loading	– a priori selection of specific hardening rules
simple treatment of hardening behavior by an interpolation rule	

5.9 PRANDTL-REUSS STRESS-STRAIN RELATIONS

In this Section, we shall derive the incremental stress-strain relations for the Prandtl-Reuss hardening material before the description of the formulation of the general stress-strain relations for hardening materials as mentioned in the previous Section.

The *flow rule* for the Prandtl-Reuss material can be carried over with a fairly simple modification from the perfect plasticity theory described in Chapter 4 to the work-hardening idealization. Unlike the theory of perfect plasticity, the neutral loading will not cause plastic flow, while the unloading remains elastic. Plastic deformation can take place only when the stress increment $d\sigma_{ij}$ moves in the outward direction of the initial yield surface.

5.9.1 Prandtl-Reuss equations

We shall consider now Fig. 5.26 where the stress increment $d\sigma_{ij}$ is decomposed into two components: one is normal to and other is tangent to the current yield surface. According to our previous discussion, the tangential component sets up neutral loading which is associated with the elastic strain. The neutral loading, however, is not responsible for the plastic deformation. To have a better physical picture, let us examine Fig. 5.27. Hereby, a thin-walled tube is tested under the combined tension and torsion. The specimen is first loaded to the initial yield state (denoted by point A) and then pulled in tension only until point B is reached. Since $d\sigma_{11}$ moves outward and, in this case, normal to the initial yield surface, we would expect the tensile response of the material to be elastic-plastic. Suppose at point B, we apply a pure torsion so that a shear stress σ_{12} has the direction tangent to the current yield surface. Will the shear response be elastic-plastic or fully elastic? The answer is of course fully elastic. The argument has been favorably supported by

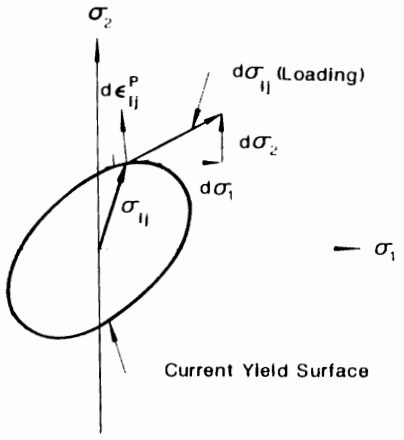

Fig. 5.26. Elastic-plastic work-hardening behavior.

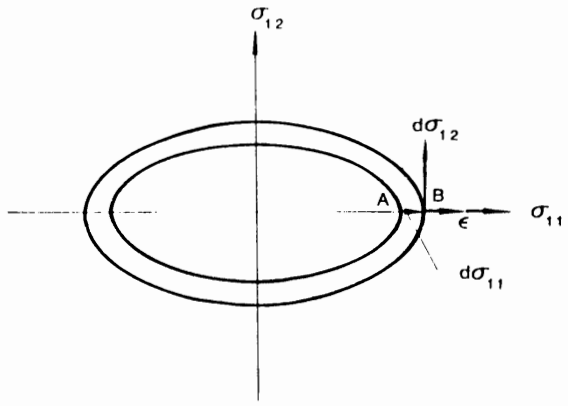

Fig. 5.27. Thin-walled tube test under combined tension and shear

experimental data. As for the flow rule described in Section 5.2.3, it would therefore be justified to assume that the magnitude of plastic strain increment $d\epsilon_{ij}^{p}$ is directly proportional to the projection of the stress increment, $d\sigma_{ij}$, onto the direction of the normal, $\partial f/\partial\sigma_{ij}$, that is, $(\partial f/\partial\sigma_{ij})\, d\sigma_{ij}$ of $d\sigma_{ij}$ where f is the yield function or the yield surface. Accordingly, we can derive the flow rule for the Prandtl-Reuss hardening material in the mathematical form as follows:

The Prandtl-Reuss equations can be rewritten as:

$$d\epsilon_{ij}^{p} = \tfrac{3}{2} d\lambda\, s_{ij} \tag{5.107}$$

where the term s_{ij} gives the direction, $3/2$ is inserted for convenience in subsequent equations and the proportionality factor $d\lambda$ can be similarly written from Eq. (5.5) as:

$$d\lambda = \frac{1}{H'}\left[\frac{\partial f}{\partial\sigma_{mn}} d\sigma_{mn}\right] \tag{5.108}$$

then the plastic strain increment $d\epsilon_{ij}^{p}$ can be expressed by:

$$d\epsilon_{ij}^{p} = \frac{3}{2}\frac{1}{H'}\left[\frac{\partial f}{\partial\sigma_{mn}} d\sigma_{mn}\right] s_{ij} \tag{5.109}$$

Equation (5.109) is, in fact, the most general form of the plastic stress-strain relations for the Prandtl-Reuss work-hardening material.

If we select an isotropic material of the J_2 or von Mises type as the yield function, f, we find:

$$\frac{\partial f}{\partial\sigma_{mn}} d\sigma_{mn} = \frac{\partial J_2}{\partial\sigma_{mn}} d\sigma_{mn} = dJ_2 \tag{5.110}$$

so that Eq. (5.109) reduces to:

$$d\epsilon_{ij}^{p} = \frac{3}{2}\frac{1}{H'}\,dJ_2 s_{ij} \tag{5.111}$$

Hardening modulus H'

To gain some physical insight into the Prandtl-Reuss flow rule of Eq. (5.111), we shall examine the typical stress-strain curve from a simple tension test. For this case, we can write $d\epsilon_{11}^{p}$ as:

$$d\epsilon_{11}^{p} = \frac{d\sigma_{11}}{E_p} \tag{5.112}$$

where E_p is the *plastic tangent modulus* in simple tension. In the most general case, $d\lambda$ is a function of $d\sigma_{ij}$, σ_{ij} and the prior history of loading as well. Now, we shall proceed to relate H' to E_p. For simplicity, consider again a work-hardening material associated with the J_2-theory under simple tension state. Since $J_2 = \frac{1}{3}\sigma_{11}^2$, dJ_2 can be written as:

$$dJ_2 = \tfrac{2}{3}\sigma_{11}\,d\sigma_{11} = \tfrac{2}{3}\sigma_{11}^2\,d\sigma_{11}/\sigma_{11} = 2J_2\,d\sigma_{11}/\sigma_{11} \tag{5.113}$$

Substituting dJ_2 into Eq. (5.111) and realizing that $s_{11} = \frac{2}{3}\sigma_{11}$, we have:

$$d\epsilon_{11}^{p} = \frac{1}{H'}\,2J_2\,d\sigma_{11} = d\sigma_{11}/E_p \tag{5.114}$$

Therefore, we find:

$$H' = 2J_2 E_p \tag{5.115}$$

Once H' is known, the plastic strain increment $d\epsilon_{ij}^{p}$ can be calculated directly from Eq. (5.111). In the following, we will extend the present one-dimensional stress state to the multi-dimensional stress state and describe an effective means to obtain H' from experimental data.

Effective stress and effective plastic strain increment

For tests other than the simple tension, the expressions for E_p will be different. In fact, there are several ways to select the coordinates for plotting the stress-strain curves from test data. For example, we can plot either $\sigma \sim \epsilon$, or $\tau \sim \gamma$, or $\tau_{oct} \sim \gamma_{oct}$, or $\tau_{max} \sim \gamma_{max}$ or even $\sigma \sim \gamma$, or $\tau \sim \epsilon$, etc. Each of these curves will of course be different and so is H'. The immediate need, therefore, is to find a variable or variables that combine all these quantities. When plotted, the new variables will give a curve that will match adequately with most of these simple tests. As a result, the

hardening function E_p in Eq. (5.115) corresponding to the simple tension test can be used as H_p defined as the *plastic tangent modulus* of the material under a general three-dimensional stress condition.

For this purpose, the two commonly used variables are the *equivalent* or *effective stress* σ_e and the *equivalent* or *effective plastic strain increment* $d\epsilon_p$ (See effective plastic strain increment $d\bar{\epsilon}_p$ defined in Section 4.8).

If the von Mises yield condition is used, the effective stress and the effective plastic strain increments may be defined, after Hill (1950), as:

$$\sigma_e = \frac{1}{\sqrt{2}}\left[(\sigma_{11}-\sigma_{22})^2 + (\sigma_{22}-\sigma_{33})^2 + (\sigma_{33}-\sigma_{11})^2 + 6(\sigma_{12}^2+\sigma_{23}^2+\sigma_{31}^2)\right]^{1/2} \quad (5.116)$$

and

$$d\epsilon_p = \frac{\sqrt{2}}{3}\left[(d\epsilon_{11}^p - d\epsilon_{22}^p)^2 + (d\epsilon_{22}^p - d\epsilon_{33}^p)^2 + (d\epsilon_{33}^p - d\epsilon_{11}^p)^2 + 6(d\epsilon_{12}^p)^2 + 6(d\epsilon_{23}^p)^2 + 6(d\epsilon_{31}^p)^2\right]^{1/2} \quad (5.117)$$

If we consider a uniaxial tension test, for example, in the x_1-direction, then, Eqs. (5.116) and (5.117) reduce to:

$$\sigma_e = \sigma_{11} \quad (5.118a)$$

and

$$d\epsilon_p = d\epsilon_{11}^p \quad (5.118b)$$

Another identical form of the effective stress and the effective plastic strain increment may be expressed as:

$$\sigma_e = \frac{3}{\sqrt{2}}\tau_{oct} = (3J_2)^{1/2} \quad (5.119)$$

and

$$d\epsilon_p = \frac{2}{\sqrt{3}}\left(\tfrac{1}{2}d\epsilon_{ij}^p\, d\epsilon_{ij}^p\right)^{1/2} \quad (5.120)$$

and the effective plastic strain becomes:

$$\epsilon_p = \int d\epsilon_p \quad (5.121)$$

As an example, the plot of the $\sigma_e \sim \epsilon_p$ curve is shown in Fig. 5.28. The curve does not start from the origin since the initial effective stress σ_e produces only elastic

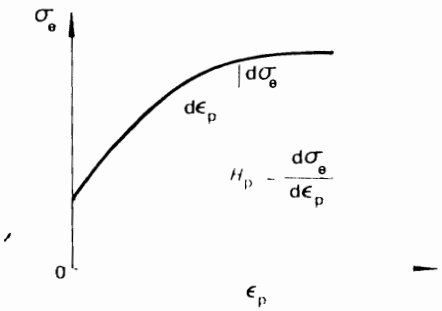

Fig. 5.28. Effective stress – effective strain curve.

strain. This $\sigma_e \sim \epsilon_p$ relation varies with the type of material but can be obtained from any simple test data.

In the following, we shall present the steps for the determination of H'. From Eqs. (2.45) and (5.119), we have:

$$J_2 = \tfrac{1}{3}\sigma_e^2 = \tfrac{1}{2}s_{ij}s_{ij} \tag{5.122}$$

so that

$$s_{ij}s_{ij} = \tfrac{2}{3}\sigma_e^2 \tag{5.123}$$

and

$$dJ_2 = \tfrac{2}{3}\sigma_e\, d\sigma_e = s_{ij}\, ds_{ij} \tag{5.124}$$

Using Eqs. (5.111), (5.123) and (5.124), Eq. (5.120) can be written as:

$$d\epsilon_p = \left(\frac{2}{3}\right)^{1/2}\left[\left\{\frac{3}{2}\frac{1}{H'}dJ_2 s_{ij}\right\}\left\{\frac{3}{2}\frac{1}{H'}dJ_2 s_{ij}\right\}\right]^{1/2}$$

$$= \left(\frac{2}{3}\right)^{1/2}\left[\frac{9}{4}\frac{1}{H'^2}(dJ_2)^2 s_{ij}s_{ij}\right]^{1/2} = \left(\frac{3}{2}\right)^{1/2}\left[\frac{1}{H'^2}(dJ_2)^2\left(\tfrac{2}{3}\sigma_e^2\right)\right]^{1/2}$$

$$\frac{1}{H'}dJ_2\sigma_e = \frac{1}{H'}\left(\tfrac{2}{3}\sigma_e\, d\sigma_e\right)\sigma_e = \frac{1}{H'}\tfrac{2}{3}\sigma_e^2\, d\sigma_e \tag{5.125}$$

Therefore, H' can be written as:

$$H' = \tfrac{2}{3}\sigma_e^2\frac{d\sigma_e}{d\epsilon_p} \tag{5.126a}$$

or

$$H' = \tfrac{2}{3}\sigma_e^2 H_p \tag{5.126b}$$

where

$$H_p = \frac{d\sigma_e}{d\epsilon_p} \tag{5.127}$$

Substituting dJ_2 and H' of Eqs. (5.124) and (5.126b) into Eq. (5.111), the general plastic stress-strain relation becomes:

$$d\epsilon_{ij}^p = \frac{3}{2}\frac{d\sigma_e}{\sigma_e H_p} s_{ij} \tag{5.128}$$

The plastic stress-strain relationship (5.128) is for the isotropic Prandtl-Reuss hardening material whose yield criterion is of the J_2 or the von Mises type. If the data from simple tests as well as from those combined tests are plotted on the $\sigma_e \sim \epsilon_p$ coordinates, these data points will generally form a narrow band along a single curve. This single curve can therefore be used to determine the magnitude of H_p. However, in case the scattering of the data points is noticeable and the band is not sufficiently narrow, the effective stress definition can be improved by introducing the invariant J_3 into σ_e. For example, we may select the two coordinates where:

$$\sigma_e = \tau_{oct}\left(1 - 2.25J_3^2/J_2^3\right)^{1/6} \tag{5.129a}$$

and

$$\epsilon_p = \gamma_{oct}^p \tag{5.129b}$$

Osgood (1947) used Eq. (5.129) and plotted the test results of thin-walled tubes under the combined tension and interior pressure. The plot is shown in Fig. 5.29. Clearly, the band is so narrow that it can be replaced by a single curve.

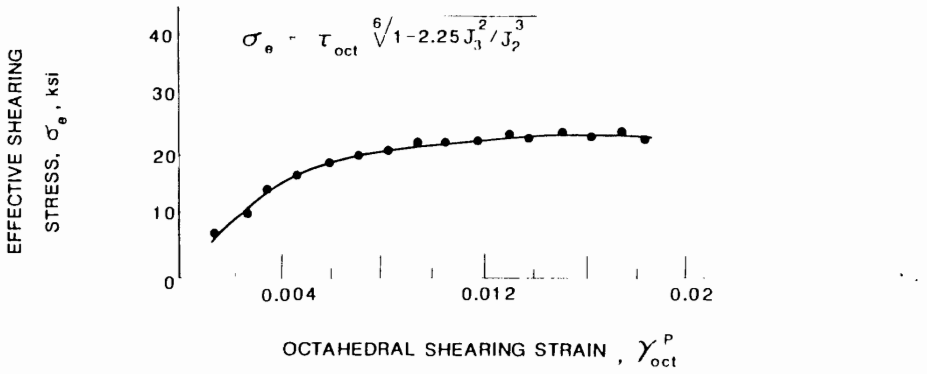

Fig. 5.29. Osgood's test on thin-walled tube under tension and interior pressure.

Experimental verification

The early experimental investigation to determine the validity of the plastic stress-strain relations was made by Lode (1926). For the principal stresses, Lode introduced the following parameter:

$$\mu = \frac{2\sigma_2 - \sigma_1 - \sigma_3}{\sigma_1 - \sigma_3}$$

$$= \frac{2s_2 - s_1 - s_3}{s_1 - s_3} = \frac{3s_2}{s_1 - s_3} = \frac{\sigma_2 - (\sigma_1 + \sigma_3)/2}{(\sigma_1 - \sigma_3)/2} \tag{5.130}$$

when $\sigma_1 > \sigma_2 > \sigma_3$.

According to the Mohr circles shown in Fig. 5.30, the term $(\sigma_1 + \sigma_3)/2$ is the abscissa of the center A, so the numerator is the distance $\overline{A\sigma_2}$; the denominator is the radius of the largest circle $\overline{A\sigma_1}$. Therefore, we have:

$$\mu = \overline{A\sigma_2}/\overline{A\sigma_1} \tag{5.131}$$

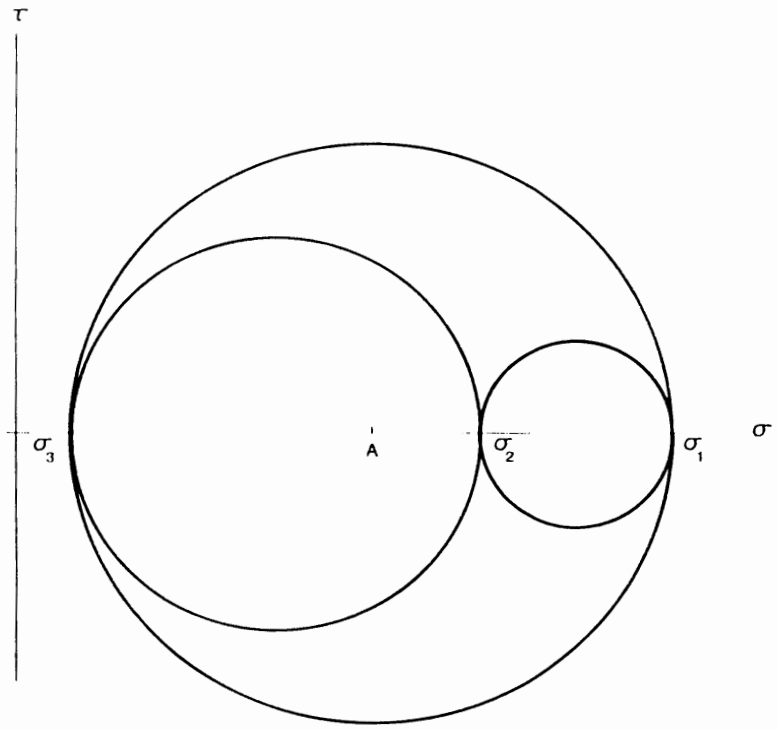

Fig. 5.30. Mohr's circles

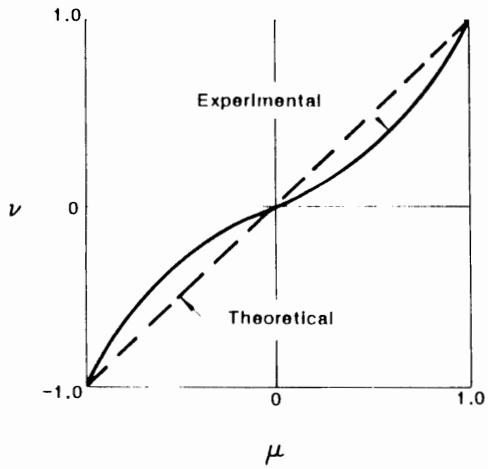

Fig. 5.31. Results of Lode's tests.

The strain increment circles are described by the parameter such as:

$$\nu = \frac{d\epsilon_2^p - (d\epsilon_1^p + d\epsilon_3^p)/2}{(d\epsilon_1^p - d\epsilon_3^p)/2} \tag{5.132}$$

Recalling the conditions:

$$s_1 + s_2 + s_3 = d\epsilon_1^p + d\epsilon_2^p + d\epsilon_3^p = 0 \tag{5.133}$$

the origin for the plastic strain increment diagram coincides with that of the deviatoric stress diagram. If the Prandtl-Reuss relations are valid, the scaling factor between the diagrams should be $\frac{1}{2}d\lambda$ as required by Eq. (5.107). This leads to the relationship:

$$\mu = \nu \tag{5.134}$$

Thus, the plot of $\nu = \mu$ is a straight line of unit slope. The results of Lode's tests on tubular specimens under the combined tension and torsion are illustrated in Fig. 5.31 and are further confirmed by Taylor and Quinney (1931) in Fig. 5.32. For a simple tension test, the stresses are $(\sigma_1, 0, 0)$ and the plastic strain increments are $d\epsilon_1^p$, $d\epsilon_2^p = -\frac{1}{2}d\epsilon_1^p$ and $d\epsilon_3^p = -\frac{1}{2}d\epsilon_1^p$ so that:

$$\mu = \sigma_1/\sigma_1 = 1 \tag{5.135a}$$

$$\nu = \frac{(d\epsilon_1^p/2) - \{d\epsilon_1^p - (d\epsilon_1^p/2)\}/2}{\{d\epsilon_1^p + (d\epsilon_1^p/2)\}/2} = -1 \tag{5.135b}$$

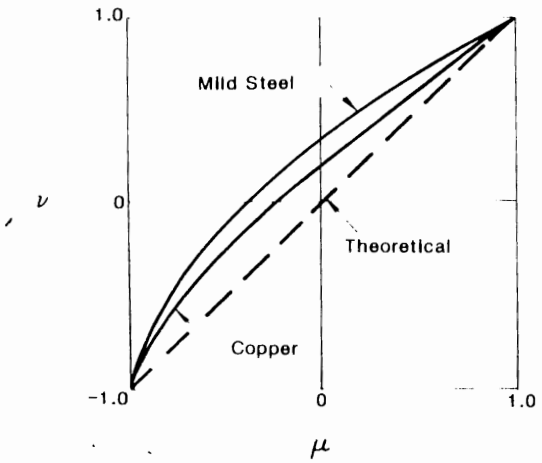

Fig. 5.32. Results of Taylor and Quinney's tests.

For a simple compression test $\mu = \nu = +1$ and for a pure shear test, we have $\mu = \nu = 0$. The deviation is not significant and the Prandtl-Reuss relations are therefore acceptable for all practical purpose. According to Prager (1956), the deviation can be reduced if a refined yield function rather than the simple form of J_2 is utilized. The additional complexity however has not been found worthwhile for general use.

5.9.2 *Matrix form of Prandtl-Reuss equations*

Referring to the Prandtl-Reuss equations (5.128) and the linear isotropic elastic relations in Chapter 3, the total increment of strain becomes:

$$d\epsilon_{ij} - d\epsilon_{ij}^{e} + d\epsilon_{ij}^{p} = \left[\frac{ds_{ij}}{2G} + \frac{d\sigma_{kk}}{9K}\delta_{ij} \right] + \frac{3}{2}\frac{d\sigma_e}{\sigma_e H_p}s_{ij} \tag{5.136}$$

Inverting these equations, the stress increment $d\sigma_{ij}$ can be expressed in terms of $d\epsilon_{ij}$ as well as s_{ij}. This inversion procedure is given below: The total deviatoric strain increment can be written as:

$$de_{ij} \quad de_{ij}^{e} + de_{ij}^{p} = de_{ij}^{e} + d\epsilon_{ij}^{p} = \frac{1}{2G}ds_{ij} + \tfrac{3}{2}d\lambda s_{ij} \tag{5.137}$$

Multiplying both sides of Eq. (5.137) by s_{ij}, we have:

$$s_{ij}\,de_{ij} \quad \frac{1}{2G}s_{ij}\,ds_{ij} + \tfrac{3}{2}d\lambda\, s_{ij}\,s_{ij} \tag{5.138}$$

Using $d\lambda = d\sigma_e/(\sigma_e H_p)$, Eqs. (5.123) and (5.124), Eq. (5.138) can be rewritten as:

$$s_{ij}\, de_{ij} = \frac{1}{2G}\left[\tfrac{2}{3}\sigma_e^2 H_p\, d\lambda\right] + \sigma_e^2\, d\lambda \tag{5.139}$$

Therefore, we obtain $d\lambda$ as:

$$d\lambda = \frac{s_{ij}\, de_{ij}}{\sigma_e^2\left(1 + H_p/3G\right)} \tag{5.140}$$

or using $s_{ij}\, de_{ij} = s_{ij}\, d\epsilon_{ij}$:

$$d\lambda = \frac{s_{ij}\, d\epsilon_{ij}}{\sigma_e^2\left(1 + H_p/3G\right)} \tag{5.141}$$

We then proceed to find $d\sigma_{ij}$ from the elastic stress-strain relation where:

$$\begin{aligned} d\sigma_{ij} &= 2G\, de_{ij}^e + K\, d\epsilon_{kk}^e \delta_{ij} \\ &= 2G\left(d\epsilon_{ij} - d\epsilon_{ij}^p - \tfrac{1}{3} d\epsilon_{kk}^e \delta_{ij}\right) + K\, d\epsilon_{kk}^e \delta_{ij} \\ &= 2G\left(d\epsilon_{ij} - \tfrac{3}{2} d\lambda s_{ij} - \tfrac{1}{3} d\epsilon_{kk}^e \delta_{ij}\right) + K\, d\epsilon_{kk}^e \delta_{ij} \end{aligned} \tag{5.142}$$

Substitution of $d\lambda$ in Eq. (5.141) and $d\epsilon_{kk}^e = d\epsilon_{kk}$ leads to:

$$d\sigma_{ij} = 2G\left[d\epsilon_{ij} - \frac{3}{2}\frac{s_{mn}\, d\epsilon_{mn} s_{ij}}{\sigma_e^2\left(1 + H_p/3G\right)}\right] - \left(\tfrac{2}{3}G - K\right) d\epsilon_{kk}\delta_{ij} \tag{5.143}$$

Equation (5.143) gives the stress increment $d\sigma_{ij}$ in terms of the current state of stress and the change in total strain. Yamada et al. (1968) presented Eq. (5.143) by introducing the Poisson's ratio, ν, into the equation and led to the form:

$$d\sigma_{ij} = 2G\left[d\epsilon_{ij} + \frac{\nu}{1 - 2\nu} d\epsilon_{kk}\delta_{ij} - s_{ij}\, \frac{s_{mn}\, d\epsilon_{mn}}{\tfrac{2}{3}\sigma_e^2\left(1 + H_p/3G\right)}\right] \tag{5.144}$$

In the following, matrix forms of the incremental stress-strain relations for the Prandtl-Reuss hardening material are described for the three-dimensional, plane stress, and plane strain cases, respectively.

(a) Three-dimensional case

Equation (5.144) can be written in the matrix form as:

$$\{d\sigma\} = [C^{ep}]\{d\epsilon\} \tag{5.145a}$$

where

$$\{d\sigma\} = [d\sigma_{11}, d\sigma_{22}, d\sigma_{33}, d\sigma_{12}, d\sigma_{23}, d\sigma_{31}]^T \tag{5.145b}$$

$$\{d\epsilon\} = [d\epsilon_{11}, d\epsilon_{22}, d\epsilon_{33}, d\gamma_{12}, d\gamma_{23}, d\gamma_{31}]^T \tag{5.145c}$$

and the elastic-plastic constitutive matrix $[C^{ep}]$ is symmetric and can be expressed in the explicit form by:

$$[C^{ep}] = 2\frac{G}{S}\begin{bmatrix} C_{11}^{ep} & C_{12}^{ep} & C_{13}^{ep} & C_{14}^{ep} & C_{15}^{ep} & C_{16}^{ep} \\ & C_{22}^{ep} & C_{23}^{ep} & C_{24}^{ep} & C_{25}^{ep} & C_{26}^{ep} \\ & & C_{33}^{ep} & C_{34}^{ep} & C_{35}^{ep} & C_{36}^{ep} \\ & & & C_{44}^{ep} & C_{45}^{ep} & C_{46}^{ep} \\ & & & & C_{55}^{ep} & C_{56}^{ep} \\ & & & & & C_{66}^{ep} \end{bmatrix} \tag{5.146}$$

in which its components are:

$$C_{11}^{ep} = \frac{1-\nu}{1-2\nu}S - s_{11}^2; \quad C_{12}^{ep} = \frac{\nu}{1-2\nu}S - s_{11}s_{22}; \quad C_{13}^{ep} = \frac{\nu}{1-2\nu}S - s_{11}s_{33}$$

$$C_{14}^{ep} = -s_{11}\sigma_{12}; \quad C_{15}^{ep} = -s_{11}\sigma_{23}; \quad C_{16}^{ep} = -s_{11}\sigma_{31}$$

$$C_{22}^{ep} = \frac{1-\nu}{1-2\nu}S - s_{22}^2, \quad C_{23}^{ep} = \frac{\nu}{1-2\nu}S - s_{22}s_{33}; \quad C_{24}^{ep} = -s_{22}\sigma_{12}$$

$$C_{25}^{ep} = -s_{22}\sigma_{23}; \quad C_{26}^{ep} = -s_{22}\sigma_{31}; \quad C_{33}^{ep} = \frac{1-\nu}{1-2\nu}S - s_{33}^2$$

$$C_{34}^{ep} = -s_{33}\sigma_{12}; \quad C_{35}^{ep} = -s_{33}\sigma_{23}; \quad C_{36}^{ep} = -s_{33}\sigma_{31}$$

$$C_{44}^{ep} = \tfrac{1}{2}S - \sigma_{12}^2; \quad C_{45}^{ep} = -\sigma_{12}\sigma_{23}; \quad C_{46}^{ep} = -\sigma_{12}\sigma_{31}$$

$$C_{55}^{ep} = \tfrac{1}{2}S - \sigma_{23}^2; \quad C_{56}^{ep} = -\sigma_{23}\sigma_{31}; \quad C_{66}^{ep} = \tfrac{1}{2}S - \sigma_{31}^2$$

and S is given as:

$$S = \tfrac{4}{9}\sigma_e^2(1 + H_p/3G)$$

It should be emphasized that Eq. (5.145a) is the general form of the elastic-plastic stress-strain relations for general three-dimensional problems involving *isotropic materials* only. Also, it is based on the Prandtl-Reuss relations employing the von Mises yield criterion.

(b) Plane stress case

For the plane stress problems where:

$$d\sigma_{31} = d\sigma_{32} = d\sigma_{33} = 0 \tag{5.147}$$

we must convert $d\epsilon_{33}$ into the components of strain increments and substitute back into $[C^{ep}]$ so that we have the two-dimensional stress-strain relations in matrix form as:

$$\begin{Bmatrix} d\sigma_{11} \\ d\sigma_{22} \\ d\sigma_{12} \end{Bmatrix} = [C^{ep}] \begin{Bmatrix} d\epsilon_{11} \\ d\epsilon_{22} \\ d\gamma_{12} \end{Bmatrix} \tag{5.148}$$

where

$$[C^{ep}] = \frac{E}{Q} \begin{bmatrix} s_{22}^2 + 2P & -s_{11}s_{22} + 2\nu P & \dfrac{-(s_{11} + \nu s_{22})}{1+\nu}\sigma_{12} \\ & s_{11}^2 + 2P & \dfrac{-(s_{22} + \nu s_{11})}{1+\nu}\sigma_{12} \\ \text{Symmetric} & & \dfrac{R}{2(1+\nu)} + \dfrac{2H_p}{9E}(1-\nu)\sigma_e^2 \end{bmatrix} \tag{5.149}$$

in which:

$$P = \frac{2H_p}{9E}\sigma_e^2 + \frac{\sigma_{12}^2}{1+\nu} \tag{5.150a}$$

$$Q = R + 2(1-\nu^2)P \tag{5.150b}$$

$$R = s_{11}^2 + 2\nu s_{11}s_{22} + s_{22}^2 \tag{5.150c}$$

(c) Plane strain case

The condition for plane strain requires:

$$d\epsilon_{33} = d\gamma_{32} = d\gamma_{31} = 0 \tag{5.151}$$

so that the plastic stress-strain matrix now becomes:

$$[C^{ep}] = 2\frac{G}{S} \begin{bmatrix} \dfrac{1-\nu}{1-2\nu}S - s_{11}^2 & \dfrac{\nu}{1-2\nu}S - s_{11}s_{22} & -s_{11}\sigma_{12} \\ & \dfrac{1-\nu}{1-2\nu}S - s_{22}^2 & -s_{22}\sigma_{12} \\ \text{Symmetric} & & \frac{1}{2}S - \sigma_{12}^2 \end{bmatrix} \tag{5.152}$$

It should be realized that $d\sigma_{33}$ is not equal to zero in the plane strain problems. If required, it can be obtained from:

$$d\sigma_{33} = 2\frac{G}{S}\left[\left(\frac{\nu}{1-2\nu}S - s_{11}s_{33}\right)d\epsilon_{11} + \left(\frac{\nu}{1-2\nu}S - s_{22}s_{33}\right)d\epsilon_{22} - s_{33}\sigma_{12}\,d\gamma_{12}\right] \tag{5.153}$$

Example 5.1: An initially unstressed and unstrained thin-walled circular tube is subjected to the combined axial-tension and twisting-moment loading history which produces the successive straight line path in $\sigma_{11} - \sigma_{12}$ space (see Fig. 5.33). Units are in pounds per square inch (tension stress σ_{11}, shear stress σ_{12}).
Path (i) (0, 0) to (0, 10,000)
Path (ii) (0, 10,000) to (30,000, 10,000)
Path (iii) (30,000, 10,000) to (30,000, − 10,000)
Path (iv) (30,000, − 10,000) to (0, 0)

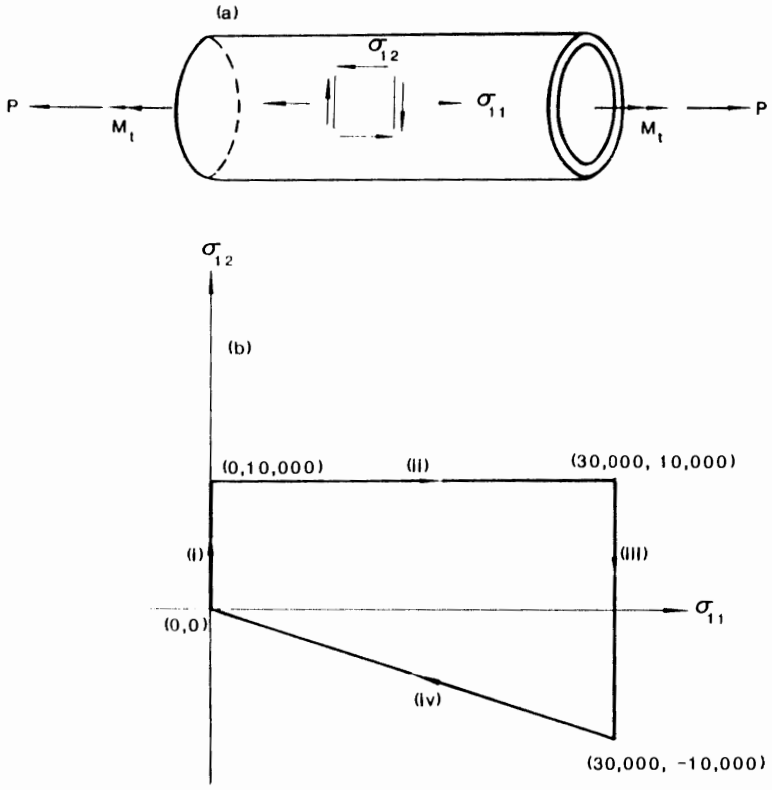

Fig. 5.33. Thin-walled circular tube test: (a) thin-walled circular tube; (b) combined axial tension and twisting moment loading history.

The material of the tube is assumed to be elastic-plastic. The elastic response is linear; the plastic response is of the Prandtl-Reuss type with the von Mises (J_2) isotropic stress-hardening model. For the first loading in simple tension, the stress σ-strain ϵ curve is given by:

$$\epsilon = 10^{-7}\sigma + 10^{-15}\sigma^3 \tag{5.154}$$

with σ in pounds per square inch. The first term in Eq. (5.154) represents the elastic strain, or recoverable response; the second term is the plastic strain.

(a) Write the stress-strain relation in component form explicitly in terms of σ_{11}, σ_{12}, $d\sigma_{11}$, and $d\sigma_{12}$.
(b) Find the elastic and the plastic components of strain at the end of each path (i), (ii), (iii), and (iv) by computing the change which takes place along each path.
(c) Draw successive yield curves at the beginning, the middle, and the end of each path.
(d) Show normality of $d\epsilon_{ij}^p$. In a qualitative manner, discuss the answer to problem (b) in terms of the normality relation.
(e) On the basis of normality and the yield curves of problem (c), contrast in quantitative but careful terms the final deformation of the tube for the complete cycle (i), (ii), (iii), (iv) with the cycle traced in reversed order, (−iv), (−iii), (−ii), (−i) that is, (0, 0) to (30,000, −10,000), (30,000, −10,000) to (30,000, 10,000), etc.

Solutions:

(a) Stress-strain relations:

For the case of simple tension test ($\sigma_{11} = \sigma$, and the others are zero), the axial plastic strain increment $d\epsilon_{11}^p$ can be written from Eq. (5.111) as:

$$d\epsilon_{11}^p = \frac{3}{2}\frac{1}{H'}\,dJ_2 s_{11} = \frac{3}{2}\frac{1}{H'}\left(\tfrac{2}{3}\sigma\,d\sigma\right)\left(\tfrac{2}{3}\sigma\right) = \frac{2}{3}\frac{1}{H'}\sigma^2\,d\sigma \tag{5.155}$$

On the other hand, the axial plastic strain increment $d\epsilon_{11}^p$ can be obtained from the second term of Eq. (5.154) as:

$$d\epsilon_{11}^p = 3 \times 10^{-15}\sigma^2\,d\sigma \tag{5.156}$$

Comparing Eqs. (5.155) with (5.156), we find:

$$H' = \tfrac{2}{9} \times 10^{15}\ (\text{psi})$$

From the first term of Eq. (5.154), we find Young's modulus $E = 10^7$ (psi). Therefore, using the incremental form of linear isotropic elastic stress-strain rela-

tions and Eq. (5.111), the general stress-strain relation for this case can be written as:

$$d\epsilon_{ij} = \left[\frac{1+\nu}{E} d\sigma_{ij} - \frac{\nu}{E} d\sigma_{kk}\delta_{ij}\right] + \frac{3}{2}\frac{1}{H'} dJ_2 s_{ij}$$

$$= \left[(1+\nu)\, d\sigma_{ij} - \nu\, d\sigma_{kk}\delta_{ij}\right] \times 10^{-7} + \tfrac{27}{4} \times 10^{-15} dJ_2 s_{ij} \tag{5.157}$$

For the combined stress case ($\sigma_{11} - \sigma_{12}$), Eq. (5.157) can be further reduced to:

$$d\epsilon_{11} = 10^{-7}\, d\sigma_{11} + 3 \times 10^{-15}\left(\sigma_{11}^2\, d\sigma_{11} + 3\sigma_{11}\sigma_{12}\, d\sigma_{12}\right) \tag{5.158a}$$

$$d\gamma_{12} = 2 \times 10^{-7}(1+\nu)\, d\sigma_{12} + 9 \times 10^{-15}\left(\sigma_{11}\sigma_{12}\, d\sigma_{11} + 3\sigma_{12}^2\, d\sigma_{12}\right) \tag{5.158b}$$

$$d\epsilon_{22} = d\epsilon_{33} = -\nu\, d\sigma_{11} \times 10^{-7} - \tfrac{3}{2} \times 10^{-15}\left(\sigma_{11}^2\, d\sigma_{11} + 3\sigma_{11}\sigma_{12}\, d\sigma_{12}\right) \tag{5.158c}$$

since $s_{11} = \frac{2}{3}\sigma_{11}$, $s_{12} = \sigma_{12}$, and $dJ_2 = \frac{2}{3}\sigma_{11}\, d\sigma_{11} + 2\sigma_{12}\, d\sigma_{12}$.

It should be noted here that the elastic-plastic stress-strain relations in Eq. (5.158) are valid only when the current stress state and stress increment satisfy the loading condition in Eq. (5.2). In the following, the strain history for ϵ_{11} and γ_{12} is presented.

(b) Stress path

Path (i): As the shearing stress σ_{12} increases gradually up to 10,000 psi from the stress-free state, it can be expected that the yield (or loading) surface expands correspondingly in the $\sigma_{11} - \sigma_{12}$ stress space. Mathematically, we have:

$$dJ_2 = 2\sigma_{12}\, d\sigma_{12} \geq 0 \tag{5.159}$$

since $\sigma_{11} = d\sigma_{11} = 0$, $\sigma_{12} \geq 0$ and $d\sigma_{12} > 0$. Therefore, for this stress path, Eq. (5.158) can be applied for the calculation of the elastic and the plastic strain increments. From Eq. (5.158a), strains at the end of this path are:

$$\epsilon_{11}^e = \epsilon_{11}^p = 0$$

On the other hand, from Eq. (5.158b), the elastic and plastic strain increments γ_{12}^e and γ_{12}^p are, respectively:

$$\gamma_{12}^e = 2 \times 10^{-7}(1+\nu)\int_0^{10{,}000} d\sigma_{12} = 2 \times 10^{-3}(1+\nu)$$

$$\gamma_{12}^p = 9 \times 10^{-15}\int_0^{10{,}000} 3\sigma_{12}^2\, d\sigma_{12} = 9 \times 10^{-3}$$

At the end of stress path (i), the current loading surface becomes:

$$J_2 = \tfrac{1}{3}\sigma_{11}^2 + \sigma_{12}^2 = 10^8 \tag{5.160}$$

Path (ii): Since $\sigma_{11} > 0$, $\sigma_{12} > 0$, $d\sigma_{11} > 0$ and $d\sigma_{12} = 0$ during stress path (ii), dJ_2 becomes:

$$dJ_2 = \tfrac{2}{3}\sigma_{11}\, d\sigma_{11} \geq 0 \tag{5.161}$$

which also indicates the condition of loading. Thus, we find:

$$\epsilon_{11}^e = 10^{-7}\int_0^{30,000} d\sigma_{11} = 3 \times 10^{-3}$$

$$\epsilon_{11}^p = 3 \times 10^{-15}\int_0^{30,000} \sigma_{11}^2 d\sigma_{11} = 2.7 \times 10^{-2}$$

$$\gamma_{12}^e = 0$$

$$\gamma_{12}^p = 9 \times 10^{-15}\int_0^{30,000} 10{,}000\sigma_{11}\, d\sigma_{11} = 4.05 \times 10^{-2}$$

At the end of stress path (ii), the new loading surface becomes:

$$J_2 = \tfrac{1}{3}\sigma_{11}^2 + \sigma_{12}^2 = 4 \times 10^8 \tag{5.162}$$

Path (iii): During stress path (iii), the value of J_2 decreases gradually and at the end of path (iii), it becomes again the same value as that at the beginning of stress path (iii). This implies that the response is fully elastic during this stress path. Therefore, we obtain:

$$\epsilon_{11}^e = 0$$

$$\epsilon_{11}^p = 0$$

$$\gamma_{12}^e = 2 \times 10^{-7}(1+\nu)\int_{10,000}^{10,000} d\sigma_{12} = -4 \times 10^{-3}(1+\nu)$$

$$\gamma_{12}^p = 0$$

The loading surface remains the same during the loading path (iii).
Path (iv): Here, as in path (iii), the response is elastic. Thus, we find only the elastic strains:

$$\epsilon_{11}^e = 10^{-7}\int_{30,000}^{0} d\sigma_{11} = -3 \times 10^{-3}$$

$$\epsilon_{11}^p = 0$$

$$\gamma_{12}^e = 2 \times 10^{-7}(1+\nu)\int_{10,000}^{0} d\sigma_{12} = 2 \times 10^{-3}(1+\nu)$$

$$\gamma_{12}^p = 0$$

TABLE 5.4

Total elastic and plastic strains

Path	ϵ_{11}^e	ϵ_{11}^p	γ_{12}^e	γ_{12}^p
i	0	0	$2\times10^{-3}(1+\nu)$	9×10^{-3}
ii	3×10^{-3}	2.7×10^{-2}	$2\times10^{-3}(1+\nu)$	4.95×10^{-2}
iii	3×10^{-3}	2.7×10^{-2}	$-2\times10^{-3}(1+\nu)$	4.95×10^{-2}
iv	0	2.7×10^{-2}	0	4.95×10^{-2}

Table 5.4 shows the total elastic and plastic strains accumulated at the end of each stress path.

(c) Loading surfaces

Based on Eqs. (5.160) and (5.162), loading surfaces at the beginning, the middle, and the end of each path are shown respectively in Fig. 5.34.

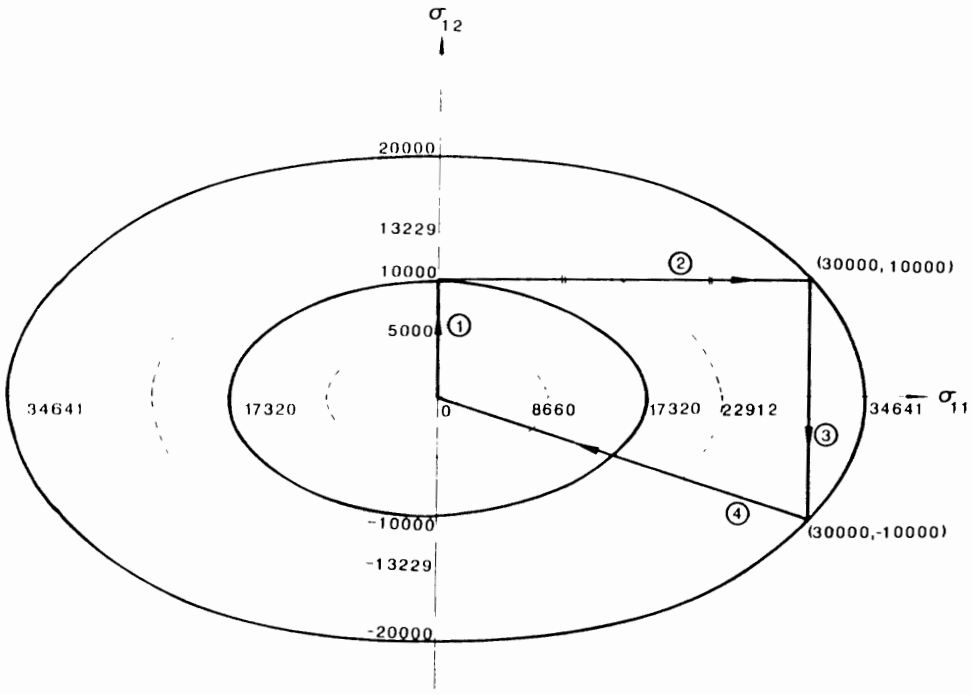

Fig. 5.34. Loading surfaces in σ_{11}-σ_{12}-space.

(d) Normality

From the Prandtl-Reuss equation (5.107), we have:

$$\frac{d\gamma_{12}^{p}}{d\epsilon_{11}^{p}} = \frac{2d\epsilon_{12}^{p}}{d\epsilon_{11}^{p}} = \frac{2s_{12}}{s_{11}} = \frac{3\sigma_{12}}{\sigma_{11}} \tag{5.163}$$

From $dJ_2 = \frac{2}{3}\sigma_{11}\, d\sigma_{11} + 2\sigma_{12}\, d\sigma_{12} = 0$ for a J_2-surface with constant value, we find:

$$\frac{d\sigma_{12}}{d\sigma_{11}} = -\frac{\sigma_{11}}{3\sigma_{12}} \tag{5.164}$$

Since the product of Eqs. (5.163) and (5.164) is -1, these two vectors, as shown schematically in Fig. 5.35, are perpendicular to each other. Thus, the normality condition is satisfied. From Eq. (5.158), the plastic strain increments $d\epsilon_{11}^{p}$ and $d\gamma_{12}^{p}$ are respectively given by:

$$d\epsilon_{11}^{p} = 3 \times 10^{-15}\left(\sigma_{11}^{2}\, d\sigma_{11} + 3\sigma_{11}\sigma_{12}\, d\sigma_{12}\right) \tag{5.165a}$$

$$d\gamma_{12}^{p} = 9 \times 10^{-15}\left(\sigma_{11}\sigma_{12}\, d\sigma_{11} + 3\sigma_{12}^{2}\, d\sigma_{12}\right) \tag{5.165b}$$

Since $d\sigma_{11} = 0$ for stress path (i), Eq. (5.165) is written as:

$$d\epsilon_{11}^{p} = 9 \times 10^{-15}\sigma_{11}\sigma_{12}\, d\sigma_{12} \tag{5.166a}$$

$$d\gamma_{12}^{p} = 27 \times 10^{-15}\sigma_{12}^{2}\, d\sigma_{12} \tag{5.166b}$$

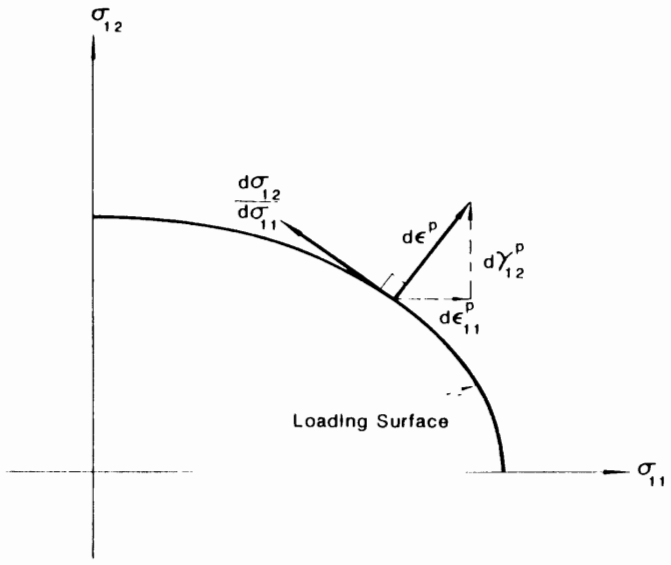

Fig. 5.35. Normality condition in σ_{11}-σ_{12}-space.

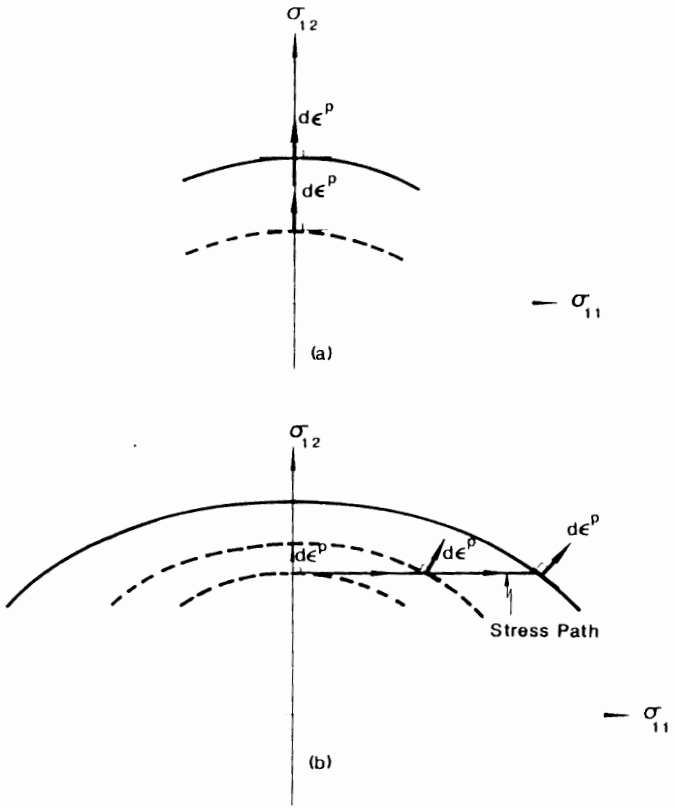

Fig. 5.36. Directions of plastic strain increment: (a) plastic strain increment during path (i); (b) plastic strain increment during path (ii).

Using Eq. (5.166), we find:

$$\frac{d\gamma_{12}^{p}}{d\epsilon_{11}^{p}} = \frac{27 \times 10^{15}\sigma_{12}^{2}\, d\sigma_{12}}{9 \times 10^{15}\sigma_{11}\sigma_{12}\, d\sigma_{12}} = \frac{3\sigma_{12}}{\sigma_{11}}$$

which satisfies the normality condition. In this case, $d\gamma_{12}^{p}/d\epsilon_{11}^{p}$ becomes infinite so that the direction of the resultant plastic strain vector coincides with that of stress path (i), as can be seen in Fig. 5.36a.

As for stress path (ii), Eq. (5.165) can be written as:

$$d\epsilon_{11}^{p} = 3 \times 10^{15}\sigma_{11}^{2}\, d\sigma_{11} \tag{5.167a}$$

$$d\gamma_{12}^{p} = 9 \times 10^{15}\sigma_{11}\sigma_{12}\, d\sigma_{11} \tag{5.167b}$$

TABLE 5.5

Total elastic and plastic strains for the reversed stress paths

Path	ϵ_{11}^e	ϵ_{11}^p	γ_{12}^e	γ_{12}^p
− iv	3×10^{-3}	3.6×10^{-2}	$-2\times10^{-3}(1+\nu)$	-3.6×10^{-2}
iii	3×10^{-3}	3.6×10^{-2}	$2\times10^{-3}(1+\nu)$	3.6×10^{-2}
ii	0	3.6×10^{-2}	$2\times10^{-3}(1+\nu)$	3.6×10^{-2}
− i	0	3.6×10^{-2}	0	-3.6×10^{-2}

From Eq. (5.167), we also find that the normality condition is satisfied, since:

$$\frac{d\gamma_{12}^p}{d\epsilon_{11}^p} = \frac{9\times10^{-15}\sigma_{11}\sigma_{12}\,d\sigma_{11}}{3\times10^{-15}\sigma_{11}^2\,d\sigma_{11}} = \frac{3\sigma_{12}}{\sigma_{11}}$$

In this case, the direction of the resultant plastic strain vector changes gradually from infinite (parallel to σ_{12}-axis) to unity (45 degrees to σ_{11} or σ_{12}-axis), since $\sigma_{12} = 10{,}000$ and $0 < \sigma_{11} < 30{,}000$ (see Fig. 5.36b). It can be understood that the directions of stress path and the resultant plastic strain vector do not coincide with each other.

(e) Reversed stress path

In a similar manner to that in (b), the elastic and plastic strains can be calculated. Since the loading surface has expanded isotropically large enough during the first stress path (− iv), the behavior for path (− iii) through path (− i) is only elastic. The total elastic and plastic strains at the end of each stress path are shown in Table 5.5. As can be recognized from Tables 5.4 and 5.5, the final states of strains are different.

5.10 GENERALIZED STRESS-STRAIN RELATIONS

So far we have demonstrated how to obtain the plastic stress-strain relationships following the procedures used by Prandtl and Reuss. Accordingly, we assume the axes of the principal plastic strain increments to coincide with those of the principal stresses. As pointed out previously in Chapter 4, these relations imply the von Mises yield function. Generally, there are limitless yield functions, loading functions and stress-strain relations which may be derived. In this Section, the elastic-plastic stress-strain relations for a general hardening plasticity model are derived in a manner that is different from that of the previous Section.

5.10.1 Incremental stress-strain relations

We shall express the plastic strain increment $d\epsilon_{ij}^p$ in terms of the total strain increment $d\epsilon_{ij}$. From the relation $d\epsilon_{ij} = d\epsilon_{ij}^e + d\epsilon_{ij}^p$ and the incremental stress-strain

relation of the linear isotropic elastic material in Chapter 3, we can write again:

$$d\sigma_{ij} = C_{ijkl}(d\epsilon_{kl} - d\epsilon^{p}_{kl}) \tag{5.168}$$

Multiplying by $\partial f/\partial\sigma_{ij}$ and substituting $d\epsilon^{p}_{ij} = (1/H')(\partial f/\partial\sigma_{mn})\, d\sigma_{mn}(\partial g/\partial\sigma_{ij})$ under the non-associated flow rule assumption, we obtain:

$$\frac{\partial f}{\partial\sigma_{ij}} d\sigma_{ij} = \frac{\partial f}{\partial\sigma_{ij}} C_{ijkl}\, d\epsilon_{kl} - \frac{1}{H'}\left(\frac{\partial f}{\partial\sigma_{mn}} d\sigma_{mn}\right)\frac{\partial f}{\partial\sigma_{ij}} C_{ijkl}\frac{\partial g}{\partial\sigma_{kl}} \tag{5.169}$$

where f and g are respectively the yield function and the plastic potential function. Solving Eq. (5.169) with respect to $(\partial f/\partial\sigma_{ij}\, d\sigma_{ij})$, we find:

$$\frac{\partial f}{\partial\sigma_{ij}} d\sigma_{ij} = \frac{\dfrac{\partial f}{\partial\sigma_{ij}} C_{ijkl}\, d\epsilon_{kl}}{1 + \dfrac{1}{H'}\dfrac{\partial f}{\partial\sigma_{ab}} C_{abcd}\dfrac{\partial g}{\partial\sigma_{cd}}} \tag{5.170}$$

Substituting Eq. (5.170) into Eq. (5.7), we find the plastic strain increment:

$$d\epsilon^{p}_{ij} = \frac{\dfrac{\partial f}{\partial\sigma_{kl}} C_{klmn}\, d\epsilon_{mn}}{H' + \dfrac{\partial f}{\partial\sigma_{ab}} C_{abcd}\dfrac{\partial g}{\partial\sigma_{cd}}}\frac{\partial g}{\partial\sigma_{ij}} \tag{5.171}$$

Thus, substitution of $d\epsilon^{p}_{ij}$ in Eq. (5.171) into Eq. (5.168) leads to the relationship between the stress increment $d\sigma_{ij}$ and the total strain increment $d\epsilon_{kl}$, that is:

$$d\sigma_{ij} = \left[C_{ijkl} - \frac{\dfrac{\partial g}{\partial\sigma_{rs}} C_{ijrs} C_{mnkl}\dfrac{\partial f}{\partial\sigma_{mn}}}{H' + \dfrac{\partial f}{\partial\sigma_{ab}} C_{abcd}\dfrac{\partial g}{\partial\sigma_{cd}}} \right] d\epsilon_{kl} \tag{5.172}$$

Equation (5.172) is the general form of the elastic-plastic constitutive equations for perfect plastic, isotropic strain-hardening, and anisotropic strain-hardening materials. The hardening modulus H' in Eq. (5.172) plays an important role in describing the behavior of material, and it has different forms for various types of materials. In what follows, the hardening modulus H' is represented for isotropic hardening and anisotropic hardening materials.

Example 5.2: Show that the hardening modulus H' in Eq. (5.172) becomes zero for a perfect plasticity material.

Solution: A perfect plasticity model contains a "failure envelope" or a "yield surface" fixed in the stress invariant space. Its function is in general expressed by:

$$f = f(\sigma_{ij}) \tag{5.173}$$

During the plastic flow, the yield function f should satisfy the consistency condition $\mathrm{d}f = 0$. That is:

$$\mathrm{d}f = \frac{\partial f}{\partial \sigma_{ij}} \mathrm{d}\sigma_{ij} = 0 \tag{5.174}$$

Since $(\partial f/\partial \sigma_{ij})\,\mathrm{d}\sigma_{ij}$ is equal to zero, H' is obtained from Eq. (5.170). Thus, we have:

$$H' \quad 0 \tag{5.175}$$

Namely, for a perfectly plastic material, its hardening modulus H' is equal to zero along the fixed surface.

5.10.2 *Isotropic hardening*

Strain hardening

The isotropic strain-hardening models generally contain; (1) a "failure envelope" or "yield surface" on which the material element fails or hardens due to shear stress and (2) in some cases, a "hardening surface" by which the rate of plastic volumetric change is controlled in terms of the magnitude of the first invariant of stress tensor, I_1. The general function for such surfaces can be expressed by:

$$f = f\left[\sigma_{ij},\ x(\epsilon^{\mathrm{p}}_{ij}),\ \kappa(\epsilon_{\mathrm{p}})\right] \tag{5.176}$$

in which σ_{ij}, $x(\epsilon^{\mathrm{p}}_{ij})$, and $\kappa(\epsilon_{\mathrm{p}})$ are respectively the stress tensor, hardening parameter which is a function of the plastic strain tensor $\epsilon^{\mathrm{p}}_{ij}$, and the material parameter κ which is a function of the effective plastic strain, $\epsilon_{\mathrm{p}} = C\int(\mathrm{d}\epsilon^{\mathrm{p}}_{ij}\ \mathrm{d}\epsilon^{\mathrm{p}}_{ij})^{1/2}$ where the parameter C is constant depending on the yield function. For example, C is $\sqrt{2}/3$ for the von Mises yield function and $(\alpha + 1/\sqrt{3})/(3\alpha^2 + \frac{1}{2})^{1/2}$ for the Drucker-Prager yield function. From the consistency condition, $\mathrm{d}f = 0$, we obtain:

$$\mathrm{d}f = \frac{\partial f}{\partial \sigma_{ij}} \mathrm{d}\sigma_{ij} + \frac{\partial f}{\partial x}\frac{\partial x}{\partial \epsilon^{\mathrm{p}}_{ij}} \mathrm{d}\epsilon^{\mathrm{p}}_{ij} + \frac{\partial f}{\partial \kappa}\frac{\mathrm{d}\kappa}{\mathrm{d}\epsilon_{\mathrm{p}}} \mathrm{d}\epsilon_{\mathrm{p}} = 0 \tag{5.177a}$$

or

$$\mathrm{d}f = \frac{\partial f}{\partial \sigma_{ij}} \mathrm{d}\sigma_{ij} + \frac{\partial f}{\partial x}\frac{\partial x}{\partial \epsilon^{\mathrm{p}}_{ij}} \mathrm{d}\epsilon^{\mathrm{p}}_{ij} + \frac{\partial f}{\partial \kappa}\frac{\mathrm{d}\kappa}{\mathrm{d}\epsilon_{\mathrm{p}}} C\left(\mathrm{d}\epsilon^{\mathrm{p}}_{ij}\ \mathrm{d}\epsilon^{\mathrm{p}}_{ij}\right)^{1/2} = 0 \tag{5.177b}$$

Substituting Eq. (5.7) into Eq. (5.177b), solution for the hardening modulus H' is expressed by:

$$H' = \frac{\partial f}{\partial \chi}\frac{\partial \chi}{\partial \epsilon_{ij}^{p}}\frac{\partial g}{\partial \sigma_{ij}} - C\frac{\partial f}{\partial \kappa}\frac{d\kappa}{d\epsilon_{p}}\left(\frac{\partial g}{\partial \sigma_{ij}}\frac{\partial g}{\partial \sigma_{ij}}\right)^{1/2} \tag{5.178}$$

Work hardening

Consider now the isotropic work-hardening model whose function is expressed by:

$$f = f\left[\sigma_{ij}, \kappa(W_{p})\right] \tag{5.179}$$

where κ is a function of the plastic work W_{p} defined by:

$$W_{p} = \int \sigma_{ij}\, d\epsilon_{ij}^{p} \tag{5.180}$$

In this case, the consistency condition is:

$$df = \frac{\partial f}{\partial \sigma_{ij}}d\sigma_{ij} + \frac{\partial f}{\partial \kappa}\frac{d\kappa}{dW_{p}}dW_{p} = 0 \tag{5.181a}$$

or

$$df = \frac{\partial f}{\partial \sigma_{ij}}\, d\sigma_{ij} + \frac{\partial f}{\partial \kappa}\frac{d\kappa}{dW_{p}}\sigma_{ij}\, d\epsilon_{ij}^{p} = 0 \tag{5.181b}$$

Thus, substitution of $d\epsilon_{ij}^{p}$ in Eq. (5.7) leads to the solution of the hardening modulus H' expressed by:

$$H' = \frac{\partial f}{\partial \kappa}\frac{d\kappa}{dW_{p}}\sigma_{ij}\frac{\partial g}{\partial \sigma_{ij}} \tag{5.182}$$

The hardening modulus, H', in Eq. (5.178), is used in the generalized Cap models to be discussed in more details in Chapter 6 as well as used in the isotropic strain-hardening type of Coulomb, Tresca and von Mises criteria, while H' in Eq. (5.182) is used for the models such as the Lade-Duncan model, and the Lade model where the hardening parameter is a function of the plastic work W_{p}.

5.10.3 Kinematic hardening

General derivation

The yield function for the pure kinematic hardening rule is written as:

$$f = f(\sigma_{ij} - \alpha_{ij}) \tag{5.183}$$

where α_{ij} denotes the translation of the center of a yield surface in stress space, that is usually assumed to be a function of the plastic strain tensor ϵ^{p}_{ij}. The consistency condition is written as:

$$df = \frac{\partial f}{\partial \sigma_{ij}}(d\sigma_{ij} - d\alpha_{ij}) = 0 \tag{5.184a}$$

or

$$df = \frac{\partial f}{\partial \sigma_{ij}} d\sigma_{ij} - \frac{\partial f}{\partial \sigma_{ij}} \frac{\partial \alpha_{ij}}{\partial \epsilon^{p}_{kl}} d\epsilon^{p}_{kl} = 0 \tag{5.184b}$$

Therefore, H' becomes:

$$H' = \frac{\partial f}{\partial \sigma_{ij}} \frac{\partial \alpha_{ij}}{\partial \epsilon^{p}_{kl}} \frac{\partial g}{\partial \sigma_{kl}} \tag{5.185}$$

As special cases, Prager's and Ziegler's kinematic hardening rules are considered in what follows.

Prager's rule

According to Prager's hardening rule, the translation of the center, $d\alpha_{ij}$, is generally expressed by:

$$d\alpha_{ij} = c\, d\epsilon^{p}_{ij} \quad \text{or} \quad \alpha_{ij} = c\epsilon^{p}_{ij} \tag{5.186}$$

where c is the work-hardening constant, characteristic for a given material. Substitution of the relationship in Eq. (5.186) into Eq. (5.185) yields:

$$H' = c \frac{\partial f}{\partial \sigma_{ij}} \frac{\partial g}{\partial \sigma_{ij}} \tag{5.187}$$

Ziegler's rule

On the other hand, the Ziegler's hardening rule assumes the rate of translation to take place in the direction of the reduced-stress vector $\bar{\sigma}_{ij} = \sigma_{ij} - \alpha_{ij}$ in the form:

$$d\alpha_{ij} = d\mu\, \bar{\sigma}_{ij} = d\mu(\sigma_{ij} - \alpha_{ij}) \tag{5.188}$$

where $d\mu$ is a positive proportionality factor which depends on the history of the deformation. For simplicity, the factor $d\mu$ can be assumed in the form:

$$d\mu = a\, d\epsilon_{p} \tag{5.189}$$

where a is a positive constant, characteristic for a given material. The plastic hardening modulus H' for this material thus takes the form:

$$H' = aC \frac{\partial f}{\partial \sigma_{ij}} \left(\frac{\partial g}{\partial \sigma_{kl}} \frac{\partial g}{\partial \sigma_{kl}} \right)^{1/2} (\sigma_{ij} - \alpha_{ij}) \tag{5.190}$$

5.10.4 *Mixed hardening*

General derivation

In engineering applications for soils, the concept of combined isotropic and kinematic hardening, called the *mixed hardening*, is attractive;, i.e., the yield surface is allowed both to expand and to translate. The general loading function for an *anisotropic hardening* material can be expressed as a combination of the kinematic hardening with the isotropic hardening rules. For example, it has the form:

$$f = f\left[\sigma_{ij} \quad \alpha_{ij}, \ x(\epsilon^{\mathrm{p}}_{ij}), \ \kappa(\epsilon_{\mathrm{p}})\right] \tag{5.191}$$

The consistency condition implies:

$$\mathrm{d}f = \frac{\partial f}{\partial \sigma_{ij}} (\mathrm{d}\sigma_{ij} - \mathrm{d}\alpha_{ij}) + \frac{\partial f}{\partial x} \frac{\partial x}{\partial \epsilon^{\mathrm{p}}_{ij}} \mathrm{d}\epsilon^{\mathrm{p}}_{ij} + \frac{\partial f}{\partial \kappa} \frac{\mathrm{d}\kappa}{\mathrm{d}\epsilon_{\mathrm{p}}} C (\mathrm{d}\epsilon^{\mathrm{p}}_{ij} \ \mathrm{d}\epsilon^{\mathrm{p}}_{ij})^{1/2} = 0 \tag{5.192a}$$

or

$$\mathrm{d}f \quad \frac{\partial f}{\partial \sigma_{ij}} \mathrm{d}\sigma_{ij} \quad \frac{\partial f}{\partial \sigma_{ij}} \frac{\partial \alpha_{ij}}{\partial \epsilon^{\mathrm{p}}_{kl}} \mathrm{d}\epsilon^{\mathrm{p}}_{kl} + \frac{\partial f}{\partial x} \frac{\partial x}{\partial \epsilon^{\mathrm{p}}_{ij}} \mathrm{d}\epsilon^{\mathrm{p}}_{ij} + \frac{\partial f}{\partial \kappa} \frac{\mathrm{d}\kappa}{\mathrm{d}\epsilon_{\mathrm{p}}} C (\mathrm{d}\epsilon^{\mathrm{p}}_{ij} \ \mathrm{d}\epsilon^{\mathrm{p}}_{ij})^{1/2} = 0 \tag{5.192b}$$

The hardening modulus H' can therefore be written from Eq. (5.192b) as:

$$H' \quad \frac{\partial f}{\partial \sigma_{ij}} \frac{\partial \alpha_{ij}}{\partial \epsilon^{\mathrm{p}}_{kl}} \frac{\partial g}{\partial \sigma_{kl}} - \frac{\partial f}{\partial x} \frac{\partial x}{\partial \epsilon^{\mathrm{p}}_{ij}} \frac{\partial g}{\partial \sigma_{ij}} - \frac{\partial f}{\partial \kappa} \frac{\mathrm{d}\kappa}{\mathrm{d}\epsilon_{\mathrm{p}}} C \left(\frac{\partial g}{\partial \sigma_{ij}} \frac{\partial g}{\partial \sigma_{ij}} \right)^{1/2} \tag{5.193}$$

Example 5.3: We shall derive the hardening modulus H' for the mixed hardening model whose loading function can be written as:

$$f \quad f\left[\sigma_{ij} \quad \alpha_{ij}, \ \kappa(\epsilon_{\mathrm{p}})\right] \tag{5.194}$$

where κ is a function of the *reduced-effective plastic strain* which is similarly defined as:

$$\bar{\epsilon}_{\mathrm{p}} = \int \mathrm{d}\bar{\epsilon}_{\mathrm{p}} = C \int (\mathrm{d}\bar{\epsilon}^{\mathrm{p}}_{ij} \ \mathrm{d}\bar{\epsilon}^{\mathrm{p}}_{ij})^{1/2} \tag{5.195}$$

This quantity governs the process of isotropic hardening; the increment of reduced plastic strain $d\bar{\epsilon}^{p}_{ij}$ is defined in what follows:

The increment of plastic strain is now simply split into two collinear components such as:

$$d\epsilon^{p}_{ij} = d\epsilon^{p(i)}_{ij} + d\epsilon^{p(k)}_{ij} \tag{5.196}$$

where $d\epsilon^{p(i)}_{ij}$ is associated with the expansion of the yield surface and $d\epsilon^{p(k)}_{ij}$ is associated with the translation of the yield surface. These two plastic strain components may be written as:

$$d\epsilon^{p(i)}_{ij} = M\, d\epsilon^{p}_{ij} \tag{5.197a}$$

$$d\epsilon^{p(k)}_{ij} = (1 - M)\, d\epsilon^{p}_{ij} \tag{5.197b}$$

where M is a material parameter which takes the value in the range:

$$-1 \leq M \leq 1 \tag{5.198}$$

The parameter M defines the share of the isotropic hardening in the total amount of hardening. M is therefore called the parameter of *mixed hardening*. Since the parameter M can also assume negative values, isotropic softening may also be considered. This implies that during the translation, the yield surface is assumed either to expand or to contract. Such a contraction is sometimes observed in experimental studies.

The isotropic part of the plastic strain increment $d\epsilon^{p(i)}_{ij}$ associated with the expansion of the yield surface is now used to define the reduced-plastic strain increment $d\bar{\epsilon}^{p}_{ij}$, that is:

$$d\bar{\epsilon}^{p}_{ij} = d\epsilon^{p(i)}_{ij} = M\, d\epsilon^{p}_{ij} \tag{5.199}$$

On the other hand, the kinematic part of the plastic strain increment $d\epsilon^{p(k)}_{ij}$ is used to define the rate of translation of the yield surface.

Prager's rule

For the case of Prager's hardening rule, the relationship between $d\alpha_{ij}$ and $d\epsilon^{p(k)}_{ij}$ is given by:

$$d\alpha_{ij} = c\, d\epsilon^{p(k)}_{ij} = c(1 - M)\, d\epsilon^{p}_{ij} \tag{5.200}$$

The consistency condition for this type of mixed hardening material is:

$$df = \frac{\partial f}{\partial \sigma_{ij}}\, d\sigma_{ij} - \frac{\partial f}{\partial \sigma_{ij}}\, d\alpha_{ij} + \frac{\partial f}{\partial \kappa}\frac{d\kappa}{d\bar{\epsilon}_{p}}\, d\bar{\epsilon}_{p} = 0 \tag{5.201}$$

Substituting $d\alpha_{ij}$ of Eq. (5.200) and $d\bar{\epsilon}_p$ of Eq. (5.195) into Eq. (5.201), we obtain:

$$df = \frac{\partial f}{\partial \sigma_{ij}} d\sigma_{ij} - c(1-M)\frac{\partial f}{\partial \sigma_{ij}} d\epsilon^p_{ij} + CM\frac{\partial f}{\partial \kappa}\frac{d\kappa}{d\bar{\epsilon}_p}(d\epsilon^p_{ij}\, d\epsilon^p_{ij})^{1/2} = 0 \tag{5.202}$$

Further substituting Eq. (5.7) and solving for hardening modulus H', we obtain:

$$H' = c(1-M)\frac{\partial f}{\partial \sigma_{ij}}\frac{\partial g}{\partial \sigma_{ij}} - CM\frac{\partial f}{\partial \kappa}\frac{d\kappa}{d\bar{\epsilon}_p}\left(\frac{\partial g}{\partial \sigma_{ij}}\frac{\partial g}{\partial \sigma_{ij}}\right)^{1/2} \tag{5.203}$$

Ziegler's Rule

For the case of Ziegler's hardening rule, the relationship between $d\alpha_{ij}$ and $d\epsilon^{p(k)}_{ij}$ is given by:

$$\begin{aligned} d\alpha_{ij} &= aC\left[d\epsilon^{p(k)}_{mn}\, d\epsilon^{p(k)}_{mn}\right]^{1/2}(\sigma_{ij} - \alpha_{ij}) \\ &= aC(1-M)(d\epsilon^p_{mn}\, d\epsilon^p_{mn})^{1/2}(\sigma_{ij} - \alpha_{ij}) \end{aligned} \tag{5.204}$$

Therefore, hardening modulus H' takes the following form:

$$H' = aC(1-M)\frac{\partial f}{\partial \sigma_{ij}}\left(\frac{\partial g}{\partial \sigma_{kl}}\frac{\partial g}{\partial \sigma_{kl}}\right)^{1/2}(\sigma_{ij} - \alpha_{ij}) - CM\frac{\partial f}{\partial \kappa}\frac{d\kappa}{d\bar{\epsilon}_p}\left(\frac{\partial g}{\partial \sigma_{ij}}\frac{\partial g}{\partial \sigma_{ij}}\right)^{1/2} \tag{5.205}$$

Comments on the hardening modulus

Since the translation increment of the center of a yield surface $d\alpha_{ij}$ has been so far described explicitly in terms of the plastic strain increment $d\epsilon^p_{ij}$, the hardening modulus H' can be easily obtained. However, the increment of translation $d\alpha_{ij}$ may in general take an implicit form with respect to the plastic strain increment $d\epsilon^p_{ij}$. For instance, in the nested yield surface models proposed by Mróz (1967) and Prévost (1977, 1978), the hardening modulus H' is first assumed to be a constant or a function of the effective plastic strain ϵ_p and then the kinematic hardening rule is determined to satisfy the consistency condition.

5.11 STIFFNESS FORMULATION

In this Section, Eq. (5.172) will be transformed into a form readily applicable for a direct use in a finite element stress analysis. To this end, a general description of Eq. (5.172) is given in a matrix form for several hardening plasticity models.

5.11.1 General description

Since an anisotropic hardening model is a homogeneous function in $(\sigma_{ij} - \alpha_{ij})$, $\partial f/\partial \sigma_{ij}$ and $\partial g/\partial \sigma_{ij}$ can be generally written respectively as:

$$\frac{\partial g}{\partial \sigma_{ij}} = \frac{\partial g}{\partial \bar{\sigma}_{ij}} = \frac{\partial g}{\partial \bar{I}_1}\frac{\partial \bar{I}_1}{\partial \sigma_{ij}} + \frac{\partial g}{\partial \bar{J}_2}\frac{\partial \bar{J}_2}{\partial \sigma_{ij}} + \frac{\partial g}{\partial \bar{J}_3}\frac{\partial \bar{J}_3}{\partial \sigma_{ij}} \tag{5.206b}$$

$$\frac{\partial f}{\partial \sigma_{ij}} = \frac{\partial f}{\partial \bar{\sigma}_{ij}} = \frac{\partial f}{\partial \bar{I}_1}\frac{\partial I_1}{\partial \sigma_{ij}} + \frac{\partial f}{\partial \bar{J}_2}\frac{\partial J_2}{\partial \sigma_{ij}} + \frac{\partial f}{\partial \bar{J}_3}\frac{\partial J_3}{\partial \sigma_{ij}} \tag{5.206a}$$

where $\bar{\sigma}_{ij}$ is the *reduced-stress tensor* denoted by $(\sigma_{ij} - \alpha_{ij})$, $I_1 = \sigma_{ii}$, $J_2 = \frac{1}{2}s_{ij}s_{ij}$, and $J_3 = \frac{1}{3}s_{ij}\bar{s}_{jk}\bar{s}_{ki}$ in which s_{ij} is the *reduced-deviatoric stress tensor* denoted by:

$$\bar{s}_{ij} = s_{ij} - \left(\alpha_{ij} - \tfrac{1}{3}\alpha_{kk}\delta_{ij}\right) \tag{5.207a}$$

or writing $\beta_{ij} = \alpha_{ij} - \frac{1}{3}\alpha_{kk}\delta_{ij}$:

$$\bar{s}_{ij} = s_{ij} - \beta_{ij} \tag{5.207b}$$

Since

$$\frac{\partial \bar{I}_1}{\partial \sigma_{ij}} = \delta_{ij} \tag{5.208a}$$

$$\frac{\partial \bar{J}_2}{\partial \sigma_{ij}} = \bar{s}_{ij} \tag{5.208b}$$

$$\frac{\partial \bar{J}_3}{\partial \sigma_{ij}} = \bar{t}_{ij} = \bar{s}_{ik}\bar{s}_{kj} - \tfrac{2}{3}\bar{J}_2\delta_{ij} \tag{5.208c}$$

Eq. (5.206) can be represented as:

$$\frac{\partial f}{\partial \sigma_{ij}} = \frac{\partial f}{\partial \bar{\sigma}_{ij}} = \frac{\partial f}{\partial \bar{I}_1}\delta_{ij} + \frac{\partial f}{\partial \bar{J}_2}\bar{s}_{ij} + \frac{\partial f}{\partial \bar{J}_3}\bar{t}_{ij} \tag{5.209a}$$

$$\frac{\partial g}{\partial \sigma_{ij}} = \frac{\partial g}{\partial \bar{\sigma}_{ij}} = \frac{\partial g}{\partial \bar{I}_1}\delta_{ij} + \frac{\partial g}{\partial \bar{J}_2}\bar{s}_{ij} + \frac{\partial g}{\partial \bar{J}_3}\bar{t}_{ij} \tag{5.209b}$$

Utilizing Eqs. (5.209) and $C_{ijkl} = \lambda\delta_{ij}\delta_{kl} + \mu(\delta_{ik}\delta_{jl} + \delta_{il}\delta_{jk})$ into Eq. (5.172), after some simplifications, we obtain the following incremental stress-strain relations:

$$d\sigma_{ij} = C^{ep}_{ijkl}\, d\epsilon_{kl} \tag{5.210}$$

where C^{ep}_{ijkl} is the elastic-plastic constituent tensor given by:

$$C^{ep}_{ijkl} = C_{ijkl} - \frac{1}{H} H^*_{ij} H_{kl} \tag{5.211}$$

in which

$$H = 3AL(3\lambda + 2\mu) + 2B\mu\left(2M\bar{J}_2 + 3N\bar{J}_3\right) + 2C\mu\left(3M\bar{J}_3 + N\bar{s}_{ik}\bar{s}_{kj}\bar{s}_{ji} - \tfrac{4}{3}N\bar{J}_2^2\right) + H' \tag{5.212a}$$

$$H_{ij} = A(3\lambda + 2\mu)\delta_{ij} + 2\mu B\bar{s}_{ij} + 2\mu C\bar{t}_{ij} \tag{5.212b}$$

$$H^*_{ij} = L(3\lambda + 2\mu)\delta_{ij} + 2\mu M\bar{s}_{ij} + 2\mu N t_{ij} \tag{5.212c}$$

$$A = \frac{\partial f}{\partial I_1}, \quad B = \frac{\partial f}{\partial J_2}, \quad C = \frac{\partial f}{\partial J_3} \tag{5.212d}$$

$$L = \frac{\partial g}{\partial I_1}, \quad M = \frac{\partial g}{\partial J_2}, \quad N = \frac{\partial g}{\partial J_3} \tag{5.212e}$$

where λ and μ are Lamé constants.

For the special case of plane strain condition, the elastic-plastic matrix reduces to:

$$\begin{Bmatrix} d\sigma_{11} \\ d\sigma_{22} \\ d\sigma_{12} \\ d\sigma_{33} \end{Bmatrix} = \begin{bmatrix} \lambda + 2\mu - \frac{1}{H}H^*_{11}H_{11} & \lambda - \frac{1}{H}H^*_{11}H_{22} & -\frac{1}{H}H^*_{11}H_{12} \\ \lambda - \frac{1}{H}H^*_{22}H_{11} & \lambda + 2\mu - \frac{1}{H}H^*_{22}H_{22} & -\frac{1}{H}H^*_{22}H_{12} \\ \frac{1}{H}H^*_{12}H_{11} & -\frac{1}{H}H^*_{12}H_{22} & \mu - \frac{1}{H}H^*_{12}H_{12} \\ \lambda - \frac{1}{H}H^*_{33}H_{11} & \lambda - \frac{1}{H}H^*_{33}H_{22} & -\frac{1}{H}H^*_{33}H_{12} \end{bmatrix} \begin{Bmatrix} d\epsilon_{11} \\ d\epsilon_{22} \\ d\gamma_{12} \end{Bmatrix} \tag{5.213}$$

Similarly, the stiffness matrices for plane stress and axisymmetric conditions can be obtained from Eq. (5.211).

As can be understood from Eq. (5.211), the stiffness matrix is not symmetric for a non-associated flow rule material but becomes symmetric for the associated flow rule material.

It should be noted that the stiffness formulation derived above for an anisotropic hardening material is readily applicable for an isotropic hardening material, by

simply replacing the reduced-stress tensor $\bar{\sigma}_{ij}$ and the reduced-deviatoric stress tensor s_{ij} with σ_{ij} and s_{ij} respectively, i.e., by setting $\alpha_{ij} = 0$ and by taking off the superscript "-".

Example 5.4: Derive the hardening modulus H' for the Coulomb, Tresca, von Mises, and Drucker-Prager materials with the isotropic hardening rule (allowed to expand isotropically).

Solution: Material constant c contained in the Coulomb model, and material constant k in the Tresca, von Mises and Drucker-Prager models are now assumed to be functions of the effective plastic strain ϵ_p. From Eq. (5.178), H' is respectively written as:
for the Coulomb model

$$H' = -C\frac{\partial f}{\partial c}\frac{\mathrm{d}c}{\mathrm{d}\epsilon_p}\left(\frac{\partial g}{\partial \sigma_{ij}}\frac{\partial g}{\partial \sigma_{ij}}\right)^{1/2} \tag{5.214a}$$

or for the Tresca, von Mises and Drucker-Prager models

$$H' = -C\frac{\partial f}{\partial k}\frac{\mathrm{d}k}{\mathrm{d}\epsilon_p}\left(\frac{\partial g}{\partial \sigma_{ij}}\frac{\partial g}{\partial \sigma_{ij}}\right)^{1/2} \tag{5.214b}$$

where $\mathrm{d}c/\mathrm{d}\epsilon_p$ or $\mathrm{d}k/\mathrm{d}\epsilon_p$ is obtained from experimental data. Substituting Eqs. (5.209a) and (5.209b) into Eqs. (5.214a) and (5.214b), after an elaborate calculation, we find:

$$H' = -C\frac{\partial f}{\partial c}\frac{\mathrm{d}c}{\mathrm{d}\epsilon_p}\left[3L^2 + 2M^2J_2 + 6MNJ_3 + N^2\left(s_{ik}s_{kl}s_{ij}s_{lj} - \tfrac{4}{3}J_2^2\right)\right]^{1/2} \tag{5.215a}$$

or

$$H' = -C\frac{\partial f}{\partial k}\frac{\mathrm{d}k}{\mathrm{d}\epsilon_p}\left[3L^2 + 2M^2J_2 + 6MNJ_3 + N^2\left(s_{ik}s_{kl}s_{ij}s_{lj} - \tfrac{4}{3}J_2^2\right)\right]^{1/2} \tag{5.215b}$$

If the associated flow rule is assumed, the expressions for L, M, and N are respectively obtained from the yield functions.

5.11.2 *Stiffness coefficients*

In the following, the hardening modulus H' and the expressions for A, B, C, L, M, and N are derived for several hardening plasticity models such as the isotropic work-hardening models by Lade and Duncan, by Lade, and the anisotropic models by Prévost, under the assumption of the associated flow rule as well as a non-associated flow rule.

(A) Lade-Duncan model

The isotropic work-hardening model of Lade and Duncan (1973, 1975) has the loading surface whose size is controlled by the plastic work done in the course of the plastic deformation. The function of the loading surface is written again as:

$$f = I_1^3 - \kappa(W_p) I_3 \tag{5.216a}$$

or

$$f = I_1^3 - \kappa(W_p)\left(\tfrac{1}{27} I_1^3 - \tfrac{1}{3} I_1 J_2 + J_3\right) \tag{5.216b}$$

where κ has a constant value depending on the stress level, and it is a function of the plastic work W_p.

On the other hand, the plastic potential function is expressed by a similar function such as:

$$g = I_1^3 - \kappa_2\left(\tfrac{1}{27} I_1^3 - \tfrac{1}{3} I_1 J_2 + J_3\right) \tag{5.217}$$

where κ_2 is a function of κ.

The stiffness coefficients are thus derived by utilizing these functions, f and g:

$$\frac{\partial f}{\partial I_1} = A = 3I_1^2 - \kappa(W_p)\left(\tfrac{1}{9} I_1^2 - \tfrac{1}{3} J_2\right) \tag{5.218a}$$

$$\frac{\partial f}{\partial J_2} = B = \tfrac{1}{3}\kappa(W_p) I_1 \tag{5.218b}$$

$$\frac{\partial f}{\partial J_3} = C = -\kappa(W_p) \tag{5.218c}$$

Similarly:

$$\frac{\partial g}{\partial I_1} = L = 3I_1^2 - \kappa_2\left(\tfrac{1}{9} I_1^2 - \tfrac{1}{3} J_2\right) \tag{5.219a}$$

$$\frac{\partial g}{\partial J_2} = M = \tfrac{1}{3}\kappa_2 I_1 \tag{5.219b}$$

$$\frac{\partial g}{\partial J_3} = N = -\kappa_2 \tag{5.219c}$$

The hardening modulus, H', in Eq. (5.182) for the isotropic work-hardening model is again expressed by:

$$H' = -\frac{\partial f}{\partial \kappa}\frac{\mathrm{d}\kappa}{\mathrm{d}W_p}\sigma_{ij}\frac{\partial g}{\partial \sigma_{ij}} \tag{5.220}$$

where $\partial f/\partial \kappa$ and $d\kappa/dW_p$ are respectively from Eqs. (5.216b) and (5.34):

$$\frac{\partial f}{\partial \kappa} = -\left(\tfrac{1}{27} I_1^3 - \tfrac{1}{3} I_1 J_2 + J_3\right) \tag{5.221a}$$

$$\frac{d\kappa}{dW_p} = \frac{1}{a}\left[1 - d(\kappa - \kappa_t)\right]^2 \tag{5.221b}$$

The parameters a, d and κ_t are material characteristics determined from experimental results. Since $\sigma_{ij}\partial g/\partial \sigma_{ij} = 3g$, we finally obtain H' in the form:

$$H' = \frac{3g}{a}\left[1 - d(\kappa - \kappa_t)\right]^2\left(\tfrac{1}{27} I_1^3 - \tfrac{1}{3} I_1 J_2 + J_3\right) \tag{5.222}$$

(B) Lade model

The Lade-Duncan model whose yield surface grows isotropically due to the plastic work can be extended by adding a spherical yield cap surface at the end along the hydrostatic axis. The effect of isotropic consolidation on the plastic deformation of soils is therefore controlled by the cap surface.

Loading surfaces. The function of the conical curved-yield surface is described by Eq. (5.39) in terms of the first and the third stress invariants, I_1 and I_3:

$$f = I_1^3 - \left[27 + f_p(W_p)(p_a/I_1)^m\right] I_3 \tag{5.223}$$

where the parameter f_p and m are the two constants to be determined for a specific density of soils, and p_a is the atmospheric pressure whose dimension is the same as that of stress. The plastic potential function, g, of the yield surface is modeled similarly by:

$$g = I_1^3 - \left[27 + \eta_2(p_a/I_1)^m\right] I_3 \tag{5.224}$$

where η_2 is a constant for given values of f_p and the confining pressure σ_3. Replacing the third stress invariant of I_3 by the stress invariants I_1, J_2, and J_3, the yield and plastic potential functions in Eqs. (5.223) and (5.224) are respectively written as:

$$f = I_1^3 - \left[27 + f_p(W_p')(p_a/I_1)^m\right]\left(\tfrac{1}{27} I_1^3 - \tfrac{1}{3} I_1 J_2 + J_3\right) \tag{5.225}$$

and

$$g = I_1^3 - \left[27 + \eta_2(p_a/I_1)^m\right]\left(\tfrac{1}{27} I_1^3 - \tfrac{1}{3} I_1 J_2 + J_3\right) \tag{5.226}$$

Thus, the stiffness coefficients for the conical curved-yield surface can be derived as follows:

$$\frac{\partial f}{\partial I_1} = A = 3I_1^2 + f_p(W_p)m(p_a/I_1)^m(1/I_1)\left(\tfrac{1}{27}I_1^3 - \tfrac{1}{3}I_1J_2 + J_3\right)$$

$$-\left[27 + f_p(W_p)(p_a/I_1)^m\right]\left(\tfrac{1}{9}I_1^2 - \tfrac{1}{3}J_2\right) \tag{5.227a}$$

$$\frac{\partial f}{\partial J_2} \quad B = \tfrac{1}{3}I_1\left[27 + f_p(W_p)(p_a/I_1)^m\right] \tag{5.227b}$$

and

$$\frac{\partial f}{\partial J_3} = C = -\left[27 + f_p(W_p)(p_a/I_1)^m\right] \tag{5.227c}$$

Similarly, for the coefficients L, M, and N, we have:

$$\frac{\partial g}{\partial I_1} = L = 3I_1^2 + \eta_2 m(p_a/I_1)^m(1/I_1)\left(\tfrac{1}{27}I_1^3 - \tfrac{1}{3}I_1J_2 + J_3\right)$$

$$-\left[27 + \eta_2(p_a/I_1)^m\right]\left(\tfrac{1}{9}I_1^2 - \tfrac{1}{3}J_2\right) \tag{5.228a}$$

$$\frac{\partial g}{\partial J_2} = M = \tfrac{1}{3}I_1\left[27 + \eta_2(p_a/I_1)^m\right] \tag{5.228b}$$

and

$$\frac{\partial g}{\partial J_3} = N = -\left[27 + \eta_2(p_a/I_1)^m\right] \tag{5.228c}$$

The hardening modulus, H', is expressed in a similar manner to that of Eq. (5.220) as:

$$H' = \frac{\partial f}{\partial f_p}\frac{\mathrm{d}f_p}{\mathrm{d}W_p}\sigma_{ij}\frac{\partial g}{\partial \sigma_{ij}} \tag{5.229}$$

where $\partial f/\partial f_p$ and $\mathrm{d}f_p/\mathrm{d}W_p$ are respectively obtained from Eqs. (5.225) and (5.43), that is:

$$\frac{\partial f}{\partial f_p} = -(p_a/I_1)^m\left(\tfrac{1}{27}I_1^3 - \tfrac{1}{3}I_1J_2 + J_3\right) \tag{5.230a}$$

$$\frac{\mathrm{d}f_p}{\mathrm{d}W_p} = f_p(W_p)\left(\frac{1}{rW_p} - b\right) \tag{5.230b}$$

The parameters b and r in Eq. (5.230b) are constants for a given value of the confining pressure σ_3. Further, $\sigma_{ij}(\partial g/\partial \sigma_{ij})$ can be reduced to the form consisting of the stiffness coefficients derived above. Thus, they can be used directly for finite-element applications.

Cap surfaces. The spherical yield cap function, f, can be written from Eq. (5.38) in terms of the first and the second stress invariants as:

$$f = I_1^2 - 2I_2 - f_c(W_c) \tag{5.231}$$

where f_c is the hardening parameter which is a function of the plastic work, W_c. For the spherical yield cap surface, the associated flow rule is employed, i.e., the plastic potential function g is identical to the cap yield function f. Equation (5.231) can be expressed in terms of I_1 and J_2 by:

$$f = g = \tfrac{1}{3}I_1^2 + 2J_2 - f_c(W_c) \tag{5.232}$$

Therefore, the stiffness coefficients are similarly obtained:

$$\frac{\partial f}{\partial I_1} = \frac{\partial g}{\partial I_1} = A = L = \tfrac{2}{3}I_1 \tag{5.233a}$$

$$\frac{\partial f}{\partial J_2} = \frac{\partial g}{\partial J_2} = B = M = 2 \tag{5.233b}$$

$$\frac{\partial f}{\partial J_3} = \frac{\partial g}{\partial J_3} = C = N = 0 \tag{5.233c}$$

and the hardening modulus, H', is expressed by:

$$H' = -\frac{\partial f}{\partial f_c}\frac{\mathrm{d}f_c}{\mathrm{d}W_c}\sigma_{ij}\frac{\partial g}{\partial \sigma_{ij}} \tag{5.234}$$

The derivatives $(\partial f/\partial f_c)$ and $(\mathrm{d}f_c/\mathrm{d}W_c)$ are respectively obtained from Eqs. (5.231) and (5.42) as:

$$\frac{\partial f}{\partial f_c} = -1 \tag{5.235a}$$

$$\frac{\mathrm{d}f_c}{\mathrm{d}W_c} = \frac{p_a}{Cq}\left(f_c/p_a^2\right)^{1-q} \tag{5.235b}$$

where C and q are constants. Further, the calculation of $\sigma_{ij}(\partial g/\partial \sigma_{ij})$ yields:

$$\sigma_{ij}\frac{\partial g}{\partial \sigma_{ij}} = 2f_c(W_c) \tag{5.236}$$

Thus, the hardening modulus, H', can be written as:

$$H' = \frac{2p_a}{Cq} f_c(W_c)\left(f_c/p_a^2\right)^{1-q} \tag{5.237}$$

Stiffness treatment at corner. So far we have derived stiffness coefficients corresponding to each yield or hardening surface of the Lade model. Next, we shall discuss the corner treatment of the model where the state of stress reaches or lies at the corner of the yield surface intersecting with the hardening cap surface.

As a general consideration, we shall assume that, at the corner where each of the n-yield (or failure) surfaces intersects, each yield (or failure) surface produces plastic strain increments whose sum makes up the total plastic strain increments, $d\epsilon_{ij}^p$, that is:

$$d\epsilon_{ij}^p = d\epsilon_{ij}^{p1} + d\epsilon_{ij}^{p2} + \ldots + d\epsilon_{ij}^{pk} + \ldots + d\epsilon_{ij}^{pn} \tag{5.238}$$

where $d\epsilon_{ij}^{pk}$ is the plastic strain increments associated with the k-th yield (or failure) surface ($1 \le k \le n$). Each plastic strain increment $d\epsilon_{ij}^{pk}$ is expressed by:

$$d\epsilon_{ij}^{pk} = d\lambda^{(k)} \frac{\partial g_k}{\partial \sigma_{ij}} \tag{5.239}$$

where $d\lambda^{(k)}$ and g_k are the proportionality factor and the plastic potential function associated with the k-th yield surface. Since the strain increment tensor $d\epsilon_{ij}$ consists of six independent components, the maximum number of independent plastic strain increments is five, i.e., $n \le 5$, because one independent strain increment is elastic.

Substitution of Eqs. (5.238) and (5.239) into the linear elastic stress-strain relations leads to:

$$d\sigma_{ij} = C_{ijkl}(d\epsilon_{kl} - d\epsilon_{kl}^p)$$

$$C_{ijkl}\left[d\epsilon_{kl} - d\lambda^{(1)} \frac{\partial g_1}{\partial \sigma_{kl}} - \ldots - d\lambda^{(k)} \frac{\partial g_k}{\partial \sigma_{kl}} - \ldots - d\lambda^{(n)} \frac{\partial g_n}{\partial \sigma_{kl}}\right] \tag{5.240}$$

where C_{ijkl} is the fourth-order constituent tensor for the linear isotropic elastic material described in Chapter 3.

Unlike a single yield surface, Eq. (5.240) contains n unknown proportionality factors. Thus, the following process should be performed in order to determine these n unknowns. Consider the general n isotropic work-hardening functions f_k ($1 \le k \le n \le 5$) expressed by:

$$f_k = f_k\left[\sigma_{ij}, \eta_k(W_{pk})\right] \tag{5.241}$$

where

$$W_{pk} = \int \sigma_{ij}\, d\epsilon_{ij}^{pk} \tag{5.242}$$

The consistency condition for each function f_k can therefore be written as:

$$df_k = \frac{\partial f_k}{\partial \sigma_{ij}}\, d\sigma_{ij} + \frac{\partial f_k}{\partial W_{pk}} \frac{\partial W_{pk}}{\partial \epsilon_{ij}^{pk}}\, d\epsilon_{ij}^{pk} = 0 \tag{5.243}$$

Substituting $d\sigma_{ij}$ of Eq. (5.240) and $d\epsilon_{ij}^{pk}$ of Eq. (5.239) into Eq. (5.243) results in:

$$\frac{\partial f_k}{\partial \sigma_{ij}} C_{ijkl} \left| d\epsilon_{kl} - d\lambda^{(1)} \frac{\partial g_1}{\partial \sigma_{kl}} - \cdots - d\lambda^{(k)} \frac{\partial g_k}{\partial \sigma_{kl}} - \cdots - d\lambda^{(n)} \frac{\partial g_n}{\partial \sigma_{kl}} \right|$$

$$+ d\lambda^{(k)} \frac{\partial f_k}{\partial W_{pk}} \frac{\partial W_{pk}}{\partial \epsilon_{ij}^{pk}} \frac{\partial g_k}{\partial \sigma_{ij}} = 0 \tag{5.244}$$

Equation (5.244) is a simultaneous equation corresponding to n proportionality factors. Solving the above equations for $d\lambda^{(1)}, \ldots, d\lambda^{(n)}$, we finally obtain the elastic-plastic constitutive equations after substitution into Eq. (5.240). In this case, the corner treatment has been done with a relative ease since the parameter η_k in each yield function f_k is related to ϵ_{ij}^{pk}. However, the mathematical treatment at corner will be more difficult for the present case, because the parameter η_k is a function of the total plastic strain ϵ_{ij}^{p}.

For the special case of the Lade model, we shall describe the corner treatment caused by two surfaces, i.e., the yield surface and the hardening cap surface expressed respectively by Eqs. (5.225) and (5.232). The yield and hardening cap surfaces are now denoted by f_1 and f_2, respectively. Further, their plastic potential surfaces are similarly given by g_1 and g_2 $(= f_2)$. Simultaneous equations are thus written as:

$$d\lambda^{(1)} A_{11} + d\lambda^{(2)} A_{12} = B_1 \tag{5.245a}$$

$$d\lambda^{(1)} A_{21} + d\lambda^{(2)} A_{22} = B_2 \tag{5.245b}$$

where $d\lambda^{(1)}$ and $d\lambda^{(2)}$ are the positive proportionality factors and the coefficients A_{11}, A_{12}, A_{21}, A_{22}, B_1, and B_2 are expressed by:

$$A_{11} = \frac{\partial f_1}{\partial \sigma_{ij}} C_{ijkl} \frac{\partial g_1}{\partial \sigma_{kl}} - \frac{\partial f_1}{\partial f_p} \frac{df_p}{dW_p} \frac{\partial W_p}{\partial \epsilon_{ij}^{p}} \frac{\partial g_1}{\partial \sigma_{ij}} \tag{5.246a}$$

$$A_{12} = \frac{\partial f_1}{\partial \sigma_{ij}} C_{ijkl} \frac{\partial g_2}{\partial \sigma_{kl}} \tag{5.246b}$$

$$A_{21} = \frac{\partial f_2}{\partial \sigma_{ij}} C_{ijkl} \frac{\partial g_1}{\partial \sigma_{kl}} \tag{5.246c}$$

$$A_{22} = \frac{\partial f_2}{\partial \sigma_{ij}} C_{ijkl} \frac{\partial g_2}{\partial \sigma_{kl}} - \frac{\partial f_2}{\partial f_c} \frac{\mathrm{d}f_c}{\mathrm{d}W_c} \frac{\partial W_c}{\partial \epsilon_{ij}^c} \frac{\partial g_2}{\partial \sigma_{ij}} \tag{5.246d}$$

$$B_1 = \frac{\partial f_1}{\partial \sigma_{ij}} C_{ijkl}\, \mathrm{d}\epsilon_{kl} \tag{5.246e}$$

$$B_2 = \frac{\partial f_2}{\partial \sigma_{ij}} C_{ijkl}\, \mathrm{d}\epsilon_{kl} \tag{5.246f}$$

Solutions for $\mathrm{d}\lambda^{(1)}$ and $\mathrm{d}\lambda^{(2)}$ are thus obtained as follows:

$$\mathrm{d}\lambda^{(1)} = \frac{B_1 A_{22} - B_2 A_{12}}{A_{11} A_{22} - A_{12} A_{21}} \tag{5.247a}$$

$$\mathrm{d}\lambda^{(2)} = \frac{B_2 A_{11} - B_1 A_{21}}{A_{11} A_{22} - A_{12} A_{21}} \tag{5.247b}$$

Substitution of $\mathrm{d}\lambda^{(1)}$ and $\mathrm{d}\lambda^{(2)}$ into Eq. (5.240) yields the elastic-plastic stress-strain relations at the corner of the Lade model.

(C) Anisotropic plasticity model

The stiffness coefficients of the nested yield surface models for the undrained and drained cases by Prévost (1977, 1978) are presented in what follows. Note that the hardening moduli H' for several plasticity models have been derived previously from the consistency condition. However, the hardening moduli for multi-yield surfaces are assumed to be constant or a function of the effective plastic strain ϵ_p, from the experimental data.

Undrained case (pressure-independent). For the undrained model, the function of nested yield surface f_m can be written as:

$$f_m = \tfrac{3}{2}\left[s_{ij} - \beta_{ij}^{(m)}\right]\left[s_{ij} - \beta_{ij}^{(m)}\right] - \left[k^{(m)}\right]^2 = 0 \tag{5.248}$$

where $\beta_{ij}^{(m)}$ is the center of a yield surface in the deviatoric plane. Since the associated flow rule is assumed, $\partial f_m/\partial \sigma_{ij}$ $(= \partial g_m/\partial \sigma_{ij})$ has the value:

$$\frac{\partial f_m}{\partial \sigma_{ij}} = 3\left[s_{ij} - \beta_{ij}^{(m)}\right] \tag{5.249a}$$

or

$$\frac{\partial f_m}{\partial \sigma_{ij}} = 3 s_{ij}^{(m)} \tag{5.249b}$$

where $s_{ij}^{(m)}$ is the reduced-deviatoric stress tensor denoted by $[s_{ij} \quad \beta_{ij}^{(m)}]$. Thus, we have the following stiffness coefficients:

$$A = L = 0, \quad B = M = 3, \quad C = N = 0 \tag{5.250}$$

Drained case (pressure-dependent). For the drained model, the yield function for the m-th nested yield surface has the form:

$$f_m = \frac{1}{2}\left[s_{ij} - \beta_{ij}^{(m)}\right]\left[s_{ij} - \beta_{ij}^{(m)}\right] + C^2\left[\frac{1}{3}I_1 \quad \gamma^{(m)}\right]^2 \quad \left[k^{(m)}\right]^2 \quad 0 \tag{5.251}$$

where $\beta_{ij}^{(m)}$, $\gamma^{(m)}$ are the location of the center of a yield surface in the deviatoric plane and along the hydrostatic axis respectively, and C is a material parameter which is usually taken as $3/\sqrt{2}$. The derivatives of f_m with respect to σ_{ij} can take the form:

$$\frac{\partial f_m}{\partial \sigma_{ij}} = 3\left[s_{ij} - \beta_{ij}^{(m)}\right] + 3\left[\frac{1}{3}I_1 - \gamma^{(m)}\right]\delta_{ij} \tag{5.252a}$$

or

$$\frac{\partial f_m}{\partial \sigma_{ij}} = 3\bar{s}_{ij}^{(m)} + 3\left[\frac{1}{3}I_1 - \gamma^{(m)}\right]\delta_{ij} \tag{5.252b}$$

Therefore, we obtain the following stiffness coefficients:

$$A = 3\left(\frac{1}{3}I_1 - \gamma^{(m)}\right) \tag{5.253a}$$

$$B = 3 \tag{5.253b}$$

$$C = 0 \tag{5.253c}$$

Similarly, $\partial g_m / \partial \sigma_{ij}$ can be written from Eqs. (5.67) through (5.70) as:

$$\frac{\partial g_m}{\partial \sigma_{ij}} = 3\bar{s}_{ij}^{(m)} + \left[3\left\{\frac{1}{3}I_1 - \gamma^{(m)}\right\} + 3A_m\left(\bar{s}_{kl}^{(m)}\bar{s}_{kl}^{(m)}\right)^{1/2}\right]\delta_{ij} \tag{5.254}$$

where A_m is a parameter related to the centers of the current and outermost yield

surfaces which are measured along the hydrostatic pressure axis. Thus, we obtain:

$$L = 3\left[\tfrac{1}{3}I_1 - \gamma^{(m)}\right] + 3A_m\left(\bar{s}_{kl}^{(m)}\bar{s}_{kl}^{(m)}\right)^{1/2} \tag{5.255a}$$

$$M = 3 \tag{5.255b}$$

$$N = 0 \tag{5.255c}$$

For the outermost yield surface, L, M, and N are respectively identical to the coefficients such as A, B, and C in Eq. (5.253).

5.12 SUMMARY

This Chapter presents the basic concept, a general discussion of various plasticity models with strain- or work-hardening, and their stress-strain relations for a nonlinear stress analysis in geotechnical engineering problems.

In developing the elastic-plastic model for a hardening material, the following three basic assumptions are generally needed:

1. The existence of an initial yield surface and subsequent loading surfaces.
2. The formulation of an appropriate hardening rule that describes the evolution of the subsequent loading surfaces.
3. A flow rule that specifies the general form of the stress-strain relationship.

The first assumption states that a stress function which defines the limit of elasticity of the material exists. It is called the *initial yield function* before plastic deformations occur and called the *loading function* beyond the initial yielding. These functions, f, are viewed respectively as the initial yield surface and the subsequent yield surfaces (or loading surfaces) in the multi-dimensional stress space.

The second assumption is related to the hardening rule. In this Chapter, three types of hardening rules are considered:

1. Isotropic hardening
2. Kinematic hardening
3. Mixed hardening

The choice of a specific hardening rule depends on the ease with which it can be applied and its ability to represent the hardening behavior of the material being considered.

The third assumption states that the direction of the plastic strain increment vector $d\epsilon_{ij}^p$ is normal to the surface defined by the *plastic potential function*, g, i.e.,

$$d\epsilon_{ij}^p = d\lambda \frac{\partial g}{\partial \sigma_{ij}}$$

where $d\lambda$ is a proportionality factor determining the magnitude of the plastic strain increments. This factor can be further rewritten as:

$$d\lambda = \frac{1}{H'}\left(\frac{\partial f}{\partial \sigma_{mn}}\, d\sigma_{mn}\right)$$

where H' is the hardening modulus. As can be understood, the magnitude of $d\lambda$ depends on the magnitude of the hardening modulus and the normal component of a stress increment to the yield surface. This flow rule is generally called a *non-associated flow*.

The flow rule is of the *associated type* if the plastic potential function takes the same form as that of the yield function, that is:

$$d\epsilon_{ij}^{p} = d\lambda \frac{\partial f}{\partial \sigma_{ij}}.$$

For a stable, work-hardening material satisfying the *Drucker's stability postulate*, it can be shown that the associated flow rule or the normality condition is assured.

The plasticity models developed in this Chapter are based on these three basic assumptions. Here, as in Chapter 4, plasticity models are developed ranging from simple, perfectly plastic idealizations, to the more complex, anisotropic hardening yield surfaces such as the models proposed by Mróz (1967) and Iwan (1967). No one model can adequately reproduce the behavior of all soils under all conditions. Rather the selection of a particular model should be made while keeping in mind the important characteristics of the soil and disturbing forces (e.g., monotonic, cyclic, etc.) to be captured.

Many of the recent plasticity models appear to be rather complex, difficult to relate to physical behavior, and usually require more detailed experimental results. The successful transition from a research to practical applications of a constitutive model generally involves two stages. The first stage is of development and practical implementation. The developer, or proponent of a particular model should present the tool which is mathematically correct from the mechanics viewpoint; is simple to understand; requires a minimum of material parameters which may be obtained from common laboratory testing procedures; requires a minimum amount of user judgement with respect to calibration. The second stage is of education. The user should understand the assumptions and limitations of the model as well as the consequences of violating these criteria; the data (experimental results) necessary to calibrate the model, together with the relative sensitivity study to variations in the material parameters.

In examining the advantages and shortcomings of the isotropic hardening formulation for soils, Drucker (1966) concluded that yield surfaces are a matter of definition and the choice is not an absolute one, but is determined by the most significant features of the problem to be solved. Thus, if a small-strain-offset definition of yielding is used, the comparison of actual yield surfaces for soils with

isotropic hardening models is found rather poor in a detailed look at the yield surfaces and at the corresponding stress-strain relations. However, if a large offset definition of yielding is taken instead, a much less complicated picture emerges for variety of loading paths which does not differ much from an isotropic hardening model. For practical design purposes, the crude measure of yielding may be more relevant than the refined small strain definition.

Isotropic work-hardening model for cohesionless soils by Lade and Duncan (1973, 1975) consists of a shear loading surface which expands asymptotically to the failure surface as the shearing continues. The form of this model is simple, and it includes the effects of hydrostatic pressure, as well as the dependence of $\sqrt{J_2}$ on the Lode angle θ. However, the failure surface depicts still a straight line in $I_1 - \sqrt{J_2}$-space.

The modified Lade-Duncan surface proposed by Lade (1977) overcomes this shortcoming, taking into account the curvature of the trace of the failure surface in the meridian plane. This failure surface indicates a decreasing friction angle with an increasing confining pressure, and a θ-dependence of $\sqrt{J_2}$ on the deviatoric planes. The Lade model is an isotropic double work-hardening type which consists of a volumetric loading surface and a shear loading surface. The model has been found adequate to describe the behavior of a wide range of pressure for both sands and normally consolidated clays.

It is generally noted that adequate results for monotonic and proportional loading may be obtained from simple isotropic formulations. Difficulties arise, however, when stress paths change directions. Materials with significant anisotropic strength and deformation characteristics are particularly difficult to represent when rotations in the principal stress axis occur. The difficulties originate in the assumption of an initially isotropic material description. Mróz (1967), Iwan (1967), and Prévost (1981) have attempted to introduce the effects of anisotropy through the use of nested yield surfaces.

Prévost's nested, or multi-surface model (Fig. 5.21) is represented by ellipsoids of revolution with their initial positions defined by the pre-consolidation state. A material which has been isotropically consolidated has the centers of each ellipse on the hydrostatic axis, otherwise, it is expected the centers would fall along a line related to K_0-consolidation. It is this flexibility in defining the initial surface locations which allows the simulation of anisotropic behavior. It should be noted that the elastic description is still one of the isotropic form.

Prévost's model allows each surface to translate and expand as plastic loading occurs. A non-associated flow rule is adopted for the inner surfaces, while the associated flow rule is used for the outermost surface. Strain-softening is admitted for the outermost surface only. The translation of the surfaces is prescribed to be in the direction of a point on the next surface with the same outward normal direction.

While this model provides a realistic representation of material behavior, it is somewhat complex. Furthermore, it appears that the manner in which the individual surfaces harden may be difficult to characterize, for arbitrary three-dimensional paths, using only ordinary triaxial data.

The fact that the loading surface at large strains is almost independent of loading path leads to the concept of bounding surface models where the subsequent loading surfaces are allowed to move isotropically inside a *limit surface* or *bounding surface*. Various types of strain-hardening plasticity models have been recently employed based on such bounding (consolidation or limiting) surface concept introduced earlier for metals (e.g., Dafalias and Popov, 1975; and Krieg, 1975). A two-surface model of this type was proposed by Mróz et al. (1978, 1979) for clays. A bounding surface, $F = 0$, representing the consolidation history of the soil, and a yield surface, $f = 0$, defining the elastic domain within the bounding surface (Fig. 5.25) were employed in the model.

The bounding surface is assumed only to expand or contract isotropically, but the yield surface is allowed to translate, and expand or contract. The translation of the yield surface is governed by the same rule as the multi-surface models described earlier (i.e., the yield surface f will translate towards the bounding surface along PR in Fig. 5.25).

The hardening modulus on the yield surface is assumed to vary with the distance δ between the yield and bounding surfaces. Unlike the nested yield surface models, the bounding surface models have the definite advantages of a smooth transition from the elastic to the fully plastic state for general reversed loading which is generally observed experimentally on soils. In fact, the bounding surface model can be considered as a smooth extension of the nested yield surface model with an analytical function to replace the nest of several loading surfaces. A very detailed discussion of the present model and its application to represent the behavior of clays under monotonic and cyclic triaxial test conditions have been given by Mróz et al. (1979).

In later parts of this Chapter, the stress-strain relations for Prandtl-Reuss material with work-hardening are presented as a special case in which the J_2-criterion is used as the yield surface under the assumption of the associated flow rule.

On the other hand, the generalized stress-strain relations for various hardening materials under the assumption of the associated or a non-associated flow rule are given by:

$$d\sigma_{ij} = C^{ep}_{ijkl}\, d\epsilon_{kl}$$

where C^{ep}_{ijkl} is the fourth-order elastic-plastic constitutive tensor expressed by:

$$C^{ep}_{ijkl} = \left[C_{ijkl} - \frac{1}{H} H^{*}_{ij} H_{kl} \right] d\epsilon_{kl}$$

in which C_{ijkl} is the fourth-order elastic constitutive tensor, and H, H^{*}_{ij}, and H_{ij} have respectively different forms corresponding to different material models. This matrix form is useful for direct application to computer implementation of stress-strain relations for various forms of yield functions.

REFERENCES

Besseling, J.F., 1958. A theory of elastic, plastic and creep deformation of an initially isotropic material showing strain hardening, creep recovery and secondary creep. J. Appl. Mech., Trans., ASME, 25: 529–536.

Chen, W.F., 1982. Plasticity in Reinforced Concrete. McGraw-Hill, New York, NY, 474 pp.

Chen, W.F., 1984. Soil mechanics, plasticity and landslides. In: G.J. Dvorak and R.T. Shield (Editors), Mechanics of Material Behavior. Elsevier, Amsterdam, Netherlands, pp. 31–58.

Dafalias, Y.F. and Herrmann, L.R., 1980. A bounding surface soil plasticity model. International Symposium on Soils under Cyclic and Transient Loading, Swansea, U.K., Vol. 1, pp. 335–345.

Dafalias, Y.F. and Herrmann, L.R., 1982. A generalized bounding surface constitutive model for clays. In: R.N. Yong and E.T. Selig (Editors), Application of Plasticity and Generalized Stress-Strain in Geotechnical Engineering. ASCE, New-York, NY, pp. 78–95.

Dafalias, Y.F. and Popov, E.P., 1975. A model of nonlinearly hardening materials for complex loadings. Acta Mech., 21: 173–192.

Dafalias, Y.F. and Popov, E.P., 1976. Plastic internal variables formalism of cyclic plasticity. J. Appl. Mech., 98(4): 645–650.

Drucker, D.C., 1951. A more fundamental approach to plastic stress-strain relations. Proc., 1st U.S. National Congress on Applied Mechanics, ASME, 1951, pp. 487–491.

Drucker, D.C., 1966. Concepts of path independence and material stability for soils. In: J. Kravtchenko and P.M. Sirieys (Editors), Rhéol. Mécan. Soils Proc. IUTAM Symp. Grenoble. Springer, Berlin, pp. 23–43.

Duncan, J.M. and Chang, C.Y., 1970. Nonlinear analysis of stress and strain in soils. J. Soil Mech. Found. Div., ASCE, 96 (SM5): 1629–1653.

Duwez, P., 1935. On the plasticity of crystals. Phys. Rev., 47: 494–501.

Green, G.E. and Bishop, A.W., 1969. A note on the drained strength of sand under generalized strain conditions. Geotechnique (London, England), 19(1): 144–149.

Hill, R., 1950. The Mathematical Theory of Plasticity. Oxford University Press, London, 355 pp.

Hodge, P.G., Jr., 1957. Discussion [of Prager (1956)]. J. Appl. Mech., 23: 482–484.

Iwan, W.D., 1967. On a class of models for the yielding behavior of continuous and composite systems. J. Appl. Mech., 34: 612–617.

Joyner, W.B. and Chen, A.T.F., 1976. Calculation of nonlinear ground response in earthquakes. Bull. Seismol. Soc. Am., 65(5), 1315–1336.

Ko, H-Y. and Scott, R.F., 1968. Deformation of sand at failure. J. Soil Mech. Found. Div., ASCE, 94(SM4): 883–898.

Krieg, R.D., 1975. A practical two-surface plasticity theory. J. Appl. Mech., 42, 641–646.

Lade, P.V., 1977. Elasto-plastic stress-strain theory for cohesionless soil with curved yield surfaces. Int. J. Solids Struct., 13: 1014–1035.

Lade, P.V., 1978. Prediction of undrained behavior of sand. J. Geotech. Eng. Div., ASCE, 104(GT6): 721–735.

Lade, P.V. and Duncan, J.M., 1973. Cubical triaxial tests on cohesionless soil. J. Soil Mech. Found. Div., ASCE, 99(SM10): 793–812.

Lade, P.V. and Duncan, J.M., 1975. Elastoplastic stress-strain theory for cohesionless soil. J. Geotech. Eng. Div., ASCE, 101(GT10): 1037–1053.

Lade, P.V. and Musante, H.M., 1978. Three-dimensional behavior of remoulded clay. J. Geotech. Eng. Div., ASCE, 104(GT2): 193–209.

Lode, W., 1926. Versuche über den Einfluss der mittleren Hauptspannung auf das Fliessen der Metalle Eisen Kupfer und Nickel. Z. Phys., 36: 913–939.

Masing, G., 1926. Eigenspannungen and Verfestingung beim Messing. Proc. 2nd Int. Cong. Applied Mechanics, Zurich, Switzerland, pp. 332–335.

Mróz, Z., 1967. On the description of anisotropic hardening. J. Mech. Phys. Solids, 15: 163–175.

Mróz, Z. and Pietruszczak, ST., 1983. A constitutive model for sand with anisotropic hardening rule. Int. J. Numer. Anal. Methods Geomech., 7: 305–320.

Mróz, Z., Norris, V.A. and Zienkiewicz, O.C., 1978. An anisotropic hardening model for soils and its application to cyclic loading. Int. J. Numer. Anal. Methods Geomech., 2: 203–221.

Mróz, Z., Norris, V.A. and Zienkiewicz, O.C., 1979. Application of an anisotropic hardening model in the analysis of elastoplastic deformation of soils. Geotechnique, 29(1): 1–34.

Mróz, Z., Norris, V.A. and Zienkiewicz, O.C., 1981. An anisotropic critical state model for soils subjected to cyclic loading. Geotechnique, 31(4): 451–469.

Osgood, W.R., 1947. Combined-stress tests on 24S-T aluminum-alloy tubes. J. Appl. Mech., 14: A-147–A-153.

Pietruszczak, S.T. and Mróz, Z., 1983. On hardening anisotropy of K_0 consolidated clays. Int. J. Numer. Anal. Methods Geomech., 7: 19–38.

Prager, W., 1955. The theory of plasticity: a survey of recent achievements (James Clayton Lecture). Proc. Inst. Mech. Eng., 69(41): 3–19.

Prager, W., 1956. A new method of analyzing stress and strains in work-hardening solids. J. Appl. Mech. ASME, 23: 493–496.

Prévost, J.H., 1977. Mathematical modeling of monotonic and cyclic undrained clay behavior. Int. J. Numer. Anal. Methods Geomech., 1: 195–216.

Prévost, J.H., 1978. Plasticity theory for soil stress-strain behavior. J. Eng. Mech. Div., ASCE, 104(EM5): 1177–1194.

Prévost, J.H., Cuny, B., Hughes, T.J.R. and Scott, R.F., 1981. Offshore gravity structures: Analysis. J. Geotech. Eng. Div., ASCE, 107(GT2): 143–165.

Procter, D.C. and Barden, L., 1969. Correspondence on Green and Bishop: A note on the drained strength of sand under generalized strain conditions. Geotechnique (London, England), 19(3): 424–426.

Taylor, G.I. and Quinney, H., 1931. The plastic distortion of metals. Philos. Trans. R. Soc. London, Ser. A, 230: 323–362.

Yamada, Y., Yoshimura, N. and Sakurai, T., 1968. Plastic stress-strain matrix and its application for the solution of elastic-plastic problem by the finite element method. Int. J. Mech. Sci., 10: 343–354.

Ziegler, H., 1959. A modification of Prager's hardening rule. Appl. Math., 17: 55–65.

Zienkiewicz, O.C., Norris, V.A. and Naylor, D.J., 1977. Plasticity and visco-plasticity in soil mechanics with special reference to cyclic loading problems. In: P.G. Bergan et al. (Editors), Finite Elements in Non-Linear Mechanics. Tapir, Trondheim, Vol. 2, pp. 455–485.

Part III

MATERIAL NONLINEARITY—CAP MODELS

Chapter 6

CAP MODEL FORMULATION AND CALIBRATION

6.1 INTRODUCTION

A good soil plasticity model should meet the following four basic requirements:

1. The mathematical formulation should result in a unique and stable stress-strain relationship.
2. The constitutive equation should reflect the key characteristics of experimental data.
3. The mathematical relationship should be defined by only a few parameters which can be determined from standard test data.
4. The mathematical model should encompass the well-known Coulomb criterion as a special case.

The *cap models* and their special versions satisfy all these requirements.

Before proceeding with a general description of the cap-type of strain-hardening models, it is helpful to review the behavior of soils subjected to hydrostatic and shear type of loadings.

Figure 6.1 shows an *isotropic consolidation curve* for a remoulded clay, accompanied by an unload/reload sequence. The following four aspects of soil behavior are evident:

1. The response is path-dependent and nonlinear.
2. The behavior during unloading and reloading (path BCD) is essentially elastic with a small amount of hysteresis.
3. Unloading exposes some irrecoverable (or plastic) strain.
4. Reloading to levels greater than that previously experienced proceeds along essentially the same path as that which would have been followed had unloading not occurred.

A similar but more complicated behavior is expected for the shear type of loading.

The behavior of two specimens subjected to triaxial compression tests will now be considered. *Overconsolidated* specimen 1 (at 1 in Fig. 6.2) and *normally consolidated* specimen 2 (at 2 in Fig. 6.2) have the same void ratio. For an *undrained* triaxial compression test, both specimens respond in a constant volume manner and fail at nearly the same shear stress (point A in Fig. 6.3). The normally consolidated specimen fails with a *positive* pore pressure, while the overconsolidated specimen fails with a *negative* pore pressure. The responses of specimens 1 and 2, if instead, subjected to *drained* triaxial compression tests, show quite different behavior (Figs. 6.2 and 6.4). The normally consolidated specimen 2 contracts and eventually fails after arriving at point B. The overconsolidated sample, however, initially contracts

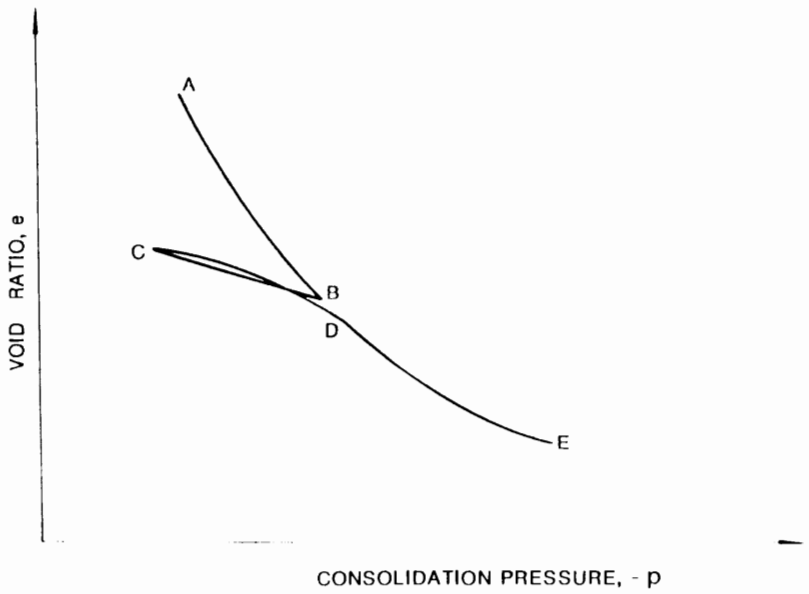

Fig. 6.1. Isotropic consolidation curve.

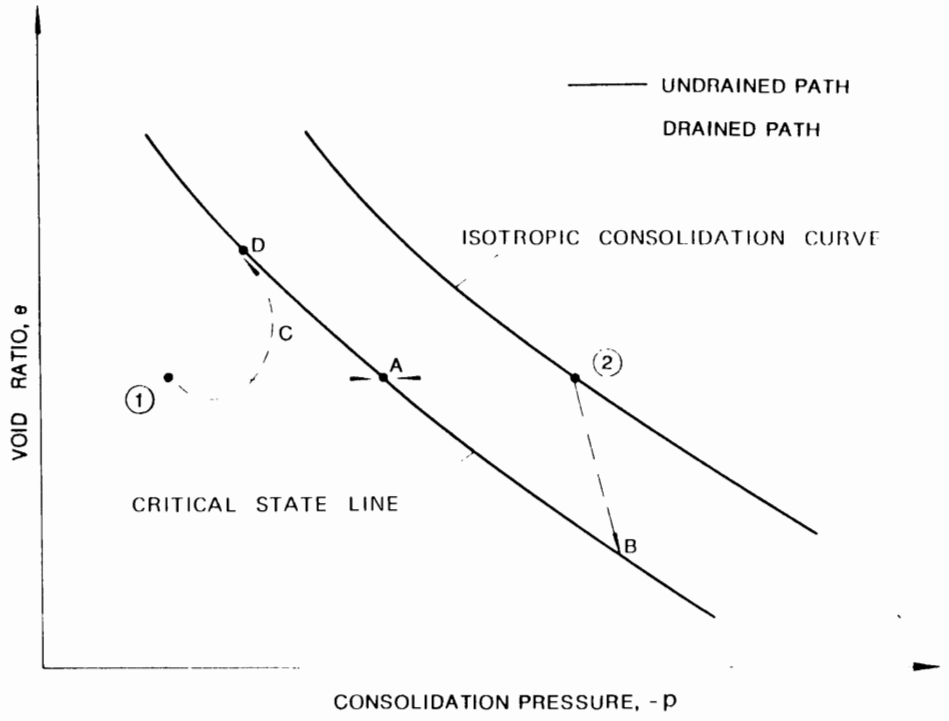

Fig. 6.2. Loading response in e p-plane.

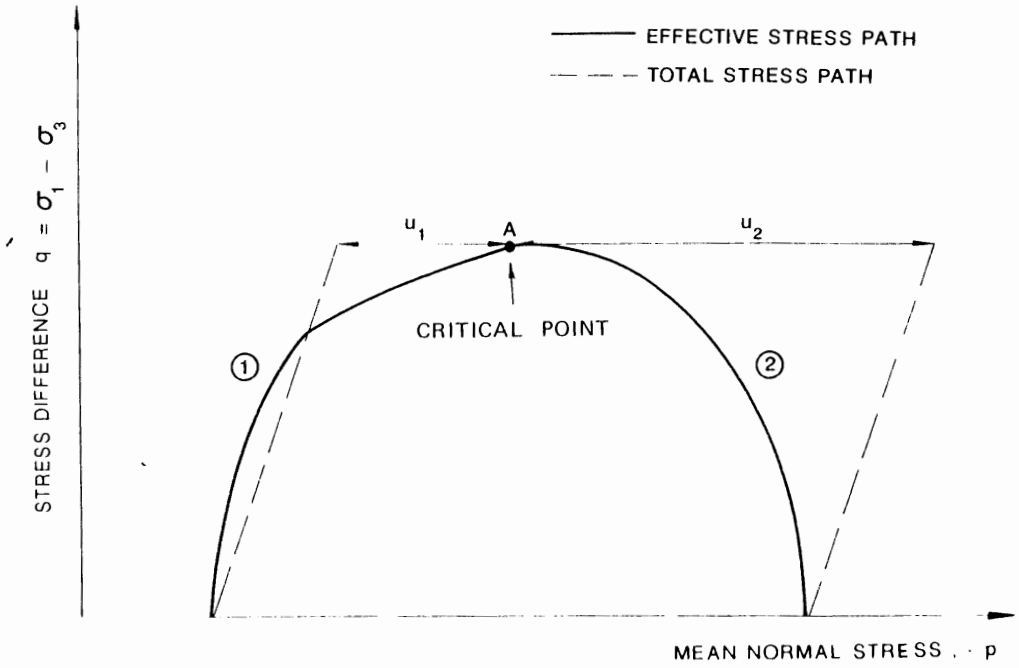

Fig. 6.3. Undrained response in q p-plane.

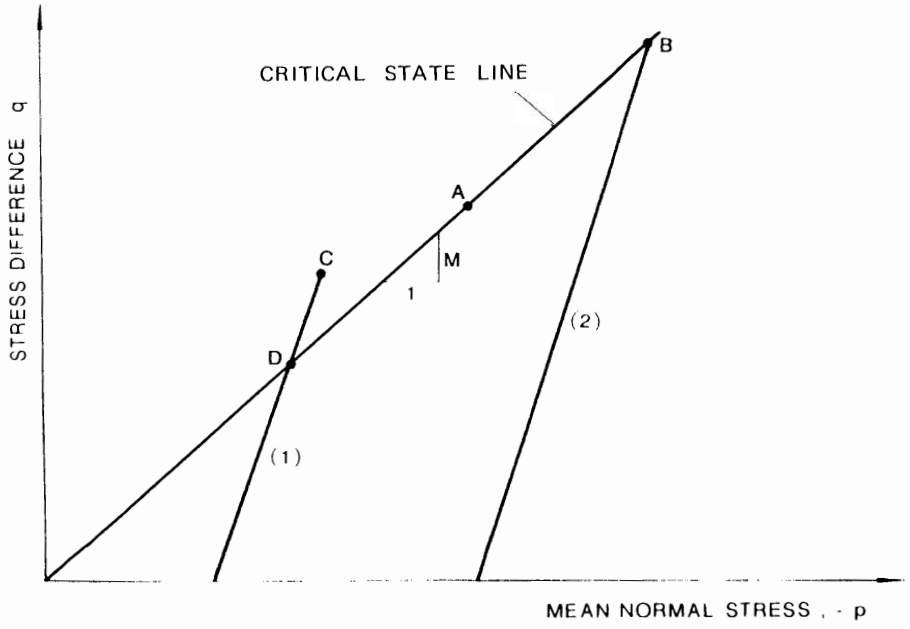

Fig. 6.4. Drained response in q p-plane.

before reaching its peak strength (point C), then dilates as it reaches its residual strength (point D). The drained and undrained tests appear to end along a unique line in the mean normal stress p – stress difference q ($= \sigma_1 - \sigma_3$)-plane (see Fig. 6.4).

In order to model the behavior of soils as shown in Figs. 6.1 through 6.4, recent research has focused on the application of the strain- or work-hardening theory of plasticity to such soil media. From the theoretical point of view, strain-hardening models, particularly, the cap type of strain-hardening models, are very attractive because they are capable of treating the conditions of *unloading*, *stress path-dependency*, *dilatancy*, and the effect of *intermediate principal stress* (see Fig. 6.4).

Two strain-hardening cap models will be developed in some details in Sections 6.3 and 6.4 after a brief historical sketch of these developments presented in the following Section.

6.2 HISTORICAL DEVELOPMENTS

Drucker et al. (1957) were the first to suggest that soil might be modeled as an elastic-plastic strain-hardening material. They introduced a spherical end-cap to the Drucker-Prager model, as shown in Fig. 6.5, in order to control the plastic

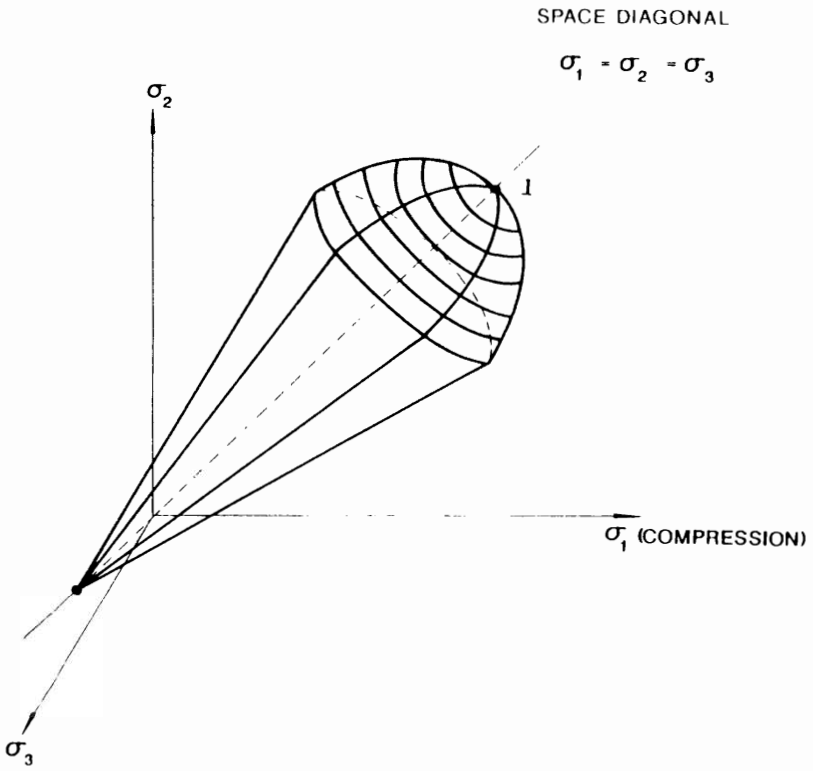

Fig. 6.5. Drucker-Prager type of strain-hardening cap model.

volumetric change of soil, or dilatancy. As the soil strain-hardens, both the cone and cap expand. In the development of their model, there are two important innovations included. The first is the introduction of the idea of spherical cap fitted to the cone. The second is the use of current soil density (specific volume or void ratio) as the strain-hardening parameter to determine the successive loading surfaces, such as the surface marked "1" in Fig. 6.5 for a particular value of soil density. There will be a succession of such surfaces, all geometrically similar, but of different sizes, for different densities. This strain- or work-hardening model was a major step toward a more realistic representation of soil behavior. Two specific isotropic hardening cap models are reviewed in the following.

6.2.1 Cambridge models (concept of critical state)

Researchers have investigated the possibility of modeling soils as a strain-hardening material. The Cambridge group in U.K., under the leadership of Roscoe, extended the basic concept of Drucker et al. (1957) and developed several plasticity-based soil models based on experimental data from triaxial tests. Roscoe et al. (1958) published a paper that contained the basis for a number of subsequent strain-hardening models for soil. Later, Roscoe et al. (1963) utilized the strain-hardening theory of plasticity to formulate a complete stress-strain model for normally consolidated or lightly overconsolidated clay in a triaxial test. These results are presented together in the book entitled "Critical State Soil Mechanics" (Schofield and Wroth, 1968) in which the models for sand and for normally consolidated or lightly overconsolidated clay are named, respectively, *Granta-gravel* and *Cam-clay models*. In the former model, volumetric strain and shearing strain are both assumed to be irrecoverable. In the latter model, however, only volumetric strain is assumed to be partially recoverable but shearing strain is irrecoverable. Important characteristics such as *Roscoe* and *Hvorslev surfaces, critical-state line*, and *elastic wall* in the mean normal stress-deviatoric stress void ratio space are advanced based on the work by Roscoe et al. (1958), and Parry (1958). These significant characteristics involved in the critical-state concept are shown schematically in Fig. 6.6, and summarized briefly in the following:

1. The *Roscoe surface* across which the load paths of normally and lightly overconsolidated (*wet*) samples move prior to failure.
2. The *Hvorslev surface* across which the load paths of heavily overconsolidated (*dry*) samples move prior to failure.
3. A *critical-state line* which is the locus of failure points for all shear test under both drained and undrained conditions, and at which the Roscoe and Hvorslev surfaces meet together. This line has the crucial property that at this critical state large shear distortions occur without any change in stress.
4. An *elastic wall* in which elastic behavior, for example, for overconsolidated samples, occurs.

The complete surface of Roscoe and Hvorslev surfaces is often termed a *state boundary surface* (e.g., Roscoe and Burland, 1968; Atkinson and Bransby, 1978).

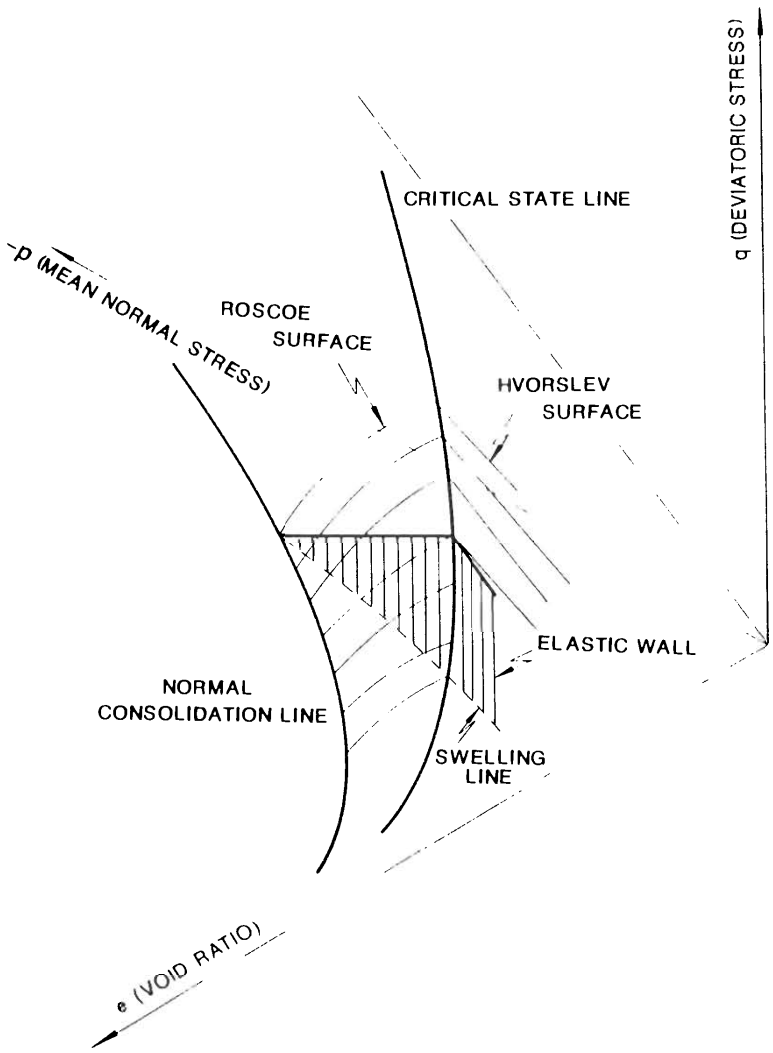

Fig. 6.6. State boundary surface and elastic wall.

Roscoe explained that the projection of the critical-state line appeared to be a straight line in the $p - q$-plane for $e = 0$. The implication is that if the initial state $(p, q, e)_i$ of a sample is known the failure conditions $(p, q, e)_f$ are uniquely determined for a particular stress path (for example, Figs. 6.2 through 6.4).

The original *Cam-clay model* assumes the Roscoe surface to be "bullet"-shaped, as shown in Fig. 6.7. However, the model predicts larger shear deformations than those observed for small levels of shear stress. In order to overcome this limitation, a modified version of the Cam-clay model was suggested by Burland (1965)

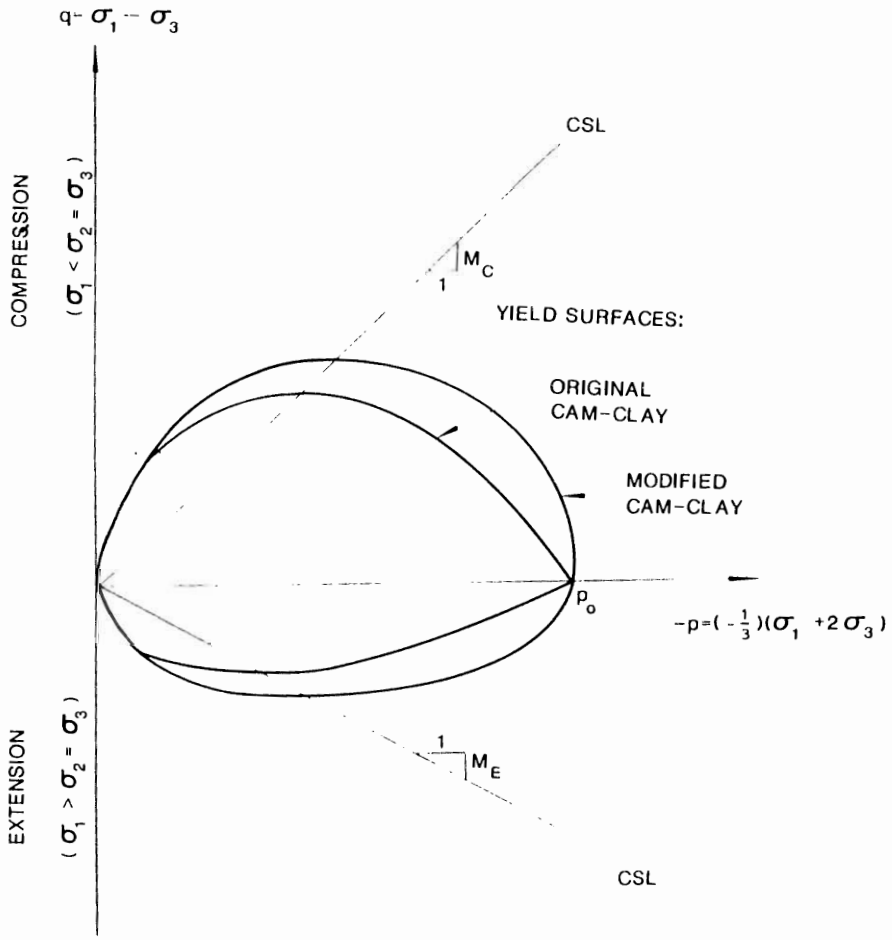

Fig. 6.7 Cam-clay yield surface in triaxial plane.

TABLE 6.1

Advantages and limitations of Cam-clay models

Advantages	Limitations
simple, qualitative judgements regarding material behavior are easily made	isotropic form, circular trace in deviatoric plane
material parameters may be determined from conventional triaxial test data	not applicable to heavily overconsolidated clays

replacing the bullet-shaped surface of the Cam-clay model with an elliptic shape and subsequently was extended by Roscoe and Burland (1968) to a model, now known as the *modified Cam-clay model*, for a general three-dimensional stress state.

The advantages and limitations of the Cam-clay model are summarized in Table 6.1.

6.2.2 Cap models

In recent years, the concept of state boundary surface, particularly the Roscoe surface, has been further modified and refined by DiMaggio and Sandler (1971), and Baladi and Rohani (1979a), among others. These models are generally called *cap model*.

The cap model falls within the classical incremental theory of hardening plasticity for materials which exhibit temperature- and time-independent properties. Further, its mathematical formulation statisfies the Drucker's postulate for stability, uniqueness, and continuity. Initially developed for sands, the cap model has now been successfully extended to other materials, such as clays and rocks (Sandler et al., 1976; Sandler, 1979; Baladi and Sandler, 1981).

The loading function for the cap model shown in Fig. 6.8 is assumed to be isotropic and consists of the following two parts: A failure surface for a perfectly plastic material response:

$$f_1(I_1, J_2) = 0 \tag{6.1}$$

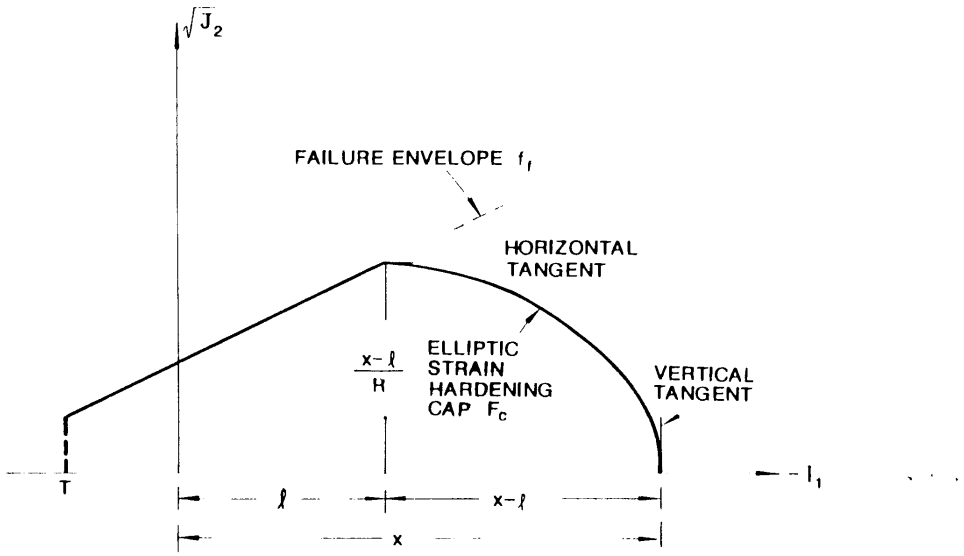

Fig. 6.8. Elliptic cap model in $I_1 - \sqrt{J_2}$-space.

and an elliptic strain-hardening cap:

$$f_c(I_1, J_2, \kappa) = 0 \tag{6.2}$$

which expands isotropically about the hydrostatic axis. Thus, three types of material response may be represented; elastic, perfectly plastic, and strain-hardening, under the assumption of the associated flow rule.

The movement of the cap is controlled by the increase or decrease in the plastic volumetric strain through the hardening parameter κ:

$$\kappa = \kappa(\epsilon_{kk}^{p}) \quad \text{or} \quad \kappa(\epsilon_{v}^{p}) \tag{6.3}$$

Thus, the dilation/compaction properties of soils may be represented.

Consider, for example, a sample initially isotropically consolidated up to some level A (Fig. 6.9) with a plastic volumetric strain that corresponds to the current hardening parameter κ of Eq. (6.3). If the sample is now subjected to the stress path AB, subsequent yielding occurs on the failure surface at B. The associated flow rule requires a plastic volumetric expansion that results in the change in the hardening parameter κ of Eq. (6.3). Since the strain-hardening is reversible in this model, a contraction of the cap towards the origin is allowed. This contraction continues until the corner of the cap coincides with the stress point B. When this occurs the potential surface may be chosen to coincide with the loading surface of the cap. The incremental plastic strain vector now becomes vertical and plastic volumetric expansion ceases. Such a mechanism leads to an effective control on dilatancy,

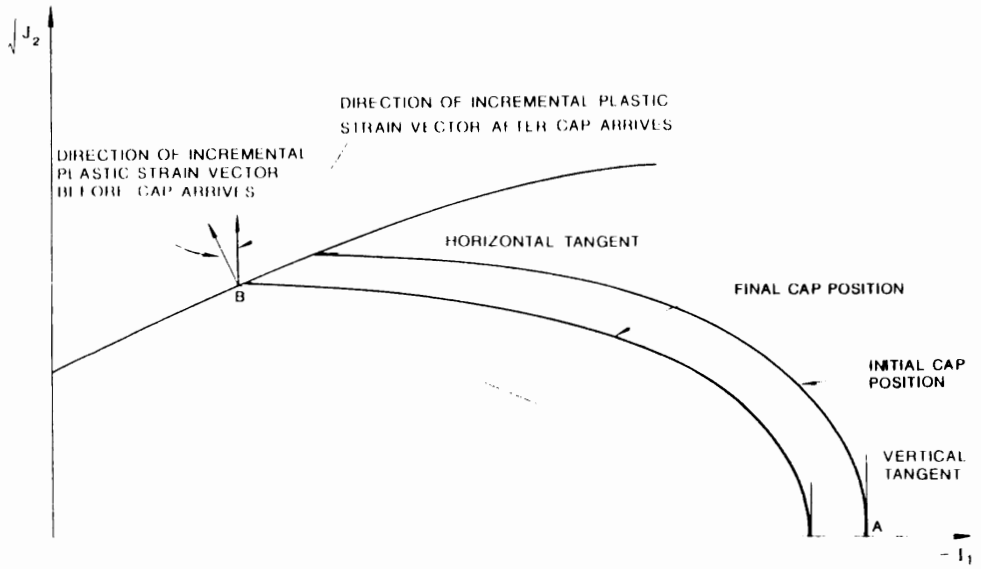

Fig. 6.9. Control of plastic dilatation for cap model.

TABLE 6.2

Advantages and limitations of Cap models

Advantages	Limitations
satisfy the theoretical requirements of stability	trial and error method to fit test data
give a proper control of plastic dilation	isotropic in form, circular trace in deviatoric plane
applicable to several materials	relatively complicated

which can be kept quite small (effectively zero) as required for many soils. This model has also been adopted for rocks (Sandler and Baron, 1976) by allowing only expansion but not contraction of the cap (i.e., hardening). In this case, the cap movement is assumed to depend only on the maximum value of the plastic volumetric strain previously attained, and thus, the cap is not reversible. This modification allows the model to predict a relatively large amount of dilatancy, which is often observed during the failure of rocks at low confining pressures. The functional forms for both the perfectly plastic and the strain-hardening portions of these models can be quite general and allow for the fitting of a wide range of material properties. Some of the more common forms of the generalized cap models are presented in Section 6.4.

These generalized cap models have also been extended to include rate effect, and anisotropic behavior within the yield surface and viscoplastic behavior during yielding (e.g., Nelson, 1978; Sandler and Baron, 1979). Many of these variations of the generalized cap models are now widely used in ground shock computations (e.g., Nelson et al., 1971; Sandler and Baron, 1976; Nelson, 1978; Nelson and Baladi, 1977).

A historical review of the cap type of strain-hardening model development is summarized by Chen (1980, 1982) and Mizuno and Chen (1986), among others.

The advantages and limitations of cap model are summarized in Table 6.2.

6.3 MODIFIED CAM-CLAY MODEL

The *modified Cam-clay model* (Roscoe and Burland, 1968) is an isotropic, nonlinear elastic strain-hardening plastic model. In this model, only volumetric strain is assumed to be partially recoverable, that is, elastic distortional strain (shearing strain) is assumed to be identically zero. Elastic volumetric strain is nonlinearly dependent on hydrostatic pressure and is independent of deviatoric stresses. In order to define the elastic bulk modulus K and the shear modulus G, an idealized response of Cam-clay material to hydrostatic pressure is presented in Fig. 6.10. The virgin isotropic consolidation line is assumed to be linear. The rebound

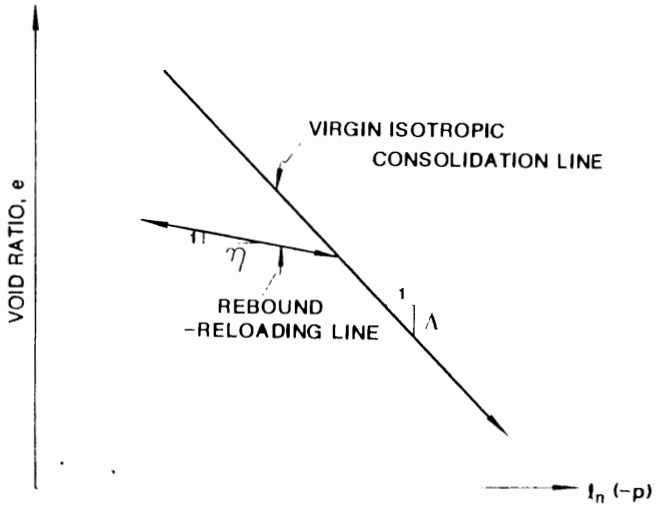

Fig. 6.10 Response of idealized soil to hydrostatic pressure.

and reloading curves are parallel. The equation for the virgin isotropic consolidation line is expressed by:

$$e = e_1 - \lambda \ln(-p) \tag{6.4}$$

where e is the *void ratio* of soil, the natural logarithm (logarithm to the base e) is denoted by ln, and e_1 and λ are material constants. A generic rebound-reloading curve is similarly defined by:

$$e = e_2 - \eta \ln(-p) \tag{6.5}$$

where e_2 and η are material constants.

Referring to Fig. 6.10, consider now the void ratio change associated with the hydrostatic pressure change. For the isotropic consolidation line, we have:

$$de = -\lambda \frac{dp}{p} \tag{6.6}$$

where p is the current hydrostatic pressure and dp is the increment of hydrostatic pressure. For the rebound-reloading line, we have:

$$de = -\eta \frac{dp}{p} \tag{6.7}$$

Introducing the relationship between the void ratio change de and the volumetric strain change $d\epsilon_{kk}$ (or $d\epsilon_v$), that is:

$$d\epsilon_{kk} = \frac{de}{1+e} \tag{6.8}$$

we have the volumetric strain increment expressed by:

$$d\epsilon_{kk} = -\frac{A}{(1+e)p}\,dp \tag{6.9}$$

Also, the recoverable or elastic component of the volumetric strain increment, $d\epsilon^e_{kk}$, is expressed by:

$$d\epsilon^e_{kk} = -\frac{\eta}{(1+e)p}\,dp \tag{6.10}$$

While, from Eqs. (6.9) and (6.10), the irrecoverable or plastic component is:

$$d\epsilon^p_{kk} = -\frac{(A-\eta)}{(1+e)p}\,dp \tag{6.11}$$

since:

$$d\epsilon^p_{kk} = d\epsilon_{kk} - d\epsilon^e_{kk} \tag{6.12}$$

From the definition of elastic bulk modulus K in Chapter 3, we find the tangential bulk modulus:

$$K = -\frac{(1+e)}{\eta}p \tag{6.13}$$

On the other hand, elastic distortional strain is assumed to be identically zero. Therefore, elastic shear modulus G can be made quite large, perhaps one hundred times the elastic bulk modulus, if we desire to keep the computational model as close as possible to the modified Cam-clay.

A modified Cam-clay yield surface and the projection of the critical state line in $p - \sqrt{J_2}$-space are shown in Fig. 6.11. The yield curve in the $p - \sqrt{J_2}$-space has an elliptic shape and is expressed by:

$$f = p^2 - p_0 p + \frac{J_2}{M^2} = 0 \tag{6.14}$$

where M is a material constant and p_0 is a strain-hardening parameter representing

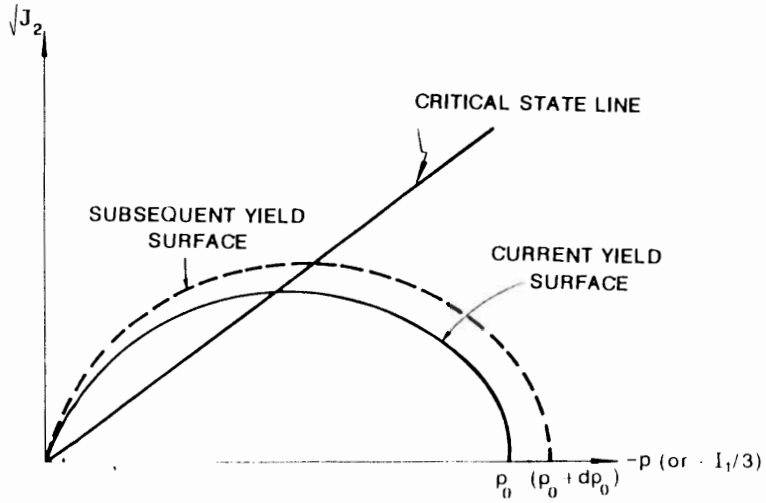

Fig. 6.11 Modified Cam-clay yield surface in p – $\sqrt{J_2}$-space.

the value of p at the intersection of the yield cap with the p-axis. Using the invariants I_1 and J_2, Eq. (6.14) can be further written as:

$$f = I_1^2 - I_1^0 I_1 + 9\frac{J_2}{M^2} = 0 \tag{6.15}$$

where I_1^0 is the value of I_1 at the intersection of yield cap with the I_1-axis; $I_1^0 = 3p_0$. Referring to Fig. 6.11, the relationship between the hardening parameter change, dI_1^0, and the change in plastic volumetric strain, $d\epsilon_{kk}^p$, is written from Eq. (6.11) as:

$$d\epsilon_{kk}^p = \frac{\lambda - \eta}{(1+e)I_1^0}\, dI_1^0 \tag{6.16}$$

or

$$dI_1^0 = \frac{(1+e)I_1^0}{\lambda - \eta}\, d\epsilon_{kk}^p \tag{6.17}$$

On the other hand, the critical-state line, which controls the failure of material, intersects the elliptic yield surface at its maximum point and may be defined by an extended von Mises type expression:

$$\sqrt{J_2} = Mp \tag{6.18}$$

To see the essential features of this model, consider the stress path of a lightly overconsolidated sample at A subjected to a drained triaxial compression test (Figs.

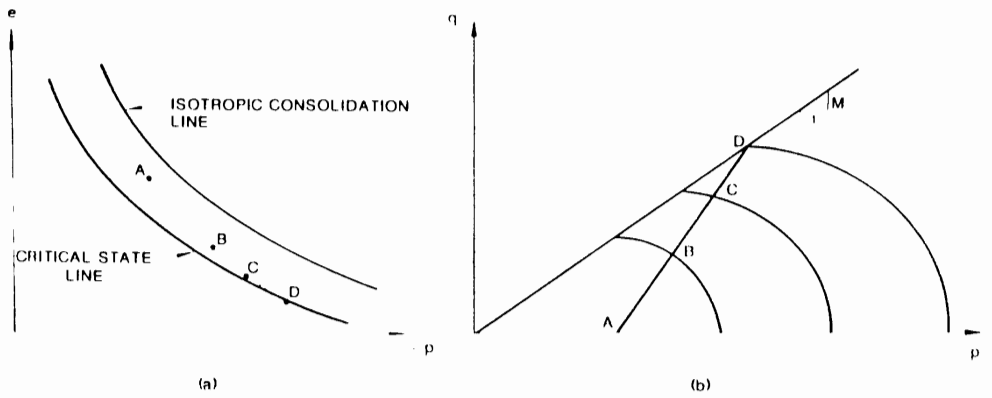

Fig. 6.12. Modified Cam-clay response during hardening: (a) e – p-plane, (b) q – p-plane

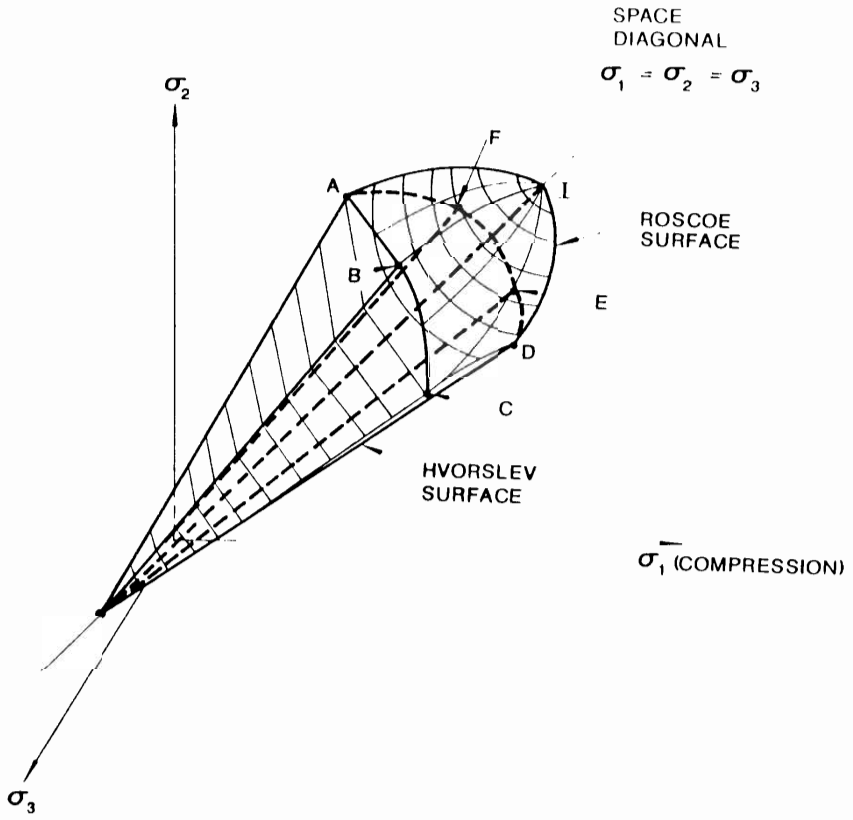

Fig. 6.13. Complete state boundary surface in principal stress space: Cambridge type of strain-hardening cap model (Atkinson and Bransby, 1978).

6.12a and b). As the test begins, the load path progresses from A to B with only elastic changes in the void ratio (shear distortions are assumed to be irrecoverable). A further loading produces an elastic-plastic response and subsequent yield surfaces are reached (C), each with the same shape (isotropic hardening). Eventually, the load path arrives at the critical-state line (D), where the associated flow rule demands that deformations may continue only in a constant volume manner. Thus, failure is implied.

The three-dimensional view of the modified Cam-clay model by Roscoe and Burland (1968) is shown in Fig. 6.13. The Hvorslev surface may be fitted to the Coulomb's surface since soil is governed by the Coulomb criterion at failure. The failure (or yield) surface corresponding to the Coulomb criterion in principal stress space is an irregular hexagon pyramid whose apex lies on the space diagonal (Fig. 6.13). The three-dimensional cap of the Roscoe surface, marked "I" in the figure, corresponds to a specific volume. The Roscoe surface intersects with the Hvorslev surface in a line ABCDEFA. This line is called the *critical-state locus*, and it is simply a line which separates the two surfaces corresponding to one fixed value of the specific volume (or void ratio). There will be similar surfaces of different sizes corresponding to different values of specific volume.

Since the development of Cambridge models, many attempts have been made to use various versions of these models in the numerical solutions of boundary value problems and predictions of soil behavior in the field (see, for example, Palmer, 1973). Also, extensive reviews of various types of Cambridge models have been given in two symposia (Parry, 1972; Palmer, 1973).

6.4 GENERALIZED CAP MODELS

In Section 6.2.2, the general form and behavior of cap models have been described. Herein, two specific functional forms of generalized cap models called the elliptic cap model and the plane cap model are presented.

6.4.1 Elliptic cap model

The schematic shape of this model is shown in Fig. 6.8. Its loading functions consist of the following three parts:

1. The failure function may be assumed to be the same as the Drucker-Prager function:

$$f_1 = \alpha I_1 + \sqrt{J_2} - k = 0 \tag{6.19}$$

where α and k are material parameters related to the cohesion c and the angle of

internal friction ϕ. Alternatively, the following function is assumed by Sandler et al. (1976) and Baladi and Rohani (1979a, b):

$$f_f = \sqrt{J_2} - \left[a - b \exp(cI_1)\right] = 0 \tag{6.20}$$

in which a, b, and c are material constants.

2. The strain-hardening cap function has the form of a quarter of an ellipse:

$$f_c = \left[I_1 - L(I)\right]^2 + R^2 J_2 - \left[x - L(I)\right]^2 = 0 \tag{6.21}$$

in which I is the value of I_1 at the center of the elliptic cap, $L(I) = I$ for $I < 0$ (in compression range) and $L(I) = 0$ for $I > 0$ (in tension range), R is the ratio of the major to minor axis lengths for the elliptic cap which may be taken as constant for simplicity or as a function of $L(I)$, and x is the hardening function. The location x of the cap is related to the history-dependent functional ϵ_{kk}^{p} of the plastic volumetric strain, and this relation is given by the following relation:

$$x = \frac{1}{D} \ln(1 + \epsilon_{kk}^{p}/W) \tag{6.22a}$$

where D and W are material constants. The incremental form $d\epsilon_{kk}^{p}$ is defined as:

$$d\epsilon_{kk}^{p} = d\epsilon_{kk}^{p} \quad \text{if } d\epsilon_{kk}^{p} \leq 0, \text{ or } I < I_1 \text{ and } I < 0$$

$$= 0 \qquad \text{otherwise} \tag{6.22b}$$

The physical meaning of ϵ_{kk}^{p} is not exactly the same as that of the current plastic volumetric strain, in a strict sense. However, this quantity can be treated in a similar way to the plastic volumetric strain, for example, for the derivation of the stiffness coefficients. Details of the numerical treatment for this cap-hardening function will be explained in Chapter 7.

3. The tension cut-off limit plane is introduced:

$$f_t = I_1 - T = 0 \tag{6.23}$$

where T is the tension cut-off limit.
This model can prevent an excessive dilatancy on the failure surface under high hydrostatic pressure I_1. Although this model can predict strain-softening as well as strain-hardening of soil, it may not exactly predict the hysteresis loop under shear loading. This is because the hardening function x in this model is assumed to be controlled only by the plastic volumetric strain ϵ_{kk}^{p}.

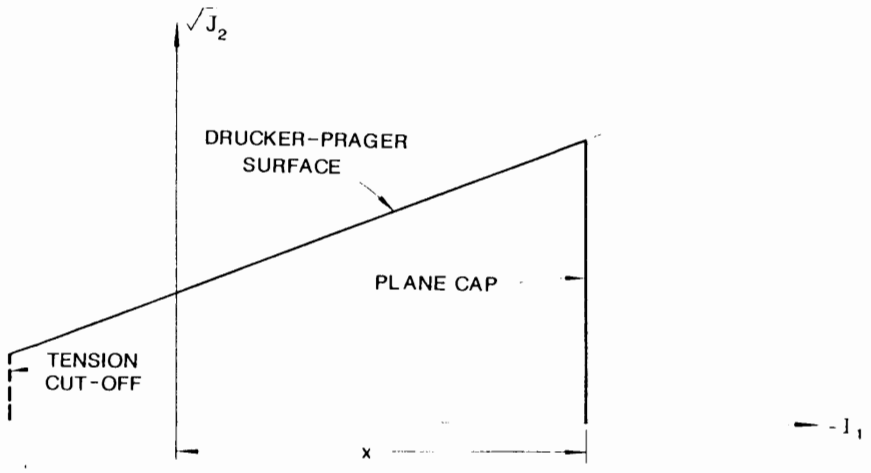

Fig. 6.14. Plane cap model in $I_1 - \sqrt{J_2}$-space.

6.4.2 Simple plane cap model

Bathe et al. (1980) and Sandler et al. (1976) have used the plane cap (Fig. 6.14) for rock materials. Similar to the elliptic cap model, the loading functions for this model consist of the following three surfaces:

1. Drucker-Prager type of failure surface or a curved failure surface similar to those in Eqs. (6.19) and (6.20).
2. Compression plane cap surface:

$$f_c = I_1 - \chi(\epsilon^p_{kk}) = 0 \tag{6.24}$$

3. Tension cut-off limit plane.

6.5 STRESS-STRAIN RELATIONS

Since failure and strain-hardening functions involved in the cap type of strain-hardening models such as the Cambridge and generalized cap models are employed under the associated flow rule assumption, the plastic strain increments $d\epsilon^p_{ij}$ can be written directly from the flow rule equation given in Chapter 5 as:

$$d\epsilon^p_{ij} = d\lambda \frac{\partial f}{\partial \sigma_{ij}} \tag{6.25}$$

where $d\lambda$ is expressed again by:

$$d\lambda = \frac{1}{H'}\left(\frac{\partial f}{\partial \sigma_{mn}} d\sigma_{mn}\right) \tag{6.26}$$

Substituting Eqs. (6.25) and (6.26) into the incremental linear isotropic elastic

stress-strain relations (Chapter 3), $d\sigma_{ij} = C_{ijkl}(d\epsilon_{kl} - d\epsilon^{p}_{kl})$ where C_{ijkl} is a fourth-order elastic constituent tensor, and multiplying both sides by $(\partial f/\partial \sigma_{ij})$, we have:

$$\frac{\partial f}{\partial \sigma_{ij}} d\sigma_{ij} = \frac{\partial f}{\partial \sigma_{ij}} C_{ijkl} d\epsilon_{kl} - \frac{1}{H'} \left(\frac{\partial f}{\partial \sigma_{mn}} d\sigma_{mn} \right) \frac{\partial f}{\partial \sigma_{ij}} C_{ijkl} \frac{\partial f}{\partial \sigma_{kl}} \tag{6.27}$$

Solving Eq. (6.27) for $(\partial f/\partial \sigma_{ij})\, d\sigma_{ij}$, we obtain:

$$\frac{\partial f}{\partial \sigma_{ij}} d\sigma_{ij} = \frac{(\partial f/\partial \sigma_{ij}) C_{ijkl}\, d\epsilon_{kl}}{1 + (1/H')(\partial f/\partial \sigma_{ab}) C_{abcd} (\partial f/\partial \sigma_{cd})} \tag{6.28}$$

Thus, substitution of Eq. (6.28) into Eq. (6.26) results in the proportionality factor, $d\lambda$, in the form:

$$d\lambda = \frac{(\partial f/\partial \sigma_{kl}) C_{klmn}\, d\epsilon_{mn}}{H' + (\partial f/\partial \sigma_{ab}) C_{abcd} (\partial f/\partial \sigma_{cd})} \tag{6.29}$$

Finally, we can write the relationship between stress increment and total strain increment in the tensorial form:

$$d\sigma_{ij} = C^{ep}_{ijkl}\, d\epsilon_{kl} \tag{6.30}$$

where C^{ep}_{ijkl} is a fourth-order constituent elastic-plastic tensor given by:

$$C^{ep}_{ijkl} = C_{ijkl} - \frac{(\partial f/\partial \sigma_{rs}) C_{ijrs} C_{mnkl} (\partial f/\partial \sigma_{mn})}{H' + (\partial f/\partial \sigma_{ab}) C_{abcd} (\partial f/\partial \sigma_{cd})} \tag{6.31}$$

The expression (6.31) is identical with those hardening models described previously in Chapter 5, except that in this case the associated flow rule ($f = g$) is assumed. Thus, the fourth-order constituent tensor C^{ep}_{ijkl} is now symmetrical.

6.6 STIFFNESS FORMULATION

In this Section, a detailed stiffness formulation for the cap type of hardening models is presented in a form that is convenient for direct use in a finite-element code.

6.6.1 General description

In general, the function involved in the cap type of hardening models may be expressed in the general form:

$$f = f\left[\sigma_{ij},\ x(\epsilon^{p}_{v} \text{ or } \epsilon^{p}_{kk})\right] \tag{6.32}$$

where $\kappa(\epsilon_v^p$ or $\epsilon_{kk}^p)$ is the hardening parameter which is a function of the plastic volumetric strain.
The derivative form $(\partial f/\partial \sigma_{ij})$ may be written as:

$$\frac{\partial f}{\partial \sigma_{ij}} = \frac{\partial f}{\partial I_1}\,\delta_{ij} + \frac{\partial f}{\partial J_2}\,s_{ij} + \frac{\partial f}{\partial J_3}\,t_{ij} \tag{6.33}$$

since $\delta_{ij} = (\partial I_1/\partial \sigma_{ij})$, $s_{ij} = (\partial J_2/\partial \sigma_{ij})$, and $t_{ij} = (\partial J_3/\partial \sigma_{ij})$ where t_{ij} can be written as $t_{ij} = s_{ik}s_{kj} - \frac{2}{3}J_2\,\delta_{ij}$. Substituting Eq. (6.33) and $C_{ijkl} = \lambda\,\delta_{ij}\,\delta_{kl} + \mu(\delta_{ik}\,\delta_{jl} + \delta_{il}\,\delta_{jk})$ into Eq. (6.31), after some simplifications, we obtain the constitutive equations in the form:

$$d\sigma_{ij} = \left[\lambda\,\delta_{ij}\,\delta_{kl} + \mu(\delta_{ik}\,\delta_{jl} + \delta_{il}\,\delta_{jk}) - \frac{1}{H}H_{ij}H_{kl}\right] d\epsilon_{kl} \tag{6.34}$$

In a similar manner to that of Chapter 5, using the notations:

$$A = \partial f/\partial I_1, \quad B = \partial f/\partial J_2, \quad \text{and} \quad C = \partial f/\partial J_3 \tag{6.35}$$

the functions H and H_{ij} are defined as:

$$H = 3A'(3\lambda + 2\mu) + 2B\mu(2BJ_2 + 3CJ_3) + 2C\mu\left(3BJ_3 + Cs_{ik}s_{kj}s_{ij}s_{ji} - \tfrac{4}{3}CJ_2^2\right) + H' \tag{6.36a}$$

$$H_{ij} = A(3\lambda + 2\mu)\,\delta_{ij} + 2\mu Bs_{ij} + 2\mu Ct_{ij} \tag{6.36b}$$

where λ and μ are Lamé constants.

For the special case of plane strain condition, the elastic-plastic matrix for cap models takes the form:

$$\begin{Bmatrix} d\sigma_{11} \\ d\sigma_{22} \\ d\sigma_{12} \\ d\sigma_{33} \end{Bmatrix} = \begin{bmatrix} \lambda + 2\mu - \frac{1}{H}H_{11}^2 & \lambda - \frac{1}{H}H_{11}H_{22} & -\frac{1}{H}H_{11}H_{12} \\ \lambda - \frac{1}{H}H_{22}H_{11} & \lambda + 2\mu - \frac{1}{H}H_{22}^2 & -\frac{1}{H}H_{22}H_{12} \\ -\frac{1}{H}H_{12}H_{11} & -\frac{1}{H}H_{12}H_{22} & \mu - \frac{1}{H}H_{12}^2 \\ \lambda - \frac{1}{H}H_{33}H_{11} & \lambda - \frac{1}{H}H_{33}H_{22} & -\frac{1}{H}H_{33}H_{12} \end{bmatrix} \begin{Bmatrix} d\epsilon_{11} \\ d\epsilon_{22} \\ d\gamma_{12} \end{Bmatrix} \tag{6.37}$$

Similarly, other special conditions such as plane stress and axisymmetric cases can be obtained.

6.6.2 Stiffness coefficients

Herein, the hardening modulus H' and stiffness coefficients for the modified Cam-clay and generalized cap models are presented.

(A) Modified Cam-clay model

The function of elliptic strain-hardening surface can be written as:

$$f = I_1^2 - I_1^0(\epsilon_{kk}^p)\, I_1 + \frac{9}{M^2} J_2 = 0 \tag{6.38}$$

where I_1^0 that is a function of the plastic volumetric strain ϵ_{kk}^p, gives the value of I_1 at the intersection of the yield cap with the I_1-axis, and M is a material constant. The stiffness coefficients such as A, B, and C are expressed as:

$$\frac{\partial f}{\partial I_1} = A = 2I_1 - I_1^0 \tag{6.39a}$$

$$\frac{\partial f}{\partial J_2} = B = \frac{9}{M^2} \quad \text{and} \quad \frac{\partial f}{\partial J_3} = C = 0 \tag{6.39b}$$

Further, from the definition (5.178) of the hardening modulus H', it takes the following form:

$$H' = -\frac{\partial f}{\partial I_1^0} \frac{\partial I_1^0}{\partial \epsilon_{kk}^p} \frac{\partial \epsilon_{kk}^p}{\partial \epsilon_{ij}^p} \frac{\partial f}{\partial \sigma_{ij}} \tag{6.40}$$

Substituting Eqs. (6.16) and (6.38) into Eq. (6.40), we find:

$$H' = -\frac{3(1+e) I_1^0 I_1}{A - \eta} \left(2I_1 - I_1^0\right) \tag{6.41}$$

To overcome the numerical difficulty in the treatment of the strain-softening region such as $I_1 > \frac{1}{2} I_1^0$, we shall introduce a perfectly plastic idealization of the critical-state line by using a perfectly plastic yield surface. To this end, the von Mises type expression may be utilized to obtain the stiffness coefficients. The treatment of flow rule at the corner of the von Mises type of failure surface with the strain-hardening surface will be discussed later.

(B) Generalized cap models

Generalized cap models consist of the Drucker-Prager type of failure (or yield) surface or a curved failure surface together with a plane cap or an elliptic cap hardening surface.

Failure surfaces. The stiffness coefficients for the Drucker-Prager type expression have already been presented in Chapter 4. To prevent an excessive amount of dilatancy on the failure surface, a modified version of the Drucker-Prager expression with a curved surface, such as that given by Eq. (6.20), has been recently utilized. The function for the modified surface is written as:

$$f = \sqrt{J_2} - [a - b\exp(cI_1)] \tag{6.42}$$

where a, b, and c are material constants. For the associated flow rule case, the stiffness coefficients are expressed by:

$$\frac{\partial f}{\partial I_1} = A = bc\exp(cI_1) \tag{6.43a}$$

$$\frac{\partial f}{\partial J_2} = B = \frac{1}{2\sqrt{J_2}} \quad \text{and} \quad \frac{\partial f}{\partial J_3} = C = 0 \tag{6.43b}$$

Further, Desai et al. (1982) proposed the following form of a failure surface:

$$f = \alpha I_1 + \beta\exp(\gamma I_1) + \sqrt{J_2} - \theta \tag{6.44}$$

where α, β, γ, and θ are material constants determined from the conventional triaxial tests. For this case, the stiffness coefficients are expressed under the associated flow rule assumption by:

$$\frac{\partial f}{\partial I_1} = A = \alpha + \beta\gamma\exp(\gamma I_1) \tag{6.45a}$$

$$\frac{\partial f}{\partial J_2} = B = \frac{1}{2\sqrt{J_2}} \quad \text{and} \quad \frac{\partial f}{\partial J_3} = C = 0 \tag{6.45b}$$

Note that the hardening modulus H' for this case is zero because of the fixed failure surface.

Cap surfaces. The stiffness coefficients corresponding to the plane cap and elliptic cap hardening surfaces are described as follows:
For the plane cap strain-hardening function (6.24), we have:

$$A = 1, \quad B = 0, \quad C = 0 \tag{6.46a}$$

and from the definition (5.178) of hardening modulus:

$$H' = 3/D(\epsilon_v^p + W) \tag{6.46b}$$

where D and W are material constants of the strain-hardening function (6.22a). For the elliptic cap strain-hardening function (6.21), we have:

$$A = 2\left[I_1 - L(I)\right], \quad B = R^2, \quad C = 0 \tag{6.47a}$$

and from the definition of hardening modulus:

$$H' = 12\{x - L(I)\}\{I_1 - L(I)\}/D(\epsilon_v^p + W) \tag{6.47b}$$

Example 6.1: Examine the corner treatment for the plane cap and elliptic cap models, as described previously in "Corner treatment of Lade model" in Chapter 5.

Solution: Plane and elliptic cap models contain the failure surface and cap hardening surface functions of the forms:

$$f_1 = f_1(\sigma_{ij}) \tag{6.48}$$

and

$$f_2 = f_2\left[\sigma_{ij}, x(\epsilon_{kk}^p)\right] \tag{6.49}$$

Here, as in Chapter 5, we find the following simultaneous equations corresponding to the proportionality factors, after some rigorous simplifications:

$$d\lambda^{(1)}A_{11} + d\lambda^{(2)}A_{12} = B_1 \tag{6.50a}$$

$$d\lambda^{(1)}A_{21} + d\lambda^{(2)}A_{22} = B_2 \tag{6.50b}$$

where $d\lambda^{(1)}$ and $d\lambda^{(2)}$ are respectively the positive proportionality factors related to the failure function and cap hardening function. The coefficients A_{11}, A_{12}, A_{21}, A_{22}, B_1, and B_2 are:

$$A_{11} = \frac{\partial f_1}{\partial \sigma_{ij}} C_{ijkl} \frac{\partial f_1}{\partial \sigma_{kl}}, \quad A_{12} = \frac{\partial f_1}{\partial \sigma_{ij}} C_{ijkl} \frac{\partial f_2}{\partial \sigma_{kl}} \tag{6.51a}$$

$$A_{21} = \frac{\partial f_2}{\partial \sigma_{ij}} C_{ijkl} \frac{\partial f_1}{\partial \sigma_{kl}} - 3\frac{\partial f_2}{\partial x}\frac{dx}{d\epsilon_{kk}^p}\frac{\partial f_1}{\partial I_1}, \quad A_{22} = \frac{\partial f_2}{\partial \sigma_{ij}} C_{ijkl} \frac{\partial f_2}{\partial \sigma_{kl}} - 3\frac{\partial f_2}{\partial x}\frac{dx}{d\epsilon_{kk}^p}\frac{\partial f_2}{\partial I_1} \tag{6.51b}$$

$$B_1 = \frac{\partial f_1}{\partial \sigma_{ij}} C_{ijkl}\, d\epsilon_{kl}, \quad B_2 = \frac{\partial f_2}{\partial \sigma_{ij}} C_{ijkl}\, d\epsilon_{kl} \tag{6.51c}$$

Solutions for $d\lambda^{(1)}$ and $d\lambda^{(2)}$ are thus obtained:

$$d\lambda^{(1)} = \frac{B_1 A_{22} - B_2 A_{12}}{A_{11} A_{22} - A_{12} A_{21}} \tag{6.52a}$$

$$d\lambda^{(2)} = \frac{B_2 A_{11} - B_1 A_{21}}{A_{11} A_{22} - A_{12} A_{21}} \tag{6.52b}$$

Substitution of $d\lambda^{(1)}$ and $d\lambda^{(2)}$ into Eq. (5.240) leads to the elastic-plastic stress-strain relationships at the corner for the cap models under the associated flow rule assumption:

$$d\sigma_{ij} = \left[C_{ijkl} - \frac{1}{H} C_{ijmn} C_{rskl} \left(A_{22} \frac{\partial f_1}{\partial \sigma_{mn}} \frac{\partial f_1}{\partial \sigma_{rs}} - A_{12} \frac{\partial f_1}{\partial \sigma_{mn}} \frac{\partial f_2}{\partial \sigma_{rs}} \right.\right.$$
$$\left.\left. + A_{11} \frac{\partial f_2}{\partial \sigma_{mn}} \frac{\partial f_2}{\partial \sigma_{rs}} - A_{21} \frac{\partial f_2}{\partial \sigma_{mn}} \frac{\partial f_1}{\partial \sigma_{rs}} \right) \right] d\epsilon_{kl} \tag{6.53}$$

where H is $A_{11}A_{22} - A_{12}A_{21}$.

6.7 CAP MODEL IN FITTING PROCEDURE

Before the application of a cap model to a boundary value problem, an analyst must first determine adequately the material parameters or material constants in the model with a certain fitting procedure, and then examine their responses on typical stress paths or strain paths in experimental level. In the following, the emphasis is placed on the necessary background for the determination of material parameters or constants in the cap model from standard experimental data.

For convenience, the description used in this Section follows the usual soil mechanics sign convention, that is, compressive and tensile stresses are taken as positive and negative values, respectively.

6.7.1 Stress paths in experiments

In this Section, stress paths tracing the changes in stress state experienced by a soil element in the commonly used conventional and true triaxial tests are described. All tests are assumed to start from an initial hydrostatic state (isotropic consolidation state), $\sigma_1^0 = \sigma_2^0 = \sigma_3^0 = \sigma_c$, where σ_c is defined as the initial confining pressure. The state of initial confining pressure in principal stress space is shown in Fig. 6.15 where deviatoric and triaxial planes are also presented. These stress paths in commonly used triaxial tests are in general proportional loading. Namely, the soil

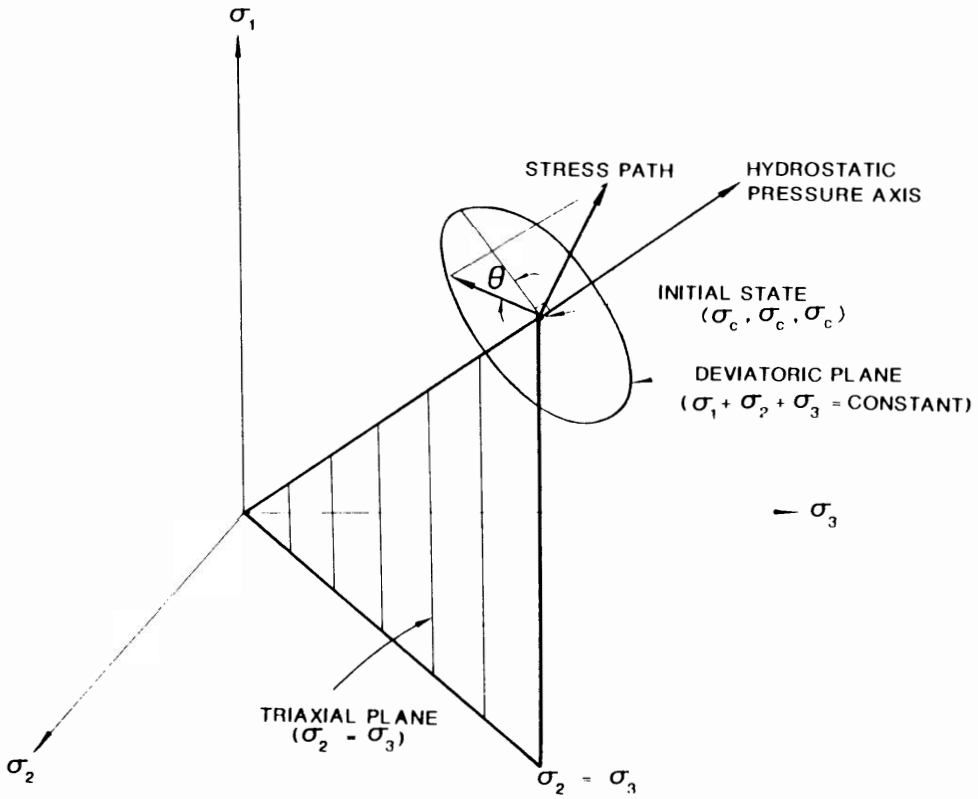

Fig. 6.15 Stress path in principal stress space

element under the initial hydrostatic state is subjected to the added stress increments (or changes) $\Delta\sigma_1$, $\Delta\sigma_2$, and $\Delta\sigma_3$ in the three principal directions such that $\Delta\sigma_1 : \Delta\sigma_2 : \Delta\sigma_3 = 1 : \alpha_1 : \alpha_2$ where α_1 and α_2 are constant parameters. All the stress paths in tests to be discussed in the following can be considered as special cases of this general straight-line stress path. Such stress paths are illustrated in Fig. 6.16 for triaxial stress plane, meridian plane (or $I_1 - \sqrt{J_2}$ stress space) and deviatoric (octahedral) plane. In the *triaxial compression (TC) tests*, *triaxial extension (TE) test*, and *simple shear (SS) test*, the stress components are changed such that the first stress invariant I_1 remains constant ($I_1 = \sigma_1 + \sigma_2 + \sigma_3 = 3\sigma_c$). For the stress paths in *conventional triaxial compression (CTC) test*, *conventional triaxial extension (CTE) test*, *reduced triaxial compression (RTC) test*, and *reduced triaxial extension (RTE) test*, the condition $\sigma_2 = \sigma_3$ is always satisfied.

The stress paths used in the tests can be characterized by the stress ratio b given by:

$$b = \frac{\sigma_{int} - \sigma_{min}}{\sigma_{max} - \sigma_{min}} \tag{6.54}$$

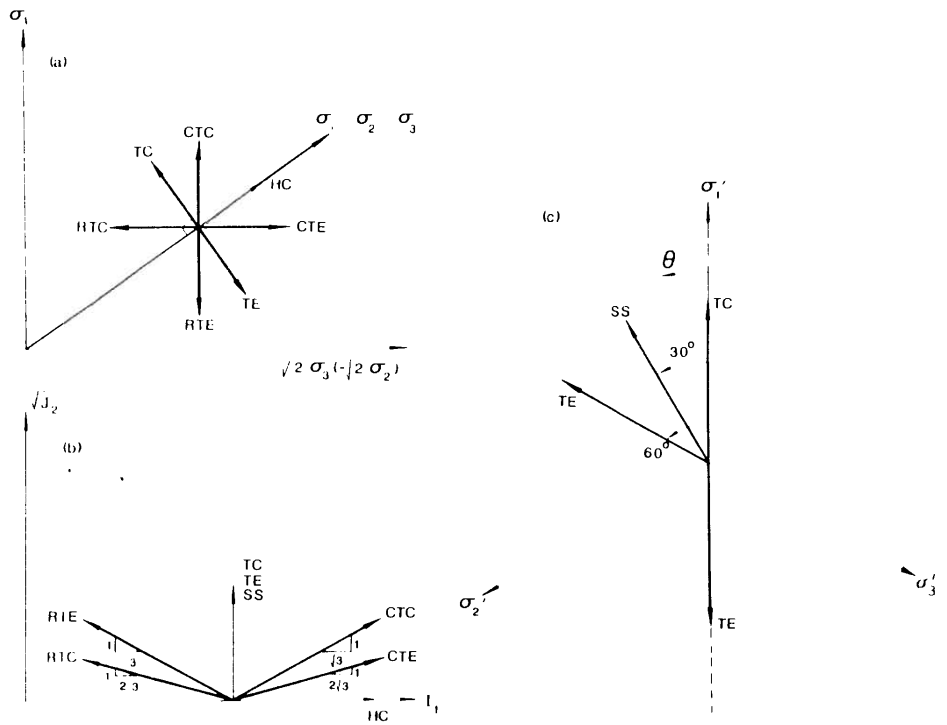

Fig. 6.16. Stress paths for common tests in different stress spaces: (a) triaxial stress plane; (b) meridian planes (θ = constant); (c) deviatoric (octahedral) plane.

where σ_{max}, σ_{int}, and σ_{min} are respectively maximum, intermediate, and minimum principal stresses applied to the cylindrical or cubic soil specimen. The particular order of applied principal stresses, σ_1, σ_2, and σ_3 as maximum, intermediate, and minimum principal stresses depends on the type of test described. The stress ratio b in Eq. (6.54) takes a value between 0 and 1. For instance, the stress path with the ratio $b = 0$ or $b = 1$ corresponds to the CTC test or CTE test. If the Lode angle θ is defined on the deviatoric plane from the plane with $b = 0$ (from σ'_{max}-axis in Fig. 6.17c), then the relation between θ and b is given by:

$$\cos 3\theta = \frac{(2 - b)(1 - 2b)(1 + b)}{2(b^2 - b + 1)^{3/2}} \tag{6.55}$$

The projection of stress path with a ratio b onto the deviatoric plane can be seen in Fig. 6.17. A brief description of some typical stress paths is given below:

Hydrostatic Compression (HC) tests. Since stress path corresponding to this test remains along the hydrostatic axis ($\sigma_1 = \sigma_2 = \sigma_3$) as shown Figs. 6.15, 6.16a, and

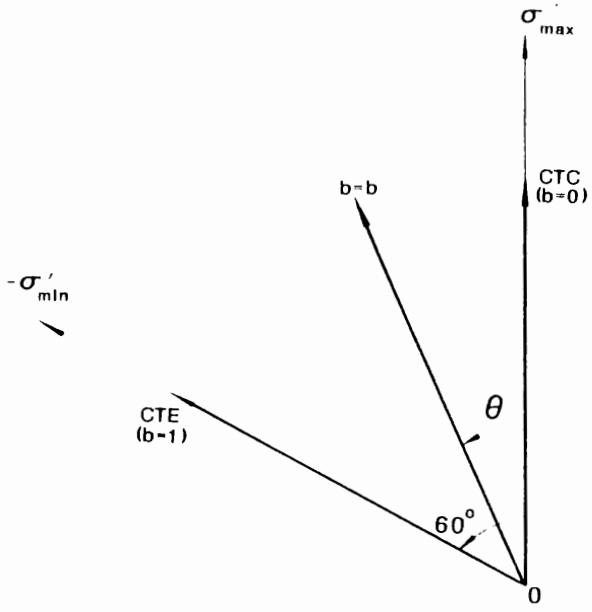

Fig. 6.17. Projected stress path with stress ratio b onto π-plane.

6.16b, it follows that the changes in stress rates are the same such that $\Delta\sigma_1 = \Delta\sigma_2 = \Delta\sigma_3 = \Delta\sigma_c$. Thus, in this case, the stress ratio in Eq. (6.54) and the Lode angle in Eq. (6.55) cannot be defined. The changes in stress invariants I_1 and J_2 are given by:

$$\Delta I_1 = 3\,\Delta\sigma_c, \quad \Delta J_2 = 0 \tag{6.56}$$

The hydrostatic stress test provides information on the volumetric behavior of the soil. For example, expressions for the bulk modulus K can be obtained from the experimental results of this test.

Conventional Triaxial Compression (CTC) test. This test is the most commonly employed in soil mechanics. Two of the principal stresses are kept constant (say, $\sigma_2 = \sigma_3 = \sigma_c$) while the third principal stress σ_1 is increased in the compression side as shown in Figs. 6.16a and 6.16b. In this case, σ_1 becomes the maximum principal stress, and σ_2 and σ_3 are the intermediate and minimum principal stresses, respectively. As a result, the stress ratio b in Eq. (6.54) and the Lode angle θ in Eq. (6.55) both take the value zero. The projected path on π-plane is shown in Fig. 6.17. The incremental stress invariants ΔI_1 and $\Delta\sqrt{J_2}$ are given by the expressions:

$$\Delta I_1 = \Delta\sigma_1 \tag{6.57a}$$

$$\Delta\sqrt{J_2} = \left(1/\sqrt{3}\right)\,\Delta\sigma_1 \tag{6.57b}$$

where $\Delta\sigma_1$ is the change in the maximum principal stress σ_1. Thus, the slope of the stress path in CTC test becomes $1/\sqrt{3}$ (Fig. 6.16b).

Reduced Triaxial Extension (RTE) test. In contrast with CTC test, the principal stress σ_1 is reduced while $\sigma_2 = \sigma_3$ remains constant. In this case, σ_2 and σ_3 become the maximum and intermediate principal stresses, and σ_1 is the minimum principal stress. Therefore, the stress ratio b and the Lode angle θ are respectively 1 and 60°. The stress path corresponding to this test is shown in Figs. 6.16a and 6.16b. The changes in stress invariants are given by the same expressions as Eqs. (6.57a) and (6.57b), but note that $\Delta\sigma_1$ is now negative for Eq. (6.57a) (decreasing).

Conventional Triaxial Extension (CTE) test. This test is carried out with one of principal stresses held constant, while the other two are increased equally. For the case when σ_1 is held constant, while σ_2 and σ_3 are increased equally, the stress ratio b and the Lode angle θ take the values of 1 and 60° from the σ_2' or σ_3'-axis, respectively. This projected stress path on π-plane is shown in Fig. 6.17. The incremental stress invariants ΔI_1 and $\Delta\sqrt{J_2}$ are:

$$\Delta I_1 \quad 2\ \Delta\sigma_2 \tag{6.58a}$$

$$\Delta\sqrt{J_2} \quad -(1/\sqrt{3})\ \Delta\sigma_2 \tag{6.58b}$$

in which $\Delta\sigma_2$ is the increment in the principal stress σ_2. The slope of the CTE stress path in Fig. 6.16b is given by $1/2\sqrt{3}$.

Reduced Triaxial Compression (RTC) test. In this case, σ_1 is held constant, while σ_2 and σ_3 are equally reduced. Similar to the CTC test, the stress ratio b and the Lode angle θ are zero so that the projected stress path onto the π-plane is also identical to each other. The incremental stress invariants ΔI_1 and $\Delta\sqrt{J_2}$ are obtained from Eqs. (6.58a) and (6.58b), but with $\Delta\sigma_2$ negative for Eq. (6.58a); that is, I_1 is decreased (Fig. 6.16b).

Triaxial Compression (TC) test. In this test, the stress increments $\Delta\sigma_1$, $\Delta\sigma_2$, and $\Delta\sigma_3$ are applied in such a manner that the first invariant of stress tensor I_1 remains always constant. For example, σ_1 is increased by $\Delta\sigma_1$, while both σ_2 and σ_3 are decreased such that $\Delta\sigma_2 = \Delta\sigma_3 = -\frac{1}{2}\Delta\sigma_1$. Therefore, the stress path is in the deviatoric plane (Fig. 6.15) and proceeds along the σ_1'-axis, that is, the Lode angle $\theta = 0°$. The incremental stress invariants are:

$$\Delta\sqrt{J_2} \quad (\sqrt{3}/2)\ \Delta\sigma_1 \tag{6.59}$$

Triaxial Extension (TE) test. In this stress path, σ_1 is decreased, while both σ_2 and σ_3 are equally increased such that $\Delta\sigma_1 + \Delta\sigma_2 + \Delta\sigma_3 = 0$. The stress path in TE test is

also in the deviatoric plane and proceeds in the opposite direction to that of the TC test. The incremental stress invariant is obtained from Eq. (6.59), but with the absolute value of $\Delta\sigma_1$.

Simple Shear (SS) test. The SS test, as in TC and TE tests, the hydrostatic pressure I_1 is kept constant, that is, the SS path lies always in the deviatoric plane corresponding to the initial hydrostatic state. In this case, for example, σ_3 remains constant while σ_1 and σ_3 are respectively increased and decreased by the same amount; that is, $\Delta\sigma_3 = -\Delta\sigma_1$ where $\Delta\sigma_1$ is the increase in σ_1. Therefore, the maximum, intermediate, and minimum principal stresses become respectively σ_1, σ_2, and σ_3. The stress ratio b in Eq. (6.54) and the Lode angle θ in Eq. (6.55) take the values of 0.5 and 30° from the σ_1'-axis as shown in Fig. 6.16c. The incremental stress invariant is given by:

$$\Delta\sqrt{J_2} = \Delta\sigma_1 \tag{6.60}$$

Effective stress paths. All stress paths described above are *total stress paths*. To describe the deformational and strength characteristics of soils during such total stress paths in experiments, soils are assumed to be a *two-phase* material; in which only fully saturated or completely dry soils are considered. For fully saturated soils, depending on the type of test such as *drained* or *undrained*, the total stress σ_{ij} in experiment can be expressed mathematically as (Terzaghi, 1943):

$$\sigma_{ij} = \sigma_{ij}^* + u\,\delta_{ij} \tag{6.61}$$

where σ_{ij}^* is the *effective stress* which is carried by the skeleton of solid particles (interparticle stresses) and is responsible for deformation, yielding, or failure of

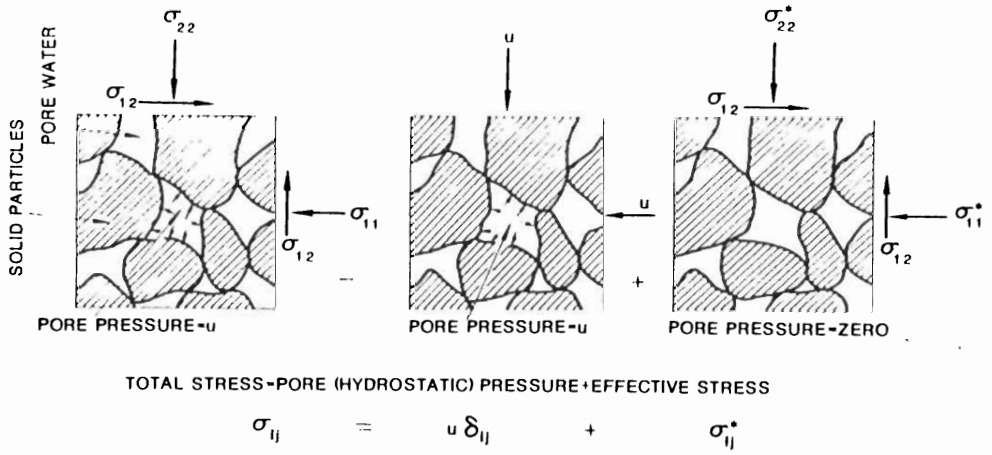

Fig. 6.18. Total and effective stresses in saturated soils.

soils, and u is the pore water pressure. This *principle of effective stress* for a fully saturated soil is schematically shown in Fig. 6.18

When the total stress is applied so slowly that some of the water can escape from the voids and the induced excess pore pressure is negligible, the soil is then said to be in a *drained condition*. In this case, any changes in the applied total stress result in identical changes in the effective stress. On the other hand, under an *undrained condition*, the total stress is assumed to be applied very rapidly so that the excess pore water pressure induced by the total stress does not have time to dissipate. In such a case, no volumetric strain can occur (constant volume condition). Precisely, undrained condition implies no change in water content; and constant volume condition is an approximation based on the incompressibility assumption for pore water and solid particles. The effective stress paths for undrained triaxial tests can be easily determined based on the pore water pressure measurements.

6.7.2 *Determination of material constants*

The material constants involved in cap models are elastic moduli such as the shear modulus G and the bulk modulus K, and the parameters in the failure function [Eq. (6.19) or Eq. (6.20)], in the elliptic cap function [Eq. (6.21)], and in the hardening function [Eq. (6.22)]. In the following, a procedure for the determination of these material constants will be described in some details.

Bulk and shear moduli. Since the cap model is assumed to behave isotropically and elastically during an unloading, the first step in a fitting procedure is to utilize these unloading portions of the hydrostatic loading test, the triaxial test, the uniaxial strain test, and so on, for the determination of appropriate elastic moduli. The bulk modulus K is independently determined from the slope of unloading curves related to the hydrostatic pressure and volumetric strain relationship from hydrostatic loading tests (Fig. 6.19a). The unloading portion may exhibit a linear or nonlinear behavior. For such cases, the bulk modulus K may be fitted as constant or a function of the stress invariant, I_1.

On the other hand, the shear modulus G is obtained from the stress-difference/strain-difference unloading curves corresponding to the drained triaxial compression or extension tests conducted at different levels of confining pressure (Fig. 6.19b). For these unloading curves, for example, their stress increment and elastic strain increment relation with the tangential moduli G and K may be written as:

$$d\sigma_1 = 2G\, de_1 + K\, d\epsilon_{kk} \tag{6.62a}$$

$$d\sigma_2 - d\sigma_3 = 2G\, de_2 + K\, d\epsilon_{kk} - 2G\, de_3 + K\, d\epsilon_{kk} \tag{6.62b}$$

where $d\sigma_i$ ($i = 1, 2, 3$) is a principal stress increment, de_i ($i = 1, 2, 3$) is a principal deviatoric strain increment and $d\epsilon_{kk}$ is a volumetric strain increment.

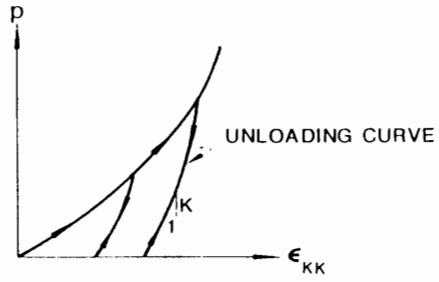

(a) HYDROSTATIC LOADING TEST

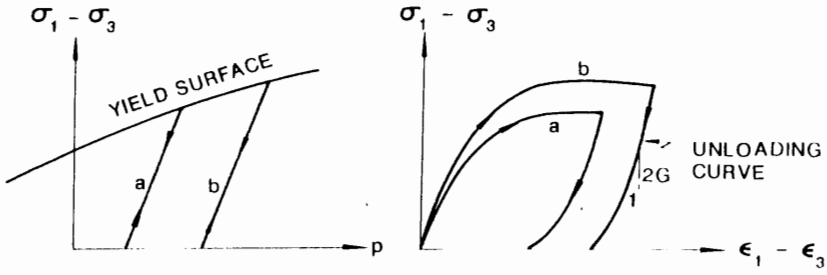

(b) DRAINED TRIAXIAL TEST

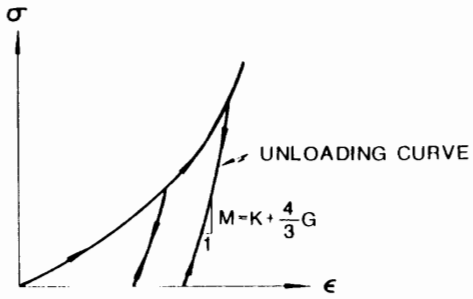

(c) UNIAXIAL STRAIN TEST

Fig. 6.19. Determination of elastic material moduli: (a) hydrostatic loading test; (b) drained triaxial test; (c) uniaxial strain test

From both equations, the stress increment difference and strain increment difference are connected by the following expression:

$$\mathrm{d}\sigma_1 - \mathrm{d}\sigma_3 = 2G\ \mathrm{d}(e_1 - e_3) \tag{6.63a}$$

or

$$d\sigma_1 - d\sigma_3 = 2G\, d(\epsilon_1 - \epsilon_3) \tag{6.63b}$$

The shear modulus G can therefore be obtained from the stress-difference/strain-difference unloading curve.

Furthermore, the combination of bulk and shear moduli is estimated by the stress-strain unloading curves from a uniaxial strain test (Fig. 6.19c). The elastic relationship between the axial principal stress increment $d\sigma_1$ and axial principal strain increment $d\epsilon_1$ is given by:

$$d\sigma_1 = \left(K + \tfrac{4}{3}G\right) d\epsilon_1 \tag{6.64}$$

Other tests, if available, may be used to check or adjust the overall fit. From these soil tests, elastic material moduli, K and G, may be assumed to be constant values or sometimes functions of the first invariant of stress tensor, I_1, and the second invariant of deviatoric stress tensor, J_2, respectively, or both. However, these modulus functions must be selected so that the *integrability condition* is kept from the viewpoint of thermodynamics requirement (see Chapter 3). Baladi (1979) used the following modulus functions:

$$K = K(I_1) \tag{6.65a}$$

$$G = G\left(\sqrt{J_2}, \epsilon^{\mathrm{p}}_{kk}\right) \tag{6.65b}$$

Failure surface. The next step in the fitting procedure is to establish the function of failure surface such as the Drucker-Prager type [Eq. (6.19)] or its modified type with a curved surface [Eq. (6.20)]. These failure surfaces are generally determined from data corresponding to failure, for example, from the triaxial compression or extension tests, and also from several proportional loading tests. These data are generally fitted as a function of the stress invariants I_1 and J_2, by utilizing a nonlinear regression analysis.

Cap surface. The final step in the fitting procedure is to determine the elliptic cap yield function (6.21) and the hardening function (6.22) which are usually the most difficult parts. The hardening parameters, W and D in the hardening function represent respectively the maximum plastic volumetric strain and the rate at which soil compaction occurs with pressure. These parameters can be determined from the data of hydrostatic compression tests, that is, a relation between the hydrostatic pressure and the plastic volumetric strain. The determination of the shape factor R in the elliptic cap yield function is conducted in several ways, for example, by a trial-and-error procedure where the value of R is first moderately assumed on the basis of some test results such as the hydrostatic pressure tests and the conventional

triaxial tests, and then the computed soil behavior corresponding to these parameters is compared with the experimental data available. If the resulting fit requires a further improvement of the parameters, a new set of parameters is tried and the same procedure is repeated until a satisfactory value is determined.

6.8 CAP MODEL IN SIMPLE TESTS

The mathematical representations of the elliptic cap model are given for the special cases of uniaxial strain, isotropic consolidation, drained and undrained triaxial shear tests. For simplicity, the elastic behavior is assumed to be linear isotropic type.

6.8.1 Uniaxial strain test

For a uniaxial strain in the x_1-direction, the following relation holds:

Initial conditions

Free stress and strain states are assumed.

Strains

$$\epsilon_{11},\ \epsilon_{22} = \epsilon_{33} = \epsilon_{12} = \epsilon_{23} = \epsilon_{31} = 0 \tag{6.66a}$$

Stresses

$$\sigma_{11},\ \sigma_{22} = \sigma_{33} \tag{6.66b}$$

Incremental strains

$$d\epsilon_{kk} = d\epsilon_{11} \tag{6.66c}$$

$$de_{11} = \tfrac{2}{3}\, d\epsilon_{11} \tag{6.66d}$$

$$de_{22} = de_{33} = -\tfrac{1}{3}\, d\epsilon_{11} \tag{6.66e}$$

$$de_{12} = de_{23} = de_{31} = 0 \tag{6.66f}$$

Deviatoric stresses

$$s_{11} = \tfrac{2}{3}(\sigma_{11} - \sigma_{22}) \tag{6.66g}$$

$$s_{22} = s_{33} = -\tfrac{1}{3}(\sigma_{11} - \sigma_{22}) = -\tfrac{1}{2}s_{11} \tag{6.66h}$$

$$s_{12} = s_{23} = s_{31} = 0 \tag{6.66i}$$

Stress invariants

$$I_1 = \sigma_{11} + 2\sigma_{22} \tag{6.66j}$$

$$\sqrt{J_2} = \frac{1}{\sqrt{3}}|\sigma_{11} - \sigma_{22}| = \frac{\sqrt{3}}{2}|s_{11}| \tag{6.66k}$$

Consider the case in which the cap position x is located at some distance from the origin of the stress space ($I_1 - \sqrt{J_2}$-space). In this case, the material behaves elastically from the stress/strain free states until the stress state hits the elliptic hardening cap. After the stress state hits the cap surface, the material exhibits an elastic-plastic behavior. In the following, the incremental elastic-plastic behavior is described mathematically.

Using Eqs. (6.33), (6.66) and $C_{ijkl} = (K - \frac{2}{3}G)\,\delta_{ij}\,\delta_{kl} + G(\delta_{ik}\,\delta_{jl} + \delta_{il}\,\delta_{jk})$, the proportionality factor $d\lambda$ in Eq. (6.29) can be reduced to:

$$d\lambda = \frac{3K(\partial f_c/\partial I_1) + 2Gs_{11}(\partial f_c/\partial J_2)}{H' + 9K(\partial f_c/\partial I_1)^2 + 4GJ_2(\partial f_c/\partial J_2)^2}\, d\epsilon_{11} \tag{6.67}$$

Substituting the elliptic cap function [Eq. (6.21)] and the plastic hardening modulus [Eq. (6.47b)] into Eq. (6.67), we obtain:

$$d\lambda = \frac{6K\{I_1 - L(l)\} + 2GR^2 s_{11}}{36K\{I_1 - L(l)\}^2 + 4GR^4 J_2 + 12\{x - L(l)\}\{I_1 - L(l)\}/D(\epsilon^p_{kk} + W)}\, d\epsilon_{11} \tag{6.68}$$

The increments of s_{11} and I_1 can now be expressed in terms of $d\lambda$:

$$ds_{11} - 2G(de_{11} - de^p_{11}) = 2G(\tfrac{2}{3}\,d\epsilon_{11} - d\lambda R^2 s_{11}) \tag{6.69a}$$

$$dI_1 = 3K(d\epsilon_{kk} - d\epsilon^p_{kk}) = 3K\left[d\epsilon_{11} - 6\,d\lambda\{I_1 - L(l)\}\right] \tag{6.69b}$$

where

$$de^p_{11} = d\lambda R^2 s_{11} \quad \text{and} \quad d\epsilon^p_{kk} = 6\,d\lambda\{I_1 - L(l)\} \tag{6.69c}$$

Therefore, $d\sigma_{11}$ is given by:

$$\begin{aligned} d\sigma_{11} &= \tfrac{1}{3}\,dI_1 + ds_{11} \\ &= K\left[d\epsilon_{11} - 6\,d\lambda\{I_1 - L(l)\}\right] + 2G(\tfrac{2}{3}\,d\epsilon_{11} - d\lambda R^2 s_{11}) \\ &= (K + \tfrac{4}{3}G)\,d\epsilon_{11} - \left[6K\{I_1 - L(l)\} + 2GR^2 s_{11}\right] d\lambda \end{aligned} \tag{6.70a}$$

The slope of the axial stress-axial strain curve has the value:

$$\frac{\mathrm{d}\sigma_{11}}{\mathrm{d}\epsilon_{11}} = K + \tfrac{4}{3}G - \left[6K\{I_1 - L(l)\} + 2GR^2 s_{11}\right]\frac{\mathrm{d}\lambda}{\mathrm{d}\epsilon_{11}} \tag{6.70b}$$

Equations (6.68) through (6.70) may be integrated numerically to obtain the complete stress-strain curve for a uniaxial strain test. In the numerical integration, $\mathrm{d}\lambda$ in Eq. (6.68) is first evaluated for an assumed value of the total axial strain increment $\mathrm{d}\epsilon_{11}$. After each incremental calculation, the variables in Eq. (6.68) must be updated for the next calculation.

This can always be done except the following case:

$$\frac{\partial f}{\partial I_1} = \sqrt{J_2} = 0 \tag{6.71}$$

which can happen for the present model if and only if the location of the cap and the current state of stress are at the origin of the stress space, i.e.:

$$s_{11} = I_1 = \epsilon_{kk}^{\mathrm{p}} = x = 0 \tag{6.72}$$

Since the value of x is zero, from the geometry of the elliptic cap surface and the failure surface, the value of l becomes in general greater than zero. Thus, we reset $L(l) = 0$ until l takes a negative value. To solve this special case, we can employ an asymptotic approach where all quantities that vanish are expanded about the origin in the stress space (Baladi, 1979). However, it may be numerically carried out by setting a cap position near the origin in the stress space, that is, by taking a relatively small negative value of x.

6.8.2 Isotropic consolidation test

During an isotropic consolidation test, only the volumetric strain ϵ_{kk} consisting of elastic part, $\epsilon_{kk}^{\mathrm{e}}$ and plastic part, $\epsilon_{kk}^{\mathrm{p}}$, is generated from the hardening cap portion of the model. The following relations hold:

Initial conditions

Free stress and strain states are assumed.

Stresses

$$\sigma_{11} = \sigma_{22} = \sigma_{33} = \tfrac{1}{3}I_1 = p \tag{6.73a}$$

Strains

$$\epsilon_{11} = \epsilon_{22} = \epsilon_{33} = \tfrac{1}{3}\epsilon_{kk} \tag{6.73b}$$

Deviatoric stresses

$$s_{11} = s_{22} = s_{33} = s_{12} = s_{23} = s_{31} = 0 \tag{6.73c}$$

Deviatoric strains

$$e_{11} = e_{22} = e_{33} = e_{12} = e_{23} = e_{31} = 0 \tag{6.73d}$$

The relationship between the increment of mean normal stress (hydrostatic pressure), $\mathrm{d}p$, and the elastic volumetric strain increment, $\mathrm{d}\epsilon^{\mathrm{e}}_{kk}$, has the usual form:

$$\mathrm{d}p = K\ \mathrm{d}\epsilon^{\mathrm{e}}_{kk} \tag{6.74}$$

On the other hand, the plastic volumetric strain increment, $\mathrm{d}\epsilon^{\mathrm{p}}_{kk}$, must be calculated from the cap hardening function in Eq. (6.22), assuming that the initial location of cap is at the origin ($I_1 = 0$). Thus, we have:

$$\mathrm{d}p = \frac{1}{3WD\,\mathrm{e}^{DX}}\ \mathrm{d}\epsilon^{\mathrm{p}}_{kk} \tag{6.75}$$

Hence, the relationship between the total volumetric strain increment, $\mathrm{d}\epsilon_{kk}$, and the hydrostatic pressure, $\mathrm{d}p$, can be written as:

$$\mathrm{d}p = \tilde{K}\ \mathrm{d}\epsilon_{kk} \tag{6.76}$$

where $\tilde{K}$ is the *apparent bulk modulus* of the material and it has the value:

$$\tilde{K} = \frac{1}{1/K + 3WD\,\mathrm{e}^{DX}} \tag{6.77a}$$

or

$$\tilde{K} = \frac{1}{1/K + 3D(\epsilon^{\mathrm{p}}_{kk} + W)} \tag{6.77b}$$

The second term in the denominator of Eq. (6.77) produces an apparent softening of the bulk modulus due to a plastic volumetric compaction. At a high pressure, the softening term goes to zero, and the apparent bulk modulus approaches the elastic bulk modulus.

The behavior of the cap model under loading-unloading isotropic consolidation tests on sands is schematically shown in Fig. 6.20. After the elastic tangent bulk modulus, K, is determined from an unloading curve, the material parameters W and D in Eq. (6.22), are estimated by choosing arbitrarily two points on the loading curve (1 → 2 in Fig. 6.20).

6.8.3 Drained triaxial shear test

For a drained triaxial shear test, the following relations hold (total stresses = effective stresses):

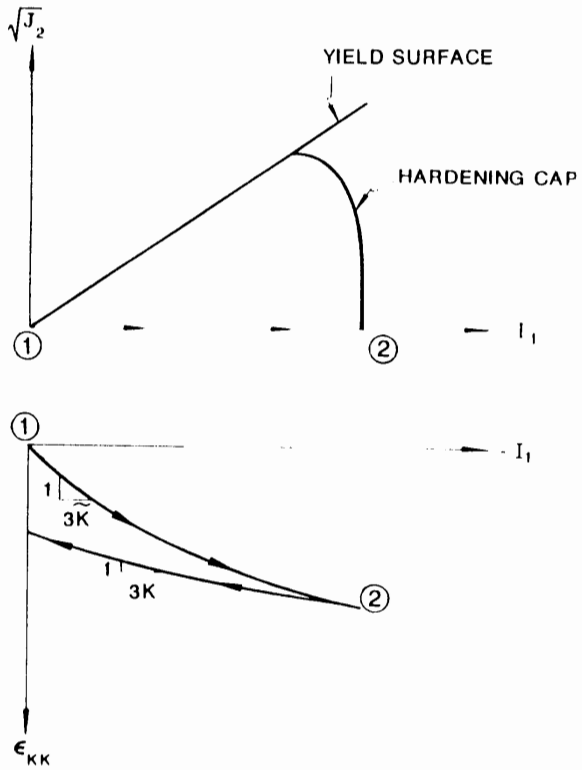

Fig. 6.20. Behavior of cap model under loading-unloading isotropic consolidation.

Initial stresses

$$\sigma_{11} = \sigma_{22} = \sigma_{33} = \sigma_c \text{ (on the cap)} \tag{6.78a}$$

Stress increments

$$d\sigma_{11},\ d\sigma_{22} = d\sigma_{33} = 0 \tag{6.78b}$$

Strain increments

$$d\epsilon_{11},\ d\epsilon_{22} = d\epsilon_{33} \tag{6.78c}$$

Deviatoric stress increments

$$ds_{11} = \tfrac{2}{3}\, d\sigma_{11} \tag{6.78d}$$

$$ds_{22} = ds_{33} = -\tfrac{1}{2}\, ds_{11} = -\tfrac{1}{3}\, d\sigma_{11} \tag{6.78e}$$

Deviatoric strain increments

$$de_{11} = \tfrac{2}{3}(d\epsilon_{11} - d\epsilon_{22}) \tag{6.78f}$$

$$de_{22} = de_{33} = -\tfrac{1}{2}\, de_{11} = -\tfrac{1}{3}(d\epsilon_{11} - d\epsilon_{22}) \tag{6.78g}$$

Stress invariants

$$I_1 = \sigma_{11} + 2\sigma_{22} \tag{6.78h}$$

$$\sqrt{J_2} = \frac{1}{\sqrt{3}}|\sigma_{11} - \sigma_{22}| = \frac{\sqrt{3}}{2}|s_{11}| \tag{6.78i}$$

Utilizing these equations, the proportionality factor $d\lambda$ in Eq. (6.29) is determined:

$$d\lambda = \frac{6K\{I_1 - L(l)\}\, d\epsilon_{kk} + 2GR^2 s_{11}(d\epsilon_{11} - d\epsilon_{22})}{36K\{I_1 - L(l)\}^2 + 4GR^4 J_2 + 12\{x - L(l)\}\{I_1 - L(l)\}/D(\epsilon^p_{kk} + W)} \tag{6.79}$$

The increments of s_{11} and I_1 can now be expressed in terms of $d\lambda$:

$$ds_{11} = 2G(de_{11} - de^p_{11}) = 2G\left[\tfrac{2}{3}\, d(\epsilon_{11} - \epsilon_{22}) - d\lambda R^2 s_{11}\right] \tag{6.80a}$$

$$dI_1 = 3K(d\epsilon_{kk} - d\epsilon^p_{kk}) = 3K\left[d\epsilon_{kk} - 6\, d\lambda\{I_1 - L(l)\}\right] \tag{6.80b}$$

since $de^p_{11} = d\lambda R^2 s_{11}$ and $d\epsilon^p_{kk} = 6\, d\lambda\{I_1 - L(l)\}$.
From Eq. (6.80a), we obtain the ratio of stress difference increment to the strain difference increment:

$$\frac{d(\sigma_{11} - \sigma_{22})}{d(\epsilon_{11} - \epsilon_{22})} = 2G\left[1 - \frac{d(\epsilon^p_{11} - \epsilon^p_{22})}{d(\epsilon_{11} - \epsilon_{22})}\right] \tag{6.80c}$$

since $ds_{11} = \tfrac{2}{3}d(\sigma_{11} - \sigma_{22})$ and $d\lambda R^2 s_{11} = \tfrac{2}{3}\, d(\epsilon^p_{11} - \epsilon^p_{22})$. Equation (6.80c) implies that the *apparent shear modulus* decreases as the ratio of incremental plastic strain difference to incremental strain difference increases.

By representing the proportionality factor $d\lambda$ from Eqs. (6.79), (6.80a) and (6.80b) in terms of the stress increment $d\sigma_{11}$, the complete stress-strain curve of the model for a drained triaxial shear test may be integrated numerically.

Parameter R

On the other hand, the shape parameter R which represents the ratio of the major axis to the minor axis of the elliptic cap may be estimated from data on

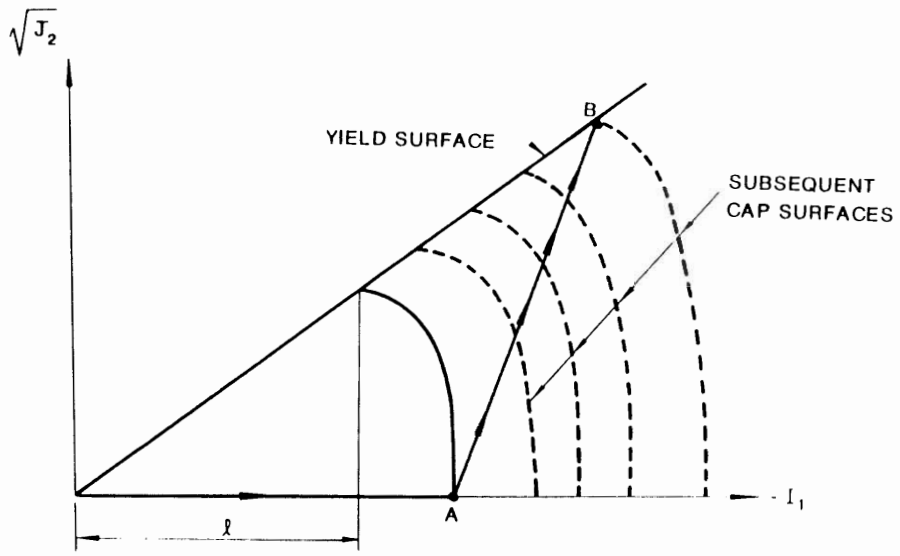

Fig. 6.21. Behavior of cap model under triaxial shear test.

triaxial compression or extension tests. Suppose that the specimen is first isotropically compressed up to a point A and then becomes in a normally consolidated state, as shown in Fig. 6.21. At point A, the initial cap location x and initial plastic volumetric strain ϵ_{kk}^{p} are known. During this shearing test, the stress state is always on the cap surface. As the stress state moves from point A to point B, the cap surface is pushed outward (Fig. 6.21). The plastic volumetric strain increments $d\epsilon_{kk}^{p}$ caused by the changes in stress state σ_{11} can be evaluated from the shear test data on the volumetric strain ϵ_{kk} and the bulk modulus K obtained from other test:

$$d\epsilon_{kk}^{p} = d\epsilon_{kk} - d\sigma_{11}/3K \tag{6.81}$$

A new cap location x after a stress increment $d\sigma_{11}$ can be estimated from using the plastic volumetric strain increment $d\epsilon_{kk}^{p}$ and Eq. (6.22a). At this stage, the known quantities for the cap surface are a new stress state (I_1, J_2) and a new cap location x. From Eq. (6.21), we have the relation between l and R:

$$l = \frac{1}{2(I_1 - x)}\left(I_1^2 + R^2 J_2 - x^2\right) \tag{6.82}$$

On the other hand, from the relation between the failure surface f_c and cap surface, we obtain R:

$$R f_f(l) = l - x \tag{6.83}$$

The shape ratio R can be obtained by solving Eqs. (6.82) and (6.83). If I in Eq. (6.82) is positive, R is again estimated by setting $I = 0$. Thus, ratio R becomes:

$$R = \left[\left(x^2 \quad I_1^2 \right) / J_2 \right]^{1/2} \tag{6.84}$$

From experimental data on triaxial shear tests and isotropic consolidation tests, the value of R may be estimated to be either a constant or a function of I as proposed by Baladi (1979).

6.8.4 Undrained triaxial shear test

For an undrained triaxial shear test, the following relations hold:
Initial stresses

$$\sigma_{11}^* = \sigma_{22}^* = \sigma_{33}^* = \sigma_c \text{ (on the cap)} \tag{6.85a}$$

Stress increments

$$d\sigma_{11} = d\sigma_{11}^* + du \tag{6.85b}$$

$$d\sigma_{22} = d\sigma_{33} = d\sigma_{22}^* + du = d\sigma_{33}^* + du = 0 \tag{6.85c}$$

where $d\sigma_{ij}^*$ is the increment of effective stress and du is the increment of pore water pressure.

Strain increments

$$d\epsilon_{11} + d\epsilon_{22} + d\epsilon_{33} = 0 \tag{6.85d}$$

$$d\epsilon_{22} = d\epsilon_{33} = -\tfrac{1}{2}\, d\epsilon_{11} \tag{6.85e}$$

Deviatoric stress increments

$$ds_{11} \quad \tfrac{2}{3}(d\sigma_{11}^* \quad d\sigma_{22}^*) - \tfrac{2}{3}(d\sigma_{11} \quad d\sigma_{22}) = \tfrac{2}{3}\, d\sigma_{11} \tag{6.85f}$$

$$ds_{22} \quad ds_{33} \qquad \tfrac{1}{2}\, ds_{11} - \quad \tfrac{1}{3}(d\sigma_{11}^* \quad d\sigma_{22}^*) - - \tfrac{1}{3}(d\sigma_{11} \quad d\sigma_{22}) = - \tfrac{1}{3}\, d\sigma_{11} \tag{6.85g}$$

Deviatoric strain increments

$$de_{11} = d\epsilon_{11} \tag{6.85h}$$

$$de_{22} = de_{33} = -\tfrac{1}{2}\, d\epsilon_{11} \tag{6.85i}$$

Stress invariants

$$I_1 = I_1^* + 3u \tag{6.85j}$$

$$\sqrt{J_2} = \frac{1}{\sqrt{3}}|\sigma_{11}^* - \sigma_{22}^*| = \frac{1}{\sqrt{3}}|\sigma_{11}| \tag{6.85k}$$

Using these conditions, $d\lambda$ in Eq. (6.29) is reduced to:

$$d\lambda = \frac{3GR^2 s_{11}\, d\epsilon_{11}}{36K\{I_1^* - L(l)\}^2 + 4GR^4 J_2 + 12\{x - L(l)\}\{I_1^* - L(l)\}/D(\epsilon_{kk}^p + W)} \tag{6.86}$$

The increments of s_{11} and I_1^* can therefore be expressed in terms of $d\lambda$ in Eq. (6.86):

$$ds_{11} = 2G(de_{11} - de_{11}^p) = 2G(d\epsilon_{11} - d\lambda R^2 s_{11}) \tag{6.87a}$$

$$dI_1^* = 3K(d\epsilon_{kk} - d\epsilon_{kk}^p) = -18K\, d\lambda[I_1^* - L(l)] \tag{6.87b}$$

since $de_{11}^p = d\lambda R^2 s_{11}$ and $d\epsilon_{kk}^p = 6\, d\lambda[I_1^* - L(l)]$.
Equations (6.86) and (6.87) may be integrated numerically to obtain the effective or total stress-strain curve of the cap model for an undrained triaxial shear test, assuming an axial strain increment $d\epsilon_{11}$ for each step of integration.

Example 6.2: Examine numerically the elliptic cap model behavior in drained and undrained triaxial compression tests on Reid-Bedford model sand with a relative density of 20%, under the initial confining pressures σ_c = 2.8 kg/cm^2 (274.4

TABLE 6.3

Material constants for Reid-Bedford model sand

Material constants	Units	
K_i	kg/cm^2	300
K_1		0.85
K_2	(kg/cm^2)$^{-1}$	0.1
G_i	kg/cm^2	160
G_1		0.8
G_2	(kg/cm^2)$^{-1}$	0.6
α		0.2309
k	kg/cm^2	0
W		0.0075
D	(kg/cm^2)$^{-1}$	0.14
R		4.33

kPa) and 5.6 kg/cm^2 (-548.8 kPa), respectively. The elliptic cap model consists of the Drucker-Prager failure surface and the elliptic cap hardening surface. The material constants used for the model simulation of these tests are listed in Table 6.3 (Baladi and Rohani, 1979a). The following functions for the bulk and shear moduli are used:

$$K = \left| K_1/(1 - K_1) \right| \left[1 - K_1 \exp(K_2 I_1) \right] \tag{6.88a}$$

$$G = \left| G_1/(1 - G_1) \right| \left[1 - G_1 \exp\left(- G_2 \sqrt{J_2} \right) \right] \tag{6.88b}$$

in which K_i = initial elastic bulk modulus; K_1 and K_2 = material constants; and G_i initial elastic shear modulus; G_1 and G_2 = material constants, respectively.

Solutions:

Initial state. The specimens are first isotropically compressed up to the confining pressures σ_c $-$ 2.8 kg/cm^2 ($-$ 274.4 kPa), and $\sigma_c = -5.6$ kg/cm^2 (-548.8 kPa), respectively. If the cap is assumed to be located at the origin of $I_1 - \sqrt{J_2}$-space before the isotropic consolidation test, the corresponding hardening cap surfaces must move forward to x ($= 3\sigma_c$) $= -8.4$ kg/cm^2 (-823.2 kPa), and -16.8 kg/cm^2 (1646.4 kPa). The generated plastic volumetric strain ϵ_{kk}^p can be evaluated from ϵ_{kk}^p $W[\exp(Dx)$ 1], i.e., for $x = -8.4$ kg/cm^2 (-823.2 kPa):

$$\epsilon_{kk}^p = 0.0075\left[\exp(0.14 \times -8.4) - 1\right] = -0.005186\ (-0.5186\%)$$

and for x 16.8 kg/cm^2 (1646.4 kPa):

$$\epsilon_{kk}^p = 0.0075\left[\exp(0.14 \times -16.8) - 1\right] = -0.006786\ (-0.6786\%)$$

At the beginning of a triaxial test, the following initial conditions for stresses, material constants, and hardening cap are used:
For the specimen under $\sigma_c = -2.8$ kg/cm^2 (-274.4 kPa):

I_1 8.4 kg/cm^2 (823.2 kPa), $\sqrt{J_2} = 0$, $s_{11} = 0$

$$K = \frac{300}{1 \quad 0.85}\{1 - 0.85 \exp[0.1 \times (-8.4)]\} = 1266.1 \text{ kg/cm}^2 \text{ (124 MPa)}$$

$$G \quad 1 \quad \frac{160}{0.8}\left[1 \quad 0.8 \exp(-0.6 \times 0)\right] = 160 \text{ kg/cm}^2 \text{ (15.68 MPa)}$$

$$I = \frac{x}{1 + \alpha R} = \frac{-8.4}{1 + 0.2309 \times 4.33} = -4.2 \text{ kg/cm}^2 \ (-411.6 \text{ kPa})$$

and for the specimen under σ_c 5.6 kg/cm^2 (548.8 kPa):

$I_1 =$ 16.8 kg/cm^2 (1646.4 kPa), $\sqrt{J_2} = 0$, s_{11} 0

$$K = \frac{300}{1 - 0.85}\{1 - 0.85 \exp[0.1 \times (-16.8)]\} = 1683.2 \text{ kg/cm}^2 \text{ (165 MPa)}$$

$G = 160$ kg/cm^2 (15.68 MPa)

$l = -8.4$ kg/cm^2 (-823.2 kPa)

Numerical procedure for drained case: We shall explain first the procedure for obtaining the stress-strain relationship in a drained triaxial test. Substituting $d(\epsilon_{11} \epsilon_{22})$ of Eq. (6.80a) and $d\epsilon_{kk}$ of Eq. (6.80b) into $d\lambda$ in Eq. (6.79), we can solve for $d\lambda$:

$$d\lambda = \frac{2\{I_1 - L(l)\} + R^2 s_{11}}{12\{x - L(l)\}\{I_1 - L(l)\}/D(\epsilon^p_{kk} + W)}\, d\sigma_{11} \tag{6.89}$$

In this case, we first assume an increment of the axial stress, $d\sigma_{11}$, to obtain the corresponding proportionality factor $d\lambda$. This is different from the procedure used previously for the uniaxial strain case in which the axial strain increment $d\epsilon_{11}$ is first assumed at each incremental step [see Eq. (6.68)].

The general procedure for an incremental calculation at the i-th step is summarized below.

1. The proportionality factor, $d\lambda^{(i)}$, is obtained by substituting into Eq. (6.89) the stress increment $d\sigma_{11}$ and the updated values at the end of the $(i-1)$-th step such as $I_1^{(i-1)}$, $I^{(i-1)}$, $s_{11}^{(i-1)}$, $x^{(i-1)}$, and $\epsilon_{kk}^{p(i-1)}$.
2. Substitution of the $d\lambda^{(i)}$ so obtained into the associated flow rule equation $d\epsilon^p_{ij} = d\lambda\, \partial f_c/\partial \sigma_{ij}$ leads to the plastic strain increments such as $d\epsilon_{11}^{p(i)}$, $d\epsilon_{22}^{p(i)}$ and $d\epsilon_{33}^{p(i)}$. Also, the elastic strain components $d\epsilon_{11}^{e(i)}$, $d\epsilon_{22}^{e(i)}$ and $d\epsilon_{33}^{e(i)}$ are obtained using the bulk and shear moduli $K[I_1^{(i-1)}]$ and $G[\sqrt{J_2}^{(i-1)}]$ at the beginning of the incremental calculation at the i-th step. Therefore, the total strain increments are:

$$\begin{aligned} d\epsilon_{11}^{(i)} &= d\epsilon_{11}^{e(i)} + d\epsilon_{11}^{p(i)} \\ &= \frac{1}{2G\left[\sqrt{J_2}^{(i-1)}\right]}\, ds_{11} + \frac{1}{9K\left[I_1^{(i-1)}\right]}\, dI_1 + d\lambda^{(i)}\left[\frac{\partial f_c}{\partial I_1} + \frac{\partial f_c}{\partial J_2} s_{11}^{(i-1)}\right] \\ &= \frac{1}{3G\left[\sqrt{J_2}^{(i-1)}\right]}\, d\sigma_{11} + \frac{1}{9K\left[I_1^{(i-1)}\right]}\, d\sigma_{11} \\ &\quad + d\lambda^{(i)}\left[2\left\{I_1^{(i-1)} - L(l)^{(i-1)}\right\} + R^2 s_{11}^{(i-1)}\right] \end{aligned} \tag{6.90a}$$

$$d\epsilon_{22}^{(i)} \quad d\epsilon_{33}^{(i)} \qquad \frac{1}{6G\left[\sqrt{J_2}^{(i-1)}\right]} d\sigma_{11} + \frac{1}{9\bar{K}\left[I_1^{(i-1)}\right]} d\sigma_{11}$$

$$+ d\lambda^{(i)}\left[2\left\{I_1^{(i-1)} - L(l)^{(i-1)}\right\} + R^2 s_{22}^{(i-1)}\right] \tag{6.90b}$$

3. For the next increment, all information required for the evaluation of a new $d\lambda^{(i+1)}$, such as the current stress state $[I_1^{(i)}, \sqrt{J_2}^{(i)}, s_{11}^{(i)}, s_{22}^{(i)}]$, strain state $[\epsilon_{11}^{(i)}, \epsilon_{22}^{(i)}, \epsilon_{kk}^{p(i)}]$, cap location $[x^{(i)}, l^{(i)}]$, and the current bulk modulus $K[I_1^{(i)}]$ and shear modulus $G[\sqrt{J_2}^{(i)}]$ are updated. These are:

$$I_1^{(i)} = I_1^{(i-1)} + d\sigma_{11} \tag{6.91a}$$

$$\sqrt{J_2}^{(i)} = \sqrt{J_2}^{(i-1)} + \frac{1}{\sqrt{3}} |d\sigma_{11}| \tag{6.91b}$$

$$s_{11}^{(i)} = s_{11}^{(i-1)} + \tfrac{2}{3} d\sigma_{11} \tag{6.91c}$$

$$s_{22}^{(i)} = s_{22}^{(i-1)} - \tfrac{1}{3} d\sigma_{11} \tag{6.91d}$$

$$s_{33}^{(i)} = s_{33}^{(i-1)} - \tfrac{1}{3} d\sigma_{11} \tag{6.91e}$$

$$\epsilon_{11}^{(i)} = \epsilon_{11}^{(i-1)} + d\epsilon_{11}^{(i)} \tag{6.91f}$$

$$\epsilon_{22}^{(i)} = \epsilon_{22}^{(i-1)} + d\epsilon_{22}^{(i)} \tag{6.91g}$$

$$\epsilon_{kk}^{p(i)} = \epsilon_{kk}^{p(i-1)} + 6\, d\lambda^{(i)}\left[I_1^{(i-1)} - L(l)^{(i-1)}\right] \tag{6.91h}$$

$$x^{(i)} = \frac{1}{D} \ln\left[1 + \epsilon_{kk}^{p(i)}/W\right] \tag{6.91i}$$

$$l^{(i)} = x^{(i)}/(1 + \alpha R) \tag{6.91j}$$

$$K^{(i)} \quad [K_1/(1 \quad K_1)]\left[1 \quad K_1 \exp(K_2 I_1^{(i)})\right] \tag{6.91k}$$

$$G^{(i)} = \left[G_1/(1 - G_1)\right]\left[1 - G_1 \exp\left(-G_2\sqrt{J_2}^{(i)}\right)\right] \tag{6.91l}$$

4. The same procedure is repeated until the stress state reaches the Drucker-Prager failure envelope, at which the material exhibits an unrestricted plastic flow.

The cap model behavior in a drained triaxial test under the confining pressures σ_3 2.8 kg/cm^2 (274.4 kPa) and 5.6 kg/cm^2 (548.8 kPa) are respectively shown in Fig. 6.22 in the form of the principal stress difference-axial strain relation.

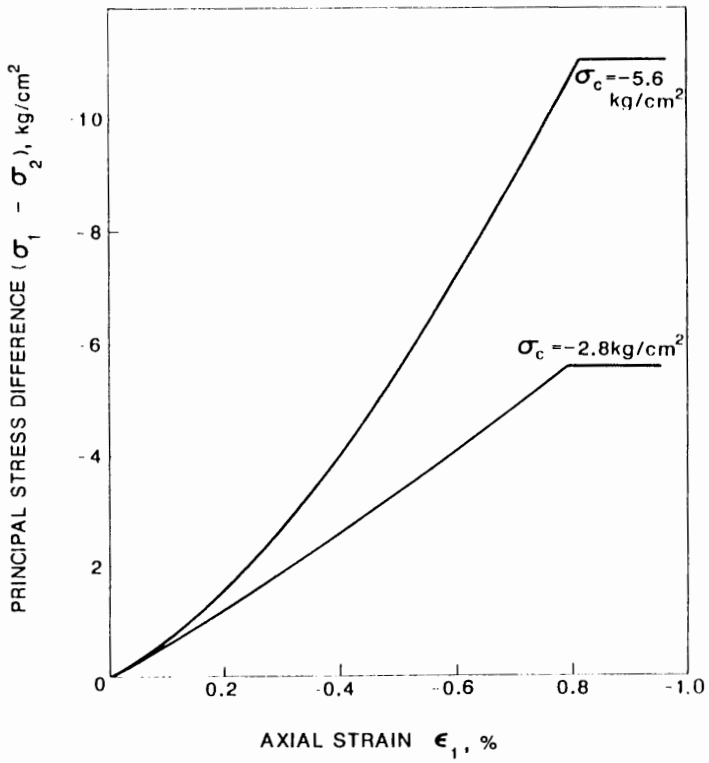

Fig. 6.22. Axial strain–principal stress difference relations under confining pressure σ_c = -2.8 kg/cm^2 and σ_c = -5.6 kg/cm^2

Numerical procedure for undrained case: A numerical technique at the i-th incremental step for obtaining the total or effective stress- strain relation in an undrained triaxial test is presented below.

1. The proportionality factor, $d\lambda^{(i)}$, can be obtained by substituting into Eq. (6.86) the axial strain increment $d\epsilon_{11}$ and the updated values at the end of the $(i-1)$-th incremental step such as $I_1^{*(i-1)}$, $\sqrt{J_2}^{(i-1)}$, $s_{11}^{(i-1)}$, $I^{(i-1)}$, $x^{(i-1)}$, $K^{(i-1)}$, and $G^{(i-1)}$.
2. Similar to the drained case, the substitution of $d\lambda^{(i)}$ into the associated flow rule equation leads to the plastic strain increments, $d\epsilon_{11}^{p(i)}$, $d\epsilon_{22}^{p(i)}$, and $d\epsilon_{33}^{p(i)}$. Since in this case the total strain increments are given as the input at the beginning of each step, the components of elastic strain increment are calculated:

$$d\epsilon_{11}^{e(i)} = d\epsilon_{11} - d\epsilon_{11}^{p(i)} = d\epsilon_{11} - d\lambda^{(i)}\left[2\left\{I_1^{*(i-1)} - L(I)^{(i-1)}\right\} + R^2 s_{11}^{(i-1)}\right] \tag{6.92a}$$

$$d\epsilon_{22}^{e(i)} = d\epsilon_{33}^{e(i)} = -\tfrac{1}{2}\, d\epsilon_{11} - d\lambda^{(i)}\left[2\left\{I_1^{*(i-1)} - L(I)^{(i-1)}\right\} + R^2 s_{22}^{(i-1)}\right] \tag{6.92b}$$

Further, the effective stress increments $d\sigma_{11}^{*(i)}$, $d\sigma_{22}^{*(i)}$, and $d\sigma_{33}^{*(i)}$ are respectively obtained from Eqs. (6.87a) and (6.87b) as:

$$d\sigma_{11}^{*(i)} = ds_{11}^{(i)} + \tfrac{1}{3}\, dI_1^{*(i)}$$

$$2G^{(i-1)}\left[d\epsilon_{11} - d\lambda^{(i)} R^2 s_{11}^{(i-1)}\right] - 6K^{(i-1)}\, d\lambda^{(i)}\left[I_1^{*(i-1)} - L(l)^{(i-1)}\right] \tag{6.93a}$$

$$d\sigma_{22}^{*(i)} = d\sigma_{33}^{*(i)} = ds_{22}^{(i)} + \tfrac{1}{3}\, dI_1^{*(i)}$$

$$= -G^{(i-1)}\left[d\epsilon_{11} - d\lambda^{(i)} R^2 s_{11}^{(i-1)}\right] - 6K^{(i-1)}\, d\lambda^{(i)}\left[I_1^{*(i-1)} - L(l)^{(i-1)}\right] \tag{6.93b}$$

Therefore, dI_1^* can be found as:

$$dI_1^{*(i)} = -18K^{(i-1)}\, d\lambda^{(i)}\left[I_1^{*(i-1)} - L(l)^{(i-1)}\right] \tag{6.93c}$$

The total stress increment $d\sigma_{11}^{(i)}$ is calculated by:

$$d\sigma_{11}^{(i)} = d\sigma_{11}^{*(i)} + du = d\sigma_{11}^{*(i)} - d\sigma_{22}^{*(i)}$$

$$3G^{(i-1)}\left[d\epsilon_{11} - d\lambda^{(i)} R^2 s_{11}^{(i-1)}\right] \tag{6.93d}$$

3. For the next increment, the current stress state $[I_1^{*(i)},\ I_1^{(i)},\ \sqrt{J_2}^{(i)},\ s_{11}^{(i)},\ s_{22}^{(i)}]$, strain state $[\epsilon_{11}^{(i)},\ \epsilon_{22}^{(i)},\ \epsilon_{kk}^{p(i)}]$, cap location $[x^{(i)},\ l^{(i)}]$, and bulk modulus $K^{(i)}$ and shear modulus $G^{(i)}$ are updated. These are:

$$I_1^{*(i)} = I_1^{*(i-1)} - 18K^{(i-1)}\, d\lambda^{(i)}\left[I_1^{*(i-1)} - L(l)^{(i-1)}\right] \tag{6.94a}$$

$$I_1^{(i)} = I_1^{(i-1)} + 3G^{(i-1)}\left[d\epsilon_{11} - d\lambda^{(i)} R^2 s_{11}^{(i-1)}\right] \tag{6.94b}$$

$$\sqrt{J_2}^{(i)} = \sqrt{J_2}^{(i-1)} + \frac{1}{\sqrt{3}}\left|d\sigma_{11}^{(i)}\right| \tag{6.94c}$$

$$s_{11}^{(i)} = s_{11}^{(i-1)} + \tfrac{2}{3}\, d\sigma_{11}^{(i)} \tag{6.94d}$$

$$s_{22}^{(i)} = s_{33}^{(i)} = s_{22}^{(i-1)} - \tfrac{1}{3}\, d\sigma_{11}^{(i)} \tag{6.94e}$$

$$\epsilon_{11}^{(i)} = \epsilon_{11}^{(i-1)} + d\epsilon_{11} \tag{6.94f}$$

$$\epsilon_{22}^{(i)} = \epsilon_{22}^{(i-1)} - \tfrac{1}{2}\, d\epsilon_{11} \tag{6.94g}$$

$$\epsilon_{kk}^{p(i)} = \epsilon_{kk}^{p(i-1)} + 6\,d\lambda^{(i)}\left[I_1^{*(i-1)} - I_c(I)^{(i-1)}\right] \tag{6.94h}$$

$$x^{(i)} = \frac{1}{D}\ln\left[1 + \epsilon_{kk}^{p(i)}/W\right] \tag{6.94i}$$

$$I^{(i)} = x^{(i)}/(1 + \alpha R) \tag{6.94j}$$

$$K^{(i)} = \left[K_i/(1 - K_1)\right]\left[1 - K_1\exp\left(K_2 I_1^{*(i)}\right)\right] \tag{6.94k}$$

$$G^{(i)} = \left[G_i/(1 - G_1)\right]\left[1 - G_1\exp\left(-G_2\sqrt{J_2}^{(i)}\right)\right] \tag{6.94l}$$

4. The same procedure is repeated until the effective stress state reaches the Drucker-Prager failure envelope.

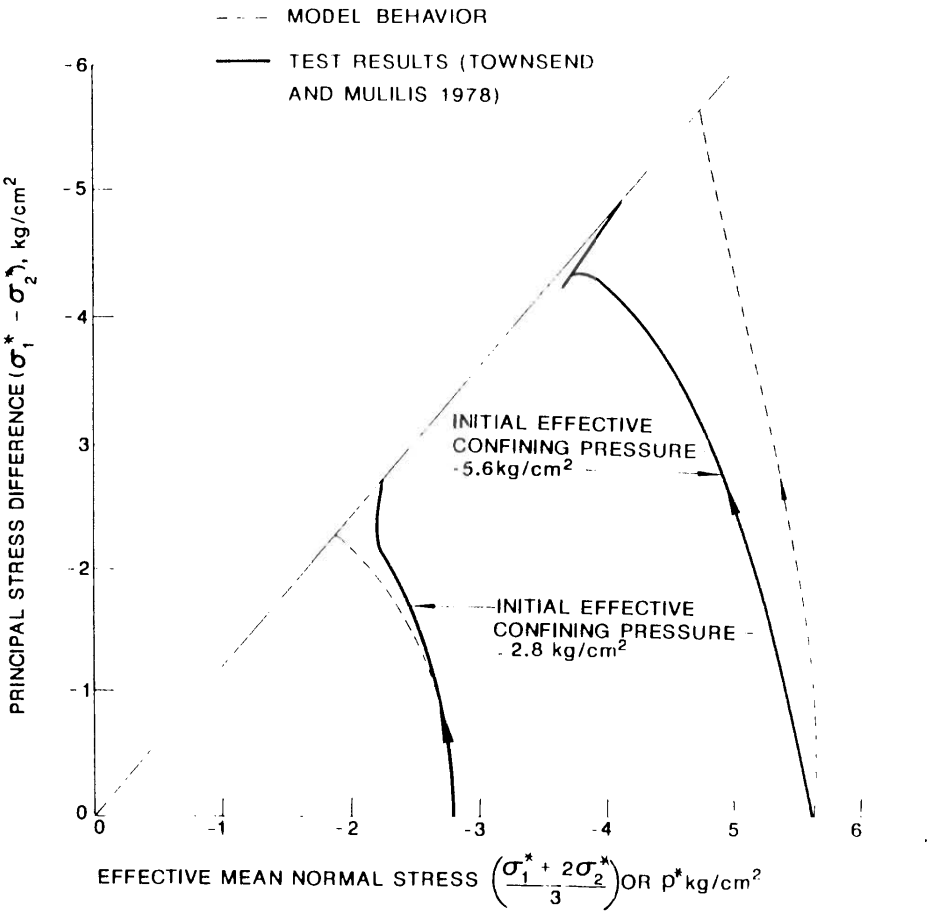

Fig. 6.23. Effective stress path under $\sigma_c = -2.8$ kg/cm² and $\sigma_c = -5.6$ kg/cm² in an undrained triaxial test.

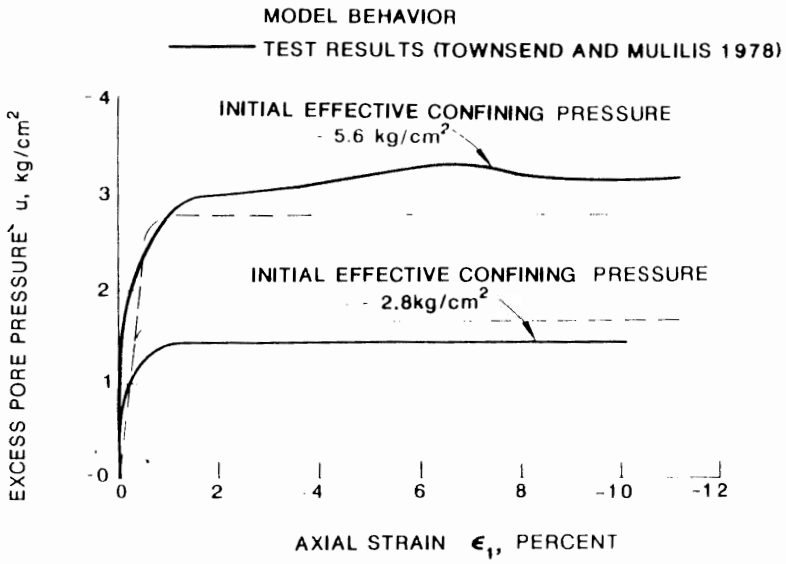

Fig. 6.24. Excess pore pressure generated under σ_c = 2.8 kg/cm² and σ_c = 5.6 kg/cm² in an undrained triaxial test.

The predicted behaviors of the cap model in an undrained triaxial test under the confining pressures $\sigma_c = -2.8$ kg/cm² (−274.4 kPa), and −5.6 kg/cm² (−548.8 kPa) are respectively shown in Figs. 6.23 through 6.25 in the form of the effective mean normal stress − principal stress difference, axial strain − excess pore pressure, axial strain − principal stress difference relationships. These figures show that the cap model behavior agrees reasonably well with the experimental data (Townsend and Mulilis, 1978) and qualitatively simulates the response of the material.

6.9 CAP MODEL IN TYPICAL FIELD CONDITIONS

At the IUTAM William Prager Symposium (Bazánt, 1985), Gudehus (1985) proposed several tests which may be used to evaluate a constitutive model for soils. It was suggested that the suitability of a particular material law, for use in boundary value problems, could be partially evaluated by examining the response to some typical strain paths associated with laboratory and field conditions. These test criteria are intended to simulate the conditions of: drained and undrained loadings; active and passive earth pressure problems; monotonic bilinear strain paths.

Figures 6.26 and 6.27, taken from Gudehus (1985), represent the behavior of drained and undrained earth pressure problems. In both cases the soil has experienced some previous stress history consisting of soil deposition (path 0-1) and erosion (path 1-2). Thus, the soil is in an overconsolidated condition at point 2. The

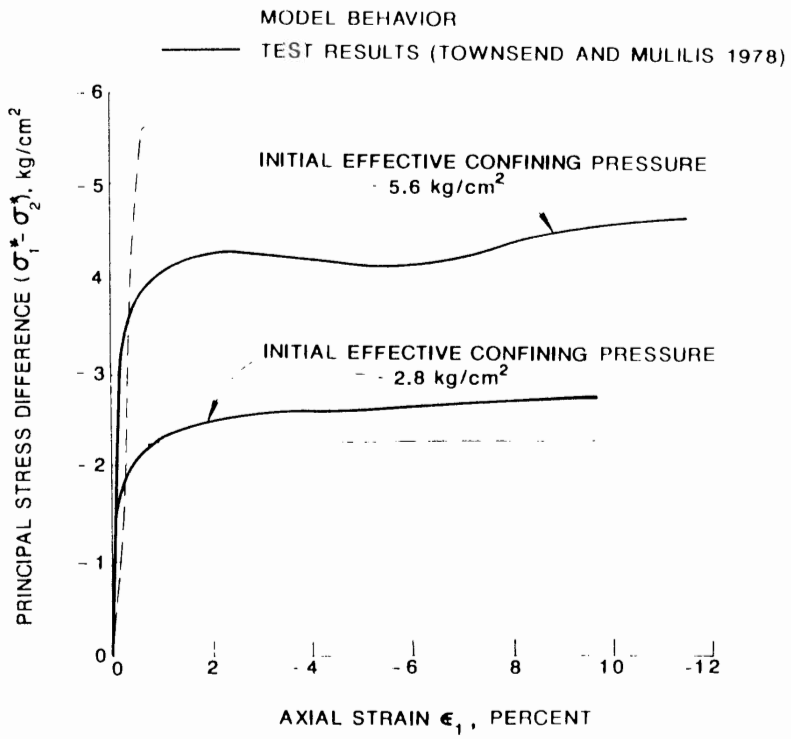

Fig. 6.25. Stress difference axial strain relation under σ_c = 2.8 kg/cm² and σ_c = 5.6 kg/cm² in an undrained triaxial test.

state of strain at this time is completely defined by the vertical strain ϵ_1, with $\epsilon_2 = \epsilon_3 = 0$ (axisymmetric conditions).

The stress paths for the drained condition (Fig. 6.26) are characterized by a constant vertical compressive stress σ_1 as a result of equilibrium requirements. The length of the path to the active failure condition is shorter than that to passive failure. The reason for this is easily seen when one considers the more conventional plot of the Coulomb failure envelope in Fig. 6.28.

The undrained condition (Fig. 6.27) is more interesting. Here the condition of incompressibility requires:

$$d\epsilon_2 = -d\epsilon_1 \tag{6.95}$$

during rapid loading (path 2-3-4). In the active case, the pore pressure decreases so that the compressive effective stress σ_1^* increases; the opposite happens in the passive case. Subsequent drainage, or pore pressure dissipation of excess pore pressures (path 4-5) returns the vertical stress to equilibrium with the overburden

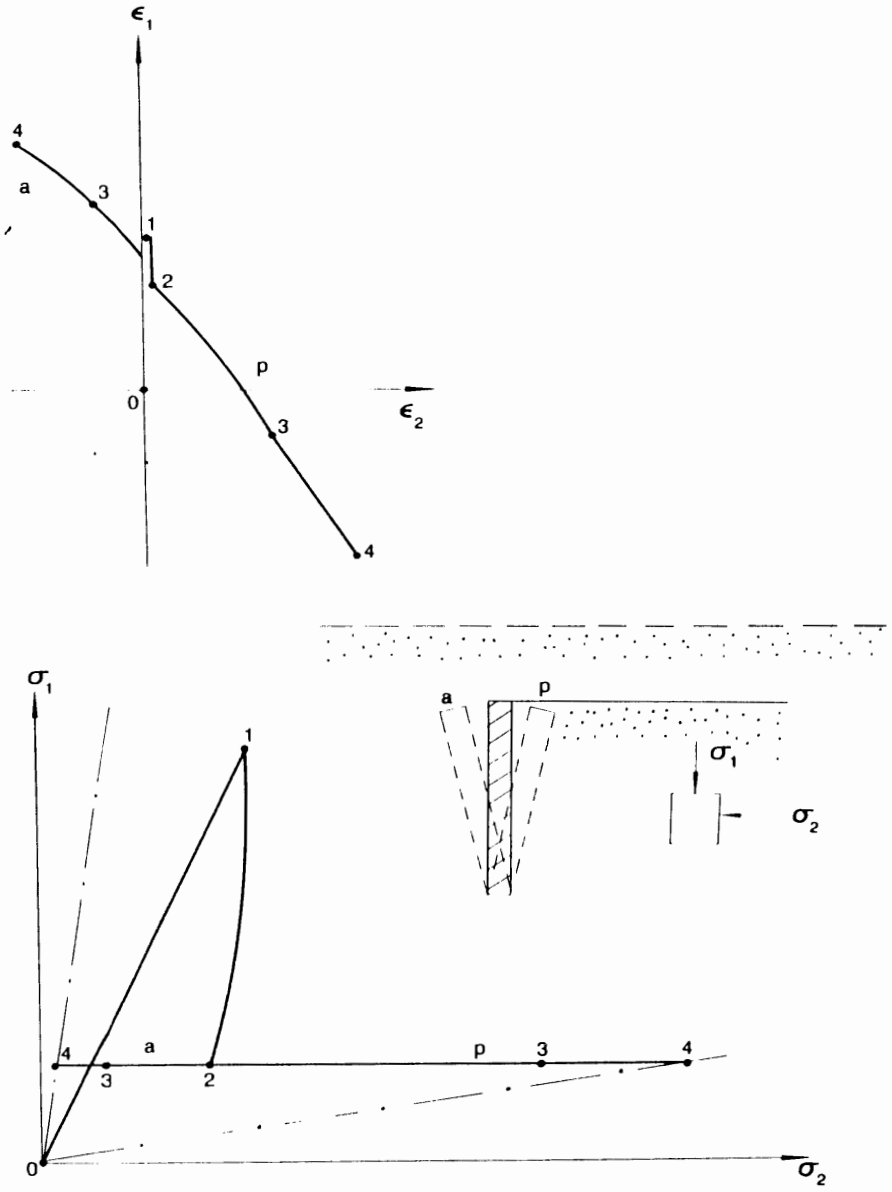

Fig. 6.26. Test paths for drained earth pressure response (Gudehus, 1985)

pressure. Dissipation of pore pressure is accompanied by a volume expansion in the active case and a volume contraction in the passive case.

Figure 6.29 shows the stress-strain relationship for bilinear strain paths. Here it is shown the stress path approaches that path which would have been produced had a

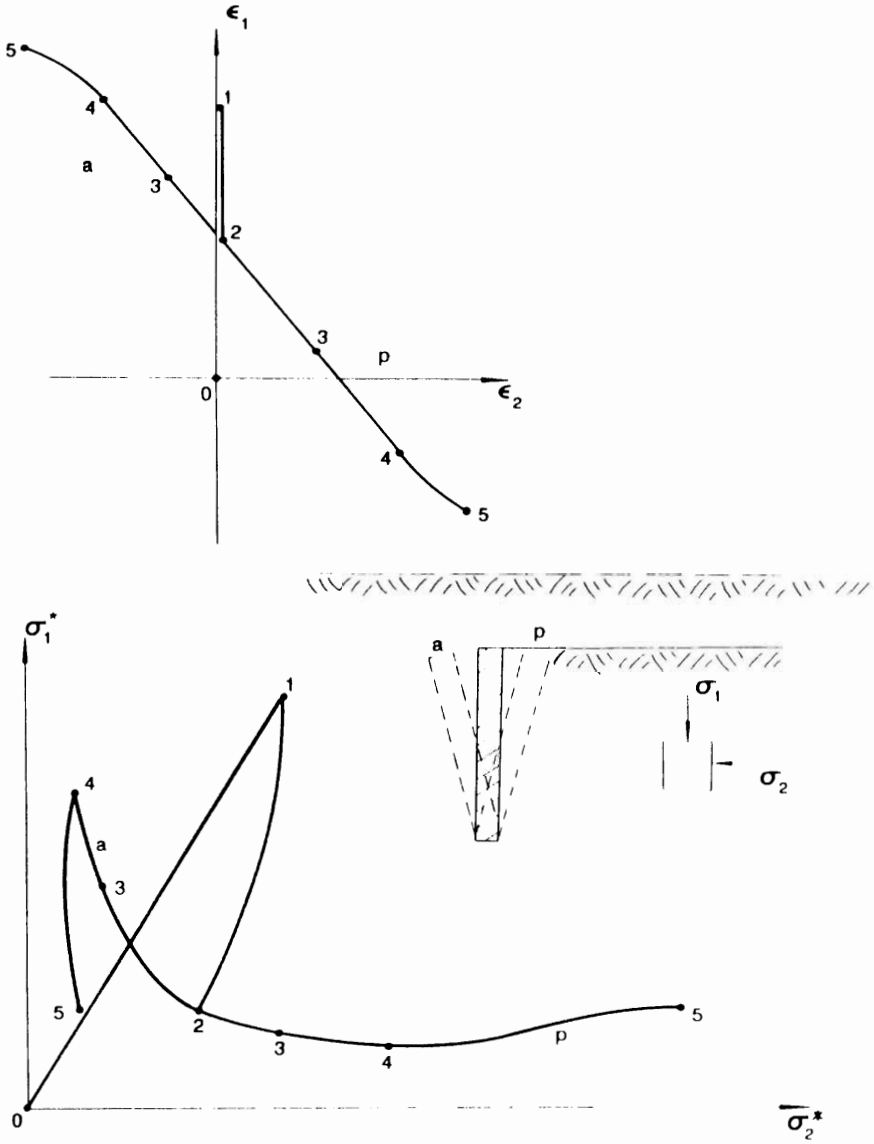

Fig. 6.27. Test paths for undrained earth pressure response (Gudehus, 1985).

proportional strain path of second type been followed from the beginning. The implication is that the long second strain path removes from material memory of any influence of the first strain path. Gudehus described these states of stress reached after sufficiently long monotonic loading as *swept-out-memory* (SOM) states.

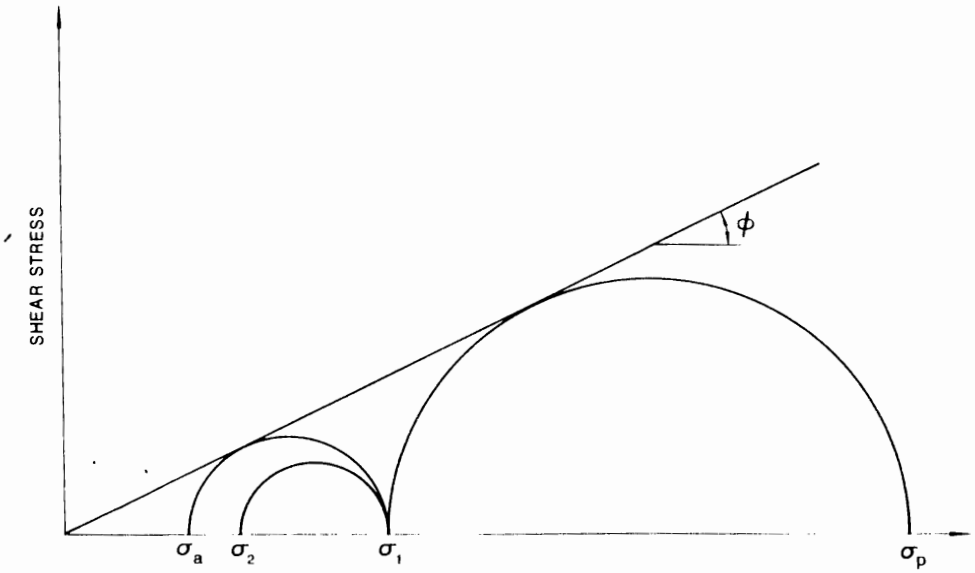

Fig. 6.28. Coulomb failure conditions for active and passive earth pressures.

Figures 6.30 through 6.32 show the response predicted by the cap model for the three problems just described (Chen, 1985; Chen and McCarron, 1986). The simple cap model described by the Drucker-Prager failure surface [Eq. (6.19)] and the elliptic cap yield surface [Eq. (6.21)] is used. The hardening function is that in Eq. (6.22). The following values of the material constants are used in the present

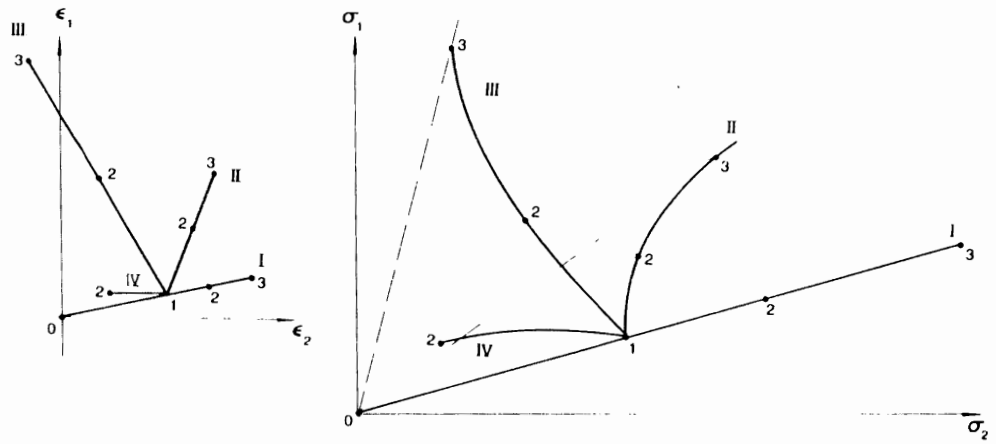

Fig. 6.29. Test paths for bilinear stram paths (Gudehus, 1985).

demonstration since they are available from previous work for a specific material (Baladi and Rohani, 1979b):

$$\phi = 49.1^\circ \quad R = 4.33$$

$$c = 0 \quad W = 0.0075 \tag{6.96}$$

$$\nu = 0.2736 \quad D = 6.78 \times 10^{-5}\ \text{ft}^2/\text{lb}\ (1.415 \times 10^{-6}\ \text{m}^2/\text{N})$$

$$E = 841400\ \text{lb}/\text{ft}^2\ (4.03 \times 10^7\ \text{N}/\text{m}^2)$$

For the plane strain condition, we have (Chen and Saleeb, 1982):

$$\alpha = 0.2309 \quad \text{and} \quad k = 0. \tag{6.97}$$

The initial cap position, I_1, is assumed to be at the origin of the $I_1 - \sqrt{J_2}$-space.

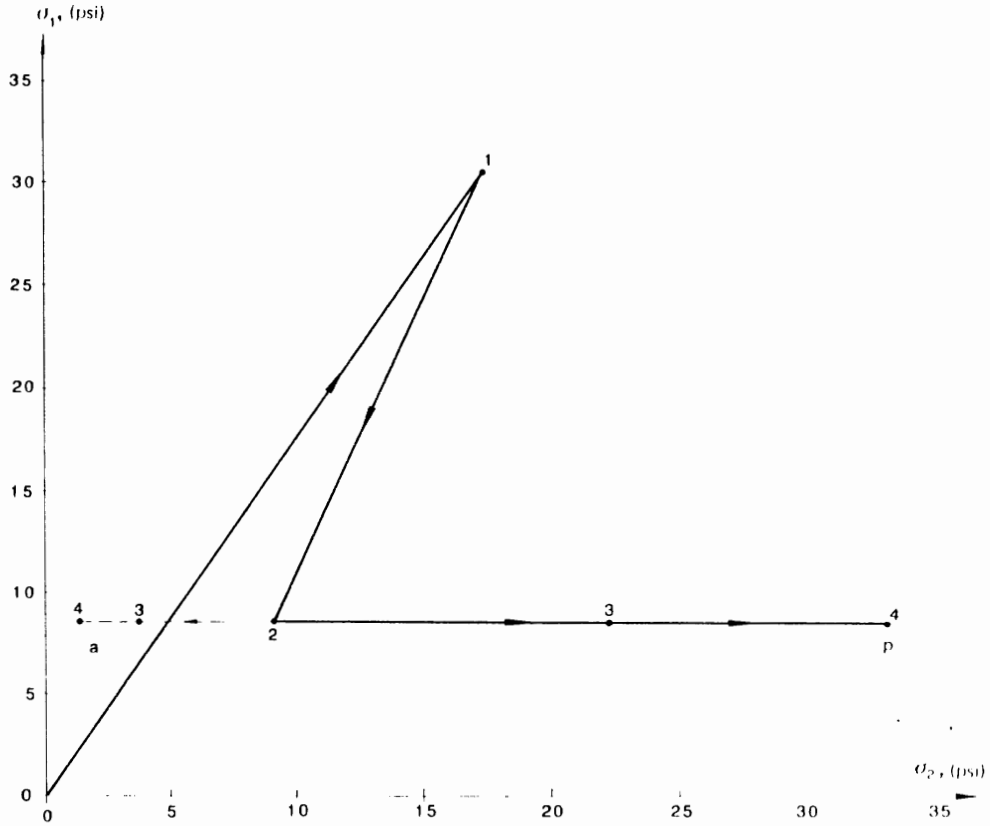

Fig. 6.30. Cap model response for drained test paths.

The plane strain earth pressure problem for drained loading is depicted in Fig. 6.30. The results are obtained in the following manner:

1. The material is loaded under a uniaxial strain condition until a vertical stress of 30 psi (in compression) is achieved (path 0-1). During this interval the stress state is on the cap for the entire path.
2. Unloading (uniaxial strain) then occurs until the vertical stress becomes a value of −8.5 psi (path 1-2). The stress-strain relation is linearly elastic along this path.
3. For the passive case, an iterative procedure is used to follow the stress path (constant σ_1). The material is first linearly elastic and then elastic-plastic when loading begins on the cap (path 2-3-4).
4. For the active case, the stress path is also followed. The material behaves elastically until the failure surface is reached (path 2-3-4).

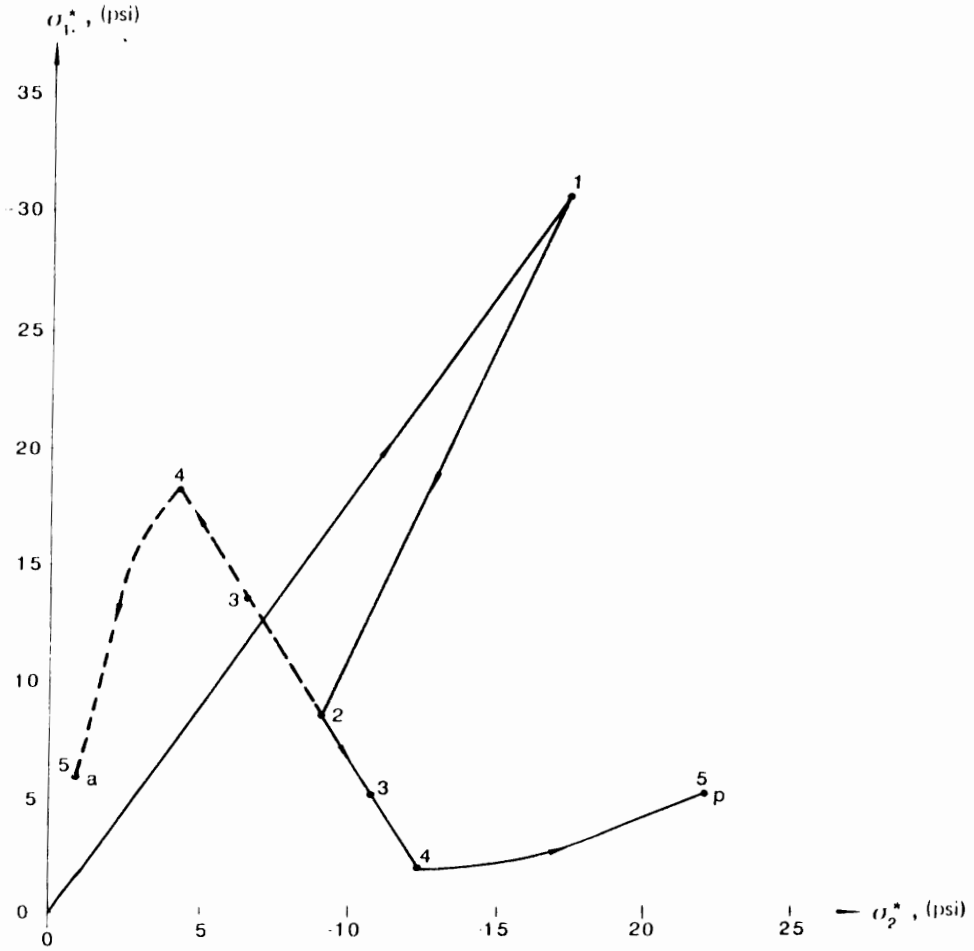

Fig. 6.31 Cap model response for undrained test paths.

The stress path in this model can not be followed after active or passive state is reached failure surface under drained condition.

The corresponding earth pressure problem for undrained loading is shown in Fig. 6.31. The results are summarized in the following:

1. The initial loading sequence (path 0-1-2) is identical to that of the drained case. Further loading along paths 2-3-4 occurs in a constant volume manner ($d\epsilon_1 = -d\epsilon_2$, $\epsilon_3 = 0$).
2. For the passive case, the response is initially elastic until the failure surface is reached (path 2-3-4). If loading continues in a constant volume manner the state of stress eventually becomes constant (unchanged) at point 4. At this point, the state of stress coincides with the intersection of the cap and failure surface (corner loading). The direction of the stress path is then altered so that the volume decreases (path 4-5).

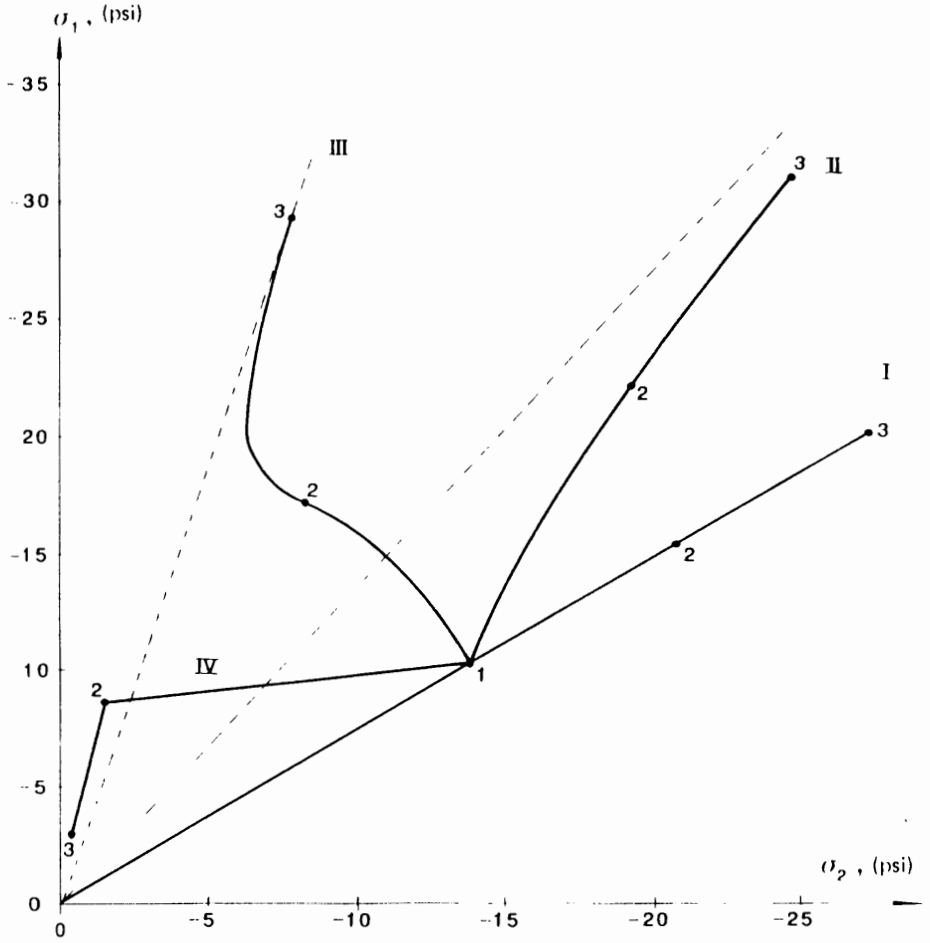

Fig. 6.32. Cap model response for bilinear strain test paths.

3. For the active case, the same procedure is followed except that the volume-conserving strain path is terminated when it reaches the failure surface (path 2-3-4). A volume-increasing path is then followed (path 4-5). If the original volume-constant path had been followed along the failure surface, the stress path would change directions so that both compressive effective stresses σ_1^* and σ_2^* would increase, and the stress path would be opposite to that for path 4-5.

The material response predicted for the four bilinear strain paths is shown in Fig. 6.32. The following four strain paths are used for the calculations:

For path I: The strain ratio $(d\epsilon_1 : d\epsilon_2 : d\epsilon_3)$ is $(1 : 3 : 0)$

For path II: The strain ratio is $(3 : 1 : 0)$

For path III: the strain ratio is $(3 : -2 : 0)$

For path IV: The strain ratio is $(1 : -4 : 0)$

Paths I, II, and III have continuous loading on the cap. Path IV loads first on the cap when the strain path is parallel to path I. When the incremental strain direction changes at point 1, the response is first elastic and then elastic-plastic with loading on the failure surface and then at the intersection of the failure surface and cap (corner loading).

From these demonstrations, it is concluded that the cap model is capable of handling and predicting the complicated situations such as nonlinear, nonproportional loading and unloading, stress path-dependency, and dilatancy as reviewed by Gudehus on some typical boundary value problems in soil mechanics.

6.10 CAP MODEL IN BOSTON BLUE CLAY

The successful application of a soil model requires that the model addresses, at least qualitatively, the significant characteristics of the soil response for the problem at hand.

The observations by Tavenas and his colleagues (Tavenas and Leroueil, 1980; Tavenas et al., 1978) confirm the applicability of the capped work-hardening plasticity models to the analysis of saturated clays subjected to embankment loads. The accumulation of a significant amount of laboratory and field observations regarding the behavior of Boston blue clay presents a unique opportunity to evaluate the performance of a constitutive model.

This Section outlines (1) a method of calibrating the cap model for analysis of saturated soils, (2) comparison of numerical results with laboratory measurements, (3) the analysis procedure for the three embankments constructed on Boston blue clay, and (4) comparison of the numerical results with measured quantities in situ.

The present method treats the soil as an elastic-plastic material and the pore water as an elastic material resisting only volumetric deformations. Although the soil-fluid response is considered, the method is time-independent, no attempt to consider time-dependent processes is implied in the present Section.

The cap model used in this analysis consists of the Drucker-Prager type of failure

surface and an elliptic strain-hardening surface (see Fig. 6.8). The mathematical forms of these surfaces are now written in terms of effective stress invariants.
For the Drucker-Prager failure surface:

$$f_1 = \alpha I_1^* + \sqrt{J_2} - k = 0 \tag{6.98}$$

where α and k are material constants, I_1^* is the first invariant of the effective stress tensor σ_{ij}^* and J_2 is the second invariant of the deviatoric stress tensor. The invariants I_1^* and J_2 are defined as:

$$I_1^* = \sigma_{11}^* + \sigma_{22}^* + \sigma_{33}^* \tag{6.99a}$$

$$J_2 = \frac{1}{6}\left[(\sigma_{11}^* - \sigma_{22}^*)^2 + (\sigma_{22}^* - \sigma_{33}^*)^2 + (\sigma_{33}^* - \sigma_{11}^*)^2 + 6\sigma_{12}^{*2} + 6\sigma_{23}^{*2} + 6\sigma_{31}^{*2}\right] \tag{6.99b}$$

For the strain-hardening cap surface:

$$f_c = \left[I_1^* - L(l)\right]^2 + R^2 J_2 - \left[x - L(l)\right]^2 = 0 \tag{6.100}$$

where R is material parameter representing the aspect ratio (ratio of horizontal to vertical axis) of the elliptic cap, l is the center of the ellipse, and x is a hardening parameter which is a function of the plastic volumetric strain in the form of $x = x(\epsilon_{kk}^p)$.

In the following Sections, the work on the response of Boston blue clay (McCarron and Chen, 1987) is summarized in some details.

6.10.1 Simulation of pore pressure

The formulation of a constitutive relation for the combined solid-fluid medium may be achieved in a simple manner by simply superimposing over the soil stiffness, a relationship representing the influence of the fluids (Naylor et al., 1981). The incremental constitutive matrix $[C]$ is then:

$$[C] = [C_s] + [C_f] \tag{6.101}$$

where $[C]$ is the total stiffness matrix, $[C_s]$ is the soil stiffness matrix and $[C_f]$ is the stiffness matrix of the fluids. Since the fluid component may not resist shear distortions, the matrix $[C_f]$ must have the following form of an isotropic elastic material with a zero shear modulus:

$$[C_f] = \begin{bmatrix} K_w & K_w & K_w & 0 & 0 & 0 \\ & K_w & K_w & 0 & 0 & 0 \\ & & K_w & 0 & 0 & 0 \\ & & & 0 & 0 & 0 \\ \text{Symmetric} & & & & 0 & 0 \\ & & & & & 0 \end{bmatrix} \tag{6.102}$$

where K_w represents the bulk modulus of the fluid. In practice, it is not necessary to use the actual bulk modulus of water, but merely a value several times larger than that of the soil.

Given a particular displacement field, the incremental effective stress is written as:

$$\{d\sigma^*\} = [C_e]\{d\epsilon\} \tag{6.103a}$$

where

$$\{d\sigma^*\} = [d\sigma_{11}^* \; d\sigma_{22}^* \; d\sigma_{33}^* \; d\sigma_{12}^* \; d\sigma_{23}^* \; d\sigma_{31}^*]^T \tag{6.103b}$$

and

$$\{d\epsilon\} = [d\epsilon_{11} \; d\epsilon_{22} \; d\epsilon_{33} \; d\gamma_{12} \; d\gamma_{23} \; d\gamma_{31}]^T \tag{6.103c}$$

The increment of pore water pressure, du developed, is represented by:

$$du = K_w \, d\epsilon_{kk} \tag{6.104a}$$

where $d\epsilon_{kk}$ is the volumetric strain increment written as:

$$d\epsilon_{kk} = d\epsilon_{11} + d\epsilon_{22} + d\epsilon_{33} \tag{6.104b}$$

The incremental total stress is then written as:

$$\{d\sigma\} = \{d\sigma^*\} + du\{I\} \tag{6.105a}$$

where

$$\{I\} = [1 \; 1 \; 1 \; 0 \; 0 \; 0]^T \tag{6.105b}$$

6.10.2 Comments on simulation of undrained response by Cap model

Principal limitations of the Cap model presented in this Chapter are: the assumptions of symmetry about the hydrostatic axis, the use of a circular trace in the deviatoric plane and the use of a perfectly plastic representation of the Drucker-Prager surface. Indeed, as pointed out below, these aspects appear to be responsible for some difficulties in calibrating the Cap model and errors in the prediction of excess pore water pressure. The use of the circular trace in the deviatoric plane implies identical strengths for triaxial compression and extension. Thus, it is not possible to accurately reproduce along both of these stress paths with a single set of model parameters.

Current research in the modeling of soils is focusing on removing the assumption of symmetry about the hydrostatic axis and incorporating the effects of K_0 consolidation (Anandarajah et al., 1984). Alternative traces in the deviatoric plane are also in use (Desai and Siriwardane, 1984).

The method of simulating undrained response is, of course, a simplification. The principal argument against using this procedure in a boundary value problem is that one must assume before hand whether a particular problem, or portion thereof, behaves in an undrained manner. The alternative is to perform a coupled diffusion (consolidation) analysis. While this may relieve one of having to decide between drained and undrained response, it requires many more assumptions concerning permeability, partial saturation, location of free drainage services, etc. Time must also enter into the solution explicitly. The method of superimposing the stiffness of materials required by compatibility to undergo identical deformations is well established and has been in use for some time (Agarwal and Broutman, 1980).

6.10.3 Model calibration

In this Section, a method for calibration of the Cap model is presented. Comparisons of model predictions and laboratory measurements for various stress paths are also made in the following.

One-dimensional compression tests data—Calibration of bulk modulus and hardening parameters

The development of plastic volumetric strain controls the position of the hardening surface for the Cap model. The accumulation of plastic volumetric strain is best observed during hydrostatic loading and unloading. However, for the present case, only the results of one-dimensional compression test were immediately available. Figure 6.33 indicates the average values of $C_c/(1 + e_0)$ and $C_r/(1 + e_0)$ are 0.2 and 0.02 respectively, where C_c and C_r are the *compression* and *rebound moduli* respectively, and e_0 is the initial void ratio. The compression modulus C_c and rebound modulus C_r that are defined usually in the one-dimensional compression test are given respectively as the slopes of the normal consolidation line and the rebound line in the relationship between the void ratio e and $\log_{10}|\sigma_v^*|$, where σ_v^* is the effective vertical stress (compressive stress). These are defined as:

$$C_c = -de/d(\log_{10}|\sigma_v^*|) \quad \text{for normal consolidation line} \tag{6.106a}$$

$$C_r = -de/d(\log_{10}|\sigma_v^*|) \quad \text{for rebound line} \tag{6.106b}$$

Using $\log_{10}|\sigma_v^*| = 0.434 \ln|\sigma_v^*|$, we have:

$$C_c = -2.303\, de/d(\ln|\sigma_v^*|) \quad \text{for normal consolidation line} \tag{6.107a}$$

$$C_r = -2.303\, de/d(\ln|\sigma_v^*|) \quad \text{for rebound line} \tag{6.107b}$$

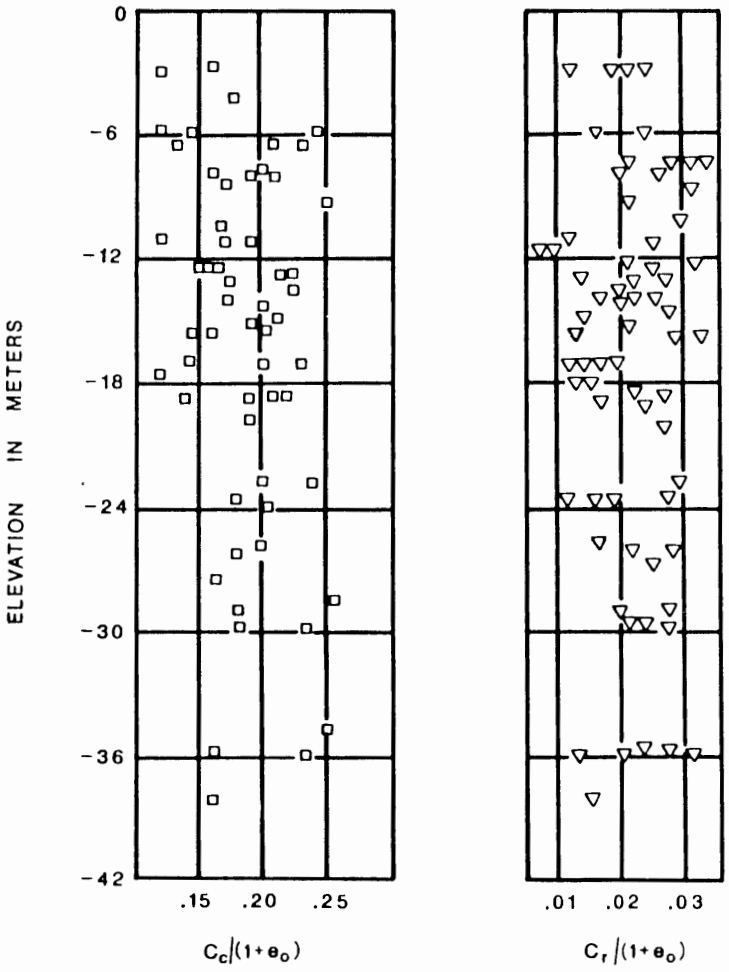

Fig. 6.33. Compression and rebound indexes for Boston blue clay (MIT, 1969a).

Noting that the volumetric strain increment $d\epsilon_v$ (compression is negative) is given by:

$$d\epsilon_v = dv/(1+v) \tag{6.108}$$

and $d\sigma_v^*/\sigma_v^* = dp^*/p^*$ where p^* is an effective mean stress (K_o has a constant value for one-dimensional normal consolidation) and that the plastic volumetric strain is merely the difference between the total and recoverable volumetric strains, then we have:

$$d\epsilon_{kk}^p = -\frac{1}{2.303}\frac{C_c - C_r}{1+e}\frac{dp^*}{p^*} \tag{6.109}$$

The implicit assumption here is that the one-dimensional compression and rebound curves are parallel to the respective curves for hydrostatic loading. Integration of Eq. (6.109) gives:

$$\Delta\epsilon^{p}_{kk} = -\frac{1}{2.303}\frac{C_c - C_r}{1+e}\ln\frac{p_2^*}{p_1^*} \tag{6.110}$$

where $\Delta\epsilon^{p}_{kk}$ represents the change in plastic volumetric strain between the hydrostatic pressures p_1^* and p_2^*. In Eq. (6.110), it has been assumed the ratios of C_c and C_r to the value $(1 + e)$ are constant for all values of p^*. For a reference pressure of unity, Eq. (6.110) becomes:

$$\epsilon^{p}_{kk} = -\frac{1}{2.303}\frac{C_c - C_r}{1+e}\ln|p^*| \tag{6.111}$$

On the other hand, the elastic portion of the volumetric strain is given by:

$$d\epsilon^{e}_{kk} = -\frac{1}{2.303}\frac{C_r}{1+e}\frac{dp^*}{p^*} \tag{6.112}$$

from which the bulk modulus K may be written as:

$$K = \frac{dp^*}{d\epsilon^{e}_{kk}} = -2.303p^*\frac{1+e}{C_r} \tag{6.113}$$

which implies a linear relationship between the bulk modulus K and the hydrostatic pressure p^* for constant ratio of $C_r/(1 + e)$.

The present version of the Cap model allows for a pressure-dependent bulk modulus K and nonlinear evolution of plastic volumetric strain ϵ^{p}_{kk} in the form:

$$K = K_{max}\left[1 - K_1\exp(K_2 I_1)\right] \tag{6.114}$$

$$\epsilon^{p}_{kk} = W\left[\exp(Dx) - 1\right] \tag{6.115}$$

where K_{max}, K_1, K_2, W and D are material parameters, and x is the intersection of the hardening surface with the hydrostatic pressure axis.

These material constants in Eqs. (6.114) and (6.115) are respectively matched with the generated data from Eqs. (6.113) and (6.111) over the stress range of interest. In retrospect, it would have been more convenient to use Eqs. (6.111) and (6.113) directly. For the range of stresses used here, these material parameters for bulk modulus and hardening rule are respectively determined:

$K_{max} = 6000$ ksf (287 MPa)

$K_1 = 0.99$

$K_2 = 0.006\ \text{ft}^2/\text{kip}\ (1.25 \times 10^{-4}\ \text{m}^2/\text{kN})$

$D = 0.03\ \text{ft}^2/\text{kip}\ (6.26 \times 10^{-4}\ \text{m}^2/\text{kN})$

$W = 0.3$

Triaxial test data—Calibration of failure surface and shape of hardening surface

While the one-dimensional and hydrostatic compression tests may serve to define the bulk modulus and evaluation of plastic volumetric strain, other stress paths are necessary to define the shape of the hardening surface and the position of the Drucker-Prager surface.

The position of the Drucker-Prager surface may be determined by examining data from triaxial and proportional loading tests. The most commonly reported result of these tests is the angle of internal friction ϕ. The angle of internal friction (measured under triaxial conditions) for Boston blue clay is generally reported to be in the range of 26 degrees (Ladd, et al., 1971). We shall adopt this value.

(A) Failure surface. In the case of triaxial compression tests, the angle of internal friction is related to the slope of the Drucker-Prager surface through the following relation (Chen, 1982):

$$\alpha = \frac{2 \sin \phi}{\sqrt{3}\,(3 - \sin \phi)} \tag{6.116}$$

and the cohesion c is related to the parameter k through the relation:

$$k = \frac{6c \cos \phi}{\sqrt{3}\,(3 - \sin \phi)} \tag{6.117}$$

For normally consolidated clays we may select $c = 0$ and $\phi = 26°$. Equations (6.116) and (6.117) then give:

$$\alpha = 0.2 \quad \text{and} \quad k = 0. \tag{6.116}$$

(B) Shape of hardening surface. The shape of the hardening surface has a significant influence on the stress path for undrained shear. Undrained shear tests on isotropically consolidated specimens of Boston blue clay indicate that, for the normally consolidated condition (OCR = 1), the ratio of undrained strength (ultimate shear strength s_u) to the absolute value of effective overburden pressure $|\sigma_{vo}^*|$, that is, $s_u/|\sigma_{vo}^*|$, is 0.3 (Ladd et al., 1971). Thus, given the initial condition, the final stress state is specified and the shape of the hardening surface may be determined. Figure 6.34 shows, qualitatively, the response of an initially normally consolidated specimen subjected to undrained triaxial shear loading.

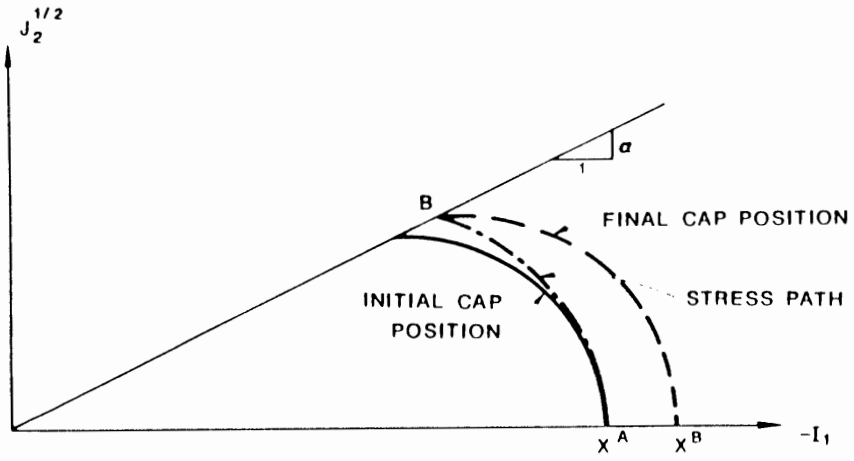

Fig. 6.34. Cap model response for undrained shear.

As an example, consider the initial hydrostatic condition such as:

$$\sigma_{ij}^{*} = \begin{vmatrix} -5 & 0 & 0 \\ 0 & -5 & 0 \\ 0 & 0 & -5 \end{vmatrix} \quad \text{(unit in ksf)} \tag{6.119}$$

The failure condition is then given by:

$$s_u / |\sigma_{xo}^{*}| = 0.3 \tag{6.120a}$$

or

$$s_u = \tfrac{1}{2}(\sigma_1 - \sigma_3) = 0.3|\sigma_{xo}^{*}| \tag{6.120b}$$

where σ_1 and σ_3 are respectively the maximum and minimum principal stresses (note that tensile stress is positive). Then, substituting $\sigma_{xo}^{*} = -5$ ksf into Eq. (6.120b), we find:

$$s_u = 1.5 \quad \text{(ksf)} \tag{6.120c}$$

The shear stress at state B expressed in terms of J_2 is:

$$J_2 = \tfrac{1}{3}(\sigma_1 - \sigma_3)^2 \tag{6.121a}$$

or from Eq. (6.120b), we have:

$$J_2 = \tfrac{4}{3}s_u^2 \tag{6.121b}$$

Substituting $s_u = 1.5$ ksf into Eq. (6.121b), we find:

$$J_2 = \frac{3}{4} \times (1.5)^2 = 3(\text{ksf})^2 \tag{6.122}$$

From the Drucker-Prager equation (6.98), the hydrostatic component of the effective stress at failure is (for $k = 0$ and $\alpha = 0.2$):

$$I_1^{*B} = \sqrt{J_2}/\alpha = 8.66 \quad (\text{ksf}) \tag{6.123}$$

The elastic volumetric strain is then calculated as:

$$\Delta\epsilon_{kk}^e = \left(I_1^{*B} - I_1^{*A}\right)/3K \tag{6.124}$$

Using an average bulk modulus K of 465 ksf (22.3 MPa) obtained from Eq. (6.114) and $I_1^{*A} = -15$ ksf, we find:

$$\Delta\epsilon_{kk}^e = 0.0045 \tag{6.125}$$

For undrained behavior we have (since $\Delta\epsilon_{kk} = 0$):

$$\Delta\epsilon_{kk}^p = \Delta\epsilon_{kk}^e \tag{6.126}$$

Through the use of Eq. (6.115) the current position of the cap x^B may be computed:

$$\epsilon_{kk}^{pB} = \epsilon_{kk}^{pA} + \Delta\epsilon_{kk}^p = 0.1087 + 0.0045 = 0.1132 \tag{6.127}$$

then:

$$x^B = \frac{1}{D}\ln\left(\frac{\epsilon_{kk}^p}{W} + 1\right) = 15.79 \quad (\text{ksf}) \tag{6.128}$$

The value of R is then:

$$R = \left(x^B - I_1^{*B}\right)/\alpha I_1^{*B} = 4.0 \tag{6.129}$$

(C) Shear modulus. It now remains to determine the shear modulus G. Ideally, the shear modulus could be determined from the unloading portion of triaxial or one-dimensional compression tests. Unfortunately, these data were not directly available. Ladd (1964), however, has published data describing the undrained modulus E_u of Boston blue clay at various stress levels. Also presented were test results for undrained triaxial compression tests on isotropically consolidated speci-

mens ($\overline{\text{CTUC}}$ tests). The following initial secant moduli (in normalized form) for Boston blue clay were determined by Ladd (1964):

For OCR = 1, $E_u/|\sigma_{xo}^*| = 240$

For OCR = 6, $E_u/|\sigma_{xo}^*| = 570$

The initial overburden pressures for the OCR's of 1 and 6 were 12.3 and 2.0 ksf (590 and 96 kPa), respectively. Here the OCR is defined as the ratio of the maximum previous vertical stress to the current vertical stress.

The elastic shear modulus G may be evaluated as:

$$G = \tfrac{1}{3}E_u \tag{6.130}$$

for the undrained condition and stress levels well below the failure stress. The resulting shear moduli are then evaluated as 980 and 380 ksf (47 and 18 MPa) for the OCR's 1 and 6, respectively. As expected, the above values did not provide accurate predictions when coupled with the previously determined parameters. Subsequently, the shear moduli were modified to values of 600 and 200 ksf (29 and 9.6 MPa) for OCR's of 1 and 6, respectively. It is likely that these values are valid for the present stress and OCR states only. The use of a higher shear modulus for the normally consolidated state does not necessarily insure a stiffer response than the overconsolidated state, since plastic deformation occurs for loading in the normally consolidated condition.

(D) Predictions and comparison. Figure 6.35 compares the undrained response of Boston blue clay with that predicted by the Cap model. Note that the stresses and

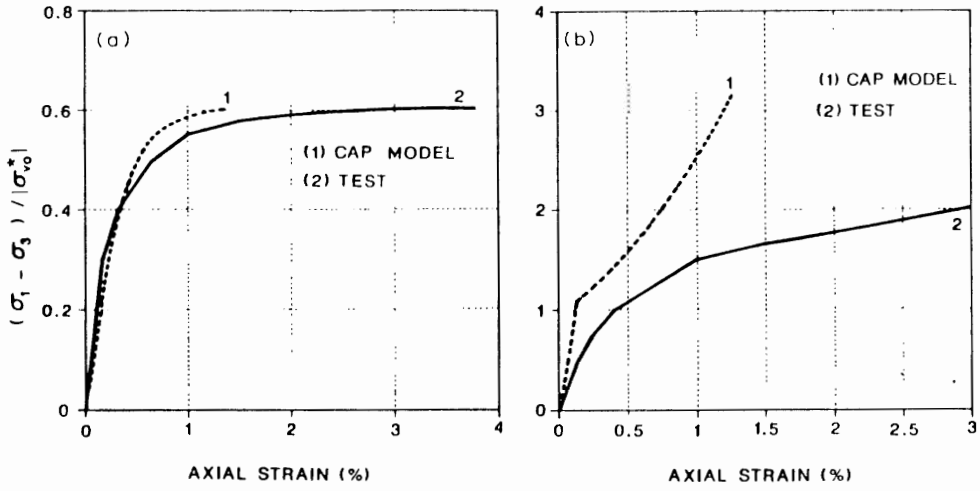

Fig. 6.35. Undrained triaxial compression tests for Boston blue clay: (a) OCR = 1; (B) OCR = 6.

strains in the figures are followed by the soil mechanics sign convention (compressive stress and strain are taken positive). In the case of OCR = 1, the overall match is quite good.

Results for the case of OCR = 6 are less encouraging. Here, it appears that a nonlinear shear modulus would provide improved results. However, this would not improve the strength prediction. Comparison with Ladd's data (1971) indicates the overestimation of strength is accompanied by a larger than observed negative pore pressure.

Plane strain test data – Predictions and comparison

Detailed information concerning the plane strain behavior of Boston blue clay has been presented in a report (Ladd et al., 1971). This report contains results from a program of 23 plane strain tests. *Active* and *passive* load conditions were considered at OCR's of 1, 2, and 4.

The specimens used by Ladd were consolidated from a clay slurry under K_o (one-dimensional) conditions. The plane strain equipment, developed at MIT (Bovee and Ladd, 1970), uses a sample with dimensions 3.5 in. high by 3.5 in. wide by 1.4 in. deep (8.9 cm by 8.9 cm by 3.6 cm). The vertical and horizontal stresses may be independently varied. The device allows measurements of the three principal stresses as well as the pore pressure.

In the following, only the results of *active* pressure tests are considered. An active pressure condition refers to a failure state in which the major principal stress direction acts in the in-situ vertical direction. Thus, if K_o is less than one, σ_1 always acts in the vertical direction and no rotation of the principal stresses occurs during shear.

The strength ratio ($s_u/|\sigma_{vo}^*|$) in plane strain active pressure conditions ($\overline{CK_oUPSA}$) is consistently greater than that observed in undrained triaxial compression conditions ($\overline{CTUC}$) (Ladd et al., 1971). This apparent increase in strength leads to questions regarding the determination of material model parameters. In particular, "Are model parameters evaluated for one load path valid for conditions which are very different?".

The differences between the initial shape of yield surfaces for isotropically and K_o-consolidated soils have been discussed by Tavenas and Leroueil (1977) and Leroueil et al. (1978). The essential difference is that the yield surface for the K_o condition appears to be symmetrical about the K_o-consolidation line rather than the hydrostatic axis, as can be seen in Fig. 6.36. It has also been noted that the yield surface may become distorted during loading (Leroueil et al., 1979). Thus, it is not surprising that K_o-consolidated specimens exhibit behavior different from that for initially isotropically consolidated specimens.

(A) Influence of the cap aspect ratio R on undrained and drained behaviors. Figure 6.37 compares the predicted response for various aspect ratio of the hardening surface under $\overline{CK_oUPSA}$ test conditions (OCR = 1). In each case, the initial stress state and model parameters are identical, only the aspect ratio of the cap changes.

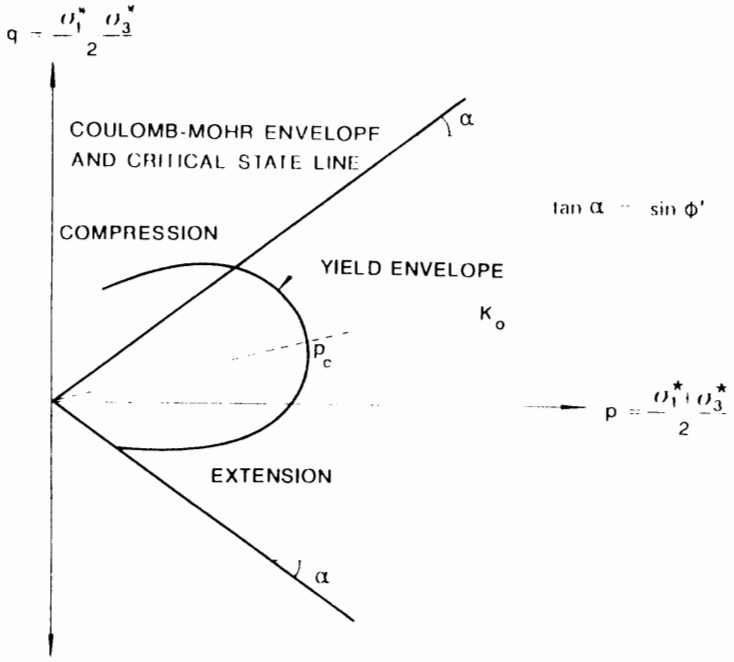

Fig. 6.36. Yield envelope for K_o-consolidated clay (Crooks, 1981).

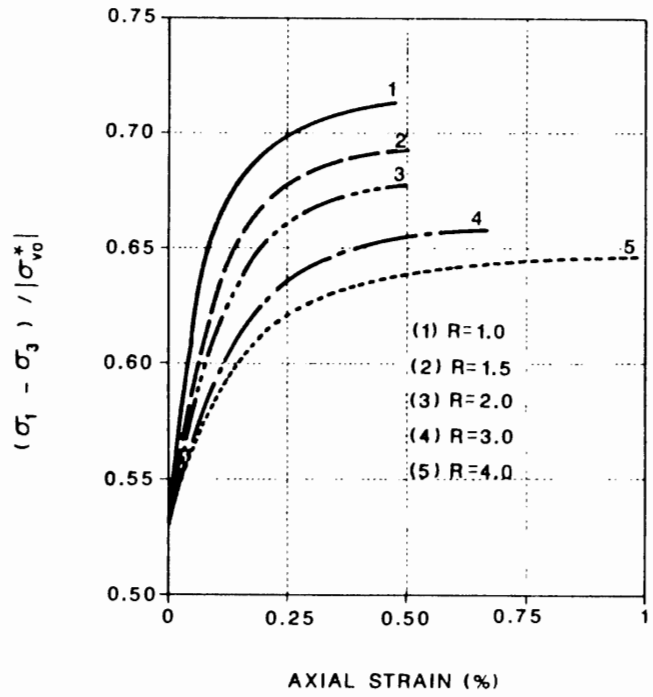

Fig. 6.37. Influence of the cap aspect ratio on undrained shear strength.

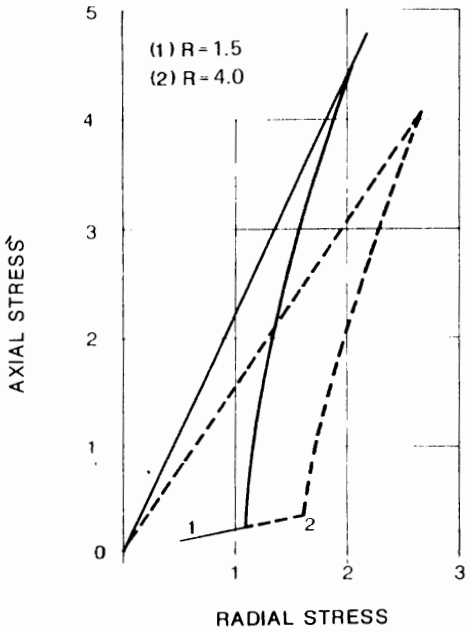

Fig. 6.38. Influence of the cap aspect ratio on uniaxial strain tests.

This implies the intersection of the cap surface with both the Drucker-Prager surface and hydrostatic axis changes. It is apparent the aspect ratio of 4.0 determined for $\bar{C}I\bar{U}\bar{C}$ test conditions does not correctly predict the plane strain failure condition (compare with the experimental result in Fig. 6.39a). Figure 6.37 indicates that an aspect ratio of 1.5 provides a good representation of the failure strength $(\sigma_1 - \sigma_3)/|\sigma_{xo}^*| = 0.7$. Further, an important influence of the aspect ratio is evident: larger values of R result in lower shear strengths.

The effect of the aspect ratio of the hardening surface for drained loading is demonstrated in Fig. 6.38 where results from uniaxial strain tests are presented. The load path here acts continuously on the hardening surface, representing virgin loading. Figure 6.38 indicates the aspect ratio of 1.5 results in K_o value of 0.45, while an aspect ratio of 4.0 gives a value of 0.6 for K_o. The K_o value of 0.45 compares well with the range of values (generally 0.45 to 0.55) reported by Ladd et al. (1971).

(B) Predictions and comparisons. Figure 6.39 compares the predicted response for OCR's of 1 and 2 for $\bar{C}\bar{K}_o\bar{U}PSA$ loading conditions. The axial stresses were 8 and 4 ksf (380 and 190 kPa) for OCR's of 1 and 2, respectively. Figure 6.39a compares the predicted response for shear moduli of 600 and 200 ksf (29 and 9.6 MPa) with the range of response found by Ladd for the normally consolidated conditions. Figure 6.39b compares the predicted response for the same two values of shear moduli with the measured response for the overconsolidated condition. In the case of the

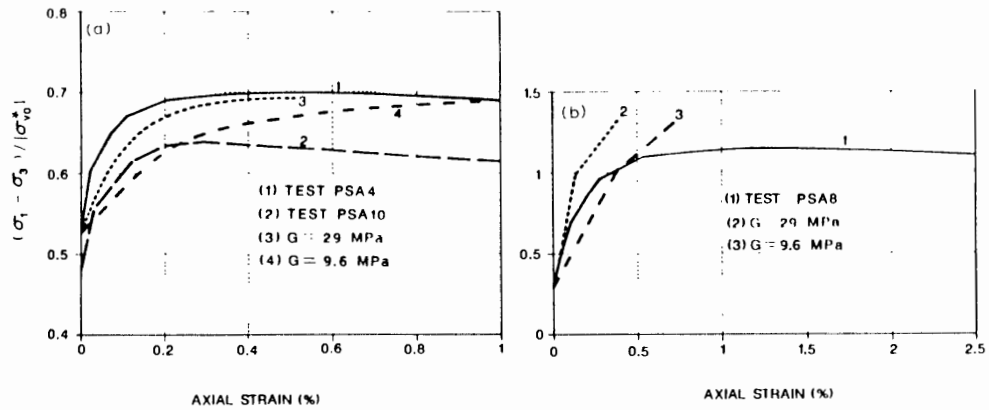

Fig. 6.39. $\overline{CK_oU}$PSA results for Boston blue clay: (a) OCR = 1, (b) OCR = 2.

normally consolidated specimen, the shear modulus of 200 ksf results in a response which is too soft. For the overconsolidated condition, arguments could be made for either value of shear modulus. However, it is noted the predicted strength is too high in both instances. The use of shear modulus of 600 ksf raises some objections since the combination of the stress dependent bulk modulus and constant shear modulus results in a negative Poisson's ratio for the present case.

The tendency to overpredict the failure strength of overconsolidated samples was common for both triaxial and plane strain conditions. Figure 6.40 compares the predicted strength $s_u/|\sigma_{vo}^*|$ and pore pressure parameters A_f with value determined by Ladd (Ladd et al., 1971). The qualitative behavior is correct in both cases, however, a tendency to diverge from the measured response is observed. The predictions presented in Fig. 6.40 are based on identical Cap model parameters in

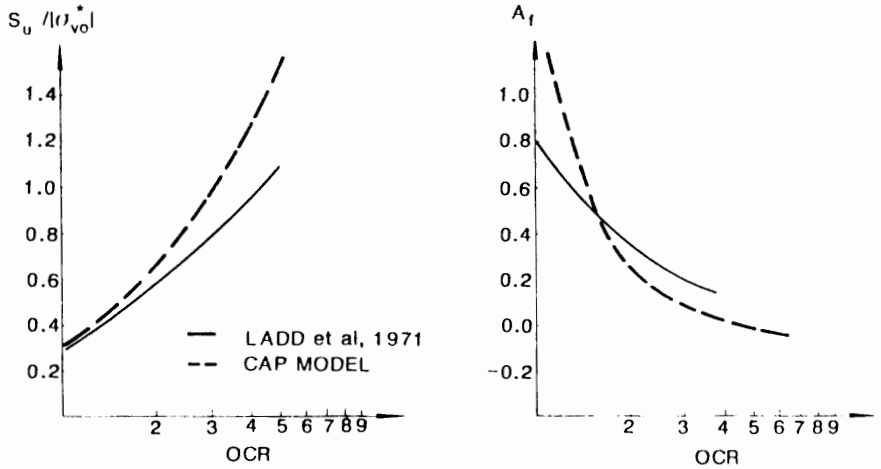

Fig. 6.40. Strength ratio and pore pressure parameter for Boston blue Clay.

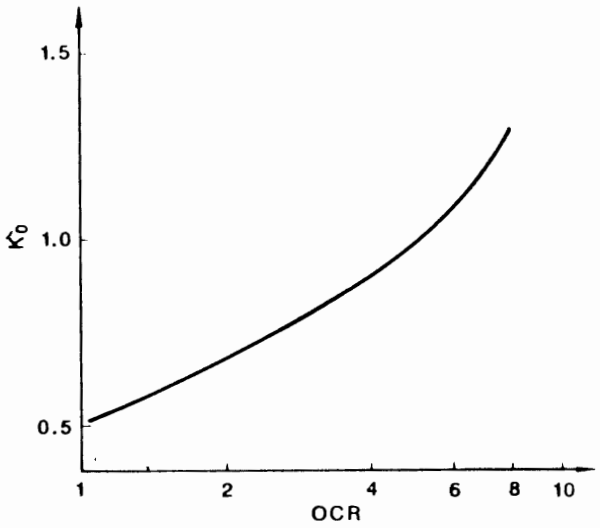

Fig. 6.41 Relationship between K_o and OCR for Boston blue clay (D'Appolonia et al., 1971).

each case. The initial position of the cap is defined by the normally consolidated position. Only the initial state of stress varies in each analysis.

The variation of K_o with degree of overconsolidation is given in Fig. 6.41. The results in Fig. 6.40 were obtained using the K_o values in Fig. 6.41.

In the present model, the effect of pore pressure is introduced by modifying the constitutive relation of the soil to account for the relative incompressibility of the pore water. The effective bulk modulus of the soil-fluid system is then:

$$K = K_s + K_w = K_s(1 + \beta) \tag{6.131}$$

where; K_s is the elastic bulk modulus of soil, K_w is the adopted value for the bulk modulus of water, and β is the ratio of K_w to K_s.

Figure 6.42 provides a more detailed account of the model behavior for normally consolidated soils subjected to undrained active pressure loading. Results in Fig. 6.42 are for β values of 1.0 and 9.0. The qualitative behavior of the model is very good. Better predictions for the present case might be obtained for a different aspect ratio of the cap. However, the object here is to provide representative behavior for the range of response expected (Fig. 6.39). The main shortcoming of the model appears to be in the magnitude of the predicted pore pressures. The errors in the pore pressure prediction may be traced to the previously discussed limitations of the effective stress response of the model.

An examination of Fig. 6.42e indicates the principal differences in the predicted and actual responses of the normally consolidated specimen may be due to the orientation of the hardening surface. The measured response indicates the mean stress is initially increasing. The model predicts a decreasing value of mean effective

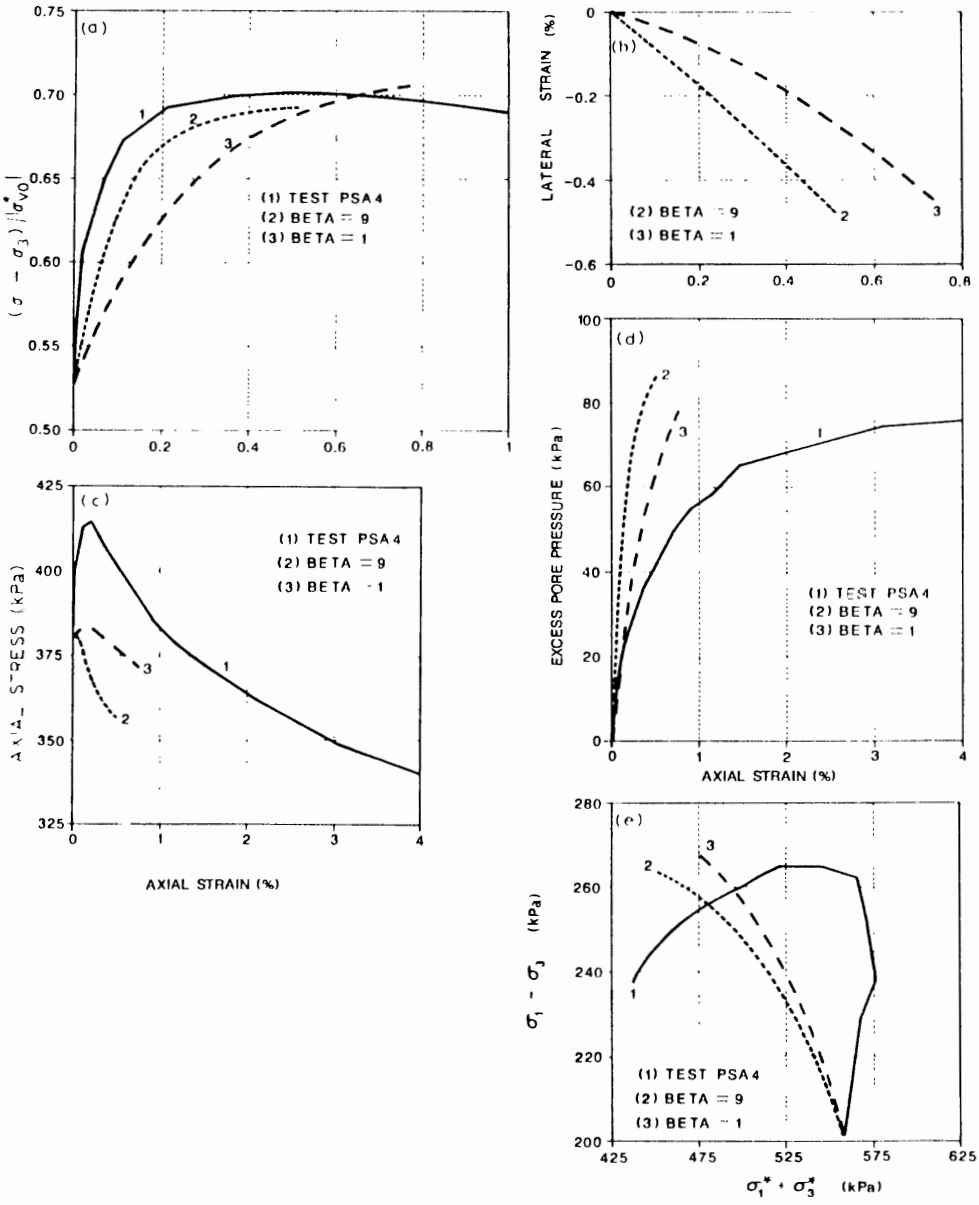

Fig. 6.42 $\bar{C}K_oUPSA$ test for Boston blue clay ($\beta = 1$ and 9): (a) axial strain $(\sigma_1 - \sigma_3)/|\sigma_{vo}^*|$ relation; (b) axial strain–lateral strain relation; (c) axial strain–axial stress relation; (d) axial strain–pore pressure relation; (e) $(\sigma_1^* + \sigma_3^*)$ vs $(\sigma_1 - \sigma_3)$ relation.

stress, consistent with the *critical-state theory* for normally consolidated clays. The difference between the predicted and measured responses is probably due to the condition of K_0 consolidation and the resultant distortion of the initial yield surface. This discrepancy is the source of the erroneous pore pressure predictions for normally consolidated states.

(C) Comments on the cap model calibration. Calibration of the Cap model above made use of constant shear moduli for various stress and OCR conditions. While this is useful for preliminary effort, in general one would expect the shear modulus to be both stress and history dependent. In the analyses which follow, both constant shear moduli and Poisson's ratio ν are used. A value of 0.1 is used for Poisson's ratio. This value was arrived at by considering the stress levels encountered for the problems considered. These levels are similar to those used in the Ladd's plane strain tests (Ladd et al., 1971). As an example of the influence of this assumption, initial shear moduli of 600 and 380 ksf (29 and 18 MPa) are obtained for the plane strain OCR conditions of 1 and 2, respectively, discussed above. These values are arrived at by considering the relationship between G, ν and K.

Difficulties were encountered in the selection of a cap aspect ratio R. Values of 4.0 and 1.5 were suggested for triaxial and plane strain conditions, respectively. This contradiction is a result of simplifications in the model. In this case, the assumption of model symmetry about the hydrostatic axis appears to be main difficulty. While the model behaves in the classical critical state manner, the K_0-consolidated specimens do not (see stress path in Fig. 6.42e). Thus, it is not surprising that difficulties in selecting the aspect ratio R arise. The selection of the aspect ratio of 1.5 for plane strain conditions here and below is one of convenience since it gives results which are acceptable for normally consolidated samples.

The final point to be considered here is the form of the Drucker-Prager surface used. Contrary to the model parameters used, overconsolidated clays do not behave as cohesionless materials. Thus, the use of $k = 0$ above is not correct. The work by McCarron and Chen (1987) was not successful in identifying a single combination of k and α, which would result in accurate strength and deformation predictions for all OCR conditions. This stems from the assumption of perfect plasticity for the Drucker-Prager surface. Thus, it was decided to set $k = 0$, keep α constant, and modify the position of the cap to give the correct shear strength for the overconsolidated states. This is a matter of convenience which is necessitated by simplification in the model.

6.10.4 Analyses of three embankments

This Section presents the analysis techniques and results for three embankments constructed on Boston blue clay. Predictions are compared with actual measured response. The analyses were performed with the finite-element program NFAP (Chang, 1980), which allows for consideration of material and geometric nonlinearities. Large deformations are included through the use of an updated Lagrangian

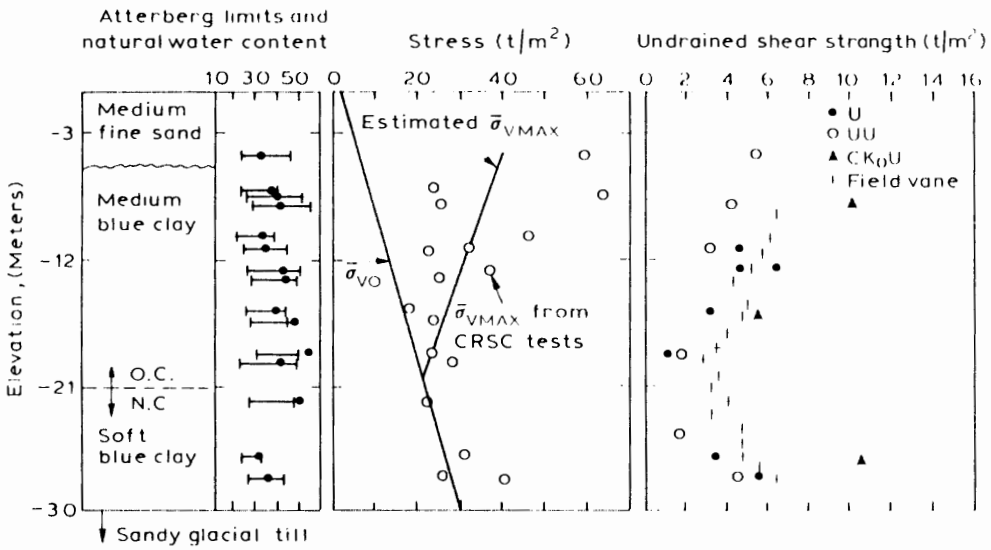

Fig. 6.43. Subsoil conditions for MIT symposium test embankment (MIT, 1975).

formulation (Bathe, 1982). In each of the plane strain analyses, the foundation has been modeled with the eight-node quadrilateral isoparametric elements (see Chapter 9 for more details of finite element).

Figure 6.43 describes the initial subsoil conditions at the location of the MIT Symposium test embankment (MIT, 1975). The information in Fig. 6.44 is typical of the embankments to be considered. In each of the analyses, the initial stress state within the foundation is specified. The horizontal stresses have been determined

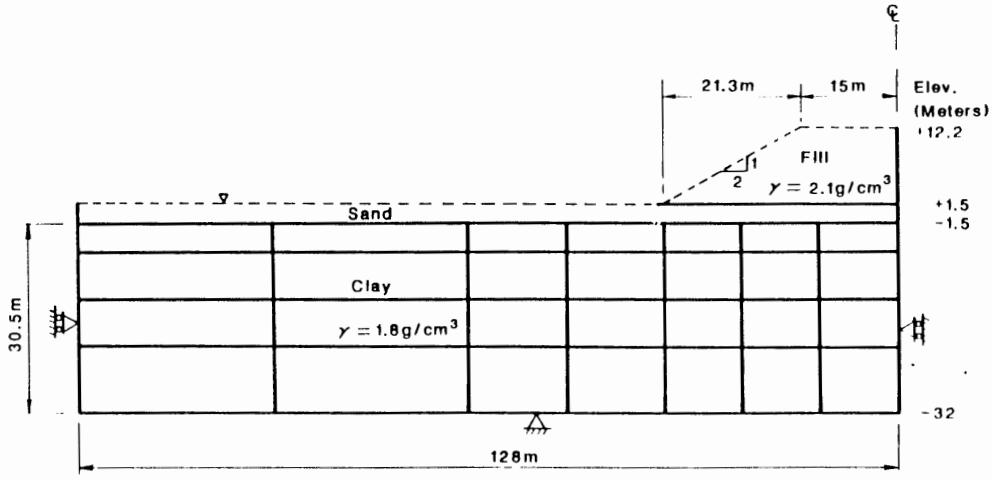

Fig. 6.44. Foundation model for Northeast test embankment.

through the preconsolidation stress information in Fig. 6.43 and the K_o relationship in Fig. 6.41.

The embankment construction is modeled by gravity build-up. The stiffening effect of the embankment and overlaying peat and sand layers are neglected, and only the resultant overburden pressure is included. The following material parameters are used to describe the Drucker-Prager and cap surfaces for the present analyses:

$\alpha = 0.2 \quad k = 0.1$ ksf (0.5 kPa) $\quad R = 1.5$

The circular cross section of the Drucker-Prager model in the deviatoric plane does not allow for an accurate representation of the material response for all load paths. Therefore, in the present analyses, the model has been calibrated for *active pressure conditions*. It is believed the active pressure condition beneath the embankment dominates the response.

(A) Northeast test embankment

General descriptions of the Northeast embankment site, foundation material, construction schedule and measured foundation response are provided by Lambe (1973), and MIT (1969a, b). The Northeast embankment was constructed over an eight-week period beginning in August 1957. The first 25 ft (7.6 m) in fill were placed over the first 5 weeks of construction. Construction was halted for period of approximately 2 weeks before the final 10.8 ft. (3 m) of fill were placed.

Figure 6.44 presents the embankment geometry and finite-element model of the foundation. Symmetry about the centerline is assumed. The gravity load is applied as a surface pressure. For the purpose of finite-element representation, each layer of element is assigned a separate set of material properties. The purpose for this is only to describe: different initial cap positions, different coefficients of lateral earth pressure K_o, and a drained or undrained layer. In order to compensate for errors previously encountered in the predicted strengths of overconsolidated specimens, the initial cap positions were adjusted to give the measured strength ratios shown in Fig. 6.40. The initial cap position (I, Fig. 6.8) and K_o value for each layer are given below:

for layer 1 $\quad I = 8.3$ ksf, $K_o = 1.20$

for layer 2 $\quad I = 8.7$ ksf, $K_o = 0.80$

for layer 3 $\quad I = 7.9$ ksf, $K_o = 0.55$

for layer 4 $\quad I =$ normally consolidated position, $K_o = 0.50$

Although it might be suggested that the cap locations were arbitrarily set to match the strength characteristics of the overconsolidated soils, consistent values are used for the cap locations in each of the embankment analyses below.

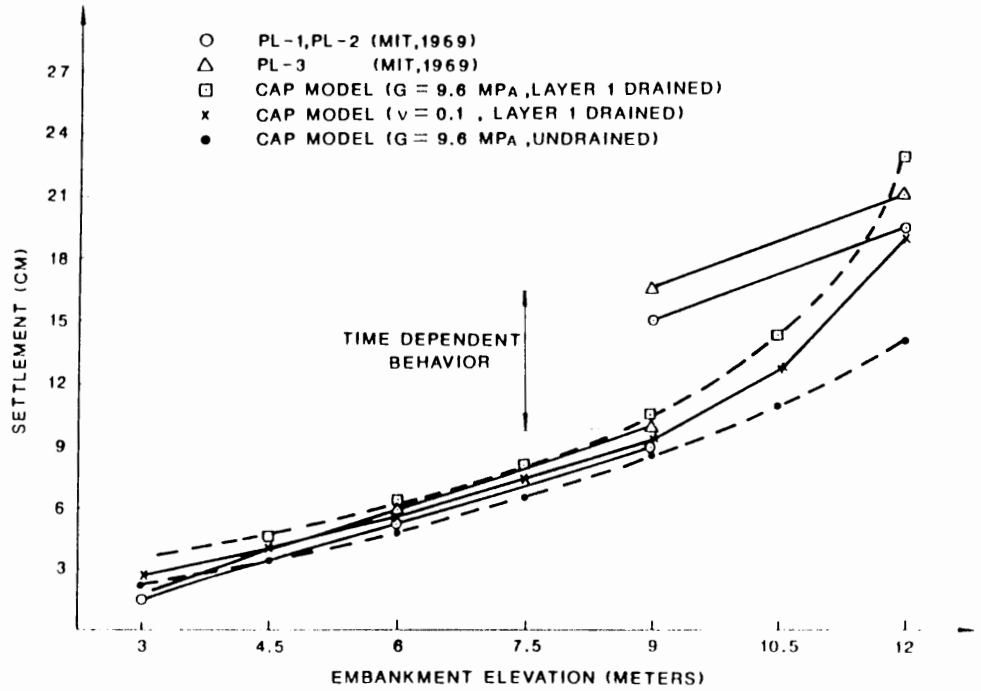

Fig. 6.45. Centerline settlement at Northeast test embankment.

Figure 6.45 compares the predicted centerline displacement with the measured values at three settlement plates along the embankment centerline. The results are presented for the following three analyses:

1. In the first analysis, a constant Poisson's ratio of 0.1 is adopted. The use of a constant Poisson's ratio and stress dependent bulk modulus results in a stress dependent shear modulus.
2. As a second case, a shear modulus of 200 ksf (9.6 MPa) is assumed. Both of these analyses assume the top layer of elements behaves in a drained manner.
3. The third analysis adopts a shear modulus of 200 ksf and assumes an undrained response for the entire foundation.

Good correlation is observed from Fig. 6.45 for all three analyses.

(B) MIT test embankment

The MIT test embankment is the most thoroughly documented out of the three embankments. The reports written at MIT (1969a, b) are especially complete. Various aspects of the embankment behavior have also been reviewed by Lambe (1973) and D'Appolonia et al. (1971). The embankment geometry and finite-element description of the foundation are shown in Fig. 6.46.

Two analyses were performed for the MIT test embankment. In both analyses, the first layer is assumed to be drained. However, again the conditions of a constant

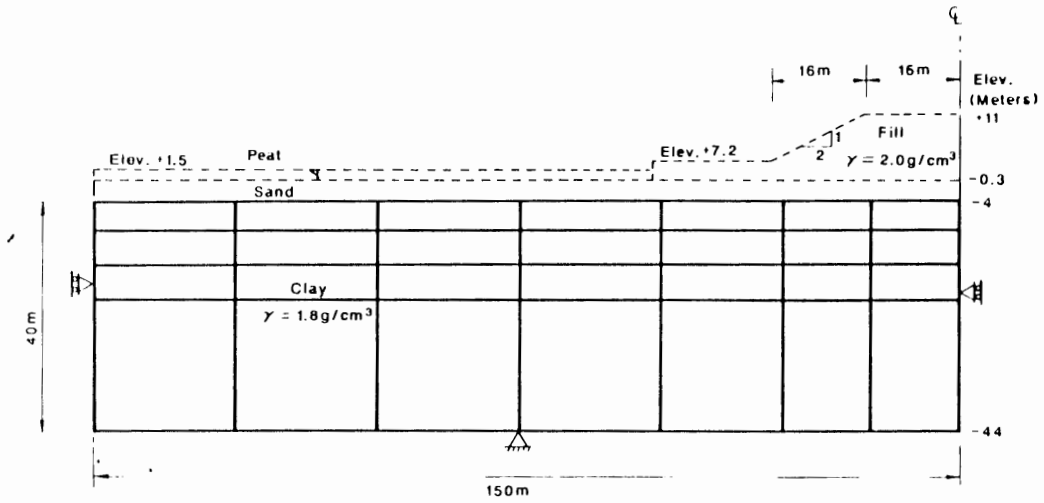

Fig. 6.46 Foundation model for MIT test embankment

Poisson's ratio (0.1) and a constant shear modulus (200 ksf) have been assumed. The initial cap positions and K_o values for the MIT test embankment are given below:

for layer 1 I 8.3 ksf, $K_o = 1.20$

for layer 2 $I = -8.7$ ksf, $K_o = 0.80$

for layer 3 $I = -7.8$ ksf, $K_o = 0.55$

for layer 4 I = normally consolidated position, $K_o = 0.50$

Figures 6.47 through 6.49 compare the predicted and measured deformations and pore pressure within the foundation. Figure 6.47a compares the measured and predicted settlement histories at the embankment centerline for the case $G = 200$ ksf. Figure 6.47b compares the measured response with the predicted quantities for the case of a constant Poisson's ratio. The settlements shown are those which occurred after the initial 9.5 feet (2.9 m) of fill had been deposited. Time scales are also included for the reader's reference.

Examination of Fig. 6.47 reveals that the recorded response of the normally consolidated layer (below Elev. -70 ft, or -21.3 m) is initially stiffer than the predicted range. However, as loading continues, the response falls within this range.

The predicted pore pressures (Fig. 6.48) at the end of construction compare well with the measured values. However, beneath the centerline of the embankment, where the pore pressures are greatest, the predicted values are too high. Figure 6.48 includes measured pore pressure values from both sides of the centerline. The values

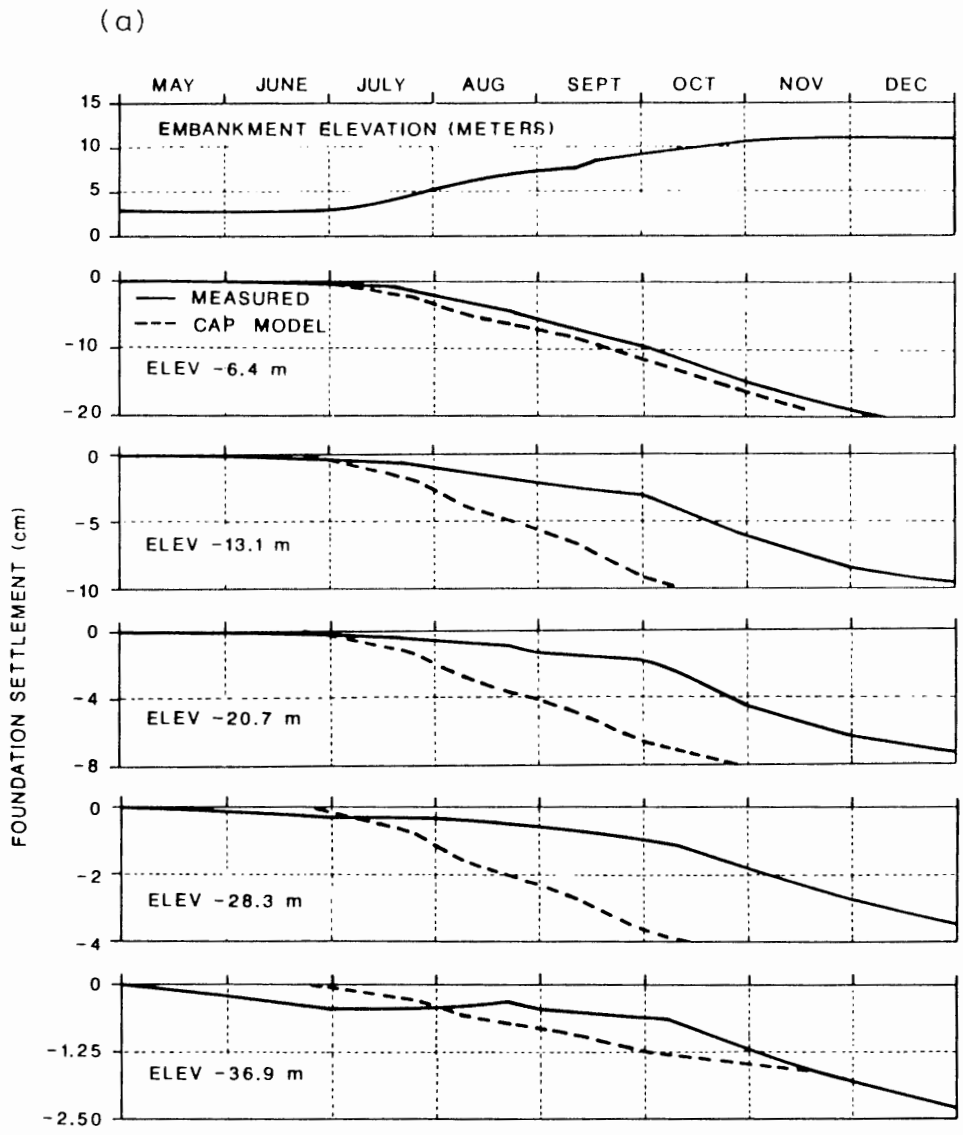

Fig. 6.47. Centerline settlements for MIT test embankment: (a) $G = 200$ ksf; (b) $\nu = 0.1$.

presented in Fig. 6.48 are for the case of $G = 200$ ksf. Values predicted for the second case ($\nu = 0.1$) were generally the same, or a little less.

Figure 6.49 compares the predicted and measured lateral displacements within the foundation at the end of construction. The predicted displacements are for a distance of 170 feet (51.8 m) from the centerline, while the measured values are for

(b)

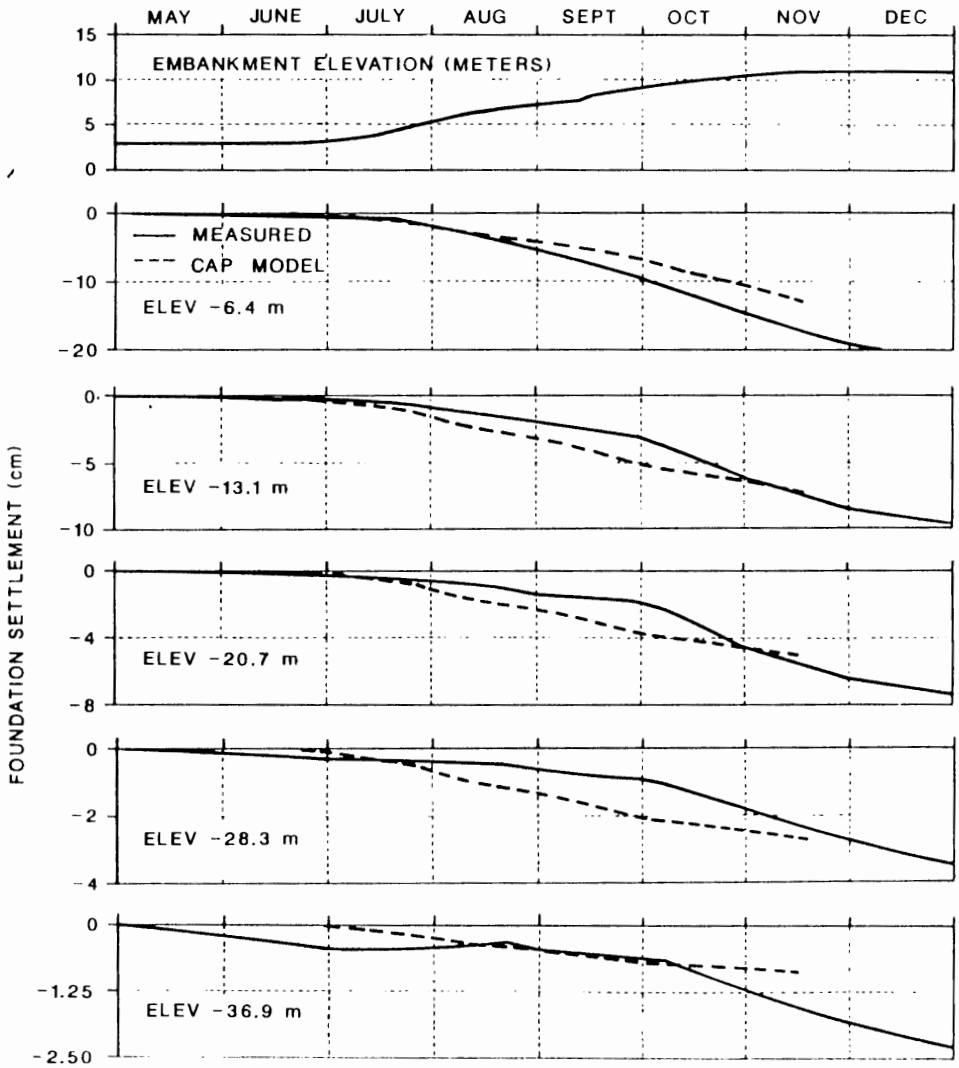

Fig. 6.47 (continued).

160 feet (48.8 m) from the centerline. The two analyses bound the actual measurements.

(C) MIT symposium embankment

The MIT symposium embankment was the subject of the Foundation Prediction

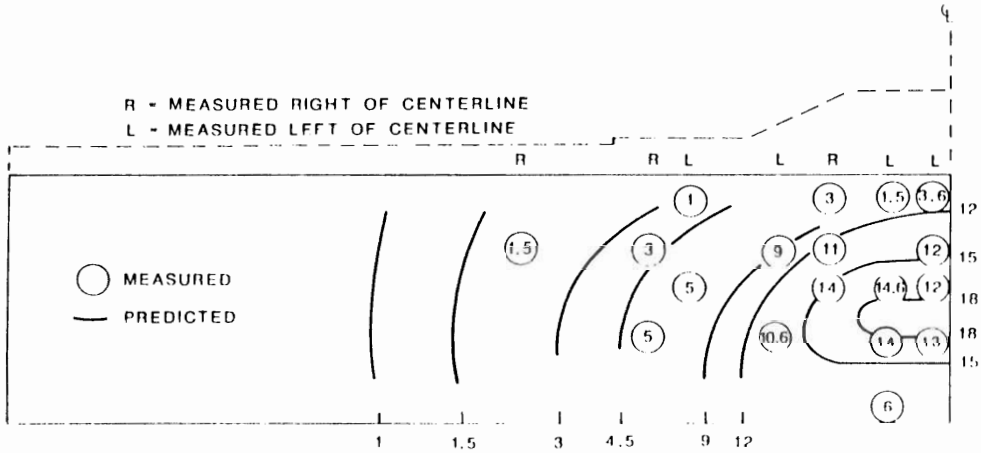

Fig. 6.48. Measured and predicted excess pore pressures (meters of water) at the MIT test embankment

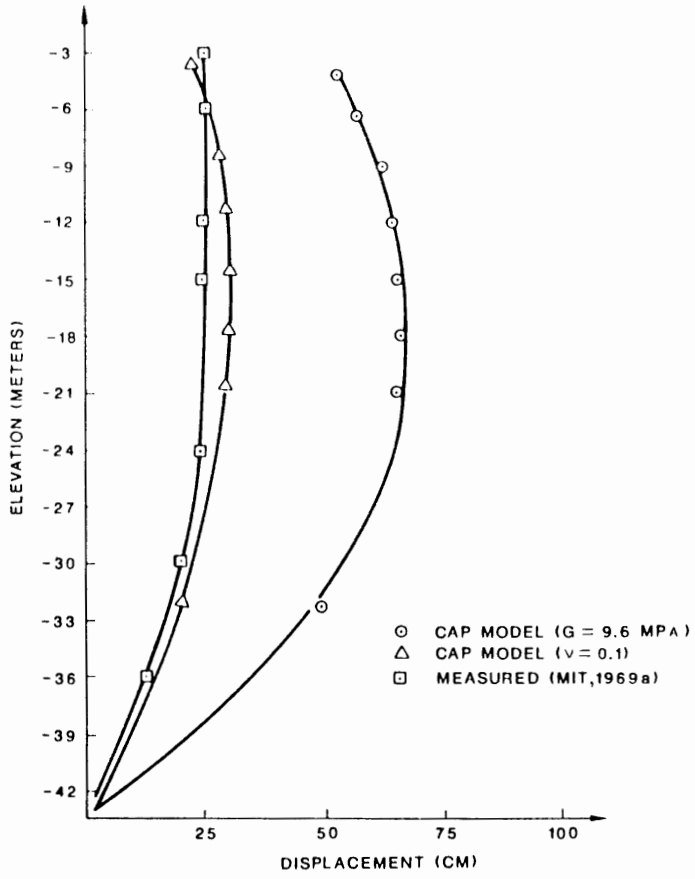

Fig. 6.49. Lateral displacements within the MIT embankment foundation.

Symposium (MIT, 1975). The purpose of the symposium was to examine current design methodology for embankment loads placed on soft foundations by comparing the predicted and measured performance of a full-scale field test.

The test embankment was initially constructed in the period 1967–1969. Following the surface preparation, the original embankment fill was placed in the periods of April to November 1968 and April to May 1969. In 1974, as part of the Foundation Prediction Symposium, construction was resumed and embankment was built to failure. The embankment failed after 18.7 ft (5.7 m) of fill had been added over a period of 25 days in August and September 1974. Several teams from the professional and educational community were challenged to make predictions regarding settlement, pore pressures, and the height of the embankment at failure.

The task of making these predictions was complicated by the time lag from initial construction, and subsurface geometry (Fig. 6.50). Each predictor was requested to make the following predictions:

1. Additional height of fill necessary to cause a stability failure.
2. When 6 feet (1.8 m) of fill had been added:
   (a) Additional horizontal movements of SI-3 and SI-4 at elevation −30 and −70 feet (−9.1 and −21.3 m).
   (b) Additional settlement of SP-1.
   (c) Additional pore pressures at P-3, P-4, and P-6.
3. Pore pressures at P-3, P-4, and P-6 at failure.

The instrument locations and original embankment geometry are shown in Fig. 6.50. The finite-element representation of the foundation is shown in Fig. 6.51.

In the following, results for two analyses are presented; (a) the entire foundation is assumed to be undrained and (b) the top layer is considered to be drained.

The present analyses do not consider the time-dependent deformations occurring during the five years between the initial and final construction sequences. The analyses were performed assuming a constant Poisson's ratio (0.1). The initial cap

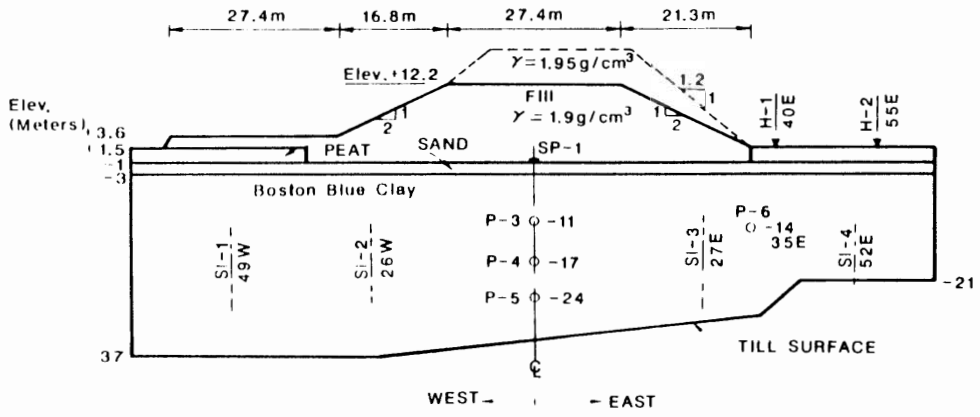

Fig. 6.50. MIT symposium test embankment

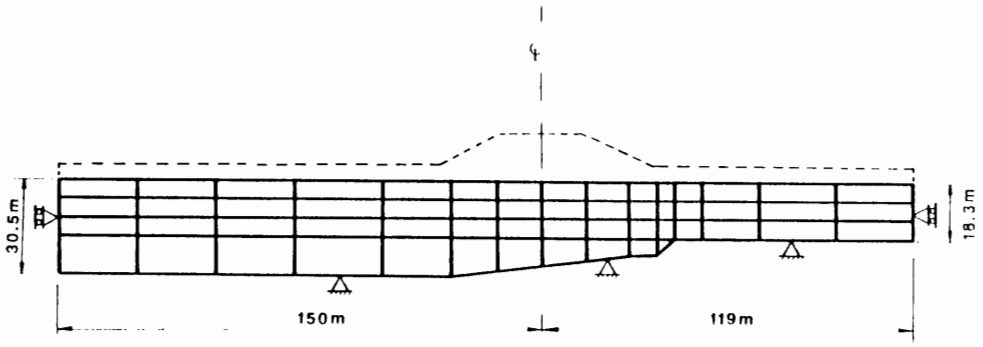

Fig. 6.51 Foundation model for the MIT symposium test embankment.

positions and K_o values for the MIT symposium embankment are given below:

for layer 1 $I = -8.3$ ksf, $K_o = 1.20$

for layer 2 $I = -8.7$ ksf, $K_o = 0.80$

for layer 3 $I = -7.8$ ksf, $K_o = 0.55$

for layer 4 I = normally consolidated position, $K_o = 0.50$

TABLE 6.4

Predicted and measured response of the MIT symposium embankment after six feet of fill added

Item predicted	Measured response	Predicted		Wroth	Symposium Predictors
		Undrained	Drained		
Horizontal movement (inches)	(Range)				(Range)
AT SI-3, ELEV −30	0.5–0.7	0.33	0.31	1.6	0.17 8.6
AT SI-3, ELEV −70	0.3 0.6	0.27	0.23	0.6	0.02 8.6
AT SI-4, ELEV −30	0 0.8	0.21	0.15	0.7	0.25 5.3
AT SI-4, ELEV −70	0	0	0	0	0
Additional settlement of SP-1 (inches)	0.66	0.82	3.7	2.6	0.76 13.7
Additional pore pressure (ft. of water)					
AT P-3	9.4	8.2	10.0	9.0	6.0 26.0
AT P-4	6.4	12.7	13.1	9.6	7.2 – 22.0
AT P-6	5.7	12.0	12.7	5.8	2.5 13.0
Additional heave (inches)					
AT H-1	−0.12	0.10	0.16	0	0 4.8
AT H-2	−0.15	0.07	0.12	0	0 6.2

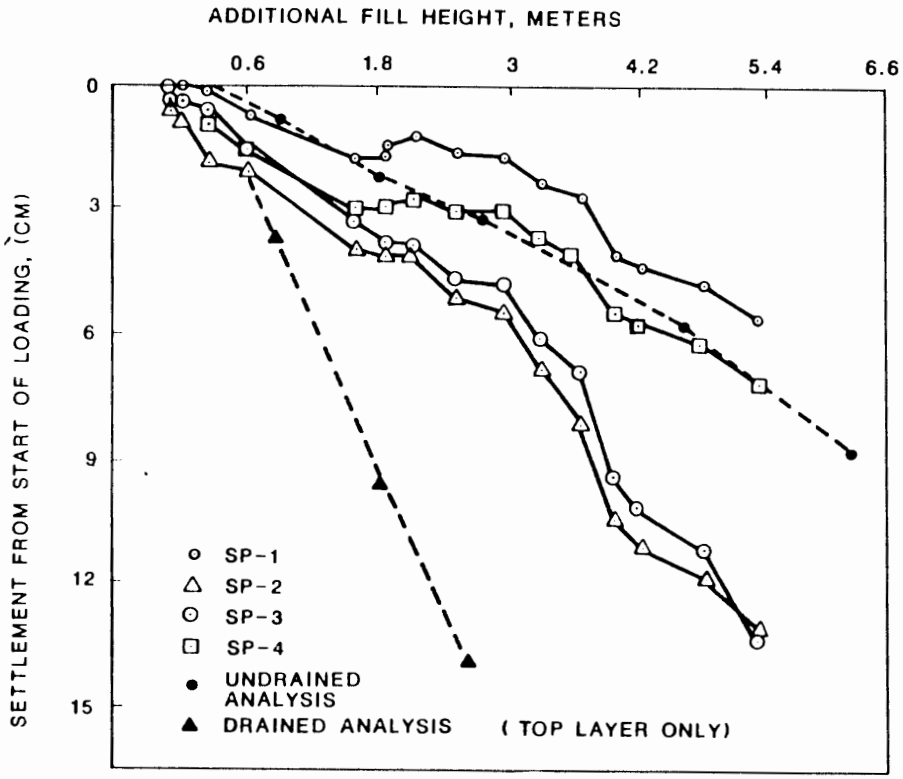

Fig. 6.52. Settlements at the MIT symposium test embankment.

The following sequence of events was followed in each analysis.

1. Application of gravity load for original embankment; $\gamma = 119$ pcf (1910 kg/m^3).
2. Application of gravity load for build-up of east side of embankment; $\gamma = 122$ pcf (1950 kg/m^3).
3. Application of fill load to top of embankment; $\gamma = 122$ pcf, (1950 kg/m^3).

Table 6.4 compares the predicted and measured data after six feet of fill had been added to the embankment. Figure 6.52 compares the predicted centerline settlements for the two analyses with the measured response at SP-1. The locations of settlement plates 2, 3, and 4 are not known. Lateral deformations at inclinometers SI-3 and SI-4 are compared in Fig. 6.53. The measurements presented are those occurring after the initial embankment construction. The analysis considering the top layer as undrained provides the most representative settlement history. Two inclinometer readings, separated by three days, were made after six feet of fill were added. The predicted values compare favorably with these measurements. Both analyses overpredict pore pressures beneath the embankment (see Table 6.4).

Table 6.4 also contains the predictions of Wroth (MIT, 1975; Wroth, 1977), one of the symposium predictors, as well as the range of values submitted by the

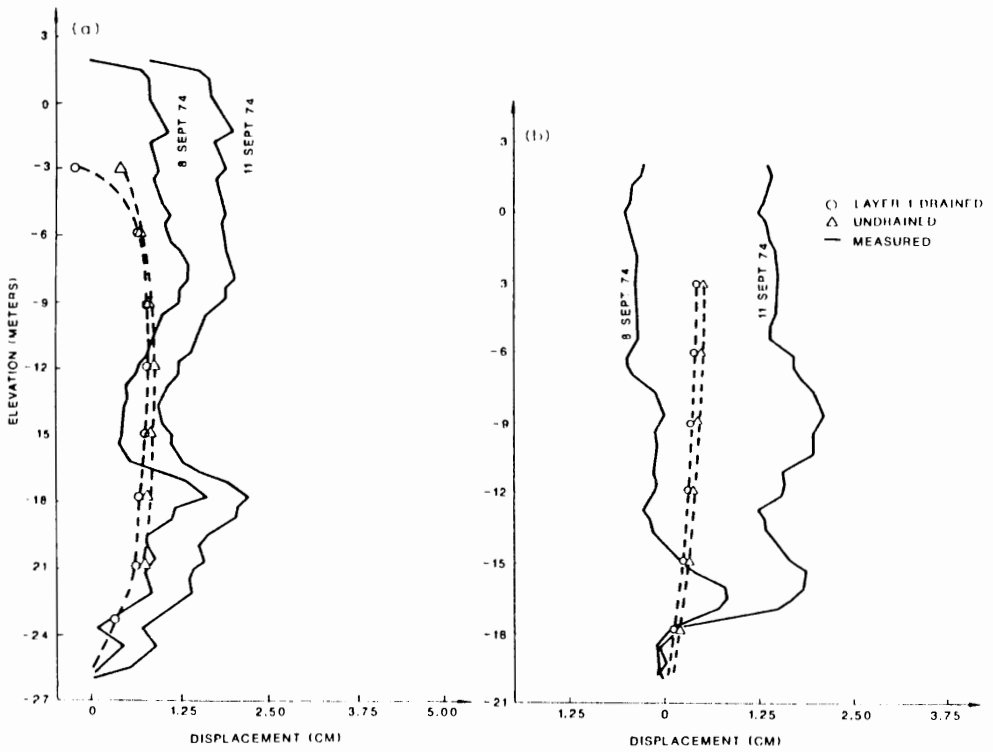

Fig. 6.53. Lateral displacements within the foundation for the MIT symposium test embankment: (a) SI-3; (b) SI-4.

predictors at the Symposium. Wroth used the modified Cam-clay model (Roscoe and Burland, 1968), a critical-state formulation, in his calculations. Wroth's predictions compare well with the actual values, and as a whole were probably the most accurate submitted to the symposium.

While it is not possible to review the methods and results of each of the symposium predictors, it should be noted that Wroth's predictions, and the present analyses, closely match the measured response. This success provides further validity of the Cap and Critical state models.

In each of the analyses, the embankment loading was carried well beyond the fill height which actually caused collapse. Figure 6.54 shows the predicted load-displacement relationship for the undrained case at a point 22.5 feet (6.9 m) east of the embankment centerline. The peculiar rebound shown is due to the second increment of load as described above. The recorded displacements at the centerline (Fig. 6.52) indicate a similar behavior, but much later in the construction sequence. The magnitude of the load reported represents the sum of the embankment surcharge applied to the foundation. While a foundation failure was not predicted, the tendency towards a limit condition is seen. A review of the Proceedings of the MIT

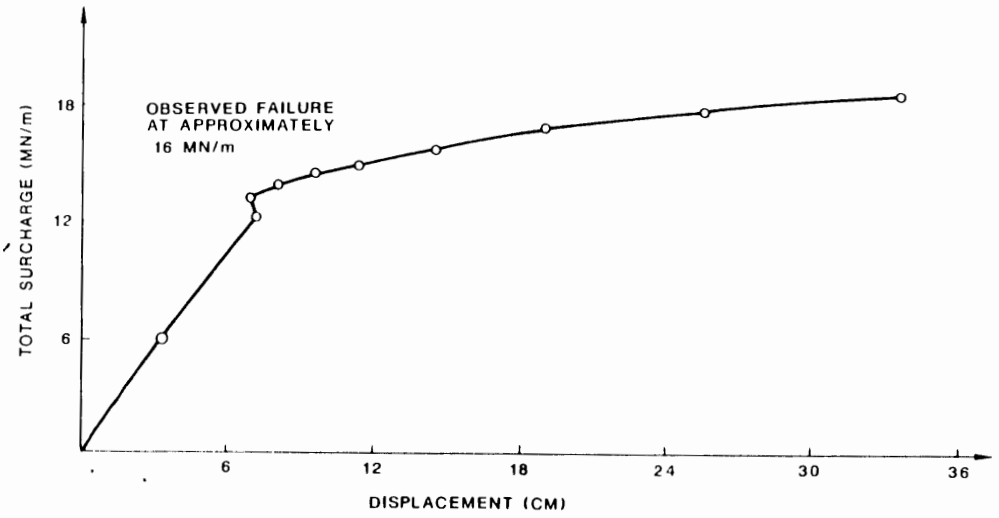

Fig. 6.54. Predicted settlement history 22.5 feet east of the MIT symposium embankment centerline (undrained analysis).

Symposium indicates the embankment failure occurred after a surcharge of approximately 1100 kips per foot embankment length (16 MN/m) had been applied. The final loading for the cap model analysis represents a surcharge of 1233 kips per foot length (18 MN/m).

The analysis results indicate that the overestimation of the foundation strength is partially attributed to material hardening in the overconsolidated layers. This could be overcome by selecting different parameters for the Drucker-Prager surface, or by using a yield surface with a shape different from the Drucker-Prager criterion. Some forms of the critical-state models could be expected to provide more realistic predictions of the overconsolidated material behavior. The selection of an associated flow rule, circular description of strength criterion in the deviatoric plane, and the neglect of material softening also influence the strength prediction.

6.10.5 Concluding remarks

The following conclusions can be made from the present analyses:

1. The model accurately predicts the strength and deformation characteristics of normally consolidated Boston blue clay in undrained triaxial compression and undrained active pressure plane strain conditions. The method tends to overpredict the magnitude of excess pore pressures. Results indicate a single configuration of the Drucker-Prager surface does not adequately describe the strength and deformation characteristics of both normally consolidated and overconsolidated clays.

2. The analysis of three embankments constructed on Boston blue clay indicates that the model accurately predicts deformations within the foundation. However, the excess pore pressures tend to be overestimated.

6.11 SUMMARY

The well-known Coulomb failure criterion is an irregular hexagonal pyramid in a three-dimensional principal stress space. Its singularities along the edges of this criterion are difficult to handle in a numerical stress analysis. Thus, the Drucker-Prager criterion is used instead to approximate smoothly this well-known failure condition. These earlier models of perfect plasticity, however, can not predict the compaction prior to the failure of soils. To this end, the cap type of hardening surfaces is introduced to the criterion. This concept marks the beginning of the modern developments of a consistent theory of *soil plasticity*.

The Cam-clay model, for normally consolidated and lightly overconsolidated clays, was developed at Cambridge University to predict the response of remoulded specimens subjected to drained or undrained triaxial compression tests. Since their development, the Cam-clay models have been extended to general three-dimensional analyses with some success. The formulation does not allow for an adequate treatment of the strain-softening behavior of heavily overconsolidated clays.

On the other hand, the Cap model is generally applicable to a wide range of geological materials and may be used to handle complicated situations such as nonlinear loading and unloading, stress path-dependency, and dilatancy. In the overconsolidated condition, the behavior is controlled by a perfectly plastic failure surface. Soils which are normally consolidated to lightly overconsolidated, however, behave like a work-hardening solid. The basic form of the cap model satisfies the Drucker's stability postulate and leads to a unique solution for a boundary value problem.

Both the Cam-clay and Cap models suffer from the disadvantage that their respective yield surfaces are generated about the hydrostatic axis. Experimental evidence for natural soils suggests that these surfaces in fact revolve about an axis which is defined by the K_o-consolidation condition.

Since the development of strain-hardening cap models that take the soil density or void ratio as the hardening parameter, several modified versions of hardening plasticity models have been proposed. Prévost and Höeg (1975) suggested a *double-hardening model* consisting of a shear loading surface controlled by the plastic shear strain and a volumetric loading surface controlled by the plastic volumetric strain. A similar double hardening elastic-plastic model was established by Vermeer (1978) for the initial loading, unloading and reloading of sand. Further, the modified Cam-clay model was extended by Van Eekelen and Potts (1978) for Drammen clay under cyclic loading. In this model development, the pre-failure behavior of clay is governed by a shear loading surface and the cap type of volumetric loading surface, while, at failure, the clay is governed by the Coulomb criterion.

As for cap models involving more complicated load histories, Sandler (1979) developed a kinematic hardening model for application to cyclic loading conditions. Baladi and Rohani (1979) presented a model which included both the strain-softening and pore-pressure generation capabilities. Further, Baladi and Sandler (1981) developed a model for use with materials which display transversely isotopic strength and deformation properties.

Current literatures and state-of-the-art papers on soil plasticity models and their applications can be found in the two earlier symposia (Parry, 1972; Palmer, 1973), as well as in the two recent ASCE workshop and symposium proceedings (Pande and Zienkiewicz, 1980; Yong and Ko, 1981; Yong and Selig, 1982). An up-to-date, summary is given in the book "Soil Plasticity: Theory and Implementation" by Chen and Baladi (1985) and the Proceedings of the 1st and 2nd international conferences on "Constitutive Laws for Engineering Materials" edited by Desai and Gallagher (1985), and Desai et al. (1987).

For a direct application of the cap hardening plasticity models, the stress-strain relations can be written in the general form:

$$d\sigma_{ij} = C^{ep}_{ijkl}\, d\epsilon_{kl} = \left(C_{ijkl} - \frac{1}{H} H_{ij} H_{kl}\right) d\epsilon_{kl}$$

where C^{ep}_{ijkl} is the elastic-plastic constituent tensor whose components are symmetrical since the cap hardening models are developed on the basis of the associated flow rule assumption.

To determine the material constants, the following fitting procedures with simple tests are suggested:

1. Use the unloading portions of the stress-strain data to determine all elastic material constants.
2. Establish the failure function from the usual triaxial compression or extension tests and proportional loading tests.
3. Determine the cap hardening function by a trial-and-error procedure.

As a demonstration of eligibility of the Cap model, it was calibrated in details against the simple shear and triaxial tests and then was applied to predict the behavior of Boston blue clay under embankment.

REFERENCES

Agarwal, B.D. and Broutman, L.J., 1980. Analysis and Performance of Fiber Composites. Wiley-Interscience, New York, NY..

Anandarajah, A., Dafalias, Y.F. and Herrmann, L.R., 1984. A bounding surface plasticity model for anisotropic clays. Proc. 5th Eng. Mech. Div. Spec. Conf., ASCE, Laramie, Wyoming, Vol. 2, pp. 937–940.

Atkinson, J.H. and Bransby, P.L., 1978. The Mechanics of Soils – An Introduction to Critical State Soil Mechanics. McGraw-Hill, New York, NY, 375 pp.

Baladi, G.Y., 1979. Lecture notes on the cap-type constitutive model. Lecture on Constitutive Equations given at Purdue University, Nov., 1979, pp. 22–29.

Baladi, G.Y. and Rohani, B., 1979a. Elastic-plastic model for saturated sand. J. Geotech. Eng. Div. ASCE, 105 (GT4): 465–480.

Baladi, G.Y. and Rohani, B., 1979b. An elastic-plastic constitutive model for saturated sands subjected to monotonic and/or cyclic loading. Third Int. Conf. Numer. Methods in Geomech. Aachen, West Germany, Vol. 1, pp. 389–404.

Baladi, G.Y. and Sandler, I.S., 1981. Examples of the use of the cap model for simulating the stress-strain behavior of soils. In: R.N. Yong and H-Y. Ko (Editors), Limit Equilibrium, Plasticity and Generalized Stress-Strain in Geotechnical Engineering. ASCE, 1981, New York, NY, pp. 649–710.

Bathe, K.J., 1982. Finite Element Procedures in Engineering Analysis. Prentice-Hall, Englewood Cliffs, NJ, 735 pp.

Bathe, K.J., Snyder, M.D., Cimento, A.P. and Rolph, W.D., 1980. On some current procedures and difficulties in finite element analysis of elastic-plastic response. Comput. Struct. 12: 607–624.

Bazánt, Z.P. (Editor), 1985. IUTAM William Prager Symposium on Mechanics of Geomaterials: Rocks, Concrete, Soils. John-Wiley, London, U.K.

Bovee, R. and Ladd, C.C., 1970. MIT plane strain device, Res. Earth Phys. Phase Rep. No. 12, Dep. Civ. Eng. Res. Rep., R70-24, MIT, Cambridge, MA.

Burland, J.B., 1965. The yielding and dilation of clay. Correspondence, Geotechnique, 15(2): 211–214.

Chang, T.Y., 1980. A Nonlinear Finite Element Analysis Program, NFAP, Vols. 1 and 2. University of Akron, Akron, OH.

Chen, W.F., 1980. Plasticity in soil mechanics and landslides. J. Eng. Mech. Div., ASCE, 106 (EM3): 443–464.

Chen, W.F., 1982. Plasticity in Reinforced Concrete. McGraw-Hill, New York, NY, 1982, 474 pp.

Chen, W.F., 1985. In: Z.P. Bazánt (Editor), Mechanics of Geomaterials. Chapter 5-Constitutive Relations for Concrete, Rock and Soils: Discusser's Report, John Wiley, U.K., pp. 65–86.

Chen, W.F. and Baladi, G.Y., 1985. Soil Plasticity: Theory and Implementation. Elsevier, Amsterdam, The Netherlands, 231 pp.

Chen, W.F. and McCarron, W.O., 1986. Modeling of soils and rocks based on concepts of plasticity. In: A.S. Balasubramanian, S. Chandra and D.T. Bergado (Editors), AIT Symposium and Course of Laboratory & Field Tests and Analysis of Geotechnical Problems. A.A. Balkema, Rotterdam, Netherlands, pp. 467–510.

Chen, W.F. and Saleeb, A.F., 1982. Constitutive Equations for Engineering Materials, Vol. 1: Elasticity and Modeling. John Wiley Interscience, New York, NY, 580 pp.

Chen, W.F., 1991. Constitutive Equations for Engineering Materials, Vol. 2: Plasticity and Modelling. Elsevier, Amsterdam, in press.

Crooks, J.H.A., 1981. A qualitative stress-strain (time) model for soft clays. In: R.N. Yong and F.C. Townsend (Editors), Laboratory Shear Strength of Soil. ASTM, STP 740, pp. 685–699.

D'Appolonia, D.J., Lambe, T.W. and Poulos, H.G., 1971. Evaluation of pore pressure beneath an embankment. J. Soil Mech. Found. Div., ASCE, 97 (SM6): 881–897.

Desai, C.S. and Gallagher, R.H. (Editors), 1985. Proceeding of the 1st International Conference on Constitutive Laws for Engineering Materials: Theory and Application. Tucson, 604 pp.

Desai, C.S. and Siriwardane, H.J., 1984. Constitutive Laws for Engineering Materials. Prentice-Hall, Englewood Cliffs, NJ.

Desai, C.S., Phan, H.V. and Perumpral, J.V., 1982. Mechanics of three-dimensional soil-structure interaction. J. Eng. Mech. Div., ASCE, 108 (EM5): 731–747.

Desai, C.S., Krempl, E., Kiousis, P.D. and Kundu, T. (Editors), 1987. Proceeding of the 2nd International Conference on Constitutive Laws for Engineering Materials, Tucson, Elsevier, New York, 1491 pp., two-volume.

DiMaggio, F.L. and Sandler, I.S., 1971. Material models for granular soils. J. Eng. Mech. Div./ASCE, 97 (EM3): 935–950.

Drucker, D.C., Gibson, R.E., and Henkel, D.J., 1957. Soil mechanics and work-hardening theories of plasticity. Trans. ASCE, 122: 338–346.

Gudehus, G., 1985. Requirements of constitutive relations for soils. In: Z.P. Bazánt (Editor), IUTAM William Prager Symposium Volume on Mechanics of Geomaterials: Rocks, Concrete, Soils. John Wiley, London, U.K.

Ladd, C.C., 1964. Stress-strain modulus of clay in undrained shear. J. Soil Mech. Found. Div., ASCE, 90 (SM5): 103–132.

Ladd, C.C., Bovee, R.J., Edgards, L. and Rixner, J.J., 1971. Consolidated-undrained plane strain shear test on Boston blue clay. Res. Earth Phys., Phase Report No. 15; U.S. Army Engineer Waterways Experimental Station, Contract Rep. No. 3-101.

Lambe, T.W., 1973. Predictions in soil engineering. Geotechnique, 23 (2): 149–202.

Leroueil, S., Tavenas, F., Trak, B., La Rochelle, P. and Roy, M., 1978. Construction pore pressures in clay foundations under embankments, Part 1: The Saint-Alban test fills. Can. Geotech. J., 15: 54–82.

Leroueil, S., Tavenas, F., Brucy, F., La Rochelle, P. and Roy, M., 1979. Behavior of destructured natural clays. J. Geotech. Eng. Div., ASCE, 105 (GT6): 759–778.

McCarron, W.O. and Chen, W.F., 1987. A capped plasticity model applied to Boston blue clay. Can. Geotech. J., 24(4): 630–644.

MIT, 1969a. Performance of an Embankment on Clay, Interstate-95. Dep. Civ. Eng. R69-67, MIT, Cambridge, MA.

MIT, 1969b. Soil Instrumentation for Interstate 95 Embankment, Saugus, MA. Dep. Civ. Eng., R69-10. MIT, Cambridge, MA.

MIT, 1975. Proceedings of the Foundation Deformation Prediction Symposium, Vol. 1, 2. Dep. Civ. Eng., R75-32, MIT, Cambridge, MA.

Mizuno, E. and Chen, W.F., 1986. Plasticity modeling and its application to geomechanics. In: A.S. Balasubramanian, S. Chandra and D.T. Bergado (Editors), AIT Symposium and Course on Laboratory & Field Tests and Analysis of Geotechnical Problems. A.A. Balkema, Rotterdam, Netherlands, pp. 391–426.

Naylor, D.J., Pande, G.N., Simpson, B. and Tabb, R., 1981. Finite Elements in Geotechnical Engineering. Pineridge Press, Swansea.

Nelson, I., 1978. Constitutive models for use in numerical computations. Proceedings of the International Symposium on Dynamic Methods in Soil and Rock Mechanics, Vol. 2, Balkema, Rotterdam, pp. 45–97.

Nelson, I. and Baladi, G.Y., 1977. Outrunning ground shock computed with different models. J. Eng. Mech. Div. ASCE, 103 (EM3): 377–393.

Nelson, I., Baron, M.L. and Sandler, I.S., 1971. Mathematical models for geological materials for wave propagation studies. In: Shock Waves and the Mechanical Properties of Solids. Syracuse University Press, Syracuse, NY, pp. 289–351.

Palmer, A.C. (Editor), 1973. Proceedings of the Symposium on the Role of Plasticity in Soil Mechanics. Cambridge University, Cambridge, England, 314 pp.

Pande, G.N. and Zienkiewicz, O.C. (Editors), 1980. Proceedings of the International Symposium on Soils under Cyclic and Transient Loading. Balkema, Rotterdam.

Parry, R.H.G., 1958. Correspondence on "On the Yielding of Soils". Geotechnique, 8: 185–186.

Parry, R.H.G. (Editor), 1972. Roscoe Memorial Symposium: Stress-Strain Behavior of Soils. Henley-on-Thames, Cambridge University, England, 752 pp.

Prévost, J.H. and Höeg, K., 1975. Effective stress-strain-strength model for soils. J. Geotech. Eng. Div., ASCE, 101 (GT3): 259–278.

Roscoe, K.H. and Burland, J.B., 1968. On the generalized stress-strain behavior of 'wet' clay. In: J. Heyman and F.A. Leckie (Editors), Engineering Plasticity. Cambridge University Press, Cambridge, England, pp. 535–609.

Roscoe, K.H., Schofield, A.N. and Worth, C.P., 1958. On the yielding of soils. Geotechnique, 8 (1): 22–53.

Roscoe, K.H., Schofield, A.N. and Thurairajah, A., 1963. Yielding of clays in state wetter than critical. Geotechnique, 13(3): 211–240.

Sandler, I.S., 1979. Capped plasticity models for cyclic behavior of soils. Proc. Third Engineering Mechanics Division Specialty Conference, ASCE, New York, NY, pp. 619–625.

Sandler, I.S. and Baron, M.L., 1976. Material models of geological materials in ground shock. Numerical Methods in Geomechanics, ASCE, New York, NY, pp. 219–231.

Sandler, I.S. and Baron, M.L., 1979. Recent development in the constitutive modeling of geological materials, Proc. 3rd International Conference on Numerical Methods in Geomechanics, Aachen, Germany, Vol. 1, pp. 363–376.

Sandler, I.S., DiMaggio, F.L. and Baladi, G.Y., 1976. Generalized cap model for geological materials. J. Geotech. Eng. Div., ASCE, 102 (GT7): 683–699.

Schofield, A.N. and Wroth, C.P., 1968. Critical State Soil Mechanics. McGraw-Hill, New York, NY, 310 pp.

Tavenas, F. and Leroueil, S., 1977. Effects of stresses and time on yielding of clays. Proc. 9th, Int. Conf. Soil Mechanics and Foundations Engineering, Vol. 1, pp. 319–326.

Tavenas, F. and Leroueil, S., 1980. The behavior of embankments on clay foundations. Can. Geotech. J., 17: 236–260.

Tavenas, F., Blanchet, R., Garneau, R. and Leroueil, S., 1978. The stability of stage-constructed embankments on soft clays. Can. Geotech. J., 15: 283–305.

Terzaghi, K., 1943. Theoretical Soil Mechanics. John Wiley and Sons, New York, NY, 510 pp.

Townsend, F.C. and Mulilis, J.P., 1978. Liquefaction potential of sands under static and cyclic loading. Research Report S-76-2, Report 6, U.S. Army Engineer Waterways Experiment Station, CE, Vicksburg, MS.

Van Eekelen, H.A.M. and Potts, D.M., 1978. The behavior of Drammen clay under cyclic loading. Geotechnique, 28 (2): 173–196.

Vermeer, P.A., 1978. A double hardening model for sand. Geotechnique, 28 (4): 413–433.

Wroth, C.P., 1977. The predicted performance of soft clay under a trial embankment loading based on the Cam-clay model. In: F. Gudehus (Editor), Finite Elements in Geomechanics. John-Wiley, New York, NY, pp. 191–208.

Yong, R.N. and Ko, H-Y. (Editors), 1981. Limit Equilibrium, Plasticity and Generalized Stress-Strain in Geotechnical Engineering. ASCE, New York, NY, 871 pp.

Yong, R.N. and Selig, E.T. (Editors), 1982. Application of Plasticity and Generalized Stress-Strain in Geotechnical Engineering. ASCE, New York, NY, 356 pp.

Chapter 7

CAP MODEL IMPLEMENTATION AND PREDICTIONS

7.1 INTRODUCTION

The elastic-plastic stress-strain relations derived in the preceding Chapters 4 through 6 are combined with the *equations of equilibrium* and the *equations of compatibility* to form a set of basic differential equations that can be used to determine the state of stress or strain for a given boundary value problem. However, in the plastic or nonlinear range, these governing differential equations are highly *nonlinear* and often intractable, only in rare instances, will it be feasible to obtain the *exact* solution by the use of formal mathematics. Almost always, recourse must be made to approximate the answer on the basis of such simple methods as the *limit analysis* for a direct load-carrying capacity determination or the numerical method such as the *finite element* for a step-by-step progressive failure analysis.

The *finite-element method* is a computer-based solution technique that discretizes the *whole* region to be analyzed into many small subregions or finite elements which are interconnected only at a discrete number of nodal points situated on their boundaries, as shown in Fig. 7.1. Unlike the *finite-difference method* which gives a *pointwise* approximation (solution of region as an array of grid points) to the governing equation, the finite-element method plays an important role on evaluating the *piecewise* approximation in the nonlinear analysis of engineering in general, and

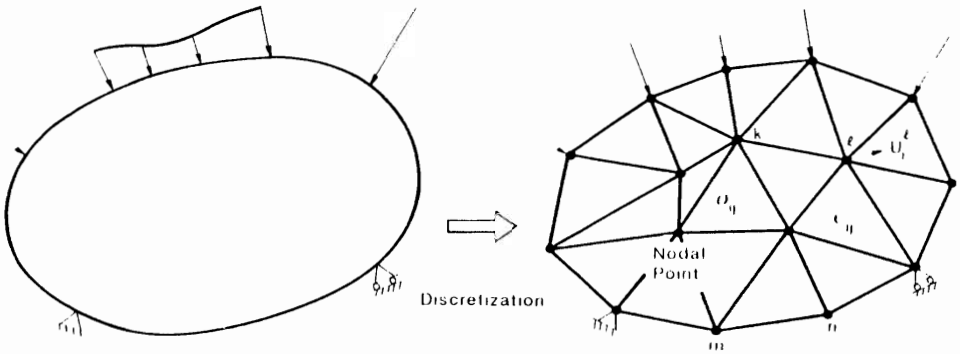

Fig. 7.1. Finite-element discretization.

structural and geotechnical engineering in particular, when their closed form solutions are difficult to be found.

Such discretization by the finite-element method can reduce the problems of continuous body with infinite number of unknowns to the problems of discretized body with finite number of unknowns corresponding to the *nodes* or the *nodal points*, although in fact, the infinite number of unknown values of the field variables ϕ such as displacements u_i, stresses σ_{ij}, or other quantities exist corresponding to any generic point inside a continuous body.

By utilizing the equations of compatibility and the constitutive equations, the finite-element procedure transforms in general the nonlinear equations of equilibrium for the elastic-plastic problems to the *incremental form of linearized finite-element equations*. The simplified incremental form is described as:

$$[K]\{dU\} = \{dR\} \tag{7.1}$$

where the matrix $[K]$ is a *total stiffness matrix* of the structure, which relates a vector $\{dR\} = [dR_1, dR_2, \ldots, dR_n]^T$ of the n total load increments to a vector $\{dU\} = [dU_1, dU_2, \ldots, dU_n]^T$ of the nodal displacement increments for the complete structure. These basic finite-element equations can be solved by any standard solution techniques.

Once the nodal displacement increments $\{dU\}$ are obtained for the total load increments $\{dR\}$ from Eq. (7.1), the strain increments $\{d\epsilon\} = [d\epsilon_{11}, d\epsilon_{22}, d\epsilon_{33}, d\gamma_{12}, d\gamma_{23}, d\gamma_{31}]^T$ and stress increments $\{d\sigma\} = [d\sigma_{11}, d\sigma_{22}, d\sigma_{33}, d\sigma_{12}, d\sigma_{23}, d\sigma_{31}]^T$ at any point inside a continuous body can be found from the kinematic relations and the constitutive relations, respectively.

Unlike the linear elastic problem, the applications of the finite-element method for a nonlinear analysis in geotechnical engineering require particular numerical techniques, in order to meet satisfactorily the basic three requirements of the kinematic condition, the constitutive relation and the equilibrium condition.

The kinematic equations and the equilibrium equations will be presented in some details together with the fundamentals of the *geometric nonlinearity* in Chapter 8, followed by a discussion in Chapter 9 of the finite-element implementation and of the general finite-element solution techniques for a nonlinear stress analysis problem involving both material and geometric nonlinearities.

As the first implementation for one of three basic equations for a continuous body, in this Chapter, we shall discuss the details of a numerical finite-element implementation procedure for the *stress-strain relation*, to find the stress increment vector $\{d\sigma\}$ corresponding to a given strain increment vector $\{d\epsilon\}$, for the perfect plastic material models such as the Drucker-Prager model and the Coulomb model, and for the strain-hardening cap model applied to the *material nonlinear analysis only*, under the assumption of the *small deformation*. Further, the implementation procedures for these models are codified in the form of *subroutines* that can be used directly in an existing finite-element program.

The numerical treatment of stress-strain relation (constitutive law) for the *large deformation analysis* will be discussed in the next Chapter 8.

7.2 GENERAL IMPLEMENTATION OF ELASTIC-PLASTIC MODELS

In this Section, we shall present a general numerical procedure for incorporating the *isotropic* elastic-plastic constitutive models into computer programs (Chen, 1982). The input quantities in the present discussion are the stress components $\{\sigma\}^n$, the hardening parameters $x^n(\epsilon_{ij}^p)$, and $k^n(\epsilon_p)$ obtained at the end of the n-th loading increment, and the components of the new strain increments $\{d\epsilon\}^{n+1}$, which are obtained from the solution for the nodal displacement increments $\{dU\}^{n+1}$ at the $(n+1)$-th load increment $\{dR\}^{n+1}$ acting on the structure:

$$\{dU\}^{n+1} = [K]_n^{-1}\{dR\}^{n+1} \tag{7.2}$$

where the values of total nodal displacements $\{U\}^n$ and tangent stiffness $[K]_n$ at the end of the n-th loading increment are known. The output quantities required are the new values of the stress components:

$$\{\sigma\}^{n+1} = \{\sigma\}^n + \{d\sigma\}^{n+1} \tag{7.3}$$

A general outline of the total computational procedure to achieve Eq. (7.3) is explained below.

7.2.1 *Elastic stress increment*

In the first step of the numerical algorithm, a set of elastic trial stresses $\{\sigma^e\}$ is computed by:

$$\{\sigma^e\} = \{\sigma\}^n + \{d\sigma^e\} = \{\sigma\}^n + [C^e]\{d\epsilon\}^{n+1} \tag{7.4}$$

where $\{d\sigma^e\}$ is a vector of elastic stress increments and $[C^e]$ is the elastic constituent matrix. These trial stresses are then tested with respect to the loading surface for the isotropic hardening material (see Chapter 5), that is:

$$f\left[\{\sigma\}, x(\epsilon_{ij}^p), k(\epsilon_p)\right] = 0 \tag{7.5}$$

If the trial stresses do not violate the loading condition, i.e., $f < 0$, the behavior of the material is truly elastic, then hardening parameters $x^n(\epsilon_{ij}^p)$ and $k^n(\epsilon_p)$ remain unchanged, and the final stresses at the end of the $(n+1)$-th loading increment are simply set to:

$$\{\sigma\}^{n+1} = \{\sigma^e\} \tag{7.6}$$

Note that the elastic moduli at the end of the n-th loading increment are assumed to be constant during the $(n+1)$-th loading increment. The effect of this assumption on the accuracy of the computations is negligible if the given strain increments

$\{d\epsilon\}^{n+1}$ are relatively small. For relatively large strain increments, on the other hand, accuracy will suffer accordingly for a nonlinear elastic material. This problem can be overcome, however, by splitting the given strain increment into several equal increments and sequentially going through the numerical algorithm several times, using updated values for elastic moduli each time.

7.2.2 *Scaling factor*

If the loading surface is violated by the elastic trial stresses, $f > 0$, the element is under a plastic loading. This is shown schematically in Fig. 7.2. At the outset we assume that the current stress path has reached point A at the end of the n-th loading increment, for which the stress state $\{\sigma^a\}$ satisfies:

$$f\left[\{\sigma^a\},\ x^n\left(\epsilon_{ij}^p\right),\ k^n(\epsilon_p)\right] = f_0 < 0 \tag{7.7}$$

which indicates that the stress $\{\sigma^a\}$ is in an elastic state. Because of the finite load increment, a fully elastic trial stress path would reach the point B with the stress state $\{\sigma^b\}$ penetrating the yield surface at the point C for a proportional loading. The condition:

$$f\left[\{\sigma^b\},\ x^n\left(\epsilon_{ij}^p\right),\ k^n(\epsilon_p)\right] = f_1 > 0 \tag{7.8}$$

violates the yield condition (7.5) and indicates that a *transition* from elastic to plastic states occurs during this $(n+1)$-th load increment. In this case, then, the load increment is subdivided into two parts, a fully elastic portion for the path AC and an elastic-plastic portion governing the behavior after the yield surface has been

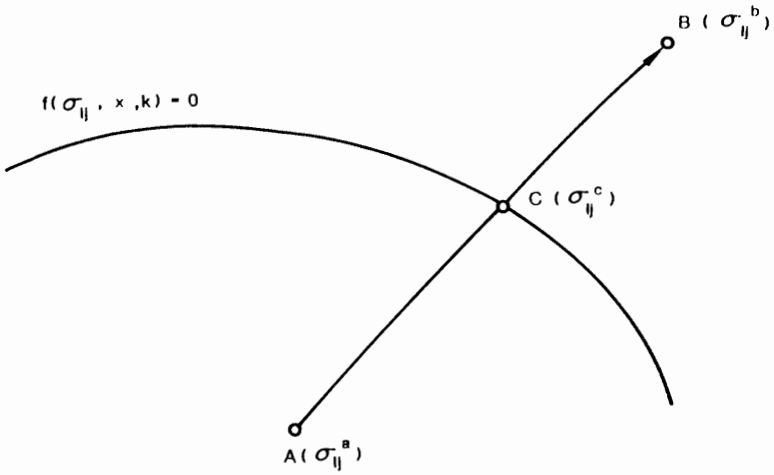

Fig. 7.2. Transition form an elastic to a plastic state.

reached at C. This requires the determination of the penetration point C, which is a geometric problem of intersecting a surface with a line. If we denote:

$$\{\sigma^c\} = \{\sigma^a\} + r\{d\sigma^c\} \tag{7.9}$$

where $r\{d\sigma^c\}$ is the portion of the stress increment at which the plastic behavior is first encountered, i.e., when:

$$f\left[\{\sigma^c\},\ x^n(\epsilon_{ij}^p),\ k^n(\epsilon_p)\right] = f\left[\{\sigma^a\} + r\{d\sigma^c\},\ x^n(\epsilon_{ij}^p),\ k^n(\epsilon_p)\right] = 0 \tag{7.10}$$

is reached, in principle, at least, the scaling factor r can be determined from Eq. (7.10). In actual applications, explicit expressions for r can be derived only for simple types of loading functions. The simplest approximate value of $r = r_1$ from Eq. (7.10) is determined by a linear interpolation in f (Zienkiewicz et al., 1969), that is:

$$r_1 = -f_0/(f_1 - f_0) \tag{7.11}$$

Due to nonlinearity in the function f, however:

$$f\left[\{\sigma^a\} + r_1\{d\sigma^c\},\ x^n(\epsilon_{ij}^p),\ k^n(\epsilon_p)\right] = f_2 \neq 0 \tag{7.12}$$

Therefore, a better estimate can now be obtained by assuming the higher-order term dr_1, that is:

$$f\left[\{\sigma^a\} + r_1\{d\sigma^c\} + dr_1\{d\sigma^c\},\ x^n(\epsilon_{ij}^p),\ k^n(\epsilon_p)\right] = 0 \tag{7.13}$$

Expanding the above equation around $\{\sigma^a\} + r_1\{d\sigma^c\}$, we find:

$$f\left[\{\sigma^a\} + r_1\{d\sigma^c\},\ x^n(\epsilon_{ij}^p),\ k^n(\epsilon_p)\right] + \{\partial f/\partial\sigma\}^T dr_1\{d\sigma^c\} = 0 \tag{7.14}$$

Substituting Eq. (7.12) into Eq. (7.14) and solving for dr_1 lead to:

$$dr_1 = -\frac{f_2}{\{\partial f/\partial\sigma\}^T\{d\sigma^c\}} \tag{7.15}$$

An improved value of r is thus given (Nayak and Zienkiewicz, 1972) by:

$$r = r_1 + dr_1 = r_1 - \frac{f_2}{\{\partial f/\partial\sigma\}^T\{d\sigma^c\}} \tag{7.16}$$

7.2.3 Plastic stress increment

Once the elastic portion of the strain increment $r\{d\epsilon\}$ and the plastic portion of the strain increment $(1-r)\{d\epsilon\}$ have been determined, the *initial-stress* or *plastic-stress* increment can be calculated:

$$\{d\sigma^p\} = \int_{r\,d\epsilon}^{d\epsilon} [C^{ep}]\{d\epsilon\} \tag{7.17}$$

where $[C^{ep}] = [C^e] - [C^{ep}]$ in which $[C^{ep}]$ is an elastic-plastic constitutive matrix. This plastic stress increment is required to restore the elastic stress increment:

$$\{d\sigma^e\} = \int_0^{d\epsilon} [C^e]\{d\epsilon\} = [C^e]\{d\epsilon\} \tag{7.18}$$

to the correct elastic-plastic values as required by the constitutive equation:

$$\begin{aligned}\{d\sigma\} &= \int_0^{d\epsilon} [C^{ep}]\{d\epsilon\} \\ &= \int_0^{d\epsilon} ([C^e] - [C^p])\{d\epsilon\} = \int_0^{r\,d\epsilon} [C^e]\{d\epsilon\} + \int_{r\,d\epsilon}^{d\epsilon} ([C^e] - [C^p])\{d\epsilon\} \\ &= \int_0^{d\epsilon} [C^e]\{d\epsilon\} - \int_{r\,d\epsilon}^{d\epsilon} [C^p]\{d\epsilon\} = \{d\sigma^e\} - \{d\sigma^p\}\end{aligned} \tag{7.19}$$

Since the plastic material stiffness $[C^p]$ varies with the current state of stress, the computation of the stress trajectory of Eq. (7.17) requires a numerical integration. The simplest approximation of Eq. (7.17) is to use the linear relation such as:

$$\{d\sigma^p\} = (1-r)[C^p]\{d\epsilon\} \tag{7.20}$$

Such a process is admissible if small load (or strain) increments are used. For large increments, however, a more accurate procedure is desirable. This can be achieved by dividing the strain interval $(1-r)\{d\epsilon\}$ into several smaller intervals and using Eq. (7.20) for each of these smaller intervals. The matrix $[C^p]$ is thus updated from time to time.

7.2.4 Stress scaling back to yield surface

Since Eq. (7.20) is an approximation to the more exact equation (7.17), where the value r is already an approximation to the actual solution of Eq. (7.10), the final stresses at the end of the $(n+1)$-th loading increment are also approximate:

$$\{\sigma\}^{n+1} = \{\sigma\}^n + \{d\sigma^e\} - \{d\sigma^p\} \tag{7.21}$$

and therefore, in general, we expect:

$$f\left[\{\sigma\}^{n+1},\ x^{n+1}(\epsilon_{ij}^{p}),\ k^{n+1}(\epsilon_{p})\right] = f_3 \neq 0 \tag{7.22}$$

and a small departure from the yield surface is obtained. Such a departure will be cumulative; since in analysis it is important to preserve the yield condition at least, a correction of stress onto the current yield surface must therefore be performed. The following two methods are provided here as example procedures for this purpose:

Method 1: The correction is achieved in a manner similar to that given in the previous refinement for a better value of the scaling factor r. Assume that the stress change or correction is along the direction of the normal to the current yield surface:

$$\{\delta\sigma\} = a\left\{\frac{\partial f}{\partial \sigma}\right\} \tag{7.23}$$

where a is a scalar and $\{\delta\sigma\}$ is the stress correction vector. Substituting Eq. (7.23) into Eq. (7.22):

$$f\left[\{\sigma\}^{n+1} + a\left\{\frac{\partial f}{\partial \sigma}\right\},\ x^{n+1}(\epsilon_{ij}^{p}),\ k^{n+1}(\epsilon_{p})\right] = 0 \tag{7.24}$$

and expanding the above equation around $\{\sigma\}^{n+1}$:

$$f - f_3 + \left\{\frac{\partial f}{\partial \sigma}\right\}^{T} a\left\{\frac{\partial f}{\partial \sigma}\right\} = 0 \tag{7.25}$$

lead to:

$$a\left\{\frac{\partial f}{\partial \sigma}\right\} \quad \{\delta\sigma\} \qquad \frac{\{\partial f/\partial\sigma\} f_3}{\{\partial f/\partial\sigma\}^{T}\{\partial f/\partial\sigma\}} \tag{7.26}$$

Method 2: An alternative procedure to correct the stresses onto the current yield surface is to assume that the stresses are scaled back by keeping the same magnitude of the first stress invariant I_1 for the hydrostatic pressure component and also by keeping the same directions of the principal stress axes of the current stress state:

$$I_1^{n+1} = \sigma_{11}^{n+1} + \sigma_{22}^{n+1} + \sigma_{33}^{n+1} \tag{7.27}$$

$$\begin{aligned}\{s\}^{n+1} &= \left[s_{11}^{n+1} s_{22}^{n+1} s_{33}^{n+1} s_{12}^{n+1} s_{23}^{n+1} s_{31}^{n+1}\right]^{T} \\ &= \left[\sigma_{11}^{n+1} \sigma_{22}^{n+1} \sigma_{33}^{n+1} \sigma_{12}^{n+1} \sigma_{23}^{n+1} \sigma_{31}^{n+1}\right]^{T} - \tfrac{1}{3} I_1^{n+1}[1\ 1\ 1\ 0\ 0\ 0]^{T}\end{aligned} \tag{7.28}$$

where $\{s\}^{n+1}$ is the vector of deviatoric stresses. Thus, the problem is now to find the condition satisfying the following equation:

$$f\left[\{\sigma\}^{n+1} + r\{s\}^{n+1},\ x^{n+1}(\epsilon_{ij}^{p}),\ k^{n+1}(\epsilon_{p})\right] = 0 \tag{7.29}$$

where r is a scaling factor. Again, expanding Eq. (7.29) around $\{\sigma\}^{n+1}$:

$$f = f_3 + \left\{\frac{\partial f}{\partial \sigma}\right\}^{T} r\{s\}^{n+1} = 0 \tag{7.30}$$

we obtain the correction vector of the deviatoric stresses:

$$r\{s\}^{n+1} = -\frac{f_3\{s\}^{n+1}}{\{\partial f/\partial \sigma\}^{T}\{s\}^{n+1}} \tag{7.31}$$

The accuracy of this calculation depends on the proximity of the calculated stress $\{\sigma\}^{n+1}$ to the yield surface f^{n+1}. The methods described above represent two examples of several possible methods to insure the final state of stress lies on the current yield surface.

7.3 IMPLEMENTATION OF COULOMB AND DRUCKER-PRAGER MODELS

The general numerical procedures for treating the constitutive relations of materials have been described in the preceding Section. In the following, we shall explain the details of the computer implementations of the perfectly plastic *Coulomb* and *Drucker-Prager* models (Mizuno, 1981). The implementation procedure described here is suitable for incorporation with the *mid-point integration method*, the details of which will be discussed in Chapter 9. The mid-point integration method avoids the *iterative procedure*, reduces the computational time, and at the same time provides the necessary accuracy of the solution within the small strain increment. Davidson and Chen (1974) used this method to solve the large-deformation bearing-capacity problems of footing and showed its applicability to a general class of nonlinear stress analysis problems in geotechnical engineering.

7.3.1 Implementation for mid-increment

We shall consider here a material element whose equilibrium stresses and strains are respectively σ_{ij}^{n} and ϵ_{ij}^{n} at the end of the n-th loading increment. According to the stress state (*elastic* or *plastic*) in an element, either the elastic constitutive matrix $[C^{e}]^{n}$ or the elastic-plastic constitutive matrix $[C^{ep}]^{n}$ is used to calculate the current element tangent stiffness.

Applying first the half of the incremental loads to the discretized soil structure stiffness $[K]_n$, incremental strains $d\epsilon_{ij}^{n+1/2}$ at the $(n+\frac{1}{2})$-th increment are first estimated from the kinematic condition:

$$\{dU\}^{n+1/2} = [K]_n^{-1}\{\tfrac{1}{2}\, dR\} \quad \text{in structural level} \tag{7.32a}$$

$$\{d\epsilon\}^{n+1/2} = [B]\{dU\}^{n+1/2} \quad \text{in an element level} \tag{7.32b}$$

where $[B]$ is a *transformation matrix* which relates the nodal displacement increments to the strain increments at any generic point inside an element (see Chapter 9).

Subsequently, the corresponding stress increments $d\sigma_{ij}^{n+1/2}$ in all elements are estimated by using the current constitutive matrix $[C^e]^n$ or $[C^{ep}]^n$. Then, the stresses $\sigma_{ij}^{n+1/2}$ for all elements at the end of the $(n+\frac{1}{2})$-th loading increment are approximated from the stresses σ_{ij}^n:

$$\{d\sigma\}^{n+1/2} = [C^{ep}]^n\{d\epsilon\}^{n+1/2} \text{ or } \{d\sigma\}^{n+1/2} = [C^e]^n\{d\epsilon\}^{n+1/2} \tag{7.33a}$$

$$\{\sigma\}^{n+1/2} = \{\sigma\}^n + \{d\sigma\}^{n+1/2} \tag{7.33b}$$

The main purpose of the calculation made at the mid-increment step is to correct the stresses $\sigma_{ij}^{n+1/2}$ in all elements if necessary and to construct for each element a new element constitutive matrix, particularly the elastic-plastic tangent stiffness matrix $[C^{ep}]^{n+1/2}$, which will be used in the subsequent steps to evaluate the final displacement increments $\{dU\}^{n+1}$ at the end of the $(n+1)$-th loading increment by applying the full $(n+1)$-th loading increment $\{dR\}$. The schematic concept of the

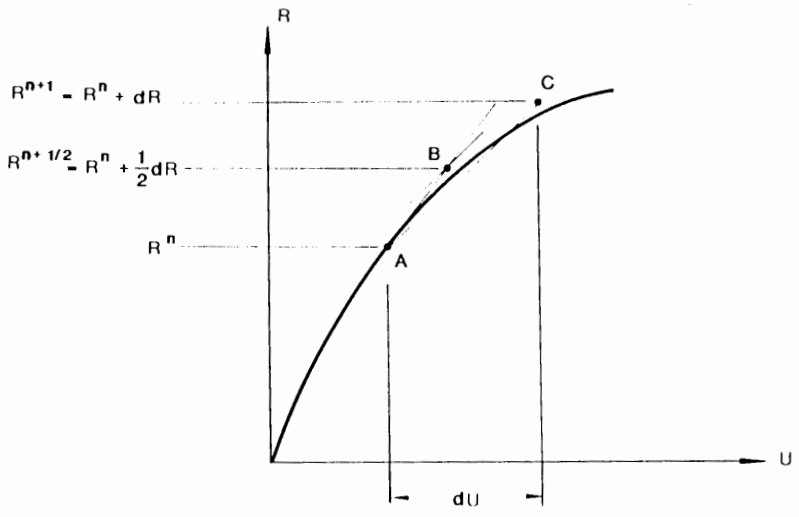

Fig. 7.3. Mid-point integration rule.

mid-point integration method is illustrated in Fig. 7.3. In the following, the calculation steps at mid-increment are presented.

Step 1: Preliminary calculation

The invariants of stress tensor and stress deviatoric tensor are computed:
For the *Drucker-Prager model*, we need:

$$\sqrt{J_2}^{n+1/2} = \left[\frac{1}{6}\left\{\left(\sigma_{11}^{n+1/2} - \sigma_{22}^{n+1/2}\right)^2 + \left(\sigma_{22}^{n+1/2} - \sigma_{33}^{n+1/2}\right)^2 + \left(\sigma_{33}^{n+1/2} - \sigma_{11}^{n+1/2}\right)^2\right\}\right.$$
$$\left. + \left(\sigma_{12}^{n+1/2}\right)^2 + \left(\sigma_{23}^{n+1/2}\right)^2 + \left(\sigma_{31}^{n+1/2}\right)^2\right]^{1/2} \quad (7.34a)$$

$$I_1^{n+1/2} = \left(\sigma_{11}^{n+1/2} + \sigma_{22}^{n+1/2} + \sigma_{33}^{n+1/2}\right) \quad (7.34b)$$

and for the *Coulomb model*, we need the following variables in addition:

$$J_3^{n+1/2} = \left(\sigma_{11}^{n+1/2} - p^{n+1/2}\right)\left(\sigma_{22}^{n+1/2} - p^{n+1/2}\right)\left(\sigma_{33}^{n+1/2} - p^{n+1/2}\right)$$
$$- \left(\sigma_{12}^{n+1/2}\right)^2\left(\sigma_{33}^{n+1/2} - p^{n+1/2}\right) - \left(\sigma_{23}^{n+1/2}\right)^2\left(\sigma_{11}^{n+1/2} - p^{n+1/2}\right)$$
$$- \left(\sigma_{13}^{n+1/2}\right)^2\left(\sigma_{22}^{n+1/2} - p^{n+1/2}\right) + 2\sigma_{12}^{n+1/2}\sigma_{23}^{n+1/2}\sigma_{31}^{n+1/2} \quad (7.35a)$$

$$\theta^{n+1/2} = \tfrac{1}{3}\cos^{-1}\left[3\sqrt{3}J_3/2J_2^{3/2}\right] \quad (7.35b)$$

where J_3 is the third invariant of the stress deviatoric tensor, θ is the *Lode angle*, and $p^{n+1/2}$ is the hydrostatic pressure equal to $\frac{1}{3}I_1^{n+1/2}$. The Coulomb equation f in terms of stress invariants has the form:

$$f = \frac{2\sin\phi}{3(1-\sin\phi)\sin\theta + \sqrt{3}(3+\sin\phi)\cos\theta} I_1 + \sqrt{J_2}$$
$$- \frac{6c\cos\phi}{3(1-\sin\phi)\sin\theta + \sqrt{3}(3+\sin\phi)\cos\theta} = 0 \quad (7.36)$$

where c and ϕ are respectively the cohesion and the angle of internal friction of soils. The Drucker-Prager equation, $f = \alpha I_1 + \sqrt{J_2} - k = 0$, is mathematically equivalent to the Coulomb equation (7.36), if the constants α and k are matched with the constants c and ϕ in the following manner:

$$\alpha^{n+1/2} = \frac{2\sin\phi}{3(1-\sin\phi)\sin\theta^{n+1/2} + \sqrt{3}(3+\sin\phi)\cos\theta^{n+1/2}} \quad (7.37a)$$

$$k^{n+1/2} = \frac{6c\cos\phi}{3(1-\sin\phi)\sin\theta^{n+1/2} + \sqrt{3}(3+\sin\phi)\cos\theta^{n+1/2}} \quad (7.37b)$$

Step 2: Check for tension cracking

When the stress state exceeds the apex of the yield surface, for the *Drucker-Prager model*:

$$-\alpha I_1^{n+1/2} + k = \Delta T < 0 \tag{7.38a}$$

and for the *Coulomb model*:

$$-\alpha^{n+1/2} I_1^{n+1/2} + k^{n+1/2} = \Delta T < 0 \tag{7.38b}$$

we shall shift the hydrostatic stress component to the corresponding hydrostatic pressure at the apex (see Fig. 7.4):

$$\tilde{\sigma}_{11}^{n+1/2} = \sigma_{11}^{n+1/2} - \frac{1}{3}\left(I_1^{n+1/2} - \frac{k}{\alpha}\right) \tag{7.39a}$$

$$\tilde{\sigma}_{22}^{n+1/2} = \sigma_{22}^{n+1/2} - \frac{1}{3}\left(I_1^{n+1/2} - \frac{k}{\alpha}\right) \tag{7.39b}$$

$$\tilde{\sigma}_{33}^{n+1/2} = \sigma_{33}^{n+1/2} - \frac{1}{3}\left(I_1^{n+1/2} - \frac{k}{\alpha}\right) \tag{7.39c}$$

Note that α and k are replaced by $\alpha^{n+1/2}$ and $k^{n+1/2}$ for the Coulomb model. Thus, the adjusted normal stresses can be estimated from Eq. (7.39), while the shearing stresses $\sigma_{12}^{n+1/2}$, $\sigma_{23}^{n+1/2}$, and $\sigma_{31}^{n+1/2}$ remain unchanged. Subsequently, the following steps should be performed.

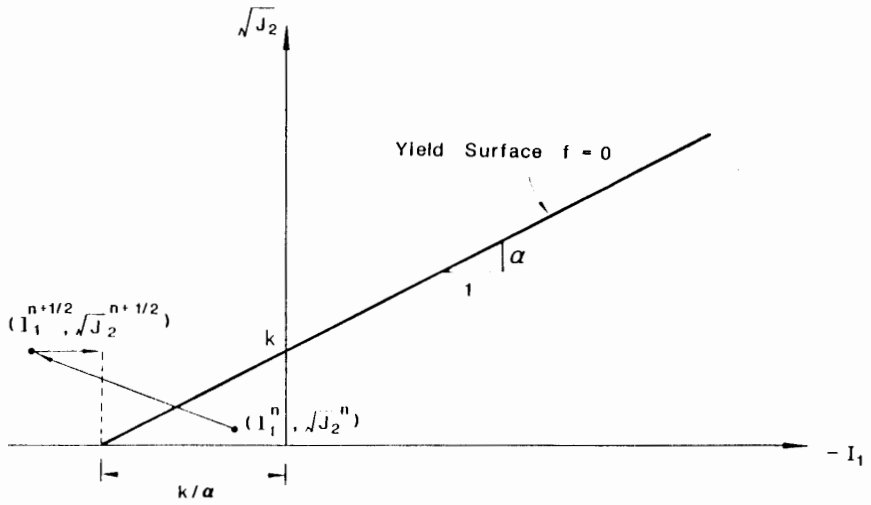

Fig. 7.4. Check for tensile stress.

Step 3: Check for a previously plastic element

For the element which is previously in a *plastic* state at the end of the n-th increment, the possible plastic unloading must be checked by calculating the proportionality factor $d\lambda$, because this may occur even though the incremental loads or displacements are monotonically increasing. For the element which is previously in an *elastic* state, a separate treatment will be performed in Step 4.

Proportionality factor $d\lambda$. The value of proportionality factor $d\lambda$ of Eq. (4.118a) in Chapter 4 is checked.

For the *Drucker-Prager model*, we have:

$$d\lambda^{n+1/2} = \frac{1}{H}\left[3K\alpha\, d\epsilon_v^{n+1/2} + G\frac{1}{\sqrt{J_2}^{n}} s_{kl}^{n}\, de_{kl}^{n+1/2}\right] \tag{7.40}$$

where s_{ij}^{n} are the deviatoric stresses at the end of the n-th load increment, $de_{kl}^{n+1/2}$ are the deviatoric strain increments at the end of the $(n+\frac{1}{2})$-th increment, and H is given from Eq. (4.118b):

$$H = 9K\alpha^2 + G \tag{7.41}$$

For the *Coulomb model*, $d\lambda^{n+1/2}$ can be calculated by:

$$d\lambda^{n+1/2} = \frac{1}{H}\left[3KA^{n}\, d\epsilon_v^{n+1/2} + 2G\left(B^{n}s_{kl}^{n} + C^{n}t_{kl}^{n}\right) d\epsilon_{kl}^{n+1/2}\right] \tag{7.42}$$

where A^n, B^n, C^n, and H are given by Eqs. (4.126) and (4.118b), using the stresses and the Lode angle θ^n at the end of the n-th increment:

$$A^{n} = \sin\phi \tag{7.43a}$$

$$B^{n} = \tfrac{1}{4}\left[3(1-\sin\phi)\sin\theta^{n} + \sqrt{3}\,(3+\sin\phi)\cos\theta^{n}\right]/\left(\sqrt{J_2}^{n}\right) + 3\sqrt{3}\,J_3^{n}\left[3(1-\sin\phi)\cos\theta^{n} - \sqrt{3}\,(3+\sin\phi)\sin\theta^{n}\right]/\left[8(J_2^{n})^{2}\sin 3\theta^{n}\right] \tag{7.43b}$$

$$C^{n} = -\sqrt{3}\left[3(1-\sin\phi)\cos\theta^{n} - \sqrt{3}\,(3+\sin\phi)\sin\theta^{n}\right]/(4J_3^{n}\sin 3\theta^{n}) \tag{7.43c}$$

$$t_{ij}^{n} = s_{ik}^{n}s_{kj}^{n} - \tfrac{2}{3}J_2^{n}\delta_{ij} \tag{7.43d}$$

$$H = 9K(A^{n})^{2} + 4GJ_2^{n}(B^{n})^{2} + 12GJ_3^{n}B^{n}C^{n} + 2G\left[s_{ik}^{n}s_{kj}^{n}s_{ji}^{n}s_{il}^{n} - \tfrac{4}{3}(J_2^{n})^{2}\right](C^{n})^{2} \tag{7.43e}$$

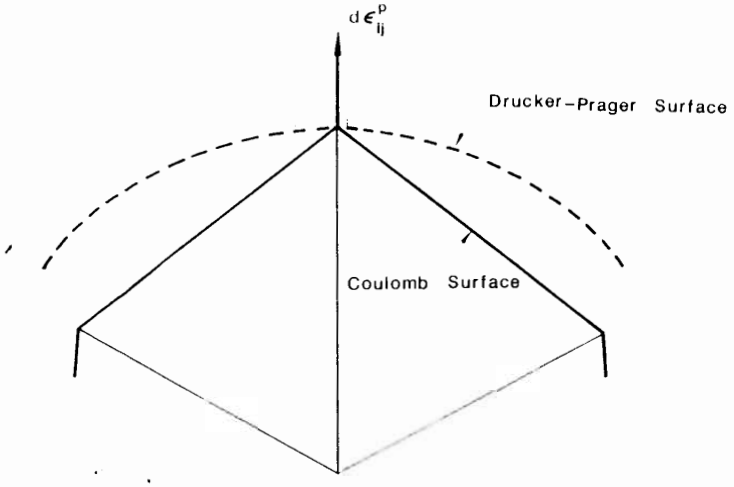

Fig. 7.5. Corner treatment of Coulomb model.

If the stress state σ_{ij}^{n} at the previous step lies just on the tensile or compressive meridian of the Coulomb model, the stiffness coefficients B^{n} and C^{n} become infinite due to the *corner singularity*. To treat this, we may use the Drucker-Prager equation to estimate $d\lambda^{n+1/2}$, as shown in Fig. 7.5. Thus, at the corner of the Coulomb model, the flow rule is taken to be identical with the projection of the axis of either the tensile or the compressive meridian on the deviatoric plane. Therefore, $d\lambda^{n+1/2}$ can be written in a similar form to Eq. (7.40) as:

$$d\lambda^{n+1/2} = \frac{1}{H}\left[3K\alpha^{n}\, d\epsilon_{v}^{n+1/2} + G\frac{1}{\sqrt{J_2}^{n}} s_{kl}^{n}\, de_{kl}^{n+1/2}\right] \tag{7.44a}$$

where H and α^{n} are given by:

$$H = 9K(\alpha^{n})^{2} + G \tag{7.44b}$$

$$\alpha^{n} = \frac{2\sin\phi}{3(1-\sin\phi)\sin\theta^{n} + \sqrt{3}\,(3+\sin\phi)\cos\theta^{n}} \tag{7.44c}$$

The implementation of these models described above is based on the associated flow rule assumption. If a non-associated flow rule is taken, a similar formulation as given previously in Chapter 5 can be utilized for such an implementation.

Plastic unloading. If $d\lambda^{n+1/2}$ has a negative value, the element is undergone a *plastic unloading*, then, the elastic constitutive element matrix $[C^{e}]$ is assigned to

compute the subsequent tangent stiffness of the structure:

$$[C^e] = \begin{bmatrix} K+\frac{4}{3}G & K-\frac{2}{3}G & K-\frac{2}{3}G & 0 & 0 & 0 \\ K-\frac{2}{3}G & K+\frac{4}{3}G & K-\frac{2}{3}G & 0 & 0 & 0 \\ K-\frac{2}{3}G & K-\frac{2}{3}G & K+\frac{4}{3}G & 0 & 0 & 0 \\ 0 & 0 & 0 & G & 0 & 0 \\ 0 & 0 & 0 & 0 & G & 0 \\ 0 & 0 & 0 & 0 & 0 & G \end{bmatrix} \tag{7.45}$$

If a nonlinear elastic model is assumed, the element stiffness must be updated from the current stresses by using the current elastic material parameters.

Plastic loading. On the other hand, if $d\lambda^{n+1/2}$ has a positive value, the element is assumed to remain plastic during the $(n+1)$-th loading increment, then, the stress state $\{\sigma\}^{n+1/2}$ is scaled back to the yield surface by employing Method 2 discussed in Section 7.2.4, i.e., the hydrostatic component I_1 and the principal directions of the stress tensor remain unchanged, while the deviatoric stress components are reduced proportionally by the scaling factor r. This process is given in the following:

Scaling back procedure. A schematic stress path associated with this stress-scaling back procedure is shown as the dotted line in Fig. 7.6. This procedure is used

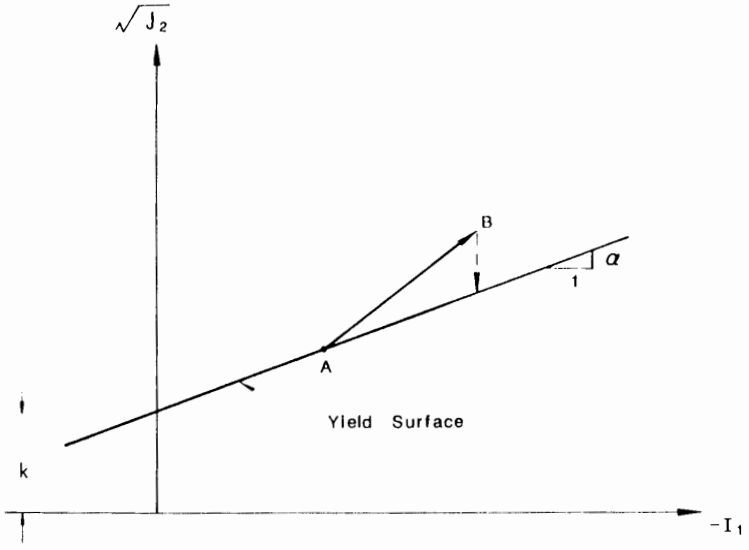

Fig. 7.6. Scheme of scale back.

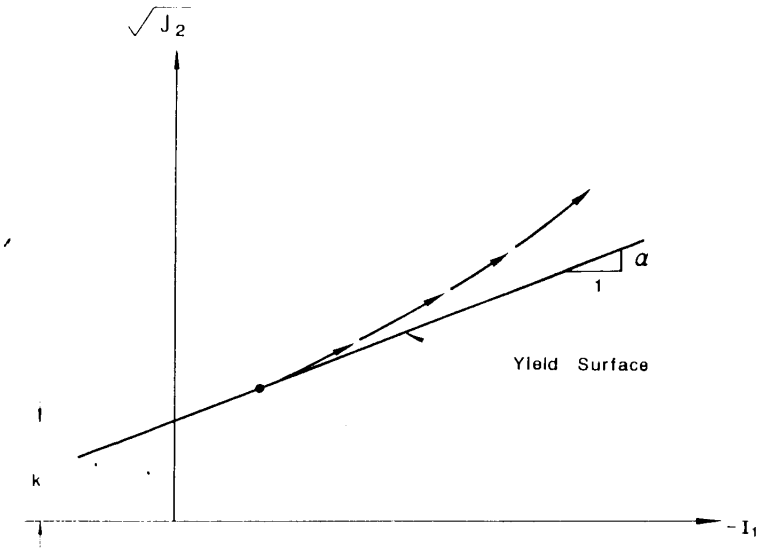

Fig. 7.7. Stress path without scale back.

because, after a number of such increments, the final stress would otherwise lie far away from the yield surface (Fig. 7.7). Introducing the scaling factor r expressed by:

$$r = \Delta T / \sqrt{J_2}^{\,n+1/2} \tag{7.46}$$

where ΔT is now the positive value defined by Eq. (7.38) in Step 2. Thus, the scaled-back stresses are given by:

$$\tilde{\sigma}_{11}^{n+1/2} = r s_{11}^{n+1/2} + \tfrac{1}{3} I_1^{n+1/2} \tag{7.47a}$$

$$\tilde{\sigma}_{22}^{n+1/2} = r s_{22}^{n+1/2} + \tfrac{1}{3} I_1^{n+1/2} \tag{7.47b}$$

$$\tilde{\sigma}_{33}^{n+1/2} = r s_{33}^{n+1/2} + \tfrac{1}{3} I_1^{n+1/2} \tag{7.47c}$$

$$\tilde{\sigma}_{12}^{n+1/2} = r s_{12}^{n+1/2} \tag{7.47d}$$

$$\tilde{\sigma}_{23}^{n+1/2} = r s_{23}^{n+1/2} \tag{7.47e}$$

$$\tilde{\sigma}_{31}^{n+1/2} = r s_{31}^{n+1/2} \tag{7.47f}$$

where $I_1^{n+1/2} = \sigma_{11}^{n+1/2} + \sigma_{22}^{n+1/2} + \sigma_{33}^{n+1/2}$. (7.47g)

Elastic-plastic constitutive matrix. Utilizing the above stress components, the elastic-plastic constitutive matrix $[C^{ep}]^{n+1/2}$ can be computed for the construction of a new tangent stiffness matrix at the mid-increment:

$$[C^{ep}]^{n+1/2} = [C^{e}]^{n+1/2} - [C^{p}]^{n+1/2} \tag{7.48}$$

where $[C^{e}]^{n+1/2}$ is the elastic constitutive matrix given previously and $[C^{p}]^{n+1/2}$ can be rewritten as:

$$[C^{p}]^{n+1/2} = \frac{1}{H}\begin{bmatrix} H_{11}^2 & H_{11}H_{22} & H_{11}H_{33} & H_{11}H_{12} & H_{11}H_{23} & H_{11}H_{31} \\ H_{22}H_{11} & H_{22}^2 & H_{22}H_{33} & H_{22}H_{12} & H_{22}H_{23} & H_{22}H_{31} \\ H_{33}H_{11} & H_{33}H_{22} & H_{33}^2 & H_{33}H_{12} & H_{33}H_{23} & H_{33}H_{31} \\ H_{12}H_{11} & H_{12}H_{22} & H_{12}H_{33} & H_{12}^2 & H_{12}H_{23} & H_{12}H_{31} \\ H_{23}H_{11} & H_{23}H_{22} & H_{23}H_{33} & H_{23}H_{12} & H_{23}^2 & H_{23}H_{31} \\ H_{31}H_{11} & H_{31}H_{22} & H_{31}H_{33} & H_{31}H_{12} & H_{31}H_{23} & H_{31}^2 \end{bmatrix} \tag{7.49}$$

where the form of H is already given in Step 3 for the Drucker-Prager and the Coulomb models, respectively. The components of this matrix are expressed as follows:

For the *Drucker-Prager model*:

$$H_{11} = 3K\alpha + G\tilde{s}_{11}^{n+1/2}/\sqrt{\tilde{J}_2}^{n+1/2} \tag{7.50a}$$

$$H_{22} = 3K\alpha + G\tilde{s}_{22}^{n+1/2}/\sqrt{\tilde{J}_2}^{n+1/2} \tag{7.50b}$$

$$H_{33} = 3K\alpha + G\tilde{s}_{33}^{n+1/2}/\sqrt{\tilde{J}_2}^{n+1/2} \tag{7.50c}$$

$$H_{12} = G\tilde{s}_{12}^{n+1/2}/\sqrt{\tilde{J}_2}^{n+1/2} \tag{7.50d}$$

$$H_{23} = G\tilde{s}_{23}^{n+1/2}/\sqrt{\tilde{J}_2}^{n+1/2} \tag{7.50e}$$

$$H_{31} = G\tilde{s}_{31}^{n+1/2}/\sqrt{\tilde{J}_2}^{n+1/2} \tag{7.50f}$$

where $\tilde{s}_{ij}^{n+1/2}$ are the scaled-back deviatoric stresses, and $\tilde{J}_2^{n+1/2}$ can be computed from the scaled-back stresses $\tilde{\sigma}_{ij}^{n+1/2}$.

For the *Coulomb model*:

$$H_{11} = 3KA^{n+1/2} + 2G\left(B^{n+1/2}\tilde{s}_{11}^{n+1/2} + C^{n+1/2}\tilde{t}_{11}^{n+1/2}\right) \tag{7.51a}$$

$$H_{22} = 3KA^{n+1/2} + 2G\left(B^{n+1/2}\tilde{s}_{22}^{n+1/2} + C^{n+1/2}\tilde{t}_{22}^{n+1/2}\right) \tag{7.51b}$$

$$H_{33} = 3KA^{n+1/2} + 2G\left(B^{n+1/2}\tilde{s}_{33}^{n+1/2} + C^{n+1/2}\tilde{t}_{33}^{n+1/2}\right) \tag{7.51c}$$

$$H_{12} = 2G\left(B^{n+1/2}\tilde{s}_{12}^{n+1/2} + C^{n+1/2}\tilde{t}_{12}^{n+1/2}\right) \tag{7.51d}$$

$$H_{23} = 2G\left(B^{n+1/2}\tilde{s}_{23}^{n+1/2} + C^{n+1/2}\tilde{t}_{23}^{n+1/2}\right) \tag{7.51e}$$

$$H_{31} = 2G\left(B^{n+1/2}\tilde{s}_{31}^{n+1/2} + C^{n+1/2}\tilde{t}_{31}^{n+1/2}\right) \tag{7.51f}$$

where $\tilde{t}_{ij}^{n+1/2}$ are calculated by:

$$\tilde{t}_{ij}^{n+1/2} = \tilde{s}_{ik}^{n+1/2}\tilde{s}_{kj}^{n+1/2} - \tfrac{2}{3}\tilde{J}_2^{n+1/2}\delta_{ij} \tag{7.51g}$$

and $A^{n+1/2}$, $B^{n+1/2}$, and $C^{n+1/2}$ are respectively calculated from the form presented in Step 3, by using the scaled-back stresses $\tilde{\sigma}_{ij}^{n+1/2}$.

As a special case of the Coulomb model, the *corner singularity* can be treated by using the Drucker-Prager equation as the failure surface for this state. The components of the plastic matrix $[C^p]^{n+1/2}$ can therefore be obtained by simply replacing α in Eqs. (7.50a) through (7.50c) with $\alpha^{n+1/2}$.

Step 4: Check for a previously elastic element

Using the stresses at the $(n+\frac{1}{2})$-th increment, the element status at the end of the $(n+1)$-th increment is estimated for the element which is previously elastic. The value of $f\ (=\alpha I_1 + \sqrt{J_2} - k)$ at the end of the n-th increment is given by:

For the *Drucker-Prager model:*

$$f^n = \alpha I_1^n + \sqrt{J_2}^n - k < 0 \tag{7.52a}$$

and for the *Coulomb model:*

$$f^n = \alpha^n I_1^n + \sqrt{J_2}^n - k^n < 0 \tag{7.52b}$$

where I_1^n and J_2^n are respectively the first and second invariants of the stress tensor and stress deviatoric tensor obtained at the n-th load increment. Note that the values α and k are constants for the Drucker-Prager model but become variables for the Coulomb model.

The value of f at the mid-increment can be evaluated as follows:

For the *Drucker-Prager model*:

$$f^{n+1/2} = \alpha I_1^{n+1/2} + \sqrt{J_2}^{n+1/2} - k \tag{7.53a}$$

and for the *Coulomb model*:

$$f^{n+1/2} = \alpha^{n+1/2} I_1^{n+1/2} + \sqrt{J_2}^{n+1/2} - k^{n+1/2} \tag{7.53b}$$

To predict the value of f at the end of the $(n+1)$-th increment, we assume the following relationship:

$$f^{n+1} = f^n + 2\left(f^{n+1/2} - f^n\right) \tag{7.54}$$

If the estimated value f^{n+1} is still *negative*, it is assumed that the element remains in the elastic range during the $(n+1)$-th increment. Thus, an elastic constitutive matrix $[C^e]^{n+1/2}$ is assigned for this element during the $(n+1)$-th incremental calculation.

Averaged matrix. On the other hand, if f^{n+1} has a positive value, it is assumed that the element yields during this increment. In this case, a *weighted* average of the elastic and elastic-plastic constitutive matrices is employed. To construct the *averaged matrix*, the stress state $\{\sigma\}^{n+1/2}$ at the mid-increment is scaled back onto the yield surface by the procedure described in Step 3, irrespective of whether this stress state lies outside or inside the yield surface. The averaged constitutive matrix is computed as:

$$\left[C_{av}^{ep}\right]^{n+1/2} = r\left[C^e\right]^{n+1/2} + (1-r)\left[C^{ep}\right]^{n+1/2} \tag{7.55}$$

where r is the scaling factor and $[C^{ep}]^{n+1/2}$ is the elastic-plastic constitutive matrix based on the scaled-back stresses. In this case, the scaling factor r may be computed by the first-order approximation discussed in Section 7.2.2, in the form:

$$r = -f^n / \left[2\left(f^{n+1/2} - f^n\right)\right] \tag{7.56}$$

Thus, the constitutive matrix of an element at the mid-increment is completely evaluated by Step 1 through Step 4.

7.3.2 Implementation for full increment

Using the constitutive matrix evaluated at the mid-increment in the previous Section for the element, the element tangent stiffness $[k]^{n+1/2}$ and the structure tangent stiffness $[K]^{n+1/2}$ can be computed. The details of these stiffness matrices

will be explained in Chapter 9. With the aid of the structure tangent stiffness $[K]^{n+\frac{1}{2}}$ after the $(n+\frac{1}{2})$-th increment, the $(n+1)$-th incremental calculation is performed to obtain the displacement increment $\{dU\}^{n+1}$ by applying the *full* load increment $\{dR\}$. Subsequently, the strain increment $\{d\epsilon\}^{n+1}$ for the element can be evaluated from the kinematic condition:

$$\{dU\}^{n+1} = [K]^{-1}_{n+1/2}\{dR\} \text{ in structural level} \tag{7.57a}$$

$$\{d\epsilon\}^{n+1} = [B]\{dU\}^{n+1} \text{ in an element level} \tag{7.57b}$$

Further, the stress increment $\{d\sigma\}^{n+1}$ can be obtained by using the current constitutive matrix $[C^e]^{n+1/2}$ or $[C^{ep}]^{n+1/2}$, and finally the stresses $\{\sigma\}^{n+1}$ can be estimated by adding the stress increment $\{d\sigma\}^{n+1}$ to the stress $\{\sigma\}^n$ at the end of the n-th increment.
For an elastic state:

$$\{d\sigma\}^{n+1} = [C^e]^{n+1/2}\{d\epsilon\}^{n+1} \tag{7.58a}$$

or for an elastic-plastic state:

$$\{d\sigma\}^{n+1} = [C^{ep}]^{n+1/2}\{d\epsilon\}^{n+1} \tag{7.58b}$$

The stress state is given by:

$$\{\sigma\}^{n+1} = \{\sigma\}^n + \{d\sigma\}^{n+1} \tag{7.58c}$$

If the analysis is based on a *large deformation formulation* under the updated Lagrangian description, the stress state at the end of the increment must first be *rotated* from a local coordinate system (the Jaumann stress state) to a global coordinate system (the Eulerian stress state). This will be discussed later in mixed incremental formulation, Section 8.7.1.

The implementation procedure for the *full increment* is in general similar to those explained in the previous Section for the *mid-increment*. Therefore, only a brief description will be given below:

Step 1: Preliminary calculation

Here as in mid-increment, the given input quantity for the Subroutine that estimates the element constitutive matrix $[C^e]^{n+1}$ or $[C^{ep}]^{n+1}$ is the stresses $\{\sigma\}^{n+1}$. As a preliminary calculation, the stress invariants such as $\sqrt{J_2}^{n+1}$, I_1^{n+1} are calculated for the *Drucker-Prager model*, and in addition, the values J_3^{n+1}, θ^{n+1}, α^{n+1}, and k^{n+1} are calculated for the *Coulomb model*.

Step 2: Check for tension cracking

If the hydrostatic stress exceeds the apex value of the yield surface, it need be

shifted to the level of the apex. The calculation procedure is the same as that illustrated in Section 7.3.1.

Step 3: Check for a previously plastic element

If the elastic-plastic matrix in Step 3 or an averaged matrix in Step 4 has been used to determine the mid-increment tangent stiffness, the stress state in the element at the end of the $(n+1)$-th increment is assumed to be *plastic* regardless of whether the stress state lies inside or outside the yield surface. The final stress state is then *scaled back* to the yield surface and the elastic-plastic constitutive matrix $[C^{ep}]^{n+1}$ is constructed for the next mid-increment calculation.

Step 4: Check for a previously elastic element

For the element whose elastic constitutive matrix is previously used to compute the mid-increment stiffness, the yield condition must be checked. If the condition:

for the *Drucker-Prager model*

$$f^{n+1} = \alpha I_1^{n+1} + \sqrt{J_2}^{n+1} - k > 0 \tag{7.59a}$$

or for the *Coulomb model*

$$f^{n+1} = \alpha^{n+1} I_1^{n+1} + \sqrt{J_2}^{n+1} - k^{n+1} > 0 \tag{7.59b}$$

is satisfied, the stresses $\{\sigma\}^{n+1}$ are scaled back to the yield surface and an elastic-plastic constitutive matrix $[C^{ep}]^{n+1}$ is assigned for the next increment. Otherwise, the stress state remains unchanged and the elastic element constitutive matrix $[C^{e}]^{n+1}$ is used for the next incremental calculation.

A schematic flow chart for the implementation of the Coulomb and Drucker-Prager models is shown in Fig. 7.8. Since the scaled-back stresses may not generally be expected to satisfy the equilibrium condition, an *iterative procedure* could be used in the finite element coding for a more accurate solution (see Section 9.4 in Chapter 9).

7.3.3 Two-dimensional finite-element subroutine

The calculation steps for the Coulomb and Drucker-Prager models have been explained to some details. In this Section, as an illustrative example, we shall present the computer SUBROUTINES developments that can be directly adopted to an existing *two-dimensional* finite-element program under the *plane strain condition*.

The two-dimensional SUBROUTINES developed include the following features: .

1. A main SUBROUTINE CDPMDL which implements the Coulomb and Drucker-Prager MODELS. It contains the following SUBROUTINES:
2. SUBROUTINE SCALE which SCALES the stresses back to the yield surface.
3. SUBROUTINE LINELS which constructs the LINear ELastic constitutive matrix.

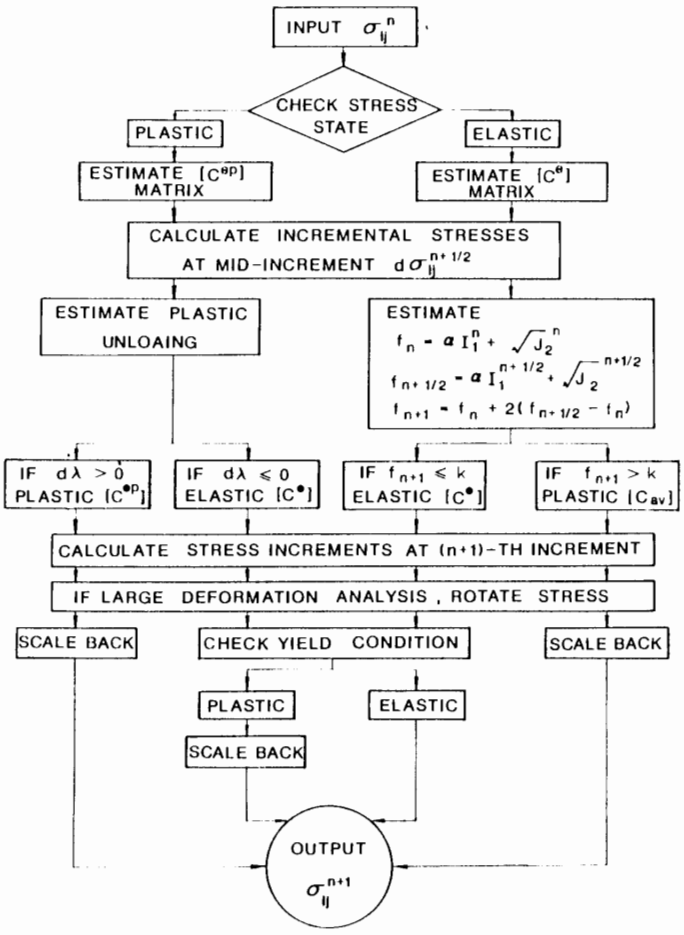

Fig. 7.8. Flow chart for the implementation of Coulomb and Drucker-Prager models.

4. SUBROUTINE EPCDP which constructs the Elastic-Plastic constitutive matrix for the Coulomb and Drucker-Prager models.
5. SUBROUTINE AVED which constructs the AVEraged constitutive matrix.

In the following, each of these subroutines will be explained in some details including the INPUT QUANTITIES, INTERNAL VARIABLES, and OUTPUT QUANTITIES.

(A) SUBROUTINE CDPMDL

INPUT QUANTITIES

1. Calculation type

KODEI : KODEI = 1 for mid-increment
: KODEI = 2 for full increment

2. Material type
   MAT : MAT = 1 for the Coulomb material
   : MAT = 2 for the Drucker-Prager material
3. Yield status
   MSTATE : Index to define the elastic or plastic state
   : MSTATE = 0 for an elastic state
   : MSTATE = 1 for a plastic state
4. Material constants
   E : Young's modulus E
   PNU : Poisson's ratio ν
   C : Cohesion c
   ALPHA : Drucker-Prager or Coulomb material constant α
   RK : Drucker-Prager or Coulomb material constant k
   PHI : Internal friction angle ϕ
5. Stress quantities
   SIGX : Stress σ_{11}
   SIGY : Stress σ_{22}
   SIGZ : Stress σ_{33}
   SIGXY : Stress σ_{12}
6. Stress quantities at previous step n
   PSIGX : Stress σ_{11}^{n}
   PSIGY : Stress σ_{22}^{n}
   PSIGZ : Stress σ_{33}^{n}
   PSIGXY : Stress σ_{12}^{n}
7. Strain increments
   EX : Strain increment $d\epsilon_{11}$
   EY : Strain increment $d\epsilon_{22}$
   EXY : Engineering shearing strain increment $d\gamma_{12}$
8. Index for yielding
   FN : $f^{n} = \alpha I_1^{n} + \sqrt{\bar{J}_2^{n}} - k$

INTERNAL VARIABLES

SI1 : First invariant of stress tensor I_1
SJ2 : Second invariant of deviatoric stress tensor J_2
SRJ2 : Square root of J_2
SJ3 : Third invariant of deviatoric stress tensor J_3
RODE : Lode angle θ
BMOD : Bulk modulus
SMOD : Shear modulus
DRAMDA : Proportionality factor $d\lambda$
TEST : Index in Eq. (7.54) to see if the plastic loading occurs for the element which was previously inelastic.

OUTPUT QUANTITIES

1. Yield status
   MSTATE

2. Scaled-back stresses
   SIGX, SIGY, SIGZ, SIGXY
3. Elastic or elastic-plastic constitutive matrix
   EPCM(4,3) for $[C^{e}]$ or $[C^{ep}]$
4. Index for yielding
   FN at the end of the $(n+1)$-th increment

In the following, the listing of SUBROUTINE CDPMDL is presented with some brief explanations that are related to the descriptions given in Sections 7.3.1 and 7.3.2.

```
00010       SUBROUTINE CDPMDL(KODEI,MAT,MSTATE,E,PNU,C,ALPHA,RK,PHI,SIGX,SIGY,
00020      &                  SIGZ,SIGXY,PSIGX,PSIGY,PSIGZ,PSIGXY,EX,EY,EXY,
00030      &                  FN,EPCM)
00040 C ***************************************************************************
00050 C *SUBROUTINE CDPMDL COMPUTES AN ELASTIC-PLASTIC CONSTITUTIVE MATRIX AT*
00060 C *MID INCREMENT OR NEXT INCREMENT                                       *
00070 C ***************************************************************************
00080 C
00090       DIMENSION EPCM(4,3),ECM(4,3),SN(3,3),SS(3,3)
00100 C
00110 C  ========================================================================
00120 C  COMPUTE VARIABLES RELATED TO THE DRUCKER-PRAGER OR COULOMB MATERIALS
00130 C  ========================================================================
00140 C
00150       SI1 =(SIGX+SIGY+SIGZ)
00160       P   =SI1/3.
00170       SJ2 =((SIGX-SIGY)**2+(SIGY-SIGZ)**2+(SIGZ-SIGX)**2)/6.+SIGXY**2
00180       SRJ2=SQRT(SJ2)
00190       BMOD=E/(3.*(1.-2.*PNU))
00200       SMOD=E/(2.*(1.+PNU))
00210 C
00220 C  IF COULOMB MATERIAL (MAT=1), THEN COMPUTE THE FOLLOWING VARIABLES
00230 C
00240       IF(MAT.NE.1) GO TO 1
00250       SJ3  =(SIGZ-P)*((SIGX-P)*(SIGY-P)-SIGXY**2)
00260       ARODE=1.0
00270       IF(SJ2.NE.0.) ARODE=1.5*SQRT(3.)*SJ3/(SJ2**1.5)
00280       IF(ABS(ARODE).GE.0.99999) ARODE=SIGN(1.,ARODE)
00290       RODE =ACOS(ARODE)/3.
00300       ALPHA=2.*SIN(PHI)/(3.*(1.-SIN(PHI))*SIN(RODE)+SQRT(3.)*
00310      &       (3.+SIN(PHI))*COS(RODE))
00320       RK   =6.*C*COS(PHI)/(3.*(1.-SIN(PHI))*SIN(RODE)+SQRT(3.)*
00330      &       (3.+SIN(PHI))*COS(RODE))
00340 C
00350 C  ========================================================================
00360 C  IF HYDROSTATIC PRESSURE EXCEEDS THE APEX OF YIELD SURFACE, THEN SHIFT
00370 C  HYDROSTATIC PRESSURE TO THE LEVEL CORRESPONDING TO THE APEX
00380 C  ------------------------------------------------------------------------
00390 C
00400 1     IF((-ALPHA*SI1+RK).GT.0.) GO TO 5
00410       TENI=RK/ALPHA-0.01
00420       SIGX=SIGX-(SI1-TENI)/3.
00430       SIGY=SIGY-(SI1-TENI)/3.
00440       SIGZ=SIGZ-(SI1-TENI)/3.
00450       SI1 =TENI
00460 C
00470 C  CHECK INCREMENT TYPE IF MID INCREMENT (KODEI=1) OR NEXT INCREMENT
00480 C  (KODEI=2)
00490 C
00500 5     IF(KODEI.EQ.2) GO TO 50
00510 C
00520 C  ========================================
00530 C  COMPUTE CONSTITUTIVE MATRIX AT MID-INCREMENT
00540 C  ----------------------------------------
00550 C
00560 C  CHECK FOR IF ELASTIC OR PLASTIC
```

```
00570 C
00580       IF(MSTATE.EQ.0) GO TO 45
00590 C
00600 C   ***** COMPUTATION FOR ELEMENT WHICH WAS PREVIOUSLY PLASTIC *****
00610 C
00620 C   COMPUTE STRESS INVARIANTS AT PREVIOUS STEP
00630 C
00640       PP   =(PSIGX+PSIGY+PSIGZ)/3.
00650       PSJ2 =((PSIGX-PSIGY)**2+(PSIGY-PSIGZ)**2+(PSIGZ-PSIGX)**2)/6.+
00660      &        PSIGXY**2
00670       PSRJ2=SQRT(PSJ2)
00680 C
00690 C   COMPUTE DEVIATORIC STRESSES
00700 C
00710       DSIGX =PSIGX-PP
00720       DSIGY =PSIGY-PP
00730       DSIGXY=PSIGXY
00740       DSIGZ =PSIGZ-PP
00750 C
00760 C   COMPUTE PROPORTIONALITY FACTOR TO CHECK PLASTIC UNLOADING FOR
00770 C   DRUCKER-PRAGER MODEL
00780 C
00790       EV  =EX+EY
00800       IF(MAT.EQ.1) GO TO 10
00810       DRAMDA=(3.*BMOD*ALPHA*EV+SMOD/PSRJ2*(DSIGX*EX+DSIGY*EY+
00820      &        DSIGXY*EXY))/(9.*BMOD*ALPHA*ALPHA+SMOD)
00830 C
00840 C   IF PROPORTIONALITY FACTOR HAS NEGATIVE VALUE, THEN ELEMENT HAS
00850 C   UNLOADED
00860 C
00870       IF(DRAMDA.GE.0.) GO TO 40
00880       CALL LINELS(BMOD,SMOD,EPCM)
00890       MSTATE=0
00900       RETURN
00910 C
00920 C   COMPUTE PROPORTIONALITY FACTOR TO CHECK PLASTIC UNLOADING FOR
00930 C   COULOMB MODEL
00940 C
00950 10    PSJ3 =(PSIGZ-PP)*((PSIGX-PP)*(PSIGY-PP)-PSIGXY**2)
00960       ARODE=1.5*SQRT(3.)*PSJ3/(PSJ2**1.5)
00970       IF(ABS(ARODE).GE.0.99999) GO TO 30
00980       RODE=ACOS(ARODE)/3.
00990       AN=SIN(PHI)
01000       BN=(3.*(1.-SIN(PHI))*SIN(RODE)+SQRT(3.)*(3.+SIN(PHI)))*
01010      &   COS(RODE))/(4.*SQRT(PSJ2))+3.*SQRT(3.)*PSJ3*(3.*(1.-SIN(PHI)))*
01020      &   COS(RODE)-SQRT(3.)*(3.+SIN(PHI))*SIN(RODE))/(8.*PSJ2*PSJ2*
01030      &   SIN(3.*RODE))
01040       CN=-SQRT(3.)*(3.*(1.-SIN(PHI))*COS(RODE)-SQRT(3.)*(3.+SIN(PHI)))*
01050      &   SIN(RODE))/(4.*PSJ2*SIN(3.*RODE))
01060       DO 15 I=1,3
01070       DO 15 J=1,3
01080 15    SN(I,J)=0.
01090       SN(1,1)=DSIGX
01100       SN(1,2)=DSIGXY
01110       SN(2,1)=SN(1,2)
01120       SN(2,2)=DSIGY
01130       SN(3,3)=DSIGZ
01140       DO 20 I=1,3
01150       DO 20 J=1,3
01160       SS(I,J)=0.
01170       DO 20 K=1,3
01180 20    SS(I,J)=SS(I,J)+SN(I,K)*SN(K,J)
01190       SSSS=0.
01200       DO 25 I=1,3
01210       DO 25 J=1,3
01220 25    SSSS=SSSS+SS(I,J)*SS(J,I)
01230       TX =SS(1,1)-2./3.*PSJ2
01240       TY =SS(2,2)-2./3.*PSJ2
01250       TZ =SS(3,3)-2./3.*PSJ2
01260       TXY=SS(1,2)
```

```
01270        H=9.*BMOD*AN*AN+4.*SMOD*PSJ2*BN*BN+12.*SMOD*PSJ3*BN*CN
01280       &  +2.*SMOD*(SSSS-4./3.*PSJ2*PSJ2)*CN*CN
01290        DRAMDA=(3.*BMOD*AN*EV+2.*SMOD*(BN*(DSIGX*EX+DSIGY*EY
01300       &        +DSIGXY*EXY)+CN*(TX*EX+TY*EY+TXY*EXY)))/H
01310        GO TO 35
01320 30     ARODE =SIGN(1.,ARODE)
01330        RODE  =ACOS(ARODE)/3.
01340        PALPHA=2.*SIN(PHI)/(3.*(1.-SIN(PHI))*SIN(RODE)+SQRT(3.)*
01350       &        (3.+SIN(PHI))*COS(RODE))
01360        DRAMDA=(3.*BMOD*PALPHA*EV+SMOD/PSRJ2*(DSIGX*EX+DSIGY*EY+
01370       &        DSIGXY*EXY))/(9.*BMOD*PALPHA*PALPHA+SMOD)
01380 C
01390 C   IF PROPORTIONALITY FACTOR HAS NEGATIVE VALUE, THEN ELEMENT HAS
01400 C   UNLOADED
01410 C
01420 35     IF(DRAMDA.GE.0.) GO TO 40
01430        CALL LINELS(BMOD,SMOD,EPCM)
01440        MSTATE=0
01450        RETURN
01460 C
01470 C   SCALE STRESSES BACK TO YIELD SURFACE
01480 C
01490 40     CALL SCALE(SIGX,SIGY,SIGZ,SIGXY,ALPHA,RK)
01500        CALL EPCDP(SIGX,SIGY,SIGZ,SIGXY,MAT,BMOD,SMOD,ALPHA,PHI,EPCM)
01510        RETURN
01520 C
01530 C   ***** COMPUTATION FOR ELEMENT WHICH WAS PREVIOUSLY ELASTIC *****
01540 C
01550 45     TEST=-FN+2.*(ALPHA*SI1+SRJ2-RK)
01560 C
01570 C   IF TEST IS NEGATIVE VALUE, THEN USE ELASTIC CONSTITUTIVE MATRIX
01580 C
01590        IF(TEST.LT.0.) RETURN
01600 C
01610 C   COMPUTE SCALING FACTOR, RATIO
01620 C
01630        RATIO=-FN/(2.*(ALPHA*SI1+SRJ2-RK-FN))
01640 C
01650 C   SCALE STRESSES BACK TO YIELD SURFACE, COMPUTE ELASTIC-PLASTIC
01660 C   CONSTITUTIVE MATRIX, AVERAGED MATRIX, SET MSTATE=1, AND RETURN TO
01670 C   MAIN PROGRAM
01680 C
01690        CALL SCALE(SIGX,SIGY,SIGZ,SIGXY,ALPHA,RK)
01700        CALL LINELS(BMOD,SMOD,ECM)
01710        CALL EPCDP(SIGX,SIGY,SIGZ,SIGXY,MAT,BMOD,SMOD,ALPHA,PHI,EPCM)
01720        CALL AVED(RATIO,EPCM,ECM)
01730        MSTATE=1
01740        RETURN
01750 C
01760 C   ======================================================
01770 C   COMPUTE CONSTITUTIVE MATRIX AT BEGINNING OF INCREMENT
01780 C   ======================================================
01790 C
01800 C   CHECK ELEMENT IF ELASTIC OR PLASTIC
01810 C
01820 50     IF(MSTATE.EQ.0) GO TO 55
01830 C
01840 C   ***** COMPUTATION FOR ELEMENT WHICH WAS PREVIOUSLY PLASTIC *****
01850 C
01860 C   SCALE STRESSES BACK TO YIELD SURFACE
01870 C
01880        CALL SCALE(SIGX,SIGY,SIGZ,SIGXY,ALPHA,RK)
01890        FN=0.
01900 C
01910 C   COMPUTE ELASTIC-PLASTIC CONSTITUTIVE MATRIX
01920 C
01930        CALL EPCDP(SIGX,SIGY,SIGZ,SIGXY,MAT,BMOD,SMOD,ALPHA,PHI,EPCM)
01940        RETURN
01950 C
01960 C   ***** COMPUTATION FOR ELEMENT WHICH WAS PREVIOUSLY ELASTIC *****
```

```
01970 C
01980 55     FN=ALPHA*SI1+SRJ2-RK
01990        IF((ALPHA*SI1+SRJ2-RK).LT.0.) RETURN
02000        MSTATE=1
02010 C
02020 C  SCALE STRESSES BACK TO YIELD SURFACE
02030 C
02040        CALL SCALE(SIGX,SIGY,SIGZ,SIGXY,ALPHA,RK)
02050        FN=0.
02060 C
02070 C  COMPUTE ELASTIC-PLASTIC CONSTITUTIVE MATRIX
02080 C
02090        CALL EPCDP(SIGX,SIGY,SIGZ,SIGXY,MAT,BMOD,SMOD,ALPHA,PHI,EPCM)
02100        RETURN
02110        END
```

A BRIEF EXPLANATION FOR LISTING

CDPMDL 150–330 This part is related to Step 1 where the first, second invariants of stress and deviatoric stress tensors I_1, J_2, and $\sqrt{J_2}$ are respectively computed as SI1, SJ2, and SRJ2. Also, compute the bulk modulus K as BMOD and shear modulus G as SMOD. For the Coulomb model, compute the third deviatoric stress invariant J_3 as SJ3, Lode angle θ as RODE, α as ALPHA, and k as RK.

CDPMDL 400–450 For the hydrostatic stress that exceeds the apex of the yield surface, shift this hydrostatic stress to the level of apex (Step 2).

CDPMDL 640–1510 This part treats the *Mid-Increment Computation* in Step 3 for an element which was *previously plastic*:

640–740 Setting stresses at the previous step as PSIGX, PSIGY, PSIGXY, PSIGZ, compute the mean normal stress $\frac{1}{3}I_1$ as PP, J_2'' as PSJ2, $\sqrt{J_2}''$ as PSRJ2, the deviatoric stresses s_{11}'', s_{22}'', s_{12}'', and s_{33}'' as DSIGX, DSIGY, DSIGXY, and DSIGZ.

790–900 Compute $d\lambda^{n+1/2}$ as DRAMDA for the *Drucker-Prager model*. If $d\lambda^{n+1/2} < 0$, assign the elastic constitutive matrix, set MSTATE = 0, and return to the main program. Otherwise, go to the Scaling Back Procedure.

950–1450 To compute $d\lambda^{n+1/2}$ for the *Coulomb model*, first compute A'', B'', and C'' as AN, BN, and CN, $s_{ik}''s_{kj}''s_{il}''s_{lj}''$ as SSSS and t_{ij}'' as TX, TY, TZ, and TXY. If $d\lambda^{n+1/2} < 0$, assign the elastic constitutive matrix, set MSTATE = 0, and return to the main program.

1490–1510 If $d\lambda^{n+1/2} > 0$ for both model cases, scale the stresses back to the yield surface, and construct the new elastic-plastic constitutive matrix.

CDPMDL 1550–1740 This part treats the *Mid-Increment Computation* in Step 4 for an element which was *previously elastic*:

	1550	Compute $f^{n+1} = f^n + 2(f^{n+1/2} - f^n)$ as TEST.
	1590–1740	If TEST < 0, return to the main program. Otherwise, scale stresses back to the yield surface, construct the elastic, elastic-plastic constitutive matrices and averaged matrix, set MSTATE = 1, and return to the main program.
CDPMDL	1880–1940	This part treats the *Full Increment Computation* in Step 3 for an element which was *previously plastic*.
CDPMDL	1980–2100	This part treats the *Full Increment Computation* in Step 4 for an element which was *previously elastic*.

(B) SUBROUTINE SCALE

INPUT QUANTITIES

1. Material constants
   ALPHA : Drucker-Prager or Coulomb material constant α
   RK : Drucker-Prager or Coulomb material constant k
2. Stress quantities
   SIGX, SIGY, SIGZ, SIGXY

INTERNAL VARIABLES

SRJ2, SI1, DSIGX, DSIGY, DSIGZ, DSIGXY
RATIO : Ratio of $[-\alpha I_1 + k]$ to current $\sqrt{J_2}$

OUTPUT QUANTITIES

1. Scaled-back stresses
   SIGX, SIGY, SIGZ, SIGXY

```
00010       SUBROUTINE SCALE(SIGX,SIGY,SIGZ,SIGXY,ALPHA,RK)
00020 C ***************************************************************
00030 C *SUBROUTINE SCALE SCALES STRESSES SUCH THAT MODIFIED STRESS STATE*
00040 C *LIES ON YIELD SURFACE                                          *
00050 C ***************************************************************
00060 C
00070 C  COMPUTE STRESS INVARIANTS I1, J2, AND DEVIATORIC STRESSES
00080 C
00090       SI1   =SIGX+SIGY+SIGZ
00100       SJ2   =((SIGX-SIGY)**2+(SIGY-SIGZ)**2+(SIGZ-SIGX)**2)/6.+SIGXY**2
00110       DSIGX =SIGX-SI1/3.
00120       DSIGY =SIGY-SI1/3.
00130       DSIGZ =SIGZ-SI1/3.
00140       DSIGXY=SIGXY
00150 C
00160 C  COMPUTE SCALING FACTOR
00170 C
00180       RATIO=(-ALPHA*SI1+RK)/SQRT(SJ2)
00190 C
00200 C  COMPUTE SCALED-BACK STRESSES
00210 C
00220       SIGX =DSIGX*RATIO+SI1/3.
00230       SIGY =DSIGY*RATIO+SI1/3.
00240       SIGZ =DSIGZ*RATIO+SI1/3.
00250       SIGXY=DSIGXY*RATIO
00260       RETURN
00270       END
```

A BRIEF EXPLANATION FOR LISTING

SCALE 90–140 Compute the stress invariants I_1, J_2 as SI1, SJ2, and also compute the deviatoric stresses s_{11}, s_{22}, s_{33}, and s_{12} as DSIGX, DSIGY, DSIGZ, and DSIGXY, respectively.

SCALE 180 Compute the scaling factor RATIO.

SCALE 220–260 Compute the scaled-back stresses and return to SUBROUTINE CDPMDL.

(C) SUBROUTINE LINELS

INPUT QUANTITIES

1. Material constants

BMOD : Bulk modulus

SMOD : Shear modulus

OUTPUT QUANTITIES

EPCM : linear elastic constitutive matrix $[4 \times 3]$ which is used to obtain the stress increments such as:

$$\begin{Bmatrix} d\sigma_{11} \\ d\sigma_{22} \\ d\sigma_{12} \\ d\sigma_{33} \end{Bmatrix} = \begin{bmatrix} K + \frac{4}{3}G & K - \frac{2}{3}G & 0 \\ K - \frac{2}{3}G & K + \frac{4}{3}G & 0 \\ 0 & 0 & G \\ K - \frac{2}{3}G & K - \frac{2}{3}G & 0 \end{bmatrix} \begin{Bmatrix} d\epsilon_{11} \\ d\epsilon_{22} \\ d\gamma_{12} \end{Bmatrix}$$

```
00010       SUBROUTINE LINELS(BMOD,SMOD,EPCM)
00020 C ************************************************************************
00030 C *SUBROUTINE LINELS COMPUTES LINEAR ELASTIC CONSTITUTIVE MATRIX UNDER*
00040 C *PLANE STRAIN CONDITION                                               *
00050 C ************************************************************************
00060 C
00070       DIMENSION EPCM(4,3)
00080 C
00090 C  COMPUTE COMPONENTS OF MATRIX EPCM
00100 C
00110       EPCM(1,1)=BMOD+4./3.*SMOD
00120       EPCM(1,2)=BMOD-2./3.*SMOD
00130       EPCM(1,3)=0.
00140       EPCM(2,1)=EPCM(1,2)
00150       EPCM(2,2)=EPCM(1,1)
00160       EPCM(2,3)=0.
00170       EPCM(3,1)=0.
00180       EPCM(3,2)=0.
00190       EPCM(3,3)=SMOD
00200       EPCM(4,1)=EPCM(1,2)
00210       EPCM(4,2)=EPCM(1,2)
00220       EPCM(4,3)=0.
00230       RETURN
00240       END
```

A BRIEF EXPLANATION FOR LISTING

LINELS 110–220 Construct the components of the linear elastic constitutive matrix $[4 \times 3]$ and return to SUBROUTINE CDPMDL.

(D) SUBROUTINE EPCDP

INPUT QUANTITIES

1. Material type

   MAT : MAT = 1 for the Coulomb material

   : MAT = 2 for the Drucker-Prager material

2. Material constants

   BMOD, SMOD, ALPHA, PHI

3. Stress quantities

   SIGX, SIGY, SIGZ, SIGXY

INTERNAL VARIABLES

SJ2, SRJ2, SI1, RODE

OUTPUT QUANTITIES

EPCM : The elastic-plastic constitutive matrix [4 × 3] which is used to obtain the stress increments such as:

$$\begin{Bmatrix} d\sigma_{11} \\ d\sigma_{22} \\ d\sigma_{12} \\ d\sigma_{33} \end{Bmatrix} = \begin{bmatrix} K+\frac{4}{3}G & K-\frac{2}{3}G & 0 \\ K-\frac{2}{3}G & K+\frac{4}{3}G & 0 \\ 0 & 0 & G \\ K-\frac{2}{3}G & K-\frac{2}{3}G & 0 \end{bmatrix} \begin{Bmatrix} d\epsilon_{11} \\ d\epsilon_{22} \\ d\gamma_{12} \end{Bmatrix}$$

$$- \frac{1}{H} \begin{bmatrix} H_{11}^2 & H_{11}H_{22} & H_{11}H_{12} \\ H_{22}H_{11} & H_{22}^2 & H_{22}H_{12} \\ H_{12}H_{11} & H_{12}H_{22} & H_{12}^2 \\ H_{33}H_{11} & H_{33}H_{22} & H_{33}H_{12} \end{bmatrix} \begin{Bmatrix} d\epsilon_{11} \\ d\epsilon_{22} \\ d\gamma_{12} \end{Bmatrix}$$

```
      SUBROUTINE EPCDP(SIGX,SIGY,SIGZ,SIGXY,MAT,BMOD,SMOD,ALPHA,PHI,
     &                 EPCM)
C ***************************************************************************
C *SUBROUTINE EPCDP COMPUTES ELASTIC-PLASTIC CONSTITUTIVE MATRIX UNDER*
C *PLANE STRAIN CONDITION                                              *
C ***************************************************************************
C
      DIMENSION S(3,3),SS(3,3),EPCM(4,3)
C
C  COMPUTE STRESS INVARIANTS
C
      SI1 =SIGX+SIGY+SIGZ
      SJ2 =((SIGX-SIGY)**2+(SIGY-SIGZ)**2+(SIGZ-SIGX)**2)/6.+SIGXY**2
      SRJ2=SQRT(SJ2)
C
C  COMPUTE DEVIATORIC STRESSES
C
      DSIGX =SIGX-SI1/3.
      DSIGY =SIGY-SI1/3.
      DSIGZ =SIGZ-SI1/3.
      DSIGXY=SIGXY
C
C  CHECK MATERIAL TYPE IF COULOMB (MAT=1) OR DRUCKER-PRAGER (MAT=2)
C
      IF(MAT.EQ.1) GO TO 1
```

```
00260 C
00270 C   ***** COMPUTE H, HX, HY, HZ, HXY FOR DRUCKER-PRAGER MATERIAL *****
00280 C
00290         H  =9.*BMOD*ALPHA**2+SMOD
00300         HX =3.*BMOD*ALPHA+SMOD/SRJ2*DSIGX
00310         HY =3.*BMOD*ALPHA+SMOD/SRJ2*DSIGY
00320         HZ =3.*BMOD*ALPHA+SMOD/SRJ2*DSIGZ
00330         HXY=SMOD/SRJ2*DSIGXY
00340         GO TO 25
00350 C
00360 C   ***** COMPUTE H, HX, HY, HZ, HXY FOR COULOMB MATERIAL *****
00370 C
00380 1       P    =SI1/3.
00390         SJ3  =(SIGZ-P)*((SIGX-P)*(SIGY-P)-SIGXY**2)
00400         ARODE=1.5*SQRT(3.)*SJ3/(SJ2**1.5)
00410         IF(ABS(ARODE).GT.0.99999) GO TO 20
00420         RODE=ACOS(ARODE)/3.
00430 C
00440 C   COMPUTE STIFFNESS COEFFICIENTS, A, B, AND C
00450 C
00460         AH=SIN(PHI)
00470         BH=(3.*(1.-SIN(PHI))*SIN(RODE)+SQRT(3.)*(3.+SIN(PHI))*
00480        &   COS(RODE))/(4.*SQRT(SJ2))+3.*SQRT(3.)*SJ3*(3.*(1.-SIN(PHI))*
00490        &   COS(RODE)-SQRT(3.)*(3.+SIN(PHI))*SIN(RODE))/(8.*SJ2*SJ2*
00500        &   SIN(3.*RODE))
00510         CH=-SQRT(3.)*(3.*(1.-SIN(PHI))*COS(RODE)-SQRT(3.)*(3.+SIN(PHI))*
00520        &   SIN(RODE))/(4.*SJ2*SIN(3.*RODE))
00530 C
00540 C   CONSTRUCT DEVIATORIC STRESS MATRIX S
00550 C
00560         DO 5 I=1,3
00570         DO 5 J=1,3
00580 5       S(I,J)=0.
00590         S(1,1)=DSIGX
00600         S(1,2)=DSIGXY
00610         S(2,1)=S(1,2)
00620         S(2,2)=DSIGY
00630         S(3,3)=DSIGZ
00640 C
00650 C   COMPUTE TWO-DIMENSIONAL MATRIX SS
00660 C
00670         DO 10 I=1,3
00680         DO 10 J=1,3
00690         SS(I,J)=0.
00700         DO 10 K=1,3
00710 10      SS(I,J)=SS(I,J)+S(I,K)*S(K,J)
00720 C
00730 C   COMPUTE SCALAR SSSS
00740 C
00750         SSSS=0.
00760         DO 15 I=1,3
00770         DO 15 J=1,3
00780 15      SSSS=SSSS+SS(I,J)*SS(J,I)
00790 C
00800 C   COMPUTE TX, TY, TZ, AND TXY
00810 C
00820         TX =SS(1,1)-2./3.*SJ2
00830         TY =SS(2,2)-2./3.*SJ2
00840         TZ =SS(3,3)-2./3.*SJ2
00850         TXY=SS(1,2)
00860 C
00870 C   COMPUTE H
00880 C
00890         H=9.*BMOD*AH*AH+4.*SMOD*SJ2*BH*BH+12.*SMOD*SJ3*BH*CH
00900        &  +2.*SMOD*(SSSS-4./3.*SJ2*SJ2)*CH*CH
00910 C
00920 C   COMPUTE HX, HY, HZ, AND HXY
00930 C
00940         HX =3.*BMOD*AH+2.*SMOD*(BH*DSIGX+CH*TX)
00950         HY =3.*BMOD*AH+2.*SMOD*(BH*DSIGY+CH*TY)
```

```
00960        HZ =3.*BMOD*AH+2.*SMOD*(BH*DSIGZ+CH*TZ)
00970        HXY=2.*SMOD*(BH*DSIGXY+CH*TXY)
00980        GO TO 25
00990 C
01000 C   COMPUTE H, HX, HY, HZ, HXY AT THE CORNER OF COULOMB MODEL
01010 C
01020 20     H  =9.*BMOD*ALPHA**2+SMOD
01030        HX =3.*BMOD*ALPHA+SMOD/SRJ2*DSIGX
01040        HY =3.*BMOD*ALPHA+SMOD/SRJ2*DSIGY
01050        HZ =3.*BMOD*ALPHA+SMOD/SRJ2*DSIGZ
01060        HXY=SMOD/SRJ2*DSIGXY
01070 C
01080 C   COMPUTE COMPONENTS OF MATRIX EPCM
01090 C
01100 25     EPCM(1,1)=BMOD+4./3.*SMOD-HX*HX/H
01110        EPCM(1,2)=BMOD-2./3.*SMOD-HX*HY/H
01120        EPCM(1,3)=-HX*HXY/H
01130        EPCM(2,1)=EPCM(1,2)
01140        EPCM(2,2)=BMOD+4./3.*SMOD-HY*HY/H
01150        EPCM(2,3)=-HY*HXY/H
01160        EPCM(3,1)=EPCM(1,3)
01170        EPCM(3,2)=EPCM(2,3)
01180        EPCM(3,3)=SMOD-HXY*HXY/H
01190        EPCM(4,1)=BMOD-2./3.*SMOD-HZ*HX/H
01200        EPCM(4,2)=BMOD-2./3.*SMOD-HZ*HY/H
01210        EPCM(4,3)=-HZ*HXY/H
01220        RETURN
01230        END
```

A BRIEF EXPLANATION FOR LISTING

ELSPLS 120 140 Compute the stress invariants, SI1, SJ2, SRJ2.

ELSPLS 180 210 Compute the deviatoric stresses, DSIGX, DSIGY, DSIGZ, DSIGXY.

ELSPLS 290 330 Compute H, H_{11}, H_{22}, H_{33}, H_{12} as H, HX, HY, HZ, HXY for the Drucker-Prager material.

ELSPLS 380 1060 Compute H, H_{11}, H_{22}, H_{33}, H_{12} for the Coulomb material:

380 420 Compute the mean normal stress p, the third deviatoric stress invariant J_3, and the Lode angle θ as P, SJ3, and RODE.

460 520 Compute the stiffness coefficients A, B, and C as AH, BH, and CH.

560 630 Construct the deviatoric stress matrix $[s_{ij}]$.

670 710 Construct the matrix for $s_{ik}s_{kj}$.

750 780 Compute the scalar $s_{ik}s_{kj}s_{il}s_{lj}$ as SSSS.

820 850 Compute t_{11}, t_{22}, t_{33}, and t_{12} as TX, TY, TZ, and TXY.

890 1060 Compute H, H_{11}, H_{22}, H_{33}, and H_{12} as H, HX, HY, HZ, and HXY.

ELSPLS 1100 1220 Construct the elastic-plastic constitutive matrix $[4 \times 3]$ for the plane strain condition and return to SUBROUTINE CDPMDL.

(E) SUBROUTINE AVED

INPUT QUANTITIES

1. Scaling factor

   RATIO : $-f''/|2(f''^{+1/2} - f'')|$

2. Elastic-plastic constitutive matrix

   EPCM : $[4 \times 3]$ matrix constructed in SUBROUTINE EPCDP.

3. Elastic constitutive matrix
   ECM : $[4 \times 3]$ matrix constructed in SUBROUTINE LINELS.

OUTPUT QUANTITIES

1. Averaged elastic-plastic constitutive matrix
   EPCM : $[4 \times 3]$ matrix calculated from $r[C^{e}] + (1 - r)[C^{ep}]$

```
00010       SUBROUTINE AVED(RATIO,EPCM,ECM)
00020 C ***************************************************************************
00030 C *SUBROUTINE AVED COMPUTES WEIGHTED AVERAGE OF ELASTIC AND ELASTIC-*
00040 C *PLASTIC CONSTITUTIVE MATRIX                                      *
00050 C ***************************************************************************
00060 C
00070       DIMENSION EPCM(4,3),ECM(4,3)
00080 C
00090 C  CONSTRUCT WEIGHTED AVERAGE OF ELASTIC AND ELASTIC-PLASTIC
00100 C  CONSTITUTIVE MATRIX
00110 C
00120       DO 1 I=1,4
00130       DO 1 J=1,3
00140 1     EPCM(I,J)=RATIO*ECM(I,J)+(1.-RATIO)*EPCM(I,J)
00150       RETURN
00160       END
```

A BRIEF EXPLANATION FOR LISTING

AVED 120 150 Using the elastic and elastic-plastic constitutive matrices, construct the averaged elastic-plastic matrix EPCM, and return to SUBROUTINE CDPMDL.

7.3.4 Utilization of the model subroutine

SUBROUTINE CDPMDL has been developed with the specific mid-point integration method, but it can also be used in finite-element programs that adopt other solution techniques such as the *direct incremental procedure* or the *iterative procedure*. In the following, we shall give a simple example to illustrate the application of the SUBROUTINE CDPMDL to the finite-element programs based on other integration techniques.

Consider an equilibrium state at a point inside the material after the n-th incremental step where the stress and strain states are respectively σ_{ij}^{n} and ϵ_{ij}^{n}. An integration procedure to estimate the stress state σ_{ij}^{n+1} corresponding to the strain state ϵ_{ij}^{n+1} after the $(n+1)$-th incremental step will now be explained:

Step 1: Divide the strain increments $d\epsilon_{ij}^{n+1}$ into several segments m, if the strain increments are not small enough.

Step 2: Obtain stress increments by applying a half of the divided strain increment, $\frac{1}{2}(d\epsilon_{ij}^{n+1}/m)$, to the current elastic or elastic-plastic constitutive matrix and add these stress increments to the current stress state.

Step 3: Set KODEI = 1 and call SUBROUTINE CDPMDL to correct the stress state and to estimate a new constitutive matrix.

Step 4: Obtain the stress increments from the latest constitutive matrix at Step 3 and the divided strain increments $d\epsilon_{ij}^{n+1}/m$. By adding these stress increments to the stress state at the beginning of Step 2, a new stress state can be estimated.

Step 5: Set KODEI = 2 and call SUBROUTINE CDPMDL to correct the stress state at Step 4 and to estimate the new constitutive matrix.

Step 6: Set stresses obtained at Step 5 as the new stress state. Repeat the same process from Step 2 to Step 5 until the stress state is renewed over the strain increments. Finally, set the renewed stress state as $\{\sigma\}^{n+1}$.

The process from Step 2 to Step 5 is in general the same as that for the mid-point integration method described in Section 7.3.1. Note that so integrated stress state does not always satisfy the equilibrium equations. In an iterative procedure, therefore, the new strain increments $d\epsilon_{ij}^{n+1}$ from an equilibrium state n are re-estimated at each iterative calculation and applied to obtain a new stress state through Step 1 to Step 6. The stress state $\{\sigma\}^n$ at the end of the n-th increment needs to be stored during an iterative calculation. This process will be continued until the equilibrium equations are satisfied within the acceptable tolerance. Finally, this currently satisfied stress state becomes $\{\sigma\}^{n+1}$ at the end of the $(n+1)$-th increment.

7.4 UNIAXIAL STRAIN BEHAVIOR: DEMONSTRATION OF SUBROUTINE CDPMDL

Using the SUBROUTINE CDPMDL, we shall demonstrate here the numerical analyses on uniaxial strain behaviors of the Prandtl-Reuss, Drucker-Prager and Coulomb materials, as being discussed previously in Examples 4.4 and 4.7, Chapter 4 for the Prandtl-Reuss and Drucker-Prager materials.

7.4.1 Initialization of input data

Initial stress and strain conditions: Here, the uniaxial strain behavior is analyzed for only one element, assuming the stress and strain conditions are uniform throughout the element. Also, the material is assumed to be initially elastic and stress and strain *free*, i.e., $\sigma_{11} = \sigma_{22} = \sigma_{33} = \sigma_{12} = 0$ and $\epsilon_{11} = \epsilon_{22} = \epsilon_{33} = \gamma_{12} = 0$:

MSTATE = 0

PSIGX = PSIGY = PSIGZ = PSIGXY = 0.

The strain increments $d\epsilon_{11}$, $d\epsilon_{22}$, and $d\gamma_{12}$ are respectively given by:

EX = $d\epsilon_{11}$

EY = 0.

EXY = 0.

Soil parameters: The following material constants of soil need to be given:

Angle of internal friction: PHI

Cohesion: C

Poisson's ratio: PNU

Young's modulus: E

Material type: Coulomb material (MAT = 1) or Drucker-Prager material (MAT = 2)

Calculation type: Mid-increment calculation KODEI = 1

Drucker-Prager material constants: The material constants α and k for the Drucker-Prager model can be determined in several ways from Eqs. (4.45), (4.46), and (4.57). For the three-dimensional matching with the compressive meridian of the Coulomb model, we have:

$$\alpha(=\text{ALPHA}) = \frac{2\sin\phi}{\sqrt{3}\,(3-\sin\phi)} \tag{7.60a}$$

and

$$k(=\text{RK}) = \frac{6c\cos\phi}{\sqrt{3}\,(3-\sin\phi)} \tag{7.60b}$$

For the three-dimensional matching with the tensile meridian of the Coulomb model, we have:

$$\alpha(=\text{ALPHA}) = \frac{2\sin\phi}{\sqrt{3}\,(3+\sin\phi)} \tag{7.61a}$$

and

$$k(=\text{RK}) = \frac{6c\cos\phi}{\sqrt{3}\,(3+\sin\phi)} \tag{7.61b}$$

For the plane strain matching with the Coulomb model having the same limit load, we have:

$$\alpha(=\text{ALPHA}) = \frac{\tan\phi}{\sqrt{9+12\tan^2\phi}} \tag{7.62a}$$

and

$$k(=\text{RK}) = \frac{3c}{\sqrt{9+12\tan^2\phi}} \tag{7.62b}$$

Stress quantities: The stress quantities such as SIGX, SIGY, SIGXY, and SIGZ needed in the SUBROUTINE CDPMDL can be calculated from the strain increments and elastic constitutive matrix.

Index for yielding: The initial values of FN for the Drucker-Prager and the Coulomb models are respectively set FN = $-$RK and FN = $-6c\cos\phi/\sqrt{3}(3-\sin\phi)$.

7.4.2 Calculation step

Our aim here is to find the stress increment of the element corresponding to a given strain increment, i.e., $d\epsilon_{ij} = [d\epsilon_1\ 0\ 0]$, under the uniaxial strain condition. A calculation step for the $(n+1)$-th increment is given below:

Step 1: Utilizing the initialized variables and applying a *half* of the full strain increment, $\frac{1}{2}d\epsilon_{11}$, compute stress increments $[d\sigma_{11}, d\sigma_{22}, d\sigma_{33}]$ from an elastic or elastic-plastic constitutive matrix (an elastic constitutive matrix is used at the beginning of the first increment from the initial free state) and also compute the stress states $[\sigma_{11}^{n+1/2}, \sigma_{22}^{n+1/2}, \sigma_{33}^{n+1/2}]$, for example, $\sigma_{11}^{n+1/2} = \sigma_{11}^{n} + d\sigma_{11}$, before going into the *mid-increment calculation* in SUBROUTINE CDPMDL.

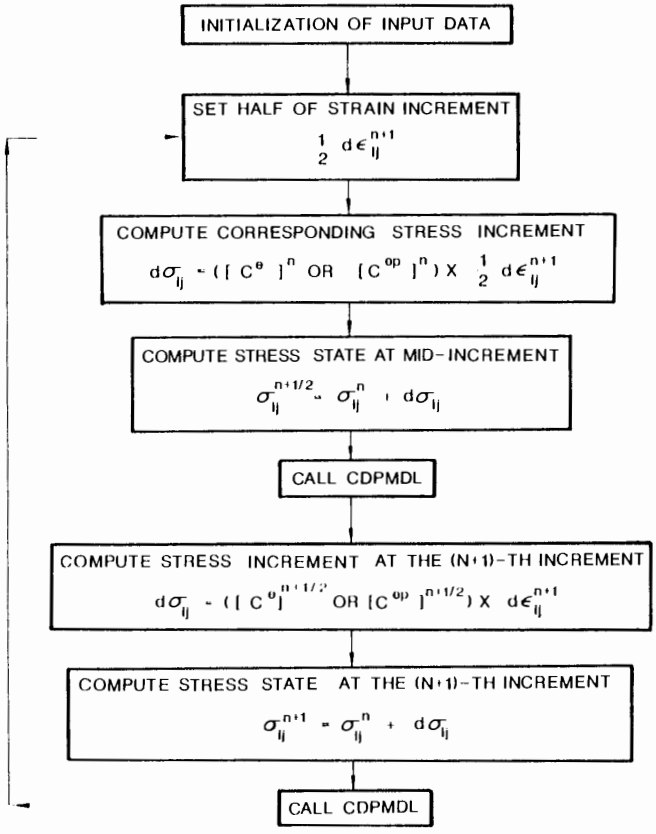

Fig. 7.9. Flow chart of strain control analysis.

Step 2: Set the material type MAT and the calculation type KODEI = 1 for the mid-increment calculation.

Step 3: Call SUBROUTINE CDPMDL and evaluate the constitutive matrix at the $(n + \frac{1}{2})$-th incremental step.

Step 4: Using the constitutive matrix at Step 3, compute the stress increments $[d\sigma_{11}, d\sigma_{22}, d\sigma_{33}]$ corresponding to the full strain increment $d\epsilon_{11}$ and also compute the stress state $[\sigma_{11}^{n+1}, \sigma_{22}^{n+1}, \sigma_{33}^{n+1}]$. Then, set the calculation type KODEI = 2.

Step 5: Call SUBROUTINE CDPMDL to modify the stress state σ_{ij}^{n+1} if necessary and evaluate the constitutive matrix after the $(n + 1)$-th incremental step.

Step 6: Using the element constitutive matrix evaluated in Step 5, repeat the same process from Step 1 to Step 5 until the incremental calculation is performed.

The flow chart for this calculation is summarized in Fig. 7.9.

7.4.3 Numerical results

In the following, we shall show the numerical results for the following three types of material models: the Prandtl-Reuss, Drucker-Prager, and Coulomb materials. The incremental value of the axial compressive strain, $d\epsilon_{11}$, is set to be -0.001%.

(A) Prandtl-Reuss material. First, we apply SUBROUTINE CDPMDL to the Prandtl-Reuss material (von Mises material). The material properties used are:

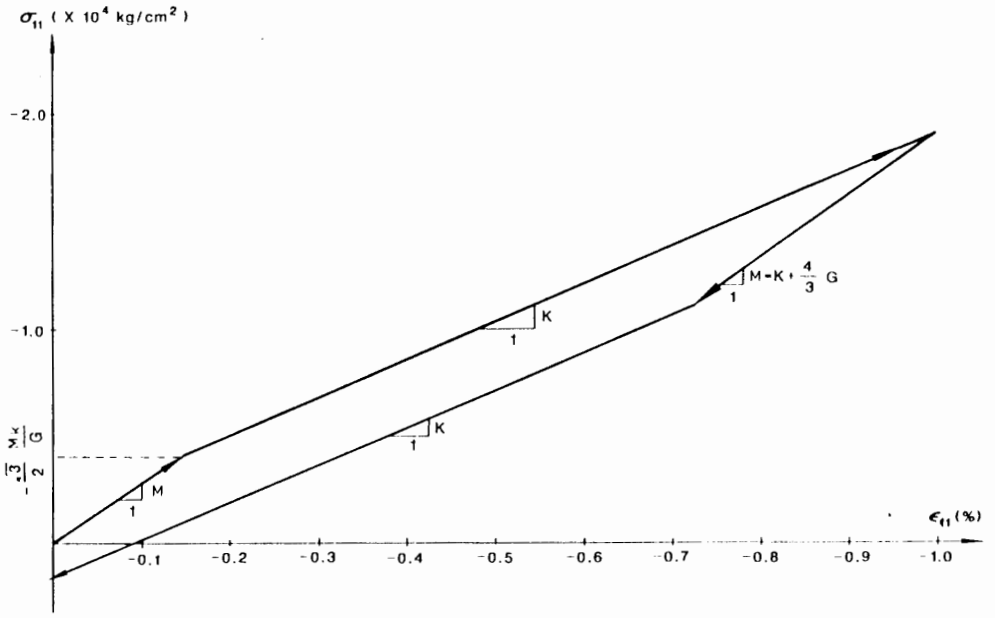

Fig. 7.10. Behavior of the Prandtl-Reuss material under the condition of uniaxial strain: vertical stress - strain relation.

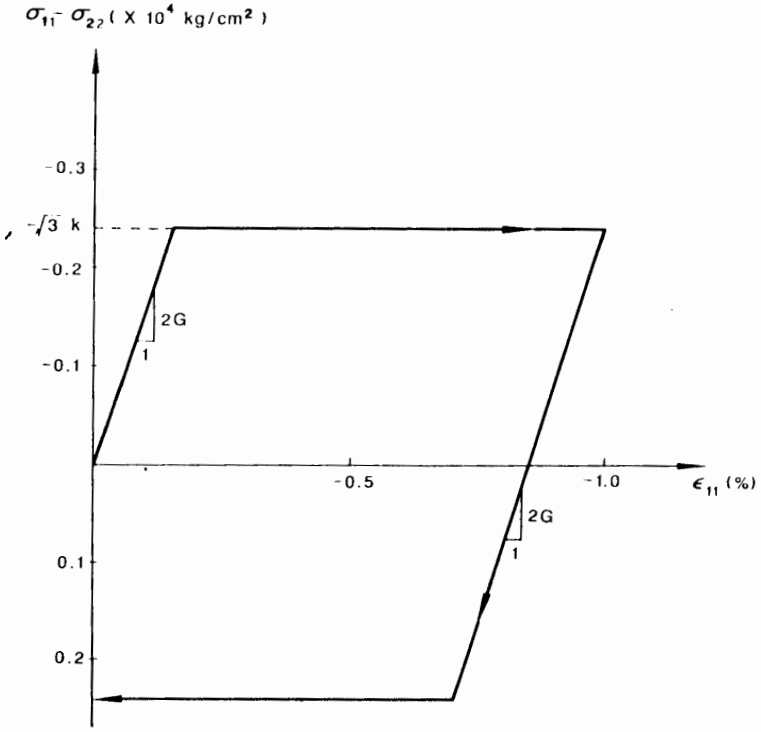

Fig. 7.11. Behavior of the Prandtl-Reuss material under the condition of uniaxial strain: principal stress difference–strain difference relation.

Yield stress $\sigma_y = 34{,}105$ psi (2400 kg/cm^2), (235.2 MPa)
Young's modulus $E = 29{,}842{,}000$ psi (2,100,000 kg/cm^2), (205,762 MPa)
Poisson's ratio $\nu = 0.3$.

Thus, the material constants α and k in the Drucker-Prager model are determined as:
$\alpha = 0$.
$k = \sigma_y/\sqrt{3} = 19{,}690.7$ psi (1,385.6 kg/cm^2), (135.8 MPa)

The axial stress-strain relation is presented in Fig. 7.10. The axial compressive strain ϵ_{11} is increased up to the level of -0.01 (-1%) and then decreased to the strain free state. The constrained modulus $M\,(= K + \frac{4}{3}G)$ and bulk modulus K are respectively obtained from the slopes in the elastic and in the plastic range. Similarly, the principal stress difference–strain difference relation, the hydrostatic pressure–volumetric strain relation, and the principal stress difference–hydrostatic pressure relation are respectively shown in Figs. 7.11, 7.12, and 7.13.

(B) Drucker-Prager material. The soil parameters used in this analysis are:
Internal friction angle $\phi = 5°$
Cohesion $c = 20$ psi (138kPa)
Young's modulus $E = 30{,}000$ psi (206.9 MPa)
Poisson's ratio $\nu = 0.3$

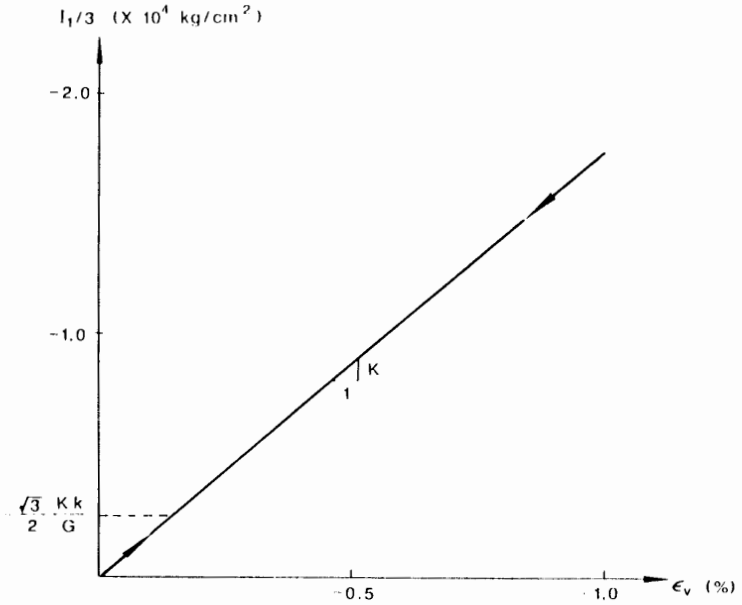

Fig. 7.12. Behavior of the Prandtl-Reuss material under the condition of uniaxial strain: hydrostatic pressure–volume strain relation.

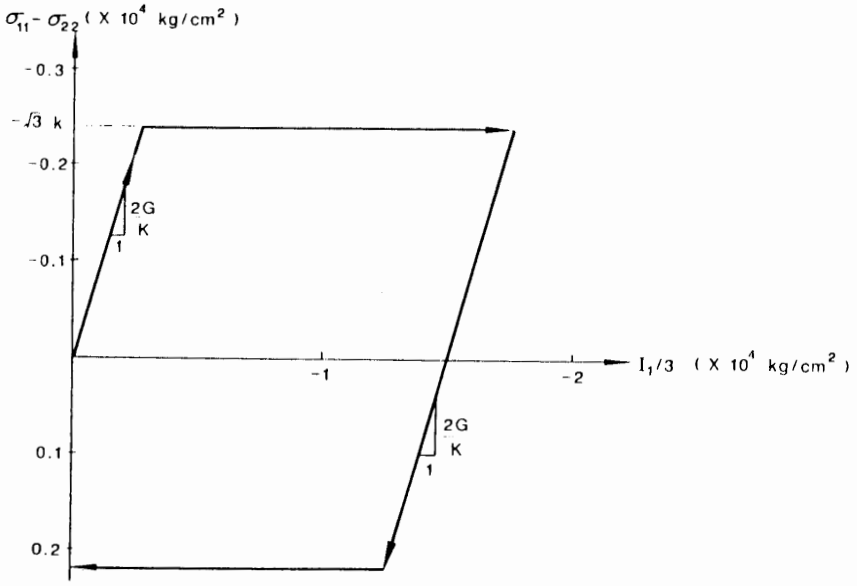

Fig. 7.13. Behavior of the Prandtl-Reuss material under the condition of uniaxial strain: principal stress difference–hydrostatic pressure relation.

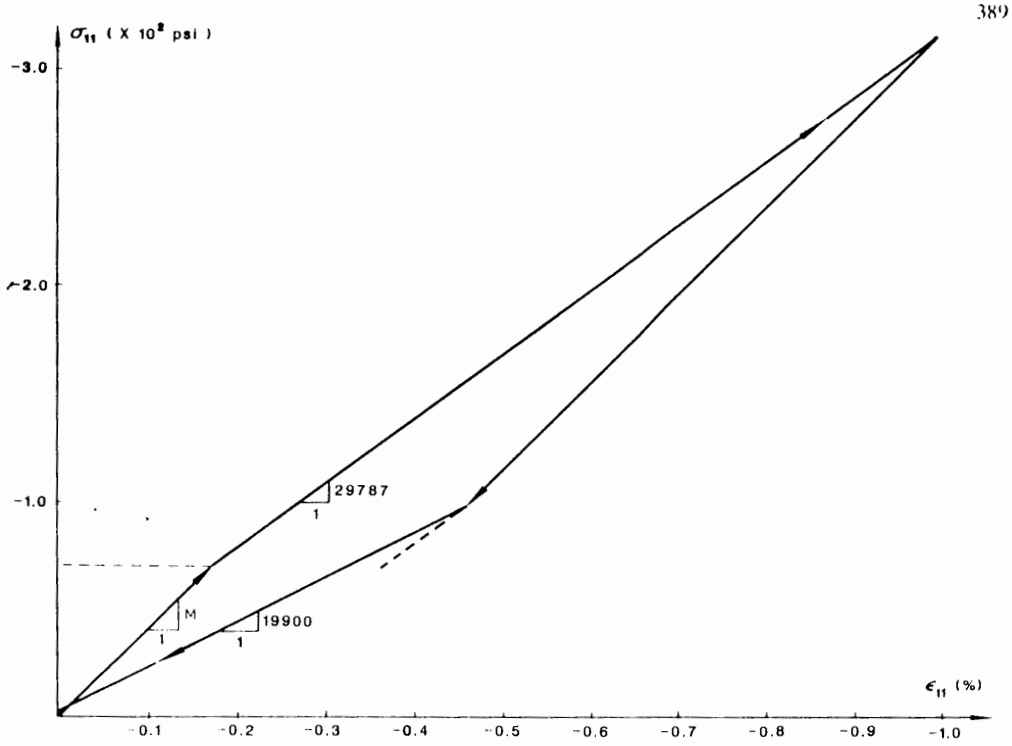

Fig. 7.14. Behavior of the Drucker-Prager material under the condition of uniaxial strain: vertical stress - strain relation.

We use the *plane strain matching* condition as given by Eqs. (7.62a) and (7.62b) for the determination of the two constants α and k:

$\alpha = 0.029$ and $k = 19{,}898$ psi

The axial stress-strain is shown in Fig. 7.14. In the initial elastic range, it is a straight line with the slope of the constrained modulus M. In the plastic range, the first and second slopes are respectively obtained from the numerical analysis as 29,787 psi (205 MPa) and 19,900 psi (137 MPa). These values are the same as those determined from Eq. (4.139). The principal stress difference - strain difference relation, the hydrostatic pressure - volumetric strain relation, and the principal stress difference - hydrostatic pressure relation are respectively shown in Figs. 7.15 through 7.17.

(C) Coulomb materials. The same soil parameters as in the Drucker-Prager material are utilized here. The first and second plastic slopes of the axial stress-strain relation in Fig. 7.18 are found respectively identical with the plastic slopes predicted by the Drucker-Prager model with the material constants that are matched each other along the compressive and tensile meridians of the Coulomb model, respec-

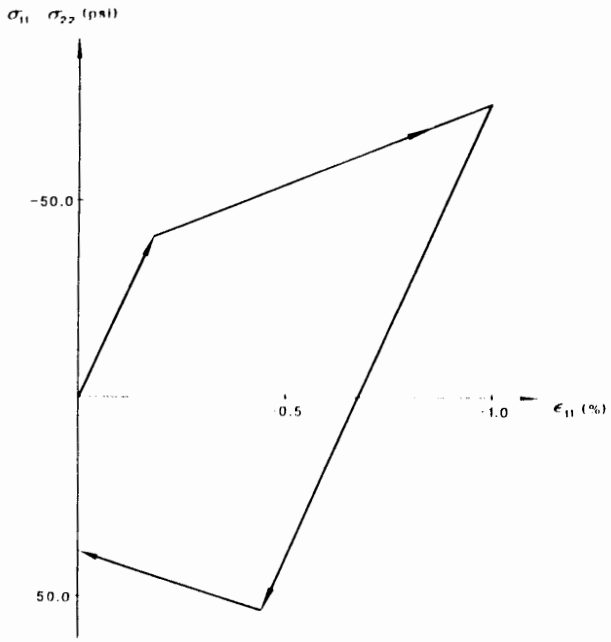

Fig. 7.15. Behavior of the Drucker-Prager material under the condition of uniaxial strain: principal stress difference–strain difference relation.

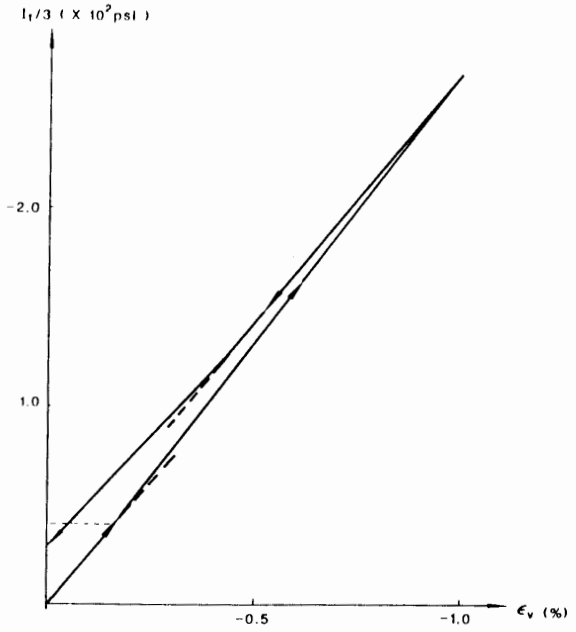

Fig. 7.16. Behavior of the Drucker-Prager material under the condition of uniaxial strain: hydrostatic pressure-volumetric strain relation.

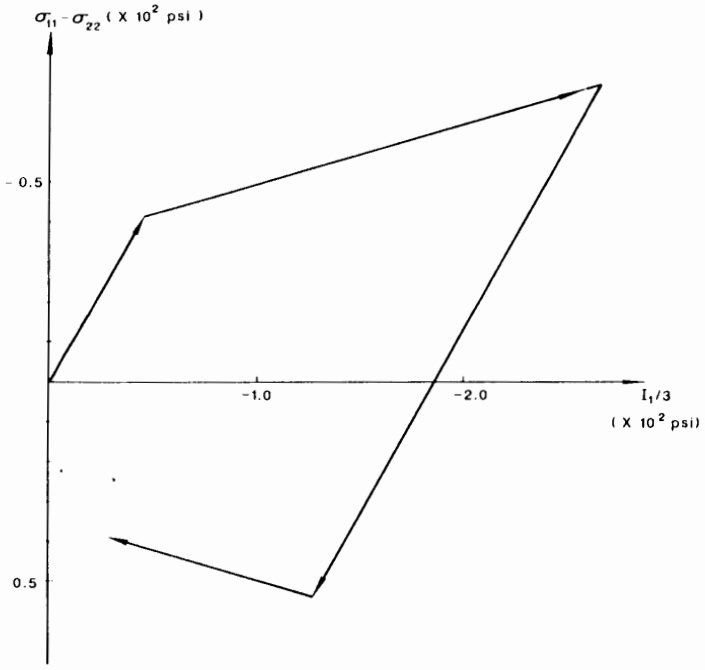

Fig. 7.17. Behavior of the Drucker-Prager material under the condition of uniaxial strain: principal stress difference-hydrostatic pressure relation.

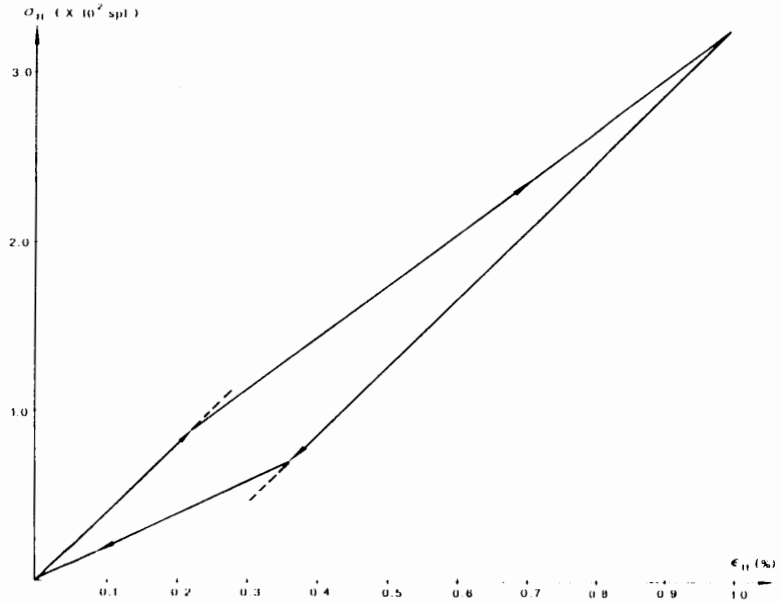

Fig. 7.18. Behavior of the Coulomb material under the condition of uniaxial strain: vertical stress - strain relation.

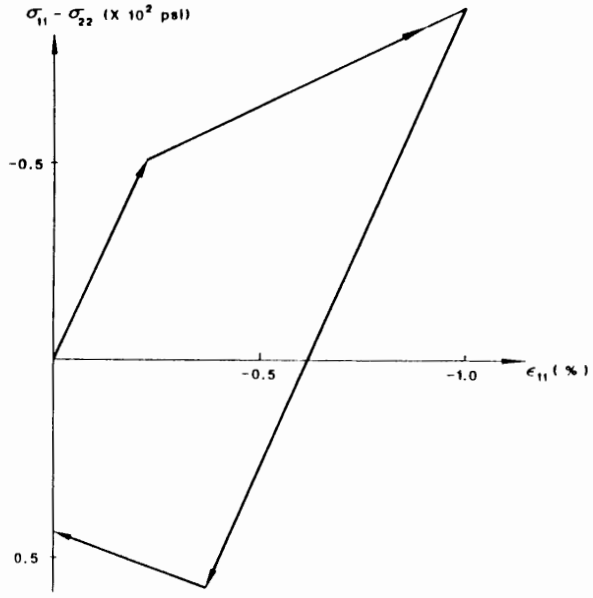

Fig. 7.19. Behavior of the Coulomb material under the condition of uniaxial strain: principal stress difference–strain difference relation.

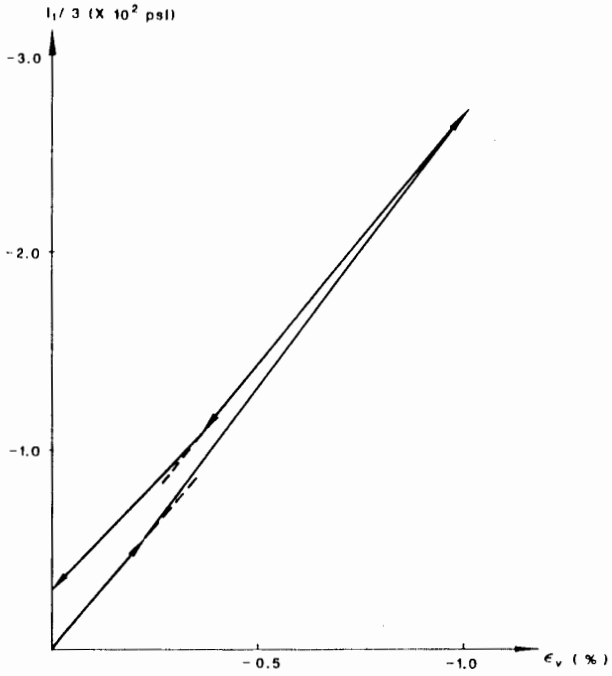

Fig. 7.20. Behavior of the Coulomb material under the condition of uniaxial strain: hydrostatic pressure–volumetric strain relation.

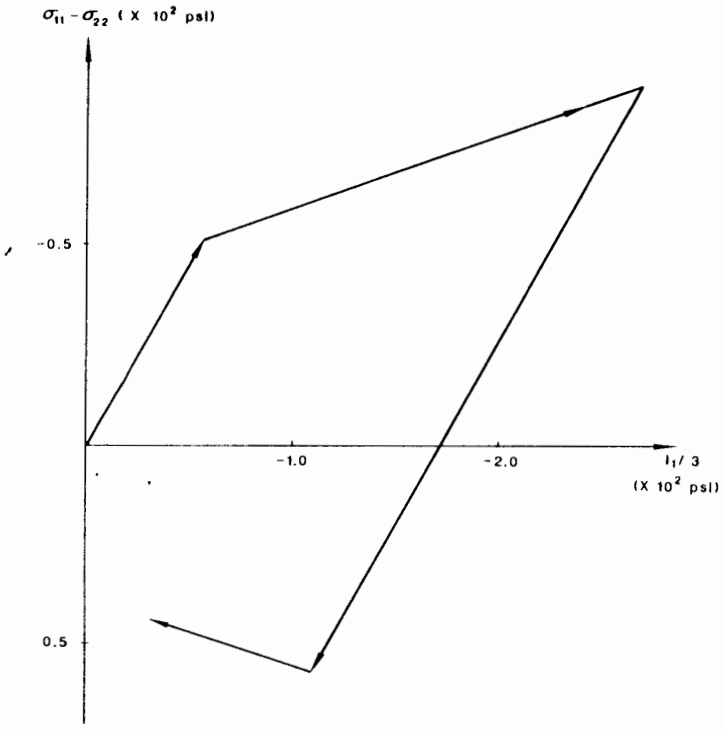

Fig. 7.21. Behavior of the Coulomb material under the condition of uniaxial strain: principal stress difference - hydrostatic pressure relation.

tively. This is because the stress state under the uniaxial strain condition is σ_{11} and $\sigma_{22} = \sigma_{33}$, so the stress state first moves on the *compressive meridian* for the first yielding and then on the *tensile meridian* for the second yielding. This leads of course to the corner singularity during the analysis that requires the use of the Drucker-Prager equation to be matched respectively with the compressive and tensile meridians of the Coulomb model. The principal stress difference - strain difference relation, the hydrostatic pressure - volumetric strain relation, and the principal stress difference - hydrostatic pressure relation are respectively shown in Figs. 7.19 through 7.21.

7.5 IMPLEMENTATION OF CAP MODELS

In this Section, the finite-element implementation of the *strain-hardening cap model* with either an elliptic or a plane cap will be presented in some details. Chen and Baladi (1985), and Sandler and Rubin (1979) suggested a procedure for implementing the cap model. Their suggested procedure will be given below. Here, as in the Coulomb and Drucker-Prager model subroutine, the *input quantities* are

the current stress components σ_{ij}^n, the hardening parameters $l^n(\epsilon_{ij}^p)$ and $x^n(\epsilon_{ij}^p)$ that have been obtained at the end of the n-th load or displacement increment, and the components of the new strain increment $d\epsilon_{ij}^{n+1}$ that are just obtained from the current finite element calculation.

The main purpose of the cap model subroutine is to determine the new stress components σ_{ij}^{n+1} for the new strain components $(\epsilon_{ij}^n + d\epsilon_{ij}^{n+1})$, and if necessary, the hardening parameter x^{n+1}.

7.5.1 Loading functions

At the end of the n-th incremental step, the cap model has the following loading functions.

(1) Drucker-Prager failure function

$$f_f = \alpha I_1 + \sqrt{J_2} - k \tag{7.63}$$

(2) Cap hardening function

The *elliptic* cap function is generally written as:

$$f_c = (I_1 - l^n)^2 + R^2 J_2 - (x^n - l^n)^2 \tag{7.64a}$$

where x^n is the cap location on the I_1-axis:

$$x^n = \frac{1}{D} \ln(1 + \epsilon_v^p / W) \tag{7.64b}$$

in which W and D are material parameters, ϵ_v^p is a history-dependent functional of the plastic volumetric strain, and its differential functional relation is given by:

$$d\epsilon_v^p = d\epsilon_v^p \quad \text{if } d\epsilon_v^p \leq 0, \quad \text{or } l^n < I_1 \quad \text{and } l^n < 0$$

$$= 0 \quad \text{otherwise} \tag{7.65}$$

Thus, if dilatancy occurs when $I_1 > 0$ (in a tension region), the contraction of the cap is limited to $l = 0$. The elliptic cap function in Eq. (7.64a) is valid as long as l^n is *negative* (in compression). In this case, the cap is called the *large cap*.

On the other hand, if l^n is *positive*, to avoid a plastic compaction in the tension region, a modified *small* cap function is assumed in the compression region by the introduction of the *von Mises yield function* in the tension region, as shown in Fig. 7.22. These are:

$$f_c = I_1^2 + R^2 J_2 - (x^n)^2 \tag{7.66a}$$

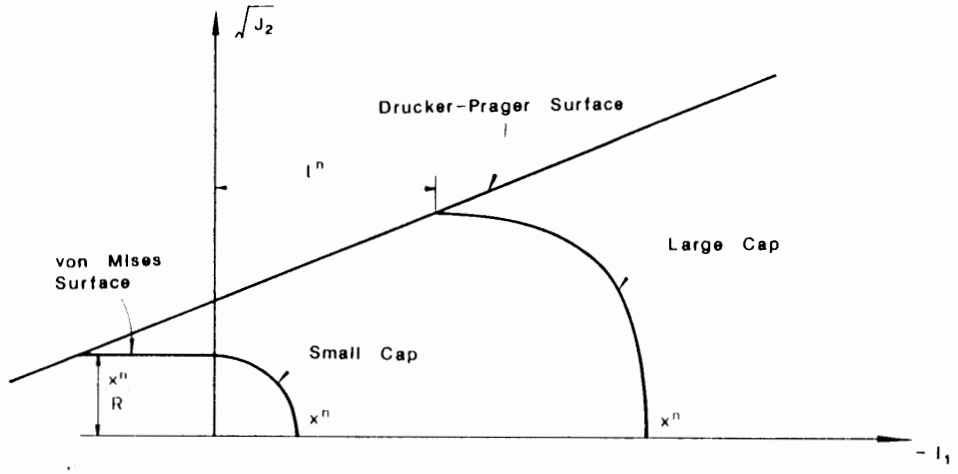

Fig. 7.22. Large cap and small cap surfaces.

and

$$f_m = \sqrt{J_2} + x^n/R \tag{7.66b}$$

Thus, the elliptic cap function f_c for both large and small caps can be written in the general form:

$$f_c = \left[I_1 - L(l^n)\right]^2 + R^2 J_2 - \left[x^n - L(l^n)\right]^2 \tag{7.67}$$

where $L(l) = l$ for $l < 0$ and $L(l) = 0$ for $l > 0$.

The *plane* cap function is a special case of the elliptic cap with $R = 0$:

$$f_c = I_1 - x^n \tag{7.68}$$

In this case, the plane cap cannot move back into the tension region.

(3) Tension cut-off function

$$f_t = I_1 \quad T \tag{7.69}$$

where T is the tensile strength of soils.

7.5.2 Elastic trial stresses

As the first step toward the determination of the new stress state σ_{ij}^{n+1}, the *elastic trial stresses* σ_{ij}^e and the *elastic trial deviatoric stresses* s_{ij}^e are computed as:

$$\sigma_{ij}^{e} = \sigma_{ij}^{n} + 2G\,\mathrm{d}e_{ij}^{n+1} + K\,\mathrm{d}\epsilon_{kk}^{n+1}\delta_{ij} \tag{7.70a}$$

$$s_{ij}^{e} = s_{ij}^{n} + 2G\,\mathrm{d}e_{ij}^{n+1} \tag{7.70b}$$

where σ_{ij}^{n}, s_{ij}^{n}, K, G, $\mathrm{d}\epsilon_{kk}^{n+1}$, and $\mathrm{d}e_{ij}^{n+1}$ are respectively the stress tensor, deviatoric stress tensor at the end of the n-th increment, bulk modulus, shear modulus, volumetric strain increment and deviatoric strain increments corresponding to the $(n+1)$-th increment. The bulk and shear moduli are assumed to be constant during the $(n+1)$-th incremental step, even if nonlinear elastic moduli are employed.

The related *trial stress invariants* I_1^e and J_2^e are expressed by:

$$I_1^{e} = \sigma_{11}^{e} + \sigma_{22}^{e} + \sigma_{33}^{e} \tag{7.71a}$$

$$J_2^{e} = \tfrac{1}{2} s_{ij}^{e} s_{ij}^{e} \tag{7.71b}$$

Since the cap model (elliptic cap or plane cap) has several loading surfaces such as the Drucker-Prager failure surface, the cap hardening surface and the tension cut-off limit plane, as shown in Fig. 7.23, the elastic trial stress invariants must be checked against each of these loading surfaces in $I_1 - \sqrt{J_2}$ space. In what follows, we shall explain the details of the finite element codings of the cap model: including *elastic coding*, *yield surface coding*, *hardening surface coding*, *corner coding*, and *tensile coding*, according to several possible elastic trial stress paths (Mizuno, 1981).

Here, as in Section 7.4, if the strain increments $\mathrm{d}\epsilon_{ij}^{n+1}$ are relatively large, we should split the given strain increments into several equal increments and sequentially go through the numerical algorithm several times, using the updated variables each time.

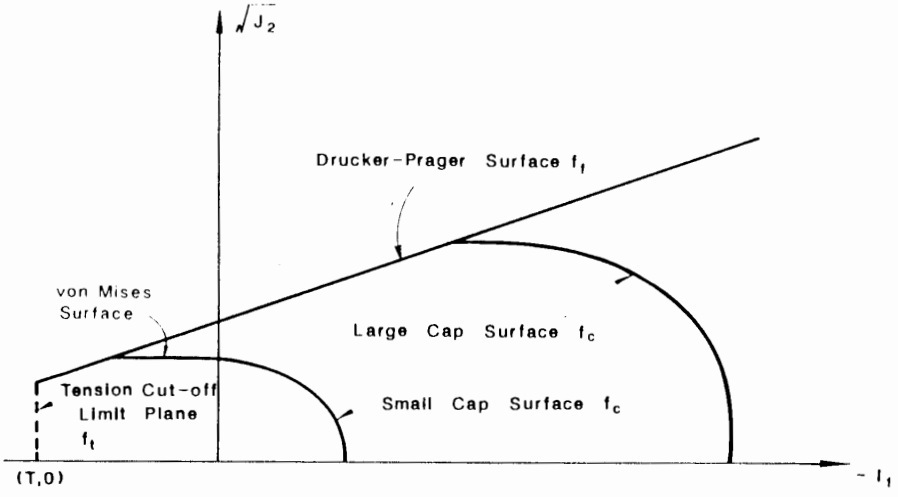

Fig. 7.23. Loading functions of cap model.

7.5.3 Elastic coding

If the trial stresses do not violate any of the loading functions, the stress state is within the following current loading surfaces:

$$f_f = \alpha I_1^e + \sqrt{J_2}^e - k < 0 \quad \text{or } f_m = \sqrt{J_2}^e + x^n/R < 0 \tag{7.72a}$$

$$f_c = f_c\left[I_1^e, \sqrt{J_2}^e, x^n\left(\epsilon_{ij}^p\right)\right] < 0 \tag{7.72b}$$

$$f_t = I_1^e - T < 0 \tag{7.72c}$$

where f_f, f_m, f_c, and f_t are respectively the Drucker-Prager failure, von Mises failure, hardening cap, and tension cut-off functions, and T is the tension limit strength. The behavior of the element is assumed to be truly elastic as shown in Fig. 7.24. The hardening parameter x^n remains unchanged, since the plastic strain increments $d\epsilon_{ij}^p$ have not been introduced during this incremental step. Thus, the final stresses σ_{ij}^{n+1} and stress invariants at the end of the $(n+1)$-th increment are written directly as:

$$\sigma_{ij}^{n+1} = \sigma_{ij}^e \tag{7.73a}$$

$$I_1^{n+1} = I_1^e \tag{7.73b}$$

$$J_2^{n+1} = J_2^e \tag{7.73c}$$

For the next incremental calculation, the *elastic* constitutive matrix $[C^e]$ in Eq. (7.45) is assigned.

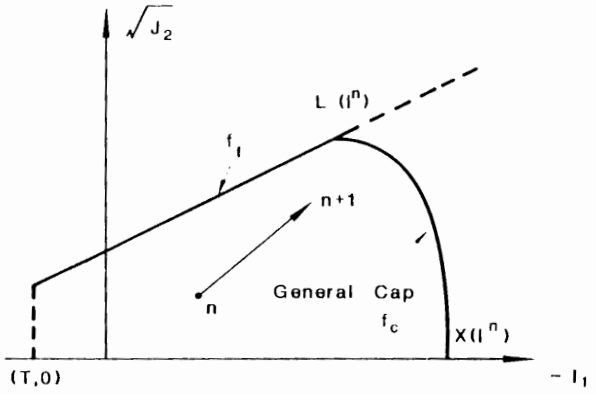

Fig. 7.24. Elastic coding.

7.5.4 *Yield surface coding*

In this coding, several possible cases for the elastic trial stress path need to be considered, particularly with respect to the condition of $l'' < 0$ or $l'' > 0$.

(A) Case for $l'' < 0$. If the yield surface f_f is violated by the elastic trial stresses as shown in Fig. 7.25, we have the conditions:

$$I_1^e \geq L(l'') = l'' \tag{7.74a}$$

and

$$f_f\left(I_1^e, \sqrt{J_2}^e\right) \geq 0 \tag{7.74b}$$

Then, the trial stresses σ_{ij}^e need to be corrected such that the final stresses at the end of the $(n+1)$-th increment satisfy the yield condition, that is, $f_f(I_1^{n+1}, \sqrt{J_2}^{n+1}) = 0$.

Since the elastic trial stresses lie outside the yield surface, the deviation of the elastic trial stresses from the yield surface ($f_f = 0$) is $f_f(I_1^e, \sqrt{J_2}^e)$ under the assumption of a small strain increment. On the other hand, the consistency condition $df_f = 0$ requires that:

$$df = \frac{\partial f_f}{\partial \sigma_{ij}} d\sigma_{ij} = \frac{\partial f_f}{\partial \sigma_{ij}} C_{ijkl}^e (d\epsilon_{kl} - d\epsilon_{kl}^p) \tag{7.75}$$

where C_{ijkl}^e is the elastic constitutive tensor. Noting that $C_{ijkl}^e d\epsilon_{kl}$ corresponds to the elastic trial stress increment $d\sigma_{ij}^e$ and also $d\epsilon_{ij}^p$ can be determined by the

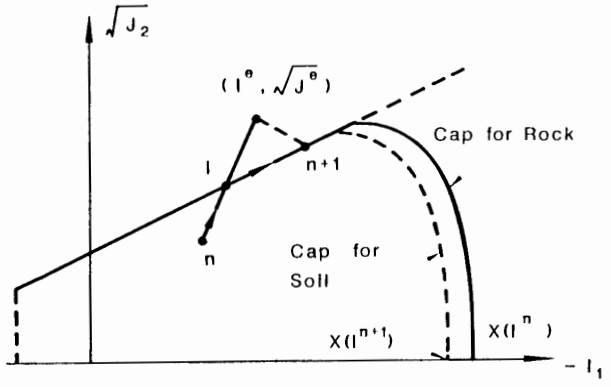

Fig. 7.25. Yield surface coding (A) — case for $l'' < 0$ with yield surface violation.

associated flow rule $d\lambda(\partial f_t/\partial \sigma_{ij})$, the proportionality factor $d\lambda$ can therefore be solved from the consistency condition (7.75):

$$d\lambda = \frac{(\partial f_t/\partial \sigma_{ij})\, d\sigma_{ij}^e}{(\partial f_t/\partial \sigma_{kl}) C_{klmn}^e (\partial f_t/\partial \sigma_{mn})} \tag{7.76}$$

Since $(\partial f_t/\partial \sigma_{ij}) d\sigma_{ij}^e$ is identical to the elastic stress deviation from the yield surface, $f_t(I_1^e, \sqrt{J_2}^e)$, $d\lambda$ can also be expressed by:

$$d\lambda = \frac{f_t\left(I_1^e, \sqrt{J_2}^e\right)}{(\partial f_t/\partial \sigma_{kl}) C_{klmn}^e (\partial f_t/\partial \sigma_{mn})} \tag{7.77}$$

Substituting $d\lambda$ into the associated flow rule $d\lambda(\partial f_t/\partial \sigma_{ij})$, the plastic strain increment $d\epsilon_{ij}^p$ can be estimated as:

$$d\epsilon_{ij}^p = \frac{f_t\left(I_1^e, \sqrt{J_2}^e\right)}{(\partial f_t/\partial \sigma_{kl}) C_{klmn}^e (\partial f_t/\partial \sigma_{mn})} \frac{\partial f_t}{\partial \sigma_{ij}} \tag{7.78}$$

It should be noted that if the stresses σ_{ij}^n are within the yield surfaces f_t, the calculation of $d\epsilon_{ij}^p$ should be made with the stresses that lie on the yield surface, as represented by the point I in Fig. 7.25. Consequently, the corresponding stress increments $d\sigma_{ij}^{n+1}$ are calculated by:

$$d\sigma_{ij}^{n+1} = K\left(d\epsilon_{kk}^{n+1} - d\epsilon_{kk}^p\right)\delta_{ij} + 2G\left(de_{ij}^{n+1} - de_{ij}^p\right) \tag{7.79}$$

where $d\epsilon_{kk}^p$ and de_{ij}^p are the increments of the plastic volumetric strain and the plastic deviatoric strain tensors, respectively.

Finally, the hardening parameter l^n, that depends only on the plastic volumetric strain, can be updated by the mathematically simple expansion of l^{n+1} about the current value l^n:

$$l^{n+1} = l^n + \left.\frac{\partial l}{\partial \epsilon_{kk}^p}\right|_{l^n} d\epsilon_{kk}^p \tag{7.80}$$

This is the *yield surface coding* for materials like *soil* for which the hardening cap is allowed to move back toward the origin. If $l^{n+1} > 0$, we set $l^{n+1} = 0$. If $L(l^{n+1}) > I_1^{n+1}$, we must use the *corner coding*. The corner coding will be discussed in details in Section 7.5.5.

On the other hand, for the material like *rock* where the hardening cap is not permitted to move back toward the origin, the hardening parameter l^n is simply set as:

$$l^{n+1} = l^n \tag{7.81}$$

For the next incremental calculation, the following *elastic-plastic constitutive matrix* of the Drucker-Prager failure surface is assigned:

$$[C^{ep}] = [C^{e}] - [C^{p}] \tag{7.82a}$$

where $[C^{e}]$ is the elastic constitutive matrix in Eq. (7.45), and $[C^{p}]$ is the plastic matrix given by:

$$[C^{p}] = \frac{1}{H}\begin{bmatrix} H_{11}^2 & H_{11}H_{22} & H_{11}H_{33} & H_{11}H_{12} & H_{11}H_{23} & H_{11}H_{31} \\ H_{22}H_{11} & H_{22}^2 & H_{22}H_{33} & H_{22}H_{12} & H_{22}H_{23} & H_{22}H_{31} \\ H_{33}H_{11} & H_{33}H_{22} & H_{33}^2 & H_{33}H_{12} & H_{33}H_{23} & H_{33}H_{31} \\ H_{12}H_{11} & H_{12}H_{22} & H_{12}H_{33} & H_{12}^2 & H_{12}H_{23} & H_{12}H_{31} \\ H_{23}H_{11} & H_{23}H_{22} & H_{23}H_{33} & H_{23}H_{12} & H_{23}^2 & H_{23}H_{31} \\ H_{31}H_{11} & H_{31}H_{22} & H_{31}H_{33} & H_{31}H_{12} & H_{31}H_{23} & H_{31}^2 \end{bmatrix} \tag{7.82b}$$

in which:

$$H_{11} = 3K\alpha + Gs_{11}^{n+1}/\sqrt{J_2}^{n+1} \tag{7.82c}$$

$$H_{22} = 3K\alpha + Gs_{22}^{n+1}/\sqrt{J_2}^{n+1} \tag{7.82d}$$

$$H_{33} = 3K\alpha + Gs_{33}^{n+1}/\sqrt{J_2}^{n+1} \tag{7.82e}$$

$$H_{12} = Gs_{12}^{n+1}/\sqrt{J_2}^{n+1} \tag{7.82f}$$

$$H_{23} = Gs_{23}^{n+1}/\sqrt{J_2}^{n+1} \tag{7.82g}$$

$$H_{31} = Gs_{31}^{n+1}/\sqrt{J_2}^{n+1} \tag{7.82h}$$

$$H = 9K\alpha^2 + G \tag{7.82i}$$

(B) Case for $l^n > 0$. If I_1^e is in the tension region and violates the von Mises yield surface as shown in Fig. 7.26, we have the conditions:

$$I_1^e \geq L(l^n) = 0 \tag{7.83a}$$

and

$$f_m\left(\sqrt{J_2}^{e}\right) \geq 0 \tag{7.83b}$$

The elastic trial stresses σ_{ij}^e are scaled back such that the corrected stress state lies

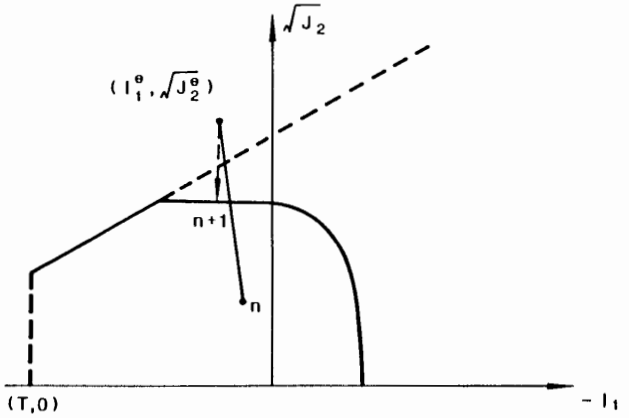

Fig. 7.26. Yield surface coding (B)—case for $l'' > 0$ with von Mises yield surface violation.

on the von Mises yield surface, keeping I_1^c unchanged. The scaling factor r is given by:

$$r = -\frac{\kappa''/R}{\sqrt{J_2}^c} \tag{7.84}$$

where $-\kappa''/R$ is the magnitude of $\sqrt{J_2}$ of the current von Mises yield surface. Thus, the final stress state at the end of the $(n+1)$-th increment becomes:

$$\sigma_{ij}^{n+1} = rs_{ij}^c + \tfrac{1}{3} I_1^c \delta_{ij} \tag{7.85}$$

Since the plastic volumetric strain increment is not allowed, the cap parameter l'' or $L(l'')$ need not be renewed. For this case, the *elastic-plastic constitutive matrix* of von Mises type is assigned to the element. The matrix is obtained directly by substituting $\alpha = 0$ in Eq. (7.82).

On the other hand, if the elastic trial stresses violate the Drucker-Prager failure surface, as shown in Fig. 7.27:

$$I_1^c > L(l'') = 0 \tag{7.86a}$$

and

$$f_1\left(I_1^c, \sqrt{J_2}^c\right) \geq 0 \tag{7.86b}$$

a similar procedure to the case of $l'' < 0$ can be utilized. However, the final cap surface and von Mises yield surface need not be corrected because $d\epsilon_v^p = 0$. The

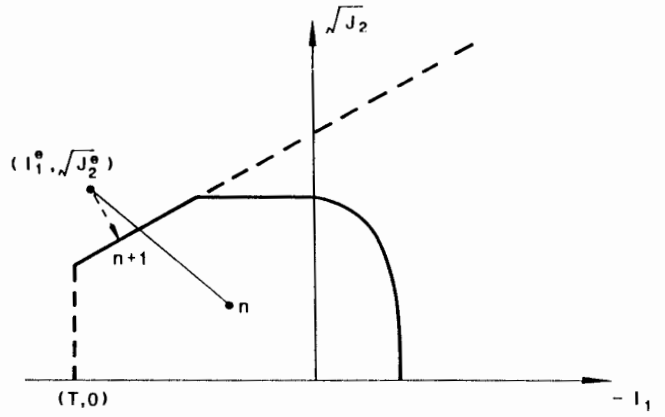

Fig. 7.27. Yield surface coding (B) – case for $I^n > 0$ with Drucker-Prager yield surface violation.

Drucker-Prager type of constitutive matrix is employed for the possible next incremental calculation.

7.5.5 *Corner coding*

The treatment of the *corner coding* depends on the characteristics of the hardening function. For soils, the hardening surface is permitted to move back toward the origin, while for rocks, it is not allowed. In the following, two different treatments for these two types of materials are discussed.

(A) Case for soil. If the value I_1^{n+1} corrected from the previous *yield surface coding* is less than the current location $L(I^{n+1})$ of the cap computed by the *yield surface coding*:

$$I_1^{n+1} < L(I^{n+1}) \tag{7.87}$$

the *corner coding* is triggered. In this case, the final stress state will be on the corner at which the yield surface intersects the cap as shown in Fig. 7.28.

The stress invariant I_1^{n+1} is calculated from the elastic trial stress invariant I_1^e and the plastic volumetric strain increment (positive *unknown* value):

$$I_1^{n+1} = I_1^e - 3K\, d\epsilon_v^p \tag{7.88}$$

On the other hand, the new location of I^{n+1} due to $d\epsilon_v^p$ is given by Eq. (7.80). Since the stress point in this case is at the intersection or corner of both surfaces, the following condition must be satisfied:

$$I_1^{n+1} = I^{n+1} \tag{7.89a}$$

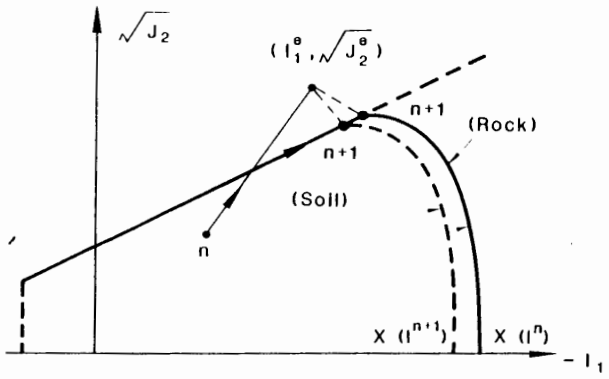

Fig. 7.28. Corner coding.

or

$$I_1^c - 3K\,d\epsilon_v^p = I^n + \left.\frac{\partial I}{\partial \epsilon_v^p}\right|_{I^n} d\epsilon_v^p \tag{7.89b}$$

Eliminating $d\epsilon_v^p$, and solving for I_1^{n+1} lead to the final corner value:

$$I_1^{n+1} = I^{n+1} = \frac{\left.\frac{\partial I}{\partial \epsilon_v^p}\right|_{I^n} I_1^c + 3KI^n}{\left.\frac{\partial I}{\partial \epsilon_v^p}\right|_{I^n} + 3K} \tag{7.90}$$

From Eq. (7.90), we see that the corner value lies somewhere between I_1^c and I^n. As a special case, if $I_1^c = I^n$, the new corner point I^{n+1} becomes identical to I^n. Substituting I_1^{n+1} back into Eq. (7.88) and solving for $d\epsilon_v^p$, we obtain:

$$d\epsilon_v^p = \frac{I_1^c - I^n}{\left.\frac{\partial I}{\partial \epsilon_v^p}\right|_{I^n} + 3K} \tag{7.91}$$

Thus, from $d\epsilon_v^p = 3d\lambda\,\partial f_c/\partial I_1$, the proportionality factor $d\lambda$ can be obtained as:

$$d\lambda = \frac{I_1^c - I^n}{3\dfrac{\partial f_c}{\partial I_1}\left[\left.\dfrac{\partial I}{\partial \epsilon_v^p}\right|_{I^n} + 3K\right]} \tag{7.92}$$

Consequently, the plastic strain increment $d\epsilon_{ij}^p$ can be calculated from the associated flow rule equation using the $d\lambda$ value so obtained. The stress increments $d\sigma_{ij}^{n+1}$ can be obtained from Eq. (7.79).

(B) Case for rock. On the other hand, for rocks, the *corner coding* is simply set to:

$$I_1^{n+1} = l^{n+1} = L(l^n) \tag{7.93}$$

Although the cap for rock materials does not move back to the origin, the increment of plastic volumetric strain is occurring at the rate to be determined by Eq. (7.91):

$$d\epsilon_v^p = (I_1^c - l^n)/3K \tag{7.94}$$

Similarly, the proportionality factor $d\lambda$ can be obtained and the new stress increment $d\sigma_{ij}^{n+1}$ can be calculated from Eq. (7.79).

Note that at the corner point of the elliptic hardening surface with the failure surface, the plastic strain increment vector is assumed to be parallel to the $\sqrt{J_2}$-axis so that no plastic volumetric strain increment will occur. The corner coding for the elliptic cap model plays an important role in controlling the excessive dilatancy of the material. The elastic-plastic constitutive matrix $[C^{ep}]$ for the elliptic cap is given by Eqs. (7.82a) and (7.82b) where H, H_{11}, H_{22}, etc. have the forms:

$$H = 36K\left[I_1^{n+1} - L(l^{n+1})\right]^2 + 4R^4GJ_2^{n+1} + 12\left[x^{n+1} - L(l^{n+1})\right]\left[I_1^{n+1} - L(l^{n+1})\right]/D(\epsilon_v^p + W') \tag{7.95a}$$

$$H_{11} = 6K\left[I_1^{n+1} - L(l^{n+1})\right] + 2R^2Gs_{11}^{n+1} \tag{7.95b}$$

$$H_{22} = 6K\left[I_1^{n+1} - L(l^{n+1})\right] + 2R^2Gs_{22}^{n+1} \tag{7.95c}$$

$$H_{33} = 6K\left[I_1^{n+1} - L(l^{n+1})\right] + 2R^2Gs_{33}^{n+1} \tag{7.95d}$$

$$H_{12} = 2R^2Gs_{12}^{n+1} \tag{7.95e}$$

$$H_{23} = 2R^2Gs_{23}^{n+1} \tag{7.95f}$$

$$H_{31} = 2R^2Gs_{31}^{n+1} \tag{7.95g}$$

Note that the term $[I_1^{n+1} - L(l^{n+1})]$ in H, H_{11}, H_{22}, and H_{33} becomes in general zero at the corner treatment.

As for the treatment of the constitutive matrix for the plane cap surface at the corner, the *mixed matrix* of the elastic-plastic matrices combining the plane hardening cap with the Drucker-Prager function may be employed (Bathe, et al., 1980). The mixed matrix $[C^{ep}]$ is given by:

$$[C^{ep}] = [C^e] - [C^p]^{D-P} - [C^p]^{PC} \tag{7.96a}$$

where $[C^e]$ is the elastic constitutive matrix, $[C^p]^{D\text{-}P}$ is the matrix given by Eq. (7.82) with the Drucker-Prager function, and $[C^p]^{PC}$ is given by Eq. (7.82b), with

their components H, H_{11}, H_{22}, etc. derived from the plane cap function (7.68). These components are:

$$H = 9K + 3/D(\epsilon_v^p + W) \tag{7.96b}$$

$$H_{11} = 3K \tag{7.96c}$$

$$H_{22} = 3K \tag{7.96d}$$

$$H_{33} = 3K \tag{7.96e}$$

$$H_{12} = 0 \tag{7.96f}$$

$$H_{23} = 0 \tag{7.96g}$$

$$H_{31} = 0 \tag{7.96h}$$

7.5.6 *Hardening surface coding*

We shall now examine the case where the hardening cap, rather than the failure surface, is violated by the elastic trial stresses. The elastic stresses are first checked against the hardening surface f_c. If:

$$f_c\left(I_1^e, \sqrt{J_2}^e, \kappa^n\right) > 0 \tag{7.97a}$$

and

$$I_1^e > L(I^n) \tag{7.97b}$$

then, the *hardening surface coding* is performed. The treatments for plane and elliptic cap surfaces are considered differently in the following:

(A) Plane hardening cap

A trial increment of hardening parameter dI^1 is first assumed, from which the corresponding increments, $d\epsilon_v^p$ and $d\epsilon_v^e$, are respectively computed (see Fig. 7.29):

$$d\epsilon_v^p = \left.\frac{\partial \epsilon_v^p}{\partial I}\right|_{I^n} dI^1 \tag{7.98a}$$

and

$$d\epsilon_v^e = \frac{I^n + dI^1 - I_1^n}{3K} \tag{7.98b}$$

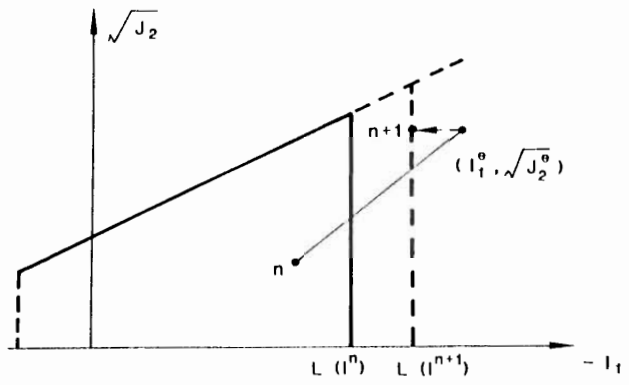

Fig. 7.29. Hardening coding for plane cap.

The estimated $d\epsilon_v^p$ and $d\epsilon_v^e$ must satisfy:

$$d\epsilon_v^{n+1} = d\epsilon_v^p + d\epsilon_v^e \tag{7.98c}$$

Obviously, the first trial value of dI^1 will not necessarily satisfy the condition (7.98c). Thus, an iterative procedure for the trial values of dI^1 is repeated until Eq. (7.98c) is satisfied within a small tolerance. Once the value of dI^1 is determined, then, the plastic volumetric strain increment $d\epsilon_v^p$ can be calculated. Similarly, the factor $d\lambda$ is determined from the flow rule equation using the $d\epsilon_v^p$ value so calculated, and the stress increment $d\sigma_{ij}^{n+1}$ is evaluated from Eq. (7.79). Since the plane cap induces only the plastic volumetric strain within the framework of the associated flow rule, the new stress state σ_{ij}^{n+1} is:

$$\sigma_{ij}^{n+1} = \sigma_{ij}^n + K\left(d\epsilon_v^{n+1} - d\epsilon_v^p\right)\delta_{ij} + 2G\, de_{ij}^{n+1} \tag{7.99}$$

(B) Elliptic hardening cap

Since now the plastic deviatoric strain increments must be considered, the hardening coding for the elliptic hardening cap (Fig. 7.30) is somewhat different from the plane cap coding. In the following, the convergence procedure will be based on the *modified regula falsi method* (Conte and Boor, 1972).

First choice of value I^1: A trial value of $I^1 = I^n + dI^1$ is first assumed. Since the final location of I^{n+1} lies somewhere between I^n and I_1^e, it follows that the first trial iterative value of I^1 may be estimated by:

$$I^1 = \frac{F^r I^l - F^l I^r}{F^r - F^l} \tag{7.100}$$

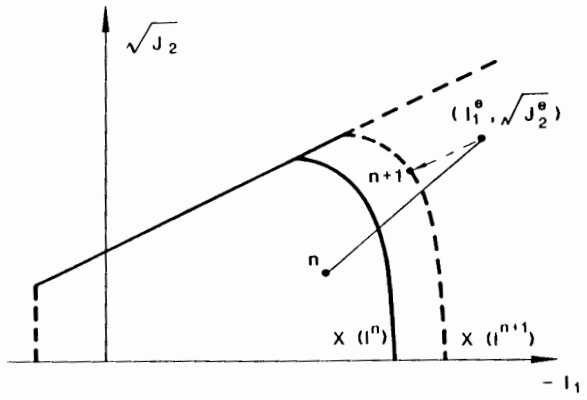

Fig. 7.30. Hardening coding for elliptic cap.

where F' and F^r are the weighting values to be explained in the forthcoming, and I' and I^r are first assumed to be I^n and I_1^c, respectively.

The following values are taken for F':
For $I_1^c < x^n$,

$$F' = \frac{I^n - I_1^c}{I^n - x^n} > 1 \tag{7.101a}$$

and for $I_1^c > x^n$,

$$F' = \frac{\sqrt{J_2}^e - \sqrt{J_2}^c}{\sqrt{J_2}^e + \sqrt{J_2}^c} < 1 \tag{7.101b}$$

where $\sqrt{J_2}^c$ is the square root of the second invariant of the deviatoric stress tensor which satisfies the current cap hardening function $f_c^n(I_1^c, \sqrt{J_2}^c, x^n) = 0$.

On the other hand, F^r is taken as:

$$F^r = \frac{x^r - I_1^r}{I_1^c - x^r} < -1 \tag{7.102a}$$

where x^r and I_1^r are respectively expressed by:

$$x^r = I_1^c - R(k - \alpha I_1^c) \tag{7.102b}$$

and

$$I_1^r - I_1^c = 3KW\left[\exp(Dx^r) - \exp(Dx^n)\right] \tag{7.102c}$$

After the trial value I_1^t is computed from Eq. (7.100), the corresponding trial values of L^t, x^t, and $d\epsilon_v^{pt}$ are computed:

$$L^t = L(I'' + dI^t) \tag{7.103a}$$

$$x^t = x(I'' + dI^t) = I^t - R(k - \alpha I^t) \tag{7.103b}$$

$$d\epsilon_v^{pt} = W\left[\exp(Dx^t) - \exp(Dx'')\right] \tag{7.103c}$$

Thus, the trial value of I_1^t is calculated by:

$$I_1^t = I_1^e - 3K\, d\epsilon_v^{pt} \tag{7.104}$$

Correction of value I^t: The first estimation of I^t will generally not lead to the correct new location of the hardening cap. If $I_1^t \le x^t$, we shall replace I' and F' in Eq. (7.100) by:

$$I' = I^t \tag{7.105a}$$

$$F' = \frac{I^t - I_1^t}{I^t - x^t} \tag{7.105b}$$

On the other hand, if $I_1^t \ge L^t$, we shall replace I^t and F^t in Eq. (7.100) by:

$$I^t = I^t \tag{7.106a}$$

$$F^t = \frac{x^t - I_1^t}{L(I^t) - x^t} \tag{7.106b}$$

Thus, the modified trial value of I^t can again be obtained from Eq. (7.100). Until the condition $L^t > I_1^t > x^t$ is satisfied, the procedure called the modified regula falsi method will be continued with the new trial value I^t.

Once this condition is satisfied, $\sqrt{J_2}^t$ is computed from the condition that the $\sqrt{J_2}^t$ lies on the trial hardening cap surface $f_c^t(I_1^t, \sqrt{J_2}^t, x^t) = 0$. Then, the trial stress state must be checked against the following condition:

$$s_{ij}^t + 2G\, de_{ij}^{pt} = s_{ij}^e \tag{7.107}$$

where s_{ij}^t and de_{ij}^{pt} are the trial deviatoric stress tensor and the increments of the trial plastic deviatoric strain tensor, respectively.

Using the estimated value of $d\epsilon_v^{pt}$, the trial value for the proportionality factor $d\lambda^t$ is approximately estimated by:

$$d\lambda^t = \left.\frac{d\epsilon_v^{pt}}{3(\partial f_c/\partial I_1)}\right|_{I_1^t, \sqrt{J_2}^t} \tag{7.108}$$

where the factor $d\lambda^t$ is computed at the stress state I_1^t. Therefore, de_{ij}^{pt} can be approximately calculated by:

$$de_{ij}^{pt} = d\lambda^t \frac{1}{2\sqrt{J_2}} \frac{\partial f_c}{\partial \sqrt{J_2}} s_{ij}^t = \left. \frac{s_{ij}^t \, d\epsilon_v^{pt} \left(\partial f_c / \partial \sqrt{J_2} \right)}{6\sqrt{J_2} \left(\partial f_c / \partial I_1 \right)} \right|_{I_1^t, \sqrt{J_2}^t} \tag{7.109}$$

Substituting Eq. (7.109) back into Eq. (7.107) leads to:

$$s_{ij}^t \left[1 + \left. \frac{G \, d\epsilon_v^{pt} \left(\partial f_c / \partial \sqrt{J_2} \right)}{3\sqrt{J_2} \left(\partial f_c / \partial I_1 \right)} \right|_{I_1^t, \sqrt{J_2}^t} \right] = s_{ij}^e \tag{7.110}$$

when squared, Eq. (7.110) becomes:

$$\sqrt{J_2}^t \left[1 + \left. \frac{G \, d\epsilon_v^{pt} \left(\partial f_c / \partial \sqrt{J_2} \right)}{3\sqrt{J_2} \left(\partial f_c / \partial I_1 \right)} \right|_{I_1^t, \sqrt{J_2}^t} \right] = \sqrt{J_2}^e \tag{7.111}$$

If Eq. (7.111) is not satisfied, the modified regula falsi method will be continued by replacing either F^r or F^ℓ with their new weighting values:

$$F^r \text{ or } F^\ell = \frac{\sqrt{J_2}^e - \sqrt{J_2}^t \left[1 + \left. \frac{G \, d\epsilon_v^{pt} \left(\partial f_c / \partial \sqrt{J_2} \right)}{3\sqrt{J_2} \left(\partial f_c / \partial I_1 \right)} \right|_{I_1^t, \sqrt{J_2}^t} \right]}{\sqrt{J_2}^e + \sqrt{J_2}^t \left[1 + \left. \frac{G \, d\epsilon_v^{pt} \left(\partial f_c / \partial \sqrt{J_2} \right)}{3\sqrt{J_2} \left(\partial f_c / \partial I_1 \right)} \right|_{I_1^t, \sqrt{J_2}^t} \right]} \tag{7.112}$$

where the value computed from Eq. (7.112) is assigned to F^ℓ, if it has the positive sign, while the negative value it is assigned to F^r. The iterative procedure is repeated until Eq. (7.111) is satisfied, i.e., the values of F^r and F^ℓ become zero.

After some iterations, the final values for l^{n+1} and hence I_1^{n+1} and $\sqrt{J_2}^{n+1}$ can be determined within the tolerance. Finally, the correct plastic strain increment $d\epsilon_{ij}^p$ is found and the corresponding stress increment $d\sigma_{ij}^{n+1}$ is determined from Eq. (7.79).

The *elastic-plastic constitutive matrices* for the plane and elliptic cap functions are then constructed for the possible calculation at the next increment. The constitutive matrix $[C^{ep}]$ for the plane cap function is given by Eqs. (7.82a), (7.82b), and (7.96b) though (7.96h), while for the elliptic cap function it is given by Eqs. (7.82a), (7.82b), and (7.95).

7.5.7 Tensile coding

When the elastic trial stresses violate the tension cut-off condition as shown in Fig. 7.31:

$$I_1^e > T \tag{7.113}$$

we shall shift the new stress state to the point $(T, 0)$ on the I_1-axis:

$$\sigma_{ij}^{n+1} = \tfrac{1}{3} T \delta_{ij} \tag{7.114}$$

The dilatancy induced by the tensile coding is considered as follows: If l^n is less than zero:

$$d\epsilon_v^p = d\epsilon_v^{n+1} - \frac{1}{3K^2}(T - I_1^n) \tag{7.115}$$

and the hardening parameter l^{n+1} is determined as:

$$l^{n+1} = l^n + \left.\frac{\partial l}{\partial \epsilon_v^p}\right|_{l^n} d\epsilon_v^p \tag{7.116}$$

On the other hand, if l^n is greater than zero, $d\epsilon_v^p$ is simply set to zero and consequently l^{n+1} is identical to l^n.

Finally, the *elastic constitutive matrix* $[C^e]$ is assigned for the next calculation.

It is worth repeating here that the above-mentioned codings are performed within the small strain increments. Furthermore, the new stress state σ_{ij}^{n+1} obtained from the *yield surface coding*, the *corner coding* and the *hardening coding* does not necessarily lie exactly on these loading surfaces. Therefore, a procedure for scaling the new stresses back onto these loading surfaces is recommended. This procedure is

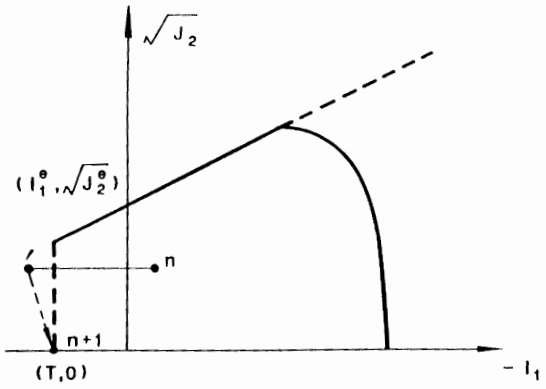

Fig. 7.31. Tensile coding.

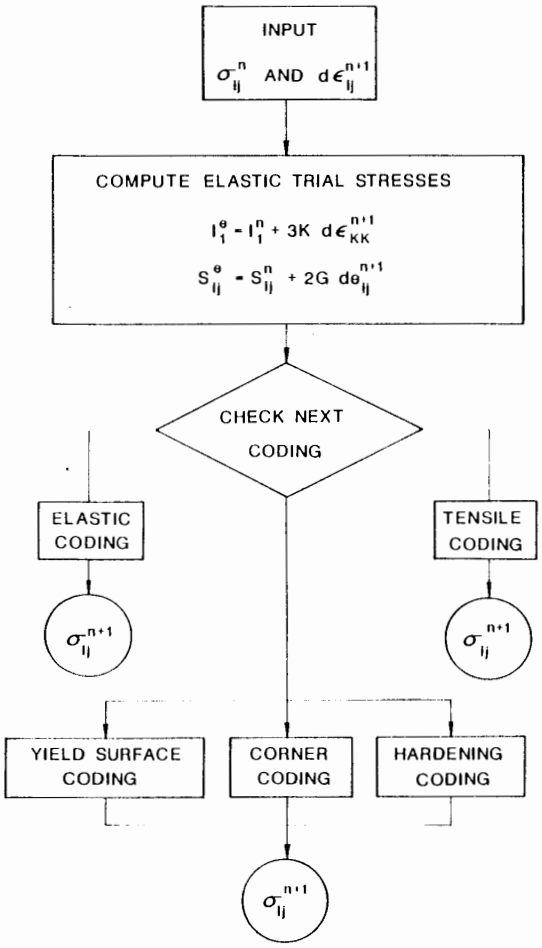

Fig. 7.32. Flow chart of computer implementation for cap model.

similar to that explained previously in Section 7.3 for the implementation of perfectly plastic models.

If a *large deformation analysis* is employed under the assumption of the updated Lagrangian formulation as in Sec. 8.7.1, the stresses must first be rotated from the local Cartesian coordinate system to the global Cartesian coordinate system for the next step of calculation. A flow chart summarizing the present implementation procedure for cap models is schematically shown in Fig. 7.32.

7.5.8 Model subroutine

The preceding algorithm forms the basis for the SUBROUTINE CAPMDL to implement CAP MODEL. This subroutine is set up for the two-dimensional problems under

the *plane strain condition*. The SUBROUTINE CAPMDL consists of:

1. SUBROUTINE LINELS in Section 7.3.3.
2. SUBROUTINE EPCDP in Section 7.3.3.
3. SUBROUTINE EPCAP constructs the Elastic-Plastic constitutive matrix for the CAP models.
4. FUNCTION FF computes $\sqrt{J_2}$ of Failure Function corresponding to I_1.
5. FUNCTION XV computes X value where the cap surface intersects with the I_1-axis.
6. FUNCTION EVP computes the accumulated volumetric plastic strain ϵ_v^p.
7. FUNCTION SRJ2C computes the Square Root of J2 on the Cap surface corresponding to I_1.

In the following, the listings of SUBROUTINES CAPMDL and EPCAP will be explained in some details with respect to the Input quantities, Internal variables, and Output quantities. As for functions FF, XV, EVP, and SRJ2C, only their listings are given.

(A) SUBROUTINE CAPMDL

INPUT QUANTITIES

1. Material type
   - MAT : MAT = 3 for the plane cap material
   - : MAT = 4 for the elliptic cap material
2. Type for movement of hardening surface
   - LTYPE : LTYPE = 1 for soil whose hardening surface is allowed to move back toward the origin.
   - : LTYPE = 2 for rock whose hardening surface is not allowed to move back.
3. Material constants
   - E : Young's modulus E
   - PNU : Poisson's ratio ν
   - ALPHA : Drucker-Prager material constant α
   - RK : Drucker-Prager material constant k
   - EL : Cap location l
   - AD : Cap material constant D
   - AW : Cap material constant W
   - R : Shape ratio R
   - TENCUT : Tension cut-off limit strength T
4. Strain increments
   - EX : Strain increment $d\epsilon_{11}$
   - EY : Strain increment $d\epsilon_{22}$
   - EXY : Engineering shearing strain increment $d\gamma_{12}$
6. Stress state at previous step
   - PSIGX : Stress σ_{11}^n
   - PSIGY : Stress σ_{22}^n
   - PSIGXY : Stress σ_{12}^n
   - PSIGZ : Stress σ_{33}^n

7. Type of material state

MSTATE : MSTATE = 0 for elastic state
MSTATE = 1 for yielding state
MSTATE = 2 for hardening state
MSTATE = 3 for corner state
MSTATE = 4 for tension cut-off state

INTERNAL VARIABLES

1. Strain increments

EV : Volumetric strain increment de_v^{n+1}
DEX : Deviatoric strain increment de_{11}^{n+1}
DEY : Deviatoric strain increment de_{22}^{n+1}
DEZ : Deviatoric strain increment de_{33}^{n+1}
DEXY : Deviatoric strain increment de_{12}^{n+1}

2. Initial deviatoric stresses and stress invariants

DSIGX : Deviatoric stress s_{11}^n
DSIGY : Deviatoric stress s_{22}^n
DSIGZ : Deviatoric stress s_{33}^n
DSIGXY : Deviatoric stress s_{12}^n
SIH : Initial stress invariant I_1^n

3. Elastic trial stresses

TDSIGX : Elastic trial deviatoric stress s_{11}^e
TDSIGY : Elastic trial deviatoric stress s_{22}^e
TDSIGZ : Elastic trial deviatoric stress s_{33}^e
TSIGXY : Elastic trial deviatoric stress s_{12}^e
TSIH : Elastic trial stress invariant I_1^e
TSRJ2 : Square root of the elastic trial deviatoric stress invariant $\sqrt{J_2}^e$

4. Scaling factor

RATIO : Ratio of $\sqrt{J_2}^{n+1}$ to $\sqrt{J_2}^e$

OUTPUT QUANTITIES

1. Yield status

MSTATE

2. Scaled-back stresses

SIGX, SIGY, SIGZ, SIGXY

3. Constitutive matrix

EPCM(4, 3) for $[C^{ep}]$ or $[C^e]$

```
00010       SUBROUTINE CAPMDL(E,PNU,EX,EY,EXY,PSIGX,PSIGY,PSIGZ,PSIGXY,
00020      &                  TENCUT,LTYPE,MAT,ALPHA,RK,EL,R,AD,AW,EPCM,
00030      &                  MSTATE)
00040 C ***************************************************************
00050 C *SUBROUTINE CAPMDL COMPUTES A CONSTITUTIVE MATRIX FOR CAP MODEL*
00060 C *UNDER PLANE STRAIN CONDITION                                   *
00070 C ***************************************************************
```

```
00080 C
00090       DIMENSION EPCM(4,3)
00100 C
00110       DATA INCRNT,NIT /10,60/
00120       DATA CONV /0.001/
00130 C
00140 C  COMPUTE ELASTIC MODULI AND MATERIAL PROPERTIES
00150 C
00160       BMOD  =E/(3.*(1.-2.*PNU))
00170       SMOD  =E/(2.*(1.+PNU))
00180       THREEK=3.*BMOD
00190       TWOG  =2.*SMOD
00200 C
00210 C  CHANGE ENGINEERING SHEAR STRAIN TO TENSORIAL STRAIN
00220 C
00230       EXY=0.5*EXY
00240 C
00250 C  COMPUTE SUBDIVIDED STRAIN INCREMENTS FOR GIVEN STRAIN INCREMENTS
00260 C
00270       EX = EX/FLOAT(INCRNT)
00280       EY = EY/FLOAT(INCRNT)
00290       EXY=EXY/FLOAT(INCRNT)
00300 C
00310 C  DO LOOP FOR COMPUTATION OF STRESS STATE FOR NEW STRAIN STATE
00320 C
00330       DO 170 INC=1,INCRNT
00340 C
00350 C  COMPUTE STRESS INVARIANTS AND DEVIATORIC STRESSES AT PREVIOUS STEP
00360 C
00370       SI1I  =PSIGX+PSIGY+PSIGZ
00380       PRESS =SI1I/3.
00390       DSIGX =PSIGX-PRESS
00400       DSIGY =PSIGY-PRESS
00410       DSIGZ =PSIGZ-PRESS
00420       DSIGXY=PSIGXY
00430 C
00440 C  COMPUTE VOLUMETRIC STRAIN INCREMENT AND DEVIATORIC STRAIN INCREMENTS
00450 C
00460       EV  =EX+EY
00470       DEX =EX-EV/3.
00480       DEY =EY-EV/3.
00490       DEZ =  -EV/3.
00500       DEXY=EXY
00510 C
00520 C  COMPUTE ACCUMULATED PLASTIC VOLUMETRIC STRAIN
00530 C
00540       XL  =XV(EL,R,ALPHA,RK)
00550       EVPI=EVP(XL,AD,AW)
00560 C
00570 C  COMPUTE ELASTIC DEVIATORIC STRESSES AND STRESS INVARIANTS
00580 C
00590       TDSIGX=DSIGX +TWOG*DEX
00600       TDSIGY=DSIGY +TWOG*DEY
00610       TDSIGZ=DSIGZ +TWOG*DEZ
00620       TSIGXY=DSIGXY+TWOG*DEXY
00630       TSI1  =SI1I+THREEK*EV
00640       TSRJ2 =SQRT(TDSIGX*TDSIGX+TDSIGY*TDSIGY+TDSIGX*TDSIGY+
00650      &        TSIGXY*TSIGXY)
00660 C
00670 C  SET INITIAL MSTATE AND SCALING FACTOR
00680 C
00690       RATIO =1.
00700       MSTATE=0
00710 C
00720 C  CHECK FOR TENSILE CODING
00730 C
00740       IF(TSI1.LT.TENCUT) GO TO 10
00750 C
00760 C  ***** TENSILE CODING *****
00770 C
00780       TSI1  =TENCUT
```

```
00790       RATIO =0.
00800       MSTATE=4
00810       IF(LTYPE.EQ.2.OR.EL.GE.0.) GO TO 160
00820 C
00830 C  TENSILE DILATANCY
00840 C
00850       ELCF  =EL+CONV*FF(EL,ALPHA,RK)
00860       ELL   =AMIN1(0.,ELCF)
00870       XLL   =XV(ELL,R,ALPHA,RK)
00880       DLDEVP=(ELL-EL)/((XLL-XL)*AD*AW*EXP(AD*XL))
00890       DEVP  =EV-(TSI1-SI1I)/THREEK
00900       EL    =EL+DEVP*DLDEVP
00910       EL    =AMIN1(0.,EL)
00920       GO TO 160
00930 C
00940 C  CHECK FOR HARDENING CODING
00950 C
00960 10    CAPL=AMIN1(0.,EL)
00970       IF(TSI1.LT.CAPL) GO TO 40
00980 C
00990 C  ***** FAILURE SURFACE CODING *****
01000 C
01010 C  CHECK FOR FAILURE SURFACE
01020 C
01030       VMISES=FF(EL,ALPHA,RK)
01040       IF(MAT.EQ.4) VMISES=SRJ2C(CAPL,XL,CAPL,R)
01050       FI1=FF(TSI1,ALPHA,RK)
01060       FD =TSRJ2-AMIN1(FI1,VMISES)
01070       IF(FD.LE.0.) GO TO 160
01080 C
01090 C  FAILURE SURFACE CALCULATION
01100 C
01110       DFDI1=0.
01120       TSCTS=TSI1+CONV*TSRJ2
01130       IF(FI1.LT.VMISES) DFDI1=(FI1-FF(TSCTS,ALPHA,RK))/(CONV*TSRJ2)
01140       DEVP =3.*DFDI1*FD/(3.*THREEK*DFDI1**2+0.5*TWOG)
01150       TSI1E=TSI1
01160       TSI1 =TSI1-THREEK*DEVP
01170 C
01180 C  SET MSTATE FOR YIELD SURFACE ZONE
01190 C
01200       MSTATE=1
01210 C
01220 C  ***** DILATANCY AND CORNER CODING *****
01230 C
01240       IF(LTYPE.EQ.1.AND.EL.LT.0.) GO TO 20
01250       TSI1=AMAX1(TSI1,CAPL)
01260       GO TO 30
01270 20    ELCTS =EL+CONV*FF(EL,ALPHA,RK)
01280       ELL   =AMIN1(TSI1E,ELCTS)
01290       XLL   =XV(ELL,R,ALPHA,RK)
01300       DLDEVP=(ELL-EL)/((XLL-XL)*AD*AW*EXP(AD*XL))
01310       ELINT =EL
01320       ELDD  =ELINT+DEVP*DLDEVP
01330       EL    =AMIN1(0.,ELDD)
01340       IF(TSI1.GE.EL) GO TO 30
01350       TSI1=(DLDEVP*TSI1E+THREEK*ELINT)/(DLDEVP+THREEK)
01360       EL  =AMIN1(0.,TSI1)
01370       IF(TSI1.LE.0.) MSTATE=3
01380 30    FI1  =FF(TSI1,ALPHA,RK)
01390       SLOPE=ALPHA
01400       IF(VMISES.LT.FI1) SLOPE=0.
01410       RATIO=AMIN1(FI1,VMISES)/TSRJ2
01420       GO TO 160
01430 C
01440 C  ***** HARDENING CODING FOR PLANE CAP SURFACE *****
01450 C
01460 40    IF(MAT.EQ.4) GO TO 70
01470       DL=0.5*(TSI1-EL)
01480       ED=EL+DL
```

```
01490        DO 50 I=1,NIT
01500        DEVP1=(TSI1-ED)/THREEK
01510        DEVP2=AW*(EXP(AD*ED)-EXP(AD*EL))
01520        FR    =(DEVP1-DEVP2)/DEVP1
01530        IF(ABS(FR).LT.0.001) GO TO 60
01540        DL=0.5*DL
01550        IF(ABS(DEVP1).LT.ABS(DEVP2)) ED=ED-DL
01560        IF(ABS(DEVP1).GT.ABS(DEVP2)) ED=ED+DL
01570 50     CONTINUE
01580 60     DEVP  =DEVP1
01590        EL    =ED
01600        MSTATE=2
01610        TSI1  =EL
01620        RATIO =1.
01630        IF(TSRJ2.GE.FF(EL,ALPHA,RK)) RATIO =FF(EL,ALPHA,RK)/TSRJ2
01640        IF(TSRJ2.GT.FF(EL,ALPHA,RK)) MSTATE=3
01650        GO TO 160
01660 C
01670 C   ***** HARDENING CODING FOR ELLIPTIC CAP SURFACE *****
01680 C
01690 70     IF(TSI1.LT.XL) GO TO 80
01700        IF(TSRJ2.LE.SRJ2C(TSI1,XL,CAPL,R)) GO TO 160
01710 C
01720 C   INITIAL SET OF CAP LOCATION
01730 C
01740 80     TSI1E =TSI1
01750        TSRJ2E=TSRJ2
01760        ELL   =EL
01770        ELR   =TSI1E
01780        IF(TSI1E.LE.XL) FL=(EL-TSI1E)/(EL-XL)
01790        IF(TSI1E.GT.XL) FL=2.*TSRJ2E/(TSRJ2E+SRJ2C(TSI1E,XL,CAPL,R))-1.
01800        XR    =AMIN1(0.,XV(ELR,R,ALPHA,RK))
01810        TSI1R=TSI1E-THREEK*(EVP(XR,AD,AW)-EVPI)
01820        FR    =(XR-TSI1R)/(ELR-XR)
01830        COMP =CONV*FF((FL*XR-FR*XL)/(FL-FR),ALPHA,RK)
01840        IF((ABS(TSI1)+TSRJ2).LT.COMP) GO TO 160
01850        MSTATE=2
01860        FOLD  =0.
01870 C
01880 C   EMPLOY A MODIFIED REGULA FALSI METHOD TO DETERMINE CAP LOCATION
01890 C
01900        DO 130 IT=1,NIT
01910        EL   =(FL*ELR-FR*ELL)/(FL-FR)
01920        XL   =AMIN1(0.,XV(EL,R,ALPHA,RK))
01930        DEVP=EVP(XL,AD,AW)-EVPI
01940        TSI1=TSI1E-THREEK*DEVP
01950        CAPL=AMIN1(0.,EL)
01960        IF(TSI1.LT.XL)    FC=(EL-TSI1)/(EL-XL)
01970        IF(TSI1.GT.CAPL) FC=(XL-TSI1)/(CAPL-XL)
01980        IF(TSI1.LT.XL.OR.TSI1.GT.CAPL) GO TO 110
01990        TSRJ2=SRJ2C(TSI1,XL,CAPL,R)
02000        DELI1=CONV*(XL-TSI1)
02010        DESP =0.
02020        IF(DELI1) 90,100,90
02030 90     DESP =(DEVP/6.)*R*SQRT((XL-CAPL)**2-(TSI1-CAPL)**2)/(TSI1-CAPL)
02040 100    SRJ2T=TSRJ2+TWOG*DESP
02050        FC    =(TSRJ2E-SRJ2T)/(TSRJ2E+SRJ2T)
02060        IF(ABS(TSRJ2E-SRJ2T).LE.COMP) GO TO 140
02070        IF(FC.GT.0..AND.(TSI1-CAPL).GE.DELI1) GO TO 140
02080 110    IF(FC.GT.0.) GO TO 120
02090        ELR=EL
02100        FR =FC
02110        IF(FOLD.LT.0.) FL=0.5*FL
02120        GO TO 130
02130 120    ELL=EL
02140        FL =FC
02150        IF(FOLD.GT.0.) FR=0.5*FR
02160 130    FOLD=FC
02170 C
02180 C   IF A MODIFIED FALSI METHOD DOES NOT CONVERGE, SET A FINAL CAP
```

```
02190 C
02200       TSI1=AMAX1(TSI1,XL)
02210       IF(TSI1.GT.AMIN1(0.,EL)) TSI1=CAPL
02220       TSRJ2=SRJ2C(TSI1,XL,CAPL,R)
02230 140   RATIO=0.
02240 C
02250 C  CHECK FOR CORNER
02260 C
02270       SRJ2T=FF(TSI1,ALPHA,RK)
02280       ERR  =TSRJ2/SRJ2T
02290       IF(ERR.GE.0.99.AND.ERR.LE.1.) MSTATE=3
02300       IF(TSRJ2E) 150,160,150
02310 150   RATIO=TSRJ2/TSRJ2E
02320 C
02330 C  ***** COMPUTE STRESS STATE CORRESPONDING TO NEW STRAIN STATE *****
02340 C
02350 C  SCALE BACK ELASTIC TRIAL DEVIATORIC STRESS
02360 C
02370 160   DSIGX =RATIO*TDSIGX
02380       DSIGY =RATIO*TDSIGY
02390       DSIGXY=RATIO*TSIGXY
02400       DSIGZ =RATIO*TDSIGZ
02410 C
02420 C  COMPUTE FINAL STRESSES
02430 C
02440       PRESS=TSI1/3.
02450       SIGX =PRESS+DSIGX
02460       SIGY =PRESS+DSIGY
02470       SIGXY=DSIGXY
02480       SIGZ =PRESS+DSIGZ
02490 C
02500 C  COMPUTE ACCUMULATED PLASTIC VOLUMETRIC STRAIN
02510 C
02520       XL   =XV(EL,R,ALPHA,RK)
02530       TEVP=EVP(XL,AD,AW)
02540 C
02550 C  INITIALIZE STRESS STATE AS PREVIOUS STRESS STATE
02560 C
02570       PSIGX =SIGX
02580       PSIGY =SIGY
02590       PSIGXY=SIGXY
02600       PSIGZ =SIGZ
02610 170   CONTINUE
02620 C
02630 C  CONSTRUCT A NEW CONSTITUTIVE MATRIX
02640 C
02650       IF(MSTATE.EQ.0.OR.MSTATE.EQ.4) CALL LINELS(BMOD,SMOD,EPCM)
02660       IF(MSTATE.EQ.1)
02670      &   CALL EPCDP(SIGX,SIGY,SIGZ,SIGXY,2,BMOD,SMOD,SLOPE,0.,EPCM)
02680       IF(MSTATE.EQ.2.OR.MSTATE.EQ.3)
02690      &   CALL EPCAP(SIGX,SIGY,SIGZ,SIGXY,MAT,EL,R,AD,AW,TEVP,BMOD,SMOD,
02700      &                ALPHA,RK,MSTATE,EPCM)
02710       RETURN
02720       END
```

A BRIEF EXPLANATION FOR LISTING

CAPMDL 160–190 Compute the bulk modulus K, the shear modulus G, $3K$, and $2G$ as BMOD, SMOD, THREEK, and TWOG, respectively.

CAPMDL 230 Change the engineering shearing strain $d\gamma_{12}$ to the tensorial shear strain $d\epsilon_{12}$.

CAPMDL 270–290 The strain increments $d\epsilon_{11}^{n+1}$, $d\epsilon_{22}^{n+1}$, and $d\epsilon_{12}^{n+1}$ are subdivided into several equal intervals, as EX, EY, and EXY, respectively.

CAPMDL

330 2610 Do loop to integrate the stress state over each subdivided strain increments:

370 420 Compute the stress invariant I_1'' as SIII and the deviatoric stresses s_{11}'', s_{22}'', s_{33}'', and s_{12}'' as DSIGX, DSIGY, DSIGZ and DSIGXY, related to the previous step.

460 500 Compute the volumetric strain increment $d\epsilon_v^{n+1}$ as EV and the deviatoric strain increments de_{11}^{n+1}, de_{22}^{n+1}, de_{33}^{n+1}, and de_{12}^{n+1} as DEX, DEY, DEZ, and DEXY.

540 550 Compute the accumulated plastic volumetric strain ϵ_v^p as EVPI, related to the previous step.

590 650 Compute the elastic trial deviatoric stresses s_{11}^e, s_{22}^e, s_{33}^e, and s_{12}^e as TDSIGX, TDSIGY, TDSIGZ, and TSIGXY, and the elastic trial stress invariants I_1^e and $\sqrt{J_2}^e$ as TSII and TSRJ2, respectively.

690 700 Set the initial material state MSTATE = 0 and the scaling factor RATIO = 1.

740 Check the tensile coding in Eq. (7.113).

780 920 The *tensile coding* in Section 7.5.7 is performed. If the determined cap location I^{n+1} as EL has a negative value, then a dilatancy in the tensile region is triggered. For the rock material, the tensile dilatancy is not carried out.

960 970 Check the hardening coding in Eq. (7.97).

1030–1200 *Failure surface coding* in Section 7.5.4 is performed. The Drucker-Prager or von Mises type of failure surface is checked for the elastic trial stresses, by using Eqs. (7.74) and (7.83). If the Drucker-Prager failure surface is violated, the dilatancy coding is performed. If the von Mises failure surface is violated, the dilatancy is not performed. The type of material state is set to "failure surface zone", that is, MSTATE = 1.

1240–1420 The *dilatancy* and *corner coding* in Section 7.5.5 is performed. If the corrected cap location EL moves over the corrected stress state toward the origin, then, the corner treatment is triggered so that the stress state becomes at the corner of the Drucker-Prager surface with the cap surface. For the rock material, the cap location is not renewed but remains constant.

1460–1650 The *hardening coding* for the plane cap surface in Section 7.5.6(A) is performed. A new location for the plane cap surface is first assumed. Subsequently, the plastic and elastic strain increments are evaluated and then the stress state is estimated from the elastic strain increments. If this stress state is not on the assumed plane cap surface, a new location for the plane cap surface is again taken until the consistency condition is satisfied.

1690–2310 The *hardening coding* for the elliptic cap surface in Section 7.5.6(B) is performed. Similar to the coding for the plane cap surface, a trial cap location is first assumed. This is performed by the modified regula falsi method until the stress state lies on the assumed hardening cap within the tolerance.

2370–2610 The elastic trial stresses are scaled back to the corresponding loading surface so that the hydrostatic pressure and the direction of the principal stress are not changed. Then, the new cap location and the plastic volumetric strain are updated for the possible next incremental calculation. The currently updated stress state is set as the "previous stress state" and the process is repeated until the stresses are integrated over all the subdivided strain increments.

CAPDMI 2650–2700 Construct the new constitutive matrix corresponding to the new stress state. This matrix is then used to make an element tangent stiffness matrix.

(B) SUBROUTINE EPCAP

INPUT QUANTITIES

1. Material type
   MAT
2. Material constants
   BMOD, SMOD, ALPHA, RK, EL, R, AD, AW
3. Stress state
   SIGX, SIGY, SIGZ, SIGXY
4. Accumulated plastic volumetric strain
   TEVP
5. Type of material state
   MSTATE

INTERNAL VARIABLES

1. Deviatoric stresses
   DSIGX, DSIGY, DSIGZ, DSIGXY
2. Stress invariants
   PRESS, SJ2, SRJ2
3. Stiffness coefficients
   AH, BH, DEDX
4. Matrix components
   H, HX, HY, HZ, HXY

OUTPUT QUANTITIES

Constitutive matrix
EPCM(4, 3) for $[C^{ep}]$

```
00010       SUBROUTINE EPCAP(SIGX,SIGY,SIGZ,SIGXY,MAT,EL,R,AD,AW,TEVP,BMOD,
00020      &                 SMOD,ALPHA,RK,MSTATE,EPCM)
```

```
00030 C   ***************************************************************
00040 C   *SUBROUTINE EPCAP COMPUTES ELASTO-PLASTIC CAP CONSTITUTIVE MATRIX*
00050 C   *UNDER PLANE STRAIN CONDITION                                   *
00060 C   ***************************************************************
00070 C
00080       DIMENSION EPCM(4,3)
00090 C
00100 C   COMPUTE STRESS INVARIANTS AND DEVIATORIC STRESSES
00110 C
00120       PRESS =(SIGX+SIGY+SIGZ)/3.
00130       SJ2   =((SIGX-SIGY)**2+(SIGY-SIGZ)**2+(SIGZ-SIGX)**2)/6.
00140      &       +SIGXY**2
00150       SRJ2  =SQRT(SJ2)
00160       DSIGX =SIGX-PRESS
00170       DSIGY =SIGY-PRESS
00180       DSIGZ =SIGZ-PRESS
00190       DSIGXY=SIGXY
00200 C
00210 C   CHECK IF CAP IS PLANE (MAT=3) OR ELLIPTIC (MAT=4)
00220 C
00230       IF(MAT.EQ.4) GO TO 10
00240 C
00250 C   COMPUTE STIFFNESS COEFFICIENTS OF PLANE CAP MODEL
00260 C
00270       AH  =1.
00280       BH  =0.
00290       DFDX=-1.
00300       GO TO 20
00310 C
00320 C   COMPUTE STIFFNESS COEFFICIENTS OF ELLIPTIC CAP MODEL
00330 C
00340 10    CAPL=AMIN1(0.,EL)
00350       AH  =2.*(3.*PRESS-CAPL)
00360       BH  =R*R
00370       DFDX=-2.*(XV(EL,R,ALPHA,RK)-CAPL)
00380 C
00390 C   COMPUTE H, HX, HY, HZ, AND HXY
00400 C
00410 20    H   =9.*BMOD*AH*AH+4.*BH*BH*SJ2*SMOD-3.*AH*DFDX/(AD*(AW+TEVP))
00420       HX  =3.*BMOD*AH+2.*BH*DSIGX*SMOD
00430       HY  =3.*BMOD*AH+2.*BH*DSIGY*SMOD
00440       HZ  =3.*BMOD*AH+2.*BH*DSIGZ*SMOD
00450       HXY=2.*BH*DSIGXY*SMOD
00460 C
00470 C   COMPUTE COMPONENTS OF A CONSTITUTIVE MATRIX
00480 C
00490       EPCM(1,1)=BMOD+4./3.*SMOD-HX*HX/H
00500       EPCM(1,2)=BMOD-2./3.*SMOD-HX*HY/H
00510       EPCM(1,3)=-HX*HXY/H
00520       EPCM(2,1)=EPCM(1,2)
00530       EPCM(2,2)=BMOD+4./3.*SMOD-HY*HY/H
00540       EPCM(2,3)=-HY*HXY/H
00550       EPCM(3,1)=EPCM(1,3)
00560       EPCM(3,2)=EPCM(2,3)
00570       EPCM(3,3)=SMOD-HXY*HXY/H
00580       EPCM(4,1)=BMOD-2./3.*SMOD-HZ*HX/H
00590       EPCM(4,2)=BMOD-2./3.*SMOD-HZ*HY/H
00600       EPCM(4,3)=-HZ*HXY/H
00610       IF((MAT.EQ.4).OR.(MAT.EQ.3.AND.MSTATE.EQ.2)) RETURN
00620 C
00630 C   COMPUTE STIFFNESS COEFFICIENTS OF DRUCKER-PRAGER MODEL
00640 C
00650       H   =9.*BMOD*ALPHA**2+SMOD
00660       HX  =3.*BMOD*ALPHA+SMOD/SRJ2*DSIGX
00670       HY  =3.*BMOD*ALPHA+SMOD/SRJ2*DSIGY
00680       HZ  =3.*BMOD*ALPHA+SMOD/SRJ2*DSIGZ
00690       HXY=SMOD/SRJ2*DSIGXY
00700 C
00710 C   COMPUTE COMPONENTS OF CONSTITUTIVE MATRIX AT CORNER FOR PLANE CAP
00720 C
```

```
00730         EPCM(1,1)=EPCM(1,1)-HX*HX/H
00740         EPCM(1,2)=EPCM(1,2)-HX*HY/H
00750         EPCM(1,3)=EPCM(1,3)-HX*HXY/H
00760         EPCM(2,1)=EPCM(1,2)
00770         EPCM(2,2)=EPCM(2,2)-HY*HY/H
00780         EPCM(2,3)=EPCM(2,3)-HY*HXY/H
00790         EPCM(3,1)=EPCM(1,3)
00800         EPCM(3,2)=EPCM(2,3)
00810         EPCM(3,3)=EPCM(3,3)-HXY*HXY/H
00820         EPCM(4,1)=EPCM(4,1)-HZ*HX/H
00830         EPCM(4,2)=EPCM(4,2)-HZ*HY/H
00840         EPCM(4,3)=EPCM(4,3)-HZ*HXY/H
00850         RETURN
00860         END
```

A BRIEF EXPLANATION FOR LISTING

EPCAP 120–190 Compute the stress invariant $\sqrt{J_2}$ as SRJ2 and the deviatoric stresses s_{11}, s_{22}, s_{33}, and s_{12} as DSIGX, DSIGY, DSIGZ, and DSIGXY, respectively.

EPCAP 270 370 Compute the stiffness coefficients A and B for the plane cap and the elliptic cap models as AH and BH.

EPCAP 410 450 Compute H, H_{11}, H_{22}, H_{33}, and H_{12} in Eqs. (7.95) and (7.96) as H, HX, HY, HZ, and HXY, respectively.

EPCAP 490–610 Compute the components of the constitutive matrix for the plane cap and the elliptic cap models under the plane strain condition.

EPCAP 650 840 Compute the components of the constitutive matrix for the plane cap model at the corner, as a special case.

```
00010         FUNCTION XV(EL,R,ALPHA,RK)
00020 C  ************************************************************************
00030 C  *FUNCTION XV COMPUTES THE VALUE OF SI1 WHERE CAP SURFACE INTERSECTS*
00040 C  *WITH HYDROSTATIC AXIS                                                 *
00050 C  ************************************************************************
00060 C
00070         XV=EL-R*(-ALPHA*EL+RK)
00080         RETURN
00090         END
00010         FUNCTION FF(SI1,ALPHA,RK)
00020 C  ************************************************************************
00030 C  *FUNCTION FF COMPUTES THE VALUE OF SQURE ROOT OF J2 CORRESPONDING*
00040 C  *TO SI1                                                                 *
00050 C  ************************************************************************
00060 C
00070         FF  ALPHA*SI1+RK
00080         RETURN
00090         END
00010         FUNCTION EVP(XLL,AD,AW)
00020 C  ************************************************************************
00030 C  *FUNCTION EVP COMPUTES THE ACCUMULATED VOLUMETRIC PLASTIC STRAIN*
00040 C  ************************************************************************
00050 C
00060         EVP=AW*(EXP(AD*XLL)-1.)
00070         RETURN
00080         END
00010         FUNCTION SRJ2C(SI1,XL,CAPL,R)
00020 C  ************************************************************************
00030 C  *FUNCTION SRJ2C COMPUTES THE VALUE OF SRJ2 TO SI1 ON THE ELLIPTIC*
00040 C  *CAP                                                                    *
00050 C  ************************************************************************
00060 C
00070         SRJ2C=SQRT(ABS(XL-CAPL)**2-(SI1-CAPL)**2)/R
00080         RETURN
00090         END
```

7.6 UNIAXIAL STRAIN BEHAVIOR: DEMONSTRATION OF SUBROUTINE CAPMDL

The SUBROUTINE CAPMDL can be incorporated directly into an existing finite element program. As a numerical example of using the SUBROUTINE CAPMDL, the behavior of sand under the uniaxial strain condition is solved here with the three plasticity models: the Drucker-Prager model without hardening cap, the Drucker-Prager model with a plane hardening cap, and the Drucker-Prager model with an elliptic hardening cap. The associated flow rule is employed in the present analysis. Since the stress and strain states in the uniaxial strain condition are assumed to be uniform throughout the material, only one element analysis is here considered.

7.6.1 Input data

INITIAL STRESS AND STRAIN CONDITIONS

Both initial stress and strain conditions are assumed to be in the *free* state, that is, $\sigma_{11} = \sigma_{22} = \sigma_{33} = \sigma_{12} = 0$ and $\epsilon_{11} = \epsilon_{22} = \epsilon_{33} = \epsilon_{12} = 0$.

SOIL PARAMETERS

The soil parameters for sand are chosen as follows:

ϕ = the angle of internal friction = 49.093°,
c = cohesion = 0 psf,
ν = Poisson's ratio = 0.2736,
E = Young's modulus = 841,396 psf or 40.3 MPa
R = shape ratio = 0 for the plane cap, $R = 4.33$ for the elliptic cap,
W = 0.0075, and
D = 6.781×10^{-5} ft^2/lb or 1.42 MPa^{-1}

MATERIAL TYPE

The material types considered are MAT = 3 for the plane cap material and MAT = 4 for the elliptic cap model.

DRUCKER-PRAGER MATERIAL CONSTANTS

The Drucker-Prager material constants α and k are determined from the soil parameters c and ϕ in the Coulomb model. For the three-dimensional matching along the *compressive meridian*, they have the values:

$$\alpha = \frac{2 \sin \phi}{\sqrt{3}\,(3 - \sin \phi)} = 0.3889$$

$$k = \frac{6c \cos \phi}{\sqrt{3}\,(3 - \sin \phi)} = 0.$$

For the three-dimensional matching along the *tensile meridian*, they are:

$$\alpha = \frac{2 \sin \phi}{\sqrt{3}\,(3 + \sin \phi)} = 0.2324$$

$$k = \frac{6c \cos \phi}{\sqrt{3}\,(3 + \sin \phi)} = 0.$$

For the *plane strain* matching with the same limit load, the values are:

$$\alpha = \frac{\tan \phi}{\sqrt{9 + 12 \tan^2 \phi}} = 0.2309$$

$$k = \frac{3c}{\sqrt{9 + 12 \tan^2 \phi}} = 0.$$

In the present numerical example, the material constants from the plane strain matching are selected.

Initial cap location

The initial cap location is assumed to be at the origin in the $I_1 - \sqrt{J_2}$-space. For the plane model:

$\text{EL} = \text{XL} = 0.$

For the elliptic cap model:

$$\text{EL} = \frac{Rk}{1 + \alpha R}$$

$\text{XL} = 0.$

7.6.2 *Numerical results*

(A) Plane cap prediction

The curve for the axial stress-strain relationship is shown in Fig. 7.33 for the plane cap model. The axial compressive strain is increased up to -3.25% and then decreased to zero (free) state under the static condition. The broken line in Fig. 7.33 shows the axial stress-strain curve predicted by the Drucker-Prager model without a cap. In this case, the relationship is linearly elastic under the strain-increasing path as well as the strain-decreasing path. As can be seen from the inset of Fig. 7.33, the stress invariant path in $I_1 - \sqrt{J_2}$ space for this case is a straight line within the failure envelope.

The solid line in Fig. 7.33 shows the behavior predicted by the Drucker-Prager model with a simple plane cap under the same strain-path condition. At the beginning of straining, the plane cap is situated at the origin in the $I_1 - \sqrt{J_2}$ space. As the strain increases, the state of stress that lies on the corner, moves along the

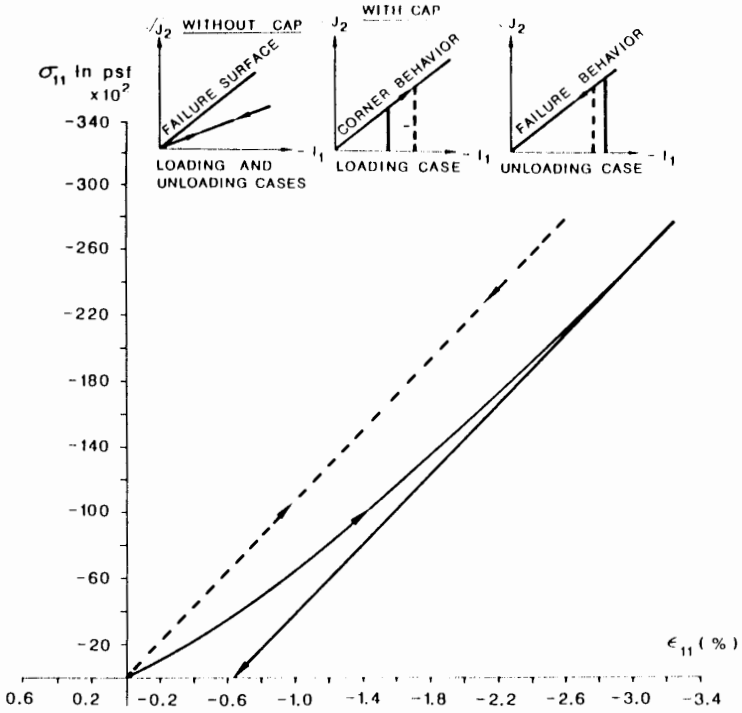

Fig. 7.33. Behavior of the plane cap material under the condition of uniaxial strain: vertical stress - strain relation.

failure envelope with the plane cap. Here, the *corner coding* described in Section 7.5.5 is performed up to the strain level of -2.3% and then the *hardening surface coding* in Section 7.5.6 is employed up to -3.25% strain level in the present analysis. Finally, the maximum *equivalent* axial compressive stress σ_{11} becomes $-27,800$ psf (-1.33 MPa).

In the case of the strain-decreasing path, the stress path is initially directed toward the elastic region, but it soon reaches the failure surface and then moves along the failure envelope toward the origin. Thus, the *yield surface coding* in Section 7.5.4 is utilized in this case. At the same time, the plane cap contracts gradually toward the origin due to the dilatancy. From the axial stress-strain curve shown in Fig. 7.33 with a solid line, however, it can be seen that the behavior for the strain-decreasing path is similar to the elastic behavior. At the strain level -0.619%, the stresses become free state and further straining does not change the stress states which remain at free state. The stress difference–strain difference relation, the hydrostatic pressure-volumetric strain relation, and the stress difference–hydrostatic pressure relation are shown respectively in Figs. 7.34 through 7.36. The behaviors in Figs. 7.34 and 7.35 are generally similar to those of Fig. 7.33. From these figures, it appears that as the strain increases, each behavior approaches the elastic behavior.

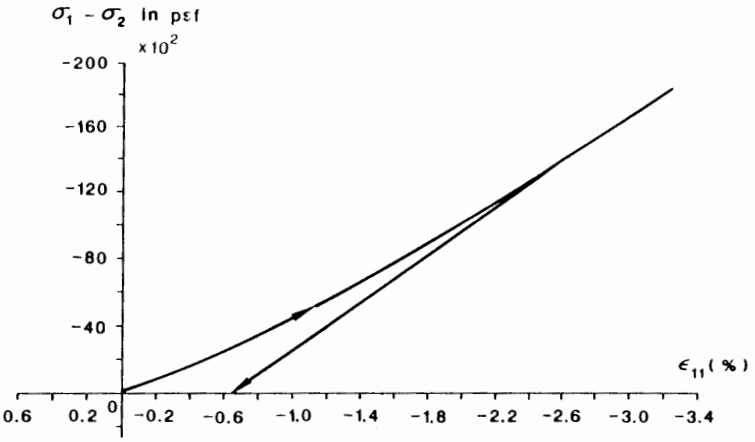

Fig. 7.34. Behavior of the plane cap material under the condition of uniaxial strain: principal stress difference strain difference relation.

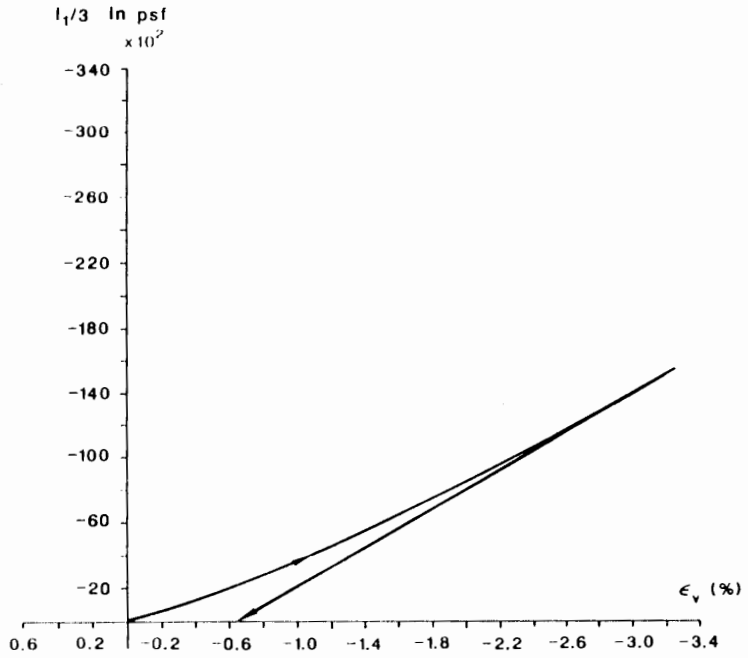

Fig. 7.35. Behavior of the plane cap material under the condition of uniaxial strain: hydrostatic pressure volumetric strain relation.

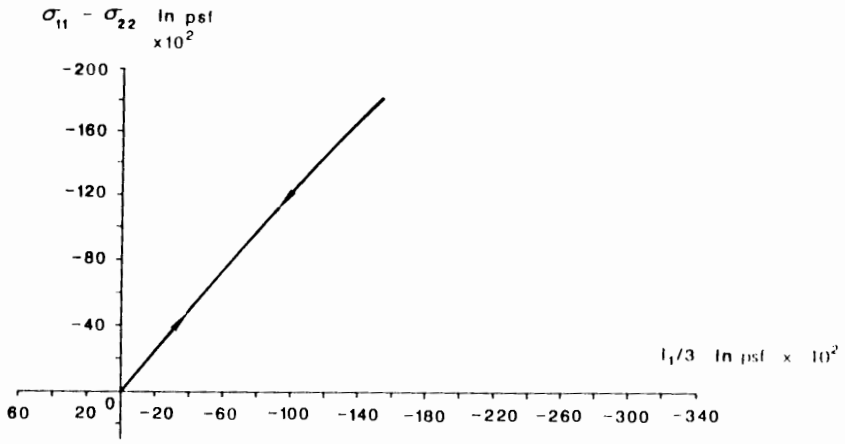

Fig. 7.36. Behavior of the plane cap material under the condition of uniaxial strain: principal stress difference–hydrostatic pressure relation.

From Fig. 7.36, on the other hand, it can be seen that the stress path moves entirely on the failure surface during both straining paths.

(B) Elliptic cap prediction

Similarly, the axial stress-strain curves for the strain-increasing and decreasing paths are presented in Fig. 7.37 with the elliptic cap model. The stress path in the $I_1 - \sqrt{J_2}$ space during the strain-increasing path is seen to move first within the failure envelope and then later to situate on the elliptic cap surface. A *hardening surface coding* in Section 7.5.6 is therefore employed here. At the axial compressive strain of -3.25%, the equivalent axial compressive stress σ_{11} becomes $-21{,}687$ psf (-1.04 MPa) which is smaller than that for the plane cap model. On the other hand, the stress state during the strain-decreasing path moves within the current elastic region while the elliptic cap remains fixed in the stress space. Consequently, the axial stress-strain curve is linearly elastic until the stress state touches the failure surface. This occurs at -1.26% axial strain. Once the stress state reaches the failure envelope, the *yield surface coding* is utilized to determine the plastic volume expansion or dilatancy. As a result of this dilatancy, the cap contracts toward the origin. The cap contraction stops at the current stress state, and this leads to the development of the corner point between the elliptic cap and the failure surface at the current stress state. Consequently, the *corner coding* is triggered until the stress state reaches the origin. The stress difference–strain difference relation, the hydrostatic pressure–volumetric strain relation, and the stress difference–hydrostatic pressure relation are respectively shown in Figs. 7.38 to 7.40. The main difference between the predictions of the plane cap model and the elliptic cap model is that they follow a different stress path during the strain-decreasing path.

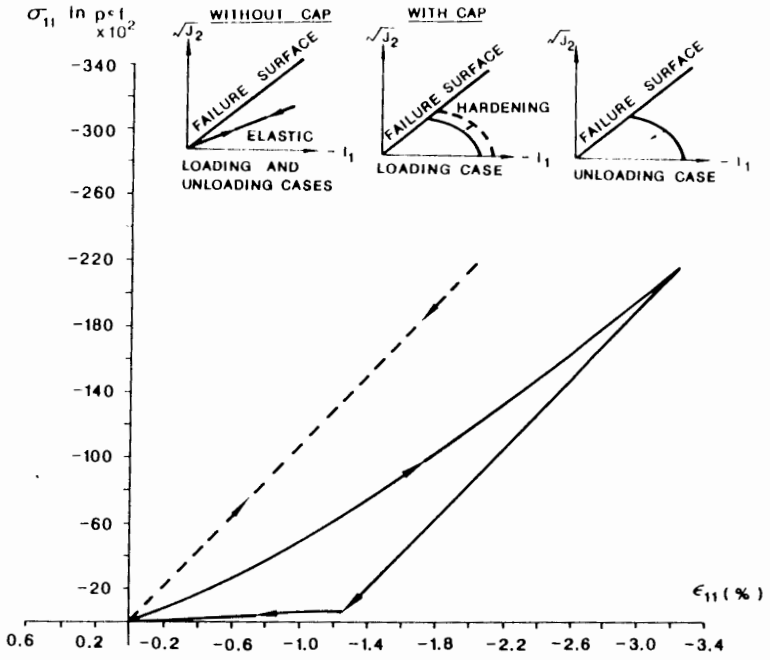

Fig. 7.37. Behavior of the elliptic cap material under the condition of uniaxial strain: vertical stress - strain relation.

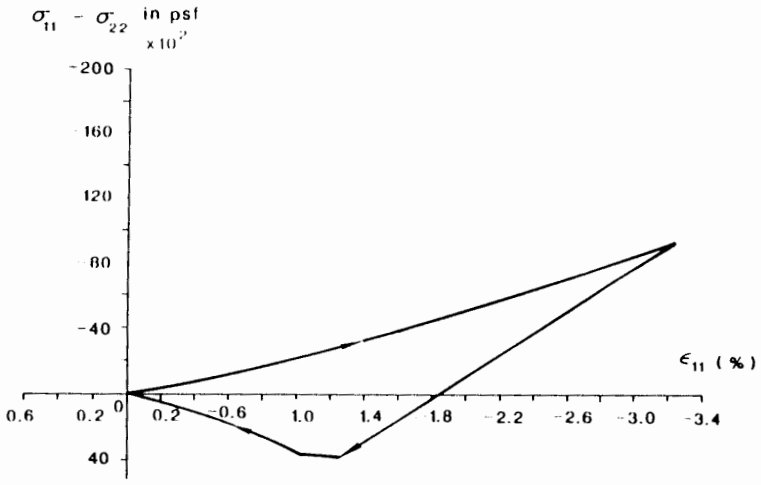

Fig. 7.38. Behavior of the elliptic cap material under the condition of uniaxial strain: principal stress difference–strain difference relation.

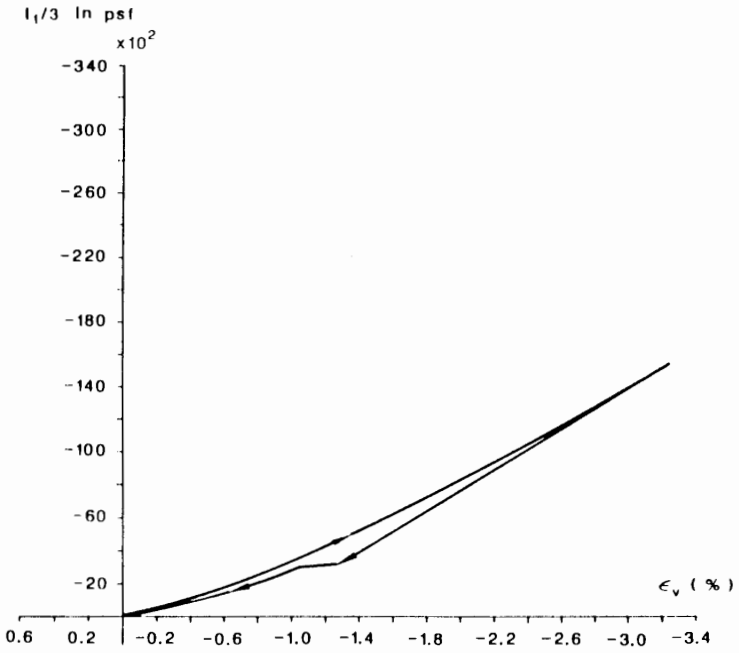

Fig. 7.39. Behavior of the elliptic cap material under the condition of uniaxial strain: hydrostatic pressure–volume strain relation.

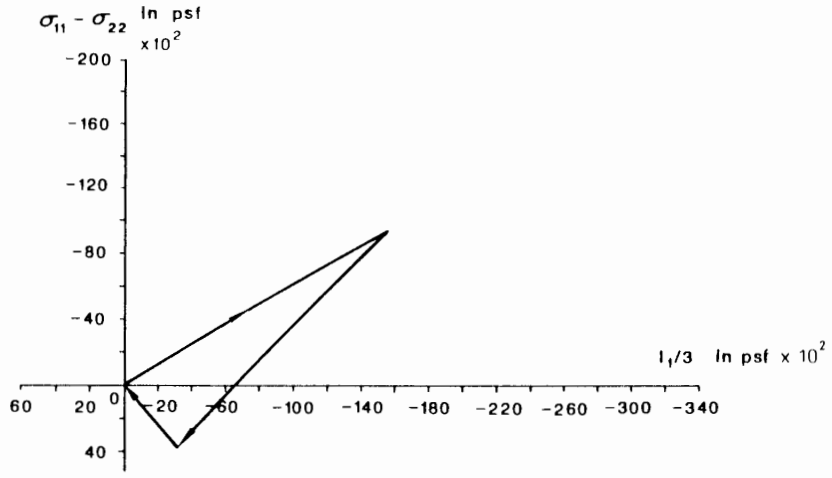

Fig. 7.40. Behavior of the elliptic cap material under the condition of uniaxial strain: principal stress difference–hydrostatic pressure relation.

7.7 SUMMARY

The finite-element computer implementations for the perfectly plastic models of the Coulomb and Drucker-Prager types and for the strain-hardening cap models of the plane and elliptical types are presented in some details. For any nonlinear stress analysis problems in geotechnical engineering, we must consider the following three conditions:

1. *Equilibrium equations* for the soil–structure system
2. *Kinematic relations* for the compatibility between strain and displacement, and
3. *Constitutive relations* for the stress and strain behavior of the material

The great error in currently available techniques for the nonlinear finite-element analysis lies in the selection of an appropriate material model. Once the material model is selected, the stress state can be evaluated for a given strain state, the strain state is estimated from the incremental equilibrium equations of the entire soil structure system and subsequently from the kinematic relations.

The implementation of material models in a finite-element computer program requires not only the knowledge of the incremental elastic and elastic-plastic constitutive matrices developed previously in Chapters 4 through 6, but also we need to estimate, at each load or displacement incremental step, the yielding state of the material element inside the discretized structure. Subsequently, the stress state must be integrated over the strain increments for the material element in the plastic region so that it lies on the current yield surface. Such a general implementation procedure for plasticity-based models is explained in Section 7.2.

Implementation of the Coulomb and the Drucker-Prager Models

The implementation of the Coulomb model and the Drucker-Prager model to a finite element program in the form of a subroutine has been described in some details. The SUBROUTINE CDPMDL so developed can be incorporated directly into an existing finite element program. Although the SUBROUTINE CDPMDL has been developed on the basis of the mid-point integration method, it can readily be used for any iterative procedure. The input quantities for the SUBROUTINE CDPMDL are the *stress state* that was obtained in the previous calculation, the material constants that were associated with the failure criterion used, and the *strain increments* that were obtained from the previous calculation step. The updated stress state is then corrected to ensure that it lies on the current loading surfaces. Finally, the updated constitutive matrix is constructed for a possible calculation for the next increment.

At the mid-increment step, the following procedures are carried out: If the material element is elastic at the end of the previous calculation step, the stress increments evaluated twice at the mid-increment are added to the stresses at the previous step. This is then followed by the stress checked against the failure or current yield surface. If the stress state does not violate the current loading surfaces, the material element is assumed to remain in the elastic state at the end of the full-increment. Otherwise, the material element is assumed to be in the plastic state.

In this case, an averaged constitutive matrix of elastic and elastic-plastic matrices is estimated as:

$$[C^{ep}]_{av} = r[C^{e}] + (1 - r)[C^{ep}]$$

where r is the scaling factor.

If the material element is in the plastic state at the end of the previous step, the material element is checked to determine whether it has undergone the *plastic unloading*. To this end, the *proportionality factor* $d\lambda$ is calculated using the stress state at the previous step and the strain increments estimated from the current finite element analysis. If the value of $d\lambda$ is positive, the material element is assumed to be in the plastic state even plastic unloading may occur at the end of the full-increment. The stress state is then scaled back onto the yield surface in such a manner that the magnitude of hydrostatic pressure and the principal directions of the stress state remain unchanged. If the proportionality factor $d\lambda$ has a negative value, the material element is assumed to be elastic.

At the full-increment step, on the other hand, the following procedures are taken: For the material element that was elastic at the mid-increment step, the stress state is checked against the failure or the current yield surfaces. If it violates either one of these surfaces, the stress state is scaled back onto the failure or yield surfaces. Otherwise, it is assumed to be elastic.

On the other hand, if the material element was plastic at the mid-increment step, stress state is scaled back onto the failure or yield surfaces regardless whether the stress state lies inside or outside the failure or yield surfaces.

The SUBROUTINE CDPMDL has been applied to the uniaxial strain problem and showed its efficiency in treating the perfectly plastic type of material models.

Implementation of the cap models

The cap model of the plane and elliptic caps has been implemented in the SUBROUTINE CAPMDL. In this subroutine, the input quantity is the *strain increments* obtained from the current incremental equilibrium equations and the kinematic relations. Using the strain increments, the *elastic trial stresses* are first estimated from the stress state at the previous step. Depending upon the location of the elastic trial stresses on the current loading surfaces, the coding treatments are divided into the following four cases:

1. *Tensile coding*
2. *Yield surface coding*
3. *Corner coding*
4. *Hardening surface coding*

If the elastic trial stresses violate none of the current loading surfaces, then, the stress state is assumed to be elastic. On the other hand, if it violates any one of the current loading surfaces, the corresponding coding described above is triggered so that the new loading surface is updated if necessary and the new stress state will

always be on this surface. The SUBROUTINE CAPMDL has also been applied to the uniaxial strain problem to check its algorithms.

Both SUBROUTINE CDPMDL and CAPMDL are directly applicable to existing finite element programs and can be easily extended to the three-dimensional conditions. The procedures described in the present subroutines are applicable for solving both static and dynamic nonlinear stress analysis problems in geotechnical engineering.

For the case of relatively large strain increments, the given strain increments should be divided further into several subsections, and then the same numerical algorithm is repeated until the stresses are integrated over the full strain increments.

For a nonlinear stress or deformation analysis in geotechnical engineering, the algorithms for an efficient and reliable finite-element solution must be selected according to the required accuracy of the analysis, constitutive laws, computing capacity available etc. For example, if the necessary laboratory or field tests for the determination of the material properties or soil field conditions are not economically justified, or if the finite-element grid is relatively coarse because of the computing capacity limitation, then, a more refined unified algorithm may not be necessary for such an analysis.

REFERENCES

Bathe, K.J., Snyder, M.D., Cimento, A.P. and Rolph, W.D., 1980. On some current procedures and difficulties in finite element analysis of elastic-plastic response. Comput. Struct., 12: 607–624.

Chen, W.F., 1982. Plasticity in Reinforced Concrete. McGraw-Hill, New York, NY, 474 pp.

Chen, W.F. and Baladi, G.Y., 1985. Soil Plasticity: Theory and Implementation. Elsevier, Amsterdam, 231 pp.

Conte, S.D. and de Boor, C., 1972. Elementary Numerical Analysis. McGraw-Hill, New York, NY.

Davidson, H.L. and Chen, W.F., 1974. Elastic-Plastic Large Deformation Response of Clay to Footing Loads. Rep. No. 355.18, Fritz Eng. Lab. Lehigh University, PA, 181 pp.

Mizuno, E., 1981. Plasticity modeling of soils and finite element applications. Ph.D. Thesis, School of Civil Engineering, Purdue University, West Lafayette, IN, 320 pp.

Nayak, G.C. and Zienkiewicz, O.C., 1972. Elasto-plastic analysis, a generalization for various constitutive relations including strain softening. Int. J. Numer. Methods Eng. 5: 113–135.

Sandler, I.S. and Rubin, D., 1979. An algorithm and a modular subroutine for the cap model. Int. J. Numer. Anal. Methods Geomech., 3: 173–186.

Zienkiewicz, O.C., Valliappan, S. and King, I.P., 1969. Elasto-plastic solutions of engineering problems; Initial stress finite element approach. Int. J. Numer. Methods Eng., 1: 75–100.

Part IV

GEOMETRIC NONLINEARITY—LARGE-DEFORMATION ANALYSES

Chapter 8

LARGE-DEFORMATION FORMULATION AND SIMPLIFICATION

8.1 INTRODUCTION

We have so far treated the *material nonlinearity* and its computer implementation in the finite-element analysis. Another *nonlinearity* is due to the effect of deformation on the overall *geometry change* of structures which has been recognized in several types of structures. This *geometrical nonlinearity* may have either a stiffening effect or a softening effect on the overall load-displacement response of structures. For example, cable structures generally display a stiffening behavior, while shallow arches may first soften and then stiffen, a behavior known as the *snap-through buckling*. Although not as tangible, the behavior of a continuum is similarly affected.

In order to describe the actual physical phenomena of structures considering the change in geometry in the formulation, the concept of *finite strain* must be introduced instead of the usual *small-strain assumption* discussed in Chapter 2. Although the small-strain assumption is acceptable and used extensively in many structural engineering applications, the effect of deformation upon the overall geometry of structures may not be ignored in many geotechnical engineering problems. The progressive failure responses of a soft ground to footing load (Davidson and Chen, 1974, 1977; Carter et al., 1977; Kiousis et al., 1986) and of the soil slope (Snitbhan and Chen, 1976; Mizuno and Chen, 1983) are typical examples that exhibit strong geometrical nonlinearities.

An examination of the current literature reveals several *large-deformation* or *large-displacement formulations* for the finite-element applications. The differences result mainly from the different simplifications of the kinematic relations and the different assumptions regarding the form of stress rate. Gadala et al. (1984) presented a discussion of several numerical techniques that are capable of dealing with nonlinear problems involving geometrical changes of structures.

In the first part of this Chapter, we shall present the theoretical basis and numerical techniques associated with large-displacement and/or large-deformation continuum problems. The equilibrium equations are then developed by introducing the appropriate stress-strain relations into the virtual work equations that take account of the changes in geometry of the soil medium. In this development, the effect of deformations in soil medium upon the overall geometry of the problem is considered when constructing the equilibrium equations.

To this end, we shall deal first with the fundamentals of finite deformations such as the measure of strains, strain rates, the measure of stresses, and stress rates, and then with the constitutive equation used in the finite deformation formulations, and finally with the modifications of the equilibrium equations as required by the virtual work equations. A brief description of the two most commonly used solution procedures for analysis of large-strain and large-displacement continuum problems will be followed. These are the *total Lagrangian* description and the *updated Lagrangian* description. Special attention will be given here for the updated Lagrangian formulations and their simplifications as used by Davidson and Chen (1974).

8.2 MEASURES OF STRAIN

In this Section, several definitions of strain commonly associated with large deformation formulations will be introduced and explained. For continuity, we shall begin first with a discussion of *small strains* and then extend the concept of infinitesimal strain to *finite strains* of the Lagrangian and Eulerian types.

8.2.1 Small strains

In general, surface tractions and/or body forces give rise to movements and deformations in the body. When the relative position of any two points in a continuous body is changed, the body is said to be *deformed* or *strained*. If the distance between every pair of points in the body remains constant during motions of the body, then the body undergoes *rigid-body motion*. The displacements of a rigid-body motion consist of *translations* and *rotations*; translations and rotations are therefore called *rigid-body displacements*. As will be understood later, when the displacements and displacement gradients are considerably small, the small-strain assumption for the deformation of the continuous body is rigorously correct.

Let us consider a line element PQ inside the body where the points P and Q have the coordinates (X_1, X_2, X_3) and $(X_1 + \mathrm{d}X_1, X_2 + \mathrm{d}X_2, X_3 + \mathrm{d}X_3)$, respectively, as shown in Fig. 8.1. After an increment of external forces, the element PQ is translated, rotated and stretched to the deformed configuration pq whose new coordinates are (x_1, x_2, x_3) and $(x_1 + \mathrm{d}x_1, x_2 + \mathrm{d}x_2, x_3 + \mathrm{d}x_3)$. Denoting the displacement of point P by $u_i = u_i(X_1, X_2, X_3)$, the relative displacement $\mathrm{d}u_i$ of point Q relative to point P is written as:

$$\mathrm{d}u_i = \frac{\partial u_i}{\partial X_j}\,\mathrm{d}X_j \tag{8.1}$$

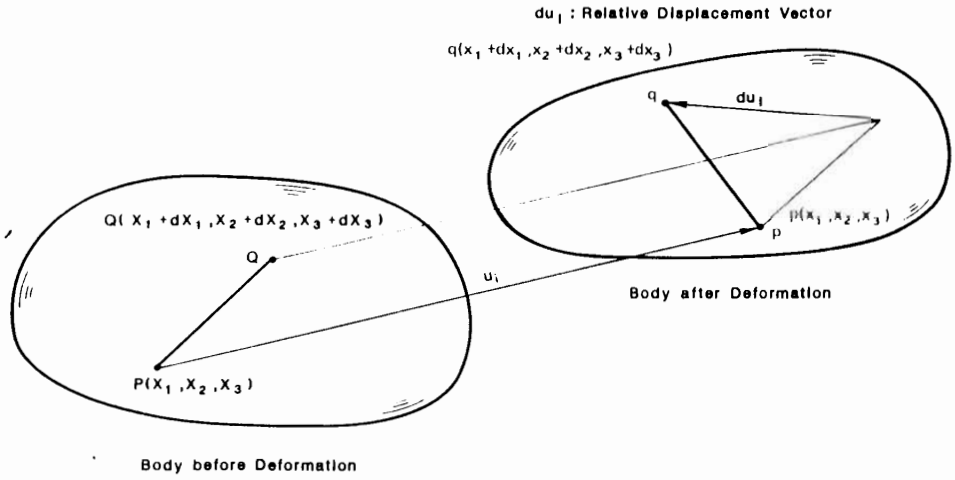

Fig. 8.1. Relative displacement vector.

Therefore, the components of *unit relative displacement* $\mathrm{d}u_i/\mathrm{d}S$ (Malvern, 1969) can be written as:

$$\frac{\mathrm{d}u_1}{\mathrm{d}S} = \frac{\partial u_1}{\partial X_1}\frac{\mathrm{d}X_1}{\mathrm{d}S} + \frac{\partial u_1}{\partial X_2}\frac{\mathrm{d}X_2}{\mathrm{d}S} + \frac{\partial u_1}{\partial X_3}\frac{\mathrm{d}X_3}{\mathrm{d}S}$$

$$\frac{\mathrm{d}u_2}{\mathrm{d}S} = \frac{\partial u_2}{\partial X_1}\frac{\mathrm{d}X_1}{\mathrm{d}S} + \frac{\partial u_2}{\mathrm{d}X_2}\frac{\mathrm{d}X_2}{\mathrm{d}S} + \frac{\partial u_2}{\partial X_3}\frac{\mathrm{d}X_3}{\mathrm{d}S} \tag{8.2a}$$

$$\frac{\mathrm{d}u_3}{\mathrm{d}S} = \frac{\partial u_3}{\partial X_1}\frac{\mathrm{d}X_1}{\mathrm{d}S} + \frac{\partial u_3}{\partial X_2}\frac{\mathrm{d}X_2}{\mathrm{d}S} + \frac{\partial u_3}{\partial X_3}\frac{\mathrm{d}X_3}{\mathrm{d}S}$$

or in indicial form:

$$\frac{\mathrm{d}u_i}{\mathrm{d}S} = \frac{\partial u_i}{\partial X_j}n_j \tag{8.2b}$$

where $\mathrm{d}S$ is the length of element PQ, $\partial u_i/\partial X_j$ is the *displacement gradient* tensor, and n_j the directional cosines $\mathrm{d}X_i/\mathrm{d}S$ of the element in the initial configuration. Since the current position coordinates of the point change from X_i to $x_i = X_i + u_i$ during the continuous deformation process of the body, the strict distinction between X_i and x_i must be made when the displacement gradients are evaluated. If the displacements u_i are small enough, however, it may not be necessary to distinguish these two coordinates and the displacement gradients may be expressed by $\partial u_i/\partial X_j$ based on the initial coordinates of the point.

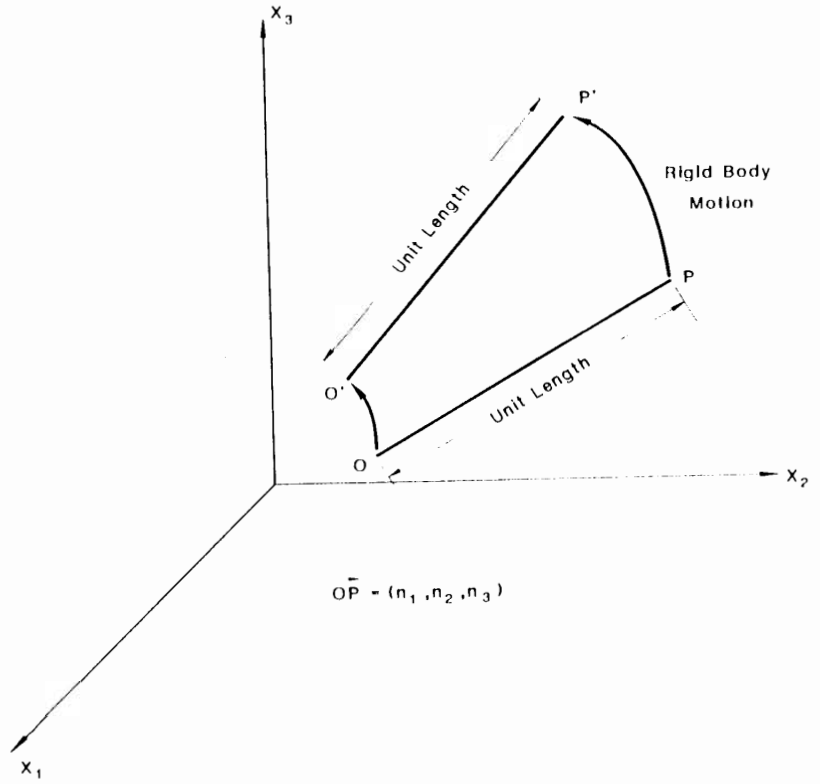

Fig. 8.2. Rigid-body motion.

A rigid-body motion, as mentioned earlier, is characterized by the fact that the length of any line element joining any two points in the body remains unchanged. In the following, the conditions for the components of the displacement gradient tensor $\partial u_i/\partial X_j$ to satisfy this requirement for rigid-body motion are introduced.

Consider the unit line element OP with the component n_i, as shown in Fig. 8.2, and assume that after a pure rigid-body motion, the element assumes the new positions O′P′ as shown. Since the length of the unit vector will not change during a rigid body motion, it follows that:

$$|\dot{n}|^2 = \left|\dot{n} + \frac{\mathrm{d}\dot{u}}{\mathrm{d}S}\right|^2 \cong |\dot{n}|^2 + 2\dot{n} \cdot \frac{\mathrm{d}\dot{u}}{\mathrm{d}S} \tag{8.3a}$$

or

$$n_i n_i = \left(n_i + \frac{\mathrm{d}u_i}{\mathrm{d}S}\right)\left(n_i + \frac{\mathrm{d}u_i}{\mathrm{d}S}\right) \cong n_i n_i + 2n_i \frac{\mathrm{d}u_i}{\mathrm{d}S} \tag{8.3b}$$

where the higher-order term in du_i/dS is neglected because of the infinitesimal deformation assumption, i.e., the displacement gradients du_i/dX_j are small compared with unity. Substituting du_i/dS from Eq. (8.2b) into Eq. (8.3b), we get:

$$n_i \cdot \frac{du_i}{dS} = n_i \frac{du_i}{dS} = n_i \left(\frac{\partial u_i}{\partial X_j} n_j \right) = 0$$

or when written out in full:

$$\frac{\partial u_i}{\partial X_j} n_i n_j = \frac{\partial u_1}{\partial X_1} n_1^2 + \frac{\partial u_2}{\partial X_2} n_2^2 + \frac{\partial u_3}{\partial X_3} n_3^2 + \left(\frac{\partial u_1}{\partial X_2} + \frac{\partial u_2}{\partial X_1} \right) n_1 n_2 + \left(\frac{\partial u_2}{\partial X_3} + \frac{\partial u_3}{\partial X_2} \right) n_2 n_3$$

$$+ \left(\frac{\partial u_3}{\partial X_1} + \frac{\partial u_1}{\partial X_3} \right) n_3 n_1 = 0 \tag{8.4}$$

Since Eq. (8.4) must be true for all values of n_1, n_2, and n_3, the necessary and sufficient conditions that tensor $\partial u_i/\partial X_j$ represents a rigid-body rotation are given by:

$$\frac{\partial u_1}{\partial X_1} = \frac{\partial u_2}{\partial X_2} = \frac{\partial u_3}{\partial X_3} = 0$$

$$\frac{\partial u_1}{\partial X_2} + \frac{\partial u_2}{\partial X_1} = \frac{\partial u_2}{\partial X_3} + \frac{\partial u_3}{\partial X_2} = \frac{\partial u_3}{\partial X_1} + \frac{\partial u_1}{\partial X_3} = 0$$

or

$$\frac{\partial u_i}{\partial X_j} = -\frac{\partial u_j}{\partial X_i} \tag{8.5}$$

That is, for a rigid-body rotation, the displacement gradient tensor $\partial u_i/\partial X_j$ should be *skew-symmetric*.

Since every second-order tensor can be decomposed into the sum of a symmetrical tensor and a skew-symmetric tensor in one and only one way, it follows that the skew-symmetric part represents a rigid-body rotation, whereas the symmetrical part represents a *pure deformation*. Thus, we can write:

$$\frac{\partial u_i}{\partial X_j} = u_{i,j} = \tfrac{1}{2}(u_{i,j} + u_{j,i}) + \tfrac{1}{2}(u_{i,j} - u_{j,i}) \tag{8.6}$$

or

$$\frac{\partial u_i}{\partial X_j} = \epsilon_{ij} + \Omega_{ij} \tag{8.7}$$

in which:

$$\epsilon_{ij} = \tfrac{1}{2}(u_{i,j} + u_{j,i}) \tag{8.8}$$

and

$$\Omega_{ij} = \tfrac{1}{2}(u_{i,j} - u_{j,i}) \tag{8.9}$$

where $u_{i,j}$ is $\partial u_i/\partial X_j$, ϵ_{ij} is called the *strain tensor* for small displacement conditions, and Ω_{ij} is called the *rotation tensor*. If the motion is purely rigid body, the terms ϵ_{ij} are identically zero. If the motion is purely distortion (strain), the terms Ω_{ij} are zero. Expanding both ϵ_{ij} and Ω_{ij}, we obtain:

$$\epsilon_{ij} = \begin{bmatrix} u_{1,1} & \tfrac{1}{2}(u_{1,2} + u_{2,1}) & \tfrac{1}{2}(u_{1,3} + u_{3,1}) \\ \tfrac{1}{2}(u_{2,1} + u_{1,2}) & u_{2,2} & \tfrac{1}{2}(u_{2,3} + u_{3,2}) \\ \tfrac{1}{2}(u_{3,1} + u_{1,3}) & \tfrac{1}{2}(u_{3,2} + u_{2,3}) & u_{3,3} \end{bmatrix} \tag{8.10}$$

$$\Omega_{ij} = \begin{bmatrix} 0 & \tfrac{1}{2}(u_{1,2} - u_{2,1}) & \tfrac{1}{2}(u_{1,3} - u_{3,1}) \\ \tfrac{1}{2}(u_{2,1} - u_{1,2}) & 0 & \tfrac{1}{2}(u_{2,3} - u_{3,2}) \\ \tfrac{1}{2}(u_{3,1} - u_{1,3}) & \tfrac{1}{2}(u_{3,2} - u_{2,3}) & 0 \end{bmatrix} \tag{8.11}$$

Substituting $\partial u_i/\partial X_j$ from Eq. (8.7) into Eq. (8.2b), we obtain:

$$\frac{\mathrm{d}u_i}{\mathrm{d}S} = \epsilon_{ij} n_j + \Omega_{ij} n_j \tag{8.12}$$

The first part of Eq. (8.12) represents the pure deformation whereas the second part represents the rigid-body rotation.

The unit relative displacement vector corresponding to the pure deformation is called the *strain vector*, and is denoted by δ:

$$\delta_i = \epsilon_{ij} n_j = \epsilon_{ji} n_j \tag{8.13}$$

The unit relative displacement vector corresponding to a rigid-body rotation is called the *rotation vector*, and is denoted by Ω:

$$\Omega_i = \Omega_{ij} n_j = -\Omega_{ji} n_j \tag{8.14}$$

The approximations involved in the small-strain definition of Eq. (8.8) will become evident in the following Section.

Example 8.1: Show that the rotation vector $\Omega_{ij}n_j$ in Eq. (8.14) gives the same unit relative displacements as the vector product $\vec{\omega} \times \vec{n}$ where the components of $\vec{\omega}$ are defined as:

$$\omega_i = -\tfrac{1}{2}e_{ijk}\Omega_{jk} \tag{8.15}$$

in which e_{ijk} is the *permutation symbol.*

Solution: The vector product $\vec{\omega} \times \vec{n}$ can be expressed by $\vec{\omega} \times \vec{n} = e_{ijk}\omega_j n_k$. Substitution of $\omega_j = -\tfrac{1}{2}e_{jlm}\Omega_{lm}$ yields the following expression:

$$\vec{\omega} \times \vec{n} = -\tfrac{1}{2}e_{ijk}e_{jlm}\Omega_{lm}n_k$$

With the characteristic of *permutation symbol*, i.e., $e_{ijk} = -e_{jik}$ and the e-δ identity $e_{jik}e_{jlm} = \delta_{il}\delta_{km} - \delta_{im}\delta_{kl}$ (Chen and Saleeb, 1982), we find:

$$\vec{\omega} \times \vec{n} = \tfrac{1}{2}e_{jik}e_{jlm}\Omega_{lm}n_k = \tfrac{1}{2}(\delta_{il}\delta_{km} - \delta_{im}\delta_{kl})\Omega_{lm}n_k$$

$$= \tfrac{1}{2}(\Omega_{ik}n_k - \Omega_{ki}n_k) = \Omega_{ik}n_k = \Omega_{ij}n_j$$

Example 8.2: When the displacement components u_i are given by:

$$u_1 = \alpha X_1 X_3, \quad u_2 = \alpha X_2 X_3, \quad u_3 = 2\alpha(X_1 + X_2)X_3$$

where α is a constant small enough to ensure the validity of the assumption of the small-deformation theory:

(a) Express the components of the small-strain tensor and the rotation tensor as a function of X_1, X_2, and X_3.

(b) Calculate these components at the point $(X_1, X_2, X_3) = (1, 1, 1)$.

Solutions:

(a) The definitions of small-strain tensor ϵ_{ij} and of rotation tensor Ω_{ij} are given by Eqs. (8.10) and (8.11). The components of displacement gradients are:

$$u_{1,1} = \alpha X_3, \quad u_{1,2} = 0, \quad u_{1,3} = \alpha X_1$$
$$u_{2,1} = 0, \quad u_{2,2} = \alpha X_3, \quad u_{2,3} = \alpha X_2$$
$$u_{3,1} = 2\alpha X_3, \quad u_{3,2} = 2\alpha X_3, \quad u_{3,3} = 2\alpha(X_1 + X_2)$$

The matrices of small strain tensor ϵ_{ij} and of rotation tensor Ω_{ij} are:

$$\epsilon_{ij} = \begin{bmatrix} \alpha X_3 & 0 & \tfrac{1}{2}\alpha(X_1 + 2X_3) \\ 0 & \alpha X_3 & \tfrac{1}{2}\alpha(X_2 + 2X_3) \\ \tfrac{1}{2}\alpha(X_1 + 2X_3) & \tfrac{1}{2}\alpha(X_2 + 2X_3) & 2\alpha(X_1 + X_2) \end{bmatrix}$$

$$\Omega_{ij} = \begin{bmatrix} 0 & 0 & \tfrac{1}{2}\alpha(X_1 - 2X_3) \\ 0 & 0 & \tfrac{1}{2}\alpha(X_2 - 2X_3) \\ -\tfrac{1}{2}\alpha(X_1 - 2X_3) & -\tfrac{1}{2}\alpha(X_2 - 2X_3) & 0 \end{bmatrix}$$

(b) Substitution of the coordinate $(X_1, X_2, X_3) = (1, 1, 1)$ into the above matrices leads to:

$$\epsilon_{ij} = \begin{bmatrix} \alpha & 0 & \frac{3}{2}\alpha \\ 0 & \alpha & \frac{3}{2}\alpha \\ \frac{3}{2}\alpha & \frac{3}{2}\alpha & 4\alpha \end{bmatrix}$$

$$\Omega_{ij} = \begin{bmatrix} 0 & 0 & -\frac{1}{2}\alpha \\ 0 & 0 & -\frac{1}{2}\alpha \\ \frac{1}{2}\alpha & \frac{1}{2}\alpha & 0 \end{bmatrix}$$

8.2.2 *Finite strains*

When the displacement gradient components at a point are large, their symmetrical and skew-symmetric parts will not represent respectively the pure deformation and the rigid rotation of the point. As a result, the strain definition (8.8) becomes incomplete and an alternative form must be adopted. In the following, we shall describe a general measurement of strains with respect to both the initially undeformed configuration and the current deformed configuration. The former approach is known as the *Lagrangian formulation*, while the latter is called *Eulerian formulation*. In the case of small displacements, the two definitions yield identical results.

General description of motion

Consider two independent systems of coordinates in a body. The system with coordinate X^K (X^1, X^2, X^3) as shown in Fig. 8.3 is measured with respect to the undeformed (reference) state while the other system x^k (x^1, x^2, x^3) is referred to the deformed (current) state. Such systems become in general curvilinear coordinate systems if the reference configuration of the body $\mathring{V}$ at time $t = 0$ and the deformed configuration V at time t are both referred to their fixed Cartesian frames $\mathring{Z}^t$ and z^t with unit base vectors $\mathring{i}_t$ and $\dot{i}_t$, respectively. Referring to Fig. 8.3, the position vectors for the point P_0 with the curvilinear coordinate X^t and point P with x^t can be described in their fixed Cartesian frames $\mathring{Z}^t$ and z^t respectively as:

$$\mathring{r} = O'\mathring{P}_0 = \mathring{Z}^K(X^1, X^2, X^3, 0)\mathring{i}_K \tag{8.16}$$

$$\dot{r} = O\dot{P} = z^k(x^1, x^2, x^3, t)\dot{i}_k \tag{8.17}$$

Denoting the infinitesimal line elements in the reference and current body by P_0Q_0

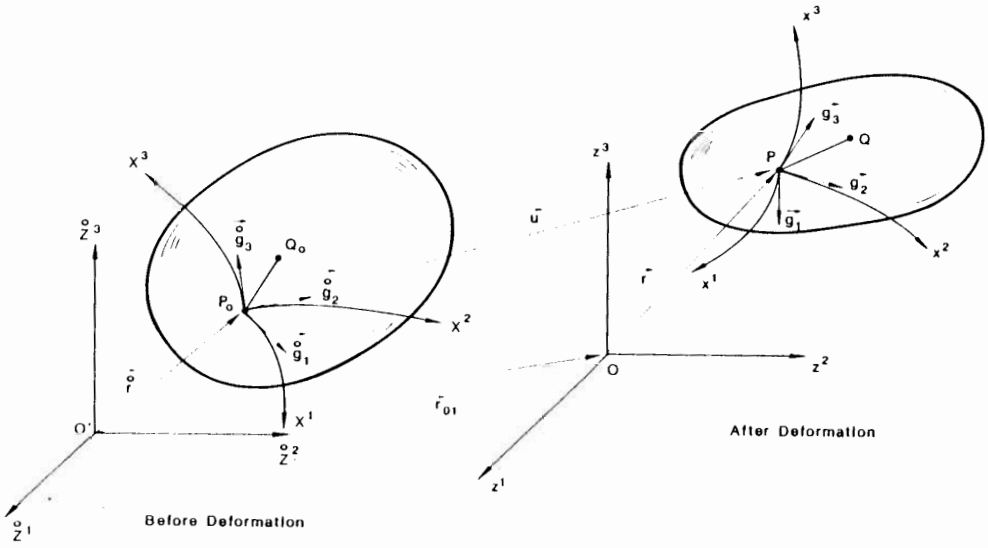

Fig. 8.3. General motion of body.

and PQ, respectively, these element vectors $\mathrm{d}\vec{\vec{r}}$ and $\mathrm{d}\vec{r}$ are expressed from Eqs. (8.16) and (8.17) as:

$$\mathrm{d}\vec{\vec{r}} = \frac{\partial \vec{\vec{r}}}{\partial X^{\Lambda}}\,\mathrm{d}X^{\Lambda} = \vec{\vec{g}}_{\Lambda}\,\mathrm{d}X^{\Lambda} \tag{8.18}$$

$$\mathrm{d}\vec{r} = \frac{\partial \vec{r}}{\partial x^{k}}\,\mathrm{d}x^{k} = \vec{g}_{k}\,\mathrm{d}x^{k} \tag{8.19}$$

where $\vec{\vec{g}}_{\Lambda}$ and $\vec{g}_{k}$ are called the *covariant base vectors* in reference and current curvilinear coordinate systems, respectively. Note that the capital indices are used in the reference configuration and the small indices in the current configuration. The components of covariant base vectors $\vec{\vec{g}}_{\Lambda}$ and $\vec{g}_{k}$ in their fixed Cartesian coordinate systems $\vec{\vec{Z}}^{\Lambda}$ and z^{k} respectively are written as:

$$\vec{\vec{g}}_{\Lambda} = \frac{\partial \vec{\vec{r}}}{\partial X^{\Lambda}} = \frac{\partial \vec{\vec{Z}}^{1}}{\partial X^{\Lambda}}\vec{\vec{i}}_{1} + \frac{\partial \vec{\vec{Z}}^{2}}{\partial X^{\Lambda}}\vec{\vec{i}}_{2} + \frac{\partial \vec{\vec{Z}}^{3}}{\partial X^{\Lambda}}\vec{\vec{i}}_{3} \tag{8.20}$$

$$\vec{g}_{k} = \frac{\partial \vec{r}}{\partial x^{k}} = \frac{\partial z^{1}}{\partial x^{k}}\vec{i}_{1} + \frac{\partial z^{2}}{\partial x^{k}}\vec{i}_{2} + \frac{\partial z^{3}}{\partial x^{k}}\vec{i}_{3} \tag{8.21}$$

since $\vec{\vec{r}} = \vec{\vec{Z}}^{1}\vec{\vec{i}}_{1} + \vec{\vec{Z}}^{2}\vec{\vec{i}}_{2} + \vec{\vec{Z}}^{3}\vec{\vec{i}}_{3}$ and $\vec{r} = z^{1}\vec{i}_{1} + z^{2}\vec{i}_{2} + z^{3}\vec{i}_{3}$.

Using Eqs. (8.18) and (8.19), the squares of the infinitesimal elements $d\mathring{s}^2$ and ds^2 in the reference and the current configurations are expressed as:

$$d\mathring{s}^2 = d\mathring{\vec{r}} \cdot d\mathring{\vec{r}} = \mathring{g}_{KL}\, dX^K\, dX^L \tag{8.22}$$

$$ds^2 = d\vec{r} \cdot d\vec{r} = g_{kl}\, dx^k\, dx^l \tag{8.23}$$

where $\mathring{g}_{KL}$ and g_{kl} are respectively called the *metric tensors* of curvilinear coordinate systems X^K and x^k, written as:

$$\mathring{g}_{KL} = \frac{\partial \mathring{Z}^M}{\partial X^K} \frac{\partial \mathring{Z}^M}{\partial X^L} \tag{8.24}$$

$$g_{kl} = \frac{\partial z^m}{\partial x^k} \frac{\partial z^m}{\partial x^l} \tag{8.25}$$

Example 8.3: Show that the determinants of the metric tensors $\mathring{g}_{KL}$ and g_{kl} are respectively denoted by:

$$|\mathring{g}_{KL}| = \left| \frac{\partial \mathring{Z}^K}{\partial X^I} \right|^2$$

$$|g_{kl}| = \left| \frac{\partial z^k}{\partial x^l} \right|^2$$

Solution: The determinant of tensor A_{ij} can be written in the form:

$$|A_{ij}| = e_{ijk} A_{i1} A_{j2} A_{k3}$$

where e_{ijk} is the permutation symbol. Applying this formula, $|\mathring{g}_{KL}|$ can be expressed by:

$$|\mathring{g}_{KL}| = e_{MNO} \mathring{g}_{M1} \mathring{g}_{N2} \mathring{g}_{O3}$$

where

$$\mathring{g}_{M1} = \frac{\partial \mathring{Z}^P}{\partial X^M} \frac{\partial \mathring{Z}^P}{\partial X^1}, \quad \mathring{g}_{N2} = \frac{\partial \mathring{Z}^Q}{\partial X^N} \frac{\partial \mathring{Z}^Q}{\partial X^2}, \quad \mathring{g}_{O3} = \frac{\partial \mathring{Z}^R}{\partial X^O} \frac{\partial \mathring{Z}^R}{\partial X^3}$$

Substituting these relations into the equation for $|\mathring{g}_{KL}|$, we obtain:

$$|\mathring{g}_{KL}| = e_{MNO} \frac{\partial \mathring{Z}^P}{\partial X^M} \frac{\partial \mathring{Z}^P}{\partial X^1} \frac{\partial \mathring{Z}^Q}{\partial X^N} \frac{\partial \mathring{Z}^Q}{\partial X^2} \frac{\partial \mathring{Z}^R}{\partial X^O} \frac{\partial \mathring{Z}^R}{\partial X^3}$$

$$= e_{MNO} \left(\frac{\partial \mathring{Z}^P}{\partial X^M} \frac{\partial \mathring{Z}^Q}{\partial X^N} \frac{\partial \mathring{Z}^R}{\partial X^O} \right) \left(\frac{\partial \mathring{Z}^P}{\partial X^1} \frac{\partial \mathring{Z}^Q}{\partial X^2} \frac{\partial \mathring{Z}^R}{\partial X^3} \right)$$

Using the relationships:

$$e_{PQR}\left|\frac{\partial \overset{\circ}{Z}{}^K}{\partial X^L}\right| = e_{MNO}\frac{\partial \overset{\circ}{Z}{}^P}{\partial X^M}\frac{\partial \overset{\circ}{Z}{}^Q}{\partial X^N}\frac{\partial \overset{\circ}{Z}{}^R}{\partial X^O}$$

and

$$\left|\frac{\partial \overset{\circ}{Z}{}^K}{\partial X^L}\right| = e_{PQR}\frac{\partial \overset{\circ}{Z}{}^P}{\partial X^1}\frac{\partial \overset{\circ}{Z}{}^Q}{\partial X^2}\frac{\partial \overset{\circ}{Z}{}^R}{\partial X^3}$$

we can derive:

$$|\overset{\circ}{g}_{KL}| = \left|\frac{\partial \overset{\circ}{Z}{}^K}{\partial X^L}\right|^2$$

Similarly, $|g_{kl}| = |\partial z^k/\partial x^l|^2$ is easily understood.

General description of deformation

We have described so far the infinitesimal elements of a deformable body in the reference and current states. To define the large deformation of the body, we consider the infinitesimal elements $\mathrm{d}X^K$ and $\mathrm{d}x^k$ (K, $k = 1$, 2 and 3). We shall derive the general relationship between the infinitesimal element $\mathrm{d}X^K$ in the undeformed body and the same element $\mathrm{d}x^k$ in the body after deformation. To begin with, we shall assume the general relationship between X^K and x^k coordinates by the equations:

$$x^k = x^k(X^K, t) \tag{8.26a}$$

or

$$X^K = X^K(x^k, t) \tag{8.26b}$$

If the components $\mathrm{d}X^K$ and $\mathrm{d}x^k$ are small, they can be expressed as:

$$\mathrm{d}x^k = x^k_{,K}\,\mathrm{d}X^K \tag{8.27a}$$

or

$$\mathrm{d}X^K = X^K_{,k}\,\mathrm{d}x^k \tag{8.27b}$$

in which $x^k_{,K}$ and $X^K_{,k}$ are respectively called the *deformation gradient* and *spatial deformation gradient* given by:

$$x^k_{,K} = \frac{\partial x^k}{\partial X^K} \tag{8.28a}$$

or

$$X^K_{,k} = \frac{\partial X^K}{\partial x^k} \tag{8.28b}$$

where K and k are respectively large and small subscripts running from 1 to 3.

The deformation gradient introduced here operates on an infinitesimal line element $\mathrm{d}X^K$ in the original or material coordinates to produce the deformed description $\mathrm{d}x^k$ in the spatial coordinates, in the manner of Eq. (8.27a). The inverse relation (8.27b) also holds.

Substitution of Eq. (8.27b) into Eq. (8.22) for the square of the line element leads to:

$$\mathrm{d}\hat{s}^2 = \mathring{g}_{KL} X^K_{,k} X^L_{,l} \, \mathrm{d}x^k \, \mathrm{d}x^l = c_{kl} \, \mathrm{d}x^k \, \mathrm{d}x^l \tag{8.29}$$

where c_{kl} is called the *Cauchy deformation tensor* which gives the relation between the square of undeformed line element and the components of the deformed line element. In a similar manner, the square of the deformed line element $\mathrm{d}s^2$ is represented by:

$$\mathrm{d}s^2 = g_{kl} x^k_{,K} x^l_{,L} \, \mathrm{d}X^K \, \mathrm{d}X^L = \mathring{c}_{KL} \, \mathrm{d}X^K \, \mathrm{d}X^L \tag{8.30}$$

where $\mathring{c}_{KL}$ is called the *Green deformation tensor* which gives the relation between the square of deformed line element and the components of the undeformed line element.

Strain tensors in general coordinates

The strain tensors of finite displacement may be defined by the change in the square of the line elements for the reference and the current configurations. These can be described in two different ways: one is measured on the basis of the components $\mathrm{d}X^K$ of the reference line element:

$$\mathrm{d}s^2 - \mathrm{d}\hat{s}^2 = [\mathring{c}_{KL} - \mathring{g}_{KL}] \, \mathrm{d}X^K \, \mathrm{d}X^L = 2E_{KL} \, \mathrm{d}X^K \, \mathrm{d}X^L \tag{8.31}$$

where $E_{KL} = \frac{1}{2}[\mathring{c}_{KL} - \mathring{g}_{KL}]$ is defined as the *Lagrangian strain tensor*.

Another is measured on the basis of the components $\mathrm{d}x^k$ of the current line element:

$$\mathrm{d}s^2 - \mathrm{d}\hat{s}^2 = [g_{kl} - c_{kl}] \, \mathrm{d}x^k \, \mathrm{d}x^l = 2e_{kl} \, \mathrm{d}x^k \, \mathrm{d}x^l \tag{8.32}$$

where $e_{kl} = \frac{1}{2}[g_{kl} - c_{kl}]$ is defined as the *Eulerian strain tensor*. Details of this continuum mechanics development based on the curvilinear coordinate system are given by Prager (1961), Fung (1965), Oden (1972) and Mason (1980), among others.

Example 8.4: If both curvilinear coordinates X^K and x^k are such that they retain their values during the motion of the body, i.e., $X^K = x^k$, these coordinates are called *convected coordinates*. Derive the strain tensors defined in the convected coordinate system.

Solution: Assume $\theta^k = X^K = x^k$. The undeformed and deformed line elements $d\ddot{s}^2$ and ds^2 are respectively expressed by:

$$d\ddot{s}^2 = \ddot{g}_{KL}\, dX^K\, dX^L = \ddot{g}_{kl}\, d\theta^k\, d\theta^l \quad \text{and} \quad ds^2 = g_{kl}\, dx^k\, dx^l = g_{kl}\, d\theta^k\, d\theta^l$$

The difference in ds^2 and $d\ddot{s}^2$ is thus given by:

$$ds^2 - d\ddot{s}^2 = (g_{kl} - \ddot{g}_{kl})\, d\theta^k\, d\theta^l$$

From the definition of strain tensor, both the Lagrangian and Eulerian strain tensors in the convected coordinate system are written as:

$$E_{KL} = e_{kl} = \frac{1}{2}(g_{kl} - \ddot{g}_{kl})$$

Since there is no distinction between X^K and x^k in this case, both strain tensors have the same form that presents the change in the base vector of the undeformed coordinate system to that of the deformed coordinate system.

Strain tensors in Cartesian coordinates

As a special and simple case of the strain tensors defined above, we shall consider the strain tensors defined in the Cartesian coordinate system, instead of the general curvilinear coordinate system.

Assume $r_{01}' = 0$ in Fig. 8.3, the fixed Cartesian coordinate systems $(\ddot{Z}^1, \ddot{Z}^2, \ddot{Z}^3)$ and (z^1, z^2, z^3) become identical to each other. Further, we shall assume the curvilinear coordinates X^K and x^k are Cartesian coordinates so that they are the same as the fixed coordinates, as shown in Fig. 8.4. In this case, we need not distinguish the *covariant* and *contravariant base vectors* in the curvilinear coordinates (Fung, 1965). These vectors become the *unit base vectors* in the Cartesian coordinates, and $\ddot{g}_{KL}$ and g_{kl} reduce to the Kronecker's delta δ_{KL} and δ_{kl}, respectively. In the following, we shall use the Cartesian coordinate system, and all indices will be written with the small subscripts such as i, j, and k, etc. The change in the square of the line elements in Eq. (8.31) is now written as:

$$ds^2 - d\ddot{s}^2 = \left[x_{k,I}x_{k,J} - \delta_{IJ}\right] dX_I\, dX_J \tag{8.33a}$$

where the small subscript after a comma denotes the partial derivative with respect

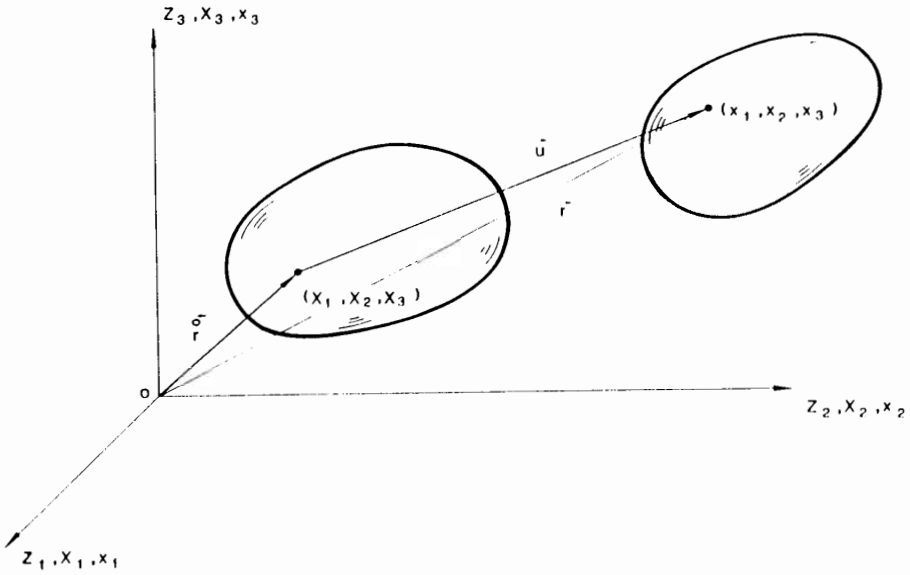

Fig. 8.4. Motion of body in Cartesian coordinate system.

to the reference coordinates X_i. The Lagrangian strain tensor E_{ij} can be expressed by:

$$E_{ij} = \tfrac{1}{2}\left[x_{k,i}x_{k,j} - \delta_{ij}\right] \tag{8.33b}$$

Similarly, Equation (8.32) can be rewritten as:

$$\mathrm{d}s^2 - \mathrm{d}\mathring{s}^2 = \left[\delta_{ij} - X_{k/i}X_{k/j}\right] \mathrm{d}x_i\, \mathrm{d}x_j \tag{8.34a}$$

where the small subscript after a slash denotes the partial derivative with respect to the spatial coordinates x_i. The Eulerian strain tensor e_{ij} can be expressed by:

$$e_{ij} = \tfrac{1}{2}\left[\delta_{ij} - X_{k/i}X_{k/j}\right] \tag{8.34b}$$

Introducing the displacement vector u_k, the relationship between both coordinates X_k and x_k may be expressed by:

$$x_k = X_k + u_k(X_1, X_2, X_3) \tag{8.35}$$

Therefore, $x_{k,i} = \partial x_k/\partial X_i$ can be obtained from Eq. (8.35) as:

$$x_{k,i} = \frac{\partial x_k}{\partial X_i} = \delta_{ki} + \frac{\partial u_k}{\partial X_i} \tag{8.36}$$

Substitution of Eq. (8.36) into Eq. (8.33b) leads to the Lagrangian strain tensor E_{ij} in terms of the displacement components:

$$E_{ij} = \frac{1}{2}\left(\frac{\partial u_i}{\partial X_j} + \frac{\partial u_j}{\partial X_i} + \frac{\partial u_k}{\partial X_i}\frac{\partial u_k}{\partial X_j}\right) \tag{8.37}$$

On the other hand, $X_{k,i} = \partial X_k / \partial x_i$ can be similarly expressed by:

$$X_{k,i} = \frac{\partial X_k}{\partial x_i} = \delta_{ki} - \frac{\partial u_k}{\partial x_i} \tag{8.38}$$

Substitution of Eq. (8.38) into Eq. (8.34b) yields the Eulerian strain tensor e_{ij} in terms of the displacement components:

$$e_{ij} = \frac{1}{2}\left(\frac{\partial u_i}{\partial x_j} + \frac{\partial u_j}{\partial x_i} - \frac{\partial u_k}{\partial x_i}\frac{\partial u_k}{\partial x_j}\right) \tag{8.39}$$

Note that Eqs. (8.37) and (8.39) represent exact definitions of strain and not an approximation. There is a difference in form between Eqs. (8.37) and (8.39) in that a plus sign in front of the product term in Eq. (8.37) corresponds to a minus sign in Eq. (8.39). Each of E_{ij} and e_{ij} is symmetric in its two subscripts. A necessary and sufficient condition that there be no deformation is that each of E_{ij} and e_{ij} vanishes. If the displacement gradients $u_{i,j}$ and $u_{i/j}$ are so small compared with unity, the nonlinear terms in Eqs. (8.37) and (8.39) can be neglected and then the strain tensors reduce to:

$$E_{ij} = \tfrac{1}{2}(u_{i,j} + u_{j,i}) \tag{8.40}$$

and

$$e_{ij} = \tfrac{1}{2}(u_{i/j} + u_{j/i}) \tag{8.41}$$

Thus, both Lagrangian and Eulerian descriptions yield the linear strain displacement relations (8.40) and (8.41). If displacements and displacement gradients are small, then, it is immaterial whether the derivatives in Eqs. (8.37) and (8.39) are calculated using the coordinates X_i or x_i. In this case, both Lagrangian and Eulerian descriptions yield the same strain-displacement relations just as the strain tensor ϵ_{ij} defined by the small-strain definition.

Example 8.5: The displacement components u_i at a point in a body are given by the functional components:

$$u_1 = 10X_1 + 3X_2, \quad u_2 = 3X_1 + 2X_2, \quad \text{and } u_3 = 6X_3$$

Show that there is no rotation if the deformations are assumed to be small. Assuming large deformations, find the components of Lagrangian and Eulerian strain tensors.

Solutions: The components of displacement gradient $\partial u_i/\partial X_j$ can be computed as:

$$\begin{aligned} u_{1,1} &= 10, & u_{1,2} &= 3, & u_{1,3} &= 0 \\ u_{2,1} &= 3, & u_{2,2} &= 2, & u_{2,3} &= 0 \\ u_{3,1} &= 0, & u_{3,2} &= 0, & u_{3,3} &= 6 \end{aligned}$$

Therefore, the rotation matrix for the small-strain assumption (Section 8.2.1) has the form:

$$\Omega_{ij} = \begin{bmatrix} 0 & \frac{1}{2}(u_{1,2} - u_{2,1}) & \frac{1}{2}(u_{1,3} - u_{3,1}) \\ \frac{1}{2}(u_{2,1} - u_{1,2}) & 0 & \frac{1}{2}(u_{2,3} - u_{3,2}) \\ \frac{1}{2}(u_{3,1} - u_{1,3}) & \frac{1}{2}(u_{3,2} - u_{2,3}) & 0 \end{bmatrix} = \begin{bmatrix} 0 & 0 & 0 \\ 0 & 0 & 0 \\ 0 & 0 & 0 \end{bmatrix}$$

Thus, there is no rotation in such a displacement field.

Using the displacement gradient obtained above, the Lagrangian strain tensor can be computed by:

$$E_{ij} = \tfrac{1}{2}(u_{i,j} + u_{j,i} + u_{k,i}u_{k,j})$$

or in matrix form, we have:

$$E_{ij} = \begin{bmatrix} 64.5 & 21 & 0 \\ 21 & 8.5 & 0 \\ 0 & 0 & 24 \end{bmatrix}$$

To compute the Eulerian strain tensor, we shall first consider the deformed coordinates x_i which are expressed by $x_i = X_i + u_i$, that is:

$$x_1 = X_1 + (10X_1 + 3X_2) = 11X_1 + 3X_2$$

$$x_2 = X_2 + (3X_1 + 2X_2) = 3X_1 + 3X_2$$

$$x_3 = X_3 + (6X_3) = 7X_3$$

The inversed form can be written as:

$$X_1 = \tfrac{1}{8}(x_1 - x_2)$$

$$X_2 = -\tfrac{1}{24}(3x_1 - 11x_2)$$

$$X_3 = \tfrac{1}{7}x_3$$

Substitution of X_i into the displacement components u_i yields the expression in terms of the deformed coordinates x_i:

$$u_1 = \tfrac{1}{8}(7x_1 + x_2)$$

$$u_2 = \tfrac{1}{24}(3x_1 + 13x_2)$$

$$u_3 = \tfrac{6}{7}x_3$$

The components of displacement gradient with respect to the spatial coordinate x_i can be computed:

$$u_{1,1} = \tfrac{7}{8}, \qquad u_{1,2} = \tfrac{1}{8}, \qquad u_{1,3} = 0$$
$$u_{2,1} = \tfrac{1}{8}, \qquad u_{2,2} = \tfrac{13}{24}, \qquad u_{2,3} = 0$$
$$u_{3,1} = 0, \qquad u_{3,2} = 0 \qquad u_{3,3} = \tfrac{6}{7}$$

Recalling the definition for the Eulerian strain tensor:

$$e_{ij} = \tfrac{1}{2}(u_{i,j} + u_{j,i} - u_{k,i}u_{k,j})$$

we can compute its components of Eulerian strain tensor:

$$e_{ij} \quad \begin{bmatrix} \frac{41}{64} & \frac{7}{192} & 0 \\ \frac{7}{192} & \frac{223}{576} & 0 \\ 0 & 0 & \frac{24}{49} \end{bmatrix}$$

Example 8.6: Find the relationship between the undeformed surface element $\mathrm{d}\vec{A}_i = \mathrm{d}\vec{A}N_i$ and the deformed surface element $\mathrm{d}A_i = \mathrm{d}An_i$ where N_i and n_i are respectively the unit normal vector to surfaces $\mathrm{d}\vec{A}$ and $\mathrm{d}A$. Also, find the relationship between the infinitesimal volumes $\mathrm{d}\vec{V}$ and $\mathrm{d}V$ in the undeformed and deformed configurations.

Solution: We shall consider two different infinitesimal line elements $\mathrm{d}X_i$ and δX_i in the undeformed body, as shown in Fig. 8.5. The area vector $\mathrm{d}\vec{A}_i$ produced by these two line elements is calculated by the vector product, i.e.:

$$\mathrm{d}\vec{A}_i = e_{ijk}\,\mathrm{d}X_j\delta X_k$$

where e_{ijk} is the permutation symbol. Assuming the deformed line elements $\mathrm{d}x_i$ and δx_i, the relation between $\mathrm{d}X_i$(or δX_i) and $\mathrm{d}x_i$ (or δx_i) can be expressed by:

$$\mathrm{d}X_i = \frac{\partial X_i}{\partial x_j}\,\mathrm{d}x_j \quad \text{or} \quad \delta X_i = \frac{\partial X_i}{\partial x_j}\delta x_j$$

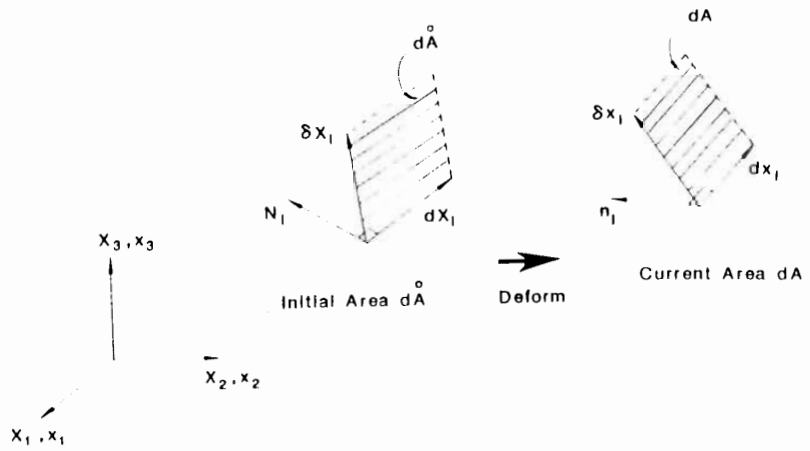

Fig. 8.5. Change of area.

Substituting these relations into the first equation, we have:

$$\mathrm{d}\mathring{A}_i = e_{ijk}\frac{\partial X_j}{\partial x_l}\frac{\partial X_k}{\partial x_m}\,\mathrm{d}x_l\delta x_m$$

Multiplying both sides of this equation by $\partial X_i/\partial x_n$:

$$\frac{\partial X_i}{\partial x_n}\,\mathrm{d}\mathring{A}_i = e_{ijk}\frac{\partial X_i}{\partial x_n}\frac{\partial X_j}{\partial x_l}\frac{\partial X_k}{\partial x_m}\,\mathrm{d}x_l\delta x_m$$

and noting that $e_{ijk}(\partial X_i/\partial x_n)(\partial X_j/\partial x_l)(\partial X_k/\partial x_m) = e_{nlm}\,|\partial X_j/\partial x_k\,|$, we obtain:

$$\frac{\partial X_i}{\partial x_n}\,\mathrm{d}\mathring{A}_i = e_{nlm}\left|\frac{\partial X_j}{\partial x_k}\right|\mathrm{d}x_l\delta x_m$$

On the other hand, since the area vector $\mathrm{d}A_i$ in the deformed state shown in Fig. 8.5 can be written as $\mathrm{d}A_i = e_{ijk}\,\mathrm{d}x_j\delta x_k$:

$$\frac{\partial X_i}{\partial x_n}\,\mathrm{d}\mathring{A}_i = \left|\frac{\partial X_j}{\partial x_k}\right|\mathrm{d}A_n \tag{8.42a}$$

or arranging the free and dummy indices:

$$\frac{\partial X_i}{\partial x_j}\,\mathrm{d}\mathring{A}_i = \left|\frac{\partial X_k}{\partial x_j}\right|\mathrm{d}A_j \tag{8.42b}$$

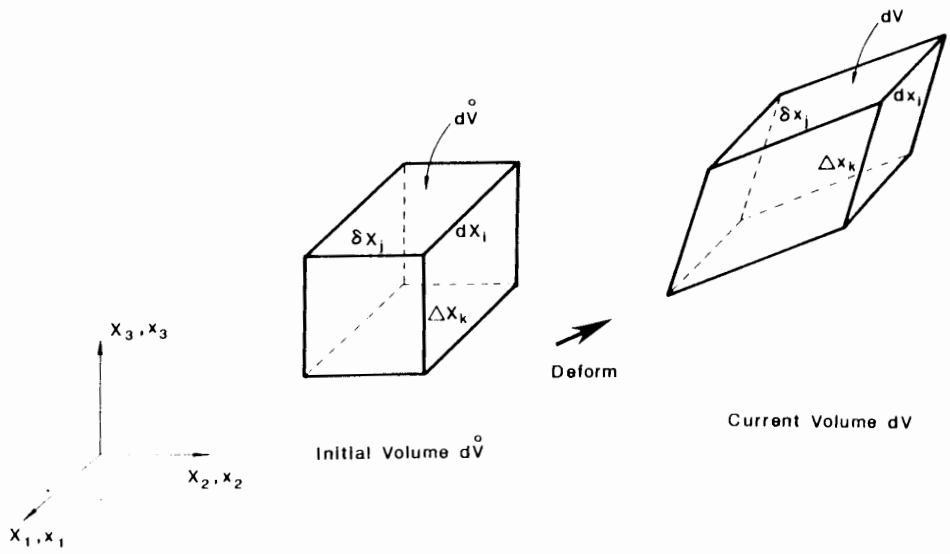

Fig. 8.6. Change of volume.

Multiplying both sides of Eq. (8.42b) by $\partial x_j/\partial X_k$ and rearranging again the index, we obtain:

$$\mathrm{d}\vec{A}_i = \left|\frac{\partial X_k}{\partial x_l}\right| \frac{\partial x_j}{\partial X_i}\,\mathrm{d}A_j = J^{-1}\frac{\partial x_j}{\partial X_i}\,\mathrm{d}A_j \tag{8.42c}$$

or in its inversed form:

$$\mathrm{d}A_j = \left|\frac{\partial x_l}{\partial X_k}\right| \frac{\partial X_i}{\partial x_j}\,\mathrm{d}\vec{A}_i = J\frac{\partial X_i}{\partial x_j}\,\mathrm{d}\vec{A}_i \tag{8.42d}$$

where $|\partial x_l/\partial X_k|$ is known as the determinant of the *Jacobian* matrix and is denoted by J.

We shall now consider the relation between volumes of infinitesimal cubic elements in the undeformed and deformed states, as shown in Fig. 8.6. The volume $\mathrm{d}\vec{V}$ in the undeformed state is calculated by:

$$\mathrm{d}\vec{V} = e_{ijk}\,\mathrm{d}X_i\delta X_j\,\Delta X_k = e_{ijk}\frac{\partial X_i}{\partial x_l}\frac{\partial X_j}{\partial x_m}\frac{\partial X_k}{\partial x_n}\,\mathrm{d}x_l\delta x_m\,\Delta x_n$$

$$= e_{lmn}J^{-1}\,\mathrm{d}x_l\delta x_m\,\Delta x_n = J^{-1}\,\mathrm{d}V \tag{8.43a}$$

or in its inversed form:

$$dV = J\, d\overset{\circ}{V} \tag{8.43b}$$

From the conservation of mass $\rho_0\, d\overset{\circ}{V} = \rho\, dV$ where ρ_0 and ρ are respectively the densities per unit volume in the undeformed and deformed states, we find the following relation:

$$\frac{\rho_0}{\rho} = \frac{dV}{d\overset{\circ}{V}} = J \tag{8.43c}$$

These area and volume relations will be utilized later in the total and updated Lagrangian formulations in Sections 8.5.1 and 8.5.2.

8.3 RATE OF DEFORMATION AND STRAIN RATES

When we consider an instantaneous equilibrium state of a body during the deformation by employing the virtual velocity or virtual work equation, the *rate of deformation*, the *rate of Lagrangian strain*, the *variation in infinitesimal strain* at the current state, or the *variation in Lagrangian strain* becomes more important than the total strain E_{ij} or e_{ij} defined in the previous Section.

Rate of deformation tensor

Define $v_i = v_i(x_1, x_2, x_3)$ as the velocity vector for a current particle at $x_i = (x_1, x_2, x_3)$ in a deforming body. The relative velocity dv_i at the neighborhood of x_i can be expressed as:

$$dv_i = \frac{\partial v_i}{\partial x_j}\, dx_j \tag{8.44}$$

where $\partial v_i/\partial x_j$ is defined as the *velocity gradients* which can be decomposed into:

$$\frac{\partial v_i}{\partial x_j} = \frac{1}{2}\left(\frac{\partial v_i}{\partial x_j} + \frac{\partial v_j}{\partial x_i}\right) + \frac{1}{2}\left(\frac{\partial v_i}{\partial x_j} - \frac{\partial v_j}{\partial x_i}\right) = V_{ij} + W_{ij} \tag{8.45}$$

in which the first tensor V_{ij} in Eq. (8.45) is called the *rate of deformation tensor* and the second W_{ij} the *spin tensor*. The rate of deformation tensor is symmetric whereas the spin tensor is skew-symmetric.

We shall consider an instantaneous rate of change at time t in the square of line element $ds^2 = dx_i\, dx_i$. Taking the material derivative with time t, $[d(\,)/dt = \partial(\,)/\partial t + \partial(\,)/\partial x_i\, \partial x_i/\partial t]$, we have:

$$\frac{d}{dt}(ds^2) = \frac{d}{dt}(dx_i\, dx_i) = 2\, dx_i \frac{d}{dt}(dx_i) \tag{8.46a}$$

Since dx_i is expressed by $dx_i = (\partial x_i/\partial X_J)\, dX_J$, $d(dx_i)/dt$ can be expressed by:

$$\frac{d}{dt}(dx_i) = \frac{d}{dt}\left(\frac{\partial x_i}{\partial X_J}\right) dX_J + \frac{\partial x_i}{\partial X_J}\frac{d}{dt}(dX_J) \tag{8.46b}$$

Noting that the components of the reference line element dX_J do not change with time, i.e., $d(dX_J)/dt = 0$, we have:

$$\frac{d}{dt}(dx_i) = \frac{d}{dt}\left(\frac{\partial x_i}{\partial X_J}\right) dX_J = \frac{\partial v_i}{\partial X_J}\, dX_J = dv_i \tag{8.46c}$$

Therefore, Eq. (8.46c) becomes identical to Eq. (8.44):

$$\frac{d}{dt}(dx_i) = \frac{\partial v_i}{\partial x_j}\, dx_j \tag{8.46d}$$

Substitution of Eq. (8.46d) into Eq. (8.46a) leads to:

$$\frac{d}{dt}(ds^2) = 2\, dx_i \frac{\partial v_i}{\partial x_j}\, dx_j = 2V_{ij}\, dx_i\, dx_j + 2W_{ij}\, dx_i\, dx_j \tag{8.47}$$

Since $W_{ij} = -W_{ji}$ and $dx_i\, dx_j = dx_j\, dx_i$, we find the second term of Eq. (8.47) $W_{ij} dx_i\, dx_j = 0$. Hence, Eq. (8.47) can be rewritten as:

$$\frac{d}{dt}(ds^2) = 2V_{ij}\, dx_i\, dx_j \tag{8.48}$$

It can be understood from the above discussion that the rate of change in the square of the line element ds^2 at the current configuration is related to the rate of deformation tensor V_{ij} and the components of the instantaneous line element dx_i.

Example 8.7: Consider the time derivative of the strain tensor ϵ_{ij} defined by the small-strain definition in Section 8.2 and compare it with the rate of deformation tensor V_{ij}.

Solution: The time derivative of the strain tensor ϵ_{ij} in the small-strain assumption is computed by:

$$\frac{d}{dt}(\epsilon_{ij}) = \frac{d}{dt}\left[\tfrac{1}{2}(u_{i,j} + u_{j,i})\right]$$

where the subscript after a comma denotes the derivative with respect to the coordinate X_i. Since the relation $d(u_{i,j})/dt = v_{i,j}$ holds, we obtain:

$$\frac{d}{dt}(\epsilon_{ij}) = \tfrac{1}{2}(v_{i,j} + v_{j,i})$$

On the other hand, the rate of deformation tensor V_{ij} defined in Eq. (8.45) can be rewritten as $V_{ij} = \frac{1}{2}(v_{i,j} + v_{j,i})$. As can be seen easily from both equations, the difference is that the strain rate in the small-strain assumption shows the derivative form with respect to the reference coordinates X_i whereas the rate of deformation tensor shows the derivative form with respect to the spatial coordinates x_i.

Example 8.8: The motion of a particle with the spatial coordinates x_i in a body can be described in terms of the reference coordinates X_i and the current time t:

$$x_1 = \tfrac{1}{2}(X_1 + X_2)\exp t + \tfrac{1}{2}(X_1 - X_2)\exp(-t)$$

$$x_2 = \tfrac{1}{2}(X_1 + X_2)\exp t - \tfrac{1}{2}(X_1 - X_2)\exp(-t)$$

$$x_3 = X_3 \exp(-t)$$

(a) Describe the velocity components in terms of the reference coordinates and time t.
(b) Describe the velocity components in terms of the spatial coordinates and time t.
(c) Derive the rate of deformation tensor.
(d) Describe the small strain components in terms of the reference coordinates and time t.
(e) Compute the rate of change $\mathrm{d}\epsilon_{ij}/\mathrm{d}t$ of the small-strain components and the rate of deformation tensor V_{ij} at time $t = 0.1$, respectively.

Solutions:
(a) Since the velocity v_i can be computed by $\mathrm{d}(x_i)/\mathrm{d}t$, we obtain:

$$v_1 = \frac{\mathrm{d}}{\mathrm{d}t}(x_1) = \tfrac{1}{2}(X_1 + X_2)\exp t - \tfrac{1}{2}(X_1 - X_2)\exp(-t)$$

$$v_2 = \frac{\mathrm{d}}{\mathrm{d}t}(x_2) = \tfrac{1}{2}(X_1 + X_2)\exp t + \tfrac{1}{2}(X_1 - X_2)\exp(-t)$$

$$v_3 = \frac{\mathrm{d}}{\mathrm{d}t}(x_3) = -X_3 \exp(-t)$$

(b) The velocity components v_1, v_2, and v_3 derived in (a) can be directly written as:

$$v_1 = x_2$$

$$v_2 = x_1$$

$$v_3 = -x_3$$

(c) Using the results in (b), the velocity gradients $v_{i/j}$ can be computed as:

$$
\begin{aligned}
&v_{1/1} = 0, \qquad v_{1/2} = 1, \qquad v_{1/3} = \ \ 0\\
&v_{2/1} = 1, \qquad v_{2/2} = 0, \qquad v_{2/3} = \ \ 0\\
&v_{3/1} = 0, \qquad v_{3/2} = 0, \qquad v_{3/3} = -1
\end{aligned}
$$

Since the rate of deformation tensor $V_{ij} = \frac{1}{2}(v_{i/j} + v_{j/i})$, we have:

$$
V_{ij} = \begin{bmatrix} 0 & 1 & 0 \\ 1 & 0 & 0 \\ 0 & 0 & -1 \end{bmatrix}
$$

(d) Using the relation $x_i = X_i + u_i$, the displacement vector u_i can be obtained:

$$u_1 = \tfrac{1}{2}(X_1 + X_2)\exp t + \tfrac{1}{2}(X_1 - X_2)\exp(-t) - X_1$$

$$u_2 = \tfrac{1}{2}(X_1 + X_2)\exp t - \tfrac{1}{2}(X_1 - X_2)\exp(-t) - X_2$$

$$u_3 = X_3\exp(-t) - X_3$$

The components of displacement gradient with respect to the X_i coordinates are:

$$
\begin{aligned}
&u_{1,1} = \tfrac{1}{2}\exp t + \tfrac{1}{2}\exp(-t) - 1, \qquad u_{1,2} = \tfrac{1}{2}\exp t - \tfrac{1}{2}\exp(-t),\\
&u_{2,1} = \tfrac{1}{2}\exp t - \tfrac{1}{2}\exp(-t), \qquad\qquad u_{2,2} = \tfrac{1}{2}\exp t + \tfrac{1}{2}\exp(-t) - 1,\\
&u_{3,1} = 0, \qquad\qquad\qquad\qquad\qquad\ \ u_{3,2} = 0
\end{aligned}
$$

$$
\begin{aligned}
&u_{1,3} = 0\\
&u_{2,3} = 0\\
&u_{3,3} = \exp(-t) - 1
\end{aligned}
$$

The small-strain tensor ϵ_{ij} can be represented in terms of time t by:

$$
\epsilon_{ij} = \begin{bmatrix} \tfrac{1}{2}\exp t + \tfrac{1}{2}\exp(-t) - 1 & \tfrac{1}{2}\exp t - \tfrac{1}{2}\exp(-t) & 0 \\ \tfrac{1}{2}\exp t - \tfrac{1}{2}\exp(-t) & \tfrac{1}{2}\exp t + \tfrac{1}{2}\exp(-t) - 1 & 0 \\ 0 & 0 & \exp(-t) - 1 \end{bmatrix}
$$

(e) Using the result in (d), the rate of change $\mathrm{d}(\epsilon_{ij})/\mathrm{d}t$ can be computed by:

$$
\frac{\mathrm{d}}{\mathrm{d}t}(\epsilon_{ij}) = \begin{bmatrix} \tfrac{1}{2}\exp t - \tfrac{1}{2}\exp(-t) & \tfrac{1}{2}\exp t + \tfrac{1}{2}\exp(-t) & 0 \\ \tfrac{1}{2}\exp t + \tfrac{1}{2}\exp(-t) & \tfrac{1}{2}\exp t - \tfrac{1}{2}\exp(-t) & 0 \\ 0 & 0 & -\exp(-t) \end{bmatrix}
$$

Substituting $t = 0.1$, we obtain the rate of small strain at $t = 0.1$:

$$\frac{\mathrm{d}}{\mathrm{d}t}(\epsilon_{ij}) = \begin{bmatrix} 0.10017 & 1.0050 & 0 \\ 1.0050 & 0.10017 & 0 \\ 0 & 0 & -0.90484 \end{bmatrix}$$

Since the rate of deformation tensor V_{ij} obtained in (c) does not have the time variable but constant values, it remains unchanged even though the time t varies. Note that at the time $t = 0$ the rate of small strain becomes identical to the rate of deformation tensor.

Strain rates

We shall consider first the *rate of Lagrangian strain tensor* E_{ij}. Recalling the difference in square of the undeformed and deformed line elements, $\mathrm{d}s^2 - \mathrm{d}\bar{s}^2 = 2E_{ij}\,\mathrm{d}X_i\,\mathrm{d}X_j$ and taking the material derivative of both sides, we have:

$$\frac{\mathrm{d}}{\mathrm{d}t}(\mathrm{d}s^2) = 2\frac{\mathrm{d}E_{ij}}{\mathrm{d}t}\,\mathrm{d}X_i\,\mathrm{d}X_j \tag{8.49}$$

Also, we can write $\mathrm{d}(\mathrm{d}s^2)/\mathrm{d}t$ from Eq. (8.48):

$$\frac{\mathrm{d}}{\mathrm{d}t}(\mathrm{d}s^2) = 2V_{ij}\,\mathrm{d}x_i\,\mathrm{d}x_j = 2V_{ij}\frac{\partial x_i}{\partial X_k}\frac{\partial x_j}{\partial X_l}\,\mathrm{d}X_k\,\mathrm{d}X_l \tag{8.50}$$

Comparing Eqs. (8.49) with (8.50) for an arbitrary $\mathrm{d}X_i$ yields the rate of Lagrangian strain tensor $\mathrm{d}E_{ij}/\mathrm{d}t$ which is related to the rate of deformation tensor:

$$\frac{\mathrm{d}E_{ij}}{\mathrm{d}t} = V_{kl}\frac{\partial x_k}{\partial X_i}\frac{\partial x_l}{\partial X_j} \tag{8.51}$$

When the displacement gradients $\partial u_i/\partial X_j$ are small compared with unity, Eq. (8.51) becomes $\mathrm{d}E_{ij}/\mathrm{d}t = V_{ij}$.

Similarly, the *rate of Eulerian strain tensor* e_{ij} may be derived as follows: The Eulerian strain tensor can be written as:

$$e_{ij} = \tfrac{1}{2}(\delta_{ij} - X_{k,i}X_{k,j}) = \frac{1}{2}\left(\delta_{ij} - \frac{\partial X_k}{\partial x_i}\frac{\partial X_k}{\partial x_j}\right) \tag{8.52}$$

Taking the material derivative of Eq. (8.52), we have:

$$\frac{\mathrm{d}e_{ij}}{\mathrm{d}t} = -\frac{1}{2}\left[\frac{\mathrm{d}}{\mathrm{d}t}\left(\frac{\partial X_k}{\partial x_i}\right)\frac{\partial X_k}{\partial x_j} + \frac{\partial X_k}{\partial x_i}\frac{\mathrm{d}}{\mathrm{d}t}\left(\frac{\partial X_k}{\partial x_j}\right)\right] \tag{8.53}$$

where the material derivative $\mathrm{d}[\partial X_i/\partial x_j]/\mathrm{d}t$ can be expressed by:

$$\frac{\mathrm{d}}{\mathrm{d}t}\left[\frac{\partial X_i}{\partial x_j}\right] = \frac{\partial}{\partial t}\left[\frac{\partial X_i}{\partial x_j}\right] + \frac{\partial}{\partial x_k}\left[\frac{\partial X_i}{\partial x_j}\right]\frac{\partial x_k}{\partial t} = \frac{\partial}{\partial t}\left[\frac{\partial X_i}{\partial x_j}\right] + \frac{\partial}{\partial x_k}\left[\frac{\partial X_i}{\partial x_j}\right]v_k$$

$$= \frac{\partial}{\partial x_j}\left[\frac{\partial X_i}{\partial t} + v_k\frac{\partial X_i}{\partial x_k}\right] - \frac{\partial v_k}{\partial x_j}\frac{\partial X_i}{\partial x_k} \tag{8.54a}$$

Since the material derivative of X_i vanishes, $\mathrm{d}(X_i)/\mathrm{d}t = \partial(X_i)/\partial t + v_j\,\partial X_i/\partial x_j = 0$, Eq. (8.54a) becomes:

$$\frac{\mathrm{d}}{\mathrm{d}t}\left[\frac{\partial X_i}{\partial x_j}\right] = -\frac{\partial v_k}{\partial x_j}\frac{\partial X_i}{\partial x_k} \tag{8.54b}$$

Substituting Eq. (8.54b) into Eq. (8.53) and using the following relation:

$$\frac{\partial X_m}{\partial x_i}\frac{\partial X_m}{\partial x_k} = \delta_{ik} - 2e_{ik}$$

we obtain:

$$\frac{\mathrm{d}e_{ij}}{\mathrm{d}t} = \frac{1}{2}\left[\frac{\partial v_m}{\partial x_i}\frac{\partial X_k}{\partial x_m}\frac{\partial X_k}{\partial x_j} + \frac{\partial X_k}{\partial x_i}\frac{\partial v_m}{\partial x_j}\frac{\partial X_k}{\partial x_m}\right]$$

$$- \frac{1}{2}\left[\frac{\partial v_m}{\partial x_i}(\delta_{mj} - 2e_{mj}) + \frac{\partial v_m}{\partial x_j}(\delta_{mi} - 2e_{mi})\right]$$

$$= V_{ij} - \frac{\partial v_k}{\partial x_j}e_{ik} - \frac{\partial v_k}{\partial x_i}e_{jk} \tag{8.55}$$

where $\mathrm{d}(e_{ij})/\mathrm{d}t$ becomes identical to the rate of deformation tensor only when the second and third terms vanish, i.e., $e_{ij} = 0$.

By comparing the rates of Lagrangian and Eulerian strain tensors respectively, the rate of Lagrangian strain tensor can be obtained directly as a transformation of the rate of deformation tensor whereas the rate of Eulerian strain tensor includes the rate of deformation tensor V_{ij}, Eulerian strain tensor e_{ij}, and velocity gradient $\partial v_i/\partial x_j$.

Consider the neighborhood of a particle showing a rigid-body motion, i.e., $V_{ij} = 0$. Since in this case there is no guarantee that the rate of Eulerian strain tensor vanishes, $\mathrm{d}(e_{ij})/\mathrm{d}t$ may not be utilized in a constitutive law. On the other hand, the rate of Lagrangian strain tensor vanishes when the neighborhood of a particle exhibits a rigid-body motion, i.e., $V_{ij} = 0$, $\mathrm{d}(E_{ij})/\mathrm{d}t$ can be employed in a constitutive law.

Example 8.9: Derive the rate of Eulerian strain tensor $\mathrm{d}(e_{ij})/\mathrm{d}t$ by taking the material derivative of the square of line element $\mathrm{d}s^2$.

Solution: The material derivative of $\mathrm{d}s^2$ can be expressed by:

$$\frac{\mathrm{d}}{\mathrm{d}t}(\mathrm{d}s^2) = \frac{\mathrm{d}}{\mathrm{d}t}[\mathrm{d}s^2 - \mathrm{d}\mathring{s}^2] = 2\frac{\mathrm{d}}{\mathrm{d}t}\left[e_{ij}\,\mathrm{d}x_i\,\mathrm{d}x_j\right]$$

$$= 2\frac{\mathrm{d}}{\mathrm{d}t}(e_{ij})\,\mathrm{d}x_i\,\mathrm{d}x_j + 2e_{ij}\frac{\mathrm{d}}{\mathrm{d}t}(\mathrm{d}x_i)\,\mathrm{d}x_j + 2e_{ij}\,\mathrm{d}x_i\frac{\mathrm{d}}{\mathrm{d}t}(\mathrm{d}x_j)$$

In view of Eq. (8.46d), then, we obtain:

$$\frac{\mathrm{d}}{\mathrm{d}t}(\mathrm{d}s^2) = 2\frac{\mathrm{d}}{\mathrm{d}t}(e_{ij})\,\mathrm{d}x_i\,\mathrm{d}x_j + 2e_{ij}\frac{\partial v_i}{\partial x_k}\,\mathrm{d}x_k\,\mathrm{d}x_j + 2e_{ij}\,\mathrm{d}x_i\frac{\partial v_j}{\partial x_k}\,\mathrm{d}x_k$$

$$= 2\left[\frac{\mathrm{d}}{\mathrm{d}t}(e_{ij}) + e_{kj}\frac{\partial v_k}{\partial x_i} + e_{ik}\frac{\partial v_k}{\partial x_j}\right]\mathrm{d}x_i\,\mathrm{d}x_j$$

Comparing with Eq. (8.48), $\mathrm{d}(\mathrm{d}s^2)/\mathrm{d}t = 2V_{ij}\,\mathrm{d}x_i\,\mathrm{d}x_j$ for an arbitrary $\mathrm{d}x_i$, we have the following relationship:

$$V_{ij} = \frac{\mathrm{d}}{\mathrm{d}t}(e_{ij}) + e_{kj}\frac{\partial v_k}{\partial x_i} + e_{ik}\frac{\partial v_k}{\partial x_j}$$

Finally, we obtain the rate of Eulerian strain tensor $\mathrm{d}(e_{ij})/\mathrm{d}t$ expressed in a similar manner to that of Eq. (8.55):

$$\frac{\mathrm{d}}{\mathrm{d}t}(e_{ij}) = V_{ij} - e_{kj}\frac{\partial v_k}{\partial x_i} - e_{ik}\frac{\partial v_k}{\partial x_j}$$

8.4 MEASURES OF STRESS

In this Section, several definitions of stresses such as the *Eulerian stress*, *Lagrangian stress* (or *first Piola Kirchhoff stress*), and *second Piola Kirchhoff stress* will be described in the Cartesian coordinate frame. These stresses are important in the subsequent development of large-displacement and large-deformation formulations.

8.4.1 Stress tensors

Eulerian stress tensor

Consider the infinitesimal force $\mathrm{d}P_j$ acting on the current surface element $\mathrm{d}A_i = \mathrm{d}An_i$ where n_i is the unit normal vector on the current surface $\mathrm{d}A$, referring

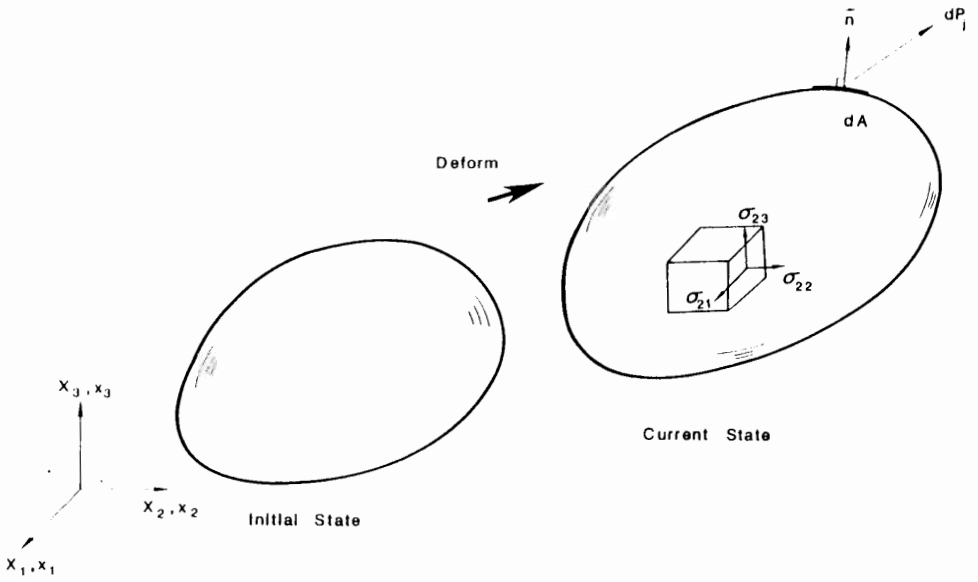

Fig. 8.7. Eulerian stresses.

to the global Cartesian coordinate system shown in Fig. 8.7. Defining the stress tensor σ_{ij} introduced in Chapter 2 as the *Eulerian stress tensor*, we have the usual relation:

$$\mathrm{d}P_i = \sigma_{ij}\,\mathrm{d}An_i \tag{8.56}$$

where σ_{ij} is a symmetric tensor, i.e., $\sigma_{ij} = \sigma_{ji}$. In this case, the Eulerian stress is a *real* stress acting on the cubic element in the deformed body. The term *real stress* implies the usual definition of force per unit deformed area, while the term *pseudo stress* will be used in the following to indicate the definition of force per unit undeformed area.

Lagrangian stress tensor

The *Lagrangian stress tensor* (or called the *first Piola-Kirchhoff stress tensor*) T_{ij} is defined by referring to the reference surface element $\mathrm{d}\ddot{A}_i = \mathrm{d}\ddot{A}N_i$ where N_i is the unit normal vector on the reference surface shown in Fig. 8.8. The Lagrangian stress tensor T_{ij} is a *pseudo* stress since it is defined to be the force per unit area of the undeformed (reference) body. Therefore, $\mathrm{d}P_i$ acting on the area in the deformed body can be written as:

$$\mathrm{d}P_i = T_{ij}\,\mathrm{d}\ddot{A}N_i \tag{8.57}$$

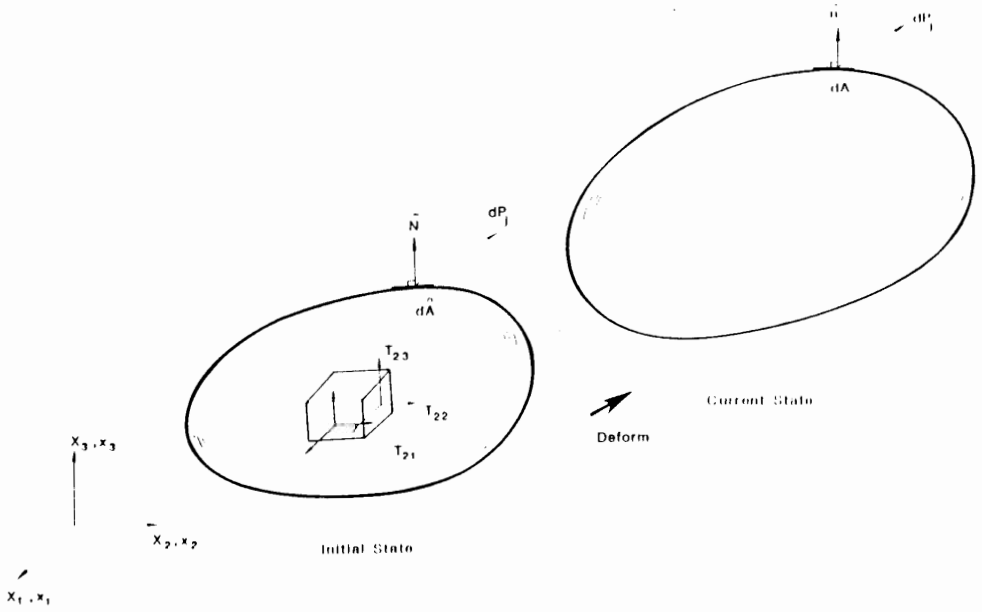

Fig. 8.8. Lagrangian stresses.

This stress tensor is related to the actual stress σ_{ij} acting in the deformed body through the following equations.

Substituting the relationship between surface elements dA and $d\bar{A}$, that is $dAn_i = J(\partial X_k/\partial x_i)\, d\bar{A}N_k$ from example 8.6, into Eq. (8.56), the relation between σ_{ij} and T_{ij} can be written directly from their definitions (8.56) and (8.57):

$$\sigma_{ij} J \frac{\partial X_k}{\partial x_i}\, d\bar{A}N_k = T_{ij}\, d\bar{A}N_i \tag{8.58a}$$

or

$$\left(\sigma_{ij} J \frac{\partial X_k}{\partial x_i} - T_{kj}\right) d\bar{A}N_k = 0 \tag{8.58b}$$

Since the unit normal vector N_k is related to an arbitrary surface element $d\bar{A}$, it follows that:

$$T_{kj} = J \frac{\partial X_k}{\partial x_i}\sigma_{ij} \quad \text{or} \quad T_{ij} = J \frac{\partial X_i}{\partial x_k}\sigma_{kj} \tag{8.58c}$$

where T_{kj} or T_{ij} are components of *pseudo-stresses* and not symmetric in general.

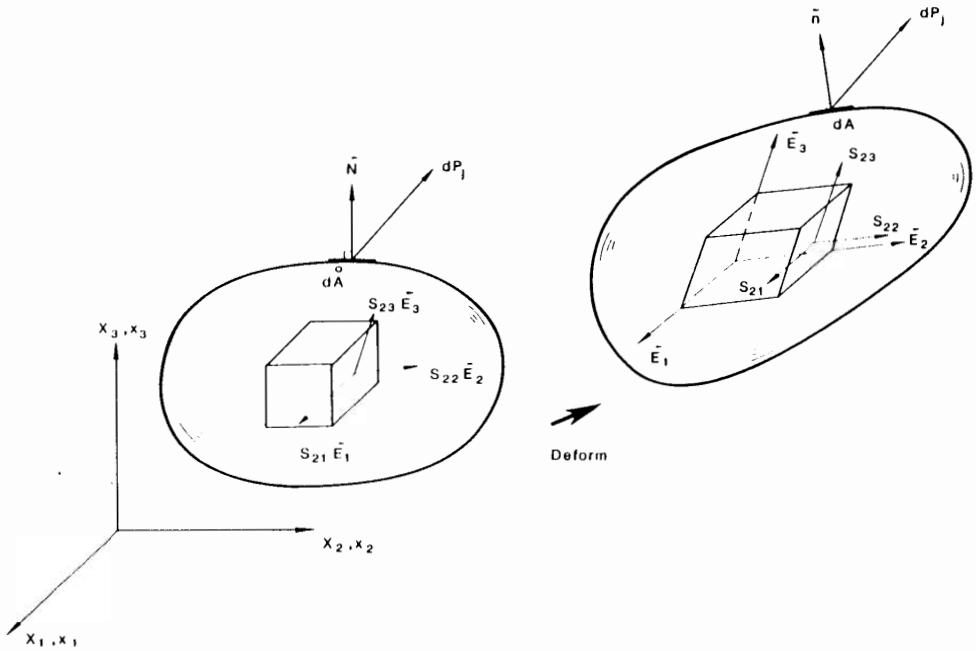

Fig. 8.9. Second Piola-Kirchhoff stresses.

Second Piola-Kirchhoff stress tensor

The *second Piola-Kirchhoff stress tensor* S_{ij} (or called the *Kirchhoff stress tensor*) is also a *pseudo-stress* that is defined on the deformed surface of a parallelepipedon and measured per unit undeformed area, as shown in Fig. 8.9. The direction j of S_{ij} acting on the surface element $\mathrm{d}\ddot{A}_\zeta$ is identical to that of the *base vector* $\dot{E}_j$ in the deformed state. The base vector $\dot{E}_j$ can be determined as follows:

Considering the infinitesimal line element $\mathrm{d}X_j$ before the deformation, the deformed line element $\mathrm{d}x_i$ can be expressed by:

$$\mathrm{d}x_i = \frac{\partial x_i}{\partial X_j}\,\mathrm{d}X_j \tag{8.59}$$

Equation (8.59) implies that if the undeformed line element $\mathrm{d}X_j$ is taken to be the unit base vector $\dot{i}_j$ in the undeformed state, then, after deformation, it becomes the *new base vector* $\dot{E}_j$ in the deformed state:

$$\dot{E}_j = \frac{\partial x_i}{\partial X_j}\dot{i}_i \quad \text{or} \quad \dot{E}_i = \frac{\partial x_j}{\partial X_i}\dot{i}_j \tag{8.60a}$$

or in matrix form:

$$\begin{Bmatrix} \dot{E}_1 \\ \dot{E}_2 \\ \dot{E}_3 \end{Bmatrix} = \begin{bmatrix} \frac{\partial x_1}{\partial X_1} & \frac{\partial x_2}{\partial X_1} & \frac{\partial x_3}{\partial X_1} \\ \frac{\partial x_1}{\partial X_2} & \frac{\partial x_2}{\partial X_2} & \frac{\partial x_3}{\partial X_2} \\ \frac{\partial x_1}{\partial X_3} & \frac{\partial x_2}{\partial X_3} & \frac{\partial x_3}{\partial X_3} \end{bmatrix} \begin{Bmatrix} \dot{i}_1 \\ \dot{i}_2 \\ \dot{i}_3 \end{Bmatrix} \tag{8.60b}$$

From the above discussion, by substituting $\dot{E}_J = (\partial x_k / \partial X_J)\dot{i}_k$ into the relationship $\mathrm{d}\bar{P}_J \dot{E}_J = \mathrm{d}P_J \dot{i}_J$ where $\mathrm{d}\bar{P}_J = S_{iJ}\,\mathrm{d}\mathring{A}N_i$, the infinitesimal force $\mathrm{d}P_k$ can be expressed by:

$$\mathrm{d}P_k = S_{iJ} \frac{\partial x_k}{\partial X_J}\,\mathrm{d}\mathring{A}N_i \tag{8.61}$$

Since $\mathrm{d}P_k = \sigma_{ik} J(\partial X_J / \partial x_i)\,\mathrm{d}\mathring{A}N_J$ from Eq. (8.58a), comparing with Eq. (8.61), we find the following relationship:

$$\sigma_{ik} J \frac{\partial X_J}{\partial x_i}\,\mathrm{d}\mathring{A}N_J = S_{iJ} \frac{\partial x_k}{\partial X_J}\,\mathrm{d}\mathring{A}N_i \tag{8.62a}$$

or

$$\left(J\sigma_{Jk} \frac{\partial X_i}{\partial x_J} - S_{iJ} \frac{\partial x_k}{\partial X_J} \right) \mathrm{d}\mathring{A}N_i = 0 \tag{8.62b}$$

For an arbitrary unit normal vector N_i, S_{iJ} can be expressed in terms of σ_{kJ} by:

$$S_{iJ} = J\sigma_{kJ} \frac{\partial X_i}{\partial x_k} \frac{\partial X_J}{\partial x_J} \tag{8.63}$$

Since σ_{kJ} is symmetric, S_{iJ} is also a symmetric tensor. Further, using Eq. (8.58c), S_{iJ} can be expressed in terms of T_{ik}, that is:

$$S_{iJ} = T_{ik} \frac{\partial X_J}{\partial x_k} \tag{8.64a}$$

or in inversed form:

$$T_{ik} = S_{iJ} \frac{\partial x_k}{\partial X_J} \quad \text{or} \quad T_{iJ} = S_{ik} \frac{\partial x_J}{\partial X_k} \tag{8.64b}$$

It can be easily understood from Eq. (8.64b) that the first Piola-Kirchhoff stress T_{ij} is equivalent to the decomposed stress of the second Piola-Kirchhoff stress into the Cartesian coordinate system x_i. Further, it is important to note that the second Piola-Kirchhoff stress tensor S_{ij} is not affected by the rigid-body motion but the first Piola-Kirchhoff stress tensor T_{ij} is.

When the displacements and displacement gradients are small, the Eulerian stress, the first and second Piola-Kirchhoff stresses become approximately equal to each other, since $J \cong 1$ and $\partial x_i/\partial X_j \cong \delta_{ij}$.

Example 8.10: Consider the static equilibrium condition of the body subjected to the body force F_i and the surface fraction T_i as shown in Fig. 8.10. The static equilibrium equation can be generally written in terms of the current variables corresponding to the deformed body, i.e., the so-called *Eulerian description*:

$$\int_A \sigma_{ji} n_j \, dA + \int_V F_i \rho \, dV = 0 \tag{8.65a}$$

where σ_{ji} is the Eulerian stress tensor, n_j the unit normal vector to the current surface of the body, F_i body force per unit mass, and ρ density per unit volume. Express the static equilibrium equation in terms of the variables corresponding to the undeformed body (*Lagrangian description*).

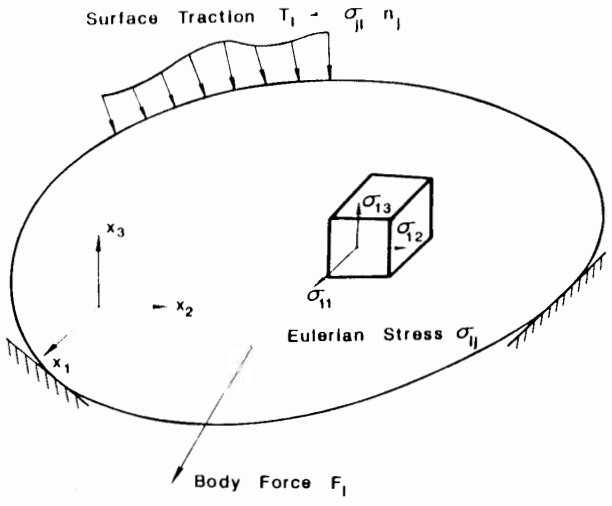

Fig. 8.10. Equilibrium of body.

Solution: The relationships between the variables in the undeformed and deformed states are summarized as follows:

Variables	Undeformed	Deformed
Coordinates	X_i	x_i
Volume	$\mathrm{d}\mathring{V}$	$\mathrm{d}V$
Area	$\mathrm{d}\mathring{A}$	$\mathrm{d}A$
Unit normal vector	N_i	n_i
Density	ρ_0	ρ
Body force	F_{0i}	F_i
Stresses	T_{ij} (Lagrangian) S_{ij} (Kirchhoff)	σ_{ij} (Eulerian)

The conservation of mass requires that $\rho_0\,\mathrm{d}\mathring{V} = \rho\,\mathrm{d}V$ whereas the body force per unit mass remains unchanged during a deformation, i.e., $F_{0i} = F_i$. Using the *divergence theorem*, a simpler *Eulerian description* of Eq. (8.65a) may be expressed by:

$$\int_V (\sigma_{ji,j} + F_i\rho)\,\mathrm{d}V = 0 \quad \text{or} \quad \sigma_{ji,j} + F_i\rho = 0 \tag{8.65b}$$

where the subscript after the slash denotes the derivative with respect to the spatial coordinates x_i.

We shall now consider the static equilibrium equation written in terms of variables in the undeformed state:

$$\int_A \sigma_{ji} n_j\,\mathrm{d}A + \int_V F_i\rho\,\mathrm{d}V = \int_{\mathring{A}} T_{ji} N_j\,\mathrm{d}\mathring{A} + \int_{\mathring{V}} F_{0i}\rho_0\,\mathrm{d}\mathring{V}$$

$$= \int_{\mathring{V}} (T_{ji,j} + F_{0i}\rho_0)\,\mathrm{d}\mathring{V} = 0$$

where the subscript after a comma denotes the derivative with respect to the reference coordinates X_i. Thus, we obtain the *Lagrangian description* of the static equilibrium equation:

$$T_{ji,j} + F_{0i}\rho_0 = 0 \tag{8.65c}$$

Substituting into Eq. (8.65c) the relation between the Lagrangian stress T_{ij} and the second Piola-Kirchhoff stress S_{ij}, that is, $T_{ji} = \partial x_i/\partial X_m S_{jm}$, we obtain:

$$\frac{\partial}{\partial X_j}\left(\frac{\partial x_i}{\partial X_m} S_{jm}\right) + \rho_0 F_{0i} = 0 \tag{8.65d}$$

Further substitution of $\partial x_i/\partial X_m = \delta_{im} + u_{i,m}$ into Eq. (8.65d) yields:

$$\frac{\partial}{\partial X_j}\left[S_{jm}(\delta_{im} + u_{i,m})\right] + \rho_0 F_{oi} = 0 \tag{8.65e}$$

8.4.2 Stress rates

The rate of deformation tensor V_{ij} is suitable for the application to a constitutive law because it vanishes when the body exhibits a rigid-body motion. Thus, the stress rate used for a constitutive law must be invariant with respect to the rigid-body rotation. The material derivative $d\sigma_{ij}/dt$ does not in general satisfy the invariance by a rigid-body rotation. For example, consider an element which is subjected to the normal stress σ_{11} only, as shown in Fig. 8.11. If the element performs the rigid-body rotation by 90°, the stress acting on the element becomes σ_{22} whose magnitude is the same as that of σ_{11} before the rotation. Thus, the rigid-body rotation alters the stress tensor, even though the stress state acting on the element remains unchanged.

In the following, the stress rates such as the *Jaumann stress rate* and the *Truesdell stress rate* which are invariant with the rigid-body rotation will be introduced in some details.

Jaumann stress rate

Consider again an element in the body where the Eulerian stress σ_{ij} referred to the fixed Cartesian coordinate x_i is acting at the instant time t. Take the origin of the coordinate system x_i at the point P in the body as shown in Fig. 8.12. Also, we consider another Cartesian coordinate system x_i' which rotates with the body, has the same origin at the point P and coincides with the x_i-axis at time t.

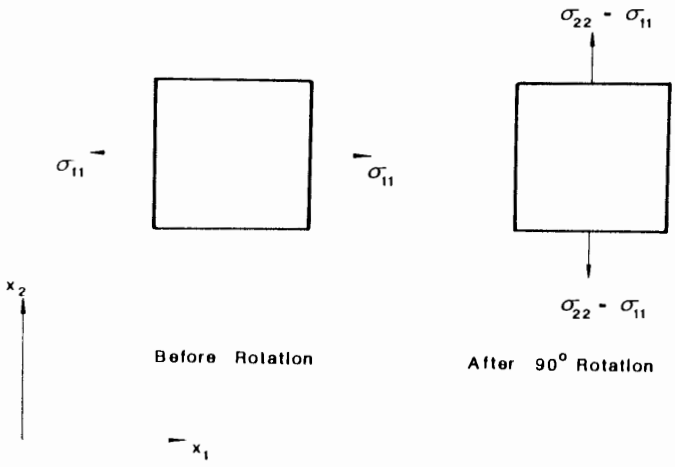

Fig. 8.11. Stress change by rigid-body rotation.

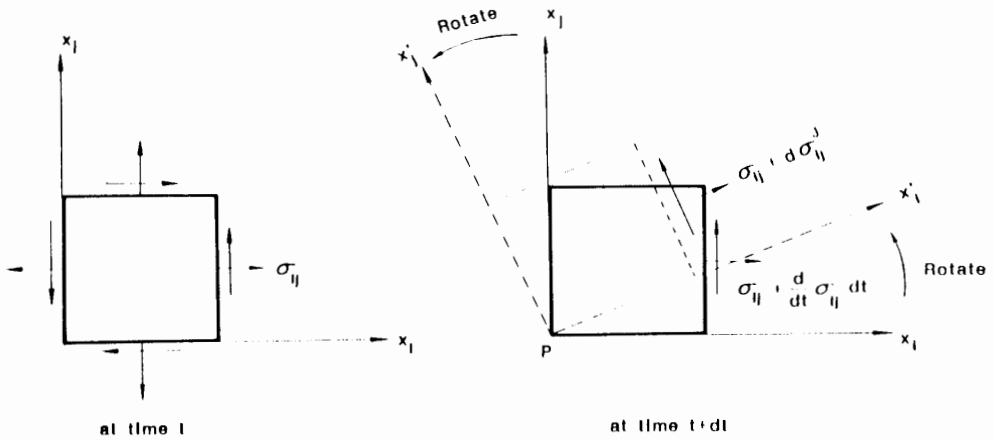

Fig. 8.12. Jaumann stress rate.

The stress tensors at time t referred to the x_i and x'_i systems are respectively denoted by $\sigma_{ij}(t)$ and $\sigma'_{ij}(t)$, and $\sigma_{ij}(t) = \sigma'_{ij}(t)$. Further, assuming the stress tensor $\sigma'_{ij}(t + dt)$ at the instant time $t + dt$ referred to the rotating Cartesian coordinate system x'_i, the *Jaumann stress rate* $\dot{\sigma}^{J}_{ij}$ can be defined as (Fung, 1965):

$$\dot{\sigma}^{J}_{ij} = \lim_{dt \to 0} \frac{1}{dt}\left[\sigma'_{ij}(t + dt) - \sigma'_{ij}(t)\right] \tag{8.66}$$

On the other hand, the stress tensor $\sigma_{ij}(t + dt)$ referred to the fixed Cartesian coordinate system x_i can be expressed by:

$$\sigma_{ij}(t + dt) = \sigma_{ij}(t) + \frac{d}{dt}\left[\sigma_{ij}(t)\right] dt \tag{8.67}$$

We shall now consider the *spin tensor* W_{ij} for the rotation axis x'_i. The spin tensor W_{ij} has the form:

$$W_{ij} = \frac{1}{2}\left[\frac{\partial v_i}{\partial x_j} - \frac{\partial v_j}{\partial x_i}\right] \tag{8.68}$$

The instantaneous velocity v_i of the axis x'_i at time t can be expressed by:

$$v_i = \frac{1}{2}\left[\frac{\partial v_i}{\partial x_j} - \frac{\partial v_j}{\partial x_i}\right] x_j \tag{8.69}$$

Therefore, the coordinates x_i' at time $t + \mathrm{d}t$ ($x_i' = x_i$ at time t) can be written in terms of x_i as:

$$x_i' = x_i - \frac{1}{2}\left[\frac{\partial v_i}{\partial x_j} - \frac{\partial v_j}{\partial x_i}\right] x_j \, \mathrm{d}t = x_i - W_{ij} x_j \, \mathrm{d}t \tag{8.70}$$

From Eq. (8.70), the stress tensor $\sigma_{ij}(t + \mathrm{d}t)$ referred to the x_i coordinate system can be transformed to the stress tensor $\sigma_{ij}'(t + \mathrm{d}t)$ referred to the x_i' coordinate system, that is:

$$\sigma_{ij}'(t + \mathrm{d}t) = \frac{\partial x_i'}{\partial x_k} \frac{\partial x_j'}{\partial x_l} \sigma_{kl}(t + \mathrm{d}t)$$

$$= (\delta_{ik} - W_{ik} \, \mathrm{d}t)(\delta_{jl} - W_{jl} \, \mathrm{d}t)\left[\sigma_{kl}(t) + \frac{\mathrm{d}}{\mathrm{d}t}(\sigma_{kl}) \, \mathrm{d}t\right] \tag{8.71}$$

Neglecting the higher-order terms with respect to $\mathrm{d}t$, we find the relation:

$$\sigma_{ij}'(t + \mathrm{d}t) = \sigma_{ij}(t) + \left[\frac{\mathrm{d}}{\mathrm{d}t}(\sigma_{ij}) - \sigma_{il}(t) W_{jl} - \sigma_{kj}(t) W_{ik}\right] \mathrm{d}t \tag{8.72}$$

From Eq. (8.66), the Jaumann stress rate $\dot{\sigma}_{ij}^{\mathrm{J}}$ can therefore be expressed by:

$$\dot{\sigma}_{ij}^{\mathrm{J}} = \frac{\mathrm{d}}{\mathrm{d}t}(\sigma_{ij}) - \sigma_{il}(t) W_{jl} - \sigma_{kj}(t) W_{ik} \tag{8.73}$$

For the finite motion during time $\mathrm{d}t$, the Jaumann stress increment $\mathrm{d}\sigma_{ij}^{\mathrm{J}}$ can be denoted by:

$$\mathrm{d}\sigma_{ij}^{\mathrm{J}} = \mathrm{d}\sigma_{ij} - \sigma_{ik} \, \mathrm{d}\Omega_{jk} - \sigma_{jk} \, \mathrm{d}\Omega_{ik} \tag{8.74}$$

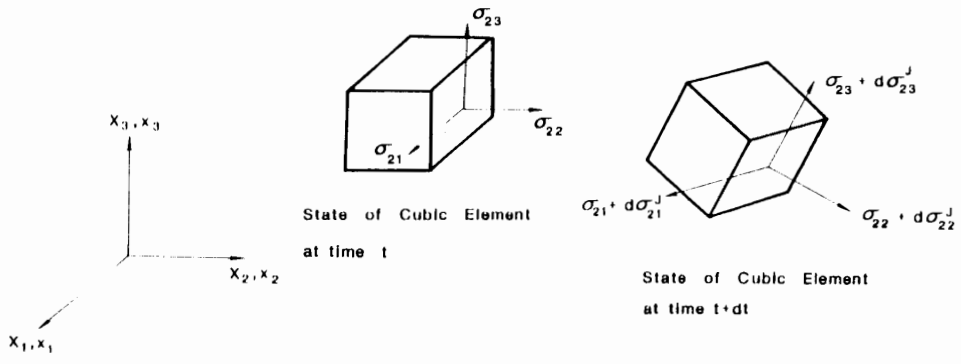

Fig. 8.13. Three-dimensional view of Jaumann stress increments.

where $d\Omega_{jk}$ is the increment of the rotation tensor given by $W_{jk}\,dt$. The three-dimensional view of the Jaumann stress increment $d\sigma_{ij}^{J}$ is shown in Fig. 8.13.

When the body performs only a pure rigid-body motion during time dt, for example, the Jaumann stress increment $d\sigma_{ij}^{J}$ remains unchanged, but the Eulerian stress increment $d\sigma_{ij}$ due to this rigid body rotation becomes, from Eq. (8.74):

$$d\sigma_{ij} = \sigma_{ik}\,d\Omega_{jk} + \sigma_{jk}\,d\Omega_{ik} \tag{8.75}$$

Truesdell stress rate

The relationship between the Eulerian stress σ_{ij} and the second Piola-Kirchhoff stress S_{ij} has been presented in Eq. (8.63). By taking the material derivative of Eq. (8.63), the relationship between the second Piola-Kirchhoff stress rate and the *Truesdell stress rate* $\mathring{\sigma}_{ij}^{1}$ can be obtained as follows: Considering the second Piola-Kirchhoff stress rate $d(S_{ij})/dt$, the right-hand side of Eq. (8.63) can be expressed by (Prager, 1961):

$$\frac{d}{dt}(S_{ij}) = \frac{d}{dt}(J)\frac{\partial X_i}{\partial x_k}\frac{\partial X_j}{\partial x_l}\sigma_{kl} + J\frac{d}{dt}\left(\frac{\partial X_i}{\partial x_k}\right)\frac{\partial X_j}{\partial x_l}\sigma_{kl} + J\frac{\partial X_i}{\partial x_k}\frac{d}{dt}\left(\frac{\partial X_j}{\partial x_l}\right)\sigma_{kl}$$

$$+ J\frac{\partial X_i}{\partial x_k}\frac{\partial X_j}{\partial x_l}\frac{d}{dt}(\sigma_{kl}) \tag{8.76}$$

Since $d(J)/dt$ may be expressed by $d(\rho_0/\rho)/dt$, (see Example 8.11):

$$\frac{d}{dt}(J) = \frac{d}{dt}\left(\frac{\rho_0}{\rho}\right) = -\left(\frac{\rho_0}{\rho^2}\right)\frac{d}{dt}(\rho) = \left(\frac{\rho_0}{\rho}\right)\frac{\partial v_i}{\partial x_i} = J\frac{\partial v_i}{\partial x_i} \tag{8.77}$$

Therefore, using Eqs. (8.54b) and (8.77), we can rewrite Eq. (8.76) in the following form:

$$\frac{d}{dt}(S_{ij}) = J\left[\frac{\partial v_m}{\partial x_m}\frac{\partial X_i}{\partial x_k}\frac{\partial X_j}{\partial x_l}\sigma_{kl} - \frac{\partial v_m}{\partial x_k}\frac{\partial X_i}{\partial x_m}\frac{\partial X_j}{\partial x_l}\sigma_{kl} - \frac{\partial X_i}{\partial x_k}\frac{\partial v_m}{\partial x_l}\frac{\partial X_j}{\partial x_m}\sigma_{kl}\right.$$

$$\left. + \frac{\partial X_i}{\partial x_k}\frac{\partial X_j}{\partial x_l}\frac{d}{dt}(\sigma_{kl})\right] \tag{8.78}$$

or rearranging the dummy indices and using the symmetry of $\sigma_{kl} = \sigma_{lk}$, we obtain the final form:

$$\frac{d}{dt}(S_{ij}) = J\frac{\partial X_i}{\partial x_k}\frac{\partial X_j}{\partial x_l}\left[\frac{d}{dt}(\sigma_{kl}) + \frac{\partial v_m}{\partial x_m}\sigma_{kl} - \frac{\partial v_l}{\partial x_m}\sigma_{km} - \frac{\partial v_k}{\partial x_m}\sigma_{ml}\right] \tag{8.79}$$

where the quantities in the square brackets in the right-hand side of Eq. (8.79) are defined as the *Truesdell stress rate* $\dot{\sigma}_{kl}^{\mathrm{T}}$ (Prager, 1961):

$$\dot{\sigma}_{kl}^{\mathrm{T}} = \frac{\mathrm{d}}{\mathrm{d}t}(\sigma_{kl}) + \frac{\partial v_m}{\partial x_m}\sigma_{kl} - \frac{\partial v_l}{\partial x_m}\sigma_{km} - \frac{\partial v_k}{\partial x_m}\sigma_{ml} \tag{8.80}$$

It should be noted that the relation between the second Piola-Kirchhoff stress rate $\mathrm{d}(S_{ij})/\mathrm{d}t$ and the Truesdell stress rate $\dot{\sigma}_{kl}^{\mathrm{T}}$ is defined in an exactly similar manner to the relation between the second Piola-Kirchhoff stress S_{ij} and the Eulerian stress σ_{kl}. Since the velocity gradients $\partial v_m/\partial x_k$ are the sum of the rate of deformation tensor V_{mk} and the spin tensor W_{mk}, Eq. (8.80) can then be expressed by:

$$\dot{\sigma}_{kl}^{\mathrm{T}} = \frac{\mathrm{d}}{\mathrm{d}t}(\sigma_{kl}) + V_{mm}\sigma_{kl} - (V_{lm} + W_{lm})\sigma_{km} - (V_{km} + W_{km})\sigma_{ml} \tag{8.81}$$

Introducing the Jaumann stress rate $\dot{\sigma}_{kl}^{\mathrm{J}} = \mathrm{d}(\sigma_{kl})/\mathrm{d}t - W_{lm}\sigma_{km} - W_{km}\sigma_{lm}$, the Truesdell stress rate in Eq. (8.81) becomes:

$$\dot{\sigma}_{kl}^{\mathrm{T}} = \dot{\sigma}_{kl}^{\mathrm{J}} + V_{mm}\sigma_{kl} - V_{lm}\sigma_{km} - V_{km}\sigma_{lm} \tag{8.82}$$

When the neighborhood of the considered particle undergoes a rigid-body rotation, the Truesdell stress rate reduces to the Jaumann stress rate because the rate of deformation tensor vanishes. In this case, both the Jaumann and Truesdell stress rates obviously vanish.

The Truesdell stress increment $\mathrm{d}\sigma_{kl}^{\mathrm{T}}$ for the finite deformation during time $\mathrm{d}t$ can be written as:

$$\mathrm{d}\sigma_{kl}^{\mathrm{T}} = \mathrm{d}\sigma_{kl}^{\mathrm{J}} + \mathrm{d}\epsilon_{mm}\sigma_{kl} - \mathrm{d}\epsilon_{lm}\sigma_{km} - \mathrm{d}\epsilon_{km}\sigma_{lm} \tag{8.83}$$

since $\mathrm{d}\epsilon_{mm} = V_{mm}\,\mathrm{d}t$, $\mathrm{d}\epsilon_{lm} = V_{lm}\,\mathrm{d}t$, and $\mathrm{d}\epsilon_{km} = V_{km}\,\mathrm{d}t$. It is noted from Eqs. (8.79) and (8.80) that $\mathrm{d}\sigma_{kl}^{\mathrm{T}}$ becomes approximately equal to the increment of second

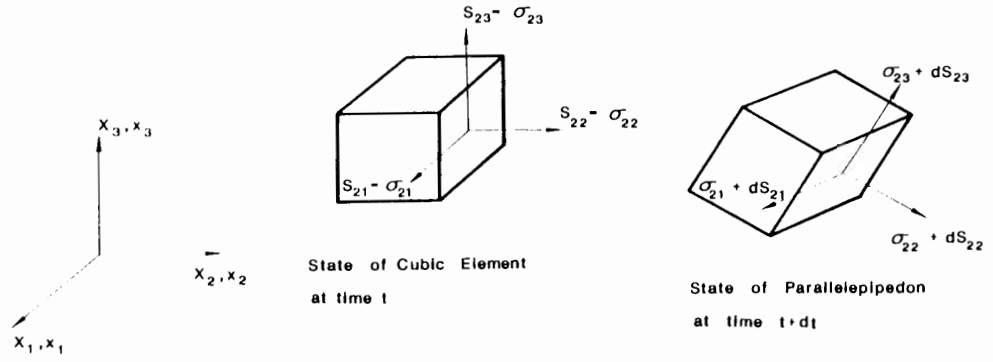

Fig. 8.14. Three-dimensional view of Truesdell stress increments.

Piola-Kirchhoff stress dS_{kl} when the displacement gradient $\partial u_i/\partial x_j$ is small compared with unity so that $J = 1$ and $\partial X_i/\partial x_j = \delta_{ij}$ are approximately held. The three-dimensional view of the Truesdell stress increment is shown in Fig. 8.14.

In a similar manner, the Lagrangian stress rate $d(T_{ij})/dt$ can be expressed by:

$$\frac{d}{dt}(T_{ij}) = \frac{d}{dt}\left(J\frac{\partial X_i}{\partial x_k}\sigma_{kj}\right) = \frac{\rho_0}{\rho}\frac{\partial X_i}{\partial x_k}\left[\frac{d}{dt}(\sigma_{kj}) + \frac{\partial v_l}{\partial x_l}\sigma_{kj} - \sigma_{lj}\frac{\partial v_k}{\partial x_l}\right]$$

$$= \frac{\rho_0}{\rho}\frac{\partial X_i}{\partial x_k}\left[\dot{\sigma}_{kj} + V_{ll}\sigma_{kj} - \sigma_{lj}(V_{kl} + W_{kl})\right] \tag{8.84a}$$

The Lagrangian stress increment dT_{ij} for the finite motion during time dt can be written by neglecting the higher-order terms:

$$dT_{ij} = d\sigma_{ij} + d\epsilon_{ll}\sigma_{ij} - \sigma_{lj}(d\epsilon_{il} + d\Omega_{il}) \tag{8.84b}$$

When the Lagrangian stress rate vanishes, the force transmitted across the surface element of the body remains unchanged irrespective of the occurrence of an instantaneous rotation and deformation.

Example 8.11: From the conservation of mass $d(m)/dt = 0$, derive the relation used in Eq. (8.77):

$$\frac{d}{dt}(\rho) = -\rho\frac{\partial v_i}{\partial x_i}$$

Solution: Assume mass m is given by $\int\rho\, dV$ where ρ denotes the density per unit volume which is a function of the current coordinates x_i and time t:

$$\rho = \rho(x_1, x_2, x_3, t)$$

The material derivative of mass m can be defined as:

$$\frac{d}{dt}(m) = \lim_{dt\to 0}\frac{1}{dt}\left[\int_{V+\Delta V}\rho(x_i, t+dt)\, dV - \int_V \rho(x_i, t)\, dV\right]$$

$$= \lim_{dt\to 0}\frac{1}{dt}\left[\int_V \rho(x_i, t+dt)\, dV + \int_{\Delta V}\rho(x_i, t+dt)\, dV - \int_V \rho(x_i, t)\, dV\right]$$

$$= \lim_{dt\to 0}\frac{1}{dt}\left[\int_V \{\rho(x_i, t+dt) - \rho(x_i, t)\}\, dV + \int_{\Delta V}\rho(x_i, t+dt)\, dV\right]$$

From the following relations:

$$\lim_{dt \to 0} \frac{1}{dt} \int_V \{ \rho(x_i, t + dt) - \rho(x_i, t) \} \, dV = \int_V \frac{\partial \rho}{\partial t} \, dV$$

and

$$dV = v_i \, dt \, n_i \, dA$$

we obtain by using the *divergence theorem*:

$$\frac{d}{dt}(m) = \int_V \frac{\partial \rho}{\partial t} \, dV + \int_A \rho v_i n_i \, dA = \int_V \left[\frac{\partial \rho}{\partial t} + \frac{\partial \rho}{\partial x_i} v_i + \rho \frac{\partial v_i}{\partial x_i} \right] dV$$

$$= \int_V \left[\frac{d\rho}{dt} + \rho \frac{\partial v_i}{\partial x_i} \right] dV = 0$$

Since $d(\rho)/dt + \rho(\partial v_i/\partial x_i) = 0$ for an arbitrary volume dV, we have therefore the relation:

$$\frac{d}{dt}(\rho) = -\rho \frac{\partial v_i}{\partial x_i}$$

Example 8.12: The Jaumann stress rate $\dot{\sigma}_{ij}^{J}$ may be considered as an actual stress rate corresponding to the rotating cubic element in the deformed body, as shown in Fig. 8.13. When we consider the rate of Kirchhoff stress corresponding to such a rotating cubic element, this stress rate is generally called the *Jaumann rate of Kirchhoff stress* $\dot{S}_{ij}^{J}$ (Yamada and Wifi, 1977). Show that $\dot{S}_{ij}^{J} = \dot{\sigma}_{ij}^{J} + \sigma_{ij} V_{kk}$.

Solution: The second Piola-Kirchhoff stress tensor S_{ij} measured in the reference coordinate system X_i may be transferred into the stress tensor (not a real stress tensor) in the spatial coordinate system x_i, as shown in Fig. 8.15. Using the transformation law, this stress tensor $\bar{S}_{ij}$ can be expressed by:

$$\bar{S}_{ij} = J\sigma_{ij} \tag{8.85}$$

Similar to that used in the preceding Section for the Jaumann rate of Eulerian stress tensor, the Jaumann rate of Kirchhoff stress tensor, $\dot{S}_{ij}^{J}$, may be obtained by simply using Eq. (8.73):

$$\dot{S}_{ij}^{J} = \frac{d}{dt}\left(\bar{S}_{ij}\right) - \bar{S}_{ik}(t) W_{jk} - \bar{S}_{jk}(t) W_{ik} = \frac{d}{dt}\left(\bar{S}_{ij}\right) - \sigma_{ik}(t) W_{jk} - \sigma_{jk}(t) W_{ik} \tag{8.86}$$

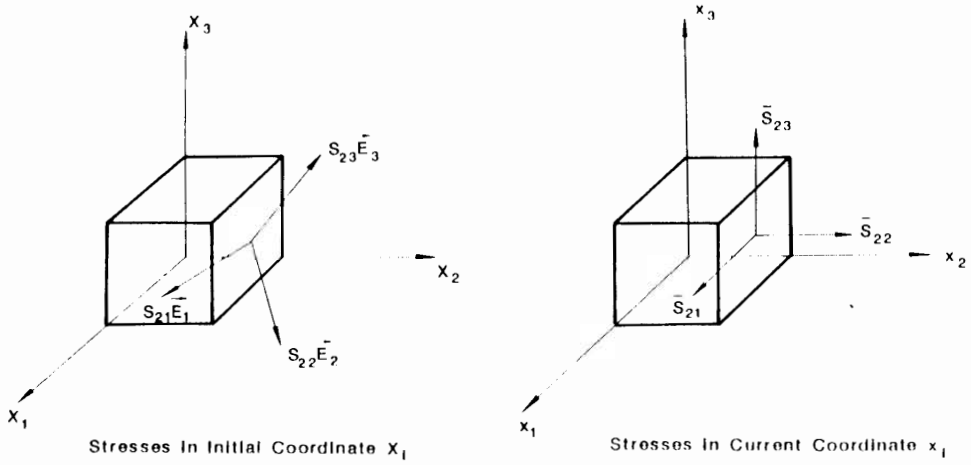

Fig. 8.15. Transformation of the second Piola-Kirchhoff stress tensor S_{ij}.

since $\bar{S}_{ij}(t) = \sigma_{ij}(t)$ at time t. Substituting Eq. (8.85) and employing the determinant of Jacobian $J = 1$ at time t lead to:

$$\begin{aligned}
\mathring{S}^{\mathrm{J}}_{ij} &= \frac{\mathrm{d}}{\mathrm{d}t}(J)\sigma_{ij} + J\frac{\mathrm{d}}{\mathrm{d}t}(\sigma_{ij}) - \sigma_{ik}(t)W_{jk} - \sigma_{jk}(t)W_{ik} \\
&= J\frac{\partial v_k}{\partial x_k}\sigma_{ij} + J\dot{\sigma}_{ij} - \sigma_{ik}(t)W_{jk} - \sigma_{jk}(t)W_{ik} \\
&= JV_{kk}\sigma_{ij} + J\dot{\sigma}_{ij} - \sigma_{ik}(t)W_{jk} - \sigma_{jk}(t)W_{ik} \\
&= \dot{\sigma}_{ij} - \sigma_{ik}(t)W_{jk} - \sigma_{jk}(t)W_{ik} + \sigma_{ij}V_{kk} = \dot{\sigma}^{\mathrm{J}}_{ij} + \sigma_{ij}V_{kk}
\end{aligned} \tag{8.87}$$

Furthermore, the Jaumann increment of Kirchhoff stress tensor $\mathrm{d}S^{\mathrm{J}}_{ij}$ for the finite motion can be written as:

$$\mathrm{d}S^{\mathrm{J}}_{ij} = \mathrm{d}\sigma^{\mathrm{J}}_{ij} + \sigma_{ij}\,\mathrm{d}\epsilon_{kk} \tag{8.88}$$

8.5 VIRTUAL WORK EQUATION

We have so far discussed the fundamentals for the large-displacement and large-deformation analyses. In this Section, with the help of this basic knowledge, we shall describe the *virtual work equation* which expresses the equality of the work done by a set of external forces and internal stresses over a set of *variational displacements*.

Assuming the external surface traction T_i and the body force F_i remain unchanged during a virtual displacement δu_i, the virtual external work δW_{ext} due to these forces is:

$$\delta W_{ext} = \int_A T_i \delta u_i \, dA + \int_V F_i \delta u_i \rho \, dV = \int_A \sigma_{ji} n_j \delta u_i \, dA + \int_V F_i \delta u_i \rho \, dV$$

$$= \int_V \left[\frac{\partial \sigma_{ji}}{\partial x_j} \delta u_i + \sigma_{ji} \frac{\partial (\delta u_i)}{\partial x_j} + F_i \delta u_i \rho \right] dV$$

$$= \int_V \left[\sigma_{ji} \frac{\partial (\delta u_i)}{\partial x_j} + \left(\frac{\partial \sigma_{ji}}{\partial x_j} + F_i \rho \right) \delta u_i \right] dV \tag{8.89a}$$

Since the second term in the square brackets is the static equilibrium equation derived previously in Example 8.10 and that $\partial(\delta u_i)/\partial x_j = \delta \epsilon_{ij} + \delta \Omega_{ij}$, we obtain:

$$\delta W_{ext} = \int_V \sigma_{ji} \frac{\partial (\delta u_i)}{\partial x_j} \, dV = \int_V \sigma_{ji} \left[\delta \epsilon_{ij} + \delta \Omega_{ij} \right] dV \tag{8.89b}$$

where $\delta \epsilon_{ij}$ and $\delta \Omega_{ij}$ are respectively the virtual strain and virtual rotation as:

$$\delta \epsilon_{ij} = \frac{1}{2} \left[\frac{\partial (\delta u_i)}{\partial x_j} + \frac{\partial (\delta u_j)}{\partial x_i} \right] \quad \text{and} \quad \delta \Omega_{ij} = \frac{1}{2} \left[\frac{\partial (\delta u_i)}{\partial x_j} - \frac{\partial (\delta u_j)}{\partial x_i} \right] \tag{8.89c}$$

Since $\sigma_{ji} \delta \Omega_{ij} = 0$, we find:

$$\delta W_{ext} = \int_V \sigma_{ji} \delta \epsilon_{ij} \, dV = \int_V \sigma_{ij} \delta \epsilon_{ij} \, dV \tag{8.89d}$$

Equation (8.89d) states that if the stress field is *statically admissible*, i.e., the equilibrium equation (8.65a) and boundary conditions $\sigma_{ji} n_j = T_i$ are both satisfied, the total virtual work of the external forces on any *kinematically admissible* virtual displacement field is identical to $\int_V \sigma_{ij} \delta \epsilon_{ij} \, dV$. The term kinematically admissible requires the variational displacements to possess continuous first-order derivatives and satisfy any imposed displacement boundary conditions.

The virtual work equation written in terms of the *Eulerian variables* has the general form:

$$\int_A T_i \delta u_i \, dA + \int_V \rho F_i \delta u_i \, dV = \int_V \sigma_{ij} \delta \epsilon_{ij} \, dV \tag{8.90a}$$

where the integrations of Eq. (8.90a) are performed over the entire deformed body. Equation (8.90a) represents the relationship between a statically admissible set of

forces and a set of kinematically admissible displacements. However, if consistent definitions of stress and strain are adopted, the virtual work equation may be written with respect to any of the previously determined equilibrium configurations.

Equation (8.90a) may be viewed as the requirement of equilibrium at some intermediate time t and can therefore be rewritten explicitly as:

$$\int_A T_i^t \delta u_i \, dA^t + \int_V \rho^t F_i^t \delta u_i \, dV^t = \int_V \sigma_{ij}^t \delta \epsilon_{ij} \, dV^t \tag{8.90b}$$

where the variables with the superscript t denote the variables at intermediate time t.

During the course of further loading and deformation, the equilibrium equation at time $(t + dt)$ also requires:

$$\int_V \sigma_{ij}^{t+dt} \delta \epsilon_{ij} \, dV^{t+dt} = R^{t+dt} \tag{8.91a}$$

where R^{t+dt} is expressed by:

$$R^{t+dt} = \int_A T_i^{t+dt} \delta u_i \, dA^{t+dt} + \int_V \rho^{t+dt} F_i^{t+dt} \delta u_i \, dV^{t+dt} \tag{8.91b}$$

The primary difficulties associated with the large-displacement and large-deformation analyses now become clear, the configuration at time $(t + dt)$ is not known, but must be arrived at by the successive solution of the appropriate equations of motion. In practice, one of the two following methods of solution is generally adopted, but both methods require the equilibrium condition to be satisfied in the deformed state. The first method, the *total Lagrangian formulation* refers all stresses and deformations to the reference (undeformed) configuration at time $t = 0$. The second method, the *updated Lagrangian formulation* refers all stresses and deformations to the current configuration at time t. These methods are described respectively in Sections 8.5.1 and 8.5.2

Example 8.13: Derive the *virtual work equation* (8.90a) using the variables in the reference state.

Solution: Consider the virtual work δW_{ext} due to the external forces as given by $\delta W_{ext} = \int_A T_i \delta u_i \, dA + \int_V F_i \rho \delta u_i \, dV$. Recalling and substituting the following relationships:

$$u_i = x_i - X_i$$

$$T_i \, dA = \sigma_{ji} n_j \, dA = T_{ji} N_j \, d\mathring{A}$$

$$F_i = F_{oi}$$

$$\rho \, dV = \rho_0 \, d\mathring{V}$$

we obtain the form of δW_{ext} in terms of the variables in the reference state:

$$\delta W_{\text{ext}} = \int_{\mathring{A}} T_{Ji} N_J \delta x_i \, \mathrm{d}\mathring{A} + \int_{\mathring{V}} F_{oi} \rho_o \delta x_i \, \mathrm{d}\mathring{V} \tag{8.92}$$

where T_{Ji} is the Lagrangian stress tensor. Employing the *divergence theorem (Gauss' theorem)*, Eq. (8.92) can be transformed into:

$$\delta W_{\text{ext}} = \int_{\mathring{V}} \left[T_{Ji} \frac{\partial(\delta x_i)}{\partial X_J} + \left(\frac{\partial T_{Ji}}{\partial X_J} + F_{oi} \rho_o \right) \delta x_i \right] \mathrm{d}\mathring{V} \tag{8.93}$$

The second term in the square brackets must vanish since it is the static equilibrium equation (8.65c) discussed in Example 8.10. Thus, we obtain the following virtual work equation in terms of variables in the reference state:

$$\delta W_{\text{ext}} = \int_{\mathring{V}} T_{Ji} \frac{\partial(\delta x_i)}{\partial X_J} \, \mathrm{d}\mathring{V} = \int_{\mathring{V}} T_{Ji} \delta \left(\frac{\partial x_i}{\partial X_J} \right) \mathrm{d}\mathring{V} \tag{8.94a}$$

or Eq. (8.92) reduces to:

$$\int_{\mathring{A}} T_{Ji} N_J \delta u_i \, \mathrm{d}\mathring{A} + \int_{\mathring{V}} F_{oi} \rho_o \delta u_i \, \mathrm{d}\mathring{V} = \int_{\mathring{V}} T_{Ji} \delta \left(\frac{\partial x_i}{\partial X_J} \right) \mathrm{d}\mathring{V} \tag{8.94b}$$

Substitution of $T_{Ji} = S_{Jk} \, \partial x_i / \partial X_k$ into Eq. (8.94a) leads to:

$$\delta W_{\text{ext}} = \int_{\mathring{V}} S_{Jk} \frac{\partial x_i}{\partial X_k} \delta \left(\frac{\partial x_i}{\partial X_J} \right) \mathrm{d}\mathring{V} = \int_{\mathring{V}} \tfrac{1}{2} S_{Jk} \delta \left[\frac{\partial x_i}{\partial X_k} \frac{\partial x_i}{\partial X_J} \right] \mathrm{d}\mathring{V} \tag{8.95a}$$

Noting that $\frac{1}{2}\delta[(\partial x_i/\partial X_k)(\partial x_i/\partial X_J)] = \delta E_{kJ}$ (see the definition of Lagrangian strain tensor, i.e., Eq. (8.33b)), we have in the final form:

$$\delta W_{\text{ext}} = \int_{\mathring{V}} S_{Jk} \delta E_{kJ} \, \mathrm{d}\mathring{V} = \int_{\mathring{V}} S_{IJ} \delta E_{IJ} \, \mathrm{d}\mathring{V} \tag{8.95b}$$

In summary, the virtual work equation can be expressed in the following forms:

$$\delta W_{\text{ext}} = \int_{V} \sigma_{ij} \delta \epsilon_{ij} \, \mathrm{d}V = \int_{\mathring{V}} T_{Ji} \delta \left(\frac{\partial x_i}{\partial X_J} \right) \mathrm{d}\mathring{V} = \int_{\mathring{V}} S_{IJ} \delta E_{IJ} \, \mathrm{d}\mathring{V} \tag{8.96}$$

in which the external virtual work δW_{ext} can be expressed in terms of either the Eulerian stress tensor σ_{ij} and the virtual change $\delta \epsilon_{ij}$ in infinitesimal strain tensor, or the first Piola-Kirchhoff stress tensor (Lagrangian stress tensor) T_{Ji} and the virtual change $\delta(\partial x_i/\partial X_J)$ of the deformation gradient, or the second Piola-Kirchhoff stress tensor S_{IJ} and the virtual change δE_{IJ} of the Lagrangian strain tensor.

8.5.1 *Total Lagrangian description in general*

The total Lagrangian formulation refers all measurements of forces, stresses, strains to the *reference* (undeformed) configuration. Thus, the virtual work equation at time t is also written with respect to the initial configuration. Considering Eq. (8.91), it is necessary to replace each of the force, stress, and strain quantities with alternative definitions which will result in an equivalent statement of the requirements of equilibrium, but written with respect to the initial configuration.

The aim of the present formulation is to obtain the subsequent state of stresses and associated displacements from some given initial state and some disturbing system of forces and/or displacements. The solution to nonlinear large-displacement and/or large-deformation problems is most effectively obtained in an *incremental* manner by linearizing the equilibrium equations at time $(t + \mathrm{d}t)$ in terms of the quantities with respect to the initial configuration.

Herein, we will only introduce the appropriate quantities for use in the virtual work equation based on the total Lagrangian description, and will leave the exact formulations to the reader. However, we shall discuss in some details the updated Lagrangian formulation in Section 8.5.2 that will be used in the subsequent applications.

Strain increments

The strain increments associated with the use of the *total Lagrangian formulation* are the *Lagrangian strain increments* $\mathrm{d}E_{ij}$. Considering Eq. (8.37) and introducing:

$$u_i^{t+\mathrm{d}t} = u_i^t + \mathrm{d}u_i \tag{8.97}$$

where $\mathrm{d}u_i$ is the displacement increment, the Lagrangian strain increments $\mathrm{d}E_{ij}$ thus become:

$$\begin{aligned}
\mathrm{d}E_{ij} &= E_{ij}^{t+\mathrm{d}t} - E_{ij}^t \\
&= \tfrac{1}{2}\left(u_{i,j}^{t+\mathrm{d}t} + u_{j,i}^{t+\mathrm{d}t} + u_{k,i}^{t+\mathrm{d}t} u_{k,j}^{t+\mathrm{d}t}\right) - \tfrac{1}{2}\left(u_{i,j}^t + u_{j,i}^t + u_{k,i}^t u_{k,j}^t\right) \\
&= \tfrac{1}{2}\left(\mathrm{d}u_{i,j} + \mathrm{d}u_{j,i} + \mathrm{d}u_{k,j} u_{k,i}^t + u_{k,j}^t\, \mathrm{d}u_{k,i} + \mathrm{d}u_{k,i}\, \mathrm{d}u_{k,j}\right)
\end{aligned} \tag{8.98}$$

where the differentiation is done with respect to the reference coordinate system X_i in the initial configuration.

Stress increments

Since the total Lagrangian formulation refers static (stress) and kinematic (strain) variables to the original undeformed configuration, the Eulerian stresses σ_{ij} must be referred back to the original configuration. This is done conveniently by relating the actual force on the deformed surface to a pseudo-force on the undeformed surface

in the manner discussed in Section 8.4 and thus required to use the second Piola-Kirchhoff stress S_{ij}.

The relationship between the second Piola-Kirchhoff stress S_{ij} and the Eulerian stress σ_{ij} can be written again as:

$$S_{ij}^t = \left(\rho_0/\rho^t\right) F_{ik}^{-1} \sigma_{kl}^t F_{jl}^{-1} = J F_{ik}^{-1} \sigma_{kl}^t F_{jl}^{-1} \tag{8.99a}$$

or in an inversed form:

$$\sigma_{ij}^t = \left(\rho^t/\rho_0\right) F_{ik} S_{kl}^t F_{jl} = \frac{1}{J} F_{ik} S_{kl}^t F_{jl} \tag{8.99b}$$

where ρ_0/ρ^t represents the ratio of the mass density ρ_0 in the original configuration to the mass density ρ^t in the current configuration, and F_{ij} denotes the deformation gradient tensor.

For the second Piola-Kirchhoff stresses during a finite deformation, we have the following incremental relationship:

$$S_{ij}^{t+\mathrm{d}t} = S_{ij}^t + \mathrm{d}S_{ij} \tag{8.100}$$

where $\mathrm{d}S_{ij}$ are the increments of second Piola-Kirchhoff stress which are related to the increments of Lagrangian strain $\mathrm{d}E_{ij}$ through:

$$\mathrm{d}S_{ij} = C_{ijkl}^* \, \mathrm{d}E_{kl} \tag{8.101}$$

where C_{ijkl}^* is not necessarily the same constitutive relation as for small displacement analyses (Bathe, 1982) and will be explained in some details in Section 8.6.

Virtual work equation

To derive the incremental equations of motion, it is necessary to linearize the virtual work expression about a known equilibrium state. The variables used in the incremental description of the total Lagrangian formulation are listed below:

Variables in the total Lagrangian formulation

	State at time t	State at time $t + \mathrm{d}t$
Kirchhoff stress	S_{ij}^t	$S_{ij}^t + \mathrm{d}S_{ij}$
Lagrangian strain	E_{ij}^t	$E_{ij}^t + \mathrm{d}E_{ij}$
Displacement	u_i^t	$u_i^t + \mathrm{d}u_i$
Body force/mass	f_{oi}	f_{oi}
Surface traction	T_{oi}^t	$T_{oi}^t + \mathrm{d}T_{oi}$

Thus, using Eqs. (8.91) and (8.96), and recalling that for the total Lagrangian formulation we relate the equilibrium requirement at time $(t + \mathrm{d}t)$ to the original configuration at time $t = 0$, we obtain:

$$\int_{\overset{0}{V}} (S_{ij}^{t} + \mathrm{d}S_{ij})\delta(E_{ij}^{t} + \mathrm{d}E_{ij})\,\mathrm{d}\overset{0}{V}$$

$$= R^{t+\mathrm{d}t} = \int_{\overset{0}{V}} F_{\omega i}\rho_0 \delta(u_i^{t} + \mathrm{d}u_i)\,\mathrm{d}\overset{0}{V} + \int_{\overset{0}{A}} (T_{\omega i}^{t} + \mathrm{d}T_{\omega i})\delta(u_i^{t} + \mathrm{d}u_i)\,\mathrm{d}\overset{0}{A} \tag{8.102}$$

Using $\delta(E_{ij}^{t} + \mathrm{d}E_{ij}) = \delta(\mathrm{d}E_{ij})$ and $\delta(u_i^{t} + \mathrm{d}u_i) = \delta(\mathrm{d}u_i)$, we find:

$$\int_{\overset{0}{V}} (S_{ij}^{t} + \mathrm{d}S_{ij})\delta(\mathrm{d}E_{ij})\,\mathrm{d}\overset{0}{V} = \int_{\overset{0}{V}} F_{\omega i}\rho_0 \delta(\mathrm{d}u_i)\,\mathrm{d}\overset{0}{V} + \int_{\overset{0}{A}} (T_{\omega i}^{t} + \mathrm{d}T_{\omega i})\delta(\mathrm{d}u_i)\,\mathrm{d}\overset{0}{A} \tag{8.103}$$

where the variation $\delta(\mathrm{d}E_{ij})$ of the Lagrangian strain increment in Eq. (8.98) can be expressed by:

$$\delta(\mathrm{d}E_{ij}) = \delta(\mathrm{d}e_{ij}) + \delta(\mathrm{d}\eta_{ij}) \tag{8.104}$$

in which $\delta(\mathrm{d}E_{ij})$ can be decomposed into the linear and nonlinear parts corresponding to the displacement increments, that is:

$$\delta(\mathrm{d}e_{ij}) = \tfrac{1}{2}\left[\delta(\mathrm{d}u_{i,j}) + \delta(\mathrm{d}u_{j,i}) + \delta(\mathrm{d}u_{k,j})u_{k,i}^{t} + u_{k,j}^{t}\delta(\mathrm{d}u_{k,i})\right] \tag{8.105a}$$

$$\delta(\mathrm{d}\eta_{ij}) = \tfrac{1}{2}\left[\delta(\mathrm{d}u_{k,i})\,\mathrm{d}u_{k,j} + \mathrm{d}u_{k,i}\delta(\mathrm{d}u_{k,j})\right] \tag{8.105b}$$

Substitution of Eqs. (8.101) and (8.104) into Eq. (8.103) and neglecting the higher-order terms lead to:

$$\int_{\overset{0}{V}} (S_{ij}^{t} + \mathrm{d}S_{ij})\left[\delta(\mathrm{d}e_{ij}) + \delta(\mathrm{d}\eta_{ij})\right]\mathrm{d}\overset{0}{V}$$

$$= \int_{\overset{0}{V}} (S_{ij}^{t} + C_{ijkl}^{*}\,\mathrm{d}E_{kl})\left[\delta(\mathrm{d}e_{ij}) + \delta(\mathrm{d}\eta_{ij})\right]\mathrm{d}\overset{0}{V}$$

$$= \int_{\overset{0}{V}} \left[S_{ij}^{t} + C_{ijkl}^{*}(\mathrm{d}e_{kl} + \mathrm{d}\eta_{kl})\right]\left[\delta(\mathrm{d}e_{ij}) + \delta(\mathrm{d}\eta_{ij})\right]\mathrm{d}\overset{0}{V}$$

$$\cong \int_{\overset{0}{V}} S_{ij}^{t}\left[\delta(\mathrm{d}e_{ij}) + \delta(\mathrm{d}\eta_{ij})\right]\mathrm{d}\overset{0}{V} + \int_{\overset{0}{V}} C_{ijkl}^{*}\,\mathrm{d}e_{kl}\delta(\mathrm{d}e_{ij})\,\mathrm{d}\overset{0}{V} = R^{t+\mathrm{d}t} \tag{8.106}$$

Bathe et al. (1975), Bathe (1982) and Gadala et al. (1984) presented further discussions on the development of the equilibrium equations for total Lagrangian formulations.

8.5.2 Updated Lagrangian description in general

Options exist for writing the equilibrium equations with respect to any of the previously determined equilibrium configurations. In practice, it is convenient to refer to either the initial or the most recent equilibrium configuration, the latter choice results in what is commonly referred to as the updated Lagrangian formulation.

Strain increments

Following the similar procedure as that described previously in the total Lagrangian formulation, Gadala et al. (1984) defined the Lagrangian strain increments for use in the *updated Lagrangian formulation* as:

$$\mathrm{d}E_{ij}^{\mathrm{a}} = \tfrac{1}{2}\left(\mathrm{d}u_{i,j} + \mathrm{d}u_{j,i} + \mathrm{d}u_{k,j}u_{k,i}^{t} + u_{k,j}^{t}\,\mathrm{d}u_{k,i}\right) \tag{8.107}$$

The differentiation is performed with respect to the current coordinates x_i in the configuration at time t and the products of incremental displacement terms have been neglected in Eq. (8.107).

Bathe (1982) and Davidson and Chen (1977) have used the following Lagrangian strain increments:

$$\mathrm{d}E_{ij}^{\mathrm{b}} = \tfrac{1}{2}\left(\mathrm{d}u_{i,j} + \mathrm{d}u_{j,i} + \mathrm{d}u_{k,i}\,\mathrm{d}u_{k,j}\right) \tag{8.108a}$$

or

$$\mathrm{d}E_{ij}^{\mathrm{b}} = \mathrm{d}\epsilon_{ij} + \mathrm{d}\eta_{ij} \tag{8.108b}$$

where $\mathrm{d}\epsilon_{ij}$ and $\mathrm{d}\eta_{ij}$ represent the linear and nonlinear components in Eq. (8.108a), respectively, and the differentiation is with respect to the current coordinates x_i in the configuration at time t.

Stress increments

Herein, we shall discuss the stress rates associated with the updated Lagrangian solution methods. The updated Lagrangian formulation provides a choice of several stress rates (Bazant, 1971), i.e., the Jaumann stress rate $\dot{\sigma}_{ij}^{\mathrm{J}}$ is the most widely used. As explained in Section 8.4.2, the Jaumann stress rate is related to the Eulerian stress rate in the manner:

$$\dot{\sigma}_{ij}^{\mathrm{J}} = \dot{\sigma}_{ij} - \sigma_{ik}^{t}W_{jk} - \sigma_{jk}^{t}W_{ik} \tag{8.109}$$

where $\dot{\sigma}_{ij}$ is the Eulerian stress rate, and W_{ij} is the spin tensor. For a finite motion, Eq. (8.109) becomes:

$$\mathrm{d}\sigma_{ij}^{\mathrm{J}} = \mathrm{d}\sigma_{ij} - \sigma_{ik}^{t}\,\mathrm{d}\Omega_{jk} - \sigma_{jk}^{t}\,\mathrm{d}\Omega_{ik} \tag{8.110}$$

where

$$d\Omega_{ij} = \tfrac{1}{2}(du_{i,j} - du_{j,i}) \tag{8.111}$$

The relationship between the increments of deformation tensor $d\epsilon_{kl}$ and the Jaumann stress increments $d\sigma^{J}_{ij}$ is commonly assumed to be:

$$d\sigma^{J}_{ij} = C_{ijkl}\, d\epsilon_{kl} \tag{8.112}$$

where C_{ijkl} may be taken the same as that for small strain analyses.

The following comments on the Jaumann stress rate are described according to the recent research. Bazant (1971) has reported that the Jaumann stress rate has no conjugate strain rate unless the material is incompressible. Several authors (Lee et al., 1983; Dafalias, 1983; Johnson and Bammann, 1984) have discussed stress oscillations which may occur when the Jaumann stress rate is combined with kinematically hardening materials.

Similar to the total Lagrangian formulation, the updated Lagrangian formulation makes use of the incremental decomposition of the stresses in the form:

$$S^{t+dt}_{ij} = S^{t}_{ij} + dS_{ij} = \sigma^{t}_{ij} + dS_{ij} \tag{8.113}$$

where the second Piola-Kirchhoff stresses S^{t}_{ij} at time t are identical to the Eulerian stresses σ^{t}_{ij}, and the second Piola-Kirchhoff stress increments dS_{ij} become the Truesdell stress increments $d\sigma^{T}_{ij}$ expressed by Eq. (8.83), that is:

$$\begin{aligned} dS_{ij} &= d\sigma^{J}_{ij} + d\epsilon_{kk}\sigma^{t}_{ij} - d\epsilon_{jk}\sigma^{t}_{ik} - d\epsilon_{ik}\sigma^{t}_{jk} \\ &= C_{ijkl}\, d\epsilon_{kl} + d\epsilon_{kk}\sigma^{t}_{ij} - d\epsilon_{jk}\sigma^{t}_{ik} - d\epsilon_{ik}\sigma^{t}_{jk} \\ &= C^{*}_{ijkl}\, dE_{kl} \end{aligned} \tag{8.114}$$

where C^{*}_{ijkl} is an elastic-plastic response function which will be explained in the following Section.

The second Piola-Kirchhoff stresses S^{t+dt}_{ij} which are measured with respect to the configuration at time t must be transformed in a manner similar to Eq. (8.99b) to obtain the true Eulerian stresses σ^{t+dt}_{ij} at time $(t + dt)$. Alternatively, using Eq. (8.110) for $d\sigma_{ij}$, the resultant stresses σ^{t+dt}_{ij} may be written as:

$$\sigma^{t+dt}_{ij} = \sigma^{t}_{ij} + d\sigma^{J}_{ij} + \sigma^{t}_{ik}\, d\Omega_{jk} + \sigma^{t}_{jk}\, d\Omega_{ik} \tag{8.115}$$

The updated Lagrangian formulation is essentially equivalent to the total Lagrangian solution with the reference configuration being the deformed body at time t. Washizu (1982) has outlined such a formulation.

Virtual work equation

The variables used in the incremental description of the updated Lagrangian formulation are listed below:

Variables in the updated Lagrangian formulation

	State at time t	State at time $t + \mathrm{d}t$
Kirchhoff stress	σ_{ij}^t	$\sigma_{ij}^t + \mathrm{d}S_{ij}$
Lagrangian strain	E_{ij}^t	$E_{ij}^t + \mathrm{d}E_{ij}$
Displacement	u_i^t	$u_i^t + \mathrm{d}u_i$
Body force/mass	F_{oi}	F_{oi}
Surface traction	T_{oi}^t	$T_{oi}^t + \mathrm{d}T_{oi}$

We can relate the equilibrium requirement at time $(t + \mathrm{d}t)$ to the current configuration at time t, that is:

$$\int_{V^t} \left(\sigma_{ij}^t + \mathrm{d}S_{ij}\right)\delta\left(E_{ij}^t + \mathrm{d}E_{ij}\right)\,\mathrm{d}V^t$$

$$= R^{t+\mathrm{d}t} = \int_{V^t} F_{oi}\rho_o\delta\left(u_i^t + \mathrm{d}u_i\right)\,\mathrm{d}V^t + \int_{A^t}\left(T_{oi}^t + \mathrm{d}T_{oi}\right)\delta\left(u_i^t + \mathrm{d}u_i\right)\,\mathrm{d}A^t \qquad (8.116)$$

Equation (8.116) represents the incremental equation of equilibrium at time t. It is at this point that assumptions regarding the descriptions of the stress and strain increments introduce differences in the final forms of the incremental equilibrium equations. For instance, Gadala et al. (1984) who used an incremental strain of the form of Eq. (8.107) derived a system of equilibrium equations which produce three contributions to the incremental stiffness. This stiffness consists of terms representing the normal *small-displacement stiffness*, the *geometric* or *initial stress stiffness*, and the *initial displacement stiffness*. On the other hand, using the incremental strain defined in Eq. (8.108), Bathe (1982) developed an incremental stiffness consisting of only the small-displacement and initial stress components (see the element stiffness matrices $[k_{\mathrm{L}}]$ and $[k_{\mathrm{NL}}]$, Section 9.3.2 in Chapter 9). Bathe's formulation is given below.

Using $\delta(E_{ij}^t + \mathrm{d}E_{ij}) = \delta(\mathrm{d}E_{ij})$ and $\delta(u_i^t + \mathrm{d}u_i) = \delta(\mathrm{d}u_i)$, we find:

$$\int_{V^t}\left(\sigma_{ij}^t + \mathrm{d}S_{ij}\right)\delta(\mathrm{d}E_{ij})\,\mathrm{d}V^t = \int_{V^t} F_{oi}\rho_o\delta(\mathrm{d}u_i)\,\mathrm{d}V^t + \int_{A^t}\left(T_{oi}^t + \mathrm{d}T_{oi}\right)\delta(\mathrm{d}u_i)\,\mathrm{d}A^t \qquad (8.117)$$

where the variation of the Lagrangian strain increment in Eq. (8.108), $\delta(\mathrm{d}E_{ij})$, can be expressed by:

$$\delta(\mathrm{d}E_{ij}) = \delta(\mathrm{d}\epsilon_{ij}) + \delta(\mathrm{d}\eta_{ij}) \qquad (8.118)$$

in which $\delta(\mathrm{d}E_{ij})$ can be decomposed into the linear and nonlinear parts corresponding to the displacement increments, that is:

$$\delta(\mathrm{d}\epsilon_{ij}) = \tfrac{1}{2}\left[\delta(\mathrm{d}u_{i,j}) + \delta(\mathrm{d}u_{j,i})\right] \tag{8.119a}$$

$$\delta(\mathrm{d}\eta_{ij}) = \tfrac{1}{2}\left[\delta(\mathrm{d}u_{k,i})\,\mathrm{d}u_{k,j} + \mathrm{d}u_{k,i}\delta(\mathrm{d}u_{k,j})\right] \tag{8.119b}$$

Substitution of Eq. (8.118) into Eq. (8.117) and neglecting the higher-order terms lead to:

$$\begin{aligned}
&\int_{V'}\left(\sigma'_{ij} + \mathrm{d}S_{ij}\right)\left[\delta(\mathrm{d}\epsilon_{ij}) + \delta(\mathrm{d}\eta_{ij})\right]\mathrm{d}V' \\
&\quad - \int_{V'}\left(\sigma'_{ij} + C^{*}_{ijkl}\,\mathrm{d}E_{kl}\right)\left[\delta(\mathrm{d}\epsilon_{ij}) + \delta(\mathrm{d}\eta_{ij})\right]\mathrm{d}V' \\
&\quad = \int_{V'}\left[\sigma'_{ij} + C^{*}_{ijkl}(\mathrm{d}\epsilon_{kl} + \mathrm{d}\eta_{kl})\right]\left[\delta(\mathrm{d}\epsilon_{ij}) + \delta(\mathrm{d}\eta_{ij})\right]\mathrm{d}V' \\
&\quad \simeq \int_{V'}\sigma'_{ij}\left[\delta(\mathrm{d}\epsilon_{ij}) + \delta(\mathrm{d}\eta_{ij})\right]\mathrm{d}V' + \int_{V'}C^{*}_{ijkl}\,\mathrm{d}\epsilon_{kl}\delta(\mathrm{d}\epsilon_{ij})\,\mathrm{d}V' \\
&\quad = R^{t+\mathrm{d}t}
\end{aligned} \tag{8.120}$$

Equation (8.120) then becomes:

$$\begin{aligned}
&\int_{V'}C^{*}_{ijkl}\,\mathrm{d}\epsilon_{kl}\delta(\mathrm{d}\epsilon_{ij})\,\mathrm{d}V' + \int_{V'}\sigma'_{ij}\delta(\mathrm{d}\eta_{ij})\,\mathrm{d}V' \\
&\quad = R^{t+\mathrm{d}t} - \int_{V'}\sigma'_{ij}\delta(\mathrm{d}\epsilon_{ij})\,\mathrm{d}V'
\end{aligned} \tag{8.121}$$

The first term of the left-hand side of Eq. (8.121) represents the normal small-displacement contribution to the stiffness and the second term results in the geometric or initial stress stiffness. Equation (8.121) may be written in a form convenient to finite-element coding (Bathe, 1982).

8.6 CONSTITUTIVE RELATIONS FOR LARGE-DEFORMATION FORMULATIONS

Several incremental constitutive relationships have been proposed corresponding to several large-displacement and large-deformation formulations. Among them, Hibbitt et al. (1970) presented a total Lagrangian formulation for finite-element problems involving large strains and large displacements. Further, Davidson and

Chen (1977) presented an updated Lagrangian formulation which resulted in nonsymmetric stiffness equations for large-strain conditions as will be formulated in details in Section 8.7. When specialized for small-strain conditions, the constitutive relation yields a symmetric set of equilibrium equations. Nagtegaal and De Jong (1981) presented an updated Lagrangian formulation which resulted in nonsymmetric equilibrium equations. However, if the material under consideration was approximately incompressible, a set of symmetric equilibrium equations could be obtained. Kiousis et al. (1986) showed a total Lagrangian formulation in which the extended von Mises plasticity model is expressed in terms of the variables in the reference configuration and corresponding constitutive relation is derived from the associated flow rule.

The difficulties in defining the appropriate constitutive relation for use in large-displacement and large-deformation analyses are attributed to the changing configuration of the body and the need for an appropriate objective stress rate. The use of an objective stress rate insures that the effects of rigid body rotation are correctly considered (Malvern, 1969; Desai and Phan, 1980). For instance, the Jaumann stress rate (Section 8.4.2) accounts for the rigid-body rotation through two terms which contain products of the existing stresses and the rate of rotation. The method is approximate and should be limited to use with sufficiently *small* incremental motions.

In the following Sections, the *elastic-plastic constitutive relations* used in the total and updated Lagrangian formulations are briefly reviewed and discussed.

8.6.1 Constitutive relation for total Lagrangian formulation

In this Section, we shall introduce and discuss an elastic-plastic constitutive relation in a total Lagrangian formulation as treated by Hibbitt et al. (1970).

Estimate of constitutive relation

In order to estimate the second Piola-Kirchhoff stress increment dS_{ij} from $C^*_{ijkl}\, dE_{kl}$ in Eq. (8.101), an appropriate constitutive response function C^*_{ijkl} must be evaluated. It should be noted that C^*_{ijkl} is not necessarily the same constitutive law as in a small strain case as that discussed in Chapters 4 through 6. Using the Jaumann stress increment $d\sigma^J_{ij}$ and the increment of deformation tensor $d\epsilon_{ij}$ which are invariant with respect to a rigid-body rotation, we have:

$$d\sigma^J_{ij} = C_{ijkl}\, d\epsilon_{kl} \tag{8.122}$$

where C_{ijkl} may be taken the same as that in the usual small-strain analysis and assumed to be known functions of current stress whereas the increment of deformation tensor $d\epsilon_{kl}$ can be expressed by:

$$d\epsilon_{kl} = \tfrac{1}{2}(du_{k,l} + du_{l,k}) \tag{8.123}$$

in which the subscript after the slash denotes the spatial derivative with respect to the coordinate system x_i. Recalling Eq. (8.79), the relationship between the second Piola-Kirchhoff stress increment dS_{ij} and the Truesdell stress increment $d\sigma^{\dagger}_{ij}$ can be rewritten as:

$$dS_{ij} = J \frac{\partial X_i}{\partial x_k} \frac{\partial X_j}{\partial x_l} d\sigma^{\dagger}_{kl} \tag{8.124a}$$

in which

$$d\sigma^{\dagger}_{kl} = d\sigma^{\dagger}_{kl} + d\epsilon_{mm}\sigma^{\dagger}_{kl} - d\epsilon_{lm}\sigma^{\dagger}_{km} - d\epsilon_{km}\sigma^{\dagger}_{lm}$$

$$= C_{klmn}\, d\epsilon_{mn} + d\epsilon_{mm}\sigma^{\dagger}_{kl} - d\epsilon_{lm}\sigma^{\dagger}_{km} - d\epsilon_{km}\sigma^{\dagger}_{lm} \tag{8.124b}$$

Since we have the relationship such as $d\epsilon_{mn} = (\partial X_r/\partial x_m)(\partial X_s/\partial x_n)\, dE_{rs}$ from Eq. (8.51), Eq. (8.124a) can be rearranged in a simple form as given by:

$$dS_{ij} = J \frac{\partial X_i}{\partial x_k} \frac{\partial X_j}{\partial x_l} \frac{\partial X_r}{\partial x_m} \left[C_{klmn} \frac{\partial X_s}{\partial x_n} + \sigma^{\dagger}_{kl} \frac{\partial X_s}{\partial x_m} - \sigma^{\dagger}_{km} \frac{\partial X_s}{\partial x_l} - \sigma^{\dagger}_{lm} \frac{\partial X_s}{\partial x_k} \right] dE_{rs} \tag{8.125}$$

The elastic-plastic constitutive tensor C^{*}_{ijrs} for a total Lagrangian formulation may thus be evaluated by:

$$C^{*}_{ijrs} = J \frac{\partial X_i}{\partial x_k} \frac{\partial X_j}{\partial x_l} \frac{\partial X_r}{\partial x_m} \left[C_{klmn} \frac{\partial X_s}{\partial x_n} + \sigma^{\dagger}_{kl} \frac{\partial X_s}{\partial x_m} - \sigma^{\dagger}_{km} \frac{\partial X_s}{\partial x_l} - \sigma^{\dagger}_{lm} \frac{\partial X_s}{\partial x_k} \right]$$

$$= J \frac{\partial X_i}{\partial x_k} \frac{\partial X_j}{\partial x_l} \frac{\partial X_r}{\partial x_m} \frac{\partial X_s}{\partial x_n} \left[C_{klmn} + \sigma^{\dagger}_{kl}\delta_{mn} - \tfrac{1}{2}\left(\sigma^{\dagger}_{km}\delta_{nl} + \sigma^{\dagger}_{kn}\delta_{ml} + \sigma^{\dagger}_{lm}\delta_{nk} + \sigma^{\dagger}_{ln}\delta_{mk} \right) \right] \tag{8.126}$$

On the other hand, Gadala et al. (1984), who presented a constitutive relation by using also the Jaumann stress rate, utilized a different expression for the second Piola-Kirchhoff stress increments dS_{ij} which may be written as:

$$dS_{ij} = J \frac{\partial X_i}{\partial x_k} \frac{\partial X_j}{\partial x_l} d\sigma_{kl} \tag{8.127}$$

where instead of the Truesdell stress increments $d\sigma^{\dagger}_{kl}$ in Eq. (8.83), the Eulerian

stress increments $\mathrm{d}\sigma_{kl}$ are employed. Substitution of Eqs. (8.74) and (8.112) into Eq. (8.127) yields:

$$\mathrm{d}S_{ij} = J\frac{\partial X_i}{\partial x_k}\frac{\partial X_j}{\partial x_l}\left(\mathrm{d}\sigma^{\mathrm{I}}_{kl} + \sigma^{\mathrm{I}}_{km}\,\mathrm{d}\Omega_{lm} + \sigma^{\mathrm{I}}_{lm}\,\mathrm{d}\Omega_{km}\right)$$

$$= J\frac{\partial X_i}{\partial x_k}\frac{\partial X_j}{\partial x_l}\left[C_{klmn}\,\mathrm{d}\epsilon_{mn} + \sigma^{\mathrm{I}}_{km}\,\mathrm{d}\Omega_{lm} + \sigma^{\mathrm{I}}_{lm}\,\mathrm{d}\Omega_{km}\right] \tag{8.128}$$

Details of this derivation can be found in the paper by Gadala et al. (1984).

Small-strain and large-rotation approximation

When the effect of a rigid body rotation on the motion of a material line element is greater than that of a pure deformation, $\partial X_i/\partial x_j$ may be written as (Hibbitt et al., 1970):

$$\frac{\partial X_i}{\partial x_j} = (\delta_{ik} + h_{ik})\,L_{kj} \tag{8.129a}$$

$$\left|\frac{\partial X_i}{\partial x_j}\right| = J^{-1} = 1 \tag{8.129b}$$

where $h_{ij} = h_{ji} \ll 1$ is related to a pure deformation and L_{kj} is an orthogonal rotation tensor. Thus, neglecting h_{ij} in comparison to unity, Eq. (8.126) may be expressed by:

$$C^{*}_{ijrs} = L_{ik}L_{jl}L_{rm}L_{sn}\left[C_{klmn} + \sigma^{\mathrm{I}}_{kl}\delta_{mn} - \tfrac{1}{2}\left(\sigma^{\mathrm{I}}_{km}\delta_{nl} + \sigma^{\mathrm{I}}_{kn}\delta_{ml} + \sigma^{\mathrm{I}}_{lm}\delta_{nk} + \sigma^{\mathrm{I}}_{ln}\delta_{mk}\right)\right] \tag{8.130}$$

Example 8.14: Herein, we shall present the constitutive relation of the extended von Mises (Drucker-Prager) plasticity model for a total Lagrangian formulation. The yield condition is first expressed in terms of the Eulerian stress tensor, and is then transformed into the reference coordinate system. The derivation of the elastic-plastic constitutive relation in incremental form will be described in what follows:

Assuming the total Lagrangian strain increments $\mathrm{d}E_{ij}$ are decomposed into elastic incremental components, $\mathrm{d}E^{\mathrm{e}}_{ij}$, and plastic incremental components, $\mathrm{d}E^{\mathrm{p}}_{ij}$, respectively, we write:

$$\mathrm{d}E_{ij} = \mathrm{d}E^{\mathrm{e}}_{ij} + \mathrm{d}E^{\mathrm{p}}_{ij} \tag{8.131}$$

The elastic Lagrangian strain increments $\mathrm{d}E^{\mathrm{e}}_{ij}$ are postulated to be a linear function of the second Piola-Kirchhoff stress increments such as:

$$dS_{ij} = D_{ijkl}\,\mathrm{d}E^{\mathrm{e}}_{kl} \tag{8.132}$$

in which D_{ijkl} is an elastic response function. The yield function of the Drucker-Prager model in Chapter 4 may be expressed in terms of the Eulerian stress tensor σ_{ij} and deviatoric components of the Eulerian stress tensor, s_{ij}:

$$F = \left(\tfrac{1}{2} s_{ij} s_{ij}\right)^{1/2} + \alpha \sigma_{ii} - k(W_p) = 0 \tag{8.133}$$

where $k(W_p)$ is a function of the plastic work W_p whose increment is $dW_p = \sigma_{ij}\, d\epsilon_{ij}^p$ in the spatial description or $dW_p = (1/J) S_{ij}\, dE_{ij}^p$ in the reference description, and α is material constant. The yield function F can be written in the reference frame as:

$$F = \left(\frac{1}{2} \left[\frac{1}{J} \frac{\partial x_i}{\partial X_k} \frac{\partial x_j}{\partial X_l} S_{kl} \frac{1}{J} \frac{\partial x_i}{\partial X_m} \frac{\partial x_j}{\partial X_n} S_{mn} \right] - \frac{1}{6} \left[\frac{1}{J} \frac{\partial x_i}{\partial X_k} \frac{\partial x_i}{\partial X_l} S_{kl} \frac{1}{J} \frac{\partial x_j}{\partial X_m} \frac{\partial x_j}{\partial X_n} S_{mn} \right] \right)^{1/2}$$

$$+ \alpha \frac{1}{J} \frac{\partial x_i}{\partial X_k} \frac{\partial x_i}{\partial X_l} S_{kl} - k = 0 \tag{8.134}$$

Equation (8.134) may be expressed in a simpler form, that is:

$$F = \left(\tfrac{1}{2} \left[J^{-2} S_{kl} S_{mn} C_{km} C_{ln} \right] - \tfrac{1}{6} \left[J^{-2} S_{kl} S_{mn} C_{kl} C_{mn} \right] \right)^{1/2} + \alpha J^{-1} S_{kl} C_{kl} - k = 0 \tag{8.135}$$

where

$$C_{kl} = \frac{\partial x_i}{\partial X_k} \frac{\partial x_i}{\partial X_l} \tag{8.136}$$

Considering the transformation of the flow rule in the spatial description to that in the material description, we obtain:

$$d\epsilon_{ij}^p = d\lambda \left(\frac{\partial F}{\partial \sigma_{ij}} \right) = d\lambda \left(\frac{\partial F}{\partial S_{kl}} \right) \left(\frac{\partial S_{kl}}{\partial \sigma_{ij}} \right)$$

$$= d\lambda \left(\frac{\partial F}{\partial S_{kl}} \right) J \left(\frac{\partial X_k}{\partial x_i} \right) \left(\frac{\partial X_l}{\partial x_j} \right)$$

Thus, we find:

$$dE_{ij}^p = d\bar{\lambda} \left(\frac{\partial F}{\partial S_{ij}} \right) \tag{8.137}$$

where the proportionality factor $d\bar{\lambda}$ in the material description can be written as:

$$d\bar{\lambda} = J\, d\lambda \tag{8.138}$$

Substitution of Eqs. (8.131) and (8.137) into Eq. (8.132) leads to:

$$dS_{ij} = D_{ijkl}\left(dE_{kl} - d\bar{\lambda}\frac{\partial F}{\partial S_{kl}}\right) \tag{8.139}$$

and

$$\frac{\partial F}{\partial S_{ij}}\, dS_{ij} = D_{ijkl}\left(dE_{kl} - d\bar{\lambda}\frac{\partial F}{\partial S_{kl}}\right)\frac{\partial F}{\partial S_{ij}} \tag{8.140}$$

From the *consistency condition* $dF = 0$ and Eq. (8.140), we obtain:

$$\begin{aligned}
&\frac{\partial F}{\partial S_{ij}}\, dS_{ij} + \frac{\partial F}{\partial E_{ij}}\, dE_{ij} + \frac{\partial F}{\partial J}\, dJ + \frac{\partial F}{\partial k}\, dk \\
&= D_{ijkl}\left(dE_{kl} - d\bar{\lambda}\frac{\partial F}{\partial S_{kl}}\right)\frac{\partial F}{\partial S_{ij}} + \frac{\partial F}{\partial E_{ij}}\, dE_{ij} + \frac{\partial F}{\partial J}\, dJ + \frac{\partial F}{\partial k}\frac{dk}{dW_p}\frac{1}{J}S_{ij}\, d\bar{\lambda}\frac{\partial F}{\partial S_{ij}} \\
&= 0
\end{aligned} \tag{8.141}$$

Solving $d\bar{\lambda}$ from Eq. (8.141) and substituting $d\bar{\lambda}$ so obtained in Eq. (8.139), we obtain the incremental stress strain relationship:

$$dS_{ij} = D_{ijkl}\left[dE_{kl} - \frac{D_{qrst}\frac{\partial F}{\partial S_{qr}}\, dE_{st} + \frac{\partial F}{\partial E_{qr}}\, dE_{qr} + \frac{\partial F}{\partial J}\, dJ}{D_{mnop}\frac{\partial F}{\partial S_{mn}}\frac{\partial F}{\partial S_{op}} - \frac{\partial F}{\partial k}\frac{dk}{dW_p}S_{mn}J^{-1}\frac{\partial F}{\partial S_{mn}}}\frac{\partial F}{\partial S_{kl}}\right] \tag{8.142}$$

To express Eq. (8.142) in the form of $dS_{ij} = C^{*}_{ijkl}\, dE_{kl}$, the following expression for J in terms of the Lagrangian strain invariants is used:

$$J = (1 + 2I_L + 4II_L + 8III_L)^{1/2} \tag{8.143}$$

where

$$I_L = E_{ii}$$

$$II_L = \tfrac{1}{2}(E_{ii}E_{jj} - E_{ij}E_{ij})$$

$$III_L = \tfrac{1}{6}(2E_{ij}E_{jk}E_{ki} - 3E_{ij}E_{ij}E_{kk} + E_{ii}E_{jj}E_{kk})$$

Thus, the constitutive response function C^{*}_{ijkl} can be written as:

$$C^{*}_{ijkl} = D_{ijmn}\left[\delta_{km}\delta_{ln} - \frac{D_{stkl}\dfrac{\partial F}{\partial S_{st}}\dfrac{\partial F}{\partial S_{mn}} + \dfrac{\partial F}{\partial E_{kl}}\dfrac{\partial F}{\partial S_{mn}} + \dfrac{\partial F}{\partial J}\dfrac{\partial F}{\partial S_{mn}}R_{kl}}{D_{opqr}\dfrac{\partial F}{\partial S_{op}}\dfrac{\partial F}{\partial S_{qr}} - \dfrac{\partial F}{\partial k}\dfrac{\mathrm{d}k}{\mathrm{d}W_{\mathrm{p}}}S_{op}J^{-1}\dfrac{\partial F}{\partial S_{op}}}\right] \tag{8.144}$$

where

$$R_{kl} = \frac{1}{2J}\left[2\delta_{kl} + 4\delta_{kl}E_{mm} - 4E_{kl} + 8E_{lm}E_{mk} - 8E_{kl}E_{mm} - 4\delta_{kl}E_{mn}E_{mn} + 4\delta_{kl}E_{mm}E_{nn}\right] \tag{8.145}$$

8.6.2 Constitutive relation for updated Lagrangian formulation

The difference between the total and the updated Lagrangian formulations lies in the choice of different reference configurations for the kinematic and static variables. Therefore, the elastic-plastic constitutive tensor C^{*}_{ijkl} for an updated Lagrangian formulation may be obtained by simply eliminating J and $\partial X_i/\partial x_j$ in Eq. (8.126). Subsequently, this is utilized in the virtual work equations, in order to evaluate the second Piola-Kirchhoff stress increments $\mathrm{d}S_{ij}$.

Gadala et al. (1984) used the Eulerian stress increments $\mathrm{d}\sigma_{ij}$ as the second Piola-Kirchhoff stress increments $\mathrm{d}S_{ij}$. This idea together with Eqs. (8.74) and (8.122) leads to:

$$\begin{aligned}\mathrm{d}S_{ij} = \mathrm{d}\sigma_{ij} &= \mathrm{d}\sigma^{\mathrm{J}}_{ij} + \sigma^{t}_{ik}\,\mathrm{d}\Omega_{jk} + \sigma^{t}_{jk}\,\mathrm{d}\Omega_{ik} \\ &= C_{ijkl}\,\mathrm{d}\epsilon_{kl} + \sigma^{t}_{ik}\,\mathrm{d}\Omega_{jk} + \sigma^{t}_{jk}\,\mathrm{d}\Omega_{ik}\end{aligned} \tag{8.146}$$

The introduction of the last two terms in Eq. (8.146) requires an additional term to be included in the virtual work equation (Gadala et al., 1984). Thus, the virtual work equation (8.121) then becomes:

$$\begin{aligned}&\int_{V^t}\left(C_{ijkl}\,\mathrm{d}\epsilon_{kl} + \sigma^{t}_{ik}\,\mathrm{d}\Omega_{jk} + \sigma^{t}_{jk}\,\mathrm{d}\Omega_{ik}\right)\delta(\mathrm{d}\epsilon_{ij})\mathrm{d}V^t + \int_{V^t}\sigma^{t}_{ij}\delta(\mathrm{d}\eta_{ij})\,\mathrm{d}V^t \\ &\quad = R^{t+\mathrm{d}t} - \int_{V^t}\sigma^{t}_{ij}\delta(\mathrm{d}\epsilon_{ij})\mathrm{d}V^t\end{aligned} \tag{8.147}$$

It may be seen that the inclusion of the rotation terms in Eq. (8.147) results in a set of nonsymmetric equilibrium equations. On the other hand, instead of the second Piola-Kirchhoff stress increments $\mathrm{d}S_{ij}$, Bathe (1982) and Malvern (1969)

proposed to use the Jaumann stress increments $d\sigma_{ij}^{J}$ in Eq. (8.112) which may be incorporated directly as dS_{ij} into the virtual work equation, thus eliminating the nonsymmetrical stiffness. Similar assumptions have been incorporated by Davidson and Chen (1977) into the updated Lagrangian formulation. The details of this development will be presented in the next Section.

Clearly, different forms of the virtual work will be obtained for different choices of stress rates, assumptions regarding the nature of material deformation (compressible or incompressible), and the magnitude of the incremental strains. The choice of stress and strain rates is not completely arbitrary. The pair should be conjugate, thus insuring that the virtual work equation is appropriately stated (Bazant, 1971).

8.7 UPDATED LAGRANGIAN FORMULATION AND SIMPLIFICATION

The purpose of this Section is to develop the governing differential equations for finite-element analysis (large strain and large rotation, or small strain and large rotation) by introducing the stress-strain relations that reflect the material nonlinearity into the equilibrium equations that reflect the change in geometry of the overall soil masses.

Herein, a set of equilibrium equations (in virtual work form) is formulated in the updated Lagrangian description for a small increment of deformation superimposed on a currently deformed and stressed body (initial configuration).

To formulate the incremental equilibrium equations in continuum mechanics, as already mentioned in the preceding Section, either the *Eulerian formulation* or the *Lagrangian formulation* can be generally utilized. Briefly, in a Lagrangian formulation all quantities (i.e., stress and strain) are referred to the coordinates X_i associated with some reference configuration, for example, the initially undeformed configuration of the body. In an Eulerian formulation, on the other hand, all quantities are referred to the coordinate x_i associated with the currently deforming configuration of the body. The incremental equilibrium equations in this Section will be derived using the *mixed incremental formulation* or *updated Lagrangian incremental formulation* (Davidson and Chen, 1974). Both total Lagrangian and mixed incremental formulations employ a known material reference state. However, the difference between these two incremental formulations is the reference state utilized in each formulation. The reference state for the total Lagrangian incremental formulation is the same for all increments and is usually the undeformed, unstressed state of the body.

On the other hand, the reference state for the mixed incremental formulation (updated Lagrangian incremental formulation) is the currently updated configuration of the body, i.e., the current Eulerian coordinates of the body, and this reference state is updated at each incremental step. In the following Section, the mixed incremental formulation by Davidson and Chen (1974) will be utilized to formulate the incremental equilibrium equations.

8.7.1 *Mixed incremental formulation*

In this Section, two different configurations of the body: the *initial* (or *current*) configuration and the *subsequent* configuration, are used to formulate the incremental equilibrium equations governing an increment of deformation. The stresses, strains, and displacements in the initial configuration are assumed to be known and have been determined through a sequence of incremental steps.

Because the updated Lagrangian incremental formulation is employed here, the equilibrium equations for the subsequent configuration are written in terms of the geometry of the initial configuration. Note that the *initial* stresses are referred to a global reference frame, and that the *initial* geometry is a currently deformed geometry determined through a sequence of previous increments.

Before going into the incremental formulation, it might be helpful to summarize again some of the terminology about *stresses* and *strains* which are used in the context of large rotations and deformations.

Stress tensors

Three different stress tensors are defined here:

σ_{ij} Initial Cartesian stress tensor referred to a global reference frame. This is physical stress representing force per unit of area of the initial geometry. This tensor is called Eulerian stress tensor in engineering mechanics literature. In addition, $\bar{\sigma}_{ij}$ is the Eulerian stress tensor in the subsequent configuration.

τ_{ij} A Cartesian stress tensor referred to a locally rotated Cartesian frame in the subsequent configuration where the frame varies from point to point. This is physical stress, that is, force per unit of area of the subsequent geometry.

S_{ij} The second Piola-Kirchhoff stress tensor. This stress tensor describes the stress state in the subsequent configuration as referred to the geometry of the initial configuration. This is not physical stress as defined above. The relationship between the second Piola-Kirchhoff stress tensor S_{ij} and Cartesian stress tensor $\bar{\sigma}_{ij}$ can be defined from Eq. (8.63) in Section 8.4.

Strain increments

Two different strain increments are introduced. Increments of Lagrangian strain tensor are defined as:

$$\mathrm{d}E_{ij} = \tfrac{1}{2}(\mathrm{d}u_{i,j} + \mathrm{d}u_{j,i} + \mathrm{d}u_{k,i}\,\mathrm{d}u_{k,j}) \tag{8.148}$$

and the infinitesimal strain increment tensor is defined as:

$$\mathrm{d}\epsilon_{ij} = \tfrac{1}{2}(\mathrm{d}u_{i,j} + \mathrm{d}u_{j,i}) \tag{8.149}$$

where $\mathrm{d}u_i$ is the increment of displacement vector from the initial (current) state to

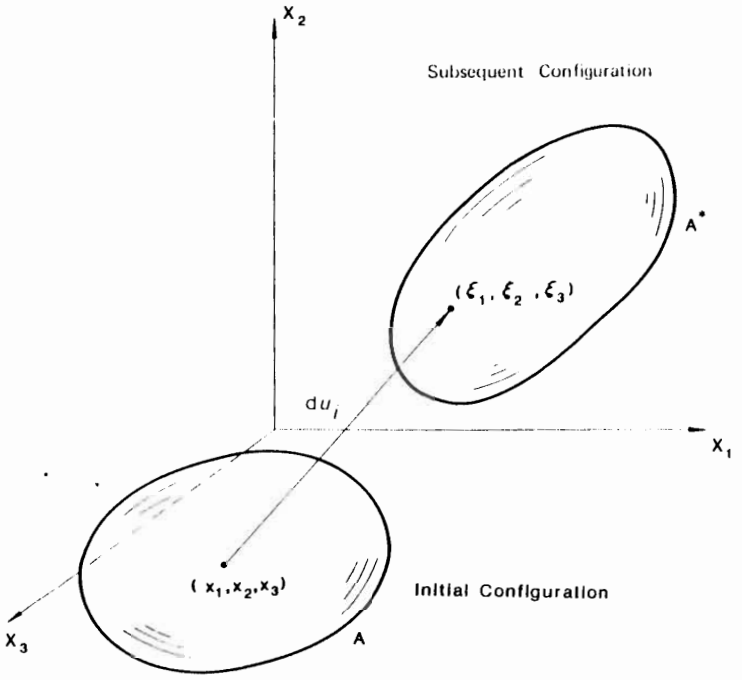

Fig. 8.16. Initial and subsequent configurations.

the subsequent state, and the comma followed by a subscript indicates a partial derivative with respect to the initial (current) material coordinates x_i.

Virtual work equation

Let us consider now a body situated in a fixed Cartesian reference frame (X_1, X_2, X_3) as shown in Fig. 8.16 where "A" denotes the boundary surface of the body in its initial configuration and "A*" denotes the boundary surface in the subsequent configuration. Let (x_1, x_2, x_3) be the initial Cartesian coordinates of an arbitrary point in the body, and let (ξ_1, ξ_2, ξ_3) be the Cartesian coordinates of the same material point after an increment of deformation. Subsequent Cartesian coordinates ξ_i can be written as:

$$\xi_i = x_i + \mathrm{d}u_i \tag{8.150}$$

We shall consider the equilibrium conditions of the initial state and the subsequent state by using the virtual work equation. Firstly, the equilibrium equation of the body at the initial state is expressed by:

$$\int_A T_i \delta(\mathrm{d}u_i)\,\mathrm{d}A + \int_V \rho_0 F_i(x_j)\delta(\mathrm{d}u_i)\,\mathrm{d}V = \int_V \sigma_{ij}\delta(\mathrm{d}\epsilon_{ij})\,\mathrm{d}V \tag{8.151}$$

where T_i is the boundary traction vector per unit of initial area, and $F_i(x_j)$ is the body force vector per unit mass and ρ_0 is the mass density of the initial state. It is assumed that the body force is purely a function of position in the fixed reference frame. The virtual strain increment field $\delta(\mathrm{d}\epsilon_{ij})$ is expressed in terms of the virtual displacement increment field $\delta(\mathrm{d}u_i)$, as seen in Eq. (8.149). Thus:

$$\delta(\mathrm{d}\epsilon_{ij}) = \frac{1}{2}\left[\delta(\mathrm{d}u_i)_{,j} + \delta(\mathrm{d}u_j)_{,i}\right] \tag{8.152}$$

where $\delta(\mathrm{d}u_i)_{,j}$ is the partial derivative of $\delta(\mathrm{d}u_i)$ with respect to the initial Cartesian coordinate x_j, namely:

$$\delta(\mathrm{d}u_i)_{,j} = \frac{\partial\{\delta(\mathrm{d}u_i)\}}{\partial x_j} \tag{8.153}$$

Secondly, we shall consider the equilibrium of the body in the subsequent configuration. Recall that the equation of equilibrium for the subsequent configuration is to be written in terms of the geometry of the initial configuration. Note that the internal virtual work per unit of initial volume is the product of the second Piola-Kirchhoff stress tensor and the variation of increments of Lagrangian strain tensor, that is:

$$\delta W_i = \int_V S_{ij}\delta(\mathrm{d}E_{ij})\,\mathrm{d}V \tag{8.154}$$

where the second Piola-Kirchhoff stress tensor in the subsequent configuration is defined as:

$$S_{ij} = \frac{\rho_0}{\rho}\frac{\partial x_i}{\partial \xi_k}\frac{\partial x_j}{\partial \xi_l}\bar{\sigma}_{kl} \tag{8.155}$$

where ρ_0 and ρ are the mass densities in the current and subsequent configurations respectively, and $\bar{\sigma}_{kl}$ is the Eulerian stress tensor in the subsequent configuration.

The equilibrium of the subsequent configuration is then implied by the virtual work equation:

$$\int_A (T_i + \mathrm{d}T_i)\delta(\mathrm{d}u_i)\,\mathrm{d}A + \int_V \rho_0\{F_i(x_j) + \mathrm{d}F_i\}\delta(\mathrm{d}u_i)\,\mathrm{d}V = \int_V S_{ij}\delta(\mathrm{d}E_{ij})\,\mathrm{d}V \tag{8.156}$$

where $\mathrm{d}T_i$ is the increment of surface traction vector per unit of initial area and $\mathrm{d}F_i$ is the increment of body force vector per unit mass of initial configuration.

After an increment of deformation, the second Piola-Kirchhoff stress in the subsequent configuration S_{ij} may be expressed by:

$$S_{ij} = \sigma_{ij} + \mathrm{d}S_{ij} \tag{8.157}$$

where dS_{ij} are the increments of the second Piola-Kirchhoff stress tensor. Using Eq. (8.148), the variation of increments of Lagrangian strain tensor, $\delta(dE_{ij})$, can be given by:

$$\delta(dE_{ij}) = \delta(d\epsilon_{ij}) + \tfrac{1}{2}\left\{du_{k,i}\delta(du_k)_{,j} + du_{k,j}\delta(du_k)_{,i}\right\} \tag{8.158}$$

Substituting Eqs. (8.157) and (8.158) into Eq. (8.156), we obtain:

$$\begin{aligned}
&\int_A dT_i\delta(du_i)\,dA + \int_V \rho_0\, dF_i\delta(du_i)\,dV \\
&+ \left\{\int_A T_i\delta(du_i)\,dA + \int_V \rho_0 F_i(x_j)\delta(du_i)\,dV - \int_V \sigma_{ij}\delta(d\epsilon_{ij})\,dV\right\} \\
&- \int_V \tfrac{1}{2}\sigma_{ij}\left\{du_{k,i}\delta(du_k)_{,j} + du_{k,j}\delta(du_k)_{,i}\right\}dV + \int_V dS_{ij}\delta(dE_{ij})\,dV
\end{aligned} \tag{8.159}$$

It should be noted that the expression in brackets { } on the left-hand side of Eq. (8.159) would be identically zero if the initial stress distributions satisfied the equation of equilibrium in Eq. (8.151). Realizing however that these stresses have been determined through a sequence of approximate calculations, we retain the expression in brackets as an *equilibrium correction term* (Hofmeister et al., 1971). If the incremental stress and displacement distribution satisfying Eq. (8.159) could be found for all kinematically admissible virtual displacement increments, the subsequent configuration would be in an equilibrium state.

8.7.2 Linearized incremental equation (large strain and large rotation)

Equation (8.159) represents the exact condition of equilibrium for the subsequent configuration. In this Section, Eq. (8.159) will be linearized under the conditions of large strain and large rotation without making any assumptions concerning the relative magnitudes of strains and rotations. The following two points should be noted firstly for this development:

1. In the context of small displacements, the elastic-plastic constitutive equation discussed in Chapters 4 to 6 relates the physical Cartesian stress increment to the infinitesimal strain increment, and
2. In the context of large strain and large rotation, care must be taken to relate the proper stress increment to the proper strain increment.

Consider the Eulerian stress tensor σ_{ij} for a three-dimensional body as shown in Fig. 8.17. During an increment of deformation, the neighborhood of a generic point translates, rotates and deforms. The rotation increment to the first order is defined by:

$$d\Omega_{ij} \quad \frac{1}{2}\left[\frac{\partial(du_i)}{\partial x_j} - \frac{\partial(du_j)}{\partial x_i}\right] \tag{8.160}$$

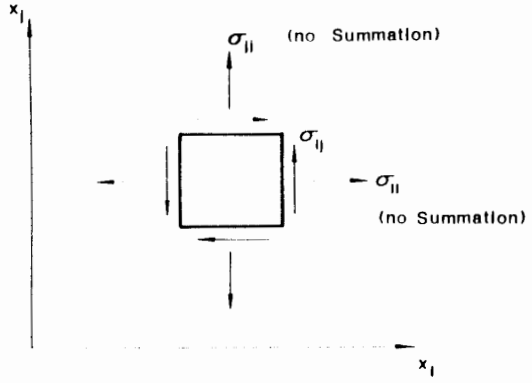

Fig. 8.17. Stress state in initial configuration.

Physical stresses τ_{ij} in the subsequent configuration, referred to a local coordinate system rotated by an amount $d\Omega_{ij}$ from the fixed reference frame, are sketched in Fig. 8.18. The relation between τ_{ij} and σ_{ij} is written as:

$$\tau_{ij} = \sigma_{ij} + d\tau_{ij} \tag{8.161}$$

where $d\tau_{ij}$ is the incremental Cartesian stress tensor for the subsequent configuration referred to a local coordinate. Note that $d\tau_{ij}$ is identical to the Jaumann stress increment, $d\sigma_{ij}^{J}$ discussed previously. $d\tau_{ij}$ is obtained from the following general form (Davidson and Chen, 1974):

$$d\tau_{ij} = C_{ijkl}^{ep}\, d\epsilon_{kl} \tag{8.162}$$

where C_{ijkl}^{ep} is the elastic-plastic constitutive tensor defined by the usual small strain assumption.

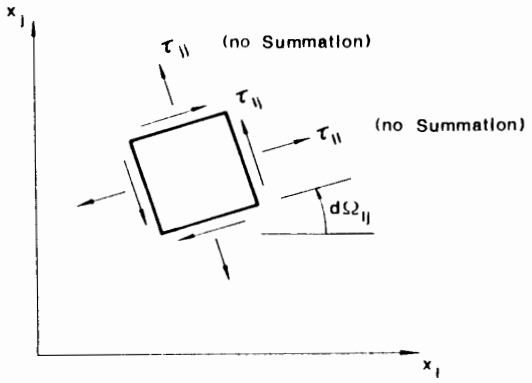

Fig. 8.18. Stress state in subsequent configuration.

It is necessary to express the increments of the second Piola-Kirchhoff stress dS_{ij} in Eq. (8.159) in terms of $d\tau_{ij}$, σ_{ij} and $d\epsilon_{ij}$ so that Eq. (8.159) can be linearized to the equation for large strain and large rotation. The second Piola-Kirchhoff stress increment dS_{ij} related to the Jaumann stress increment $d\tau_{ij}$ to the first order is generally written as:

$$dS_{ij} = d\tau_{ij} + \psi_{ijkl}\, d\epsilon_{kl} \tag{8.163}$$

where ψ_{ijkl} is in general expressed in terms of the current stress components, σ_{ij}.

Substituting the general form of Eq. (8.163) into Eq. (8.159) and rearranging some terms lead to the following incremental equilibrium equation:

$$\int_A (T_i + dT_i)\delta(du_i)\, dA + \int_V \rho_0 \{F_i(x_j) + dF_i\}\delta(du_i)\, dV - \int_V \sigma_{ij}\delta(d\epsilon_{ij})\, dV$$

$$= \int_V \sigma_{ij}\, du_{k,i}\delta(du_k)_{,j}\, dV + \int_V (d\tau_{ij} + \psi_{ijkl}\, d\epsilon_{kl})\delta(dE_{ij})\, dV \tag{8.164}$$

Note that the $[\psi]$ matrix is nonsymmetric in general. If a finite-element procedure is employed in conjunction with Eq. (8.164), the nonsymmetry of the $[\psi]$ matrix will cause the set of discrete equilibrium equations to be nonsymmetric, too.

To linearize the incremental equilibrium equation (8.164), recall that the incremental deformations and rotations are "small". This implies that the relative elongations and distortions as defined by Novozhilov (1953) are given by the increments of Lagrangian strain tensor in Eq. (8.148). Incorporating the following identity:

$$du_{i,j} = d\epsilon_{ij} + d\Omega_{ij} \tag{8.165}$$

into the incremental form of Lagrangian strain tensor in Eq. (8.148) yields:

$$dE_{ij} = d\epsilon_{ij} + \tfrac{1}{2}(d\epsilon_{ki} + d\Omega_{ki})(d\epsilon_{kj} + d\Omega_{kj}) \tag{8.166a}$$

or

$$dE_{ij} = d\epsilon_{ij} + \tfrac{1}{2}(d\epsilon_{ki}\, d\epsilon_{kj} + d\epsilon_{ki}\, d\Omega_{kj} + d\Omega_{ki}\, d\epsilon_{kj} + d\Omega_{ki}\, d\Omega_{kj}) \tag{8.166b}$$

Therefore, the variation of increments of Lagrangian strain tensor, $\delta(dE_{ij})$, can be written as:

$$\delta(dE_{ij}) = \delta(d\epsilon_{ij}) + \tfrac{1}{2}\big[\delta(d\epsilon_{ki})\, d\epsilon_{kj} + d\epsilon_{ki}\delta(d\epsilon_{kj}) + \delta(d\epsilon_{ki})\, d\Omega_{kj} + d\epsilon_{ki}\delta(d\Omega_{kj})$$

$$+ \delta(d\Omega_{ki})\, d\epsilon_{kj} + d\Omega_{ki}\delta(d\epsilon_{kj}) + \delta(d\Omega_{ki})\, d\Omega_{kj} + d\Omega_{ki}\delta(d\Omega_{kj})\big] \tag{8.167}$$

Substituting Eqs. (8.165) and (8.167) into Eq. (8.164), and eliminating the products of incremental quantities, we obtain:

$$\int_A (T_i + \mathrm{d}T_i)\delta(\mathrm{d}u_i)\,\mathrm{d}A + \int_V \rho_0\{F_i(x_j) + \mathrm{d}F_i\}\delta(\mathrm{d}u_i)\,\mathrm{d}V - \int_V \sigma_{ij}\delta(\mathrm{d}\epsilon_{ij})\,\mathrm{d}V$$

$$= \int_V \sigma_{ij}\left[\mathrm{d}\epsilon_{ki}\delta(\mathrm{d}\epsilon_{kj}) + \mathrm{d}\epsilon_{ki}\delta(\mathrm{d}\Omega_{kj}) + \mathrm{d}\Omega_{ki}\delta(\mathrm{d}\epsilon_{kj}) + \mathrm{d}\Omega_{ki}\delta(\mathrm{d}\Omega_{kj})\right]\mathrm{d}V$$

$$+ \int_V (\mathrm{d}\tau_{ij} + \psi_{ijkl}\,\mathrm{d}\epsilon_{kl})\delta(\mathrm{d}\epsilon_{ij})\,\mathrm{d}V \tag{8.168}$$

Although Eq. (8.168) is an approximate equation governing the incremental response of soil mass, it may describe the response of large deformation (large strain and large rotation).

Example 8.15: Derive the increments of the second Piola-Kirchhoff stress tensor $\mathrm{d}S_{ij}$ in Eq. (8.163) for the three-dimensional case and two-dimensional cases of plane strain, plane stress, and axisymmetric conditions (Mizuno, 1981).

Three-dimensional condition

We shall consider first an infinitesimal element for which the initial configuration is cubic ($\mathrm{d}x_1$, $\mathrm{d}x_2$, $\mathrm{d}x_3$) and whose sides are parallel to the global coordinate system as shown in Fig. 8.17. In the subsequent configuration, the cube has been rotated by $\mathrm{d}\Omega_{ij}$ (to the first order) and has been deformed into a parallelepiped (Fig. 8.19). In the figure, ξ, η, and ζ denote the shear strain increments $\mathrm{d}\epsilon_{12}$, $\mathrm{d}\epsilon_{13}$, and $\mathrm{d}\epsilon_{23}$, respectively, and the stress components $\bar{\tau}_{ij}$ are referred to this *locally convected coordinate system* and defined as force per unit of area in the subsequent configuration.

According to Novozhilov (1953), the relationships between the second Piola-Kirchhoff stresses S_{ij} and stresses $\bar{\tau}_{ij}$ mentioned above are given by:

$$S_{11} = \frac{A_1^*}{A_1}\frac{\bar{\tau}_{11}}{1+\Lambda_1}, \quad S_{12} = \frac{A_1^*}{A_1}\frac{\bar{\tau}_{12}}{1+\Lambda_2}, \quad S_{13} = \frac{A_1^*}{A_1}\frac{\bar{\tau}_{13}}{1+\Lambda_3} \tag{8.169a}$$

$$S_{21} = \frac{A_2^*}{A_2}\frac{\bar{\tau}_{21}}{1+\Lambda_1}, \quad S_{22} = \frac{A_2^*}{A_2}\frac{\bar{\tau}_{22}}{1+\Lambda_2}, \quad S_{23} = \frac{A_2^*}{A_2}\frac{\bar{\tau}_{23}}{1+\Lambda_3} \tag{8.169b}$$

$$S_{31} = \frac{A_3^*}{A_3}\frac{\bar{\tau}_{31}}{1+\Lambda_1}, \quad S_{32} = \frac{A_3^*}{A_3}\frac{\bar{\tau}_{32}}{1+\Lambda_2}, \quad S_{33} = \frac{A_3^*}{A_3}\frac{\bar{\tau}_{33}}{1+\Lambda_3} \tag{8.169c}$$

where Λ_1, Λ_2, and Λ_3 are respectively *relative elongation* of the elements, $\mathrm{d}x_1$, $\mathrm{d}x_2$, and $\mathrm{d}x_3$, and A_i and A_i^* ($i = 1, 2, 3$) are areas before deformation and after

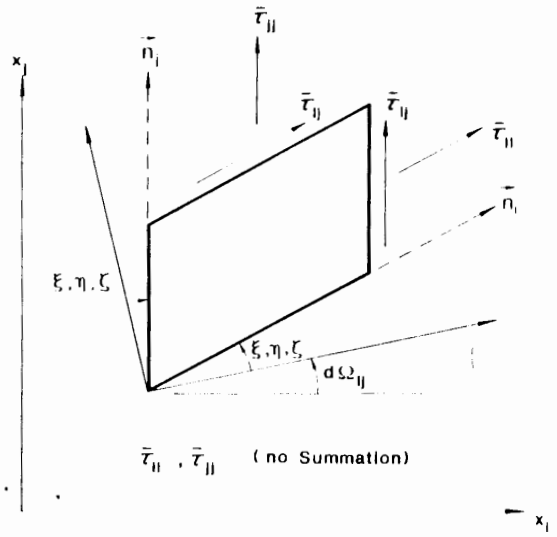

Fig. 8.19. Subsequent physical stress referred to a convected coordinate system.

deformation. A_1^*/A_1, A_2^*/A_2, and A_3^*/A_3 are defined as follows:

$$A_1^*/A_1 = \left[(1 + 2\,\mathrm{d}E_{22})(1 + 2\,\mathrm{d}E_{33}) - 4(\mathrm{d}E_{23})^2\right]^{1/2} \tag{8.170a}$$

$$A_2^*/A_2 = \left[(1 + 2\,\mathrm{d}E_{11})(1 + 2\,\mathrm{d}E_{33}) - 4(\mathrm{d}E_{13})^2\right]^{1/2} \tag{8.170b}$$

and

$$A_3^*/A_3 = \left[(1 + 2\,\mathrm{d}E_{11})(1 + 2\,\mathrm{d}E_{22}) - 4(\mathrm{d}E_{12})^2\right]^{1/2} \tag{8.170c}$$

Also, $(1 + \Lambda_1)$, $(1 + \Lambda_2)$, and $(1 + \Lambda_3)$ are given by:

$$1 + \Lambda_1 = \left[1 + 2\,\mathrm{d}E_{11}\right]^{1/2} \tag{8.171a}$$

$$1 + \Lambda_2 = \left[1 + 2\,\mathrm{d}E_{22}\right]^{1/2} \tag{8.171b}$$

and

$$1 + \Lambda_3 = \left[1 + 2\,\mathrm{d}E_{33}\right]^{1/2} \tag{8.171c}$$

The stresses $\bar{\tau}_{ij}$ in the convected coordinate system can be expressed in terms of the stresses τ_{ij} in the local coordinate system and the shear strain increments. The

unit vectors n_1^*, n_2^*, and n_3^* along three edges of the parallelepiped in Fig. 8.19 are given by:

$$n_1^* = \left[\cos(\xi^2 + \eta^2)^{1/2} \quad \sin\xi \quad \sin\eta\right] \tag{8.172a}$$

$$n_2^* = \left[\sin\xi \quad \cos(\xi^2 + \zeta^2)^{1/2} \quad \sin\zeta\right] \tag{8.172b}$$

$$n_3^* = \left[\sin\eta \quad \sin\zeta \quad \cos(\zeta^2 + \eta^2)^{1/2}\right] \tag{8.172c}$$

where ξ, η, and ζ are the shear strain increments related to $d\epsilon_{12}$, $d\epsilon_{13}$ and $d\epsilon_{23}$, respectively. By calculating a normal vector to each plane of parallelepiped, by using the Cauchy's formula and by eliminating the higher-order terms related to the products of shear strain increments, we have the following relations between the stresses $\bar{\tau}_{ij}$ and τ_{ij}:

$$\bar{\tau}_{11} = \tau_{11} - 2\xi\tau_{12} - 2\eta\tau_{13} \tag{8.173a}$$

$$\bar{\tau}_{12} = \tau_{12} - \xi\tau_{11} - \xi\tau_{22} - \eta\tau_{23} - \zeta\tau_{13} \tag{8.173b}$$

$$\bar{\tau}_{13} = \tau_{13} - \eta\tau_{11} - \eta\tau_{33} - \xi\tau_{23} - \zeta\tau_{12} \tag{8.173c}$$

$$\bar{\tau}_{22} = \tau_{22} - 2\xi\tau_{12} - 2\zeta\tau_{23} \tag{8.173d}$$

$$\bar{\tau}_{23} = \tau_{23} - \zeta\tau_{22} - \zeta\tau_{33} - \xi\tau_{13} - \eta\tau_{12} \tag{8.173e}$$

$$\bar{\tau}_{33} = \tau_{33} - 2\eta\tau_{13} - 2\zeta\tau_{23} \tag{8.173f}$$

Substitution of Eqs. (8.170a–c), (8.171a–c) and (8.173a–f) into Eq. (8.169) and elimination of the higher-order products of the shear strain increments lead to the simplified expressions for the second Piola-Kirchhoff stresses S_{ij} in terms of τ_{ij} and $d\epsilon_{ij}$, for example:

$$\begin{aligned}
S_{11} &= \frac{A_1^*}{A_1}\frac{\bar{\tau}_{11}}{1 + A_1} \\
&= \left(1 + 2\,dE_{22} + 2\,dE_{33} + 4\,dE_{22}\,dE_{33} - 4\,dE_{23}^2\right)^{1/2}\left(1 + 2\,dE_{11}\right)^{-1/2} \\
&\quad \times (\tau_{11} - 2\xi\tau_{12} - 2\eta\tau_{13}) \\
&\cong (1 + dE_{22} + dE_{33})(1 - dE_{11})(\tau_{11} - 2\xi\tau_{12} - 2\eta\tau_{13}) \\
&\cong (1 - dE_{11} + dE_{22} + dE_{33})(\tau_{11} - 2\xi\tau_{12} - 2\eta\tau_{13}) \\
&\cong (1 - d\epsilon_{11} + d\epsilon_{22} + d\epsilon_{33})(\tau_{11} - 2\,d\epsilon_{12}\tau_{12} - 2\,d\epsilon_{13}\tau_{13}) \\
&\cong \tau_{11} - \tau_{11}\,d\epsilon_{11} + \tau_{11}\,d\epsilon_{22} + \tau_{11}\,d\epsilon_{33} - 2\tau_{12}\,d\epsilon_{12} - 2\tau_{13}\,d\epsilon_{13}
\end{aligned} \tag{8.174}$$

Further use of the relations such as $S_{11} = \sigma_{11} + dS_{11}$, $\tau_{11} = \sigma_{11} + d\tau_{11}$, $\tau_{12} = \sigma_{12} + d\tau_{12}$, and $\tau_{13} = \sigma_{13} + d\tau_{13}$ into the above equation and elimination of the higher-order terms yield the incremental form for the second Piola-Kirchhoff stress:

$$dS_{11} = d\tau_{11} - \sigma_{11}\, d\epsilon_{11} + \sigma_{11}\, d\epsilon_{22} + \sigma_{11}\, d\epsilon_{33} - 2\sigma_{12}\, d\epsilon_{12} - 2\sigma_{13}\, d\epsilon_{13}$$

$$= d\tau_{11} - \sigma_{11}\, d\epsilon_{11} + \sigma_{11}\, d\epsilon_{22} + \sigma_{11}\, d\epsilon_{33} - \sigma_{12}\, d\gamma_{12} - \sigma_{13}\, d\gamma_{13} \tag{8.175}$$

Similarly, the incremental forms for other stresses dS_{12}, ... and dS_{33} can be obtained. The general matrix form for dS_{ij} in terms of $d\tau_{ij}$, σ_{ij} and $d\epsilon_{ij}$ can be written as:

$$\begin{Bmatrix} dS_{11} \\ dS_{22} \\ dS_{33} \\ dS_{12} \\ dS_{23} \\ dS_{31} \end{Bmatrix} = \begin{Bmatrix} d\tau_{11} \\ d\tau_{22} \\ d\tau_{33} \\ d\tau_{12} \\ d\tau_{23} \\ d\tau_{31} \end{Bmatrix} + \begin{bmatrix} \sigma_{11} & \sigma_{11} & \sigma_{11} & -\sigma_{12} & 0 & -\sigma_{13} \\ \sigma_{22} & \sigma_{22} & \sigma_{22} & -\sigma_{12} & -\sigma_{23} & 0 \\ \sigma_{33} & \sigma_{33} & \sigma_{33} & 0 & \sigma_{23} & \sigma_{13} \\ 0 & 0 & \sigma_{12} & -\tfrac{1}{2}(\sigma_{11}+\sigma_{22}) & -\tfrac{1}{2}\sigma_{13} & -\tfrac{1}{2}\sigma_{23} \\ \sigma_{23} & 0 & 0 & -\tfrac{1}{2}\sigma_{13} & -\tfrac{1}{2}(\sigma_{22}+\sigma_{33}) & -\tfrac{1}{2}\sigma_{12} \\ 0 & \sigma_{13} & 0 & -\tfrac{1}{2}\sigma_{23} & -\tfrac{1}{2}\sigma_{12} & -\tfrac{1}{2}(\sigma_{11}+\sigma_{33}) \end{bmatrix} \begin{Bmatrix} d\epsilon_{11} \\ d\epsilon_{22} \\ d\epsilon_{33} \\ d\gamma_{12} \\ d\gamma_{23} \\ d\gamma_{31} \end{Bmatrix} \tag{8.176}$$

where $d\tau_{ij}$ are Jaumann stress increments and the transformation matrix $[\psi]$ for ψ_{ijkl} can be expressed by a nonsymmetric form.

Plane strain condition

We shall first reduce Eq. (8.169) to the *plane strain* condition where $dE_{31} = dE_{32} = dE_{33} = 0$. Thus, we find:

$$S_{11} = \left[\frac{1 + 2\, dE_{22}}{1 + 2\, dE_{11}}\right]^{1/2} \bar{\tau}_{11} \tag{8.177a}$$

$$S_{22} = \left[\frac{1 + 2\, dE_{11}}{1 + 2\, dE_{22}}\right]^{1/2} \tau_{22} \tag{8.177b}$$

$$S_{12} = \tau_{12} \tag{8.177c}$$

The following transformation equations of stress τ_{ij} to stress $\bar{\tau}_{ij}$ are given by substituting $\eta = \zeta = 0$ into Eq. (8.173):

$$\bar{\tau}_{11} = \tau_{11} - 2\xi\tau_{12} \tag{8.178a}$$

$$\bar{\tau}_{22} = \tau_{22} - 2\xi\tau_{12} \tag{8.178b}$$

$$\bar{\tau}_{12} = -\xi\tau_{11} - \xi\tau_{22} + \tau_{12} \tag{8.178c}$$

Substituting Eqs. (8.178a c) into Eqs. (8.177a c) and taking the linear Taylor expansion with respect to $\mathrm{d}E_{11}$ and $\mathrm{d}E_{22}$, S_{ij} is thus obtained:

$$S_{11} = (1 - \mathrm{d}E_{11} + \mathrm{d}E_{22})(\tau_{11} - 2\xi\tau_{12}) \tag{8.179a}$$

$$S_{22} = (1 + \mathrm{d}E_{11} - \mathrm{d}E_{22})(\tau_{22} - 2\xi\tau_{12}) \tag{8.179b}$$

$$S_{12} = -\xi\tau_{11} - \xi\tau_{22} + \tau_{12} \tag{8.179c}$$

Also, substituting Eqs. (8.157) and (8.161) into Eqs. (8.179a c), replacing increments of Lagrangian strain tensor $\mathrm{d}E_{ij}$ with increments of infinitesimal strain tensor $\mathrm{d}\epsilon_{ij}$, and eliminating terms which are nonlinear with respect to the incremental variables, we have finally the expressions:

$$\mathrm{d}S_{11} = \mathrm{d}\tau_{11} - \sigma_{11}\,\mathrm{d}\epsilon_{11} + \sigma_{11}\,\mathrm{d}\epsilon_{22} - \sigma_{12}\,\mathrm{d}\gamma_{12} \tag{8.180a}$$

$$\mathrm{d}S_{22} = \mathrm{d}\tau_{22} + \sigma_{22}\,\mathrm{d}\epsilon_{11} - \sigma_{22}\,\mathrm{d}\epsilon_{22} - \sigma_{12}\,\mathrm{d}\gamma_{12} \tag{8.180b}$$

$$\mathrm{d}S_{12} = \mathrm{d}\tau_{12} - \tfrac{1}{2}(\sigma_{11} + \sigma_{22})\,\mathrm{d}\gamma_{12} \tag{8.180c}$$

or in matrix form:

$$\begin{Bmatrix} \mathrm{d}S_{11} \\ \mathrm{d}S_{22} \\ \mathrm{d}S_{12} \end{Bmatrix} = \begin{Bmatrix} \mathrm{d}\tau_{11} \\ \mathrm{d}\tau_{22} \\ \mathrm{d}\tau_{12} \end{Bmatrix} + \begin{bmatrix} -\sigma_{11} & \sigma_{11} & -\sigma_{12} \\ \sigma_{22} & -\sigma_{22} & -\sigma_{12} \\ 0 & 0 & -\tfrac{1}{2}(\sigma_{11} + \sigma_{22}) \end{bmatrix} \begin{Bmatrix} \mathrm{d}\epsilon_{11} \\ \mathrm{d}\epsilon_{22} \\ \mathrm{d}\gamma_{12} \end{Bmatrix} \tag{8.181}$$

Plane stress condition

Herein, we shall derive $\mathrm{d}S_{ij}$ for the plane stress condition. Carrying out the same procedure as that for the plane strain case, we obtain:

$$\mathrm{d}S_{11} = \mathrm{d}\tau_{11} - \sigma_{11}\,\mathrm{d}\epsilon_{11} + \sigma_{11}\,\mathrm{d}\epsilon_{22} + \sigma_{11}\,\mathrm{d}\epsilon_{33} - \sigma_{12}\,\mathrm{d}\gamma_{12} \tag{8.182a}$$

$$\mathrm{d}S_{22} = \mathrm{d}\tau_{22} + \sigma_{22}\,\mathrm{d}\epsilon_{11} - \sigma_{22}\,\mathrm{d}\epsilon_{22} + \sigma_{22}\,\mathrm{d}\epsilon_{33} - \sigma_{12}\,\mathrm{d}\gamma_{12} \tag{8.182b}$$

$$\mathrm{d}S_{12} = \mathrm{d}\tau_{12} + \sigma_{12}\,\mathrm{d}\epsilon_{33} - \tfrac{1}{2}(\sigma_{11} + \sigma_{22})\,\mathrm{d}\gamma_{12} \tag{8.182c}$$

where $d\epsilon_{33}$ can be obtained from the constitutive equation derived in Chapters 4 to 6, in terms of $d\epsilon_{11}$, $d\epsilon_{22}$, and $d\gamma_{12}$. It has the form:

$$d\epsilon_{33} = \alpha_1\, d\epsilon_{11} + \alpha_2\, d\epsilon_{22} + \alpha_3\, d\gamma_{12} \tag{8.183}$$

in which

$$\alpha_1 = \frac{H_{33}^* H_{11} - \lambda H}{(\lambda + 2\mu) H - H_{33}^* H_{33}} \tag{8.184a}$$

$$\alpha_2 = \frac{H_{33}^* H_{22} - \lambda H}{(\lambda + 2\mu) H - H_{33}^* H_{33}} \tag{8.184b}$$

$$\alpha_3 = -\frac{H_{33}^* H_{12}}{(\lambda + 2\mu) H - H_{33}^* H_{33}} \tag{8.184c}$$

Back substituting $d\epsilon_{33}$ into Eq. (8.182) and rearranging with respect to $d\epsilon_{11}$, $d\epsilon_{22}$, and $d\gamma_{12}$, dS_{ij} can be written as:

$$dS_{11} = d\tau_{11} + (\alpha_1 - 1)\sigma_{11}\, d\epsilon_{11} + (1 + \alpha_2)\sigma_{11}\, d\epsilon_{22} + (\alpha_3\sigma_{11} - \sigma_{12})\, d\gamma_{12} \tag{8.185a}$$

$$dS_{22} = d\tau_{22} + (1 + \alpha_1)\sigma_{22}\, d\epsilon_{11} + (\alpha_2 - 1)\sigma_{22}\, d\epsilon_{22} + (\alpha_3\sigma_{22} - \sigma_{12})\, d\gamma_{12} \tag{8.185b}$$

$$dS_{12} = d\tau_{12} + \alpha_1\sigma_{12}\, d\epsilon_{11} + \alpha_2\sigma_{12}\, d\epsilon_{22} + \left(\alpha_3\sigma_{12} - \tfrac{1}{2}\sigma_{11} - \tfrac{1}{2}\sigma_{22}\right) d\gamma_{12} \tag{8.185c}$$

or in matrix form:

$$\begin{Bmatrix} dS_{11} \\ dS_{22} \\ dS_{12} \end{Bmatrix} = \begin{Bmatrix} d\tau_{11} \\ d\tau_{22} \\ d\tau_{12} \end{Bmatrix} + \begin{bmatrix} (\alpha_1 - 1)\sigma_{11} & (1 + \alpha_2)\sigma_{11} & (\alpha_3\sigma_{11} - \sigma_{12}) \\ (1 + \alpha_1)\sigma_{22} & (\alpha_2 - 1)\sigma_{22} & (\alpha_3\sigma_{22} - \sigma_{12}) \\ \alpha_1\sigma_{12} & \alpha_2\sigma_{12} & \left(\alpha_3\sigma_{12} - \tfrac{1}{2}\sigma_{11} - \tfrac{1}{2}\sigma_{22}\right) \end{bmatrix} \begin{Bmatrix} d\epsilon_{11} \\ d\epsilon_{22} \\ d\gamma_{12} \end{Bmatrix} \tag{8.186}$$

Axisymmetric condition

By changing the coordinate symbols (1, 2, 3) to the (r, z, θ) for the axisymmetric condition, we have dS_{ij}:

$$dS_{rr} = d\tau_{rr} - \sigma_{rr}\, d\epsilon_{rr} + \sigma_{rr}\, d\epsilon_{zz} + \sigma_{rr}\, d\epsilon_{\theta\theta} - \sigma_{rz}\, d\gamma_{rz} \tag{8.187a}$$

$$dS_{zz} = d\tau_{zz} + \sigma_{zz}\, d\epsilon_{rr} - \sigma_{zz}\, d\epsilon_{zz} + \sigma_{zz}\, d\epsilon_{\theta\theta} - \sigma_{rz}\, d\gamma_{rz} \tag{8.187b}$$

$$dS_{\theta\theta} = d\tau_{\theta\theta} + \sigma_{\theta\theta}\, d\epsilon_{rr} + \sigma_{\theta\theta}\, d\epsilon_{zz} - \sigma_{\theta\theta}\, d\epsilon_{\theta\theta} \tag{8.187c}$$

$$dS_{rz} = d\tau_{rz} + \sigma_{rz}\, d\epsilon_{\theta\theta} - \tfrac{1}{2}(\sigma_{rr} + \sigma_{zz})\, d\gamma_{rz} \tag{8.187d}$$

or in matrix form:

$$\begin{Bmatrix} \mathrm{d}S_{rr} \\ \mathrm{d}S_{zz} \\ \mathrm{d}S_{\theta\theta} \\ \mathrm{d}S_{rz} \end{Bmatrix} = \begin{Bmatrix} \mathrm{d}\tau_{rr} \\ \mathrm{d}\tau_{zz} \\ \mathrm{d}\tau_{\theta\theta} \\ \mathrm{d}\tau_{rz} \end{Bmatrix} + \begin{bmatrix} -\sigma_{rr} & \sigma_{rr} & \sigma_{rr} & -\sigma_{rz} \\ \sigma_{zz} & -\sigma_{zz} & \sigma_{zz} & -\sigma_{rz} \\ \sigma_{\theta\theta} & \sigma_{\theta\theta} & -\sigma_{\theta\theta} & 0 \\ 0 & 0 & \sigma_{rz} & -\tfrac{1}{2}(\sigma_{rr}+\sigma_{zz}) \end{bmatrix} \begin{Bmatrix} \mathrm{d}\epsilon_{rr} \\ \mathrm{d}\epsilon_{zz} \\ \mathrm{d}\epsilon_{\theta\theta} \\ \mathrm{d}\gamma_{rz} \end{Bmatrix} \tag{8.188}$$

8.7.3 Linearized incremental equation (small strain and large rotation)

In this Section, the incremental equilibrium equation (8.159) will be linearized by assuming the order of magnitude of the incremental strains $\mathrm{d}\epsilon_{ij}$ is less than that of the incremental rotations $\mathrm{d}\Omega_{ij}$. Further, if we assume that the increments of Lagrangian strain tensor, $\mathrm{d}E_{ij}$, are an order of magnitude less than the increments of rotation tensor, $\mathrm{d}\Omega_{ij}$, the linear incremental equations are rendered symmetric. Thus, Eq. (8.166b) can be reduced to:

$$\mathrm{d}E_{ij} \cong \mathrm{d}\epsilon_{ij} + \tfrac{1}{2}(\mathrm{d}\epsilon_{ki}\,\mathrm{d}\Omega_{kj} + \mathrm{d}\Omega_{ki}\,\mathrm{d}\epsilon_{kj} + \mathrm{d}\Omega_{ki}\,\mathrm{d}\Omega_{kj}) \tag{8.189}$$

Considering again Eq. (8.163) and recalling the assumption that incremental deformations are very small, the following approximation by Novozhilov (1953), is incorporated:

$$\mathrm{d}S_{ij} \cong \mathrm{d}\tau_{ij} \tag{8.190}$$

The new incremental equilibrium equation for small strain and large rotation can therefore be written as:

$$\int_A (T_i + \mathrm{d}T_i)\delta(\mathrm{d}u_i)\,\mathrm{d}A + \int_V \rho_0\{F_i(x_j) + \mathrm{d}F_i\}\delta(\mathrm{d}u_i)\,\mathrm{d}V - \int_V \sigma_{ij}\delta(\mathrm{d}\epsilon_{ij})\,\mathrm{d}V$$

$$= \int_V \sigma_{ij}\left[\mathrm{d}\epsilon_{ki}\delta(\mathrm{d}\Omega_{kj}) + \mathrm{d}\Omega_{ki}\delta(\mathrm{d}\epsilon_{kj}) + \mathrm{d}\Omega_{ki}\delta(\mathrm{d}\Omega_{kj})\right]\mathrm{d}V + \int_V \mathrm{d}\tau_{ij}\delta(\mathrm{d}\epsilon_{ij})\,\mathrm{d}V \tag{8.191}$$

Equation (8.191) leads to a set of symmetric equations under the assumption that incremental deformations are an order smaller than that of incremental rotations.

8.8 Summary

In this Chapter, the definitions of stress and strain for a *finite deformation* of a deformable body and subsequently the general incremental virtual work equations

have been discussed and developed for the large-deformation analysis of soil response.

Strain tensors

Instead of the usual *small-strain* assumption that assumes approximately the same configuration of the body in the undeformed and deformed states, the concept of *finite strain* is essential and powerful for the analysis of finite deformation of the body. According to the finite deformation theory, the strain tensor is classified into the following two definitions:

1. *Lagrangian strain tensor* E_{ij} is taken with respect to the reference (original) coordinates X_i. The Lagrangian strain tensor E_{ij} is defined by the change in the square of the line elements $\mathrm{d}\ddot{s}^2$ and $\mathrm{d}s^2$ in the reference and current configurations. This relation has the form:

$$\mathrm{d}s^2 - \mathrm{d}\ddot{s}^2 = 2E_{kl}\,\mathrm{d}X_k\,\mathrm{d}X_l$$

2. *Eulerian strain tensor* e_{ij} is taken with respect to the spatial (current) coordinates x_i. Similar to the definition of E_{ij}, the Eulerian strain tensor e_{ij} is defined as:

$$\mathrm{d}s^2 - \mathrm{d}\ddot{s}^2 = 2e_{kl}\,\mathrm{d}x_k\,\mathrm{d}x_l$$

Note that if the displacements and displacement gradients are small both strain tensors reduce to the usual small strain tensor ϵ_{ij}.

Strain rates

The *velocity gradient* $\partial v_i/\partial x_j$ can be decomposed into the *rate of deformation tensor* V_{ij} and the *spin tensor* W_{ij}. The rate of deformation tensor is responsible for the rate of change in the square of the line element $\mathrm{d}s^2$ at the current configuration, as can be understood from Eq. (8.48). On the other hand, the spin tensor W_{ij} contributes only to the rigid body motion of the body, but not to the deformation.

The rate of Lagrangian strain tensor $\mathrm{d}E_{ij}/\mathrm{d}t$ can be represented as a transformation of the rate of deformation tensor as:

$$\frac{\mathrm{d}E_{ij}}{\mathrm{d}t} = V_{kl}\frac{\partial x_k}{\partial X_i}\frac{\partial x_l}{\partial X_j}$$

The rate of Eulerian strain tensor $\mathrm{d}e_{ij}/\mathrm{d}t$ includes the rate of deformation tensor V_{ij}, the Eulerian strain tensor e_{ij}, and the velocity gradient $\partial v_i/\partial x_j$, namely:

$$\frac{\mathrm{d}e_{ij}}{\mathrm{d}t} = V_{ij} - \frac{\partial v_k}{\partial x_j}e_{ik} - \frac{\partial v_k}{\partial x_i}e_{jk}$$

As can be seen from the comparison of both strain rates, the rate of Lagrangian strain tensor $\mathrm{d}E_{ij}/\mathrm{d}t$ vanishes when the neighborhood of a particle exhibits a

rigid-body motion, i.e., $V_{ij} = 0$ whereas the rate of Eulerian strain tensor $\mathrm{d}e_{ij}/\mathrm{d}t$ may not vanish in general. Therefore, $\mathrm{d}E_{ij}/\mathrm{d}t$ should be used in the constitutive law rather than $\mathrm{d}e_{ij}/\mathrm{d}t$.

Stress tensors

The stress tensors defined in the large-deformation formulation are:

1. *Eulerian stress tensor* σ_{ij}
2. *Lagrangian stress tensor* (*first Piola-Kirchhoff stress tensor*) T_{ij} and
3. *Second Piola-Kirchhoff stress tensor* S_{ij}.

The Eulerian stress tensor is a physically *real* stress which is measured in the currently deformed configuration. On the other hand, the first and second Piola-Kirchhoff stress tensors are *not* real stresses. The relationship between these three stresses are:

$$T_{ij} = J \frac{\partial X_i}{\partial x_k} \sigma_{kj}$$

$$S_{ij} = J \frac{\partial X_i}{\partial x_k} \frac{\partial X_j}{\partial x_l} \sigma_{kl}$$

$$S_{ij} = \frac{\partial X_j}{\partial x_k} T_{ik}$$

When the displacements and displacement gradients are small enough, the Eulerian stress, the first and second Piola-Kirchhoff stresses become approximately equal to each other under the usual small-strain assumption.

Stress rates

The stress rate used in the constitutive law must be invariant with respect to the rigid-body rotation. The *Jaumann stress rate* $\dot{\sigma}^{\mathrm{J}}_{ij}$ is defined as:

$$\dot{\sigma}^{\mathrm{J}}_{ij} = \frac{\mathrm{d}}{\mathrm{d}t}(\sigma_{ij}) - \sigma_{ik}W_{jk} - \sigma_{jk}W_{ik}$$

The *Truesdell stress rate* $\dot{\sigma}^{\mathrm{T}}_{ij}$ is defined as:

$$\dot{\sigma}^{\mathrm{T}}_{ij} = \frac{\mathrm{d}}{\mathrm{d}t}(\sigma_{ij}) + \frac{\partial v_k}{\partial x_k}\sigma_{ij} - \frac{\partial v_j}{\partial x_k}\sigma_{ik} - \frac{\partial v_i}{\partial x_k}\sigma_{kj}$$

or introducing the Jaumann stress rate $\dot{\sigma}^{\mathrm{J}}_{ij}$, these two stress rates are related by:

$$\dot{\sigma}^{\mathrm{T}}_{ij} = \dot{\sigma}^{\mathrm{J}}_{ij} + V_{kk}\sigma_{ij} - V_{jk}\sigma_{ik} - V_{ik}\sigma_{jk}$$

When the neighborhood of the considered particle undergoes a rigid-body rotation, the Truesdell stress rate reduces to the Jaumann stress rate.

Total Lagrangian description

The total Lagrangian formulation refers all measurements of forces, stresses, and strains to the *reference* configuration. The incremental form of the virtual work equation requires the consideration of the following quantities:

1. Lagrangian strain increments $\mathrm{d}E_{ij}$ based on the reference state.
2. Second Piola-Kirchhoff stress increments $\mathrm{d}S_{ij}$ based on the reference state.

The virtual work equation has the form:

$$\int_V \left(S_{ij}^t + \mathrm{d}S_{ij}\right)\delta\left(\mathrm{d}E_{ij}\right)\,\mathrm{d}\overset{\circ}{V} = \int_V F_{oi}^t \rho_o \delta(\mathrm{d}u_i)\,\mathrm{d}\overset{\circ}{V} + \int_A \left(T_{oi}^t + \mathrm{d}T_{oi}\right)\delta(\mathrm{d}u_i)\,\mathrm{d}\overset{\circ}{A}$$

To relate the increments of second Piola-Kirchhoff stress tensor $\mathrm{d}S_{ij}$ to the increments of the Lagrangian strain tensor $\mathrm{d}E_{kl}$, the constitutive relation in Section 8.6.1 is used:

$$\mathrm{d}S_{ij} = C_{ijkl}^{*}\,\mathrm{d}E_{kl}$$

Updated Lagrangian description

The updated Lagrangian formulation refers all measurements of forces, stresses, and strains to the *currently deformed* configuration. The incremental form of the virtual work equation utilizes the following quantities:

1. Lagrangian strain increments $\mathrm{d}E_{ij}$ based on the currently deformed state.
2. Second Piola-Kirchhoff stress increments $\mathrm{d}S_{ij}$ based on the currently deformed state.

The virtual work equation has the form:

$$\int_{V^t} \left(\sigma_{ij}^t + \mathrm{d}S_{ij}\right)\delta\left(\mathrm{d}E_{ij}\right)\,\mathrm{d}V^t = \int_{V^t} F_{oi}^t \rho_o \delta(\mathrm{d}u_i)\,\mathrm{d}V^t + \int_{A^t} \left(T_{oi}^t + \mathrm{d}T_{oi}\right)\delta(\mathrm{d}u_i)\,\mathrm{d}A^t$$

The increments of second Piola-Kirchhoff stress tensor $\mathrm{d}S_{ij}$ may be evaluated by the Eulerian stress increments $\mathrm{d}\sigma_{ij}$ as:

$$\mathrm{d}S_{ij} = \mathrm{d}\sigma_{ij} - C_{ijkl}\,\mathrm{d}\epsilon_{kl} + \sigma_{ik}^t\,\mathrm{d}\Omega_{jk} + \sigma_{jk}^t\,\mathrm{d}\Omega_{ik}$$

The inclusion of the rotation terms results in a set of nonsymmetric equilibrium equations. An alternative approach is simply to use the Jaumann stress increments $\mathrm{d}\sigma_{ij}^{\mathrm{J}}$ as $\mathrm{d}S_{ij}$:

$$\mathrm{d}S_{ij} = \mathrm{d}\sigma_{ij}^{\mathrm{J}} = C_{ijkl}\,\mathrm{d}\epsilon_{kl}$$

Updated Lagrangian formulation (Davidson and Chen, 1974)

Although the solution of a nonsymmetric set of linear simultaneous equations resulting from the large-strain and large-rotation formulation as given in Eq. (8.168) presents no conceptual difficulties, there are some practical drawbacks, e.g., the core storage required for the equation, the computational time required to solve the equations, etc. On the other hand, if Eq. (8.191) for small strain and large rotation is utilized, then a greater number of increments must be employed to obtain the same accuracy of solution as that obtained from Eq. (8.168). However, the choice is not clear since a greater computational effort is required per each increment if the nonsymmetric equations are employed.

Although the soil response is generally nonlinear, the material nonlinearity usually dominates the geometric nonlinearity. The size of the increment is generally governed by the severity of the material nonlinearity. With this point in mind, the symmetric incremental finite-element equation (small strain and large rotation) will be utilized for the analysis of slope stability to be given in Chapter 9. However, it should be understood that we are not claiming here that soil response is characterized by small strain and large rotation. Rather, it is still our intention to capture large-strain and large-rotation analysis through the incremental procedure.

REFERENCES

Bathe, K.J., Ramm, E. and Wilson, E.L., 1975. Finite element formulations for large deformation dynamic analysis. Int. J. Numer. Method Eng., 9: 353–386.

Bathe, K.J., 1982. Finite Element Procedures in Engineering Analysis. Prentice-Hall, Englewood Cliffs, NJ, 735 pp.

Bazant, Z.P., 1971. A correlational study of formulations of incremental deformation and stability of continuous bodies. J. Appl. Mech. ASME, 38: 919–928.

Carter, J.P., Booker, J.R. and Davis, E.H., 1977. Finite deformation of an elasto-plastic soil. Int. J. Numer. Anal. Methods Geomech., 1: 25–43.

Chen, W.F. and Saleeb, A.F., 1982. Constitutive Equations for Engineering Materials, Vol. 1: Elasticity and Modeling. John Wiley & Sons, New York, NY, 580 pp.

Dafalias, Y.F., 1983. Corotational rates for kinematic hardening at large plastic deformations. J. Appl. Mech. ASME, 50: 561–565.

Davidson, H.L. and Chen, W.F., 1974. Elastic-plastic large deformation response of clay to footing loads. Rep. No. 355.18, Fritz Eng. Lab. Leihigh University, PA, 181 pp.

Davidson, H.L. and Chen, W.F., 1977. Elastic-plastic, large deformation response of soft clay to footing load. Int. Symposium on Soft Clay, Bangkok, Thailand, 5–6 July, 1977, pp. 629–646.

Desai, C.S. and Phan, H.V., 1980. Three-dimensional finite element analysis including material and geometric nonlinearities. In: J.T. Oden (Editor), Computational Methods in Nonlinear Mechanics. Proceedings of the TICOM Second International Conference, Austin, Texas, March 26–29, 1979. Elsevier, Amsterdam, pp. 205–224.

Fung, Y.C., 1965. Foundations of Solid Mechanics. Prentice-Hall, Englewood Cliffs, NJ, pp. 434–439.

Gadala, M.S., Dokainish, M.A. and Oravas, G.AE., 1984. Formulation methods of geometric and material nonlinearity problems. Int. J. Numer. Methods Eng., 20: 887–914.

Hibbitt, H.D., Marcal, P.V. and Rice, J.R., 1970. A finite element formulation for problems of large strain and large displacement. Int. J. Solids Struct. 6: 1069–1086.

Hofmeister, L.D., Greenbaum, G.A. and Evensen, D.A., 1971. Large strain elastic-plastic finite element analysis. AIAA J., 9: 1248–1254.

Johnson, G.C. and Bammann, D.J., 1984. A discussion of stress rates in finite deformation problems. Int. J. Solids Struct., 20 (8): 725–737.

Kiousis, P.D., Voyiadjis, G.Z. and Tumay, M.T., 1986. A large strain theory for the two-dimensional problems in geomechanics. Int. J. Numer. Anal. Methods Geomech. 10: 17–39.

Lee, E.H., Mallett, R.L. and Wertheimer, T.B., 1983. Stress analysis for anisotropic hardening in finite deformation plasticity. J. Appl. Mech. ASME, 50: 554–560.

Malvern, L.E., 1969. Introduction to the Mechanics of a Continuous Medium. Prentice-Hall, Englewood Cliffs, NJ, 713 pp.

Mason, J., 1980. Variational, Incremental and Energy Methods in Solid Mechanics and Shell Theory. Elsevier, Amsterdam, 368 pp.

Mizuno, E., 1981. Plasticity modeling of soils and finite element applications. Ph.D. Thesis, School of Civil Engineering, Purdue University, West Lafayette, IN, 320 pp.

Mizuno, E. and Chen, W.F., 1983. Plasticity analysis of slope with different flow rules. Comput. Struct., 17 (3): 375–388.

Nagtegaal, J.C. and De Jong, J.E., 1981. Some computational aspects of elastic-plastic large strain analysis. Int. J. Numer. Methods Eng., 17: 13–41.

Novozhilov, V.V., 1953. Foundations of the Non-Linear Theory of Elasticity. Graylock Press, Rochester, NY, 233 pp.

Oden, J.T., 1972. Finite Elements of Nonlinear Continua. McGraw-Hill, New York, NY, 432 pp.

Prager, W., 1961. Introduction to Mechanics of Continua. Ginn and Company, 230 pp.

Snitbhan, N. and Chen, W.F., 1976. Finite element analysis of large deformation in slopes. Proc. Second Int. Conference on Numerical Methods in Geomechanics, Blacksburg, VA, Vol. 2, pp. 744–756.

Washizu, K., 1982. Variational Methods in Elasticity and Plasticity. Pergamon Press, New York, NY, 630 pp.

Yamada, Y. and Wifi, A.S., 1977. Large strain analysis of some geomechanics problems by the finite element method. Int. J. Numer. Anal. Methods Geomech., 1: 299–318.

Chapter 9

LARGE-DEFORMATION IMPLEMENTATION AND PREDICTIONS

9.1 INTRODUCTION

The first step in any finite-element analyses to solve the governing equations with certain boundary conditions is the derivation of the *total stiffness matrix* $[K]$, which relates the vector $\{dU\}$ of the nodal displacement increments to the vector $\{dR\}$ of the total load increments. This relation is known as the *incremental finite-element equations*. To derive these equations, we must use the following three conditions discussed in Chapter 8:

1. *Kinematic assumptions* which relate the displacement field to the strain field within the framework of the large-deformation description as well as the small-deformation description.
2. *Constitutive relations* which have several forms under assumption of the total Lagrangian formulation and of the updated Lagrangian formulation, and these relations are incorporated into the large-deformation virtual work equations based on the two different Lagrangian formulations.
3. *Equilibrium equations* which are represented by the two types of large-deformation virtual work equations.

As the first step to the finite-element implementation in displacement analysis, a field variable $\phi(x, y, z)$ for displacements in a three-dimensional element may be constructed by the *generalized coordinates* α_i:

$$\phi = \alpha_1 + \alpha_2 x + \alpha_3 y + \alpha_4 z + \alpha_5 x^2 + \alpha_6 xy + \alpha_7 y^2 + \alpha_8 yz + \dots \tag{9.1a}$$

or it may be written in terms of the *interpolation functions* N_i and the values Φ_i of field variable corresponding to the specified points inside the element and on the element boundaries, i.e.:

$$\phi = \Phi_1 N_1 + \Phi_2 N_2 + \dots + \Phi_n N_n \tag{9.1b}$$

where Φ_i ($i = 1, 2, \dots$ and n) may involve in some cases the values of derivative of the field variable at the specified points (generally called *nodes* or *nodal points*) of the element, N_i may also involve the interpolation functions (or the shape functions) corresponding to the derivative quantities at the nodal points, and n is the number of the degree of freedom of the element with respect to the field variable.

In this Chapter, limiting our discussion to such finite-element implementation in displacement analysis, the *displacement models* are firstly introduced into several types of finite elements. By utilizing them in the incremental virtual work equation with the effects of the geometrical nonlinearity as well as the material nonlinearity, the incremental finite-element equation and *element stiffness matrix* $[k]$ are derived for each element. Further, each incremental finite-element equation is assembled to construct a *total stiffness matrix* $[K]$ for the whole region.

In the later part of this Chapter, the appropriate solution techniques such as the *incremental procedure* and *iteration procedure* including the *initial-strain technique* and the *initial-stress technique* are discussed with respect to their advantages and limitations when they are applied to the nonlinear problems.

Our special concern is to discuss the large-deformation finite-element implementation and to present the large-deformation finite-element analysis of a vertical slope, as a numerical example where the two-dimensional finite elements such as the constant-strain triangular element and the four-node quadrilateral element are applied (Davidson and Chen, 1974, 1976; and Mizuno, 1981).

9.2 DISPLACEMENT MODELS AND SHAPE FUNCTIONS

In this Section, as a basic concept of the finite-element method, the *generalized-coordinate displacement model* and *interpolation displacement model* are briefly presented by introducing the *shape functions* N_i (or the *interpolation functions*) in Eq. (9.1) for the construction of the field variable ϕ for the displacement. Further, several shape functions used in the finite-element method are derived.

Herein, we limit our discussion to the shape functions of finite elements (continuum elements) for the C^0-problem in which the field variable ϕ is continuous at the element interfaces. For more details of the shape functions and their basic requirements, and for more higher-order problems such as C^1- and C^2-problems in which the first and the second derivatives are required to be respectively continuous, the reader can refer to the books by Desai and Abel (1972), Huebner (1975), Zienkiewicz (1978), and Bathe (1982), among others.

9.2.1 Generalized coordinate displacement model

In the finite-element analysis, the displacements at an element node are often taken as unknowns. The field variable ϕ for displacement is generally expressed in the form of *polynomials* whose numerical integrations and derivatives are easily performed. For example, the m-th order polynomial function corresponding to a certain displacement field, $\phi(x, y)$, in the two-dimensional space (x, y), can be generally written as:

$$\phi(x, y) = \sum_{k=1}^{n} \alpha_k x^i y^j, \quad i + j \leq m \tag{9.2}$$

where the coefficients α_k are the *generalized coordinates* of the element and n is the number of terms in the polynomial given by:

$$n = \tfrac{1}{2}(m+1)(m+2) \tag{9.3}$$

The number of coefficients in the polynomial, n, is equal to the number of nodal variables Φ_i of the element, i.e., the number of nodes.

For $m = 1$ and $n = 3$, for example, we have a polynomial function ϕ for a displacement field written as:

$$\phi = \alpha_1 + \alpha_2 x + \alpha_3 y \tag{9.4a}$$

or in matrix form:

$$\phi = \begin{bmatrix} 1 & x & y \end{bmatrix} \begin{bmatrix} \alpha_1 & \alpha_2 & \alpha_3 \end{bmatrix}^{\mathrm{T}} \tag{9.4b}$$

where [ ] denotes the row vector and the superscript T the transpose.

For $m = 2$ and $n = 6$, similarly we have another displacement field such as:

$$\phi = \alpha_1 + \alpha_2 x + \alpha_3 y + \alpha_4 x^2 + \alpha_5 xy + \alpha_6 y^2 \tag{9.5a}$$

or in matrix form:

$$\phi = \begin{bmatrix} 1 & x & y & x^2 & xy & y^2 \end{bmatrix} \begin{bmatrix} \alpha_1 & \alpha_2 & \alpha_3 & \alpha_4 & \alpha_5 & \alpha_6 \end{bmatrix}^{\mathrm{T}} \tag{9.5b}$$

and so on.

The displacement model so constructed is called the *generalized-coordinate displacement model*. In the following, we shall derive the displacement fields of several simple elements frequently used in the finite-element analyses of structural and geotechnical engineering problems.

Truss element

The simplest truss element in the two-dimensional space has a node at each end, as shown in Fig. 9.1. The displacement at each node can be decomposed into the displacements in the x- and y-directions, respectively. Since the coordinates x and y within the truss element have a unique relation, i.e., $y = [1/(x_2 - x_1)][(y_2 - y_1)x + (y_1 x_2 - x_1 y_2)]$ where (x_1, y_1) and (x_2, y_2) are the coordinates of the nodes, either of the variable x or y becomes dependent to each other. Therefore, the displacement model (9.2) for the truss element can be reduced to the one-dimensional problem. Eliminating the y-variable in Eq. (9.4), for example, we have:

$$\phi = \alpha_1^* + \alpha_2^* x \tag{9.6a}$$

or in matrix form:

$$\phi = \begin{bmatrix} 1 & x \end{bmatrix} \begin{bmatrix} \alpha_1^* & \alpha_2^* \end{bmatrix}^{\mathrm{T}} \tag{9.6b}$$

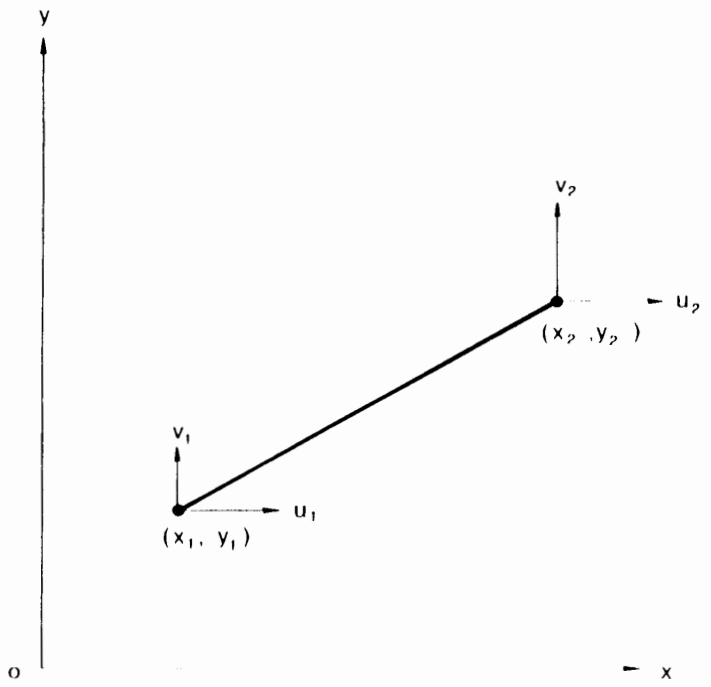

Fig. 9.1. Truss element in two dimensions.

Therefore, the variable of displacement field at each node is obtained by substituting the coordinates x_1 and x_2, respectively:

$$\phi_1 = \alpha_1^* + \alpha_2^* x_1 \tag{9.7a}$$

$$\phi_2 = \alpha_1^* + \alpha_2^* x_2 \tag{9.7b}$$

or in matrix form:

$$\begin{Bmatrix} \phi_1 \\ \phi_2 \end{Bmatrix} = \begin{bmatrix} 1 & x_1 \\ 1 & x_2 \end{bmatrix} \begin{Bmatrix} \alpha_1^* \\ \alpha_2^* \end{Bmatrix} \tag{9.8}$$

The solutions for the generalized coordinates α_1^* and α_2^* are written as from Eq. (9.7):

$$\alpha_1^* = \frac{\phi_1 x_2 - \phi_2 x_1}{x_2 - x_1} \tag{9.9a}$$

$$\alpha_2^* = \frac{\phi_2 - \phi_1}{x_2 - x_1} \tag{9.9b}$$

or in matrix form:

$$\begin{Bmatrix} \alpha_1^* \\ \alpha_2^* \end{Bmatrix} = \frac{1}{x_2 - x_1} \begin{bmatrix} x_2 & -x_1 \\ -1 & 1 \end{bmatrix} \begin{Bmatrix} \Phi_1 \\ \Phi_2 \end{Bmatrix} \tag{9.10}$$

Substitution of the generalized coordinates (α_1^*, α_2^*) in Eq. (9.10) into Eq. (9.6) leads to:

$$\phi = \frac{1}{x_2 - x_1} [x_2 - x \quad x - x_1][\Phi_1 \quad \Phi_2]^T = [N_1 \quad N_2][\Phi_1 \quad \Phi_2]^T \tag{9.11a}$$

in which

$$[N_1 \quad N_2] = \begin{bmatrix} \dfrac{x_2 - x}{x_2 - x_1} & \dfrac{x - x_1}{x_2 - x_1} \end{bmatrix} \tag{9.11b}$$

N_1 and N_2 are the so-called *linear shape functions* corresponding to the displacement field variables Φ_1 and Φ_2, respectively. Note that a linear shape function N_1 has values of unit and zero at nodes 1 and 2, respectively, while N_2 has such values at nodes 2 and 1. Since the displacement at a node is decomposed into the two directions such as the x- and y-directions, i.e., (U_1, V_1) at node 1 and (U_2, V_2) at node 2, the functions of displacement fields u and v are expressed by utilizing Eq. (9.11):

$$\begin{Bmatrix} u \\ v \end{Bmatrix} = \begin{bmatrix} N_1 & N_2 & 0 & 0 \\ 0 & 0 & N_1 & N_2 \end{bmatrix} \begin{Bmatrix} U_1 \\ U_2 \\ V_1 \\ V_2 \end{Bmatrix} \tag{9.12}$$

Triangular element

Here, we shall present a procedure to construct the shape functions of the simplest three-node triangular element which is most often used in the two-dimensional analysis of continuum mechanics, as shown in Fig. 9.2. Since the three-node triangular element has three different values of displacement field at three nodes, Eq. (9.4a) can be used as the polynomial function for the displacement field ϕ. Equation (9.4a) may be expressed in matrix form:

$$\phi = [A]\{\alpha\} \tag{9.13a}$$

in which

$$[A] = [1 \quad x \quad y] \tag{9.13b}$$

$$\{\alpha\} = [\alpha_1 \quad \alpha_2 \quad \alpha_3]^T \tag{9.13c}$$

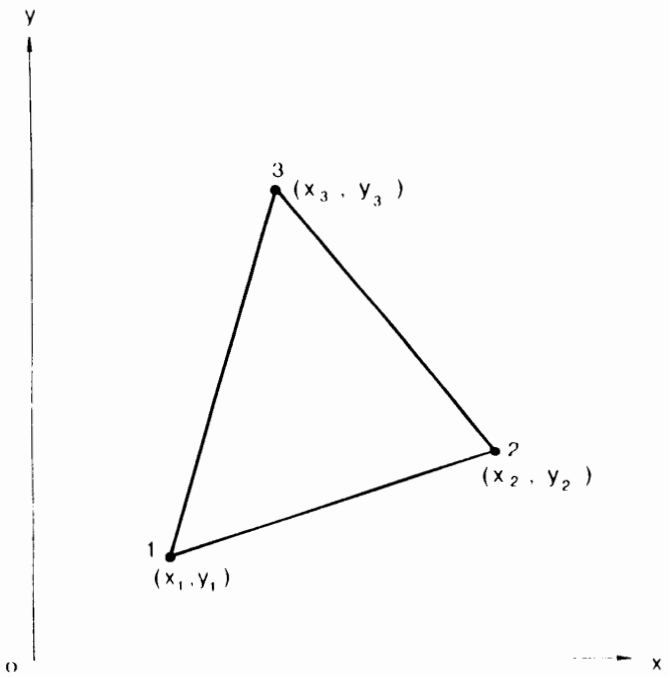

Fig. 9.2. Triangular element in two dimensions.

The values of field variable for displacement at three nodes corresponding to the coordinates (x_1, y_1), (x_2, y_2), and (x_3, y_3) are respectively:

$$\phi_1 = \alpha_1 + \alpha_2 x_1 + \alpha_3 y_1 \tag{9.14a}$$

$$\phi_2 = \alpha_1 + \alpha_2 x_2 + \alpha_3 y_2 \tag{9.14b}$$

$$\phi_3 = \alpha_1 + \alpha_2 x_3 + \alpha_3 y_3 \tag{9.14c}$$

or in matrix form:

$$\{\phi\} = [G]\{\alpha\} \tag{9.15a}$$

in which

$$\{\phi\} = [\phi_1 \quad \phi_2 \quad \phi_3]^T \tag{9.15b}$$

$$[G] = \begin{bmatrix} 1 & x_1 & y_1 \\ 1 & x_2 & y_2 \\ 1 & x_3 & y_3 \end{bmatrix} \tag{9.15c}$$

The vector of generalized coordinates, $\{\alpha\}$, can be solved from Eq. (9.15a), that is:

$$\{\alpha\} = [G]^{-1}\{\Phi\} \tag{9.16}$$

Substituting Eq. (9.16) into Eq. (9.13a), we find the general displacement field variable for the triangular element:

$$\phi = [A][G]^{-1}\{\Phi\} = [N]\{\Phi\} \tag{9.17a}$$

in which

$$[N] = [N_1 \quad N_2 \quad N_3] \tag{9.17b}$$

Similar to the case of truss element, the displacement field functions u and v in the x- and y-directions can be represented by utilizing Eq. (9.17), i.e.:

$$\begin{Bmatrix} u \\ v \end{Bmatrix} = \begin{bmatrix} [N] & [0] \\ [0] & [N] \end{bmatrix} \begin{Bmatrix} \{U\} \\ \{V\} \end{Bmatrix} \tag{9.18a}$$

where

$$\{U\} = [U_1 \quad U_2 \quad U_3]^T \tag{9.18b}$$

$$\{V\} = [V_1 \quad V_2 \quad V_3]^T \tag{9.18c}$$

Rectangular element

As shown in Fig. 9.3, we shall consider a rectangular element which has four corner nodes. As the field variable ϕ of displacement, the four-term polynomial can be employed in this case by substituting $\alpha_4 = \alpha_6 = 0$ into Eq. (9.5a), that is:

$$\phi(x, y) = \alpha_1 + \alpha_2 x + \alpha_3 y + \alpha_5 xy \tag{9.19a}$$

or in matrix form:

$$\phi(x, y) = [A]\{\alpha\} \tag{9.19b}$$

in which

$$[A] = [1 \quad x \quad y \quad xy] \tag{9.19c}$$

$$\{\alpha\} = [\alpha_1 \quad \alpha_2 \quad \alpha_3 \quad \alpha_5]^T \tag{9.19d}$$

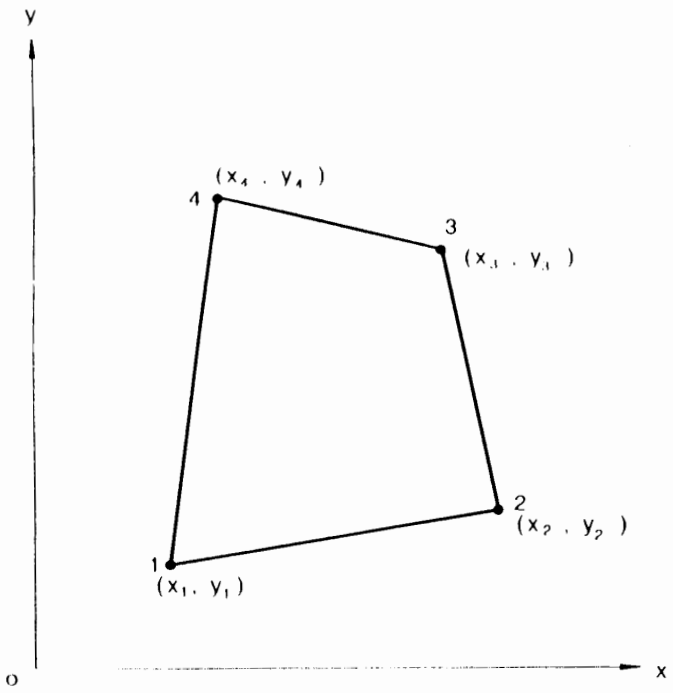

Fig. 9.3. Rectangular element in two dimensions.

The values Φ_i of field variable ϕ at the four nodes are:

$$\Phi_1 = \alpha_1 + \alpha_2 x_1 + \alpha_3 y_1 + \alpha_5 x_1 y_1 \tag{9.20a}$$

$$\Phi_2 = \alpha_1 + \alpha_2 x_2 + \alpha_3 y_2 + \alpha_5 x_2 y_2 \tag{9.20b}$$

$$\Phi_3 = \alpha_1 + \alpha_2 x_3 + \alpha_3 y_3 + \alpha_5 x_3 y_3 \tag{9.20c}$$

$$\Phi_4 = \alpha_1 + \alpha_2 x_4 + \alpha_3 y_4 + \alpha_5 x_4 y_4 \tag{9.20d}$$

or in matrix form:

$$\{\Phi\} = [G]\{\alpha\} \tag{9.21}$$

where $\{\Phi\} = [\Phi_1 \quad \Phi_2 \quad \Phi_3 \quad \Phi_4]^T$, $\{\alpha\} = [\alpha_1 \quad \alpha_2 \quad \alpha_3 \quad \alpha_5]^T$, and matrix $[G]$ can be written as:

$$[G] = \begin{bmatrix} 1 & x_1 & y_1 & x_1 y_1 \\ 1 & x_2 & y_2 & x_2 y_2 \\ 1 & x_3 & y_3 & x_3 y_3 \\ 1 & x_4 & y_4 & x_4 y_4 \end{bmatrix} \tag{9.22}$$

The general field variable ϕ for displacement can be similarly expressed by the form of Eq. (9.17), and therefore the displacement field functions u and v can be given by Eq. (9.18a) where $\{U\} = [U_1 \quad U_2 \quad U_3 \quad U_4]^T$ and $\{V\} = [V_1 \quad V_2 \quad V_3 \quad V_4]^T$. Using the same procedure for the generalized coordinate displacement model discussed above, the displacement field for the three-dimensional elements can also be constructed.

9.2.2 *Interpolation displacement model*

To find the function of field variable ϕ as well as the shape functions N_i by employing the generalized-coordinate displacement model in the preceding Section, we need always to compute the inverse of matrix $[G]$. In some cases, however, it would happen that the form of $[G]^{-1}$ may not be obtained (Irons et al., 1968). Even when it exists, much computational efforts will be required for a large number of elements with many degrees of freedom. In this Section, therefore, we shall introduce an alternative procedure to find the function of field variable ϕ and the interpolation functions N_i directly by employing the *natural coordinate system* presented in the following.

Natural coordinate systems

The *natural coordinate system* is a local coordinate system associated with each discretized element in a structure. It is important to note that magnitude of each natural coordinate is designed not to exceed the unity; it has generally a unit value at one node of element and zero value at the other nodes. An advantage of the natural coordinate system is a simple calculation of volume integration when an *element stiffness matrix* is constructed. In the following, we shall introduce various natural coordinate systems in one, two, and three dimensions.

One-dimensional case. As an example of the natural coordinate system in one dimension, we shall consider a line element as shown in Fig. 9.4. As the natural coordinates we select L_1 and L_2 given by:

$$L_1 = l_2/l \tag{9.23a}$$

$$L_2 = l_1/l \tag{9.23b}$$

where l is the length of line element, and l_1 and l_2 are respectively the distances

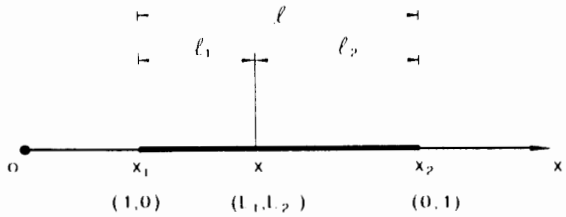

Fig. 9.4. Length coordinates.

between the left node 1 and the arbitrary point within the line element, and between the right node 2 and the arbitrary point, then the *linear* geometrical relationship between the natural coordinates (L_1, L_2) and the global coordinate x within a line element is thus written as:

$$x = L_1 x_1 + L_2 x_2 \tag{9.24}$$

where x_1 and x_2 are respectively the global coordinates at nodes 1 and 2. Note that since we have a relation of $L_1 + L_2 = 1$ from Eq. (9.23), only one of the natural coordinates is independent. Also, the matrix form of Eqs. (9.23) and (9.24) can be represented as:

$$\begin{Bmatrix} 1 \\ x \end{Bmatrix} = \begin{bmatrix} 1 & 1 \\ x_1 & x_2 \end{bmatrix} \begin{Bmatrix} L_1 \\ L_2 \end{Bmatrix} \tag{9.25}$$

The inversed form for the natural coordinates (L_1, L_2) is then written as:

$$\begin{Bmatrix} L_1 \\ L_2 \end{Bmatrix} = \frac{1}{l} \begin{bmatrix} x_2 & -1 \\ -x_1 & 1 \end{bmatrix} \begin{Bmatrix} 1 \\ x \end{Bmatrix} \tag{9.26}$$

Such natural coordinates L_1 and L_2 are known as the *length coordinates*.

Two-dimensional case.

(A) *Triangular element*. Firstly, we shall consider the natural coordinates of a triangular element. By choosing the natural coordinates L_1, L_2, and L_3 which have respectively a zero value along one boundary of a triangle and a unit value at the node opposite to its boundary, as shown in Fig. 9.5, the *linear* geometrical relationship between the global coordinates (x, y) and the natural coordinates (L_1, L_2, L_3) within a triangular element may be written as:

$$x = L_1 x_1 + L_2 x_2 + L_3 x_3 \tag{9.27a}$$

$$y = L_1 y_1 + L_2 y_2 + L_3 y_3 \tag{9.27b}$$

where x_i and y_i ($i = 1, 2, 3$) are the global coordinates at the node i. At the nodes 1, 2, and 3 in Fig. 9.5, the natural coordinates (L_1, L_2, L_3) are respectively (1, 0, 0), (0, 1, 0), and (0, 0, 1). Similar to the one-dimensional case, we impose an additional condition such as:

$$L_1 + L_2 + L_3 = 1 \tag{9.27c}$$

Also, the matrix form of Eqs. (9.27a - c) can be represented as:

$$\begin{Bmatrix} 1 \\ x \\ y \end{Bmatrix} = \begin{bmatrix} 1 & 1 & 1 \\ x_1 & x_2 & x_3 \\ y_1 & y_2 & y_3 \end{bmatrix} \begin{Bmatrix} L_1 \\ L_2 \\ L_3 \end{Bmatrix} \tag{9.28}$$

Solving Eq. (9.28) for the natural coordinates L_1, L_2, and L_3, we obtain:

$$L_1 = A_1/A \tag{9.29a}$$

$$L_2 = A_2/A \tag{9.29b}$$

$$L_3 = A_3/A \tag{9.29c}$$

where A, A_1, A_2, and A_3 are respectively the area of triangle element and subareas as shown in Fig. 9.5. These are written in terms of the global coordinates as:

$$A = \tfrac{1}{2}\left[(y_2 - y_3)(x_1 - x_3) - (x_2 - x_3)(y_1 - y_3)\right] \tag{9.30a}$$

$$A_1 = \tfrac{1}{2}\left[(y - y_2)(x_3 - x_2) - (x - x_2)(y_3 - y_2)\right] \tag{9.30b}$$

$$A_2 = \tfrac{1}{2}\left[(y - y_3)(x_1 - x_3) - (x - x_3)(y_1 - y_3)\right] \tag{9.30c}$$

$$A_3 = \tfrac{1}{2}\left[(y - y_1)(x_2 - x_1) - (x - x_1)(y_2 - y_1)\right] \tag{9.30d}$$

The inverse form of Eq. (9.28) can then be presented as:

$$\begin{Bmatrix} L_1 \\ L_2 \\ L_3 \end{Bmatrix} = \frac{1}{2A}\begin{bmatrix} a_1 & b_1 & c_1 \\ a_2 & b_2 & c_2 \\ a_3 & b_3 & c_3 \end{bmatrix}\begin{Bmatrix} 1 \\ x \\ y \end{Bmatrix} \tag{9.31}$$

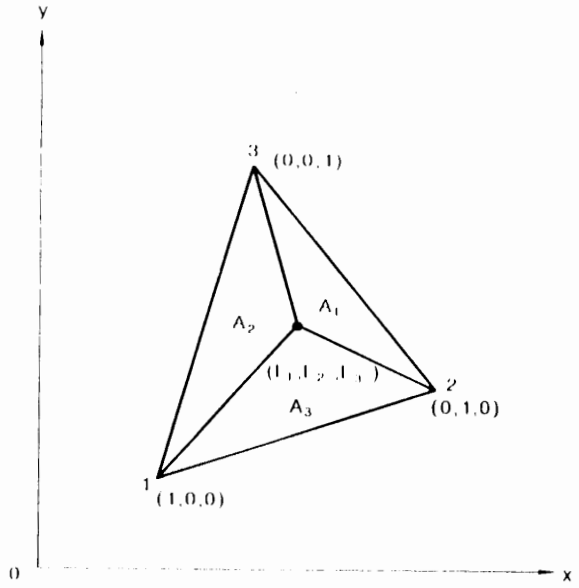

Fig. 9.5. Area coordinates.

where

$$a_1 = x_2y_3 - y_2x_3, \quad b_1 = y_2 - y_3, \quad c_1 = x_3 - x_2 \tag{9.32a}$$

$$a_2 = x_3y_1 - y_3x_1, \quad b_2 = y_3 - y_1, \quad c_2 = x_1 - x_3 \tag{9.32b}$$

$$a_3 = x_1y_2 - y_1x_2, \quad b_3 = y_1 - y_2, \quad c_3 = x_2 - x_1 \tag{9.32c}$$

The natural coordinates L_1, L_2, and L_3 described above are generally called the *area coordinates*.

(B) *Quadrilateral element*. Secondly, we shall consider the natural coordinates of the quadrilateral element in two dimensions, as shown in Fig. 9.6 where the natural coordinates (ξ, η) take values between -1 and $+1$, respectively. The *linear* geometrical relationship between the global coordinates and the natural coordinates inside an element is written as:

$$x = L_1x_1 + L_2x_2 + L_3x_3 + L_4x_4 \tag{9.33a}$$

$$y = L_1y_1 + L_2y_2 + L_3y_3 + L_4y_4 \tag{9.33b}$$

where x_i and y_i $(i = 1, 2, 3, 4)$ are the global coordinates at the node i and L_i are defined as:

$$L_1 = \tfrac{1}{4}(1 - \xi)(1 - \eta), \quad L_2 = \tfrac{1}{4}(1 + \xi)(1 - \eta) \tag{9.34a}$$

$$L_3 = \tfrac{1}{4}(1 + \xi)(1 + \eta), \quad L_4 = \tfrac{1}{4}(1 - \xi)(1 + \eta) \tag{9.34b}$$

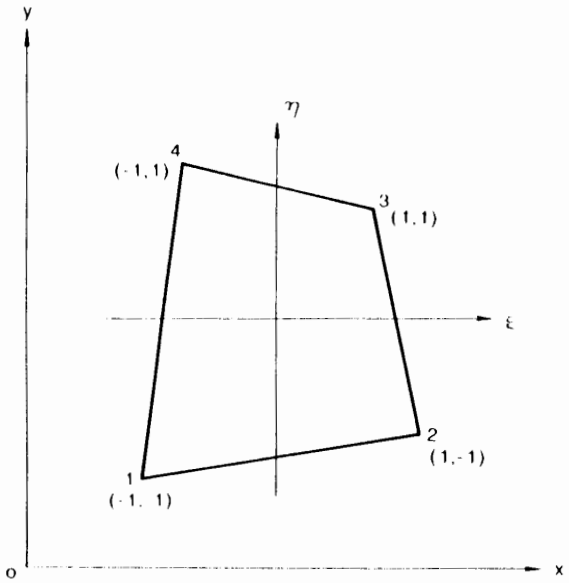

Fig. 9.6. Quadrilateral coordinates.

It should be noted that L_i takes a unit value at node i and zero values at the other nodes, respectively.

Three-dimensional case

(A) *Tetrahedral element.* Extending the procedure for the construction of the natural coordinates (the area coordinates) of the triangular element, we shall herein introduce the natural coordinates of a tetrahedron element in three dimensions, as shown in Fig. 9.7. Introducing the natural coordinates, L_1, L_2, L_3, and L_4, which have respectively a unit value at a corresponding node and zero value on a plane constructed by the other three nodes, a linear geometrical relationship between the global coordinates and the natural coordinates inside an element may be written in an analogous manner to the triangular element, that is:

$$1 = L_1 + L_2 + L_3 + L_4 \tag{9.35a}$$

$$x = L_1x_1 + L_2x_2 + L_3x_3 + L_4x_4 \tag{9.35b}$$

$$y = L_1y_1 + L_2y_2 + L_3y_3 + L_4y_4 \tag{9.35c}$$

$$z = L_1z_1 + L_2z_2 + L_3z_3 + L_4z_4 \tag{9.35d}$$

or in matrix form:

$$\begin{Bmatrix} 1 \\ x \\ y \\ z \end{Bmatrix} = \begin{bmatrix} 1 & 1 & 1 & 1 \\ x_1 & x_2 & x_3 & x_4 \\ y_1 & y_2 & y_3 & y_4 \\ z_1 & z_2 & z_3 & z_4 \end{bmatrix} \begin{Bmatrix} L_1 \\ L_2 \\ L_3 \\ L_4 \end{Bmatrix} \tag{9.36}$$

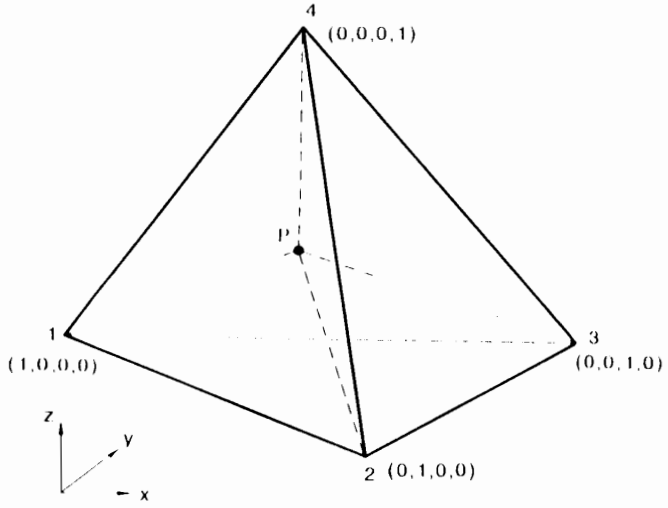

Fig. 9.7. Tetrahedral coordinates.

Solving Eq. (9.35a–d) for natural coordinates L_i ($i = 1$–4), we obtain:

$$L_i = \frac{V_i}{V} \tag{9.37}$$

where V and V_i are respectively the volume of tetrahedron 1-2-3-4 and subtetrahedron P-2-3-4, P-1-3-4, P-1-2-4, or P-1-2-3 as shown in Fig. 9.7, and these are written as:

$$V = \frac{1}{6}\begin{vmatrix} 1 & 1 & 1 & 1 \\ x_1 & x_2 & x_3 & x_4 \\ y_1 & y_2 & y_3 & y_4 \\ z_1 & z_2 & z_3 & z_4 \end{vmatrix} \tag{9.38}$$

and

$$V_i = a_i + b_i x + c_i y + d_i z \quad (i = 1\text{–}4) \tag{9.39}$$

As an example, a_1, b_1, c_1, and d_1 are written as follows:

$$a_1 = \frac{1}{6}\begin{vmatrix} x_2 & x_3 & x_4 \\ y_2 & y_3 & y_4 \\ z_2 & z_3 & z_4 \end{vmatrix}, \quad b_1 = -\frac{1}{6}\begin{vmatrix} 1 & 1 & 1 \\ y_2 & y_3 & y_4 \\ z_2 & z_3 & z_4 \end{vmatrix} \tag{9.40a}$$

$$c_1 = \frac{1}{6}\begin{vmatrix} 1 & 1 & 1 \\ x_2 & x_3 & x_4 \\ z_2 & z_3 & z_4 \end{vmatrix}, \quad d_1 = -\frac{1}{6}\begin{vmatrix} 1 & 1 & 1 \\ x_2 & x_3 & x_4 \\ y_2 & y_3 & y_4 \end{vmatrix} \tag{9.40b}$$

The other constants a_2, b_2, ..., c_4, and d_4 can be simply obtained by a cyclic permutation of subscripts, 1, 2, 3, and 4. The natural coordinates L_i defined in Eq. (9.37) are generally called the *volume coordinates*.

(B) *Hexahedral element*. Extending the natural coordinates (ξ, η) in two-dimensional quadrilateral element, we shall explain the natural coordinates (ξ, η, ζ) of the hexahedral element in three dimensions, as shown in Fig. 9.8. The natural coordinates (ξ, η, ζ) take the value between -1 and $+1$. The *linear* geometrical relationship between the global and natural coordinates inside an element can be presented by:

$$x = L_1 x_1 + L_2 x_2 + L_3 x_3 + L_4 x_4 + L_5 x_5 + L_6 x_6 + L_7 x_7 + L_8 x_8 \tag{9.41a}$$

$$y = L_1 y_1 + L_2 y_2 + L_3 y_3 + L_4 y_4 + L_5 y_5 + L_6 y_6 + L_7 y_7 + L_8 y_8 \tag{9.41b}$$

$$z = L_1 z_1 + L_2 z_2 + L_3 z_3 + L_4 z_4 + L_5 z_5 + L_6 z_6 + L_7 z_7 + L_8 z_8 \tag{9.41c}$$

where x_i and y_i ($i = 1$–8) are the global coordinates at the node i, and L_i are

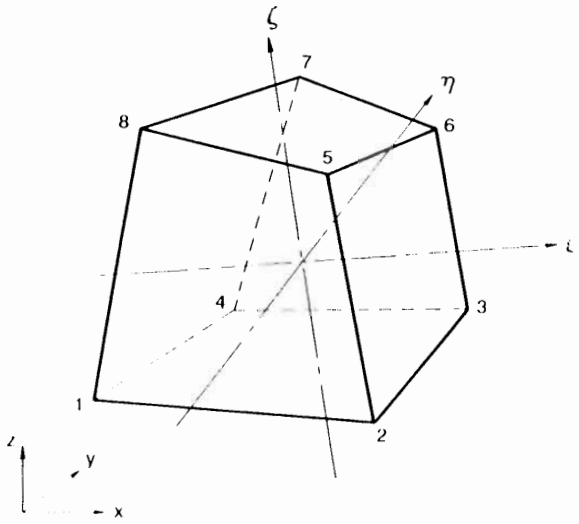

Fig. 9.8. Hexahedral coordinates.

functions of the natural coordinates (ξ, η, ζ) and take a unit value at node i and zero values at the other seven nodes. Similar to the quadrilateral element, these can be written as:

$$\begin{aligned} I_1 &= \tfrac{1}{8}(1-\xi)(1-\eta)(1-\zeta), \quad & I_2 &= \tfrac{1}{8}(1+\xi)(1-\eta)(1-\zeta) \\ I_3 &= \tfrac{1}{8}(1+\xi)(1+\eta)(1-\zeta), \quad & I_4 &= \tfrac{1}{8}(1-\xi)(1+\eta)(1-\zeta) \\ I_5 &= \tfrac{1}{8}(1+\xi)(1-\eta)(1+\zeta), \quad & I_6 &= \tfrac{1}{8}(1+\xi)(1+\eta)(1+\zeta) \\ I_7 &= \tfrac{1}{8}(1-\xi)(1+\eta)(1+\zeta), \quad & I_8 &= \tfrac{1}{8}(1-\xi)(1-\eta)(1+\zeta) \end{aligned} \tag{9.42}$$

or in indicial notation:

$$I_i = \tfrac{1}{8}(1+\xi_i\xi)(1+\eta_i\eta)(1+\zeta_i\zeta), \quad i = 1,\ldots,8 \tag{9.43}$$

where ξ_i, η_i, and ζ_i are the natural coordinates at node i.

Concept of the interpolation displacement model

Utilizing the natural coordinate system presented above, we shall here explain the procedure to construct directly the interpolation functions or shape functions, N_i, which have unit value at node i and zero values at all other nodes. A displacement field so constructed is in general called the *interpolation displacement model*. Being different from the generalized-coordinate displacement model discussed previously, the calculation of the inversed matrix $[G]^{-1}$ is no longer required for the interpolation displacement model.

For example, consider the displacement field constructed by the interpolation function for the one-dimensional line element. The field variable ϕ for displacement may be expressed as:

$$\phi = N_1\Phi_1 + N_2\Phi_2 \tag{9.44a}$$

or in matrix form:

$$\phi = [N_1 \quad N_2][\Phi_1 \quad \Phi_2]^{\mathrm{T}} \tag{9.44b}$$

where Φ_1 and Φ_2 are values of field variable ϕ at nodal points, and N_1 and N_2 are respectively written directly in terms of the natural coordinates such as the length coordinates L_1 and L_2 defined by Eq. (9.26), that is:

$$N_1 = L_1 = \frac{1}{l}(x_2 - x) \tag{9.45a}$$

$$N_2 = L_2 = \frac{1}{l}(-x_1 + x) \tag{9.45b}$$

The schematic aspect of the linear interpolation functions N_1 and N_2 is shown in Fig. 9.9.

As can be understood from the comparison between Eqs. (9.24) and (9.44a), the *geometrical field* x and *displacement field* ϕ can be presented respectively by the same form:

$$x = [N_1 \quad N_2][x_1 \quad x_2]^{\mathrm{T}} \quad \text{and} \quad \phi = [N_1 \quad N_2][\Phi_1 \quad \Phi_2]^{\mathrm{T}} \tag{9.46}$$

When the field variable ϕ for displacement is presented in the same form and the

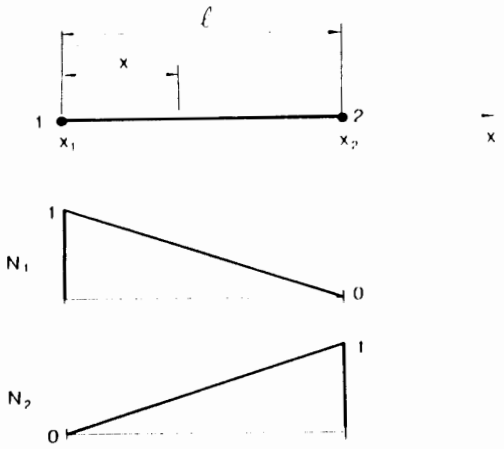

Fig. 9.9. Linear interpolation functions for a line element.

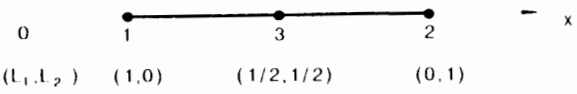

Fig. 9.10. Three-node truss element.

same order as that of the geometrical field, a finite-element constructed in such a manner is called the *isoparametric element* (Zienkiewicz et al., 1969).

Substituting Eq. (9.45) into Eq. (9.44a), the displacement field is expressed as:

$$\phi = \frac{1}{l}(x_2 - x)\Phi_1 + \frac{1}{l}(-x_1 + x)\Phi_2$$

$$= \frac{1}{l}(x_2\Phi_1 - x_1\Phi_2) + \frac{1}{l}(\Phi_2 - \Phi_1)x \tag{9.47}$$

Note that the above equation has exactly the same form as that of Eq. (9.6a) with Eq. (9.9) that is given by the generalized-coordinate displacement model in Section 9.2.1.

Next, consider the interpolation functions N_i of the three-node truss element as shown in Fig. 9.10. In this case, the interpolation functions N_1, N_2, and N_3 corresponding to the nodal points 1, 2, and 3 are expressed in the quadratic form of the length coordinates L_1 and L_2, i.e.:

$$N_1 = L_1(2L_1 - 1) \tag{9.48a}$$

$$N_2 = L_2(2L_2 - 1) \tag{9.48b}$$

$$N_3 = 4L_1L_2 \tag{9.48c}$$

These three quadratic interpolation functions are shown in Fig. 9.11 where each magnitude of the interpolation functions becomes a unit value at a specific node and zero values at other two nodes. The field variable ϕ for displacement is thus written as:

$$\phi = N_1\Phi_1 + N_2\Phi_2 + N_3\Phi_3 \tag{9.49a}$$

or in matrix form:

$$\phi = [N_1 \quad N_2 \quad N_3][\Phi_1 \quad \Phi_2 \quad \Phi_3]^T \tag{9.49b}$$

The linear interpolation functions N_1, N_2, and N_3 of the two-dimensional triangular element as shown in Fig. 9.5 can be presented directly in terms of the natural coordinates, i.e., the area coordinates:

$$N_1 = L_1, \quad N_2 = L_2, \quad N_3 = L_3 \tag{9.50}$$

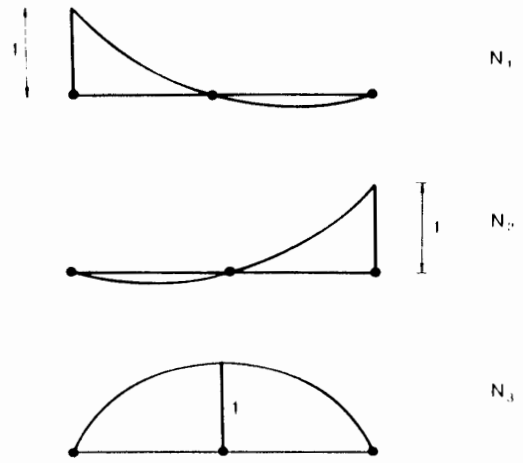

Fig. 9.11. Interpolation functions for a three-node line element.

As an example, the schematic aspect of the linear interpolation function N_1 of the triangular element is shown in Fig. 9.12. Therefore, the displacement fields u in the x-direction and v in the y-direction can be expressed by:

$$u = L_1U_1 + L_2U_2 + L_3U_3 \tag{9.51a}$$

$$v = L_1V_1 + L_2V_2 + L_3V_3 \tag{9.51b}$$

or in matrix form:

$$\begin{Bmatrix} u \\ v \end{Bmatrix} = \begin{bmatrix} L_1 & L_2 & L_3 & 0 & 0 & 0 \\ 0 & 0 & 0 & L_1 & L_2 & L_3 \end{bmatrix} \{U\} \tag{9.52}$$

where $\{U\} = [U_1 \quad U_2 \quad U_3 \quad V_1 \quad V_2 \quad V_3]^T$.

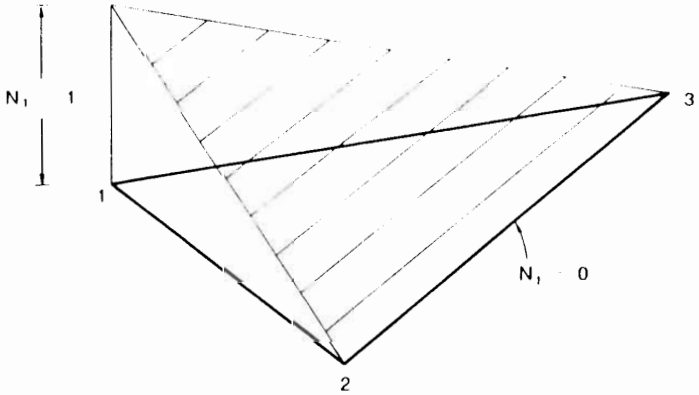

Fig. 9.12. Interpolation function N_1 for a triangular element.

9.2.3 *Shape functions for various finite elements*

In this Section, we shall introduce the several more shape functions N_i (or interpolation functions) constructed on the basis of natural coordinates explained in the preceding Section.

Triangular elements

The shape functions N_i of the higher-order triangular elements as shown in Figs. 9.13a–9.13d become the 2nd-, 3rd-, 4th- and 5th-order polynomials that require the values of the field variable at 6 nodes, 10 nodes, 15 nodes, and 21 nodes, respectively. In the following, we shall explain the procedure to obtain the general shape functions for the higher-order triangular elements (Silvester, 1969).

By introducing the three-digit identification (α, β, γ) for an arbitrary nodal point within the element as shown in Fig. 9.14, Silvester (1969) presented the general interpolation function $N_{\alpha\beta\gamma}$ at the nodal point with three-digit identification (α, β, γ) for the mth-order triangular element that has the nodal points of $\frac{1}{2}(m+1)(m+2)$, that is:

$$N_{\alpha\beta\gamma} = N_\alpha(L_1)\,N_\beta(L_2)\,N_\gamma(L_3) \tag{9.53}$$

where L_1, L_2, and L_3 are the area coordinates discussed in Section 9.2.2, α, β, and γ are integers satisfying the condition $\alpha + \beta + \gamma = m$ for the identification of an arbitrary nodal point within the element, and the functions of N_α, N_β, and N_γ are

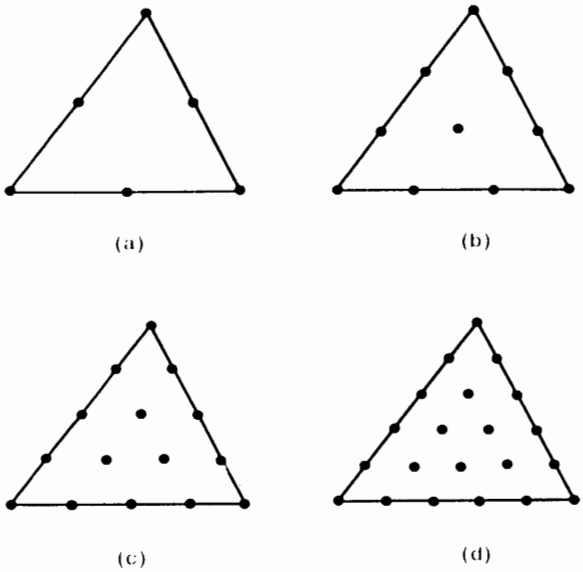

Fig. 9.13. Higher-order triangular elements.

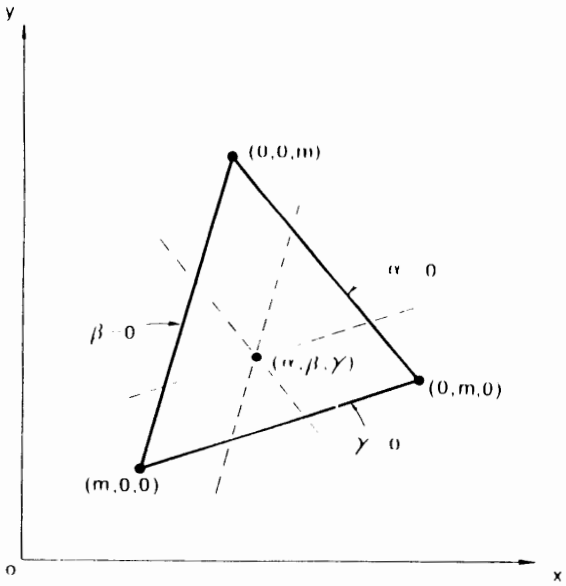

Fig. 9.14. Node identification for triangular elements.

written in terms of the natural coordinates L_1, L_2, and L_3, respectively, for example:

$$N_\alpha(L_1) = \prod_{i}^{\alpha}{}_{1}\left[\frac{1}{i}(mL_1 - i + 1)\right] \quad \text{for } \alpha \geq 1 \tag{9.54a}$$

$$= 1 \qquad \text{for } \alpha = 0 \tag{9.54b}$$

in which Π denotes the product of all terms running from $i = 1$ to $i = \alpha$ and a similar form is applied to the functions $N_\beta(L_2)$ and $N_\gamma(L_3)$, respectively.

Utilizing the above formula (9.54), for example, we can construct the interpolation functions of the 10-node triangular element ($m = 3$) as shown in Fig. 9.13b. In this case, the interpolation functions such as N_{003}, N_{012}, N_{111}, and so on become the cubic polynomial and then the field variable ϕ for displacement is presented as:

$$\phi = N_{300}\Phi_1 + N_{030}\Phi_2 + N_{003}\Phi_3 + N_{210}\Phi_4 + N_{120}\Phi_5 + N_{021}\Phi_6 + N_{012}\Phi_7 + N_{102}\Phi_8 + N_{201}\Phi_9 + N_{111}\Phi_{10} \tag{9.55}$$

where $\Phi_1, \ldots, \Phi_{10}$ are the values of the field variable ϕ for displacement at 10 nodes, and the shape functions such as N_{300}, $N_{030}, \ldots$ and N_{111} are written from Eqs. (9.53) and (9.54), for example:

$$N_{030} = N_0(L_1)N_3(L_2)N_0(L_3) \tag{9.56}$$

in which

$$N_0(L_1) = 1 \tag{9.57a}$$

$$N_3(L_2) = \prod_{i}^{3} \prod_{1} \left[\frac{1}{i}(3L_2 - i + 1) \right]$$

$$= \tfrac{1}{1}(3L_2 - 1 + 1)\tfrac{1}{2}(3L_2 - 2 + 1)\tfrac{1}{3}(3L_2 - 3 + 1)$$

$$= \tfrac{1}{2}L_2(3L_2 - 1)(3L_2 - 2) \tag{9.57b}$$

$$N_0(L_3) = 1 \tag{9.57c}$$

Equation (9.56) can thus be expressed by:

$$N_{030} = \tfrac{1}{2}L_2(3L_2 - 1)(3L_2 - 2) \tag{9.58}$$

Similarly, the interpolation functions are constructed for the other two corner nodes:

$$N_{300} = \tfrac{1}{2}L_1(3L_1 - 1)(3L_1 - 2), \quad N_{003} = \tfrac{1}{2}L_3(3L_3 - 1)(3L_3 - 2) \tag{9.59a}$$

for the six nodes along the sides:

$$N_{210} = \tfrac{9}{2}L_1L_2(3L_1 - 1), \quad N_{120} = \tfrac{9}{2}L_1L_2(3L_2 - 1)$$

$$N_{021} = \tfrac{9}{2}L_2L_3(3L_2 - 1), \quad N_{012} = \tfrac{9}{2}L_2L_3(3L_3 - 1) \tag{9.59b}$$

$$N_{102} = \tfrac{9}{2}L_1L_3(3L_3 - 1), \quad N_{201} = \tfrac{9}{2}L_1L_3(3L_1 - 1)$$

and for the center node:

$$N_{111} = 27L_1L_2L_3 \tag{9.59c}$$

The shape functions for more higher-order triangular elements shown in Figs. 9.13c and 9.13d can be obtained in an analogous manner proposed by Silvester (1969).

Rectangular elements

For the four-node rectangular element, the *bilinear* shape functions (or interpolation functions) N_i are assumed to be the same as those from Eq. (9.34), on the basis of the isoparametric concept that the geometry and displacement within the element can be written in terms of the same parameter and of the same order, that is:

$$N_1 = L_1 = \tfrac{1}{4}(1 - \xi)(1 - \eta), \quad N_2 = L_2 = \tfrac{1}{4}(1 + \xi)(1 - \eta) \tag{9.60a}$$

$$(9.60b)$$

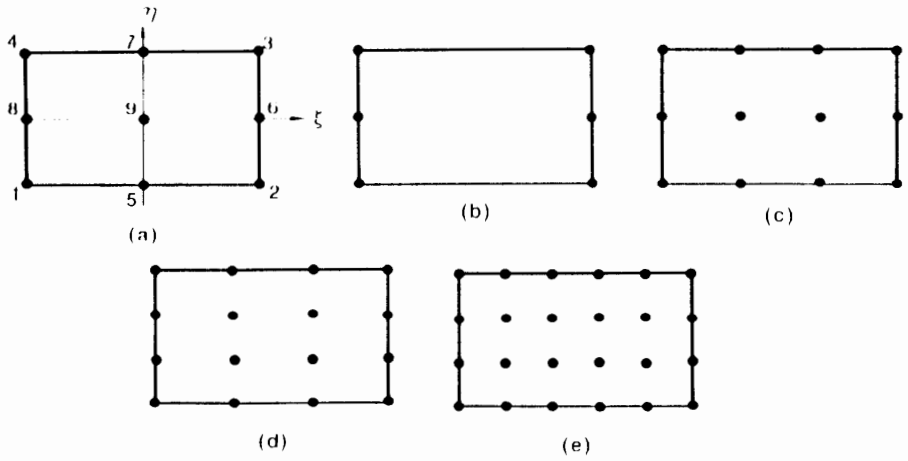

Fig. 9.15. Lagrange family of rectangular elements.

or in indicial notation:

$$N_i = \tfrac{1}{4}(1 + \xi_i \xi)(1 + \eta_i \eta) \tag{9.60c}$$

where ξ and η are the natural coordinates whose magnitudes take values between -1 and 1, and ξ_i and η_i are coordinates at node i.

Further, consider more higher-order rectangular elements shown in Fig. 9.15. The shape functions $N_k(\xi, \eta)$ for an arbitrary node k of such rectangular elements are written as the product of the *Lagrange polynomials*:

$$N_k(\xi, \eta) = L_k(\xi) L_k(\eta) \tag{9.61}$$

where L_k is the *Lagrange polynomial*. For example, the mth-order Lagrange polynomial $L_k(\xi)$ is defined as:

$$L_k(\xi) = \prod_{\substack{n=0 \\ n \neq k}}^{m} \frac{\xi - \xi_n}{\xi_k - \xi_n}$$

$$= \frac{(\xi - \xi_0) \ldots (\xi - \xi_{k-1})(\xi - \xi_{k+1}) \ldots (\xi - \xi_m)}{(\xi_k - \xi_0) \ldots (\xi_k - \xi_{k-1})(\xi_k - \xi_{k+1}) \ldots (\xi_k - \xi_m)} \tag{9.62}$$

The Lagrange polynomial $L_k(\eta)$ can also be written in a similar form as that of Eq. (9.62). The Lagrange polynomials $L_k(\xi)$ and $L_k(\eta)$ are characterized by giving unit value at a specified node k and zero values at the other nodes. For the bi-quadratic rectangular element in Fig. 9.15a, the shape functions are derived for four corner nodes:

$$N_1 = \tfrac{1}{4}\xi\eta(\xi - 1)(\eta - 1), \quad N_2 = \tfrac{1}{4}\xi\eta(\xi + 1)(\eta - 1),$$

$$N_3 = \tfrac{1}{4}\xi\eta(\xi + 1)(\eta + 1), \quad N_4 = \tfrac{1}{4}\xi\eta(\xi - 1)(\eta + 1)$$

or in indicial notation:

$$N_i = \tfrac{1}{4}\xi\eta(\xi + \xi_i)(\eta + \eta_i) \quad (i = 1, 2, 3 \text{ and } 4) \tag{9.63a}$$

for the four side nodes:

$$N_5 = \tfrac{1}{2}\eta(\eta - 1)(1 - \xi^2), \quad N_6 = \tfrac{1}{2}\xi(\xi + 1)(1 - \eta^2),$$

$$N_7 = \tfrac{1}{2}\eta(\eta + 1)(1 - \xi^2), \quad N_8 = \tfrac{1}{2}\xi(\xi - 1)(1 - \eta^2) \tag{9.63b}$$

and for the center node:

$$N_9 = (1 - \xi^2)(1 - \eta^2) \tag{9.63c}$$

In a similar manner, the shape functions for other higher-order rectangular finite elements (Fig. 9.15b–e) can be constructed. These elements are of the *Lagrange family*.

Next, consider the rectangular elements as shown in Fig. 9.16. These elements are known as the quadratic and cubic elements of the *serendipity family* (Ergatoudis et al., 1968). To construct the shape functions of such family, the Lagrange polynomial may not be directly utilized but may be obtained by *inspection*. We shall derive the shape function N_1 at node 1 with the natural coordinate $(\xi, \eta) = (-1, -1)$ for the quadratic element in Fig. 9.16a. The shape function N_1 can be evaluated by:

$$N_1 = N_1 \mid_{\text{bilinear}} - \tfrac{1}{2}N_5 - \tfrac{1}{2}N_8 \tag{9.64a}$$

where $N_1 \mid_{\text{bilinear}}$ is the bilinear shape function as given in Eq. (9.60a), and N_5 and N_8 are respectively the shape functions at the nodes 5 and 8, that is:

$$N_5 = \tfrac{1}{2}(1 - \xi^2)(1 - \eta), \quad N_8 = \tfrac{1}{2}(1 - \eta^2)(1 - \xi) \tag{9.64b}$$

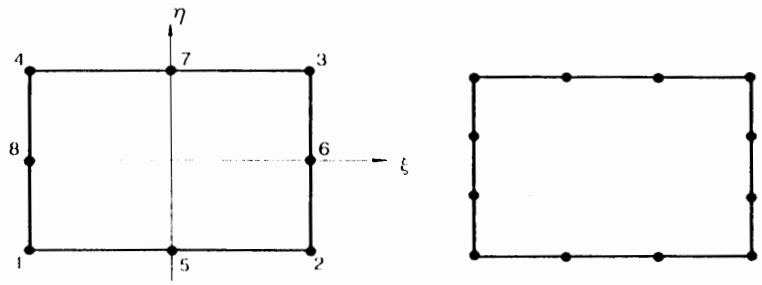

(a) Quadratic Type (b) Cubic Type

Fig. 9.16. Serendipity family of rectangular elements.

Substitution of (9.64b) into Eq. (9.64a) leads to:

$$N_1 = \tfrac{1}{4}(1-\xi)(1-\eta) - \tfrac{1}{4}(1-\xi^2)(1-\eta) - \tfrac{1}{4}(1-\eta^2)(1-\xi)$$
$$-\tfrac{1}{4}(1-\xi)(1-\eta)(-\xi-\eta-1) \tag{9.65a}$$

In general, the shape functions for four corner nodes can be presented in indicial notation ($i = 1, 2, 3$, and 4):

$$N_i = \tfrac{1}{4}(1+\xi_i\xi)(1+\eta_i\eta)(\xi_i\xi+\eta_i\eta-1) \tag{9.65b}$$

Also, for nodes 5 and 7 at $\xi = 0$, $\eta = \pm 1$, we have:

$$N_i = \tfrac{1}{2}(1-\xi^2)(1+\eta_i\eta) \tag{9.65c}$$

and for the nodes 6 and 8 at $\xi = \pm 1$ and $\eta = 0$, we have:

$$N_i = \tfrac{1}{2}(1+\xi_i\xi)(1-\eta^2) \tag{9.65d}$$

The shape functions for the cubic element in Fig. 9.16b are summarized in the following:

$$N_i = \tfrac{1}{32}(1+\xi_i\xi)(1+\eta_i\eta)\left[9(\xi^2+\eta^2)-10\right] \quad \text{for nodes at } \xi = \pm 1 \text{ and } \eta = \pm 1 \tag{9.66a}$$

$$N_i = \tfrac{9}{32}(1+\xi_i\xi)(1-\eta^2)(1+9\eta_i\eta) \quad \text{for nodes at } \xi = \pm 1 \text{ and } \eta = \pm \tfrac{1}{3} \tag{9.66b}$$

$$N_i = \tfrac{9}{32}(1+\eta_i\eta)(1-\xi^2)(1+9\xi_i\xi) \quad \text{for nodes at } \xi = \pm \tfrac{1}{3} \text{ and } \eta = \pm 1 \tag{9.66c}$$

Note that under the isoparametric assumption, the relation between the global coordinates (x, y) and the natural coordinates (ξ, η) is given by Eq. (9.33).

Tetrahedral elements

Consider now the shape functions of the family of tetrahedral elements shown in Fig. 9.17. The tetrahedral element is considered the extension of the two-dimensional triangular element to the three-dimensional element. Similar to that of the triangular element, Silvester (1972) expressed the general shape functions $N_{\alpha\beta\gamma\delta}$ of the mth-order tetrahedral element by assigning the four-digit identification $(\alpha, \beta, \gamma, \delta)$ to an arbitrary node within an element, that is:

$$N_{\alpha\beta\gamma\delta} = N_\alpha(L_1)\,N_\beta(L_2)\,N_\gamma(L_3)\,N_\delta(L_4)$$
$$\alpha+\beta+\gamma+\delta = m \tag{9.67}$$

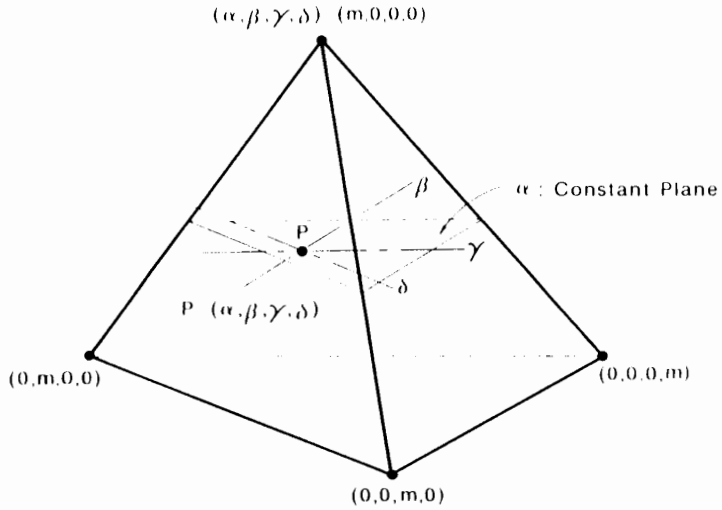

Fig. 9.17. Node identification for tetrahedral elements.

where L_i ($i = 1, 2, 3$ and 4) are in this case the volume coordinates and N_α, N_β, N_γ and N_δ are expressed respectively in terms of the volume coordinate, for example:

$$N_\alpha(L_1) = \prod_{i}^{\alpha} \prod_{1} \left[\frac{1}{i} (mL_1 - i + 1) \right] \quad \text{for } \alpha \geq 1 \tag{9.68a}$$

$$= 1 \qquad \text{for } \alpha = 0 \tag{9.68b}$$

where $\prod$ denotes the product of all terms and m is the order of the polynomial. The

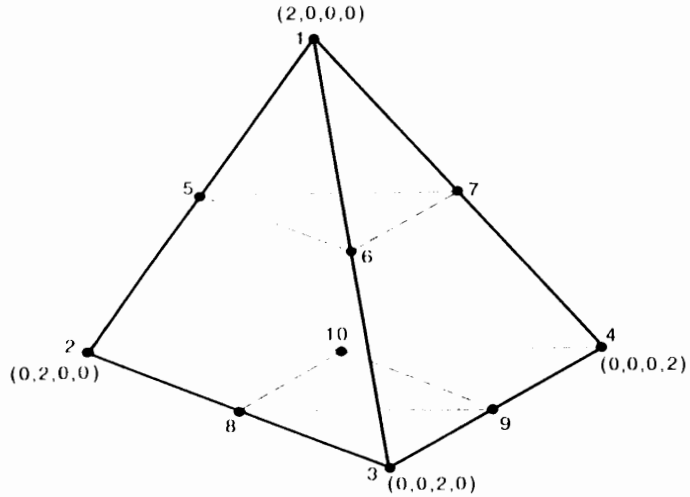

Fig. 9.18. 10-node tetrahedral element.

three other functions of N_β, N_γ and N_δ can be constructed in a similar manner as the form of Eq. (9.68).

Consider now the 10-node tetrahedral element as shown in Fig. 9.18. Since $m = 2$ in this case, for the corner node 1, we have:

$$N_{2000} = N_2(L_1)N_0(L_2)N_0(L_3)N_0(L_4)$$

$$= \tfrac{1}{1}(2L_1 - 1 + 1)\tfrac{1}{2}(2L_1 - 2 + 1) = L_1(2L_1 - 1) \tag{9.69a}$$

For the three other nodes, similar forms can be obtained:

$$N_{0200} = L_2(2L_2 - 1), \quad N_{0020} = L_3(2L_3 - 1), \quad N_{0002} = L_4(2L_4 - 1) \tag{9.69b}$$

For the six mid-nodes such as 5, 6, 7, 8, 9, and 10 along the boundaries, we have respectively:

$$N_{1100} = N_1(L_1)N_1(L_2)N_0(L_3)N_0(L_4) = 4L_1L_2 \tag{9.69c}$$

$$N_{1010} = 4L_1L_3, \quad N_{1001} = 4L_1L_4, \quad N_{0110} = 4L_2L_3,$$

$$N_{0011} = 4L_3L_4, \quad N_{0101} = 4L_2L_4 \tag{9.69d}$$

Similarly, the other higher-order elements can be constructed from formula (9.68).

Hexahedral elements

The Lagrange family and serendipity family of the rectangular elements in two dimensions can be easily extended to the hexahedral elements in three dimensions. We shall first consider the shape functions of the higher-order Lagrange element as shown in Fig. 9.19. Introducing the natural coordinates (ξ, η, ζ), the shape functions at an arbitrary node i of the mth-order hexahedral element are generally expressed as the product of the Lagrange polynomials L_i in the ξ-, η- and ζ-directions:

$$N_i(\xi, \eta, \zeta) = L_i(\xi)L_i(\eta)L_i(\zeta) \tag{9.70}$$

For example, the shape functions of the 27-node element shown in Fig. 9.19c are respectively written in indicial notation, for the eight corner nodes, $\xi = \pm 1$, $\eta = \pm 1$, and $\zeta = \pm 1$:

$$N_i = \tfrac{1}{8}\xi\eta\zeta(\xi + \xi_i)(\eta + \eta_i)(\zeta + \zeta_i) \tag{9.71a}$$

for the four side nodes, $\xi = \pm 1$, $\eta = \pm 1$, and $\zeta = 0$:

$$N_i = \tfrac{1}{4}\xi\eta(\xi + \xi_i)(\eta + \eta_i)(1 - \zeta^2) \tag{9.71b}$$

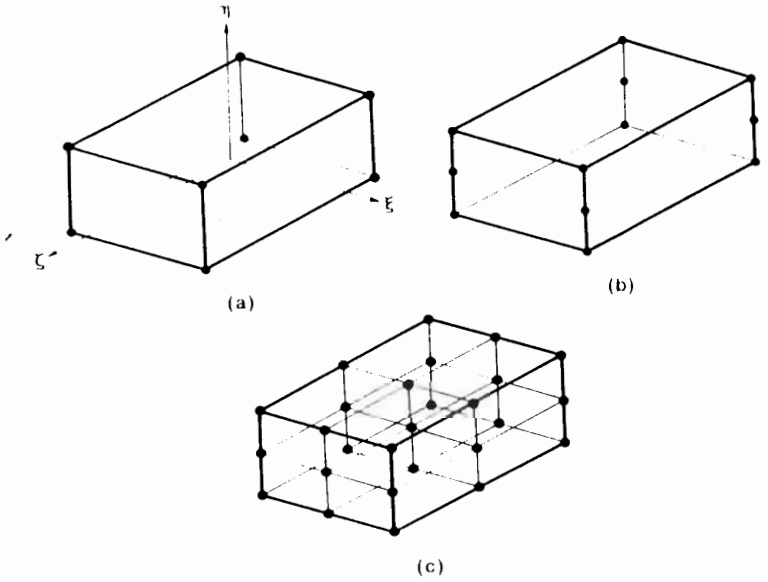

Fig. 9.19. Lagrange family of hexahedral elements.

for the four side nodes, $\xi = \pm 1$, $\eta = 0$, and $\zeta = \pm 1$:

$$N_i = \tfrac{1}{4}\xi\zeta(\xi + \xi_i)(1 - \eta^2)(\zeta + \zeta_i) \tag{9.71c}$$

for the four side nodes, $\xi = 0$, $\eta = \pm 1$, and $\zeta = \pm 1$:

$$N_i = \tfrac{1}{4}\eta\zeta(1 - \xi^2)(\eta + \eta_i)(\zeta + \zeta_i) \tag{9.71d}$$

for the two interior nodes, $\xi = \pm 1$, $\eta = 0$, and $\zeta = 0$:

$$N_i = \tfrac{1}{2}\xi(\xi + \xi_i)(1 - \eta^2)(1 - \zeta^2) \tag{9.71e}$$

for the two interior nodes, $\xi = 0$, $\eta = \pm 1$, and $\zeta = 0$:

$$N_i = \tfrac{1}{2}\eta(\eta + \eta_i)(1 - \xi^2)(1 - \zeta^2) \tag{9.71f}$$

for the two interior nodes, $\xi = 0$, $\eta = 0$, and $\zeta = \pm 1$:

$$N_i = \tfrac{1}{2}\zeta(\zeta + \zeta_i)(1 - \xi^2)(1 - \eta^2) \tag{9.71g}$$

and for the center node, $\xi = \eta = \zeta = 0$:

$$N_{\text{center}} = (1 - \xi^2)(1 - \eta^2)(1 - \zeta^2) \tag{9.71h}$$

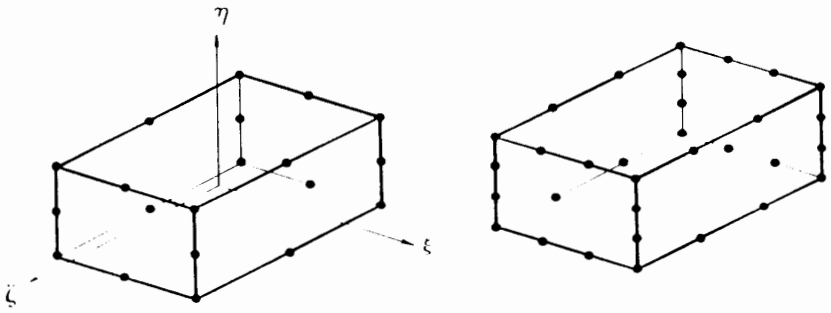

(a) 20 Node Element (b) 32 Node Element

Fig. 9.20. Serendipity family of hexahedral elements.

Furthermore, the shape functions of the serendipity family of the higher-order hexahedral elements as shown in Fig. 9.20 are summarized in the following:

20-node element (Fig. 9.20a)

For the eight corner nodes, $\xi = \pm 1$, $\eta = \pm 1$, and $\zeta = \pm 1$:

$$N_i = \tfrac{1}{8}(1 + \xi_i\xi)(1 + \eta_i\eta)(1 + \zeta_i\zeta)(\xi_i\xi + \eta_i\eta + \zeta_i\zeta - 2) \tag{9.72a}$$

For the four side nodes, $\xi = 0$, $\eta = \pm 1$, and $\zeta = \pm 1$:

$$N_i = \tfrac{1}{4}(1 - \xi^2)(1 + \eta_i\eta)(1 + \zeta_i\zeta) \tag{9.72b}$$

For the four side nodes, $\xi = \pm 1$, $\eta = 0$, and $\zeta = \pm 1$:

$$N_i = \tfrac{1}{4}(1 + \xi_i\xi)(1 - \eta^2)(1 + \zeta_i\zeta) \tag{9.72c}$$

For the four side nodes, $\xi = \pm 1$, $\eta = \pm 1$, and $\zeta = 0$:

$$N_i = \tfrac{1}{4}(1 + \xi_i\xi)(1 + \eta_i\eta)(1 - \zeta^2) \tag{9.72d}$$

32-node element (Fig. 9.20b)

For the eight corner nodes, $\xi = \pm 1$, $\eta = \pm 1$, and $\zeta = \pm 1$:

$$N_i = \tfrac{1}{64}(1 + \xi_i\xi)(1 + \eta_i\eta)(1 + \zeta_i\zeta)\left[9(\xi^2 + \eta^2 + \zeta^2) - 19\right] \tag{9.73a}$$

For the eight side nodes, $\xi = \pm \frac{1}{3}$, $\eta = \pm 1$, and $\zeta = \pm 1$:

$$N_i = \tfrac{9}{64}(1 - \xi^2)(1 + 9\xi_i\xi)(1 + \eta_i\eta)(1 + \zeta_i\zeta) \tag{9.73b}$$

For the eight side nodes, $\xi = \pm 1$, $\eta = \pm \frac{1}{3}$, and $\zeta = \pm 1$:

$$N_i = \tfrac{9}{64}(1 + \xi_i\xi)(1 - \eta^2)(1 + 9\eta_i\eta)(1 + \zeta_i\zeta) \tag{9.73c}$$

For the eight side nodes, $\xi = \pm 1$, $\eta = \pm 1$, and $\zeta = \pm \frac{1}{3}$:

$$N_i = \tfrac{9}{64}(1 + \xi_i\xi)(1 + \eta_i\eta)(1 - \zeta^2)(1 + 9\zeta_i\zeta) \tag{9.73d}$$

We have so far presented the shape functions of several finite elements which are used for the C^0-problems. Unlike the derivations discussed above, the manner to construct the shape functions by degenerating the number of the nodal points, i.e., from the quadrilateral element to the triangular element, from the hexahedral element to the tetrahedral element or to the triangular prism element, and so on, can be found in the book by Bathe (1982).

9.3 INCREMENTAL FINITE-ELEMENT EQUATIONS

Utilizing the shape functions N_i (or the interpolation functions) for the interpolation displacement model discussed in the preceding Section, we shall herein derive the incremental finite-element equations for the continuous medium involving both material and geometrical nonlinearities under the total Lagrangian description and updated Lagrangian description.

9.3.1 General equation based on total Lagrangian description

Virtual work equation

Recall the incremental virtual work equation (8.106) that gives the equilibrium condition at time $(t + \mathrm{d}t)$ to the reference configuration at time $t = 0$:

$$\int_V {}_0C^*_{ijkl}\,\mathrm{d}e_{kl}\delta(\mathrm{d}e_{ij})\,\mathrm{d}\overset{\circ}{V} + \int_V S^t_{ij}\delta(\mathrm{d}\eta_{ij})\,\mathrm{d}\overset{\circ}{V}$$

$$= \int_V F_{oi}\rho_o\delta(\mathrm{d}u_i)\,\mathrm{d}\overset{\circ}{V} + \int_{\overset{\circ}{A}}\left(T^t_{oi} + \mathrm{d}T_{oi}\right)\delta(\mathrm{d}u_i)\,\mathrm{d}\overset{\circ}{A} - \int_V S^t_{ij}\delta(\mathrm{d}e_{ij})\,\mathrm{d}\overset{\circ}{V} \tag{9.74}$$

The main objective in this Section is to represent Eq. (9.74) in the three-dimensional matrix form suitable for the finite-element analysis. Before going to our derivation, we shall consider the increments of the displacement field variables, $\mathrm{d}u_i (i = 1, 2,$ and $3)$, for a finite element within the discretized body.

Displacement fields

The increments of the three-dimensional displacement field, $\mathrm{d}u_i$ $(i = 1, 2,$ and $3)$, are written in terms of the incremental values $\mathrm{d}U_i^m$ of displacement field variables at node m and the corresponding general shape functions N_m $(m = 1, 2, \ldots,$ and $n)$ where n is the number of nodes within the element, i.e.:

$$\mathrm{d}u_i = N_1\,\mathrm{d}U_i^1 + N_2\,\mathrm{d}U_i^2 + \ldots + N_n\,\mathrm{d}U_i^n \tag{9.75a}$$

or in indicial notation:

$$du_i = N_m \, dU_i^m \quad (m = 1, \ldots, n \text{ and } i = 1, 2, 3) \tag{9.75b}$$

Note that N_m is a function of the reference coordinates (X_1, X_2, X_3) of the material at time $t = 0$. Equation (9.75b) can also be expressed in the matrix form:

$$\{du\} = [N]\{dU\} \tag{9.75c}$$

in which

$$\{du\} = [du_1 \quad du_2 \quad du_3]^T,$$

$$\{dU\} = \left[dU_1^1 \quad dU_2^1 \quad dU_3^1 \quad \ldots \quad dU_1^n \quad dU_2^n \quad dU_3^n\right]^T$$

$$[N] = \begin{bmatrix} N_1 & 0 & 0 & N_2 & 0 & 0 & \ldots & N_n & 0 & 0 \\ 0 & N_1 & 0 & 0 & N_2 & 0 & \ldots & 0 & N_n & 0 \\ 0 & 0 & N_1 & 0 & 0 & N_2 & \ldots & 0 & 0 & N_n \end{bmatrix}$$

Similarly, we can also construct the displacement field u_i' at time t:

$$u_i' = N_m U_i^m \quad (m = 1, \ldots, n) \tag{9.76a}$$

or in matrix form:

$$\{u'\} = [N]\{U\} \tag{9.76b}$$

in which

$$\{u'\} = \left[u_1' \quad u_2' \quad u_3'\right]^T, \quad \{U\} = \left[U_1^1 \quad U_2^1 \quad U_3^1 \quad \ldots \quad U_1^n \quad U_2^n \quad U_3^n\right]^T$$

Matrix forms for virtual work equation

Using the incremental displacement field du_i in Eq. (9.75) and displacement field u_i' in Eq. (9.76), we consider here to represent the virtual work equation (9.74) in matrix form.

To represent the first term, $\int_V C_{ijkl}^* \, de_{kl} \delta(de_{ij}) \, d\mathring{V}$, in the left-hand side of Eq. (9.74) in matrix form, consider firstly the variation in the linear part of the Lagrangian strain increment, $\delta(de_{ij})$:

$$\delta(de_{ij}) = \tfrac{1}{2}\left[\delta(du_{i,j}) + \delta(du_{j,i}) + \delta(du_{k,j}) u_{k,i}' + u_{k,j}' \delta(du_{k,i})\right] \tag{9.77}$$

where the subscript after the comma denotes the partial derivative with respect to the reference coordinates X_i. Using Eqs. (9.75) and (9.76), we obtain respectively the

following expressions for the first two and the last two terms of the right-hand side of Eq. (9.77):

$$\tfrac{1}{2}\left[\delta(\mathrm{d}u_{i,j}) + \delta(\mathrm{d}u_{j,i})\right] = \tfrac{1}{2}\left[N_{m,j}\delta(\mathrm{d}U_i^m) + N_{m,i}\delta(\mathrm{d}U_j^m)\right] \tag{9.78a}$$

and

$$\tfrac{1}{2}\left[\delta(\mathrm{d}u_{k,j})u_{k,i}^l + u_{k,j}^l\delta(\mathrm{d}u_{k,i})\right] = \tfrac{1}{2}\left[N_{m,j}\delta(\mathrm{d}U_k^m)N_{l,i}U_k^l + N_{m,j}U_k^m N_{l,i}\delta(\mathrm{d}U_k^l)\right]$$
$$\tfrac{1}{2}\left[N_{m,j}N_{l,i}U_k^l + N_{m,i}N_{l,j}U_k^l\right]\delta(\mathrm{d}U_k^m) \tag{9.78b}$$

where the scripts l, $m = 1, \ldots, n$ and i, j, $k = 1, 2, 3$. Now introducing the column matrices:

$$\{\delta\mathrm{d}e\} = [\delta\mathrm{d}e_{11} \quad \delta\mathrm{d}e_{22} \quad \delta\mathrm{d}e_{33} \quad 2\delta\mathrm{d}e_{12} \quad 2\delta\mathrm{d}e_{23} \quad 2\delta\mathrm{d}e_{31}]^{\mathrm{T}} \tag{9.79a}$$

and

$$\{\delta\mathrm{d}U\} = [\delta\mathrm{d}U_1^1 \quad \delta\mathrm{d}U_2^1 \quad \delta\mathrm{d}U_3^1 \quad \delta\mathrm{d}U_1^2 \quad \delta\mathrm{d}U_2^2 \quad \delta\mathrm{d}U_3^2 \quad \ldots \delta\mathrm{d}U_1^n \quad \delta\mathrm{d}U_2^n \quad \delta\mathrm{d}U_3^n]^{\mathrm{T}} \tag{9.79b}$$

the tensorial form in Eq. (9.77) can be expressed by the following matrix form:

$$\{\delta\mathrm{d}e\} = [B_{\mathrm{L}}]\{\delta\mathrm{d}U\} \tag{9.80}$$

in which

$$[B_{\mathrm{L}}] = [B_{\mathrm{L}0}] + [B_{\mathrm{L}1}] \tag{9.81a}$$

and the matrices $[B_{\mathrm{L}0}]$ and $[B_{\mathrm{L}1}]$ are expressed as:

$$[B_{\mathrm{L}0}] = \begin{bmatrix} N_{1,1} & 0 & 0 & N_{2,1} & 0 & 0 & \ldots & N_{n,1} & 0 & 0 \\ 0 & N_{1,2} & 0 & 0 & N_{2,2} & 0 & \ldots & 0 & N_{n,2} & 0 \\ 0 & 0 & N_{1,3} & 0 & 0 & N_{2,3} & \ldots & 0 & 0 & N_{n,3} \\ N_{1,2} & N_{1,1} & 0 & N_{2,2} & N_{2,1} & 0 & \ldots & N_{n,2} & N_{n,1} & 0 \\ 0 & N_{1,3} & N_{1,2} & 0 & N_{2,3} & N_{2,2} & \ldots & 0 & N_{n,3} & N_{n,2} \\ N_{1,3} & 0 & N_{1,1} & N_{2,3} & 0 & N_{2,1} & \ldots & N_{n,3} & 0 & N_{n,1} \end{bmatrix} \tag{9.81b}$$

and

$$[B_{\mathrm{L}1}] = \begin{bmatrix} l_{11}N_{1,1} & l_{12}N_{1,1} & l_{13}N_{1,1} & l_{11}N_{2,1} & \ldots \\ l_{21}N_{1,2} & l_{22}N_{1,2} & l_{23}N_{1,2} & l_{21}N_{2,2} & \ldots \\ l_{31}N_{1,3} & l_{32}N_{1,3} & l_{33}N_{1,3} & l_{31}N_{2,3} & \ldots \\ (l_{11}N_{1,2} + l_{21}N_{1,1}) & (l_{12}N_{1,2} + l_{22}N_{1,1}) & (l_{13}N_{1,2} + l_{23}N_{1,1}) & (l_{11}N_{2,2} + l_{21}N_{2,1}) & \ldots \\ (l_{21}N_{1,3} + l_{31}N_{1,2}) & (l_{22}N_{1,3} + l_{32}N_{1,2}) & (l_{23}N_{1,3} + l_{33}N_{1,2}) & (l_{21}N_{2,3} + l_{31}N_{2,2}) & \ldots \\ (l_{11}N_{1,3} + l_{31}N_{1,1}) & (l_{12}N_{1,3} + l_{32}N_{1,1}) & (l_{13}N_{1,3} + l_{33}N_{1,1}) & (l_{11}N_{2,3} + l_{31}N_{2,1}) & \ldots \end{bmatrix}$$

$$
\begin{vmatrix}
\cdots & I_{11}N_{n,1} & I_{12}N_{n,1} & I_{13}N_{n,1} \\
\cdots & I_{21}N_{n,2} & I_{22}N_{n,2} & I_{23}N_{n,2} \\
\cdots & I_{31}N_{n,3} & I_{32}N_{n,3} & I_{33}N_{n,3} \\
\cdots & (I_{11}N_{n,2} + I_{21}N_{n,1}) & (I_{12}N_{n,2} + I_{22}N_{n,1}) & (I_{13}N_{n,2} + I_{23}N_{n,1}) \\
\cdots & (I_{21}N_{n,3} + I_{31}N_{n,2}) & (I_{22}N_{n,3} + I_{32}N_{n,2}) & (I_{23}N_{n,3} + I_{33}N_{n,2}) \\
\cdots & (I_{11}N_{n,3} + I_{31}N_{n,1}) & (I_{12}N_{n,3} + I_{32}N_{n,1}) & (I_{13}N_{n,3} + I_{33}N_{n,1})
\end{vmatrix} \tag{9.81c}
$$

in which

$$I_{ij} = N_{k,i}U_j^k \tag{9.81d}$$

Therefore, the first term in Eq. (9.74) can be written as the following matrix form:

$$\int_V C_{ijkl}^* \, \mathrm{d}e_{kl}\delta(\mathrm{d}e_{ij}) \, \mathrm{d}\bar{V} = \int_V \{\delta \mathrm{d}U\}^{\mathrm{T}}[B_{\mathrm{L}}]^{\mathrm{T}}[C^*][B_{\mathrm{L}}]\{\mathrm{d}U\} \, \mathrm{d}\bar{V}$$

$$= \{\delta \mathrm{d}U\}^{\mathrm{T}} \int_V [B_{\mathrm{L}}]^{\mathrm{T}}[C^*][B_{\mathrm{L}}] \, \mathrm{d}\bar{V}\{\mathrm{d}U\} \tag{9.82}$$

where the matrix $[C^*]$ is a constitutive matrix with the size $[6 \times 6]$.

Next, consider the matrix form for the second term, $\int_V S_{ij}^{\prime}\delta(\mathrm{d}\eta_{ij}) \, \mathrm{d}\bar{V}$, in the left-hand side of Eq. (9.74). The variation in the nonlinear part of the Lagrangian strain increment, $\delta(\mathrm{d}\eta_{ij})$, can be written as:

$$\delta(\mathrm{d}\eta_{ij}) = \tfrac{1}{2}\left[\delta(\mathrm{d}u_{k,i}) \, \mathrm{d}u_{k,j} + \mathrm{d}u_{k,i}\delta(\mathrm{d}u_{k,j})\right]$$

Since the terms $\delta(\mathrm{d}u_{k,i})$ and $\mathrm{d}u_{k,i}$ involved in the nonlinear quantity $\delta(\mathrm{d}\eta_{ij})$ are respectively expressed by:

$$\delta(\mathrm{d}u_{k,i}) = N_{m,i}\delta(\mathrm{d}U_k^m), \quad \mathrm{d}u_{k,i} = N_{m,i} \, \mathrm{d}U_k^m \tag{9.83a}$$

or in matrix form:

$$\{\delta \mathrm{d}\bar{u}\} = [B_{\mathrm{NL}}]\{\delta \mathrm{d}U\}, \quad \{\mathrm{d}\bar{u}\} = [B_{\mathrm{NL}}]\{\mathrm{d}U\} \tag{9.83b}$$

where

$$\{\delta \mathrm{d}\bar{u}\} = [\delta \mathrm{d}u_{1,1} \;\; \delta \mathrm{d}u_{1,2} \;\; \delta \mathrm{d}u_{1,3} \;\; \delta \mathrm{d}u_{2,1} \;\; \delta \mathrm{d}u_{2,2} \;\; \delta \mathrm{d}u_{2,3} \;\; \delta \mathrm{d}u_{3,1} \;\; \delta \mathrm{d}u_{3,2} \;\; \delta \mathrm{d}u_{3,3}]^{\mathrm{T}}$$

$$\{\mathrm{d}\bar{u}\} = [\mathrm{d}u_{1,1} \;\; \mathrm{d}u_{1,2} \;\; \mathrm{d}u_{1,3} \;\; \mathrm{d}u_{2,1} \;\; \mathrm{d}u_{2,2} \;\; \mathrm{d}u_{2,3} \;\; \mathrm{d}u_{3,1} \;\; \mathrm{d}u_{3,2} \;\; \mathrm{d}u_{3,3}]^{\mathrm{T}}$$

and

$$[B_{\mathrm{NL}}] = \begin{bmatrix} N_{1,1} & 0 & 0 & N_{2,1} & 0 & 0 & \dots & N_{n,1} & 0 & 0 \\ N_{1,2} & 0 & 0 & N_{2,2} & 0 & 0 & \dots & N_{n,2} & 0 & 0 \\ N_{1,3} & 0 & 0 & N_{2,3} & 0 & 0 & \dots & N_{n,3} & 0 & 0 \\ 0 & N_{1,1} & 0 & 0 & N_{2,1} & 0 & \dots & 0 & N_{n,1} & 0 \\ 0 & N_{1,2} & 0 & 0 & N_{2,2} & 0 & \dots & 0 & N_{n,2} & 0 \\ 0 & N_{1,3} & 0 & 0 & N_{2,3} & 0 & \dots & 0 & N_{n,3} & 0 \\ 0 & 0 & N_{1,1} & 0 & 0 & N_{2,1} & \dots & 0 & 0 & N_{n,1} \\ 0 & 0 & N_{1,2} & 0 & 0 & N_{2,2} & \dots & 0 & 0 & N_{n,2} \\ 0 & 0 & N_{1,3} & 0 & 0 & N_{2,3} & \dots & 0 & 0 & N_{n,3} \end{bmatrix} \tag{9.83c}$$

we obtain the following matrix form for the second term:

$$\begin{aligned} \int_{V^0} S'_{ij}\delta(\mathrm{d}\eta_{ij})\,\mathrm{d}\overset{0}{V} &= \int_{V^0} S'_{ij}\tfrac{1}{2}\left[\delta(\mathrm{d}u_{k,i})\,\mathrm{d}u_{k,j} + \mathrm{d}u_{k,i}\delta(\mathrm{d}u_{k,j})\right]\mathrm{d}\overset{0}{V} \\ &= \int_{V^0} \{\delta \mathrm{d}U\}^{\mathrm{T}}[B_{\mathrm{NL}}]^{\mathrm{T}}[S'][B_{\mathrm{NL}}]\{\mathrm{d}U\}\,\mathrm{d}\overset{0}{V} \\ &= \{\delta \mathrm{d}U\}^{\mathrm{T}}\int_{V^0}[B_{\mathrm{NL}}]^{\mathrm{T}}[S'][B_{\mathrm{NL}}]\,\mathrm{d}\overset{0}{V}\{\mathrm{d}U\} \end{aligned} \tag{9.84}$$

in which

$$[S'] = \begin{bmatrix} S'_{11} & S'_{12} & S'_{13} & 0 & 0 & 0 & 0 & 0 & 0 \\ S'_{21} & S'_{22} & S'_{23} & 0 & 0 & 0 & 0 & 0 & 0 \\ S'_{31} & S'_{32} & S'_{33} & 0 & 0 & 0 & 0 & 0 & 0 \\ 0 & 0 & 0 & S'_{11} & S'_{12} & S'_{13} & 0 & 0 & 0 \\ 0 & 0 & 0 & S'_{21} & S'_{22} & S'_{23} & 0 & 0 & 0 \\ 0 & 0 & 0 & S'_{31} & S'_{32} & S'_{33} & 0 & 0 & 0 \\ 0 & 0 & 0 & 0 & 0 & 0 & S'_{11} & S'_{12} & S'_{13} \\ 0 & 0 & 0 & 0 & 0 & 0 & S'_{21} & S'_{22} & S'_{23} \\ 0 & 0 & 0 & 0 & 0 & 0 & S'_{31} & S'_{32} & S'_{33} \end{bmatrix}$$

Finally, introducing the following column matrices for the body force $\rho_0 F_{0i}$, for

the surface traction force $T_{oi}^{t+dt} = T_{oi}^{t} + dT_{oi}$ and for the second Piola-Kirchhoff stress S_{ij}^{t}:

$$\{F\} = [\rho_o F_{o1} \quad \rho_o F_{o2} \quad \rho_o F_{o3}]^T \tag{9.85a}$$

$$\{T^{t+dt}\} = [T_{o1}^{t+dt} \quad T_{o2}^{t+dt} \quad T_{o3}^{t+dt}]^T \tag{9.85b}$$

$$\{\bar{S}\} = [S_{11}^{t} \quad S_{22}^{t} \quad S_{33}^{t} \quad S_{12}^{t} \quad S_{23}^{t} \quad S_{31}^{t}]^T \tag{9.85c}$$

the right-hand side of the virtual work equation (9.74) can be represented by:

$$\begin{aligned}
&\int_{V^o} \rho_o F_{oi} \delta(du_i)\, dV^o + \int_{A^o} T_{oi}^{t+dt} \delta(du_i)\, dA^o - \int_{V^o} S_{ij}^{t} \delta(de_{ij})\, dV^o \\
&= \int_{V^o} \{\delta dU\}^T [N]^T \{F\}\, dV^o + \int_{A^o} \{\delta dU\}^T [N]^T \{T^{t+dt}\}\, dA^o \\
&\quad - \int_{V^o} \{\delta dU\}^T [B_L]^T \{\bar{S}\}\, dV^o \\
&= \{\delta dU\}^T \int_{V^o} [N]^T \{F\}\, dV^o + \{\delta dU\}^T \int_{A^o} [N]^T \{T^{t+dt}\}\, dA^o \\
&\quad - \{\delta dU\}^T \int_{V^o} [B_L]^T \{\bar{S}\}\, dV^o
\end{aligned} \tag{9.86}$$

Finite-element equation

From the derivation presented above, the virtual work equation (9.74) for an element in the discretized body:

$$\begin{aligned}
&\int_{V^o} C_{ijkl}^{*}\, de_{kl} \delta(de_{ij})\, dV^o + \int_{V^o} S_{ij}^{t} \delta(d\eta_{ij})\, dV^o \\
&= \int_{V^o} \rho_o F_{oi} \delta(du_i)\, dV^o + \int_{A^o} T_{oi}^{t+dt} \delta(du_i)\, dA^o - \int_{V^o} S_{ij}^{t} \delta(de_{ij})\, dV^o
\end{aligned}$$

can be written in the finite-element matrix form:

$$\begin{aligned}
&\{\delta dU\}^T \left(\int_{V^o} [B_L]^T [C^*][B_L]\, dV^o + \int_{V^o} [B_{NL}]^T [S^t][B_{NL}]\, dV^o \right) \{dU\} \\
&= \{\delta\, dU\}^T \left(\int_{V^o} [N]^T \{F\}\, dV^o + \int_{A^o} [N]^T \{T^{t+dt}\}\, dA^o - \int_{V^o} [B_L]^T \{\bar{S}\}\, dV^o \right)
\end{aligned} \tag{9.87}$$

Now extending the displacement increment vector $\{dU\}$ for an element to that for the total element assemblage, we obtain the finite-element equation for the entire structure:

$$\{\delta dU\}^{\mathrm{T}}\left(\sum\int_{\mathring{V}}[B_{\mathrm{L}}]^{\mathrm{T}}[C^{*}][B_{\mathrm{L}}]\,d\mathring{V}+\sum\int_{\mathring{V}}[B_{\mathrm{NL}}]^{\mathrm{T}}[S^{\mathrm{t}}][B_{\mathrm{NL}}]\,d\mathring{V}\right)\{dU\}$$

$$=\{\delta dU\}^{\mathrm{T}}\left(\sum\int_{\mathring{V}}[N]^{\mathrm{T}}\{F\}\,d\mathring{V}+\sum\int_{\mathring{A}}[N]^{\mathrm{T}}\{T^{t+dt}\}\,d\mathring{A}\right.$$

$$\left.-\sum\int_{\mathring{V}}[B_{\mathrm{L}}]^{\mathrm{T}}\{\bar{S}\}\,d\mathring{V}\right) \tag{9.88}$$

where Σ denotes the sum of total element matrices and vectors. Note that Eq. (9.88) is true only when the contribution of all elements is assumed in the manner of the conventional direct stiffness method and that the element surface integrals are identically zero unless part of the element boundary is coincident with the body boundary.

Further employing the principle of virtual displacements, we find:

$$\left(\sum[k_{\mathrm{L}}]\right)\{dU\}+\left(\sum[k_{\mathrm{NL}}]\right)\{dU\}=\sum\left[\{r_{\mathrm{B}}\}+\{r_{\mathrm{S}}\}-\{r_{\mathrm{I}}\}\right] \tag{9.89a}$$

in which the matrices $[k_{\mathrm{L}}]$ and $[k_{\mathrm{NL}}]$ are respectively called the *linear element stiffness matrix* and *nonlinear element stiffness matrix*:

$$[k_{\mathrm{L}}]=\int_{\mathring{V}}[B_{\mathrm{L}}]^{\mathrm{T}}[C^{*}][B_{\mathrm{L}}]\,d\mathring{V} \tag{9.89b}$$

$$[k_{\mathrm{NL}}]=\int_{\mathring{V}}[B_{\mathrm{NL}}]^{\mathrm{T}}[S^{\mathrm{t}}][B_{\mathrm{NL}}]\,d\mathring{V} \tag{9.89c}$$

and also the column matrices $\{r_{\mathrm{B}}\}$, $\{r_{\mathrm{S}}\}$ and $\{r_{\mathrm{I}}\}$ are respectively called the *load vectors* including the effect of the element body force, the element surface traction force, and element initial stress:

$$\{r_{\mathrm{B}}\}=\int_{\mathring{V}}[N]^{\mathrm{T}}\{F\}\,d\mathring{V} \tag{9.89d}$$

$$\{r_{\mathrm{S}}\}=\int_{\mathring{A}}[N]^{\mathrm{T}}\{T^{t+dt}\}\,d\mathring{A} \tag{9.89e}$$

$$\{r_{\mathrm{I}}\}=\int_{\mathring{V}}[B_{\mathrm{L}}]^{\mathrm{T}}\{\bar{S}\}\,d\mathring{V} \tag{9.89f}$$

To eliminate the degrees of freedom with respect to the internal nodes within an

element and to make the size of an element stiffness matrix smaller, a numerical process called *condensation* is in general carried out (for example, Huebner, 1975).

Further, denoting $\Sigma[k_L]$, $\Sigma[k_{NL}]$, $\Sigma\{r_B\}$, $\Sigma\{r_S\}$, and $\Sigma\{r_I\}$ as the *total stiffness matrices* $[K_L]$ and $[K_{NL}]$, and the *total load vectors* $\{R_B\}$, $\{R_S\}$, and $\{R_I\}$, the finite-element equation (9.89a) can be represented as:

$$([K_L] + [K_{NL}])\{dU\} = \{R_B\} + \{R_S\} - \{R_I\} = \{dR\} \tag{9.90}$$

where $\{dR\}$ is a vector of the external load increments from the previous equilibrium state. Equation (9.90) is the *general total Lagrangian finite-element equation* including both material and geometrical nonlinearities.

Example 9.1: Element stiffness matrices for quadrilateral element

Herein, utilizing the finite-element derivation described above, we shall present an example derivation of the element stiffness matrices $[k_L]$ and $[k_{NL}]$ for the *two*-dimensional four-node quadrilateral element under the plane strain condition, with the total Lagrangian description. The configurations of the original element at time $t = 0$ and the current element at time t are shown in Fig. 9.21.

The total node displacements U_i^m at time t, measured with respect to the reference configuration and the reference coordinates X_i^m at a node m are respectively given by:

$$U_1^1 = 0, \quad U_2^1 = 0, \quad U_1^2 = 0.5, \quad U_2^2 = 0.5$$

$$U_1^3 = 1, \quad U_2^3 = 1, \quad U_1^4 = 0.5, \quad U_2^4 = 0.5$$

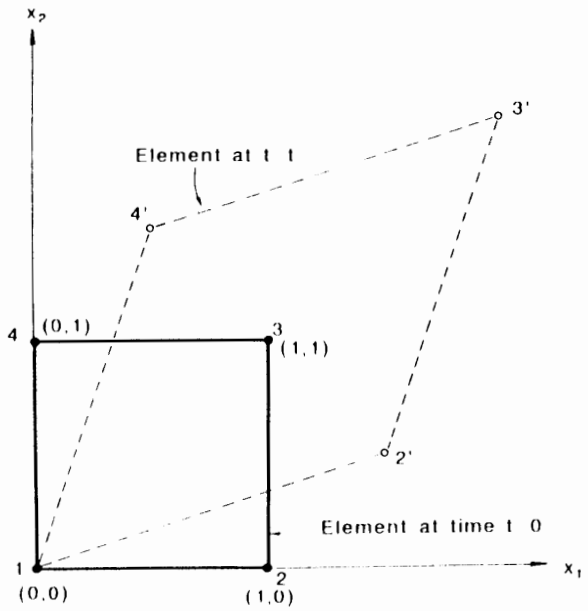

Fig. 9.21. Large deformation of a quadrilateral element.

and

$$X_1^1 = 0, \quad X_2^1 = 0, \quad X_1^2 = 1, \quad X_2^2 = 0$$

$$X_1^3 = 1, \quad X_2^3 = 1, \quad X_1^4 = 0, \quad X_2^4 = 1$$

Geometrical field and displacement field: The geometrical field (X_1, X_2) and the displacement field (u_1, u_2) are respectively expressed in terms of the same shape functions (9.60) that are written by the natural coordinates (ξ, η), under the isoparametric assumption:

$$X_1(\xi, \eta) = N_1 X_1^1 + N_2 X_1^2 + N_3 X_1^3 + N_4 X_1^4 = N_2 + N_3 \tag{9.91a}$$

$$X_2(\xi, \eta) = N_1 X_2^1 + N_2 X_2^2 + N_3 X_2^3 + N_4 X_2^4 = N_3 + N_4 \tag{9.91b}$$

and

$$u_1(\xi, \eta) = N_1 U_1^1 + N_2 U_1^2 + N_3 U_1^3 + N_4 U_1^4 = 0.5N_2 + N_3 + 0.5N_4 \tag{9.92a}$$

$$u_2(\xi, \eta) = N_1 U_2^1 + N_2 U_2^2 + N_3 U_2^3 + N_4 U_2^4 = 0.5N_2 + N_3 + 0.5N_4 \tag{9.92b}$$

in which

$$N_1(\xi, \eta) = \tfrac{1}{4}(1 - \xi)(1 - \eta), \; N_2(\xi, \eta) = \tfrac{1}{4}(1 + \xi)(1 - \eta)$$

$$N_3(\xi, \eta) = \tfrac{1}{4}(1 + \xi)(1 + \eta), \; N_4(\xi, \eta) = \tfrac{1}{4}(1 - \xi)(1 + \eta) \tag{9.92c}$$

Strain-displacement relation: The plane strain condition is herein assumed. The two-dimensional relation between the linear vector $\{de\}$ of the Lagrangian strain increment and the displacement increment vector $\{dU\}$ is denoted in a similar form to Eq. (9.80) by:

$$\{de\} = [B_L]\{dU\} \tag{9.93a}$$

in which

$$\{de\} = [de_{11} \quad de_{22} \quad 2\,de_{12}]^T \tag{9.93b}$$

$$\{dU\} = [dU_1^1 \quad dU_2^1 \quad dU_1^2 \quad dU_2^2 \quad dU_1^3 \quad dU_2^3 \quad dU_1^4 \quad dU_2^4]^T \tag{9.93c}$$

and the matrix $[B_L]$ is given by:

$$[B_L] = [B_{L0}] + [B_{L1}] \tag{9.93d}$$

Reduction of Eqs. (9.81b) and (9.81c) to those under the plane strain condition leads to the following matrices $[B_{L0}]$ and $[B_{L1}]$:

$$[B_{L0}] = \begin{bmatrix} N_{1,1} & 0 & N_{2,1} & 0 & N_{3,1} & 0 & N_{4,1} & 0 \\ 0 & N_{1,2} & 0 & N_{2,2} & 0 & N_{3,2} & 0 & N_{4,2} \\ N_{1,2} & N_{1,1} & N_{2,2} & N_{2,1} & N_{3,2} & N_{3,1} & N_{4,2} & N_{4,1} \end{bmatrix} \tag{9.94a}$$

and

$$[B_{L1}]$$

$$\begin{bmatrix} l_{11}N_{1,1} & l_{12}N_{1,1} & \cdots & l_{11}N_{4,1} & l_{12}N_{4,1} \\ l_{21}N_{1,2} & l_{22}N_{1,2} & \cdots & l_{21}N_{4,2} & l_{22}N_{4,2} \\ (l_{11}N_{1,2} + l_{21}N_{1,1}) & (l_{12}N_{1,2} + l_{22}N_{1,1}) & \cdots & (l_{11}N_{4,2} + l_{21}N_{4,1}) & (l_{12}N_{4,2} + l_{22}N_{4,1}) \end{bmatrix} \tag{9.94b}$$

where the subscript after the comma denotes the derivative with respect to the reference coordinate X_i ($i = 1, 2$) and l_{ij} is given by $N_{k,i}U_j^k$ (i, $j = 1, 2$, and $k = 1, 2, 3$, and 4).

On the other hand, the nonlinear strain displacement relation (9.83b) is rewritten as:

$$\{d\bar{u}\} = [B_{NL}]\{dU\} \tag{9.95a}$$

in which:

$$\{d\bar{u}\} = [du_{1,1} \quad du_{1,2} \quad du_{2,1} \quad du_{2,2}]^t \tag{9.95b}$$

and

$$[B_{NL}] = \begin{bmatrix} N_{1,1} & 0 & N_{2,1} & 0 & N_{3,1} & 0 & N_{4,1} & 0 \\ N_{1,2} & 0 & N_{2,2} & 0 & N_{3,2} & 0 & N_{4,2} & 0 \\ 0 & N_{1,1} & 0 & N_{2,1} & 0 & N_{3,1} & 0 & N_{4,1} \\ 0 & N_{1,2} & 0 & N_{2,2} & 0 & N_{3,2} & 0 & N_{4,2} \end{bmatrix} \tag{9.95c}$$

Note that the derivatives of the shape functions $N_i(\xi, \eta)$ with respect to the reference coordinates X_i can be obtained numerically from Eq. (9.91). The derivative forms of $\partial N_i/\partial\xi$ and $\partial N_i/\partial\eta$ are expressed as:

$$\begin{aligned} \frac{\partial N_i}{\partial \xi} &= \frac{\partial N_i}{\partial X_1}\frac{\partial X_1}{\partial \xi} + \frac{\partial N_i}{\partial X_2}\frac{\partial X_2}{\partial \xi} \\ \frac{\partial N_i}{\partial \eta} &= \frac{\partial N_i}{\partial X_1}\frac{\partial X_1}{\partial \eta} + \frac{\partial N_i}{\partial X_2}\frac{\partial X_2}{\partial \eta} \end{aligned} \tag{9.96a}$$

or in matrix form:

$$\begin{Bmatrix} \dfrac{\partial N_i}{\partial \xi} \\ \dfrac{\partial N_i}{\partial \eta} \end{Bmatrix} = \begin{bmatrix} \dfrac{\partial X_1}{\partial \xi} & \dfrac{\partial X_2}{\partial \xi} \\ \dfrac{\partial X_1}{\partial \eta} & \dfrac{\partial X_2}{\partial \eta} \end{bmatrix} \begin{Bmatrix} \dfrac{\partial N_i}{\partial X_1} \\ \dfrac{\partial N_i}{\partial X_2} \end{Bmatrix} \tag{9.96b}$$

in which

$$\frac{\partial X_1}{\partial \xi} = \frac{\partial}{\partial \xi}(N_2 + N_3) = \frac{1}{2}, \quad \frac{\partial X_1}{\partial \eta} = \frac{\partial}{\partial \eta}(N_2 + N_3) = 0$$

$$\frac{\partial X_2}{\partial \xi} = \frac{\partial}{\partial \xi}(N_3 + N_4) = 0, \quad \frac{\partial X_2}{\partial \eta} = \frac{\partial}{\partial \eta}(N_3 + N_4) = \frac{1}{2}$$

Therefore, the derivative forms of $\partial N_i/\partial X_1$ and $\partial N_i/\partial X_2$ are obtained as the inversed form of Eq. (9.96b):

$$\begin{Bmatrix} \dfrac{\partial N_i}{\partial X_1} \\ \dfrac{\partial N_i}{\partial X_2} \end{Bmatrix} = \begin{bmatrix} \dfrac{\partial X_1}{\partial \xi} & \dfrac{\partial X_2}{\partial \xi} \\ \dfrac{\partial X_1}{\partial \eta} & \dfrac{\partial X_2}{\partial \eta} \end{bmatrix}^{-1} \begin{Bmatrix} \dfrac{\partial N_i}{\partial \xi} \\ \dfrac{\partial N_i}{\partial \eta} \end{Bmatrix} = \begin{bmatrix} 2 & 0 \\ 0 & 2 \end{bmatrix} \begin{Bmatrix} \dfrac{\partial N_i}{\partial \xi} \\ \dfrac{\partial N_i}{\partial \eta} \end{Bmatrix} \tag{9.97}$$

With the help of Eqs. (9.92c) and (9.97), the components of the matrices $[B_{10}]$, $[B_{11}]$, and $[B_{N1}]$ in Eqs. (9.94a), (9.94b) and (9.95c) can be respectively calculated as:

$$[B_{10}] = \frac{1}{2}\begin{bmatrix} (1-\eta) & 0 & 1-\eta & 0 & 1+\eta & 0 & (1+\eta) & 0 \\ 0 & -(1-\xi) & 0 & -(1+\xi) & 0 & 1+\xi & 0 & 1-\xi \\ (1-\xi) & -(1-\eta) & -(1+\xi) & 1-\eta & 1+\xi & 1+\eta & 1-\xi & -(1+\eta) \end{bmatrix} \tag{9.98a}$$

$$[B_{11}] = \frac{1}{4}\begin{bmatrix} -(1-\eta) & -(1-\eta) & 1-\eta & 1-\eta & 1+\eta & 1+\eta & (1+\eta) & (1+\eta) \\ (1-\xi) & -(1-\xi) & -(1+\xi) & -(1+\xi) & 1+\xi & 1+\xi & 1-\xi & 1-\xi \\ 2+\xi+\eta & 2+\xi+\eta & \xi-\eta & \xi-\eta & 2+\xi+\eta & 2+\xi+\eta & \xi-\eta & \xi-\eta \end{bmatrix} \tag{9.98b}$$

$$[B_{N1}] = \frac{1}{2}\begin{bmatrix} (1-\eta) & 0 & 1-\eta & 0 & 1+\eta & 0 & -(1+\eta) & 0 \\ (1-\xi) & 0 & (1+\xi) & 0 & 1+\xi & 0 & 1-\xi & 0 \\ 0 & -(1-\eta) & 0 & 1-\eta & 0 & 1+\eta & 0 & (1+\eta) \\ 0 & -(1-\xi) & 0 & -(1+\xi) & 0 & 1+\xi & 0 & 1-\xi \end{bmatrix} \tag{9.98c}$$

Note that in this case $J_{11} = J_{12} = J_{21} = J_{22} = \frac{1}{2}$ are used to calculate the components in Eq. (9.98b).

Element stiffness matrices: Since the components of the matrices shown above involve the natural coordinates ξ and η, the linear and nonlinear quadrilateral element stiffness matrices $[k_L]$ and $[k_{NL}]$ in Eqs. (9.89b) and (9.89c) may be easily integrated over the region $[-1, 1]$ defined by the natural coordinates. We here introduce the relation between the volume $d\bar{V}$ defined in the reference coordinates (X_1, X_2) and the volume $d\bar{V}$ defined in the natural coordinates (ξ, η), i.e., $d\bar{V} = J\, d\bar{V}$, referring to Eq. (8.43b), where J is the determinant of the *Jacobian matrix*. The Jacobian determinant J is calculated as:

$$J = \begin{vmatrix} \dfrac{\partial X_1}{\partial \xi} & \dfrac{\partial X_2}{\partial \xi} \\ \dfrac{\partial X_1}{\partial \eta} & \dfrac{\partial X_2}{\partial \eta} \end{vmatrix} = \begin{vmatrix} \dfrac{1}{2} & 0 \\ 0 & \dfrac{1}{2} \end{vmatrix} = \frac{1}{4}$$

Finally, we have the following form for the matrix $[k_L]$:

$$[k_L] = \int_{\bar{V}} [B_L]^T [C^*] [B_L]\, d\bar{V} = \int_{\bar{V}} [B_L]^T [C^*] [B_L]\, J\, d\bar{V}$$

$$= \int_{\bar{V}} \frac{1}{4} [B_L]^T [C^*] [B_L]\, d\xi\, d\eta \tag{9.99a}$$

where the matrix $[C^*]$ is a constitutive matrix with a size of $[3 \times 3]$ for the plane strain condition under the total Lagrangian description and also we have for the matrix $[k_{NL}]$:

$$[k_{NL}] = \int_{\bar{V}} [B_{NL}]^T [S^t] [B_{NL}]\, d\bar{V} = \int_{\bar{V}} \frac{1}{4} [B_{NL}]^T [S^t] [B_{NL}]\, d\xi\, d\eta \tag{9.99b}$$

in which the matrix $[S^t]$ is the Second Piola-Kirchhoff stress matrix with a size of $[4 \times 4]$ for the plane strain condition, i.e.:

$$[S^t] = \begin{bmatrix} S^t_{11} & S^t_{12} & 0 & 0 \\ S^t_{21} & S^t_{22} & 0 & 0 \\ 0 & 0 & S^t_{11} & S^t_{12} \\ 0 & 0 & S^t_{21} & S^t_{22} \end{bmatrix}$$

9.3.2 *General equation based on updated Lagrangian description*

Following the similar process for the total Lagrangian description in the previous Section, we shall consider herein to represent the virtual work equation (8.121) based on the updated Lagrangian description for the three-dimensional finite-element equation.

Virtual work equation

The virtual work equation (8.121) at time $t + \mathrm{d}t$, based on the updated Lagrangian description, can be again written as:

$$\int_{V^t} C^*_{ijkl}\, \mathrm{d}\epsilon_{kl}\delta(\mathrm{d}\epsilon_{ij})\, \mathrm{d}V^t + \int_{V^t} \sigma^t_{ij}\delta(\mathrm{d}\eta_{ij})\, \mathrm{d}V^t$$

$$= \int_{V^t} F_{oi}\rho_0\delta(\mathrm{d}u_i)\, \mathrm{d}V^t + \int_{A^t} \left(T^t_{oi} + \mathrm{d}T_{oi}\right)\delta(\mathrm{d}u_i)\, \mathrm{d}A^t - \int_{V^t} \sigma^t_{ij}\delta(\mathrm{d}\epsilon_{ij})\, \mathrm{d}V^t \qquad (9.100)$$

All variables used in the above equation refer to the current configuration of the deformed body at time t.

Displacement fields

Exactly the same notations and the same forms as Eqs. (9.75) and (9.76) in the total Lagrangian description are also used for the displacement fields. Note here that the shape functions N_m are the functions of the current coordinates (x_1, x_2, x_3) of the material at time t.

Matrix forms for virtual work equation

To write the matrix form for the first term in the left-hand side of Eq. (9.100), first consider the matrix form for the variation in the linear part of the Lagrangian strain increments, $\delta(\mathrm{d}\epsilon_{ij})$:

$$\delta(\mathrm{d}\epsilon_{ij}) = \tfrac{1}{2}\left[\delta(\mathrm{d}u_{i,j}) + \delta(\mathrm{d}u_{j,i})\right]$$

$$= \tfrac{1}{2}\left[N_{m,j}\delta(\mathrm{d}U^m_i) + N_{m,i}\delta(\mathrm{d}U^m_j)\right] \qquad (9.101)$$

where the subscripts i and j ($i, j = 1, 2, 3$) after the comma denote respectively the partial derivatives with respect to the *current coordinates* x_i and x_j at time t, and m ($m = 1, \ldots, n$: n is the number of nodes in the element) represents the nodal number assigned locally inside an element. Now introducing the following column matrix for the variation in the linear strain increments:

$$\{\delta\mathrm{d}\epsilon\} = \left[\delta\mathrm{d}\epsilon_{11} \quad \delta\mathrm{d}\epsilon_{22} \quad \delta\mathrm{d}\epsilon_{33} \quad 2\delta\mathrm{d}\epsilon_{12} \quad 2\delta\mathrm{d}\epsilon_{23} \quad 2\delta\mathrm{d}\epsilon_{31}\right]^{\mathrm{T}} \qquad (9.102)$$

and the column matrix for the variation (9.79b) in the displacement, the tensorial form for the variation (9.101) in the linear strain can be expressed as:

$$\{\delta \mathrm{d}\epsilon\} = [B_{\mathrm{L}}]\{\delta \mathrm{d}U\} \tag{9.103}$$

where in this case, the matrix $[B_{\mathrm{L}}]$ does not include the matrix $[B_{\mathrm{L1}}]$ as given in Eq. (9.81c) but has the same form as $[B_{\mathrm{L0}}]$ in Eq. (9.81b). Therefore, we obtain the following matrix form for the first term in Eq. (9.100):

$$\int_{V'} C^*_{ijkl}\, \mathrm{d}\epsilon_{kl}\delta(\mathrm{d}\epsilon_{ij})\, \mathrm{d}V' = \{\delta \mathrm{d}U\}^{\mathrm{T}} \int_{V'} [B_{\mathrm{L}}]^{\mathrm{T}} [C^*][B_{\mathrm{L}}]\, \mathrm{d}V' \{\mathrm{d}U\} \tag{9.104}$$

where the matrix $[C^*]$ is a constitutive matrix with a size $[6 \times 6]$ constructed for the updated Lagrangian formulation.

Similarly, the matrix form for the second term in the left hand side of Eq. (9.100) is given by:

$$\int_{V'} \sigma'_{ij}\delta(\mathrm{d}\eta_{ij})\, \mathrm{d}V' = \{\delta \mathrm{d}U\}^{\mathrm{T}} \int_{V'} [B_{\mathrm{NL}}]^{\mathrm{T}} [\sigma'][B_{\mathrm{NL}}]\, \mathrm{d}V' \{\mathrm{d}U\} \tag{9.105}$$

where the matrix $[B_{\mathrm{NL}}]$ has the same form as that of Eq. (9.83c) and the stress matrix $[\sigma']$ can be written as:

$$[\sigma'] = \begin{bmatrix} \sigma'_{11} & \sigma'_{12} & \sigma'_{13} & 0 & 0 & 0 & 0 & 0 & 0 \\ \sigma'_{21} & \sigma'_{22} & \sigma'_{23} & 0 & 0 & 0 & 0 & 0 & 0 \\ \sigma'_{31} & \sigma'_{32} & \sigma'_{33} & 0 & 0 & 0 & 0 & 0 & 0 \\ 0 & 0 & 0 & \sigma'_{11} & \sigma'_{12} & \sigma'_{13} & 0 & 0 & 0 \\ 0 & 0 & 0 & \sigma'_{21} & \sigma'_{22} & \sigma'_{23} & 0 & 0 & 0 \\ 0 & 0 & 0 & \sigma'_{31} & \sigma'_{32} & \sigma'_{33} & 0 & 0 & 0 \\ 0 & 0 & 0 & 0 & 0 & 0 & \sigma'_{11} & \sigma'_{12} & \sigma'_{13} \\ 0 & 0 & 0 & 0 & 0 & 0 & \sigma'_{21} & \sigma'_{22} & \sigma'_{23} \\ 0 & 0 & 0 & 0 & 0 & 0 & \sigma'_{31} & \sigma'_{32} & \sigma'_{33} \end{bmatrix}$$

Using the similar column matrices $\{F\}$ in Eq. (9.85a) for the body force and $\{T'^{+\mathrm{d}t}\}$ in Eq. (9.85b) for the surface traction force and introducing the column for the current stresses:

$$\{\bar{\sigma}\} = \begin{bmatrix} \sigma'_{11} & \sigma'_{22} & \sigma'_{33} & \sigma'_{12} & \sigma'_{23} & \sigma'_{31} \end{bmatrix}^{\mathrm{T}} \tag{9.106}$$

the right-hand side of the virtual work equation (9.100) can be represented by:

$$\int_{V^t} \rho_0 F_{0i} \delta(\mathrm{d}u_i)\, \mathrm{d}V^t + \int_{A^t} T_{0i}^{t+\mathrm{d}t} \delta(\mathrm{d}u_i)\, \mathrm{d}A^t - \int_{V^t} \sigma_{ij}^t \delta(\mathrm{d}\epsilon_{ij})\, \mathrm{d}V^t$$

$$= \{\delta \mathrm{d}U\}^{\mathrm{T}} \int_{V^t} [N]^{\mathrm{T}} \{F\}\, \mathrm{d}V^t + \{\delta \mathrm{d}U\}^{\mathrm{T}} \int_{A^t} [N]^{\mathrm{T}} \{T^{t+\mathrm{d}t}\}\, \mathrm{d}A^t$$

$$- \{\delta \mathrm{d}U\}^{\mathrm{T}} \int_{V^t} [B_{\mathrm{L}}]^{\mathrm{T}} \{\bar{\sigma}\}\, \mathrm{d}V^t \tag{9.107}$$

Finite-element equation

In the following, the matrix forms presented for each term in the virtual work equation are used to construct the finite-element equation for the whole element assemblage. After extending the displacement increment vector $\{\mathrm{d}U\}$ for an element to that for the total element assemblage and then employing the principle of virtual displacements, we obtain a similar finite element equation to that given in Eq. (9.89a) for the virtual work equation (9.100), that is:

$$\left(\sum [k_{\mathrm{L}}]\right)\{\mathrm{d}U\} + \left(\sum [k_{\mathrm{NL}}]\right)\{\mathrm{d}U\} = \sum \left[\{r_{\mathrm{B}}\} + \{r_{\mathrm{S}}\} - \{r_{\mathrm{I}}\}\right] \tag{9.108a}$$

in which the matrices $[k_{\mathrm{L}}]$ and $[k_{\mathrm{NL}}]$ are respectively called the linear element stiffness matrix and the nonlinear element stiffness matrix, i.e.:

$$[k_{\mathrm{L}}] = \int_{V^t} [B_{\mathrm{L}}]^{\mathrm{T}} [C^*] [B_{\mathrm{L}}]\, \mathrm{d}V^t \tag{9.108b}$$

$$[k_{\mathrm{NL}}] = \int_{V^t} [B_{\mathrm{NL}}]^{\mathrm{T}} [\sigma^t] [B_{\mathrm{NL}}]\, \mathrm{d}V^t \tag{9.108c}$$

and $\{r_{\mathrm{B}}\}$, $\{r_{\mathrm{S}}\}$, and $\{r_{\mathrm{I}}\}$ are called the load vectors with the effects of the element body force, the element surface traction force, and the element initial stress, respectively:

$$\{r_{\mathrm{B}}\} = \int_{V^t} [N]^{\mathrm{T}} \{F\}\, \mathrm{d}V^t \tag{9.108d}$$

$$\{r_{\mathrm{S}}\} = \int_{A^t} [N]^{\mathrm{T}} \{T^{t+\mathrm{d}t}\}\, \mathrm{d}A^t \tag{9.108e}$$

and

$$\{r_{\mathrm{I}}\} = \int_{V^t} [B_{\mathrm{L}}]^{\mathrm{T}} \{\bar{\sigma}\}\, \mathrm{d}V^t \tag{9.108f}$$

Introducing the following total stiffness matrices $[K_L]$ and $[K_{NL}]$, and the total load vectors $\{R_B\}$, $\{R_S\}$, and $\{R_I\}$ such as:

$$[K_L] = \sum [k_L], \quad [K_{NL}] = \sum [k_{NL}]$$

$$\{R_B\} = \sum \{r_B\}, \quad \{R_S\} = \sum \{r_S\} \quad \text{and} \quad \{R_I\} = \sum \{r_I\}$$

we have finally the same simplified finite-element equation as that given by Eq. (9.90):

$$([K_L] + [K_{NL}])\{dU\} = \{R_B\} + \{R_S\} - \{R_I\} = \{dR\}$$

Example 9.2: Element stiffness matrices for quadrilateral element

Herein, by taking the same example problem as that used in the previous Section 9.3.1 but with the updated Lagrangian description, we shall derive the element stiffness matrices $[k_L]$ and $[k_{NL}]$ at time t for the *two*-dimensional quadrilateral element under the plane strain condition.

In this case, the quantities of the total displacements at four nodes are not important to calculate the element stiffness matrices but the current coordinates x_1 and x_2 at time t are needed. These are:

$$x_1^1 = 0 \quad x_2^1 = 0 \quad x_1^2 = 1.5 \quad x_2^2 = 0.5$$

$$x_1^3 = 2 \quad x_2^3 = 2 \quad x_1^4 = 0.5 \quad x_2^4 = 1.5$$

Geometrical field and displacement field: Employing the isoparametric assumption, the geometrical field (x_1, x_2) and the displacement field (u_1, u_2) with respect to the current configuration of the material at time t are expressed in terms of the shape functions as:

$$x_1(\xi, \eta) = N_1 x_1^1 + N_2 x_1^2 + N_3 x_1^3 + N_4 x_1^4 = 1.5N_2 + 2N_3 + 0.5N_4 \tag{9.109a}$$

$$x_2(\xi, \eta) = N_1 x_2^1 + N_2 x_2^2 + N_3 x_2^3 + N_4 x_2^4 = 0.5N_2 + 2N_3 + 1.5N_4 \tag{9.109b}$$

$$u_1(\xi, \eta) = N_1 U_1^1 + N_2 U_1^2 + N_3 U_1^3 + N_4 U_1^4 \tag{9.110a}$$

$$u_2(\xi, \eta) = N_1 U_2^1 + N_2 U_2^2 + N_3 U_2^3 + N_4 U_2^4 \tag{9.110b}$$

in which N_i ($i = 1, 2, 3$ and 4) are the shape functions written in terms of the natural coordinates ξ and η, as given by Eq. (9.92c).

Strain-displacement relation: Reducing the three-dimensional linear and nonlinear strain-displacement relations into the two-dimensional relations, we have the similar forms to those given by Eqs. (9.93) and (9.95). Note that the derivatives of the shape

functions N_i are performed with respect to the current coordinates x_i at time t by utilizing the *Jacobian transformation matrix*, i.e.:

$$\begin{aligned}\frac{\partial N_i}{\partial \xi} &= \frac{\partial N_i}{\partial x_1}\frac{\partial x_1}{\partial \xi} + \frac{\partial N_i}{\partial x_2}\frac{\partial x_2}{\partial \xi} \\ \frac{\partial N_i}{\partial \eta} &= \frac{\partial N_i}{\partial x_1}\frac{\partial x_1}{\partial \eta} + \frac{\partial N_i}{\partial x_2}\frac{\partial x_2}{\partial \eta}\end{aligned} \tag{9.111a}$$

or in matrix form:

$$\begin{Bmatrix} \dfrac{\partial N_i}{\partial \xi} \\ \dfrac{\partial N_i}{\partial \eta} \end{Bmatrix} = \begin{bmatrix} \dfrac{\partial x_1}{\partial \xi} & \dfrac{\partial x_2}{\partial \xi} \\ \dfrac{\partial x_1}{\partial \eta} & \dfrac{\partial x_2}{\partial \eta} \end{bmatrix} \begin{Bmatrix} \dfrac{\partial N_i}{\partial x_1} \\ \dfrac{\partial N_i}{\partial x_2} \end{Bmatrix} \tag{9.111b}$$

in which

$$\frac{\partial x_1}{\partial \xi} = \frac{\partial}{\partial \xi}(1.5N_2 + 2N_3 + 0.5N_4) = \frac{3}{4}, \quad \frac{\partial x_1}{\partial \eta} = \frac{\partial}{\partial \eta}(1.5N_2 + 2N_3 + 0.5N_4) = \frac{1}{4}$$

$$\frac{\partial x_2}{\partial \xi} = \frac{\partial}{\partial \xi}(0.5N_2 + 2N_3 + 1.5N_4) = \frac{1}{4}, \quad \frac{\partial x_2}{\partial \eta} = \frac{\partial}{\partial \eta}(0.5N_2 + 2N_3 + 1.5N_4) = \frac{3}{4}$$

Therefore, the derivative forms $\partial N_i/\partial x_1$ and $\partial N_i/\partial x_2$ are calculated as the inversed form of Eq. (9.111b):

$$\begin{Bmatrix} \dfrac{\partial N_i}{\partial x_1} \\ \dfrac{\partial N_i}{\partial x_2} \end{Bmatrix} = \begin{bmatrix} \dfrac{\partial x_1}{\partial \xi} & \dfrac{\partial x_2}{\partial \xi} \\ \dfrac{\partial x_1}{\partial \eta} & \dfrac{\partial x_2}{\partial \eta} \end{bmatrix}^{-1} \begin{Bmatrix} \dfrac{\partial N_i}{\partial \xi} \\ \dfrac{\partial N_i}{\partial \eta} \end{Bmatrix} = \begin{bmatrix} \dfrac{3}{2} & -\dfrac{1}{2} \\ -\dfrac{1}{2} & \dfrac{3}{2} \end{bmatrix} \begin{Bmatrix} \dfrac{\partial N_i}{\partial \xi} \\ \dfrac{\partial N_i}{\partial \eta} \end{Bmatrix} \tag{9.112}$$

The components of the matrices $[B_1]$ and $[B_{N1}]$ are thus calculated as:

$$[B_1] \quad \frac{1}{8}\begin{bmatrix} 2(\xi+3\eta) & 0 & 4+\xi-3\eta & 0 & 2(-\xi+3\eta) & 0 & -4+\xi & 3\eta & 0 \\ 0 & 2+3\xi & \eta & 0 & -4 & 3\xi+\eta & 0 & 2+3\xi & -\eta & 0 & -4 & 3\xi+\eta \\ 2+3\xi & \eta & 2(\xi+3\eta) & -4 & 3\xi+\eta & 4+\xi & 3\eta & 2+3\xi & \eta & 2(\xi+3\eta) & -4 & 3\xi+\eta & -4+\xi & 3\eta \end{bmatrix} \tag{9.113a}$$

$$[B_{N1}] \quad \frac{1}{8}\begin{bmatrix} 2(\xi+3\eta) & 0 & 4+\xi & 3\eta & 0 & 2(\xi+3\eta) & 0 & 4+\xi & 3\eta & 0 \\ 2+3\xi & \eta & 0 & -4 & 3\xi+\eta & 0 & 2+3\xi & \eta & 0 & 4 & 3\xi+\eta & 0 \\ 0 & 2(\xi+3\eta) & 0 & 4+\xi & 3\eta & 0 & 2(\xi+3\eta) & 0 & 4+\xi & 3\eta \\ 0 & 2+3\xi & \eta & 0 & -4 & 3\xi+\eta & 0 & 2+3\xi & \eta & 0 & 4 & 3\xi+\eta \end{bmatrix} \tag{9.113b}$$

Element stiffness matrices: Similar to the total Lagrangian description, the element stiffness matrices $[k_1]$ and $[k_{N1}]$ are integrated over the region $[-1, 1]$ defined by the natural coordinates. Since the determinant of the Jacobian matrix, J, is calculated as:

$$J = \begin{vmatrix} \dfrac{\partial x_1}{\partial \xi} & \dfrac{\partial x_2}{\partial \xi} \\ \dfrac{\partial x_1}{\partial \eta} & \dfrac{\partial x_2}{\partial \eta} \end{vmatrix} = \begin{vmatrix} \dfrac{3}{4} & \dfrac{1}{4} \\ \dfrac{1}{4} & \dfrac{3}{4} \end{vmatrix} = \frac{1}{2}$$

we have:

$$[k_1] = \int_{-1}^{1} [B_1]^{\mathrm{T}} [C^*] [B_1] \, \mathrm{d}\xi \, \mathrm{d}\eta \tag{9.114a}$$

where $[C^*]$ is a constitutive matrix $[3 \times 3]$ for the plane strain condition under the updated Lagrangian description and:

$$[k_{\mathrm{NL}}] = \int_{-1}^{1} [B_{\mathrm{NL}}]^{\mathrm{T}} [\sigma'] [B_{\mathrm{NL}}] \, \mathrm{d}\xi \, \mathrm{d}\eta \tag{9.114b}$$

where the matrix $[\sigma']$ is the Eulerian stress matrix with a size of $[4 \times 4]$ for the plane strain condition:

$$[\sigma'] = \begin{bmatrix} \sigma'_{11} & \sigma'_{12} & 0 & 0 \\ \sigma'_{21} & \sigma'_{22} & 0 & 0 \\ 0 & 0 & \sigma'_{11} & \sigma'_{12} \\ 0 & 0 & \sigma'_{21} & \sigma'_{22} \end{bmatrix}$$

A comparison between both the total and updated Lagrangian formulations presented above makes it clear that for the total Lagrangian finite-element equation the derivatives of shape functions with respect to the reference coordinates (X_1, X_2) remain unchanged during the step-by-step calculation once they are calculated at the beginning whereas for the updated Lagrangian finite-element equation these derivatives with respect to the current coordinates (x_1, x_2) must be carried out each time when the current coordinates of the material are updated.

9.3.3 Updated Lagrangian formulation equation

In this Section, we shall present the finite-element equations for the virtual work equation (8.168) with the large strain and large rotation, and for the virtual work equation (8.191) with the small strain and large rotation, which have been derived by Davidson and Chen (1974) with the updated Lagrangian formulation.

(A) *Finite-element equation for large strain and large rotation*

Virtual work equation

The virtual work equation (8.168) based on the updated Lagrangian formulation can be rewritten as:

$$\int_V \sigma_{ij}\left[\mathrm{d}\epsilon_{ki}\delta(\mathrm{d}\epsilon_{kj}) + \mathrm{d}\epsilon_{ki}\delta(\mathrm{d}\Omega_{kj}) + \mathrm{d}\Omega_{ki}\delta(\mathrm{d}\epsilon_{kj}) + \mathrm{d}\Omega_{ki}\delta(\mathrm{d}\Omega_{kj})\right] \mathrm{d}V$$

$$+ \int_V (\mathrm{d}\tau_{ij} + \psi_{ijkl}\,\mathrm{d}\epsilon_{kl})\delta(\mathrm{d}\epsilon_{ij})\,\mathrm{d}V$$

$$= \int_A (T_i + \mathrm{d}T_i)\delta(\mathrm{d}u_i)\,\mathrm{d}A + \int_V \rho_0\{F_i(x_j) + \mathrm{d}F_i\}\delta(\mathrm{d}u_i)\,\mathrm{d}V - \int_V \sigma_{ij}\delta(\mathrm{d}\epsilon_{ij})\,\mathrm{d}V \tag{9.115}$$

Displacement fields

The same notations and forms as those in the preceding Section are also assumed here.

Matrix forms for virtual work equation

Introducing the following column matrices, in which the upper part is related to incremental strain components $\mathrm{d}\epsilon_{ij}$ and the lower part is to incremental rotation components $\mathrm{d}\Omega_{ij}$:

$$\{\mathrm{d}\tilde{\epsilon}\} = [\mathrm{d}\epsilon_{11} \quad \mathrm{d}\epsilon_{22} \quad \mathrm{d}\epsilon_{33} \quad 2\,\mathrm{d}\epsilon_{12} \quad 2\,\mathrm{d}\epsilon_{23} \quad 2\,\mathrm{d}\epsilon_{31} \quad \mathrm{d}\Omega_{12} \quad \mathrm{d}\Omega_{23} \quad \mathrm{d}\Omega_{31}]^{\mathrm{T}} \tag{9.116a}$$

$$\{\delta\mathrm{d}\tilde{\epsilon}\} = [\delta\mathrm{d}\epsilon_{11} \quad \delta\mathrm{d}\epsilon_{22} \quad \delta\mathrm{d}\epsilon_{33} \quad 2\delta\mathrm{d}\epsilon_{12} \quad 2\delta\mathrm{d}\epsilon_{23} \quad 2\delta\mathrm{d}\epsilon_{31} \quad \delta\mathrm{d}\Omega_{12} \quad \delta\mathrm{d}\Omega_{23} \quad \delta\mathrm{d}\Omega_{31}]^{\mathrm{T}} \tag{9.116b}$$

the first term in the left-hand side of the virtual work equation (9.115) can be represented in matrix form as

$$\int_V \sigma_{ij}\left[\mathrm{d}\epsilon_{ki}\delta(\mathrm{d}\epsilon_{kj}) + \mathrm{d}\epsilon_{ki}\delta(\mathrm{d}\Omega_{kj}) + \mathrm{d}\Omega_{ki}\delta(\mathrm{d}\epsilon_{kj}) + \mathrm{d}\Omega_{ki}\delta(\mathrm{d}\Omega_{kj})\right] \mathrm{d}V$$

$$= \int_V \{\delta\,\mathrm{d}\tilde{\epsilon}\}^{\mathrm{T}}[A]\{\mathrm{d}\tilde{\epsilon}\}\,\mathrm{d}V \tag{9.117a}$$

where the matrix $[A]$ is a symmetric matrix consisting of the Cartesian stresses σ_{ij} as expressed by:

$$[A] = \begin{bmatrix}
\sigma_{11} & 0 & 0 & \frac{1}{2}\sigma_{12} & 0 & \frac{1}{2}\sigma_{13} & \sigma_{13} & 0 & \sigma_{11} \\
 & \sigma_{22} & 0 & \frac{1}{2}\sigma_{21} & \frac{1}{2}\sigma_{23} & 0 & -\sigma_{21} & \sigma_{23} & 0 \\
 & & \sigma_{33} & 0 & \frac{1}{2}\sigma_{32} & \frac{1}{2}\sigma_{31} & 0 & -\sigma_{32} & \sigma_{31} \\
 & & & \frac{1}{4}(\sigma_{11}+\sigma_{22}) & \frac{1}{4}\sigma_{13} & \frac{1}{4}\sigma_{23} & \frac{1}{2}(\sigma_{22}-\sigma_{11}) & \frac{1}{2}\sigma_{13} & \frac{1}{2}\sigma_{23} \\
 & & & & \frac{1}{4}(\sigma_{22}+\sigma_{33}) & \frac{1}{4}\sigma_{21} & -\frac{1}{2}\sigma_{31} & \frac{1}{2}(\sigma_{33}-\sigma_{22}) & \frac{1}{2}\sigma_{21} \\
 & & & & & \frac{1}{4}(\sigma_{11}+\sigma_{33}) & \frac{1}{2}\sigma_{32} & \frac{1}{2}\sigma_{12} & \frac{1}{2}(\sigma_{11}-\sigma_{33}) \\
 & & & & & & \sigma_{11}+\sigma_{22} & -\sigma_{13} & -\sigma_{23} \\
 & & & & & & & \sigma_{22}+\sigma_{33} & \sigma_{21} \\
 & & \text{Symmetric} & & & & & & \sigma_{11}+\sigma_{33}
\end{bmatrix} \tag{9.117b}$$

Using the relation $d\Omega_{ij} = \frac{1}{2}(\partial du_i/\partial x_j - \partial du_j/\partial x_i)$ and the incremental displacement vector $\{du\} = [N]\{dU\}$, the column matrices $\{d\tilde{\epsilon}\}$ and $\{\delta d\tilde{\epsilon}\}$ are respectively expressed as:

$$\{d\tilde{\epsilon}\} = [\tilde{B}]\{dU\} \tag{9.118a}$$

$$\{\delta d\tilde{\epsilon}\} = [\tilde{B}]\{\delta dU\} \tag{9.118b}$$

in which

$$\{dU\} = \left[dU_1^1 \quad dU_2^1 \quad dU_3^1 \quad dU_1^2 \quad dU_2^2 \quad dU_3^2 \quad \dots \quad dU_1^n \quad dU_2^n \quad dU_3^n\right]^T \tag{9.119a}$$

$$[\tilde{B}] = \begin{bmatrix}
N_{1,1} & 0 & 0 & N_{2,1} & 0 & 0 & \dots & N_{n,1} & 0 & 0 \\
0 & N_{1,2} & 0 & 0 & N_{2,2} & 0 & \dots & 0 & N_{n,2} & 0 \\
0 & 0 & N_{1,3} & 0 & 0 & N_{2,3} & \dots & 0 & 0 & N_{n,3} \\
N_{1,2} & N_{1,1} & 0 & N_{2,2} & N_{2,1} & 0 & \dots & N_{n,2} & N_{n,1} & 0 \\
0 & N_{1,3} & N_{1,2} & 0 & N_{2,3} & N_{2,2} & \dots & 0 & N_{n,3} & N_{n,2} \\
N_{1,3} & 0 & N_{1,1} & N_{2,3} & 0 & N_{2,1} & \dots & N_{n,3} & 0 & N_{n,1} \\
\frac{1}{2}N_{1,2} & -\frac{1}{2}N_{1,1} & 0 & \frac{1}{2}N_{2,2} & -\frac{1}{2}N_{2,1} & 0 & \dots & \frac{1}{2}N_{n,2} & -\frac{1}{2}N_{n,1} & 0 \\
0 & \frac{1}{2}N_{1,3} & -\frac{1}{2}N_{1,2} & 0 & \frac{1}{2}N_{2,3} & -\frac{1}{2}N_{2,2} & \dots & 0 & \frac{1}{2}N_{n,3} & \frac{1}{2}N_{n,2} \\
-\frac{1}{2}N_{1,3} & 0 & \frac{1}{2}N_{1,1} & -\frac{1}{2}N_{2,3} & 0 & \frac{1}{2}N_{2,1} & \dots & -\frac{1}{2}N_{n,3} & 0 & \frac{1}{2}N_{n,1}
\end{bmatrix} \tag{9.119b}$$

Therefore, substitution of Eqs. (9.118a) and (9.118b) into the right-hand side of Eq.

(9.117a) leads to:

$$\int_{V'} \{\delta \mathrm{d}\tilde{\epsilon}\}^{\mathrm{T}} [A] \{\mathrm{d}\tilde{\epsilon}\} \, \mathrm{d}V = \{\delta \mathrm{d}U\}^{\mathrm{T}} \int_{V'} [\tilde{B}]^{\mathrm{T}} [A] [\tilde{B}] \, \mathrm{d}V \{\mathrm{d}U\} \tag{9.120}$$

Note that Eq. (9.120) should give the identical form to that given by Eq. (9.105).

Next introducing the following matrices:

$$\{\mathrm{d}\tau\} = [\mathrm{d}\tau_{11} \quad \mathrm{d}\tau_{22} \quad \mathrm{d}\tau_{33} \quad \mathrm{d}\tau_{12} \quad \mathrm{d}\tau_{23} \quad \mathrm{d}\tau_{31}]^{\mathrm{T}} \tag{9.121a}$$

$$\{\mathrm{d}\epsilon\} = [\mathrm{d}\epsilon_{11} \quad \mathrm{d}\epsilon_{22} \quad \mathrm{d}\epsilon_{33} \quad 2\,\mathrm{d}\epsilon_{12} \quad 2\,\mathrm{d}\epsilon_{23} \quad 2\,\mathrm{d}\epsilon_{31}]^{\mathrm{T}} \text{ and} \tag{9.121b}$$

$$[\psi] = \text{transformation matrix} \tag{9.121c}$$

where $\{\mathrm{d}\tau\}$ is column vector for incremental Cartesian stresses referred to the local coordinate frame in the subsequent configuration, $\{\mathrm{d}\epsilon\}$ is column vector for incremental linear strains and $[\psi]$ is a transformation matrix with a size of $[6 \times 6]$ given in Eq. (8.176) for the 4th-order tensor ψ_{ijkl}, the second term in the left-hand side of Eq. (9.115) can thus be expressed as:

$$\int_V (\mathrm{d}\tau_{ij} + \psi_{ijkl} \, \mathrm{d}\epsilon_{kl}) \delta(\mathrm{d}\epsilon_{ij}) \, \mathrm{d}V = \int_{V'} \{\delta \mathrm{d}\epsilon\}^{\mathrm{T}} (\{\mathrm{d}\tau\} + [\psi]\{\mathrm{d}\epsilon\}) \, \mathrm{d}V \tag{9.122}$$

Further substitution of $\{\delta \mathrm{d}\epsilon\}^{\mathrm{T}} = \{\delta \mathrm{d}U\}^{\mathrm{T}} [B_{\mathrm{L}}]^{\mathrm{T}}$, $\{\mathrm{d}\epsilon\} = [B_{\mathrm{L}}]\{\mathrm{d}U\}$ and $\{\mathrm{d}\tau\} = [C]\{\mathrm{d}\epsilon\} = [C][B_{\mathrm{L}}]\{\mathrm{d}U\}$, where $\{\mathrm{d}U\}$ is the column matrix given in Eq. (9.119a) for incremental displacements of the body and $[C]$ is an elastic-plastic constitutive matrix under the small strain assumption, leads to:

$$\int_V \{\delta \mathrm{d}\epsilon\}^{\mathrm{T}} (\{\mathrm{d}\tau\} + [\psi]\{\mathrm{d}\epsilon\}) \, \mathrm{d}V = \{\delta \mathrm{d}U\}^{\mathrm{T}} \int_{V'} [B_{\mathrm{L}}]^{\mathrm{T}} ([C] + [\psi]) [B_{\mathrm{L}}] \{\mathrm{d}U\} \, \mathrm{d}V \tag{9.123}$$

Using the column matrices $\{T' + \mathrm{d}T\}$ for surface traction forces, $\{F\} = \rho_0 [F_1 + \mathrm{d}F_1 \quad F_2 + \mathrm{d}F_2 \quad F_3 + \mathrm{d}F_3]^{\mathrm{T}}$ for body forces and $\{\bar{\sigma}\} = [\sigma'_{11} \quad \sigma'_{22} \quad \sigma'_{33} \quad \sigma'_{12} \quad \sigma'_{23} \quad \sigma'_{31}]^{\mathrm{T}}$ for the Cartesian stresses referred to the global coordinates, the right-hand side of the virtual work equation (9.115) becomes identical form to that of Eq. (9.107).

Finite-element equation

Extending the displacement increment vector $\{\mathrm{d}U\}$ for a single element to that of all elements, the matrix form for the virtual equation (9.115) can thus be written

as:

$$\{\delta \mathrm{d}U\}^{\mathrm{T}} \sum \left(\int_A [N]^{\mathrm{T}} \{T^{t+\mathrm{d}t}\} \, \mathrm{d}A \right) + \{\delta \mathrm{d}U\}^{\mathrm{T}} \sum \left(\int_V [N]^{\mathrm{T}} \{F\} \, \mathrm{d}V \right)$$

$$- \{\delta \mathrm{d}U\}^{\mathrm{T}} \sum \left(\int_V [B_{\mathrm{L}}]^{\mathrm{T}} \{\bar{\sigma}\} \, \mathrm{d}V \right)$$

$$\{\delta \mathrm{d}U\}^{\mathrm{T}} \sum \left(\int_V [\tilde{B}]^{\mathrm{T}} [A] [\tilde{B}] \, \mathrm{d}V \right) \{\mathrm{d}U\}$$

$$+ \{\delta \mathrm{d}U\}^{\mathrm{T}} \sum \left(\int_V [B_{\mathrm{L}}]^{\mathrm{T}} [[C] + [\psi]] [B_{\mathrm{L}}] \, \mathrm{d}V \right) \{\mathrm{d}U\} \tag{9.124}$$

where Σ denotes the sum of total element matrices and vectors.

Since Eq. (9.124) must be satisfied for all kinematically admissible virtual nodal displacement increments, it follows that:

$$\sum \left(\int_V [\tilde{B}]^{\mathrm{T}} [A] [\tilde{B}] \, \mathrm{d}V \right) \{\mathrm{d}U\} + \sum \left(\int_V [B_{\mathrm{L}}]^{\mathrm{T}} [[C] + [\psi]] [B_{\mathrm{L}}] \, \mathrm{d}V \right) \{\mathrm{d}U\}$$

$$= \sum \left(\int_A [N]^{\mathrm{T}} \{T^{t+\mathrm{d}t}\} \, \mathrm{d}A \right) + \sum \left(\int_V [N]^{\mathrm{T}} \{F\} \, \mathrm{d}V \right) - \sum \left(\int_V [B_{\mathrm{L}}]^{\mathrm{T}} \{\bar{\sigma}\} \, \mathrm{d}V \right) \tag{9.125}$$

Now introducing the element stiffness matrices $[k_{\mathrm{m}}]$ and $[k_{\mathrm{g}}]$, and the load vectors $\{r_{\mathrm{S}}\}$, $\{r_{\mathrm{B}}\}$ and $\{r_{\mathrm{I}}\}$, Eq. (9.125) can be simply expressed as:

$$\sum [k_{\mathrm{g}}] \{\mathrm{d}U\} + \sum [k_{\mathrm{m}}] \{\mathrm{d}U\} = \sum \{r_{\mathrm{S}}\} + \sum \{r_{\mathrm{B}}\} - \sum \{r_{\mathrm{I}}\} \tag{9.126}$$

where $[k_{\mathrm{g}}]$ and $[k_{\mathrm{m}}]$ are the so-called *geometrical stiffness matrix* (or *initial stress stiffness matrix*) and the *material stiffness matrix* respectively. The matrix $[k_{\mathrm{g}}]$ is a *symmetric* matrix while the matrix $[k_{\mathrm{m}}]$ becomes *nonsymmetric* for the large strain and large rotation case and *symmetric* for the small strain and large rotation case, due to the effects of nonsymmetric matrix $[\psi]$. The column matrices $\{r_{\mathrm{S}}\}$, $\{r_{\mathrm{B}}\}$ and $\{r_{\mathrm{I}}\}$ are respectively the load vectors with the effects of the element surface traction force, the element body force and the element initial stresses. These are written as:

$$[k_{\mathrm{g}}] = \int_V [\tilde{B}]^{\mathrm{T}} [A] [\tilde{B}] \, \mathrm{d}V \tag{9.127a}$$

$$[k_{\mathrm{m}}] = \int_V [B_{\mathrm{L}}]^{\mathrm{T}} [[C] + [\psi]] [B_{\mathrm{L}}] \, \mathrm{d}V \tag{9.127b}$$

$$\{r_S\} = \int_A [N]^T \{T^{t+dt}\}\, dA \tag{9.127c}$$

$$\{r_B\} = \int_V [N]^T \{F\}\, dV \tag{9.127d}$$

$$\{r_I\} = \int_V [B_L]^T \{\bar{\sigma}\}\, dV \tag{9.127e}$$

Further introduction of the *total stiffness matrices* $[K_G] = \Sigma[k_g]$ and $[K_M] = \Sigma[k_m]$, and the *total load vectors* $\{R_S\} = \Sigma\{r_S\}$, $\{R_B\} = \Sigma\{r_B\}$ and $\{R_I\} = \Sigma\{r_I\}$ leads to the simplified finite-element equation:

$$([K_G] + [K_M])\{dU\} = \{R_S\} + \{R_B\} - \{R_I\} = \{dR\} \tag{9.128}$$

(B) *Finite-element equation for small strain and large rotation*

Virtual work equation

The virtual work equation (8.191) for the small-strain and large-rotation case can be rewritten as:

$$\int_V \sigma_{ij}\left[d\epsilon_{kl}\delta(d\Omega_{kj}) + d\Omega_{ki}\delta(d\epsilon_{kj}) + d\Omega_{ki}\delta(d\Omega_{kj})\right] dV + \int_V d\tau_{ij}\delta(d\epsilon_{ij})\, dV$$

$$= \int_A (T_i + dT_i)\delta(du_i)\, dA + \int_V \rho_0\{F_i(x_j) + dF_i\}\delta(du_i)\, dV - \int_V \sigma_{ij}\delta(d\epsilon_{ij})\, dV \tag{9.129}$$

Note that the above equation has no terms for $d\epsilon_{ki}\delta(d\epsilon_{kj})$ and $\psi_{ijkl}\, d\epsilon_{kl}$, compared with Eq. (9.115) with the large-strain and large-rotation effect.

Matrix forms for virtual work equation

The first term in the left-hand side of Eq. (9.129) can be expressed in the same form as that given by Eq. (9.120). It should be noted, however, that for this case the matrix $[A]$ is given by:

$$[A] = \begin{bmatrix} 0 & 0 & 0 & 0 & 0 & 0 & \sigma_{12} & 0 & -\sigma_{13} \\ & 0 & 0 & 0 & 0 & 0 & -\sigma_{21} & \sigma_{23} & 0 \\ & & 0 & 0 & 0 & 0 & 0 & -\sigma_{32} & \sigma_{31} \\ & & & 0 & 0 & 0 & \tfrac{1}{2}(\sigma_{22}-\sigma_{11}) & \tfrac{1}{2}\sigma_{13} & -\tfrac{1}{2}\sigma_{23} \\ & & & & 0 & 0 & -\tfrac{1}{2}\sigma_{31} & \tfrac{1}{2}(\sigma_{33}-\sigma_{22}) & \tfrac{1}{2}\sigma_{21} \\ & & & & & 0 & \tfrac{1}{2}\sigma_{32} & -\tfrac{1}{2}\sigma_{12} & \tfrac{1}{2}(\sigma_{11}-\sigma_{33}) \\ & & & & & & \sigma_{11}+\sigma_{22} & -\sigma_{13} & -\sigma_{23} \\ & \text{Symmetric} & & & & & & \sigma_{22}+\sigma_{33} & -\sigma_{21} \\ & & & & & & & & \sigma_{11}+\sigma_{33} \end{bmatrix} \tag{9.130}$$

The matrix form for the second term is obtained by substituting $[\psi] = [0]$ into Eq. (9.123).

Finite-element equation

The finite-element equation has the same forms as those for Eqs. (9.126) and (9.128), except the material stiffness matrix $[k_m]$ for an element is written as:

$$[k_m] = \int_V [B_L]^T [C][B_L] \, dV \tag{9.131}$$

where for the small-strain and large-rotation case, the material stiffness matrix becomes symmetric.

Example 9.3: Element stiffness matrices for triangular element. Here, we shall demonstrate the construction of the element stiffness matrices $[k_m]$ and $[k_\sigma]$ for the two-dimensional three-node triangular element (*constant strain triangular element*) under plane strain, plane stress and axisymmetric conditions, respectively.

Considering a triangular element shown in Fig. 9.22, as a simple expansion of displacement field in Eq. (9.52), the incremental displacement field over the triangle element can be rewritten as:

$$\{du\} = [N]\{dU\} \tag{9.132}$$

where the column matrix $\{du\}$ has the components of du_1 and du_2, representing

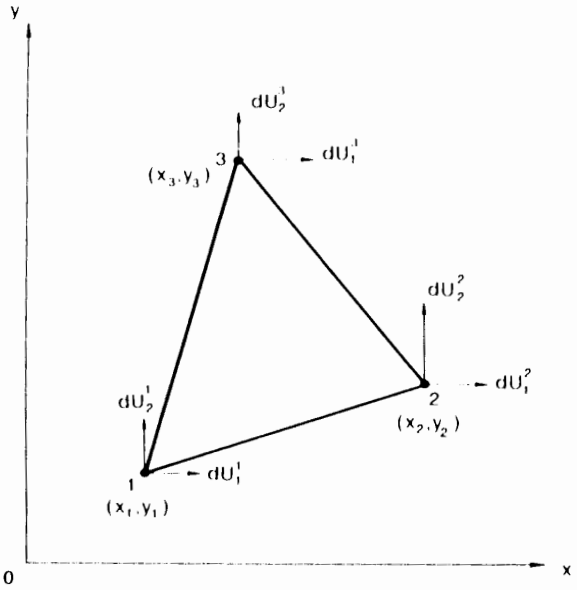

Fig. 9.22. Constant strain triangular element.

the displacement increments in the x- and y-directions respectively at an arbitrary point inside an element, and $\{dU\}$ is a column matrix of displacement increments at nodes, i.e.:

$$\{dU\} = \left[dU_1^1 \quad dU_2^1 \quad dU_1^2 \quad dU_2^2 \quad dU_1^3 \quad dU_2^3\right]^t \tag{9.133}$$

where, for example, dU_2^1 is the displacement increment in the y-direction, at node 1. For this case, the shape function matrix $[N]$ is rewritten from Eq. (9.52) as:

$$[N] = \begin{bmatrix} L_1 & 0 & L_2 & 0 & L_3 & 0 \\ 0 & L_1 & 0 & L_2 & 0 & L_3 \end{bmatrix} \tag{9.134}$$

where L_1, L_2 and L_3 are the so-called area coordinates of the triangular element, which are defined as:

$$L_1 = \frac{1}{2A}(a_1 + b_1 x + c_1 y) \tag{9.135a}$$

$$L_2 = \frac{1}{2A}(a_2 + b_2 x + c_2 y) \tag{9.135b}$$

$$L_3 = \frac{1}{2A}(a_3 + b_3 x + c_3 y) \tag{9.135c}$$

in which

$$a_1 = x_2 y_3 - x_3 y_2, \quad b_1 = y_2 - y_3, \quad c_1 = x_3 - x_2 \tag{9.136a}$$

$$a_2 = x_3 y_1 - x_1 y_3, \quad b_2 = y_3 - y_1, \quad c_2 = x_1 - x_3 \tag{9.136b}$$

$$a_3 = x_1 y_2 - x_2 y_1, \quad b_3 = y_1 - y_2, \quad c_3 = x_2 - x_1 \tag{9.136c}$$

and A is the area of the triangular element, given as:

$$A = \tfrac{1}{2}\left[(y_2 - y_3)(x_1 - x_3) - (x_2 - x_3)(y_1 - y_3)\right] \tag{9.136d}$$

Element stiffness matrices for plane strain and plane stress cases: For the plane strain and plane stress conditions, Eqs. (9.121b) and (9.116a) are reduced to:

$$\{d\epsilon\} = \begin{Bmatrix} d\epsilon_{11} \\ d\epsilon_{22} \\ d\gamma_{12} \end{Bmatrix} = \begin{Bmatrix} \partial(du_1)/\partial x \\ \partial(du_2)/\partial y \\ \partial(du_1)/\partial y + \partial(du_2)/\partial x \end{Bmatrix} = [B_L]\{dU\} \tag{9.137a}$$

and

$$\{d\tilde{\epsilon}\} = \begin{Bmatrix} d\epsilon_{11} \\ d\epsilon_{22} \\ d\gamma_{12} \\ d\Omega_{12} \end{Bmatrix} = [\tilde{B}]\{dU\} \tag{9.137b}$$

where the matrices $[B_L]$ in Eq. (9.127b) and $[\tilde{B}]$ in Eq. (9.127a) are obtained by utilizing Eqs. (9.132) through (9.135) with the kinematic relations (9.137a) and (9.137b). Thus, we have:

$$[B_L] = \frac{1}{2A}\begin{bmatrix} b_1 & 0 & b_2 & 0 & b_3 & 0 \\ 0 & c_1 & 0 & c_2 & 0 & c_3 \\ c_1 & b_1 & c_2 & b_2 & c_3 & b_3 \end{bmatrix} \tag{9.138a}$$

and

$$[\tilde{B}] = \frac{1}{2A}\begin{bmatrix} b_1 & 0 & b_2 & 0 & b_3 & 0 \\ 0 & c_1 & 0 & c_2 & 0 & c_3 \\ c_1 & b_1 & c_2 & b_2 & c_3 & b_3 \\ \frac{1}{2}c_1 & -\frac{1}{2}b_1 & \frac{1}{2}c_2 & -\frac{1}{2}b_2 & \frac{1}{2}c_3 & -\frac{1}{2}b_3 \end{bmatrix} \tag{9.138b}$$

Next, the matrix $[A]$ in Eq. (9.127a) is determined. First, the matrix $[A]$ for the large-strain and large-rotation analysis is reduced from Eq. (9.117b). Since $\sigma_{13} = \sigma_{23} = d\gamma_{13} = d\gamma_{23} = d\epsilon_{33} = 0$ or $\sigma_{13} = \sigma_{23} = \sigma_{33} = d\gamma_{13} = d\gamma_{23} = 0$ and $d\Omega_{13} = d\Omega_{23} = 0$, we have:

$$[A] = \begin{bmatrix} \sigma_{11} & 0 & \frac{1}{2}\sigma_{12} & \sigma_{12} \\ & \sigma_{22} & \frac{1}{2}\sigma_{12} & -\sigma_{12} \\ & & \frac{1}{4}(\sigma_{11}+\sigma_{22}) & -\frac{1}{2}(\sigma_{11}-\sigma_{22}) \\ & \text{Symmetric} & & (\sigma_{11}+\sigma_{22}) \end{bmatrix} \tag{9.139a}$$

Also, the matrix $[A]$ for small strain and large rotation analysis is reduced from Eq. (9.130). Thus, we have:

$$\begin{bmatrix} 0 & 0 & 0 & \sigma_{12} \\ & 0 & 0 & \sigma_{22} \\ & & \frac{1}{4}(\sigma_{11}+\sigma_{22}) & -\frac{1}{2}(\sigma_{11}-\sigma_{22}) \\ \text{Symmetric} & & & (\sigma_{11}+\sigma_{22}) \end{bmatrix}$$

The constitutive matrix $[C]$ in Eq. (9.127b) is shown in Chapters 3 to 6 for several material models under plane strain and plane stress conditions. On the other hand, the matrix $[\psi]$ in Eq. (9.127b) can be written from Eqs. (8.181) and (8.186) for plane strain and plane stress cases, respectively. For plane strain case, we have:

$$[\psi] = \begin{bmatrix} -\sigma_{11} & \sigma_{11} & -\sigma_{12} \\ \sigma_{22} & -\sigma_{22} & -\sigma_{12} \\ 0 & 0 & -\frac{1}{2}(\sigma_{11}+\sigma_{22}) \end{bmatrix} \tag{9.140a}$$

and for plane stress case, we have:

$$[\psi] = \begin{bmatrix} (\alpha_1 - 1)\sigma_{11} & (1+\alpha_2)\sigma_{11} & (\alpha_3\sigma_{11} - \sigma_{12}) \\ (1+\alpha_1)\sigma_{22} & (\alpha_2 - 1)\sigma_{22} & (\alpha_3\sigma_{22} - \sigma_{12}) \\ \alpha_1\sigma_{12} & \alpha_2\sigma_{12} & \left(\alpha_3\sigma_{12} - \frac{1}{2}\sigma_{11} - \frac{1}{2}\sigma_{22}\right) \end{bmatrix} \tag{9.140b}$$

in which

$$\alpha_1 = \frac{H_{33}^* H_{11} - \lambda H}{(\lambda + 2\mu)H - H_{33}^* H_{33}}$$

$$\alpha_2 = \frac{H_{33}^* H_{22} - \lambda H}{(\lambda + 2\mu)H - H_{33}^* H_{33}}$$

$$\alpha_3 = \frac{H_{33}^* H_{12}}{(\lambda + 2\mu)H - H_{33}^* H_{33}}$$

Note that for an analysis with small strain and large rotation, the components in matrix $[\psi]$ are null. Since the matrices $[B_L]$, $[\tilde{B}]$, $[A]$, $[C]$ and $[\psi]$ presented above have *constant* components with respect to the two-dimensional coordinates (x, y), the geometrical element stiffness matrix $[k_g]$ and material element stiffness matrix $[k_m]$ for the constant strain triangular element are written respectively from Eqs. (9.127a) and (9.127b) as:

$$[k_g] = [\tilde{B}]^T [A][\tilde{B}]V \tag{9.141a}$$

and

$$[k_m] = [B_L]^T [[C] + [\psi]][B_L]V \tag{9.141b}$$

where V is the volume of a triangular element.

Element stiffness matrix for axisymmetric case: Similarly, the matrices $[B_L]$ and $[\tilde{B}]$ for axisymmetric condition are determined by taking into account the additional

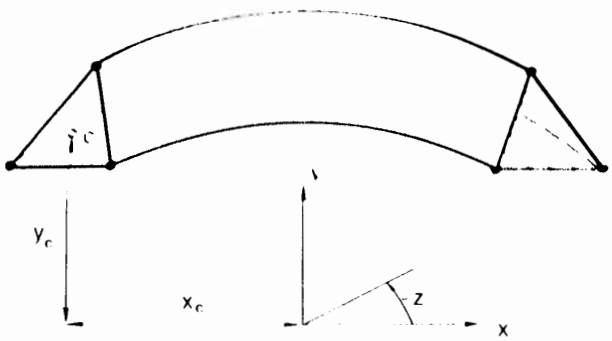

Fig. 9.23. Triangular element in axisymmetric condition.

stress and strain in the circumferential direction. Utilizing coordinates (x, y, z) as shown in Fig. 9.23, we have the following forms for the vectors $\{d\epsilon\}$ and $\{d\tilde{\epsilon}\}$:

$$\{d\epsilon\} = \begin{Bmatrix} d\epsilon_{11} \\ d\epsilon_{22} \\ d\epsilon_{33} \\ d\gamma_{12} \end{Bmatrix} = \begin{Bmatrix} \partial(du_1)/\partial x \\ \partial(du_2)/\partial y \\ du_1/x \\ \partial(du_1)/\partial y + \partial(du_2)/\partial x \end{Bmatrix} = [B_1]\{dU\} \tag{9.142a}$$

$$\{d\tilde{\epsilon}\} = \begin{Bmatrix} d\epsilon_{11} \\ d\epsilon_{22} \\ d\epsilon_{33} \\ d\gamma_{12} \\ d\Omega_{12} \end{Bmatrix} = [\tilde{B}]\{dU\} \tag{9.142b}$$

where x is the distance from the center-line of axisymmetricity in Fig. 9.23 and these matrices $[B_1]$ and $[\tilde{B}]$ are written as:

$$[B_1] = \frac{1}{2A}\begin{bmatrix} b_1 & 0 & b_2 & 0 & b_3 & 0 \\ 0 & c_1 & 0 & c_2 & 0 & c_3 \\ L_1/x & 0 & L_2/x & 0 & L_3/x & 0 \\ c_1 & b_1 & c_2 & b_2 & c_3 & b_3 \end{bmatrix} \tag{9.143a}$$

$$[\tilde{B}] = \frac{1}{2A}\begin{bmatrix} b_1 & 0 & b_2 & 0 & b_3 & 0 \\ 0 & c_1 & 0 & c_2 & 0 & c_3 \\ L_1/x & 0 & L_2/x & 0 & L_3/x & 0 \\ c_1 & b_1 & c_2 & b_2 & c_3 & b_3 \\ \frac{1}{2}c_1 & -\frac{1}{2}b_1 & \frac{1}{2}c_2 & -\frac{1}{2}b_2 & \frac{1}{2}c_3 & -\frac{1}{2}b_3 \end{bmatrix} \tag{9.143b}$$

The matrix $[A]$ can be reduced from Eqs. (9.117b) and (9.130) respectively for the large-strain and large-rotation case:

$$[A] = \begin{bmatrix} \sigma_{11} & 0 & 0 & \frac{1}{2}\sigma_{12} & \sigma_{12} \\ & \sigma_{22} & 0 & \frac{1}{2}\sigma_{21} & -\sigma_{21} \\ & & \sigma_{33} & 0 & 0 \\ & & & \frac{1}{4}(\sigma_{11}+\sigma_{22}) & \frac{1}{2}(\sigma_{22}-\sigma_{11}) \\ & \text{Symmetric} & & & \sigma_{11}+\sigma_{22} \end{bmatrix} \tag{9.144a}$$

and for the small-strain and large-rotation case:

$$[A] = \begin{bmatrix} 0 & 0 & 0 & 0 & \sigma_{12} \\ & 0 & 0 & 0 & -\sigma_{21} \\ & & 0 & 0 & 0 \\ & & & 0 & \frac{1}{2}(\sigma_{22}-\sigma_{11}) \\ & \text{Symmetric} & & & \sigma_{11}+\sigma_{22} \end{bmatrix} \tag{9.144b}$$

The constitutive matrix $[C]$ for axisymmetric condition can be obtained from Chapters 3 through 6. The matrix $[\psi]$ in Eq. (9.127b) is written from Eq. (8.188) as:

$$[\psi] = \begin{bmatrix} -\sigma_{11} & \sigma_{11} & \sigma_{11} & -\sigma_{12} \\ \sigma_{22} & -\sigma_{22} & \sigma_{22} & -\sigma_{12} \\ \sigma_{33} & \sigma_{33} & -\sigma_{33} & 0 \\ 0 & 0 & \sigma_{12} & -\frac{1}{2}(\sigma_{11}+\sigma_{22}) \end{bmatrix} \tag{9.145}$$

Since the matrices $[B_1]$ and $[\tilde{B}]$ contain the coordinates (x, y) for this case, it is not so simple to integrate Eqs. (9.127a) and (9.127b), compared with the plane strain and plane stress conditions. An approximate method is simply to use the centroid coordinates (x_c, y_c) of a triangular element instead of the arbitrary coordinates (x, y) (Zienkiewicz, 1978). In this case, the components of all matrices become constant and thus the element stiffness matrices $[k_g]$ and $[k_m]$ in Eqs. (9.127a) and (9.127b) can be represented by the same forms in Eqs. (9.141a) and (9.141b).

In this Section, general incremental finite-element equations were developed for the large-deformation analysis of soil response. Since our interest is sometimes in the analysis of soil response for two-dimensional cases, the element stiffness matrices developed above can be utilized in the finite-element coding for such large-strain and large-rotation analysis or small-strain and large-rotation analysis.

A direct sum of element stiffness matrices and load vectors yields a set of displacement increment equilibrium equations for the discretized body. Subsequently, the displacement increments can be obtained by solving the incremental equilibrium equations for each incremental load. However, the displacement increments do not usually satisfy the equilibrium of the discretized body at the next configuration because of *material nonlinearity* as well as *geometric nonlinearity*. As a result, various iterative numerical procedures have been developed and applied to finite-element analysis. The choice of a particular procedure depends on the loading condition, the accuracy required for the analysis, constitutive laws, capacity of the computer to be used, and computational time.

Since the geometrical and material nonlinearity problems are employed here, displacement increments are considered rather than the total quantity of displacements. Thus, the incremental displacement-load equilibrium equations (9.90) and (9.128) as derived in the previous Section are rewritten as:

$$[K]\{dU\} = \{dR\} \tag{9.146}$$

where $\{dU\}$ and $\{dR\}$ are respectively the vectors of displacement increments and load increments for the discretized body. The matrix $[K]$ is the sum of the total geometrical stiffness and total material stiffness matrices, is the current tangent stiffness of the discretized body, and is a function of the current stress state and current configuration of the body.

In the following, the numerical procedures to treat Eq. (9.146) in nonlinear problems are briefly reviewed with respect to their advantages and limitations in finite-element analysis.

9.4.1 *Incremental procedure*

As can be understood from Eq. (9.146), perhaps the simplest way to approximate the nonlinear response during a load (or displacement) increment is to use the *Euler integration method* (Ketter and Prawel, 1968) in which the tangent stiffness $[K]$ at the beginning of an increment is directly utilized to obtain a linear approximation for the incremental response. For example, referring to Fig. 9.24a, we suppose that the solution at Point A is known at the beginning and we want to determine incremental displacements $\{dU\}$ associated with applied incremental load $\{dR\}$. We project along a tangent at Point A to obtain an approximate solution denoted by Point B. However, we can expect that after a number of increments, the approximate solution diverges from the true solution, as shown in Fig. 9.24b. Although this kind of analytical error can be reduced by keeping the incremental load (or displacement) small, the number of increments will be correspondingly greater, causing an increase in computational time.

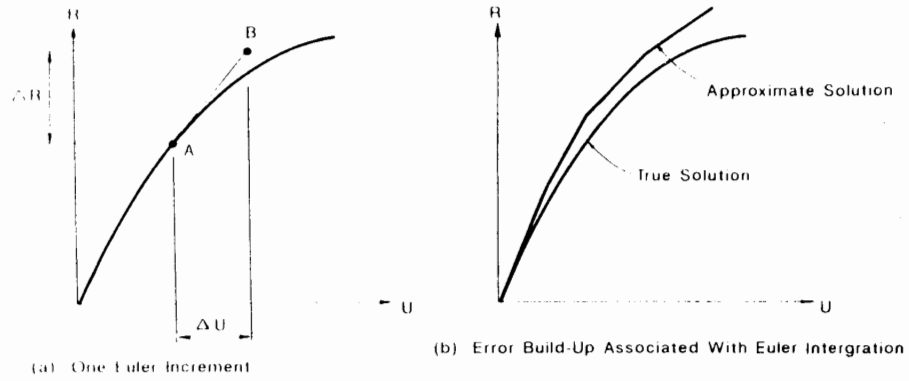

Fig. 9.24. Euler integration: (a) one Euler increment; (b) error build-up associated with Euler integration.

In conjunction with a finite-element approach, variations of the Euler integration method have been used by Pope (1965), Swedlow et al., (1965), Marcal and King (1967), and Yamada and Yoshimura (1968) to solve elastic-plastic problems.

In order to obtain a more accurate solution, a particular method known as the *mid-point integration rule* based on *Runge-Kutta method* (Ketter and Prawel, 1968) is explained as follows. This technique has been used previously by Felippa (1966), Akyuz and Merwin (1968) and Fernandez and Christian (1971) to solve elastic-plastic, geometrically nonlinear problems. A nonlinear one-dimensional load-displacement curve is shown in Fig. 9.25a. Suppose that the actual state of equilibrium is known at Point A, and we want to compute the incremental displacement vector $\{dU\}$ associated with the incremental load vector $\{dR\}$ which is applied at Point A in equilibrium.

The mid-point integration rule is motivated by the idea that the secant stiffness denoted by line AD can probably be closely approximated by the tangent stiffness

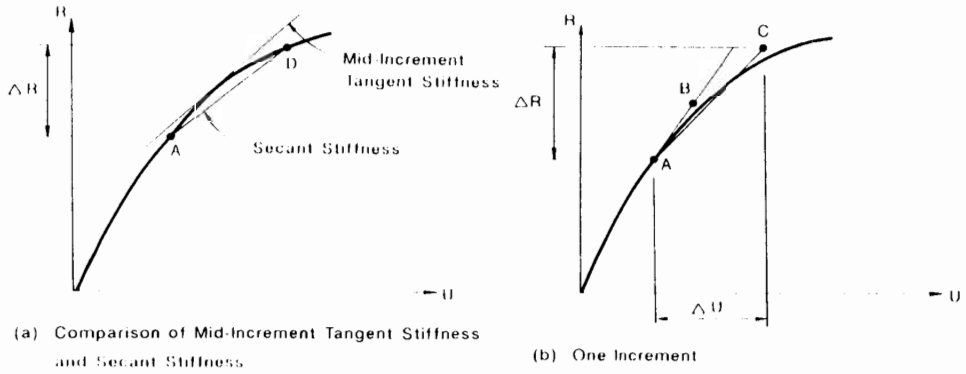

Fig. 9.25. Mid-point integration rule: (a) Comparison of mid-increment tangent stiffness and secant stiffness; (b) One increment.

evaluated at mid increment (half of the load increment). The mid increment stiffness, of course, is not known but we can estimate it. Referring to Fig. 9.25b, we first apply half of incremental load vector, $\frac{1}{2}\{dR\}$. The tangent stiffness at Point A is used to obtain the mid-incremental solution denoted by Point B. Subsequently, the complete incremental load and the tangent stiffness evaluated at Point B are used to obtain an approximate incremental solution denoted by point C. Thus, two sets of linear, simultaneous equations must be solved in each increment.

The elastic-plastic constitutive matrix is modified at mid-increment to reflect mid-increment stresses. However, neither the geometry nor the geometrical stiffness matrix is updated at mid-increment, rather their value at the beginning of the increment is used to compute mid-increment tangent stiffness. This is done to save computation time, under the assumption that the geometrical nonlinearity would not be as severe as the material nonlinearity.

9.4.2 Iterative procedure

Iterative procedure is the method by which the calculation is continued until the nonlinear equilibrium equations are satisfied. Since a constant or variable element stiffness is used during each iterative calculation, equilibrium is not necessarily satisfied. Consequently, a *correction load vector*, which is an unequal force vector obtained from the external load vectors and the stress state at the previous iterative step, is then applied to approximate the displacement increment at the next iterative step. This procedure can be repeated until the correction load vector becomes negligible. During an iteration, two different stiffness matrices are considered. One is based on the tangent stiffness method (the *Newton-Raphson method*) and the other on the *modified Newton-Raphson method*. In the former case, the tangent stiffness matrix is recalculated at each time during an iteration as shown in Fig. 9.26 and therefore convergence of the solution is not guaranteed if the tangent stiffness becomes weak. In the latter case, the stiffness matrix evaluated at the previous step is used throughout the iteration as shown in Fig. 9.27. Therefore, the number of iteration increases until the solution converges.

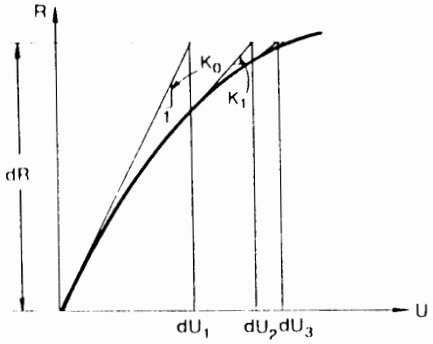

Fig. 9.26. Newton-Raphson method.

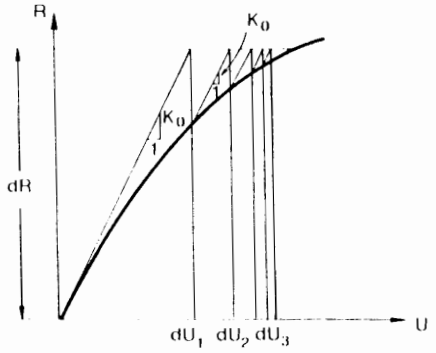

Fig. 9.27. Modified Newton-Raphson method.

The following numerical procedures are generally performed within the framework of the iterative calculation of nonlinear analysis.

Initial strain procedure: A number of incremental solution techniques, which do not require formulation of the tangent stiffness, have appeared in the literature in 1960's. One of these techniques, utilized in elastic-plastic problems, is called the *initial strain method*.

Gallagher et al. (1962) suggested the following approach for the analysis of nonlinear elastic, hardening materials subjected to small displacement. Now consider the analysis of an elastic-plastic problem associated with the large-strain and large-rotation analysis, under the updated Lagrangian formulation, as explained in Section 9.3.3. The incremental stress-strain relationship of a generic finite element is written as:

$$\{d\tau\} = [C]\{d\epsilon\} \tag{9.147}$$

where $[C]$ is an elastic-plastic constitutive matrix evaluated at the beginning of the increment, $\{d\tau\}$ is incremental Cartesian stress vector referred to the local coordinate frame in the subsequent configuration, and $\{d\epsilon\}$ denotes the small strain increment vector. An equivalent constitutive relationship is from Fig. 9.28:

$$\{d\tau\} = [C^e](\{d\epsilon\} - \{d\epsilon^p\}) \tag{9.148}$$

where $[C^e]$ and $\{d\epsilon^p\}$ are respectively the elastic constitutive matrix and the plastic strain increment vector expected during an increment.

If somehow we knew the value of incremental plastic strain vector $\{d\epsilon^p\}$ in Eq. (9.148), we could use Eq. (9.148) rather than Eq. (9.147) to evaluate the element stiffness. For example, substitution of $\{d\tau\}$ in Eq. (9.148) into Eq. (9.122) leads to

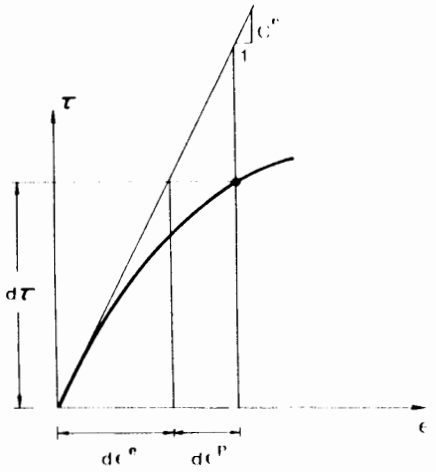

Fig. 9.28. Initial strain method.

the following finite-element equation:

$$\sum\left(\int_V [\tilde{B}]^T [A][\tilde{B}]\, dV\right)\{dU\} + \sum\left(\int_V [B_L]^T [[C^e] + [\psi]][B_L]\, dV\right)\{dU\}$$

$$- \sum\left(\int_V [B_L]^T [C^e]\{d\epsilon^p\}\, dV\right)$$

$$= \sum\left(\int_A [N]^T \{T^{t+dt}\}\, dA\right) + \sum\left(\int_V [N]^T \{F\}\, dV\right)$$

$$- \sum\left(\int_V [B_L]^T \{\bar{\sigma}\}\, dV\right) \tag{9.149}$$

The third integral in the left-hand side of the above equation corresponds to an *effective load vector* which can be shifted to the right-hand side. Since the incremental plastic strain vector $\{d\epsilon^p\}$ is not known at the beginning of an increment, $\{d\epsilon^p\}$ determined in the immediately preceding incremental step may be firstly used to estimate the incremental plastic strain vector in the current increment. For example, once the strain increment vector $\{d\epsilon\}$ and the stress increment vector $\{d\tau\}$ have been evaluated, the vector of plastic strain increment can be computed as:

$$\{d\epsilon^p\} = \{d\epsilon\} - [C^e]^{-1}[C]\{d\epsilon\} \tag{9.150a}$$

or

$$\{d\epsilon^p\} = [C]^{-1}\{d\tau\} - [C^e]^{-1}\{d\tau\} \tag{9.150b}$$

where the superscript -1 denotes matrix inverse. Equation (9.150a) is associated with the so-called *constant strain method* of computing incremental plastic strain vector, while Eq. (9.150b) is associated with the so-called *constant stress method* (Lansing et al., 1965).

As has often been noted that the constant stress method breaks down for the perfect plasticity model since matrix $[C]$ contains no inverse. The initial strain technique as proposed by Gallagher et al. (1962) was used by Lansing et al. (1965) and Armen et al. (1968) to analyze elastic-plastic problems.

Considering again Eq. (9.148), if we could choose an incremental plastic strain vector such that the incremental solution satisfied Eq. (9.147), the initial strain method would be identical to an Euler method. This suggests an iteration technique in which the vector of plastic strain increment $\{d\epsilon^p\}$ estimated from either Eq. (9.150a) or (9.150b) is again applied into Eq. (9.149) as an unbalanced load vector and then the vector of updated plastic strain increment is obtained in a similar manner to the previous step. This process is continued until satisfied convergence is obtained. Finally, an elastic-plastic constitutive matrix $[C]$ is updated at the end of the increment.

The above approach was suggested by Argyris (1965). A somewhat similar technique was proposed by Capurso (1969), where a proof of convergence was presented. An interesting variation of the method was used by Witmer and Kotanchik (1968) to analyze perfectly plastic materials. The iterative technique is such that the total stress state at the end of the increment is guaranteed to satisfy the yield inequality, while the incremental stresses and incremental strains satisfy the constitutive relation (9.147) where, however, the elastic-plastic constitutive matrix $[C]$ is now evaluated at the end of the increment.

Initial stress procedure: Zienkiewicz et al. (1969) discussed a so-called *initial stress iteration technique* for elastic-plastic problems. In a similar manner to that of the initial strain procedure, the first estimate of the strain increments is obtained from an elastic solution. The revised stress increments are estimated from Eq. (9.147) using the strain increments obtained at the first elastic-calculation. The new

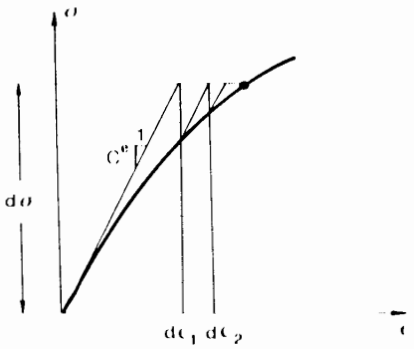

Fig. 9.29. Initial stress method.

mate of stress increments does not satisfy equilibrium for the discretized body. The resultant unbalanced nodal force is then distributed using the elastic stiffness. This procedure is continued until the unbalanced nodal forces are negligible (see Fig. 9.29). At each stage of the iteration process the constitutive matrix is evaluated using the most recently determined stress state. This technique is similar to the so-called *modified Newton-Raphson iterative technique*.

A variant of the initial stress method has been presented by Nayak and Zienkiewicz (1972). The first solution for the strain is calculated by using the tangent stiffness at the beginning of the increment. Then a revised stress state is obtained by numerically integrating the stress-increment strain-increment equations over the first estimate of strain increments. Since the stress state can not in general satisfy equilibrium of the discretized body, unbalanced nodal forces exist. The unbalanced nodal forces are distributed to the system using either the current tangent stiffness or the initial tangent stiffness evaluated at the beginning of the increment. This process is repeated until the acceptable convergence is obtained. If at each stage the current tangent stiffness is used to distribute the unbalanced nodal forces, the procedure is similar to the Newton-Raphson iteration. On the other hand, if the initial tangent stiffness is used for all iterations, the procedure is similar to the modified Newton-Raphson iteration.

The accuracy of the iteration procedures just described is of course dependent upon increment size as is the case with all of the methods discussed above. Even if a Newton-Raphson like procedure is employed, we must still use a fairly large number of increments in order to obtain an accurate solution. This is the case regardless of the convergence criterion used and simply reflects the fact that we employ incremental plasticity theory.

9.4.3 Iterative solution techniques

The solution techniques for nonlinear problems described in the previous Section are all based on a piecewise linear method in which the stiffness of structure is assumed constant and an iterative procedure is pursued until equilibrium is satisfied.

At the beginning of the $(n+1)$-th incremental step, the incremental load vector $\{\mathrm{d}R\}^{n+1}$ is given as the difference between the total load level $\{R_B\}^{n+1} + \{R_S\}^{n+1}$ and the resisting forces $\{R_I\}^n$ obtained by integration of the element stresses at the end of the previous n-th step:

$$\{\mathrm{d}R\}^{n+1} = \{R_B\}^{n+1} + \{R_S\}^{n+1} - \{R_I\}^n \tag{9.151}$$

The incremental displacements are then obtained as:

$$\{\mathrm{d}U\}^{n+1} = [K]_{n+1}^{-1}\{\mathrm{d}R\}^{n+1} \tag{9.152}$$

where $[K]_{n+1}$ is the global stiffness of structure at the beginning of the $(n+1)$-th increment.

Due to the assumption of a constant stiffness within the load step, the displacement increments $\{dU\}^{n+1}$ will, in general, be in error. If left uncorrected, such errors will accumulate and solution will diverge from the correct load path. Therefore, some iterative procedure should be implemented to insure that the solution obtained is sufficiently close to the true equilibrium position. Bathe (1982) describes several iterative solution techniques including the full Newton-Raphson, the modified Newton-Raphson, and the initial stress method. Crisfield (1979) has presented an efficient solution acceleration scheme for the modified Newton-Raphson technique.

Convergence of the iterative solution is generally measured using either a *displacement criterion* or a *residual force criterion*. The first method compares the norms of two consecutive trial solutions. Convergence is satisfied when the difference between the two norms is less than some specified tolerance:

$$\frac{\left|\{U\}_{i+1}^{n+1}\right| - \left|\{U\}_{i}^{n+1}\right|}{\left|\{U\}_{i}^{n+1}\right|} \leq \text{Tol} \tag{9.153a}$$

or defining $\{dU\}_{i}^{n+1} = \{U\}_{i+1}^{n+1} - \{U\}_{i}^{n+1}$, we have:

$$\frac{\left|\{dU\}_{i}^{n+1}\right|}{\left|\{U\}_{i}^{n+1}\right|} \leq \text{Tol} \tag{9.153b}$$

where the subscript i is the iteration number and the norm of a vector $\{A\}$ is defined as:

$$\text{Norm}\ \{A\} = |\{A\}| = \sqrt{\{A\}^T \{A\}} \tag{9.154}$$

Equations (9.153a) and (9.153b) represent two options for measuring displacement convergence.

Alternatively, one may compare the norm of the residual (unbalanced) force vector $\{\psi\}$ to the norm of the total external load vector $\{R\}^{n+1} = \{R_B\}^{n+1} + \{R_S\}^{n+1}$:

$$\frac{|\{\psi\}|}{|\{R\}^{n+1}|} \leq \text{Tol} \tag{9.155}$$

where the residual force vector is defined as:

$$\{\psi\} = \{R\}^{n+1} - \{R_I\}_{i+1}^{n+1} \tag{9.156}$$

Nayak and Zienkiewicz (1972) have suggested the tolerance for these criteria should be on the order of 10^{-4} to 10^{-5}. This seems rather restrictive for geological

materials. Good results have been obtained using a *displacement convergence tolerance* in Eq. (9.153b) on the order of 10^{-2} to 10^{-3} when predicting the theoretical collapse load of footings, as to be presented in the next Section. It should be noted that the displacement convergence criterion represents an indirect method of minimizing the residual loads.

9.4.4 Applicability of the finite-element method

The plane strain elastic-plastic response of clay strata subjected to footing loads has been investigated previously by Davidson and Chen (1977, 1978), and Mizuno and Chen (1983b), among others. These authors considered the effects of large deformations, material hardening, and non-associated flow rules.

Figure 9.30 shows the effect of element selection on the response of a strip footing resting on a von Mises type material ($\phi = 0$) for three cases. Chen (1975) used rectangular finite elements composed of four constant strain triangular (CST) elements. The remaining analyses were obtained with the finite-element program NFAP (Nonlinear Finite Element Analysis Program). One analysis made use of four-node (linear) rectangular elements with isoparametric formulation and 2×2 Gauss quadrature. The remaining analysis used eight-node, or parabolic elements with 3×3 Gauss quadrature.

The analyses performed by Chen (1975) and that using the linear isoparametric element made use of Mesh 1 in Fig. 9.31a. The analyses with the parabolic element

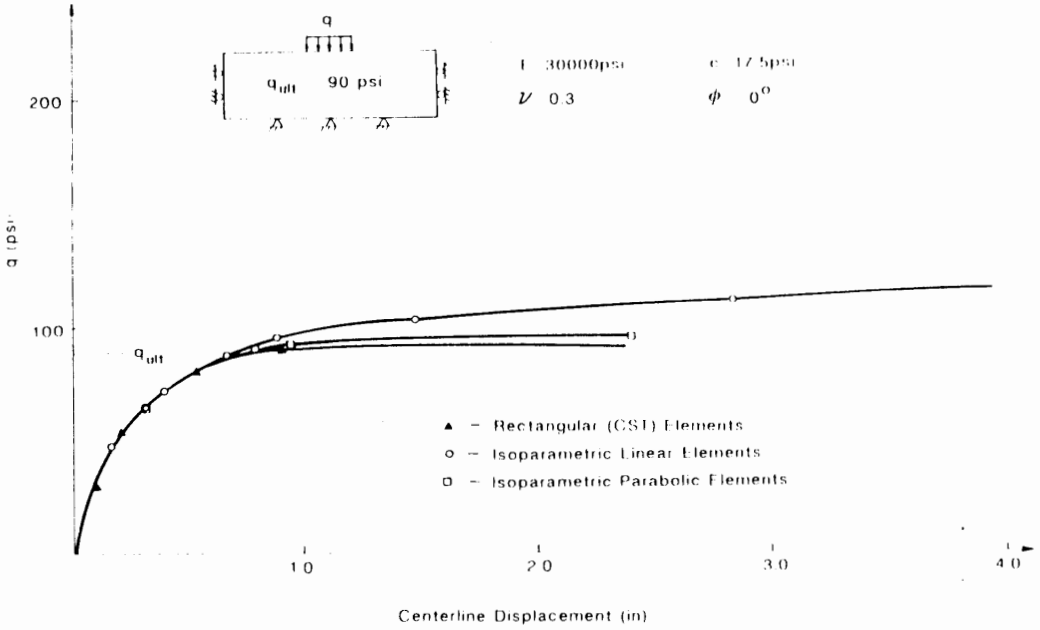

Fig. 9.30. Footing response on von Mises material.

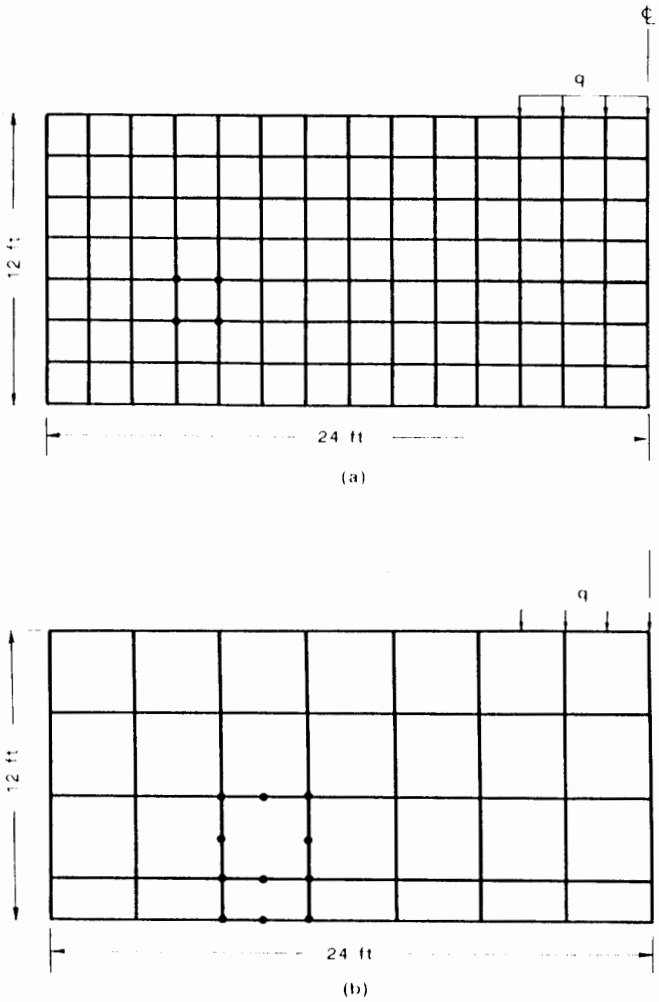

Fig. 9.31. Element mesh used for footing analysis.

used Mesh 2 in Fig. 9.31b. Mesh 1 contains 98 elements, 120 nodes and 196 net degrees of freedom. Mesh 2 contains 28 elements, 99 nodes, and 154 net degrees of freedom.

As shown in Fig. 9.30, the analysis using the linear isoparametric element displays the "locking" phenomenon discussed by Nagtegaal et al. (1974). The remaining analyses are consistent with the exact collapse load. The validity of these elements for present type analysis has been discussed by Sloan and Randolph (1982). It is interesting to note the second mesh provides a better solution with the use of less elements, degrees of freedom, and total Gauss points. It is expected, therefore, that the use of parabolic elements will be more economical. Both

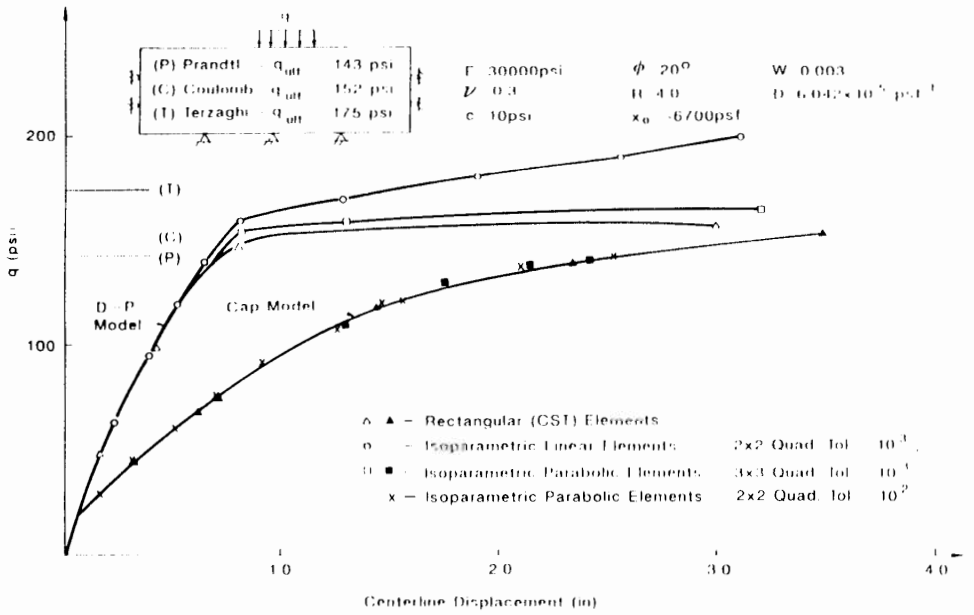

Fig. 9.32. Footing response on frictional material.

solutions obtained with NFAP used a convergence tolerance in Eq. (9.153b) of 10^{-2}.

Using the same mesh geometries and element formulations, the results for the analysis of a strip footing resting on a frictional material have been obtained and shown in Fig. 9.32. The frictional behavior of the soil is represented by matching the Drucker–Prager criterion with the plane strain failure condition of the Mohr-Coulomb criterion (Chen and Saleeb, 1982). Results are presented in Fig. 9.32 for the Drucker–Prager model with and without the cap. The limiting cases are compared with the collapse solutions of Prandtl, Coulomb and Terzaghi. The analysis performed with the rectangular elements composed of the CST elements were made by Mizuno (1981) and details of this analysis are presented as one of numerical examples, in Chapter 10.

A comparison of the load-displacement relations predicted by the Drucker–Prager, and Cap models shows that the Cap model predicts larger settlements at low stresses. This is a reasonable development since the Drucker–Prager model neglects the influence of plastic volumetric compaction. However, both materials are valid for collapse predictions.

The "locking" phenomenon is found again for the linear isoparametric formulation in both the Drucker–Prager model and the Cap model (not shown).

The analyses for the Drucker–Prager model were performed with a convergence tolerance of 10^{-2}. For the Cap model, the analyses were performed with a tolerance

of both 10^{-2} and 10^{-3}. In the case of the more restrictive criterion with a tolerance of 10^{-3}, the Cap model last converged at a load level of 142 psi. However, the residual force vector $\{\psi\}$ in Eq. (9.155) was rather smaller at the next greater level, 145 psi. This appears to indicate that an equilibrium position does exist, but a rather large displacement increment made it difficult to satisfy the displacement convergence criterion. In the case of a tolerance of 10^{-2}, essentially the same load-displacement response was predicted, with convergence last obtained at a load of 148 psi.

A study of the influence of the order of Gauss integration was also performed. A 2×2 integration scheme resulted in essentially the same predictions as those for the 3×3 integration scheme previously discussed in the footing response on the von Mises material (Fig. 9.30). A slightly softer response was observed at higher stress levels. An analysis using 2×2 integration and a solution tolerance of 10^{-2} resulted in the same predictions as that of 3×3 integration and a tolerance of 10^{-3}, while requiring less than half the CPU time (Fig. 9.32).

9.5 LARGE-DEFORMATION FINITE-ELEMENT PREDICTIONS OF VERTICAL SLOPE

Utilizing the finite-element method with large-deformation formulation as well as the small deformation formulation to perform elastic-plastic analyses of a vertical slope in a homogeneous soil, Snitbhan and Chen (1975, 1978) concluded that the effect of large deformation on the response of slopes is extremely significant. In their work, the soil was modeled as a linear elastic-perfectly plastic material with the Drucker–Prager yield criterion and its associated flow rule.

In this Section, we shall apply the Drucker–Prager model with a non-associated flow rule as well as the model with the associated flow rule to solve the same type of two-dimensional slope problem under the plane strain condition, by using the finite element method with large deformation effect (small strain and large rotation effect). These finite-element results (Mizuno and Chen, 1983a) are presented and compared with the earlier work by Snitbhan and Chen (1975, 1978). Further, the limit load and failure mechanism are discussed in view of the present large-deformation finite-element solution and the limit analysis solution.

9.5.1 *Analyses of vertical slopes with Drucker–Prager models*

Analytical model

To perform an elastic-plastic effective stress analysis of a vertical slope subjected to gravitational load, a 30-ft (9.15-m) high vertical slope as shown in Fig. 9.33 is considered. To simulate an infinite soil mass, the vertical boundaries and bottom boundary are placed respectively at 300 ft (91.5 m) and 150 ft (45.75 m) away from the toe of the slope. Movement on the vertical boundaries is constrained horizontally only, while movement on the bottom boundary is constrained in both horizontal and vertical directions. A mesh consisting of 250 nodes and 216 rectangular

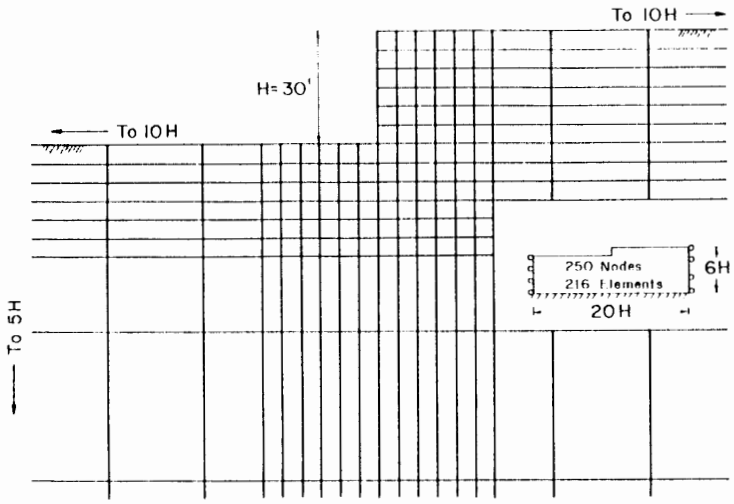

Fig. 9.33. Finite-element model of a vertical slope.

elements is utilized in the finite element analysis (Fig. 9.33). A rectangular element contains four constant-strain triangular elements.

Loading conditions and analytical procedure

Sequential loading to simulate a cut-down or build-up process is not considered. Instead, for a given slope, the complete load-displacement-stress response of the slope is investigated quantitatively by increasing the internal force due to the weight of soil until a collapse is observed. During each load increment, the incremental equilibrium equations are formulated with respect to the current slope configuration (updated Lagrangian formulation) to capture the large-deformation effect.

Material constants

The following three sets of the material constants of cohesion c and internal friction angle ϕ are assumed:

Type (a) $c = 810$ psf (38.8 kPa) and $\phi = 10°$

Type (b) $c = 650$ psf (31.1 kPa) and $\phi = 20°$

Type (c) $c = 540$ psf (25.9 kPa) and $\phi = 30°$

Also, Young's modulus, E, and Poisson's ratio, ν, are assumed to be 5×10^5 psf (2.4×10^4 kPa) and 0.3 for all three cases. The material constants, α and k, in the Drucker–Prager model are obtained from matching with the Coulomb criterion in the plane strain condition. For the analysis with a non-associated flow rule, the von Mises type of function is used as the plastic potential function. Thus, the internal friction angle ϕ^p, corresponding to this function, is set zero.

In what follows, the comparative study on the large-deformation problem of the

vertical slope is discussed with respect to (1) load-displacement curves, (2) deformed shape, (3) limit loads, (4) stress distributions, (5) yield zones and (6) velocity fields.

9.5.2 *Load-displacement curves*

The response of a body to an applied load is generally illustrated by its load-displacement relationship. In the bearing-capacity problems to be presented in Chapter 10, the load is applied through a footing toe where the displacement is recorded. In the present slope analysis, however, soil weight is applied uniformly throughout the soil mass, and thus a reference point for recording the displacement is not obvious. Snitbhan and Chen (1975, 1978) carefully investigated bulging of the vertical slope line, while the gravitational load is applied incrementally. It was found that, of all the nodal points located along the vertical slope line, the one immediately above the toe experiences the largest horizontal displacement. Therefore, we choose this nodal point as the reference from which the displacement data are presented in the load-displacement curves.

Type (a)

The complete load-displacement curves for the case of $\phi = 10°$ are shown in Fig. 9.34 where the value of horizontal displacement immediately above the toe is taken as the quantity of displacement. The curves with the solid and broken lines are responses predicted by the models with the associated and non-associated flow rules, respectively. Both curves behave identically to $\gamma = 40$ pcf (6.28 kN/m^3) and thereafter show slightly different responses with the intersection at about $\gamma = 140$

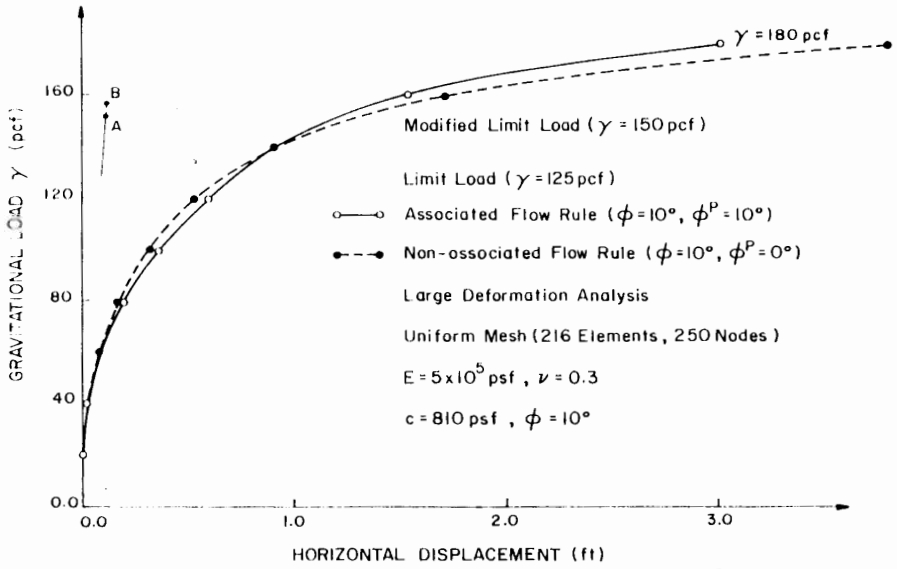

Fig. 9.34. Gravitational load-horizontal displacement curves for the $\phi = 10°$ case.

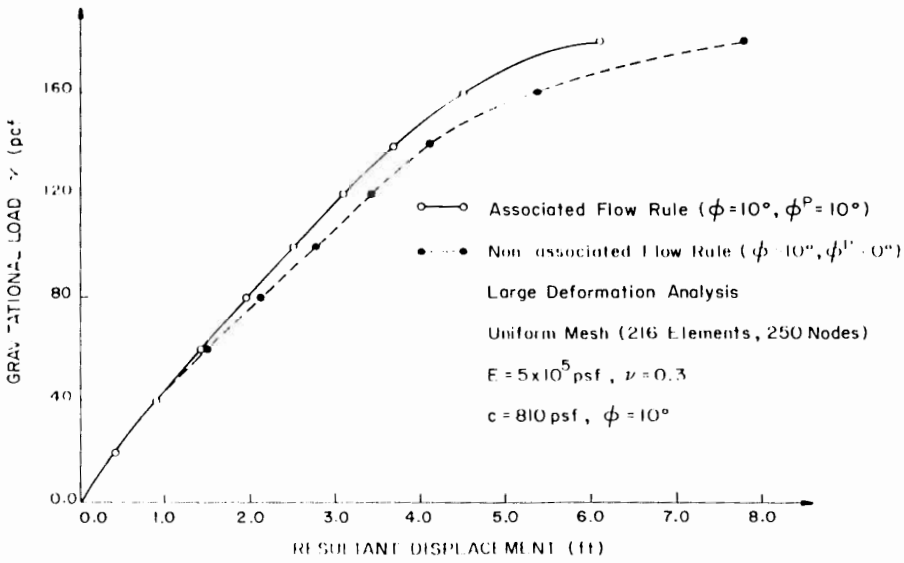

Fig. 9.35. Gravitational load-resultant displacement curves for the $\phi = 10°$ case.

pcf. As a common trend of response, the curves bend over smoothly and approach the final value of $\gamma = 180$ pcf. Although it was found from the analysis of bearing-capacity problem (Mizuno and Chen, 1983b, see Chapter 10) that the curve for the case of the non-associated flow rule presents a much larger displacement at the same load level than that for the case of the associated flow rule, this can not be seen from the curves in Fig. 9.34.

On the other hand, Fig. 9.35 shows the load-displacement curves which utilize the resultant displacement at the nodal point above the toe. From this figure, it is clear that the curve for the case of the non-associated flow rule presents larger resultant displacement than that for the case of the associated flow rule. However, the behavior of collapse can not be so clearly visualized.

Type (b) and Type (c)

Similarly, the two types of load-displacement curves for $\phi = 20°$ and $30°$ cases are illustrated in Figs. 9.36 through 9.39. In the case of $\phi = 20°$ in Fig. 9.36, both curves show initial yield at 40 pcf and intersect at about 135 pcf. Although the general trend for both curves is similar to the case of $\phi = 10°$, it can be seen that the non-associated flow rule curve is stiffer than the associated flow rule curve, and shows drastic collapse behavior. As expected, the response for both flow rule cases becomes stiffer as the internal friction angle ϕ increases, and the curves bend over more sharply than those for the case of $\phi = 10°$. The approximate collapse loads for the cases of associated and non-associated flow rules are $\gamma = 160$ pcf and 142 pcf respectively. Further, the load-resultant displacement curves are shown in Fig. 9.37.

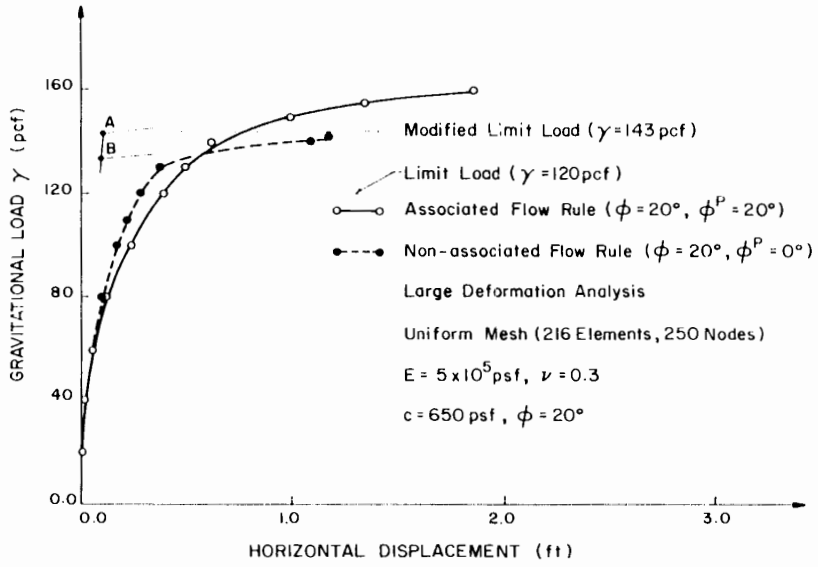

Fig. 9.36. Gravitational load-horizontal displacement curves for the $\phi = 20°$ case.

Their relationship is similar to that in the case of $\phi = 10°$. For the non-associated flow rule case, the curve also shows a sudden reduction of stiffness.

The load displacement curves for the $\phi = 30°$ case (Fig. 9.38) are stiffer and show a clearer difference in deformational behavior between the two flow rule cases.

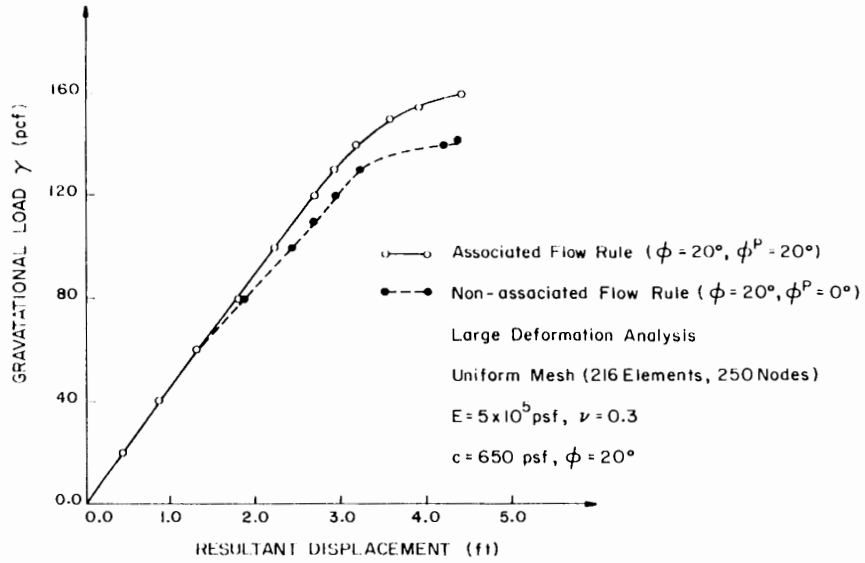

Fig. 9.37. Gravitational load-resultant displacement curves for the $\phi = 20°$ case.

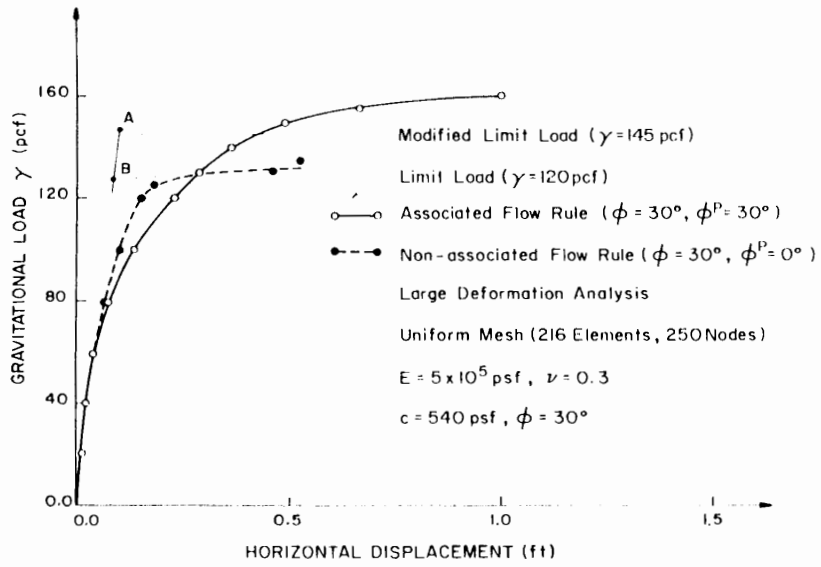

Fig. 9.38. Gravitational load-horizontal displacement curves for the $\phi = 30°$ case.

For the non-associated flow rule case, the curve rises almost linearly until collapse occurs. The approximate collapse loads for the associated and non-associated flow rule cases are $\gamma = 160$ pcf and 135 pcf respectively. The load-resultant displacement curves in Fig. 9.39 are seen to be almost linear except for the last two increments.

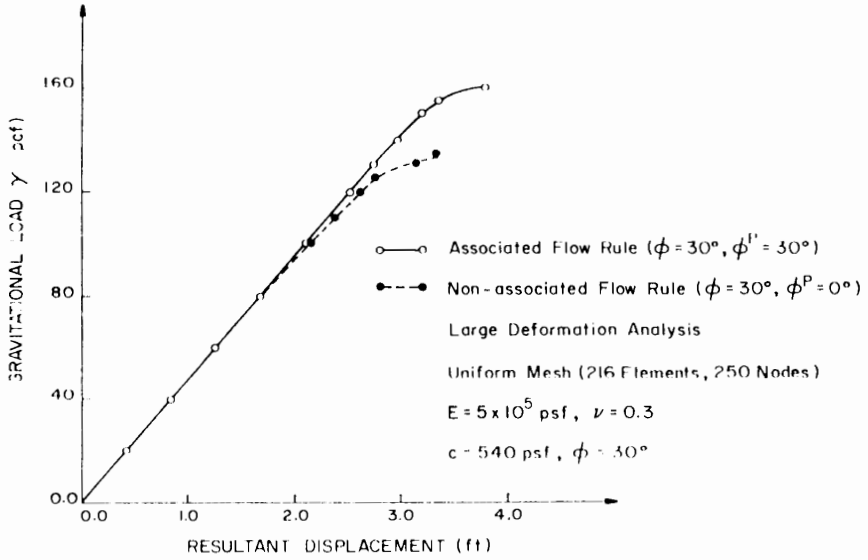

Fig. 9.39. Gravitational load-resultant displacement curves for the $\phi = 30°$ case.

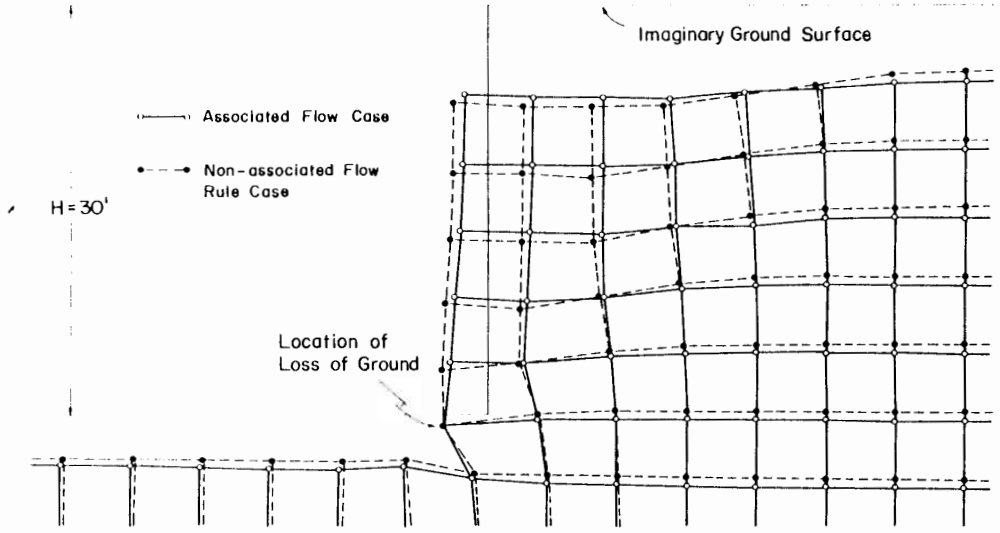

Fig. 9.40. Deformed shape of slope at sliding stage ($\gamma = 180$ pcf and $\phi = 10°$). The length of one original finite-element unit is 5 ft (1.5 m).

9.5.3 *Deformed shape*

Figure 9.40 shows the deformed geometry of the slope prior to collapse ($\gamma = 180$ pcf or 28.3 kN/m^3) in the $\phi = 10°$ case. In the figure, the resultant displacement at the nodal point above the toe is used as a normalized unit length so that the difference between the geometric changes of the slope for both flow rule cases can be seen. The deformed shape for the associated flow rule case is shown with the solid line and that for the non-associated flow rule case is shown with the broken line. In the associated and non-associated flow rule cases, respectively, the ground surface at the crest has settled approximately 6 ft (1.83 m) and 8.5 ft (2.59 m) and the lateral bulging extends 3 ft (0.92 m) and 3.8 ft (1.16 m) from the original vertical slope line. The collapse shape for the non-associated flow rule case is more severe than that for the associated flow rule case. The sliding of the mass is similar to the rigid mass failure mechanisms used in the limit analysis method. Further, in confirmation of a previous report (Snitbhan and Chen, 1975), the present analysis shows that for the associated flow rule case the loss of ground, which is identified by the largest horizontal displacement along the vertical slope line, occurs at a distance of approximately one-sixth the total height above the toe of the slope. However, for the non-associated flow rule case, the occurrence of loss of ground is observed at three nodal points above the toe.

9.5.4 *Limit loads*

According to the study by Snitbhan and Chen (1975, 1978), it appears reasonable to consider bulging or loss of ground as an instability criterion. In the large-defor-

mation finite-element analysis, the limit load is determined to be the weight of soil, γ, where the increment of load is terminated. From the load-displacement curves in Figs. 9.34, 9.36, and 9.38, the limit loads of the associated flow rule materials are approximated respectively as 180 pcf (28.28 kN/m^3), 160 (25.14), and 160 (25.14) for the $\phi = 10°$, 20°, and 30° cases. On the other hand, those of the non-associated flow rule materials are estimated to be 180, 142, and 135 pcf, respectively.

If the limit analysis or limit equilibrium methods were to be used to calculate the limit load, then it might be suggested, from the previous discussion on the deformed shape of the slope, that the "reduced" height (25 ft or 7.63 m) could be utilized in both methods. The limit analysis method using the reduced height (25 ft) predicts the modified limit loads to be 150, 143, and 145 pcf for the $\phi = 10°$, 20°, and 30° cases, respectively. Note here that the limit analysis method using the full height (30 ft) would predict corresponding values of 125, 120, and 120 pcf.

An alternative evaluation of the limit loads may be made by superimposing upon the load-displacement curves the type of idealization which would be compatible with the limit analysis and limit equilibrium methods. This has been done graphically in Figs. 9.34, 9.36, and 9.38 by extending the initial tangent modulus and approximating the final tangent modulus. The intersection point between these two straight lines represents the "equivalent" limit load. Although the graphical idealization does not illustrate precisely the perfectly plastic behavior assumed by the limit analysis and limit equilibrium methods, it does maintain similar condition that a slight increase in load beyond this limit load will result in an excessively large displacement. These intersections as the definition of limit load for the associated and non-associated flow rule cases are designated "A" and "B" in Figs. 9.34, 9.36, and 9.38. Accordingly, the limit loads so obtained for the $\phi = 10°$, 20°, and 30° cases are predicted to be, respectively, 152, 144, and 147 pcf for the associated flow rule case and 156, 134, and 127 pcf for the non-associated flow rule case. It can be understood that the limit loads for the associated flow rule material give a good agreement with those predicted by the limit analysis method using the reduced height.

9.5.5 *Stress distributions*

In Figs. 9.41 through 9.49, the distributions of vertical stress σ_y, horizontal stress σ_x and shearing stress τ_{xy} within the slopes at $\gamma = 180$ pcf (28.28 kN/m^3), 140 pcf (22), 130 pcf (20.4) are illustrated for the $\phi = 10°$, 20° and 30°, respectively. In all cases, the stresses are given along the vertical line near the vertical slope surface and along three other vertical lines located at 10 ft (3.05 m), 20 ft (6.1 m) and 30 ft (9.15 m) behind the crest of the slope. Note that in these figures the stress distributions with solid and broken lines are from the analyses with associated and non-associated flow rules, respectively, and that the stresses follow the soil mechanics sign convention (i.e., compressive stresses are positive).

Referring to Fig. 9.41 showing the distribution of vertical stresses for the $\phi = 10°$ case, it can be seen that in the associated flow rule case the variation of stress with

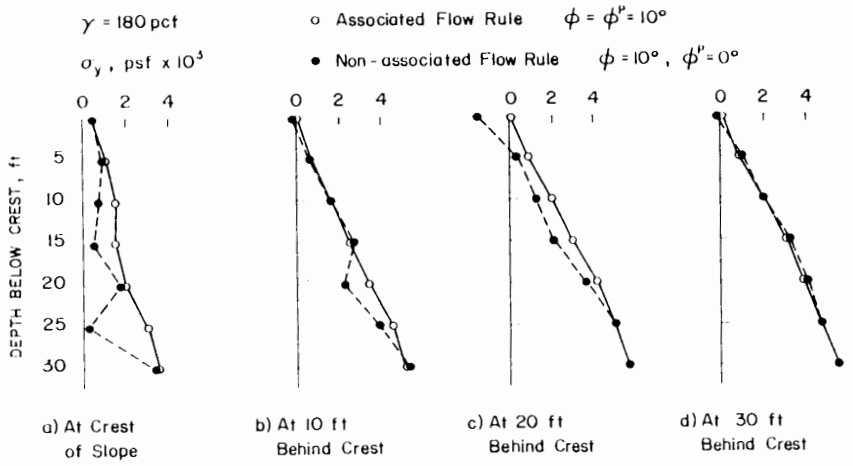

Fig. 9.41. Vertical stress distributions for the $\phi = 10°$ case.

depth is virtually the same at all locations except the vertical slope line. In the non-associated flow rule case, the stress distribution predicted at 30 ft. behind the crest is almost identical to that of the associated flow rule case. However, the stresses predicted at 10 and 20 ft. behind the crest show, as a whole, smaller values than those of the associated flow rule case. In particular, a tensile stress is predicted near the surface at 20 ft. behind the crest. The stresses near the vertical slope line are smaller for both flow rule cases than those at the three other locations. Further, the stresses in the non-associated flow rule case are smaller than those in the associated flow rule case.

As for the $\phi = 20°$ and $30°$ cases shown in Figs. 9.42 and 9.43, the variation of stress is particularly the same at all locations, except near the vertical slope line

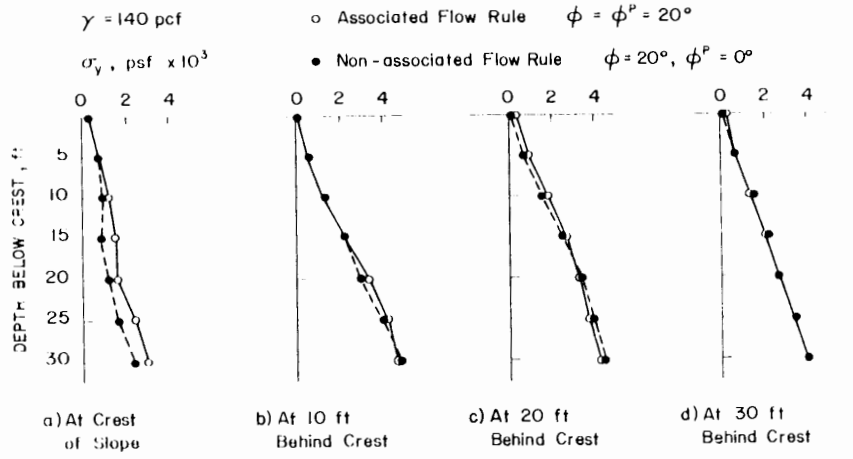

Fig. 9.42. Vertical stress distributions for the $\phi = 20°$ case.

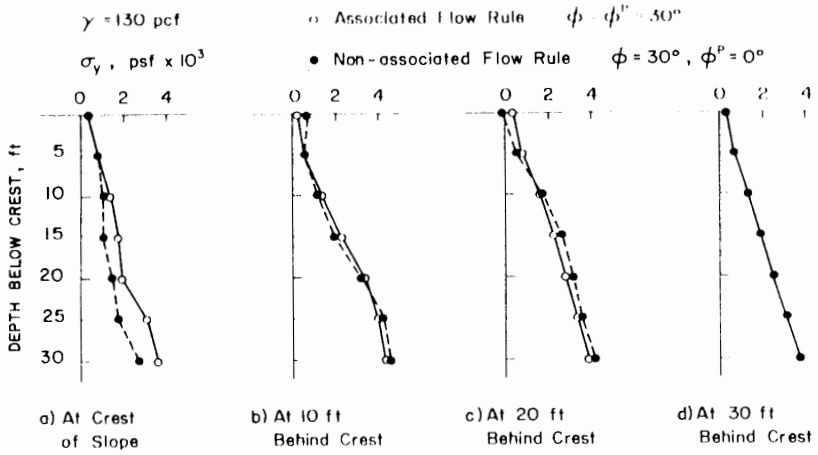

Fig. 9.43. Vertical stress distributions for the $\phi = 30°$ case.

where the stresses in the non-associated flow rule are found to be smaller than those in the associated flow rule case.

As the location of the vertical line becomes far away from the face of the slope, the magnitude of vetrical stress σ_v at any depth, H, may be approximated by:

$$\sigma_v = \gamma H \tag{9.157}$$

This simple equation (9.157) is normally used to calculate the overburden stress at any depth below the ground surface. The distribution of vertical stress at 30 ft. behind the crest of the slope presents very good agreement with Eq. (9.157) for all the cases of $\phi = 10°$, $20°$, and $30°$.

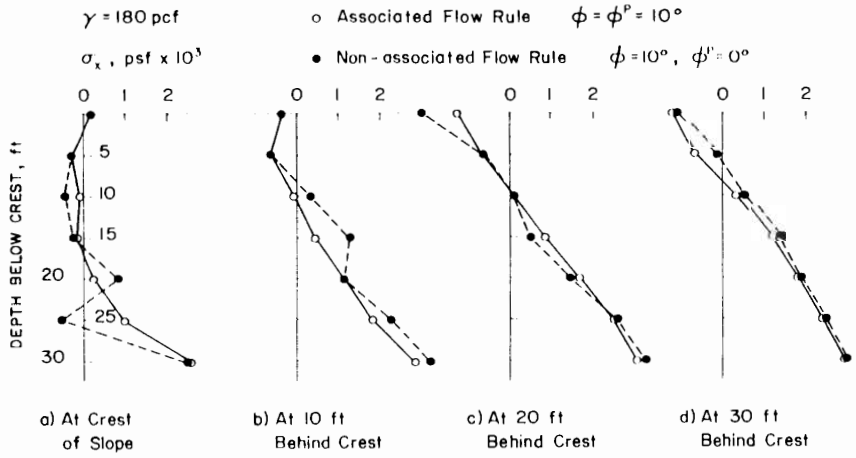

Fig. 9.44. Horizontal stress distributions for the $\phi = 10°$ case.

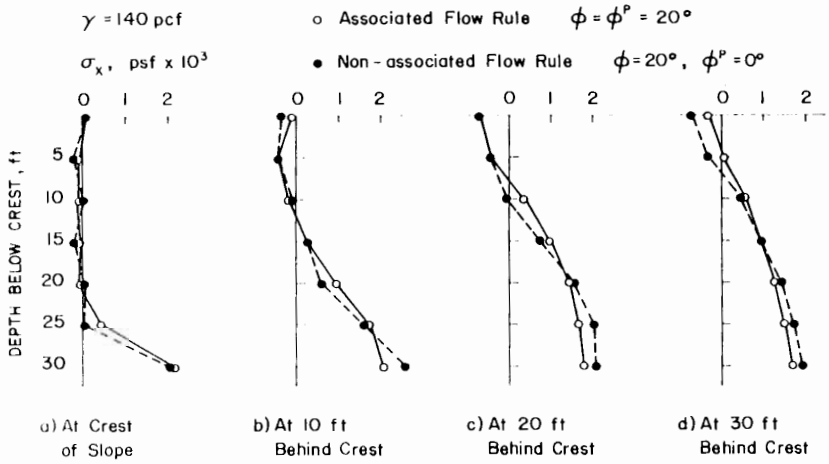

Fig. 9.45. Horizontal stress distributions for the $\phi = 20°$ case.

Next, the distributions of horizontal stresses, σ_x, at the four locations are given in Fig. 9.44 for the $\phi = 10°$ case. In the associated flow rule case (solid line), the results indicate that the vertical slope line is approximately a stress-free boundary, except at the toe area where high stress concentrations are expected due to the corner geometry. In addition, the stress distributions show a tensile zone which covers a region from near the ground surface to about one-half the total height of the slope at the vertical slope line, and approximately one-third at the other locations. Beyond the tensile zone, the horizontal stress reverses direction to become compressive stress. At all locations except the vertical slope line, the compressive stress varies almost linearly with depth.

In the non-associated flow rule case, the distributions of stress at 20 and 30 ft.

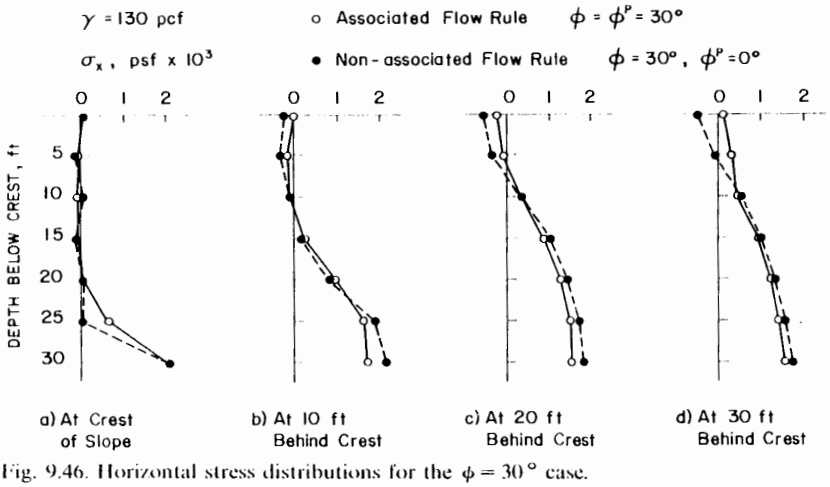

Fig. 9.46. Horizontal stress distributions for the $\phi = 30°$ case.

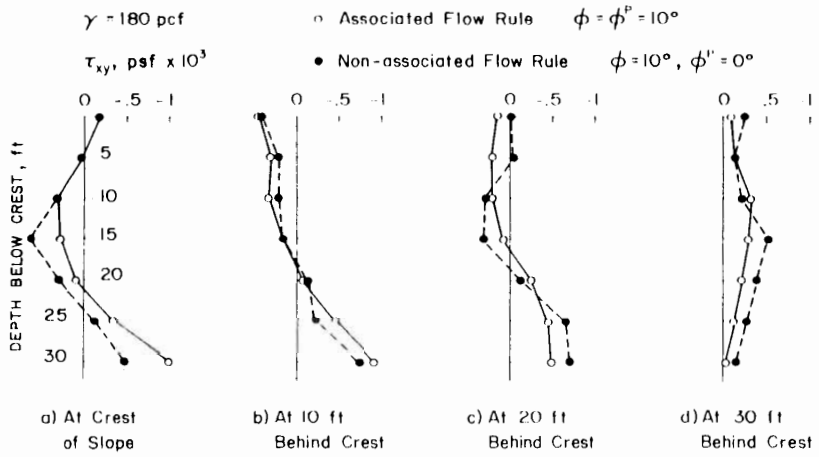

Fig. 9.47. Shearing stress distributions for the $\phi = 10°$ case.

behind the crest agree relatively well with those of the associated flow rule case. For the cases of $\phi = 20°$ and 30°, similar observations can be made from Figs. 9.45 and 9.46. All the results are very close for both flow rule cases, and the stress distributions at the vertical slope line show clearly the stress-free boundary except at the toe area.

Just as a K_o value can be defined to indicate the ratio of horizontal stress, σ_x, to vertical stress, σ_y, inside infinite ground, so also a general relationship between σ_x and σ_y may be found in the region beyond the tensile zone at all locations except the vertical slope line.

Finally, the distributions of shearing stress, τ_{xy}, along vertical lines at the four

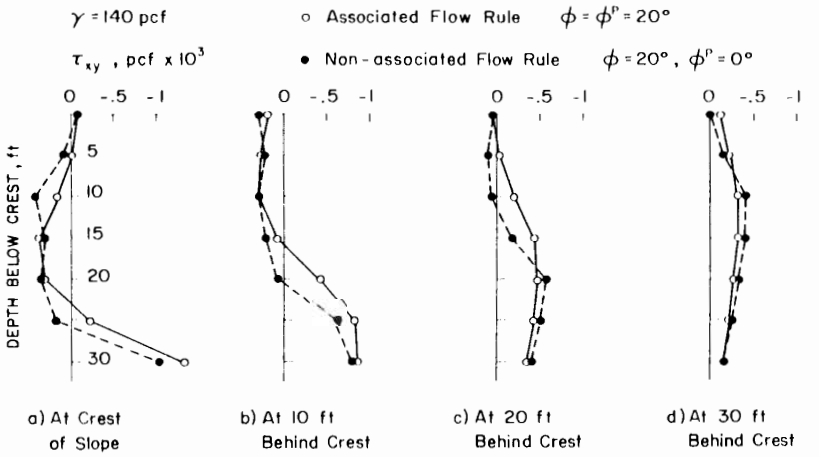

Fig. 9.48. Shearing stress distributions for the $\phi = 20°$ case.

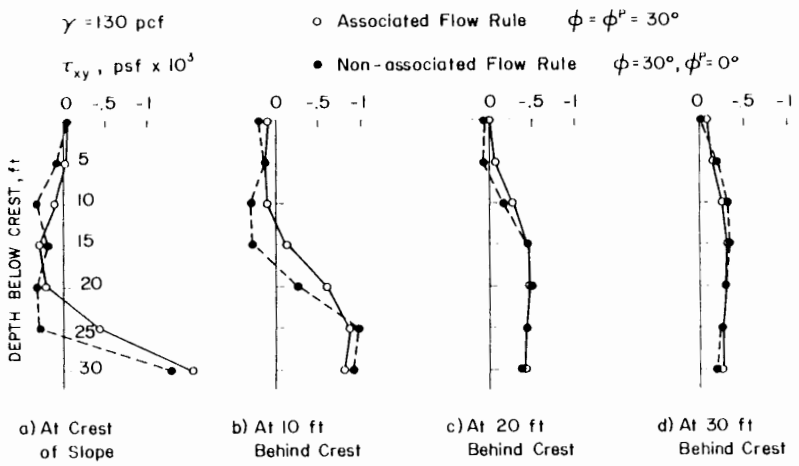

Fig. 9.49. Shearing stress distributions for the $\phi = 30°$ case.

locations are shown for the $\phi = 10°$, 20°, and 30° cases in Figs. 9.47, 9.48, and 9.49, respectively. If the ground surface were infinite, we would expect the state of stress at any point to have no shearing stress component. This condition can be observed in these figures. The magnitude of shearing for both flow rule cases decreases, on the whole, as the reference line is further away from the slope line. Also, the difference in magnitude of stress between both cases appears to become smaller. Particularly, at 30 ft. behind the crest, the distributions of shearing stress become almost the same except for the $\phi = 10°$ case.

9.5.6 *Yielded zones*

In Figs. 9.50 through 9.55, the yielded zones at four different loads (40, 80, 120, and 160 pcf or 6.28, 12.57, 18.85, and 25.14 kN/m^3) are presented for the $\phi = 10°$, 20°, and 30° cases. Considering first the yielded zones for the $\phi = 10°$ case, at $\gamma = 40$ pcf yielding first occurs at the toe area and above the bottom boundary for both flow rule cases (Figs. 9.50 and 9.51). As the gravitational load increases, the yielded zones then spread upwards toward the ground surface behind crest. In particular, the yielded zone at the toe area spreads diagonally upwards along the slip surface, as would be predicted by the limit analysis method. At $\gamma = 160$ pcf the yielded zone reaches the upper ground surface. However, the region near the lower ground surface, except for the area adjacent to the toe, does not yield even at the collapse load. This may be accounted for by some heaving of the lower ground surface which helps to reduce the potential of yielding. Further, a small region at the crest of the slope and a large region near the upper ground surface beginning at a distance of about the slope height from the crest remain in the elastic state up to the collapse load. As can be seen by comparing Figs. 9.50 and 9.51, the spreading of the yielded zones is practically the same.

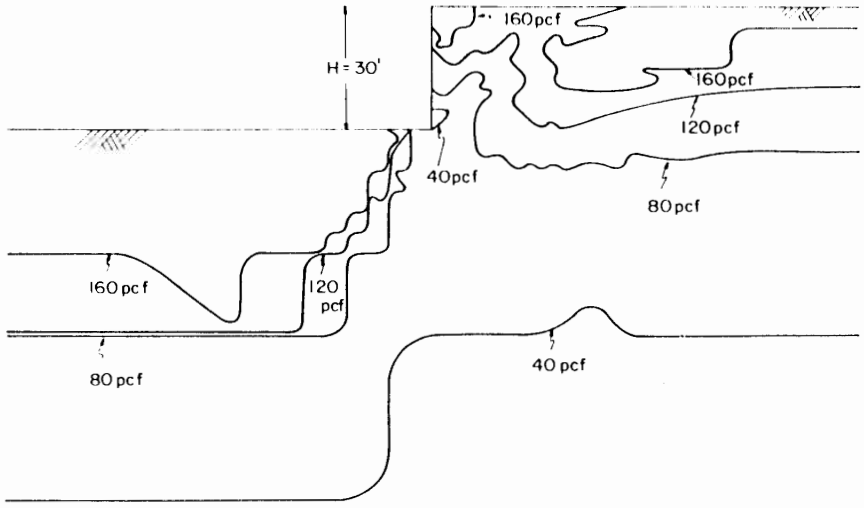

Fig. 9.50. Spread of yielded zone in associated flow rule material slope ($\phi = \phi^p = 10°$).

In Figs. 9.52 and 9.53, the yielded zones of both flow rule materials are presented at the four different load levels for the $\phi = 20°$ case. The trend of the spreading of the yielded zones appears to be similar to that in the $\phi = 10°$ case. At $\gamma = 160$ pcf, the yielded zone reaches the upper ground surface for the associated flow rule case. On the other hand, for the non-associated flow rule case, the yielded zone reaches this surface at a lower load of $\gamma = 140$ pcf. Compared to the $\phi = 10°$ case, these yielded zones do not spread as close to the ground. Consequently, larger elastic

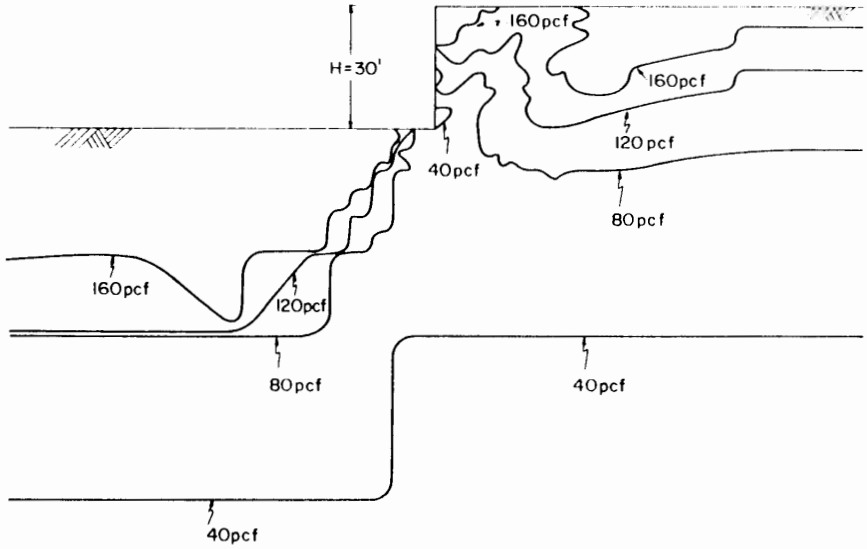

Fig. 9.51. Spread of yielded zone in non-associated flow rule material slope ($\phi = 10°$, $\phi^p = 0°$).

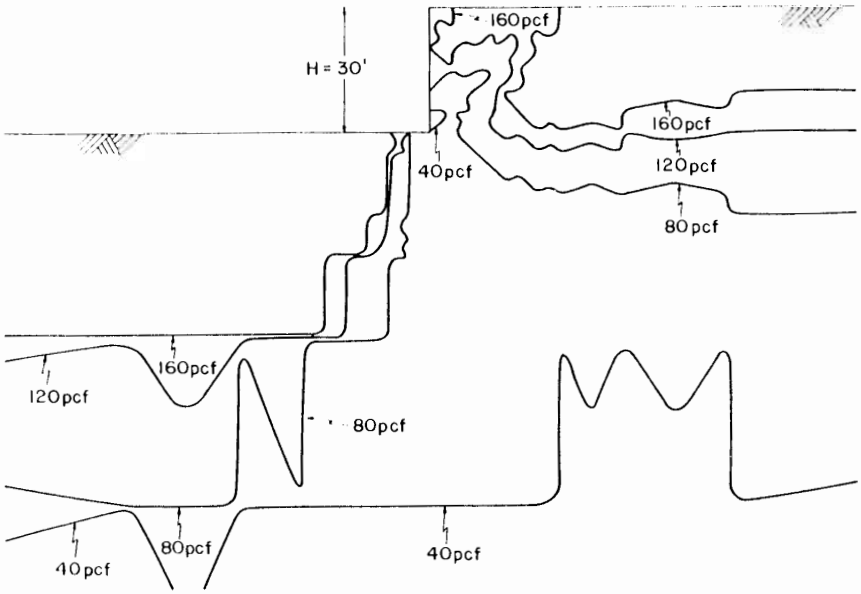

Fig. 9.52. Spread of yielded zone in associated flow rule material slope ($\phi = \phi^p = 20°$).

zones remain in the regions near the lower ground surface and upper ground surface. For the non-associated flow rule case, it can be seen in Fig. 9.53 that, at $\gamma = 120$ and 140 pcf, small yielded zones appear on the lower ground surface.

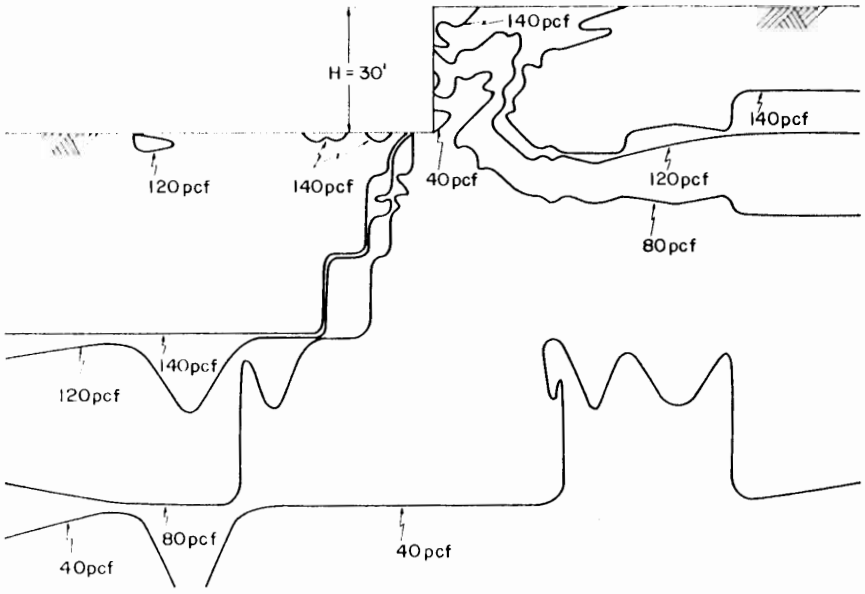

Fig. 9.53. Spread of yielded zone in non-associated flow rule material slope ($\phi = 20°$, $\phi^p = 0°$).

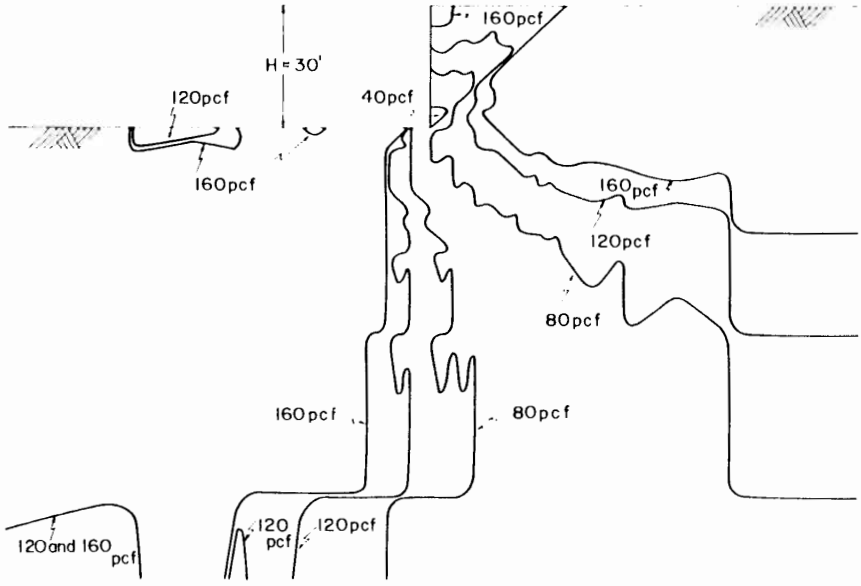

Fig. 9.54. Spread of yielded zone in associated flow rule material slope ($\phi = \phi^p = 30°$).

The spreading of the yielded zones ($\phi = 30°$ case) in Figs. 9.54 and 9.55 shows a rather different pattern than those in the last two cases. In particular, the yielding spreads upwards from the bottom boundary to the right-hand side of the toe. In

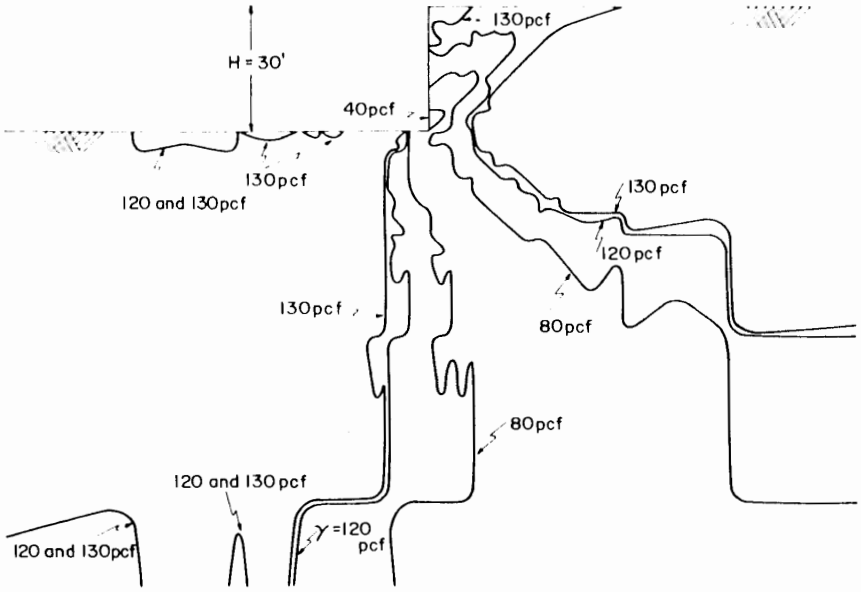

Fig. 9.55. Spread of yielded zone in non-associated flow rule material slope ($\phi = 30°$, $\phi^p = 0°$).

addition, the toe area yields and then the yielded zone spreads diagonally upwards along the slip surface of the limit analysis method. Finally, it reaches the upper ground surface and shows clearly a sharp zone of yielding inside the slope. Yielding also occurs in small regions on the lower ground surface for both flow rule cases.

9.5.7 *Velocity fields*

Snitbhan and Chen (1975, 1978) were the first to point out that there exists a "discontinuity" between the velocity fields on either side of the *modified log-spiral slip surface*, which passes from the most deformed point on the vertical slope line to a point somewhere on the upper ground surface. Further, they checked the variation in direction of the displacement vector on the slip surface and concluded that a possible slip or sliding surface of the soil mass may occur above this slip surface rather than the *conventional log-spiral slip surface*. Here, we discuss the velocity fields of both flow rule materials, and compare them with the modified log-spiral slip surface of the limit analysis method.

The velocity fields at the collapse stage are presented in Figs. 9.56, 9.57, and 9.58, for the $\phi = 10°$, $20°$, and $30°$ cases, respectively. The magnitude and direction of the velocity at each node are represented by an arrow, and the resultant-displacement increment at the nodal point above the toe is taken as a normalized unit length. The solid and broken lines in the figure are the outlines of the modified and conventional log-spiral slip surfaces, respectively.

Type (a)

Considering first the $\phi = 10°$ case in Fig. 9.56, the velocity fields of both flow rule materials seem to agree well with the modified log-spiral slip surfaces. In the associated flow rule case, the largest increment of horizontal displacement on the vertical slope line is located at a distance of one-sixth the slope height above the toe. On the other hand, in the non-associated flow rule case, three points above the toe show the largest increments of horizontal diplacement. As has been reported by Snitbhan and Chen (1975), the "discontinuity" between velocity fields on either side of the modified log-spiral slip surface can be seen in Figs. 9.56a and 9.56b. Although the magnitude of the velocity vectors in the region between the two slip surfaces is smaller than that in the sliding zone above the modified slip surface, its direction seems to follow the conventional slip surface, except at the toe.

Further, the angle between the modified slip surface and the velocity vector at the point immediately above the toe is measured from the figures. For the associated flow rule case, it is measured as 7.5°. It is expected that, if the load were increased, the angle would approach 10° as predicted by the limit analysis method. On the other hand, the angle in the non-associated flow rule case appears to be zero degree, i.e., the direction of the velocity is almost identical to the tangential direction of the modified slip surface. This means that dilatancy has not been developed on the slip surface. This condition is expected because the von Mises type of plastic potential function was assumed in the non-associated flow rule case.

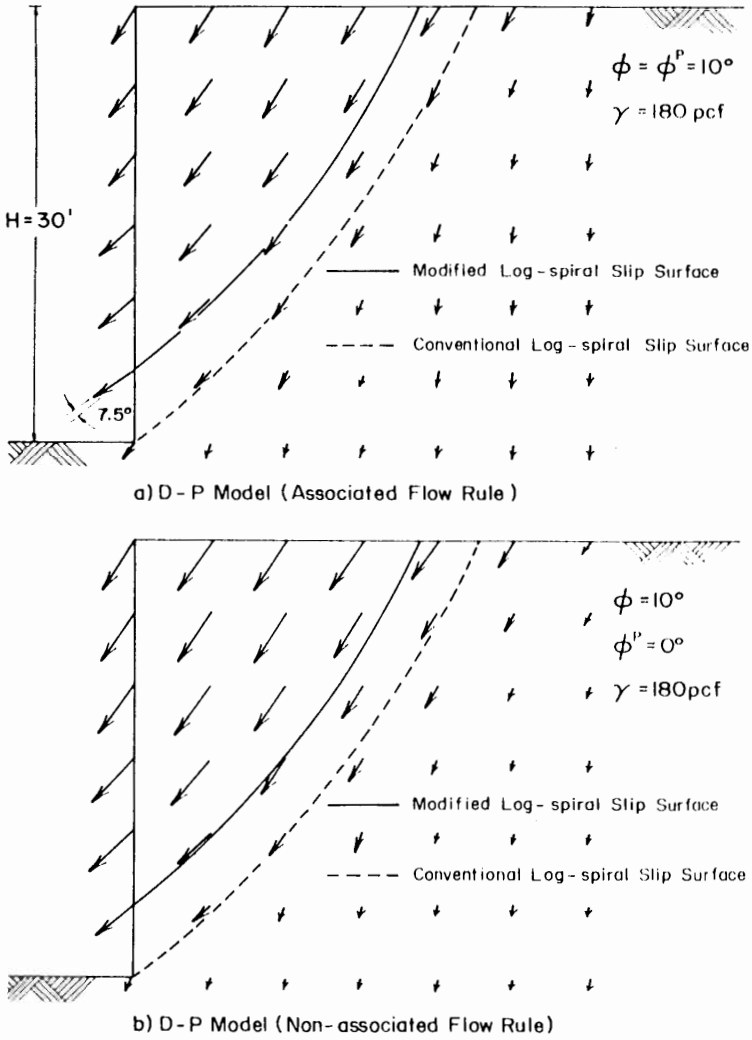

Fig. 9.56. Velocity field at the final load increment for the $\phi = 10°$ case.

Type (b)

The velocity fields of the $\phi = 20°$ case are presented in Figs. 9.57a and 9.57b. In the associated flow rule case, the "discontinuity" between velocity fields on either side of the modified slip surface is seen more clearly (Fig. 9.57a). The angle between the velocity vector and the modified slip surface at the vertical slope line is measured as 15° which is close to $\phi = 20°$. In the non-associated flow rule case, the "discontinuity" is not so clear in the region near the upper ground surface. Rather, it appears to occur near the conventional log-spiral slip surface. Also, the angle between the velocity vector and modified slip surface at the vertical slope line is approximately zero.

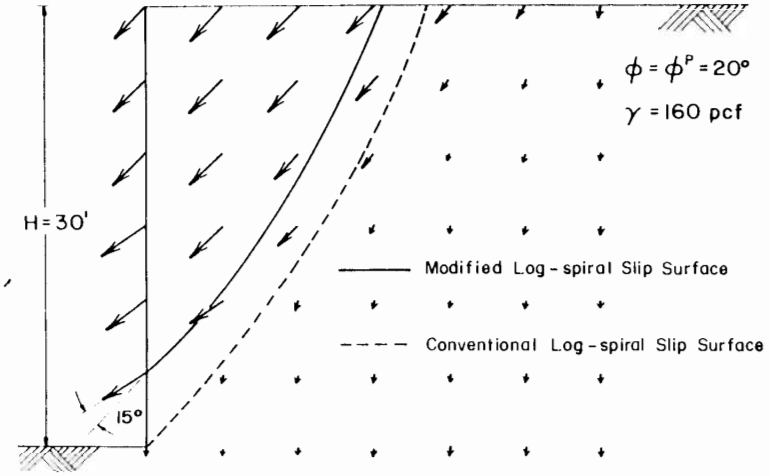

a) D-P Model (Associated Flow Rule)

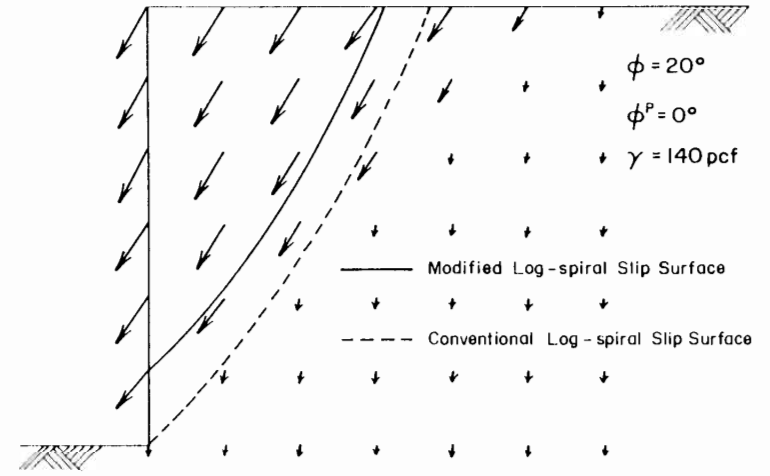

b) D-P Model (Non-associated Flow Rule)

Fig. 9.57. Velocity field at the final load increment for the $\phi = 20°$ case.

Type (c)

Similar results can be observed in Fig. 9.58a and 9.58b, for the $\phi = 30°$ case. In the associated flow rule case, the "discontinuity" can be seen clearly, and the angle between the velocity vector immediately above the toe and the slip surface is measured as 26°. On the other hand, in the non-associated flow rule case, the velocity field near the upper ground surface does not seem to agree with either of the slip surfaces. The angle between the velocity vector and the slip surface at the vertical slope line is approximately zero.

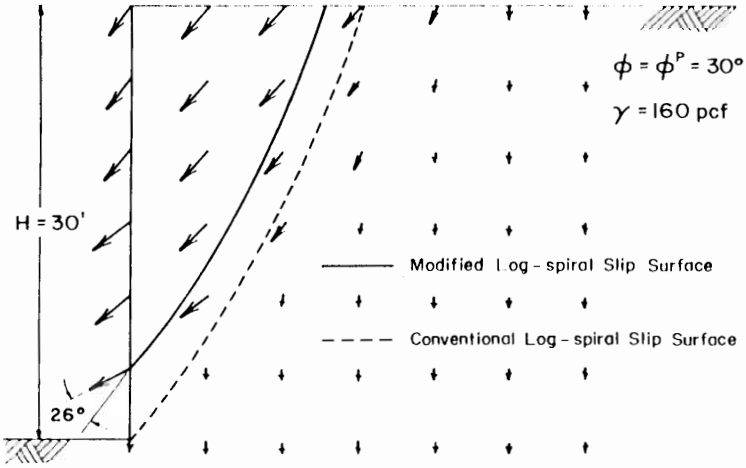

a) D-P Model (Associated Flow Rule)

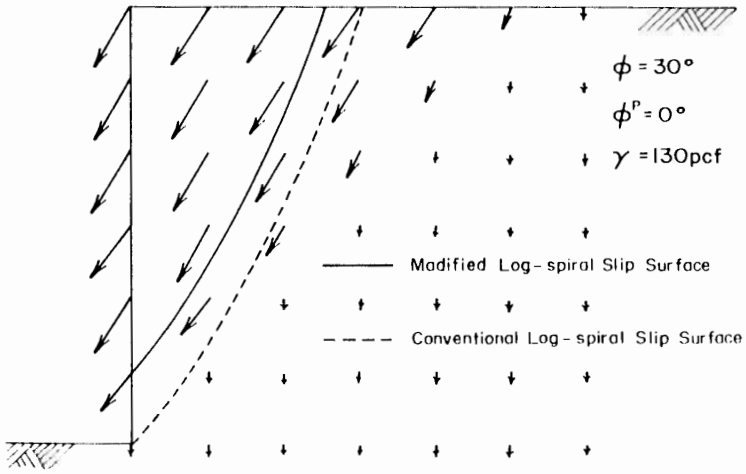

b) D-P Model (Non-associated Flow Rule)

Fig. 9.58. Velocity field at the final load increment for the $\phi = 30°$ case.

9.5.8 *Concluding remarks*

The following conclusions can be made from the present large-deformation finite-element analysis of slope:

1. As expected, the load-displacement curves in both flow rule cases exhibit very different behavior as the value of the internal friction angle ϕ increases. For three different values of ϕ, the non-associated flow rule model generally predicts a lower limit load.
2. From the geometry of the deformed slope at the collapse stage, it has been confirmed that, in the associated flow rule case, the nodal point immediately

above the toe has the largest displacement on the vertical slope line which indicates the loss of ground. On the other hand, in the non-associated flow rule case, the largest displacements occur at three nodal points above the toe. However, it appears that the collapse occurs at a distance of approximately one-sixth the total slope height above the toe, for both flow rule cases.

3. The analyses with the associated flow rule give the higher limit loads than the "modified" limit loads as predicted by the limit analysis method. On the other hand, the analyses with the non-associated flow rule give the lower limit loads than the modified limit loads for the $\phi = 20°$ and $30°$ cases. Further, a proposed graphical procedure based on the finite-element solution of the associated flow rule case may give a reasonable limit load.
4. The spreading of yielded zones inside a slope is found to be consistent with that of the limit analysis method. For the $\phi = 30°$ case, this aspect is particularly clear.
5. The velocity field of the associated flow rule materials appears to be reasonable, compared with that of the modified log-spiral slip surface of the limit analysis method. From the measurements of the angle between the velocity vector and the slip surface, it has been confirmed that slip or sliding of the soil mass occurs above the "modified" log-spiral slip surface. However, in the non-associated flow rule case, the velocity field near the ground surface does not agree so well with that of the "modified" slip surface for higher values of internal friction angle ϕ. Rather, it seems to agree better with that of the *plane slip surface*.

9.6 SUMMARY

As a tool to find approximate solutions of the nonlinear equilibrium equations such as the total Lagrangian equations, updated Lagrangian equations derived in the preceding Chapter, the basic concepts of *finite-element method* are introduced in the earlier part of this Chapter.

Each step in the application of the finite-element method is summarized below:

1. The *whole* region of the continuous body considered is discretized into many *parts* of finite element. Inside the continuous body, in fact, the infinite number of unknown values such as displacements u_i, stresses σ_{ij}, or other quantities exist corresponding to each generic point. However, such discretization can reduce a problem with infinite number of unknowns to a problem with a finite number of unknowns.
2. The model for the field variable ϕ and the finite element are selected with respect to the problem considered. The field variable ϕ inside a three-dimensional element is approximated by utilizing the *generalized coordinates* α_i:

$$\phi = \alpha_1 + \alpha_2 x + \alpha_3 y + \alpha_4 z + \alpha_5 x^2 + \alpha_6 xy + \alpha_7 y^2 + \ldots$$

or the field variable ϕ is written in terms of the interpolation functions N_i and the values of field variables Φ_i corresponding to the specified points inside the element and on the element boundaries:

$$\phi = \Phi_1 N_1 + \Phi_2 N_2 + \ldots + \Phi_n N_n$$

where n is the number of the degree of freedom of an element with respect to the field variable.

3. Utilizing the incremental virtual work equation, which can include the geometrical as well as material nonlinearities, the incremental finite-element equations based on the total Lagrangian formulation and updated Lagrangian formulation are constructed for each element. Substitution of the field variables at each specified point into the equilibrium equation gives an *element stiffness matrix* $[k]$.
4. Each incremental finite-element equation is assembled to construct a *total stiffness matrix* $[K]$ for the whole region.
5. The total incremental finite-element equilibrium equation in a matrix form, $[K]\{dU\} = \{dR\}$ where $\{dU\}$ and $\{dR\}$ are respectively the vector of displacement increments and the vector of external load increments, is solved for the vector $\{dU\}$ of displacement increments at the nodal points. When the nonlinear problem is treated, the appropriate solution techniques such as the *incremental procedure* and *iterative procedure* including the *initial strain technique*, and the *initial stress technique* are selected and applied.
6. Utilizing the values of the field variables Φ_i for displacement increments at nodal points, as obtained from the total incremental equilibrium equation, the stress states inside the element are computed. Namely, stress states are estimated from the displacement-strain relation (the kinematic assumption) and the stress-strain relation (the constitutive law).

As can be understood through the items described above, the finite-element procedure relies upon idealization, or discretization, of a problem so that an approximate solution to the governing differential equations may be obtained. The accuracy of this solution depends on the assumptions made during the discretization of a problem and the numerical techniques used to obtain the solution. Some common sources of errors are:

1. Constitutive relations.
2. Element selection and mesh refinement.
3. Solution of the equilibrium equations.

A constitutive relation which does not adequately reproduce the significant characteristics of the problem at hand can not hope to provide a solution in which one may have a great degree of confidence. However, even with the use of a correct stress-strain law, numerical errors may be introduced through the linearization and integration of the stress-strain relation (9.147) over a finite load path. These errors may be minimized by a separation of the strain increment into a number of smaller subincrements and varying the constitutive relation over the strain path. The importance of satisfying the consistency condition, $df = 0$, during plastic loading is also emphasized. Chen (1975) has shown this correction provides improved accuarcy with little additional computational effort.

The effects of mesh refinement are well understood. The influence of element selection is not so clear. An element which behaves well during an elastic response may provide completely erroneous results when a plastic behavior is dominant.

Several authors (Nagtegaal et al., 1974; Nagtegaal and De Jong, 1981; Argyris et al., 1974; and Sloan and Randolph, 1982) have discussed the phenomena of "locking" exhibited by some elements and mesh configurations. The problem is particularly severe when an extensive plastic behavior occurs in conjunction with a von Mises type material. Here, the condition of incompressibility imposes additional constraints on the manner in which deformations may occur. Lower-order elements are often unable to satisfy these constraints, leading to errors in the predicted load-displacement response.

As a numerical example for the large-deformation finite-element analyses, in the latter part of this Chapter, the Drucker–Prager models with the associated and non-associated flow rules have been applied to the analyses of vertical slopes and then their results have been presented as a comparative study. Among these results, the limit loads and failure mechanisms obtained from the finite-element method are discussed and compared with those obtained by the limit analysis method.

REFERENCES

Akyuz, F.A. and Merwin, J.E., 1968. Solution of nonlinear problems of elastoplasticity by finite element method. AIAA J., 6 (10): 1825–1831.

Argyris, J.H., 1965. Elasto-plastic matrix displacement analysis of three-dimensional continua. J. R. Aeronautical Soc., 69: 633–636.

Argyris, J.H., Dunne, P.C., Angelopoulos, T. and Bichat, B., 1974. Large natural strains and some special difficulties due to non-linearity and incompressibility in finite elements. Comput. Methods Appl. Mech. Eng., 4: 219–278.

Armen, H., Pifko, A. and Levine, H.S., 1968. A finite element method for the plastic bending analysis of structures. Proc. Second Conference on Matrix Method in Structural Mechanics, Wright-Patterson Air Force Base, AFFDL-TR-68-150, 1968, pp. 1301–1339.

Bathe, K.J., 1982. Finite Element Procedures in Engineering Analysis. Prentice-Hall, Englewood Cliffs, NJ, 1982, 735 pp.

Capurso, M., 1969. A general method for the incremental solution of elastic-plastic problems. Meccanica, 4 (4): 267–280.

Chen, W.F., 1975. Limit Analysis and Soil Plasticity. Amsterdam, The Netherlands, Elsevier, 638 pp.

Chen, W.F. and Saleeb, A.F., 1982. Constitutive Equations for Engineering Materials, Vol. 1. John-Wiley, New York, NY, 580 pp.

Crisfield, M.A., 1979. A faster modified Newton–Raphson iteration. Comput. Methods Appl. Mech. Eng., 20: 267–278.

Davidson, H.L. and Chen, W.F., 1974. Elastic-plastic large deformation response of clay to footing loads. Rep. No. 355.18, Fritz Eng. Lab., Lehigh University, PA, 181 pp.

Davidson, H.L. and Chen, W.F., 1976. Non-linear analysis in soil and solid mechanics. In: C.S. Desai (Editor), Numerical Methods in Geomechanics. ASCE, Vol. 1, pp. 205–216.

Davidson, H.L. and Chen, W.F., 1977. Large deformation response of clay to loads. Proc. Int. Conf. on Finite Elements in Nonlinear Solid and Structural Mechanics, Geilo, Norway, Aug. 29–Sept. 1, 1977, Two Volumes, DO 2-1, DO 2-20, (Vol. 2).

Davidson, H.L. and Chen, W.F., 1978. Nonlinear response of drained clay to footings. Comput. Struct. 8: 281–290.

Desai, C.S. and Abel, J.F., 1972. Introduction to the Finite Element Method. Van Nostrand Reinhold Company, New York, NY, 477 pp.

Ergatoudis, I.G., Irons, B.M. and Zienkiewicz, O.C., 1968. Curved isoparametric quadrilateral elements for finite element Analysis. Int. J. Solids Struct. 4: 31–42.

Felippa, C.I., 1966. Refined finite element analysis of linear and nonlinear two-dimensional structures. Thesis presented to the University of California, at Berkeley, in partial fulfillment of the requirements of the degree of Doctor of Philosophy.

Fernandez, R.M. and Christian, J.T., 1971. Finite element analysis of large strains in soils. NASA Res. Rep. R71-37, Sept.

Gallagher, R.H., Padlog, J. and Bijlaard, P.P., 1962. Stress analysis of heated complex shapes. ARS J., 32 (5): 700–707.

Huebner, K.H., 1975. The Finite Element Method for Engineers. John Wiley & Sons, New York, NY, 500 pp.

Irons, B.M., Ergatoudis, I.G., and Zienkiewicz, O.C., 1968. Discussion of the paper by P. Dunne. Aeronaut. J., 72.

Ketter, R.L. and Prawel, S.P., 1968. Modern Methods of Engineering Computation. McGraw-Hill, New York, NY, 492 pp.

Lansing, W., Jensen, W.R. and Falby, W., 1965. Matrix analysis methods for inelastic structures. Matrix Methods in Structural Mechanics, Proc. Conf. held at Wright-Patterson Air Force Base, AFFDL-TR-66-80, pp. 605–633.

Marcal, P.V. and King, I.P., 1967. Elastic-plastic analysis of two-dimensional stress systems by the finite element method. Int. J. Mech. Sci., 9: 143–155.

Mizuno, E., 1981. Plasticity modeling of soils and finite element applications. Thesis presented to Purdue University, West Lafayette, in partial fulfillment of requirements of the degree of Doctor of Philosophy, 320 pp.

Mizuno, E. and Chen, W.F., 1983a. Plasticity analysis of slope with different flow rules. Comput. Struct., 17 (3): 375–388.

Mizuno, E. and Chen, W.F., 1983b. Cap models for clay strata to footing loads. Comput. Struct., 17 (4): 511–528.

Nagtegaal, J.C., Parks, D.M. and Rice, J.R., 1974. On numerically accurate finite element solutions in the fully plastic range. Comput. Methods Appl. Mech. Eng., 4: 153–177.

Nagtegaal, J.C. and De Jong, J.E., 1981. Some computational aspects of elastic-plastic large strain analysis. Int. J. Numer. Methods Eng., 17: 14–41.

Nayak, G.C. and Zienkiewicz, O.C., 1972. Elasto-plastic stress analysis. A generalization for various constitutive relations including strain softening. Int. J. Numer. Methods Eng., 5: 113–135.

Pope, G.G., 1965. The application of the matrix displacement method in plane elasto-plastic problems. Matrix Methods in Structural Mechanics, Proc. Conf. held at Wright-Patterson Air Force Base, AFFDL-TR-66-80, pp. 635–654.

Silvester, P., 1969. Higher-order polynomial triangular finite elements for potential problems. Int. J. Eng. Sci. 7 (8): 849–861.

Silvester, P., 1972. Tetrahedral polynomial finite elements for the Helmholtz equation. Int. J. Numer. Methods Eng., 4 (3): 405–413.

Sloan, S.W. and Randolph, M.F., 1982. Numerical predictions of collapse loads using finite element methods. Int. J. Numer. Analyt. Methods Geomech., 6: 47–76.

Snitbhan, N. and Chen, W.F., 1975. Plasticity solutions for slopes in aniosotropic, inhomogeneous soil. Rep. No. 355.21, Fritz Eng. Lab., Lehigh University, PA, 169 pp.

Snitbhan, N. and Chen, W.F., 1978. Elastic-plastic large deformation analysis of soil slopes. Comput. Struct., 9: 567–577.

Swedlow, J.L., Williams, M.L. and Yang, W.H., 1965. Elasto-plastic stresses and strains in cracked plates. Proc. First Int. Conf. on Fracture, 1: 259–282.

Witmer, E.A. and Kotanchik, J.J., 1968. Progress report on discrete-element elastic and plastic analyses of shells of revolution subjected to axisymmetric and asymmetric loadings. Proc. Second Conference on Matrix Methods of Structural Mechanics, Wright-Patterson Air Force Base, AFFDL-TR-68-150, pp. 1341–1453.

Yamada, Y. and Yoshimura, N., 1968. Plastic stress-strain matrix and its application for the solution of elastic-plastic problems by the finite element method. Int. J. Mech. Sci. 10: 343–354.

Zienkiewicz, O.C., 1978. The Finite Element Method. McGraw-Hill, New York, NY, 787 pp.

Zienkiewicz, O.C., Valliappan, S. and King, I.P., 1969. Elasto-plastic solutions of engineering problems: "Initial stress" finite element approach. Int. J. Numer. Methods Eng., 1: 75–100.

Part V

CASE STUDY

Chapter 10

CASE STUDIES

10.1 INTRODUCTION

The applicability and predictive capability of constitutive model (particularly the cap model) with *material nonlinearity* can be checked by solving typical geotechnical problems with the finite-element method based on the small-deformation formulation as well as the large-deformation formulation with *geometrical nonlinearity*.

One of the typical check problems is the analysis of horizontal clay strata subjected to vertical loads such as those transmitted by a footing. The study of static response of a homogeneous clay stratum to footing loads has been reported by Davidson and Chen (1974, 1977, 1978), among others. In their work, the effect of *large deformations* on the response of clay was considered within the framework of finite-element analysis with a mid-point integration rule. The clay was modeled as a linear elastic-perfectly plastic material with the Drucker–Prager yield condition and its associated flow rule. It was found from their analyses that (1) the Drucker–Prager model with the associated flow rule can predict plastic collapse loads that are comparable with those of the limit analysis method based on the Coulomb criterion and (2) for rigid footings bearing on clay, the effect of changing soil geometry is to strengthen the system.

It is of great interest here to apply the strain-hardening cap model to study the same problem, and to compare these responses of soil strata to footing loads with those of the perfectly plastic models based on a non-associated as well as the associated flow rule. In the first two Sections of this Chapter, therefore, the analytical work of Davidson and Chen (1974) on bearing-capacity problems for a two-dimensional shallow stratum of clay is extended by considering several plasticity models. The analyses of (1) flexible and smooth strip footings (Section 10.2) and (2) rigid and rough strip footings (Section 10.3) on stratum of clay are respectively presented under the assumption of the *small deformation* (Mizuno and Chen, 1983).

Another typical check problem is the stability analysis of slopes during earthquake loading, which has often been performed by the conventional "*pseudo-static method of analysis*". In this analysis, the inertia force is treated as an equivalent concentrated horizontal force acting at some critical point (usually the center of gravity) in the critical sliding mass of the limit analysis and limit equilibrium methods. Although the inadequacies of this analysis for slope stability problems have been pointed out by some researchers (Chen, 1980; Daddazio et al., 1987), the pseudo-static method is simple to implement and has generally been used with

may continue to be used by the practitioner for the analysis of geotechnical engineering problems, until an alternative simple method can be found.

The limit analysis techniques of perfect plasticity have been modified and extended to the pseudo-static method of slope stability analysis (see Chen et al., 1978; Chang et al., 1984). Chang and Chen (1983) have developed computer programs for the calculation of *yield acceleration* i.e., the acceleration at which sliding just begins to occur, and the displacements corresponding to subsequent accelerations. However, the progressive failure behavior of soil slopes prior to sliding of the mass is still not available from this analysis. In Section 10.4, therefore, the development and verification of the "pseudo-static" method using finite-element analysis with the elliptic cap model as well as the Drucker Prager model are presented, and a comparative study is made with the limit analysis method (Chen, 1975). Emphasis is placed here on the effect of large deformation on the evaluation of the overall slope stability problems. Further, of particular concern is the comparison of failure modes and limit loads with those assumed in the limit analysis method (Mizuno and Chen, 1984).

10.2 EXAMPLE 1. FLEXIBLE AND SMOOTH STRIP FOOTINGS ON STRATUM OF CLAY

Analytical model

Zienkiewicz et al. (1975) analyzed a shallow layer of clay as shown in Fig. 10.1 employing the Coulomb yield condition with a non-associated flow rule as well as

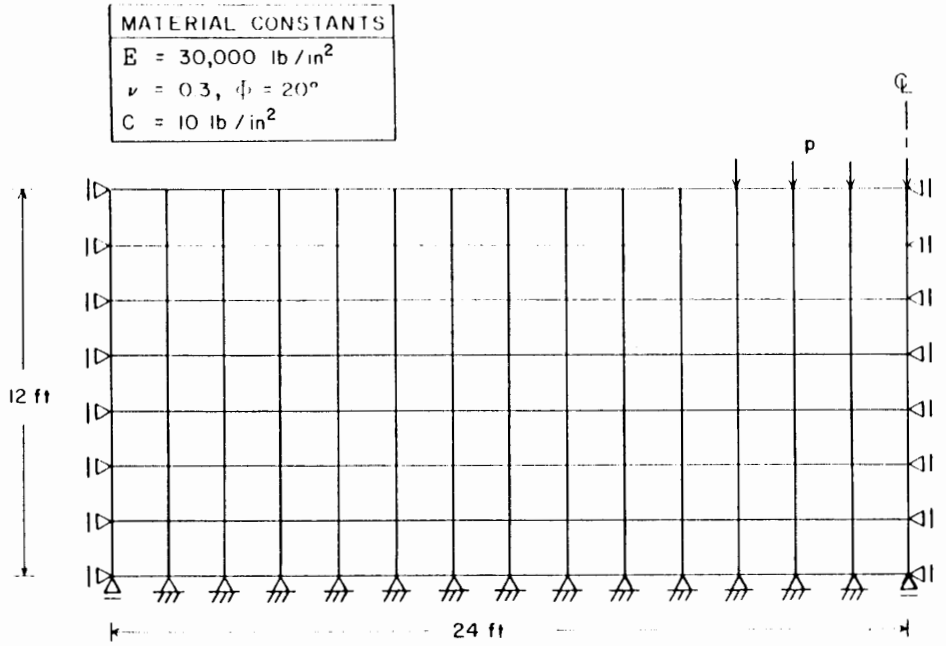

Fig. 10.1. Analytical model for shallow stratum of clay.

the associated flow rule. The footing was assumed to be *flexible* and *smooth* so that the stresses beneath the footing are distributed vertically and uniformly.

The analytical model used for the present *plane strain analyses* is a 10.28-ft (3.14-m)-wide strip footing (Fig. 10.1) bearing on a shallow stratum supported by a rigid and perfectly rough base. The horizontal extent of the stratum is set at 24 ft (7.32 m) from the footing center and the depth of the stratum is 12 ft (3.66 m). The vertical boundary is assumed to be perfectly smooth and rigid.

Finite-element mesh

The finite-element mesh consists of 120 nodes and 98 uniform *rectangular elements* as shown in Fig. 10.1. Here, each quadrilateral element is subdivided into four triangles connected to the fifth node located at the quadrilateral centroid. In the finite-element process, the *static condensation* is used to reduce the $[10 \times 10]$ quadrilateral element stiffness matrix to the desired $[8 \times 8]$ element stiffness matrix. The stiffness of the triangle element is based on a linear displacement expansion (*constant strain triangles*).

Type of analysis

Here, we analyze the following three items (1) through (3), using the finite-element method with the *small-deformation assumption*:

1. Analyses by the Drucker–Prager models with different methods in determining material constants, using the associated flow rule.
2. Analyses by the Drucker–Prager models with the associated and non-associated flow rules.
3. Analyses by a plane cap and an elliptic cap models with the associated flow rule.

10.2.1 Drucker–Prager models with different material constants

In this Section, the response of the clay stratum to footing loads is analyzed by the Drucker–Prager model, for which determination of material constants is different.

Material constants

The following material constants are used: Young's modulus $E = 3 \times 10^4$ psi (2.07×10^5 kPa), Poisson's ratio $\nu = 0.3$, cohesion $c = 10$ psi (69 kPa), angle of internal friction $\phi = 20°$, and the effect of weight of soil is neglected.

For the Drucker–Prager model, careful selection of material constants α and k is required so that it matches with the well-known Coulomb criterion, as discussed in Chapter 4. In the following, three types of material constants as given by Eqs. (4.45), (4.46) and (4.57) are used in the analysis with the associated flow rule. These constants are obtained from matching the Drucker-Prager model with the Coulomb model along the compressive meridian, along the tensile meridian, and under plane strain conditions, respectively. The values of material constants α and k are 0.149 and 12.25 psi (84.53 kPa), 0.118 and 9.74 psi (67.21 kPa), and 0.112 and 9.22 psi (63.62 kPa) respectively.

Analytical procedure

Here, the incremental integration scheme known as the mid-point rule is used. In the present elastic-plastic analysis, scaling stress back to the Drucker–Prager yield surface as discussed in Chapter 7 and distributing the unbalanced nodal forces during the next increment are employed. At each increment, a relatively small load increment is applied in order to obtain an accurate solution.

Load-displacement curves

The following discussions on the load-displacement curves can be made from the finite-element results.

The complete load-displacement response of the strip footing is shown in Fig. 10.2 where the applied pressure is plotted versus the centerline displacement directly beneath the footing for each case. The circles plotted in Fig. 10.2 correspond to some actually computed points obtained from the small-deformation analysis. As can be seen, the analysis using material constants matched with the compressive meridian of the Coulomb criterion in three-dimensional space results in a collapse

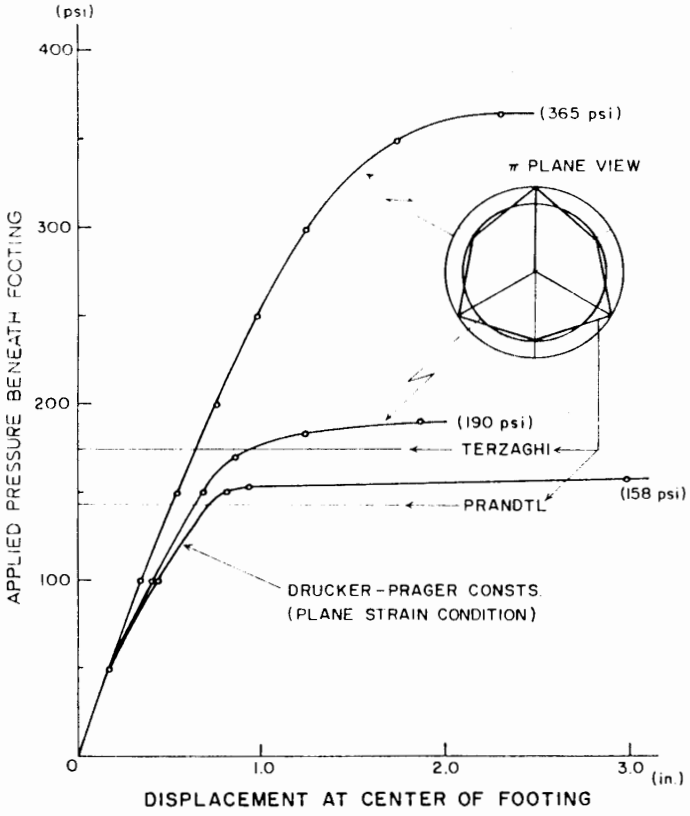

Fig. 10.2. Load-displacement curves by the Drucker–Prager models with different material constants.

load (365 psi or 2520 kPa) which is almost twice that of the other analyses (158, 190 psi or 1090, 1310 kPa). This load-displacement curve is characterized by linear elastic response to approximately 150 psi and nonlinear elastic-plastic response to the collapse load. On the other hand, the Drucker–Prager criterion with material constants matched with the tensile meridian of the Coulomb criterion predicts a collapse load (190 psi) which is somewhat higher than that of 175 psi given by Terzaghi. Further, the collapse load (158 psi) predicted by the Drucker-Prager criterion matched with the Coulomb criterion in the plane strain condition is, as expected, almost the same as that of 152 psi predicted by the Coulomb criterion (Zienkiewicz et al., 1975). This load is close to the loads (175 psi and 143 psi) given by the Terzaghi and Prandtl solutions.

As a result, the analysis with the material constants of Eq. (4.45) does not agree with the well-known Terzaghi and Prandtl solutions. The important point to be noted here in using the Drucker–Prager model is the careful selection of material constants. In order for this criterion to represent a proper generalization of the Coulomb or modified Coulomb criteria under multi-dimensional stress states, its material constants α and k must be properly defined. These constants should not be treated as fixed expressions for all types of applications. Rather, their choice depends on the particular problems to be solved.

10.2.2 Drucker–Prager models with non-associated flow rule

In this Section, the Drucker–Prager model with a non-associated flow rule is utilized so that comparisons can be made with the analyses by the associated flow rule model in the previous Section.

Material constants

For the associated flow rule case, the material constants α and k obtained from Eq. (4.57) by matching the Coulomb model under plane strain conditions are used in the failure function f and the plastic potential function $g = f$.

For the case of a non-associated flow rule, the failure function is the same as that for the associated flow rule case, but a von Mises type of function (no plastic volumetric strain) is taken as the plastic potential function.

Analytical procedure

The mid-point integration scheme with an *interative procedure* is used.

In the following, the finite-element results are discussed with respect to (A) load-displacement curves, (B) yield zones and (C) velocity fields.

(A) Load-displacement curves

Figure 10.3 shows the load-displacement curves predicted by both flow rule cases. These curves are the same up to an applied load of 40 psi (276 kPa) because the state of stress in all elements at this load level is still within the elastic region. Then, as the load is gradually increased, their behavior becomes different. The

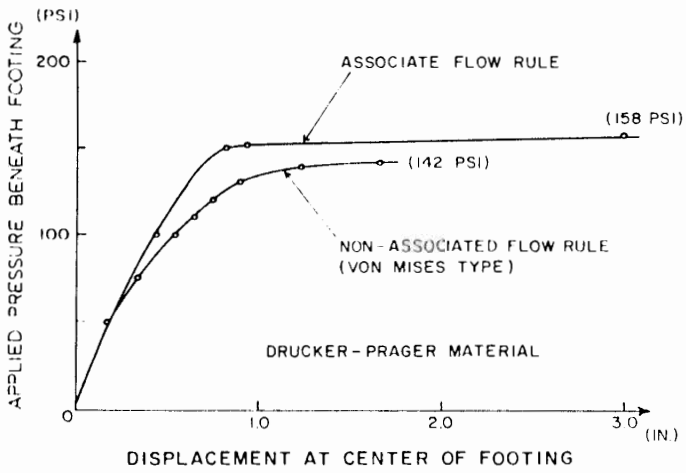

Fig. 10.3. Load-displacement curves by the Drucker–Prager models with associated and non-associated flow rules (flexible and smooth footing).

load-displacement curve for the associated flow rule case bends sharply at a load of 150 psi and reaches a plastic limit load of 158 psi. On the other hand, the curve for the non-associated flow rule case deviates gradually from the associated flow rule curve at a load of 40 psi, and exhibits a significantly nonlinear response to its collapse load of 142 psi. This collapse load is less than that of the associated flow rule case. This collapse load agrees quite well with the loads of 143 psi and 147 psi given by the solutions of Prandtl, and of Coulomb with a non-associated flow rule (Zienkiewicz et al., 1975).

(B) Yield zones

The spreading of yielded zones corresponding to various load levels is shown schematically in Figs. 10.4a and 10.4b for the cases of associated and non-associated flow rules. For the associated flow rule case, yielding occurs at a load of 42 psi (290 kPa) in regions under the footing (Fig. 10.4a). As the load increases, the yielded zone expands outward, reaching both the surface and the base of the clay stratum at a load of 70 psi. At this load, yielding has occurred for most of the area under the footing except some portions immediately below the footing and near the base of the stratum. The zone of yielding continues to spread laterally, particularly for regions near the base. Yielding also continues slowly near the center of the footing and the center of the base. On the other hand, the yielded zone near the surface expands very little as the load increases from 70 psi to 120 psi. At a load of 157 psi, which is near the collapse load of 158 psi, yielding has occurred for virtually the entire stratum of the clay as shown in Fig. 10.4a.

A similar trend can be seen for the non-associated flow rule case (Fig. 10.4b). However, the yielded zones at a load of 120 psi are somewhat different from those for the associated flow rule case. In this case, yielding is spreading diagonally

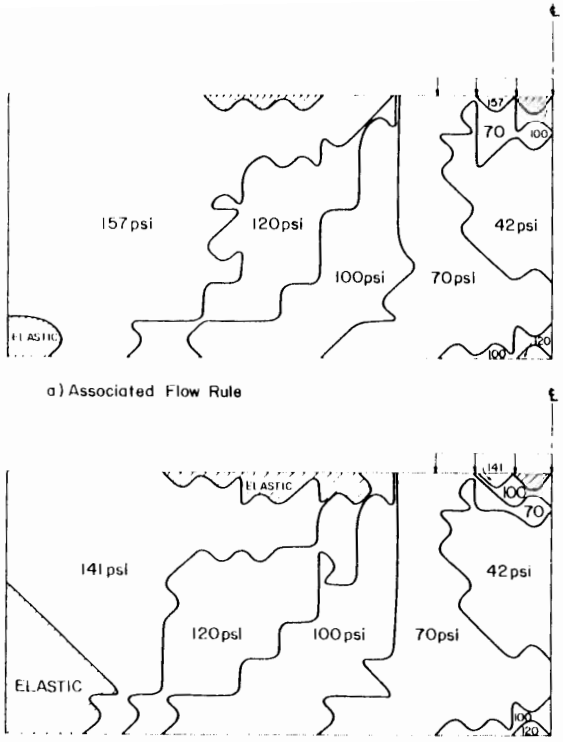

Fig. 10.4. Spread of yielded zone in the Drucker–Prager perfectly plastic material stratum (flexible and smooth footing).

towards the upper edge of the clay stratum. At a load of 141 psi, which is near the collapse load of 142 psi, yielding has occurred for a significant portion of the stratum.

(C) Velocity fields

In Fig. 10.5, the velocity fields at the collapse load are presented for both cases. The broken and solid lines in the figure are outlines of Terzaghi and Prandtl velocity fields respectively. The magnitude and direction of velocity at each node are represented by an arrow, and the displacement increment at the center of the footing is taken as a normalized unit length. As shown in Fig. 10.5a, the numerically obtained velocity field for the associated flow rule material is seen to be in fair agreement with that of the Prandtl solution. Further, it can be seen that the magnitude of velocity becomes gradually larger along the slip flow in the "radial shearing zone" and the "near-surface zone" in the Prandtl mechanism. This is due to the nature of dilatancy in soil during plastic flow. In other case, the velocity field (Fig. 10.5b) for the non-associated flow rule material appears to agree with that of the Terzaghi solution. In this case, the magnitude of velocity becomes gradually smaller, or remains nearly the same, along the slip flow in the "radial shearing zone". Here, because the von Mises type of plastic potential function is assumed,

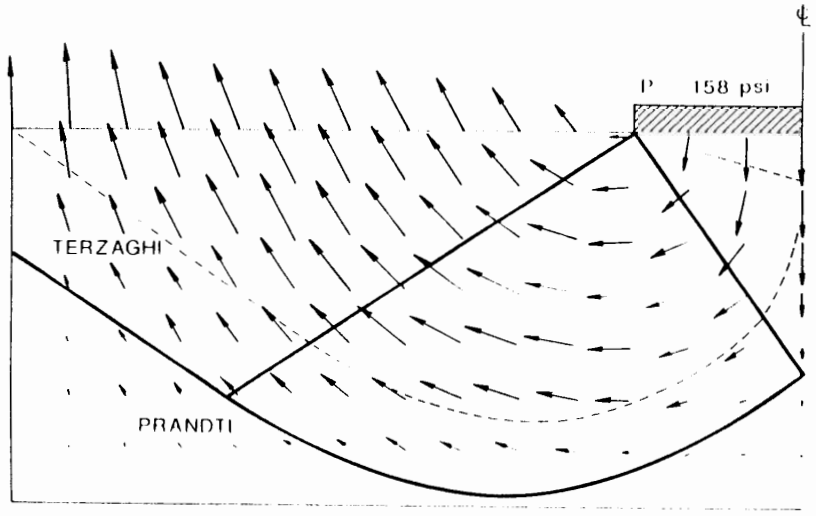

(a) DRUCKER-PRAGER Model (Associated Flow Rule)

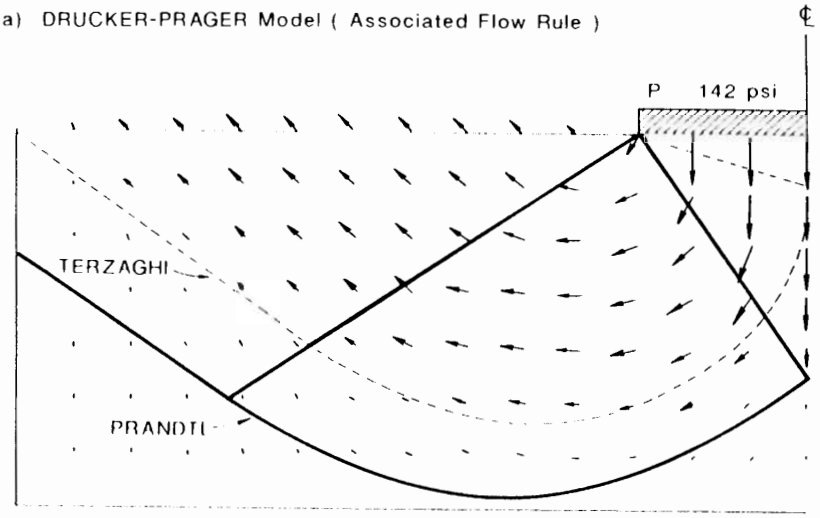

(b) DRUCKER-PRAGER Model (Non- associated Flow Rule)

Fig. 10.5. Velocity field by the Drucker–Prager models at the numerical limit load (flexible and smooth footing).

dilatancy does not contribute to the flow. The velocity field in Fig. 10.5b is consistent with this condition.

10.2.3 Cap models with associated flow rule

In this Section, the strain-hardening plane cap and elliptic cap models with the associated flow rule are employed to solve the same problem.

Material constants

The material constants W and D in the hardening function [Eq. (6.22a)] are assumed to be 0.003 (the maximum compaction of plastic volumetric strain) and 6.042×10^{-5} ft^2/lb (1.26×10^{-6} Pa^{-1}), respectively. In addition, the shape of an elliptic cap, R, is assumed to be 4. Further, the initial intersection of both cap-hardening surfaces with the I_1-axis is situated at the point of -6700 psf on that axis. In this analysis, these caps are allowed to expand and to contract if necessary as the plastic volumetric strain increases and decreases.

As for the yield surface, the Drucker–Prager type of yield surface based on material constants matched with the Coulomb criterion under the plane strain condition is used.

Note that since the weight of clay is not considered, the initial state of stress inside the clay stratum is set at the origin in $I_1 - \sqrt{J_2}$-space at the beginning of analysis.

Analytical procedure

Iterative procedure with initial stress method is employed.

In the following, the finite-element results are discussed with respect to (A) load-displacement curves, (B) zones of stress state and (C) velocity fields.

(A) Load-displacement curves

In Fig. 10.6, the load-displacement curves for the cap models are compared with those obtained previously. Initially, all the curves are the same. After yielding, the

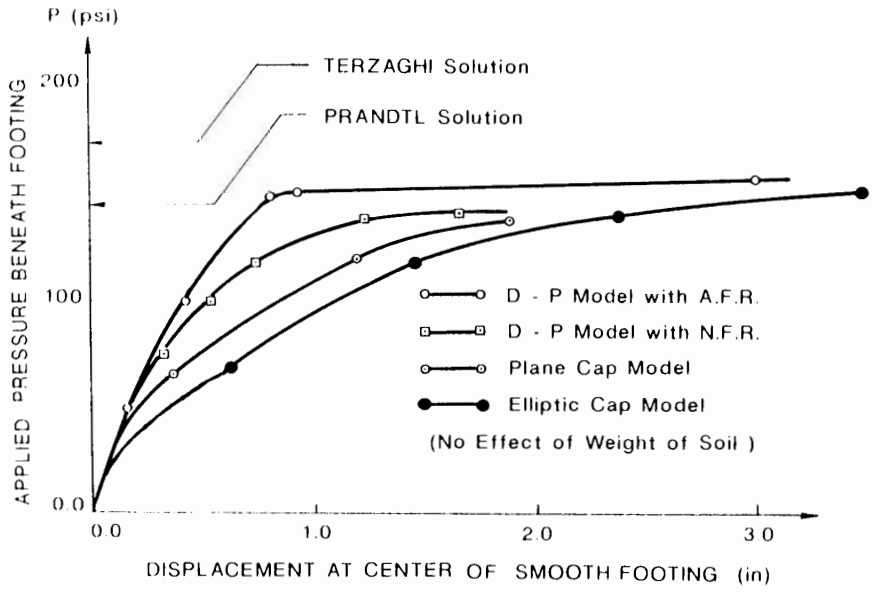

Fig. 10.6. Load-displacement curves by the cap and Drucker–Prager models (flexible and smooth footing).

plane cap model curve deviates from the Drucker Prager model curves at approximately 40 psi (276 kPa), and thereafter rises to a load of 139 psi. Beyond this point the iterative procedure of the computer solution seems not to give a good convergence. Thus, this load is approximately defined as the collapse load. Compared with the collapse loads discussed in the previous Section, the present estimated collapse load agrees quite well with that of 142 psi predicted by the Drucker Prager non-associated flow rule model, and with that of 143 psi given by the Prandtl solution.

On the other hand, the elliptic cap model curve starts to deviate at a much earlier load of 25 psi. This is because the initial elastic zone of the elliptic cap model is smaller, in compressive $I_1 - \sqrt{J_2}$-space, than that of the plane cap model. However, the curve behaves in a similar manner to that of the plane cap model and asymptotically approaches the curve predicted by the Drucker Prager associated flow rule model.

(B) Zones of stress state

The stress states here are classified as *elastic state*, *tension state*, *hardening state* and *corner state* as described in Chapter 7. Figure 10.7 shows the zones of stress state predicted by the plane cap model at various load levels. At a load of 28 psi (193 kPa), hardening occurs immediately below the footing (Fig. 10.7a). As the load increases, yielding first develops in regions along the boundary between the "rigid zone" under the footing and the "radial shearing zone" in the Prandtl mechanism, and then spreads upward to the edge of the footing. As the load continues to increase, soil in the yielded zone gradually changes to the corner zone because stresses on the yield surface begin to reach the corner of the hardening surface. The stress states at a load of 49 psi are shown in Fig. 10.7b. With a further increasing load, the corner zone under the footing spreads downward and then outward as shown in Figs. 10.7c and 10.7d. At a load of 97 psi, yielded zones are developing along the leading edge of the corner zone, and are advancing through the stratum in a line that sweeps radially from the edge of the footing. As the load approaches the collapse state, the size of these yielded zones becomes larger, and another yielded zone appears at the upper edge of the stratum (Fig. 10.7e). These yielded zones merge at a higher level of load. Also, small yielded zones develop inside the large corner zone. Near the collapse load, the yielded zone below the footing grows, penetrating the corner zone. In the meantime, the corner zone continues to spread outward. Thus, the zones of stress state near the collapse load become very complicated (Fig. 10.7f).

The zones of stress state as predicted by the elliptic cap model at various load levels are shown in Fig. 10.8. The hardening zone under the footing spreads downwards first and then, after reaching the base of stratum, gradually expands outwards. This can be seen in Figs. 10.8a through 10.8d. As the load increases to 125 psi, the hardening zone reaches the edge of the stratum while a corner zone appears under the footing, spreading along the boundary between the "rigid zone" and "radial shearing zone" of the Prandtl mechanism, as shown in Fig. 10.8e. The

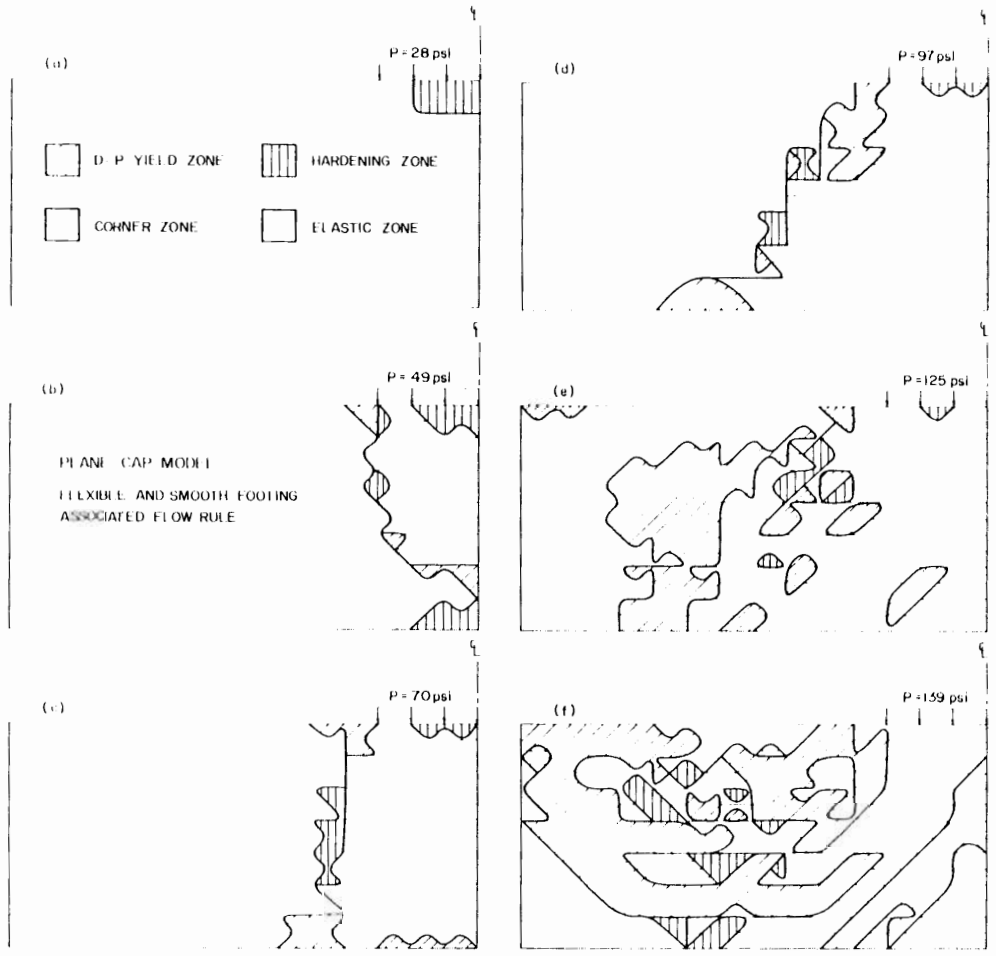

Fig. 10.7. Zones of stress state in the plane cap hardening material stratum (flexible and smooth footing).

corner zone then spreads downward inside the hardening zone (Figs. 10.8f and 10.8g). At the load of 154 psi, the corner zone finally touches the base of the stratum (Fig. 10.8h). With a further increasing load, it is expected that the corner zone will spread diagonally from the region near the base of the stratum to the upper edge of the stratum. The elliptic cap model predicts substantially different zones of stress state during loading from those predicted by the plane cap model. This is because yielded zones and corner zones are most important in the case of the plane cap model, while corner zones and hardening zones predominate in the case of the elliptic cap model.

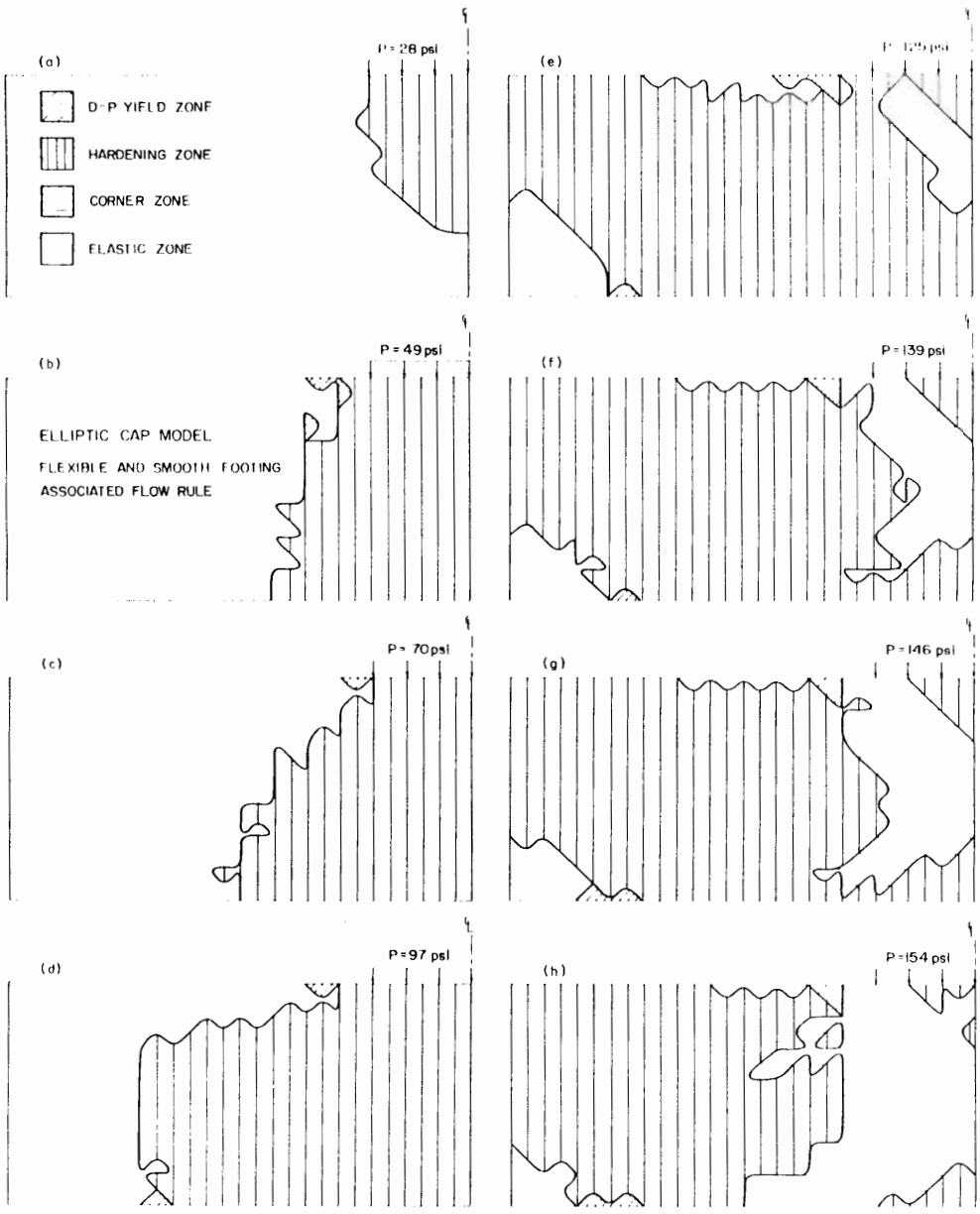

Fig. 10.8. Zones of stress state in the elliptic cap hardening material stratum (flexible and smooth footing).

(C) Velocity fields

The velocity fields corresponding to the last load increment for both cap models are shown in Fig. 10.9. For the plane cap model, the velocity field (Fig.10.9a) agrees

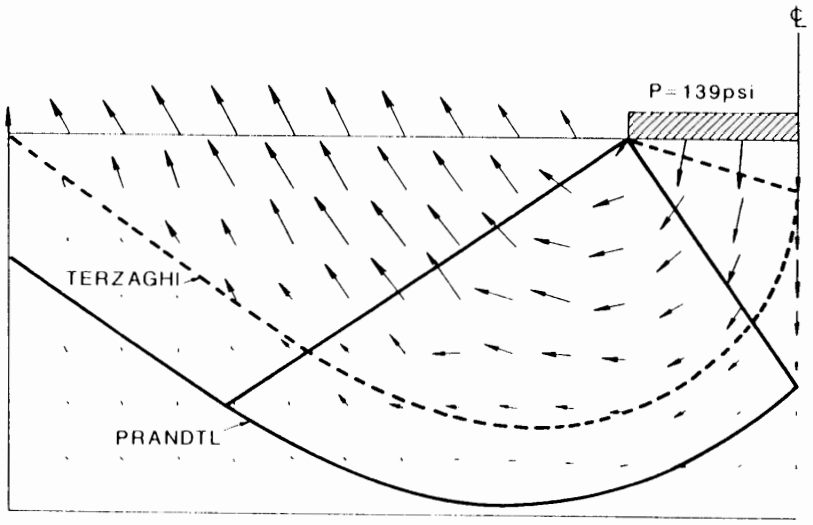

(a) Plane Cap Model

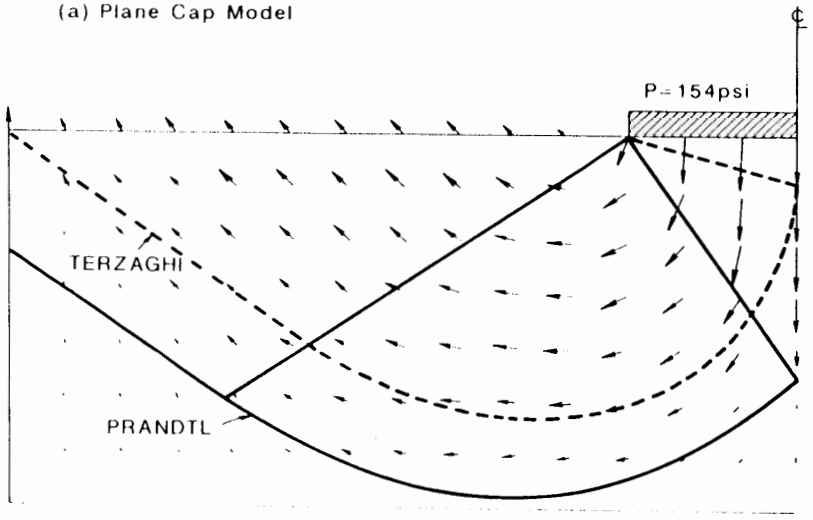

(b) Elliptic Cap Model

Fig. 10.9. Velocity field by the cap models at numerical limit load (flexible and smooth footing).

quite well with that of the Terzaghi solution (broken line). The magnitude of velocity is large inside the Terzaghi zone compared with that along the boundary surface. The velocity field appears to lie between those predicted by the various Drucker Prager models.

The velocity field predicted by the elliptic cap model corresponds reasonably well with the Prandtl field (Fig. 10.9b). Since the stress states are either in a corner zone

or a hardening zone for almost all the elements as shown in Fig. 10.8h, little dilatancy is expected. Thus, the velocity field is close to that predicted by the Drucker–Prager non-associated flow rule model.

10.3 EXAMPLE II. RIGID AND ROUGH STRIP FOOTINGS ON STRATUM OF CLAY

The preceding soil–structure interaction problem between footing and ground is now changed from a flexible and smooth boundary to a rigid and rough boundary. The displacements beneath the footing are assumed to be vertically uniform. As a result of this change, the *displacement incremental method* is utilized in the finite-element analysis with the iterative initial stress procedure. Note that the footing pressure in this Section is defined as the average pressure under the footing.

Type of analysis

Plane strain analyses of the rigid and rough footings on stratum of clay are performed with respect to following two items:

1. Analyses by the Drucker–Prager models with the associated and non-associated flow rules.
2. Analyses by a plane cap and an elliptic cap models with the associated flow rule.

Analytical procedure

Iterative procedure with the initial stress method is employed in the following Sections 10.3.1 and 10.3.2.

10.3.1 Drucker–Prager models

Here, the finite-element results such as (A) load-displacement curves, (B) yield zones and (C) velocity fields predicted by the Drucker–Prager models are presented.

(A) Load-displacement curves

Figure 10.10 shows the load-displacement curves predicted by the Drucker–Prager models. The curve for the associated flow rule case rises linearly to about 65 psi (449 kPa), then exhibits a mild nonlinear behavior and finally a severe reduction of the stiffness. The model predicts a much stiffer curve compared with that of the flexible and smooth footing problem. The collapse load is approximately 171 psi which is quite close to the Terzaghi's solution (175 psi) but considerably higher than that of 158 psi as predicted by the same model for the flexible and smooth footing problem.

The curve corresponding to the non-associated flow rule case deviates from the associated flow rule curve at a load of 65 psi, and then shows nonlinear behavior until it reaches the collapse load of approximately 154 psi. The collapse load lies between those of 158 psi and 142 psi predicted by the same models for the flexible

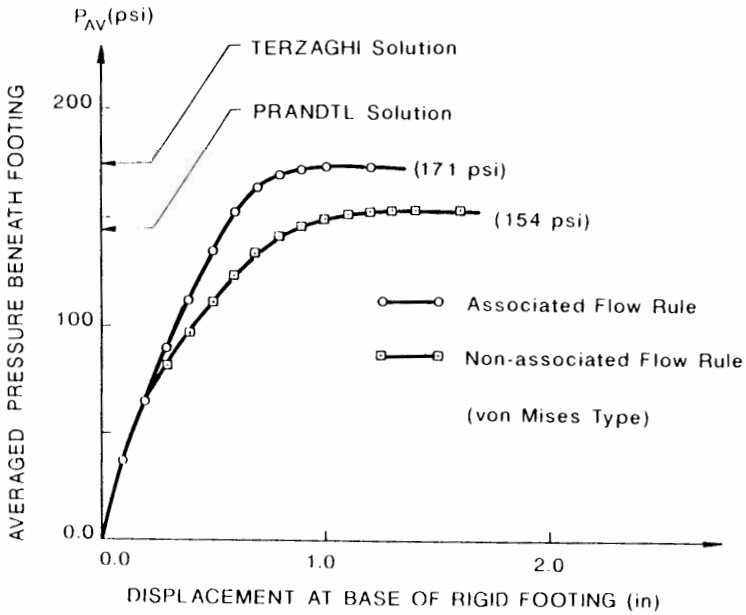

Fig. 10.10. Load-displacement curves by the Drucker–Prager models with associated and non-associated flow rules (rigid and rough footing).

and smooth footing problem. Also, this load is close to that of 143 psi given by the Prandtl solution.

(B) Yield zones

The yielded zones for both flow rule materials are predicted at various levels of footing displacement in Fig. 10.11. For the associated flow rule case, a displacement of 0.1 in. (0.254 cm) causes yielding in the vicinity of the footing edge (Fig. 10.11a). As displacement increases to 0.5 in., the yielded zone spreads over most of the internal regions of the Prandtl mechanism. As displacement increases further to 0.6 in., the "near-surface zone" in the Prandtl mechanism becomes substantially yielded. At a displacement of 1.0 in., yielding has gradually expanded downward, leaving only a small elastic zone (shaded) at the lower edge of the stratum.

The yielded zone predicted by the non-associated flow rule model is shown in Fig. 10.11b. At footing displacements of 0.1, 0.2, and 0.4 in., the spread of yielding is similar to that of the previous case. However, as displacement increases, appreciable difference between the two cases is seen. For the non-associated flow rule case, the yielded zone reaches the upper edge of stratum at the footing displacement of 0.8 in., while for the associated flow rule case, a significant portion of the stratum becomes yielded at the displacement of 0.6 in.

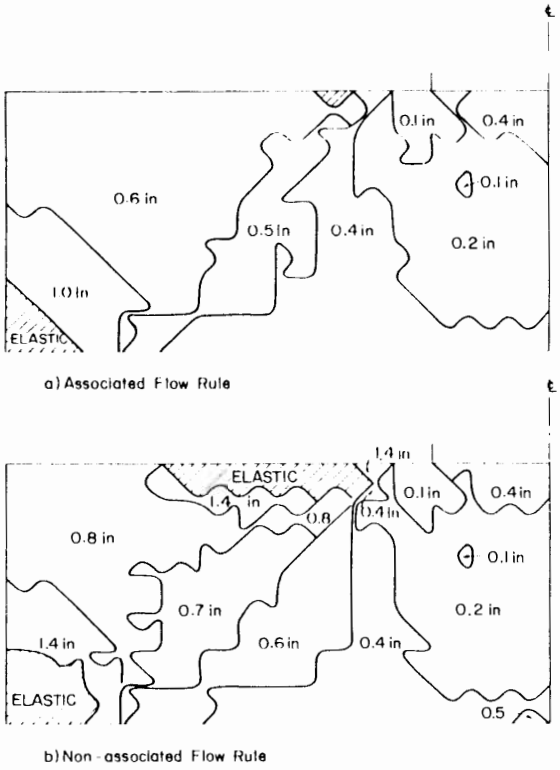

Fig. 10.11. Spread of yielded zone in the Drucker–Prager perfectly plastic material stratum (rigid and rough footing).

(C) Velocity fields

The velocity fields for both models at the last displacement increment are shown in Fig. 10.12. The magnitude and direction of velocity at each node are denoted by an arrow and, the uniform displacement increment at the base of the footing is taken as a normalized unit length. Figure 10.12a shows the velocity field predicted by the associated flow rule model. The velocity field agrees quite well with that of the Prandtl solution, as represented by the solid line. The magnitude of the velocity field is much larger than that predicted by the same model for the flexible and smooth footing problem. Further, its magnitude at the surface becomes two or three times that beneath the footing. This is due to the large amount of dilatancy at this increment.

The velocity field predicted by the model with the non-associated flow rule (Fig. 10.12b) has a relatively small and uniform magnitude in the "radial shearing zone" and the "near-surface zone". The velocity field agrees well with that of the Prandtl solution. As expected, dilatancy in the stratum is restricted at this increment, as can be seen from the velocity field on the surface.

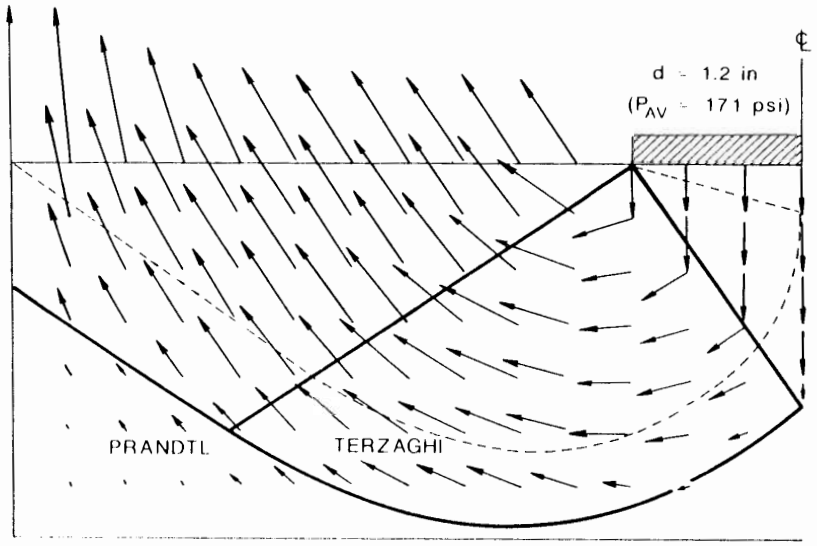

(a) DRUCKER-PRAGER Model (Associated Flow Rule)

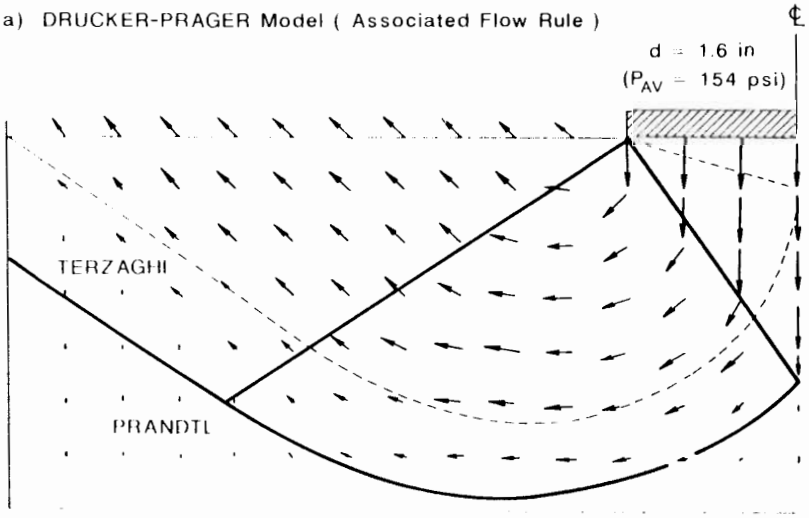

(b) DRUCKER-PRAGER Model (Non- associated Flow Rule $\phi^P = 0^o$)

Fig. 10.12. Velocity field by the Drucker Prager models at the numerical limit load (rigid and rough footing).

In the present analysis, the direction of velocity in the "triangle rigid zone" in the Prandtl mechanism is found to be vertically downwards (Fig. 10.12), while it is not uniformly vertical for the flexible and smooth footing problem (see Fig. 10.5).

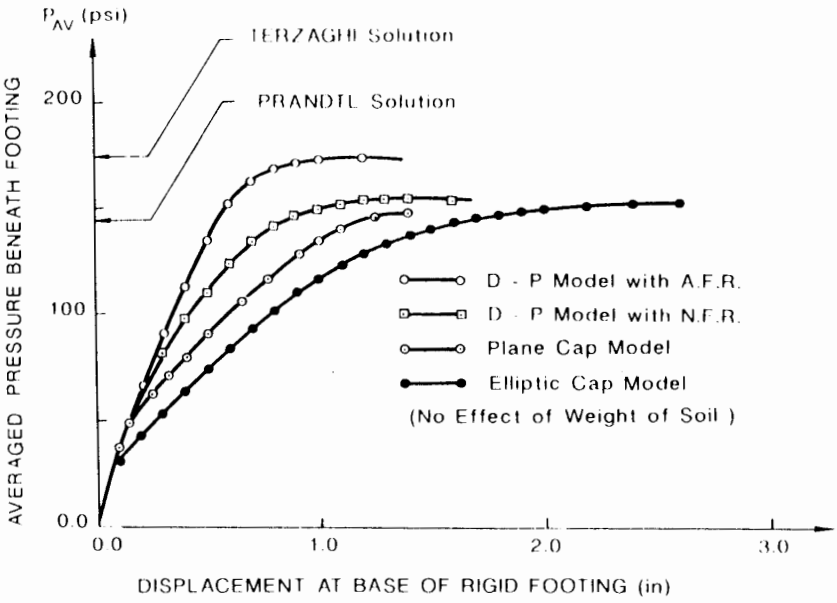

Fig. 10.13. Load-displacement curves by the cap and Drucker–Prager models (rigid and rough footing).

10.3.2 Cap models

Herein, finite-element results predicted by cap models are presented.

(A) Load-displacement curves

The load-displacement curves predicted by both cap models are shown in Fig. 10.13, and compared with those predicted by the Drucker–Prager models. Initially, all the curves are similar. After yielding, the cap model curves start to deviate from each other. Here, as in the Drucker–Prager models, these curves are stiffer than those of the flexible and smooth footing problem (Fig. 10.6). For the plane cap model, yielding starts at about 40 psi (276 kPa). Thereafter, the cap surface expands, hardens, and reaches the collapse state at 148 psi. This load is quite close to those (143 psi, 154 psi) predicted by the Prandtl solution and the Drucker–Prager model with the non-associated flow rule. Note that this collapse load is slightly higher than that (139 psi) predicted by the same model for the flexible and smooth footing problem.

As for the elliptic cap model, yielding starts at 30 psi, and reaches the collapse load of 152 psi, which is greater than that (143 psi) of the Prandtl solution but quite close to that (148 psi) predicted by the plane cap model.

(B) Zones of stress state

The stress states predicted by the plane cap model are shown in Fig. 10.14 at various levels of footing displacement. At a footing displacement of $d = 0.1$ in.

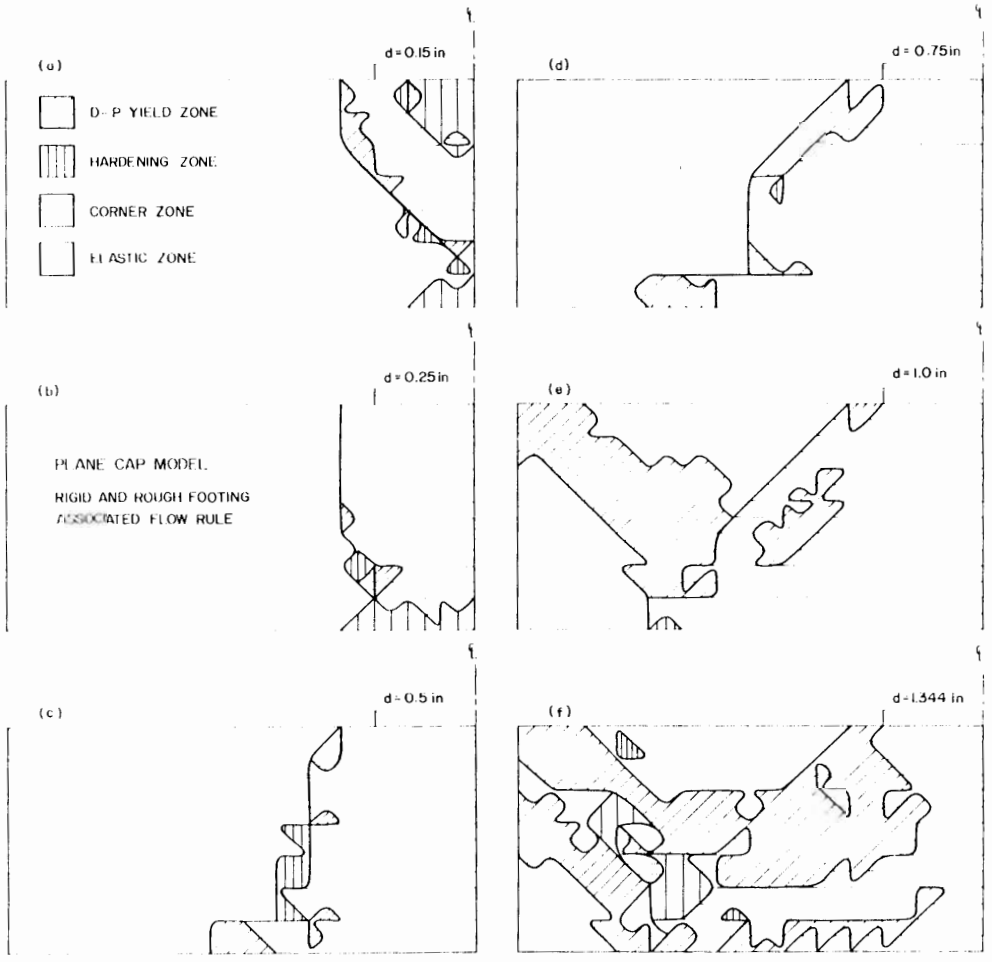

Fig. 10.14. Zones of stress state in the plane cap hardening material stratum (rigid and rough footing).

(0.254 cm), a yielded zone and a corner zone develop near the edge of the footing and then spread downward with increasing displacement. In particular, the corner zone spreads diagonally and downward. The hardening zone spreads mainly in the area directly beneath the footing. This is shown in Fig. 10.14a for $d = 0.15$ in. and also in Fig. 10.14b for $d = 0.25$ in. At $d = 0.5$ in. and 0.75 in., the corner zone spreads outward, and small yielded zones and hardening zones appear on the leading edge of the corner zone (Figs. 10.14c and d). At $d = 1.0$ in., Fig. 10.14e, yielding has developed in the upper edge of the stratum, spreads diagonally downward, and finally merges with another yielded zone which has started in the lower region. At the collapse state, $d = 1.344$ in., Fig. 10.14f, the yielded zone spreads inward over the corner zone, and the stress state in the stratum becomes

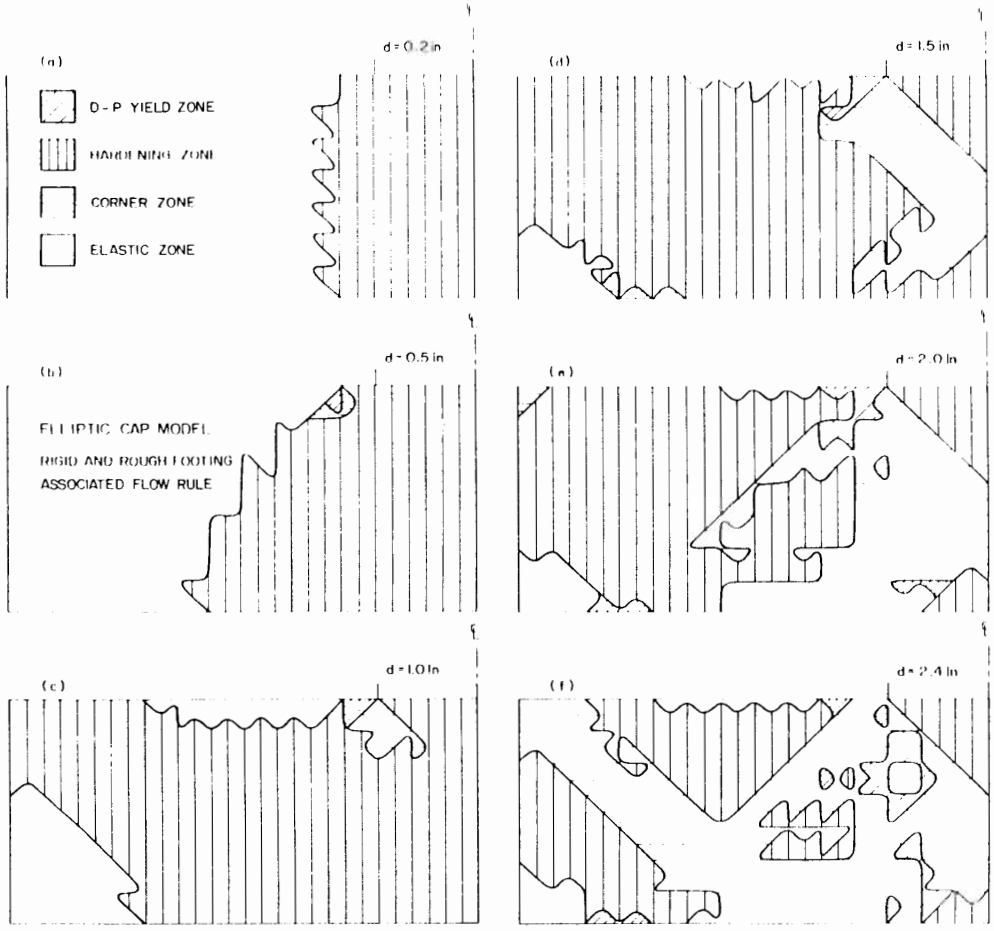

Fig. 10.15. Zones of stress state in the elliptic cap hardening material stratum (rigid and rough footing).

very complicated. In the present analysis, yielded zones and corner zones dominate the response of the stratum.

As for the elliptic cap model, the stress states for various levels of footing displacement are shown in Fig. 10.15. At a displacement of $d = 0.2$ in., the hardening zone spreads directly beneath the footing to the base of the stratum as shown in Fig. 10.15a, and then expands laterally. As the footing displacement increases to 0.5 in. (Fig.10.15b), small yield and corner zones develop near the edge of the footing. At $d = 1.0$ in., Fig. 10.15c, the corner zone starts to expand diagonally inward from the footing edge. With further displacement, it reaches the center of the clay stratum, changes direction, and further expands diagonally outward at $d = 1.5$ in. (Fig. 10.15d). At $d = 2.0$ in. (Fig. 10.15e), another corner zone develops at the upper edge of the stratum and starts to spread diagonally toward the

stratum base. At $d = 2.4$ in., Fig. 10.15f, the two corner zones merge and the footing approaches its collapse stage. Therefore, for the elliptic cap model, it can be concluded that corner and hardening zones are most important in the response of the soil stratum to footing load.

(C) Velocity fields

The velocity fields associated with both models are presented in Fig. 10.16. The velocity field by the plane cap model, Fig. 10.16a, agrees quite well with that of

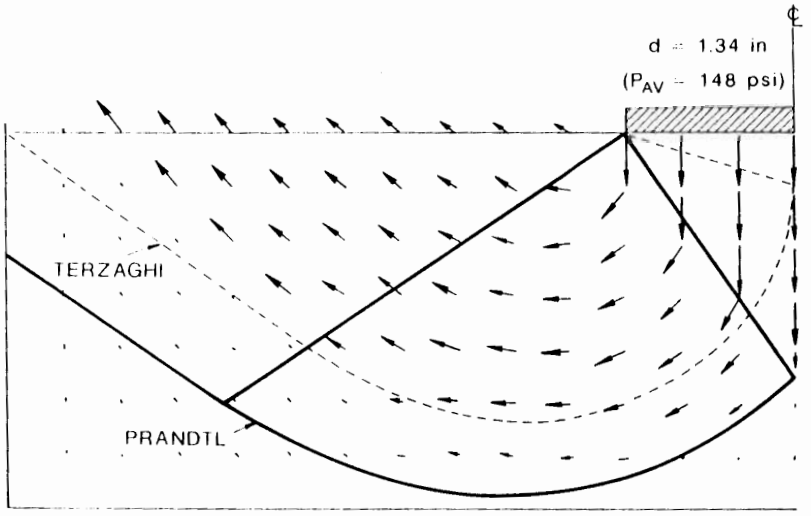

(a) Plane Cap Model

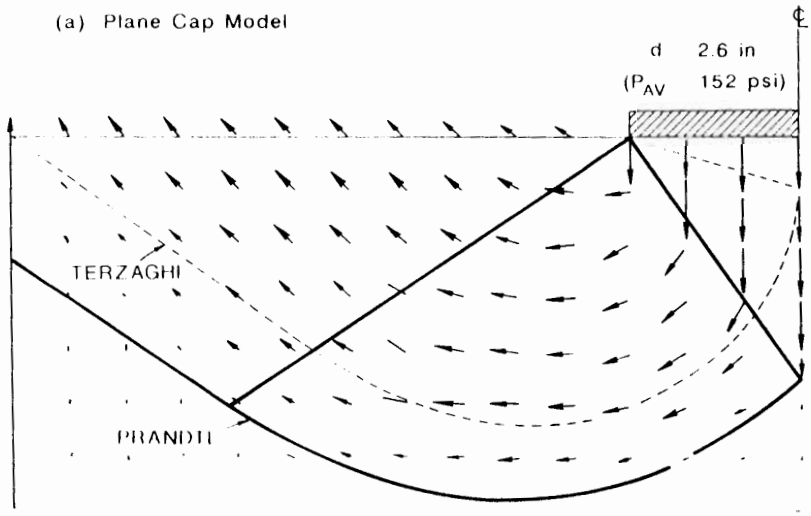

(b) Elliptic Cap Model

Fig. 10.16. Velocity field by the cap models at the numerical limit load (rigid and rough footing).

Terzaghi solution in the "radial shearing zone" and "near-surface zone". However, the velocity under the footing follows that of the Prandtl field and its direction is almost vertical.

The velocity field predicted by the elliptic cap model, Fig. 10.16b, agrees quite well with that of the Prandtl solution. Its magnitude is comparable to that of the plane cap model.

Both models have much less dilatancy than that required by the Drucker–Prager model with the associated flow rule.

10.4 EXAMPLE III. SEISMIC ANALYSES OF SLOPES

In this Section, the cap model as well as the Drucker–Prager model with the assumption of the associated flow rule are applied to the large-deformation finite-element analyses of slopes during the seismic loadings, for the verification and development of the "pseudo-static" method.

Analytical model

A 30 ft (9.15 m) high vertical slope, as analyzed in Chapter 9 is considered under *plane strain condition* (refer to Fig. 9.33). The vertical boundaries and bottom boundary are placed respectively at 300 and 150 ft away from the toe of the expected slope surface as shown in Fig. 9.33. Movement on the vertical boundaries is constrained horizontally only and that along the bottom boundary is constrained in both directions.

Finite-element mesh

The same mesh consisting of 250 nodes and 216 *rectangular elements* is utilized in the finite-element analysis.

Analytical procedure

The *iterative procedure* with initial stress method is employed through the following Sections.

Material constants

The following material constants of soil are assumed: Young's modulus $E = 5 \times 10^5$ psf (2.4×10^7 Pa), Poisson's ratio $\nu = 0.3$, cohesion $c = 810$ psf (3.88×10^4 Pa), internal friction angle $\phi = 10°$, weight of soil $\gamma = 120$ pcf (18.85 kN/m^3).

Comments on material constants

The material constants, α and k, in the Drucker–Prager model are obtained from matching with the Coulomb criterion under the plane strain condition. The material constants, W and D, in the hardening function [Eq. (6.22a)] are assumed to be 0.06 (the maximum compaction of plastic volumetric strain) and 6.042×10^{-5} psf^{-1} (1.26×10^{-6} Pa^{-1}), respectively. The shape ratio of the elliptic cap surface, R, is

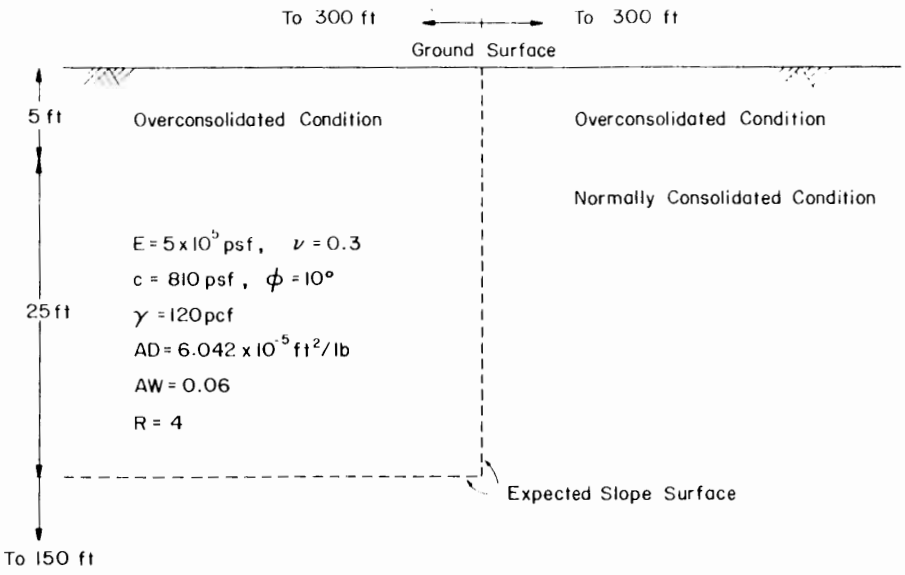

Fig. 10.17. Initial condition of ground.

assumed to be 4. Further, the initial intersection of the elliptic cap surface with the I_1-axis is situated at the point of $I_1 = -6700$ psf (compression side) for soil elements above 5 ft (1.53 m) in depth. In this case, the initial stress states, whose vertical stress, σ_y, and horizontal stresses, $\sigma_x = \sigma_z$, are respectively assumed to be γH and $[\nu/(1-\nu)]\gamma H$ where H is the depth, are within the initial elliptic cap surface. Thus, soil above the 5-ft-level is in the overconsolidated condition. On the other hand, for soil elements below the 5-ft-level, the locations of the cap surfaces are determined according to the initial stress states so that the stress states lie on the corresponding cap surfaces. Thus, soil below 5 ft in depth is in a normally consolidated condition. This ground condition is illustrated in Fig. 10.17. As for the yield surface in the elliptic cap model, the same surface as that of the Drucker–Prager model assumed above is utilized.

Note that since the gravitational load increases from zero to the natural weight of soil ($\gamma = 120$ pcf) the initial stress state for all elements is situated at the origin of stress-invariant space $I_1 \sqrt{J_2}$ in both model analyses while the initial location of the elliptic cap surfaces for all elements can be determined in a similar manner as described above for the elliptic cap model analysis.

10.4.1 Prior to seismic loadings

In order to simulate the slope condition after the completion of the ground excavation, an elastic-plastic effective stress analysis of the slope is performed in this Section. A sequential loading to simulate a cut-down or build-up process is not considered here. Instead, the final configuration of the slope, the stress distribution

inside the slope, and the spreading of yielded zones are investigated quantitatively by increasing the internal force due to weight of soil from zero to the natural soil weight of $\gamma = 120$ pcf (18.85 kN/m^3).

In what follows, (A) the load-displacement curves, (B) deformed shape of slopes, (C) stress distributions and (D) yielded zones and zones of stress state are discussed in some details.

(A) Load-displacement curves

The complete load-displacement curves loaded to $\gamma = 120$ pcf (18.85 kN/m^3) are shown in Fig. 10.18 where the value of horizontal displacement at a distance of approximately one-sixth the slope height above the toe is taken as the reference displacement, in a similar manner to the slope analysis in Chapter 9. The curves with solid and broken lines are the responses predicted by the Drucker Prager and elliptic cap models, respectively. The two curves behave identically to $\gamma = 60$ pcf, but then gradually separate as the load increases. A clear difference between the

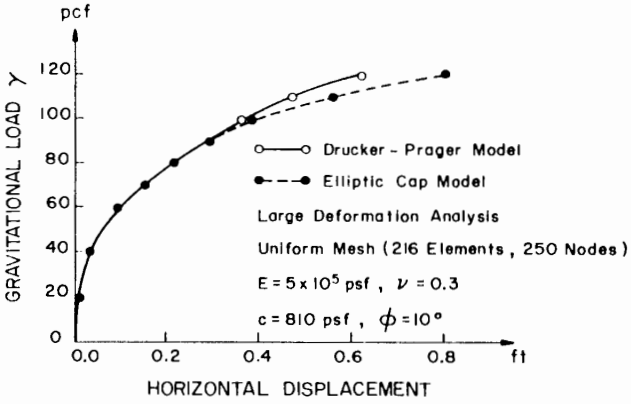

Fig. 10.18. Gravitational load- horizontal displacement curves by the cap and Drucker- Prager models.

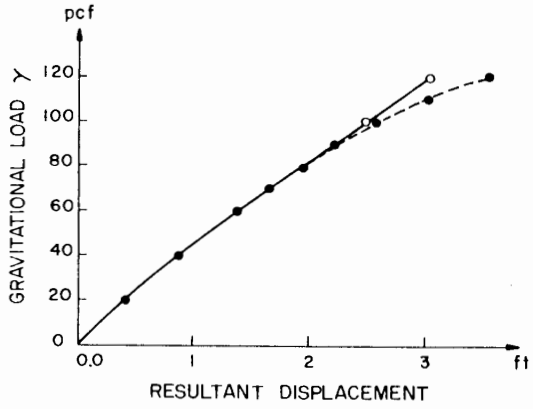

Fig. 10.19. Gravitational load-resultant displacement curves by the cap and Drucker–Prager models.

curves can be recognized above $\gamma = 90$ pcf. In the case of the Drucker-Prager model, a horizontal displacement of 0.604 ft (0.184 m) to the left is observed at the final load level of $\gamma = 120$ pcf. On the other hand, it is approximately 0.804 ft (0.245 m) for the case of the elliptic cap model. Further, the load-displacement curves corresponding to the resultant displacement at the nodal point above the toe are shown in Fig. 10.19. The curve predicted by Drucker–Prager model rises linearly to $\gamma = 120$ pcf with a resultant displacement of about 3 ft (0.915 m). As for the elliptic cap model, the response curve is almost the same as that of the former case to $\gamma = 90$ pcf, but thereafter shows a larger resultant displacement. At $\gamma = 120$ pcf, it has the computed value of 3.55 ft (1.08 m).

(B) Deformed shape of slopes

The deformed geometries of slopes after excavation are presented with solid lines in Figs. 10.20 and 10.21. In these figures, the deformed shapes are drawn to the scale of one unit original finite-element to 5 ft. In the Drucker Prager model case (Fig. 10.20), the ground surface behind the crest settles approximately 3.2 ft (0.98 m) and the bulging extends 0.604 ft (0.184 m) from the original vertical slope line. For the elliptic cap model case (Fig. 10.21), larger amounts of ground settlement (3.8 ft or 1.16 m) and bulging (0.804 ft or 0.245 m) in the horizontal direction are observed. However, deformed geometries of the two slopes are still similar at this load level, regardless of the relatively large difference in ground settlement. Further, it seems clear from the present analysis that for both model cases the loss of ground, which is usually evaluated by the largest horizontal displacement along the vertical slope line, would occur at the nodal point immediately above the toe.

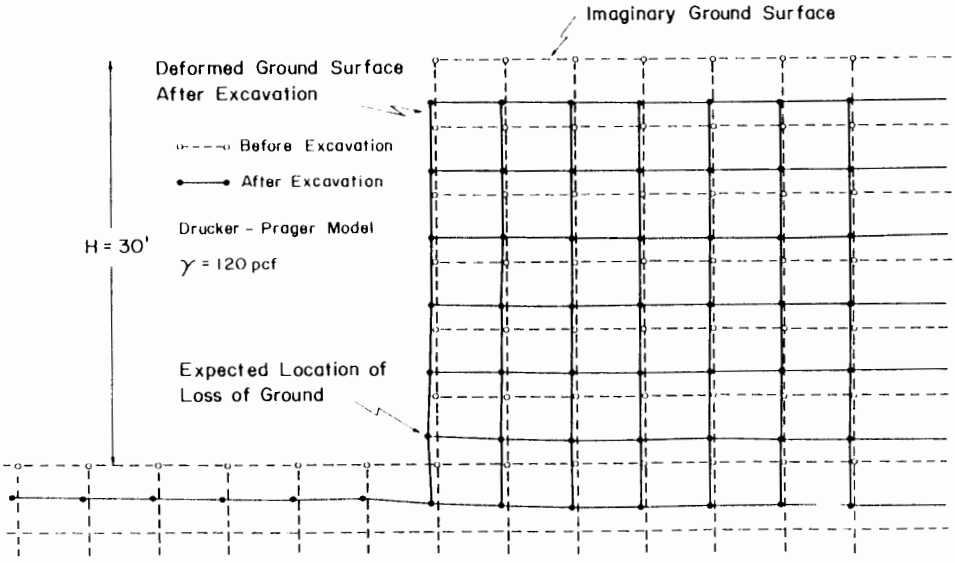

Fig. 10.20. Geometry of slope after excavation (Drucker-Prager model).

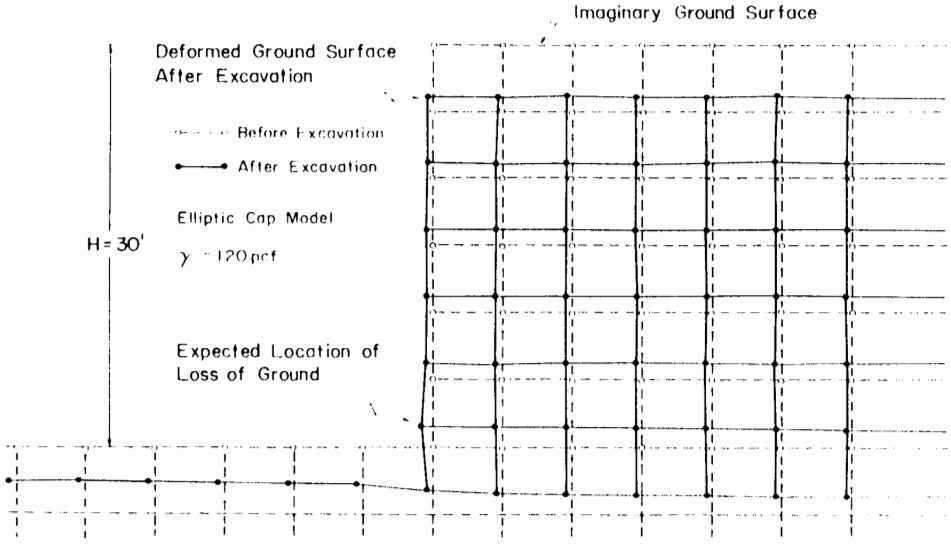

Fig. 10.21. Geometry of slope after excavation (elliptic cap model).

(C) Stress distributions

The distributions of vertical stress σ_y, horizontal stresses σ_x and σ_z, and shearing stress τ_{xy} within the slopes at $\gamma = 120$ pcf (18.85 kN/m^3) are illustrated respectively in Figs. 10.22 through 10.25, for both model cases. In all figures, stresses are given along the vertical line near the vertical slope line (free surface) as well as three other vertical lines located at 10, 20, and 30 ft (3.05, 6.1, and 9.15 m) behind the crest of the slope. The stress distributions with solid and broken lines are from analyses with the Drucker–Prager and elliptic cap models respectively. Note that the stresses in the figures follow the usual soil mechanics sign convention (compressive stresses are positive).

Considering the distributions of vertical stress σ_y in Fig. 10.22, the variations of stress with depth are almost the same at all locations except the vertical slope line for both model cases. The stress distributions at three locations behind the crest almost follow the simple relation $\sigma_y = \gamma H$. As a whole, there is little difference between the vertical stresses predicted by the two models except at the nodal point above the toe.

Similarly, the distributions of horizontal stresses, σ_x and σ_z, at the four locations are presented in Figs. 10.23 and 10.24, respectively. The horizontal stress, σ_x, acts in the direction normal to the vertical slope plane. The other horizontal stress, σ_z, is associated with a strain of zero as required by the plane strain condition. The distribution of horizontal stress, σ_x, near the vertical slope line indicates an almost stress-free boundary except at the toe area where a high stress concentration is expected due to the corner geometry (Fig. 10.23). Although both models present

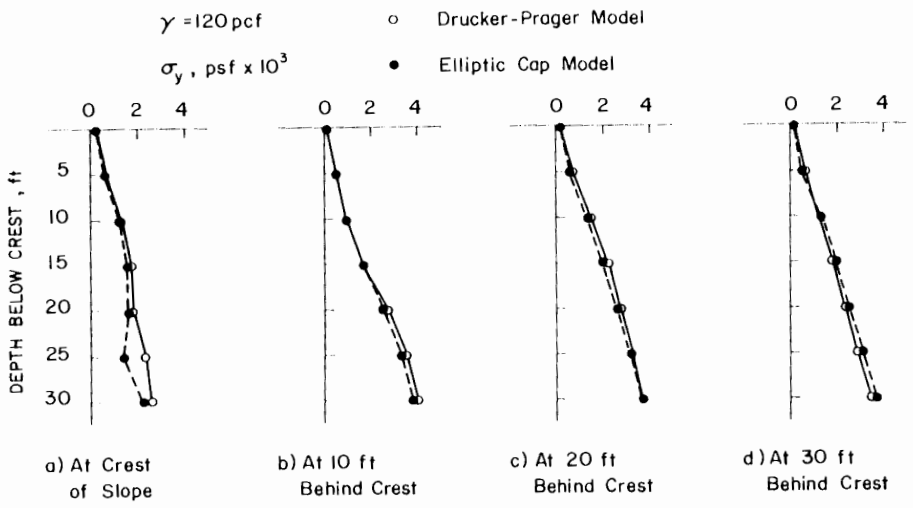

Fig. 10.22. Vertical stress distributions after excavation.

practically the same tensile stress distributions to a depth of 20 ft, the stress predicted at 25 ft in depth is compressive for the Drucker–Prager model case and tensile for the elliptic cap model case. As the vertical line situates further away from the vertical slope line, the stress distributions predicted by the elliptic cap model for depths below one-half the slope height present larger values than those predicted by the Drucker Prager model. In the Drucker-Prager model case, the distributions of stress at 30 ft behind the crest seem to agree well with the simple relation $\sigma_x = [\nu/(1-\nu)]\gamma H$ for depths below one-half the slope height.

As for the distributions of horizontal stress, σ_x, in Fig. 10.24, tensile stress never

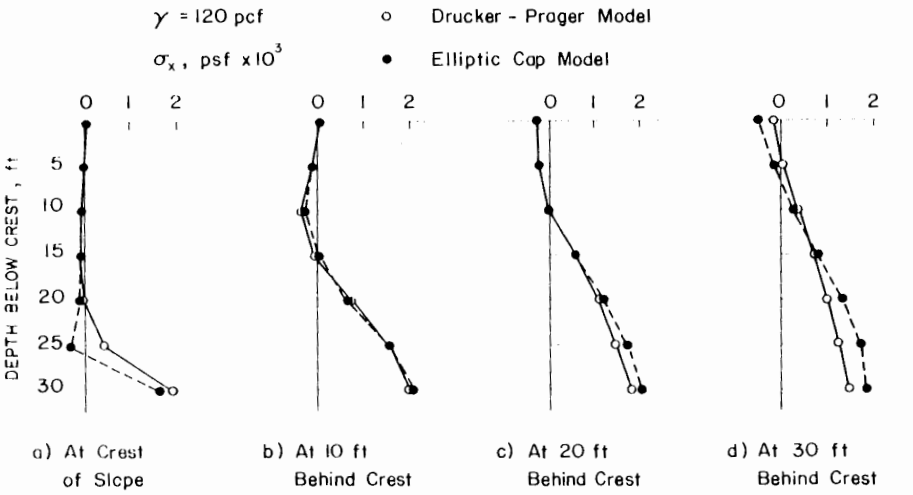

Fig. 10.23. Horizontal stress distributions after excavation.

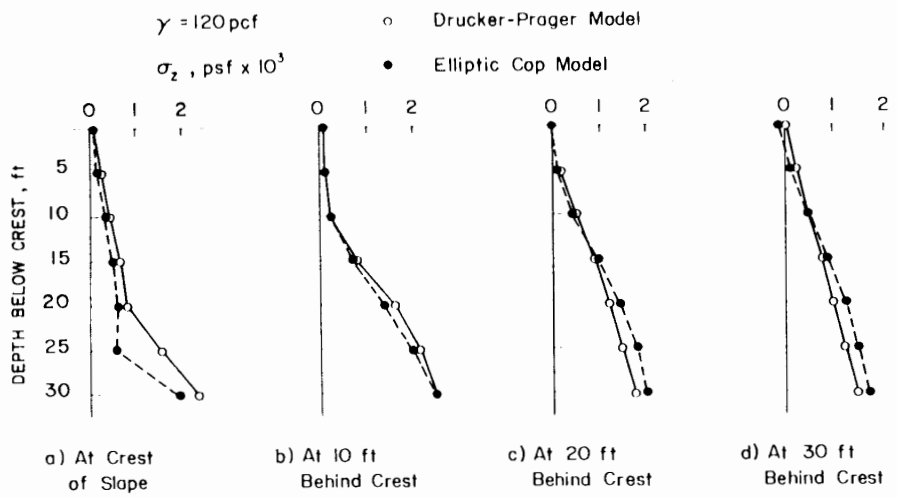

Fig. 10.24. Horizontal stress distributions after excavation.

occurs at any location except near the ground surface at 30 ft behind the crest. Here, as in the case of horizontal stress, σ_x, the stress distributions predicted by the elliptic cap model present larger values than those of the Drucker–Prager model as the location of vertical lines becomes far away from the vertical slope line. Also, the distributions of stress at 20 and 30 ft behind the crest almost coincide with the relation $\sigma_z = [\nu/(1-\nu)]\gamma H$, for the Drucker–Prager model.

Finally, the distributions of shearing stress, τ_{xy}, are shown in Fig. 10.25 for both model cases. If the ground surface were infinite, it would be expected that the state of stress at any point would have no shearing stress component. This condition can

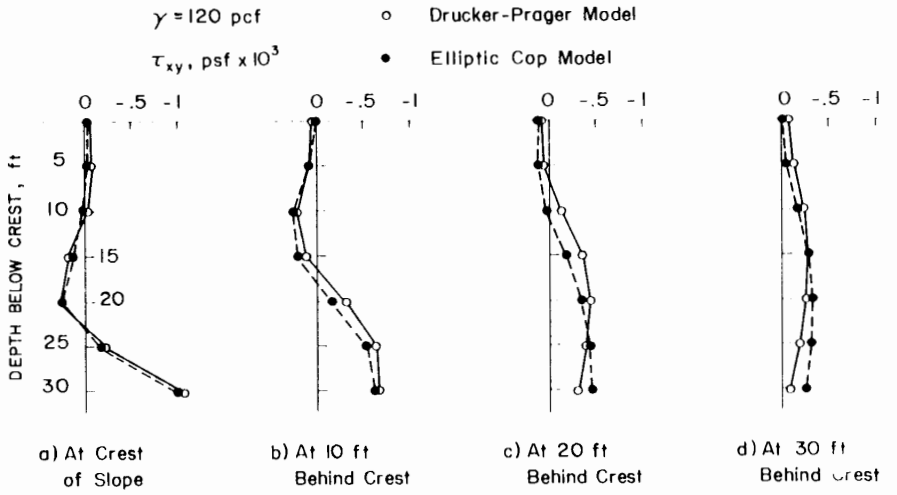

Fig. 10.25. Shearing stress distributions after excavation.

be observed from the fact that the magnitude of shearing stress for both model cases decreases as the vertical line becomes far away from the vertical slope line. The stress distributions in both model cases are almost the same at the vertical slope line. However, those at the three other locations present slightly different values.

(D) Yielded zones and zones of stress state

In Fig. 10.26a, the yielded zones at four different loads ($\gamma = 40$, 60, 80, and 120 pcf or $\gamma = 6.28$, 9.43, 12.57, and 18.85 kN/m^3) are presented for the Drucker–Prager model case. Further, the zones of stress state such as the Drucker–Prager yielded zone, hardening zone, corner zone and elastic zone are illustrated in Fig. 10.26b at $\gamma = 120$ pcf, for the elliptic cap model case. Considering first the spreading of yielded zones in Fig. 10.26a, at $\gamma = 40$ pcf the yielding occurs first around the toe area and above the bottom boundary. As the load increases, the yielded zone above the bottom boundary spreads upwards toward the ground surface behind the crest and seems to merge with the yielded zone around the toe area, at $\gamma = 60$ pcf. The merged zone of yielding then spreads upward into the slope and laterally into the lower ground located in front of the toe. In particular, the yielded zone appears to spread diagonally along the slip surface as would be predicted by the limit analysis method. Finally, the yielded zone spreads to within 5 ft of the upper ground surface, at $\gamma = 120$ pcf.

For the elliptic cap model case, the Drucker–Prager yielded zone spreads in the same manner as that of Fig. 10.26a to a load of $\gamma = 60$ pcf. As the load increases to $\gamma = 120$ pcf, some parts of the yielded zones and almost all of the elastic zones on

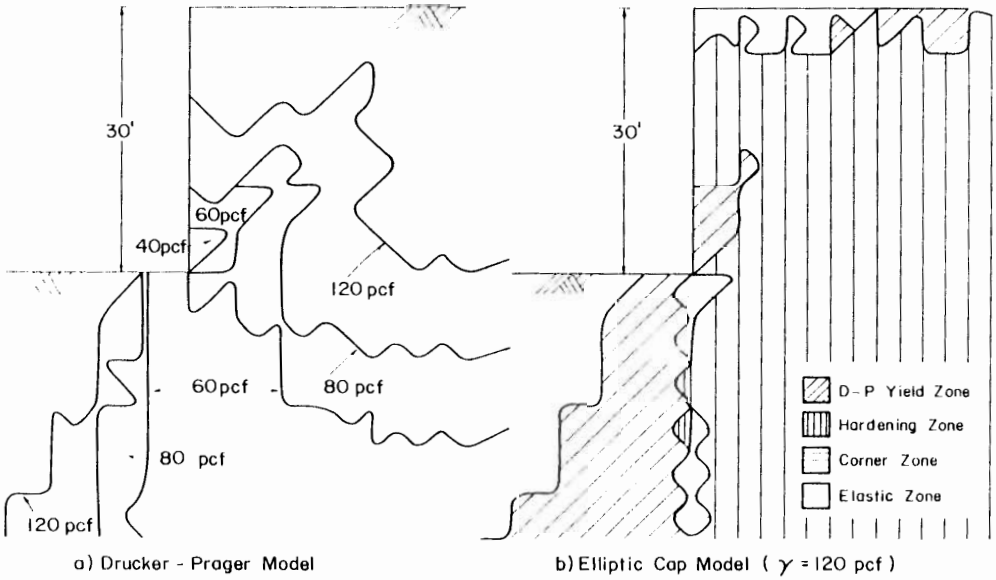

Fig. 10.26. Spread of yielded zone in the Drucker–Prager perfectly plastic material slope and zones of stress state in the elliptic cap hardening material slope.

the right-hand side of the toe change into the hardening zone. The zones of yielding spread diagonally upward near the toe, throughout the area in front of the toe, and near the ground surface behind the crest. Further, the corner zone spreads directly downward from the toe. The zones of stress state for the cap model at $\gamma = 120$ pcf are seen to be quite different inside slope compared to those of the Drucker–Prager case.

10.4.2 During seismic loadings

Based on the analysis described in the previous Section, the seismic large-deformation analyses of the vertical slopes are performed in this Section by employing the *pseudo-static method*. The 1934 El Centro (S–N direction) accelerogram, as shown in Fig. 10.27, is used as input for the seismic loadings which are obtained as the product of soil mass, m, and acceleration, a. In the present analysis, the horizontal acceleration data between time $t = 1.5$ seconds and $t = 4.5$ seconds in the accelerogram are applied to the deformed shape of the slope after excavation. For simplicity, the distribution of acceleration is here assumed to be uniform throughout the slope. It acts to the right when its sign is positive.

Herein, the *effective stress analysis* is performed, in a similar manner to that of the previous Section. In the following, the finite element results are presented with respect to (A) response of the slopes during seismic loading, (B) stress distributions, and (C) velocity fields at the collapse stage.

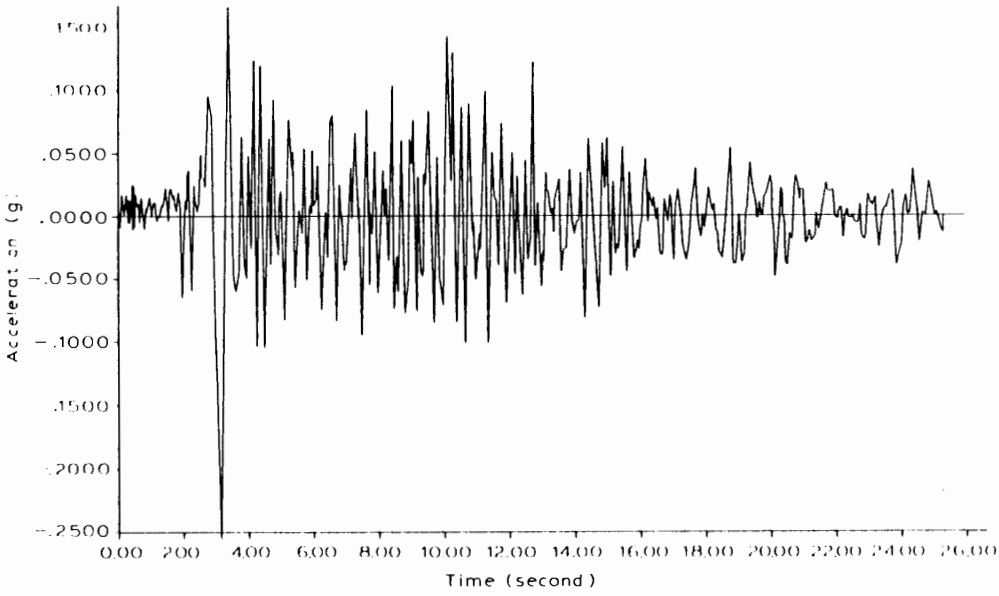

Fig. 10.27. Accelerogram (S-N direction) of 1934 El Centro earthquake.

(A) Response of slopes

In Fig. 10.28, the acceleration-time-displacement curves are presented for both model cases. Note that the horizontal displacement at the nodal point above the toe is taken as the reference displacement in the figure, and that displacement is measured from the deformed shape of the slope after excavation, not from the original shape. The displacement response curves with the solid and broken lines are results from the analyses with the Drucker–Prager and elliptic cap models, respectively. Further, the zones of yielding during seismic loading are presented in Fig. 10.29 for both model cases. The yielded zones in the Drucker–Prager model and elliptic cap model cases are illustrated in parallel in the upper and lower halves of the figure respectively. Note that the yielded zones in the elliptic cap model case are

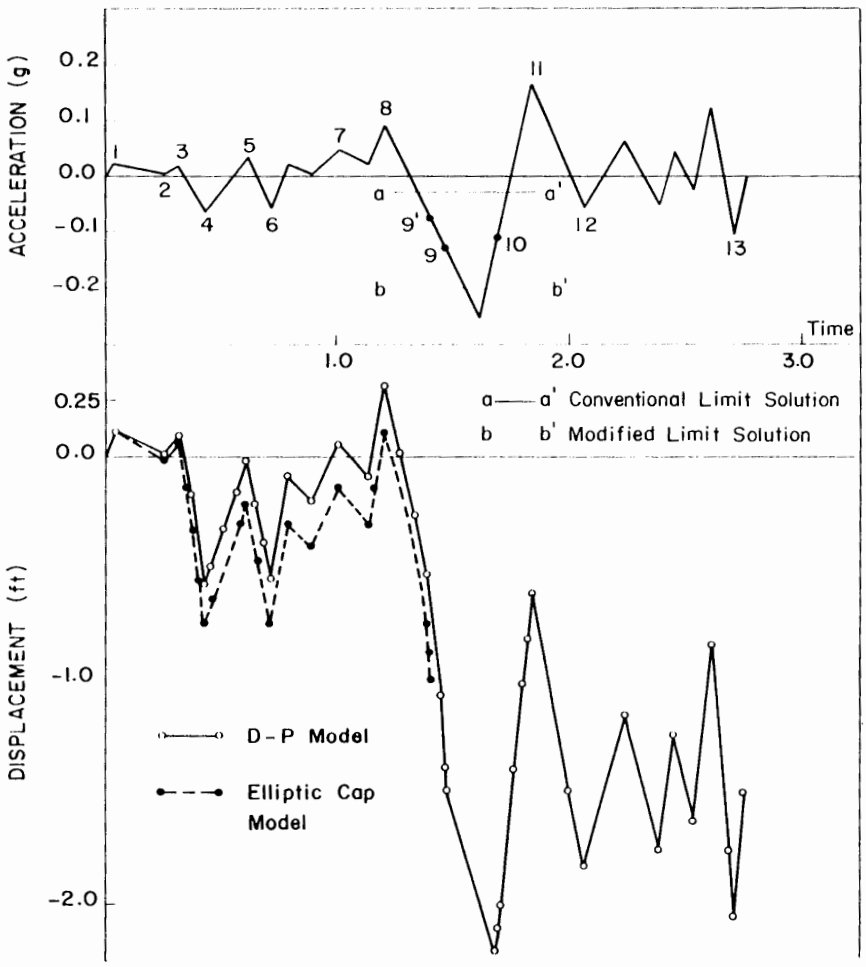

Fig. 10.28. Acceleration-time-displacement curves by the Drucker–Prager and elliptic cap models.

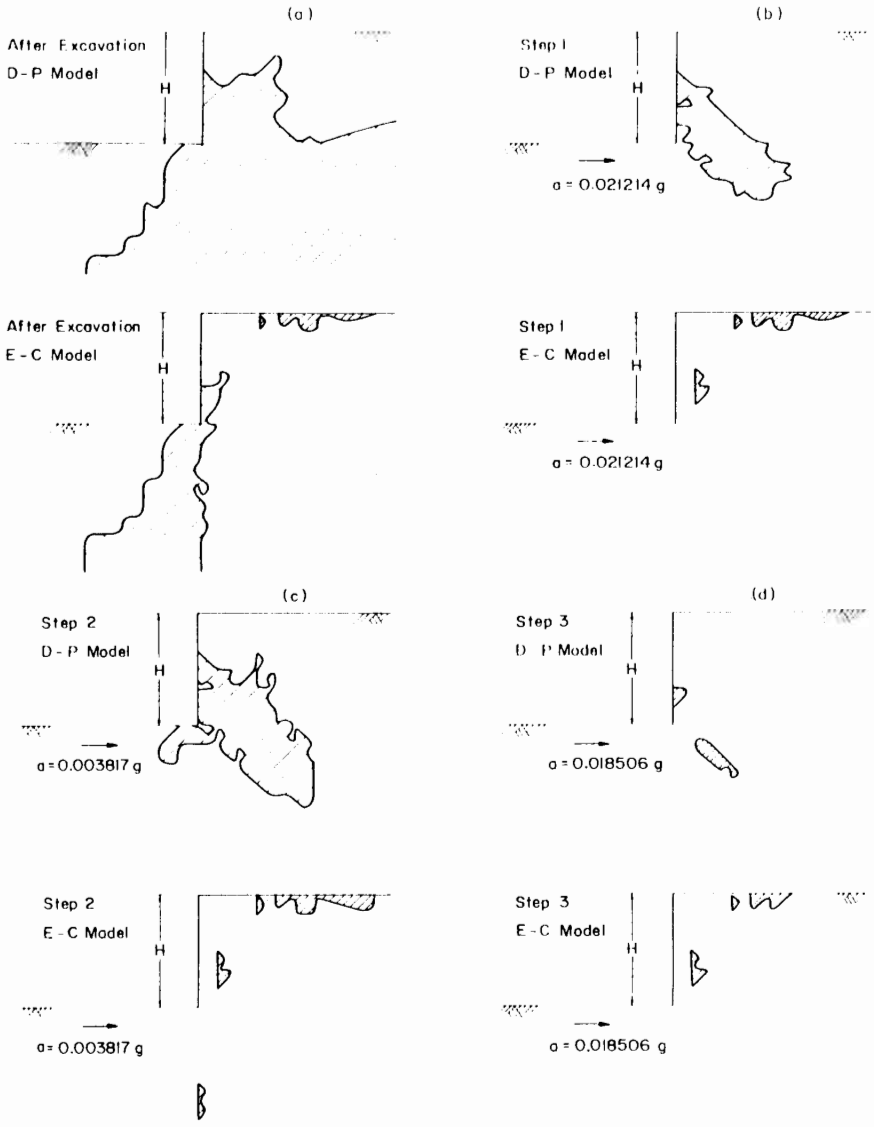

Fig. 10.29. Yielded zones in the Drucker–Prager perfectly plastic material and elliptic cap hardening material slopes during seismic loading.

taken to be the combination of the Drucker–Prager yielded zones and corner zones, but not the hardening zones.

The seismic loadings with small magnitude act horizontally and uniformly to the right during the incipient period. This can be seen from the accelerogram in Fig.

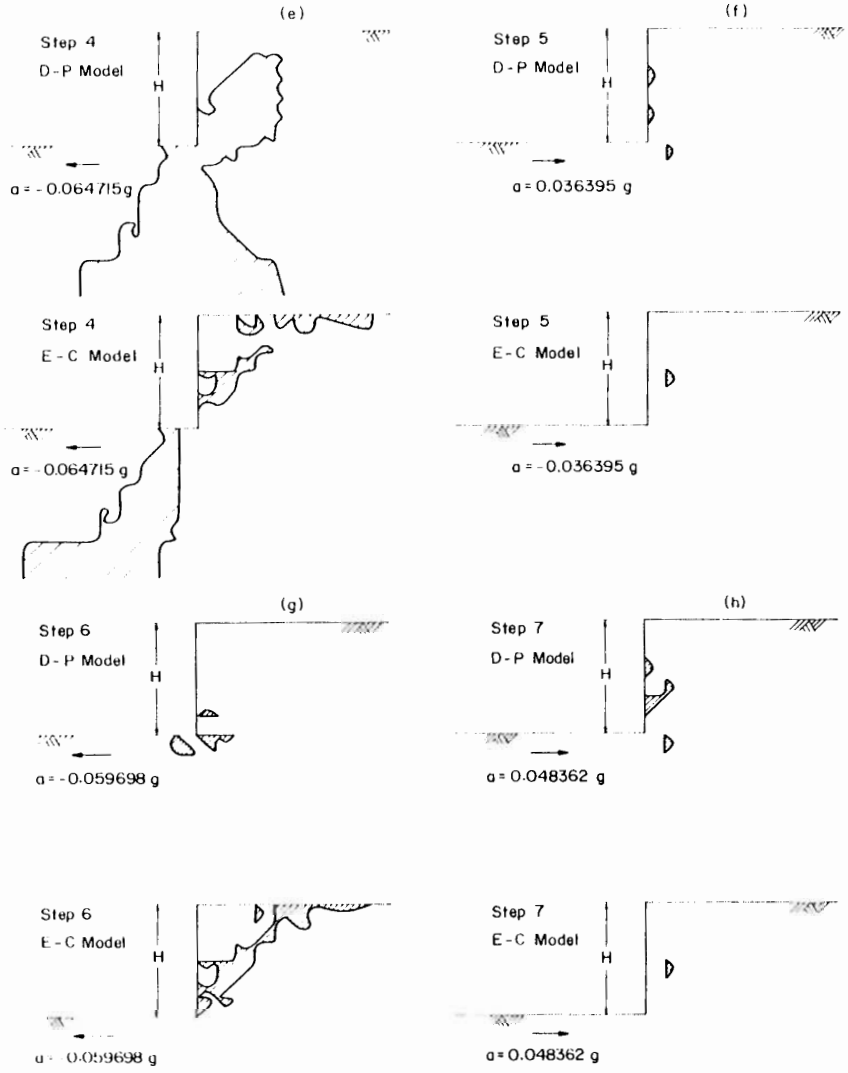

Fig. 10.29 (continued).

10.28. Consequently, the direction of horizontal displacement at the nodal point above the toe is to the right and it prevents the slope from sliding.

The displacements predicted by both models during the period between step 1 and step 3 as marked in Fig. 10.28 are almost the same. Further, the yielded zone predicted by the Drucker Prager model contracts dramatically at step 1, as shown in Fig. 10.29b, compared with that (Fig. 10.29a) at the beginning of the seismic loading. In this case, the yielded zone is located just to the right of the toe and

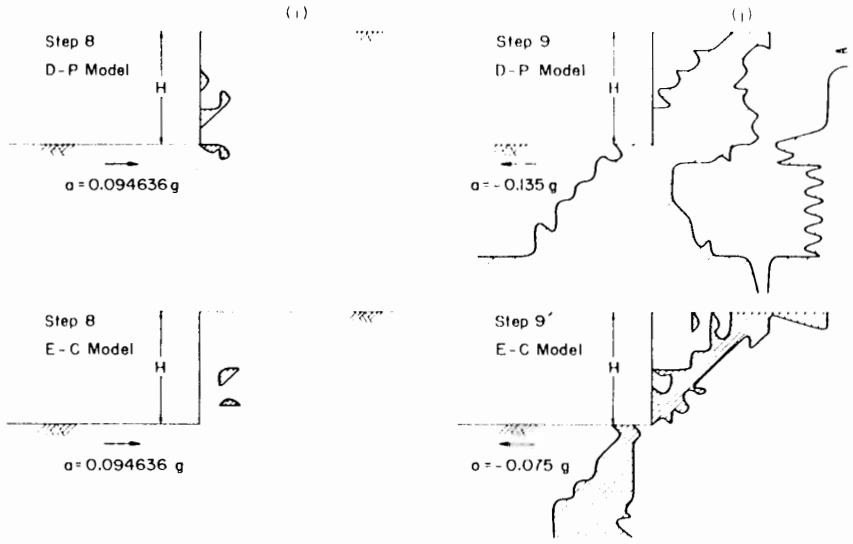

Fig. 10.29 (continued).

oriented diagonally downward. At step 2, it grows in size and then contracts again at step 3 (Figs. 10.29c and d). The yielded zones for the elliptic cap model case show a similar response during this period. However, the nature of the spreading of yielded zones is quite different from that in the other case. In particular, the spreading occurs at the upper ground surface behind the crest.

During the period between step 3 and step 4, the seismic load changes direction and acts to the left so that sliding of the slope is likely to occur. At step 4 with $a = -0.065\ g$, the horizontal displacements are predicted to be 0.58 ft (0.177 m) and 0.73 ft (0.223 m) by the Drucker–Prager and elliptic cap models, respectively. For the Drucker–Prager model case, the yielding spreads into the area below the toe and along the slip surface as would be predicted in the limit analysis method (Fig. 10.29e). For the elliptic cap model case, it spreads over this same general area but also at the ground surface behind the crest. In this case, the yielded zones show a clearer picture of a potential sliding of the slope.

At step 5, however, the important spreading of yielded zones to cause possible sliding of the slope is not observed in Fig. 10.29f for both model cases because the load now acts to the right. As a result, the zones of yielding contract.

At step 6 where the direction of loading is again reversed, the growth of yielded zone is limited to a small area around the toe for the Drucker–Prager model case (Fig. 10.29g). However, for the elliptic cap model case, the yielded zone spreads along the entire slip surface of the limit analysis method.

During the period between step 7 and step 8, yielded zones spread over a small area near the vertical slope line for the Drucker–Prager model case and inside the slope for the elliptic cap model case (Figs. 10.29h and i). These yielded zones do not appear to affect the critical behavior of the slope.

The behavior of the displacement during the period between step 4 and step 8 shows a similar pattern of variation for both model cases, although there is a difference in magnitude. It is clear from Fig. 10.28 that the elliptic cap model predicts a larger displacement than that of the Drucker–Prager model.

Beyond step 8, the seismic load acts to the left and directs toward a level corresponding to an acceleration of $a = -0.255\ g$. Since potential sliding of the slope is observed at step 4 (Fig. 10.29e) with $a = -0.064\ g$, it is expected that the sliding mechanism would develop during this loading. Based on the finite-element calculation, the sliding of the slope is estimated to occur at approximately $a = -0.135\ g$ and $-0.075\ g$, for the Drucker–Prager and elliptic cap model cases, respectively. On the other hand, the limit analysis method predicts the occurrence of sliding at $a = -0.0287\ g$ and $-0.196\ g$ by applying the full slope height of 30 ft (9.15 m) and the modified slope height of 25 ft (7.63 m), respectively. Thus, the finite element solutions lie between the two extreme solutions of the limit analysis method.

Further, at this sliding stage the horizontal displacement is predicted to be 1.49 ft (0.454 m) and 0.99 ft (0.302 m) for the Drucker–Prager and elliptic cap model cases, respectively, as can be seen in Fig. 10.28. The yielded zone predicted by the Drucker–Prager model spreads downward into below the toe, diagonally upward along portions of the slip surface of the limit analysis method, and vertically in the area approximately 40 ft behind the crest. On the other hand, for the elliptic cap model case, it spreads into the ground below the front of the toe, within a narrow area along the slip surface, and at the ground surface behind the crest. In this case, the zones of yielding are quite different from those of the Drucker–Prager model

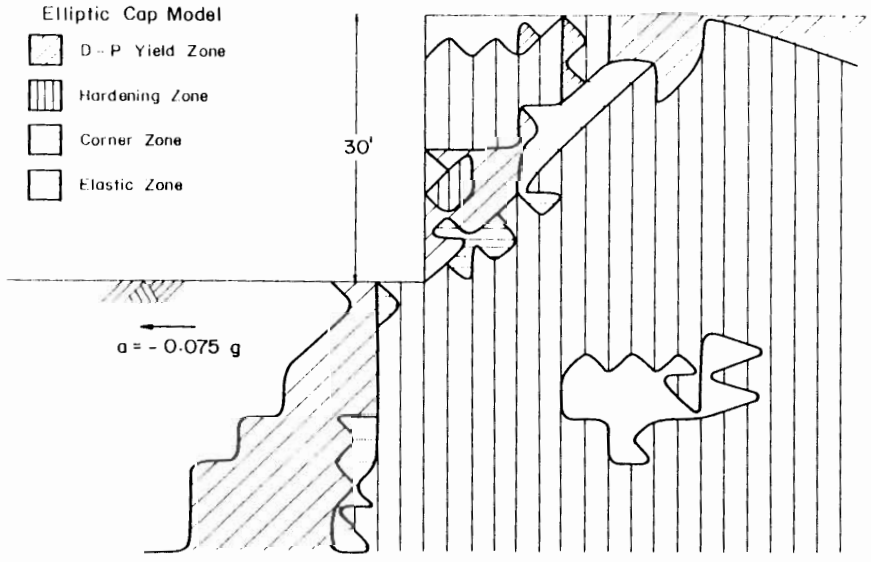

Fig. 10.30. Zones of stress state in the elliptic cap hardening material slope at sliding stage.

case. Also, a much clearer picture of spreading of the yielded zone can be seen along the slip surface.

The zones of different stress states at the sliding stage are illustrated in Fig. 10.30 for the elliptic cap model case. The Drucker Prager yielded zone spreads downward into the region in front of the toe, along the slip surface near the toe, and at the ground surface behind the crest. The corner zone spreads along portions of the slip surface, and vertically below the front of the toe. Further, the hardening zone spreads over almost the entire region to the right of the vertical slope line. Finally, a large elastic zone remains on the left-hand side, and a smaller one inside the hardening region.

(B) Stress distributions

In Figs. 10.31 through 10.38, the distributions of vertical stress σ_y, horizontal stresses σ_x and σ_z, and shearing stress τ_{xy} at the sliding stage are compared with those after the excavation, for both model cases. The solid and broken lines represent respectively the stress distributions at the sliding stage and prior to the seismic loading. Considering first the vertical stress, σ_y, predicted by the Drucker Prager model, the stress distributions are very similar at all four locations, as shown in Fig. 10.31. However, as can be seen in Fig. 10.32, the distribution of horizontal stress, σ_x, changes significantly as the vertical line becomes far away from the vertical slope line. At the vertical slope line, the horizontal stresses do not change and still keep the stress-free boundary. At the other three locations, larger tensile stresses are observed above a depth of one-half the slope height, and larger compressive stresses are observed below that depth. This is expected because only horizontal seismic forces are considered in the present analysis. As for the horizontal stress, σ_z, which is normal to the section of the slope, and the shearing stress, τ_{xy},

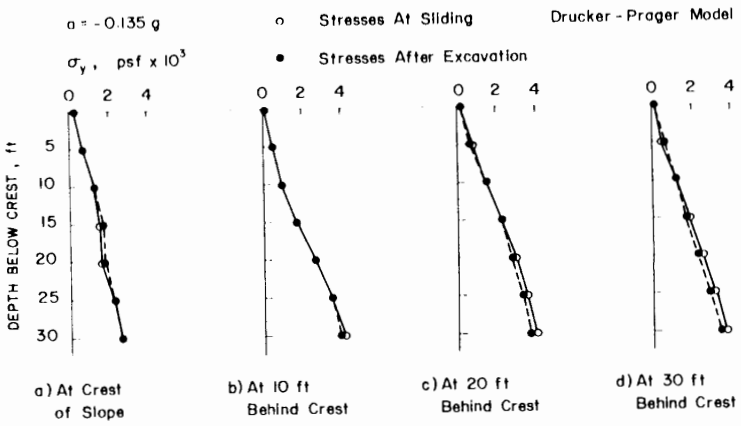

Fig. 10.31. Vertical stress distributions at sliding (Drucker–Prager model).

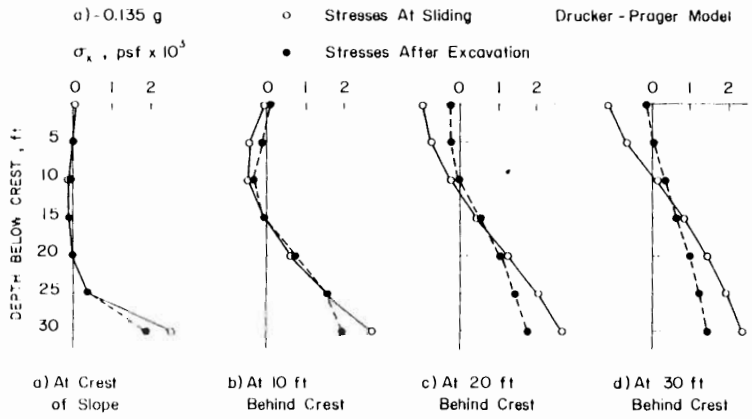

Fig. 10.32. Horizontal stress distributions at sliding (Drucker–Prager model).

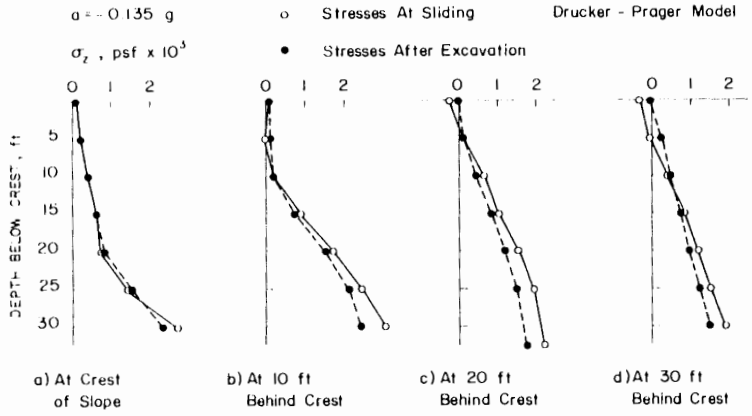

Fig. 10.33. Horizontal stress distributions at sliding (Drucker–Prager model).

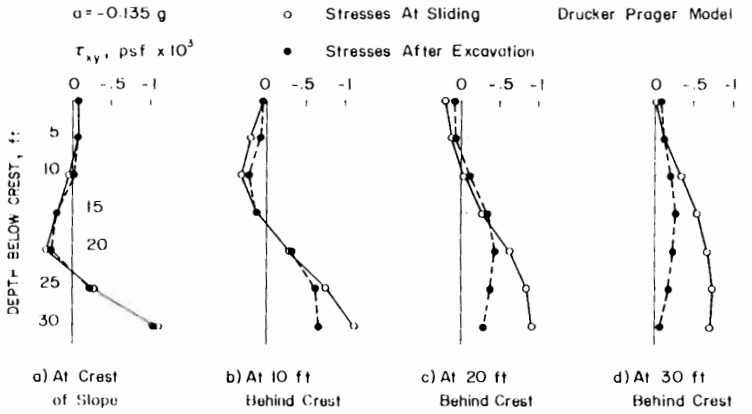

Fig. 10.34. Shearing stress distributions at sliding (Drucker–Prager model).

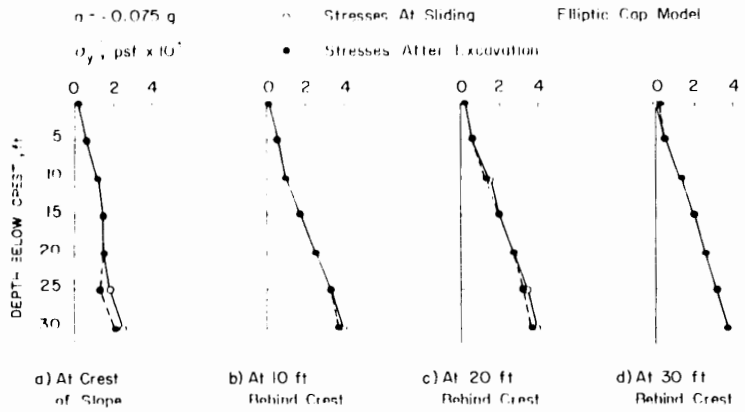

Fig. 10.35. Vertical stress distributions at sliding (elliptic cap model).

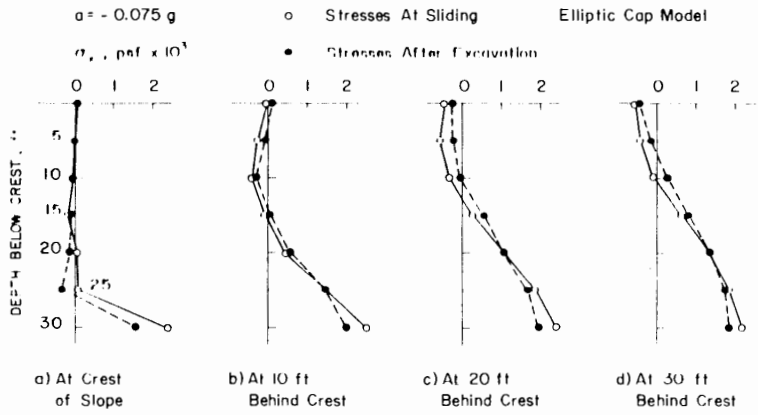

Fig. 10.36. Horizontal stress distributions at sliding (elliptic cap model).

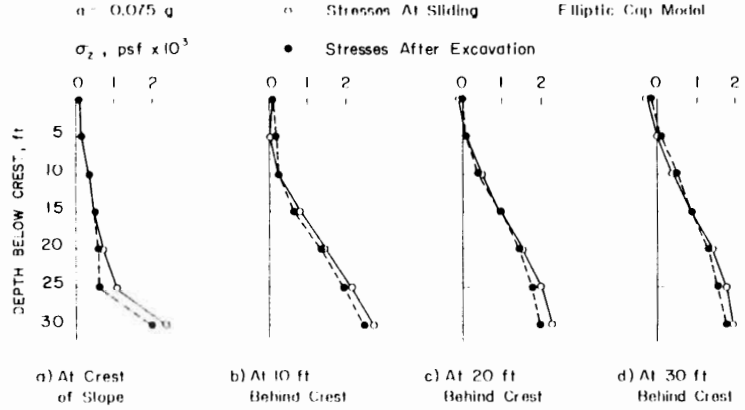

Fig. 10.37. Horizontal stress distributions at sliding (elliptic cap model).

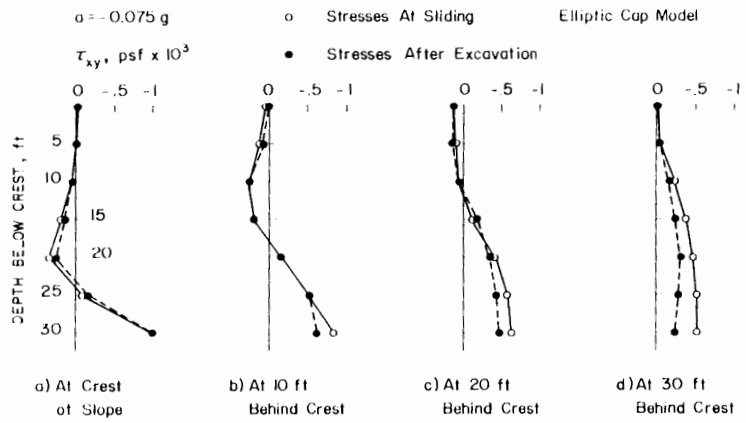

Fig. 10.38. Shearing stress distributions at sliding (elliptic cap model).

roughly similar responses can be seen from Figs. 10.33 and 10.34 respectively. However, the distribution of horizontal stress, σ_z, changes less with distance from the crest than those of σ_y and τ_{yz}.

A similar pattern of stress variation can be seen from Figs. 10.35 through 10.38 for the elliptic cap model case. In this case, however, the magnitude of stress is less because the acceleration ($a = -0.075\ g$) at the sliding stage is smaller than that ($a = -0.135\ g$) of the Drucker–Prager model case.

(C) Velocity fields

Herein, the *relative velocity fields* rather than total velocity fields are discussed. The relative velocity is defined here as the difference between the displacement increment at a nodal point and that at the toe. The relative velocity fields at the sliding stage are presented in Fig. 10.39, for both model cases. The magnitude and direction of each relative velocity vector are shown by an arrow, and the resultant of the relative-displacement increment at the nodal point above the toe is taken as a normalized unit length. Further, the modified and conventional log-spiral slip surfaces of the limit analysis method are illustrated with the solid and broken lines, respectively. The former and latter slip surfaces are obtained by using slope heights of 25 ft (7.63 m) and 30 ft (9.15 m) in the limit analysis solution. Also note that the modified and conventional slip surfaces correspond to failure mechanisms at $a = -0.196\ g$ and $-0.0287\ g$, respectively. Since loss of ground appears to occur at a distance of approximately one-sixth the total height above the toe as discussed previously, the relative velocity fields of both models agree well with the modified slip surface. Further, a very clear velocity "discontinuity" between the relative velocity fields on either side of the modified slip surface is seen in both Figs. 10.39a and 10.39b.

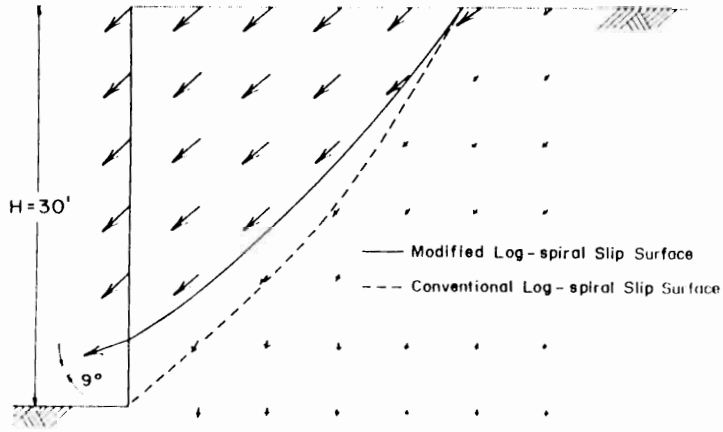

a) Relative Velocity Field (D-P Model), a = -0.135g.

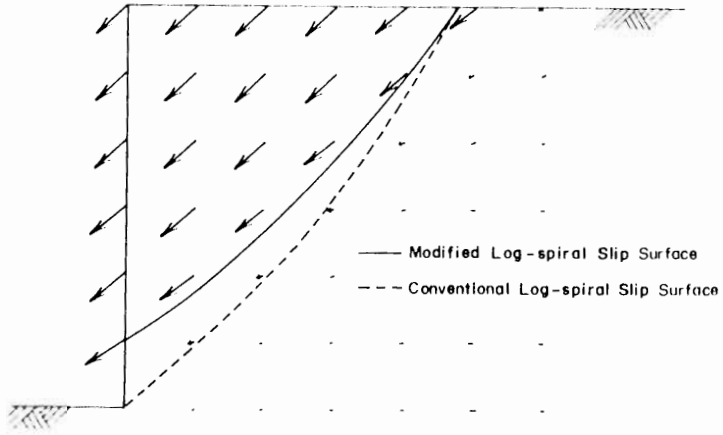

b) Relative Velocity Field (Elliptic Cap Model), a = -0.075g.

Fig. 10.39. Relative velocity field at sliding.

The angle between the modified slip surface and the relative velocity vector at the nodal point above the toe is measured from the figures. For the Drucker Prager model case, it is measured as 9°. It is expected that if the seismic load is increased slightly, this angle would approach 10° as would be predicted by the limit analysis method. On the other hand, the angle in the elliptic cap model case seems to be nearly zero. This means that the dilatancy has not been developed so much along the slip surface. Referring to Fig. 10.30, some stress states along the slip surface are in the corner zone. Consequently, the dilatancy on the slip surface is prevented to some extent.

10.4.3 After slidings

It is usually difficult to continue an elastic-plastic analysis with the finite-element method beyond the loading which causes instability of the slope, because the stiffness matrix itself becomes unstable. However, a method to calculate the post-sliding behavior of the slope under seismic loading conditions is proposed (Mizuno and Chen, 1984).

To perform the post-sliding analysis, "pseudo-velocity" inside the sliding mass at the sliding stage is first defined. Here, it is assumed that the pseudo-velocity can be calculated as follows:

$$V_p = du/dt \tag{10.1}$$

where du and dt are respectively the relative-displacement increment inside the sliding mass and the time interval corresponding to the last seismic loading increment before the sliding stage.

As can be observed from Fig. 10.39, the relative velocity vectors above the modified log-spiral slip surface are almost uniform in magnitude and have the same direction of approximately 45° downward to the left, except the vector at the point above the toe. Consequently, rigid-body movement is assumed to start after sliding occurs and to continue until the magnitude of acceleration becomes again the same as that at the beginning of sliding. Finally, the "*pseudo-displacement*" of the sliding mass is calculated as a product of the pseudo-velocity V_p and the time interval during which the acceleration is beyond the one at the beginning of the sliding. The pseudo-velocities at step 9 and step 9′ in Fig. 10.28 are approximated to be 6.3 ft/sec (1.92 m/sec) and 18.2 ft/sec (5.5 m/sec) for the Drucker–Prager and elliptic cap model cases, respectively. Thus, the corresponding pseudo-displacements are calculated to be 1.05 ft (0.32 m) and 4.55 ft (1.39 m).

To resume the finite-element analysis, the pseudo-displacement is then introduced as the rigid-body movement of sliding mass into the configuration of the slope system at the beginning of sliding. However, note that direct addition of the full pseudo-displacement causes numerical problems, because the sudden change of updated Lagrangian system generates large unbalanced nodal forces along the slip surface. Here, we gradually add this displacement by dividing it into several increments. If iteration causes numerical problems during this process, then the acceleration at the beginning of sliding is slightly reduced. At each new stage, the remaining quantity of pseudo-displacement is again added into the latest configuration of the slope. In this way, the addition of the pseudo-displacement of 1.05 ft (0.32 m) into the slope at the beginning of sliding has been completed at step 10 of $a = 0.11\ g$ in Fig. 10.28, for the Drucker–Prager model case. Figure 10.40 presents three geometries of the slope: before seismic loading, at occurrence of sliding, and the addition of the pseudo-displacement. For the elliptic cap model case, the "pseudo-displacement" of 4.55 ft (1.39 m) has been estimated to cause

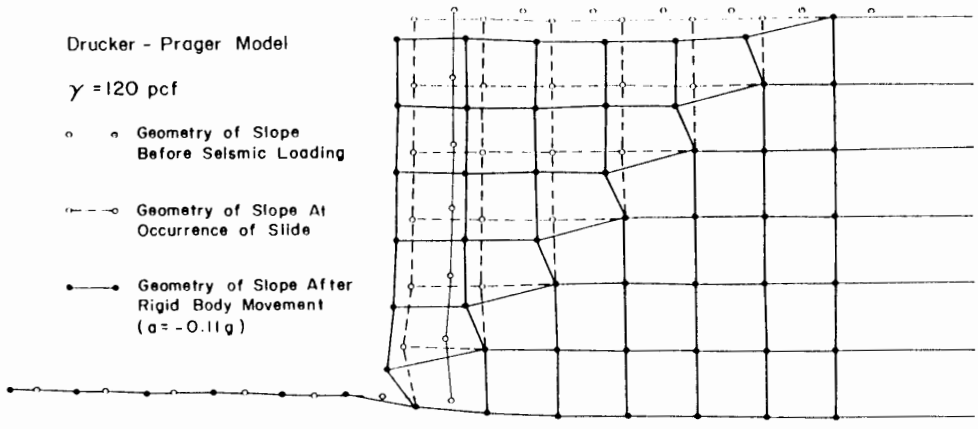

Fig. 10.40. Geometries of the Drucker Prager perfectly plastic material slope: before seismic loading, at sliding and after rigid body movement.

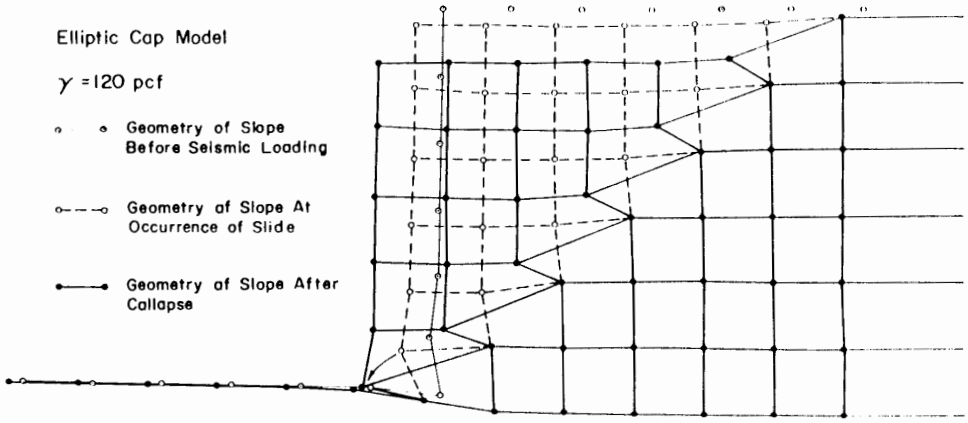

Fig. 10.41. Geometries of the elliptic cap hardening material slope: before seismic loading, at sliding and after collapse.

collapse of the slope. In a similar manner to that of the former case, the corresponding geometries of the slope are presented in Fig. 10.41 for the cap model.

Using this procedure, the post-sliding behavior has been analyzed for the Drucker–Prager model case. Figure 10.42 presents the zones of yielding during he seismic loading after the step 10. After the addition of the pseudo-displacement, the yielded zone spreads over a very narrow area along the slip surface as shown in Fig.

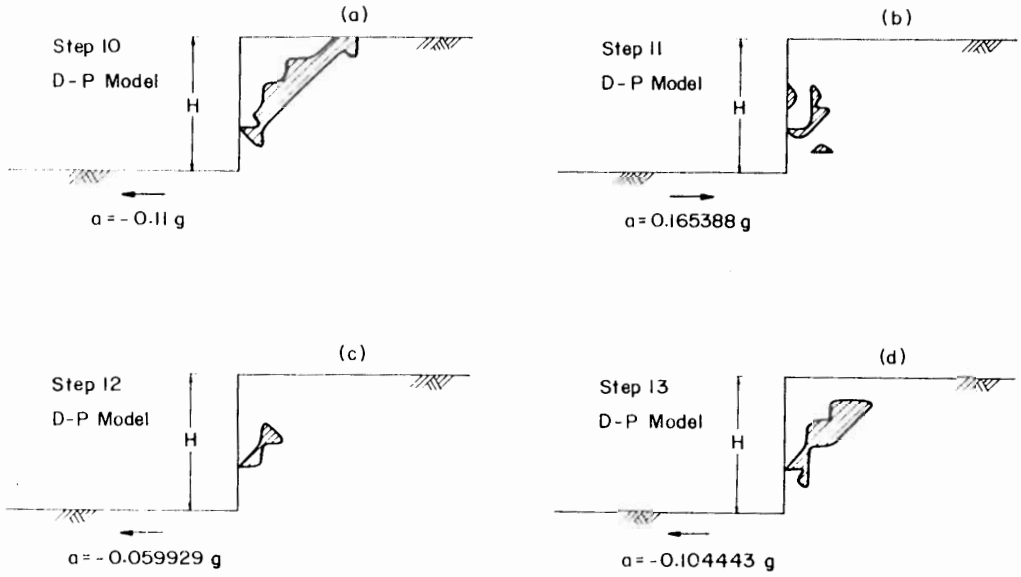

Fig. 10.42. Yielded zone in the Drucker–Prager perfectly plastic material slope after sliding.

10.42a. This spreading of yielded zone is very interesting because it is consistent with the assumption of the limit analysis method. As the seismic load acts to the right during step 11, the yielded zone contracts as shown in Fig. 10.42b. The yielded zones at steps 12 and 13 are illustrated in Figs. 10.42c and d. As the loading acts to the left, the yielding begins to spread along the slip surface toward the ground surface behind the crest.

On the other hand, the response of displacement is found to be almost elastic from step 10 to step 13, in spite of the existence of the yielded zones.

10.5 SUMMARY

In this Chapter, the applicability and predictive capability of the Cap model and the Drucker–Prager model as applied to geotechnical engineering problems using the finite-element analysis are discussed in some details by comparing their numerical results with those of the limit analysis method.

In Sections 10.2 and 10.3, the Drucker–Prager models with the associated flow rule as well as with a non-associated flow rule, together with the cap models are applied to obtain solutions for problems of (1) flexible smooth footings, and (2) rigid rough footings resting on stratum of clay. From these case studies, the following conclusions can be made:

1. The load-displacement curves predicted by the Drucker–Prager models are found to be much stiffer than those predicted by the cap models.

2. All collapse loads lie between those of the Terzaghi and Prandtl solutions.
3. In the case of Drucker–Prager models applied to the flexible and smooth footing problem, yielding occurs under the footing along the boundary area of the "rigid zone" of the Prandtl mechanism. For the rigid and rough footing problem, yielding occurs near the edge of the footing.
4. In the case of plane cap model, the corner zone controls, for the most part, the response of the stratum during loading prior to collapse. As the load approaches the collapse state, both corner zones and yielded zones coexist and play important roles in the collapse. In the case of elliptic cap model, hardening zones and corner zones dominate the response of the stratum.
5. The velocity fields predicted by the plane cap model for both types of footing problems do not agree with that of the Prandtl solution in the "radial shearing zone" and "near the surface zone". The velocity fields predicted by the Drucker–Prager and elliptic cap models agree well with that of the Prandtl solution for both footing problems.

In Section 10.4, the large-deformation seismic analyses of vertical slopes have been performed by employing the Drucker–Prager and elliptic cap models. The main purpose is to make a comparative study between the finite-element method and the limit analysis method. Development and verification of the "pseudo-static" method of the finite-element analysis after the sliding of slope as well as before the sliding of slope are also studied. Based on these case studies, the following conclusions can be made:

1. The spreading of yielded zones predicted by the elliptic cap model is very different from that of the Drucker–Prager model in all situations: after excavation, during seismic loading and at sliding.
2. Although the distributions of stress as predicted by both models have somewhat different magnitudes, the patterns of variation appear to be similar.
3. The limit analysis method predicts the yield acceleration to be $-0.0287\ g$ and $-0.196\ g$, by applying the full slope height of 30 ft (9.15 m) and the modified slope height of 25 ft (7.63 m), respectively. On the other hand, the finite-element method associated with the Drucker–Prager and elliptic cap models predicts the corresponding values to be $-0.135\ g$ and $-0.075\ g$, which lie between the solutions of the limit analysis method. In a sense, it may be concluded that the finite-element solution gives a reasonable and possibly more accurate solution compared with those of the limit analysis method.
4. The concept of "pseudo-velocity" and "pseudo-displacement" during sliding of the slope makes the analysis of post-sliding behavior of the slope with the finite-element method possible.

REFERENCES

Chang, C.J., and Chen, W.F. 1983. Seismic safety analysis of submarine slopes. Proceedings of the Shanghai Symposium on Marine Geotechnology and Nearshore/Offshore Structures, Tongji University, Shanghai, China, November 1–4, 1983, pp. 262–295.

Chang, C.J., Chen, W.F. and Yao, J.T.P., 1984. Seismic displacements in slopes by limit analysis. J. Geotech. Eng. Div., ASCE, 110 (GT7): 860–874.

Chen, W.F., 1975. Limit Analysis and Soil Plasticity. Elsevier, Amsterdam, The Netherlands, 638 pp.

Chen, W.F., 1980. Plasticity in soil mechanics and landslides. J. Eng. Mech., ASCE, 107 (EM3): 443–464.

Chen, W.F., Chang, C.J. and Yao, J.T.P., 1978. Limit analysis of earthquake-induced slope failure. R.L. Sierakowski (Editor), Proc. of the 15th Annual Meeting of the Society of Engineering Science. University of Florida, Gainesville, FL, pp. 533–538.

Daddazio, R.P. Ettouney, M.M. and Sandler, I.S., 1987. Nonlinear dynamic slope stability analysis. J. Geotech. Eng. Div., ASCE, 113 (GT4): 285–298.

Davidson, H.L. and Chen, W.F., 1974. Elastic-plastic large deformation response of clay to footing loads. Rep. No. 355.18, Fritz Eng. Lab. Lehigh University, PA, 181 pp.

Davidson, H.L. and Chen, W.F., 1977. Nonlinear response of undrained clay to footings. Computers Struct., 7: 539–546.

Davidson, H.L. and Chen, W.F., 1978. Nonlinear response of drained clay to footings. Computers Struct., 8: 281–290.

Mizuno, E. and Chen, W.F., 1983. Cap models for clay strata to footing loads. Computers Struct., 17 (4): 511–528.

Mizuno, E. and Chen, W.F., 1984. Plasticity models for seismic analyses of slopes. Soil Dynamics Earthquake Eng., 3 (1): 2–7.

Zienkiewicz, O.C., Humpheson, C. and Lewis, R.W., 1975. Associated and non-associated visco-plasticity and plasticity in soil mechanics. Geotechnique, 25 (4): 671–689.

SUBJECT INDEX

AUTHOR INDEX